WILEY-VCH

Edited by
Zbigniew L. Pianowski

# Molecular Photoswitches

## Chemistry, Properties, and Applications

Foreword by B. L. Feringa

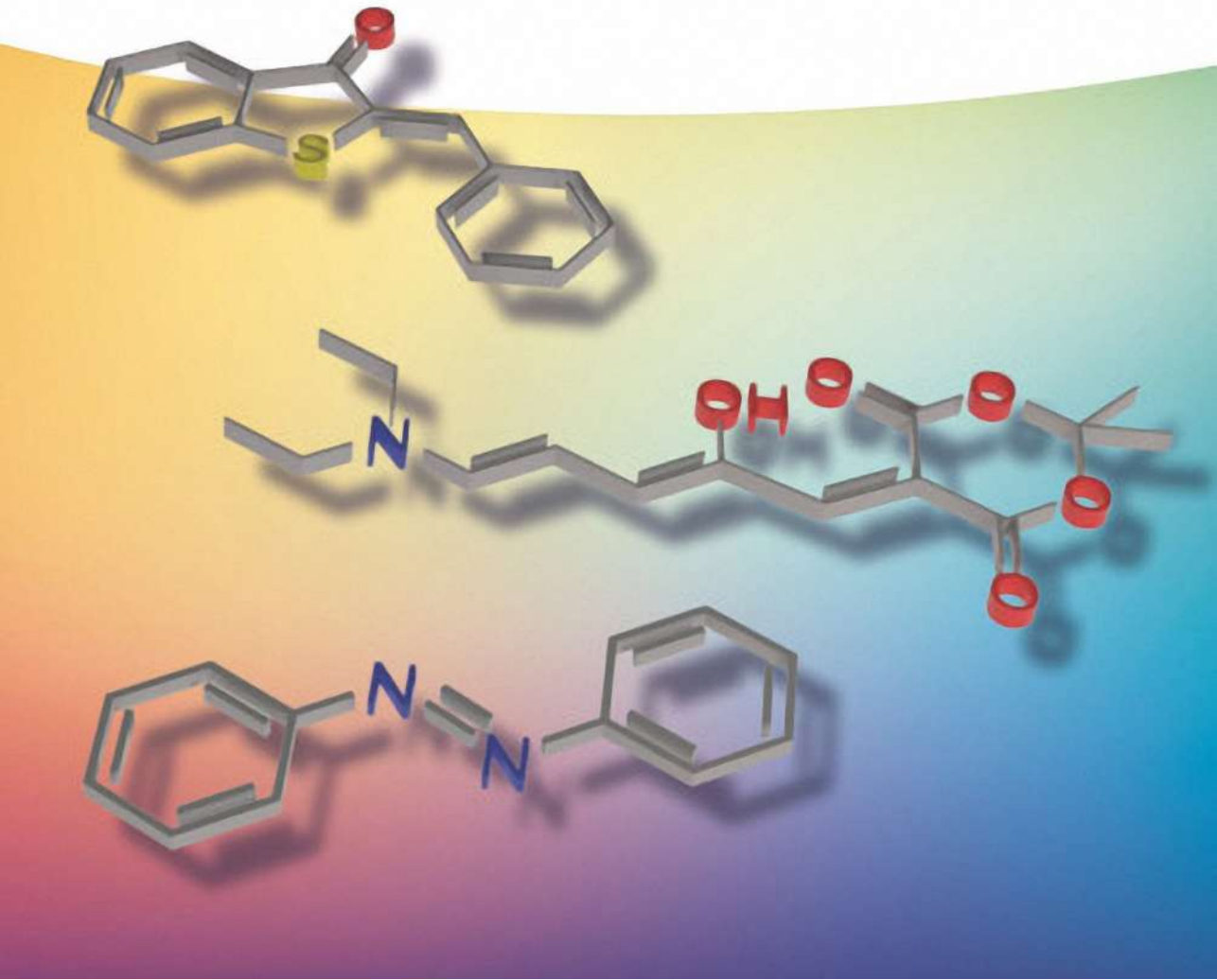

**Molecular Photoswitches**

# Molecular Photoswitches

Chemistry, Properties, and Applications

*Edited by*
*Zbigniew L. Pianowski*

Volume 1

WILEY-VCH

# Molecular Photoswitches

Chemistry, Properties, and Applications

*Edited by*
*Zbigniew L. Pianowski*

Volume 2

WILEY-VCH

***Editor***

***Dr. Zbigniew L. Pianowski***
Karlsruhe Institute of Technology
Institute of Organic Chemistry
Fritz-Haber-Weg 6
76131 Karlsruhe
Germany

Karlsruhe Institute of Technology
Institute of Biological and Chemical
Systems – Functional Molecular Systems
(IBCS-FMS)
Hermann-von-Helmholtz-Platz 1
76344 Eggenstein-Leopoldshafen
Germany



**Library of Congress Card No.:** applied for

**British Library Cataloguing-in-Publication Data**
A catalogue record for this book is available from the British Library.

**Bibliographic information published by the Deutsche Nationalbibliothek**
The Deutsche Nationalbibliothek lists this publication in the Deutsche Nationalbibliografie; detailed bibliographic data are available on the Internet at <http://dnb.d-nb.de>.



**Print ISBN:** 978-3-527-35103-9
**ePDF ISBN:** 978-3-527-82760-2
**ePub ISBN:** 978-3-527-82761-9
**oBook ISBN:** 978-3-527-82762-6

**Cover Design** SCHULZ Grafik-Design, Fußgönheim, Germany
**Typesetting** Straive, Chennai, India

Printed on acid-free paper

10 9 8 7 6 5 4 3 2 1

# Contents

# Contents

**Volume 2**



# Foreword

That you can read the title of this book "Molecular Photoswitches" and do not get lost during a fascinating journey through it is due to the billions of tiny molecular switches working frantically in your eyes. Arguably vision is one of the most magnificent results of biological evolution, and it is intriguing that the fundamental process behind it is in fact a *Z*–*E* photoisomerization of an alkene unit in the cis-retinal photoswitch triggered by visible light. But it is more than this as the photoswitch does not operate on its own. To exert its function, the switch is integrated within a dynamic multicomponent system that interfaces it with the complex machinery of life. This duality is reflected in several of current research objectives in the field of artificial molecular photoswitches.

Unsurprisingly, beyond tuning the well-known classes of switches for specific functions, the design of novel molecular photoswitches, and elucidating the fundamental mechanisms of the photochemical event itself, major future challenges are associated with the exploration of these trigger elements in complex dynamic systems ranging from responsive materials all the way to the control of biological function in cells. Drawing inspiration from Nature, numerous chemists have contributed over the last decades to the blooming field of artificial molecular photoswitches, which is testimony to its prominent role in the transition from molecules to dynamic molecular systems in contemporary chemical sciences.

In this timely volume the "Molecular Photoswitch Community" has joined forces to provide an in-depth and balanced account of the progress as well as challenges and perspectives in this flourishing and highly dynamic field under the editorship of Zbigniew Pianowski.

The study of the interplay of light and matter, i.e. photoresponsive molecules, continues to offer remarkable new insights not in the least due to the advances in transient spectroscopies and computational methods. These developments guide the design of novel photoswitches toward specific applications. It is amazing how "revisiting" more classical photochromic compounds, such as azobenzenes, stilbenes, and spiropyrans, is stimulated by the quest for visible light switching, enhanced bistability or compatibility with the molecular systems or materials in which they are to exert their function. It has initiated many unforeseen opportunities. The introduction of new classes of switches such as overcrowded alkenes, arylhydrazones, diazocines, indigoids, and Stenhouse adducts has significantly

enlarged our playground for instance toward multistate or multicomponent orthogonal switching systems.

The discussion of adaptive materials based on molecular photoswitches in Section II again illustrates a vibrant research field. Introducing switching functions in liquid crystal polymers, a variety of soft materials, and supramolecular systems enables the amplification of the molecular triggering event along the length scales to macroscopic function, ranging from responsive surfaces to mechanical muscle-type movement. In addition, the confinement of photoswitches on nanoparticles or in 2D and 3D assemblies, including porous frameworks, addresses issues of functioning at interfaces and cooperative action, and brings entirely new dimensions to the field.

Among the most spectacular developments over the past decade is the use of molecular switches for the photomodulation of biological systems. It is evident that the rapidly emerging area of photopharmacology has its roots in the field of photoswitches, in particular azobenzenes which were reported by Mitscherlich as early as 1834. The control of the activity of a drug by light with high spatiotemporal precision holds promise for precision therapy, smart pharmaceuticals, and imaging techniques. In addition, Section III illustrates how photochromic systems can be applied in a much broader perspective, including control of peptides, oligonucleotides, saccharides, and ion channels. Photoregulation of specific pathways in complex biochemical networks, cellular communication, transcription, or membrane transport are fascinating examples of the opportunities that emerge. It is also evident that the photoswitch community has to tackle many challenges entering the realm of biology – not least in how to make these molecular switches biocompatible, operate in the aqueous environment of the cells, be compatible with multi-chromophore functional systems, and switchable with visible or NIR light. Answering these questions will ultimately allow the application of molecular photoswitches in vivo.

Arguably the question as to how to use molecular switches and achieve controlled movement at the nanoscale has been essential in the discoveries leading toward molecular machines. With the expected key role of chemistry in future complex systems, molecular information science, and soft robotics, taking advantage of the solid basis in molecular photoswitches as presented here will likely become increasingly important. Indeed, this book showcases many novel approaches and opportunities in this vibrant field and without doubt will guide molecular explorers in their odyssey in the world of responsive molecular systems.

*Ben L. Feringa*

# Preface

Light is a traceless reagent, which can be dosed with high spatiotemporal precision. It has been consciously used for almost 200 years to perform chemical reactions, since the report of light-induced rearrangement followed by dimerization of α-santonin by Trommsdorff in 1834. A few decades later, light-induced processes resulting in reversible color changes have been described: photooxidation of tetracene by Fritzche (1867), photoisomerization of benzylidenehydrazines (Wislicenus 1893), osazones (Blitz 1899), or the reversible color change of 2,3,4,4-tetrachloronaphthalen-1(4H)-one in the solid state by Markwald (1899). The latest author introduced the German term "Phototropie," which evolved into what we now call "photochromism" – the reversible transformation of a chemical species between two forms with distinct absorption spectra, by the absorption of electromagnetic radiation. Photochromism often manifests itself as a reversible change of color upon exposure to light.

In 43 chapters of this book, authors describe photochromic organic compounds – molecular photoswitches – which undergo reversible photoisomerization and change their molecular properties, such as geometry, polarity, or rigidity. Properly designed systems containing molecular photoswitches can transform the energy of light into a wide range of functions. Very often, fascinating macroscopic effects can be achieved, which go far beyond the simple color change.

After introductory chapters on the photophysics of the switches and relevant computational methods, the first volume of the book demonstrates the broad variety of classes of photochromic chemical compounds. The photochromic scaffolds established for decades, such as spiropyrans, diarylethenes, or azobenzenes, are followed by compounds whose photochromism was just recently exploited – such as indigoids or donor–acceptor Stenhouse adducts. Some classes have a distinctive functional bias, such as molecular motors for chirooptical switches, conversion of the solar energy by norbornadienes, or molecular electronic systems relying on dihydroazulenes. This section is complemented with a report on photochromic coordination compounds and on systems used for photomodulation of catalytic processes.

The second volume of this book is dedicated to the variety of materials based on molecular photoswitches. Its scope spans from light-induced phase transitions, through photochromic porous materials, liquid crystals, or nanoparticles, to light-responsive molecular machines and logic devices. The last section in

the same volume pertains to the applications of molecular photoswitches in the biological context. There, properties and applications of photoswitchable biopolymers – oligonucleotides, peptides, or saccharides – are described. Other contributions are focused on photochromic bioactive small molecules and their applications – such as light-modulated antibiotics, cytotoxins, or ion channel inhibitors. This section is concluded with light-propelled artificial muscles and implementation of molecular photoswitches into computational design of proteins.

The aim of this book is to provide a balanced overview – to specialists and non-experts – on the rapidly growing field of molecular photoswitches, with a particular focus on the achievements and discoveries from the last decade. We hope that this book may inspire younger colleagues to enter into the fascinating realm of photochromic compounds and materials. We also hope that it will support lecturers worldwide in preparing courses related to this subject. In the name of all the readers, the editor wants to appreciate the effort of contributing authors in providing clear and balanced chapters, rich in carefully selected information and complemented with sources for the further advanced reading. The editor also sincerely apologizes for the omissions and mistakes that might appear in the book despite the careful planning and revision process.

Germany *Dr. Zbigniew L. Pianowski*

# Section I

# Interplay of Light and Matter

# 1 Physicochemical Aspects of Photoswitching

Petr Klán and Jakob Wirz

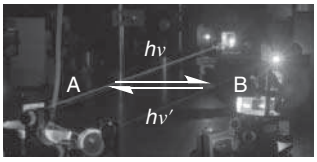


**Characteristic Features**

This chapter offers a short prologue to the basics of photophysics and photochemistry and introduces fundamental concepts such as quantum yield and photostationary state. On two examples of common photoswitches, the reader is acquainted with steady-state and time-resolved spectroscopic methods commonly used to study photochromic systems.

**Key References**

Klan, P. and Wirz, J. (2009). *Photochemistry of Organic Compounds: From Concepts to Practice*, 1st ed. Chichester: Wiley.

Ward, C.L. and Elles, C.G. (2012). Controlling the excited-state reaction dynamics of a photochromic molecular switch with sequential two-photon excitation. *J. Phys. Chem. Lett.*, 3: 2995–3000.

Quick, M., Dobryakov, A.L., Gerecke, M. et al. (2014). Photoisomerization dynamics and pathways of *trans*- and *cis*-azobenzene in solution from broadband femtosecond spectroscopies and calculations. *J. Phys. Chem. B*, 118: 8756–8771.

# 1

# Physicochemical Aspects of Photoswitching

*Petr Klán*[1] *and Jakob Wirz*[2]

[1] *Department of Chemistry and RECETOX, Faculty of Science, Masaryk University, Kamenice 5, 62500, Brno, Czech Republic*
[2] *Department of Chemistry, Institute of Physical Chemistry, University of Basel, Klingelbergstrasse 80, CH-4056, Basel, Switzerland*

## 1.1 Introduction

The expression photochromism is used for reversible structural rearrangements that are triggered by light in one or both directions, which connect two related species (isomers) with different absorption spectra [1]. Such molecules are also called photoswitches. Photoactivation can give access to a thermodynamically less stable isomer. Several types of photoreactions can be involved, such as light-triggered electrocyclization, cycloaddition, *E*,*Z*-isomerization, intramolecular hydrogen, group or electron transfer, or dissociation. Each of them requires specific reaction and illumination conditions and, in particular, detailed knowledge of the mechanism when sufficient control over the scope of photoswitching is needed. Photoswitches have attracted attention in many fields, spanning from applications of optical filters, photography, protection from sunlight, actinometry, imaging, holography, solar energy conversion, energy storage, and molecular electronics to drug delivery and photopharmacology [2–9].

Azobenzene derivatives, spiropyrans, fulgides, and diarylethenes (Scheme 1.1) are probably the most common classes of organic photochromic compounds. The *E*- and *Z*-forms of azobenzene possess similar and strongly overlapping absorption spectra, whereas the two forms of the latter photoswitches are distinctively different thanks to a considerable change of electron distribution during the electrocyclization reaction.

When designing a chromophore as a photoswitch, the number of cycles that a molecule can repeat without degradation is of utmost importance; the loss of any of the photochromic component during irradiation, for example, by oxidative degradation, is termed "fatigue" [1]. Thus, one needs to consider the following properties depending on the application aimed at:

- A reliable, simple synthesis and variability for tailor-made compounds
- Photoswitching efficiency (quantum yield)

*Molecular Photoswitches: Chemistry, Properties, and Applications*,
First Edition. Edited by Zbigniew L. Pianowski.


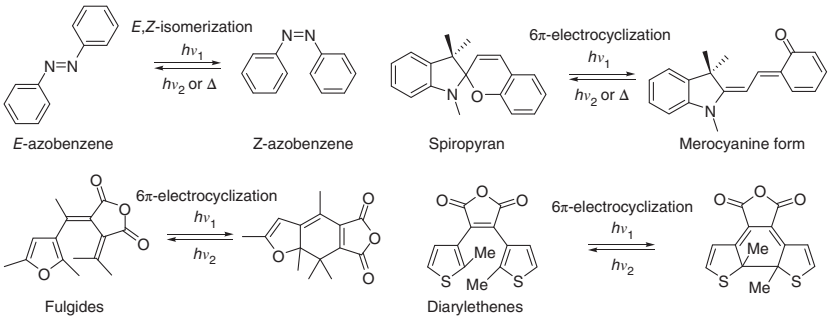


**Scheme 1.1** Major families of photochromic compounds.

- Sufficiently different absorption spectra of both isomers
- Excitation wavelength
- Reversibility and bidirectional switching
- Photodegradation, fatigue
- The desired lifetime of switch setting:
  - T-type: rapid thermal reversion
  - P-type: thermally irreversible or slow
- Fluorescence

## 1.2 Essentials of Photophysics

Some knowledge of photochemistry is required to design and study a photoswitch. Here, we give a short introduction to the basics of photophysics and photochemistry.

We start with a short introduction defining photophysical processes, which are usually depicted in a *Jabłonski diagram* [10] (Figure 1.1). Molecular electronic states are represented by thick horizontal lines (—) that are arranged in a vertical order to indicate relative energies and are labeled consecutively by increasing energy, beginning with the singlet ground state $S_0$, followed by excited singlet

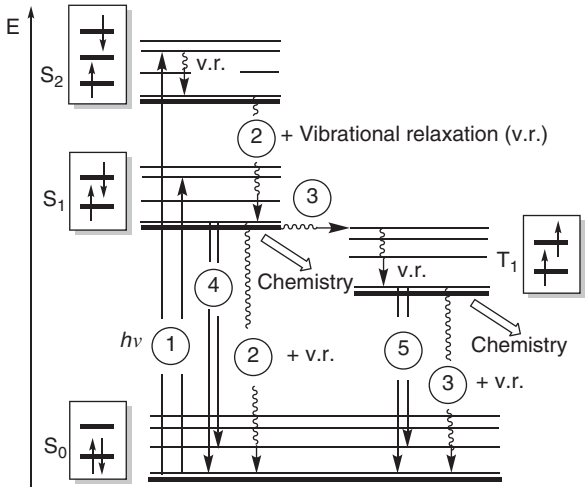


**Figure 1.1** Jabłonski diagram.

states $S_1$, $S_2$, etc. Vibrational states, represented here by thin lines (—), are usually not shown explicitly. States of a given *multiplicity* (singlet, triplet) are collected in separate columns. Horizontal displacement does *not* indicate a change in structure. The energy levels represent minima on the potential energy surfaces of a given electronic state. The corresponding structures will be somewhat different for each state. For molecules with a singlet ground state, the left-hand column collects the electronic singlet states and that to the right the triplet states. The lowest triplet state is labeled $T_1$, followed by $T_2$, etc.

*Photophysical processes* are *radiative* or *radiationless transitions* by which molecules are promoted from one electronic state to another. No chemical change takes place, although the bond lengths and angles generally differ somewhat in different electronic states. Radiative transitions are associated with the absorption or emission of a photon and are represented as straight arrows (↑ or ↓), while radiationless transitions, including vibrational relaxation (v.r.), are not associated with absorption or emission and are shown as wavy arrows (↝).

The major transitions depicted in Figure 1.1 involve: ① *Absorption* of a photon generating an electronically excited state ($S_0$ to $S_1$ and $S_0$ to $S_2$ shown); ② *internal conversion* (IC) as a radiationless transition between two electronic states of the same multiplicity ($S_2$ to $S_1$ and $S_1$ to $S_0$ shown); ③ *intersystem crossing* (ISC) as a radiationless transition between two electronic states of different multiplicity ($S_1$ to $T_1$ and $T_1$ to $S_0$ shown); ④ *fluorescence* – emission of a photon associated with the generation of a lower-energy state of the same multiplicity ($S_1$ to $S_0$ shown); and ⑤ *phosphorescence* – emission of a photon associated with the generation of a lower-energy state of different multiplicity ($T_1$ to $S_0$ shown). IC ② and ISC ③ are isoenergetic processes of energy redistribution within the excited molecule by which electronic energy is distributed over many vibrational modes of the lower excited state. IC and ISC are essentially irreversible processes because they are associated with an entropy increase (high density of states in the lower-energy electronic state) and because the following vibrational relaxation is very fast (picosecond timescale) in solution. The lowest $S_1$ and $T_1$ states are typically not only associated with emission but also with primary chemical processes (depicted as "chemistry").

### 1.2.1 Quantum Yield

The term *quantum yield* $\Phi_x(\lambda)$ is equal to the amount $n_x$ of photochemical or photophysical events x that have occurred, divided by the amount $n_p$ of photons at the irradiation wavelength $\lambda$ that were absorbed by the reactant, Eq. (1.1) [10].

$$\Phi_x(\lambda) = n_x/n_p \tag{1.1}$$

Both $n_x$ and $n_p$ are measured in moles or einstein (1 einstein = 1 mol of photons) and the dimension of $\Phi_x$ is unity. The photochemical or photophysical process x must be defined explicitly. In general, quantum yields lie in the range $0 \leq \Phi_x \leq 1$ and represent the probability that a molecule undergoes the defined process x after absorption of a photon.

According to *Kasha's rule*, polyatomic molecules generally luminesce only from the lowest excited state of a given multiplicity [10]. By extension of Kasha's rule,

quantum yields are often independent of the excitation wavelength. The same rule can be applied to photochemical processes as depicted in Figure 1.1. There are many exceptions, however.

### 1.2.2 Photostationary State

In a reversible photoreaction between two photoswitch isomers A and B that are stable in the dark, the ratio of their amounts, $n_A$ and $n_B$, formed by exhaustive irradiation at a given wavelength $\lambda_{irr}$, is given by Eq. (1.2) [10],

$$\mathrm{A} \underset{h\nu'}{\overset{h\nu}{\rightleftharpoons}} \mathrm{B}$$

$$\frac{n_B}{n_A}(\lambda_{irr}) = \frac{\Phi_{A\to B}\varepsilon_A(\lambda_{irr})}{\Phi_{B\to A}\varepsilon_B(\lambda_{irr})} \tag{1.2}$$

where $\varepsilon_A(\lambda_{irr})$ and $\varepsilon_B(\lambda_{irr})$ are the molar absorption coefficients of A and B at the wavelength of irradiation, and $\Phi_{A\to B}$ and $\Phi_{B\to A}$ are the quantum yields of photoisomerization of A to B and of B to A, respectively. The ratio $n_B/n_A$ is called the photostationary state (PSS); it defines how well the position of a photoswitch can be controlled by monochromatic irradiation at a given wavelength $\lambda_{irr}$.

### 1.2.3 Photoactivation

Photoswitching processes are typically activated by one-photon excitation, by UV light at least in one direction, and the interconversion itself can originate from either the singlet or triplet excited state. The nature of the excited state, its lifetime, and susceptibility to undergo unwanted competing side reactions, such as oxidation in the presence of oxygen, is one of the main factors in the design and application of photoswitches. When a visible- or near-infrared-light phototrigger is needed, specific modifications of the chromophore, such as the extension of a π-system or designing a push–pull system, can be utilized [11]. In another approach, a high-energy excited state can also be accessed via two-photon excitation [12].

In biological or medical applications, the wavelengths of photoactivation are restricted by the adverse effects of UV light, by tissue absorption due to endogenous chromophores, and by optical scattering, which restrict the depth of tissue penetration. Thus, photolysis by light within the so-called tissue-transparent or phototherapeutic window, limited by the absorption of hemoglobin below 600 nm and by the absorption of water above 900 nm [13], is important for biological and medical applications, and there is a demand for photoswitches that can be activated in this wavelength range.

## 1.3 Spectroscopy of Photoswitching

Steady-state absorption and emission spectroscopies provide invaluable information about the electronic properties and structures of individual photoswitch forms, and

they can also be used for the determination of the composition of reaction mixtures and the identification of reaction (unwanted) side products, especially in combination with other analytical techniques, such as HPLC. The time evolution of the absorbance spectra is particularly important for the evaluation of the photokinetics of slow transformations. Global analysis of spectral data is a very useful tool to validate a proposed model of photoswitch transformation [10].

NMR spectroscopy became one of the essential tools in the structural identification of long-lived intermediates and photoproducts formed during a photochromic process, in conformational analyses, and it can be used for monitoring the extent of photoswitching [14]. NMR can also provide valuable quantitative information about the mixtures without the need to perform other analytical determination methods. Detailed examination of the chemical shifts and spin–spin couplings in the spectra gives additional information about intermolecular interactions, aggregations, etc.

The primary reactions of photoswitches are commonly very fast, taking place on a picosecond timescale and faster. Such reactions can be studied using modern spectroscopy of short-lived reaction intermediates. Following excitation of the photoswitch by an intense, short laser pulse, the resulting transient intermediates are commonly observed by their absorption (transient absorbance difference spectroscopy). More informative spectroscopic techniques for the detection and identification of reactive intermediates have been developed, in particular EPR, IR and Raman spectroscopy, NMR, mass spectrometry, electron microscopy, and X-ray diffraction.

Most optical flash photolysis apparatuses with excitation pulses of nanosecond and longer duration operate in the kinetic mode, that is, the transient absorption is monitored with a photomultiplier at a single wavelength as a function of time, providing accurate reaction rate constants up to about $10^8\ s^{-1}$ [10]. For faster reactions, excitation by laser pulses of shorter duration is required. The pump–probe method provides transient absorption spectra at a given time delay with respect to the excitation pulse. The laser pulse is split into two portions. The major part of the laser pulse (the pump pulse) is used to excite the sample and trigger the process under investigation; the rest (the probe pulse) is focused onto some material to produce a supercontinuum pulse with a strongly broadened spectrum, which is then sent to the sample over an optical delay line. As the speed of light is $c = 3 \times 10^8\ m\ s^{-1} = 0.3\ m\ ns^{-1}$, a delay line of 30 cm length delays the probe pulse by 1 ns with respect to the pump pulse. The probe signal is typically averaged over many pulses. A fast detector is not required. The temporal resolution is fundamentally limited only by the duration of the pump and probe pulses. By varying the time delay between the pump and probe pulses, it is possible to assemble absorption spectra as a function of time after the excitation pulse. Basically, both the kinetic and the pump–probe spectrographic setup measure one-dimensional slices of the same physical information that consists of a two-dimensional array A of absorbances $A\ (\lambda,t)$ as a function of wavelength $\lambda$ and time $t$ after excitation of the sample.

Time-resolved IR and Raman spectroscopies have also been recognized as excellent methods for the characterization of transient chemical species [10]. Both IR and

Raman spectra provide fingerprints that allow for unambiguous identification of simple molecules or their mixtures. The dynamics of fast chemical transformations of photoswitches are successfully evaluated with sensitive Fourier-transform instruments. In picosecond and femtosecond time-resolved Raman spectroscopy, the sample is pumped and probed by well-defined laser pulses, producing a full vibrational spectrum in the 1000–2000 $cm^{-1}$ range with up to <100 fs temporal and < 35 $cm^{-1}$ spectral resolution.

## 1.4 Two Case Examples

This chapter provides two examples of spectroscopic approaches used to study the transformations of photoswitches and highlights some difficulties that can occur in interpreting data. The provided information is not comprehensive; it should only introduce the reader to the spectroscopic methods, which are used to study photochemistry of photoswitches.

### 1.4.1 Diarylethenes

Photochemically induced 6π-electrocyclic cyclization and cycloreversion of diarylethenes (Scheme 1.2) are very fast processes, and their reaction dynamics can be studied by ultrafast time-resolved spectroscopic methods [15–17]. The photocyclization of the simplest example of diarylethenes, (*Z*)-stilbene, occurs from the singlet $^1\pi,\pi^*$ state [10]. The orbital symmetry allowed conrotatory closure results in the formation of *trans*-dihydrophenanthrene, which can be oxidized to phenanthrene in nearly quantitative yield [18, 19] (Scheme 1.2). Many derivatives of 1,2-bis(hetero)arylethenes, in which the phenyl groups of stilbene are replaced with five-membered heterocyclic (e.g. thiophene or furan) rings, have received special attention as photoswitches [16, 17].

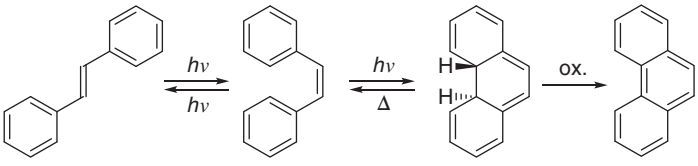


**Scheme 1.2** Stilbene photochemistry.

For example, the photochromic pair of compounds **1a** and **1b** (Scheme 1.3) is a fatigue-resistant [20] photoswitch showing distinct absorption spectra of the open- and closed-ring forms (Figure 1.2) [21, 22]. The π-conjugated system of **1a** is localized on the UV-absorbing thiophene rings, whereas the visible-light-absorbing π-system of **1b** is delocalized throughout the molecule. The lack of absorption of **1a** above 400 nm allows for a complete cycloreversion of **1b** upon irradiation by visible light.

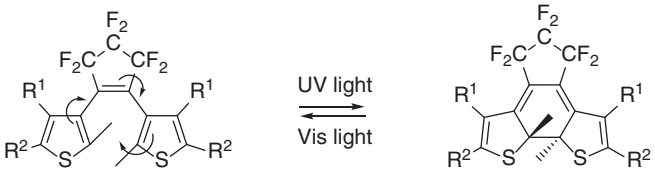


**1a**: $R^1 = CH_3$, $R^2$ = Ph — **1b**
**2a**: $R^1 = CH_3$, $R^2 = p\text{-}(C_6H_4)N(C_2H_5)_2$ — **2b**
**3a**: $R^1$ = H, $R^2$ = Ph — **3b**
**4a**: $R^1$ = H, $R^2 = CH_3$ — **4b**

**Scheme 1.3** Photochemical cyclization and cycloreversion of dithienylethenes.

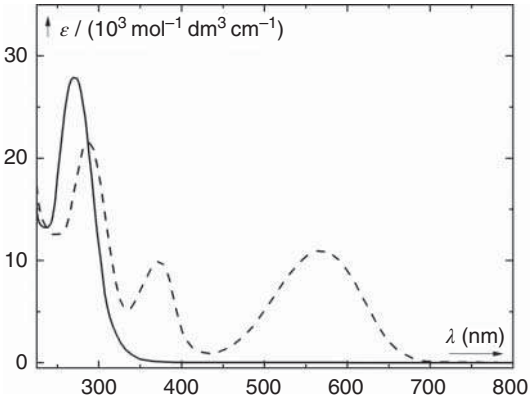


**Figure 1.2** Absorption spectra of **1a** (solid line) and **1b** (dashed line) (R = Ph) in hexane. Source: Adapted from Ward et al. [21].

The **1b→1a** conversion ($x$/%) in dilute solutions is calculated under photostationary-state conditions according to Eq. (1.3) [22]. When the ratio of $\boldsymbol{\Phi_{1b\rightarrow 1a}\varepsilon_{1b}/\Phi_{1a\rightarrow 1b}\varepsilon_{1a}}$ is high, the conversion is large.

$$x = \frac{\boldsymbol{\Phi_{1b\rightarrow 1a}\varepsilon_{1b}}}{\boldsymbol{\Phi_{1b\rightarrow 1a}\varepsilon_{1b} + \Phi_{1a\rightarrow 1b}\varepsilon_{1a}}} \times 100 \tag{1.3}$$

The quantum yields and the efficiencies of any side-reactions may vary with temperature, the nature of substituents, solvent, conformational behavior, etc. [16]. For example, the ring-opening quantum yields decrease by introducing an electron-donating substituent to the *p*-position of the phenyl $R^2$ groups in **2a** (Scheme 1.3) [22]. 1,2-Bis(hetero)arylethenes attain two conformations with the two rings in a parallel or antiparallel arrangement, but the photocyclization can occur only from the latter conformation (Scheme 1.4) [22, 23]. In the case that

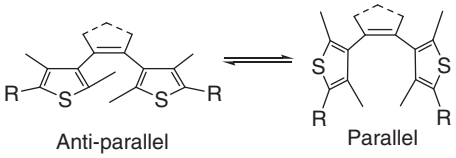


**Scheme 1.4** Antiparallel and parallel arrangements of 1,2-bis(hetero)arylethenes.

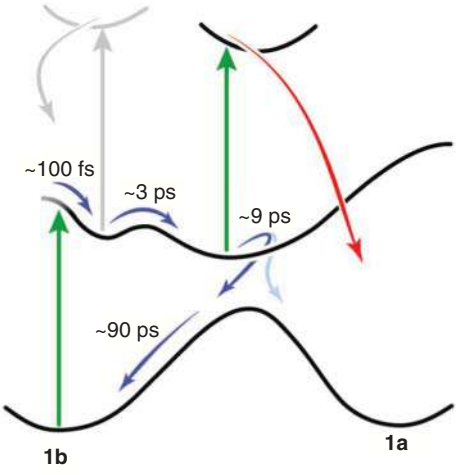


**Figure 1.3** The reaction dynamics for one- and two-photon excitation of **1b**. Source: Reproduced by permission of Ward and Elles [26].

the population ratio of the two conformers is 1 : 1, the cyclization quantum yield cannot exceed 0.5. This ratio, and thus the magnitude of the quantum yield, can be controlled by structural changes and confined environment [16, 17].

Ultrafast kinetics of the cyclization and cycloreversion reactions have been investigated by pico- and femtosecond time-resolved absorption spectroscopy [15, 24]. Polarization-selective nonlinear transient-absorption spectroscopy with a 90–110 fs time resolution was used to study the ring-closing reaction of **3a** (Scheme 1.3) in cyclohexane by Duppen and coworkers [25]. The population and orientational dynamics supported by theoretical calculations revealed that, upon excitation, three events follow: pre-switching due to excited state mixing (50 fs), the ring closure (0.9 ps), and post-switching related to vibrational cooling (100 ps). The fs pump–probe one- [26] and two-color [21] pump–repump–probe spectroscopies were used to study the cycloreversion of **1b** (Scheme 1.3). The excited molecule $^{1}$**1b*** has to cross an activation barrier in ~3 ps, before reaching the access to a conical intersection with the ground state (Figure 1.3). When a secondary excitation with a delay of ~5 ps between the primary and secondary excitation events is used, the highest cycloreversion efficiency to give **1a** is observed [26]. It was suggested that the method can be used to selectively control the extent of photoswitching.

A different approach was utilized with picosecond time-resolved Stokes and anti-Stokes Raman spectroscopies to study the cyclization and cycloreversion reactions of **4a**, **4b** (Scheme 1.3) photochemical interconversion [27]. The cyclization, monitored by the time evolution of specific Raman bands attributed to the ring-closed form **4b**, was found to occur in 4 ps followed by vibrational cooling within 10 ps.

Femtosecond transient absorption spectroscopy and ultrafast electron diffraction crystallography [28–30] were also utilized in the study of the cyclization reaction of **1a** in a single crystal. While there is a coexistence of two conformations of **1a** in solution (Figure 1.4), the conformation in the crystal is confined in an antiparallel arrangement, allowing for the cyclization. Femtosecond time-resolved diffraction experiments showed that an initial motion occurring upon excitation brings the central carbon atoms involved in the bond formation into close proximity [30].

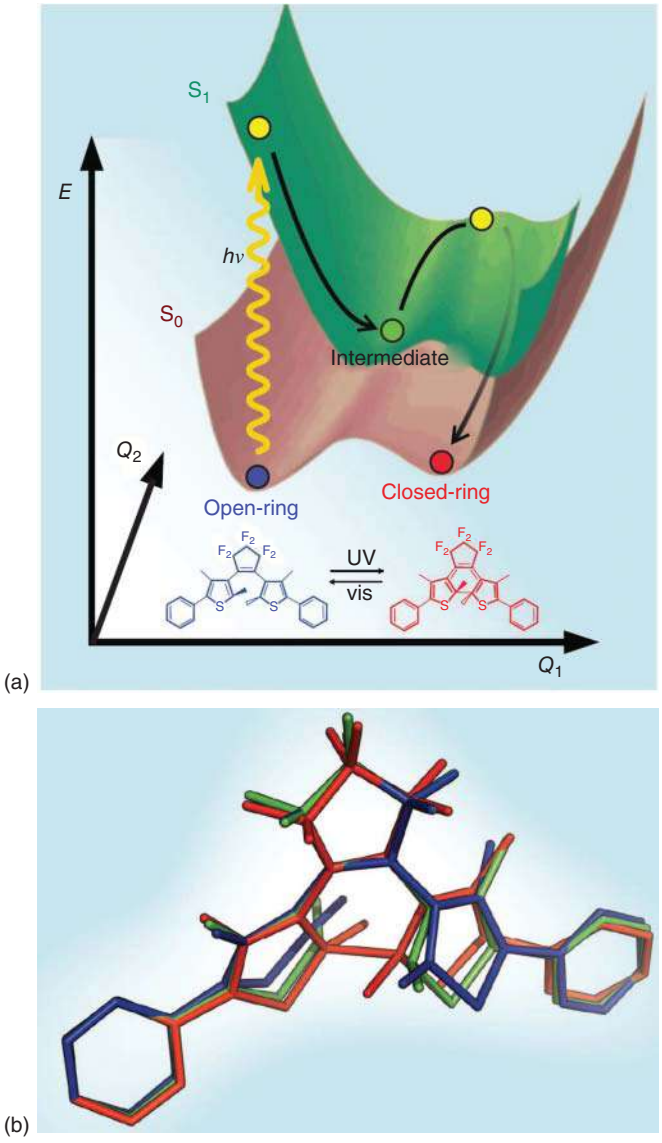


**Figure 1.4** (a) The primary motions involved in the photocyclization of **1a** in a single crystal studied by femtosecond time-resolved diffraction and a simplified reaction coordinate. (b) Motions determined by fs electron diffraction studies. Source: Reproduced by permission of Miller [30].

### 1.4.2 Azobenzene and Its Derivatives

Azobenzene and its derivatives are the most commonly used photoswitches, which undergo a reversible *E*–*Z* photoisomerization (Scheme 1.1) [31–36]. Both isomers possess weak ($n$,$\pi^*$; $S_0 \rightarrow S_1$) and strong ($\pi$,$\pi^*$; $S_0 \rightarrow S_2$) absorption bands. These transitions can be very close in energy in azobenzenes bearing electron-donating

substituents, and the π,π* state becomes the $S_0 \rightarrow S_1$ transition in push–pull systems. Differences in the absorption properties of (*E*)- and (*Z*)-azobenzene allow us to select the irradiation wavelength to obtain the (*Z*)-isomer preferentially, and the photostationary ratio (Eq. (1.2)) of the isomers can be affected by competing thermal $Z \rightarrow E$ processes. The forward and back isomerization quantum yields depend on the irradiation wavelength, the solvent, and the excited-state multiplicity [37].

Precise knowledge of the absorption spectra of both photoisomers is essential to choose the optimum wavelength for switching in either direction and to determine the quantum yields. A recent study [38] revealed that in all previous work, the reported spectrum of *E*-azobenzene had been contaminated by small amounts of the *Z*-isomer. For azobenzene in methanol solution the ratio $\varepsilon_E/\varepsilon_Z$ is the highest at 347 nm reaching 91, and the inverse ratio $\varepsilon_Z/\varepsilon_E$ is the highest at 413 nm reaching 3.3 (Figure 1.5) [39]. These wavelengths of irradiation provide the highest purity of the desired isomer. For complete photoswitching, these numbers should be ∞ and 0, respectively.

The rate constant for the *thermal* $Z \rightarrow E$ isomerization is $1.2 \times 10^{-5}$ $s^{-1}$ at 45 °C, so that essentially pure *E*-azobenzene is obtained by keeping a methanol solution in the dark at 45 °C for five days. At 25 °C, the rate constant amounts to $1.1 \times 10^{-6}$ $s^{-1}$ [39], which is sufficiently slow for many applications. The reaction enthalpy of $Z \rightarrow E$ isomerization in *n*-heptane was reported to be $\Delta H = \sim 48.9$ kJ $mol^{-1}$ [40]. Clearly, the properties of azobenzene fulfill many requirements for a P-type photoswitch. Several structure–property relationship studies helped to design azobenzene photoswitches that possess high *Z*-isomer stability, as complete photoswitching as possible, and bathochromically shifted spectra [31, 32]. For example, *para*-electron-donating substituents of azobenzene can accelerate this thermal back isomerization [41], whereas *ortho*-chloro [42], fluoro [43, 44], or methoxy [45] substituents slow it down.

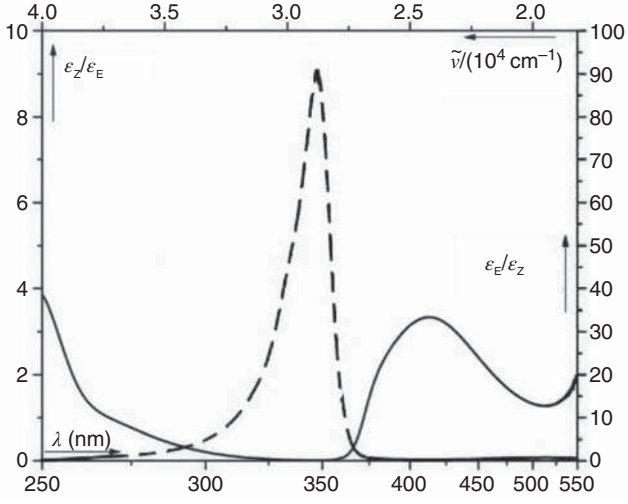


**Figure 1.5** The ratio of molar absorption coefficients $\varepsilon_Z/\varepsilon_E$ (solid line) and $\varepsilon_E/\varepsilon_Z$ (dashed line) of azobenzene in methanol. Source: Adapted from Vetráková et al. [38].

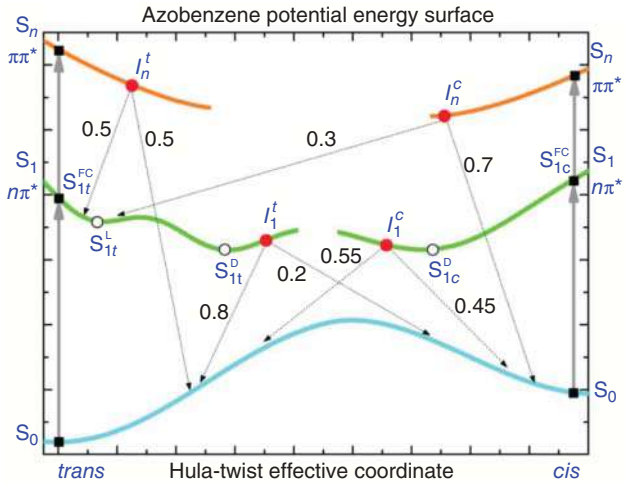


**Figure 1.6** Potential energy surface and relaxation/isomerization pathways of azobenzene [46]. Filled squares mark wavepacket positions upon $n,\pi^*$ ($S_1$) or $\pi,\pi^*$ ($S_n$) excitation, while open and filled circles show stationary points and conical intersections ($I$), respectively. Dotted arrows marked with yields indicate relaxation/isomerization via the intersections. Source: Reproduced by permission of Quick et al. [46].

The quantum yields of isomerization are less than unity and depend on the excitation wavelength, thus violating Kasha rule [37]; in methanol solution, they amount to $\Phi_{E\to Z}(280\,\text{nm}, \pi,\pi^*) = 0.16$, $\Phi_{Z\to E}(280\,\text{nm}, \pi,\pi^*) = 0.36$; $\Phi_{E\to Z}(313\,\text{nm}, \pi,\pi^*) = 0.14$, $\Phi_{Z\to E}(313\,\text{nm}, \pi,\pi^*) = 0.33$; $\Phi_{E\to Z}(405\,\text{nm}, \text{n},\pi^*) = 0.29$, $\Phi_{Z\to E}(405\,\text{nm}, n,\pi^*) = 0.45$ [39].

The excited-state evolution of azobenzene is summarized in the potential energy scheme (Figure 1.6). The photoisomerization was studied by broadband transient absorption spectroscopy [46]. Following $n,\pi^*$-excitation at 444 nm in acetonitrile, the $E\to Z$ reaction takes place with a lifetime of 16 ps, and the reverse reaction rate is bi-exponential with lifetimes of 0.1 and 1 ps. The 16-ps time constant of the former is attributed to the isomerization process that encounters a barrier of 12 kJ mol$^{-1}$, and not to vibrational cooling. Upon $\pi,\pi^*$-excitation, 50% of the population relaxes to an $S_1$ region, which is not accessible under n,$\pi^*$-excitation. The fast decay of the excited states prevents any side reactions, so that the switch can be operated indefinitely without noticeable fatigue.

Time-resolved Raman spectroscopy also provides valuable information about the dynamics of singlet excited states of azobenzene [31, 47]. With the probe wavelength at 410 nm in resonance with a transient absorption appearing after the $S_0\to S_2$ ($\pi,\pi^*$) photoexcitation, transient Raman bands assigned to the $S_1$ state are found. Its lifetime is solvent-dependent; the values of ~2.5 ps in ethylene glycol and ~1 ps in hexane were determined [48].

Nitrogen atoms of the N=N bond of azobenzene possess an in-plane lone electron pair in an n orbital involved in two limiting mechanisms of photoisomerization (rotation akin to that of simple alkenes or in-plane inversion) [10, 31]. A femtosecond

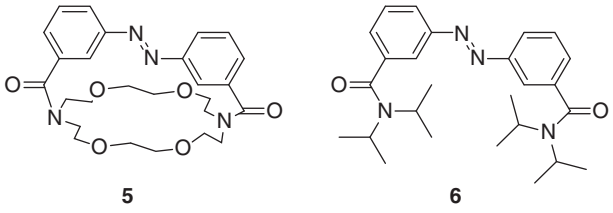

**Figure 1.7** Azobenzene derivatives **5** and **6**.

time-resolved fluorescence up-conversion spectroscopy of rotation-restricted **5** and rotation-free **6** *E*-azobenzene derivatives (Figure 1.7) revealed very similar fluorescence lifetimes [49]. Because **5** cannot isomerize by rotation about the central N=N bond, it was suggested that the interconversion occurs via the inversion mechanism.

## References


1 Dürr, H. and Bouas-Laurent, H. (2003). *Photochromism: Molecules and Systems*. Amsterdam: Elsevier Science.

2 Abdollahi, A., Roghani-Mamaqani, H., and Razavi, B. (2019). Stimuli-chromism of photoswitches in smart polymers: recent advances and applications as chemosensors. *Prog. Polym. Sci.* 98, 101149.

3 Boelke, J. and Hecht, S. (2019). Designing molecular photoswitches for soft materials applications. *Adv. Opt. Mater.* 7, 1900404.

4 Jia, S., Fong, W.K., Graham, B., and Boyd, B.J. (2018). Photoswitchable molecules in long-wavelength light-responsive drug delivery: from molecular design to applications. *Chem. Mater.* 30: 2873–2887.

5 Sun, C.L., Wang, C.X., and Boulatov, R. (2019). Applications of photoswitches in the storage of solar energy. *ChemPhotoChem* 3: 268–283.

6 Tian, Z.Y., Wu, W.W., and Li, A.D.Q. (2009). Photoswitchable fluorescent nanoparticles: preparation, properties and applications. *ChemPhysChem* 10: 2577–2591.

7 Zhou, X.X. and Lin, M.Z. (2013). Photoswitchable fluorescent proteins: ten years of colorful chemistry and exciting applications. *Curr. Opin. Chem. Biol.* 17: 682–690.

8 Broichhagen, J., Frank, J.A., and Trauner, D. (2015). A roadmap to success in photopharmacology. *Acc. Chem. Res.* 48: 1947–1960.

9 Morstein, J. and Trauner, D. (2019). New players in phototherapy: photopharmacology and bio-integrated optoelectronics. *Curr. Opin. Chem. Biol.* 50: 145–151.

10 Klan, P. and Wirz, J. (2009). *Photochemistry of Organic Compounds: From Concepts to Practice*, 1st ed. Chichester: Wiley.

11 Bléger, D. and Hecht, S. (2015). Visible-light-activated molecular switches. *Angew. Chem. Int. Ed.* 54: 11338–11349.

12 Kobayashi, Y., Mutoh, K., and Abe, J. (2018). Stepwise two-photon absorption processes utilizing photochromic reactions. *J. Photochem. Photobiol. C* 34: 2–28.


**13** Konig, K. (2000). Multiphoton microscopy in life sciences. *J. Microsc.* 200: 83–104.

**14** Delbaere, S. and Vermeersch, G. (2008). NMR spectroscopy applied to photochromism investigations. *J. Photochem. Photobiol. C* 9: 61–80.

**15** Kumpulainen, T., Lang, B., Rosspeintner, A., and Vauthey, E. (2017). Ultrafast elementary photochemical processes of organic molecules in liquid solution. *Chem. Rev.* 117: 10826–10939.

**16** Irie, M., Fukaminato, T., Matsuda, K., and Kobatake, S. (2014). Photochromism of diarylethene molecules and crystals: memories, switches, and actuators. *Chem. Rev.* 114: 12174–12277.

**17** Irie, M. (2000). Diarylethenes for memories and switches. *Chem. Rev.* 100: 1685–1716.

**18** Waldeck, D.H. (1991). Photoisomerization dynamics of stilbenes. *Chem. Rev.* 91: 415–436.

**19** Laarhoven, W.H. (1983). Photochemical cyclizations and intramolecular cycloadditions of conjugated arylolefins. Part I: photocyclization with dehydrogenation. *Recl. Trav. Chim. Pays-Bas* 102: 185–204.

**20** Irie, M., Lifka, T., Uchida, K. et al. (1999). Fatigue resistant properties of photochromic dithienylethenes: by-product formation. *Chem. Commun.* 747–750.

**21** Ward, C.L. and Elles, C.G. (2014). Cycloreversion dynamics of a photochromic molecular switch via one-photon and sequential two-photon excitation. *J. Phys. Chem. A* 118: 10011–10019.

**22** Irie, M., Sakemura, K., Okinaka, M., and Uchida, K. (1995). Photochromism of dithienylethenes with electron-donating substituents. *J. Org. Chem.* 60: 8305–8309.

**23** Uchida, K., Nakayama, Y., and Irie, M. (1990). Thermally irreversible photochromic systems. reversible photocyclization of 1,2-bis(benzo[*b*]thiophen-3-yl) ethene derivatives. *Bull. Chem. Soc. Jpn.* 63: 1311–1315.

**24** Tamai, N. and Miyasaka, H. (2000). Ultrafast dynamics of photochromic systems. *Chem. Rev.* 100: 1875–1890.

**25** Hania, P.R., Telesca, R., Lucas, L.N. et al. (2002). An optical and theoretical investigation of the ultrafast dynamics of a bisthienylethene-based photochromic switch. *J. Phys. Chem. A* 106: 8498–8507.

**26** Ward, C.L. and Elles, C.G. (2012). Controlling the excited-state reaction dynamics of a photochromic molecular switch with sequential two-photon excitation. *J. Phys. Chem. Lett.* 3: 2995–3000.

**27** Okabe, C., Nakabayashi, T., Nishi, N. et al. (2003). Picosecond time-resolved stokes and anti-stokes Raman studies on the photochromic reactions of diarylethene derivatives. *J. Phys. Chem. A* 107: 5384–5390.

**28** Jean-Ruel, H., Cooney, R.R., Gao, M. et al. (2011). Femtosecond dynamics of the ring closing process of diarylethene: a case study of electrocyclic reactions in photochromic single crystals. *J. Phys. Chem. A* 115: 13158–13168.

**29** Jean-Ruel, H., Gao, M., Kochman, M.A. et al. (2013). Ring-closing reaction in diarylethene captured by femtosecond electron crystallography. *J. Phys. Chem. B* 117: 15894–15902.


**30** Miller, R.J.D. (2014). Femtosecond crystallography with ultrabright electrons and X-rays: capturing chemistry in action. *Science* 343: 1108.

**31** Bandara, H.M.D. and Burdette, S.C. (2012). Photoisomerization in different classes of azobenzene. *Chem. Soc. Rev.* 41: 1809–1825.

**32** Dong, M., Babalhavaeji, A., Samanta, S. et al. (2015). Red-shifting azobenzene photoswitches for in vivo use. *Acc. Chem. Res.* 48: 2662–2670.

**33** Beharry, A.A. and Woolley, G.A. (2011). Azobenzene photoswitches for biomolecules. *Chem. Soc. Rev.* 40: 4422–4437.

**34** Natansohn, A. and Rochon, P. (2002). Photoinduced motions in azo-containing polymers. *Chem. Rev.* 102: 4139–4176.

**35** Merino, E. and Ribagorda, M. (2012). Control over molecular motion using the *cis-trans* photoisomerization of the azo group. *Beilstein J. Org. Chem.* 8: 1071–1090.

**36** Calbo, J., Thawani, A.R., Gibson, R.S.L. et al. (2019). A combinatorial approach to improving the performance of azoarene photoswitches. *Beilstein J. Org. Chem.* 15: 2753–2764.

**37** Bortolus, P. and Monti, S. (1979). *Cis-trans* photoisomerization of azobenzene. Solvent and triplet donors effects. *J. Phys. Chem.* 83: 648–652.

**38** Vetráková, Ľ., Ladányi, V., Al Anshori, J. et al. (2017). The absorption spectrum of *cis*-azobenzene. *Photochem. Photobiol. Sci.* 16: 1749–1756.

**39** Ladányi, V., Dvořák, P., Al Anshori, J. et al. (2017). Azobenzene photoisomerization quantum yields in methanol redetermined. *Photochem. Photobiol. Sci.* 16: 1757–1761.

**40** Adamson, A.W., Vogler, A., Kunkely, H., and Wachter, R. (1978). Photocalorimetry. Enthalpies of photolysis of *trans*-azobenzene, ferrioxalate and cobaltioxalate ions, chromium hexacarbonyl, and dirhenium decarbonyl. *J. Am. Chem. Soc.* 100: 1298–1300.

**41** Bahamonde, M.I., Taura, J., Paoletta, S. et al. (2014). Photomodulation of G protein-coupled adenosine receptors by a novel light-switchable ligand. *Bioconjugate Chem.* 25: 1847–1854.

**42** Konrad, D.B., Frank, J.A., and Trauner, D. (2016). Synthesis of redshifted azobenzene photoswitches by late-stage functionalization. *Chem. Eur. J.* 22: 4364–4368.

**43** Hansen, M.J., Lerch, M.M., Szymanski, W., and Feringa, B.L. (2016). Direct and versatile synthesis of red-shifted azobenzenes. *Angew. Chem. Int. Ed.* 55: 13514–13518.

**44** Bléger, D., Schwarz, J., Brouwer, A.M., and Hecht, S. (2012). *o*-Fluoroazobenzenes as readily synthesized photoswitches offering nearly quantitative two-way isomerization with visible light. *J. Am. Chem. Soc.* 134: 20597–20600.

**45** Beharry, A.A., Sadovski, O., and Woolley, G.A. (2011). Azobenzene photoswitching without ultraviolet light. *J. Am. Chem. Soc.* 133: 19684–19687.

**46** Quick, M., Dobryakov, A.L., Gerecke, M. et al. (2014). Photoisomerization dynamics and pathways of *trans*- and *cis*-azobenzene in solution from broadband femtosecond spectroscopies and calculations. *J. Phys. Chem. B* 118: 8756–8771.

**47** Fujino, T. and Tahara, T. (2000). Picosecond time-resolved Raman study of trans-azobenzene. *J. Phys. Chem. A* 104: 4203–4210.


**48** Lednev, I.K., Ye, T.Q., Matousek, P. et al. (1998). Femtosecond time-resolved UV-visible absorption spectroscopy of *trans*-azobenzene: dependence on excitation wavelength. *Chem. Phys. Lett.* 290: 68–74.

**49** Pancur, T., Renth, F., Temps, F. et al. (2005). Femtosecond fluorescence upconversion spectroscopy of a rotation-restricted azobenzene after excitation to the $S_1$ state. *Phys. Chem. Chem. Phys.* 7: 1985–1989.

# 2 Computational Methods and Photochromism

Martial Boggio-Pasqua

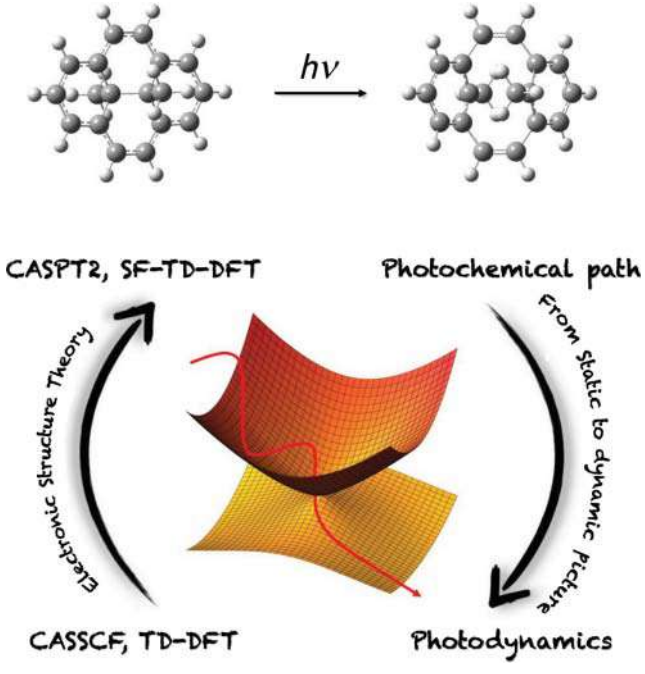


**Characteristic Features**

Computational photochemistry at work in the theoretical study of the photoswitching mechanisms of photochromic compounds. Illustration of dihydroazulene and dihydropyrene photochromism.

**Key References**

Boggio-Pasqua, M., Bearpark, M.J., Hunt, P.A. et al. (2002). Dihydroazulene/vinylheptafulvene photochromism: a model for one-way photochemistry via a conical intersection. *J. Am. Chem. Soc.* 124: 1456–1470.

Boggio-Pasqua, M., Bearpark, M.J., and Robb, M.A. (2007). Towards a mechanistic understanding of the photochromism of dimethyldihydropyrenes. *J. Org. Chem.* 72: 4497–4503.

# 2

# Computational Methods and Photochromism

*Martial Boggio-Pasqua*

*CNRS et Université Toulouse III – Paul Sabatier, LCPQ UMR 5626, 118 route de Narbonne, 31062, Toulouse, France*

## 2.1 Introduction

In the field of photochemistry, photochromism represents an increasing area of research because of its actual and potential applications [1–3]. It can be defined as a reversible phototransformation of a molecule between two forms having different spectral properties. Photochromic compounds thus convert photonic energy into chemical energy on an ultrafast timescale. The change in electronic and molecular structures following light irradiation results in a modification of physical properties, which forms the basis of many applications in biology [4], nano, and material sciences [5–13].

The vast majority of reported photochromic compounds relies on organic molecules undergoing photoinduced electrocyclic reactions, cycloadditions, *cis-trans* (*E*/*Z*) isomerizations, intramolecular hydrogen or group transfers, dissociation processes, or electron transfers (redox) [1]. Moreover, transition metal complexes have also been designed to display photochromic properties. These systems are often based on linkage isomerizations between the metal center and ambidentate ligands (e.g. nitrosyls [14, 15] and sulfoxides [16, 17]).

Given the importance and many possible applications of photoswitches to which photochromic compounds belong, a large number of computational studies have been carried out to (i) rationalize experimental observations, (ii) unravel the key steps of the underlying reaction mechanism at the origin of the photochromism, (iii) predict the properties and help in the design of new photochromic systems to be synthesized.

Computational photochemistry [18–20] is an essential tool for rationalizing the photochemical behavior of such compounds. While early interpretations of photochemical processes were based on vertical excitations at the Franck–Condon (FC) geometry, advances in electronic structures methods and in computational tools have allowed the exploration of other regions of the complex multidimensional potential energy surfaces (PESs) and the characterization of electronically

*Molecular Photoswitches: Chemistry, Properties, and Applications*,
First Edition. Edited by Zbigniew L. Pianowski.


excited-state reaction paths. The general strategy often relies on a combination of quantum chemistry calculations and nonadiabatic dynamics simulations in order to characterize the main photochemical pathways connecting the initial excited-state reactants to the final ground-state photoproducts and to simulate the photodynamics of the system. This synergy between accurate and global static calculations and either quantum or semiclassical nonadiabatic dynamics simulations has allowed major breakthroughs in the understanding of photochemical and photophysical processes, in particular in the field of photochromism. The purpose of this chapter is to provide a general introduction to the computational methods and strategies used in the theoretical studies of such compounds and to give some illustrations with notable examples in which computations were used to explain nonintuitive experimental observations.

## 2.2 Basics of Computational Photochemistry

### 2.2.1 Electronic Structure Methods

To describe the ground and excited electronic states involved in the photodynamics of a system, a quantum mechanical method that provides a balanced description of all these states is required. The method needs to describe the electronic states consistently along the entire photochemical pathway (e.g. along the photoisomerization pathway in the context of electrocyclic reactions as illustrated below), meaning that the important electronic rearrangements taking place in all the states considered must be accounted for along the reaction path. In addition, a method with analytical energy gradients available is also required to explore any photochemical process, whether statically through geometry optimizations and minimum energy path (MEP) calculations or dynamically through ab initio nonadiabatic molecular dynamics (NAMD) simulations. Because of the important nonadiabatic effects often involved in the excited-state dynamics, particularly around conical intersections (CoIns) [21], it is also desirable to use a method that allows a proper description of the electronic state couplings in the corresponding regions of the PESs.

For all these reasons, multiconfigurational wavefunction-based methods, such as the popular complete active space self-consistent field (CASSCF) method, have often been used to compute excited-state PESs or to investigate ab initio NAMD on-the-fly of photochromic compounds. Within the CASSCF framework, one chooses a set of active orbitals over which the active electrons can be distributed to generate all the electronic configurations, as in a configuration interaction (CI) calculation. Both CI coefficients and orbitals are optimized for a given (set of) state(s). The most critical feature of this kind of calculations is the choice of the active electrons and orbitals, known as the active space. A judicious choice of active space has to be selected [22] in order to describe all the electronic rearrangements that will occur during the photoisomerization of the photochromic compound under investigation. It allows a reliable description of the static (or non-dynamical) electron correlation. However, to obtain accurate PESs, post-CASSCF treatments

are usually necessary to recover the dynamic electron correlation missing at the CASSCF level. This is the case in the complete active space second-order perturbation theory (CASPT2), which has become the post-CASSCF method of reference widely employed in photochemistry today [23, 24], including for the studies of photochromic compounds. To obtain useful mechanistic information in photochemical studies, the CASSCF approximation is often sufficient. However, if quantitative agreement with experiment is sought or if CASSCF does not provide a balanced description of the excited states involved because of the lack of dynamic electron correlation, then CASPT2 becomes necessary.

However, both CASSCF and CASPT2 approaches rapidly become prohibitively expensive with the system and active space sizes. Although promising approaches to reduce the scaling of such methods have been developed recently based most notably on the density matrix renormalization group (DMRG) [25], these methods are not widely applicable yet to investigate photochemical mechanisms because of the lack of analytical energy gradients. Thus, alternative approaches capable of computing excited-state energies and their associated gradients need to be used when the system size forbids the use of CASSCF and CASPT2. This is the case of several efficient single-reference methods [26] such as time-dependent density functional theory (TD-DFT), approximate second-order coupled-cluster (CC2), and algebraic diagrammatic construction (ADC) scheme. Among these, TD-DFT is one of the most popular approaches to study excited states of medium to large-size systems, including in the context of the photoisomerization of photochromic compounds. Unlike the CASSCF and CASPT2 approaches, it is simple and straightforward to use once an appropriate functional has been chosen for the considered system. It can be efficiently used to study NAMD on the fly [27]. However, it suffers from deficiencies of the underlying mono-configurational description of the ground state in regions of bond breaking and bond formation, and it is known to encounter severe problems in describing valence states of molecules exhibiting extended $\pi$ systems, doubly excited states, charge-transfer excited states [26], and CoIns between ground and excited states [28, 29]. Triplet state instabilities [30] are also a serious issue when such states are involved in the photochemical process. For all these reasons, TD-DFT may only give qualitative information on the photoisomerization mechanisms of photochromic compounds. Note that developments in TD-DFT are ongoing to solve these issues and to make TD-DFT truly reliable in the context of computational photochemistry [31, 32].

In addition, approaches based on semiempirical configuration interaction methods (e.g. FOMO/CI [33], GUGA [34], OM2/MRCI [35], MMVB [36–38]) have also been developed specifically for excited-state calculations and for simulating photochemical processes taking place through CoIns. Such methods neglect many of the two-electron integrals computed in ab initio calculations and use parameters for most of the one- and two-electron integrals that cannot be neglected. These low-cost methods can be considered as an alternative to the ab initio methods described above for studies of photochemical processes in large-size molecules or when a large number of trajectories are necessary to simulate the dynamics of the system. However, these methods require transferable, large-scale parameterization

over many elements to obtain a single-molecule-independent set of parameters. Moreover, it is often necessary to re-optimize these parameters to generate a molecule-specific set of parameters allowing description of the excited-state critical structures (stationary points and CoIns) on the PESs to make them truly reliable for modeling photochemical processes. In such cases, the method becomes cumbersome in practice and unsatisfactory from a conceptual point of view.

For more details about the various electronic structure methods available in computational photochemistry and their capabilities, the interested reader can consult a number of excellent review articles and books dedicated to this topic [20, 28, 39–41].

### 2.2.2 Photochemical Pathway and Conical Intersections

To understand the fate of photoexcited molecules such as in the case of photochromic compounds, it is not only necessary to understand their excited-state properties but also to determine how the system will evolve chemically in terms of bond making and bond breaking in these excited states. Thus, it is crucial to understand the reaction pathway describing the passage from the excited-state reactants to the final photoproducts evolving along the PESs of the photochemically relevant electronic states (see Figure 2.1 for an illustration involving one excited state). This reaction path is called *photochemical reaction path* or *photochemical pathway*. It is determined by following the detailed relaxation and reaction paths of the molecule along the relevant PESs from the Franck-Condon (FC) point (i.e. vertically excited geometry) to the ground state. Static calculations are performed to investigate the topology of the PESs. It requires finding all the relevant critical structures (minima, saddle points, barriers, surface crossings) involved along the reaction path and

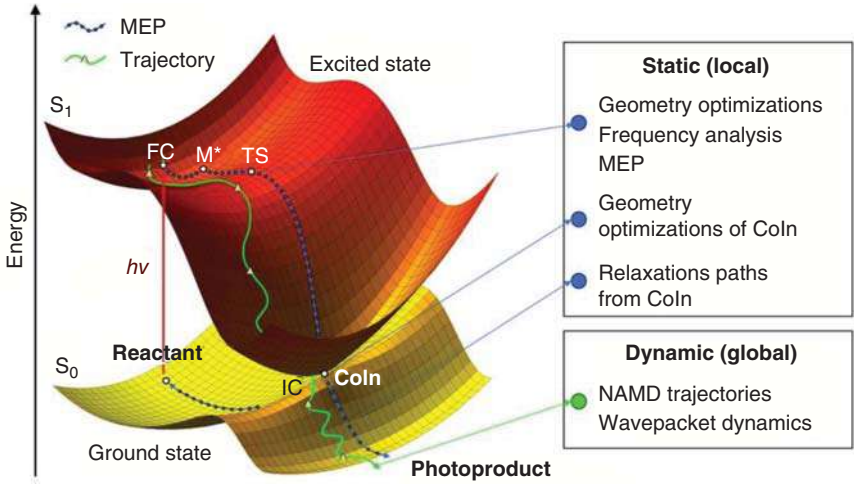


**Figure 2.1** Illustration of the photoreaction path modeling with static and dynamic approaches for a two-state photochemical reaction. FC, Franck–Condon point; M*, excited-state minimum; TS, transition state; CoIn, conical intersection; IC, internal conversion; MEP, minimum energy path.

understanding how all these critical points are interconnected on the PESs. This interconnection is often determined by MEP calculations or sometimes by exploring potential energy profiles using linearly interpolated geometries between optimized structures. Once the potential energy landscape for all the relevant electronic states is understood, very detailed mechanistic information can be derived on the photochemistry of the system such as the identification of the transient species involved, the radiative and nonradiative deactivation pathways, the barrierless or activated nature of the photochemical reaction, and its feasibility in terms of forming new photoproducts (photochemical paths) against the regeneration of the initial ground-state species (photophysical paths).

It is important to state at this stage that the photochemical reaction path requires computing relaxation pathways in the excited states up to the eventual PES crossings before exploring what are the different relaxation paths arising from such crossings down to the ground state. One of the common pitfalls is to try to deduce photoinduced reaction mechanisms based solely on the excited-state potential energy profiles computed along the ground-state (thermal) reaction paths. While these profiles can be interesting as an initial exploration of the excited-state PESs and may sometimes provide indications of possible PES crossings, they do not describe the correct reaction path in the excited states, as the nuclei feel an excited-state potential after the system is photoexcited. It is therefore crucial to follow the excited-state path along which the system is evolving, otherwise important mechanistic features of the photochemical reaction may be completely overlooked.

The information obtained from this static approach is mainly structural, i.e. the computed photochemical path describes the motion of a vibrationally cold molecule moving with infinitesimal momenta. While this path does not represent any *real* trajectory, it allows for a qualitative understanding of different experimental data such as excited-state lifetimes, nature of the photoproducts formed, and quantum yields. Beyond the static approach, detailed information about the time-evolution of a molecule after photoexcitation can be obtained from nonadiabatic dynamics simulations. Dynamics studies become all the more important when the system does not follow MEPs. In such cases, regions of the PESs far from the computed static photochemical pathway may become important, and mechanistic pictures deduced solely from the topological investigation of the PESs may be erroneous. Moreover, dynamics simulations can bring semiquantitative information on important experimental data such as excited-state lifetimes and quantum yields provided that a sufficient sampling of the system can be achieved. Thus, calculations of PESs and characterization of the static photochemical pathway are often complemented by dynamics simulations to gain a more complete understanding of the molecular photochemistry.

These simulations can be performed using two distinct strategies. The first and most conventional method is to simulate the direct dynamics of the system using semiclassical approaches such as ab initio NAMD by computing the potential energies and couplings on the fly along trajectories. This method is largely used in photochromic compounds due to the large number of internal degrees of freedom that needs to be handled. The second approach resorts to more accurate and

computationally demanding grid-based quantum wavepacket dynamics [42] such as in the multi-configuration time-dependent Hartree method [43] (MCTDH), which requires that the PESs and couplings are modeled along the most relevant (photochemically active) internal degrees of freedom using a vibronic-coupling Hamiltonian. This approach is much more challenging to use in the context of photochromic compounds, but the MCTDH dynamics study of benzopyran taken as a model compound for photochromic spiropyrans is a beautiful example [44].

Over the last three decades, it has become more and more evident that photochemical pathways were evolving through CoIns, which correspond to PES crossings responsible for efficient nonradiative decay of excited-state species. While first thought as an exception, it is now very well established that CoIns are central mechanistic features in organic photochemistry [45–47]. This is particularly the case in the photoswitching mechanisms of photochromic systems, as CoIns have been identified along the photoisomerization paths of azobenzenes [48], spiropyrans [49], aromatic Schiff bases [50], dihydroazulenes [51], dithienylethenes [52], chromenes [53], oxazines [54], dihydropyrenes [55], dihydronaphthalene [56], and fulgides [57], to cite a few examples.

Thus, CoIns need to be located as they act as funnels for electronic radiationless transitions between electronic states. In an analogy to transition states, which are bottleneck structures separating the reactant from the product in a ground-state reaction, CoIns form a bottleneck for electronic relaxation in a photochemical reaction. The main difference is that CoIns act as bifurcations leading possibly to different products, and they are not isolated crossing points on the PESs but are part of extended crossing seams [58–60]. CoIns are characterized by the two vectors (nuclear vibrations) that lift the degeneracy at first order: the gradient difference ($\mathbf{x}_1$) and the interstate coupling ($\mathbf{x}_2$) vectors, which form the so-called *branching space*. As a consequence, the two crossing PESs intersect as a double cone if they are plotted in the two dimensions of the branching space vectors. For a molecule with $N^{\text{int}}$ internal degrees of freedom, it is possible to find $N^{\text{int}} - 2$ coordinates orthogonal to the branching space, which preserve the degeneracy at first order. This $(N^{\text{int}} - 2)$-dimensional space is a hyperline of degeneracy and is also called *intersection space* or *intersection seam*. This seam will then appear as a crossing line if the two intersecting PESs are plotted along one branching space coordinate and one intersection space coordinate.

A first consequence of this intrinsic multidimensional nature of a CoIn is that it makes the state crossings all the more accessible during the course of the photochemical reaction. Moreover, this high dimensionality can be crucially important, as different regions of the associated extended crossing seam can be sampled by the system during excited-state vibrational relaxations, and these regions can potentially lead to different products. Thus, the search for the most relevant photochemical funnels aims at finding minimum energy crossing points (also called minimum energy CoIns) within the crossing seams. But one has to keep in mind that energetically accessible crossing segments away from such minima can also play a major role in the outcome of a photochemical reaction.

## 2.3 Applications: Photoswitching Mechanisms of Photochromic Compounds

In this section, we will illustrate the insightful potential of computational photochemistry with two notable examples of photochromic systems for which computations were used to explain nonintuitive experimental observations. For each system, the main experimental observations will be summarized, the computational method succinctly presented, and the main results deduced from the calculations allowing for a detailed interpretation of their photoswitching mechanism will be described.

### 2.3.1 Dihydroazulene Photochromism

The dihydroazulene (DHA)/vinylheptafulvene (VHF) photochromic couple (Scheme 2.1) has attracted a lot of interest because of its applications as photoswitch and thermoswitch. The photoinduced ring-opening reaction has a very high quantum yield (close to unity) in solution at room temperature, and the VHF photoproduct is formed on an ultrafast picosecond timescale, suggesting the presence of a CoIn [61]. Surprisingly, whereas DHA and VHF absorb in different spectral regions with no spectral overlap, irradiation of VHF in its first excited state does not produce DHA. The cyclization reaction can be achieved thermally or by two-photon excitation [62]. Moreover, no fluorescence is observed from VHF even at low temperature in contrast to DHA [63]. We will show in the following that most of these experimental observations can be explained by a CoIn between the $S_1$ and $S_0$ electronic states [49].

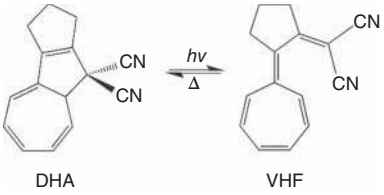


**Scheme 2.1** The dihydroazulene (DHA)/vinylheptafulvene (VHF) photochromic system.

The reference theoretical study of the photoswitching mechanism of this system was performed two decades ago [51]. It relied on the static and dynamical investigations of various model systems at the CASSCF level of theory. To account for the electronic reorganization taking place along the photoisomerization, it is necessary to include all the valence π orbitals of DHA plus the pair of σ, σ* orbitals describing the σ-bond that breaks during the ring-opening reaction. This active space naturally correlates with the full valence π system of VHF. It is important to note that CASPT2 calculations on such systems were not feasible at that time but would be required for accurate energetics of the PESs. However, the CASSCF method is sufficient to

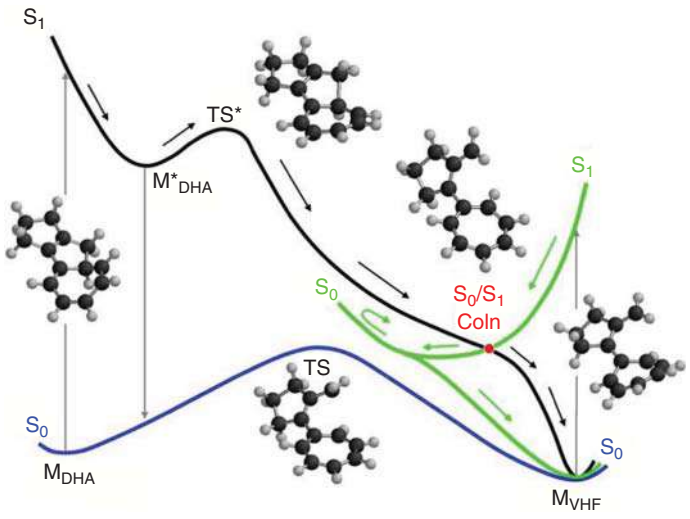


**Figure 2.2** Schematic $S_0$ and $S_1$ potential energy profiles for a model DHA/VHF system. Gray vertical arrows indicate absorption and emission processes. The black and green curves show the nonadiabatic DHA→VHF and VHF→VHF reaction pathways, respectively. Source: Adapted from Boggio-Pasqua et al. [51].

provide the correct topology of the PESs and thus the central mechanistic features for this system.

Based on this computational methodology, the $S_0$ and $S_1$ potential energy profiles obtained along the photochemical reaction path are shown in Figure 2.2 along with the main relaxation pathways. Upon photoexcitation to the $S_1$ state of DHA, the system relaxes to a local $S_1$ DHA biradicaloid minimum ($M^*_{DHA}$) following a complete inversion of single and double bonds within the π-system. Then, upon stretching the σ-bond that breaks to produce VHF, the system reaches a transition state TS* (about 10 kcal mol$^{-1}$ above $M^*_{DHA}$ but more than 20 kcal mol$^{-1}$ below the $S_1$ Franck–Condon energy) characterized by a transition vector dominated by an adiabatic σ-bond breaking. Beyond the transition structure, the system proceeds downhill to a conical intersection, $S_0/S_1$ CoIn. The associated minimum energy CoIn corresponds to the lowest energy point on the $S_1$ PES (over 50 kcal mol$^{-1}$ below $M^*_{DHA}$). This crossing presents a VHF-like structure, i.e. the 5-membered ring is opened, and at this funnel, efficient radiationless decay to $S_0$ will take place producing the VHF isomer ($M_{VHF}$). This picture is consistent with the observation of fluorescence following photoexcitation of DHA, as there is a local DHA $S_1$ minimum ($M^*_{DHA}$). The DHA→VHF isomerization quantum yield increases, at the expense of the emission efficiency, when the temperature is increased. This is consistent with the activated process to reach the funnel for photoisomerization.

In fact, the MEP calculated from TS* in the VHF direction does not actually reach the minimum energy $S_0/S_1$ CoIn itself, the lowest-energy point optimized on the intersection. Instead, the MEP terminates at a higher energy point on the intersection seam, denoted as $S_0/S_1$ CoIn*, which is over 30 kcal mol$^{-1}$ above the minimum

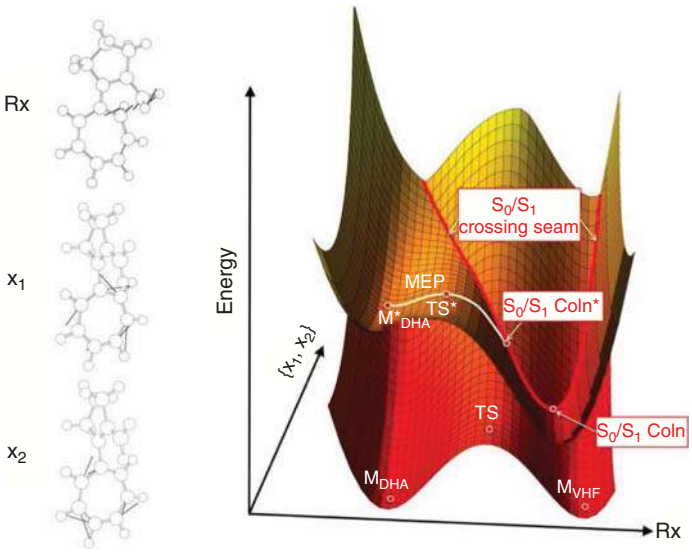


**Figure 2.3** $S_0$ and $S_1$ potential energy landscapes along the reaction path (Rx) corresponding to the DHA→VHF photoisomerization. The MEP computed at TS* is indicated by the white line and shows how it is intercepted by the intersection seam at the structure $S_0/S_1$ CoIn*, lying much higher in energy than the minimum energy conical intersection, $S_0/S_1$ CoIn. The relevant coordinates for mechanistic photochemistry are shown on the left for a DHA/VHF model system: the reaction coordinate Rx is orthogonal to the branching space.

energy CoIn (Figure 2.3). This is made possible because the ring-opening reaction coordinate involves mainly a C—C σ-bond breaking, while the branching space coordinates $\{\mathbf{x}_1, \mathbf{x}_2\}$ at the minimum energy $S_0/S_1$ CoIn are dominated by rearrangements of the seven-membered ring. Thus, the crossing seam appears as a line of degeneracy along the DHA→VHF reaction path, as illustrated in Figure 2.3. In addition to its higher energy, $S_0/S_1$ CoIn* is characterized by a shorter C—C bond distance for the broken σ-bond of 2.45 Å compared with the 3.45 Å C—C bond distance at the minimum energy $S_0/S_1$ CoIn. This confirms that the MEP is intercepted by the crossing seam well before reaching the minimum energy CoIn. Analysis of the decay routes at $S_0/S_1$ CoIn* shows that the system may return to $M_{DHA}$ or form $M_{VHF}$ but, for inertial reasons, product formation will be highly favored over reactant regeneration.

Upon photoexcitation to the $S_1$ state of VHF, the system relaxes directly toward the minimum energy $S_0/S_1$ CoIn (green arrows in Figure 2.2). The relaxation coordinate corresponds to the gradient difference $\mathbf{x}_1$ vector characterizing this crossing. Consequently, the MEP on $S_1$ is naturally driven to the minimum energy $S_0/S_1$ CoIn. The topological feature on $S_0$ around this CoIn only allows the system to reform VHF. After nonradiative decay to $S_0$ at the minimum energy CoIn, the system encounters a steep rise in the ground-state energy (Figure 2.2), and molecules approaching the minimum energy $S_0/S_1$ CoIn from the VHF side will therefore be reflected on this barrier back toward $M_{VHF}$. These particular topological features around the CoIn account for the high photostability of VHF. Moreover, the presence of the minimum

energy $S_0/S_1$ CoIn as the lowest critical point on the $S_1$ PES in the VHF region also explains the lack of fluorescence upon excitation of VHF.

Both the highly efficient DHA→VHF photoisomerization and high VHF photostability were confirmed by on-the-fly CASSCF [51] and MMVB [37] molecular dynamics. All the trajectories performed from TS* ended up producing VHF, while none of the trajectories started from VHF produced DHA. In addition, these dynamics simulations also illustrated the access of the higher energy part of the crossing seam in the region of $S_0/S_1$ CoIn* during the DHA→VHF photoisomerization.

### 2.3.2 Dihydropyrene Photochromism

Dihydropyrenes (DHPs) belong to a well-known class of photochromic compounds: the diarylethene family, whose most famous representative is the dithienylethene (DTE) photochrome [8]. However, in contrast to DTEs, DHPs have the particularity to be negative photochromes, which makes them highly interesting because the thermally stable isomer is the more colored one, while positive photochromes such as DTEs have the more stable form colorless. The colored form, associated with the highly conjugated closed-ring DHP isomer, bleaches upon exposure to visible light corresponding to the formation of the less aromatic open-ring cyclophanediene (CPD) isomer and returns to the DHP isomer upon exposure to UV light or thermally (Scheme 2.2) [64, 65]. However, the low DHP to CPD isomerization quantum yields combined with a fast rate of thermal back reaction in these compounds were representing an obstacle for their use as efficient photochromic systems.

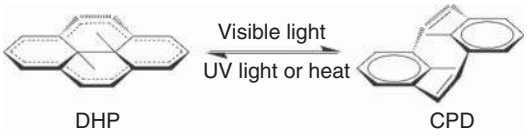


**Scheme 2.2** The dimethyldihydropyrene (DHP)/cyclophanediene (CPD) photochromic system.

The reasons behind this lack of efficiency were first rationalized based on a CASSCF/CASPT2 ab initio study of the reference compound shown in Scheme 2.2 back in 2007 [55]. Unlike the DHA/VHF system presented above, which can be approximated as a two-electronic-state problem, the DHP/CPD is much more challenging because several coupled excited states of different nature (covalent/ionic, singly-/doubly-excited) are involved in the photoswitching mechanism. In addition, the natural active space to describe this electrocyclic reaction requires to include the valence π orbitals of the annulene ring at the periphery of DHP plus the pair of σ, σ* orbitals describing the σ-transannular bond that breaks during the ring-opening reaction. This amounts to distributing 16 electrons in 16 orbitals for this unsubstituted DHP, representing a formidable task for computing CASSCF and CASPT2 PESs. An additional challenge arises from the difficulty to describe simultaneously covalent and zwitterionic excited states for which the dynamic electron correlation

is very different. In such a particular case, the CASSCF method fails to provide accurate relative energies between these states, and the CASPT2 level is necessary to obtain the right order of the states [66]. Thus, this system falls in the case where both static and dynamic electron correlations need to be described accurately between the various electronic states. The CASSCF is then only useful to optimize structures and to provide approximate adiabatic relaxation pathways assuming that these are correctly described without accurate description of the dynamic electron correlation. These relaxation pathways cannot be computed with standard MEP calculations because of their prohibitive computational cost at the CASSCF(16,16) level. More approximate paths based on linearly interpolated geometries in internal coordinates between optimized structures had to be used instead.

Following such a computational strategy, the photoisomerization path was derived from the static exploration of the PESs as represented in Figure 2.4. On this figure, only the most relevant excited states are shown. These states are (i) the $S_1(L_b)$ covalent state described as a combination of the HOMO–1→LUMO and HOMO→LUMO+1 excitations, (ii) the $S_2(L_a)$ zwitterionic state dominated by the HOMO→LUMO transition, and (iii) the $S_6(\cdot\cdot)$ biradicaloid state described by a mixture of singly and doubly excited configurations and dominated upon vibrational relaxation by the ground-state configuration and the $HOMO^2 \rightarrow LUMO^2$ excitation. Irradiation of the unsubstituted DHP (Scheme 2.2) in its first singlet excited state $S_1(L_b)$ does not lead to CPD formation, whereas photoisomerization is observed from the $S_2(L_a)$ state upon irradiation at 480 nm in aerated cyclohexane with a ring-opening quantum yield of only 0.006 [65]. This very low ring-opening quantum yield was rationalized theoretically by the efficient depopulation of the initially excited $S_2(L_a)$ photoactive state (i.e. state that leads to photoisomerization) to the lower $S_1(L_b)$ unreactive state (i.e. state that does not lead to photoisomerization). This is illustrated by the yellow path in Figure 2.4 showing the nonradiative decay from $S_2(L_a)$ to $S_1(L_b)$ via a $S_1/S_2$ CoIn. While vibrational relaxation on the $S_2$ state leads to a CPD precursor (CPD*; Figure 2.4) characterized by an elongated transannular C—C bond and a loss of planarity of the DHP core relative to the ground-state structure, the $S_1$ state relaxes to an excited-state minimum (DHP*; Figure 2.4) with a similar structure as ground-state DHP. From DHP*, the system deactivates back to the initial ground-state DHP either radiatively or nonradiatively. To undergo the DHP to CPD ring-opening reaction, the system needs to reach a biradical intermediate via the population of CPD* on $S_2$ followed by internal conversion at a CoIn between the zwitterionic and biradicaloid states. Upon population of the biradical intermediate, the system can then decay to the ground state at a nearby $S_0/S_1$ CoIn leading to product formation. This is illustrated by the purple path in Figure 2.4. Note that this path is an activated process as it needs to reach two CoIns higher in energy than CPD*. The $S_0/S_1$ CoIn is the expected photochemical funnel for CPD formation. This CoIn belongs to a well-known class of conical intersections involving three weakly coupled π-electrons. This type of CoIn has also been encountered in the photoswitching mechanism of DTEs [52].

Since this seminal theoretical study, more efficient DHP derivatives such as benzo [*e*]-fused-DHPs and pyridinium-appended-DHPs were studied computationally

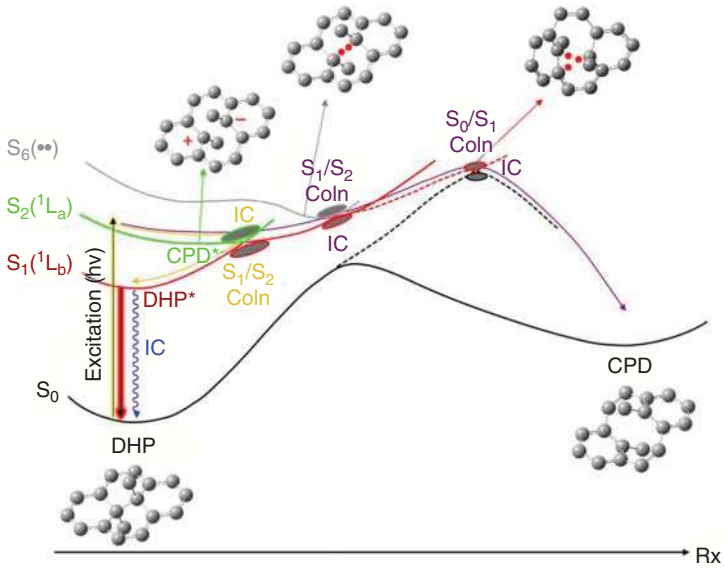


**Figure 2.4** Schematic potential energy profiles of the relevant electronic states involved in the DHP/CPD photochromism based on CASPT2 energies along CASSCF adiabatic relaxation pathways. IC: internal conversion, CoIn: conical intersection. Relevant structures for which hydrogen atoms have been omitted for clarity are shown. Yellow curved arrow: photophysical pathway; purple curved arrow: photoisomerization (photochemical) pathway.

[67, 68]. Because of the size of these derivatives, the CASSCF/CASPT2 approach employed to study the reference compound (Scheme 2.1) becomes impractical. Instead, TD-DFT can be used efficiently. While the biradicaloid excited state cannot be described with TD-DFT because of the doubly excited nature of this electronic state, TD-DFT is expected to describe the $S_2 \rightarrow S_1$ deactivation pathway, as both states result from single excitations as described above. This was first verified for the reference compound [67]. After validation of the description of the $S_2 \rightarrow S_1$ photophysical path at the TD-DFT level, the pathway leading to CPD* and to the $S_1/S_2$ CoIn was investigated for these improved DHP derivatives. Figure 2.5 illustrates this relaxation pathway for a simple benzo[*e*]-fused-DHP. For this system, the more efficient ring-opening reaction is made possible by the inversion of states occurring between $S_1$ and $S_2$, $S_1$ becoming the $L_a$ state and $S_2$ the $L_b$ state. Thus, CPD* formation takes place directly on the lowest $S_1$ PES, and no internal conversion with another excited state is involved. This study showed that in these systems, the CPD* minimum is the lowest excited-state minimum in contrast to the reference system for which it is DHP*. As CPD* is the transient species required to photoisomerize, more efficient formation of this intermediate is associated here to an improved ring-opening efficiency. More recently, it was explained theoretically why the ring-opening efficiency is dependent on the number of electron-withdrawing pyridinium groups appended to the DHP core [69].

Note that the photochemical funnels ($S_0/S_1$ CoIn) have yet to be identified in these substituted DHP derivatives. As TD-DFT is not suitable to describe such crossings

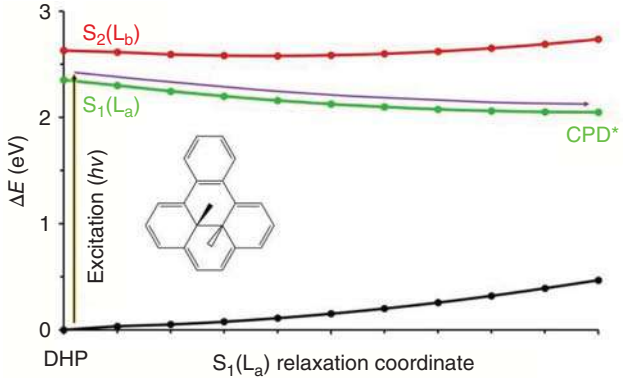


**Figure 2.5** TD-DFT potential energy profiles for the first three electronic states of a simple benzo[*e*]-fused DHP along the $S_1$ relaxation coordinate leading to CPD*. Purple curved arrow: $S_1$ relaxation pathway.

(biradical character of $S_0$ at the $S_0/S_1$ CoIn and wrong $S_0$-$S_1$ coupling at this level of theory), other variants of TD-DFT (e.g. spin-flip TD-DFT and multiconfigurational DFT) [31, 32, 70], which allow both the multiconfigurational description of the ground state and its correct electronic coupling with excited states, will be required to investigate the complete photoisomerization pathway of these systems.

## 2.4 Conclusions and Perspectives

In this chapter, we have given an outlook of the potential of computational photochemistry applied in the context of photochromic systems. Computational photochemistry is the branch of computational chemistry devoted to the study of chemical reactions induced by light. We have reviewed succinctly the various important aspects of such studies. It includes a short description of the most popular electronic structure methods allowing the reliable simultaneous description of ground and excited electronic states. We have presented the general strategy to determine a photochemical reaction mechanism with both static and dynamic exploration of the PESs allowing description of the sequence of molecular structures (traveling points on the PESs) through which the photoreaction proceeds on its way from reactant to photoproducts. We have recalled the central role of CoIns in ultrafast photochemistry in general but also in the context of the photoswitching of photochromic systems. CoIns provide the critical funnels through which the system is nonradiatively decaying between electronic states. Eventually, CoIns provide the reactive channels (photochemical funnels) for the photoproducts formation in the ground state.

Two illustrative examples of computational studies of photochromic systems have been given. The first one is the unidirectional photoswitching of DHA to VHF, which can be explained by the particular topological features of the $S_0/S_1$ CoIn seam. The second example is the low-efficient photoinduced ring opening of DHP into CPD, which can be accounted for by the presence of an unreactive

deactivation pathway via an easily accessible $S_1/S_2$ CoIn. The improved efficiency of some DHP derivatives can be rationalized theoretically by the effective removal of this unreactive deactivation pathway.

The developments of efficient and accurate quantum chemistry methods capable of describing excited-state reaction paths, CoIns, and photodynamics are needed to deal with complex and large photoactive systems. Recent advances in the field [32, 71] hold great promises in the future exploration of photochromic compounds, not only at the molecular level but also at the nanoscale [72], which is of high relevance to understand the efficiencies of photochromic materials for various optoelectronic applications. We can thus anticipate that computational photochemistry will carry on playing a major role in the understanding of photochromic compounds, and its predictive power will prove valuable in the design of novel photochromic materials in the future.

## References


1 Dürr, H. and Bouas-Laurent, H. (ed.) (1990). *Photochromism: Molecules and Systems*. Amsterdam: Elsevier.

2 Crano, J.C. and Guglielmetti, R. (1999). *Organic Photochromic and Thermochromic Compound*. New York: Plenum Press.

3 Feringa, B.L. and Browne, W.R. (ed.) (2011). *Molecular Switches*. Wiley-VCH Verlag GmbH & Co. KGaA.

4 Szymanski, W., Beierle, J.M., Kistemaker, H.A.V. et al. (2013). Reversible photocontrol of biological systems by the incorporation of molecular photoswitches. *Chem. Rev.* 113: 6114–6178.

5 Feringa, B.L. (2007). The art of building small: from molecular switches to molecular motors. *J. Org. Chem.* 72: 6635–6652.

6 Kim, T., Zhu, L., Al-Kaysi, R.O., and Bardeen, C.J. (2014). Organic photomechanical materials. *ChemPhysChem* 15: 400–414.

7 Asadirad, A.M., Boutault, S., Erno, Z., and Branda, N.R. (2014). Controlling a polymer adhesive using light and a molecular switch. *J. Am. Chem. Soc.* 136: 3024–3027.

8 Irie, M. (2000). Diarylethenes for memories and switches. *Chem. Rev.* 100: 1685–1716.

9 Berkovic, G., Krongauz, V., and Weiss, V. (2000). Spiropyrans and spirooxazines for memories and switches. *Chem. Rev.* 100: 1741–1753.

10 Yokoyama, Y. (2000). Fulgides for memories and switches. *Chem. Rev.* 100: 1717–1739.

11 Szacilowski, K. (2008). Digital information processing in molecular systems. *Chem. Rev.* 108: 3481–3548.

12 Andréasson, J. and Pischel, U. (2010). Smart molecules at work – mimicking advanced logic operations. *Chem. Soc. Rev.* 39: 174–188.

13 Pianowski, Z.L. (2019). Recent implementations of molecular photoswitches into smart materials and biological systems. *Chem. Eur. J.* 25: 5128–5144.


**14** Coppens, P., Novozhilova, I., and Kovalevsky, A. (2002). Photoinduced linkage isomers of transition-metal nitrosyl compounds and related complexes. *Chem. Rev.* 102: 861–883.

**15** Bitterwolf, T.E. (2006). Photochemical nitrosyl linkage isomerism/metastable states. *Coord. Chem. Rev.* 250: 1196–1207.

**16** Rack, J.J. (2009). Electron transfer triggered sulfoxide isomerization in ruthenium and osmium complexes. *Coord. Chem. Rev.* 253: 78–85.

**17** McClure, B.A. and Rack, J.J. (2010). Isomerization in photochromic ruthenium sulfoxide complexes. *Eur. J. Inorg. Chem.* 3895–3904.

**18** Kutateladze, A.G. (2005). *Computational Methods In Photochemistry*. CRC Press.

**19** Olivucci, M. (2005). *Computational Photochemistry*. Elsevier.

**20** Robb, M.A. (2018). *Theoretical Chemistry for Electronic Excited States*, Theoretical and Computational Chemistry Series. London: The Royal Society of Chemistry.

**21** Worth, G.A. and Cederbaum, L.S. (2004). Beyond Born-Oppenheimer: molecular dynamics through a conical intersection. *Annu. Rev. Phys. Chem.* 55: 127–158.

**22** Veryazov, V., Malmqvist, P.Å., and Roos, B.O. (2011). How to select active space for multiconfigurational quantum chemistry? *Int. J. Quantum Chem.* 111: 3329–3338.

**23** Garavelli, M. (2006). Computational organic photochemistry: strategy, achievements and perspectives. *Theor. Chem. Acc.* 116: 87–105.

**24** Roca-Sanjuán, D., Aquilante, F., and Lindh, R. (2012). Multiconfiguration second-order perturbation theory approach to strong electron correlation in chemistry and photochemistry. *WIREs Comput. Mol. Sci.* 2: 585–603.

**25** Yanai, T., Saitow, M., Xiong, X.-G. et al. (2017). Multistate complete-active-space second-order perturbation theory based on density matrix renormalization group reference states. *J. Chem. Theory Comput.* 13: 4829–4840.

**26** Dreuw, A. and Head-Gordon, M. (2005). Single-reference ab initio methods for the calculation of excited states of large molecules. *Chem. Rev.* 105: 4009–4037.

**27** Curchod, B.F.E., Rothlisberger, U., and Tavernelli, I. (2013). Trajectory-based nonadiabatic dynamics with time- dependent density functional theory. *ChemPhysChem* 14: 1314–1340.

**28** Levine, B.G., Ko, C., Quenneville, J., and Martínez, T.J. (2006). Conical intersections and double excitations in time-dependent density functional theory. *Mol. Phys.* 104: 1039–1051.

**29** Cordova, F., Doriol, L.J., Ipatov, A. et al. (2007). Troubleshooting time-dependent density-functional theory for photochemical applications: oxirane. *J. Chem. Phys.* 127: 164111.

**30** Peach, M.J.G., Williamson, M.J., and Tozer, D.J. (2011). Influence of triplet instabilities in TDDFT. *J. Chem. Theory Comput.* 7: 3578–3585.

**31** Casida, M. and Huix-Rotllant, M. (2012). Progress in time-dependent density-functional theory. *Annu. Rev. Phys. Chem.* 63: 287–323.

**32** Herbert, J.M., Zhang, X., Morrison, A.F., and Liu, J. (2016). Beyond time-dependent density functional theory using only single excitations: methods for computational studies of excited states in complex systems. *Acc. Chem. Res.* 49: 931–941.


**33** Granucci, G., Persico, M., and Toniolo, A. (2001). Direct semiclassical simulation of photochemical processes with semiempirical wave functions. *J. Chem. Phys.* 114: 10608.

**34** Koslowski, A., Beck, M.E., and Thiel, W. (2003). Implementation of a general multireference configuration interaction procedure with analytic gradients in a semiempirical context using the graphical unitary group approach. *J. Comput. Chem.* 24: 714.

**35** Silva-Junior, M.R. and Thiel, W. (2010). Benchmark of electronically excited states for semiempirical methods: MNDO, AM1, PM3, OM1, OM2, OM3, INDO/S, and INDO/S2. *J. Chem. Theory Comput.* 6: 1546–1564.

**36** Bernardi, F., Olivucci, M., and Robb, M.A. (1992). Simulation of MC-SCF results on covalent organic multi-bond reactions: molecular mechanics with valence bond (MM-VB). *J. Am. Chem. Soc.* 114: 1606–1616.

**37** Bearpark, M.J., Boggio-Pasqua, M., Robb, M.A., and Ogliaro, F. (2006). Excited states of conjugated hydrocarbons using the molecular mechanics - valence bond (MMVB) method: conical intersections and dynamics. *Theor. Chem. Acc.* 116: 670–682.

**38** Bearpark, M.J., Ogliaro, F., Vreven, T. et al. (2007). CASSCF calculations for photoinduced processes in large molecules: choosing when to use the RASSCF, ONIOM and MMVB approximations. *J. Photochem. Photobiol., A* 190: 207–227.

**39** González, L., Escudero, D., and Serrano-Andrés, L. (2012). Progress and challenges in the calculation of electronic excited states. *ChemPhysChem* 13: 28–51.

**40** Lischka, H., Nachtigallová, D., Aquino, A.J.A. et al. (2018). Multireference approaches for excited states of molecules. *Chem. Rev.* 118: 7293–7361.

**41** Mai, S. and González, L. (2020). Molecular photochemistry: recent developments in theory. *Angew. Chem. Int. Ed.* 59: 16832–16846.

**42** Kosloff, R. (1988). Time-dependent quantum-mechanical methods for molecular dynamics. *J. Phys. Chem.* 92: 2087–2100.

**43** Meyer, H.-D., Gatti, F., and Worth, G.A. (ed.) (2009). *Multidimensional Quantum Dynamics: MCTDH Theory and Applications*. Weinheim: Wiley VCH.

**44** Gonon, B., Lasorne, B., Karras, G. et al. (2019). A generalized Vibronic-coupling hamiltonian for molecules without symmetry: application to the photoisomerization of benzopyran. *J. Chem. Phys.* 150: 124109.

**45** Robb, M.A., Bernardi, F., and Olivucci, M. (1995). Conical intersections as a mechanistic feature of organic photochemistry. *Pure Appl. Chem.* 67: 783–789.

**46** Bernardi, F., Olivucci, M., and Robb, M.A. (1996). Potential energy surface crossings in organic photochemistry. *Chem. Soc. Rev.* 25: 321–328.

**47** Robb, M.A., Garavelli, M., Olivucci, M., and Bernardi, F. (2000). A computational strategy for organic photochemistry. *Rev. Comput. Chem.* 15: 87–146.

**48** Cattaneo, P. and Persico, M. (1999). An ab initio study of the photochemistry of azobenzene. *Phys. Chem. Chem. Phys.* 1: 4739–4743.

**49** Celani, P., Bernardi, F., Olivucci, M., and Robb, M.A. (1997). Conical intersection mechanism for photochemical ring opening in benzospiropyran compounds. *J. Am. Chem. Soc.* 119: 10815–10820.


**50** Zgierski, M.Z. and Grabowska, A. (2000). Photochromism of salicylideneaniline (SA). How the photochromic transient is created: a theoretical approach. *J. Chem. Phys.* 112: 6329–6337.

**51** Boggio-Pasqua, M., Bearpark, M.J., Hunt, P.A., and Robb, M.A. (2002). Dihydroazulene/vinylheptafulvene photochromism: a model for one-way photochemistry via a conical intersection. *J. Am. Chem. Soc.* 124: 1456–1470.

**52** Boggio-Pasqua, M., Ravaglia, M., Bearpark, M.J. et al. (2003). Can diarylethene photochromism be explained by a reaction path alone? A CASSCF study with model MMVB dynamics. *J. Phys. Chem. A* 107: 11139–11152.

**53** Migani, A., Gentili, P.L., Negri, F. et al. (2005). The ring-opening reaction of Chromenes: a photochemical mode-dependent transformation. *J. Phys. Chem. A* 109: 8684–8692.

**54** Maurel, F., Aubard, J., Millie, P. et al. (2006). Quantum chemical study of the photocoloration reaction in the naphthoxazine series. *J. Phys. Chem. A* 110: 4759–4771.

**55** Boggio-Pasqua, M., Bearpark, M.J., and Robb, M.A. (2007). Towards a mechanistic understanding of the photochromism of dimethyldihydropyrenes. *J. Org. Chem.* 72: 4497–4503.

**56** Tomasello, G., Ogliaro, F., Bearpark, M.J. et al. (2008). Modeling the photophysics and photochromic potential of 1,2-dihydronaphthalene (DHN): a combined CASPT2//CASSCF-topological and MMVB-dynamical investigation. *J. Phys. Chem. A* 112: 10096–10107.

**57** Tomasello, G., Bearpark, M.J., Robb, M.A. et al. (2010). Significance of a zwitterionic state for fulgide photochromism: implications for the design of mimics. *Angew. Chem. Int. Ed.* 49: 2913–2916.

**58** Yarkony, D.R. (1996). Diabolical conical intersections. *Rev. Mod. Phys.* 68: 985–1013.

**59** Robb, M.A. (2011). *Conical Intersections in Organic Photochemistry, in Conical Intersections: Theory, Computation and Experiment*, vol. 17 (ed. W. Domcke, D.R. Yarkony and H. Köppel), Chap. 1, pp. 3–50. Singapore: World Scientific.

**60** Blancafort, L. (2014). Photochemistry and photophysics at extended seams of conical intersection. *ChemPhysChem* 15: 3166–3181.

**61** Ern, J., Petermann, M., Mrozek, T. et al. (2000). Dihydroazulene/vinylheptafulvene photochromism: dynamics of the photochemical ring-opening reaction. *Chem. Phys.* 259: 331–337.

**62** De Waele, V., Schmidhammer, U., Mrozek, T. et al. (2002). Ultrafast bidirectional dihydroazulene/vinylheptafulvene (DHA/VHF) molecular switches: photochemical ring closure of vinylheptafulvene proven by a two-pulse experiment. *J. Am. Chem. Soc.* 124: 2438–2439.

**63** Görner, H., Fischer, C., Gierisch, S., and Daub, J. (1993). Dihydroazulene/vinylheptafulvene photochromism: effects of substituents, solvent, and temperature in the photorearrangement of dihydroazulene to vinylheptafulvenes. *J. Phys. Chem.* 97: 4110–4117.

**64** Mitchell, R.H. (1999). The metacyclophanediene-dihydropyrene photochromic π switch. *Eur. J. Org. Chem.* 2695–2703.

**65** Sheepwash, M.A.L., Mitchell, R.H., and Bohne, C. (2002). Mechanistic insights into the photochromism of *trans*-10b,10c-dimethyl-10b-10c-dihydropyrene derivatives. *J. Am. Chem. Soc.* 124: 4693–4700.

**66** Sarkar, R., Heitz, M.-C., Royal, G., and Boggio-Pasqua, M. (2020). Electronic excited states and UV-Vis absorption spectra of the dihydropyrene/cyclophanediene photochromic couple: a theoretical investigation. *J. Phys. Chem. A* 124: 1567–1579.

**67** Boggio-Pasqua, M. and Garavelli, M. (2015). Rationalization and design of enhanced photoinduced cycloreversion in photochromic dimethyldihydropyrenes by theoretical calculations. *J. Phys. Chem. A.* 119: 6024–6032.

**68** Roldan, D., Cobo, S., Lafolet, F. et al. (2015). A multi-addressable switch based on the dimethyldihydropyrene photochrome with remarkable proton-triggered photo-opening efficiency. *Chem. Eur. J.* 21: 455–467.

**69** Lognon, E., Heitz, M.-C., Bakkar, A. et al. (2020). Dependency of the dimethyldihydropyrene photochromic properties on the number of Pyridinium electron-withdrawing groups. *ChemPhysChem* 21: 1571–1577.

**70** Ghosh, S., Verma, P., Cramer, C.J. et al. (2018). Combining wave function methods with density functional theory for excited states. *Chem. Rev.* 118: 7249–7292.

**71** Park, J.W. and Shiozaki, T. (2017). On-the-Fly CASPT2 surface-hopping dynamics. *J. Chem. Theory Comput.* 13: 3676–3683.

**72** Levine, B.G., Esch, M.P., Fales, B.S. et al. (2019). Conical intersections at the nanoscale: molecular ideas for materials. *Annu. Rev. Phys. Chem.* 70: 21–43.

# Section II

# Chemical Classes of Molecular Photoswitches

# 3 Azobenzenes: The Quest for Visible Light Triggering

Vanessa Koch and Stefan Bräse

**Photochromism**

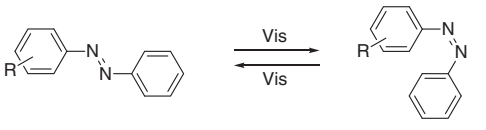


**Characteristic Features**

This chapter aims to summarize the synthetic approaches (including Mills reactions), the design concepts of different kinds of azobenzene photoswitches reversibly switchable with visible light, regarding their applications (especially in biological systems) as well as their physical properties.

**Synthetic Methods**

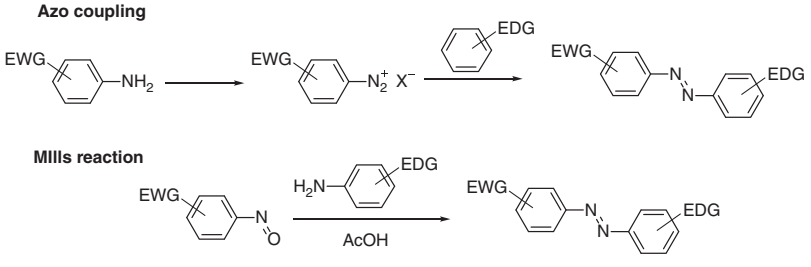


**First Reference**

Robertson, P.W. (1913). *J. Chem. Soc. Trans.* 103: 1472–1479.

**Key References**

Bléger, D., Schwarz, J., Brouwer, A.M. et al. (2012). *J. Am. Chem. Soc.* 134: 20597–20600.

Banghart, M., Borges, K., Isacoff, E. et al. (2004). *Nat. Neurosci.* 7: 1381–1386.

Dong, M., Babalhavaeji, A., Samanta, S. et al. (2015). *Acc. Chem. Res.* 48: 2662–2670.

Hansen, M.J., Lerch, M.M., Szymanski, W. et al. (2016). *Angew. Chem. Int. Ed.* 55: 13514–13518.

# 3

# Azobenzenes: The Quest for Visible Light Triggering

*Vanessa Koch*[1,2] *and Stefan Bräse*[1,2]

[1] *Karlsruhe Institute of Technology (KIT), Institute of Organic Chemistry, Organic Chemistry I, Fritz-Haber-Weg 6, Karlsruhe, 76131, Germany*
[2] *Karlsruhe Institute of Technology (KIT), Biological and Chemical Systems – Functional Molecular Systems (IBCS-FMS), Hermann-von-Helmholtz-Platz 1, Eggenstein-Leopoldshafen, D-76344, Germany*

## 3.1 Introduction

The discovery of azo compounds goes back to the mid-1800s when Eilhard Mitscherlich found that the distillation of nitrobenzene over burnt lime gave a so far unknown red solid compound that he called azobenzene (AB) due to its elemental analysis, which is ambiguous for a molecule with one or two nitrogen atoms. Its structure was determined over 30 years later by August Kekulé, but the configuration of the N=N double bond remained unsolved till G.S. Hartley discovered the photoisomerization of ABs in 1937 [1]. During his studies of the solubility properties of ABs, he observed a lack of reproducibility in the measurement of absorbance spectra and the color change of the solution when being exposed to sunlight. By a tremendous purification process, he was able to isolate the product that was responsible for the color change and determined its physical and chemical properties. As it thermally reverts to the *trans*-AB, G. S. Hartley concluded that he discovered the *cis*-form of AB and therefore also the photoisomerization of *trans*-ABs to *cis*-ABs by sunlight. In the following years, many AB derivatives were synthesized and their photophysical properties were studied.

The present book chapter aims to summarize the synthetic approaches, the design concepts of different kinds of AB photoswitches regarding their applications (especially in biological systems) as well as their physical properties. In the end, selected applications were given to show the overall potential of ABs. Thereby, the cited literature and reviews serve as sources to be consulted for deeper understanding [2–5]. Aliphatic derivatives are not covered, while heteroaromatic azoarenes (six- [6–10] or five-membered ones [11–14]) are compared with classical ones – a more detailed discussion is found in this book (Chapter 5 by Matthew Fuchter) [15]. Multiple [16] and cyclic [17] azobenzenes are only discussed very briefly.

*Molecular Photoswitches: Chemistry, Properties, and Applications*,
First Edition. Edited by Zbigniew L. Pianowski.


### 3.1.1 Azobenzene and Its Physical Characteristics

ABs have two geometric isomers (*Z*/*E* or *cis*/*trans*) from which the *E*-isomer is circa 12 kcal mol$^{-1}$ more stable than the *Z*-isomer. As the energy barrier of the photoexcited state is about 23 kcal mol$^{-1}$, the *trans*-isomer is predominant in the dark at room temperature with 99.99%. When irradiated with a wavelength between 320 and 350 nm, the *trans*-AB isomerizes to the *cis*-form on a picosecond timescale, thus being substantially faster than most biological processes, qualifying ABs for biological investigations. The reaction is reversible either by irradiation with light of a wavelength between 400 and 450 nm, heating, or thermal relaxation (milliseconds to days) the *trans*-isomer back. The reversibility of the process and the changes in physical properties, such as molecular geometry, their absorption spectra, or dipole moment, identify ABs as valuable photoswitches. The change of the geometry leads to a decrease in the end-to-end distance of *trans*-located carbons from 9.0 to 5.5 Å. This goes along with a change of the dipole moment μ as the *cis*-isomer is bent and one of the aryl rings twists 50° out of the plane to avoid electronical repulsion resulting in μ = 3.0 D while the *trans*-AB is almost flat. This effect can be also observed in the $^1$H NMR (nuclear magnetic resonance) spectrum. Due to the anisotropic effect of the π cloud of the aromatic, the aromatic signals of the *cis*-AB are shifted toward a higher field compared with those of the *trans*-AB (Figure 3.1).

The UV–vis absorption spectra of both isomers of the AB show two characteristic absorption bands, which are distinct but overlap each other. *trans*-AB shows a very intense π→π* transition band near 320 nm and a weak n→π* transition band near 440 nm – as this transition is not allowed by symmetry rules. In comparison, the *cis*-AB has a stronger n→π* transition band at a similar wavelength (as it is allowed) and two absorption bands at shorter wavelengths of 280 and 240 nm. It is worth noting that photoisomerization takes place with high quantum yields, and only negligible photobleaching is observed.

The photophysics of heterocyclic azobenzenes has been discussed in detail elsewhere [15]. Recently, azobenzenes have been used for the self-assembly of nanoparticles [18] and the design of visible-light switchable or orthogonally switchable systems [19–21].

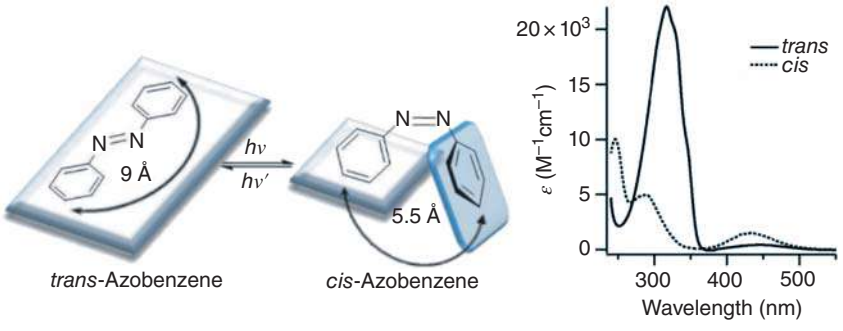


**Figure 3.1** Photoisomerization of azobenzene (Source: Reprinted from Ref. [5]) and the absorption spectrum of the two isomers. Source: Reprinted with permission from Beharry and Woolley [2].

## 3.2 Synthesis of Azobenzenes

Since ABs are broadly used both in the industry and in academia, a variety of synthetic methods have been developed since their discovery in the mid-1800s. Some of these will be presented in the following chapter, for more detailed information, several reviews can be found in the literature [22, 23]. Even though many new methods have been developed, most syntheses of ABs are still based on classical methods such as the azo coupling or the Mills reaction.

### 3.2.1 Synthesis of Symmetrical Azobenzenes by Oxidation of Anilines

The synthesis of symmetrical AB derivatives has been accomplished via the oxidation of anilines – either by electrolytic oxidation or oxidizing reagents comprising metallic and nonmetallic ones. Among the huge variety of oxidants presented in the literature reaching over $MnO_2$, $KMnO_4$, $Ag_2CO_3$ $Pb(OAc)_4$, and hypervalent iodides such as $PhI(OAc)_2$ to aerial oxidants such as $O_2$/*t*BuOK, $O_2$/$CuCl_2$/pyridine or peroxidase/$H_2O_2$, $MnO_2$, and NaOCl are most commonly used in practice. The oxidation of anilines bearing electron-withdrawing groups (EWGs) in *meta*- and/or *para*-position was realized in refluxing toluene with $MnO_2$ affording the ABs in mostly excellent yields (Scheme 3.1, top). Apart from classical methods, greener alternatives by solvent-free permanganate oxidation were provided to access ABs carrying, for example, *para*-chloro substituents, but also di-*ortho*-*para*-methyl residues (Scheme 3.1, bottom).

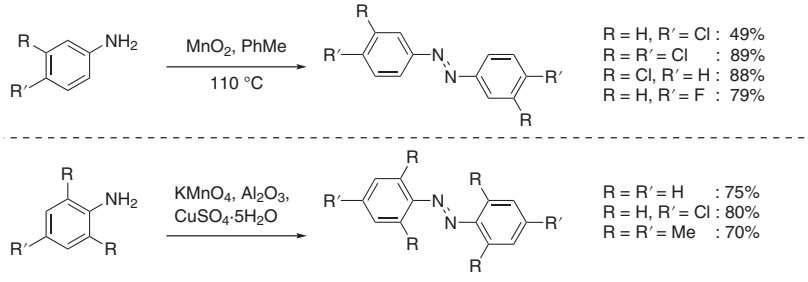


**Scheme 3.1** Oxidation of anilines with $MnO_2$ and $KMnO_4$.

The oxidation of anilines sometimes suffers from poor yields in dependency on the substitution pattern. For example, the oxidation of 2,4,6-trichloroaniline using NaOCl as oxidant afforded the tetra-*ortho*-chloro AB (**Cl4**) only in 19% yield (Scheme 3.2, left). Hence, the development of new and alternative methods is still under investigation and provides new solutions for specific synthetic problems. An approach to access different tetra-*ortho*-chloro ABs of the type **Cl4** was recently introduced by the Trauner group using a palladium-catalyzed late-stage C–H chlorination (Scheme 3.2, right) [24].

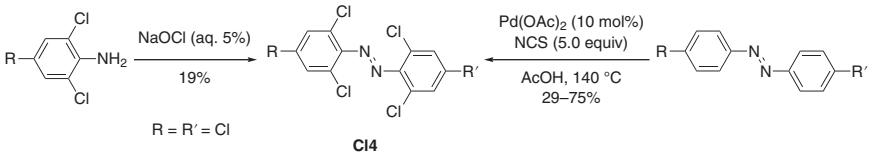


**Scheme 3.2** Oxidation of anilines and late-stage C–H chlorination for the synthesis of tetra-*ortho*-chloro azobenzene.

### 3.2.2 Azo Coupling

The most widespread and classical (1860, Grieß) method to access unsymmetrical ABs is still the azo coupling, based on the initial diazotization of an aniline derivative, which is then supposed to react with an electron-rich aromatic nucleophile carrying typical electron-donating groups (EDGs) such as ethers or amines (Scheme 3.3). The reaction proceeds usually in a short time and good yields; nevertheless, the temperature of the reaction has to be controlled and the stability of the diazonium salt has to be carefully considered as some of these are explosive. For example, diazonium chlorides are unstable – decomposing explosively when they are stored at a temperature above 5 °C, whereby tetrafluoroborates or hexafluorophosphates show higher stability in the solid state and can even be stored for longer periods.

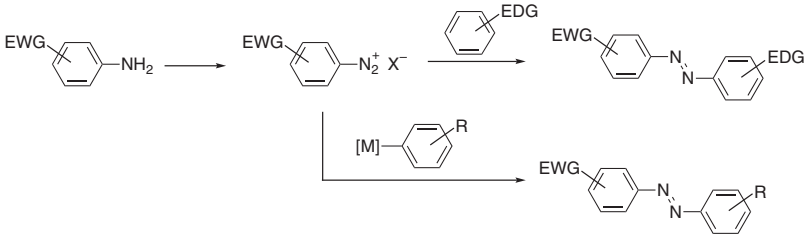


**Scheme 3.3** Azo coupling of diazonium salts and electron-rich aromatics.

Due to the electron-donating character of the nucleophile, the azo coupling occurs in *para*-position to the donor group. When this position is already occupied by another functional group, *ortho*-substitution is favored instead. An alternative is the reaction of diazonium salts with organometallics such as Grignard, lithium, or zinc reagents (see also Scheme 3.7).

### 3.2.3 Mills Reaction

Another classical method for the synthesis of unsymmetrical AB derivatives was developed by Mills and includes the reaction between an aromatic nitroso derivative and anilines under acetic conditions (Scheme 3.4). The nitroso compound was first synthesized by the oxidation of an aromatic methylhydroxyl amine,

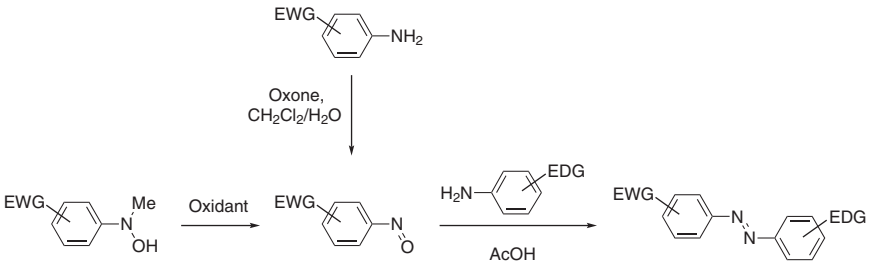


**Scheme 3.4** Mills reaction starting of the aromatic nitroso compound with anilines. The nitroso compound can be prepared by oxidation of aromatic methylhydroxyl amines or anilines.

whereby many oxidants are described in the literature, e.g. *tert*-butyl hypochlorite, $FeCl_3$, *m*-CPBA, or $H_2O_2$ in the presence of rhenium, tungsten, or molybdenum catalysts (Scheme 3.4, left). Nevertheless, the nitrosoarene is often only obtained in low yields, because competing side reactions such as the decomposition of the hydroxylamine, the overoxidation of the nitroso to nitro compound, or the condensation of the hydroxylamine and the nitro compound are difficult to control. To overcome these drawbacks, heterogeneous two-phase systems such as Oxone® in a mixture of $CH_2Cl_2$ and $H_2O$ were developed. These separate the less water-soluble nitrosoarene from the *N*-hydroxylamine intermediates and the aniline derivate and prevent therefore the condensation reaction (Scheme 3.4, top).

Variants of the Mills reaction include the deoxygenation of aromatic nitro compounds under basic reaction conditions to form the nitroso derivative, which reacts then with *N*-acylamines, or the reaction of nitroso derivatives with triphenylarsine phenylamine as a nucleophile. The latter reacts upon heating with the nitroso compound in a Wittig-type mechanism giving the corresponding azo compound (Scheme 3.5).

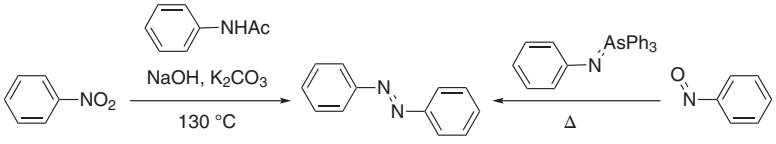


**Scheme 3.5** Modified reaction conditions of the Mills Reaction.

### 3.2.4 Modern Methods

A plethora of new methods arises in the current literature accessing azobenzenes including the usage of metal–organic reagents, late-stage C–H activation reactions, metal catalysts as well as electrocatalytic approaches from which only selected examples will be presented in the following. A particular focus relies on the synthesis of tetra-*ortho*-substituted ABs, as the yields are often unsatisfying when classical methods are applied (Scheme 3.6).

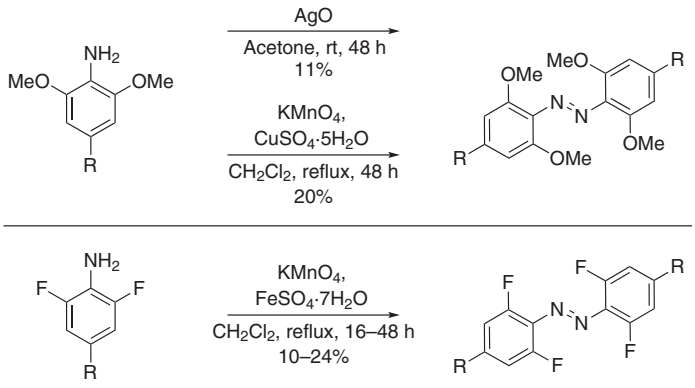


**Scheme 3.6** Classical synthetic methods toward tetra-*ortho*-substituted azobenzenes.

In addition to the *ortho*-chlorination of ABs to access tetra-*ortho*-chloroazobenzenes (Scheme 3.2) [24], Feringa and coworkers proposed to use a directed *ortho*-lithiation of the aromatic precursor and its subsequent reaction with aryldiazonium salts (Scheme 3.7). This approach accesses symmetric and unsymmetrical ABs in improved yields ranging from 77% to 92% but lacks a broad functional group tolerance as they have to be compatible with lithium organyls [25].

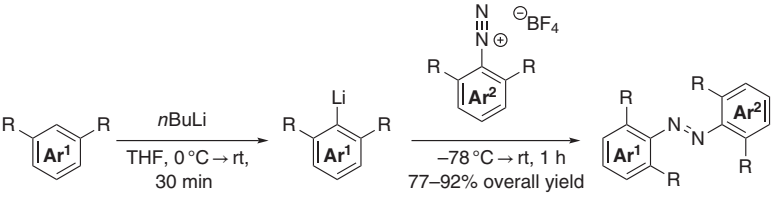


**Scheme 3.7** Novel synthetic methods toward tetra-*ortho*-substituted azobenzenes based on the addition of lithium organyls to diazonium compounds.

Lin et al. showed that symmetrical ABs can be easily synthesized by an oxidative homocoupling in a one-step procedure starting from aniline derivatives using the stable and inexpensive reagents *N*-chlorosuccinimide (NCS) and 1,8-diazabicyclo [5.4.0]undec-7-ene (DBU) (Scheme 3.8). The protocol includes the synthesis of several tetra-*ortho*-fluoroazobenzenes in good yields of c. 60% [26].

Mellah and coworker reported on an electrocatalytic approach based on the reduction of nitroarenes toward ABs using electrogenerated samarium diiodide

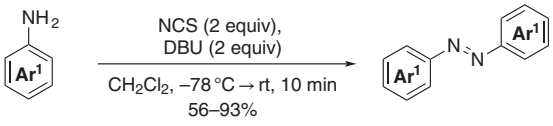


**Scheme 3.8** Oxidative coupling of aniline derivatives for the synthesis of symmetric azobenzenes.

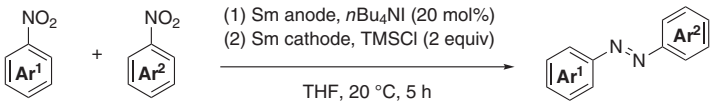


**Scheme 3.9** Novel synthetic methods for azobenzenes.

as a reducing reagent (Scheme 3.9). This method allows accessing a variety of symmetrical ABs bearing different kinds of functional groups in all positions, but also unsymmetrical ABs by using different molar ratios (1,3 of $Ar^1$-$NO_2$/$Ar^2$-$NO_2$). This includes di-*ortho*-substituted ABs in general as well as the tetra-*ortho*-methylazobenzenes [27].

## 3.3 Visible Light-Activated Azobenzenes as Photoswitches

Since UV light is highly energetic and hence, detrimental to the surroundings and sometimes even to the photoswitch itself, several strategies have been developed to avoid the irradiation with UV light and replace it with visible light or even near-infrared (NIR) light.

In principle, three different strategies divided by their mechanism were developed so far. The first strategy is based on the combination of a photoswitch with a photosensitizer such as a two-photon fluorophore, a triplet sensitizer, or an upconverting nanoparticle that can absorb the irradiated light and transfer the energy to the molecular switch. The latter can happen through different modes of action, e.g. Förster resonance energy transfer, triplet–triplet transfer, or simple emission and reabsorption.

The second strategy involves redox reactions where a sensitizer is excited either by irradiation or electrochemically and initiates the catalytic chain through photoinduced electron transfer.

The third and most direct approach tries to engineer the direct photoexcitation by influencing the energy gap between the highest occupied molecular orbital (HOMO) and the lowest occupied molecular orbital (LUMO) by the molecular design. This can be achieved by the extension of the π system resulting in a redshift of the π→π* band. Since the n→π* band is only slightly affected, the absorption bands of the two isomers overlap, and thus, the isomers cannot be addressed selectively [4]. Hence, the incorporation of EWGs or EDGs to influence the energy of the orbitals represents the preferred approach (Figure 3.2). Besides, so-called push–pull systems in which one ring of the ABs bears an EWG, while the other an EDG, were investigated. In this case, the π→π* and n→π* bands are overlapping as well, making a light-driven control of the isomerization processes impossible. Besides, it is worth mentioning that half-lives of the respective *Z*-isomers are rather short and typically range from nanoseconds to seconds. For an early example, see reference [28].

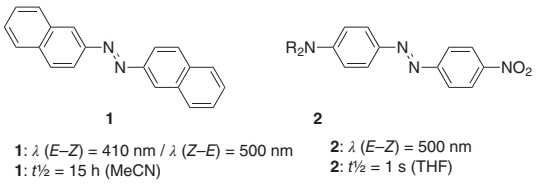


**Figure 3.2** Examples for red-shifted azobenzenes by the extension of the π system (left) or a push–pull substitution (right).

### 3.3.1 The Effect of Electron-Donating Groups on Direct Photoexcitation

Several EDGs such as alkyl, amino, methoxy, or thioalkyl residues were incorporated at all positions of the AB structure. Systematic studies on the design of ABs with EDG showed however that the *ortho*-substitution was superior over the *meta*-substitution as the thermal half-life time of the *cis*-isomer in the latter case was too short for most of applications (μs for *meta* in contrast to s for the *ortho*). When adding electron-donating alkyl groups to all four *ortho*-positions, a small separation of the n→π* transition between the *cis*- and *trans*-isomer was observed. The *ortho*-alkylation also led to longer thermal half-lives, which was attributed to the steric clashes between the substituents and the n-orbital of azo nitrogen. By the substitution with stronger EDGs such as amino groups, the absorption wavelength could be shifted toward longer wavelengths and thermal relaxation times in the range of seconds to minutes in water. The degree of the donating effect of the amine was determined by the character of the amino group. A six-membered piperidine residue, for example, caused a loss of $sp^2$ character on the azo nitrogen due to the steric interactions, which was not the case for the five-membered pyrrolidine residue or an acyclic amine. As an undesired side effect of the electron-rich nature of the AB, photobleaching occurred [29] (Figure 3.3).

To avoid photobleaching, less electron-donating methoxy groups were installed at all four *ortho*-positions of an amidoazobenzene **OMe4** (Figure 3.4). This also shifted the n→π* absorption band for the *trans*-isomer to higher wavelengths and led therefore to a separation of the transition bands between the *cis*- and *trans*-isomers ($\Delta\lambda_{n\rightarrow\pi^*} = 35$ nm). This can be explained by the comparison of the relative energies of the orbitals of each isomer. As the HOMO, located at the azo nitrogen, is close to the electron-rich oxygen atom of the methoxy group in the *trans*-isomer, its

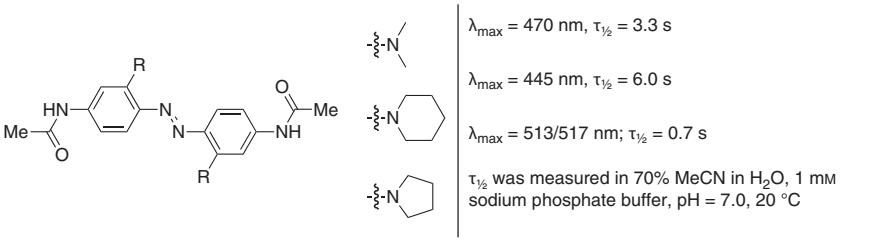


**Figure 3.3** *Ortho*-substituted aminoazobenzenes and their selected physical properties.

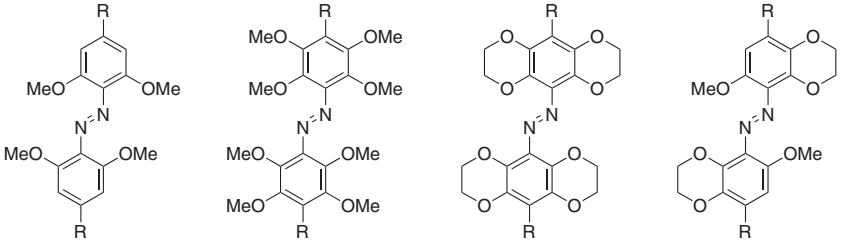


**Figure 3.4** Overview of azobenzenes bearing methoxy groups and/or dioxane rings.

relative energy is higher than in the unsubstituted AB. As a result, the required energy for the *trans*→*cis* isomerization based on the n→π* transition is decreased. For the *cis*-isomer, the methoxy group does not influence the lone pair, which is why **OMe4** shows a similar transition band to its parent compound. This *cis*-isomer was thermally stable with a half-life of 53 hours allowing that both isomers can be readily photogenerated and maintained in the dark granting, for example, the spatial localization of the *cis*-isomer in vivo. Additionally, no photobleaching or photo-oxidation occurred as the photoswitch survived multiple cycles of isomerization and constant high-intensity irradiation with a green light. To tune the (photo)physical properties, a variety of derivatives based on the same concept were explored [30–33]. According to computational studies, the functionalization of all *ortho*- and *meta*-positions of the AB with methoxy groups (**OMe8**) is supposed to lead to a loss of conjugation due to the steric clash of the methoxy groups. Therefore, the conformation was locked by the introduction of 1,4-dioxane moieties. Because of the poor solubility of azobenzene **DOM4**, only one dioxane ring per aryl residue could be attached (**DOM2**). The absorbance maximum of the *trans*-isomer was even further red-shifted to near 600 nm with a clear separation of the n→π* transition of the two isomers. By the nature of the chosen amine R in *the para*-position, the wavelength maximum was affected, but also – and even more importantly – the azonium p$K_a$. This might diminish the absorbance as the azonium and the ammonium species can coexist at physical pH having both different photophysical properties. Regarding their application in biological systems, their sensitivity toward reduction limits their usage to extracellular processes [34].

### 3.3.2 The Effect of Electron-Withdrawing Groups on Direct Photoexcitation

As was the case for EDGs, numerous studies have been carried out to investigate the effect of EWGs on ABs. *Ortho*-EWGs can stabilize both the n orbital of the *cis*-isomer and the π* orbitals of both isomers. This leads to an increased energy of the n→π* transition band for the *cis*-isomer of *ortho*-EWG substituted ABs and hence, in a blue shift of the n→π* band, while the transition energy of the corresponding *trans*-isomer is lowered, and as consequence, a redshift for n→π* transition band is observed compared with the unsubstituted ABs (Figure 3.5).

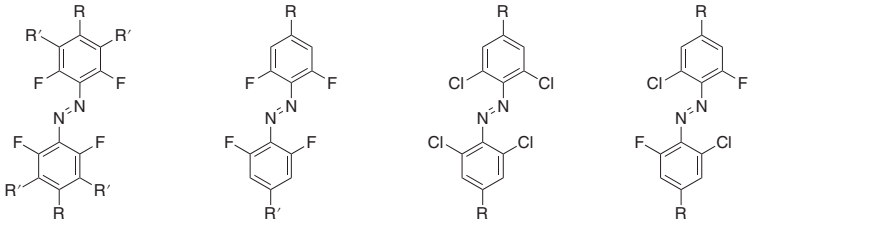


**Figure 3.5** Overview of selected examples of fluoro- and chloroazobenzenes.

As a consequence, the two n→π* transition bands of *ortho*-tetrafluoroazobenzene **F4** are well separated (42 nm) allowing the use of visible light $\lambda = 410$ nm for the $E \rightarrow Z$ isomerization and $\lambda > 500$ nm for the reverse $Z \rightarrow E$ isomerization accompanied with high quantum yields. An interesting feature of these *ortho*-fluoro substituted ABs is their planarity as well as the enhanced thermal stability of the *cis*-form due to the lowered energy of the n orbital. As expected, ABs bearing only two *ortho*-fluorine substituents cause a smaller splitting than **F4**, whereby the opposite effect of an enhanced splitting did not occur when additional fluorine atoms were added (**F6**, **F8**, or **F10**). EDGs lead to a less effective splitting of the n→π* bands and were hence not further investigated. Regarding the photoconversions, best performances were attained for *ortho*-tetrafluoroazobenzenes bearing either amide (**F4-diamide**) or ester groups (**F4-diester**), which additionally facilitate the attachment of biological systems. All fluoro-substituted ABs show longer thermal half-lives of the *cis*-isomer than the unsubstituted AB whereby symmetrical ABs with four or six fluorine atoms (**F4** and **F6**) showed half-lives of more than 90 hours in MeCN at 60 °C. Nevertheless, the studies revealed that *meta*-substitution should be avoided if one is seeking photoswitches with long thermal half-lives. Among the *ortho*-fluoroazobenzenes, **F4-ester** represents the best compromise between high photoconversions in both directions and high thermal stability including also the possibility of an attachment to other systems [35]. For completeness, it is worth mentioning that Woolley et al. investigated at the same time *ortho*-tetrachloroazobenzene **Cl4** with an even higher red-shifted absorption for the n→π* transition, but higher thermal relaxation rates [31, 36].

In most recent reports, the relation between substituents of the *ortho*-tetrachloroazobenzene **Cl4** and the photophysical properties has been in-depth investigated, both spectroscopically and theoretically [20]. Another group demonstrated deeply red-shifted azobenzenes with mixed chloro- and fluoro-substituents in the *ortho*-positions (e.g. **Cl2F2**), less synthetically challenging and more thermally stable than the original **Cl4** structure [21]. Finally, it was shown that appending the **F4** structure with conjugated unsaturated substituents (–CHO or –C=C– groups) in *para*-positions (R, R′) (but not in *meta*-) also results in bathochromic shift of the photoisomerization wavelength. In that case, red light (>630 nm) irradiation can

**Table 3.1** Spectroscopic data including the separation of the n→π* transition bands ($\Delta\lambda_{n\rightarrow\pi^*}$), the composition of the photostationary state (PSS) when irradiated at $\lambda > 500$ nm ($PSS_{(Z)}$) and $\lambda = 410$ nm ($PSS_{(E)}$), and the experimental half-lives $\tau_{1/2}$ in MeCN at 60 °C by Bléger et al. [35].

| Compound | $\Delta\lambda_{n\rightarrow\pi^*}$ (nm) | $PSS_{(Z)}$ (%) | $PSS_{(E)}$ (%) | $\tau_{1/2}$ (h) |
|---|---|---|---|---|
| AB | 14 | — | — | 4 |
| F4 | 42 | 86 | 91 | 92 |
| F6 | 36 | 94 | 91 | 95 |
| F8 | 43 | 92 | 92 | 27 |
| F10 | 40 | 91 | 90 | — |
| F4-diester | 50 | 90 | 97 | 15 |
| F4-ester | 44 | 95 | 95 | 30 |
| F4-diamide | 50 | 92 | 96 | 22 |

Source: Data from Bléger et al. [35].

produce up to 82% of the respective *cis*-isomer (for the bis-aldehyde) with thermal stability similar to the unsubstituted azobenzene (*cis*-isomer with $t_{1/2} = 3.2$ hour at 60 °C in MeCN, see Table 3.1) [37].

### 3.3.3 Further Modification Leading to Visible Light Photoswitches

There are also further approaches to tune the photoswitching properties of ABs. One of these is based on a C2-bridged azobenzene (diazocines), which also has distinct and well-separated n→π* transition bands (Scheme 3.10). In this case, the *cis*-form is thermodynamically more stable than the *trans*-form as the short bridge strains and distorts the latter. The *cis*→*trans* isomerization occurs rapidly with blue light from the near-UV range (λ = 380–400 nm) while the backward reaction is induced by green light, both in very high quantum yields [38]. A more detailed reference can be found in the chapter of Rainer Herges and coworkers [38–59].

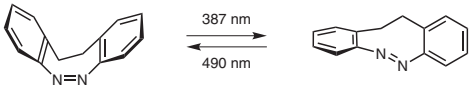


**Scheme 3.10** C2-bridged azobenzene.

Another class of visible-light addressable AB photoswitches are boron-coordinated azo compounds (Scheme 3.11). The introduction of different functional groups in the *para*-position of **azo1** gave a series of AB derivatives emitting green, yellow, orange, and red fluorescence [60, 61]. As the isomerization reaction was locked due to the coordination of the boron atom to the lone pair of the azo nitrogen, structural changes were required. Hence, azo compounds with the general structure **azo2** were synthesized showing well-separated $\pi_{nb}\rightarrow\pi^*$ transitions for the *trans*-

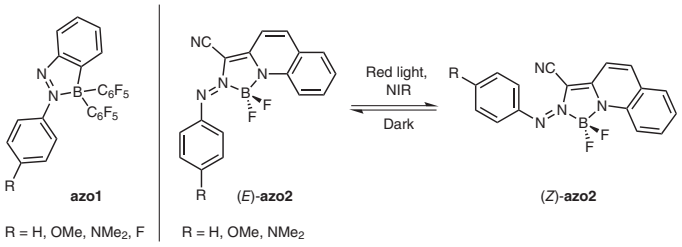


**Scheme 3.11** Boron-coordinated azobenzenes.

and the *cis*-isomer in the visible part of the light spectrum, which is caused by the complexation of the azo group with $BF_2$ in combination with an extended conjugation of the diazo π-electrons. By increasing the electron density through EDGs in the *para*-position of **azo2**, the absorption bands were shifted to the red and even NIR region. Besides the high photoconversion and high photoisomerization quantum yields, the **azo2**-compounds were relatively stable regarding their half-lives ($\tau_{1/2} \approx 10$ hours/20 minutes in deoxygenated/regular $CH_2Cl_2$) and toward reduction by glutathione [62, 63].

### 3.3.4 Complex Molecular and Supramolecular Systems Containing Azobenzenes

Azobenzenes have been incorporated into molecular systems with various degree of complexity. Many specific examples have been discussed in the following chapters of this book. However, we will list here a few representative examples: diazocine homologues with increasing sizes of the central ring [52], further macrocyclic azobenzenes [44, 64, 65], azobenzene-containing crown-ethers [66], or cyclic binaphthyls [67]. One selected example of a complex azobenzene-containing macrocyclic system is shown below (Scheme 3.12) [68].

Over the last year, a vast number of phototriggered materials based on azobenzene photoisomerization have been demonstrated, just to mention photochromic hydrogels [69–73], actuators for upconverting luminescence [74], molecular machines [75], polymers [76], and complex systems [77, 78], as well as photoswitchable MOF [6–10, 79–85] – many discussed in-depth in the following chapters in the Section II of this book.

## 3.4 Applications of Azobenzenes in Biological Systems

Visible light is an interesting tool to study biochemical processes in vivo without external interference. The usage of light offers additionally the possibility to investigate biochemical pathways and interactions with high spatial and temporal precision. Alternative methods do not show spatiotemporal control since genetic approaches often lack temporal resolution, while small molecules can be better temporally controlled but suffer from the target selectivity. To use visible light as an efficient tool, the biomolecule must carry a light-sensitive group such as an AB fulfilling

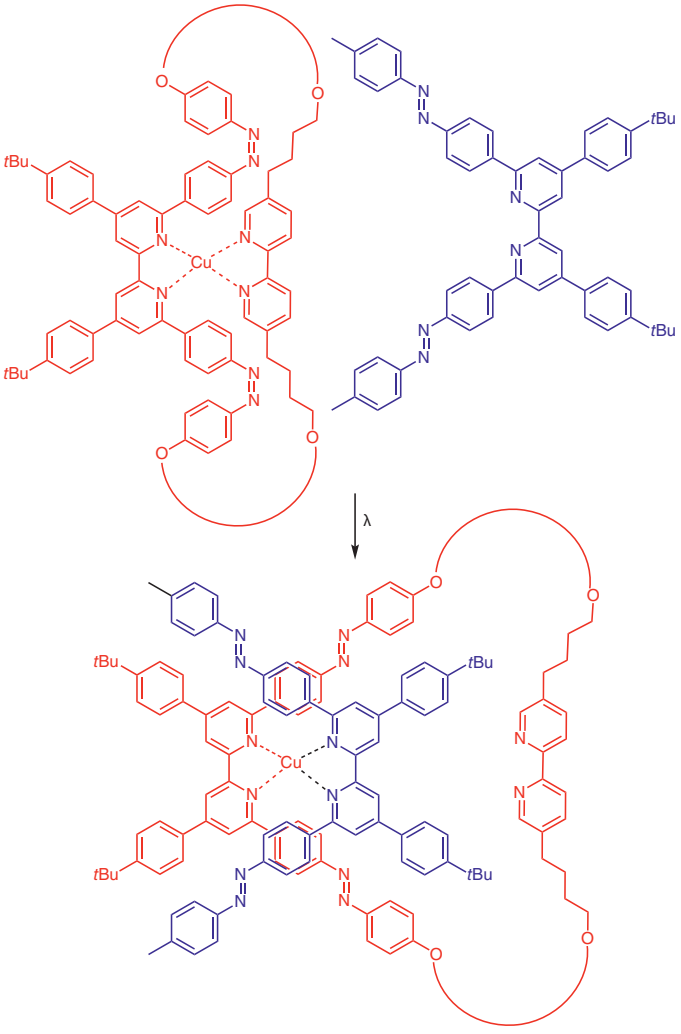


**Scheme 3.12** Switching of an azo crown ether copper complex. Source: Modified from Umeki et al. [68].

certain requirements to be applicable in biological systems. The light-sensitive group has to alter the target upon irradiation in a substantial manner to detect the changes in its biological activity caused, for example, by conformational changes. Second, the absorption of light in an efficient manner is required, meaning that the group either shows a high molar extinction coefficient or undergoes a two-photon cross section. This aspect also includes that the photochemistry of the envisioned modification is efficient to avoid the application of high dosages of light. The selected photoswitch should isomerize with visible or NIR light (between 400 and 900 nm), preferentially in the so-called therapeutic window (600–900 nm), which is only negligibly absorbed by soft body parts or hemoglobin. Hence, that light can penetrate cells

and tissues easily to induce the photoswitch, while UV light in contrast is strongly absorbed by biomolecules such as NADH and scattered by the skin. Another, but not less important, requirement for the photosensitive group is its stability under biological conditions during as well as after the irradiation, meaning that photosensitive groups should be nontoxic and stable toward hydrolysis and reduction. To fulfill these requirements, the core structure of ABs has been modified (see above).

Noteworthy, the reversibility of the photoisomerization of ABs makes them superior toward competing approaches such as the "caging" approach. So far, most applications of ABs to photomodulate biological systems were reported in vitro. For in vivo applications, the target has to be addressed selectively by the AB, or it has to be modified with the AB and then introduced into the living system, which both pose significant technical challenges. In the following section, a selection of examples will be presented to give a rough overview of the milestones that were achieved so far, but also the limitations of ABs as photoswitches.

One application of AB photoswitches to photomodulate properties of biopolymers is based on the idea to control structures of peptides to alter their function by changing their secondary/tertiary structure. As cysteine residues are rarely found in proteins and are easy to introduce by standard molecular biology techniques, cysteine residues are commonly utilized to attach ABs to peptides and proteins. The AB derivative incorporates two chloroacetamide groups to provide chemoselective covalent binding with the cysteine sulfhydryl groups in presence of other aminoacid side chains. Additionally, sulfonate groups were included into the structure of the azobenzene for higher solubility. The peptides were rationally designed after the calculations of the end-to-end distances of both isomers. The UV irradiation of a helical peptide that contains the cross-linked cysteines at the positions $i$ and $i + 11$ matching to the end-to-end distance range of the *trans*-AB leads to a decrease in helicity as the *cis*-isomer has a smaller end-to-end distance and is therefore not compatible with the helical structure (Figure 3.6). This strategy was later transferred to naturally occurring peptides such as the DNA-recognition helix to enable the photo-control of DNA binding by conformational changes [86].

The isomerization of AB has also been used in vivo to open and close pores in cellular membranes to control the transport of ions. One example was presented by Kramer and Trauner [87] using the photoisomerization of ABs to control $K^+$ channels in neurons of rats to switch action potential firing on and off (Figure 3.7). As these voltage-gated $K^+$ channels are blocked by the binding of quaternary ammonium ions, the ABs were equipped with triethylammonium residues on one side. On the other side, a maleimide linker was attached to ensure selective binding to cysteine that was introduced to the channel by exogenous expression replacing Glu422. By irradiation with $\lambda = 380$ nm, photoisomerization is induced shortening the end-to-end distance of the AB about 7 Å, which opens the channel and hence, allows the ions to pass. When the light of $\lambda = 500$ nm is applied, the photoisomerization process is reversed and the channel is blocked again.

Another example of the control of ion channels by photoisomerization is based on the allosteric control of an active site by a remote regulatory binding site and was illustrated for the ionotropic glutamate receptor (iGluR). Therefore, an AB was

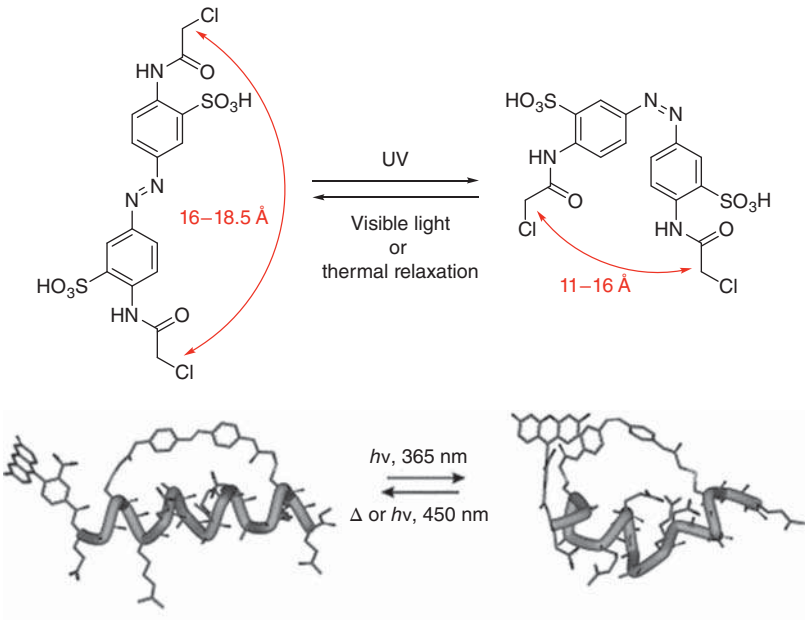


**Figure 3.6** Photocontrol of the α-helical content in secondary structures of peptides connected via two cysteines in position *i* and *i* + *11* to an azobenzene derivative. Source: Adapted with permission from Beharry et al. [86].

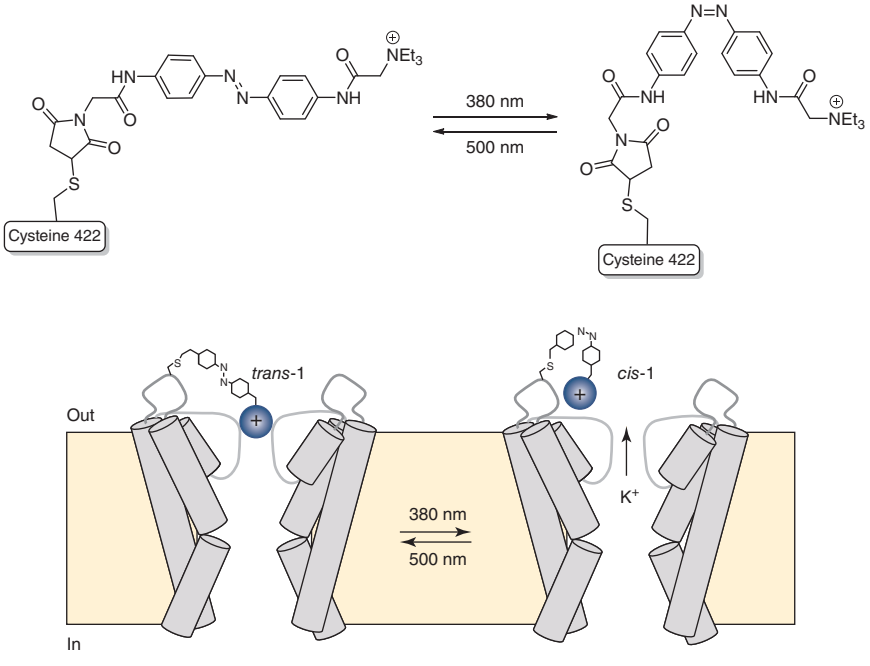


**Figure 3.7** Photocontrol of a $K^+$ channel in the cellular membrane of neurons based on the photoisomerization of an azobenzene derivative, which is connected via a maleimide to the Cys422 of the ion channel. Source: Adapted with permission from Banghart et al. [87].

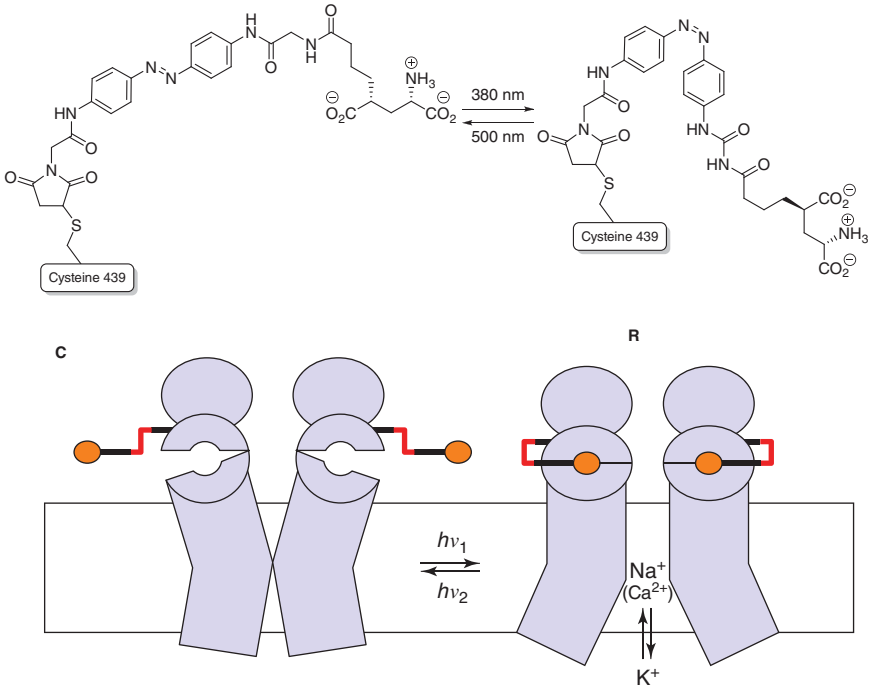


**Figure 3.8** Photocontrol of the ionotropic ion glutamate receptor by the conformational changes of an azobenzene derivative connected to the ion channel via a Cys439. Source: Source: Reprinted with permission from Volgraf et al. [88].

equipped with a maleimide residue enabling the covalent binding to the protein via a cysteine residue (again inserted by mutation, L439C) and a glutamate unit on the other side serving as an agonist for the receptor. Upon irradiation with $\lambda = 380$ nm, photoisomerization occurs allowing the interaction of the glutamate residue with the active site of the protein receptor, which leads to conformational changes of the protein and hence, to channel gating (Figure 3.8). Other applications are directed to other channels [88].

To circumvent systemic and environmental side effects of drugs, photoswitchable drugs with spatial and temporal control over its activity with light are part of numerous investigations in the emerging field of photopharmacology. In this context, Feringa et al. developed a photo-responsive, antibacterial diaminopyrimidine whose activity can be controlled by light with specific wavelengths. The antibacterial diaminopyrimidine unit was attached to a tetra-*ortho*-chloroazobenzene. Whereas (*E*)-**Cl4pyr** is nearly inactive with an $MIC_{50} > 80\,\mu M$, the irradiation with red light ($\lambda = 652$ nm) forms (*Z*)-**Cl4pyr** and leads to bacteriostasis (inhibition of bacteria growth without their destruction) down to 20 μM with an $MIC_{50} = 80\,\mu M$, which corresponds to an eightfold difference before and after irradiation [89]. (Figure 3.9).

Other examples included visible-light-responsive peptide backbone photoswitches [73, 90], intercalators for photocontrol of DNA [91], reversible and

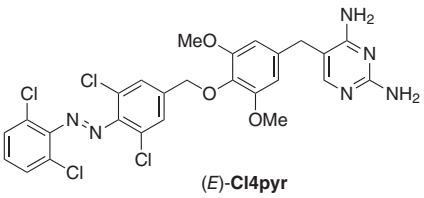


(*E*)-**Cl4pyr**

**Figure 3.9** First example of a photo-responsive antibacterial agent switchable with visible light.

tunable photoswitching of protein function [92], red-shifted azobenzene [93], or azo-bridges [94].

## 3.5 Conclusion

In this chapter, we have summarized the basic photophysical properties, photochromism, and most common synthetic methods of azobenzenes, which are among the most common molecular photoswitches. They are embedded in a variety of functional molecular scaffold and used to construct phototriggered materials and compounds with photomodulated biological activity. Selected classes and examples of such materials will be discussed in the Sections II and III of this book, respectively. Here, we attempted to provide the reader with a brief overview and more detailed references to a few selected topics. While the standard azobenzene chromophore poses numerous limitations on its application scope, the last decade witnessed numerous reports on AB structures optimized for particular applications, especially in hydrophilic biological systems. This was enabled by efficient few-step synthetic strategies available for this particular scaffold, as well as its photostability and chemical robustness.

## References

1 Hartley, G.S. (1937). Cis form of azobenzene. *Nature* 140: 281.
2 Beharry, A.A. and Woolley, G.A. (2011). Azobenzene photoswitches for biomolecules. *Chem. Soc. Rev.* 40 (8): 4422–4437.
3 Dong, M., Babalhavaeji, A., Samanta, S. et al. (2015). Red-shifting azobenzene photoswitches for in vivo use. *Acc. Chem. Res.* 48 (10): 2662–2670.
4 Bléger, D. and Hecht, S. (2015). Visible-light-activated molecular switches. *Angew. Chem. Int. Ed.* 54 (39): 11338–11349.
5 Merino, E. and Ribagorda, M. (2012). Control over molecular motion using the cis–trans photoisomerization of the azo group. *Beilstein J. Org. Chem.* 8: 1071–1090.
6 Wang, Z., Grosjean, S., Bräse, S., and Heinke, L. (2015). Photoswitchable adsorption in metal-organic frameworks based on polar guest-host interactions. *ChemPhysChem* 16 (18): 3779–3783.
7 Dommaschk, M., Peters, M., Gutzeit, F. et al. (2015). Photoswitchable magnetic resonance imaging contrast by improved light-driven coordination-induced spin state switch. *J. Am. Chem. Soc.* 137 (24): 7552–7555.

8 Fang, L., Chen, S., Zhang, Y., and Zhang, H. (2011). Azobenzene-containing molecularly imprinted polymer microspheres with photoresponsive template binding properties. *J. Mater. Chem.* 21 (7): 2320–2329.

9 Modrow, A., Zargarani, D., Herges, R., and Stock, N. (2011). The first porous MOF with photoswitchable linker molecules. *Dalton Trans.* 40 (16): 4217–4222.

10 Wang, Z., Heinke, L., Jelic, J. et al. (2015). Photoswitching in nanoporous, crystalline solids: an experimental and theoretical study for azobenzene linkers incorporated in MOFs. *Phys. Chem. Chem. Phys.* 17 (22): 14582–14587.

11 Adam, V., Prusty, D.K., Centola, M. et al. (2018). Expanding the toolbox of photoswitches for DNA nanotechnology using arylazopyrazoles. *Chem. Eur. J.* 24 (5): 1062–1066.

12 Calbo, J., Weston, C.E., White, A.J.P. et al. (2017). Tuning azoheteroarene photoswitch performance through heteroaryl design. *J. Am. Chem. Soc.* 139 (3): 1261–1274.

13 Simeth, N.A., Crespi, S., Fagnoni, M., and Koenig, B. (2018). Tuning the thermal isomerization of phenylazoindole photoswitches from days to nanoseconds. *J. Am. Chem. Soc.* 140 (8): 2940–2946.

14 Weston, C.E., Richardson, R.D., Haycock, P.J. et al. (2014). Arylazopyrazoles: azoheteroarene photoswitches offering quantitative isomerization and long thermal half-lives. *J. Am. Chem. Soc.* 136 (34): 11878–11881.

15 Fuchter, M. (2021). Arylazoheterocycles. In: *Molecular Photoswitches – Synthesis, Properties and Applications* (ed. Z. Pianowski). Wiley-VCH.

16 Heindl, A.H., Becker, J., and Wegner, H.A. (2019). Selective switching of multiple azobenzenes. *Chem. Sci.* 10 (31): 7418–7425.

17 Vela, S., Scheidegger, A., Fabregat, R., and Corminboeuf, C. (2020). Tuning the thermal stability and photoisomerization of azoheteroarenes through macrocycle strain. *ChemRxiv* 1–10.

18 Manna, D., Udayabhaskararao, T., Zhao, H., and Klajn, R. (2015). Orthogonal light-induced self-assembly of nanoparticles using differently substituted azobenzenes. *Angew. Chem. Int. Ed.* 54 (42): 12394–12397.

19 Zhao, F., Grubert, L., Hecht, S., and Bleger, D. (2017). Orthogonal switching in four-state azobenzene mixed-dimers. *Chem. Commun.* 53 (23): 3323–3326.

20 Lameijer, L.N., Budzak, S., Simeth, N.A. et al. (2020). General principles for the Design of visible-light-responsive photoswitches: tetra-ortho-chloro-azobenzenes. *Angew. Chem. Int. Ed.* 59: 21663–21670.

21 Konrad, D.B., Savasci, G., Allmendinger, L. et al. (2020). Computational design and synthesis of a deeply red-shifted and bistable azobenzene. *J. Am. Chem. Soc.* 142 (14): 6538–6547.

22 Merino, E. (2011). Synthesis of azobenzenes: the coloured pieces of molecular materials. *Chem. Soc. Rev.* 40 (7): 3835–3853.

23 Hamon, F., Djedaini-Pilard, F., Barbot, F., and Len, C. (2009). Azobenzenes—synthesis and carbohydrate applications. *Tetrahedron* 65 (49): 10105–10123.

24 Konrad, D.B., Frank, J.A., and Trauner, D. (2016). Synthesis of redshifted azobenzene photoswitches by late-stage functionalization. *Chem. Eur. J.* 22 (13): 4364–4368.


**25** Hansen, M.J., Lerch, M.M., Szymanski, W., and Feringa, B.L. (2016). Direct and versatile synthesis of red-shifted azobenzenes. *Angew. Chem. Int. Ed.* 55 (43): 13514–13518.

**26** Antoine John, A. and Lin, Q. (2017). Synthesis of azobenzenes using *N*-chlorosuccinimide and 1,8-diazabicyclo[5.4.0]undec-7-ene (DBU). *J. Org. Chem.* 82 (18): 9873–9876.

**27** Zhang, Y.-F. and Mellah, M. (2017). Convenient electrocatalytic synthesis of azobenzenes from nitroaromatic derivatives using SmI2. *ACS Catal.* 7 (12): 8480–8486.

**28** Robertson, P.W. (1913). Isomerism of p-Azophenol. *J. chem. Soc. Trans.* 103: 1472–1479.

**29** Sadovski, O., Beharry, A.A., Zhang, F., and Woolley, G.A. (2009). Spectral tuning of azobenzene photoswitches for biological applications. *Angew. Chem. Int. Ed.* 48 (8): 1484–1486.

**30** Samanta, S., Babalhavaeji, A., Dong, M.-x., and Woolley, G.A. (2013). Photoswitching of ortho-substituted azonium ions by red light in whole blood. *Angew. Chem. Int. Ed.* 52 (52): 14127–14130.

**31** Samanta, S., Beharry, A.A., Sadovski, O. et al. (2013). Photoswitching azo compounds in vivo with red light. *J. Am. Chem. Soc.* 135 (26): 9777–9784.

**32** Dong, M., Babalhavaeji, A., Hansen, M.J. et al. (2015). Red, far-red, and near infrared photoswitches based on azonium ions. *Chem. Commun.* 51 (65): 12981–12984.

**33** Beharry, A.A., Sadovski, O., and Woolley, G.A. (2011). Azobenzene photoswitching without ultraviolet light. *J. Am. Chem. Soc.* 133 (49): 19684–19687.

**34** Dong, M., Babalhavaeji, A., Collins, C.V. et al. (2017). Near-infrared photoswitching of azobenzenes under physiological conditions. *J. Am. Chem. Soc.* 139 (38): 13483–13486.

**35** Bléger, D., Schwarz, J., Brouwer, A.M., and Hecht, S. (2012). *o*-Fluoroazobenzenes as readily synthesized photoswitches offering nearly quantitative two-way isomerization with visible light. *J. Am. Chem. Soc.* 134 (51): 20597–20600.

**36** Rullo, A., Reiner, A., Reiter, A. et al. (2014). Long wavelength optical control of glutamate receptor ion channels using a tetra-ortho-substituted azobenzene derivative. *Chem. Commun.* 50 (93): 14613–14615.

**37** Leistner, A.-L., Kirchner, S., Karcher, J. et al. (2021). Fluorinated azobenzenes switchable with red light. *Chem. Eur. J.* 27 (31): 8094–8099.

**38** Böckmann, M., Doltsinis, N.L., and Marx, D. (2010). Unraveling a chemically enhanced photoswitch: bridged azobenzene. *Angew. Chem. Int. Ed.* 49 (19): 3382–3384.

**39** Herges, R. (2021). Diazocines – Bridged Azobenzenes with Unusual Properties. In: *Molecular Photoswitches – Synthesis, Properties and Applications*. Wiley-VCH.

**40** Siewertsen, R., Neumann, H., Buchheim-Stehn, B. et al. (2009). Highly efficient reversible Z-E photoisomerization of a bridged azobenzene with visible light through resolved S1(n$\pi^*$) absorption bands. *J. Am. Chem. Soc.* 131 (43): 15594–15595.


**41** Siewertsen, R., Schoenborn, J.B., Hartke, B. et al. (2011). Superior Z E and E Z photoswitching dynamics of dihydrodibenzodiazocine, a bridged azobenzene, by S1(nπ*) excitation at $\lambda$ = 387 and 490 nm. *Phys. Chem. Chem. Phys.* 13 (3): 1054–1063.

**42** Boeckmann, M., Doltsinis, N.L., and Marx, D. (2012). Enhanced photoswitching of bridged azobenzene studied by nonadiabatic ab initio simulation. *J. Chem. Phys.* 137 (22): 22A505/1–22A505/10.

**43** Samanta, S., Qin, C., Lough, A.J., and Woolley, G.A. (2012). Bidirectional photocontrol of peptide conformation with a bridged azobenzene derivative. *Angew. Chem. Int. Ed.* 51 (26): 6452–6455, S6452/1–S6452/10.

**44** Deo, C., Bogliotti, N., Metivier, R. et al. (2016). A visible-light-triggered conformational diastereomer photoswitch in a bridged azobenzene. *Chem. Eur. J.* 22 (27): 9092–9096.

**45** Hammerich, M., Schuett, C., Staehler, C. et al. (2016). Heterodiazocines: synthesis and photochromic properties, trans to cis switching within the bio-optical window. *J. Am. Chem. Soc.* 138 (40): 13111–13114.

**46** Liu, L., Wang, Y., and Fang, Q. (2017). New insights into mechanistic photoisomerization of ethylene-bridged azobenzene from ab initio multiple spawning simulation. *J. Chem. Phys.* 146 (6): 064308/1–064308/8.

**47** Glock, P., Broichhagen, J., Kretschmer, S. et al. (2018). Optical control of a biological reaction-diffusion system. *Angew. Chem. Int. Ed.* 57 (9): 2362–2366.

**48** Jun, M., Joshi, D.K., Yalagala, R.S. et al. (2018). Confirmation of the structure of trans-cyclic azobenzene by X-ray crystallography and spectroscopic characterization of cyclic azobenzene analogs. *ChemistrySelect* 3 (9): 2697–2701.

**49** Schehr, M., Hugenbusch, D., Moje, T. et al. (2018). Synthesis of mono-functionalized S-diazocines via intramolecular Baeyer-Mills reactions. *Beilstein J. Org. Chem.* 14: 2799–2804.

**50** Cabre, G., Garrido-Charles, A., Gonzalez-Lafont, A. et al. (2019). Synthetic photoswitchable neurotransmitters based on bridged azobenzenes. *Org. Lett.* 21 (10): 3780–3784.

**51** Lentes, P., Stadler, E., Roehricht, F. et al. (2019). Nitrogen bridged diazocines: photochromes switching within the near-infrared region with high quantum yields in organic solvents and in water. *J. Am. Chem. Soc.* 141 (34): 13592–13600.

**52** Maier, M.S., Huell, K., Reynders, M. et al. (2019). Oxidative approach enables efficient access to cyclic azobenzenes. *J. Am. Chem. Soc.* 141 (43): 17295–17304.

**53** Reynders, M., Matsuura, B., Berouti, M. et al. (2019). PHOTACs enable optical control of protein degradation. *ChemRxiv* 1–34.

**54** Stadler, E., Tassoti, S., Lentes, P. et al. (2019). In situ observation of photoswitching by NMR spectroscopy: a photochemical analogue to the exchange spectroscopy experiment. *Anal. Chem.* 91 (17): 11367–11373.

**55** Thapaliya, E.R., Zhao, J., and Ellis-Davies, G.C.R. (2019). Locked-azobenzene: testing the scope of a unique photoswitchable scaffold for cell physiology. *ACS Chem. Neurosci.* 10 (5): 2481–2488.


**56** Trads, J.B., Huell, K., Matsuura, B.S. et al. (2019). Sign inversion in photopharmacology: incorporation of cyclic Azobenzenes in photoswitchable potassium channel blockers and openers. *Angew. Chem. Int. Ed.* 58 (43): 15421–15428.

**57** Zhu, Q., Wang, S., and Chen, P. (2019). Diazocine derivatives: a family of azobenzenes for photochromism with highly enhanced turn-on fluorescence. *Org. Lett.* 21 (11): 4025–4029.

**58** Burk, M.H., Schroeder, S., Moormann, W. et al. (2020). Fabrication of diazocine-based photochromic organic thin films via initiated chemical vapor deposition. *Macromolecules* 53 (4): 1164–1170.

**59** Trauner, D., Reynders, M., Matsuura, B. et al. (2020). Preparation of photoswitchable PROTACs for treating diseases and inducing selective degradation of a target protein. WO2020172655A1.

**60** Yoshino, J., Furuta, A., Kambe, T. et al. (2010). Intensely fluorescent azobenzenes: synthesis, crystal structures, effects of substituents, and application to fluorescent vital stain. *Chem. Eur. J.* 16 (17): 5026–5035.

**61** Yoshino, J., Kano, N., and Kawashima, T. (2007). Synthesis of the most intensely fluorescent azobenzene by utilizing the B–N interaction. *Chem. Commun.* 6: 559–561.

**62** Yang, Y., Hughes, R.P., and Aprahamian, I. (2012). Visible light switching of a BF2-coordinated Azo compound. *J. Am. Chem. Soc.* 134 (37): 15221–15224.

**63** Yang, Y., Hughes, R.P., and Aprahamian, I. (2014). Near-infrared light activated azo-BF2 switches. *J. Am. Chem. Soc.* 136 (38): 13190–13193.

**64** Takaishi, K., Kawamoto, M., Muranaka, A., and Uchiyama, M. (2012). Fusion of photochromic reaction and synthetic reaction: photoassisted cyclization to highly strained chiral azobenzenophanes. *Org. Lett.* 14 (13): 3252–3255.

**65** Lin, C., Maisonneuve, S., Metivier, R., and Xie, J. (2017). Photoswitchable carbohydrate-based macrocyclic azobenzene: synthesis, chiroptical switching, and multi-stimuli-responsive self-assembly. *Chem. Eur. J.* 23 (60): 14996–15001.

**66** Shiga, M., Takagi, M., and Ueno, K. (1980). Azo-crown ethers. The dyes with azo group directly involved in the crown ether skeleton. *Chem. Lett.* 8: 1021–1022.

**67** Takaishi, K., Muranaka, A., Kawamoto, M., and Uchiyama, M. (2012). Photoinversion of cisoid/transoid binaphthyls. *Org. Lett.* 14 (1): 276–279.

**68** Umeki, S., Kume, S., and Nishihara, H. (2011). Switching of molecular insertion in a cyclic molecule via photo- and thermal isomerization. *Inorg. Chem.* 50 (11): 4925–4933.

**69** Tamesue, S., Takashima, Y., Yamaguchi, H. et al. (2010). Photoswitchable supramolecular hydrogels formed by cyclodextrins and azobenzene polymers. *Angew. Chem. Int. Ed.* 49 (41): 7461–7464. S7461/1-S7461/17.

**70** Dai, L., Lu, J., Kong, F. et al. (2019). Reversible photo-controlled release of bovine serum albumin by azobenzene-containing cellulose nanofibrils-based hydrogel. *Adv. Compos. Hybrid Mater.* 2 (3): 462–470.

**71** Velema, W.A., Stuart, M.C.A., Szymanski, W., and Feringa, B.L. (2013). Light-triggered self-assembly of a dichromonyl compound in water. *Chem. Commun.* 49 (44): 5001–5003.


**72** Accardo, J.V. and Kalow, J.A. (2018). Reversibly tuning hydrogel stiffness through photocontrolled dynamic covalent crosslinks. *Chem. Sci.* 9 (27): 5987–5993.

**73** Karcher, J. and Pianowski, Z.L. (2018). Photocontrol of drug release from supramolecular hydrogels with green light. *Chem. Eur. J.* 24 (45): 11605–11610.

**74** Jiang, Z., Xu, M., Li, F., and Yu, Y. (2013). Red-light-controllable liquid-crystal soft actuators via low-power excited upconversion based on triplet-triplet annihilation. *J. Am. Chem. Soc.* 135 (44): 16446–16453.

**75** Browne, W.R., Pijper, D., Pollard, M.M., and Feringa, B.L. (2009). Chiroptical molecular switches and motors. In: *Switching at the nanoscale* (ed. D.B. Amabilino), 349–390. Wiley-VCH Verlag GmbH & Co. KGaA.

**76** Yue, Y., Norikane, Y., Azumi, R., and Koyama, E. (2018). Light-induced mechanical response in crosslinked liquid-crystalline polymers with photoswitchable glass transition temperatures. *Nat. Commun.* 9 (1): 1–8.

**77** Weis, P., Wang, D., and Wu, S. (2016). Visible-Light-Responsive Azopolymers with Inhibited π-π Stacking Enable Fully Reversible Photopatterning. *Macromolecules* 49 (17): 6368–6373.

**78** Yan, H., Qiu, Y., Wang, J. et al. (2020). Wholly visible-light-responsive host-guest supramolecular gels based on methoxy azobenzene and β-cyclodextrin dimers. *Langmuir* 36 (26): 7408–7417.

**79** Fan, C.B., Liu, Z.Q., Gong, L.L. et al. (2017). Photoswitching adsorption selectivity in a diarylethene-azobenzene MOF. *Chem. Commun.* 53 (4): 763–766.

**80** Heinke, L., Cakici, M., Dommaschk, M. et al. (2014). Photoswitching in two-component surface-mounted metal-organic frameworks: optically triggered release from a molecular container. *ACS Nano* 8 (2): 1463–1467.

**81** Heinke, L., Tu, M., Wannapaiboon, S. et al. (2015). Surface-mounted metal-organic frameworks for applications in sensing and separation. *Microporous Mesoporous Mater.* 216: 200–215.

**82** Meng, H., Zhao, C., Nie, M. et al. (2018). Optically controlled molecular metallofullerene magnetism via an azobenzene-functionalized metal-organic framework. *ACS Appl. Mater. Interfaces* 10 (38): 32607–32612.

**83** Prasetya, N., Donose, B.C., and Ladewig, B.P. (2018). A new and highly robust light-responsive Azo-UiO-66 for highly selective and low energy post-combustion $CO_2$ capture and its application in a mixed matrix membrane for $CO_2/N_2$ separation. *J. Mater. Chem. A* 6 (34): 16390–16402.

**84** Wang, Z., Mueller, K., Valasek, M. et al. (2018). Series of photoswitchable azobenzene-containing metal-organic frameworks with variable adsorption switching effect. *J. Phys. Chem. C* 122 (33): 19044–19050.

**85** Heinke, L. (2021). Light-triggered metal-organic frameworks. In: *Molecular Photoswitches – Synthesis, Properties and Applications* (ed. Z. Pianowski). Wiley-VCH.

**86** Beharry, A.A., Wong, L., Tropepe, V., and Woolley, G.A. (2011). Fluorescence imaging of azobenzene photoswitching in vivo. *Angew. Chem. Int. Ed.* 50 (6): 1325–1327.

**87** Banghart, M., Borges, K., Isacoff, E. et al. (2004). Light-activated ion channels for remote control of neuronal firing. *Nat. Neurosci.* 7 (12): 1381–1386.


**88** Volgraf, M., Gorostiza, P., Numano, R. et al. (2006). Allosteric control of an ionotropic glutamate receptor with an optical switch. *Nat. Chem. Biol.* 2: 47–52.

**89** Wegener, M., Hansen, M.J., Driessen, A.J.M. et al. (2017). Photocontrol of antibacterial activity: shifting from UV to red light activation. *J. Am. Chem. Soc.* 139 (49): 17979–17986.

**90** Albert, L., Penalver, A., Djokovic, N. et al. (2019). Modulating protein-protein interactions with visible-light-responsive peptide backbone photoswitches. *ChemBioChem* 20 (11): 1417–1429.

**91** Heinrich, B., Bouazoune, K., Wojcik, M. et al. (2019). ortho-Fluoroazobenzene derivatives as DNA intercalators for photocontrol of DNA and nucleosome binding by visible light. *Org. Biomol. Chem.* 17 (7): 1827–1833.

**92** Luo, J., Samanta, S., Convertino, M. et al. (2018). Reversible and tunable photoswitching of protein function through genetic encoding of azobenzene amino acids in mammalian cells. *ChemBioChem* 19 (20): 2178–2185.

**93** John, A.A., Ramil, C.P., Tian, Y. et al. (2015). Synthesis and site-specific incorporation of red-shifted azobenzene amino acids into proteins. *Org. Lett.* 17 (24): 6258–6261.

**94** Hoppmann, C., Maslennikov, I., Choe, S., and Wang, L. (2015). In situ formation of an azo bridge on proteins controllable by visible light. *J. Am. Chem. Soc.* 137 (35): 11218–11221.

## 4 Diazocines: Photoswitches with Excellent Photophysical Properties and Inverted Stabilities

Rainer Herges and Pascal Lentes

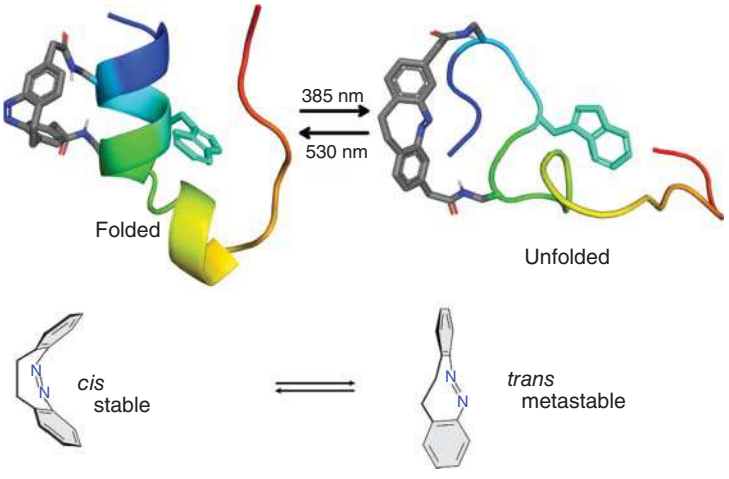


**Characteristic Features**

Diazocines are bridged azobenzenes with superior properties for application in a number of fields, such as light-controlled protein folding, photopharmacology, and materials sciences.

### First reported

R. Siewertsen, R. Herges, F. Temps et al. (2009). Highly efficient reversible Z–E photoisomerization of a bridged azobenzene with visible light through resolved S1($n\pi^*$) absorption bands. *J. Am. Chem. Soc*. 131, 15594–15595.

### Key references

M. Hammerich, C. Schütt, C. Stähler, and P. Lentes (2016). Heterodiazocines: synthesis and photochromic properties, *trans* to *cis* switching within the bio-optical window. *J. Am. Chem. Soc*. 138, 13111–13114.

P. Lentes, E. Stadler, F. Röhricht, and A. Brahms (2019). Nitrogen bridged diazocines: photochromes switching within the near-infrared region with high quantum yields in organic solvents and in water. *J. Am. Chem. Soc*.: 13592–13600.

G. Cabré, A. Garrido-Charles, À. González-Lafont, and W. Moormann (2019). Synthetic photoswitchable neurotransmitters based on bridged azobenzenes. *Org. Lett*. 21, 3780–3784.

# 4

# Diazocines: Photoswitches with Excellent Photophysical Properties and Inverted Stabilities

*Rainer Herges and Pascal Lentes*

*Christian-Albrechts-Universität zu Kiel, Otto-Diels-Institut für Organische Chemie, Otto-Hahn-Platz 4, 24098 Kiel, Germany*

## 4.1 Photophysical Properties and Conformations of Parent Diazocine

Diazocines (11,12-dihydrodibenzo[*c*,*g*][1,2]diazocines) are azobenzenes that are bridged by an ethylene linker connecting the *ortho* positions of both phenyl rings. Parent diazocine (**1**, $-CH_2-CH_2$-bridged) was first discovered in 1910 during an investigation on benzidination reactions [1]. About 100 years after the first report, it was rediscovered as a photoswitch with largely superior properties compared to the parent azobenzene system [2]. The 8-membered central "ocine" core exhibits two configurations, a stable *Z* structure in boat conformation and a metastable *E* isomer (Figure 4.1). As expected for an unsaturated 8-membered ring, the *Z*-boat structure is about 8–10 kcal mol$^{-1}$ more stable than the *E* configuration, which has a strain energy of ∼17 kcal mol$^{-1}$ [3, 4]. Diazocines, therefore, have an inverse thermal stability compared to azobenzene, which has a stable *E* configuration [5].

UV-spectra and photoisomerization mechanisms of diazocine also differ from azobenzene. Parent *E* and *Z* azobenzene exhibit ππ* transitions at 314 nm (*E*) and 275 nm (*Z*). Upon irradiation into the ππ* band of the *E* isomer of azobenzene with UV light of 290–350 nm, the *Z* isomer is formed (92%). Back-isomerization is achieved by irradiation into the nπ* band of the *Z* isomer with violet light (∼420 nm). However, the photoconversion is incomplete (79% *E*) because the nπ* bands of both isomers strongly overlap (*E*: $\lambda_{max}$ 445 nm, *Z*: $\lambda_{max}$ 435 nm). Nevertheless, a reasonable photoconversion yield is observed since the molar extinction coefficients of the nπ* bands of both isomers differ (*E*: 390, *Z*: 1100 L mol$^{-1}$ cm$^{-1}$). The difference in molar absorption arises from the fact that *E* azobenzene is planar and the nπ* transition is symmetry forbidden, whereas the *Z* isomer is slightly distorted [6, 7].

Diazocines exhibit a rather different photoswitching mechanism. In contrast to azobenzene, the nπ* bands of *Z* and *E* diazocine are clearly separated ($\lambda_{max}$: 404 and 490 nm) and have higher molar extinction coefficients (*Z*: 479; *E*: 770 L$^{-1}$ mol cm$^{-1}$)

*Molecular Photoswitches: Chemistry, Properties, and Applications*,
First Edition. Edited by Zbigniew L. Pianowski.


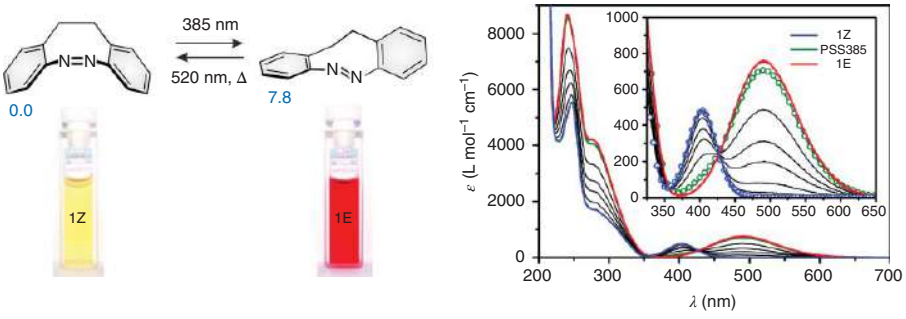


**Figure 4.1** Left: Structures of parent diazocine **1** in the *Z*-boat conformation and the *E*-twist conformation. Relative energies $E_{rel}$ in kcal mol$^{-1}$ are given in blue color. Right: UV spectra of *Z*-diazocine (blue), photostationary equilibrium upon irradiation with 385 nm (PSS 385, green, and pure *E*-diazocine [red]) [2]. Source: Adapted with permission of the American Chemical Society from Siewertsen et al. [2].

because both isomers are non-planar. Hence, the two nπ* bands can be selectively addressed with violet light (385–400 nm, $Z \rightarrow E$ isomerization) and green or yellow light (520–600 nm, $E \rightarrow Z$) (see Figure 4.1 and Table 4.1) [2]. Photoconversion yields are excellent ($E \rightarrow Z > 99\%$ and $Z \rightarrow E \sim 92\%$). The metastable $E$ configuration thermochemically isomerizes back to the stable $Z$ isomer with a half-life of 4.5 hours at 28.5 °C in hexane.

With quantum yields of 0.7 ($Z \rightarrow E$) at 385 nm and 0.9 ($E \rightarrow Z$) at 520 nm [4], parent diazocine **1** well competes with the most efficient natural systems such as rhodopsin (see Figure 4.2). Azobenzene exhibits significantly smaller quantum yields of 0.47 ($Z \rightarrow E$, 436 nm) and 0.16 ($E \rightarrow Z$, 317 nm) [9].

Efficient photochemical conversions, high quantum yields, and switching wavelengths in the visible region lead to very high efficiencies in the conversion of light to chemical energy (7.6% at 400 nm). Substituted diazocines attain efficiencies of up to 18.1% [8], which are the highest among photochromic compounds. Unexpectedly, the isomerization dynamics of parent diazocine **1** ($S_1$ life-time ~30–40 fs) are one order of magnitude faster than the isomerization of azobenzene ($S_1$ life-time ~365–400 fs). The ultrafast excited state decay is counter-intuitive since the bridge reduces the flexibility of the molecule [5, 10, 11].

As compared to azobenzene, the conformational degrees of freedom in diazocine are reduced. The ethylene bridge locks the rotation of the phenyl rings. Nevertheless, several temperature-dependent conformational movements complicate the interpretation of nuclear magnetic resonance (NMR) spectra (Figure 4.3). The stable $Z$ isomer undergoes a boat inversion, which is slow on the NMR timescale at room temperature. The calculated activation barrier is 33.3 kcal mol$^{-1}$ at the M062X(D3)/def2TZVP level of density-functional theory (DFT). The metastable $E$-diazocine exists in a twist or a chair conformation, whereby the $E$-twist conformation is about 2–3 kcal mol$^{-1}$ more stable than the $E$-chair conformation. Hence, the predominant $E$ species is the twisted form. DFT calculations revealed that both $E$-conformations (twist and chair) are rotamers and are in equilibrium with each other by a crank-type movement. Due to its $C_2$ symmetry, both $E$-twist structures are enantiomers. The chair and the twist, however, do not directly interconvert with their enantiomeric structure, the intermediate structure of the chair–chair conversion is the twist form and vice versa [12].

The nπ*-transition of the $E$-chair is almost isoenergetic with the nπ*-transition of the $Z$-boat ($\lambda_{max} \sim 400$ nm), while the nπ*-transition of the $E$-twist conformation is strongly bathochromic shifted ($\lambda_{max} = 490$ nm). This is an important finding. Upon designing new diazocine derivatives, care should be taken that the $E$-twist conformation is more stable than the $E$-chair conformation. If the $E$-chair would be the predominant species in the conformational equilibrium, this would decrease the photoconversion yield drastically due to an overlap of the $Z$-boat nπ*-transition and the $E$-chair nπ*-transition [3, 4].

The switching properties of substituted azobenzenes may differ from the unsubstituted parent system, albeit diazocines are less susceptible to substitution effects. An overview of recent literature [13–17] indicates that the energies of

**Table 4.1** Comparison of the photophysical properties of azobenzene, parent diazocine **1**, and heteroatom-bridged diazocines **18–22**.

| | **Parent azobenzene** | **Parent diazocine 1** | **O-diazocine 18** | **S-diazocine 19** | **NH-diazocine 20** | **NMe-diazocine 21** | **NAc-diazocine 22** |
|---|---|---|---|---|---|---|---|
| Stable isomer | *E* | *Z* | *Z* | *Z* | *Z* | *Z* | *Z* |
| $\Delta E_{rel}$ [a)] | −12.4 | 7.9 | 12.5 | 6.2 | 11.0 | 9.0 | 9.2 |
| $\lambda_{max(Z)}$ [b)] | 435 nm (nπ*) | 404 nm (nπ*) | 385 nm (nπ*) | 405 nm (nπ*) | 409 nm (nπ*) | 401 nm (nπ*) | 398 nm (nπ*) |
| $\lambda_{max(E)}$ [b)] | 314 nm (ππ*) | 490 nm (nπ*) | 525 nm (nπ*) | 525 nm (nπ*) | 559 nm (nπ*) | 554 nm (nπ*) | 516 nm (nπ*) |
| $t_{1/2}$ | 4 h (60 °C) | 4.5 h (28.5 °C) | 89 s (20 °C) | 3.5 d (27 °C) | 131 s (25 °C) | 40 s (25 °C) | 27 min (25 °C) |
| $\Gamma_{Z\to E}$ [c)] | > 400 nm: 79% | 385 nm: 92% | 385 nm: 80% | 405 nm: 70% | 405 nm: 65% | 405 nm: 50% | 400 nm: 88% |
| $\Phi_{Z\to E}$ [d)] | 0.47 (436 nm) | 0.72 (385 nm) | N/A | 0.43 (405 nm) | 0.57 (400 nm) | N/A | 0.48 (400 nm) |
| $\Gamma_{E\to Z}$ [a)] | 317 nm: 90% | 520 nm: > 99% | 520 nm: > 99% | 520 nm: > 99% | 520–690 nm: > 99% | 520–740 nm: > 99% | 520–590 nm: > 99% |
| $\Phi_{E\to Z}$ [d)] | 0.16 (280 nm) | 0.9 (520 nm) | N/A | N/A | 0.8 (520 nm) | N/A | 0.85 (520 nm) |

a) $\Gamma_{Z\to E}$, $\Gamma_{E\to Z}$: conversion yields $Z \to E$ and $E \to Z$ at the photostationary states upon irradiation at the given wavelengths;
b) $\Delta E_{rel} = E_E - E_Z$ in kcal mol$^{-1}$, M06-2X(D3)/def2-TZVP;
c) $\lambda_{max(Z)}$, $\lambda_{max(E)}$: maximum absorption wavelengths of the excitations used for switching (nπ* or ππ*);
d) $\Phi_{Z\to E}$, $\Phi_{E\to Z}$: quantum yields determined at the given wavelengths.

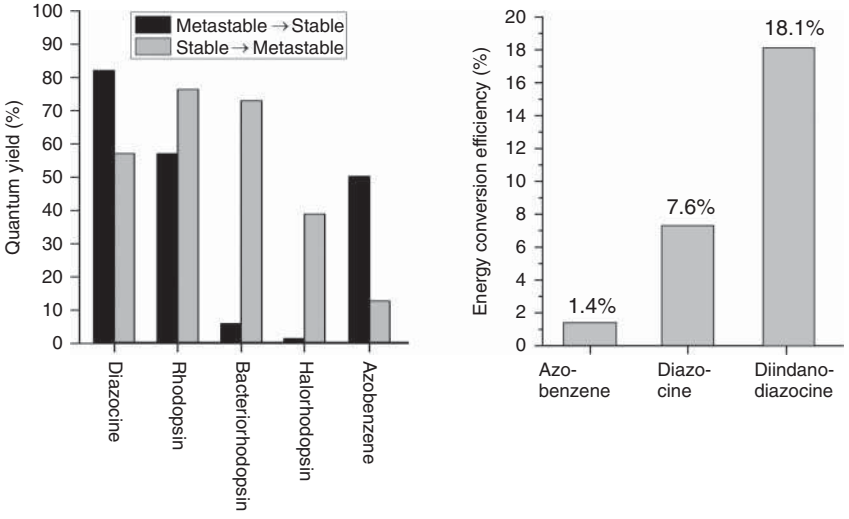


**Figure 4.2** Left: Switching quantum yields of diazocine, azobenzene, and selected natural systems. Right: Energy conversion efficiencies of light to chemical (strain) energy of azobenzene, diazocine, and a diazocine derivative [8].

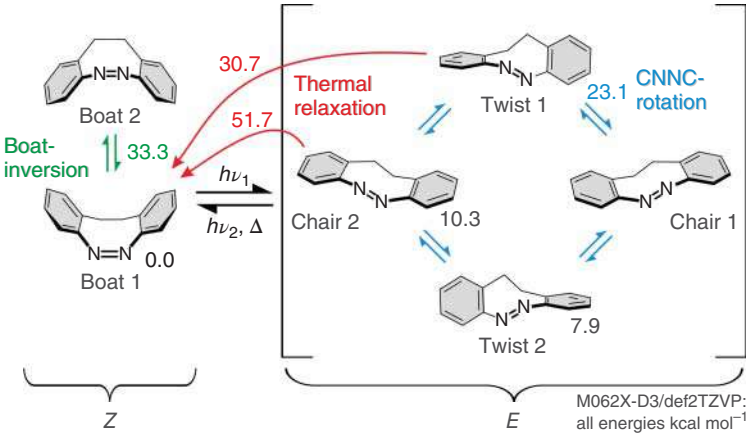


**Figure 4.3** Configurational and conformational space of the parent diazocine **1** [12]. Relative energies (relative to the most stable structure: *Z*-boat **1**) calculated at the M062X-D3/def2TZVP level of density functional theory are given. Numbers in black are minima, and numbers in green and blue color are transition-state energies.

the nπ*-transitions are not much affected by substitution, particularly if the substituents are in *meta* position with respect to the azo group (2,8-positions). The nπ*-transitions seem to be largely independent of the electronic nature of the diazocine. However, in contrast to the nπ*-transitions, the ππ*-transitions are shifting bathochromically if the π-system is enlarged, if it carries amino substituents or a push–pull substitution pattern. Large bathochromic shifts cause an overlap of the

*E* ππ*-transition with the *Z* nπ*-transition, and consequently the $Z \rightarrow E$ photostationary state decreases significantly (down to 18%: dithiophene diazocine) [13]. The ππ*-transitions are significantly affected by strong electron-donating substituents (e.g. $NH_2 > OMe$). A decoupling of these substituents from the electronic core (e.g. by inserting $CH_2$ groups) is the best strategy to retain the excellent photophysical properties of diazocines [18].

The photoconversion with visible light in both directions, the well-separated nπ*-transitions, the efficient photoconversion, the high quantum yields, and the ultrafast isomerization are outstanding properties of diazocines. Moreover, no fatigue over thousands of switching cycles was observed in the parent system. The substituted systems investigated so far are obviously long-term stable as well.

## 4.2 Synthesis of Diazocines

A key step of the synthesis of diazocines is the formation of the 8-membered ring. Cyclization can be accomplished by reduction [16, 19–21] of the nitro precursor **2** or oxidation [17] of the amino precursor **4** (Figure 4.4). Direct reduction to the diazocine with zinc or lead under milling was found to give low yields, which are hard to reproduce. Variable product distributions of azoxy, azo, and hydrazo derivatives are observed under reductive conditions, since the reduction is very sensitive to pH, the reducing reagent, or temperature. It is most convenient to reduce the nitro precursor **2** with zinc in basic solution to the hydrazine derivative **3** (58% yield) that can selectively be reoxidized with air in a copper-catalyzed reaction to the diazocine in quantitative yields. Oxidation of a dianiline precursor **4** to the diazocine **1** can be accomplished with yields up to 86% with peroxy reagents such as *m*CPBA [17]

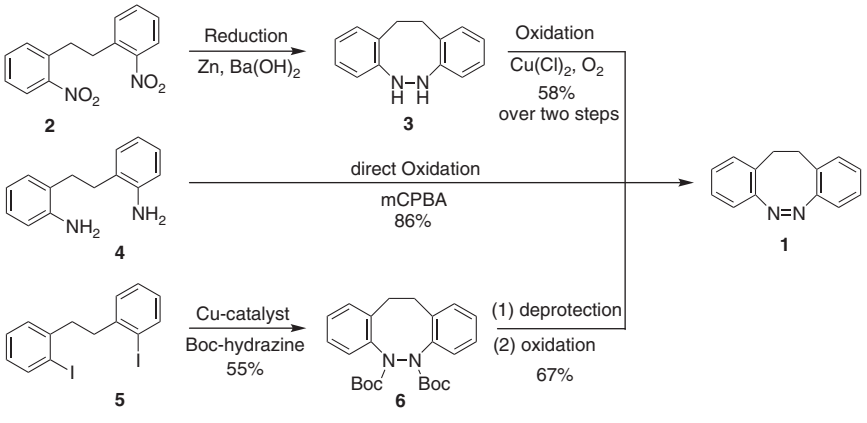


**Figure 4.4** Three strategies to close the 8-membered diazocine ring (azo-cyclization). Reductive approach (top): reduction of nitro precursor **2** via hydrazine **3** and reoxidation to diazocine **1**. Oxidative approach (middle): oxidation of amino precursor **4** with *m*CPBA or oxone. Cross-coupling approach (bottom): Ullmann–Goldberg reaction with Boc-hydrazine, followed by deprotection and oxidation of the free hydrazine.

or Oxone [22]. Another method is the C—N copper-catalyzed Ullmann–Goldberg coupling of 1,2-bis(*t*-butyloxycarbonyl)hydrazine with *o*-iodobibenzyl **5** (55% yield), followed by deprotection of the hydrazo compound **6** with TMSI and oxidation of the hydrazine with NBS in pyridine (67% yield). However, the yields of the cyclization vary strongly, dependent on the substrates (16–70%) [13]. All attempts to form the N=N bond first and to close the 8-membered ring by C—C bond formation in the last step, failed so far.

There is no electrophilic aromatic substitution with diazocines published; however, the aromatic bromination of the parent azoxy derivative was reported [20]. Substitution takes place at the phenyl ring distant from the $N^+$–$O^-$ group. Oxidation of unsymmetrically substituted diazocines and incomplete reduction of unsymmetrical bis-nitro precursors provide two isomeric azoxy compounds. Therefore, only symmetrically substituted diazocines are directly accessible via the "azoxy approach." There is a lack of general methods for the selective reduction of azoxy to azo groups. Each azoxy system requires tedious optimization of reducing agents and conditions. Frequently only moderate yields are obtained [23]. Therefore, substitution prior to cyclization, e.g. substitution of the anilines, or substitution of the nitro compounds and subsequent reduction to the anilines should be considered. Obviously, the reductive approach gives higher yields but is not always favorable.

The first step in diazocine synthesis is the formation of the ethylene bridge. Three general approaches were reported for C—C coupling – (a) Oxidative dimerization of *o*-nitrotoluenes [21], (b) Sonogashira cross-coupling [17], (c) Wittig reaction [15] (Figure 4.5).

The oxidative C—C bond formation (a) requires strongly basic conditions, since the methyl groups of the nitrotoluenes **7**, **8** have to be deprotonated. Substituents that are labile to strong bases or functional groups with more acidic protons than the methyl group in 2-position (e.g. $CH_2$-COR or amines/amides) are not compatible with this method. Moreover, the bridge formation leads to a statistical product distribution (**9**, **10**, **11**) if two different *o*-nitrotoluene molecules are connected. Monosubstituted bis(nitrophenyl)ethanes **9** are accessible by using a large excess of nitrotoluene **8**, which suppresses the self-coupling of the two substituted nitrotoluenes (**7** → **11**); however, self-addition of nitrotoluene might lead to problems to isolate the wanted unsymmetrical product **9** in the presence of large amounts of **10**. Symmetrically substituted bis(nitrophenyl)ethanes **11** are easily accessible in high yields. Moreover, a number of substituted *o*-nitrotoluenes are commercially available [8, 16, 21]. For the synthesis of unsymmetrically substituted dinitro diazocine precursors, the statistical approach **A** is often acceptable, but a C—C bond formation via cross-coupling (b) or Wittig reaction (c) might be favorable if the nitrotoluenes are less accessible or if they include functional groups that are base sensitive. Cross-coupling reactions under Sonogashira conditions (b) often lead to dehalogenation if the phenyl precursors (**12** and **13**) include further halogens (R = Br, I). Steric hindrance also impedes cross-coupling reactions. As an alternative, Wittig reaction is possible under metal-free conditions with a higher tolerance to bulky substituents [24]. Pathways (b) and (c) are resulting in an unsaturated

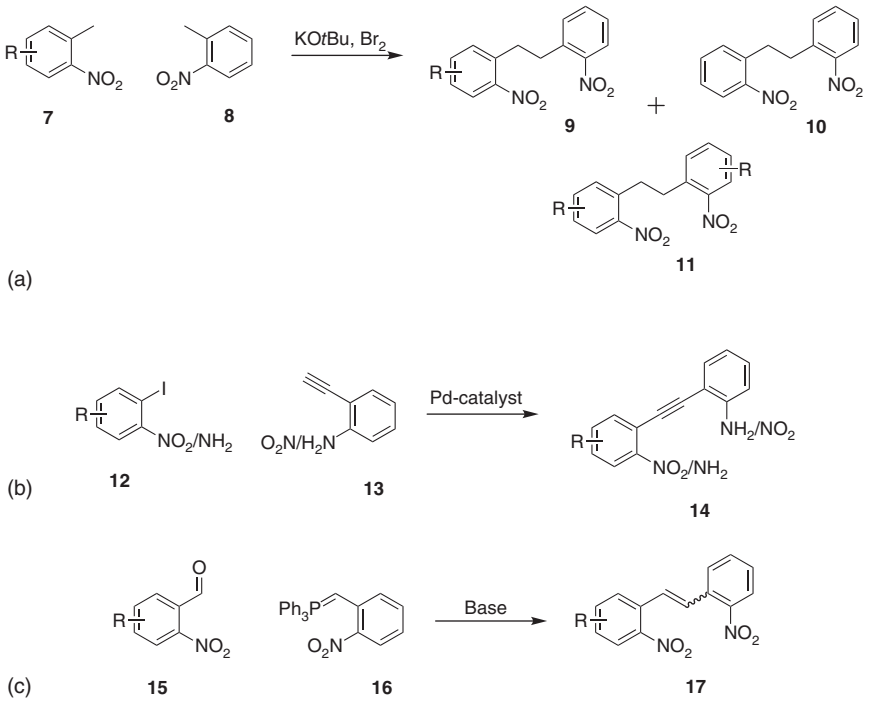


**Figure 4.5** Three C—C bond formation approaches to establish the ethylene bridging unit. (a) Oxidative C—C-coupling under basic conditions and addition of bromine, (b) Sonogashira cross-coupling reaction, (c) Wittig reaction.

bridge (**14**, **17**) that has to be reduced before the azo cyclization. For the complete reduction of stilbenes or tolanes to alkanes, catalytic hydrogenation (Pd/C) is the method of choice. However, aryl halides (R = Cl, Br, I) are partially reduced under these conditions, and therefore ways (b) and (c) are less suitable for the synthesis of halogenated diazocines (except R = F) [17]. The synthetic approach (a) starting from halogenated *o*-nitrotoluenes is most convenient for the preparation of symmetrically halogen-substituted diazocines [22]. Halogenated diazocines are an important starting point for further functionalization via crosscoupling reactions [25].

The synthetic strategies listed above allow the synthesis of a wide range of substituted diazocines [16, 17, 19, 22]. There are practically no functional group limitations. It is justified to state that the synthetic access to functionalized diazocines does not fall behind the well-elaborated preparation methods of azobenzenes. Diazocines for different applications are available or can be rationally designed.

## 4.3 Heteroatom-Bridged Diazocines

Substitution of one $CH_2$ group of the ethylene bridge by heteroatoms such as oxygen **18**, sulfur **19**, or nitrogen **20**–**22** (Figure 4.6) changes the flexibility of the bridge, and the electron-donating effects alter the photophysical properties of the

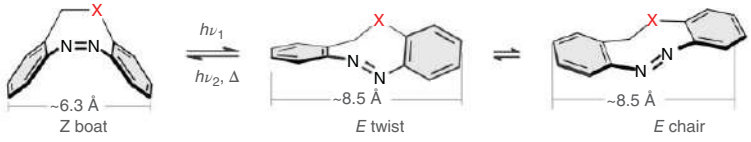


| | X | $E_{strain}$ Z | $E_{rel}$ Twist | $E_{rel}$ Chair |
|---|---|---|---|---|
| **1** | $CH_2$ | 16.3 | 7.6 | 10.5 |
| **2** | O | 19.5 | 12.5 | 15.4 |
| **3** | S | 16.5 | 5.1 | 5.1 |

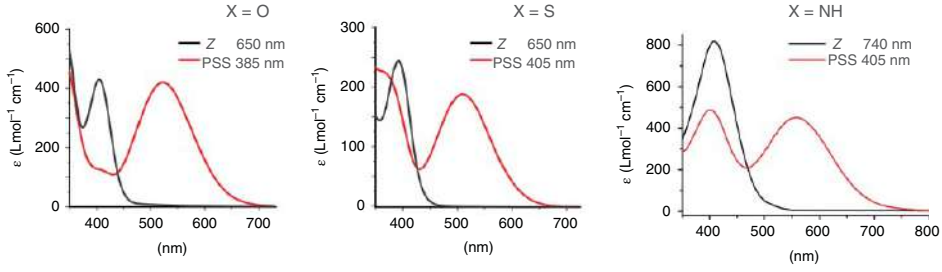


**Figure 4.6** Structures of heteroatom-bridged diazocines with their isodesmic strain energy ($E_{strain}$) and the relative energy differences ($E_{rel}$) of the different *E* conformations (M06-2X(D3)/def2-TZVP) [3, 4]. UV–vis spectra of the photostationary states of **18**, **19,** and **20** are given below. Source: Adapted with permission of the *American Chemical Society* from Hammerich et al. [3] (© 2016) and Lentes et al. [4] (© 2019).

diazocines (Table 4.1). The energy levels of the $Z \rightarrow E$ $n\pi^*$-transitions are slightly bathochromically shifted compared to parent diazocine **1**, which allows a $Z \rightarrow E$ isomerization with 400–405 nm (except O-diazocine **18**). The $E \rightarrow Z$ n$\pi^*$-transitions are strongly bathochromically shifted and a quantitative $E \rightarrow Z$ isomerization is still effective with wavelengths of >600 nm or even near-infrared (NIR) light [3, 4].

$Z \rightarrow E$ Photoconversion yields of S-diazocine **19** (70%) [3, 18], NH-diazocine **20** (60%), and NMe-diazocine **21** (50%) [4] were found to be limited by the presence of a significant amount of the *E*-chair conformation in the *E*-chair $\rightleftharpoons$ *E*-twist equilibrium, due to the overlap of the *Z*-boat and *E*-chair n$\pi^*$-transitions. In contrast to **19**, **20,** and **21**, parent diazocine **1**, O-diazocine **18,** or NAc-diazocine **22** does not suffer from this disadvantage. No significant amount of *E*-chair was observed by NMR or UV–vis spectroscopy.

A systematic investigation of the solvent dependence of the photophysical properties of $CH_2$–$CH_2$-bridged diazocines revealed that the separations of the *Z* and *E* n$\pi^*$-transitions are decreasing with increasing polarity of the solvent. In addition, there is a general trend that the quantum yields of $CH_2$–$CH_2$-bridged diazocines are favoring the $E \rightarrow Z$ and disfavor $Z \rightarrow E$ conversion with increasing solvent polarity. The two effects are systematically decreasing the photoconversion yields of the $CH_2$–$CH_2$-bridged diazocines from 92% in *n*-hexane to ∼50% in water. In case of S-diazocine **19**, there is a third effect that decreases $Z \rightarrow E$ conversion yields. The concentration of the *E* chair conformation is increasing with increasing solvent polarity causing a complete overlap with the *Z* boat n$\pi^*$-transition. Therefore, the photoconversion yield of S-diazocine **19** is decreasing from 70% in acetone to <42% in water. The lower $Z \rightarrow E$ conversion yields of $CH_2$–$CH_2$-bridged diazocines and of S-diazocine **19** reduce the efficiency of applications in aqueous media. However, NAc-diazocine **22** is an exception. There is also a decrease of the n$\pi^*$-band separation (*Z*-boat and *E*-twist), but the quantum yields are favoring the $Z \rightarrow E$ conversion with higher solvent polarity. The $Z \rightarrow E$ photoconversion yields of NAc-diazocine **22** are mostly retained in water (72%) compared to organic solvents (82%). Another advantage of NAc-diazocine **22** for applications in biological environments is the fact that it is inherently water-soluble without solubilizing substituents [18].

## 4.4 Applications of Diazocines

Diazocines exhibit inverted stabilities compared to azobenzenes. The bent and sterically more demanding *Z* configuration is thermodynamically more stable than the slender, stretched *E* isomer. This property makes them particularly suitable for applications in photopharmacology and as mechanophores (Figure 4.7).

In photopharmacology, a photoswitchable drug is administered in its biologically inactive state (off state). Upon irradiation at the site of illness (inflammation, tumor, etc.), the drug switches into the active (on) state. Spatiotemporal control of biological activity with light avoids side effects in neighboring healthy tissue, and the thermal backisomerization prevents contamination of the environment after excretion [26, 27]. There are a number of azobenzene-derivativatized, photoswitchable inhibitors published. The majority of these drugs is biologically

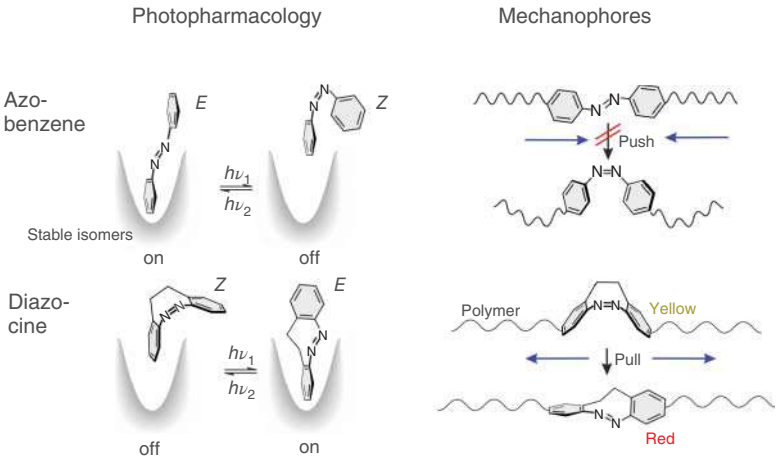


**Figure 4.7** Application of azobenzenes and diazocines in photopharmacology and as mechanophores. Diazocines are more suitable as azobenzenes in these fields because they have a bent *cis* resting state, which is converted to a stretched *trans* geometry upon irradiation (inverted stability). This allows light-induced on-switching of biological activities in photopharmacology as well as mechanically induced $Z \rightarrow E$ switching by applying a stretching force in polymers.

active in the stretched $E$ configuration and inactive in the bent $Z$ form (Figure 4.7). This is probably due to the fact that the slender $E$ configuration fits into the spatially confined active center of the target protein and the sterically more demanding $Z$ isomer does not. Since azobenzenes are stable in their active $E$ configuration, irradiation would rather switch the activity of the drug off than on, which is unfavorable. Diazocines, however, can be administered in their inactive $Z$ state (off) and activated with light (on) at the site of interest. Generally, it is more important to switch a drug effectively to the inactive than to the active state because incomplete conversion to the active state can be accounted for by increasing the concentration, whereas remaining activity of drug due to incomplete deactivation is hard to counterbalance. Off switching ($E \rightarrow Z$) of diazocines, indeed, is quantitative in all cases that were investigated so far. Another obvious advantage of diazocines are the switching wavelengths, which are in the visible region extending to the red and even near infrared (N-diazocines). UV light, needed for $E \rightarrow Z$ isomerization in azobenzenes, is tissue damaging, whereas the $E \rightarrow Z$ switching wavelengths in diazocines (>500 nm) are rather safe. Moreover, at wavelengths >650 nm, light has a larger penetration depth in blood-supported tissue (bio-optical window). Diazocines with their tricyclic structure are conformationally less flexible than azobenzenes and most other photoswitches. Therefore, the force transmission from the photoswitch to the environment should be more efficient and an induced fit of the inhibitor to the binding site of the receptor should be less likely. Diazocines are structurally similar to the family of tricyclic drugs. One can assume that if the photoswitching unit is part of such a binding motif, the change in binding affinity upon isomerization is stronger than in drugs that carry a photoswitch as a substituent.

The first applications of diazocines in photopharmacology were photoswitchable neurotransmitters. Substituted diazocines that are binding as ligands to the tetraethylammonium-binding site or glutamate receptors of potassium channels (external and internal) were used as extracellular ion channel agonists and intracellular ion channel blocker in living neurons [22, 28, 29]. The thermodynamically stable *Z* isomers of the photoswitches did not influence the postsynaptic currents, while the metastable *E* isomers exhibit a high affinity to ion channels. In the extracellular media, the ion flow was switched on, while the ion flow was switched off in intracellular experiments. Even though the conversion yield ($Z \rightarrow E$) was comparatively low (~50–60%) and does not limit this application, the dark-adapted *Z* isomer is physiologically inactive and addressable with a quantitative photoconversion yield. It was possible to trigger neuronal firing selectively and spatiotemporally resolved without any background activity in the dark. This is a big advantage compared to azobenzene-based systems, where only an increase or decrease in current flow through irradiation was achieved in similar studies due to its incomplete photostationary states or thermal relaxation to the active *E* isomers [30, 31]. Moreover, visible light (~400 nm) for the $Z \rightarrow E$ isomerization of diazocines has a higher tissue penetration depth than UV light that is required for the $E \rightarrow Z$ isomerization of azobenzene (Figure 4.8).

Substituted diazocines were also used as peptide cross-linking, amino-acid analogs in protein backbones [15, 32, 33], or for the modulation of DNA duplexes [34]. The photoinduced isomerization of diazocines allowed a selective manipulation of the three-dimensional structures of the biological macromolecules (protein folding and unfolding or interconversion of DNA duplexes with double-stranded DNA) with a high spatiotemporal resolution and non-toxic and traceless light energy. The ability to control the biological activity of macromolecules with light provides the basis to investigate mechanisms, kinetics, or biochemical pathways on a more sophisticated level as compared to classical methods.

S-diazocine derivates were used as photoswitchable VEGFR-2 Axitinib inhibitors. The sterical clash of the protein-binding site with the *Z*-configurations gave rise to a 40–50 fold difference in bioactivity upon $Z \rightarrow E$ conversion, which is a major improvement compared to previous photoswitchable kinase inhibitors. However, a derivative of parent diazocine **1** did not yield a significant decrease of the inhibitorial

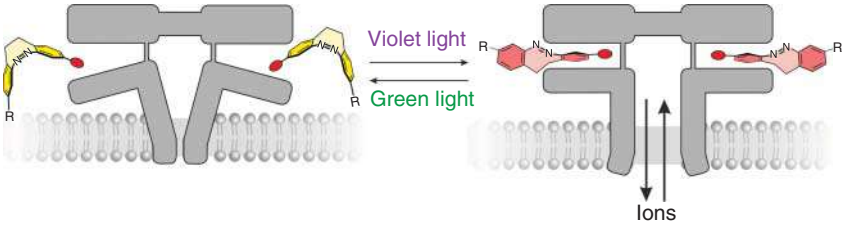


**Figure 4.8** Photoinduced firing of neuronal cells. Irradiation with deep blue light induces a $Z \rightarrow E$ photoisomerization of a diazocine ligand. The *E* isomer opens the ion channels while the *Z* isomer is completely inactive.

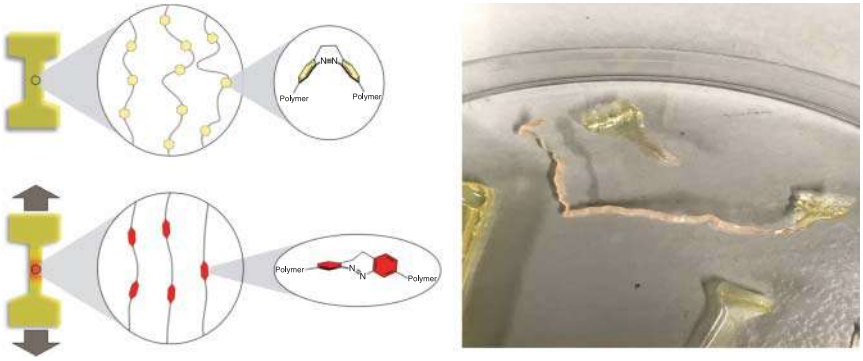


**Figure 4.9** Diazocines in a polymer backbone. The thermodynamically stable *Z* configuration isomerizes to the metastable *E* twist isomer if the material is stretched. The mechanical stress is indicated by a color change from yellow to intense red. Source: van der Schaft and Luijk [38].

strength after irradiation, because of a larger angle between the phenyl rings in its *Z* configuration and a less pronounced sterical clash compared to the S-diazocine [35].

Diazocines in their *Z* resting state are pale yellow, while the metastable *E* twist configurations are intensely red-colored. The color difference is observable with the bare eye even at very small concentrations. Tensile forces lead to the conversion of the shorter bend *Z* conformer to the stretched *E* isomer and, therefore, diazocines are suitable as mechanochromes that are indicating mechanical stress of functional materials by a color change from yellow to red. Linear urea polymers that contain amino-substituted diazocines in their backbone or siloxane copolymers, including vinylated diazocines, were reported. Irradiation caused reversible color changes and bending of the thin polymer films. These functional polymers are promising candidates for applications as smart materials such as photoresponsive mechanophores, visible-light-driven actuators, or rewriteable materials [36, 37] (Figure 4.9).

## 4.5 Conclusion

Diazocines are structurally related to azobenzenes; however, they are superior in most photophysical properties. The bridge between the two phenyl rings forming an 8-membered ring inverts the relative stability of the *E* and *Z* isomers in favor of the *Z* form. Unlike azobenzene, where ππ* ($E \rightarrow Z$) and nπ* ($Z \rightarrow E$) excitations are used for switching, both isomerizations in diazocines are induced by nπ* excitations with light in the visible range or even near infrared. The more rigid structure of diazocines improves quantum yields, light to chemical energy conversion efficiencies, and force transmission to the environment. Long-term stability studies of the parent system did not reveal any fatigue over more than 100 000 switching cycles. Recent strategies for the synthesis of diazocine derivatives improved the accessibility for a number of applications in biochemistry and materials science. Further applications in other areas are to be expected.

## Acknowledgments

The authors are grateful to the Deutsche Forschungsgemeinschaft for support via the SFB 677 Function by Switching.

## References


1 Duval, H. (1910). Recherches sur la benzidination. *Bull. Soc. Chim. Fr.* 7: 727–732.

2 Siewertsen, R., Neumann, H., Buchheim-Stehn, B. et al. (2009). Highly efficient reversible Z-E photoisomerization of a bridged azobenzene with visible light'through resolved S1(nπ*) absorption bands. *J. Am. Chem. Soc.* 131: 15594–15595.

3 Hammerich, M., Schütt, C., Stähler, C. et al. (2016). Heterodiazocines: synthesis and photochromic properties, trans to cis switching within the bio-optical window. *J. Am. Chem. Soc.* 138: 13111–13114.

4 Lentes, P., Stadler, E., Röhricht, F. et al. (2019). Nitrogen Bridged Diazocines: Photochromes Switching within the Near-Infrared Region with High Quantum Yields in Organic Solvents and in Water. *J. Am. Chem. Soc.* 141: 13592–13600.

5 Siewertsen, R., Schönborn, J.B., Hartke, B. et al. (2001). Superior Z → E and E → Z photoswitching dynamics of dihydrodibenzodiazocine, a bridged azobenzene, by S1(nπ*) excitation at λ = 387 and 490 nm. *Phys. Chem. Chem. Phys.* 13: 1054–1063.

6 Bortolus, P. and Monti, S. (1979). *Cis-trans* photoisomerization of azobenzene. Solvent and triplet donors effects. *J. Phys. Chem.* 83: 648–652.

7 Ito, Y., Ito, H., and Matsuura, T. (1988). *Trans-cis* photoisomerization of *meta*-(phenylazo) azobenzenes. *Tetrahedron Lett.* 29: 563–566.

8 Moormann, W., Tellkamp, T., Stadler, E. et al. (2020). Efficient conversion of light to chemical energy: directional, chiral photoswitches with very high quantum yields. *Angew. Chem. Int. Ed.* 132: 15081–15089.

9 Ladányi, V., Dvořák, P., Al Anshori, J. et al. (2017). Azobenzene photoisomerization quantum yields in methanol redetermined. *Photochem. Photobiol. Sci.* 16: 1757–1761.

10 Böckmann, M., Doltsinis, N.L., and Marx, D. (2010). Unraveling a chemically enhanced photoswitch: bridged azobenzene. *Angew. Chem. Int. Ed.* 49: 3382–3384.

11 Jiang, C.-W., Xie, R.-H., Li, F.-L., and Allen, R.E. (2011). Comparative studies of the trans−cis photoisomerizations of azobenzene and a bridged azobenzene. *J. Phys. Chem. A* 115: 244–249.

12 Röhricht, F. (2021). In silico design funktionaler Moleküle: Vorhersage und Erklärung molekularen Verhaltens durch Dichtefunktionaltheorie. Dissertation. Kiel University.

13 Li, S., Eleya, N., and Staubitz, A. (2020). Cross-coupling strategy for the synthesis of diazocines. *Org. Lett.* 22: 1624–1627.

**14** Sell, H., Näther, C., and Herges, R. (2013). Amino-substituted diazocines as pincer-type photochromic switches. *Beilstein J. Org. Chem.* 9: 1–7.

**15** Samanta, S., Quin, C., Lough, A.J., and Woolley, G.A. (2012). Bidirectional photocontrol of peptide conformation with a bridged azobenzene derivative. *Angew. Chem. Int. Ed.* 124: 6558–6561.

**16** Moormann, W., Langbehn, D., and Herges, R. (2019). Synthesis of functionalized diazocines for application as building blocks in photo- and mechanoresponsive materials. *Beilstein J. Org. Chem.* 15: 727–732.

**17** Maier, M.S., Hüll, K., Reynders, M. et al. (2019). Oxidative approach enables efficient access to cyclic azobenzenes. *J. Am. Chem. Soc.* 141: 17295–17304.

**18** Lentes, P., Frühwirt, P., Freißmuth, H. et al. (2021). Photoswitching of diazocines in aqueous media. *J. Org. Chem.* in press. DOI: https://doi.org/10.1021/acs.joc.1c00065.

**19** Paudler, W.W. and Zeiler, A.G. (1969). Diazocine chemistry. VI. An inquiry into the aromaticity of 5,6-dihydrodibenzo[b,f][l,Z]diazocine. *J. Org. Chem* 34: 3237–3239.

**20** Joshi, D.K., Mitchell, M.J., Bruce, D. et al. (2012). Synthesis of cyclic azobenzene analogues. *Tetrahedron* 68: 8670–8676.

**21** Moormann, W., Langbehn, D., and Herges, R. (2017). Solvent-free synthesis of diazocine. *Synthesis* 49: 3471–3475.

**22** Cabré, G., Garrido-Charles, A., González-Lafont, À. et al. (2019). Synthetic photoswitchable neurotransmitters based on bridged azobenzenes. *J. Org. Lett.* 21: 3780–3784.

**23** Merino, E. (2011). Synthesis of azobenzenes: the coloured pieces of molecular materials. *Chem. Soc. Rev.* 40: 3835–3853.

**24** Kiselyov, A.S. (1994). Reaction of *N*-fluoropyridinium salts with wittig reagents: a novel and convenient approach to symmetric trans-olefins. *Tetrahedron Lett.* 35: 8951–8954.

**25** Zhu, Q., Wang, S., and Chen, P. (2019). Diazocine derivatives: a family of azobenzenes for photochromism with highly enhanced turn-on fluorescence. *Org. Lett.* 21: 4025–4029.

**26** Hüll, K., Morstein, J., and Trauner, D. (2018). In vivo photopharmacology. *Chem. Rev.* 118: 10710–10747.

**27** Szymanski, W., Beierle, J.M., Kistemaker, H.A. et al. (2013). Reversible photocontrol of biological systems by the incorporation of molecular photoswitches. *Chem. Rev.* 113: 6114–6178.

**28** Thapaliya, E.K., Zhao, J., and Ellis-Davies, G.C.R. (2019). Locked-azobenzene: testing the scope of a unique photoswitchable scaffold for cell physiology. *ACS Chem. Neurosci.* 10: 2481–2488.

**29** Trads, J.B., Hüll, K., Matsuura, B.S. et al. (2019). Sign inversion in photopharmacology:incorporation of cyclic azobenzenes in photoswitchable potassium channel blockers and openers. *Angew. Chem. Int. Ed.* 58: 15421–15428.

**30** Mourot, A., Herold, C., Kienzler, A.M., and Lramer, R.H. (2018). Understanding and improving photo-control of ion channels in nociceptors with azobenzene photo-switches. *Br. J. Pharmacol.* 175: 2296–2311.

**31** Banghart, M.R., Mourot, A., Fortin, D.L. et al. (2009). Photochromic blockers of voltage-gated potassium channels. *Angew. Chem. Int. Ed.* 48: 9097–9101.

**32** Preußke, N., Moormann, W., Bamberg, K. et al. (2020). Visible-light-driven photocontrol of the Trp-cage protein fold by a diazocine cross-linker. *Org. Biomol. Chem.* 18: 2650–2660.

**33** Albert, L., Peñalver, A., Djokovic, N. et al. (2019). Modulating protein–protein interactions with visible-light-responsive peptide backbone photoswitches. *ChemBioChem* 20: 1417–1429.

**34** Eljabu, F., Dhruval, J., and Yan, H. (2015). Incorporation of cyclic azobenzene into oligodeoxynucleotides for the photo-regulation of DNA hybridization. *Bioorg. Med. Chem. Lett.* 25: 5594–5596.

**35** Heintze, L., Schmidt, D., Rodat, T. et al. (2020). Photoswitchable azo- and diazocine-functionalized derivatives of the VEGFR-2 inhibitor axitinib. *Int. J. Mol. Sci.* 21: 8961–8981.

**36** Li, S., Han, G., and Zhang, W. (2018). Concise synthesis of photoresponsive polyureas containing bridged azobenzenes as visible-light-driven actuators and reversible photopatterning. *Macromolecules* 51: 4290–4297.

**37** Burk, M.H., Schröder, S., Moormann, W. et al. (2020). Fabrication of diazocine-based photochromic organic thin films via initiated chemical vapor deposition. *Macromolecules* 53: 1164–1170.

**38** van der Schaft, M., and Sijbesma, R.P. Characterization of bridged azobenzenes as mechanophores in polymer networks, Bachelor Thesis, Eindhoven University of Technology 2019.


# 5 Azoheteroarenes

Jake L. Greenfield, Aditya R. Thawani, Magdalena Odaybat, Rosina S.L. Gibson, Thomas B. Jackson, and Matthew J. Fuchter

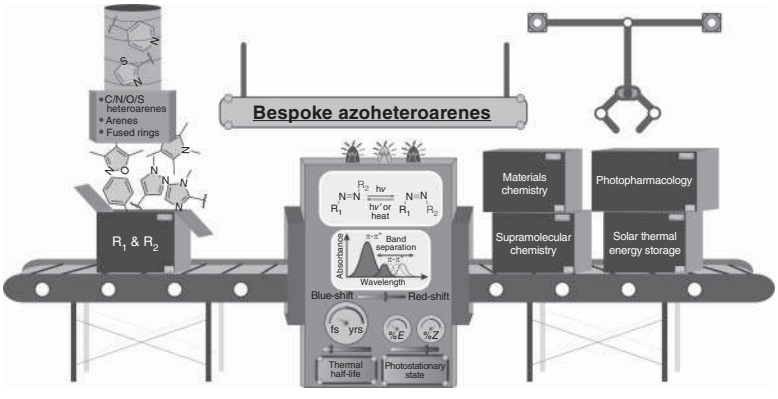


**Characteristic Features**

Azoheteroarenes are photoswitches capable of reversible, *E*–*Z* photoisomerization, where, one or both, phenyl rings in traditional azobenzene have been replaced by a heterocycle.

**Key References – Design**

Photoswitchable azoheterocycles via coupling of lithiated imidazoles with benzenediazonium Salts. *J. Org. Chem.* 2012, 77, 7: 3284–3287.

Tuning azoheteroarene photoswitch performance through heteroaryl design. *J. Am. Chem. Soc*. 2011, 139, 3: 1261–1274.

Unraveling the thermal isomerization mechanisms of heteroaryl azoswitches: phenylazoindoles as case study. *Org. Lett*. 2018, 20, 16: 4815–4879.

A combinatorial approach to improving the performance of azoarene photoswitches. *Beilstein. J. Org. Chem.* 2019, 15: 2153–2164.

Photochromic evaluation of 3(5)-arylazo-1*H*·pyrazoles. *J. Org. Chem.* 2020, 85, 6: 4019–4088.

**Key References – Applications**

Light-driven coordination-induced spin-state switching: rational design of photodissociable ligands. *Chem. Eur. J*. 2012, 18: 16358–16368.

Photoswitchable basicity through the use of azoheteroarenes. *Chem. Commun*. 2016, 52, 4521–4524.

Arylazopyrazoles for long-term thermal energy storage and optically triggered heat release below 0 °C. *J. Am. Chem. Soc*. 2020, 142, 19: 8688–8695.

Photoswitchable CENP-E inhibitor enabling the dynamic control of chromosome movement and mitotic progression. *J. Am. Chem. Soc*. 2020, 142, 4: 1763–1767.

TRPswitch—a step-function chemo-optogenetic ligand for the vertebrate TRPA1 channel. *J. Am. Chem. Soc*. 2020, 142, 41: 17457–17468.

An arylazopyrazole-based N-heterocyclic carbene as a photoswitch on gold surfaces: light-switchable wettability, work function, and conductance. *Angew. Chem. Int. Ed*. 2020, 59: 1–7.

# 5

# Azoheteroarenes

*Jake L. Greenfield, Aditya R. Thawani, Magdalena Odaybat, Rosina S.L. Gibson, Thomas B. Jackson, and Matthew J. Fuchter*

*Imperial College London, Molecular Sciences Research Hub, Department of Chemistry, 82 Wood Lane, London W12 OBZ, UK*

## 5.1 Introduction

Azobenzenes [1], an archetypal class of photoswitch [2], have been championed for a range of applications spanning several fields, including photopharmacology [3], organic energy-storage materials [4], and supramolecular chemistry [5–7]. More recently, interest has spread to the investigation of novel azobenzene analogues, the azoheteroarenes [2]; where the inclusion of heteroatoms in the ring system vastly expands the breadth of functionality and the chemical space available (Figure 5.1). With this added tunability, the various structural, electronic, and photophysical properties of these switches can be tailored to achieve specific functions, as well as engender new behaviors within the system.

Similar to azobenzenes, the photoswitching performance of azoheteroarenes can be described quantitatively using several parameters [14]. These parameters include the energy of the electronic absorption bands ($\lambda_{max}$); the extent of photoinduced switching at the photostationary state (PSS); the thermal half-life of the switched state ($t_{1/2}$); and the resistance of the switch to fatigue or degradation [2]. The heteroaromatic ring(s) of the azoheteroarenes provides a versatile way to tune such parameters. For example, exchanging one arene-ring in azobenzene for a 2-pyrrole afforded a 70 nm red-shift in the π–π* absorption band in the UV–vis spectrum (**7**, Figure 5.2) [14]. This ability to tune the energy of the electronic absorption bands, more specifically, the separation of the π–π* and n–π* electronic transitions of the *Z* and *E* isomers, respectively, can engender improved selectivity of photoexcitation and subsequently yield a PSS containing a higher proportion of the targeted isomer [15]. This is exemplified in the case of a methylated phenylazo-4-pyrazole derivative where a 106 nm separation between the n–π* of the *Z* isomer and the π–π* of the *E* isomer afforded a >98% in *Z*–*E* photoconversion (**8**, Figure 5.2) [14]. The basicity of the heteroatoms additionally grants access to charged analogues, either in acidic media or through heteroatom alkylation, that display improved

*Molecular Photoswitches: Chemistry, Properties, and Applications*,
First Edition. Edited by Zbigniew L. Pianowski.


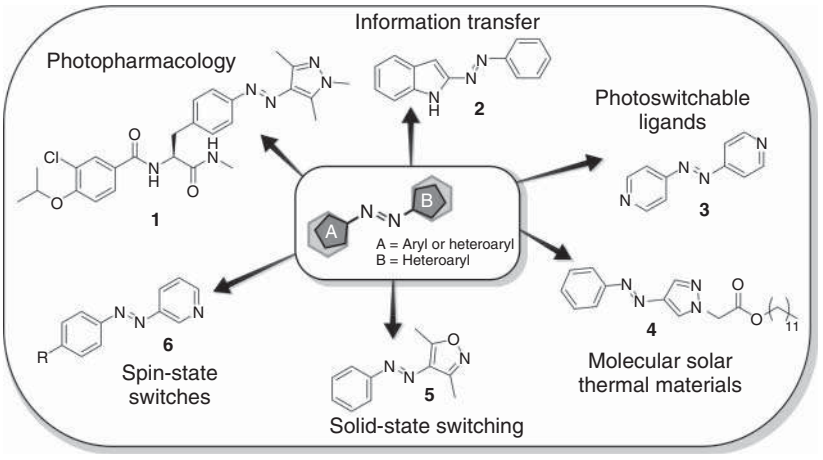


**Figure 5.1** Examples of azoheteroarene photoswitches and their applications. Switches **1** [8], **2** [9], **3** [10], **4** [11], **5** [12], and **6** [13] are discussed further in Sections 5.4–5.7 of this chapter.

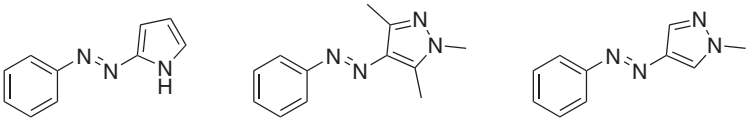

**Figure 5.2** Switches **7–9** are commonly referred to as 2pyH, 4pzMe, and 4pzH, respectively.

solubilities in aqueous media, red-shifted absorption bands (c. 70 nm for the π–π* of the *Z* isomer of phenylazo-4-pyrazole, **9**, Figure 5.2), and shortened thermal half-lives (the thermal half-life of phenylazo-4-pyrazole was reduced from ~1000 days to 8 minutes in the presence of 2 M HCl) [16]. Moreover, the propensity for heteroarenes to coordinate to metal ions allows the design of photoresponsive coordination complexes, including photoswitchable MRI contrast agents [13, 17]. By exchange of a single arene for a heteroarene, the molecules' dipole moment can be tailored, thus altering the material properties of the photoswitch (surface wettability or electrical conductance) [18], or establish push–pull tautomerization across the azo bond [19]. This latter point can greatly influence the dominant isomerization mechanism and the thermal half-life of the photoswitch. The degree of tunability over the rate of thermal isomerism of azoheteroarenes renders them ideal candidates for real-world applications from thermal energy storage, which requires relatively long thermal half-lives [11], to information transfer requiring sub-nanosecond isomerization [15, 20]. Azoheteroarenes also offer significant potential as replacements for azobenzenes in photopharmacology, due to their improved bioisosterism, polarity, lipophilicity, and solubility [21].

Due to the wide range of structural combinations and their associated properties, structure–property relationships for azoheteroarenes are currently less well

understood compared to azobenzenes [2]. This chapter provides: an overview of current knowledge surrounding such relationships, as well as synthetic methodology available to access these photoswitches; a description of how heteroarene chemical space can influence the key switching and electronic parameters of the azoswitches; and several prominent applications where the use of heteroaryl switches excels.

## 5.2 Synthetic Strategies Toward Azoheteroarenes

Many of the key synthetic routes used to synthesize azobenzene photoswitches have been adapted to generate azoheteroarene analogues. Strategies to afford symmetric azoheteroarenes have included the use of oxidative (e.g. *t*-BuOI) [22], or reductive (e.g. Zn) [23] homocouplings, from the amino- or nitro-heteroaryl unit, respectively (Scheme 5.1).

Both symmetric and asymmetric azoheteroarenes can also be accessed via diazonium-coupling or the Bayer–Mills-coupling reaction. In the former strategy, diazonium coupling has successfully afforded azoheteroarenes by either employing the heterocycle as part of the diazonium ion (Scheme 5.2a, Het = pyridine [26], pyrazole [24, 25]) or alternatively as the nucleophile (Scheme 5.2b, Het = pyrrole [14], indole [27], imidazole [28]), depending on the intrinsic reactivity of the heteroaromatic.

The main drawback to the diazonium-coupling strategy is the instability of the diazonium species and, potential safety concerns especially when working on a large scale, which is necessary for real-world applications [29]. On the other hand, challenges may arise for heterocycles with low nucleophilicity toward the diazonium species when employed as shown in Scheme 5.2b. This is exemplified in the case of unsubstituted pyrazoles (electron-rich pyrazoles, i.e. amino-substituted [30], have been reported to couple successfully), where modifications are required; 3,5-disubstituted pyrazoles require an initial coupling to form a hydrazone intermediate and a subsequent condensation with hydrazine to provide the desired azopyrazole (Scheme 5.3) [31, 32].

The nucleophilicity of the heterocycle can be increased via the *in situ* generation of a lithiated ring, as utilized in the synthesis of arylazothiophene (Scheme 5.4a) [33]. Coupling can also be directed to sites of lower nucleophilicity using a protecting group strategy: protecting the more acidic sites facilitates the selective formation of 4/5-azoimidazoles as opposed to 2-azoimidazoles (Scheme 5.4b) [34].

The Bayer–Mills reaction provides a reliable method to generate azoheteroarenes using synthetically accessible (and in many cases, commercially available) amino-heterocycles (e.g. pyrazoles, triazoles, tetrazoles) and nitrosobenzenes

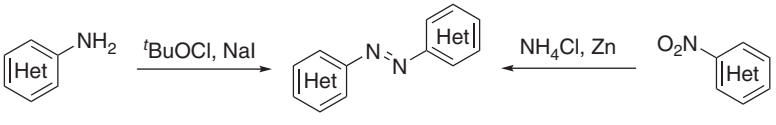


**Scheme 5.1** Example of oxidative [22] and reductive [23] homocoupling conditions for symmetric azo compounds.

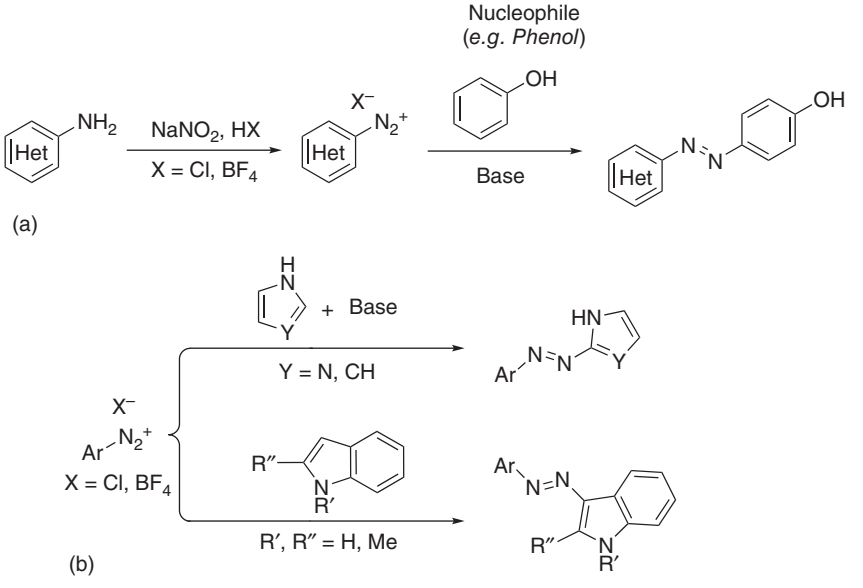


**Scheme 5.2** Examples of diazonium couplings modified for azoheteroarenes. (a) Example of the use of heteroaromatic diazonium ions (e.g. pyrazole [24, 25] or pyridine [26]). (b) Employing the heteroaromatic as the nucleophilic species (indole [27], pyrrole [14], or imidazole [28]).

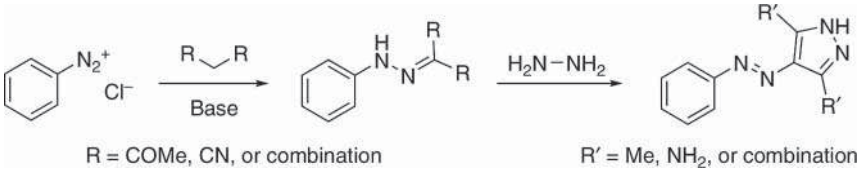


**Scheme 5.3** An alternative strategy toward the synthesis of azopyrazoles, employing an initial diazonium coupling to form a hydrazine intermediate. Sources: Weston et al. [31]; Al-Etaibi et al. [31, 32].

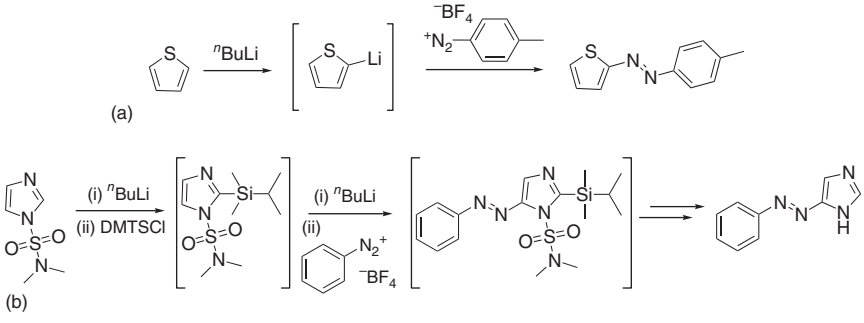


**Scheme 5.4** Formation of (a), azothiophene. Source: Slavov et al. [33]. Licensed under CC BY-4.0. , and (b) azoimidazoles [34] via lithium species. Source: Modified from Herges et al. [34].

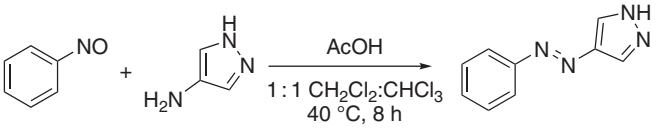


**Scheme 5.5** Bayer–Mills reaction to produce azopyrazole [14].

(Scheme 5.5) under either basic or acidic conditions [14]. Although the analogous reaction with anilines and nitrosoheteroarenes is theoretically possible, there are few documented examples in the literature thus far [35]. In principle, this should not be the result of an inability to form nitrosoheteroarenes however, as nitrosopyrazoles have been prepared successfully and studied in the literature [36].

Through the methods described above, any class of azoheteroarene should be synthetically accessible, although the choice of a method depends heavily upon the exact target molecule, including its required substitution.

## 5.3 Structure–Property Relationships

In this section, we discuss several of the key structural–property relationships inherent to azoheteroarenes, with an emphasis on how the photoswitching properties of this class of photoswitches differ from their azobenzene counterparts. The discussion is divided into phenomena that are dependent on the structure of the photoswitch and those that are dependent on external factors, including the influence of pH.

### 5.3.1 Conformational Effects on Thermal Half-Life and n–$\pi^*$ Oscillator Strength

Azoheteroarenes share broadly similar structural and mechanistic characteristics to that of azobenzene photoswitches. The *Z*-isomer of azoheteroarenes is typically the metastable state (excluding diazocines) [37], and similar to azobenzenes, three main mechanisms to describe the thermal isomerism of azobenzenes are operative: inversion, rotation, or tautomerization [2]. For azoheteroarenes, the rotation and tautomerization mechanisms are generally governed by the same factors as for azobenzenes (for example, the degree of single-bond character of the azo bridge) [2]. However, azoheteroarenes bearing aryl rings that comprise <6 atoms exhibit markedly different behavior in their inversion mechanism than azobenzene with significant deviations from the typical conformational effects reported (*vide infra*) [38]. Such effects directly influence the thermal half-life of the metastable state: azopyrazoles have demonstrated *Z*-isomer half-lives as long as 46 years (**10**, Figure 5.3) [38], an order of magnitude greater than the longest $t_{1/2}$ of an azobenzene (ca. 700 days for **11**, Figure 5.3) [39]. These dramatic differences in $t_{1/2}$ appear to arise, at least in part, from the adoption of specific metastable *Z*-isomer ground- and transition-state (TS) conformations that are only accessible to azoheteroarenes of a similar 5-membered heteroaryl ring size (*vide infra*) [14].

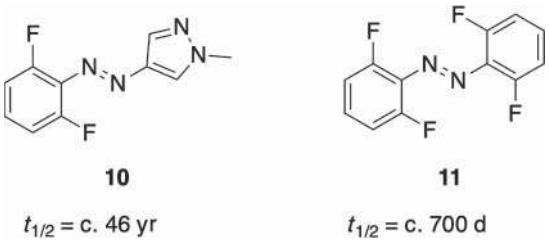


**Figure 5.3** The structures of azo-based photoswitches with the longest reported *Z* to *E* thermal half-lives (recorded in DMSO): Azoheteroarene derivative **10** and azobenzene derivative **11**. Sources: Calbo et al. [38]; Bléger et al. [39].

The works of Contreras-García and Fuchter [14] on azopyrazoles and azopyrroles provide the rationalization for the experimentally observed thermal half-lives of several 5-membered azoheteroarenes based upon their *Z*-isomer conformations. Steric considerations and the degree of favorable dispersive interactions were revealed as the dominant factors underpinning the impact of conformational effects upon the thermal half-life. These studies also rationalize the dynamic interplay between the thermodynamic and kinetic factors, which govern a given 5-membered heteroarenes *Z* to *E* thermal isomerization rate.

5-Membered azohetereoarenes can adopt a unique conformation with the heteroaryl ring twisting about the azo bridge up to a perpendicular (90°) T-shaped *Z*-isomer conformation (for unsubstituted heteroaryl rings) [14, 32, 34]. Of the possible ground-state *Z*-conformations, the T-shaped conformer is considered the lowest energy, with a greater degree of intramolecular (C–H–π) interactions between the proximal heteroaryl *ortho*-H and the aryl ring (Figure 5.4b). Notably, mono-*ortho*-substituted azoheteroarenes can interconvert between a T-shaped or twisted (<90°) *Z*-isomer conformer as a result of their asymmetry, depending upon the energetics of the system. The bis-*ortho*-substituted azoheteroarenes display a destabilizing steric effect due to the twisted nature of their *Z*-conformations (<90°). Additional computational work within the study highlighted the potential for a "compensation principle" to dominate within highly substituted azoheteroarenes, which may relate to recent work for azobenzenes [40]. The adoption of *Z*-isomer T-shaped conformations has been reported for other azoheteroarenes, including tetrazoles, triazoles, imidazoles, and thiophenylazobenzenes [14, 33, 34].

There is also a significant kinetic component to the thermal isomerization rates of such azoheteroarenes. Theoretical calculations revealed that azopyrazoles adopted a protracted T-shaped TS conformation (with minimal dispersive surface interactions, equaling a higher TS energy). This TS was identified as further contributing to the greater $t_{1/2}$ in the azopyrazoles. In contrast, the TS conformation of the azopyrroles was closer to being co-planar, whereby increased dispersive surface interactions afford a lower-energy TS. This lowering of the TS energy results in more rapid *Z* to *E* thermal isomerization via inversion, thus indicating a significant kinetic contribution to the observed $t_{1/2}$ (Figure 5.4c) [14].

Alongside influencing $t_{1/2}$, the increased molecular symmetry of T-shaped *Z*-isomers results in a considerably less intense n–π* transition, similar to that observed for the planar *E*-isomers. This outcome, in turn, impacts *Z*–*E* photoswitching, which mostly relies on excitation of the *Z*-isomer n–π* band. Thus, the T-shape conformation can serve to increase the *Z*-isomer thermodynamic stability,

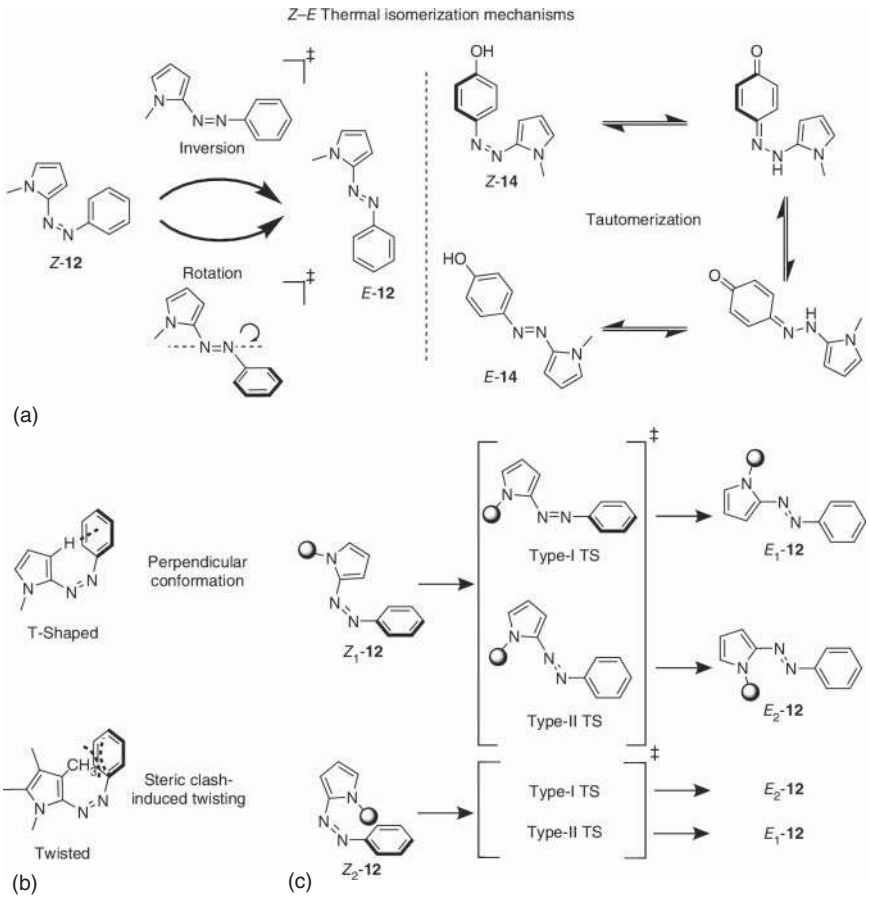


**Figure 5.4** (a) *Z*–*E* thermal isomerization mechanisms for azoheteroarenes, inversion, rotation, and tautomerization. Sources: Calbo et al. [14]; Schweighauser et al. [40]. (b) Schematic representation of the T-shape and twisted conformations of N-methylated azopyrrole **12** and **13**, respectively, highlighting the impact of ring substitution adjacent to the azo bridge. Source: Modified from Calbo et al. [14]. (c) Schematic representation of the transition-state conformations of azopyrrole. Source: Adapted from Calbo et al. [14].

a key factor in the thermal relaxation rates, but also result in a less efficient *Z*–*E* photoswitching. Conversely, switches in which the 5-membered component is more sterically hindered acquire a twisted rather than T-shaped conformation when in the *Z*-isomer. As a direct result, these systems can undergo excellent bidirectional photoswitching (although at the expense of *Z* isomer stability) due to the higher oscillator strength of their n–π* transitions arising from the lower symmetry of the twisted conformation.

### 5.3.2 Choice of Heterocycle

In recent years, an expanding list of heterocycles has been employed in azoheteroarene photoswitches. Compounds bearing 5- and 6-membered nitrogen

heterocycles such as pyridine (**15**) [41], pyrimidine (**17** and **18**) [20, 42], pyrrole (**19**) [14], pyrazole (**9**) [14], imidazole (**21**) [43] as well as some fused systems such as indole (**2**) [9] and indazole (**24**) [44] are becoming more frequently employed in the literature (Figure 5.5). Accounts of azoheteroarenes containing triazole (**22**) [14], tetrazole (**23**) [14], and purine rings (**26**) [47] are also present. In contrast, incorporation of heteroatoms other than N in the scaffold of azo switches is less explored with just a handful of examples bearing thiophene (**20**) [33], thiazole, oxazole, benzothiazole, and benzoxazole units (**27** [48], Figure 5.5). The following section includes a review of representative examples. It does not aim to give a comprehensive overview of every heterocyclic motif that has been incorporated into an azo photoswitch but emphasizes the key structure–property relationships that have been derived.

### 5.3.3 6-Membered Heterocycles

Historically, azopyridines were among the first heteroaromatic azo dyes to be synthesized and, of the azoheteroarenes, their photochromism has been the most extensively studied. [49–51] Replacing one of the phenyl groups of azobenzene with a pyridine unit does not have a dramatic effect on the position of the π–π* and n–π* bands in the absorption spectra, while in symmetrical azopyridine systems a blue shift of the π–π* transition is generally observed resulting in an increased *Z*-rich PSS (**15**, Figure 5.5) [41, 52, 53]. Perhaps the most prominent differentiating structural feature of azopyridines compared to their azobenzene counterparts is the presence of N-lone pairs available to coordinate to metals, a feature that has inspired a large body of research (see Section 5.6.2) [13, 41, 53–55].

Due to their strong electron-withdrawing abilities, pyridinium groups have attracted considerable attention for the design of push–pull azoheteroarene systems [45, 56, 57]. Simply introducing an electron-donating functionality in the structure of an azopyridinium salt results in a dramatic enhancement of the *Z* to *E* thermal isomerization rate, in some instances producing switches with thermal half-lives in the picosecond temporal domain (Figure 5.6a) through a push–pull effect [45, 56, 57]. In addition to their rapid thermal isomerization kinetics, azopyridiniums exhibit red-shifted absorption maxima compared to their azobenzene and azopyridine counterparts [45, 56, 57]. For example, in amino-azopyridinium switches (**16**, Figure 5.5) the π–π* transitions of the *E* isomer occur in the region up to 560 nm (in EtOH), while the corresponding amino-azopyridine analogues (**28**, Figure 5.6) are blue shifted (up to 444 nm in EtOH) [45]. Therefore, simply by replacing pyridine with a pyridinium unit, one can red-shift the absorption of a given switch by more than 100 nm.

Despite being known for nearly 70 years, azopyrimidines have been far less studied than their pyridine counterparts [59]. The ubiquity of the pyrimidine ring in nature renders this structural motif attractive for biological applications. The photophysics of azopyrimidines is strongly affected by the substitution pattern of the switch. For example, Velasco and coworkers have reported a biocompatible 2-phenylazopyrimidine, bearing a phenolic 4′-OH, which undergoes thermal

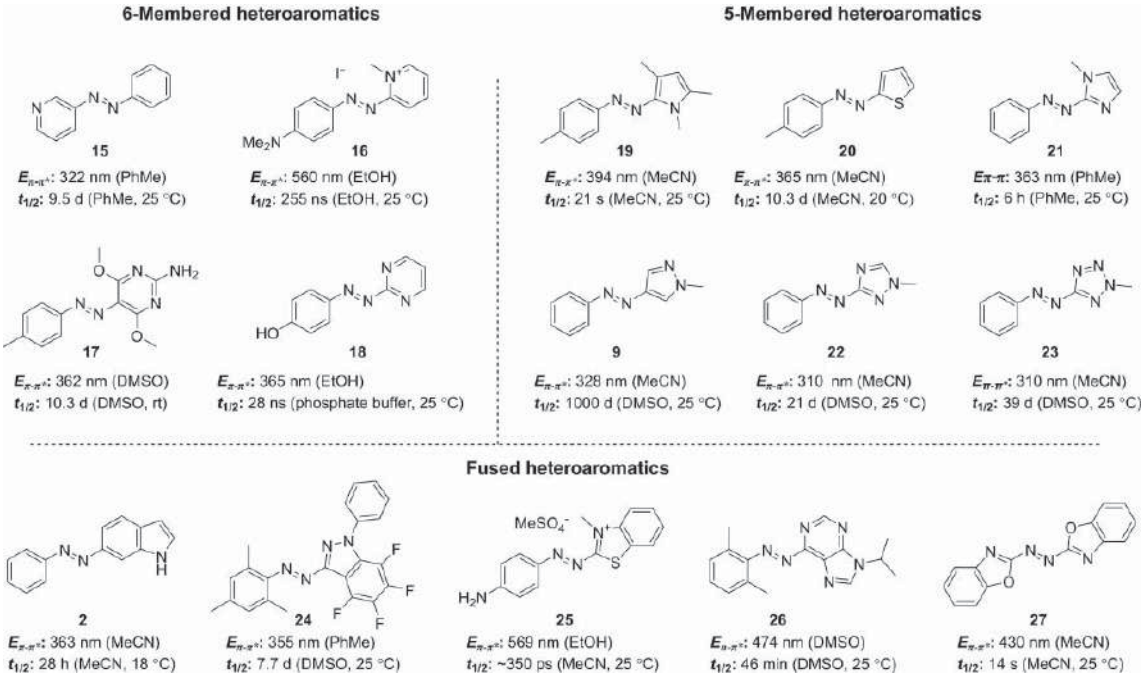


**Figure 5.5** Azoheteroarenes bearing various heterocyclic motifs: 6-membered heteroaromatics **15** [41], **16** [45], **17** [42], and **18** [20]; 5-membered heteroaromatics **19** [14], **20** [33], **21** [43], **9** [14], **22** [14], and **23** [14]; and fused heteroaromatics **2** [9], **24** [44], **25** [46], **26** [47], and **27** [48].

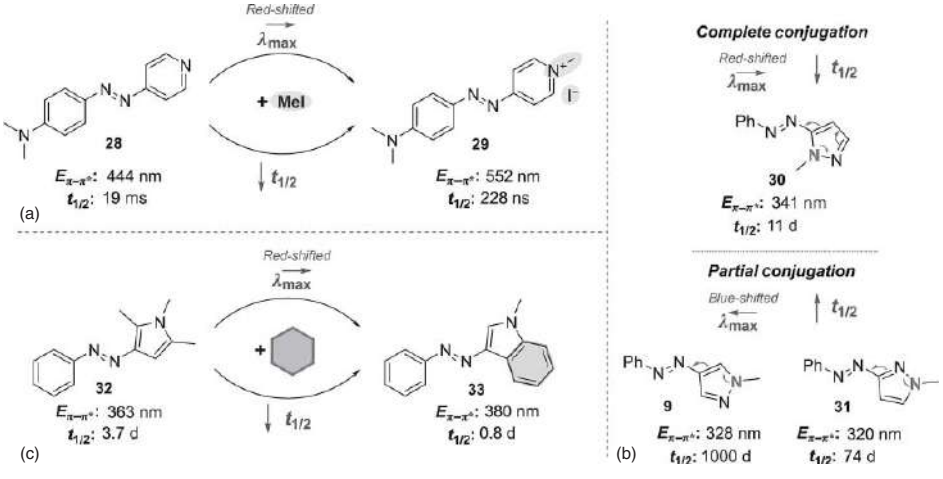


**Figure 5.6** Structural factors influencing the photophysics of azoheteroarene switch. (a) The effect of introducing a charged moiety, **29**, to the azoheteroarene system. Source: Modified from Garcia-Amorós et al. [45]. (b) The influence of the position of the heterocycle relative to the azo group, i.e. extent of donative conjugation from the *N*-methyl lone pair to the azo group. Source: Modified from Calbo et al. [14]. (c) The impact of incorporating a bicyclic ring, **33** [58], relative to a monocyclic analogue, **32** [14]. Sources: Calbo et al. [14]; Simeth et al. [58].

isomerization on the nanosecond time scale under physiological conditions (**18**, Figure 5.5) [20]. On the other hand, Procházková and coworkers have introduced a series of 2-amino-4,6-dimethoxy-5-phenylazopyrimidines that, depending on the nature of the 4′ substituent, exhibit thermal half-lives of up to 10.3 days (in DMSO-$d_6$ at r.t., **17** Figure 5.5) [42].

### 5.3.4 5-Membered Heterocycles

The structure–property relationships of azoheteroarene switches bearing various nitrogen-rich 5-membered rings have been the subject of several studies [14, 32]. The photochromism and thermal half-lives of these systems were found to strongly correlate with the identity and position of the heteroatom and the substitution pattern of the heterocyclic component. As described above in Section 5.3.1, the conformation of the ground state of the *Z*-isomer and its TS in the thermal isomerism plays a key role in governing the characteristics of the switch. Notably, *Z* isomers that exhibit slow thermal relaxation rates ($t_{1/2}$ in order of days to years) were found to adopt a T-shaped ground-state conformation, accessible only to photoswitches featuring a 5-membered heterocycle (see Section 5.3.1).

The spectroscopic properties of switches bearing 5-membered nitrogen heterocycles are correlated with the electron-donating or -withdrawing abilities of the corresponding heterocyclic unit [14, 32]. In general, the more electron-donating the heterocycle, the larger the red-shift of the *E*-isomer π–π* absorption bands (following the trend: pyrrole **19** [14] > thiophene **20** [33, 60] > imidazole **21** [14, 19, 61] > pyrazole **9** [14] > triazole **22** [14] ∼ tetrazole **23** [14]). Thus, when considering systems bearing solely methyl substituents, it becomes apparent that azopyrroles exhibit the most red-shifted π–π* transitions ($\lambda_{max}$ as high as 394 nm), followed by azothiophene (365 nm), azoimidazoles (as high as 363 nm), and azopyrazoles (as high as 341 nm). The most electron-poor azotriazole and azotetrazole have the least red-shifted π–π* bands (310 nm for both systems). The azo N=N bond length, and hence the bond order (Wiberg index [62] – WI), is also correlated with the electron-donating or -withdrawing abilities of the corresponding heterocyclic unit. In general, electron-rich systems act as better electron donors that reduce the WI and subsequently the *Z* thermal half-life (*vide supra*). Therefore, switches featuring electron-donating pyrrole and thiophene rings usually undergo thermal isomerization on the order of hours, while systems bearing weaker electron donors as pyrazole have relatively long-lived *Z* isomers with typical half-lives in the timescale of days (or even months and years) [33, 38, 60].

In addition to the nature of the heterocyclic unit, the position of the heteroatom(s) with respect to the azo linkage has a dramatic effect on the spectroscopic characteristics of the azoheteroarene switches as well as the thermal stability of the *Z* isomer (Figure 5.6b) [14]. The connectivity of the heteroaromatic ring influences the extent of N-lone pair conjugative donation into the azo-bridge. As a consequence, systems in which the N-lone pair is adjacent to the azo group exhibit a longer conjugation length (**30** vs. **9** and **31**, Figure 5.6), giving rise to red-shifted π–π* absorption bands, a decrease of the WI, and *Z*-isomers displaying reduced *Z* to *E* thermal half-lives (Figure 5.6b) [14].

### 5.3.5 Fused Heterocycles

With the exception of azoindoles, incorporation of fused heterocycles in azo photoswitches has received less attention [9, 58]. Introduction of an additional fused benzene (or heterocyclic) ring increases the extent of conjugation within the system, and in most cases results in red-shifting of the absorbance and accelerating the thermal relaxation rate for a given switch (Figure 5.6c). For example, when comparing 3-phenylazopyrrole, **32** [14], and its fused 3-phenylazoindole equivalent **33** [58], it becomes evident that the absorption maximum of the latter is red-shifted by around 20 nm (~360 nm vs. ~380 nm) and the *Z*-isomer undergoes thermal isomerization three times faster than the former analogue [14, 58].

The König group has demonstrated the utility of azoindoles (**2**, Figure 5.5) as molecular photoswitches with thermal half-lives ranging from days to nanoseconds [9, 58]. Subtle changes in the structure of the switch such as methylation of the indolic nitrogen or varying the connectivity of the heterocycle were found to dramatically affect the thermal isomerization kinetics of phenylazoindoles. The wide range of thermal half-lives accessible to this scaffold (spanning over 14 orders of magnitude) was attributed to a variation in isomerization mechanism [9]. Thus, both *N*-methylated **33** and unsubstituted 5- and 6-phenylazoindole systems exhibit long-lived *Z*-isomers, reverting back to *E* via in-plane inversion (Figure 5.6). Unsubstituted 3-phenylazoindole undergoes *Z* to *E* thermal relaxation on the millisecond time scale through rotation or tautomerization depending on the solvent present, while for the fastest isomerizing non-methylated 2-phenylazoindole (**2**, Figure 5.12a, $t_{1/2} \sim 10^{-9}$ seconds) the rotation mechanism is predicted to be the only operative mechanism as highly unfavorable aromaticity loss in the s-*cis* hydrazone renders the tautomerization mechanism unfeasible [9].

It has been demonstrated that azoindazoles have relatively stable *Z*-isomers with thermal half-lives up to several days (**24**, Figure 5.5) [44]. Interestingly, unlike the azopyrazoles, these systems are believed to thermally convert back via rotational rather than inversion mechanism [32, 44]. On the contrary, the benzothiazolium motif **25** has been utilized in the design of several push–pull azo switches, some of which characterized with half-lives in the picosecond temporal domain [46, 63]. In addition to their ultra-fast thermal isomerization kinetics, these systems have significantly red-shifted absorption spectra with π–π* absorption maxima up to 569 nm (in EtOH) for the *E*-isomers. Another example of fused heteroaryl switches addressable with visible light are the 6-azopurines **26** prepared in the search for novel photopharmacological agents [47]. These systems can undergo *E* to *Z* photoconversion following irradiation of the n–π* band with green light (530 nm, $\lambda_{max}$ 474 nm). Furthermore, Beves and coworkers have reported three symmetrical azobenzoxazoles **27** with strongly red-shifted π–π* *E*-isomer transitions that upon irradiation at the $\lambda_{max}$ (~450 nm) convert to around 80% of the *Z*-isomer [48]. These systems are characterized with good fatigue resistance and thermal half-lives of the less stable *Z*-isomers in the timescale of minutes.

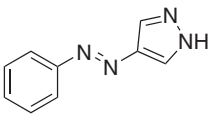

34

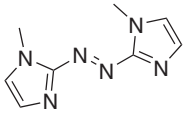

35

**Figure 5.7** Azoheteroarenes where the *Z*-isomer half-life is very sensitive to the presence of water **34** [64], or which can act as a photobase **35** [19]. Sources: Devi et al. [64]; Weston et al. [19].

### 5.3.6 External Influences

In addition to structural influences on the thermal half-life, there is a range of external factors that can control the thermal isomerization rate of azoheteroarenes. As with azobenzenes [1], thermal half-lives vary with solvent polarity due to differences in the stabilization of the ground and TSs. The thermal half-lives of arylazopyrroles appear to be particularly sensitive to the water content of the solution they are measured in. Rapid thermal reversion was observed for these switches in solutions containing a higher composition of water. For example, in the presence of water, the thermal isomerization rate of **7** increases by 10% [32]. The arylazopyrroles, along with azoimidazoles, also appear to exhibit a concentration dependence to the *Z*-isomer thermal half-life. Such behavior may be indicative of an intermolecular mechanism at play during thermal relaxation [14]. Similar behavior has been observed for an unmethylated derivative of an arylazopyrazole **34** (Figure 5.7); studies by Venkataramani suggest that intermolecular hydrogen bonding from the NH group influences *Z* to *E* isomerization rate [9, 64].

In a similar manner to tautomerization, decreasing the pH of the solution results in increased rates of isomerization for most azo switches (note that examples exist of azo switches where protonation stabilizes the *Z*-isomer, e.g. bis azoimidazole **35**, Figure 5.7) [19]. Protonation of the azo group affords an azonium species, accompanied by an increase in the rate of thermal isomerization of the *Z*-isomer, due to a contribution of resonance structures that reduce the double-bond character of the N=N bond of the azo moiety [65]; an effect known to be increased for the arylazopyrazoles compared to azobenzenes due to the additional mesomeric stabilization of the azonium ion [19]. In an analogous manner, cations have been shown to accelerate the half-lives of azoheteroarenes, as they do for azobenzenes, via coordination to the azo-nitrogen. Klajn and coworkers demonstrated that the thermal $t_{1/2}$ of **8** (4pzMe, Figure 5.2), acting as a guest molecule, was reduced upon increasing amounts of a Pd-based self-assembled coordination cage. Disassociation of the cage's ligands facilitated the coordination of **8** to the free $Pd^{2+}$ ions, which increased the rate of thermal isomerism. Metal–organic structures involving azoheteroarenes are further discussed in Section 5.3.1 [66].

## 5.4 Photopharmacological Applications

Photopharmacology using photoswitches is a promising approach to light-addressable therapeutics, whereby the activity of a given molecule can be modulated via irradiation of light. Light as a tool is non-invasive, non-toxic, readily

tunable in terms of intensity/wavelength and offers excellent spatio-temporal control in the generation of the photoresponsive molecule's pharmacologically active structure [21]. Given their significant change in shape following photoisomerization, azo photoswitches can be harnessed to generate molecules whose bioactivity can be readily toggled using light. Azoheteroarenes, by virtue of the heterocyclic component, should showcase good drug-like characteristics, including improved solubility and a larger dipole moment, which reduces lipophilicity (and likely associated promiscuous binding), as well as potentially diminishing metabolism [21]. Intermolecular interactions between heteroatoms in the photoswitch ring system and the binding site may also allow for an increase in ligand-binding efficiency [21]. Here, we highlight some representative examples of the use of azoheteroarenes in photopharmacology, noting distinct advantages they offer relative to their azobenzene counterparts [8].

### 5.4.1 Photoswitchable CENP-E Inhibitor

Centromere-associated protein E (CENP-E) plays a crucial role in the checkpoint mechanism underpinning cellular division. Specifically, it controls the progression from the metaphase to the anaphase of the mitotic cell cycle [8]. Inhibition of CENP-E triggers cell apoptosis (cell death) and has potential as a cancer therapy. Uehara, Tamaoki, and coworkers modified an existing CENP-E inhibitor to have a photoswitchable component [8]. Of the two classes of azo-photoswitch derivatives developed in their study, the azopyrazole analogue, **1**, displayed significantly better aqueous solubility (>100 μM in BRB-80 buffer +0.1% DMSO) vs. the azobenzene analogues (**37–39**, 5 μM in BRB-80 buffer +10% DMSO, Figure 5.8). The significantly improved band separation of the azopyrazole-derivative, vs. the azobenzene analogues, also enabled more complete bidirectional photoswitching. The *E*-isomer of **1** exerted anti-proliferative effects in HeLa cells that were diminished 10-fold upon irradiation with 365 nm light. The ability to toggle the activity of the CENP-E inhibitor allowed the precise role of CENP-E to be monitored in a time-dependent manner. Temporally resolved live-cell imaging – enabled by the use of a photoswitchable inhibitor – demonstrated that CENP-E is continuously required for chromosomal congression (alignment) but becomes expendable once full alignment is achieved.

### 5.4.2 Photoswitchable Ligands for a TRPA1 Chemo-Optogenetic System

Transient receptor potential ankyrin 1 (TRPA1) is a $Ca^{2+}$ potentiated ion channel expressed in the peripheral nervous system. TRPA1 is involved in an array of sensory systems controlling vision, taste, temperature, and touch (pain-sensing). The groups of Peterson and Fuchter identified **40** (Figure 5.9a) and **41** (Figure 5.9b) as reversible TRPA1 photoactuators via phenotypic screening in zebrafish [67]. Both compounds displayed zebrafish TRPA1-dependent activity upon *E* to *Z* photoswitching using violet light (352–402 nm). Notably, **41** displayed superior,

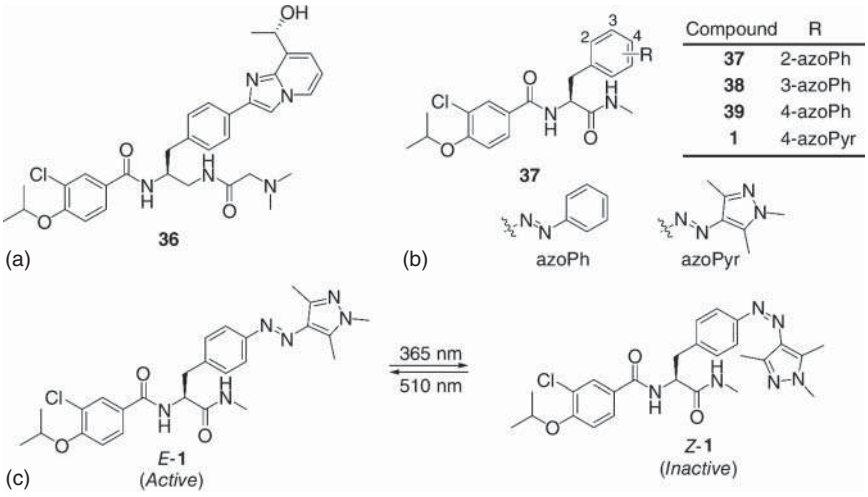


**Figure 5.8** (a) Structure of the CENP-E inhibitor. (b) Two photoswitchable analogues containing either an azobenzene (**37**–**39**) or an azopyrazole moiety (**1**). (c) Significant structural changes are observed upon switching from the *E*-isomer (CENP-E active form) to the *Z*-isomer (CENP-E inactive form). Source: Mafy et al. [8].

near-quantitative bidirectional photoswitching compared to the azobenzene analogue **40**. Photoswitch-dependent gating of the ion channel was demonstrated using a flash (one-second pulse) of violet and green light (500–600 nm) corresponding to the *E* to *Z* and *Z* to *E* photoisomerization events, respectively. When larval zebrafish exogenously expressing the ion channel in their cardiomyocytes (heart muscle cells) were treated with either **40** or **41**, they displayed no change in their cardiac rhythm vs. DMSO controls. However, their ventricular heartbeat could be put into a systolic state after a flash of violet light. Normal cardiac rhythm was immediately restored after a flash of green light. Repeated pulses of violet followed by green light allowed this process to continue in a cyclic manner (Figure 5.9c). Thus, TRPA1/**41** represents a novel, chemo-optogenetic system with a unique combination of high conductance, high efficiency, and capacity for complete bidirectional optical switching [67].

### 5.4.3 Further Pharmacological Applications of Azoheteroarenes

Hodson and Trauner reported the use of an azothiodiazole for photocontrol over pancreatic beta-cell function and insulin secretion (**42** and **43**, Figure 5.10a) [68]. Notably, this compound has a red-shifted absorbance maximum, compared to an azobenzene analogue [73], enabling yellow light-driven *E* to *Z* isomerization while being stable to bacterial azoreductase. Azopyridine-derived ligands, such as **44** (Figure 5.10b), for the $mGlu_5$ receptor have been reported with a negative allosteric modulation activity. **44** and its analogues inhibited $mGlu_5$ agonist activity, as the *E* isomer, at nanomolar to low micromolar concentrations [69]. This could be readily toggled off with violet light (*E* to *Z* isomerization). Furthermore, these compounds

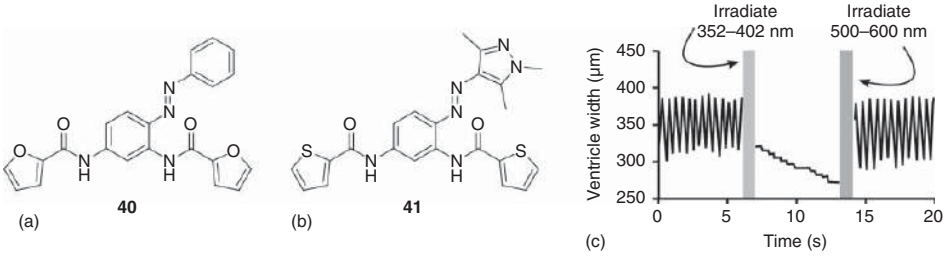


**Figure 5.9** (a) The structure of the azobenzene-based TRPA1 photoactuator, **40**. (**b)** The structure of the azopyrazole-based TRPA1 photoactuator, **41**. (c) Sequential irradiation of larval zebrafish containing **41** was found to modulate the cardiac rhythm, followed by monitoring the ventricle width as a function of time. Source: Adapted from Lam et al. [67].

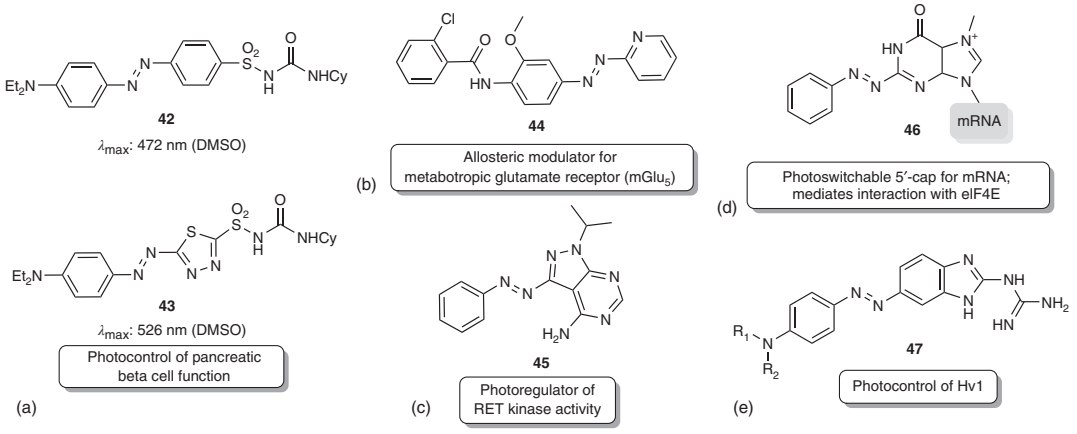


**Figure 5.10** A selection of azoheteroarene scaffolds employed in photoregulation of various biological targets. (a) Structures of photoswitches that exhibit photocontrol over pancreatic beta-cell function and insulin secretion [68]. (b) Azopyridine-based switch targeting the $mGlu_5$ receptor [69]. (c) An azopyrazolopyrimidine designed to regulate RET kinase activity [70]. (d) A photoswitchable guanosine residue to block an interaction of translation initiation factor elF4E [71]. (e) An azobenzimidazole derivative designed to grant photocontrol over Hv1 [72].

demonstrated analgesic activity in a rodent model that could be toggled off with violet light and subsequently restored (green light; *Z* to *E* isomerization) [69]. An azopyrazolopyrimidine system (**45**, Figure 5.10c) [70] allows photoregulation of RET kinase activity with an absorbance maximum that is red-shifted (375 nm) with respect to a stilbene analogue (313 nm) [74]. While photoregulation with the azopyrazolopyrimidine was robust and reversible, the corresponding stilbene underwent photoinduced side-reactions preventing a similar response. Ogasawara reported the use of a modified, photoswitchable guanosine residue, **46**, that could be tagged at the 5′-cap of an mRNA sequence (Figure 5.10d) [71]. The *E* isomer blocks an interaction between the translation initiation factor elF4E and the 5′-cap. Irradiation with 370 nm light (*E* to *Z* isomerization) allowed elF4E to bind and initiate protein translation. This photoswitchable tool was subsequently used to study the developmental biology of zebrafish embryos. Berger and coworkers reported a class of azobenzimidazoles (**47**, Figure 5.10e) for photocontrol of the voltage-gated proton channel Hv1, which is found in various cells, including macrophages and sperm [72]. The *E*-isomer inhibits Hv1 effectively, but maximal inhibition, for an exemplar compound, is reduced ~1.5-fold upon irradiation with blue light (*E* to *Z* isomerization) and a concomitant change in $IC_{50}$ from 9 to 13 μM. This in turn induced robust proton currents in sperm and macrophages. Compared to azobenzene, these compounds featured red-shifted absorbance maximum in the range of 452–468 nm.

### 5.4.4 Glutathione Stability

Metabolism of the azo bridge is an important parameter for consideration if azo photoswitches are to be serious contenders as light-addressable therapeutics. While extensive literature investigations have profiled the metabolic stability of the *E*-isomer of azobenzenes in microsomes and against oxidative and reductive enzymes, there is currently a dearth of similar surveys as applied to azoheteroarenes. Preliminary activity has been reported concerning the assessment of azoheteroarenes stability to reduction by glutathione (GSH) however – an important reductant in biological assays and cells. In this regard, the azopyrazoles measured to date have shown remarkable stability. This is highlighted in a recent study by Samanta and coworkers who found that thiomethyl-substituted arylazopyrazoles (**48**, Figure 5.11a) [75] demonstrated a markedly improved resistance toward reduction by glutathione than tetramethoxy azobenzene [65, 76] derivatives (**51**, Figure 5.11b) [75]. Ravoo and coworkers have also demonstrated that a family of 3,5-dimethylazopyrazoles have impressive stability to incubation with an effective concentration of 10 mM GSH (reduced form); **49**, see Figure 5.11a [78]. Incidentally, König, Crespi, and coworkers, under comparable experimental conditions, have demonstrated 3(5)-substituted-1*H*-pyrazoles, **50**, to undergo <5% reduction by GSH after 16 hours of exposure (Figure 5.11a) [79]. In contrast to the excellent stability of the arylazopyrazoles, Herges and coworkers reported a 2-azothiazole

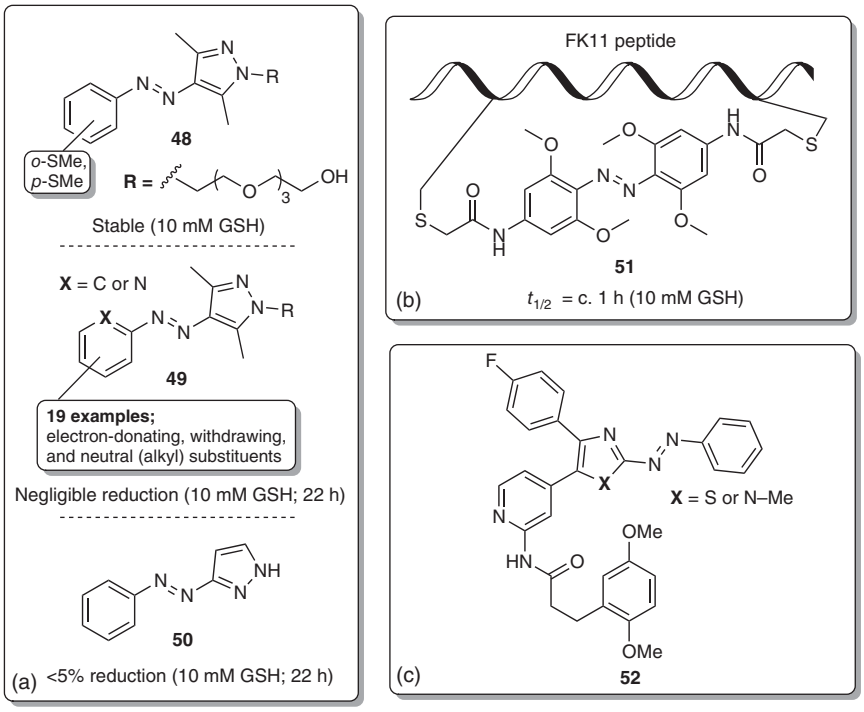


**Figure 5.11** (a) Azopyrazole derivatives appear resistant to GSH reduction [75, 78, 79]. (b) Crosslinked tetramethoxy azobenzenes undergo GSH-promoted reduction of the azo bridge [76]. (c) An azothiazole derivative, being more electron-poor than its azimidazole analogue, is prone to undergoing GSH reduction to the hydrazide [77].

photoswitchable kinase inhibitor to undergo a relatively facile reduction of the azo functionality by DTT, or GSH, in the relevant assays (**52**, Figure 5.11c) [77]. This reduction was not observed for a comparably more electron-rich 2-azoimidazole analogue. As with all azo photoswitches, GSH stability appears to be, at least in part, governed by the redox potential of the azo bridge, with electro-rich heterocycles (pyrazole and imidazole) being more resistant than electron-poor counterparts (thiazoles).

## 5.5 Materials for Electronic Applications

Materials that can robustly alter both their structural and electronic properties in response to particular stimuli continue to be of high interest for a variety of electronic applications. This is most certainly the case for azoheteroarene-based photoswitches, whereby the tunability of structure and switching properties allows them to be tailored to perform specific roles. In this section, we present several exciting applications of azoheteroarenes in electronic applications.

### 5.5.1 Information Transfer

Azoheteroarenes are promising candidates for use in information transfer [57] and molecular photo-oscillators [2, 15]. In this role, a fast rate of photoinduced $E$ to $Z$ isomerization and fast thermal $Z$ to $E$ reversion (in the dark) is required. Thus, an optical signal can induce a change in the initial state of the switch, which subsequently reverts to its initial state following the end of the optical stimulus, ready to receive the next signal. The typical time scale required for such applications is the ns–ps regime. General to azoarene-derived photoswitches is fast photoinduced isomerism, taking place on the sub-ps time scale [80]. However, the reported rates of thermal reversion can span 18 orders of magnitude; thus, it is important to select the right switch for a given application [38, 46].

Azopyridine and azopyridiunium derivatives have demonstrated short half-lives in the range of $10^3$–$10^{-10}$ seconds (measured in EtOH, Figure 5.12a) [15, 81]. These low values, relative to azobenzene (thermal $t_{1/2}$ of $Z$ to $E$ of 69 hours) [81, 82], can be attributed to either an improved ability to engineer push–pull character across the azo-moiety resulting in an azo/hydrazone tautomeric equilibrium (**54**, Figure 5.12a) [46], or via improved inversion and rotation isomerization pathways [9]. Velasco and coworkers demonstrated that the covalent attachment of two azo-switches, one being an azopyridinium derivative, afforded a system displaying two different half-life regimes, separated by $10^{15}$ seconds (**55**, Figure 5.12a). In this example, the thermal half-life of the faster azo-switch (0.2 ns in EtOH) displayed a $10^3$ seconds shorter half-life in the coupled structure than when it was in isolation (255 ns in EtOH) [57]. This observation points toward additional factors, the spatial proximity, or steric bulk, as a contributor to the rate of thermal isomerism [57]. In a subsequent study, the same group achieved thermal half-lives on the ps time scale (**25**, measured in EtOH, Figure 5.12a) by employing stronger electron-withdrawing motifs in a push–pull switch. Exchanging the pyridinium ring for thiazolium or benzothiazolium, afforded greater hydrazone character to the tautomeric equilibrium, affording the fastest reported thermal half-lives for azo-switches to date (~ps in EtOH). One common feature of the azoheteroarene-based switches possessing short thermal half-lives is their charged nature. However, charged molecules can pose challenging when incorporating these materials in device applications, due to their limited solubilities in common host materials and liquid-crystalline dopants [63, 83]. Azoheteroarenes bearing neutral push–pull systems have also afforded relatively short thermal half-lives; a switch comprising benzothiazole and pyrrole derivatives have afforded thermal half-lives of 49 μs (**53**, measured in EtOH, Figure 5.12a), while neutral azoindoles reported by König and coworkers have reached thermal half-lives as low as 5.3 ns (**2**, measured in cyclohexane, Figure 5.12a) [9, 83].

### 5.5.2 Switching in the Solid State

To date, reports of azoheteroarene switches being applied to electronic devices are scarce in the literature [18]. This may, in part, be attributed to the challenges associated with translating the properties displayed in the solution state to the solid state

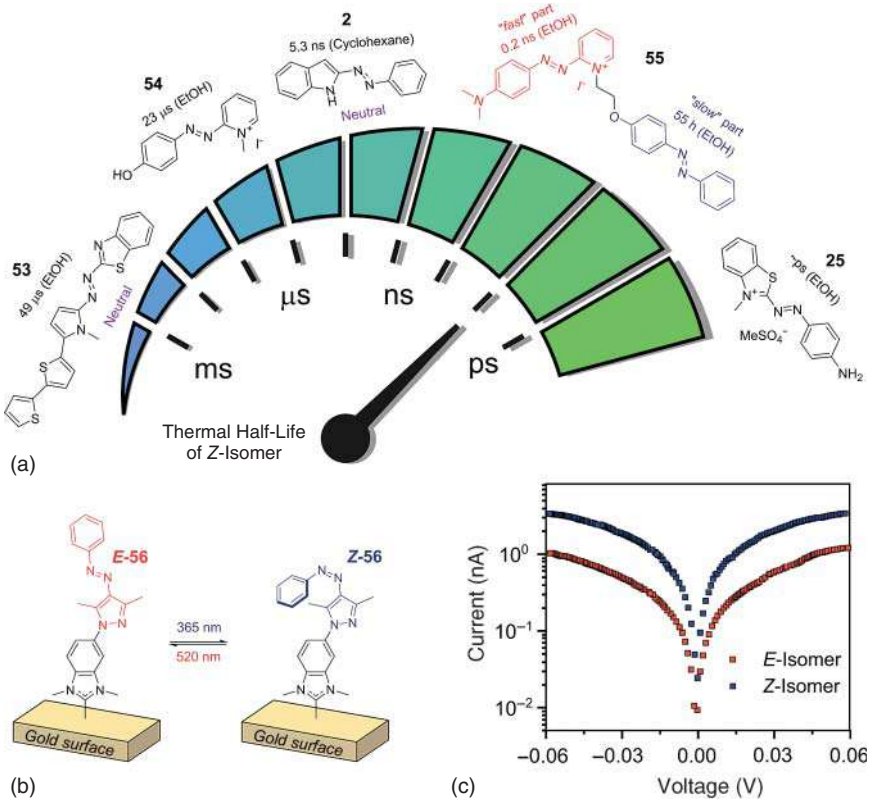


**Figure 5.12** (a) The structures of various azoheteroarene photoswitches (*i–iv)*, displaying a range of thermal half-lives, designed for information transfer applications. (b) Arylazopyrazoles can be attached to conductive gold surfaces via N-heterocyclic carbenes [18]. (c) Using conductive AFM (cAFM), the electrical current through switch **56** could be modulated as a function of the isomerism state of the switch. This behavior was rationalized as a change in resistance of the conductive pathway. Source: Modified from Nguyen et al. [18].

[7, 84]. For azo-switches in the solution state, the switching process is typically facile. However, for self-assembled monolayers and crystalline films, strong intermolecular interactions and the density of the molecular packing can severely hinder their propensity to isomerize [7]. One class of azoheteroarene that is capable of switching in the absence of solvent are the arylazoisoxazoles (**5**, Figure 5.1) [12]. These switches undergo a light-induced phase transition, from solid to liquid, upon photoisomerism from the *E*-isomer to the *Z*-isomer. The authors concluded that this behavior was facilitated by the absence of strong intermolecular interactions between the individual switches in the solid state. Therefore, arylazoisoxazoles may provide a useful platform to develop solid-state photoswitching; however, their attachment to surfaces so as to control the packing density and preserve electronic communication between the substrate and the photoswitch requires equal consideration.

Recently, Glorius and coworkers demonstrated switching of an azoheteroarene, **56**, tethered to a surface (Figure 5.12b) [18]. The covalent attachment of an arylazopyrazole to an N-heterocyclic carbene served as an effective route toward anchoring the azoswitches to a conductive substrate. The resulting system displayed complete conjugation from the arylazopyrazole to a gold substrate, allowing the electronic properties of the system to be investigated in response to photoisomerism. The surface-anchored arylazopyrazoles maintained their ability to photoswitch in response to different wavelengths of light, evidenced by a change in contact angle due to the different dipole moments of the *E* and *Z* isomers. The switch state of the arylazopyrazole, more specifically, the magnitude of dipole moment, was found to dictate the work function of the substrate and conductance of the system (Figure 5.12c). *Z*-**56** exhibited a 2.3-fold lower resistance than the *E*-**56**, attributed to a combination of a shortening of the molecule when expressed as the *Z*-isomer, in addition to the *Z*-isomer exhibiting greater intermolecular coupling. This light-mediated change in conductance may serve as a platform toward developing single-molecule photodiodes. The combination of these recent advances with the insight obtained for manipulating the thermal half-lives of these azoheteroarene photoswitches suggests that further studies into translating these molecular systems into functional electronic devices would be worthwhile.

## 5.6 Azoheteroarenes in Supramolecular Chemistry

The use of light to directly manipulate a system's chemical or physical properties, with a high degree of spatio-temporal control, has found widespread use in the field of supramolecular chemistry [5, 85, 86]. Azo-photoswitches have been employed in a variety of supramolecular applications, including the modulation of host–guest chemistry, driving systems away from equilibrium and generating responsive molecular architectures. More specifically, azoheteroarenes have become a widely studied class of photoswitches in this area due to their high degree of structural and property tuneability as well as the ability of heteroarenes to serve as ligands.

### 5.6.1 Modulation of Host–Guest Behavior

The improved separation of the π–π* and n–π* absorption bands of arylazopyrazoles has been exploited to efficiently achieve a change in host–guest properties upon irradiation [5, 78, 85]. Ravoo and coworkers demonstrated that cucurbit[8]uril (CB[8]), a host, was able to encapsulate both a molecule of methylviologen, **57**, and an arylazopyrazole, **58**, the guest molecules, affording a heteroternary inclusion complex (Figure 5.13a) [85]. The binding of **58** was selective for the *E*-isomer with the *Z*-isomer unable to fit inside the host. Irradiation of the host–guest complex with UV light results in the ejection of the *Z*-isomer of **58**. This behavior was further extended to develop photoactive biosurfaces. Covalently tethering methylviologen to a substrate, combined with a pyrazole ring containing a motif that could be recognized by receptors of a specific cell, allowed spatio-temporal control of cell

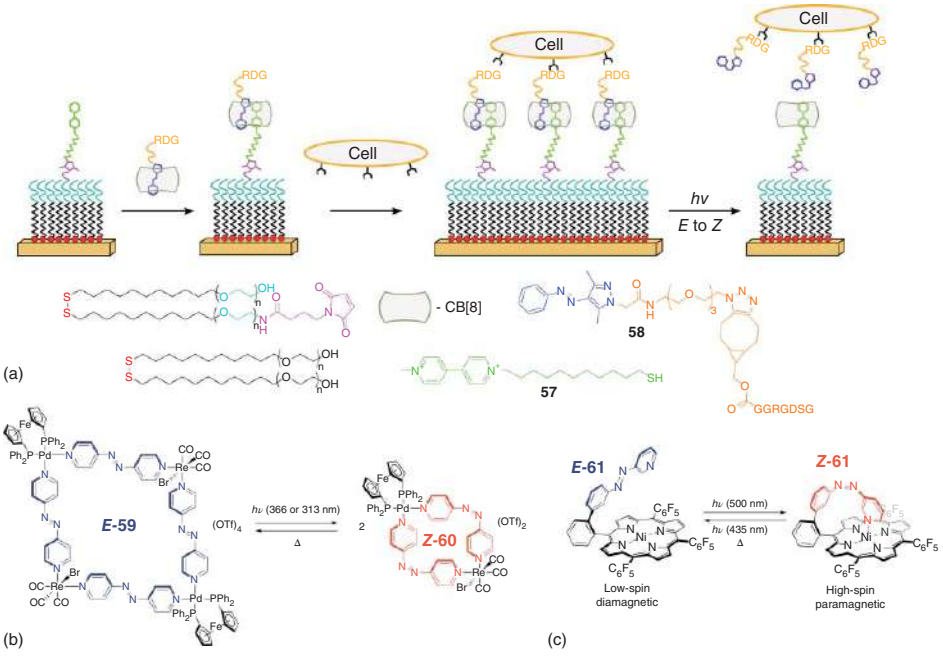


**Figure 5.13** (a) Schematic of an arylazopyrazole-based switch serving as a switchable anchor for a cell to a functionalized surface, mediated by a change in binding properties of the switch with cucurbit[8]uril (CB[8]) as a function of *E*–*Z* isomerism. Source: Modified from Wiemann et al. [85]. (b) Demonstration of an azopyridine photoswitch serving as a ligand. Source: Modified from Sun et al. [10]. Photoswitching results in a change of the macroscopic structure due to a change in the ligands' coordination vectors. (c) Spin-state switching based on an arylazopyridine photoswitch. Source: Venkataramani et al. [13].

immobilization to the surface (Figure 5.13a). Alternatively, a similar photomediated host–guest methodology has been applied to reversibly controlling the aggregation state of nanoparticles [5, 87]. Arylazopyrazoles excel in this area, whereby their improved thermal stability of the *Z*-isomer and larger PSSs affords a more complete change in the material properties trigged upon irradiation [5]. Light-dependent anchoring of molecules to surfaces and nanoparticles has led to the development of defined nano-scale cavities in which reactions can be performed, termed nanoreactors [88]. To date, these nanoreactors have adopted azobenzene photoswitches; however, the improved photoswitching behavior of arylazopyrazoles as reported by Ravoo and coworkers in similar materials may serve to maximize the performance of these nanoreactors.

### 5.6.2 Photoswitchable Ligands

Differences in the relative orientation of the heteroarene rings for the *E*/*Z* isomers can be amplified to macroscopic changes in structure [10]. Exploiting the ability for heteroarenes to coordinate to metal ions (M) [89, 90], photoresponsive 3D architectures have been developed comprising azoheteroarene ligands (L). An early example was demonstrated by Lees and coworkers, whereby the photoinduced structural change of individual azopyridine molecules was translated into a macroscopic change of a size of a macrocycle [10]. Explicitly, the size of a heterometallic macrocycle could be toggled between an $M_4L_4$ (*E*-**59**) and an $M_2L_2$ (*Z*-**60**) macrocycle using light (Figure 5.13b). In regard to converting light-induced structural changes into a function, Herges and coworkers described the use of an arylazopyridine derivative to control the spin state of a metal center (Figure 5.13c). This was achieved through tethering a phenylazo-3-pyridine arm to a $Ni^{2+}$ porphyrin [13, 91]. For the *E*-isomer, *E*-**61**, both the coordination vector and distance between the pyridyl unit and the $Ni^{2+}$ ion was insufficient to achieve coordination. Upon irradiation with 500 nm light, the *Z*-isomer, *Z*-**61**, was accessed and allowed coordination of the pyridyl fragment to the $Ni^{2+}$ center. This was accompanied by a change from low to high spin of the metal center, hence from diamagnetic to paramagnetic. Thus, light-induced spin-state switching was achieved using a photoswitch. Spin-state switching in the presence of water was realized by exchanging the azopyridine motif for azo-*N*-methylimidazole [17]. Such compounds, capable of spin-state switching under physiological conditions, are of interest as photoswitchable contrast agents in MRI applications for example [17].

## 5.7 Energy-Storage Materials

Molecular solar thermal (MOST) materials have been hailed as a promising approach for thermal energy storage. MOST materials function by absorbing the energy from sunlight and storing it in a metastable state, accessed via a photoisomerization process. Reverse isomerization results in the release of the stored energy. One of the most important properties for photoswitchable MOST materials

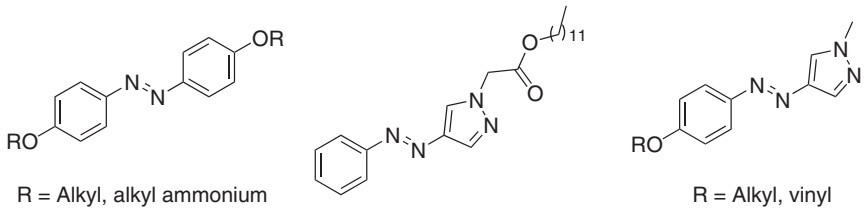


**Figure 5.14** (a) Photoswitchable ionic crystals based on switch **62**, reported by Kimizuka and coworkers. Source: Modified from Ishiba et al. [95]. (b) Dodecanoate azopyrazole derivative **4** reported by Han, Fuchter, and coworkers. Source: Modified from Gerkman et al. [11]. (c) Pyrazoles based on motif **63** reported by Moth-Poulsen, Li and coworkers. Source: Modified from Zhang and Li [96].

is the thermal half-life of the metastable state, corresponding to the lifetime of the stored energy. Azobenzenes have been previously explored as candidates for MOST materials as small molecules [92, 93] and dopants [94] in a variety of hybrid materials [4]. For azobenzene-derived MOST materials, half-lives in the solid state are limited by the half-life of the azobenzene core, as demonstrated by photoliquefiable ionic crystals of switch **62** (Figure 5.14a) whose half-life is less than half a day [95]. The energy-storage capabilities of MOST materials can be greatly extended by exchanging the azobenzene core for a heteroaryl with a significantly longer half-life, for example, the 4pzH moiety in **4**. Azo-switches comprising pyrazole derivatives, **4** and **63,** have been reported by both Han, Fuchter, and coworkers [11] (Figure 5.14b), and Moth-Poulsen, Li, and coworkers [96] (Figure 5.14c), respectively. These pyrazole-based switches have demonstrated increased half-lives, with the dodecanoate examples, notably **4** (Figure 5.14b) being reported to store energy in the solid state for weeks. The dodecanoate derivatives have the added advantage of releasing the stored energy at sub-zero temperatures due to the *Z*-isomers' liquid-phase stability at low temperatures, which may find a range of applications in colder climates. Recently, Han, Fuchter and coworkers have demonstrated efficient electrochemical switching in the condensed phase [97].

## 5.8 Final Remarks

In this chapter, we highlighted the key structure–property relationships that are generally applicable to the majority of azoheteroarene structures. However, this picture is not complete. With each new azoheteroarene motif that is reported, a thorough investigation of their structure–property relationship would fill in gaps in knowledge and thus facilitate the rational design of photoswitches to precise specification. Such improved understanding would, in turn, further allow the development of new and improved light-mediated applications. For example, in regards to photopharmacological applications, similar challenges to those faced by azobenzene motifs are also present for azoheteroarenes, notably, red-shifted absorption and stability under physiological conditions. For the former challenge,

recent advances in a two-photon absorption strategy for azobenzene motifs are likely to be applicable to azoheteroarenes [98]. For electronic-based applications, specifically, information transfer, combining the design principles of ultrafast thermal reversion with the recent advances of azoheteroarenes that are capable of switching in the solid state may help the realization of using these switches in electronic devices. Novel azoheteroarene motifs are still being frequently reported: with each new structure prepared, the number of potential applications for these switches undoubtedly increases. Thus, we look forward to seeing what unpredicted applications will emerge for this diverse class of photoswitches in the future.

## References


1 Hartley, G.S. (1938). *J. Chem. Soc.*: 633–642. https://doi.org/10.1039/JR9380000633.
2 Crespi, S., Simeth, N.A., and König, B. (2019). *Nat. Rev. Chem.* 3: 133–146.
3 Szymański, W., Beierle, J.M., Kistemaker, H.A.V. et al. (2013). *Chem. Rev.* 113: 6114–6178.
4 Dong, L., Feng, Y., Wang, L., and Feng, W. (2018). *Chem. Soc. Rev.* 47: 7339–7368.
5 Stricker, L., Fritz, E.-C., Peterlechner, M. et al. (2016). *J. Am. Chem. Soc.* 138: 4547–4554.
6 Sell, H., Gehl, A., Plaul, D. et al. (2019). *Commun. Chem.* 2: 62.
7 Klajn, R. (2010). *Pure Appl. Chem.* 82: 2247–2279.
8 Mafy, N.N., Matsuo, K., Hiruma, S. et al. (2020). *J. Am. Chem. Soc.* 142: 1763–1767.
9 Crespi, S., Simeth, N.A., Bellisario, A. et al. (2019). *J. Phys. Chem. A* 123: 1814–1823.
10 Sun, S.-S., Anspach, J.A., and Lees, A.J. (2002). *Inorg. Chem.* 41: 1862–1869.
11 Gerkman, M.A., Gibson, R.S.L., Calbo, J. et al. (2020). *J. Am. Chem. Soc.* 142: 8688–8695.
12 Kumar, P., Srivastava, A., Sah, C. et al. (2019). *Chem. Eur. J.* 25: 11924–11932.
13 Venkataramani, S., Jana, U., Dommaschk, M. et al. (2011). *Science* 331: 445–448.
14 Calbo, J., Weston, C.E., White, A.J.P.P. et al. (2017). *J. Am. Chem. Soc.* 139: 1261–1274.
15 García-Amorós, J. and Velasco, D. (2012). *Beilstein J. Org. Chem.* 8: 1003–1017.
16 Gibson, R.S.L., Calbo, J., and Fuchter, M.J. (2019). *ChemPhotoChem* 3: 372–377.
17 Heitmann, G., Schütt, C., Gröbner, J. et al. (2016). *Dalton Trans.* 45: 11407–11412.
18 Nguyen, D.T., Freitag, M., Gutheil, C. et al. (2020). *Angew. Chem. Int. Ed.* 59: 13651–13656.
19 Weston, C.E., Richardson, R.D., and Fuchter, M.J. (2016). *Chem. Commun.* 52: 4521–4524.
20 Garcia-Amorós, J., Díaz-Lobo, M., Nonell, S., and Velasco, D. (2012). *Angew. Chem. Int. Ed.* 51: 12820–12823.


**21** Fuchter, M.J. (2020). *J. Med. Chem.* 63 (20): 11436–11447. https://doi.org/10.1021/acs.jmedchem.0c00629.

**22** Okumura, S., Lin, C.-H., Takeda, Y., and Minakata, S. (2013). *J. Org. Chem.* 78: 12090–12105.

**23** Gattavecchia, E. and Tonelli, D. (1986). *J. Chem. Soc. Perkin Trans* 2: 689.

**24** Hussain, G., Ather, M., Khan, M.U.A. et al. (2016). *Dyes Pigm.* 130: 90–98.

**25** Kumar, R., Joshi, Y.C., and Joshi, P. (2005). *Heterocycl. Commun.* 11: 361–364.

**26** Gelebart, A.H., Mulder, D.J., Vantomme, G. et al. (2017). *Angew. Chem. Int. Ed.* 56: 13436–13439.

**27** Jackson, A.H. and Lynch, P.P. (1987). *J. Chem. Soc. Perkin Trans.* 53: 1215.

**28** Verma, R.K., Aggarwal, M., Bansal, M., and Kaur, I.P. (2007). *Synth. Commun.* 37: 1977–1982.

**29** Colomer, J.P. and Moyano, E.L. (2011). *Tetrahedron Lett.* 52: 1561–1565.

**30** Gompper, R., Guggenberger, R., and Zentgraf, R. (1985). *Angew. Chem. Int. Ed.* 24: 984–985.

**31** Al-Etaibi, A., El-Apasery, M., Ibrahim, M., and Al-Awadi, N. (2012). *Molecules* 17: 13891–13909.

**32** Weston, C.E., Richardson, R.D., Haycock, P.R. et al. (2014). *J. Am. Chem. Soc.* 136: 11878–11881.

**33** Slavov, C., Yang, C., Heindl, A.H. et al. (2020). *Angew. Chem. Int. Ed.* 59: 380–387.

**34** Wendler, T., Schütt, C., Näther, C., and Herges, R. (2012). *J. Org. Chem.* 77: 3284–3287.

**35** Rangnekar, D.W. and Dhamnaskar, S.V. (1988). *J. Heterocycl. Chem.* 25(6): 1663–1664.

**36** Cameron, M., Gowenlock, B.G., and Boyd, A.S.F. (1996). *J. Chem. Soc. Perkin Trans.* 2, 53: 2271.

**37** Slavov, C., Yang, C., Heindl, A.H. et al. (2018). *J. Phys. Chem. Lett.* 9: 4776–4781.

**38** Calbo, J., Thawani, A.R., Gibson, R.S.L. et al. (2019). *Beilstein J. Org. Chem.* 15: 2753–2764.

**39** Bléger, D., Schwarz, J., Brouwer, A.M., and Hecht, S. (2012). *J. Am. Chem. Soc.* 134: 20597–20600.

**40** Schweighauser, L., Strauss, M.A., Bellotto, S., and Wegner, H.A. (2015). *Angew. Chem. Int. Ed.* 54: 13436–13439.

**41** Thies, S., Sell, H., Bornholdt, C. et al. (2012). *Chem. Eur. J.* 18: 16358–16368.

**42** Čechová, L., Kind, J., Dračínský, M. et al. (2018). *J. Org. Chem.* 83: 5986–5998.

**43** Otsuki, J., Suwa, K., Narutaki, K. et al. (2005). *J. Phys. Chem. A* 109: 8064–8069.

**44** Travieso-Puente, R., Budzak, S., Chen, J. et al. (2017). *J. Am. Chem. Soc.* 139: 3328–3331.

**45** Garcia-Amorós, J., Nonell, S., and Velasco, D. (2012). *Chem. Commun.* 48: 3421.

**46** Garcia-Amorós, J., Maerz, B., Reig, M. et al. (2019). *Chem. Eur. J.* 25: 7726–7732.

**47** Kolarski, D., Szymanski, W., and Feringa, B.L. (2017). *Org. Lett.* 19: 5090–5093.

**48** Kennedy, A.D.W.W., Sandler, I., Andréasson, J. et al. (2020). *Chem. Eur. J.* 26: 1103–1110.

**49** Kirpal, A. and Böhm, W. (1932). *Ber. Dtsch. Chem. Ges.* 65: 680–682.


**50** Le Fèvre, R.J.W. and Worth, C.V. (1951). *J. Chem. Soc.*: 1814–1817.
**51** Brown, E.V. and Granneman, G.R. (1975). *J. Am. Chem. Soc.* 97: 621–627.
**52** Nakagawa, M., Rikukawa, M., Watanabe, M. et al. (1997). *Bull. Chem. Soc. Jpn.* 70: 737–744.
**53** Otsuki, J. and Narutaki, K. (2004). *Bull. Chem. Soc. Jpn.* 77: 1537–1544.
**54** Wang, Y., Ge, X., Schull, G. et al. (2010). *J. Am. Chem. Soc.* 132: 1196–1197.
**55** Matino, F., Schull, G., Jana, U. et al. (2010). *Chem. Commun.* 46: 6780.
**56** Garcia-Amorós, J., Nonell, S., and Velasco, D. (2011). *Chem. Commun.* 47: 4022.
**57** Garcia-Amorõs, J., Cuadrado, A., Reig, M. et al. (2015). *Chem. Eur. J.* 21: 14292–14296.
**58** Simeth, N.A., Crespi, S., Fagnoni, M., and König, B. (2018). *J. Am. Chem. Soc.* 140: 2940–2946.
**59** Whittaker, N. and Jones, T.S.G. (1951). *J. Chem. Soc.*: 1565–1570.
**60** Heindl, A.H. and Wegner, H.A. (2020). *Chem. Eur. J.* 26 https://doi.org/10.1002/chem.202001148.
**61** Otsuki, J., Suwa, K., Sarker, K.K., and Sinha, C. (2007). *J. Phys. Chem. A* 111: 1403–1409.
**62** Wiberg, K.B. (1968). *Tetrahedron* 24: 1083–1096.
**63** Garcia-Amorós, J., Reig, M., Castro, M.C.R. et al. (2014). *Chem. Commun.* 50: 6704–6706.
**64** Devi, S., Saraswat, M., Grewal, S., and Venkataramani, S. (2018). *J. Org. Chem.* 83: 4307–4322.
**65** Samanta, S., Babalhavaeji, A., Dong, M., and Woolley, G.A. (2013). *Angew. Chem. Int. Ed.* 52: 14127–14130.
**66** Hanopolskyi, A.I., De, S., Białek, M.J. et al. (2019). *Beilstein J. Org. Chem.* 15: 2398–2407.
**67** Lam, P., Thawani, A.R., Balderas, E. et al. (2020). *J. Am. Chem. Soc.* 142: 17457–17468.
**68** Broichhagen, J., Frank, J.A., Johnston, N.R. et al. (2015). *Chem. Commun.* 51: 6018–6021.
**69** Gómez-Santacana, X., Pittolo, S., Rovira, X. et al. (2017). *ACS Cent. Sci.* 3: 81–91.
**70** Ferreira, R., Nilsson, J.R., Solano, C. et al. (2015). *Sci. Rep.* 5: 9769.
**71** Ogasawara, S. (2017). *ACS Chem. Biol.* 12: 351–356.
**72** Rennhack, A., Grahn, E., Kaupp, U.B., and Berger, T.K. (2017). *ACS Chem. Biol.* 12: 2952–2957.
**73** Broichhagen, J., Schönberger, M., Cork, S.C. et al. (2014). *Nat. Commun.* 5: 5116.
**74** Dinér, P., Alao, J.P., Söderlund, J. et al. (2012). *J. Med. Chem.* 55: 4872–4876.
**75** Bhunia, S., Dolai, A., and Samanta, S. (2020). *Chem. Commun.* 56: 10247–10250.
**76** Samanta, S., Beharry, A.A., Sadovski, O. et al. (2013). *J. Am. Chem. Soc.* 135: 9777–9784.
**77** Schehr, M., Ianes, C., Weisner, J. et al. (2019). *Photochem. Photobiol. Sci.* 18: 1398–1407.
**78** Stricker, L., Böckmann, M., Kirse, T.M. et al. (2018). *Chem. Eur. J.* 24: 8639–8647.
**79** Rustler, K., Nitschke, P., Zahnbrecher, S. et al. (2020). *J. Org. Chem.* 85: 4079–4088.


**80** W. M. Horspool and F. Lenci. (2004). *Organic Photochemistry and Photobiology*, CRC Press: Boca Raton. https://doi.org/10.1201/9780203495902.

**81** Bujak, K., Orlikowska, H., Małecki, J.G. et al. (2019). *Dyes Pigm.* 160: 654–662.

**82** Bandara, H.M.D.D. and Burdette, S.C. (2012). *Chem. Soc. Rev.* 41: 1809–1825.

**83** Garcia-Amorós, J., Castro, M.C.R., Coelho, P. et al. (2013). *Chem. Commun.* 49: 11427–11429.

**84** Goulet-Hanssens, A., Eisenreich, F., and Hecht, S. (2020). *Adv. Mater.* 32: 1905966.

**85** Wiemann, M., Niebuhr, R., Juan, A. et al. (2018). *Chem. Eur. J.* 24: 813–817.

**86** McConnell, A.J., Wood, C.S., Neelakandan, P.P., and Nitschke, J.R. (2015). *Chem. Rev.* 115: 7729–7793.

**87** Möller, N., Hellwig, T., Stricker, L. et al. (2017). *Chem. Commun.* 53: 240–243.

**88** Wei, Y., Han, S., Kim, J. et al. (2010). *J. Am. Chem. Soc.* 132: 11018–11020.

**89** Zhang, Y., Wang, L., Hu, J. et al. (2020). *CrystEngComm* 22: 2649–2655.

**90** Wang, W., Wang, Y.X., and Yang, H.B. (2016). *Chem. Soc. Rev.* 45: 2656–2693.

**91** Thies, S., Sell, H., Schütt, C. et al. (2011). *J. Am. Chem. Soc.* 133: 16243–16250.

**92** Hu, J., Huang, S., Yu, M., and Yu, H. (2019). *Adv. Energy Mater.* 9: 1901363.

**93** Kunz, A., Heindl, A.H., Dreos, A. et al. (2019). *ChemPlusChem* 84: 1145–1148.

**94** Han, G.G.D., Deru, J.H., Cho, E.N., and Grossman, J.C. (2018). *Chem. Commun.* 54: 10722–10725.

**95** Ishiba, K., Morikawa, M., Chikara, C. et al. (2015). *Angew. Chem. Int. Ed.* 54: 1532–1536.

**96** Zhang, Z. and Li, T. (2019). *ChemRxiv* https://doi.org/10.26434/chemrxiv.9730694.v1.

**97** Greenfield, J.L., Gerkman, M.A., Gibson, R.S.L. et al. (2021). *J. Am. Chem. Soc.* 143(37): 15250–15257.

**98** Moreno, J., Gerecke, M., Dobryakov, A.L. et al. (2015). *J. Phys. Chem. B* 119: 12281–12288.


# 6 Arylhydrazones

Baihao Shao and Ivan Aprahamian

**Photochromism**

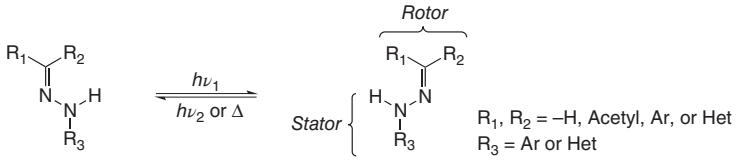


**Characteristic Features**

(1) Straightforward synthesis; (2) thermal relaxation half-lives that range from thousands of years to hours; (3) fluorescence emission that can be toggled "ON" and "OFF"; (4) photoswitching in the condensed phase and (5) switching in biologically relevant media and in the presence of glutathione.

**Synthetic Methods**

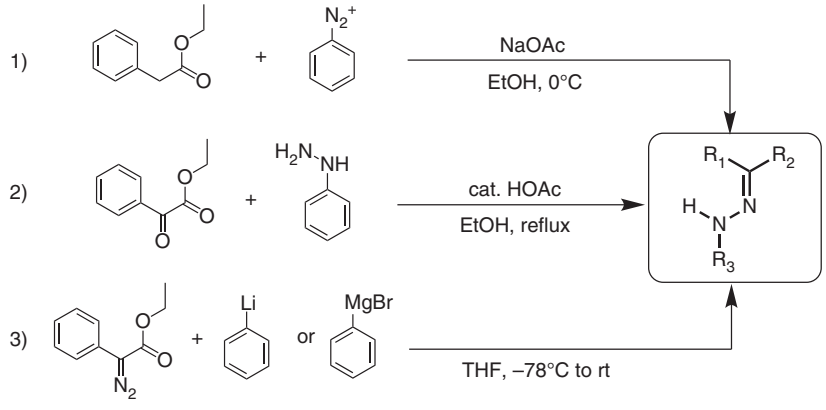


Note: Ethyl ester and phenyl groups are exemplars used in this case to represent $R_1$, $R_2$, $R_3$.

**First Reported**

Courtot, P., Pichon, R., and Le Saint, J. (1976). DETERMINATION IJU SITE DE CHELATION CHEZ LES ARYLHYDRAZONES DE TRICETONES ET D' cr-DICETONES SUBSTITUEES Tetrahedron Lett. 17: 1177–1180.

**Key References**

Chaur, M.N., Collado, D., and Lehn, J.-M. (2011). Configurational and constitutional information storage: multiple dynamics in systems based on pyridyl and acyl hydrazones. *Chem. Eur. J.* 17: 248–258.

Qian, H., Pramanik, S., and Aprahamian, I. (2017). Photochromic hydrazone switches with extremely long thermal half-lives. *J. Am. Chem. Soc.* 139: 9140–9143.

Shao, B., Qian, H., Li, Q., Aprahamian, I. (2019). Structure property analysis of the solution and solid-state properties of bistable photochromic hydrazones. *J. Am. Chem. Soc.* 141: 8364–8371.

# 6

# Arylhydrazones

*Baihao Shao and Ivan Aprahamian*

*Dartmouth College, Department of Chemistry, 6128 Burke Laboratory, Hanover, NH 03755, USA*

## 6.1 Introduction

Photochromic compounds featuring *E*/*Z* photoisomerization around double bonds (e.g. C=C, N=N, and C=N bonds) are an indispensable class of functional molecules for the development of light-responsive devices and materials [1, 2]. The most important characteristic that distinguishes this class of photoswitches from others is the large geometrical change they undergo upon *E*/*Z* isomerization. The subsequent spatial rearrangement of the position of substituents enables molecular-level functions that include bringing/moving two functional units together/apart [3], favoring/disfavoring molecular interactions [4], and affecting/altering coupled supramolecular networks [5–7], among others. Such photochromes have therefore been extensively applied in designing light-controllable reactions and catalysts [8, 9], supramolecular assemblies [10, 11], polymer and crystal actuation [12, 13], sensors [14], magnets [15], and drugs (i.e. photopharmacology) [16, 17]. The development and optimization of stilbenes [18], azobenzenes [19], and their derivatives [20] over the years have resulted in these accomplishments, while at the same time, set the stage for developing new photoswitchable systems that can overcome the limitations associated with these prevalent systems. These developments have spurred a renewed interest in new photoswitchable architectures [2], resulting in new opportunities for accessing unprecedented functions and properties.

The multifaceted and versatile hydrazone (C=N—NH) functional group, consisting of a dynamic imine bond and an acidic NH proton, has been historically used in synthesis, sensing applications, cation coordination, and dynamic covalent chemistry [21]. The use of the *E*/*Z* isomerization around the C=N double bond in the development of photoswitches on the other hand has until very recently been less explored (Scheme 6.1). This disparity stemmed from a lack of attention to the photoswitchable arylhydrazones developed by Pichon and Courtet [22–24]. The growing interest in diversifying the molecular switch toolbox, together with an appreciation that the predominant switches can be drastically improved, resulted in a surge in the exploration of chemically and photochemically activated hydrazone switches

*Molecular Photoswitches: Chemistry, Properties, and Applications*,
First Edition. Edited by Zbigniew L. Pianowski.


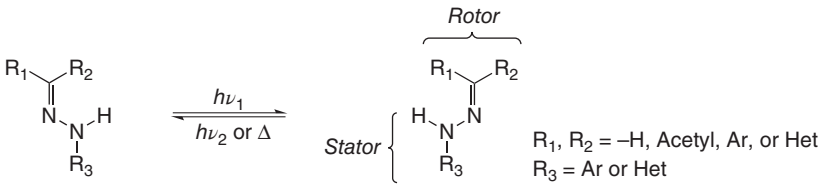


**Scheme 6.1** *E/Z* photoisomerization around the C=N double bond of arylhydrazone (The designation of rotor and stator is arbitrary).

[25]. The studies that have ensued showcased that the hydrazones (i) can undergo efficient and reversible *E*/*Z* isomerization upon chemical or light activation; (ii) have thermal relaxation half-lives ($\tau_{1/2}$) that range from thousands of years to hours; (iii) can be emissive, and that the emission can be toggled ON and OFF; (iv) can be efficiently photoswitched in the condensed phase, and (v) can be switched in biologically relevant media and in the presence of glutathione, among other advantages. In this chapter, we will survey the development of photoswitchable arylhydrazones (Scheme 6.1), and the applications that they have enabled so far.

## 6.2 Acetyl/Aroyl-Based and Pyridyl-Based Photochromic Arylhydrazones

The hydrazone-based photoswitches have a common structural feature, namely the six-membered H-bonded ring system, which connects hydrazone NH proton with the H-bond acceptor at the rotary part. The nature and strength of this H-bond determines many of the properties of the hydrazone, including the thermal isomerization rate, isomer ratio at equilibrium, whether the hydrazone will be emissive or not, and even if the system will be photoswitchable. Early studies conducted by Pichon and Courtet and coworkers focused on the photoisomerization of arylhydrazone derivatives of β-ketones, β-ketoesters, β-ketosulfonates, and β-ketophosphonates (Scheme 6.2) [22–24]. In the case of β-ketoester-based hydrazone **1**, the H-bond occurs at the acetyl group, resulting in the exclusive formation of the *E* configuration at equilibrium (>99%) in nonpolar solvents (e.g. $CCl_4$). The

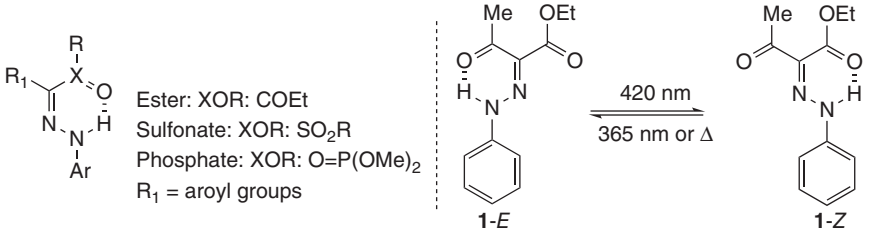


**Scheme 6.2** Left: structures of the hydrazone derivatives developed by Pichon and Courtet and coworkers. Right: light-induced *E*/*Z* photoisomerization of hydrazone **1**. Source: Refs. [22–24].

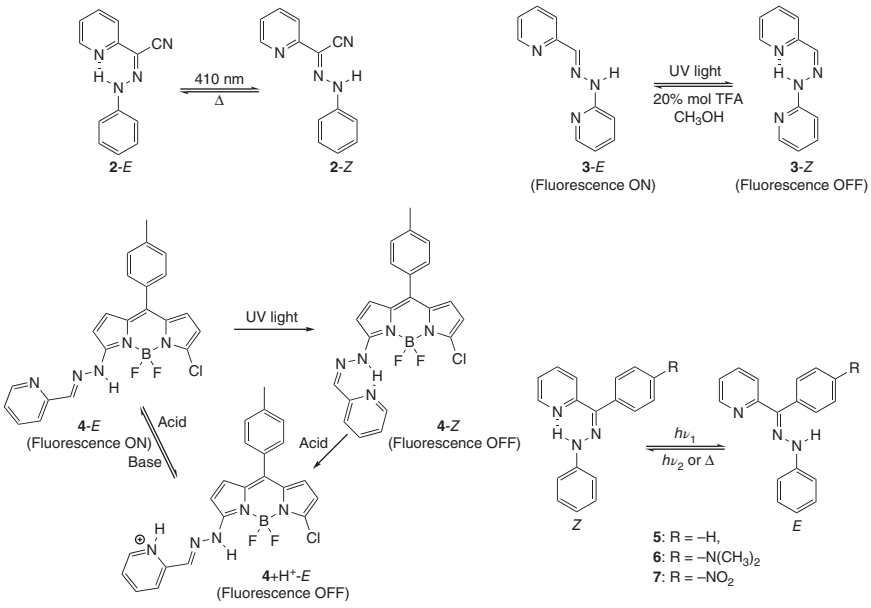


**Scheme 6.3** Upper left: light and heat-induced *E*/*Z* isomerization of hydrazone **2**. Upper right: light and heat-induced *E*/*Z* isomerization of hydrazone **3**. Lower left: *E*/*Z* isomerization and pH-responsive fluorescence of hydrazone **4**. Lower right: light-activated *E*/*Z* isomerization of hydrazones **5**–**7**.

$E \rightarrow Z$ photoisomerization can be triggered upon 420 nm light irradiation, leading to a photostationary state (PSS) containing >98% of the *Z* isomer. The reverse process can be induced by irradiation with 365 nm light, resulting in a $PSS_{365}$ consisting of 70% *E* and 30% *Z* isomers. The $Z \rightarrow E$ thermal relaxation of **1** proceeds slowly with a $\tau_{1/2}$ of over 15 days. Replacing the acetyl group of **1** with an aroyl group shifts the H-bonding toward the ester group (i.e. ester, sulfonate, or phosphate). Most of the aroyl hydrazones behave similar to **1** but differ in their thermal stability, i.e. the thermal back-isomerization is faster. When going from apolar solvents to polar ones, the thermal relaxation rates of arylhydrazones, in general, are drastically accelerated from days/hours to seconds/milliseconds.

The Aprahamian and Lehn research groups have extensively studied hydrazones having a pyridyl ring, which acts as a pH-dependent H-bond acceptor, as part of the rotor group. Hydrazone **2** (Scheme 6.3), for example, served as a synthetic precursor for a family of $BF_2$-coordinated fluorescent molecular rotors developed by the former group [26]. Ma and coworkers on the other hand studied the photoisomerization of **2** and showed that it undergoes an efficient $E \rightarrow Z$ isomerization (PSS > 95% *Z*) in both solution and the solid state, while the $Z \rightarrow E$ process can only occur thermally [27]. This system is reminiscent of the one (**3**) developed by Lehn and coworkers. Hydrazone **3** adopts the non-H-bonded configuration (*E*) as the thermally stable form, and it can be photochemically converted into the H-bonded *Z* isomer with high conversion efficiency (94%) [28]. The $E \rightarrow Z$ photoswitching process is accompanied with an ON → OFF fluorescence toggling, which is a rare occurrence in configurational

**Table 6.1** Summary of the photophysical and photochemical parameters of the hydrazone switches.

| Structure[a)] | R | $\lambda_Z$/ nm | $\lambda_E$/ nm | $PSS_{Z\rightarrow E}$ (*Z*:*E*) | $PSS_{E\rightarrow Z}$ (*Z*:*E*) | $\Phi_{Z\rightarrow E}$ | $\Phi_{E\rightarrow Z}$ | $\tau_{1/2}$[b)] |
|---|---|---|---|---|---|---|---|---|
| 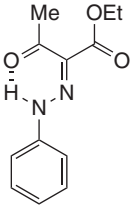 | — | 365 | 354 | 30 : 70 | 98 : 2 | — | 0.27 | >15 d[c)] |
| 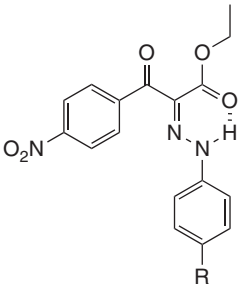 | —H | 420[d)] | 368[d)] | — | — | — | — | 150 s[e)] |
| | —$NO_2$ | 420[d)] | 371[d)] | — | — | — | — | 700 s[e)] |
| 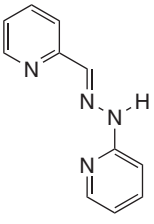 | — | 350 | 340 | — | 94 : 6 | — | — | —[f)] |
| 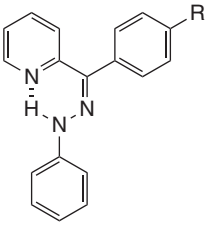 | —H | 387 | 348 | 15 : 85 | 81 : 19 | 0.03 | 0.09 | 0.7 yr[g)] |
| | —$NO_2$ | 399 | 353 | 25 : 75 | 96 : 4 | 0.17 | 0.04 | 0.5 yr[g)] |
| | —$NMe_2$ | 406 | 338 | 4 : 96 | 87 : 13 | 1.9 | 0.3 | 0.3 yr[g)] |
| 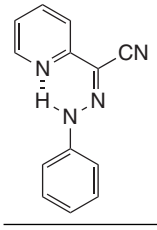 | — | 370 | 376 | — | 95 : 5 | — | — | — |

(*continued*)

**Table 6.1** (Continued)

| Structure[a] | R | $\lambda_Z$/ nm | $\lambda_E$/ nm | $PSS_{Z\rightarrow E}$ (Z:E) | $PSS_{E\rightarrow Z}$ (Z:E) | $\Phi_{Z\rightarrow E}$ | $\Phi_{E\rightarrow Z}$ | $\tau_{1/2}$[b] |
|---|---|---|---|---|---|---|---|---|
| 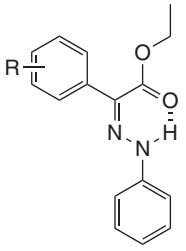 | *p*-OMe | 376 | 330 | 2:98 | 84:16 | 0.05 | 0.09 | 664 yr[g] |
| | *p*-$NMe_2$ | 395 | 343 | >1:99 | 82:18 | 0.32 | 0.15 | 213 yr[g] |
| | *m*-$NMe_2$ | 366 | 331 | >1:99 | 54:46 | 0.16 | 0.11 | 1645 yr[g] |
| | *p*-$NO_2$ | 392 | 314 | 8:92 | 52:48 | 0.12 | 0.13 | 20 yr[g] |
| | *p*-$HNMe_2^+$ | 361 | 336 | 12:88 | 76:24 | 0.07 | 0.14 | 1.4 d[g] |
| | *p*-$NMe_3^+$ | 362 | 335 | 10:90 | 72:28 | 0.02 | 0.05 | 14 yr[g] |
| 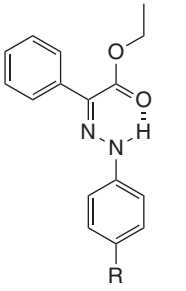 | –H | 367 | 334 | 5:95 | 76:24 | 0.08 | 0.11 | 324 yr[g] |
| | –CN | 368 | 333 | >1:99 | 86:14 | 0.04 | 0.05 | 1033 yr[g] |
| | –$NO_2$ | 391 | 366 | 2:98 | 82:18 | 0.35 | 0.11 | 1286 yr[g] |
| | –OMe | 383 | 351 | 7:93 | 88:12 | 0.05 | 0.10 | 14 d[g] |
| | –$NMe_2$ | 410 | 398 | 73:27 | — | 0.65 | — | 0.5 d[g] |
| 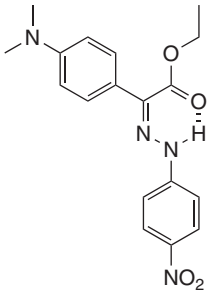 | — | 435 | 384 | >1:99 | 96:4 | 0.46 | 0.07 | 126 yr[g] |
| 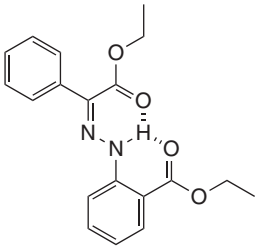 | — | 372 | 356 | 12:88 | 77:23 | 0.02 | 0.04 | 5357 yr[h] |
| 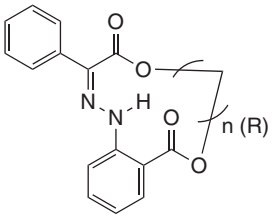 | 3 | 381 | 327 | >1:99 | 91:9 | 0.03 | 0.09 | 15 yr[h] |
| | 4 | 371 | 325 | >1:99 | 84:16 | 0.04 | 0.08 | 223 yr[h] |
| | 5 | 362 | 327 | 2:98 | 67:33 | 0.04 | 0.08 | 996 yr[h] |
| | 6 | 366 | 325 | 2:98 | 75:25 | 0.02 | 0.06 | 2.4 yr[h] |
| | 7 | 372 | 328 | >1:99 | 70:30 | 0.04 | 0.07 | 0.5 yr[h] |
| | 8 | 370 | 325 | 12:88 | 79:21 | 0.02 | 0.06 | 17 d[h] |

**Table 6.1** (Continued)

| Structure[a] | R | $\lambda_Z$/ nm | $\lambda_E$/ nm | PSS$_{Z\rightarrow E}$ ($Z:E$) | PSS$_{E\rightarrow Z}$ ($Z:E$) | $\Phi_{Z\rightarrow E}$ | $\Phi_{E\rightarrow Z}$ | $\tau_{1/2}$[b] |
|---|---|---|---|---|---|---|---|---|
| 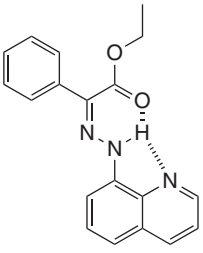 | — | 398 | 373 | 9 : 91 | 76 : 24 | 0.01 | 0.02 | 2700 yr[i] |
| 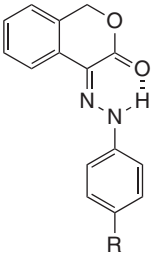 | –H | 398 | 366 | 14 : 86 | 79 : 21 | 0.06 | 0.12 | 14 d[i] |
| | –$NO_2$ | 415 | 384 | 12 : 88 | 88 : 12 | 0.03 | 0.11 | 24 d[i] |

a) The structures of the thermally stable isomers are shown.
b) Thermal relaxation $\tau_{1/2}$. s, d, and yr refer to second, day, and year, respectively.
c) Thermal $\tau_{1/2}$ were measured in $CCl_4$.
d) Data acquired in $CCl_4$.
e) Thermal $\tau_{1/2}$ were measured in EtOAc.
f) See Ref. [28].
g) Thermal $\tau_{1/2}$ were measured in toluene.
h) Thermal $\tau_{1/2}$ were measured in xylene. Note: the absorption maxima, PSSs, and $\Phi$s were determined in the same solvents as the thermal $\tau_{1/2}$, unless otherwise stated.
i) Thermal $\tau_{1/2}$ were measured in MeCN.

switches. The $Z \rightarrow E$ isomerization, on the other hand, only takes place upon heating in the presence of trifluoroacetic acid (TFA). This system was later adopted by Niu and coworkers in developing the BODIPY fluorescent dye **4** whose emission can be toggled ON and OFF as a function of light and pH inputs (Scheme 6.3) [29].

More recently, Cigan and coworkers developed the photoswitchable benzoylpyridine hydrazones (**5**–**7**) [30], whose activation wavelengths are red-shifted while having better absorption band separation relative to **3**. These hydrazones undergo reversible $E/Z$ photoisomerization with high PSSs (75–96%), though the quantum yields are low (~1%). The $\tau_{1/2}$ of **5**–**7** are around 0.3–0.7 years in toluene, which are relatively long for configurational switches.

## 6.3 Phenylacetate-Based Photochromic Arylhydrazones

In 2009, the Aprahamian group reported on a pH-activated hydrazone switch (**8**) in which the acetyl group in **1** was replaced with a pH-sensitive pyridyl group (Scheme 6.4) [31]. This structural modification allowed for the quantitative acid-induced *E*/*Z* isomerization of **8** between its neutral *E* and protonated *Z* forms [32]. While hydrazone **8** is an inefficient photoswitch, its quinolyl derivative **9** undergoes one-way light induced $E \rightarrow Z$ isomerization with a $PSS_{410}$ of 95% *Z*. It was hypothesized that having two H-bond acceptors in the rotor part, i.e. pyridyl and ester groups, is responsible for the lack of photo-reversibility in **9**. Hence, the pyridyl group was replaced with a phenyl one to obtain hydrazone **10** [32], which can be switched in both directions with light. Irradiation of **10** with 442 nm light results in a $PSS_{442}$ of 91% *E*, while subsequent 340 nm light irradiation yields a $PSS_{340}$ of 76% *Z*. What is interesting in this, and subsequently developed systems, is that the obtained photoswitches are bistable with $\tau_{1/2}$ up to >5000 years [33]. Such long thermal $\tau_{1/2}$ are rare in the context of configurational switches and open the way for using these hydrazone switches in the development of adaptive materials with multilevel and persistent functions and properties (*vide infra*).

To shed light on this unusual thermal stability and further improve on the photophysical properties of this class of arylhydrazones, Aprahamian and coworkers conducted systematic structure–property analyses [34], from which they identified two key factors that can be used in manipulating the extremely long thermal $\tau_{1/2}$ of the hydrazones (Scheme 6.5). The first one is an electronic effect that imparts, through resonance, a single bond character to the central C=N double bond thus accelerating the thermal relaxation process. Another element that regulates the thermal relaxation rate is a steric effect at the *fjord* region. When the rotary fragment of the switch is made coplanar with the rest of the molecule (**11**) [35], the *fjord* region of the thermally unstable *E* isomer gets crowded, leading to a destabilization of the ground state and thus a smaller activation barrier for isomerization. Finally, it was shown that strain buildup (i.e. angle, transannular, and torsional strain) in macrocyclic hydrazones can also be used in tuning the thermal $\tau_{1/2}$ of the hydrazones. Counterintuitively the strain is larger in bigger macrocycles resulting in orders of

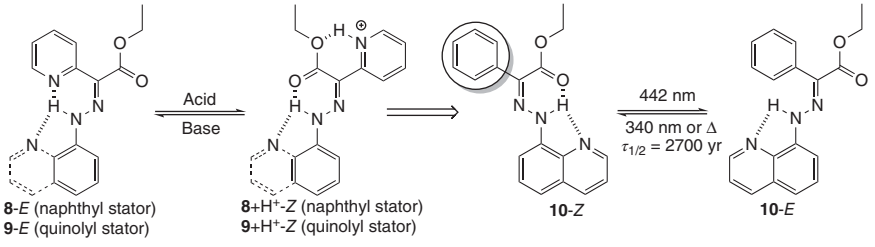


**Scheme 6.4** Left: pH-activated *E*/*Z* isomerization of hydrazones **8** and **9**. (Right) light-activated *E*/*Z* isomerization of hydrazone **10**. Source: Modified from Landge and Aprahamian [31].

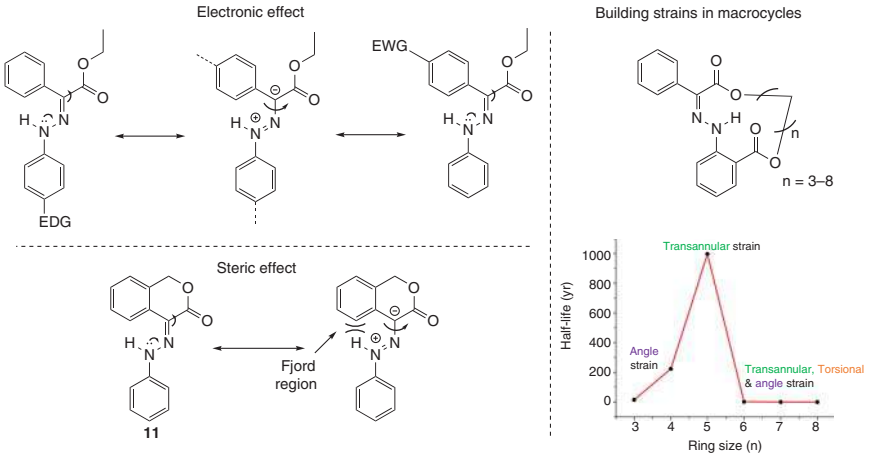


**Scheme 6.5** Top left: proposed resonance structure showing how electron-donating groups (EDGs) and electron-withdrawing groups (EWGs) accelerate the thermal relaxation by imparting single bond character on the central C=N double bond. Bottom left: proposed mechanism showing how planarization results in congestion at the *fjord* region. Right: structure of the hydrazone macrocycles and a schematic plot showing how $\tau_{1/2}$ varies as a function of ring size (for n = 3 and 6-8 there is not enough resolution on the y-axis to show the actual differences in half-lives).

magnitude acceleration in isomerization rates (Scheme 6.5) [33], Overall, electronic and steric effects can be used in tuning the thermal $\tau_{1/2}$ of hydrazones from thousands of years to a few hours.

The structure–property analyses also resulted in more efficient photoswitches and hydrazones having novel properties. For example, when a *para*-$NMe_2$ group was introduced to the rotor phenyl ring (Scheme 6.6), a fluorescent hydrazone (**12**) was obtained, whose emission can be toggled ON and OFF in solution (including aqueous buffer) and the solid state [36]. Experimental evidence, along with computational studies [37], show that the charge transfer from the rotary *para*-$NMe_2$ group, which further stabilizes the *Z* configuration by strengthening the H-bond, is responsible for the observed emission. Installing a *para*-$NO_2$ group to the stator phenyl ring of **12** results in the push-pull hydrazone **13**, which exhibits huge bathochromic shifts in the absorption bands of both the *Z* and *E* isomers, making it the first fully visible-light (i.e. 480 and 410 nm) activated hydrazone switch [34]. It is noteworthy that **13** has a long thermal relaxation $\tau_{1/2}$, which is highly unusual for push–pull systems [18].

Another important and unique property of this class of hydrazones is their solid-state emission and photoswitching, which are highly dependent on the crystal packing mode of the hydrazones (Scheme 6.7). For example, when the packing of hydrazone is tight (e.g. head-to-tail packing of **13**) the photoswitching is less efficient, the fluorescence quantum yields are lower, and larger shifts in emission wavelengths are observed relative to solution state. On the other hand, these properties are barely affected when the packing is loose (e.g. orthogonal packing of **15**).

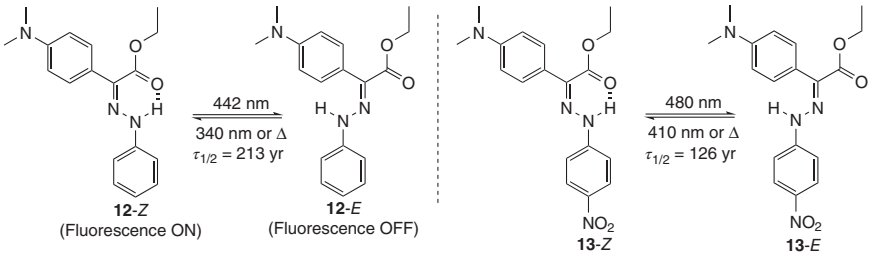


**Scheme 6.6** Left: light-activated *E*/*Z* isomerization and emission toggling of hydrazone dye **12**. Right: visible light-activated *E*/*Z* isomerization of hydrazone **13**.

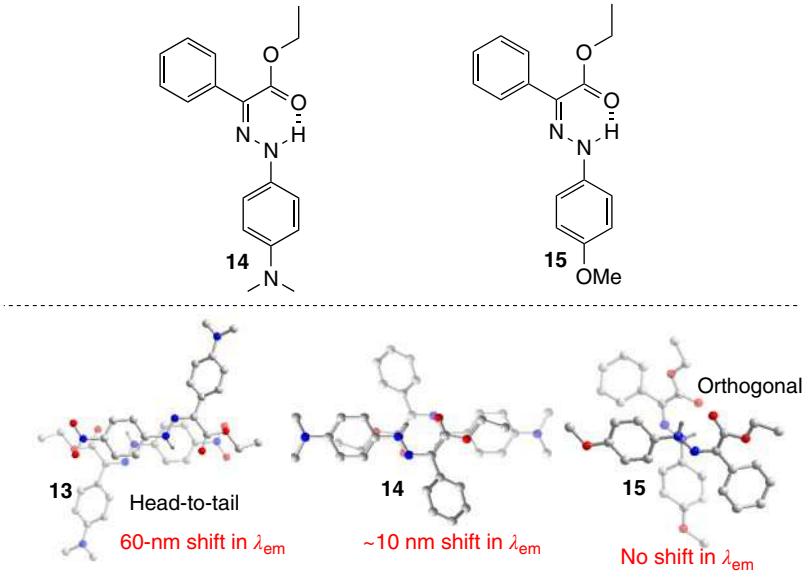


**Scheme 6.7** Top: structures of hydrazones **14** and **15**. Bottom: selected examples (**13**, **14**, and **15**) showcasing that the crystal packing mode determines the solid-state photophysical and photochemical properties of the hydrazones.

## 6.4 Applications of Bistable Photochromic Hydrazones

### 6.4.1 Kinetic Trapping of Nanostructures

Controlling the functions and properties of bulk materials and supramolecular assemblies in a multistep and persistent manner is a highly sought-after property in the context of (photo)adaptive functional materials [38]. Attaining such control though is not straightforward. In the context of photoswitches, it requires the combination of bistability with a large geometrical change upon isomerization. The latter allows for the control over the functions and properties of bulk materials within which the switches are incorporated, while the former gives access to various

non-equilibrated states, i.e. kinetically trapped ones, as a function of $E/Z$ isomer ratio (i.e. PSS), which can be controlled either by irradiation time or wavelength. The combination of these features though is rare in the vast majority of photoswitches in the literature. The hydrazone switches on the other hand are well capable of meeting these requirements because they are configurationally bistable switches. In this section, we will focus on three successful demonstrations of this concept from the Aprahamian group, in which the bistable hydrazone photoswitches were used to induce multilevel and persistent functions in smart materials.

#### 6.4.1.1 Liquid Crystal-Based Smart Window

The concept of multilevel and persistent switching was first tested with the bistable chiral dopant **16** (Figure 6.1), the photoswitching of which can be used in controlling the helical self-assembly, and hence, the photophysical properties of liquid crystals (LCs) [39]. The chiral isosorbide linker in **16** was used to impart helicity on the LC host, and the long alkyl chains were installed to increase the solubility of the dopant in LCs. Two commercially available LCs, 5CB and PCH5, were used to host the dopant **16**, yielding photoswitchable cholesteric LCs. Switching the dopant using different wavelengths of lights resulted in PSSs having different $E/Z$ isomer ratios, which were sustained indefinitely because of the bistability of the dopant. The different helical pitches resulting from these isomer ratios in turn were locked-in, resulting in the reflection of different wavelengths of light from the surface of the

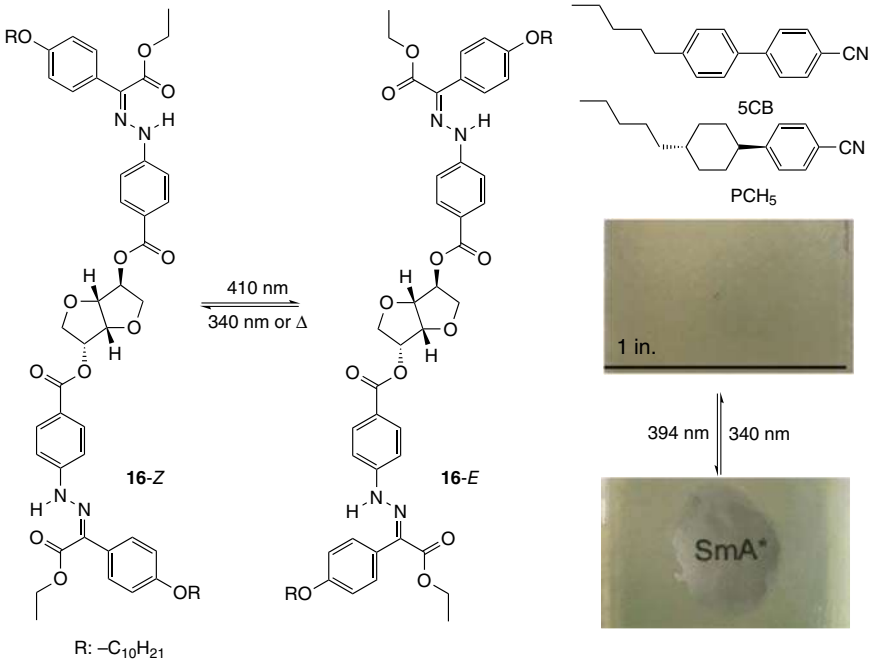


**Figure 6.1** Left: light-activated $E/Z$ isomerization of the hydrazone dopant **16**. Top right: Structures of the nematic liquid crystals 5CB and PCH5. Bottom right: a light-controllable smart window based on switch **9**. Source: Moran et al. [39].

LCs. For example, in the case of LC 5CB, the change in helical pitch as a function of PSS resulted in the reflection of different near-infrared lights from the LC surface. Most surprisingly, upon 394 nm light irradiation 5CB underwent an order-increasing phase transition from a cholesteric to a non-twisted lamellar smectic A* (SmA*) phase. It is important to note that the SmA* phase obtained using 394 nm light irradiation is an emergent phenomenon. To take advantage of this phase transition and the accompanied change in light transmission properties, the Aprahamian group developed a light-controlled smart window (Figure 6.1). Using 394 and 340 nm light irradiation, the LC can be toggled between an opaque cholesteric phase and a transparent SmA* one, thus enabling to hide and then reveal items hidden behind the LC-based window.

#### 6.4.1.2 Shape-Persistent Photoactuator

Next, and to transfer the microscopic switching event into a macroscopic motion that can be observed with the naked eye, the Aprahamian group, in collaboration with the Katsonis group [40], developed the acrylate-terminated hydrazone monomer **17**, which was then covalently incorporated into an LC elastomer as a dopant (Figure 6.2). The photoswitching of the dopant **17** within the obtained elastomer resulted in photoactuation. What distinguishes this system from others in the literature [41] is that the different polymer film shapes can be indefinitely locked-in by varying the irradiation time, i.e. $E/Z$ isomer ratio. This example showcases how bistable configurational photoswitching can be used in achieving multistage, multistable, and persistent polymer actuation. The actuation mechanism of this system is speculated to result from the order-to-order transitions that the hydrazone switches enforced on the LC elastomer, in addition to the 0.6 nm contraction in the size of the dopant upon photoisomerization.

#### 6.4.1.3 Photoresponsive Drug Release

To take advantage of bistability, $E/Z$ configurational switching, and ON/OFF emission toggling properties of hydrazone **12**, it was incorporated into a traceable drug delivery system [42]. An amphiphilic copolymer (**18**) functionalized with **12** was self-assembled into core–shell nanoparticles (Figure 6.3). The green emission of the hydrazone enabled visualization of the intracellular distribution of the nanoparticles, and the visible light activated $Z \rightarrow E$ photoisomerization was used to trigger drug release (i.e. doxorubicin) from the nanocarriers. The bistability, in this case, allowed for the locking-in of nanoparticles of varying sizes, which when combined with switchable emission, was used in regulating and even estimating where and how much drug was being released. This drug delivery mechanism was used in affecting light-triggered cytotoxicity in MDA-MB-231 cancer cells. The uniqueness of this system lies in the simplicity by which the hydrazone switch allows for the tracking of the localization of the nanoparticles in cells, while monitoring where and how much drug is being deployed.

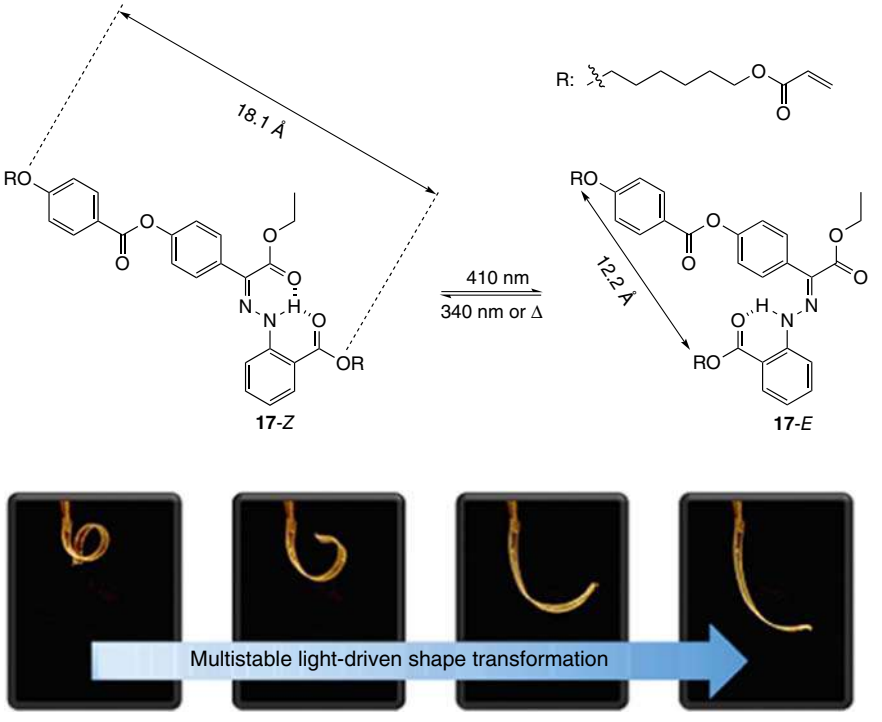


**Figure 6.2** Top: *E*/*Z* photoisomerization of the bifunctional hydrazone monomer **17** (the arrows show the contraction in size brought about by hydrazone photoisomerization). Bottom: multilevel and persistent actuation of an LC elastomeric film. Source: Ryabchun et al. [40].

### 6.4.2 Switching on Metal Surfaces

Understanding photoisomerization processes on metal surfaces can provide fundamental information for the development of surface-based smart devices and materials [43]. In general, photoswitches exhibit a dramatic enhancement in thermal isomerization rates when adsorbed on metal surfaces, which complicates the study of their surface behavior, and their use in real-life applications. The extremely long thermal $\tau_{1/2}$ of the hydrazones might mitigate this problem, allowing for a better understanding of the factors that control photoisomerization processes on surfaces. To this end, the Aprahamian and Zenobi groups reported on a detailed study of the photoisomerization of the thiol-terminated hydrazone **19** on three different metal surfaces (i.e. Au, Ag, and Cu; Figure 6.4) [44]. The six-carbon spacer was selected to minimize the length of the molecule, while still allowing for the formation of a well-organized monolayer on the metal surfaces [45]. Switch **19** undergoes an efficient *E*/*Z* photoisomerization in solution under 410 and 340 nm light irradiation, and its $E \rightarrow Z$ thermal relaxation $\tau_{1/2}$ was measured to be 789 years. The $Z \rightarrow E$ photoisomerization of **19** can also be triggered using 415 nm ($E = 3.0$ eV) light irradiation on Au ($E_{\text{d-band}} = 2.2$ eV) and Cu ($E_{\text{d-band}} = 2.1$ eV) surfaces through a substrate-mediated isomerization mechanism [46], but not on

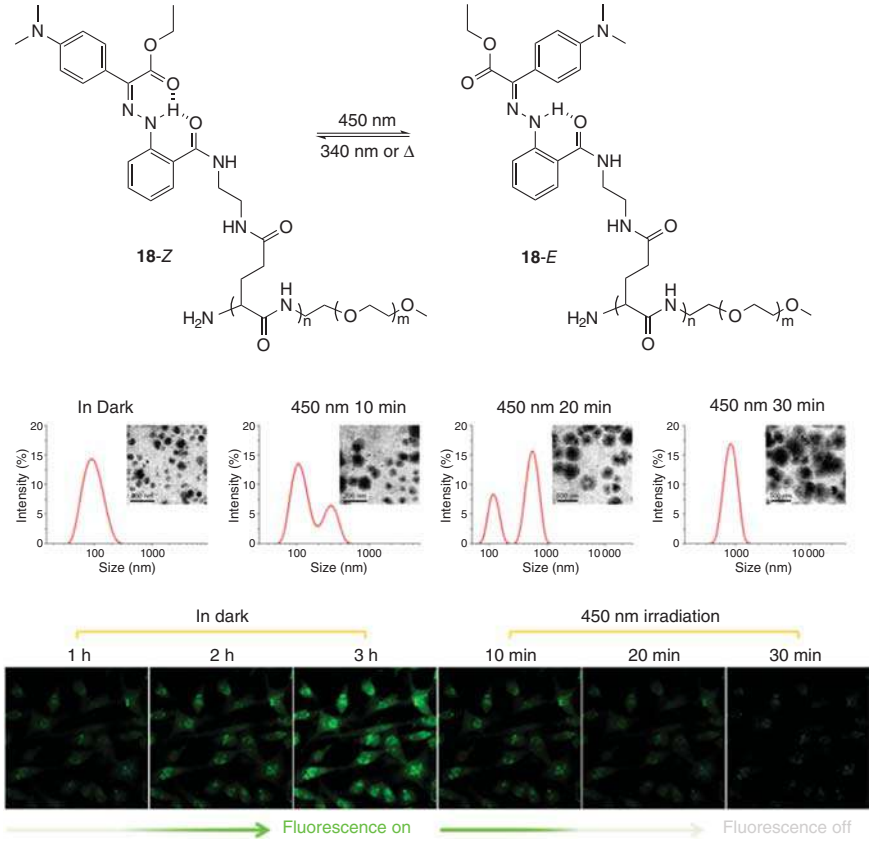


**Figure 6.3** Top: light-induced *E*/*Z* switching of the hydrazone-functionalized amphiphilic copolymer **18**. Middle: characterization of the irradiation time-dependent nanoparticle expansion using dynamic light scattering and transmission electron microscopy. Bottom: demonstration of the cellular uptake of the hydrazone-functionalized nanoparticle, and controllable fluorescence emission in MDA-MB-231 cells. Source: Guo et al. [42].

Ag surface because of its relatively low-lying d band ($E_{\text{d-band}} = 3.9$ eV). On the other hand, $E \rightarrow Z$ photoisomerization does not take place on any of these metal surfaces. A likely reason for this lack of photoisomerization is that the energies generated from the metal substrates upon light excitation lie below the threshold for *E* isomer excitation. Although the $E \rightarrow Z$ isomerization is not photochemically reversible, it can be reversed thermally with an unprecedented long thermal $\tau_{1/2}$ of 6.9 days on Au surface. This result attests to the benefits of using bistable hydrazone in such applications and opens up ample opportunities of incorporating them in robust photoresponsive surfaces.

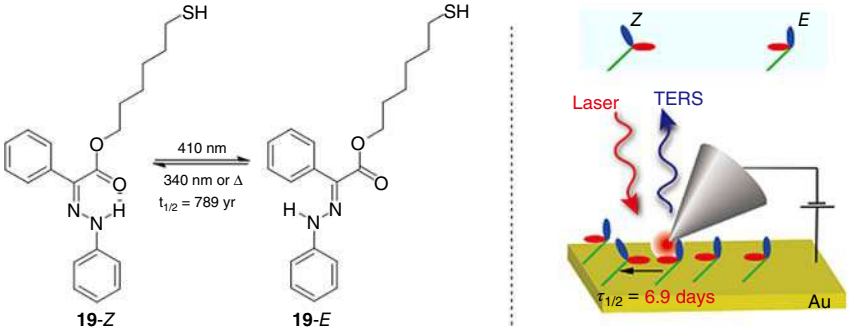


**Figure 6.4** Left: light-induced *E*/*Z* isomerization of thiol-terminated hydrazone **19**. Right: characterization of the photoswitching and thermal relaxation of **19** on Au surface using tip-enhanced Raman scattering (TERS). Source: Zheng et al. [44].

## 6.5 Conclusion

In this chapter, we showcased the benefits that can be reaped from developing new arylhydrazone-based photoswitches, while highlighting how such systems bring new opportunities to the field of adaptive functional materials. As configurational photoswitches, the bistability of the hydrazones allows for the kinetic trapping of different non-equilibrated states of polymers and supramolecular assemblies leading to multistate photoactuation and emergent phenomena that have not been observed with other photoswitches. The pronounced thermal acceleration effect observed for other photoswitches on metal surfaces also gets counteracted by the high thermal stability of the hydrazones. These properties, along with other advantages, e.g. concise synthesis, emission toggling, and switching in a broad range of media and phases, will make hydrazones excellent and competitive candidates for the development of super high-resolution imaging dyes [47], photoresponsive drugs [16], and molecular machines [48], among other applications.

## References


1 Durr, H. and Bouas-Laurent, H. (eds.) (2003). *Photochromism: Molecules and Systems*. Amsterdam: Elsevier Science.
2 Harris, J.D., Moran, M.J., and Aprahamian, I. (2018). *Proc. Natl. Acad. Sci. U.S.A.* 115: 9414–9422.
3 Blanco, V., Leigh, D.A., and Marcos, V. (2015). *Chem. Soc. Rev.* 44: 5341–5370.
4 Qu, D.-H., Wang, Q.-C., Zhang, Q.-W. et al. (2015). *Chem. Rev.* 115: 7543–7588.
5 Wang, L. and Li, Q. (2018). *Chem. Soc. Rev.* 47: 1044–1097.
6 Bisoyl, H.K. and Li, Q. (2016). *Chem. Rev.* 116: 15089–15166.


7 Xu, W.-C., Sun, S., and Wu, S. (2019). *Angew. Chem. Int. Ed.* 58: 9712–9740.
8 Peters, M.V., Stoll, R.S., Kuhn, A. et al. (2008). *Angew. Chem. Int. Ed.* 47: 5968–5972.
9 Wang, J. and Feringa, B.L. (2011). *Science* 331: 1429–1432.
10 Tamesue, S., Takashima, Y., Yamaguchi, H. et al. (2010). *Angew. Chem. Int. Ed.* 49: 7461–7464.
11 Lubbe, A.S., Liu, Q., Smith, S.J. et al. (2018). *J. Am. Chem. Soc.* 140: 5069–5076.
12 Lamsaard, S., Anger, E., Aßhoff, S.J. et al. (2016). *Angew. Chem. Int. Ed.* 55: 9908–9912.
13 Ikejiri, S., Takashima, Y., Osaki, M. et al. (2018). *J. Am. Chem. Soc.* 140: 17308–17315.
14 Wiedbrauk, S., Bartelmann, T., Thumser, S. et al. (2018). *Nat. Commun.* 9: 1456.
15 Venkataramani, S., Jana, U., Dommaschk, M. et al. (2011). *Science* 331: 445–448.
16 Broichhagen, J., Frank, J.A., and Trauner, D.A. (2015). *Acc. Chem. Res.* 48: 1947–1960.
17 Lerch, M.M., Hansen, M.J., van Dam, G.M. et al. (2016). *Angew. Chem. Int. Ed.* 55: 10978–10999.
18 Bandara, H.M.D. and Burdette, S.C. (2012). *Chem. Soc. Rev.* 41: 1809–1825.
19 García-López, V., Liu, D., and Tour, J.M. (2020). *Chem. Rev.* 120: 79–124.
20 Petermayer, C. and Dube, H. (2018). *Acc. Chem. Res.* 51: 1153–1163.
21 Su, X. and Aprahamian, I. (2014). *Chem. Soc. Rev.* 43: 1963–1981.
22 Courtot, P., Pichon, R., and Le Saint, J. (1976). *Tetrahedron Lett.* 17: 1181–1184.
23 Courtot, P., Pichon, R., and Le Saint, J. (1976). *Tetrahedron Lett.* 17: 1177–1180.
24 Pichon, R., Lesaint, J., and Courtot, P. (1981). *Tetrahedron* 37: 1517–1524.
25 Shao, B. and Aprahamian, I. (2020). *Chem* 6: 2162–2173.
26 Yang, Y., Su, X., Carroll, C.N. et al. (2012). *Chem. Sci.* 3: 610–613.
27 Ma, L., Yuan, Z., Huang, Z. et al. (2017). *Chem. Commun.* 53: 12630–12633.
28 Chaur, M.N., Collado, D., and Lehn, J.-M. (2011). *Chem. Eur. J.* 17: 248–258.
29 Zheng, H.-R., Niu, L.-Y., Chen, Y.-Z. et al. (2016). *RSC Adv.* 6: 41002–41006.
30 Mravec, B., Filo, J., Csicsai, K. et al. (2019). *Phys. Chem. Chem. Phys.* 21: 24749–24757.
31 Landge, S.M. and Aprahamian, I. (2009). *J. Am. Chem. Soc.* 131: 18269–18271.
32 Qian, H., Pramanik, S., and Aprahamian, I. (2017). *J. Am. Chem. Soc.* 139: 9140–9143.
33 Li, Q., Qian, H., Shao, B. et al. (2018). *J. Am. Chem. Soc.* 140: 11829–11835.
34 Shao, B., Qian, H., Li, Q. et al. (2019). *J. Am. Chem. Soc.* 141: 8364–8371.
35 Shao, B. and Aprahamian, I. (2020). *ChemistryOpen* 9: 191–194.
36 Shao, B., Baroncini, M., Qian, H. et al. (2018). *J. Am. Chem. Soc.* 140: 12323–12327.
37 Wang, G., Li, Y., Song, T. et al. (2020). *J. Phys. Chem. A* 124: 6411–6419.
38 Morone, M.I.F. (2018). *Chem. Eng. News* 96: 36–42.
39 Moran, M.J., Magrini, M., Walba, D.M. et al. (2018). *J. Am. Chem. Soc.* 140: 13623–13627.
40 Ryabchun, A., Li, Q., Lancia, F. et al. (2019). *J. Am. Chem. Soc.* 141: 1196–1200.
41 Lancia, F., Ryabchun, A., and Katsonis, N. (2019). *Nat. Rev. Chem.* 3: 536–551.


**42** Guo, X., Shao, B., Zhou, S. et al. (2020). *Chem. Sci.* 11: 3016–3021.

**43** Pathem, B.K., Claridge, S.A., Zheng, Y.B. et al. (2013). *Annu. Rev. Phys. Chem.* 64: 605–630.

**44** Zheng, L.-Q., Yang, S., Lan, J. et al. (2019). *J. Am. Chem. Soc.* 141: 17637–17645.

**45** Love, J.C., Estroff, L.A., Kriebel, J.K. et al. (2005). *Chem. Rev.* 105: 1103–1169.

**46** Wolf, M. and Tegeder, P. (2009). *Surf. Sci.* 603: 1506–1517.

**47** Sahl, S.J., Hell, S.W., and Jakobs, S. (2017). *Nat. Rev. Mol. Cell Biol.* 18: 685–701.

**48** Aprahamian, I. (2020). *ACS Cent. Sci.* 6: 347–358.


# 7 Spiropyran – Multifaceted Chromic Compounds

Luuk Kortekaas and Wesley R. Browne

**Photochromism and Other Structural Transformations**

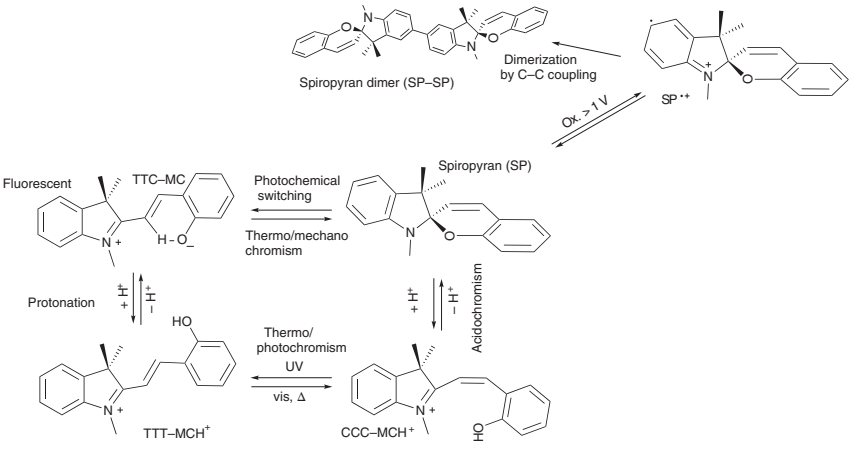


**Characteristic Features**

Spiropyrans are the Swiss Army knife of the molecular switches, with thermo-, acido-, mechano-, solvato-, and electrochromic responsivity.

**Key References**

Fischer, E. and Hirshberg, Y. (1952). Formation of coloured forms of spirans by low-temperature irradiation. *J. Chem. Soc*. 4522–4524.

Kortekaas, L. and Browne, W.R. (2019). The evolution of spiropyran: fundamentals and progress of an extraordinarily versatile photochrome. *Chem. Soc. Rev*. 48 (12): 3406–3424.

Kortekaas, L., Chen, J., Jacquemin, D., and Browne, W.R. (2018). Proton-stabilized photochemically reversible *E/Z* isomerization of spiropyrans. *J. Phys. Chem. B* 122 (24): 6423–6430.

# 7

# Spiropyran – Multifaceted Chromic Compounds

*Luuk Kortekaas and Wesley R. Browne*

*University of Groningen, Molecular Inorganic Chemistry, Stratingh institute for Chemistry, Faculty of Science and Engineering, Nijenborgh 4, Groningen 9747AG, The Netherlands*

## 7.1 Introduction

Since the discovery of their photochromism in the 1950s, spiropyrans have played a central role in the development of photochromism and more recently in their application in responsive materials [1]. This particular class of compound shows a range of chromism far beyond photoactivation, however, and a full appreciation of this versatile class opens many opportunities in material science and biology [2]. In this chapter, we will focus on the physical and chemical properties of spiropyrans and the mechanisms by which chromic switching proceeds. The earliest interest in spiropyrans, which stretches back to the 1900s, was in their solvent- and pH-dependent behavior and especially the large structural and color changes that could be induced in, for example, **1a–d** (Scheme 7.1 (1a)). Indeed, as early as 1908, Decker and Felser coined the term spiropyran to describe the center of the double pyran structure [3].

The photochromism of the spiropyran form has received the majority of interest ever since its first report over 65 years ago in a spiro compound (**2**) prepared through condensation of salicylaldehydes with Fischer bases (Scheme 7.1 (1b)) [4, 5]. Indeed, it is this specific core structure that has been focused upon in many applications of the spiropyran photochrome [1, 2]. However, a wide range of acidochromic and thermochromic spiropyrans are now known with relatively predictive tuning of behavior through substituent effects as discussed below. These aspects of the reactivity of spiropyrans are determined often by the low barriers to thermally driven interconversion between isomers. Furthermore, protonation stabilizes the merocyanine form, and so the combination of acidochromism and thermochromism allows for more complex functions [6].

## 7.2 Thermochromic Spiropyrans

The change in color that spiropyrans undergo as the temperature is raised is one of the earliest (1926) properties of spiropyrans noted (Scheme 7.1) [3],

*Molecular Photoswitches: Chemistry, Properties, and Applications*,
First Edition. Edited by Zbigniew L. Pianowski.


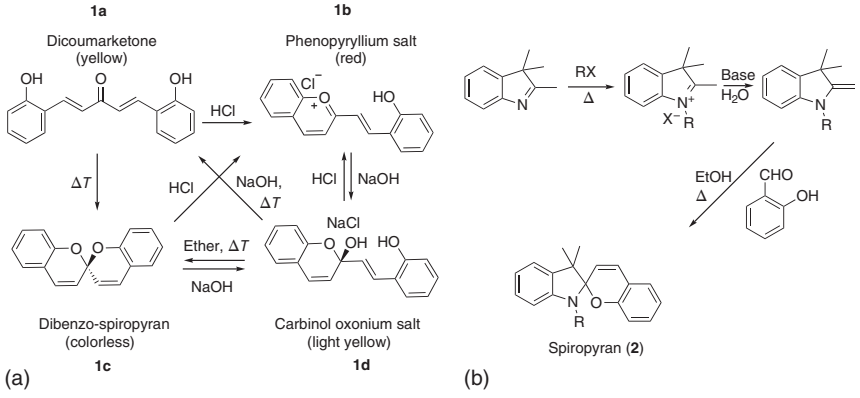


**Scheme 7.1** (a) Spiropyrans were discovered during the synthesis of coumarin-type compounds (**1a–d**) and (b) are now typically prepared in two steps from indoline.

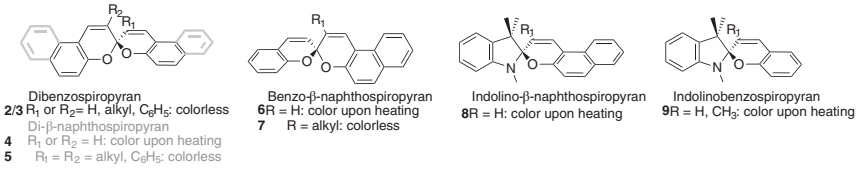


**Scheme 7.2** Spiropyrans developed for thermal and acid/base-induced switching. Isospiropyrans are thermally responsive also. Source: Modified from Day [7].

with full thermal reversibility described simultaneously by several groups for di-β-naphthospiropyran derivatives (Scheme 7.2) [7]. It goes without saying that interest in the thermochromism was stimulated by the ease of their study by the naked eye and that was the main point of attention until the 1960s [7, 8]. Wizinger's observation that an indolino moiety allowed for reversible thermochromism of benzopyrans through polarization of the spiro core was the trigger to these studies, and trends in structural dependencies emerged rapidly [9]. In general, it was an increase in temperature that triggered visible coloration and the mechanism by which thermal ring opening occurred was proposed to be ionization of the pyran and its counterpart that form the spiro-unit [10] rather than a radical dissociation pathway [11].

The structure of the so-called open form, the merocyanine, can be considered as zwitterionic and quinoidal resonance structures, the more pertinent of which depends on molecular structure and the conditions used. In general, their properties are better described by their zwitterionic form [7]. Charge delocalization is a major driver for the stability of the merocyanine form, which is heavily influenced and hence tuned by substituents. For example, benzospiropyrans have a lesser tendency to undergo ring opening compared to naphthospiropyrans, which can be rationalized by considering the quinoidal structure that requires a loss of aromaticity [12]. Thermochromism in spiropyrans requires that one of the pyran rings be at least a naphthopyran, unless the structure of the heterocyclic ring allows the delocalized

charge to be sufficiently stabilized, e.g. in the original indolinobenzospiropyrans reported by Wizinger[9] and later by Fischer [5].

Ring opening involves breaking of the carbon—oxygen bond of the spiro center, and hence electron-donating substituents on the heterocyclic ring add to the effect of electron-withdrawing substituents on the phenolate [7, 9, 13]. Steric effects and the acidity of the alkenyl hydrogen adjacent to the indoline influence ring opening also, e.g. substitution of the $C_3'$ hydrogen inhibits ring opening since it removes H-bonding between the $C_3'$–H and phenol in the ring-open form that stabilizes the merocyanine [12, 14]. Curiously, the p$K_a$ of the phenol is a poor predictive tool for the tendency of spiropyrans to undergo thermochromism. Ion pairing between the phenolate and an alkali cation does not affect the conjugation significantly but can stabilize the merocyanine form as for the non-thermochromic 3′-methylbenzo-β-naphthospiropyran, which is more acidic than the thermally responsive analogue, 3-methylbenzo-β-naphthospiropyran [12].

## 7.3 Relative Stability of the Merocyanine Isomers

Although it is more usual to discuss the merocyanine form as a pair of compounds, i.e. *Z*- and *E*-isomers, it is in fact a family of eight conformers/isomers referred to collectively as the merocyanine form, in which the configuration around the α, β, and γ bonds varies (Scheme 7.3). Although the structures are similar, they have differences in steric and intramolecular interactions that distinguish them in regard to their energy and the order in which the isomers fall relative to one another. The TTT isomer provides for the largest charge separation between the positively charged imine and negatively charged phenolate moiety and hence is expected to be lowest in energy. However, the methine $C_3'$–H is acidic and there is a lower barrier to spiro ring opening due to the intramolecular H-bonding with the phenolate moiety in the TTC conformation, making it slightly favored in general [14]. While steric arguments

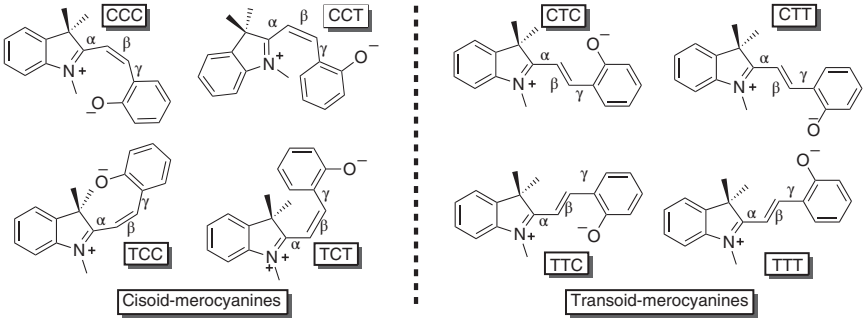


**Scheme 7.3** The merocyanine form is in fact any of a set of eight isomers, grouped into *Z*- and *E*-isomers referring to the configuration around the β-double bond. The naming of the isomers generally follows the cisoid, or transoid orientation of the three adjacent bonds α, β, and γ.

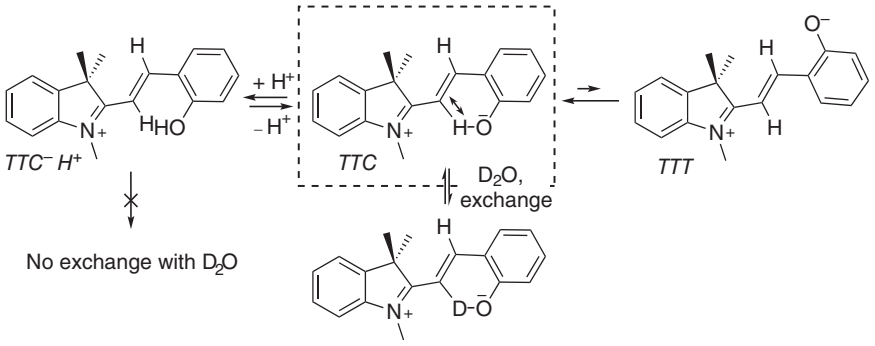


**Scheme 7.4** Intramolecular hydrogen bonding between the phenolate and the $C_3'$ hydrogen stabilizes the TTC isomer (*E*-merocyanine) to an extent that the TTT form is not observed. The stabilization is lost upon protonation and decreased by deuterium exchange at the acidic $C_3'$.

raised in analogues substituted at the $C_3'$ position argue against this, $^1$H NMR spectroscopy indicates that the H-bond interaction stabilizes the TTC isomer [15]; the $^1$H NMR signal of the $C_3'$–H is shifted to higher ppm than would be expected and exchanges with $D_2O$ or MeOD [16]. Hence, it is not a trivial task to identify the minimum on the energy surface for interconversion between the conformational isomers.

A further consideration is that the charge separation created by the indoline nitrogen and phenolate is stabilized by the delocalized/conjugated merocyanine structure [17] and that the $C_3'$ and $C_4'$ carbons are heavily polarized. The stabilization of negative charge at the $C_3'$position by the interaction between the phenolate and the $C_3'$ hydrogen in the TTC isomer is supported by $^1$H and $^{13}$C NMR spectroscopy (Scheme 7.4) [16, 18]; the $C_3'$ and $C_4'$ carbons are well separated (111 vs. 152 ppm), the C–O$^-$ carbon has double-bond character (182 ppm); and the $C_2'$ signal is shifted quite far upfield (169 ppm) due to the positively charged indoline nitrogen. Deuteration at the $C_4'$-position results in a decreased shift [18]. Under acidic conditions, the phenol moiety loses stabilization due to H-bonding with $C_3'$ hydrogen, and the rate of exchange with deuterated solvent is decreased. The *N*-methyl signals shift to 4.2 ppm reflecting the increase in positive charge on the nitrogen.

The entropic energetic stabilization granted by the conformational freedom and hydrogen bonding in the open merocyanine state, and, in particular, the relief of steric demands balance closely with the enthalpic stabilization provided by the formation of 5- and 6-membered rings at the spiro center. The accessibility of the open state was first noted in passing by Koelsch in 1951 [12], when a barrier to ring closing was noted during flash freezing of hot blue solutions of dinaphthospiropyran. The blue coloration was retained until the sample was warmed to ambient temperature (Scheme 7.5).

Although the structural differences between the isomers are readily apparent, they are energetically quite similar and hence have relatively similar absorption spectra also, making the definitive assignment of spectral features challenging. Hirshberg and Fischer described the appearance of several differently colored species

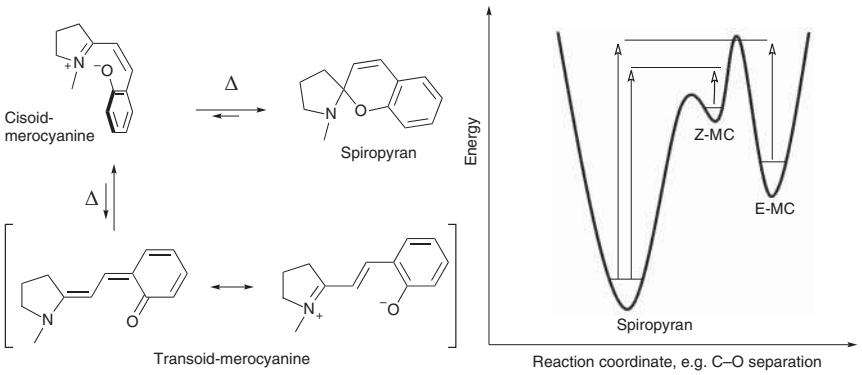


**Scheme 7.5** (Left) Ring opening of spiropyran to cisoid merocyanine followed by conversion to transoid isomer shown as two (TTC) resonance structures. (Right) Schematic reaction coordinate diagram for reactions on the ground-state surface (thermochromism).

above 105 K, generated by UV irradiation [19]. The merocyanine form of dibenzo-, di-β-naphtho, and benzo-β-naphtho-spiropyran formed several isomers (i.e. colors) depending on temperature [20]. Raising the temperature of pre-irradiated solutions steadily revealed several additional merocyanine isomers formed by a thermally activated process, leading eventually to the colorless spiropyran. This study was key to demonstrating the existence of several *cisoid* and *transoid* isomers that can interconvert thermally. Heating some spiropyrans, as Koelsch demonstrated, close to the boiling points of the solvents containing them led to the appearance of the most thermally stable of the merocyanine isomers [12].

Multi-dimensional NMR and Raman spectroscopic studies allowed for the assignment of all four *transoid* isomers of several spiropyrans in the 1980s [21], and time-resolved spectroscopic studies and quantum chemical calculations have led to the consensus that the TTC and to a lesser extent the TTT merocyanine isomers are the thermodynamically most stable *transoid* forms for the basic benzoindolinospiropyran structure [22]. Subsequent studies by $^{1}$H NMR spectroscopy allowed characterization of several isomers, for example, of the solvatochromic 6,8-dinitrobenzoindolinospiropyran [16], with time-resolved emission and 2D transient absorption spectroscopy providing insight into how and on what timescale the isomers interconvert [23, 24].

Though the TTC isomer is generally accepted to be the lowest in energy of the merocyanine isomers, even in early studies of spiropyran thermochromism, the effect of solvent on the visible absorption spectrum of solutions of spiropyrans was commented on [8]. Indeed as the polarity of the solvent used is increased, typically so too does the coloration increase due to stabilization of the polar zwitterionic merocyanine isomers and the decrease in barrier to ring opening [13]. Furthermore, a blue shift and the appearance of vibrational progression in the visible absorption spectrum are observed as solvent polarity is increased suggesting that *transoid* forms other than the TTC are present [7]. For benzospiropyrans, the merocyanine ground state is best described by the zwitterionic resonance form, whereas a

quinoidal structure best represents the electronically excited state [15], and indeed the dipole moment measured for the electronically excited state is less than that in the ground state [25]. As solvent polarity is increased, the ground state is stabilized more than the excited state therefore and $S_0$–$S_1$ energy gap increases, manifested in a blue-shift. In contrast, naphthopyrans and spiro-oxazines exhibit the opposite behavior as they are best represented by a quinoidal ground and zwitterionic excited state, primarily since they do not need to lose aromaticity to be in the quinoidal form. The solvent dependence on the relative stability of the isomers is unsurprising given the importance of H-bonding and delocalization in merocyanine stabilization discussed above [15], and the sensitivity of electronic properties to minor changes in structure is a key characteristic that gives the spiropyran family such a wide range of variability in their properties. Indeed, it is such dependence that, for example, makes them particular attractive in study of their mechanochromism [26].

## 7.4 Photochromic Properties

Fischer and Hirshberg were the first to report the photochromism of spiropyrans in 1952 [5]. The thermal barrier to reversion of the merocyanine to the spiropyran form is a key parameter in allowing photochromism to be observed. The barrier has to be sufficiently high that rapid recovery of the spiropyran does not outcompete formation of the merocyanine isomers. Indeed, as mentioned above [19], photochromism can be observed in several spiropyran structures at low temperatures, but the observation of photochromism at room temperature is less common [27, 28]. The first stage of the photochemical isomerization is loss of electronic energy by breaking of the $C_{spiro}$—O directly after excitation to the Franck–Condon state via a $^1\pi$–$\pi^*$ to form the CCC isomer, albeit in a conformation that is highly non-planar [29, 30]. The bond can then immediately reform to recover the spiropyran isomer or reduce strain through movement along the excited-state surface with the carbon—oxygen bond distance increasing sufficiently to allow for relaxation to either a *cis*- or a *trans*-oid merocyanine isomer [31]. If the *cis*-oid isomer is formed, then rapid recovery of the spiropyran occurs on the ground-state surface. The isomer formed is highly dependent on the substituents present, and by variation it has been possible to detect the four transoid isomers by spectroscopic methods [21].

Although processes on the singlet excited-state surfaces dominate the photochemistry of spiropyrans, in some cases intersystem crossing to triplet excited states has been noted. In particular, nitro 6- or 8-substituents on the pyran ring provide for ISC to triplet states via n–$\pi^*$-excited states (making use of coupling of spin and orbital angular momentum) as observed for stilbenes also [32]. The $^3\pi$–$\pi^*$ excited state absorbs at 430 nm and has a sufficiently long excited-state lifetime to form aggregates manifested in a shoulder at 630 nm [15, 33]. Furthermore, the nitro substituents serve to weaken and hence lengthen the $C_{spiro}$—O bond in the ground state [34]. Despite that, the triplet pathway increases the quantum efficiency for ring opening, it also results in increased tendency to sensitize $^3O_2$ and hence photochemical degradation [29].

Rapid recovery of the spiropyran form is typically observed for merocyanines and, indeed, the relatively late discovery of their photochromism is in large part due to the low barrier to this process. However, in the case of some indolinobenzomerocyanines, recovery is not observed and visible-light excitation resulted in a combination of radiationless relaxation and fluorescence in the case of nitro-substituted spiropyrans. It was only with the indolinonaphthomerocyanines that visible-light-induced recovery of the spiro form was reported [35]. Naphtho- and benzo-type (nitro-)substituted merocyanines show visible-light-induced ring closing to the spiro forms also [29], and it is of interest that the quantum efficiencies for both processes (ring opening and closing) are highly sensitive to the substitution pattern, making them highly versatile photochromes [36]. A drawback however is that an increase in quantum yield in one direction is in general met with a decrease in the opposite direction. The quantum efficiency for cyclization is generally higher than for opening to the merocyanine isomer, which can be inverted by involvement of triplet excited states at the cost of an increase in photochemical fatigue rates [29]. As a final note on photochemical switching, spiropyrans have unexpectedly high cross sections for 2-photon absorption, and ring opening can be induced in some cases with near-infrared light [37], even with continuous wave lasers [38].

## 7.5 Fluorescence

Spiropyrans typically do not show significant fluorescence in solution, due primarily to the deactivation channel provided by the breaking of the C—O bond. Furthermore, *cisoid* isomers formed photochemically and trapped at low temperature are also non-emissive [19]. In contrast, *transoid* merocyanine isomers occasionally show significant fluorescence, especially in polar organic solvents, competing with *E*–*Z* and intersystem crossing pathways that cause radiationless deactivation [21, 39, 40]. Indeed as an aryl alkene, it is of little surprise that the photochemistry of the merocyanine isomer is comparable with that of stilbenes, for which the *cis*-isomer is not fluorescent due to steric interactions between the aryl rings that push the structure along the reaction coordinate. In contrast the *trans*-isomer is unaffected by steric interactions and shows weak fluorescence ($\Phi_f = 0.05$) due to a longer excited-state lifetime [31]. Additionally, it is of note that for analogues of stilbene in which the geometry around the C=C bond is fixed (isomerization is not possible), the emission quantum yield is c. 1.0 [31]. In a similar manner, if *E*–*Z* isomerization is inhibited in merocyanines, e.g. through steric hindrance or low temperatures, then the emission quantum yield increases dramatically also [19, 41]. Furthermore, when in confined environments where collision-induced relaxation is precluded, quantum yields increase also. For example, shielding of the spiropyran-merocyanine system from electron transfer induced by collisions with solvent molecules in metal organic framework (MOF) structures can also considerably improve the fluorescence intensity [42, 43].

## 7.6 Acidochromism

Breaking of the $C_{spiro}$—O bond is the first step in isomerization between the spiropyran and merocyanine isomers. The thermochromism discussed above relies on the weakness of the bond and the stabilization achieved by planarization and *Z*–*E* isomerization, despite that overall the lowest energy isomer is typically the spiropyran form. Steric encumbrance at the 3- and 3′-carbons that is sufficient to block planarization reduces the tendency to ring open considerably. Protonation of the phenolate generated upon ring opening stabilizes the merocyanine isomers considerably but raises the energy of the electronically excited states manifested in a blue shift in the visible absorption of the merocyanines. The stabilization is analogous to metallochromism, i.e. ring opening due to the presence of metal ions that can bind to the phenolate [44]. The acidochromism of spiropyrans (including non-photochromic variants) was well established [8] before photochromism was reported. The phenopyrillium salt is an early example that highlighted the importance of formation of 6-membered rings over (**11**), for example, 5-membered rings (**10**) at the spiro center (Scheme 7.6).

The tendency to undergo protonation-induced ring opening is highly dependent on the relative p$K_a$ of the acid used and the merocyanine in both the *E*- and *Z*-forms. Irving and coworkers noted this already in 1929 for benzoxantho- and xanthonaphtho-spiropyran, which showed acidochromism with $CCl_3CO_2H$ and not $CH_3CO_2H$ [6], and much later by Roxburgh and Sammes for indolinobenzospiropyrans [45]. As ring opening proceeds on the electronic ground state when induced by protonation, $^1$H NMR spectroscopy is a useful spectroscopic tool for determining mechanisms/pathways involved. Roxburgh and Sammes noted an intermediate species that was assigned as a short-lived *cisoid*-species, although they could not determine the protonation state unequivocally. In a contemporary study, Zhou et al. reported that the 6′,8′-dinitrospiropyran underwent protonation-induced ring opening to form a merocyanine cisoid species that had not fully planarized, analogous to the postulated intermediate on the excited-state surface [46]. Later, Shiozaki reported [47] a clearer response to protonation in ethanol with sulfuric acid than observed with trifluoroacetic [48] and hydrochloric acids [49, 50]. The acidochromic response depends not only on the relative p$K_a$ of the acid and the *Z*- and *E*-merocyanine isomers but also on the relative p$K_a$s of the merocyanine isomers themselves (Scheme 7.7) [51].

The stabilization of the merocyanine formed upon protonation essentially converts the spiropyran to a stilbene analogue, and photochemical switching between

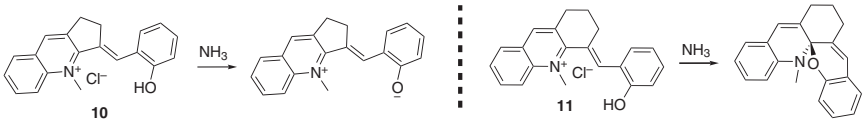


**Scheme 7.6** pH-dependent closing to form a spiro center is dependent on the ease with which the molecule can achieve planarity.

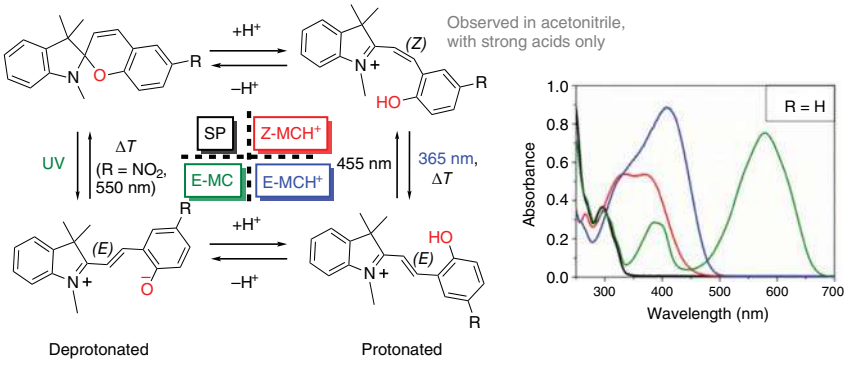


**Scheme 7.7** The 4-state pH-gated photochemical switching of indolinobenzospiropyran (R = H) and 6-nitroindolinobenzospiropyran (R = $NO_2$) is pH dependent involving 4 isomers (UV/Vis absorption spectra of spiropyran – black, *E*-merocyanine – green, $H^+$-*Z*-merocyanine – red and $H^+$-*E*-merocyanine – blue) in aprotic solvents with acids with p$K_a$ lower than that of the merocyanine isomers, e.g. $CF_3SO_3H$ (p$K_a$ 0.7) [51]. Source: Kortekaas et al. [51].

*Z*- and *E*-isomers is observed in a similar manner to that shown by Andréasson et al. [52], where the phenolate was methylated to prevent cyclisation.

The importance of solvent-leveling effects is apparent in aqueous solutions in which the near-UV absorption bands of the $H^+$-*Z*-merocyanine are not observed in the pH range 2–8, while those of $H^+$-*E*-merocyanine are (at 422 nm) [53]. For merocyanines with relatively high p$K_a$ values and hence more stable $H^+$-*E*-merocyanine, isomers isolation in solid form is possible [54]. The consistently lower p$K_a$ values of the corresponding $H^+$-*Z*-merocyanine isomers can be understood by considering the additional stabilization of the phenolate by proximity to the spiro-forming carbon center. This difference in p$K_a$ between the merocyanine isomers makes them particularly useful as reversibly switchable photoacids [55, 56].

A good example of the versatility of the spiropyran acid/base chemistry combined with photochemistry is found in an alkyl-sulfonate-modified spiropyran **12** (the sulfonate provides water solubility, Figure 7.1), which can be used to change pH reversibly with light. It should be noted however that the capacity of this system to change pH is limited both by the p$K_a$ of the two isomers and simple consideration of the logarithmic dependence of pH on proton concentration. A balance can be struck and this system works between pH 4 and 6, which requires only millimolar concentrations of the spiropyran [56, 58]. A further advantage of operating in this pH range is that hydrolysis (to yield back the starting materials for the spiropyran) is typically slow [59]. Similarly, photochemical switching of pH can be achieved by including a pyridinium moiety in the chromene half [60].

The use of spiropyrans as switchable photoacids necessitates that the p$K_a$ of the acid that is to undergo deprotonation is between that of the spiropyran/*Z*-merocyanine and that of the *E*-merocyanine isomer. In this way, the spiropyran form is innocent until it is switched with UV light to generate the *E*-isomer, which can then act as a base to deprotonate the acid present (Scheme 7.7).

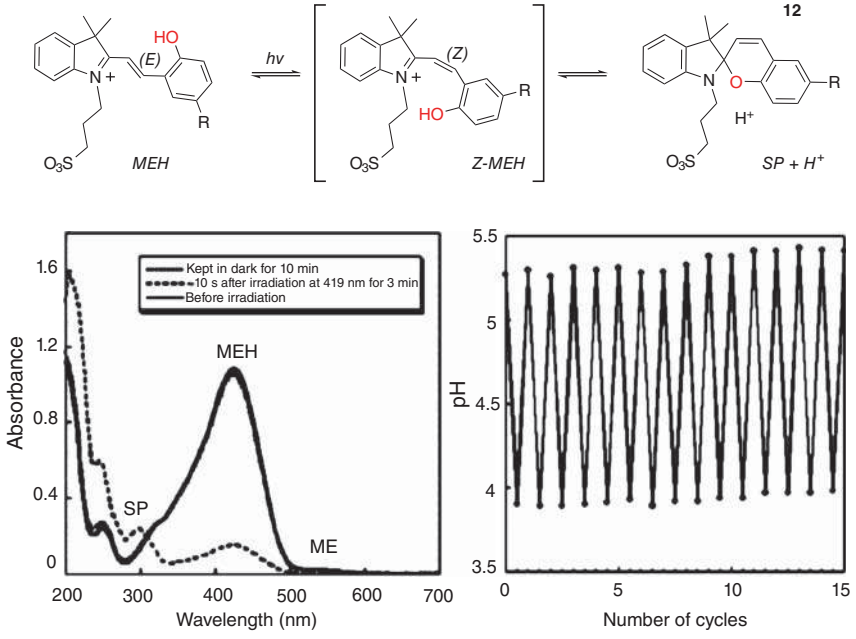


**Figure 7.1** (Top) switching between spiropyranine and merocyanine isomers upon protonation. (Bottom) UV/vis absorption spectrum of a photoacid MEH before and 10 seconds after irradiation for 3 minutes, and after the solution was held in dark for 10 minutes thereafter and pH with cycles of irradiation and darkness. Source: Liao [56] and Shi et al. [57].

Subsequent irradiation with visible (blue) light generates a strong acid in the form of $H^+$-*Z*-merocyanine, which then reprotonates the acid and regenerates the spiropyran. 6-nitroindolinobenzospiropyrans are by far the mostly widely used for this purpose [40, 50, 56, 58, 61]; however, tuning of the $pK_a$ of the *E*-merocyanine isomer can be achieved with electron-donating and -withdrawing groups on the phenol ring [56]. Indeed, in acetonitrile. the non-nitro-substituted spiropyran **13** (Figure 7.2) can act as a photoacid with near-stoichiometric phosphoric acid, whereas 6-nitroindolinobenzospiropyran cannot [51].

Although generally applied with stoichiometric equivalents of acids, trace acid can be used to catalyze photoswitching. For example, when encased in hosts, spiropyrans can undergo visible-light-induced ring closing in water even when not nitro-substituted as shown by Klajn and coworkers recently [62]. The non-protonated *E*-merocyanine isomer did not decolorize the solution upon irradiation with red light (580 nm) despite the isomer being absorbed at that wavelength. However, ring closing was observed upon irradiation at 460 nm due to switching of the trace amounts of $H^+$-*E*-merocyanine isomer to the more acidic and thermodynamically unstable $H^+$-*Z*-isomer, which then released the proton again, and in this way Le Chatelier's principle can be applied to drive ring closing. This case is by far less common and typically the protonated *E*-merocyanine form is present fully, which can be a photoacid if the $pK_a$ of the *E*- and *Z*-forms are

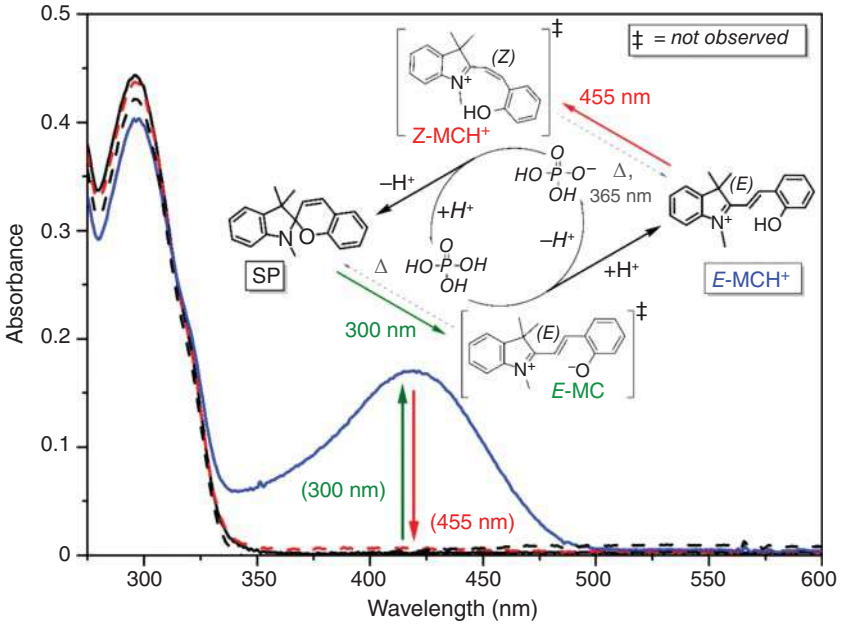


**Figure 7.2** UV/vis absorption spectrum of a spiropyran **13** (black) with 1 equiv. $H_3PO_4$ (red dashed line), which does not affect the spectrum significantly, indicating that the acid is not strong enough to protonate the *Z*-merocyanine isomer. Irradiation at 300 nm (blue spectrum) results in the appearance of the near-UV absorption of the protonated *E*-merocyanine (*E*-MC) isomer. Note that the non-protonated *E*-merocyanine of this spiropyran is not stable at room temperature and hence is locked here by protonation (the acid is strong enough to protonate it). Visible light results in reversion to the original spectrum. Source: Kortekaas et al. [51].

optimized to the conditions at hand (Scheme 7.8) [58, 63]. The combination of acid/base chemistry and photochemistry makes possible more complex operations and has been applied widely in functional systems [57, 58, 62, 63], such as chemopropulsion [64], reversible release of volatile compounds (perfumes) [65], polymerization [66, 67], solvent gelation [68] and swelling [69–71], and reversible self-assembly/disassembly of nanoparticles [72, 73].

## 7.7 Redox-Properties of Spiropyrans

Reduction of nitro-indolinospiropyrans at relatively low negative potentials was reported quite early in the last century [74]; however, the cyclic voltammetry of spiropyrans toward positive (oxidizing) potentials has received more recent attention by several groups. Campredon and coworkers reported irreversible oxidation of nitrospiropyrans at potentials above 1 V, even at 10 $V\,s^{-1}$ sweep rates [74]. The reduction on the subsequent cycle to negative potentials revealed two minor reductions at potentials below 1 V ascribed to various processes, including electrochemically driven ring opening to the merocyanine form. The changes in

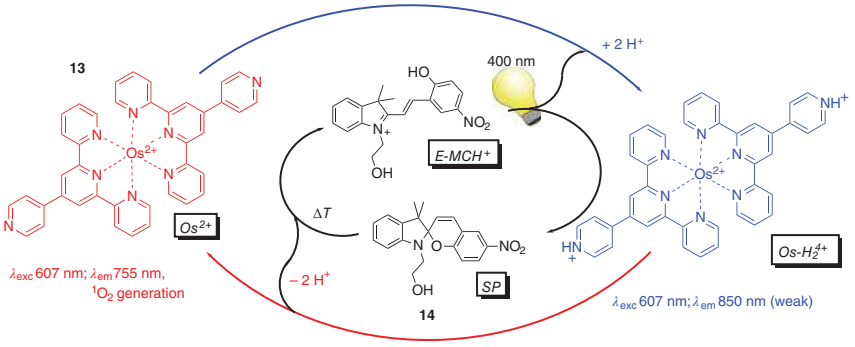


**Scheme 7.8** Phosphorescence of an osmium complex (**13**) and its ability to sensitize $^3O_2$ oxygen is controllable by a photoswitchable merocyanine (**14**) that can take up and give a proton to the pyridine units of the complex. Source: Modified from Silvi et al. [63].

color that accompany the electrochemical oxidation (electrochromism) attracted intermittent attention, but it was only after several years that the origin of the irreversibility became apparent when Giordani et al. obtained dimeric spiropyrans coupled at the indoline units following oxidation with Cu(II) [75]. The reactions involved in the formation of these dimers are essentially the same as those observed in the electrochemical coupling of *N*,*N*-dialkyl anilines [38, 76]. When the para position of the indoline unit was blocked with a methyl group, the oxidation is rendered fully reversible, i.e. redox-driven switching of structure is not observed. Hence, the electrochromic properties reported so far have predominantly been due to changes in redox state rather than structure and is complicated by protonation effects especially during electrochemical oxidation [77].

## 7.8 Photochemistry in the Solid State

In the solid state, the spiropyrans generally do not show photochromism, as expected considering the large structural changes involved in opening to the *E*-merocyanine form [62]. In more open structures, such as polymers and self-assembled monolayers, often changes in pH or temperature are needed in addition to light to achieve switching [77, 78]. Switching in the solid state can be achieved with open structures [43, 79], covalent organic frameworks (COFs) [80], and MOFs [2]. Williams et al. reported that cavities within MOF allow for switching depending on the size of the pillars and can reach solution rates of switching [81]. A simple design that shows the multi-responsiveness of spiropyran through solid-state packing was demonstrated by Wu and coworkers [79]. Using a tetraphenylethene core to control the directionality of π–π stacking to form columnar phases, the photochemistry of spiropyrans could be restored in the solid state, by creation of free volume [82]. The openness allowed for slow but reversible color change upon irradiation and with volatile small-molecule acids and bases, acidochromism could be achieved in a reversible manner.

## 7.9 Conclusions

Spiropyrans are a remarkable group of functional compounds that can respond to light, pH changes, temperature, metal ions, and electrochemical stimulation in a highly interconnected manner. Despite being known for over a century, their structural diversity and the ability to tune their properties with variation in peripheral substituents continue to provide novel functions and stimulate use in an ever-increasing area of applications in functional materials and devices. In this chapter, we have only touched on the main aspects of the "personality" of spiropyrans and the reader is directed further to the recent reviews that have collated their applications.

## Acknowledgments

Financial support was provided by The Netherlands Ministry of Education, Culture and Science (Gravity Program 024.001.035 to L.K. and W.R.B.)

## References

1 Kortekaas, L. and Browne, W.R. (2019). The evolution of spiropyran: fundamentals and progress of an extraordinarily versatile photochrome. *Chem. Soc. Rev.* 48 (12): 3406–3424.
2 Danowski, W., van Leeuwen, T., Browne, W.R., and Feringa, B.L. (2021). Photoresponsive porous materials. *Nanoscale Adv.* 3: 24–40.
3 Decker, H. and Felser, H. (1908). Über cyclische Oxoniumsalze aus Dicumaketon und über Spiropyranderivate. *Ber. Dtsch. Chem. Ges.* 41 (2): 2997–3007.
4 Fischer, E. and Hess, O. (1884). Synthese von Indolderivaten. *Ber. Dtsch. Chem. Ges.* 17 (1): 559–568.
5 Fischer, E. and Hirshberg, Y. (1952). Formation of coloured forms of spirans by low-temperature irradiation. *J. Chem. Soc.*: 4522–4524.
6 Irving, F. (1929). Styrylpyrylium salts. Part XII. Spiropyrans derived from 9-methyl- and 9-ethyl-xanthylium salts. *J. Chem. Soc.*: 1093–1095.
7 Day, J.H. (1963). Thermochromism. *Chem. Rev.* 63 (1): 65–80.
8 Mustafa, A. (1948). The chemistry of spiropyrans. *Chem. Rev.* 43 (3): 509–523.
9 Wizinger, R. and Wenning, H. (1940). Über Intramolekulare Ionisation. *Helv. Chim. Acta* 23 (1): 247–271.
10 Löwenbein, A. and Katz, W. (1926). Über substituierte spiro-Dibenzopyrane. *Ber. Dtsch. Chem. Ges. A/B* 59 (7): 1377–1383.
11 Heller, C.A., Fine, D.A., and Henry, R.A. (1961). Photochromism. *J. Phys. Chem.* 65 (10): 1908–1909.
12 Koelsch, C.F. (1951). Steric factors in thermochromism of spiropyrans and in reactivities of certain methylene groups. *J. Org. Chem.* 16 (9): 1362–1370.

**13** Knott, E.B. (1951). The colour of organic compounds. Part V. Thermochromic spirans. *J. Chem. Soc.*: 3038–3047.

**14** Dilthey, W. and Wübken, H. (1928). Zur Kenntnis der Spiropyrane. (Heteropolare Kohlenstoffverbindungen, VI.). *Ber. Dtsch. Chem. Ges. A/B* 61 (5): 963–968.

**15** Ramamurthy, V. and Schanze, K.S. (2003). *Photochemistry of Organic Molecules in Isotropic and Anisotropic Media*. New York: Marcel Dekker, Inc.

**16** Hobley, J., Malatesta, V., Millini, R. et al. (1999). Proton exchange and isomerisation reactions of photochromic and reverse photochromic spiro-pyrans and their merocyanine forms. *Phys. Chem. Chem. Phys.* 1 (14): 3259–3267.

**17** Aldoshin, S.M., Atovmyan, L.O., D'yachenko, O.A., and Gal'bershtam, M.A. (1981). Molecular and crystal structure of 1,3,3-trimethyl-6′-nitro-8′-bromospiro(indolin-2,2′-[2*H*-1]-benzopyran) and products of its photochemical conversion. *Bull. Acad. Sci. USSR, Div. Chem. Sci.* 30 (12): 2262–2270.

**18** Hobley, J., Malatesta, V., Giroldini, W., and Stringo, W. (2000). π-Cloud and non-bonding or H-bond connectivities in photochromic spiropyrans and their merocyanines sensed by 13C deuterium isotope shifts. *Phys. Chem. Chem. Phys.* 2 (1): 53–56.

**19** Hirshberg, Y. and Fischer, E. (1953). Multiple reversible color changes initiated by irradiation at low temperature. *J. Chem. Phys.* 21: 1619–1620.

**20** Hirshberg, Y. and Fischer, E. (1953). Low-temperature photochromism and its relation to thermochromism. *J. Chem. Soc.*: 629–636.

**21** Minkin, V.I. (2004). Photo-, thermo-, solvato-, and electrochromic spiroheterocyclic compounds. *Chem. Rev.* 104 (5): 2751–2776.

**22** Ernsting, N.P., Dick, B., and Arthen-Engeland, T. (1990). The primary photochemical reaction step of unsubstituted indolino-spiropyrans. *Pure Appl. Chem.* 62 (8): 1483–1488.

**23** Kim, D., Zhang, Z., and Xu, K. (2017). Spectrally resolved super-resolution microscopy unveils multipath reaction pathways of single spiropyran molecules. *J. Am. Chem. Soc.* 139 (28): 9447–9450.

**24** Kullmann, M., Ruetzel, S., Buback, J. et al. (2011). Reaction dynamics of a molecular switch unveiled by coherent two-dimensional electronic spectroscopy. *J. Am. Chem. Soc.* 133 (33): 13074–13080.

**25** Bletz, M., Pfeifer-Fukumura, U., Kolb, U., and Baumann, W. (2002). Ground- and first-excited-singlet-state electric dipole moments of some photochromic spirobenzopyrans in their spiropyran and merocyanine form†. *J. Phys. Chem. A* 106 (10): 2232–2236.

**26** Li, M., Zhang, Q., Zhou, Y.N., and Zhu, S. (2018). Let spiropyran help polymers feel force! *Prog. Polym. Sci.* 79: 26–39.

**27** Hirshberg, Y. and Fischer, E. (1954). Photochromism and reversible multiple internal transitions in some spiroPyrans at low temperatures. Part I. *J. Chem. Soc.*: 297–303.

**28** Hirshberg, Y. and Fischer, E. (1954). Photochromism and reversible multiple internal transitions in some spiroPyrans at low temperatures. Part II. *J. Chem. Soc.*: 3129–3137.


**29** Feringa, B.L. and Browne, W.R. (2011). *Molecular Switches*. Weinheim, Germany: Wiley-VCH Verlag GmbH & Co. KGaA.

**30** Anslyn, E.V. and Dougherty, D.A. (2006). *Modern Physical Organic Chemistry*. Sausalito: University Science Books.

**31** Turro, N.J., Ramamurthy, V., and Scaiano, J.C. (2009). *Principles of Molecular Photochemistry: An Introduction*. Sausalito: University Science Books.

**32** Turro, N.J. (1991). *Modern Molecular Photochemistry*. Sausalito: University Science Books.

**33** Uznanski, P. (2000). From spontaneously formed aggregates to J-aggregates of photochromic spiropyran. *Synth. Met.* 109 (1–3): 281–285.

**34** Aldoshin, S.M. and Atovmyan, L.O. (1985). Structure of a new photochromic indoline spiropyran. *Izv. Akad. Nauk. SSSR, Ser. Khim.*: 180–182.

**35** Hirshberg, Y., Frei, E.H., and Fischer, E. (1953). Reversible appearance and disappearance of coloured modifications of some compounds as a result of irradiation at low temperatures. *J. Chem. Soc.*: 2184–2185.

**36** Buback, J., Kullmann, M., Langhojer, F. et al. (2010). Ultrafast bidirectional photoswitching of a spiropyran. *J. Am. Chem. Soc.* 132 (46): 16510–16519.

**37** Parthenopoulos, D.A. and Rentzepis, P.M. (1989). Three-dimensional optical storage memory. *Science* 245 (4920): 843–845.

**38** Ivashenko, O., van Herpt, J.T., Feringa, B.L. et al. (2013). Electrochemical write and read functionality through oxidative dimerization of spiropyran self-assembled monolayers on gold. *J. Phys. Chem. C* 117 (36): 18567–18577.

**39** Bahr, J.L., Kodis, G., De la Garza, L. et al. (2001). Photoswitched singlet energy transfer in a porphyrin-spiropyran dyad. *J. Am. Chem. Soc.* 123 (29): 7124–7133.

**40** Stafforst, T. and Hilvert, D. (2009). Kinetic characterization of spiropyrans in aqueous media. *Chem. Commun.* (3): 287–288.

**41** Metelitsa, A.V., Dorogan, I.V., Lukyanov, B.S. et al. (2005). Photochromic spiro[7*H*-furo(3,2-f)-(2*H*-1)-benzopyran-7,2′-indolines]: experimental and computational evidence for the elusive intermediate of the photoinitiated ring opening reaction of spiropyrans. *Mol. Cryst. Liq. Cryst.* 430: 45–52.

**42** Chen, J., Zeng, F., Wu, S. et al. (2008). A core-shell nanoparticle approach to photoreversible fluorescence modulation of a hydrophobic dye in aqueous media. *Chem. Eur. J.* 14 (16): 4851–4860.

**43** Howlader, P., Mondal, B., Purba, P.C. et al. (2018). Self-assembled Pd(II) barrels as containers for transient merocyanine form and reverse thermochromism of spiropyran. *J. Am. Chem. Soc.* 140 (25): 7952–7960.

**44** Paramonov, S.V., Lokshin, V., and Fedorova, O.A. (2011). Spiropyran, chromene or spirooxazine ligands: insights into mutual relations between complexing and photochromic properties. *J. Photochem. Photobiol. C Photochem. Rev.* 12 (3): 209–236.

**45** Roxburgh, C.J. and Sammes, P.G. (1995). On the acid catalysed isomerisation of some substituted spirobenzopyrans. *Dyes Pigm.* 27 (1): 63–69.

**46** Zhou, J., Li, Y., Tang, Y. et al. (1995). Detailed investigation on a negative photochromic spiropyran. *J. Photochem. Photobiol., A* 90 (2–3): 117–123.


**47** Shiozaki, H. (1997). Molecular orbital calculations for acid induced ring opening reaction of spiropyran. *Dyes Pigm.* 33 (3): 229–237.

**48** Raymo, F.M., Giordani, S., White, A.J.P., and Williams, D.J. (2003). Digital processing with a three-state molecular switch. *J. Org. Chem.* 68 (11): 4158–4169.

**49** Remon, P., Li, S.M., Grotli, M. et al. (2016). An acido- and photochromic molecular device that mimics triode action. *Chem. Commun.* 52: 4659–4662.

**50** Sumaru, K., Takagi, T., Satoh, T., and Kanamori, T. (2018). Photo- and thermoresponsive dehydration of spiropyran-functionalized polymer regulated by molecular recognition. *Macromol. Rapid Commun.* 39 (1): 1700234.

**51** Kortekaas, L., Chen, J., Jacquemin, D., and Browne, W.R. (2018). Proton-stabilized photochemically reversible E/Z isomerization of spiropyrans. *J. Phys. Chem. B* 122 (24): 6423–6430.

**52** Fleming, C.L., Li, S., Grøtli, M., and Andréasson, J. (2018). Shining new light on the spiropyran photoswitch: a photocage decides between *cis* – *trans* or spiro-merocyanine isomerization. *J. Am. Chem. Soc.* 140 (43): 14069–14072.

**53** Cui, L., Zhang, H., Zhang, G. et al. (2018). Substituent effect on the acid-induced isomerization of spiropyran compounds. *Spectrochim. Acta, Part A* 202: 13–17.

**54** Colaço, M., Carletta, A., Van Gysel, M. et al. (2018). Direct access by mechanochemistry or sonochemistry to protonated merocyanines: components of a four-state molecular switch. *ChemistryOpen* 7 (7): 520–526.

**55** Martin, C.J., Rapenne, G., Nakashima, T., and Kawai, T. (2018). Recent progress in development of photoacid generators. *J. Photochem. Photobiol. C Photochem. Rev.* 34: 41–51.

**56** Liao, Y. (2017). Design and applications of metastable-state photoacids. *Acc. Chem. Res.* 50 (8): 1956–1964.

**57** Shi, Z., Peng, P., Strohecker, D., and Liao, Y. (2011). Long-lived photoacid based upon a photochromic reaction. *J. Am. Chem. Soc.* 133 (37): 14699–14703.

**58** Tatum, L.A., Foy, J.T., and Aprahamian, I. (2014). Waste management of chemically activated switches: using a photoacid to eliminate accumulation of side products. *J. Am. Chem. Soc.* 136 (50): 17438–17441.

**59** Abeyrathna, N. and Liao, Y. (2017). Stability of merocyanine-type photoacids in aqueous solutions. *J. Phys. Org. Chem.* 30 (8): e3664.

**60** Kaiser, C., Halbritter, T., Heckel, A., and Wachtveitl, J. (2017). Thermal, photochromic and dynamic properties of water-soluble spiropyrans. *ChemistrySelect* 2 (14): 4111–4123.

**61** Vallet, J., Micheau, J.C., and Coudret, C. (2016). Switching a pH indicator by a reversible photoacid: a quantitative analysis of a new two-component photochromic system. *Dyes Pigm.* 125: 179–184.

**62** Samanta, D., Galaktionova, D., Gemen, J. et al. (2018). Reversible chromism of spiropyran in the cavity of a flexible coordination cage. *Nat. Commun.* 9 (1): 641.

**63** Silvi, S., Constable, E.C., Housecroft, C.E. et al. (2009). Photochemical switching of luminescence and singlet oxygen generation by chemical signal communication. *Chem. Commun.* (12): 1484.

**64** Florea, L., Wagner, K., Wagner, P. et al. (2014). Photo-chemopropulsion-light-stimulated movement of microdroplets. *Adv. Mater.* 26 (43): 7339–7345.


**65** Wang, Z., Johns, V.K., and Liao, Y. (2014). Controlled release of fragrant molecules with visible light. *Chem. Eur. J.* 20 (45): 14637–14640.

**66** Sumaru, K., Kameda, M., Kanamori, T., and Shinbo, T. (2004). Characteristic phase transition of aqueous solution of poly(*N*-isopropylacrylamide) functionalized with spirobenzopyran. *Macromolecules* 37 (13): 4949–4955.

**67** Sumaru, K., Kameda, M., Kanamori, T., and Shinbo, T. (2004). Reversible and efficient proton dissociation of spirobenzopyran-functionalized poly(*N*-isopropylacrylamide) in aqueous solution triggered by light irradiation and temporary temperature rise. *Macromolecules* 37 (21): 7854–7856.

**68** Maity, C., Hendriksen, W.E., Van Esch, J.H., and Eelkema, R. (2015). Spatial structuring of a supramolecular hydrogel by using a visible-light triggered catalyst. *Angew. Chem. Int. Ed.* 54 (3): 998–1001.

**69** Satoh, T., Sumaru, K., Takagi, T., and Kanamori, T. (2011). Fast-reversible light-driven hydrogels consisting of spirobenzopyran- functionalized poly(*N*-isopropylacrylamide). *Soft Matter* 7 (18): 8030–8034.

**70** Ziółkowski, B., Florea, L., Theobald, J. et al. (2016). Porous self-protonating spiropyran-based NIPAAm gels with improved reswelling kinetics. *J. Mater. Sci.* 51 (3): 1392–1399.

**71** Stumpel, J.E., Liu, D., Broer, D.J., and Schenning, A.P.H.J. (2013). Photoswitchable hydrogel surface topographies by polymerisation-induced diffusion. *Chem. Eur. J.* 19 (33): 10922–10927.

**72** Silvi, S., Arduini, A., Pochini, A. et al. (2007). A simple molecular machine operated by photoinduced proton transfer. *J. Am. Chem. Soc.* 129 (44): 13378–13379.

**73** Kundu, P.K., Samanta, D., Leizrowice, R. et al. (2015). Light-controlled self-assembly of non-photoresponsive nanoparticles. *Nat. Chem.* 7 (8): 646–652.

**74** Campredon, M., Giusti, G., Guglielmetti, R. et al. (1993). Radical ions and germyloxyaminoxyls from nitrospiro[indoline-naphthopyrans]. A combined electrochemical and EPR study. *J. Chem. Soc. Perkin Trans.* 2 (11): 2089.

**75** Natali, M. and Giordani, S. (2012). Interaction studies between photochromic spiropyrans and transition metal cations: the curious case of copper. *Org. Biomol. Chem.* 10 (6): 1162–1171.

**76** Ivashenko, O., van Herpt, J.T., Rudolf, P. et al. (2013). Oxidative electrochemical aryl C–C coupling of spiropyrans. *Chem. Commun.* 49 (60): 6737.

**77** Kortekaas, L., Ivashenko, O., van Herpt, J.T.J.T., and Browne, W.R.W.R. (2016). A remarkable multitasking double spiropyran: bidirectional visible-light switching of polymer-coated surfaces with dual redox and proton gating. *J. Am. Chem. Soc.* 138 (4): 1301–1312.

**78** Khalil, T., Alharbi, A., Baum, C., and Liao, Y. (2018). Facile synthesis and photoactivity of merocyanine-photoacid polymers. *Macromol. Rapid Commun.* 39 (15): 1800319.

**79** Wu, Z., Pan, K., Mo, S. et al. (2018). Tetraphenylethene-induced free volumes for isomerization of spiropyran towards multifunctional materials in the solid state. *ACS Appl. Mater. Interfaces* 10: 30879–30886.

**80** Kundu, P.K., Olsen, G.L., Kiss, V., and Klajn, R. (2014). Nanoporous frameworks exhibiting multiple stimuli responsiveness. *Nat. Commun.* 5 (1): 3588.


**81** Williams, D.E., Martin, C.R., Dolgopolova, E.A. et al. (2018). Flipping the switch: fast photoisomerization in a confined environment. *J. Am. Chem. Soc.* 140 (24): 7611–7622.

**82** Yu, Q., Su, X., Zhang, T. et al. (2018). Non-invasive fluorescence switch in polymer films based on spiropyran-photoacid modified TPE. *J. Mater. Chem. C* 6 (8): 2113–2122.

# 8 Diarylethenes – Molecules with Good Memory

Igor V. Komarov, Sergii Afonin, Oleg Babii, Tim Schober, and Anne S. Ulrich

**Photochromism**

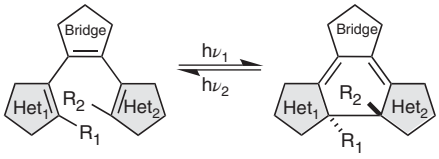


$Het_1$ and $Het_2$ – residues of (substituted) aromatic five-membered heterocycles (most often 3-thienyl) or their fused polycyclic analogs; $R_1$, $R_2$ – generic substituents (most often methyl); Bridge – a cyclic or polycyclic fragment (usually 1,2-cyclopent-1-enyl or its perfluorinated analog) $h\nu_1$ – UV or visible, $h\nu_2$ – visible light

**Characteristic Features**

high thermal stability of both photoforms (up to thousands of years at 30 °C), high photofatigue resistance (up to 14 000 photoisomerization cycles), short photoisomerization time (sub-picosecond to tenths of picosecond), high sensitivity to light, small geometrical and substantial electronic changes upon the photoisomerization, chirality of the cyclized photoform, applications in molecular electronics, optical memory media, in biological systems (imaging), medicinal chemistry (photoresponsive drug design)

**Synthetic Methods**

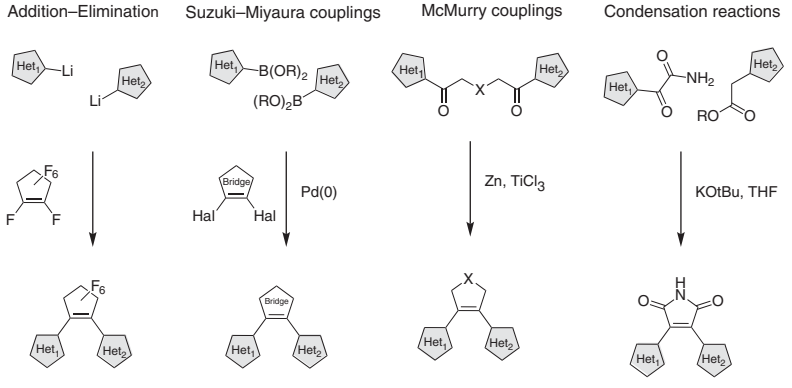


**First Reported**

Irie, M. and Mohri, M. (1988). Thermally irreversible photochromic systems. Reversible photocyclization of diarylethene derivatives. *J. Org. Chem.* 53 (4): 803–808.

**Key References**

Irie, M., Fukaminato, T., Matsuda, K. et al. (2014). Photochromism of diarylethene molecules and crystals: memories, switches, and actuators. *Chem. Rev*. 114 (24): 12174–12277.

Zhang, J. and Tian, H. (2018). The endeavor of diarylethenes: new structures, high performance, and bright future. *Adv. Opt. Mater*. 6 (6): 1701278.

# 8

# Diarylethenes – Molecules with Good Memory

*Igor V. Komarov[1], Sergii Afonin[2], Oleg Babii[2], Tim Schober[3], and Anne S. Ulrich[2,3]*

*[1] Taras Shevchenko National University of Kyiv, Institute of High Technologies (IHT), Vul. Volodymyrska 60, Kyiv 01601, Ukraine*
*[2] Karlsruhe Institute of Technology (KIT), Institute of Biological Interfaces (IBG-2), POB 3640, 76021, Karlsruhe, Germany*
*[3] Karlsruhe Institute of Technology (KIT), Institute of Organic Chemistry (IOC), Fritz-Haber-Weg 6, Karlsruhe 76131, Germany*

## 8.1 Introduction

The discovery of diarylethene photoswitches is a good example of a story where serendipity and careful analysis of experimental data led to the establishment of an entirely new, exciting branch of research. These compounds are heterocyclic analogs of *cis*-stilbene **1** (Figure 8.1), which was found to undergo photochemically induced cyclization in the 1950s [2]. In essence, this reaction is an electrocyclic ring closure in the core 1,3,5-hexatriene system. The formed product – 1,3-cyclohexadiene derivative – readily aromatizes in the case of the *cis*-stilbene and its simple heterocyclic analogs. Nevertheless, the process was known to be reversible in the absence of oxygen [3] and for non-aromatic compounds [4]. It was hypothesized that aromatization (i.e. hydrogen elimination in the presence of oxygen) would be effectively suppressed when the central carbon atoms that form the cycle bear non-hydrogen substituents. This insightful idea presumably emerged during the search for photoresponsive polymers [5]. Irie and coworkers discovered that poly[2,3-di(2,5-dimethyl-3-thienyl)butadiene] undergoes a thermally irreversible photochromic reaction [6]. This finding, in the context of the above hypothesis, eventually led them in the late 1980s to rationally design a *cis*-dithiene system. This type of compound was indeed found to undergo a fully reversible transformation between the so-called "ring-open" and "ring-closed" isomeric forms when irradiated with light of different wavelengths [1]. In Figure 8.1, an example of an early reported *cis*-dithienes, compound **2**, serves to illustrate the photoisomer nomenclature used here and the reversible photo isomerization.

The pioneering works on *cis*-dithienes revealed the intrinsic thermal stability of the two photoisomeric forms at ambient and even elevated temperatures (up to

*Molecular Photoswitches: Chemistry, Properties, and Applications*,
First Edition. Edited by Zbigniew L. Pianowski.


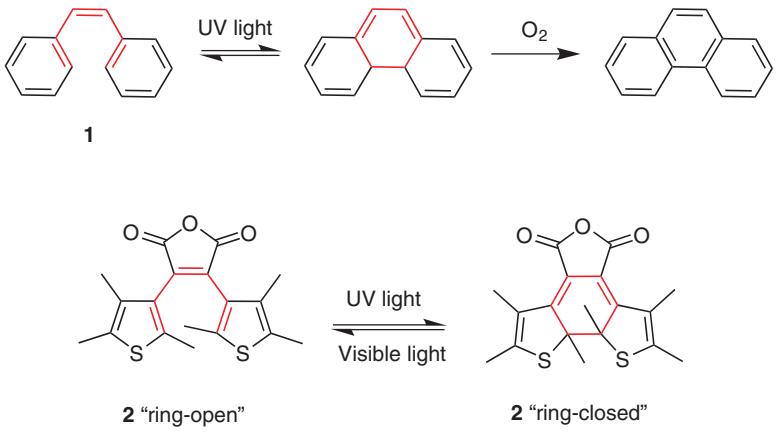


**Figure 8.1** Photochemical cyclization and subsequent aromatization of *cis*-stilbene **1** and one of the early reported diarylethenes **2** [1]. The conjugated core (red) undergoes the key light-induced electrocyclic transformation. Source: Irie and Mohri [1].

80 °C). This important property makes them very promising in the development of data storage systems based on photochromic molecules. A photochromic "molecular memory" model had been demonstrated on spiropyran systems before the discovery of *cis*-dithienes [7], but one of the spiropyran photoisomers utilized at that time was stable only at low temperatures (−70 to −100 °C). Discovery of the bistable *cis*-dithienes – compounds with exceptionally "good" memory – finally made molecular memory devices technically feasible. Other distinctive properties of *cis*-dithienes have been discovered and extensively studied since. In particular, they possess high fatigue resistance, fast photoisomerization kinetics, high sensitivity to light or other stimuli, and they undergo unique structural and specific electronic changes of the molecules upon photoisomerization. Thousands of derivatives and modifications of the original diarylethene systems were synthesized along the way, leading to many exciting ideas for practical applications. These studies have been extensively reviewed [6, 8–18]. At present, most of the studied photochromic diarylethenes can be denoted by the general formula **3** (Figure 8.2), where two heterocyclic rings ($Het_1$, $Het_2$) and their substituents can be varied to fine-tune specific properties. The central double bond is usually incorporated in a bridge, which serves, first of all, to lock the heterocyclic moieties in the *cis*-position needed for effective electrocyclic ring closure. Very often, a perfluorocyclopentene moiety is used as a bridge, as in the representative compounds **4** and **5**, shown in Figure 8.2. It has been demonstrated that this type of bridge shifts the spectral absorbance of the ring-closed form to longer wavelengths and increases the overall durability of the compounds, both of which are useful for many practical purposes [19]. However, the structure of the bridge can also be widely varied and tailored for specific targeted applications [17].

In the following sections, we will discuss the properties of diarylethenes in more detail and exemplify the utility of each property by prominent applications of the diarylethene-derived compounds in science and technology. We have selected

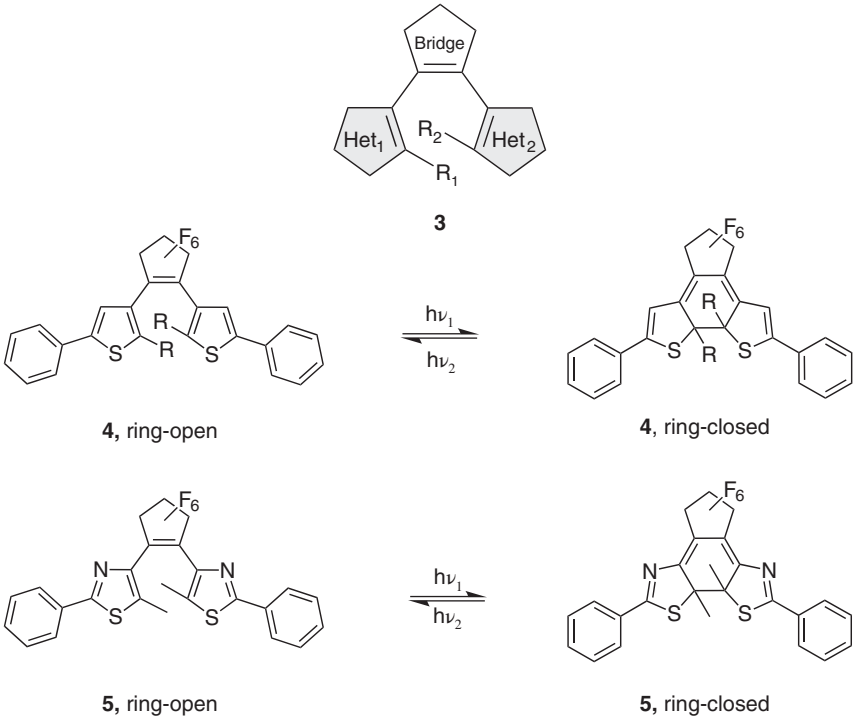


**Figure 8.2** A general formula for the diarylethene-based photochromic compounds (**3**) most often studied to date ($Het_1$ and $Het_2$ – aromatic five-membered heterocyclic moieties or their fused polycyclic analogs; $R_1$, $R_2$ – generic substituents; "Bridge" – a cyclic or polycyclic moiety connecting the 1,2-positions of the central C=C double bond); two typical examples, **4** (R: generic substituents, further discussed in Sections 8.3.1 and 8.3.2) and **5**.

only the most illustrative examples; a comprehensive discussion of the structure, properties, and countless applications of diarylethenes can be found in the cited reviews. We will finally outline the most commonly used synthetic approaches to constructing diarylethene cores and highlight the open problems in this field.

## 8.2 Photochemical Behavior of Diarylethenes

Using a typical representative example, compound **6** (Figure 8.3), which has been extensively studied by experimental and computational methods, the peculiarities of diarylethene photochemistry can be illustrated. Like most of the diarylethenes discussed in this chapter, compound **6** undergoes reversible transformations between a colorless ring-open form and a blue-colored ring-closed form under irradiation with light of different wavelengths (Figure 8.3a). Sufficiently long irradiation (minutes to hours) leads to the establishment of a photostationary state (PSS), at which point particular concentrations of the two photoforms are determined (i) by the individual absorption coefficients ε at the irradiation wavelength, and (ii) by the corresponding cyclization/cycloreversion quantum yields Φ. These parameters specify the maximal

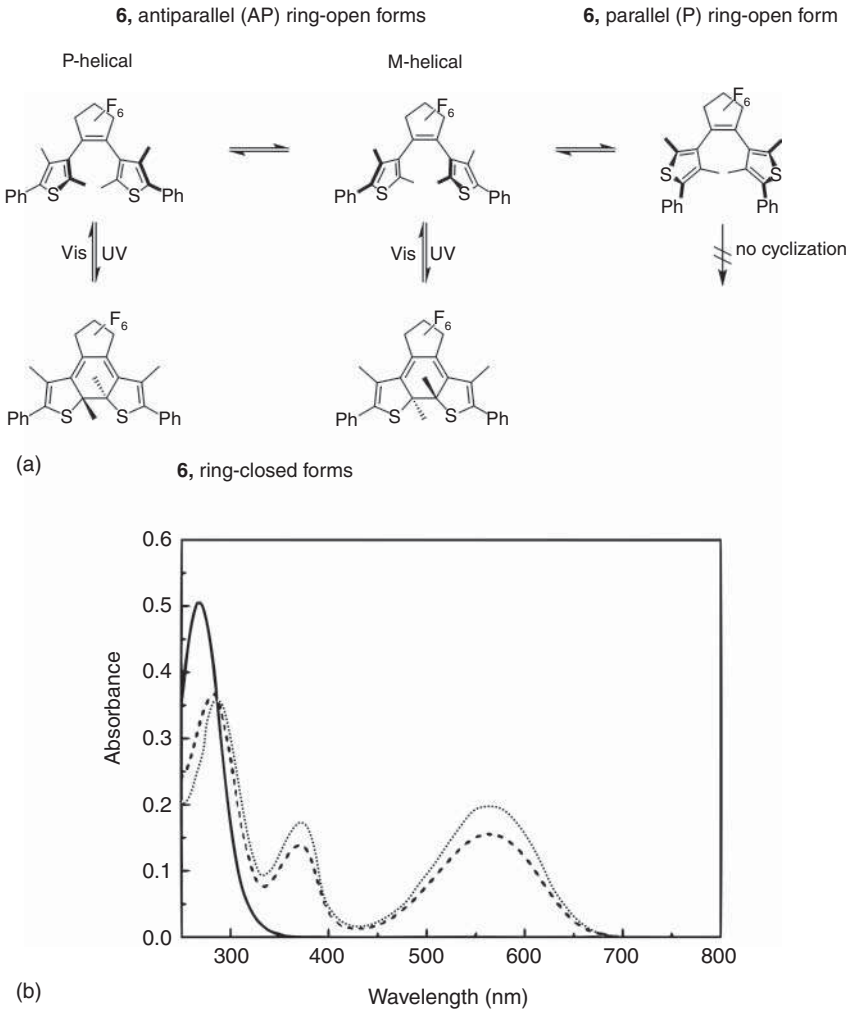


**Figure 8.3** (a) Photocyclization/cycloreversion processes for compound **6**; (b) absorption spectra of **6**. Black solid line: ring-open isomer; dotted line: ring-closed isomer; dashed line: photostationary state under irradiation at UV light. Source: Sumi et al. [20].

conversion of one photoform into another. For example, the photoconversion from the ring-open to the ring-closed isomer is defined as $100\% \times \Phi_{oc} \cdot \varepsilon_o / (\Phi_{oc} \cdot \varepsilon_o + \Phi_{co} \cdot \varepsilon_c)$, where $\Phi_{oc}$ and $\Phi_{co}$ are the quantum yields of the cyclization and cycloreversion processes, and $\varepsilon_o$ and $\varepsilon_c$ are the absorption coefficients of ring-open and ring-closed photoforms at the irradiation wavelength, respectively.

Experimental UV–vis absorption spectra of the ring-closed and ring-open **6** are illustrated in Figure 8.3b [20, 21]. The absorption of the ring-open form at 597 nm, where the ring-closed photoform has one of its absorption maxima, is negligible. Therefore, irradiation of ring-closed **6** at this wavelength leads to an almost quantitative ring opening. In the UV region, however, both photoforms

have comparable absorption coefficients. Irradiation at 313 nm hence leads to a PSS where both photoforms are present. As is typical for diarylethene photochromes [6], compound **6** is characterized by a much lower quantum yield for the ring-opening process (0.015 at 500 nm) than for the cyclization (0.45 at 313 nm). Therefore, ring closure at 313 nm is still quite efficient (~79% conversion) [20, 21]. Electron-donating substituents in the phenyl rings can further increase the conversion up to 99% [21]. Since the efficiency of photoconversion is crucial for most applications of photochromic compounds, numerous diarylethenes with practically quantitative photoswitching in both directions have been reported [22].

As illustrated in Figure 8.3a, the ring-open isomers can exist in different conformations, denoted as antiparallel (AP) and parallel (P). According to the Woodward–Hoffmann rules, a photochemical cyclization can proceed only in the conrotatory mode from the AP conformation. For compounds such as **6**, with unrestricted rotation around the C-(thienyl) bonds, the populations of the P- and AP-conformers are close to equal; hence, the quantum yield of the cyclization cannot be higher than 0.5 [21]. Much work has been done on the design and synthesis of compounds in which the AP-conformation is fixed or prevailed. Such fixation can be achieved either by covalent-bonded bridges or by noncovalent interactions, both leading to enhanced cyclization quantum yields and more efficient conversion [6]. By imposing severe rotational restrictions, it has even been possible to isolate stable atropisomers of the ring-open forms. An exciting example is compound **7**, where restrictions arise due to a bulky benzo-bis(thiadiazole) bridge connecting two similarly bulky benzothiophene residues (Figure 8.4). The photoactive AP conformer of ring-open **7** is readily isolated by column chromatography and cyclizes with extremely high quantum yield (0.73) [23].

Another peculiarity in the ring-closure reaction of diarylethenes becomes evident when we notice that the AP conformers are chiral, even for those compounds that have $C_2$ symmetry (like all diarylethenes discussed so far). The two AP conformers of ring-open **6**, P-helical and M-helical (Figure 8.3a), produce two stereoisomeric ring-closed products upon photoisomerization. For **6**, the photocyclized product is a racemic mixture, provided that no additional factors inducing enantioselectivity are involved. However, numerous chiral nonracemic diarylethene derivatives have been described [6, 24], which undergo stereoselective photochemical transformations. An illustrative example is the compound **8**. Photocyclization of **8** (Figure 8.5) in

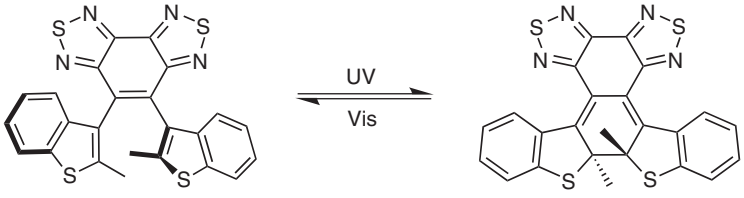


**7**, ring-open **7**, ring-closed

**Figure 8.4** The room-temperature stable AP atropisomer of **7** in the ring-open form and its photocyclization.

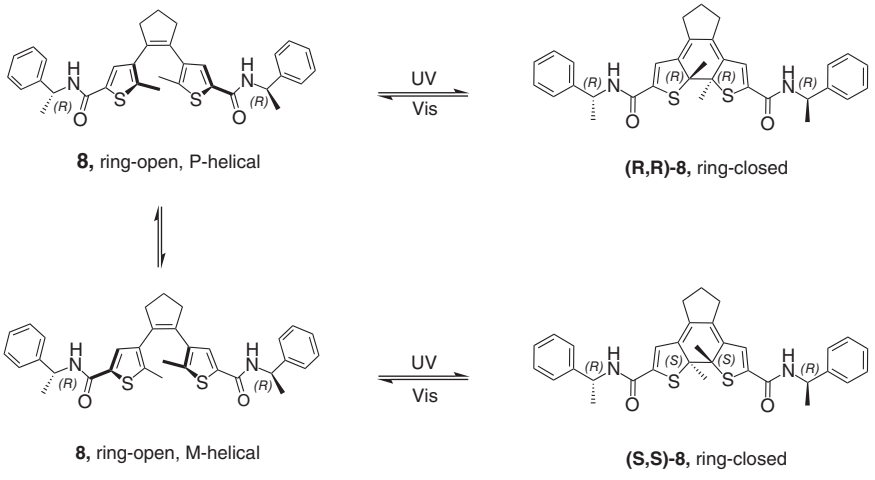


**Figure 8.5** Photochemical transformations of chiral compound **8**. Source: Modified from de Jong et al. [25].

solutions was non-diastereoselective [the ratio of the (R,R)-**8** and (S,S)-**8** ring-closed was 1 : 1], but remarkable stereoselectivity (96% de) was observed in the gel phase and attributed to hydrogen-bond-driven self-assembly of **8** [25]. Gelation of the ring-open **8** from isotropic solution proceeded with the formation of chiral fibers containing P-helical AP conformers. The supramolecular chirality upon photocyclization was thus transferred to the molecular chirality of the ring-closed form **8**.

The ring-opening reaction also has some distinctive features. It was shown that its quantum yield is sensitive to the temperature and irradiation wavelength [20]. This reflects an important detail of the ring-opening mechanism, namely the presence of a potential energy barrier along the pathway. The current mechanistic interpretation involves a conical intersection (CI) of the ground- and excited-state potential energy surfaces, a set of molecular geometry points whose potential energy surfaces are degenerate (intersect). Upon photoexcitation, the ring-open/ring-closed diarylethenes reach the CI through coupled (nonadiabatic) electron-nuclear motions that allow photoisomerization to take place. A rigorous theoretical treatment of the nonadiabatic processes around the CI is still problematic even for simple molecules such as **6**. However, model studies and plausible approximations shed light on the details of the photoisomerization mechanism. In a seminal paper [26], Boggio-Pasqua et al. reported on high-level *ab initio* and dynamics calculations for a model compound **9**. Figure 8.6 illustrates the ground-state ($S_0$) and excited-state ($S_1$) potential energy surfaces for this system, where the reaction-decisive CI ($CI_3$) is shown.

These and subsequent studies [6] revealed an important difference between the cyclization and cycloreversion processes. For ring closure, the diarylethenes can decay to the products on $S_0$ through $CI_3$ before reaching the transition state $TS_1$ on $S_1$. In contrast, cycloreversion encounters the energy barrier on $S_1$ before reaching the

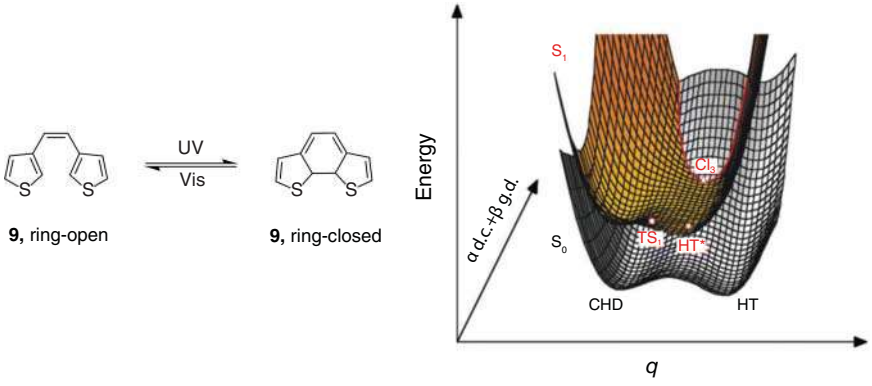


**Figure 8.6** Schematic representation of the ground-state $S_0$ (cyclohexadiene [CHD, "closed form"]) and hexatriene (HT, "open form") and excited-state $S_1$ potential surface topologies calculated for model system **9** in the reaction coordinate space (see [26] for details). The conical intersection point ($CI_3$) and transition-state $TS_1$ on the excited-state hexatriene (HT*) potential surface are shown. Source: Boggio-Pasqua et al. [26].

critical $CI_3$. This scheme explains not only the temperature and wavelength dependencies of the abovementioned ring-opening quantum yields, but it also accounts for the much lower values of the cycloreversion quantum yields compared to those of cyclization. Elucidating the electronic and nuclear driving forces that lead photoexcited diarylethene systems toward CI remains a hot topic of current research [27, 28]. Specific molecular vibrational modes have been identified by computational [29] and experimental [30] studies to be critical for ring opening.

Ample experimental data, obtained mostly by time-resolved spectroscopic studies [6, 8], have shown that the time scale of photoisomerization of typical diarylethenes is in the range of sub-picoseconds to a few tens of picoseconds in both directions. This extremely fast kinetics is crucial for the design of molecular devices for applications in molecular electronics and optical memory systems. This intrinsic kinetic behavior does not necessarily mean, however, that actual photoconversion rates in real settings will be high. Global photoconversion will depend on the actual quantum yields and many other factors, including realistic light characteristics within the reaction media, which should always be accounted for in practical applications. In particular, the rates of cyclization reaction can be very slow when the AP conformation is not easily accessible [31].

Moreover, both cyclization and cycloreversion reaction rates can be significantly slowed down by the absorption and scattering of light by the reaction media. This dependence may cause severe problems for applications of diarylethenes, e.g. in living organisms, where the light penetration depth in the tissue might become a limiting factor [32]. In this regard, we note the effort placed on the development of diarylethene systems with bathochromically shifted absorption maxima that can photoisomerize by visible or near-infrared (NIR) light in both directions. Living tissues absorb and scatter NIR light to the least extent, so photoconversion utilizing such light remains efficient even deep inside biological objects, which is important

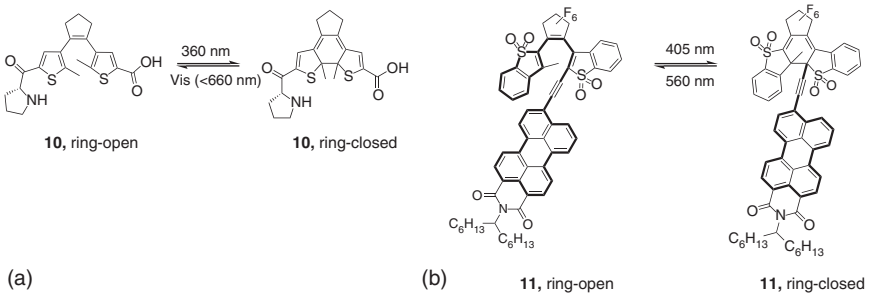


**Figure 8.7** (a) Amino acid surrogate **10** exhibiting red light-induced cycloreversion. (b) Diarylethene derivative **11** exhibiting all-visible light photochromism. The conjugated π-systems are shown bold for both photoforms. Source: Fukaminato et al. [33].

for imaging and therapeutic applications. The development of diarylethene systems that are photoisomerizable in both directions by visible light turned out to be a challenging task. Progress in this field is still slow compared to that for other photoswitches. An obvious way to achieve photoswitching with visible light throughout is to reduce the HOMO-LUMO energy gap by extending the π-conjugated system. However, it was soon discovered that this approach compromises the photoreactivity of diarylethenes. Introduction of two carbonyl substituents, at 5-5′-positions of the dithiene system, as in compound **10** (Figure 8.7a), was shown to have little effect on the photoreactivity, while providing a significant redshift of the ring-closed photoform absorbance. Compound **10** (ring-closed) has a broad absorbance band with $\lambda_{max}$ at 590 nm, which ranges up to 660 nm so that the cycloreversion process can be induced by red light. Compound **10** was successfully used to modify biologically active peptides, by directly incorporating this amino acid analogue into the peptide backbone [32]. The cyclization of **10**, however, still required UV light. A breakthrough for all-visible light photoswitches was recently reported by Irie et al. [33], who attached a perylene monoimide unit to the carbon atoms involved in bond formation/breakage during photoisomerization. The presence of the S,S-dioxide moieties and a suitable mutual orientation of the diarylethene and perylene units (allowing suppression of the intramolecular energy transfer, which otherwise hampered the cycloreversion) were the key features of the design. The best-performing compound **11** underwent photocyclization upon irradiation with 560 nm light, and cycloreversion proceeded upon irradiation with 405 nm light (Figure 8.7b).

An alternative strategy that opened exciting possibilities toward the design of all-visible light diarylethene photoswitches is based on indirect excitation of the diarylethene systems through triplet sensitizers (see the basic principle of this strategy in Figure 8.8a). Pioneering work implementing this strategy was performed on systems bearing metal complexes as the sensitizing units connected to the diarylethene core [34]. Progress with metal-free sensitizers was achieved very recently [35], and the key to success was the discovery of a sensitizing group with a narrow singlet–triplet energy gap and strong visible-light absorption. Efficient intramolecular triplet–triplet energy transfer from the sensitizer

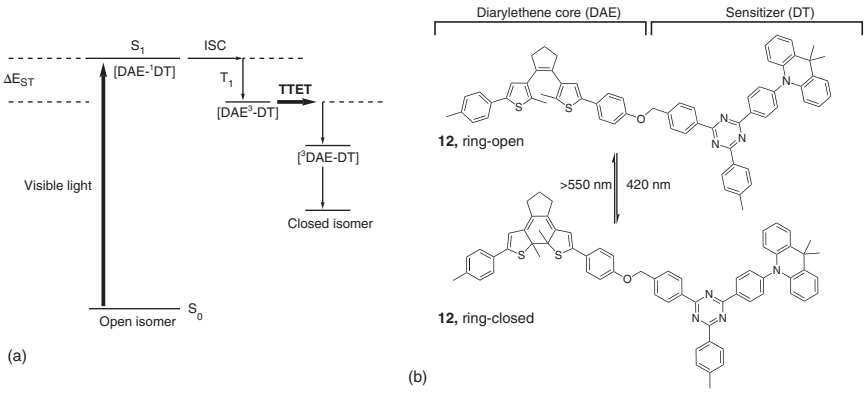


**Figure 8.8** (a) General principle for triplet sensitizer-mediated diarylethene photochromism (ISC – intersystem crossing; TTET – triplet–triplet energy transfer; ΔEST – singlet–triplet energy gap of the synthesizer). (b) Compound **12** utilizing TTET for all-visible light photoswitching.

unit to the diarylethene chromophore has thus been achieved, resulting in an efficient visible-light-driven cyclization. Compound **12**, demonstrating the proof-of-principle, is shown in Figure 8.8b. Compound **12** (ring-open) cyclized under irradiation with visible light (420 nm), and the cycloreversion proceeded under irradiation at >550 nm.

## 8.3 Distinctive Properties of Diarylethene Photoswitches

### 8.3.1 Thermal Stability of the Photoforms

Since their discovery, diarylethene photochromes have been praised for the high thermal stability of their photoisomers, which makes them truly bistable. Even today, photochromic compounds stable at ambient (20–25 °C) and elevated temperatures are quite rare. A theoretical study stemming from the Irie group [36] attempted to explain for the first time the high thermal stability of diarylethenes. This study demonstrated that the identity of the heterocyclic rings ($Het_1$ and $Het_2$) contributes significantly. While the open isomers of the diarylethenes are very stable due to the presence of the aromatic rings, cyclization leads to a loss of the stabilizing aromatic π-conjugation. Consequently, the closed-ring isomers may be unstable, thermally isomerizing to the aromatically stabilized open isomers. The ground-state energy difference between the ring-closed and ring-open photoforms appears to be inversely correlated with the energy barrier of the closed-to-open transformation, which, in turn, controls the stability of the ring-closed form. In particular, for 1,2-diphenylethene, a significant ground-state energy difference and a correspondingly small cycloreversion energy barrier were calculated by Nakamura et al. [36]. However, when the phenyl groups were replaced by 3-thienyls, characterized by a lower aromaticity change during the photoconversion, the

cycloreversion energy barrier became larger, which was later confirmed experimentally [1]. Therefore, the *cis*-dithienyl system is still the most favorably used today. The half-lives ($t_{1/2}$) for these compounds are on the order of hundreds of years at 30 °C (ring-closed **4** has $t_{1/2} \sim 1900$ years at this temperature). Numerous other thermally stable heteroaryl derivatives have been prepared, for example, azole-based diarylethenes [37]. An extraordinarily thermally stable ring-closed photoform was reported for a thiazole derivative, compound **5** (Figure 8.2), with a $t_{1/2}$ of $4.7 \times 10^5$ years at 30 °C [38]. Apart from aromatic stabilization, the thermal stability of the ring-closed forms is sensitive to the steric bulk of the substituents at the reactive positions. For example, for compounds **4** bearing different substituents R at the 2,2′-positions of the thiophenes (Figure 8.2), the thermal stability of the ring-closed photoforms becomes systematically decreased as the steric volume of the substituents is increased. The $t_{1/2}$ at 100 °C is 23 days for dimethyl-derivative (R = Me), but 40 hours for the diethyl-derivative (R = Et) and only 0.33 hours for the *i*-Pr-derivative (R = *i*Pr) [39]. The introduction of electron-withdrawing substituents at the aryl groups also decreases the thermal stability of the ring-closed forms [22]. The latter effect is explained by the weakening of the reactive carbon-carbon bonds in the ring-closed isomers.

As was initially predicted [1], the high thermal stability of both photoforms of the diarylethenes secured their leading role in the development of durable photochemical memory devices. Indeed, many such devices have been constructed to date; excellent overview of this subject was recently presented by Zhang et al. [14]. The authors of that review point out that thermal irreversibility is generally considered a vital advantage for diarylethenes, but this property should be considered in context. For certain applications, thermal reversibility is more desirable; e.g. thermally reusable photoresponsive image recordings would benefit from a thermal reactivity of the photoswitches. For biological applications, thermal reversibility could also be useful, as suggested by Feringa et al. [40]. A nonstable toxic photoform of a diarylethene-based drug could spontaneously become thermally deactivated after exerting the desired biological activity. This feature would protect the treated organisms and environment from an excessive toxicity burden (that is more likely associated with the biologically active form), and diminish the development of acquired resistance, e.g. of bacteria or cancer, to the treatment. Many diarylethenes were obtained for which the ring-closed isomers demonstrated significant thermal reversibility [41].

The design principles for highly thermally stable diarylethenes are far from being fully understood. Therefore, systems in which additional reversible chemical processes can be used to control the photo- and thermal reactivity have been proposed. Such control shall be illustrated here by diarylethenes bearing a furan moiety. These systems can be "locked" by the formation of Diels–Alder adducts involving furanyl. Branda and coworkers [42] synthesized compound **13** (Figure 8.9a), which gave a Diels–Alder adduct with a maleimide only in the ring-open photoform. The corresponding retro-Diels–Alder reaction could proceed only when the diarylethene remained in the ring-open photoform at elevated temperatures (>100 °C). UV irradiation thus led to the formation of the ring-closed isomer, for which the retro-reaction

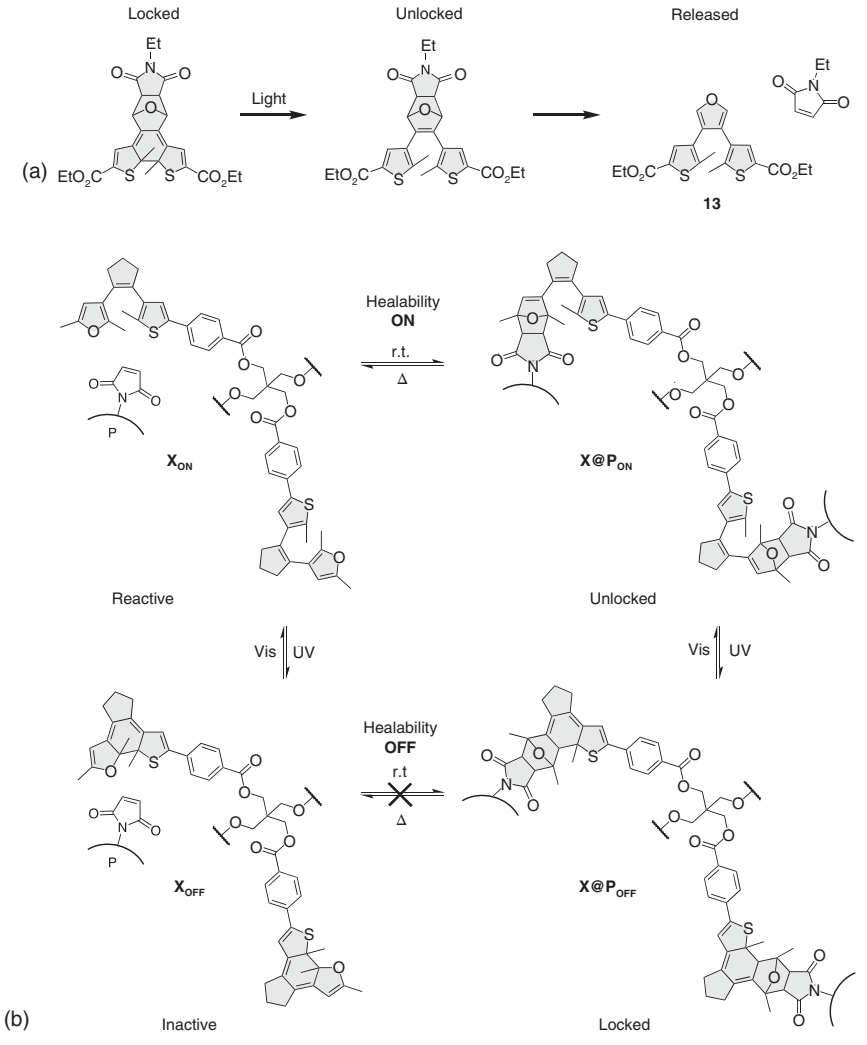


**Figure 8.9** (a) Furane-based diarylethene **13**, which can be "locked" by the Diels–Alder reaction and "unlocked" by the retro-Diels–Alder process. Source: Modified from Erno et al. [42]. (b) Photoswitchable crosslinker (X, only two of four identical units are shown for clarity) and maleimide-bearing polymer (P) forming the crosslinked polymeric network (X@P) through the Diels–Alder reaction. In its photoreactive dynamic form (X@PON), the polymer can self-heal upon heating. UV irradiation "locks" both the crosslinker and polymer, whereas visible light restores reactivity and the ability to self-heal. Source: Fuhrmann et al. [43].

was prohibited due to the absence of the cyclohexene fragment. Irradiation with visible light, however, "unlocked" the system, and the retro-Diels–Alder reaction could proceed again. The research groups of Branda and Hecht reported on "smart" self-healing polymers based on this control principle. In one of their works [43], polymerization via Diels–Alder reaction between the multivalent photoresponsive

furan-based crosslinker and maleimide-containing poly(lauryl methacrylate) proceeded only when the diarylethene moiety of the crosslinker was in the ring-open form (Figure 8.9b). UV irradiation "locked" the polymer, which became highly thermally stable. Irradiation with visible light restored the reactivity, and subsequent heating to 124 °C allowed for self-healing of mechanical defects in the polymer.

### 8.3.2 Photofatigue Resistance and Chemical Stability

Diarylethene photoswitches have been found to possess high photofatigue resistance, i.e. the ability to undergo many successive photoswitching cycles without substantial degradation. This property is indispensable in many applications of photoswitches [6]. Compounds that are extremely resistant to photodegradation have been identified among diarylethenesbearing benzothiophene rings and a perfluorocyclopentene bridge. Compound **14** (Figure 8.10), for instance, retains 90% of its performance after 14 000 cyclization/cycloreversion cycles in a methylcyclohexane solution [19], which is an extraordinary robust performance. However, not all the known photoisomerizable diarylethenes are as stable as **14**. It should be noted that the photofatigue resistance of diarylethenes, being in general very high compared to other photoswitches, may vary to a large extent with the structure and photoisomerization conditions [8]. For example, compound **4** (R = Me) can undergo only 80 cyclization/cycloreversion transformations in a hexane solution before degrading by 80% [8, 44].

Much work has been done to elucidate diarylethene photodegradation mechanisms, in order to elaborate the design principles for compounds resistant to photodegradation. Photofatigue is caused mainly by side reactions induced by irradiation. In the presence of oxygen, these side reactions can be promoted by the formation of endoperoxides, reactive oxygen species, and products of their further transformations [45]. For this reason, photodegradation is usually suppressed in the absence of oxygen; compound **4** (R = Me), for example, undergoes 200 coloration/decoloration cycles in deaerated solutions, 2.5 times more than when exposed to air [44]. It was also shown that photofatigue resistance is more pronounced in crystals than in solutions. The number of coloration/decoloration cycles for **4** (R = Me) in crystals was estimated to be larger than $10^4$ [44]. Another side reaction common to dithiene photoswitches was found to be the formation of polycyclic compounds through photochemical C—S bond cleavage and radical

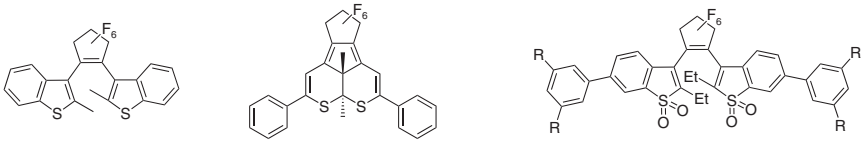


**14** **15** **16**, R = $CONHC(CH_2CH_2COOH)_3$

**Figure 8.10** Photofatigue-resistant compound **14**, a side product **15** isolated after photoisomerization of **4** (R = Me), and compound **16**, which is resistant to photodegradation in water.

migration. Such compounds were isolated and characterized by spectroscopic methods and X-ray crystallography in many cases. The byproduct of this type (compound **15**) isolated after the photodegradation of **4** (R = Me) [44] is shown in Figure 8.10.

Apart from the side reactions that are common to certain types of photoswitches and should be expected for most diarylethenes upon irradiation, other light-induced side reactions can occur, which are specific to the functional groups that decorate the central diarylethene core. An instructive illustration is the report in which photodegradation in water of the diarylethenes containing carboxyamide functionalized with ($CH_2COOH$) groups was found to proceed through C—C bond cleavage, with the extrusion of a formaldehyde molecule. To suppress this cleavage, the authors introduced *tert*-alkyl branching points at the reactive centers. Several compounds, among them **16** (Figure 8.10), demonstrated excellent photofatigue resistance in water [46].

For some applications, photofatigue is not an issue, as multiple photoswitching of the diarylethenes may not be required. For example, the use of biologically active diarylethenes in living organisms generally requires only a single cyclization/cycloreversion cycle or even just one photoisomerization [47]. In such cases, however, undesirable (not photochemical) reactions of the diarylethenes with other compounds in living tissues might cause severe problems, as such reactions could lead to toxicity or metabolic instability of diarylethene-based drugs. Most diarylethene photoswitches reported to date may be considered as reasonably inert in living tissues [48], but systematic studies on this topic are still lacking.

### 8.3.3 Molecular Geometry and Electronic Changes Upon Photoisomerization

Concerning the structure and electronic differences between the two photoforms, diarylethenes possess characteristics that are in many cases distinct from those of other known photoswitches. In particular, numerous studies have confirmed that the light-induced geometrical changes are not very large. The ring-open and ring-closed photoforms are nearly superimposable, as revealed by X-ray crystallography (Figure 8.11) [49]. Such small changes upon photoisomerization, however, turned out to be an advantage in many technologies utilizing photomechanical effects. Crystals of diarylethenes do not disintegrate by light but change only slightly in shape and size, providing exciting opportunities for their use. Various types of photomechanical motions such as contraction, expansion, bending, twisting, and "molecular popping" (photosalient behavior) have been reported [18]. The fast response time to light exposure and the possibility of miniaturizing the photoresponsive material allow for the construction of small smart photomechanical devices.

Another rapidly evolving technology, where the subtle geometrical changes of photoswitchable diarylethenes turned to be advantageous, is the optically controlled chemical separation by diarylethene-modified metal-organic frameworks (MOFs). In these MOFs, photoisomerization of the diarylethene ligands, as in crystals, does

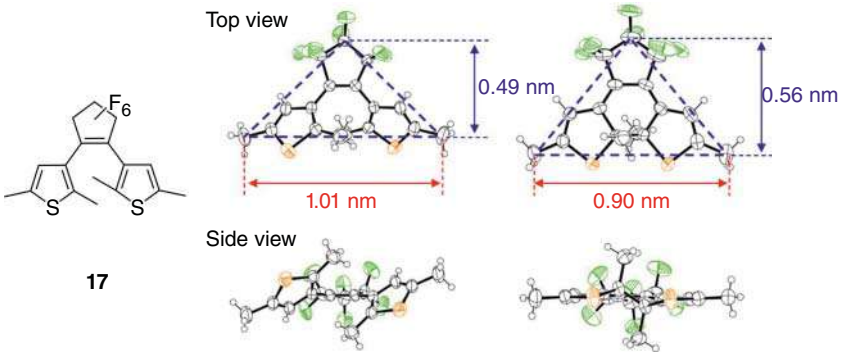


**Figure 8.11** Chemical structure of the ring-open **17** along top and side views of the crystal structures of the ring-open and ring-closed isomers of **17**. Source: Irie et al. [6].

not damage the framework, but effectively modulates the size of the MOF pores, enabling light-dependent discrimination between molecules that are very similar in size such as $C_2H_2$ and $C_2H_4$ [50].

On the other hand, it seems that the small light-induced geometrical changes discussed above may have been considered disadvantageous and have therefore discouraged chemists from the design of light-regulated biologically active derivatives and, ultimately, drugs. Diarylethene photoswitches may have been regarded inferior in the design of photoresponsive drugs due to the simplified belief that biological activity would depend only on the compound geometry and that an ideal pharmacophore would require a fixed spatial arrangement of functional groups. Compelling evidence now demonstrates that the dynamics of conformational motions modulating supramolecular interactions between biologically active ligands and their targets may be equally important [51]. Conformational dynamics is known to be of particular importance for the interactions of flexible biological targets with their ligands. Diarylethene-modified molecules can reveal excellent photoswitching performance in such systems, because the ring-open and ring-closed isomers can differentially modulate ligand conformational dynamics due to substantial alterations in molecular flexibility [52]. With a greatly enhanced rotational freedom, the ring-open isomers are much more flexible than their ring-closed counterparts. Recently, it has been demonstrated that the photoisomerizable diarylethene core in peptide ligands can serve as an enthalpy-entropy switch for protein–protein interaction [53]. The more active ring-open photoisomers of these ligands could bind better to the target protein due to a more favorable binding entropy. In contrast, the binding of the ring-closed photoisomers was predominantly enthalpy-driven. This difference in the thermodynamics of binding was suggested to originate from the different molecular flexibility of the photoisomers imposed by the diarylethene moiety.

The difference in molecular flexibility of diarylethenes may also influence their interaction with a highly mobile environment such as that in fluid lipid bilayers. Membranolytic diarylethene-derived peptidomimetics have been reported, with an efficient photoswitchable biological response. Compound **18** (Figure 8.12) demonstrated excellent photocontrolled activity, both *in vitro* (against different

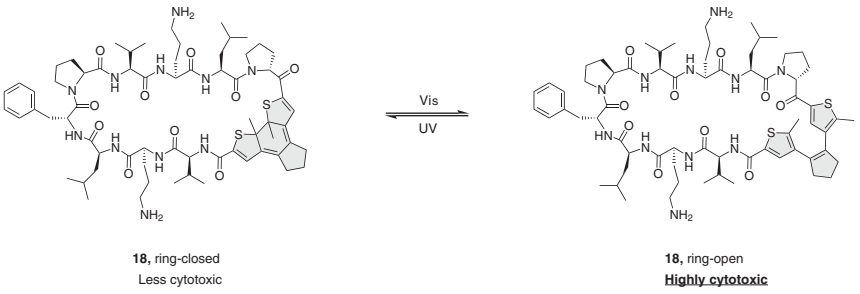


**Figure 8.12** Photoswitchable membrane-active peptidomimetic **18** (the diarylethene residue accommodated in one of the β-turns of the molecule is highlighted).

cell line cultures) and *in vivo* (in rodent cancer models) [32]. The translocation of diarylethene-modified peptides across living cell membranes could also be controlled by light [54]. In almost all these examples, the flexible ring-open forms were more biologically/membrane-active than their ring-closed isomers. Numerous analogs of **18** have been synthesized, and their structure–activity relationship was studied in detail [55]. This concept of photocontrolling the activity of a biomimetic molecule is an important step in the development of diarylethene-based drugs possessing enhanced safety. A photocontrollable drug can be safer because it can be administered in the inactive, less-toxic (photo)isomeric form, which can then be activated by light with a high level of spatiotemporal precision at the desired site of action [48].

In contrast to the geometrical effects, the changes in the electronic properties of diarylethenes upon photoisomerization are considerable. The HOMO-LUMO gap, dipole moment, electron affinity, ionization energy, and concomitant properties are fundamentally different for the ring-open and ring-closed isomers. These differences drive current applications of diarylethenes in molecular optical memory media and electronics, rapidly evolving and promising areas of applied research. As mentioned above, electronic changes are manifested in the dramatic differences of the absorbance spectra. The aromatically stabilized ring-open forms absorb mostly in the UV region. The ring-closed isomers, where the π-conjugation delocalizes to a larger extent and the HOMO-LUMO gap is smaller, absorb in the visible spectral region. These differences are appealing for use in ultrahigh density (Tbits/in.$^2$) optical storage media, given the high fatigue resistance and durability of many diarylethenes. However, the use of absorbance for a readout inevitably leads to damage to the recorded information, as this readout mode requires the use of photoisomerization-inducing UV or visible light. Fortunately, for diarylethenes, other nondestructive readouts are possible. In particular, benzothiophene-containing compounds such as **14** were found to have significantly different IR spectra for both photoisomers in the spectral range around 1590 cm$^{-1}$. As IR irradiation does not cause photoisomerization, IR light was successfully used for a nondestructive readout of the information recorded by this type of diarylethene [56].

The changes in the electronic structure of diarylethenes upon photoisomerization also dramatically alter their fluorescence behavior. In principle, photocontrolled fluorescence could also be exploited in molecular memory and molecular electronics applications, but the range of possible applications is even broader. Specific use of diarylethene-based photoswitchable fluorophores in sensing, cell imaging, and, lately, superresolution microscopy (optical microscopy beyond the diffraction limit) has been envisaged [15]. Most diarylethene derivatives effectively emit light only in their ring-open forms. For example, ring-closed **6** (Figure 8.3) shows only very weak fluorescence with a maximum at ~790 nm (excitation at 515 nm). Overlap of the absorbance and fluorescence bands for ring-closed **6** leads to intramolecular quenching of its intrinsic fluorescence. The fluorescence of the ring-open form, in contrast, is much brighter and occurs at ~425 nm (excitation at 300 nm) [27]. This fluorescence mode was termed the "turn-off" mode, i.e. upon UV irradiation these fluorescent ring-open diarylethenes will lose their fluorescence. The practical utility of the "turn-off" mode is limited, however, because the fluorescence detection *per se* will lead to ring closure, causing a loss of the desired signal. To cope with this limitation, "turn-on" fluorescent photoswitchable diarylethenes have been searched for, and many such compounds have been reported. For example, sulfone-based diarylethenes of the general formula **19** (Figure 8.13) are "turn-on" fluorescent compounds: their ring-open forms are poorly fluorescent, while the ring-closed forms demonstrate bright fluorescence. These compounds are suitable for superresolution imaging. Their properties can be fine-tuned by varying the substituents to optimize the photoswitching parameters for different types of superresolution microscopy, such as PALM, SOFI, and RESOLFT [57]. Similar systems respond very well in water, which is important for biological studies, such as the fatigue-resistant compound **16** mentioned before [46].

Another strategy that aims at efficient fluorescence photoswitching and detection, without direct interference from photoisomerization, relies on the use of a non-photoswitchable fluorophore that is connected to but not conjugated with the diarylethene core (compare with compound **11** described above). The interaction between the photochromic moiety and the fluorophore can reversibly modulate fluorescence through intramolecular energy or electron transfer. Fukaminato et al. reported a successful example based on fluorescence quenching by intramolecular electron transfer [58]. Molecule **20**, designed in that work, is shown in Figure 8.14,

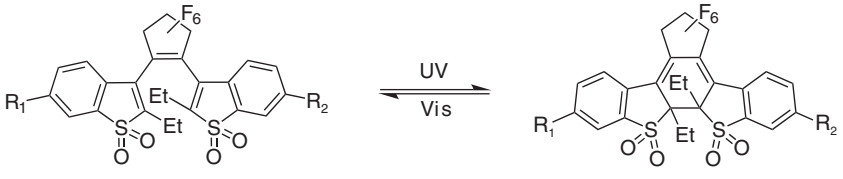


**19,** ring-open
Non-fluorescent

**19,** ring-closed
Fluorescent

**Figure 8.13** "Turn-on" photoswitchable fluorescent diarylethene **19**.

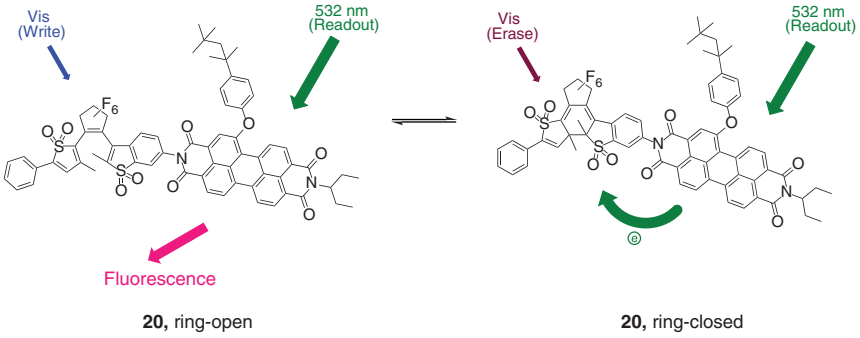


**Figure 8.14** Photocontrollable fluorescent molecule **20**, and the principle of its performance based on intramolecular electron transfer between a nonconjugated fluorophore and the diarylethene photoswitch. Source: Fukaminato et al. [58].

to illustrate the principles of utilizing such derivatives. Compound **20** was found to be sufficiently selective for a nondestructive fluorescence readout even on a single-molecule level; hence, it represents a major practical breakthrough on the way toward functional diarylethene-based molecular optical memory devices. Overall, the systems based on electron transfer seem to be advantageous, as the change in oxidation/reduction potential of the diarylethene unit caused by the electron transfer process does not induce uncontrolled photoswitching, unlike when intramolecular energy transfer is involved. As a result, electron transfer systems of this kind are more advantageous to achieve a nondestructive readout, which is needed for most practical applications.

Numerous diarylethene-based probes, alone or doped into a nanoparticle structure, have been widely used for imaging in biological systems. A significant advantage offered by such photoswitchable fluorescent probes is that they act without a need to supplement the imaging buffer with oxygen-scavenging systems and reducing agents, which is attributed to their ability to dynamically and effectively switch the fluorescent signal on and off [14].

Apart from the spectroscopic properties, other characteristics of diarylethenes are also found to change due to the electronic differences of the photoisomers. In the last two decades, one of the most studied properties has been single-molecule conductance, mostly to support the fabrication of new molecular electronic devices [14]. Diarylethene photoswitches – with their bistability, high fatigue resistance, ultrashort photoisomerization time, high quantum yields, and small geometrical changes during photoswitching – are suitable candidates for current switches, ubiquitous elements of electronic devices. The diarylethene ring-closed isomers are expected to conduct better than the ring-open isomers, as the former usually have extended conjugated π-systems, whereas the π-conjugation of the latter is localized on the aromatic rings. However, in practice, the integration of diarylethenes into molecular electronic circuits faces considerable challenges. Strong molecule–electrode coupling may often counteract diarylethene photoswitching in both directions; the first reported molecular switches were only unidirectional. Gold electrodes, for instance,

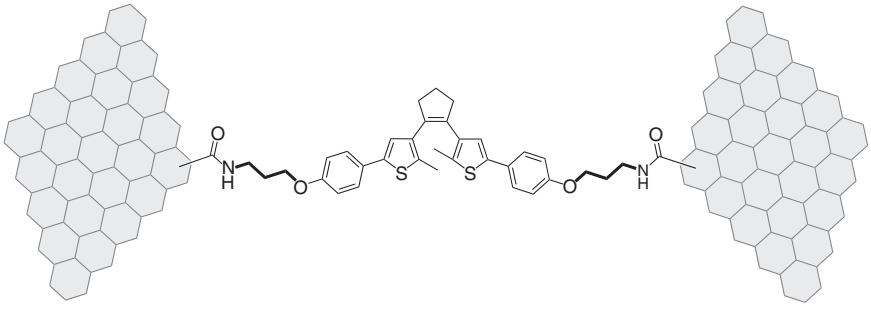


**Figure 8.15** Schematic representation of a molecular device with photoswitchable conductance: a diarylethene-based crosslinker flanked with 3x$CH_2$ "isolators" (bold) is placed between two graphene electrodes, as described in [59]. Source: Modified from Jia et al. [59].

can quench the ring-open excited states, prohibiting the cyclization. Carbon-based electrodes – single-walled nanotubes or graphene sheets – have been shown to interact with excited ring-closed diarylethenes efficiently, and therefore cycloreversion was not possible in these systems. Progress has been made only recently by introducing several "isolating" –$CH_2$– groups between an electrode-anchoring moiety and the diarylethene core. Guo and coworkers demonstrated [59], both theoretically and experimentally, that incorporation of three methylene groups on both sides of a diarylethene fragment as schematically shown in Figure 8.15, reduces the molecule–electrode interaction to an extent that bidirectional photoswitching becomes possible. They achieved a conductance on/off ratio of $107.1 \pm 56.3$ under alternating UV/vis irradiation. The devices were very stable (with no detectable operational degradation over a year) and photofatigue resistant (more than 100 photoswitching cycles were observed without any appreciable degradation).

At the end of this section, let us mention some other properties of diarylethenes that are photoswitchable due to the changes in electronic structure upon photoisomerization. Magnetic interaction in diarylethenes decorated with stable radicals was shown to be efficiently photoswitchable [60]. Light-induced modulation of the refractive index in polymers doped with diarylethenes was also reported [61]. This list is by no means exhaustive, and novel discoveries will undoubtedly expand it further.

## 8.4 Synthesis of Diarylethenes

The diarylethenes described in the pioneering work of Irie et al. [1] were prepared starting from 2,4,5-trimethyl-3-(cyanomethyl)thiophene through a coupling reaction as the key step (Figure 8.16).

This approach, however, lacks generality, and several other synthetic strategies have been developed since [62]. We already mentioned that among a large number of synthesized and studied diarylethenes, the most commonly used ones are diarylperfluorocyclopentenes. These compounds can be reliably prepared through

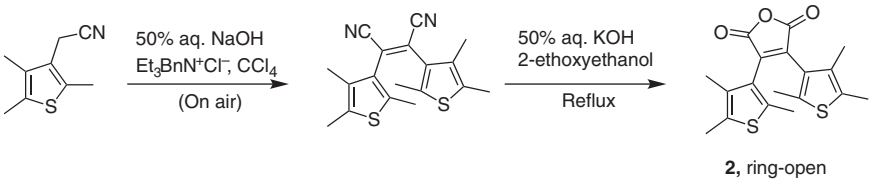


**Figure 8.16** Historical synthesis of photochromic diarylethenes.

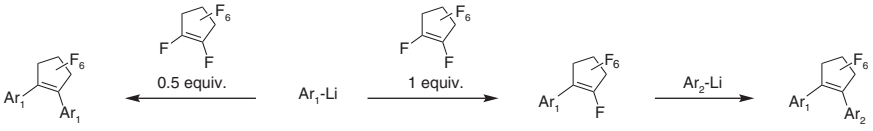


**Figure 8.17** Synthesis of diarylperfluorocyclopentenes through the addition–elimination reaction of perfluorocyclopentenes with aryllithium. Source: Modified from Hanazawa et al. [19].

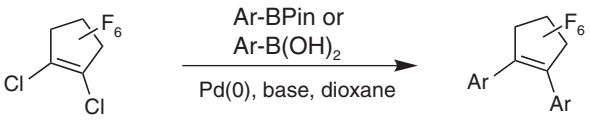


**Figure 8.18** Suzuki–Miyaura-based synthesis of diarylethenes. Source: Modified from Hiroto et al. [63].

a nucleophilic addition–elimination reaction of perfluorocyclopentene, as shown in Figure 8.17 [19]. Symmetric diarylethenes with various heterocyclic aryl groups could be obtained by the reaction of perfluorocyclopentene with two equivalents of aryllithium. The use of equimolar amounts of perfluorocyclopentene and aryllithium leads to mono-substituted perfluorocyclopentenes, which can subsequently be used in the synthesis of nonsymmetrical diarylethenes.

A technically more convenient approach, reported by Shinokubo et al. is based on the Suzuki–Miyaura coupling reaction of 1,2-dichlorohexafluorocyclopentene with arylboronic acids and esters (Figure 8.18) [63]. This approach works well for the symmetric diarylethenes and can be adapted to the synthesis of nonsymmetrical compounds, although with moderate success, because the mono-coupling proceeds non-selectively and gives a substantial amount of the bis-coupled product [62]. Using different starting compounds possessing 1,2-dihalosubstituted ethene fragments, diarylethenes with different ethane bridges can be prepared through Suzuki–Miyaura bis-coupling [64].

Fan and coworkers [65], and later Feringa and coworkers [66], have developed an alternative method for the synthesis of diarylethenes, utilizing low-valent titanium-promoted McMurry coupling for forming the cyclic alkene bridge. An example published by Feringa et al. is shown in Figure 8.19. Based on McMurry coupling, diarylethenes with different aryl groups and ethene bridges were synthesized [67]. The McMurry coupling-based strategy was also proposed for the synthesis of nonsymmetrical diarylethenes [62].

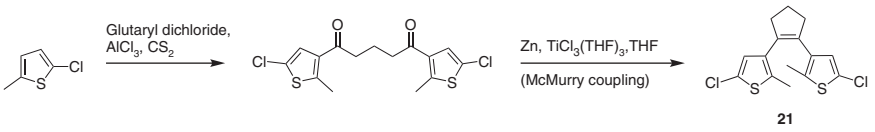


**Figure 8.19** McMurry coupling-based pathway to dithienylcyclopentenes.

Finally, numerous syntheses of functionalized diarylethenes have started from simple, readily available diarylethene precursors. The most frequently used are dihalosubstituted diarylethenes, such as compound **21** (Figure 8.19). They were functionalized through various coupling reactions or halogen–lithium exchange, followed by reactions with electrophiles [62].

## 8.5 Conclusions and Outlook

During their relatively short but fascinating history, photoisomerizable diarylethenes have evolved into a remarkable class of compounds with numerous prospects for practical applications. In our opinion, this field of research has reached the stage where numerous proof-of-principle discoveries are well established by extensive academic research. However, significant and challenging steps are still to be taken in the translation of these innovations from academia to industry. In many areas awaiting practical implementation, further improvements of the diarylethene characteristics are possible and should be made. For example, for molecular electronic devices, more fatigue-resistant diarylethenes are required. The exploitation of diarylethene-based photocontrolled biologically active compounds is still in need of optimizing the pharmacokinetic characteristics and safety – a formidable task, taking into account relatively large size of the diarylethene moiety. Applications of diarylethenes in optical storage systems require improvements in nondestructive readout methods. For all prospective applications, the synthetic procedures, fabrication of the devices, and their manipulation have to be made cheaper and more straightforward, in order to be competitive with other analogous systems that are currently being developed. We believe that the efforts and resources invested in these improvements will eventually be paid off by the advantages offered by new technologies, based on the fascinating compounds discussed in this chapter.

## References

1 Irie, M. and Mohri, M. (1988). Thermally irreversible photochromic systems. Reversible photocyclization of diarylethene derivatives. *J. Org. Chem.* 53 (4): 803–808.
2 Parker, C.O. and Spoerri, P.E. (1950). Photochemical conversion of stilbene to phenanthrene. *Nature* 166 (4223): 603–603.
3 Mallory, F.B., Wood, C.S., Gordon, J.T. et al. (1962). Photochemistry of stilbenes. I. *J. Am. Chem. Soc.* 84 (22): 4361–4362.

**4** Srinivasan, R. (1966). Photochemistry of conjugated dienes and trienes. *Adv. Photochem.* 4: 113–142.

**5** Irie, M. and Schnabel, W. (1982). Photochemical conversion of poly-2,3-diphenylbutadiene to poly-9,10-dimethylenephenanthrene. *Eur. Polym. J.* 18 (1): 15–18.

**6** Irie, M., Fukaminato, T., Matsuda, K. et al. (2014). Photochromism of diarylethene molecules and crystals: memories, switches, and actuators. *Chem. Rev.* 114 (24): 12174–12277.

**7** Hirshberg, Y. (1956). Reversible formation and eradication of colors by irradiation at low temperatures. A photochemical memory model. *J. Am. Chem. Soc.* 78 (10): 2304–2312.

**8** Irie, M. (2000). Diarylethenes for memories and switches. *Chem. Rev.* 100 (5): 1685–1716.

**9** Yokoyama, Y. and Kose, M. (2004). Reversible control of properties of materials by thermally irreversible photochromism. *J. Photochem. Photobiol. A* 166 (1–3): 9–18.

**10** Yun, C., You, J., Kim, J. et al. (2009). Photochromic fluorescence switching from diarylethenes and its applications. *J. Photochem. Photobiol. C* 10 (3): 111–129.

**11** Irie, M. (2010). Photochromism of diarylethene single molecules and single crystals. *Photochem. Photobiol. Sci.* 9 (12): 1535–1542.

**12** Shirinian, V.Z., Lonshakov, D.V., Lvov, A.G. et al. (2013). Fluorescent photochromes of diarylethene series: synthesis and properties. *Russ. Chem. Rev.* 82 (6): 511–537.

**13** Pu, S.Z., Sun, Q., Fan, C.B. et al. (2016). Recent advances in diarylethene-based multi-responsive molecular switches. *J. Mater. Chem. C* 4 (15): 3075–3093.

**14** Zhang, J. and Tian, H. (2018). The endeavor of diarylethenes: new structures, high performance, and bright future. *Adv. Opt. Mater.* 6 (6): 1701278.

**15** Fukaminato, T., Ishida, S., and Métivier, R. (2018). Photochromic fluorophores at the molecular and nanoparticle levels: fundamentals and applications of diarylethenes. *NPG Asia Mater.* 10 (9): 859–881.

**16** Dela Cruz Calupitan, J.P., Galangau, O., Nakashima, T. et al. (2019). Photochromic diarylethenes designed for surface deposition: from self-assembled monolayers to single molecules. *ChemPlusChem* 84 (6): 564–577.

**17** Lvov, A.G., Yokoyama, Y., and Shirinian, V.Z. (2020). Post-modification of the ethene bridge in the rational design of photochromic diarylethenes. *Chem. Rec.* 20 (1): 51–63.

**18** Kobatake, S. and Kitagawa, D. (2020). Photomechanical behavior of photochromic diarylethene crystals. In: *Mechanically Responsive Materials for Soft Robotics*, 1e (ed. K. Hideko). Wiley-VCH Verlag, 3–28.

**19** Hanazawa, M., Sumiya, R., Horikawa, Y. et al. (1992). Thermally irreversible photochromic systems. Reversible photocyclization of 1,2-bis(2-methylbenzo[*b*]thiophen-3-yl) perfluorocyclocoalkene derivatives. *J. Chem. Soc., Chem. Commun.* (3): 206–207.


**20** Sumi, T., Takagi, Y., Yagi, A. et al. (2014). Photoirradiation wavelength dependence of cycloreversion quantum yields of diarylethenes. *Chem. Commun.* 50 (30): 3928–3930.

**21** Irie, M., Sakemura, K., Okinaka, M. et al. (1995). Photochromism of dithienylethenes with electron-donating substituents. *J. Org. Chem.* 60 (25): 8305–8309.

**22** Gilat, S.L., Kawai, S.H., and Lehn, J.M. (1995). Light-triggered molecular devices: photochemical switching of optical and electrochemical properties in molecular wire type diarylethene species. *Chem. Eur. J.* 1 (5): 275–284.

**23** Li, W., Jiao, C., Li, X. et al. (2014). Separation of photoactive conformers based on hindered diarylethenes: efficient modulation in photocyclization quantum yields. *Angew. Chem. Int. Ed.* 53 (18): 4603–4607.

**24** Nakagawa, T., Ubukata, T., and Yokoyama, Y. (2018). Chirality and stereoselectivity in photochromic reactions. *J. Photochem. Photobiol. C Photochem. Rev.* 34: 152–191.

**25** de Jong, J.J., Lucas, L.N., Kellogg, R.M. et al. (2004). Reversible optical transcription of supramolecular chirality into molecular chirality. *Science* 304 (5668): 278–281.

**26** Boggio-Pasqua, M., Ravaglia, M., Bearpark, M.J. et al. (2003). Can diarylethene photochromism be explained by a reaction path alone? A CASSCF study with model MMVB dynamics. *J. Phys. Chem. A* 107 (50): 11139–11152.

**27** Sotome, H., Une, K., Nagasaka, T. et al. (2020). A dominant factor of the cycloreversion reactivity of diarylethene derivatives as revealed by femtosecond time-resolved absorption spectroscopy. *J. Chem. Phys.* 152 (3): 034301.

**28** Sotome, H., Okajima, H., Nagasaka, T. et al. (2020). Geometrical evolution and formation of the photoproduct in the cycloreversion reaction of a diarylethene derivative probed with molecular vibrations. *ChemPhysChem* 21 (14): 1524–1530.

**29** Chiariello, M.G., Raucci, U., Coppola, F. et al. (2019). Unveiling anharmonic coupling by means of excited state ab initio dynamics: application to diarylethene photoreactivity. *Phys. Chem. Chem. Phys.* 21 (7): 3606–3614.

**30** Jarota, A., Pastorczak, E., Tawfik, W. et al. (2019). Exploring the ultrafast dynamics of a diarylethene derivative using sub-10 fs laser pulses. *Phys. Chem. Chem. Phys.* 21 (1): 192–204.

**31** Schweigert, C., Babii, O., Afonin, S. et al. (2019). Real-time observation of diarylethene-based photoswitches in a cyclic peptide environment. *ChemPhotoChem* 3 (6): 403–410.

**32** Babii, O., Afonin, S., Garmanchuk, L.V. et al. (2016). Direct photocontrol of peptidomimetics: an alternative to oxygen-dependent photodynamic cancer therapy. *Angew. Chem. Int. Ed.* 55 (18): 5493–5496.

**33** Fukaminato, T., Hirose, T., Doi, T. et al. (2014). Molecular design strategy toward diarylethenes that photoswitch with visible light. *J. Am. Chem. Soc.* 136 (49): 17145–17154.

**34** Jukes, R.T., Adamo, V., Hartl, F. et al. (2004). Photochromic dithienylethene derivatives containing Ru(II) or Os(II) metal units. Sensitized photocyclization from a triplet state. *Inorg. Chem.* 43 (9): 2779–2792.


**35** Zhang, Z., Wang, W., Jin, P. et al. (2019). A building-block design for enhanced visible-light switching of diarylethenes. *Nat. Commun.* 10 (1): 1–9.

**36** Nakamura, S. and Irie, M. (1988). Thermally irreversible photochromic systems. A theoretical study. *J. Org. Chem.* 53 (26): 6136–6138.

**37** Lvov, A.G., Khusniyarov, M.M., and Shirinian, V.Z. (2018). Azole-based diarylethenes as the next step towards advanced photochromic materials. *J. Photochem. Photobiol. C* 36: 1–23.

**38** Takami, S., Kobatake, S., Kawai, T. et al. (2003). Extraordinarily high thermal stability of the closed-ring isomer of 1,2-bis(5-methyl-2-phenylthiazol-4-yl)perfluorocyclopentene. *Chem. Lett.* 32 (10): 892–893.

**39** Kitagawa, D., Sasaki, K., and Kobatake, S. (2011). Correlation between steric substituent constants and thermal cycloreversion reactivity of diarylethene closed-ring isomers. *Bull. Chem. Soc. Jpn.* 84 (2): 141–147.

**40** Velema, W.A., Van Der Berg, J.P., Hansen, M.J. et al. (2013). Optical control of antibacterial activity. *Nat. Chem.* 5 (11): 924–928.

**41** Kitagawa, D. and Kobatake, S. (2016). Strategy for molecular design of photochromic diarylethenes having thermal functionality. *Chem. Rec.* 16 (4): 2005–2015.

**42** Erno, Z., Asadirad, A.M., Lemieux, V. et al. (2012). Using light and a molecular switch to 'lock'and 'unlock'the Diels–Alder reaction. *Org. Biomol. Chem.* 10 (14): 2787–2792.

**43** Fuhrmann, A., Göstl, R., Wendt, R. et al. (2016). Conditional repair by locally switching the thermal healing capability of dynamic covalent polymers with light. *Nat. Commun.* 7 (1): 1–7.

**44** Irie, M., Lifka, T., Uchida, K. et al. (1999). Fatigue resistant properties of photochromic dithienylethenes: by-product formation. *Chem. Commun.* (8): 747–750.

**45** Taniguchi, H., Shinpo, A., Okazaki, T. et al. (1992). Photodegradation mechanism of photochromic diarylethene derivatives. *Nippon Kagaku Kaishi* 1992 (10): 1138–1140.

**46** Uno, K., Bossi, M.L., Irie, M. et al. (2019). Reversibly photoswitchable fluorescent diarylethenes resistant against photobleaching in aqueous solutions. *J. Am. Chem. Soc.* 141 (41): 16471–16478.

**47** Lerch, M.M., Hansen, M.J., van Dam, G.M. et al. (2016). Emerging targets in photopharmacology. *Angew. Chem. Int. Ed.* 55 (37): 10978–10999.

**48** Babii, O., Afonin, S., Schober, T. et al. (2020). Peptide drugs for photopharmacology: how much of a safety advantage can be gained by photocontrol? *Fut. Drug Discovery* 2 (1): FDD28.

**49** Yamada, T., Kobatake, S., and Irie, M. (2000). X-ray crystallographic study on single-crystalline photochromism of 1,2-bis(2,5-dimethyl-3-thienyl) perfluorocyclopentene. *Bull. Chem. Soc. Jpn.* 73 (10): 2179–2184.

**50** Fan, C.B., Le Gong, L., Huang, L. et al. (2017). Significant enhancement of $C_2H_2/C_2H_4$ separation by a photochromic diarylethene unit: a temperature-and light-responsive separation switch. *Angew. Chem. Int. Ed.* 56 (27): 7900–7906.

**51** Tzeng, S.R. and Kalodimos, C.G. (2012). Protein activity regulation by conformational entropy. *Nature* 488 (7410): 236–240.

**52** Komarov, I.V., Afonin, S., Babii, O. et al. (2018). Efficiently photocontrollable or not? Biological activity of photoisomerizable diarylethenes. *Chem. Eur. J.* 24 (44): 11245–11254.

**53** Strizhak, A.V., Babii, O., Afonin, S. et al. (2020). Diarylethene moiety as an enthalpy-entropy switch: photoisomerizable stapled peptides for modulating p53/MDM2 interaction. *Org. Biomol. Chem.* 18 (28): 5269–5482.

**54** Schober, T., Wehl, I., Afonin, S. et al. (2019). Controlling the uptake of diarylethene-based cell-penetrating peptides into cells using light. *ChemPhotoChem* 3 (6): 384–391.

**55** Babii, O., Afonin, S., Ishchenko, A.Y. et al. (2018). Structure–activity relationships of photoswitchable diarylethene-based β-hairpin peptides as membranolytic antimicrobial and anticancer agents. *J. Med. Chem.* 61 (23): 10793–10813.

**56** Uchida, K., Saito, M., Murakami, A. et al. (2003). Non-destructive readout of the photochromic reactions of diarylethene derivatives using infrared light. *Adv. Mater.* 15 (2): 121–125.

**57** Nevskyi, O., Sysoiev, D., Dreier, J. et al. (2018). Fluorescent diarylethene photoswitches – a universal tool for super-resolution microscopy in nanostructured materials. *Small* 14 (10): 1703333.

**58** Fukaminato, T., Doi, T., Tamaoki, N. et al. (2011). Single-molecule fluorescence photoswitching of a diarylethene–perylenebisimide dyad: non-destructive fluorescence readout. *J. Am. Chem. Soc.* 133 (13): 4984–4990.

**59** Jia, C., Migliore, A., Xin, N. et al. (2016). Covalently bonded single-molecule junctions with stable and reversible photoswitched conductivity. *Science* 352 (6292): 1443–1445.

**60** Matsuda, K. and Irie, M. (2000). A diarylethene with two nitronyl nitroxides: photoswitching of intramolecular magnetic interaction. *J. Am. Chem. Soc.* 122 (30): 7195–7201.

**61** Kang, J.W., Kim, J.J., and Kim, E. (2002). All-optical Mach–Zehnder modulator using a photochromic dye-doped polymer. *Appl. Phys. Lett.* 80 (10): 1710–1712.

**62** Szalóki, G. and Pozzo, J.L. (2013). Synthesis of symmetrical and nonsymmetrical bisthienylcyclopentenes. *Chem. Eur. J.* 19 (34): 11124–11132.

**63** Hiroto, S., Suzuki, K., Kamiya, H., and Shinokubo, H. (2011). Synthetic protocol for diarylethenes through Suzuki–Miyaura coupling. *Chem. Commun.* 47 (25): 7149–7151.

**64** Patel, D.G., Mitchell, T.B., Myers, S.D. et al. (2020). A Suzuki approach to quinone-based diarylethene photochromes. *J. Org. Chem.* 85 (4): 2646–2653.

**65** Xu, B.A., Huang, Z.N., Jin, S. et al. (1997). Synthesis and photochromic mechanism of 3,4-bis[2,5-dimethylthiophene-3-yl]-2,5-dihydrothiophene. *J. Photochem. Photobiol. A Chem.* 110 (1): 35–40.

**66** Lucas, L.N., Jong, J.J.D., Esch, J.H.V. et al. (2003). Syntheses of dithienylcyclopentene optical molecular switches. *Eur. J. Org. Chem.* 2003 (1): 155–166.

**67** Krayushkin, M.M., Kalik, M.A., and Migulin, V.A. (2009). McMurry reaction in the synthesis of photochromic dihetarylethenes. *Russ. Chem. Rev.* 78 (4): 329.


# 9 Fulgides and Fulgimides

Falk Renth and Friedrich Temps

## Photoisomerization

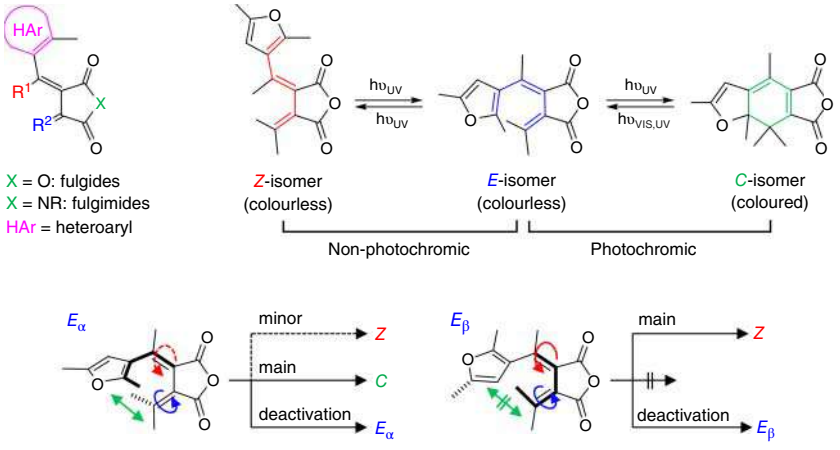


Mechanistic insight by ultrafast spectroscopy: conformer-specific photochemistry & rational design

## Characteristic Features

- Strong photochromism in the visible range of light
- Thermal irreversibility
- Very low photochemical fatigue
- Suitable for polar and aqueous environments

## First Reported

Stobbe, H. (1905). Die Farbe der "Fulgensäuren" und "Fulgide" (7. Abhandlung über Butadienverbindungen), *Ber. Dtsch. Chem. Ges.* 38: 3673–3682.

## Key References

Yokoyama, Y. (2000). Fulgides for memories and switches. *Chem. Rev*. 100: 1717–1740.

Renth, F., Siewertsen, R., and Temps, F. (2013). Enhanced photoswitching and ultrafast dynamics in structurally modified photochromic fulgides. *Int. Rev. Phys. Chem.* 32: 1–38.

Lachmann, D., Lahmy, R., and König, B. (2019). Fulgimides as light-activated tools in biological investigations, *Eur. J. Org. Chem.* 2019: 5018–5024.

# 9

# Fulgides and Fulgimides

*Falk Renth and Friedrich Temps*

*Institut für Physikalische Chemie, Christian-Albrechts-Universität zu Kiel, 24098 Kiel, Olshausenstr. 40, Germany*

## 9.1 Introduction

Fulgides and fulgimides are strongly photochromic, optically bistable photoswitches offering reversible interconversions between two isomers purely by irradiation with light of two different colors [1–5]. Their photochromism, like that of diarylethenes [6, 7], relies on the 6π-electrocyclic ring-closure and ring-opening reactions between the central 1,3,5-hexatriene (HT, open) and 1,3-cyclohexadiene (CHD, closed) moieties and extends well into the visible wavelength range [3–5]. Besides photoisomerization reactions with high conversion yields that can even be initiated in the solid state [8, 9], fulgides and fulgimides show exceptionally low photochemical fatigue and stand out for their thermal irreversibility.

Fulgides were discovered already more than a century ago when Stobbe first studied aryl-substituted derivatives of 1,3-butadiene-2,3-dicarboxylic acid and its anhydride [10]. Early fulgides suffered from limited interconversion, thermal as well as photo-induced degrading reactions, including hydrogen shifts, and a strong susceptibility toward oxidative aromatization. The subsequent structural evolution of fulgide photoswitches, as well as comprehensive research covering synthetic, structural, and photochemical aspects up to the early 2000s, has been covered in excellent previous reviews [2, 3]. This chapter first summarizes the photoswitching properties and synthesis of modern fulgides and fulgimides, and then focuses on recent developments and perspectives, in particular the effects of structural modifications, and the mechanistic picture obtained in studies of the underlying photo-induced ultrafast molecular processes. These results may guide the future rational design of new fulgide derivatives with improved functionalities. Finally, the enormous application potential of fulgide-type photoswitches is highlighted by selected examples.

*Molecular Photoswitches: Chemistry, Properties, and Applications*,
First Edition. Edited by Zbigniew L. Pianowski.


## 9.2 Photoswitching Properties

Modern fulgides and fulgimides share a common substitution pattern at the bismethylenesuccinic acid anhydride and imide cores, respectively, as shown in Figure 9.1.

The use of heteroaryl substituents (instead of an aryl group) provides bathochromic shifts resulting in strong photochromicity. Furthermore, substitution of all remaining H-atoms at the HT backbone, e.g. by alkyl groups, prevents thermal degradation by sigmatropic hydrogen rearrangements and oxidative hydrogen abstraction. Finally, the steric hindrance introduced by the substituents $R^1$ and $R^2$ enforces a non-planar, helically chiral conformation of the HT moiety that effectively blocks the disrotatory thermal ring opening and ensures thermal irreversibility [3–5, 11]. Using furylfulgide **1** as example, the right-hand side of Figure 9.1 illustrates that the photochemistry of fulgides goes beyond ring opening and closure, as there are three thermally stable isomers connected by photoisomerization reactions. The desired photo-induced electrocyclic ring-opening and -closure reactions interconvert the open *E*-isomer and the closed *C*-isomer, whereas the *E*–*Z* photoisomerization is an unwanted, photo-reversible side reaction between the open isomers. The formal *E*–*Z* photoisomerization of the *exo*-isopropylidene group leads only to electronic deactivation since reactant and photoproduct are the same for symmetrical substituents $R^2$.

Figure 9.2 shows the corresponding UV/vis absorption spectra for the three isomers. As can be seen, the open *E*- and *Z*-isomers have first absorption bands in the near UV, at much shorter wavelengths than the closed *C*-isomer. Due to the well-separated *E*- and *C*-isomer absorption bands, ring opening and closure lead to strong absorption changes. Furthermore, quantitative ring opening of the *C*-isomer can be achieved by irradiation at visible wavelengths ($\geq$ 450 nm for **1C**), where the open isomers do not absorb. Likewise, irradiation of the *E*-isomer in the near UV leads to almost quantitative conversion to the ring-closed isomer in the photostationary state (≈95% for irradiation of **1E** at 365 nm [12]). In the latter case, photochemical accumulation of the noncyclizable *Z*-isomer due to the competing *E*–*Z* isomerization is prevented by the reverse *Z*–*E* photoreaction. However,

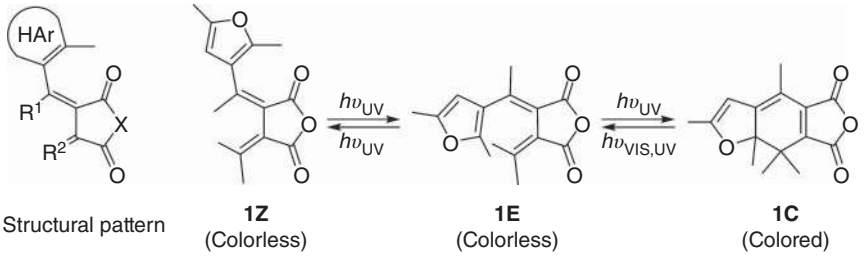


**Figure 9.1** Left: Substituent pattern for fulgides (X = O) and fulgimides (X = NR) as described in the text. HAr denotes a heteroaryl group. Right: Thermally stable *C*-, *E*-, and *Z*-isomers (**1C**, **1E**, and **1Z**) and photoisomerization reactions for the prototypical furylfulgide **1** with methyl and isopropylidene groups as $R^1$ and $R^2$.

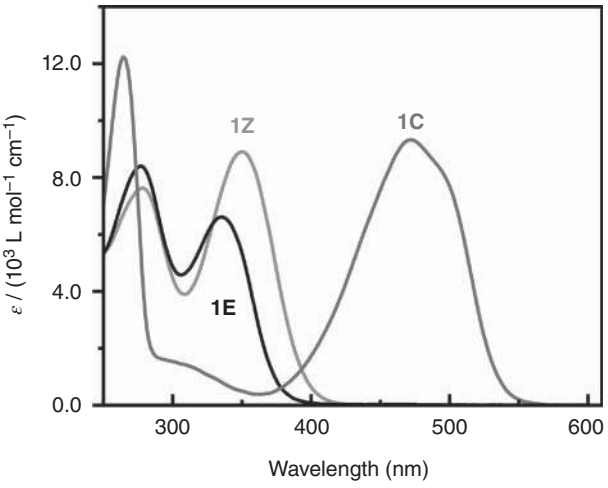


**Figure 9.2** UV/vis absorption spectra of the open *E*- and *Z*-isomers and the closed *C*-isomer (black, light, and dark gray lines, respectively) of furylfulgide **1**.

especially the quantum yields for the ring-opening reaction $\Phi_{CE}$ by irradiation at visible wavelengths are usually unsatisfying. For example, furylfulgide **1C** has a quantum yield of only $\Phi_{CE} = 0.1$, and even lower values of 0.01–0.05 are found for indolyl-derivatives [3, 12–14], a problem shared with many diarylethenes [6]. Furthermore, the competing isomerization to the noncyclizable isomer happens with similar efficiency as the desired ring closure in some cases [3, 5, 12, 13]. These issues have been targeted by substantial synthetic work.

An important aspect affecting the photoswitching behavior of fulgides and fulgimides is the equilibrium between the $E_\alpha$ and $E_\beta$ conformers [15]. Whereas the HT backbone of the $E_\alpha$ conformer has a cisoid conformation suitable for cyclization, the transoid $E_\beta$ conformer cannot undergo electrocyclic ring closure, see Figure 9.3. Shifting the conformer equilibrium toward the cyclizable $E_\alpha$ form by structural modifications thus proved a viable strategy to improve the ring-closure efficiency [13, 16]. Due to the sterical repulsion of the substituents at the HT backbone, both conformers adopt left- (*M*) or right-helical (*P*) chiral forms. As sketched in Figure 9.3, thermal equilibrium between the conformers (vertical arrows) proceeds by diastereotopomerization, a simultaneous change in helicity and conformation involving only a small energy barrier. Enantiotopomerization, i.e. the change in helicity only (horizontal arrows), is sterically hindered by the substituents at both ends of the HT backbone. Due to the lesser steric demands, only the conversion between the two $E_\beta$ enantiomers is feasible and has been observed by NMR spectroscopy with an activation barrier of 53 kJ mol$^{-1}$ [15]. The interconversion of the $E_\alpha$ conformers proceeds as a three-step process involving two diastereotopomerizations.

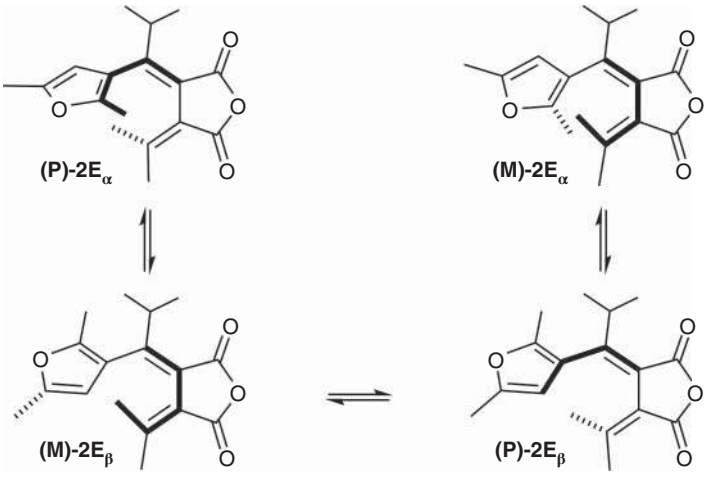


**Figure 9.3** Thermal conformer equilibria for the $E_\alpha$ and $E_\beta$ conformers of the isopropyl-furylfulgide **2**. Both conformers exist as left- (*M*) and right-helical (*P*) chiral forms. Direct enantiotopomerization (horizontal arrows) occurs only for the $E_\beta$ conformers. The vertical arrows indicate diastereotopomerization (see text).

## 9.3 Synthesis

The synthesis of fulgides and fulgimides usually follows the established route via double Stobbe condensation [3, 4, 10, 13] as depicted schematically in Figure 9.4.

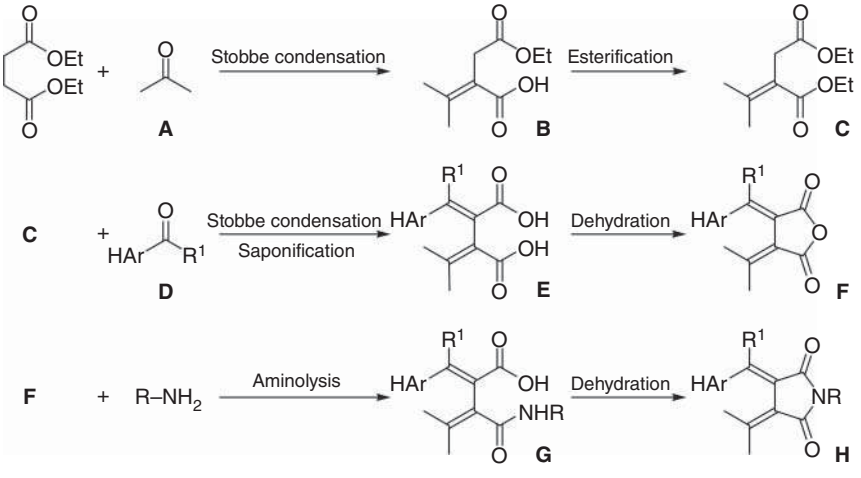


**Figure 9.4** Synthesis of fulgides **F** via double Stobbe condensation. Aminolysis and subsequent dehydration furnishes the corresponding fulgimides **H**.

For derivatives with sterically demanding substituents, a Pd-catalyzed route has also been adopted [17]. In the first Stobbe condensation, succinic acid diethylester reacts with ketone **A** under basic conditions to form the 2-alkylidene-succinic half-ester **B**, followed by esterification to the diester **C**. The heteroaryl group is introduced in the second Stobbe condensation with **C** and a heteroaromatic ketone **D** as reactants, again under basic conditions [3, 4, 13]. Depending on the reaction conditions, this yields lactones or half-esters as intermediates that are usually saponified *in situ* to a mixture of *E*- and *Z*-isomers of the diacid **E** (only one isomer is shown in Figure 9.4 for clarity). The step can be considered a bottleneck in the synthesis of fulgides, as yields are often unsatisfactory, although better results have been obtained using potassium hexamethyldisilazide as base [18, 19]. The fulgides **F** are subsequently obtained via dehydration of the diacids using, e.g. acetic anhydride, acetyl chloride, or *N,N*-dicyclohexylcarbodiimide (DCC) as agents [3, 4, 13]. The onward synthesis of fulgimides **H** usually starts with fulgides as precursor via aminolysis to the succinamic acids **G** and subsequent dehydration [3, 4]. A one-pot microwave-assisted route has been suggested recently as alternative [20]. In addition, the direct synthesis of fulgimides from 2,5-bis(trimethylsiloxy)-1-phenylpyrrole with overall yields exceeding 40% has been reported [21].

## 9.4 Effects of Chemical Structure

Substantial synthetic work has been performed to tune the photoswitching behavior of fulgides and fulgimides with respect to, e.g. photochemical fatigue, isomerization quantum yields, spectral properties, or the switching in solid or aqueous environments. Different optimization strategies were followed, leading to the identification of clear structure–property correlations [3–5].

Increased steric demands by bulky $R^1$ substituents resulted in a significant increase of the ring closure quantum yields and effective suppression of the unwanted *E*–*Z* side reaction, e.g. from $\Phi_{EC} = 0.23$ and $\Phi_{EZ} = 0.13$ for the methyl-substituted compound **1** to $\Phi_{EC} = 0.58$ and $\Phi_{EZ} \approx 0.0$ for the isopropyl-fulgide **2**. Hardly any effect on the ring-opening quantum yields was observed [3, 13, 22]. Subsequent density functional theory (DFT) calculations suggested that this behavior is due to almost quantitative shifts toward the cyclizable $E_\alpha$ conformer in thermal equilibrium for **2E**. Hence, an intramolecular bridge was introduced as a new structural element that provides effective steric constraints and simultaneously fixes the conformation to the cyclizable $E_\alpha$ rotamer [13, 16]. Conversely, larger sterical hindrance at $R^2$, e.g. via an adamantylidene group, resulted in more efficient ring opening but lowered the ring-closure quantum yield [22]. Combining steric constraints at both positions had the desired effect of higher quantum yields in both directions, but also increased the ring-opening quantum yield in the UV, hampering effective conversion from the *E*-form to the *C*-isomer [22].

The variation of the heteroaromatic π-system had effects on absorption properties, quantum yields, as well as photochemical fatigue. Electron-rich heteroaryl substituents such as indolyl groups caused favorable bathochromic shifts of the absorption bands that enabled bidirectional switching purely by visible light, and simultaneously increased photochemical stability considerably (≈ 30 times for indolyl compared to furyl derivatives [4, 23, 24]). On the downside, however, photoisomerization quantum yields were lower in both directions [3, 23]. Further improvements in terms of photochemical fatigue and thermal stability could be achieved in indolyl derivatives with an electron-withdrawing $CF_3$-group at the $R^1$ position [14, 23, 24]. While similar bathochromic shifts were also observed for other heteroaromatic systems [3, 4], the distinct changes for the ring-opening reaction depending on the specific choice of the heteroaromatic moiety point to changes of the excited-state isomerization pathways [5]. Finally, the susceptibility of fulgides to hydrolysis of the anhydride moieties was found to be reduced considerably for fulgimides, which show otherwise unchanged photochemical and photochromic properties and offer an additional reaction site for functionalization at the N-atom of the imide group [3, 4, 25]. This has been exploited for the synthesis of aqueous soluble indolylfulgimides that can be switched purely by visible light and are suitable for biomedical applications [26, 27].

## 9.5 Ultrafast Photoswitching Dynamics

The 6π-electrocyclic nature of the ring-closure and -opening reactions of fulgides was first inferred from the presence of naphthalene derivatives formed by dehydrogenation of the initial photoproducts [28], and later confirmed to occur in accordance with the Woodward–Hoffmann rules for pericyclic reactions [29] using $^1$H-NMR spectroscopy [30]. However, a detailed knowledge of the mechanism and underlying photo-induced processes on the time scale of the photoisomerization reactions is of crucial importance from a fundamental viewpoint and regarding the rational design of new fulgide switches. It is now widely recognized that the molecular dynamics of many photo-initiated reactions happens on the ultrafast time scale from femto- to picoseconds, with conical intersections (CIs) acting as photochemical funnels between different electronic states [31, 32]. Consequently, a thorough understanding of the photoisomerization reactions of fulgides and fulgimides has been achieved employing ultrafast spectroscopical techniques and quantum chemical calculations [5, 16, 33–56].

### 9.5.1 Photoisomerization Mechanism

The photo-induced ring opening of fulgides and fulgimides has been studied extensively for indolyl, furyl, and benzofuryl derivatives [5, 34–48]. The structures of the most-studied indolyl compounds are given in Figure 9.5.

For compound **4C**, transient absorption spectroscopy with visible and mid-IR detection and broadband fluorescence experiments indicated multiexponential

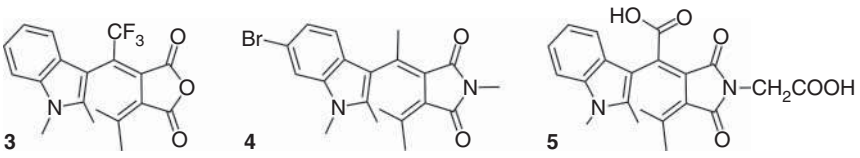


**Figure 9.5** Indolylfulgides and indolylfulgimides studied by ultrafast spectroscopy.

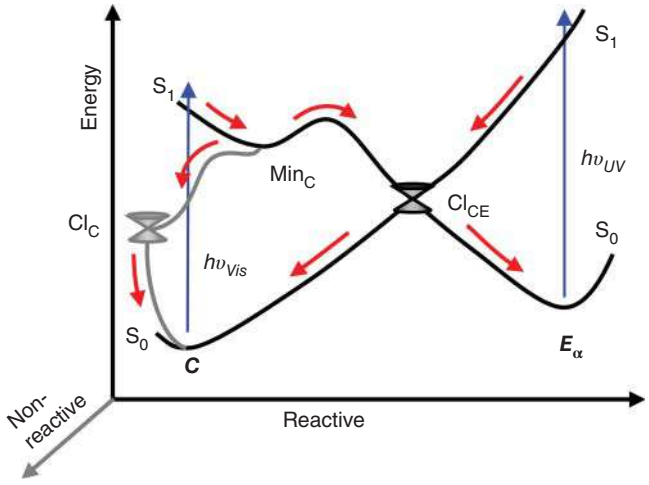


**Figure 9.6** Schematic sketch of the pathways for the ring-opening and -closure reactions of the *C*-isomers and $E_\alpha$ conformers [45, 52, 57, 58]. The conical intersections (CI) are indicated by double cones. The reactive pathways lie in the drawing plane, the non-reactive pathway leading only to electronic deactivation of the *C*-isomer is sketched in gray to emphasize its location outside the drawing plane.

molecular dynamics, comprising a sub-picosecond component and two slower components of ≈2 and 15–20 ps [34–36]. In analogy to the CHD/HT system, the results were first interpreted in favor of a very fast internal conversion from the initially excited $S_2(1B_2)$ electronic state to an optically dark, covalent $S_1(2A_1)$ state as first step, and subsequent isomerization and deactivation to the electronic ground states of the ring-opened *E*-isomer product and *C*-isomer reactant from there. The reaction was assumed to be slowed down to ≈2 ps by an energy barrier in the $S_1$ excited state, and to conclude with vibrational relaxation in the electronic ground states described by the slowest time constant [36, 37].

This interpretation has been questioned more recently [45, 52, 57, 58]. Accordingly, the $S_1$ state is optically bright and zwitterionic. Excitation of the *C*-isomers in the visible populates this state directly and involves charge transfer from the heteroaromatic ring to the anhydride moiety. The scenario is depicted in Figure 9.6.

Upon excitation, the *C*-isomer evolves quickly from the Franck–Condon (FC) region to an excited-state energy minimum ($Min_C$). From there, two pathways both involving an excited-state energy barrier are possible. Whereas the non-reactive pathway via $CI_C$ (sketched in gray) leads only back to the *C*-isomer, the reactive

pathway via $CI_{CE}$ affects both isomerization to the $E_\alpha$ conformer and electronic deactivation. The fast sub-picosecond time constant is interpreted as initial dynamics in the vicinity of the FC region going along with vibrational relaxation and/or solvent reorganization processes [43–45, 47]. The energy barriers for the excited-state processes explain the observed slower time scale (2–15 ps, depending on conditions) of the ring-opening and electronic deactivation processes. The scenario also rationalizes the faster excited-state decay and increased ring-opening quantum yields observed at higher temperatures [38, 39], upon excitation to higher excited electronic states, with optical excess energy [42, 46], or directly after a preceding UV-initiated ring closure [38, 39, 41]. The strongly polar properties of the $S_1$ excited state also explain the observed red-shift of the $S_1$ absorption band in polar solvents, as well as the decrease in quantum yields and slowing down of the ring-opening dynamics in polar aprotic environments [39, 43, 49]. The unusual dynamics for derivative **5** in the protic solvent water was ascribed to the opening of an additional deactivation pathway involving excited-state proton transfer [44]. Further, it could be shown that the ring opening is promoted by low-frequency molecular vibrational modes driving the dynamics along the ring-opening reaction coordinate, with coherent oscillations in the transient absorption signals as a direct signature that has been observed in several cases [39, 40, 43, 44, 47]. Finally, an additional efficient reactive pathway has been invoked to explain the significant increase of the ring-opening quantum yields after excitation into a higher-lying electronic state $S_n$ by two successive femtosecond pulses or by stepwise two-photon absorption using longer (15 ps) laser pulses [46, 48].

In contrast to the ring opening, the photo-induced *E–C* ring closure has turned out to be a robust, non-activated, barrierless excited-state process that occurs typically within less than a picosecond, irrespective of temperature, solvents, or optical excess energy [37, 40, 44, 45, 49, 50, 52]. Subsequent results clearly disapproved the complex reaction scheme suggested on the basis of the very first measurements [33] and were initially interpreted as sequential electronic deactivation according to the HT/CHD case. It was assumed that the ring-closure and ring-opening reactions proceed via two distinct CIs to explain the strong differences in the time-resolved emission spectra for both directions [36, 37, 49]. This interpretation has been superseded as sketched in Figure 9.6: ring closure happens in the zwitterionic $S_1$ excited state on a barrierless pathway via a common CI [45, 52, 54, 58].

An important aspect in the photochemistry of fulgides with considerable impact regarding applications is the possible competition between the desired ring closure and the unwanted *E–Z* photoisomerization, which occur with comparable quantum yields upon excitation of isomer **1E** [12, 13]. Results from transient electronic absorption spectroscopy and calculations by time-dependent density functional theory indicated that both reactions indeed occur in parallel on the sub-picosecond time scale via distinct excited-state pathways and suggested conformer-specific photochemistry in the excited state. Based on the time scale and the calculations, the *E–Z* photoisomerization was established as a barrierless, direct photoreaction proceeding via a CI between the $S_1$ and $S_0$ electronic states on a rotational pathway [52].

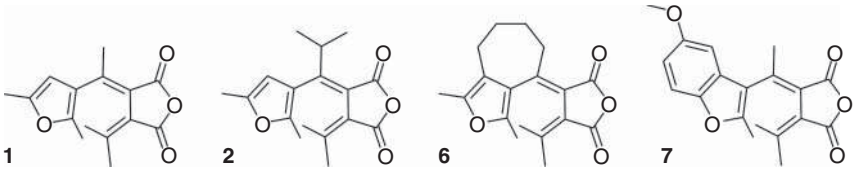


**Figure 9.7** Furyl- and benzofurylfulgides studied by ultrafast spectroscopy.

The reverse *Z*–*E* photoisomerization has been studied much less [5, 51, 53], even though it is important to restore optical bistability by preventing the photochemical accumulation of the *Z*-isomer. Results for several derivatives (see Figure 9.7) gave time constants in the range of $\tau = 0.18-0.32$ ps indicating barrierless excited-state pathways that involve a CI halfway along the carbon double-bond torsion as reaction coordinate according to calculations [55].

### 9.5.2 Tuning by Chemical Structure

A detailed understanding of the effects of chemical modifications on the mechanistic level is highly relevant for the rational design of new fulgide compounds, and has been targeted in recent comparative studies of the ultrafast photo-induced processes in fulgides with selected structural motifs [5, 16, 47, 51–56]. Both photochromic reactions and the interconversion between the two open isomers were investigated by ultrafast spectroscopy and detailed *ab initio* calculations.

The chosen derivatives (see Figure 9.7) allowed to address the effects of varied steric hindrance at the central position of the HT unit ($R^1$), as well as the influence of an extended aromatic π-system. Excitation of the closed isomers revealed very similar transient absorption changes for the furylfulgides **1C**, **2C**, and **6C**, indicating that steric modifications are without much effect on the ring opening. The observed fast excited-state dynamics in these cases could be described by two sub-picosecond time constants of $\tau_1 = 0.39-0.57$ ps and $\tau_2 = 0.66-0.92$ ps. The corresponding partial recovery of the reactant bleach and the rise of *E*-isomer product absorption within the first picosecond suggested that the slower component is related to the isomerization and electronic deactivation. In contrast, benzannulation at the furyl moiety in compound **7C** caused an excited-state decay requiring two much slower components of $\tau_2 = 4.7$ ps and $\tau_3 = 17.4$ ps, i.e. complete deactivation took ≈25 times longer. The results could be interpreted consistently according to the scenario sketched in Figure 9.6, where the observed fast dynamics suggested only small excited-state energy barriers for the furyl derivatives. Conversely, the drastic changes upon benzannulation indicated that the extended π-system leads to increased excited-state energy barriers, presumably via stabilization of the excited-state minimum $Min_C$. Moreover, the recovery of the reactant bleach with the same two time constants as for the excited-state decay provided experimental evidence for the proposed dual electronic deactivation pathways [47]. Finally, weak oscillations in the transient absorption signals were consistent with a mode-specific ring-closure reaction [43, 45].

The results for the photo-excited *E*-isomers allowed detailed insight into the conformer-specific photochemistry and the factors affecting the *E*–*C* ring closure and the *E*–*Z* isomerization reactions. In particular, furylfulgide **6** permitted to single out the photochemistry of the cyclizable $E_\alpha$ conformer, as its conformation is fixed by the intramolecular bridge. The sterically less hindered derivative **1** has similar molar fractions of $x_\alpha = 0.66$ and $x_\beta = 0.34$ for the $E_\alpha$ and $E_\beta$ conformers in thermal equilibrium and thus constituted an ideal model system to study the excited-state reaction pathways for both conformers, as well as the competition between the ring closure and the *E*–*Z* isomerization reactions.

The data proved unambiguously that the sterically less congested compounds **1E** and **7E** both undergo parallel sub-picosecond *E*–*C* and *E*–*Z* photoisomerization reactions with respective time constants of ≈0.12 and ≈0.34 ps that are apparently not much affected by the electronic modification. In contrast, the sterically constrained derivatives **2E** and **6E** reacted virtually exclusively to the *C*-isomer with high quantum yields, within only ≈50 fs. The respective time scales suggest barrierless excited-state pathways in all cases, as sketched in Figure 9.6 and as generally accepted for *E*–*Z* isomerizations [16, 31, 54, 56, 58, 59]. The results gave clear evidence for conformer-specific photoreactions, with ring closure exclusively by the $E_\alpha$ conformer and *E*–*Z* isomerization predominantly by the $E_\beta$ conformer. The situation emerging from detailed analysis complemented by quantum chemical calculations and large-scale computational simulations of the photodynamics [54, 56] is sketched in Figure 9.8.

Increased sterical hindrance was found to induce a favorable twisted pre-orientation of the furyl unit in the $E_\alpha$ conformer that leads to a decisively accelerated, extremely fast, and efficient conrotatory ring closure as main reaction path. The $E_\alpha$–*Z* channel was assigned as a minor channel that is unfavored by kinetic competition with the faster $E_\alpha$–*C* reaction and appears to be slowed down by excited-state energy barriers and kinematic effects by heavier substituents. The $E_\beta$ conformer cannot undergo ring closure. Finally, a non-reactive pathway for electronic deactivation via degenerate *E*–*Z* isomerization at the isopropylenic double bond was shown [54, 56].

The comparison for the photo-excited *Z*-isomer derivatives gave clear evidence that the *Z*–*E* photoisomerization reaction is not affected by the given structural motifs (cf. Figure 9.7) and happens within only 0.2–0.4 ps on a barrierless excited-state pathway [5, 51, 53, 55]. In line with the mechanism described in

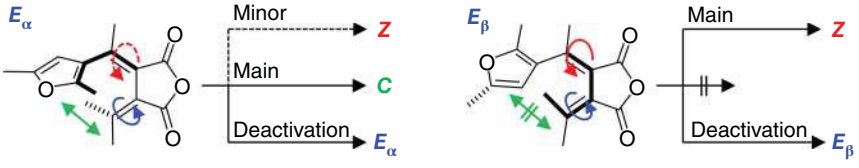


**Figure 9.8** Possible photoreactions of the $E_\alpha$ (left) and the $E_\beta$ conformers (right). For the $E_\alpha$ conformer, the *E*–*Z* pathway is disfavored. The $E_\beta$ conformer cannot undergo ring closure. Degenerate isomerization of the *exo*-isopropylidene group is a pathway for non-reactive electronic deactivation in both cases.

Section 9.5.1, the negligible effects of the selected chemical modifications on the photoisomerization were explained by torsion about the isomerizing carbon double bond as relevant coordinate, which should not be sterically hindered according to the equilibrium structures of the *Z*-isomers [13].

### 9.5.3 Implications for New Derivatives

The comprehensive results summarized above provide detailed knowledge on the photo-induced processes and molecular dynamics of fulgide and fulgimide photoswitches. In accordance with the Woodward–Hoffmann rules [29], the ring closure and opening of the central HT and CHD units happen as 6π-electrocyclic conrotatory reactions. However, unlike the HT/CHD system, photo-excitation involves charge transfer and is governed by a zwitterionic first excited electronic state. This distinguishes fulgides and fulgimides from the related diarylethenes (where a covalent $S_1(2A_1)$ state as in HT/CHD is relevant [7, 32]) and may explain their greater fatigue resistance in polar environments [60]. Increased steric hindrance at the HT unit and electronic modifications of the heteroaryl group were found to affect the ring-closure and ring-opening reactions independently, so that both may be used as orthogonal inputs for selective improvements. The advantageous effects of steric modifications on the ring closure are a combination of favorable shifts in the conformer equilibrium and a kinetic preference of the ring closure over the *E*–*Z* reaction. This suggests intramolecular bridging and heavier rather than just bulkier substituents at the $R^1$ position as viable extension of established strategies for structural optimization [3, 5]. For the ring-opening reaction, benzannulated heteroaromatic groups (as in the popular indolyl-derivatives) are probably a mixed blessing, in that positive effects like bathochromic shifts have to be balanced against potentially unfavorable changes of the excited-state pathways. Nevertheless, the potential for improvements of the ring-opening reaction by optimization of the heteroaryl unit is considerable, in particular regarding electron-donating and -withdrawing substituents. Furthermore, prevention of the so far neglected detrimental electronic deactivation by degenerate *E*–*Z* photoisomerization of the *exo*-isopropylidene group, e.g. by intramolecular bridging, should help to enhance the quantum yields of both desired photoreactions. Finally, the mode-specific nature of the ring opening suggests structural modifications targeting the relevant vibrational modes as new approach for improved ring-opening efficiency.

## 9.6 Application Examples

Fulgides and fulgimides have been employed as molecular functional units in a wide range of applications, including photo-responsive materials, films, and surfaces [61, 62], photoswitching of fluorescence or energy transfer, or molecular information processing [63, 64]. A long-standing research focus has been the development of optical memory devices [3, 4]. For example, Rentzepis and co-workers succeeded in the design of an optical storage device with non-destructive readout based on a

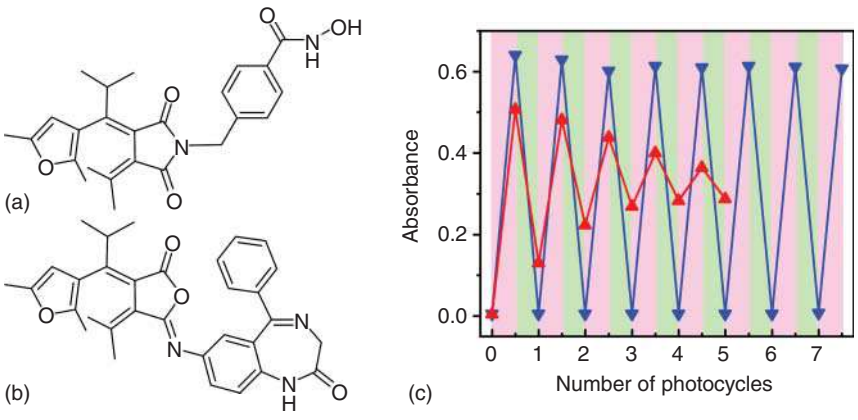


**Figure 9.9** (a) Fulgimide-based HDAC-inhibitor. (b) Fulgazepam for photocontrol of GABA receptors. (c) Switching performance over repeated photocycles using alternating irradiation with UV (pink shading) and visible light (green shading) for HDAC inhibitors functionalized with fulgimides (blue) or diarylethenes (red). Source: Modified from Wutz et al. [69].

photoswitchable dyad consisting of a fluorescing benzophenoxazine dye covalently attached to a fulgimide [65].

An emerging use of photoswitches is the control of biologically relevant systems such as peptides, nucleic acids, or receptors by light for application in optogenetics and photopharmacology [66–68]. Fulgimides have recently turned out as attractive alternatives to azobenzenes and diarylethenes in this context, as they combine thermal irreversibility and high conversion yields with superior solubility and photochemical stability in polar and aqueous environments [27, 69, 70]. Photoswitchable inhibition of histone deacetylase (HDAC) was achieved using fulgimides functionalized with aromatic hydroxamic acids for binding to the HDAC (see Figure 9.9a). Unlike the fulgimides, the corresponding dithienylethene derivatives showed significant photochemical degradation after only few photoswitching cycles due to the irreversible formation of the non-photochromic dyotropic byproduct upon UV irradiation (see Figure 9.9b) [60, 69].

Very recently, fulgimide benzodiazepine derivatives such as those displayed in Figure 9.9c have been designed and successfully applied *in vivo* for the photocontrol of γ-butyric acid (GABA) receptors. By comparison with an azobenzenenitrazepam analogue, the fulgimide compound showed no toxicity, displayed an ideal photopharmacological profile by acting as a pure potentiator in its closed form, and allowed for complete thermally irreversible photoswitching [70]. Fulgides and fulgimides thus clearly continue to be indispensable photoswitches.

## 9.7 Conclusions

The photoswitching properties of fulgides and fulgimides clearly rival those of diarylethenes, both sharing a strong, thermally irreversible photochromism and

outstanding photostability based on electrocyclic ring opening and closure photoreactions. Regardless, diarylethenes are arguably more popular, and this is probably related to the challenging synthesis of fulgides and fulgimides. On the other hand, emerging applications of fulgimide switches, e.g. in the context of photopharmacology, have witnessed their superior behavior in polar and aqueous environments and emphasized the need for new and improved fulgide-type compounds. For this purpose, recent results from ultrafast spectroscopy and theory gain importance: Knowledge of the underlying reaction mechanisms and the effects of structural modifications provides guidelines for a rational design of improved derivatives and suggests new approaches for tuning the photochemical properties. This may enable photochemists to use the known structure–property relations to full capacity for the future development of fulgides and fulgimides and their applications.

## References


1 Feringa, B.L. and Browne, W.R. (eds.) (2011). *Molecular Switches*, 2e. Weinheim: Wiley-VCH.
2 Fan, M.-G., Yu, L., and Zhao, W. (2002). Fulgide Family Compounds: Synthesis, Photochromism, and Applications. In: *Organic Photochromic and Thermochromic Compounds: Volume 1: Main Photochromic Families* (eds. J.C. Crano and R.J. Guglielmetti), 141–206. US: Springer.
3 Yokoyama, Y. (2000). *Chem. Rev.* 100: 1717–1740.
4 Rück-Braun, K., Mayer, K., Hebert, A., and Michalik, F. (2012). Fulgimides. In: *CRC Handbook of Organic Photochemistry and Photobiology*, , ch. 25, 3e, vol. 1 (eds. A. Griesbeck, M. Oelgemöller and F. Ghetti), 607–626. CRC Press.
5 Renth, F., Siewertsen, R., and Temps, F. (2013). *Int. Rev. Phys. Chem.* 32: 1–38.
6 Irie, M. (2000). *Chem. Rev.* 100: 1685–1716.
7 Irie, M., Fukaminato, T., Matsuda, K., and Kobatake, S. (2014). *Chem. Rev.* 114: 12174–12277.
8 Koshima, H., Nakaya, H., Uchimoto, H., and Ojima, N. (2012). *Chem. Lett.* 41: 107–109.
9 Harada, J., Taira, M., and Ogawa, K. (2017). *Cryst. Growth Des.* 17: 2682–2687.
10 Stobbe, H. (1905). *Ber. Dtsch. Chem. Ges.* 38: 3673–3682.
11 Heller, H.G. and Oliver, S. (1981). *J. Chem. Soc. Perkin Trans. 1*: 197–201.
12 Uhlmann, E. and Gauglitz, G. (1996). *J. Photochem. Photobiol. A* 98: 45–49.
13 Strübe, F., Siewertsen, R., Sönnichsen, F.D. et al. (2011). *Eur. J. Org. Chem.*: 1947–1955.
14 Reinfelds, M., Hermanns, V., Halbritter, T. et al. (2019). *ChemPhotoChem* 3: 441–449.
15 Yokoyama, Y., Ogawa, K., Iwai, T. et al. (1996). *Bull. Chem. Soc. Jpn.* 69: 1605–1612.
16 Siewertsen, R., Strübe, F., Mattay, J. et al. (2011). *Phys. Chem. Chem. Phys.* 13: 3800–3808.
17 Kiji, J., Okano, T., Kitamura, H. et al. (1995). *Bull. Chem. Soc. Jpn.* 68: 616–619.


**18** Zarwell, S., Dietrich, S., Schulz, C. et al. (2009). *Eur. J. Org. Chem.*: 2088–2095.

**19** Lv, N.N., Sang, A.G., and Zhang, Y. (2013). *Adv. Mater. Res.* 821–822: 522–526.

**20** Lee, W.-W.W., Gan, L.-M., and Loh, T.-P. (2007). *J. Photochem. Photobiol. A* 185: 106–109.

**21** Zerrer, R. and Simchen, G. (1992). *Synthesis*: 922–924.

**22** Yokoyama, Y., Inoue, T., Yokoyama, M. et al. (1994). *Bull. Chem. Soc. Jpn.* 67: 3297–3303.

**23** Wolak, M.A., Thomas, C.J., Gillespie, N.B. et al. (2003). *J. Org. Chem.* 68: 319–326.

**24** Islamova, N.I., Chen, X., Garcia, S.P. et al. (2008). *J. Photochem. Photobiol. A* 195: 228–234.

**25** Matsushima, R. and Sakaguchi, H. (1997). *J. Photochem. Photobiol. A* 108: 239–245.

**26** Chen, X., Islamova, N.I., Garcia, S.P. et al. (2009). *J. Org. Chem.* 74: 6777–6783.

**27** Lachmann, D., Lahmy, R., and König, B. (2019). *Eur. J. Org. Chem.*: 5018–5024.

**28** Santiago, A. and Becker, R.S. (1968). *J. Am. Chem. Soc.* 90: 3654–3658.

**29** Woodward, R.B. and Hoffmann, R. (1969). *Angew. Chem. Int. Ed. Engl.* 8: 781–853.

**30** Darcy, P.J., Heller, H.G., Strydom, P.J., and Whittall, J. (1981). *J. Chem. Soc. Perkin Trans. 1*: 202–205.

**31** Matsika, S. and Krause, P. (2011). *Annu. Rev. Phys. Chem.* 62: 621–643.

**32** Kumpulainen, T., Lang, B., Rosspeintner, A., and Vauthey, E. (2017). *Chem. Rev.* 117: 10826–10939.

**33** Handschuh, M., Seibold, M., Port, H., and Wolf, H.C. (1997). *J. Phys. Chem. A* 101: 502–506.

**34** Malkmus, S., Koller, F., Heinz, B. et al. (2006). *Chem. Phys. Lett.* 417: 266–271.

**35** Koller, F.O., Schreier, W.J., Schrader, T.E. et al. (2006). *J. Phys. Chem. A* 110: 12769–12776.

**36** Heinz, B., Malkmus, S., Laimgruber, S. et al. (2007). *J. Am. Chem. Soc.* 129: 8577–8584.

**37** Draxler, S., Brust, T., Malkmus, S. et al. (2008). *J. Mol. Liq.* 141: 130–136.

**38** Draxler, S., Brust, T., Malkmus, S. et al. (2009). *Phys. Chem. Chem. Phys.* 11: 5019–5027.

**39** Brust, T., Malkmus, S., Draxler, S. et al. (2009). *J. Photochem. Photobiol. A* 207: 209–216.

**40** Brust, T., Draxler, S., Popp, A. et al. (2009). *Chem. Phys. Lett.* 477: 298–303.

**41** Brust, T., Draxler, S., Eicher, J. et al. (2010). *Chem. Phys. Lett.* 489: 175–180.

**42** Cordes, T., Malkmus, S., DiGirolamo, J.A. et al. (2008). *J. Phys. Chem. A* 112: 13364–13371.

**43** Slavov, C., Bellakbil, N., Wahl, J. et al. (2015). *Phys. Chem. Chem. Phys.* 17: 14045–14053.

**44** Slavov, C., Boumrifak, C., Hammer, C.A. et al. (2016). *Phys. Chem. Chem. Phys.* 18: 10289–10296.

**45** Nenov, A., Schreier, W.J., Koller, F.O. et al. (2012). *J. Phys. Chem. A* 116: 10518–10528.


**46** Ishibashi, Y., Katayama, T., Ota, C. et al. (2009). *New J. Chem.* 33: 1409–1419.
**47** Siewertsen, R., Strübe, F., Mattay, J. et al. (2011). *Phys. Chem. Chem. Phys.* 13: 15699–15707.
**48** Nagasaka, T., Sotome, H., Yoshida, Y. et al. (2018). *J. Phys. Chem. C* 122: 24987–24995.
**49** Koller, F.O., Schreier, W.J., Schrader, T.E. et al. (2008). *J. Phys. Chem. A* 112: 210–214.
**50** Cordes, T., Herzog, T.T., Malkmus, S. et al. (2009). *Photochem. Photobiol. Sci.* 8: 528–534.
**51** Renth, F., Foca, M., Petter, A., and Temps, F. (2006). *Chem. Phys. Lett.* 428: 62–67.
**52** Siewertsen, R., Renth, F., Temps, F., and Sönnichsen, F. (2009). *Phys. Chem. Chem. Phys.* 11: 5952–5961.
**53** Renth, F., Siewertsen, R., Strübe, F. et al. (2014). *Phys. Chem. Chem. Phys.* 16: 19556–19563.
**54** Schönborn, J.B., Koslowski, A., Thiel, W., and Hartke, B. (2012). *Phys. Chem. Chem. Phys.* 14: 12193–12201.
**55** Schönborn, J.B. and Hartke, B. (2013). *J. Photochem. Photobiol. A* 263: 34–40.
**56** Schönborn, J.B. and Hartke, B. (2014). *Phys. Chem. Chem. Phys.* 16: 2483–2490.
**57** Schönborn, J.B., Sielk, J., and Hartke, B. (2010). *J. Phys. Chem. A* 114: 4036–4044.
**58** Tomasello, G., Bearpark, M.J., Robb, M.A. et al. (2010). *Angew. Chem. Int. Ed.* 49: 2913–2916.
**59** Levine, B.G. and Martìnez, T.J. (2007). *Annu. Rev. Phys. Chem.* 58: 613–634.
**60** Mendive-Tapia, D., Perrier, A., Bearpark, M.J. et al. (2014). *Phys. Chem. Chem. Phys.* 16: 18463–18471.
**61** Hänsel, M., Barta, C., Rietze, C. et al. (2018). *J. Phys. Chem. C* 122: 25555–25564.
**62** Klaes, S., Henry-de-Villeneuve, C., Ozanam, F. et al. (2019). *J. Phys. Chem. C* 123: 12223–12233.
**63** Cusido, J., Deniz, E., and Raymo, F.M. (2009). *Eur. J. Org. Chem.*: 2031–2045.
**64** Pischel, U., Andréasson, J., Gust, D., and Pais, V.F. (2013). *ChemPhysChem* 14: 28–46.
**65** Dvornikov, A.S., Walker, E.P., and Rentzepis, P.M. (2009). *J. Phys. Chem. A* 113: 13633–13644.
**66** Szymanski, W., Beierle, J.M., Kistemaker, H.A.V. et al. (2013). *Chem. Rev.* 113: 6114–6178.
**67** Lerch, M.M., Hansen, M.J., van Dam, G.M. et al. (2016). *Angew. Chem. Int. Ed.* 55: 10978–10999.
**68** Hüll, K., Morstein, J., and Trauner, D. (2018). *Chem. Rev.* 118: 10710–10747.
**69** Wutz, D., Gluhacevic, D., Chakrabarti, A. et al. (2017). *Org. Biomol. Chem.* 15: 4882–4896.
**70** Rustler, K., Maleeva, G., Gomila, A.M.J. et al. (2020). *Chem. Eur. J.* 26: 12722–12727.


# 10 The Negative Photochromism of Dimethyldihydropyrene π-Switches

Subhajit Bandyopadhyay

**Photoisomerization**

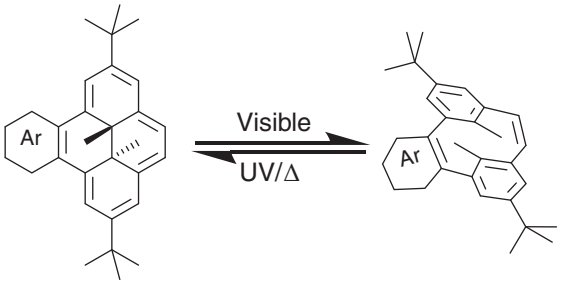


**Characteristic Features**

The dimethyldihydropyrene photoswitch is a T-type, negative photochromic system, which served primarily as a probe for aromaticity. However, its applications as a photoswitch has gained considerable attention in recent times because of the developments of novel analogs of the photochromic system with superior switching ability that can also be addressed by electrochemical stimuli.

**First Reported**

Blattmann, H. R., Meuche, D., Heilbronner, E. et al. (1965). Photoisomerization of *trans*-15,16- dimethyldihydropyrene. *J. Am. Chem. Soc*. 87 (1): 130–131.

Boekelheide, V. and Phillips, J.B. (1967). Aromatic molecules bearing substituents within the cavity of the π-electron cloud. Synthesis of *trans*-15,16-Dimethyldihydropyrene. *J. Am. Chem. Soc*. 89 (7): 1695–1704.

**Key References**

Mitchell, R.H. (2001). Measuring aromaticity by NMR. *Chem. Rev*. 101 (5): 1301–1316.

Mitchell, R.H. (1999). The metacyclophanediene-dihydropyrene photochromic π switch. *Eur. J. Org. Chem*. 1999: 2695–2703.

Sheepwash, M.A.L., Ward, T.L., Wang, Y. et al. (2002) Mechanistic studies on the photochromism of [e]-annulated dimethyldihydropyrenes. *Photochem. Photobiol. Sci*. 2: 104–112.

Andréasson, J., Kodis, G., Terazono, Y. et al. (2004). Molecule-based photonically switched half-adder. *J. Am. Chem. Soc*. 126 (49): 15926–15927.

Ghosh, S., Hossain, M.S., Chatterjee, S. et al. (2020). Light-gated modulation of electronic mobility of a dihydropyrene-based photochromic coordination polymer. *ACS Appl. Mater. Interfaces* 12 (47): 52983–52991.

# 10

# The Negative Photochromism of Dimethyldihydropyrene π-Switches

*Subhajit Bandyopadhyay*

*Department of Chemical Sciences, Indian Institute of Science Education and Research (IISER) Kolkata, Mohanpur, Nadia 741246, India*

## 10.1 The Genesis

Aromaticity has always been a puzzling topic in chemistry. More than half a century ago, some of the most stalwart chemists embarked on addressing a fundamental question of the nature of aromaticity of large Huckel polyene systems. The basic question was if the model of a donut-like π-electronic cloud with a void in the middle portrayed a realistic picture of aromatic systems. This prompted some challenging synthesis of large monocyclic polyenes. The most challenging problem of working with the large monocyclic polyenes was to maintain their planarity. To ensure the planarity, Sondheimer and Nagakawa introduced the rigid acetylenic unit in the polyene systems (**1** and **2**) [1, 2], whereas Boekelheide introduced a stable and saturated bridge in the middle (Figure 10.1) [3]. Thus, Boekelheide's target molecule, 15,16-dimethyldihydropyrene **3** with a 14-annulene scaffold at the periphery held rigidly by a saturated "butane" in its center, did address the problem and validated the model. Soon thereafter, the dihydropyrene (DHP) system (**3**) served as a probe to study the effect of the diatropic ring current on the nuclear magnetic resonance (NMR) chemical shifts. Later Mitchell used the DHP system and developed a quantitative scale for measuring the elusive property of aromaticity from the NMR chemical shifts of the internal methyl group of the DHP derivatives.

## 10.2 DHP as a Probe for Measuring Aromaticity

While this book is primarily focused on photoswitches, it is essential to understand the context of the origin of the DHP system in terms of the other important purpose it served. Over the last few decades, Mitchell has championed establishing a quantitative experimental scale of aromaticity of a number of aromatic systems by measuring the perturbation in the chemical shift of the internal methyl groups of various aromatic ring-fused DHP systems. An excellent review summarizes the results of

*Molecular Photoswitches: Chemistry, Properties, and Applications*,
First Edition. Edited by Zbigniew L. Pianowski.


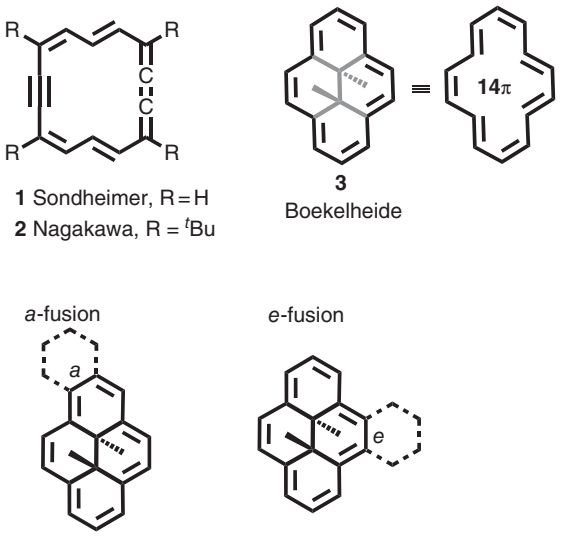


**Figure 10.1** Sondheimer's 14 annulene and Boekeldeide's DHP. Source: Boekelheide et al. [3].

Mitchell's ingenious method and the quantitative measure of aromaticity of a number of aromatic systems and is a recommended reading for the readers [4]. It is also crucial to recall the contribution of Tashiro, who provided a more accessible route to the DHPs through the simplified synthesis of 4,9-*t*-dibutyl-DHP derivatives [5].

Two recent works have been chosen here to demonstrate the estimation of aromaticity using the DHP as the probe. The first one is the aromaticity of the tropylium cation, a non-benzenoid 6π electronic Hückel system. Its structurally related tropone is considered as weakly aromatic or nonaromatic, whereas 1,3,5-cycloheptatriene is known to be a homoaromatic species. To estimate the aromaticity of these species, annelated DHP-fused tropone **4**, fused-cycloheptatriene **5**, and tropylium **6** were synthesized (Figure 10.2). The $^1$H NMR data of these species clearly demonstrated that cycloheptatriene **5** as a neutral homoaromatic species has ∼30% aromatic nature compared with benzene, whereas this number was ∼20% for tropone. On the other hand, the aromaticity of the tropylium ion was found to be ∼50% compared with benzene demonstrating its aromatic nature. These outcomes were supported by the computationally estimated nucleus-independent chemical shift (NICS) values [6]. Recently, Hecht and coworkers have reported that the DHP system can be used to estimate the loss of aromaticity due to the perturbation resulting from the electronic push–pull effect. It was observed that DHP derivative, bearing the dimethylamino and the nitro groups in the pseudo-para orientation, showed a maximum of 12% quinoid character compared with the parent benzenoid 4-nitroaniline [7]. Experimental estimate of the relative aromaticity of the cyclooctatetraene dianion was also studied using dimethyldihydropyrene as the aromaticity probe [8].

## 10.3 DHP as a Photoswitch

Although the DHP system has been used for the quantification of aromaticity, another fascinating feature of the DHP system has been its photochromic

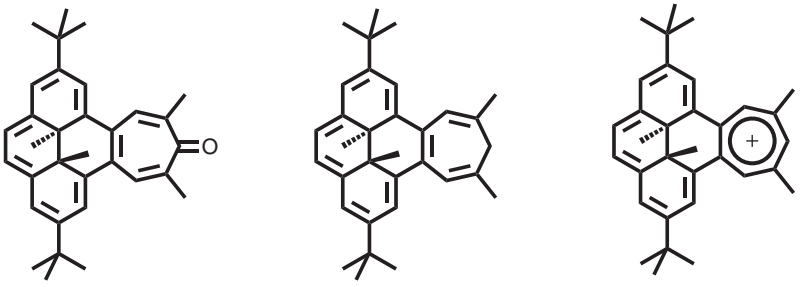


4 5 6

**Figure 10.2** DHP-fused tropone **4**, cycloheptatriene **5**, and tropylium **6**.

properties. In fact, the photochromic nature of the DHP system was apparent when Boekelheide observed that the DHP switched to a colorless form under the visible light [9]. It was realized that DHP, upon exposure to a wide range of light in the visible region, undergoes an electrocyclic ring opening to afford the corresponding *meta*-cyclophanediene (CPD) form. UV light causes a reversal of the CPD form to the original DHP form. The visible-light-induced bleaching/opening reaction for DHP has a quantum yield in the range of 0.015–0.02, and the thermal reversal of the reverse coloration/closing reaction has a first-order rate constant of the order of $k = 0.0010\ \text{min}^{-1}$ at 30 °C. The 2,7-di-*t*-butyl derivative of DHP **7** (R = *t*-butyl) has a quantum yield that is about an order of magnitude lower than the DHP without the *t*-butyl group (**7**, R = H) (Figure 10.3). The thermal reversal rate is also slower for the *t*-butyl analogue. This is because of the effect of the alkyl groups that lead to the non-radiative decay of the photochemically excited DHP from its first excited state [10].

Fusion of an aromatic ring on the DHP has a dramatic effect on the efficiency of the photochromic behavior. The aromatic fusion at the [*e*]-position of the DHP **8** enhances the DHP→CPD switching efficiency and also decreases the thermal reversal of the CPD to the DHP. Fusion in the [*a*]-position (Figure 10.1) has a detrimental effect on the switching efficiency as the thermal reversal pathway of the CPD→DHP becomes more efficient [11].

Naphthalene and anthracene fusion at the [*e*] position are also known, although the shorter synthesis and superior photoswitching of the benzo-[*e*] fused system have made the benzo-fused system a superior candidate as a photoswitch [11, 12]. The dihydrothieno[3.4-*b*]pyrazine fused system underwent a slow CPD to DHP thermal reversal, leading to the formation of an efficient photochromic material [13].

In the subsequent sections, the use of the DHP systems will be discussed for various applications, primarily from recent works. The term "DHP" will be used generally for all the DHP derivatives and their fused analogs.

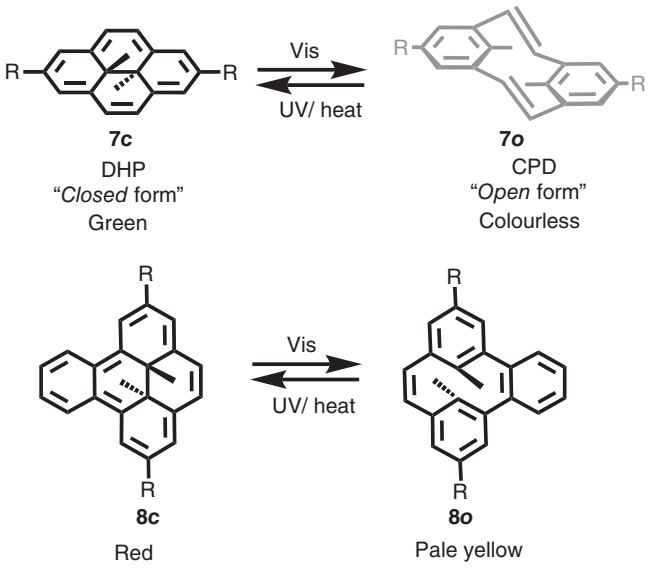


**Figure 10.3** Photoswitching of DHP and the benzo-[*e*]-fused DHP.

## 10.4 DHP as a "π-Switch": Switching of Electrical Conductivity

Photochromic systems offer reversible tunability of the electronic structures using light as the stimuli and do not require any external chemical species as the input. Therefore these systems are coveted for the development of smart materials that are addressable by light. In the DHP, the extended π-system having a delocalized 14π aromatic system is transformed to the step-like CPD form having two discrete 6π electronic phenyl rings as shown in Figure 10.1. Therefore the term "π-switch" has been coined for these systems by Mitchell [11].

The DHP π-switches have been demonstrated to switch conductivity in various systems including in a poly-(DHP-thiophene) **9A** as a conducting polymer (Figure 10.4a) [14]. The difference in electrical conductivity as measured by a positive drain current was different in the open and close forms of the DHP unit. This is one of the examples where a photochromic moiety was a part of the backbone of a conducting polymer. In the polymer, the DHP-thiophene repeat units served as the redox switch that could be addressed by light. With a different connectivity of the thiophene units, Lai's group has prepared a similar conducting copolymer **9B** where the thiophenes were connected at the 2,9-positions of the DHP (Figure 10.4b) [15]. The polymer was found to have a small bandgap of ~1.0 eV. The iodine-doped polymer had a conductivity of about 1.0 S $cm^{-1}$. The quinoidal character, as well as

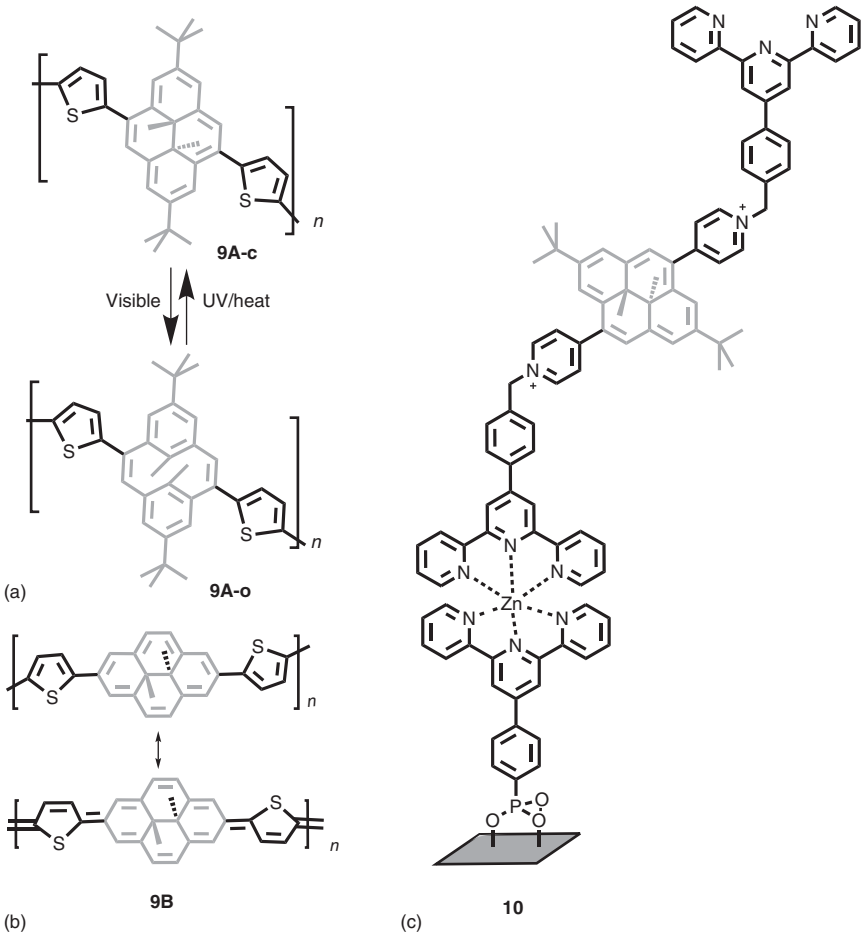


**Figure 10.4** (a and b) DHP-thiophene photoswitchable conducting copolymers with different connectivity. Source: Marsella et al. [14] and Gao and Lai [15]; (c) the bis-terpyridine-appended DHP-Zn(II) repeat units of a coordination polymer.

the low HOMO-LUMO gap of the electron-rich polymer, was responsible for the semiconducting properties of DHP–thiophene **9B** copolymer. Unfortunately, the effect of photoswitching of the DHP unit was not reported.

Switching the electrical conductivity continued to be of interest in the field of opto-electronics with other DHP-based systems. Oligothiophene-functionalized DHP photoswitches have been employed to modulate the electronic mobility through the changes in π-conjugation upon the DHP-CPD switching. 2-Naphthoyl-DHP functionalized with oligothiophenes at the 4,9-positions showed maximum changes in electrical conductivity upon isomerization where opening the switch leads to a decrease in electrical conductivity, which can be restored through closing the switch via thin film [16]. Cobo and coworkers have reported a reversible light-induced switching of thin films made out of a coordination polymer based on Zn(II)

and bis-terpyridine-appended DHP **10** as the photochromic core (Figure 10.4c). Furthermore, a reversible light-induced change of the electrical conduction of these films upon photoisomerization was demonstrated. Interestingly, with an increase in the length of the coordination polymer, the conductance was found to decrease [17].

The reversible control of conductivity has been explored in other DHP-based systems as well. The pyridine-containing DHP-CPD photochromic system **11** has been employed for the investigation of conductance in single-molecule junctions using the mechanically controllable break junction technique (Figure 10.5). The DHP to CPD photoisomerization was accompanied by a disruption in the electronic conjugation of the π-switch and triggered a drastic >1000 times decrease in the conductance as demonstrated by single-molecule experiments [18].

Recently, it has been shown that an Ag(I)-based two-dimensional coordination polymer (CP) bearing pyridines on either side of a photochromic DHP-CPD π-switch **12** can display an excellent conductance switching upon exposure of visible light (Figure 10.6). The closed form conducts more than 70 times better than the open form of the CP [19].

Although light-induced isomerization of the DHP/CPD photochromic system is the focus of this chapter, it is also interesting that the CPD form can close electrochemically to the DHP form providing an electrochemical control of the CPD to DHP isomerization process. In an organometallic Cp-Ruthenium-fused DHP, Mitchell and Berg demonstrated for the first time that the electrochemical

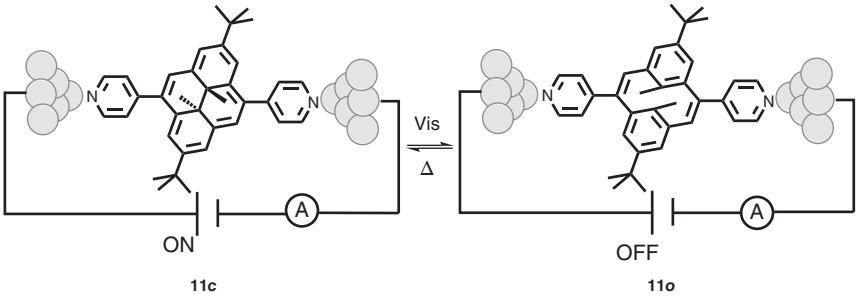


**Figure 10.5** Charge transport through DHP switches in a single-molecule junction.

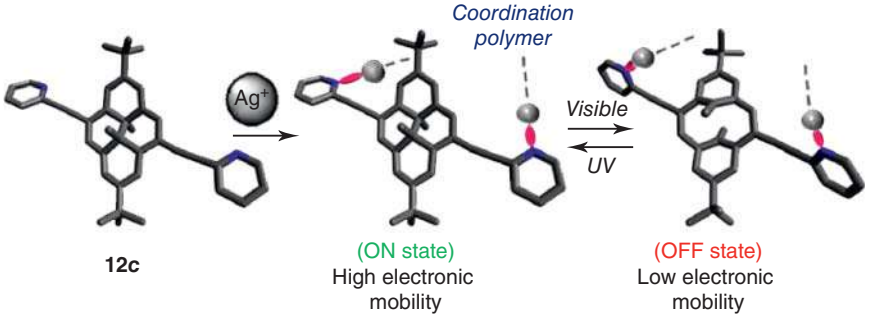


**Figure 10.6** A DHP-based coordination polymer having silver(I) as the metal ion.

ring closing of the DHP ring could be achieved at negative potentials [20]. More recently, Cobo's group has described the reversible electrochemical control of the DHP/CPD process by the substitution of DHP core with the electron-withdrawing moieties. It was found that the substitution at the opposite position does not influence the ring opening/closing phenomenon. On the other hand, substitution at the adjacent positions of the DHP unit has a significant effect on electrochemical isomerization [21]. Hecht's team showed that a pyridyl-appended DHP undergoes reversible isomerization in conjunction with the inorganic semiconductor ZnO where thermal reversal from CPD to DHP takes place at moderate temperature. The pyridine moiety of Py-DHP anchors to the ZnO surface and reversibly alters the electronic properties of the ZnO surface. This provides a reversible control of the interfacial charge injection/extraction properties. Reversible changes in the molecular structure of the py-DHP upon isomerization also lead to change in the valence electronic structure. Therefore, the dynamic tuning of the energy levels by light in an inorganic/organic interface was realized. These materials can be crucial for the development of photo-programmable optoelectronic devices [22].

## 10.5 DHP with Non-methyl Internal Groups: The New-Generation Switches

DHPs undergo reverse CPD to DHP transformation under UV light or heat. Achieving improved quantum yield for the forward DHP to CPD process and reducing the rate of the thermal process have been a challenge. Computationally designed DHP systems indicated that changing the internal methyl groups to unsaturated C=C could enhance the activation energy for the CPD-DHP thermal reversal and enhance the DHP-CPD quantum yield. The designed systems were synthesized, and the results were in excellent agreement with the theoretical studies [23]. The DHP system with the internal CHO **13a** (Figure 10.7) has a thermal half-life of 11 days for the reverse CPD to DHP thermal reversal, whereas the one with internal CN **13b** has a long half-life of 36 years. The internal nitrile group in DHP is not a robust photochromic system because of the migration of the nitrile group to the peripheral ring carbons leading to the death of its photochromic properties. Various alkenyl internal groups of DHP such as **14** and **15** displayed half-lives varying from 56 days to 10 years for the thermal CPD to DHP reversal processes [24].

## 10.6 Multistate Systems with DHP and All-Photonic Molecular Logic Gates

Systems with more than one photochromic units offer a possibility of multistate switches where various ON/OFF combinations of the switches are possible. The earliest example of a three-state light-addressable switch **16** was reported by Bandyopadhyay and Mitchell where the two benzo-[*e*]-fused DHPs were linked

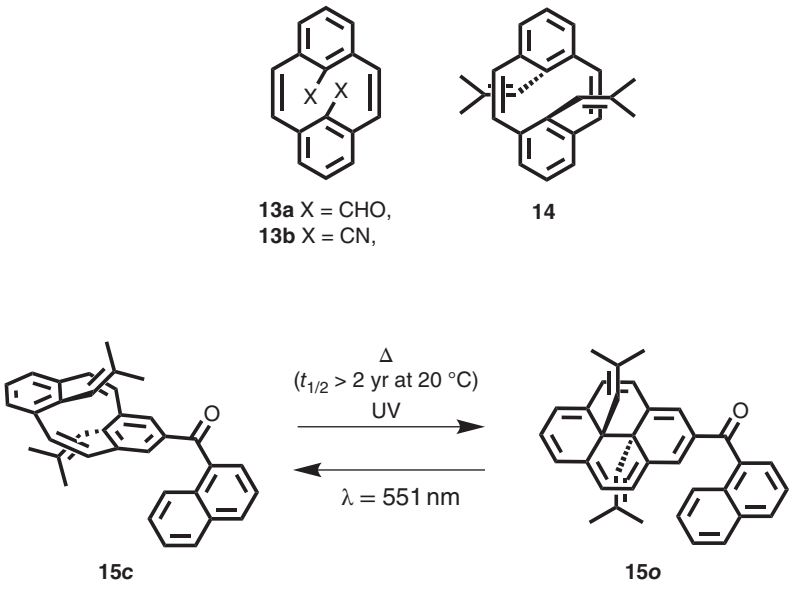


**Figure 10.7** DHP-CPD systems with non-methyl groups.

by an acetylenic linker (Figure 10.8) [25]. Interestingly, in a dimeric diarylethene (DAE) photochromic system with a similar linkage, it was observed that the bis-open form could be switched to an open-closed dimer and back to the bis-open form. No switching to closed form was observed [26]. In contrast, the DHP-based switch operated without affecting the ability of either of the photochromic units to photoswitch. The system could generate a multi-addressable three different states with the molecule, namely the DHP-DHP, DHP-CPD, and the CPD-CPD states. A molecule containing three switchable annelated dihydropyrene units has also been studied. The fused systems with multiple DHP units are synthetically challenging. Some of the multistate switches contain metal ions as the linker and have been discussed in the later part of this chapter.

The DHP-CPD photochromic system, or in fact, any photochromic system, such as a transistor, is capable of performing Boolean logic operations. Multistate switches that can be addressed photonically or electrochemically can, in principle, be used in logic devices having photons as nonchemical inputs and outputs. In a series of joint efforts by Mitchell and Gust's group, a series of logic gates and a photonic half-adder, demultiplexer for Boolean logic operations have been developed using the DHP system. These elegant all-photonic logic systems were some of the early ones to be reported with photochromic systems [27–29].

The following example in a DHP–porphyrin–fullerene (DHP–P–$C_{60}$) **17** molecular triad exploits photoinduced electron transfer (PET) processes that can be turned ON and OFF by simply toggling between the two states of the DHP/CPD photochromic unit (Figure 10.9). The excitation and the photoirradiation are achieved with two lasers and the third-harmonics generator (THG). In the DHP–P–$C_{60}$ form, the porphyrin (P) unit can be excited, and a PET process from the P to $C_{60}$ generates a

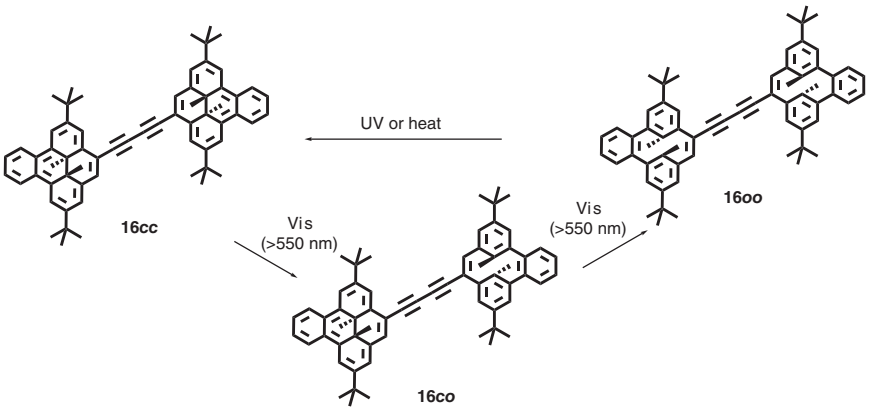


**Figure 10.8** A DHP-based multistate photoswitch. Source: Mitchell and Bandyopadhyay [25].

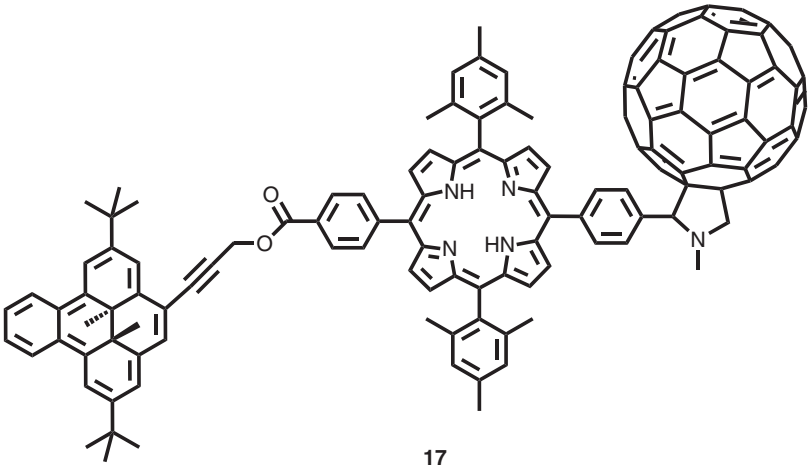


**Figure 10.9** The DHP–P–$C_{60}$ molecular triad.

DHP–$P^+$–$C_{60}^{\cdot-}$ charge-separated state. The DHP being electron-rich donates an electron to the P+ unit and generates a large DHP$^+$–P–$C_{60}^{\cdot-}$ dipolar species with a long lifetime of 2 μs (Figure 10.10). Photoisomerization of the DHP moiety to the CPD generates the CPD–P–$C_{60}$ state. Now, the excitation of the porphyrin produces a short-lived CPD–$P^{\cdot+}$–$C_{60}^{\cdot-}$ state. The CPD unit is not as electron-rich as the DHP and cannot donate an electron to the P+ unit. Again, exposure to UV light converts the CPD–P–$C_{60}$ to the DHP–P–$C_{60}$ form. Thus, the triad can be operated in many cycles. The long-lived photoinduced charge-separated state can be read out in a non-destructive fashion by the transient absorption at 1000 nm, and thus, the system can be used to perform an all-photonic AND logic operation [27].

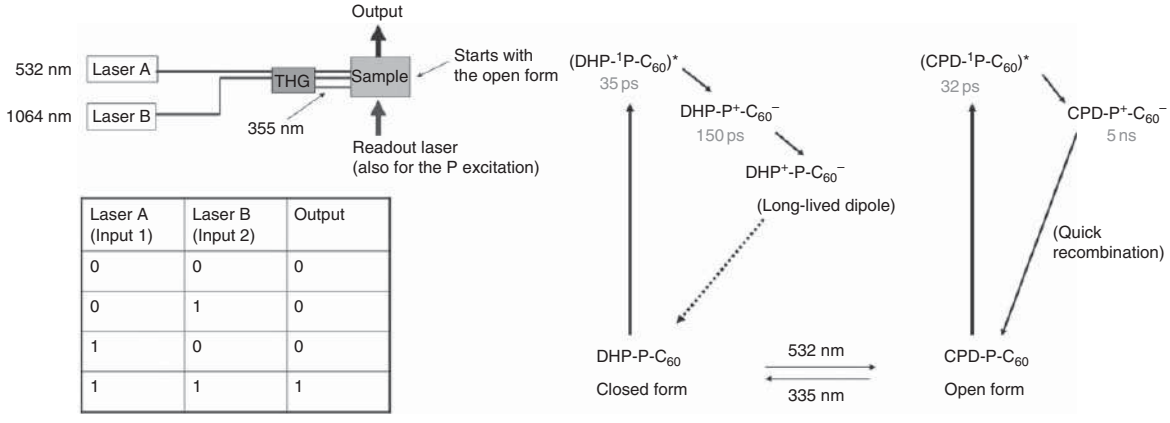


| Laser A (Input 1) | Laser B (Input 2) | Output |
|---|---|---|
| 0 | 0 | 0 |
| 0 | 1 | 0 |
| 1 | 0 | 0 |
| 1 | 1 | 1 |

**Figure 10.10** Performing the AND logic operation with triad **17** and the associated processes.

## 10.7 DHP Photoswitches Having Metal Ions

Metal ions serve multiple purposes, including tuning the photochromic properties, rendering them with tunable redox properties, or even bringing in multiple photochromic units together for various functional properties. The kinetics and efficiency of the reversible photoisomerization of the DHP-CPD photochromic system can also be fine-tuned by putting various substituents on the DHP unit. Jacquet et al. have shown that the introduction of electron-withdrawing moieties can change the photochromic properties. Thus, they have designed terpyridine ruthenium complexes linked to the DHP photochromic units through a pyridinium spacer. It was observed that incorporation of an electron-withdrawing pyridinium spacer between the photochromic core and the ruthenium complex leads to rapid, reversible, and complete conversion between the closed and the open forms compared with the parent unsubstituted DHP [30]. The development of multi-responsive molecular switches that can be addressed and transformed under different external stimuli has been a challenging problem in the field of stimuli-responsive materials. Photochromic systems featuring complete reversibility with a short response time and the metallic center having redox switching ability between its different redox states without overlap with the electrochemical response of the photochromic unit are the prerequisites in this context. Royal and coworkers have designed a bis-terpyridine containing DHP derivative having a pyridinium spacer between the DHP and the two pyridine moieties. Remarkably, the complexation of this ligand with Co(II) does not affect the kinetics or the efficiency of the photoisomerization. The Co(II)-metal center can be addressed electrochemically, whereas the DHP center can be addressed photochemically. Thus a combination of electrochemical and photochemical stimuli can give rise to four different states of the molecule, namely DHP-Co(II)-DHP, CPD-Co(II)-CPD, DHP-Co(III)-DHP, and CPD-Co(III)-CPD. Therefore, without using any chemical stimulus, a NOR and an AND molecular logic gates can be constructed with this system [31].

Photochromic units appended with terpyridyl metal complexes as multi-addressable redox- and photoswitches are also known [32]. The photoisomerization rate of the DHP unit can be controlled by the introduction of an osmium metal center tethered by terpyridine linkers. The emission of the osmium terpyridine complexes can be affected through complexation with the DHP probably owing to energy transfer from the complex center to the DHP unit. Upon isomerization with visible light, the quantum yield of osmium terpyridine complexes was found to be restored [33]. However, the presence of the ruthenium complexes based on photochromic DHP core does not have any adverse effects on the photochromic behavior of the DHP unit upon exposure to light [34]. The effect of platinum complexes on isomerization of the DHP photoswitches has been investigated in $(\text{DHP-ethynyl})_2$-Pt systems. The rate of DHP to CPD isomerization of the platinum complexes was about four times slower than the corresponding alkyne precursors. On the other hand, the thermal CPD to DHP reverse reaction was found to be 50% faster for the metal complexes than for the DHP–ethyne precursor [35]. DHP-pyridyl photochromic system can bind to a zinc(II) tetraphenylporphyrin

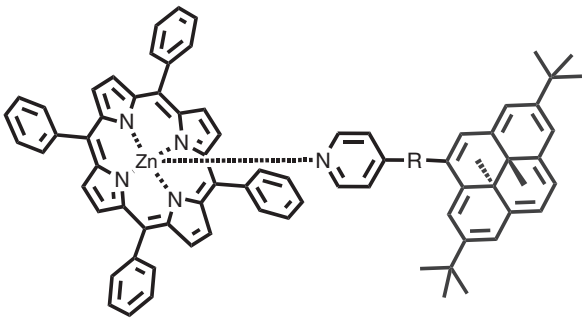


**Figure 10.11** Axial coordination of the DHP–pyridine-based ligand to the (TPP)Zn in **18**.

**18a** No spacer
**18b** R = Ph
**18c** R = $CH_2Py^+$

(TPP) via an axial coordination. Changing the spacer between the DHP and the chelating pyridine **18** (Figure 10.11), the length of conjugation and the efficiency of the DHP → CPD conversion can be modulated. Moreover, the axial coordination of the DHP–pyridine-based ligand to the (TPP)Zn unit allowed improved the photoinduced ring-opening reaction and enhanced the thermal stability of the open form [36].

Nishihara and coworker have reported conjugated DHP derivatives having two terpyridine moieties connected at the 4,9-positions of DHP photochrome via phenyl and ethynyl linkers. Depending upon the nature of the linkers, the redox potential of the DHP moiety, the absorption, and the fluorescence spectra as well as the photochromic behavior can also be altered through modification of valence orbital of the DHP and terpyridine moieties. Redox potential and photoisomerization behavior can also be modified upon complexation with $Ru(tpy)_2$ moieties [37]. Complexation of photochromic DHP core with iron carbonyl forces the large ring to deviate from its planarity by an angle of about 30° and causes a loss of its aromaticity reflected by the increased bond alternation of the ring, which leads to an adverse effect on the photochromic nature of the DHP photochrome [38].

## 10.8 Light-Triggered Molecular Recognition

Molecular recognition through photo-modulation has gained considerable attention in recent times owing to its appealing applications in various fields. Catalytic RNAs are therapeutic targets for a variety of human diseases. The DHP switch displays an aptamer-specific binding toward a hammerhead ribozyme. Using the reversible photoisomerization of the DHP-CPD system, Sen and Mitchell have reported that the catalysis with the allosteric hammerhead ribozyme can be controlled by light with a >900-fold difference in the catalytic rates with micromolar quantities of the two photoisomers [39].

Reversible control of $Cu^{2+}$-ion recognition using DHP/CPD photochromic couple via light was reported where the binding affinity of the CPD form with the metal-ion

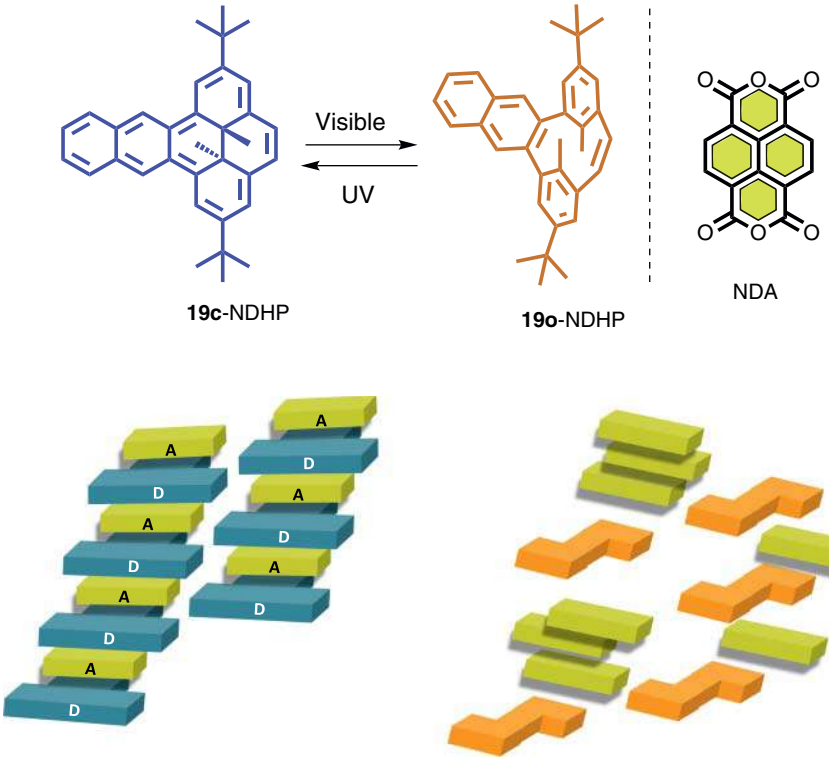


**Figure 10.12** Light-controlled assembly–disassembly of DHP-NDA π-stacks.

was found to be >10 times weaker compared with ring-closed DHP isomeric form of the (ethynylpridine)DHP ligand (Figure 10.12). This is most likely because of the altered distance between the two donor centers in the DHP and the CPD forms [40]. A supramolecular system, having an alternately stacked structure of an electron-rich naphtho-[*e*]-fused DHP system **NDHP 19** and an electron-deficient naphthalene dianhydride (**NDA**), was obtained. Upon exposure to visible light, the planar structure of the naphtho-DHP changes to the nonplanar CPD form. This changes a disruption in the supramolecular stacks and causes disassembly of donor–acceptor stacks. The system can be restored to its original structure upon exposure to the UV light via the generation of the DHP form of the photochromic system. Thus a light-induced assembly–disassembly of a donor–acceptor pi-stacked system was achieved [12].

## 10.9 Multi-addressable Switches: Proton-Triggered

Photochromic efficiency of the DHP systems can be enhanced by the substitution with the electron-withdrawing pyridinium moieties. In case of pyridinium containing DHPs, the reverse reaction, open form to closed form can be accomplished by electrochemically through the oxidation of the CPD ring. Moreover, the efficiency

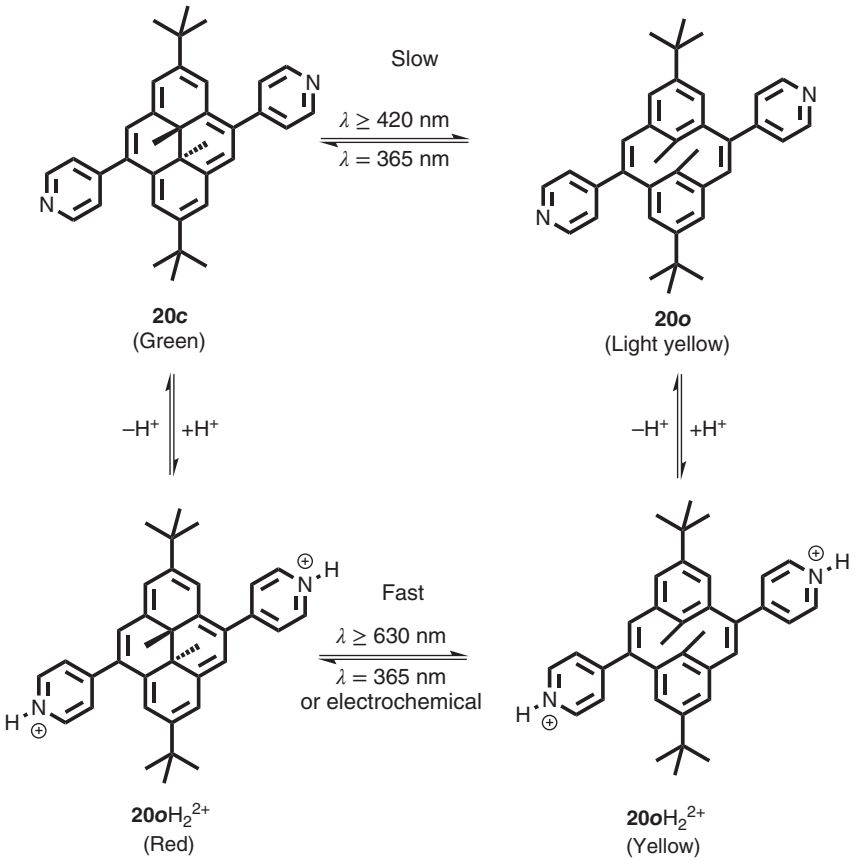


**Figure 10.13** Systems where the kinetics of photoswitching is dependent on protonation. Source: Roldan et al. [41].

of the ring-opening photoreactions of the pyridine containing DHP derivatives **20** can be controlled through protonation–deprotonation reactions (Figure 10.13) [41].

## 10.10 Electrochemically Triggered

Earlier in this chapter, the electrochemically induced isomerization of the CDP-DHP system was partially discussed [20, 21]. A series of bis(ferrocenylethynyl) DHP complexes have been reported in which the two redox-active ferrocene moieties and DHP core were connected through a π-conjugated ethynyl spacer. The ferrocenyl complexes exhibit reversible photochromic behavior and, at the same time, control of the electronic communication between the ferrocene moieties through reversible photoswitching. The complexes in the closed form show strong electronic communication between the ferrocene moieties, which drastically diminishes upon photoisomerization in the open form owing to the loss of electronic conjugation. Moreover, the redox-assisted ring-closing reaction of the complexes from CPD to DHP was also be attained through the oxidation of the ferrocene moieties [42].

## 10.11 Effect of Fluorescent Moieties on the Switching

Mitchell and Bohne have designed several fluorophore-containing DHP derivatives to enhance the switching of the photochromic system. The switches were found to possess superior switching efficiency in the presence of carbonyl-containing fluorophore moieties at the 4-position of the DHP framework without influencing the half-life of the CPD to DHP reverse thermal isomerization reaction. It is important to note that the inclusion of the fluorescent naphthyl or pyrenyl substituents for monitoring the reversible photoswitching was found to be unsuitable due to the formation of highly emissive impurities in trace quantities. However, the emission above 600 nm, attributed to the closed form of the DHP, can be considered as an outstanding way to monitoring the reversible photoswitching [43].

## 10.12 Fatigue Resistance Through Encapsulation

The mechanism of the DHP-CPD conversion has been investigated using photophysical studies by Bohne [44], and using theoretical calculations by Williams [8], and recently by Boggio-Pasqua [41]. The DHP-CPD transformation occurs through a biradical intermediate formed from the dissociation of the central C—C bond of the photoswitch upon excitation [44]. It is generally advised to perform the photoswitching experiments with degassed samples to keep them protected from the reactive oxygen species. Although Bohne and Mitchell have used cyclodextrins to encapsulate the DHP for enhancing the stability, Klajn and coworkers have recently demonstrated that the fatigue of a DHP system can be reduced by encapsulation within a Pd(II)-based octahedral $Pd^{II}{}_6L_4$ cage by protecting the reactive biradical intermediate during photoisomerization process [45]. The cavity inside the $Pd^{II}{}_6L_4$ cage was large enough to accommodate the change of the molecular structures during the photoisomerization.

## 10.13 Cooperative Photoswitching

The mechanism of light-induced DHP to CPD ring opening involves the excitation of the photoswitchable molecule to the second singlet excited state, $S_2$. The deactivation from $S_2$ to the first singlet excited state, $S_1$ state and eventually to $S_0$ is detrimental for the photoswitching process and leads to the lowering of photo-opening efficiency of the DHP switches [44]. DHP systems with proper donor–acceptor groups at the two end of a molecule can reduce this deactivation and enhance the switching efficiency of the ring opening [41, 46, 47]. Based on this, Hecht and coworkers have designed a series of DHP dimers linked through spacers with electron donors and acceptors on the two ends of each DHP units and demonstrated that cooperative photoswitching in the DHP system can be achieved in such systems. Thus, in the molecules with the general structural structure, **21**, (Figure 10.14) once the first DHP unit photoisomerizes to the CPD, the extended conjugation that was present in the closed (**21cc**) form is partially lost

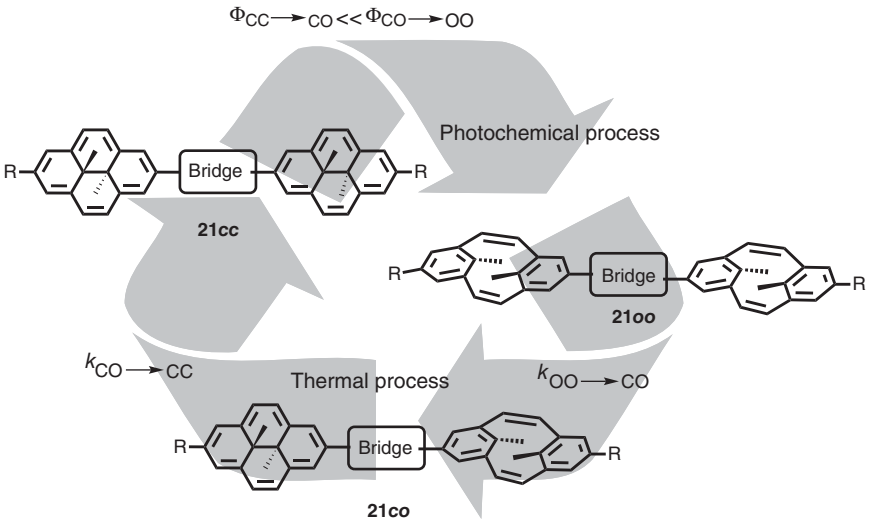


**Figure 10.14** Cooperative switching of the DHP system.

and the electron donation of the bridging π-unit to the second DHP is enhanced. Consequently, this becomes a better donor–acceptor system, and the second ring-opening process becomes more efficient. In fact, the second switching turns out to be so efficient that the closed–open (**21co**) intermediate is not observed during the light-mediated opening of these dimeric switches. This is in contrast to the observation by Bandyopadhyay and Mitchell (Figure 10.8), where there were no donor–acceptor units in the dimeric switches [25]. Therefore, the electronic nature of the bridging unit and R-group of **21** together have a pivotal role in the cooperativity of the switching [48].

In conclusion, although the DHP photochromic system is known for the last half a century, the use of the molecule was primarily of academic interest. It served predominantly as a probe to measure aromaticity of various aromatic units. In the last few decades, DHP has been used as a photoswitch, thanks to the ingenuity and tremendous work of Reg Mitchell. However, in the recent years, DHP has indeed emerged as an important and attractive photoswitch of the future for various nifty applications.

## References


1 Sondheimer, F. (1972). Annulenes. *Acc. Chem. Res.* 5 (3): 81–91.

2 Nakagawa, M. (1975). 'Acetylene–Cumulene' Dehydroannulenes. In: *The Chemistry of Nonbenzenoid Aromatic Compounds–II*, 885–924. Butterworth-Heinemann (Eds. R. Kreher and T.H. Darmstadt).

3 Boekelheide, V. and Phillips, J.B. (1967). Aromatic molecules bearing substituents within the cavity of the π-electron cloud. Synthesis of *trans*-15,16-dimethyldihydropyrene. *J. Am. Chem. Soc.* 89 (7): 1695–1704.

4 Mitchell, R.H. (2001). Measuring aromaticity by NMR. *Chem. Rev.* 101 (5): 1301–1316.

5 Tashiro, M. and Yamato, T. (1982). Metacyclophanes and related compounds. 4. Halogenations of 8,16-dialkyl-*anti*-5,13-di-*tert*-butyl[2.2]metacyclophan-1-enes and 2,7-di-*tert*-butyl-*trans*-10b,10c-dialkyl-10b,10c-dihydropyrenes. *J. Am. Chem. Soc.* 104 (13): 3701–3707.

6 Williams, R.V., Edwards, W.D., Zhang, P. et al. (2012). Experimental verification of the homoaromaticity of 1,3,5-cycloheptatriene and evaluation of the aromaticity of tropone and the tropylium cation by use of the dimethyldihydropyrene probe. *J. Am. Chem. Soc.* 134 (40): 16742–16752.

7 Garmshausen, Y., Klaue, K., and Hecht, S. (2017). Dihydropyrene as an aromaticity probe for partially quinoid push–pull systems. *ChemPlusChem* 82 (7): 1025–1029.

8 Mitchell, R.H., Zhang, P., Berg, D.J., and Williams, R.V. (2012). An experimental estimate of the relative aromaticity of the cyclooctatetraene dianion by fusion to dimethyldihydropyrene. *Chem. Commun.* 48 (65): 8144–8146.

9 Blattmann, H.R., Meuche, D., Heilbronner, E. et al. (1965). Photoisomerization of *trans*-15,16-dimethyldihydropyrene. *J. Am. Chem. Soc.* 87 (1): 130–131.

10 Mitchell, R.H., Bohne, C., Wang, Y. et al. (2006). Multistate π switches: synthesis and photochemistry of a molecule containing three switchable annelated dihydropyrene units. *J. Org. Chem.* 71 (1): 327–336.

11 Mitchell, R.H. (1999). The metacyclophanediene-dihydropyrene photochromic π switch. *Eur. J. Org. Chem.* 1999 (11): 2695–2703.

12 Krishna, V.S.R., Samanta, M., Pal, S. et al. (2016). Light-triggered assembly–disassembly of an ordered donor–acceptor π-stack using a photoresponsive dimethyldihydropyrene π-switch. *Org. Biomol. Chem.* 14 (24): 5744–5750.

13 Sawada, T., Kuroki, M., Ogawa, T. et al. (2010). Dihydropyrene annelated with dihydrothieno[3.4-*b*]pyrazine: synthesis and photoswitching property. *Tetrahedron Lett.* 51 (31): 4033–4036.

14 Marsella, M.J., Wang, Z.Q., and Mitchell, R.H. (2000). Backbone photochromic polymers containing the dimethyldihydropyrene moiety: toward optoelectronic switches. *Org. Lett.* 2 (19): 2979–2982.

15 Gao, J. and Lai, Y.H. (2009). Narrow bandgap and enhanced electroconductivity in a dihydropyrene–thiophene copolymer. *Polymer* 50 (8): 1830–1834.

16 Robinson, S.G., Sauro, V.A., and Mitchell, R.H. (2009). Oligothiophene functionalized dimethyldihydropyrenes I: syntheses and photochromicity. *J. Org. Chem.* 74 (17): 6592–6605.

17 Bakkar, A., Lafolet, F., Roldan, D. et al. (2018). Bidirectional light-induced conductance switching in molecular wires containing a dimethyldihydropyrene unit. *Nanoscale* 10 (12): 5436–5441.

18 Roldan, D., Kaliginedi, V., Cobo, S. et al. (2013). Charge transport in photoswitchable dimethyldihydropyrene-type single-molecule junctions. *J. Am. Chem. Soc.* 135 (16): 5974–5977.

19 Ghosh, S., Hossain, M.S., Chatterjee, S. et al. (2020). Light-gated modulation of electronic mobility of a dihydropyrene-based photochromic coordination polymer. *ACS Appl. Mater. Interfaces* 12 (47): 52983–52991.


**20** Mitchell, R.H., Brkic, Z., Sauro, V.A., and Berg, D.J. (2003). A photochromic, electrochromic, thermochromic Ru complexed benzannulene: an organometallic example of the dimethyldihydropyrene–metacyclophanediene valence isomerization. *J. Am. Chem. Soc.* 125 (25): 7581–7585.

**21** Bakkar, A., Lafolet, F., Boggio-Pasqua, M. et al. (2017). Electrochemical control of the switching process of photochromic dimethyldihydropyrene derivatives. *Chem. Commun.* 53 (67): 9360–9363.

**22** Wang, Q., Ligorio, G., Schlesinger, R. et al. (2019). Switching the electronic properties of ZnO surfaces with negative T-type photochromic pyridyl-dihydropyrene layers and impact of fermi level pinning. *Adv. Mater. Interfaces* 6 (10): 1900211.

**23** Ayub, K. and Mitchell, R.H. (2014). Syntheses of dihydropyrene–cyclophanediene negative photochromes containing internal alkenyl and alkynyl groups and comparison of their photochemical and thermochemical properties. *J. Org. Chem.* 79 (2): 664–678.

**24** Ayub, K., Zhang, R., Robinson, S.G. et al. (2008). Suppressing the thermal metacyclophanediene to dihydropyrene isomerization: synthesis and rearrangement of 8,16-dicyano[2.2]metacyclophane-1,9-diene and evidence supporting the proposed biradicaloid mechanism. *J. Org. Chem.* 73 (2): 451–456.

**25** Mitchell, R.H. and Bandyopadhyay, S. (2004). Linked photoswitches where both photochromes open and close. *Org. Lett.* 6 (11): 1729–1732.

**26** Kaieda, T., Kobatake, S., Miyasaka, H. et al. (2002). Efficient photocyclization of dithienylethene dimer, trimer, and tetramer: quantum yield and reaction dynamics. *J. Am. Chem. Soc.* 124 (9): 2015–2024.

**27** Liddell, P.A., Kodis, G., Andréasson, J. et al. (2004). Photonic switching of photoinduced electron transfer in a dihydropyrene–porphyrin–fullerene molecular triad. *J. Am. Chem. Soc.* 126 (15): 4803–4811.

**28** Andréasson, J., Kodis, G., Terazono, Y. et al. (2004). Molecule-based photonically switched half-adder. *J. Am. Chem. Soc.* 126 (49): 15926–15927.

**29** Straight, S.D., Andréasson, J., Kodis, G. et al. (2005). Molecular AND and INHIBIT gates based on control of porphyrin fluorescence by photochromes. *J. Am. Chem. Soc.* 127 (26): 9403–9409.

**30** Jacquet, M., Lafolet, F., Cobo, S. et al. (2017). Efficient photoswitch system combining a dimethyldihydropyrene pyridinium core and ruthenium (II) bis-terpyridine entities. *Inorg. Chem.* 56 (8): 4357–4368.

**31** Bakkar, A., Cobo, S., Lafolet, F. et al. (2016). A redox-and photo-responsive quadri-state switch based on dimethyldihydropyrene-appended cobalt complexes. *J. Mater. Chem. C* 4 (6): 1139–1143.

**32** Bakkar, A., Cobo, S., Lafolet, F. et al. (2016). Dimethyldihydropyrene–cyclophanediene photochromic couple functionalized with terpyridyl metal complexes as multi-addressable redox-and photo-switches. *Dalton Trans.* 45 (35): 13700–13708.

**33** Sakurai, H., Jacquet, M., Lafolet, F. et al. (2019). Photochemical and photophysical properties of photochromic osmium terpyridine-dimethyldihydropyrene complexes. *Dyes Pigm.* 160: 93–98.


**34** Vila, N., Royal, G., Loiseau, F., and Deronzier, A. (2011). Photochromic and redox properties of bisterpyridine ruthenium complexes based on dimethyldihydropyrene units as bridging ligands. *Inorg. Chem.* 50 (21): 10581–10591.

**35** Zhang, P., Berg, D.J., Mitchell, R.H. et al. (2012). Platinum complexes of alkynyl-substituted dimethyldihydropyrenes. *Organometallics* 31 (23): 8121–8134.

**36** Bakkar, A., Cobo, S., Lafolet, F. et al. (2016). Self-assembled dimethyldihydropyrene-pyridyl substituted ligands with zinc(II) meso-tetraphenylporphyrin via axial coordination. *Dalton Trans.* 45 (41): 16453–16462.

**37** Muratsugu, S. and Nishihara, H. (2014). π-Conjugation modification of photochromic and redox-active dimethyldihydropyrene by phenyl-and ethynyl-terpyridines and Ru (bis-terpyridine) complexes. *New J. Chem.* 38 (12): 6114–6124.

**38** Zhang, R., Fan, W., Twamley, B. et al. (2007). Synthesis and structures of dimethyldihydropyrene iron carbonyl complexes. *Organometallics* 26 (8): 1888–1894.

**39** Lee, H.W., Robinson, S.G., Bandyopadhyay, S. et al. (2007). Reversible photo-regulation of a hammerhead ribozyme using a diffusible effector. *J. Mol. Biol.* 371 (5): 1163–1173.

**40** Pal, S., Hatai, J., Srikanth, K., and Bandyopadhyay, S. (2013). Light gated reversible modulation of $Cu^{2+}$ binding. *RSC Adv.* 3 (11): 3739–3744.

**41** Roldan, D., Cobo, S., Lafolet, F. et al. (2015). A multi-addressable switch based on the dimethyldihydropyrene photochrome with remarkable proton-triggered photo-opening efficiency. *Chem. Eur. J.* 21 (1): 455–467.

**42** Muratsugu, S., Kume, S., and Nishihara, H. (2008). Redox-assisted ring closing reaction of the photogenerated cyclophanediene form of bis(ferrocenyl)dimethyldihydropyrene with interferrocene electronic communication switching. *J. Am. Chem. Soc.* 130 (23): 7204–7205.

**43** Mitchell, R.H., Bohne, C., Robinson, S.G., and Yang, Y. (2007). The effect of addition of fluorescent moieties to dihydropyrenes: enhancing photochromicity and fluorescence monitoring. *J. Org. Chem.* 72 (21): 7939–7946.

**44** Sheepwash, M.A., Mitchell, R.H., and Bohne, C. (2002). Mechanistic insights into the photochromism of *trans*-10b, 10c-dimethyl-10b, 10c-dihydropyrene derivatives. *J. Am. Chem. Soc.* 124 (17): 4693–4700.

**45** Canton, M., Grommet, A.B., Pesce, L. et al. (2020). Improving fatigue resistance of dihydropyrene by encapsulation within a coordination cage. *J. Am. Chem. Soc.* 142 (34): 14557–14565.

**46** Klaue, K., Garmshausen, Y., and Hecht, S. (2018). Taking photochromism beyond Visible: direct one-photon NIR photoswitches operating in the biological window. *Angew. Chem. Int. Ed.* 57: 1414–1417.

**47** Klaue, K., Han, W., Liesfeld, P. et al. (2020). Donor–acceptor dihydropyrenes switchable with near-infrared light. *J. Am. Chem. Soc.* 142: 11857–11864.

**48** Liesfeld, P., Garmshausen, Y., Budzak, S. et al. (2020). Highly cooperative photoswitching in dihydropyrene dimers. *Angew. Chem. Int. Ed.* 59 (43): 19352–19358.


# 11 Chiroptical Molecular Switches and Motors

Brian P. Corbet, Anouk S. Lubbe, Stefano Crespi, and Ben L. Feringa

**Photochromism**

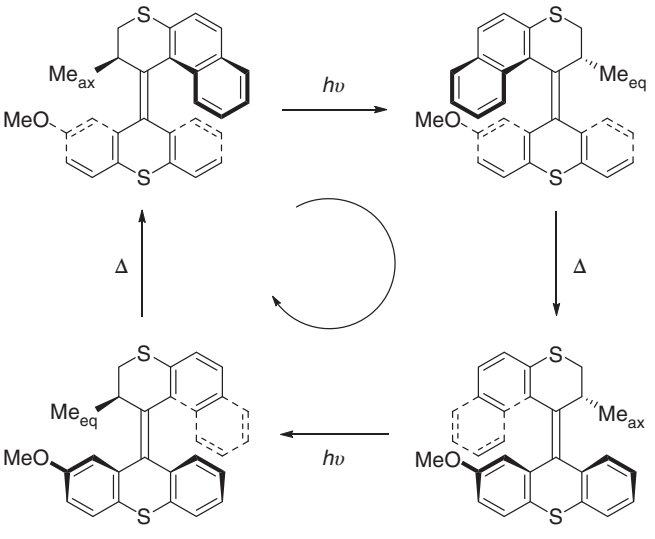


**Characteristic Features**

Rotation around overcrowded alkene axle, helical and point chirality, *E/Z*-photoisomerization, thermal helix inversion, unidirectional rotation.

**First Reported**

Feringa, B.L., Jager, W.F., de Lange, B., and Meijer, E.W. (1991). Chiroptical molecular switch. *J. Am. Chem. Soc*. 113 (14): 5468–5470.

Koumura, N., Zijlstra, R.WJ., van Delden, R.A., et al. (1999). Light-driven monodirectional molecular rotor. *Nature* 401 (6749): 152–155.

**Key References**

Koumura, N., Geertsema, E.M., Meetsma, A., and Feringa, B.L. (2000). Light-driven molecular rotor: unidirectional rotation controlled by a single stereogenic center. *J. Am. Chem. Soc*. 122 (48): 12005–12006.

Kistemaker, J.C.M., Štacko, P., Visser, J., and Feringa, B.L. (2015). Unidirectional rotary motion in achiral molecular motors. *Nat. Chem*. 7 (11): 890–896.

Kudernac, T., Ruangsupapichat, N., Parschau, M., et al. (2011). Electrically driven directional motion of a four-wheeled molecule on a metal surface. *Nature* 479 (7372): 208–211.

Wang, J., and Feringa, B.L. (2011). Dynamic control of chiral space in a catalytic asymmetric reaction using a molecular motor. *Science* 331 (6023): 1429–1432.

# 11

# Chiroptical Molecular Switches and Motors

*Brian P. Corbet, Anouk S. Lubbe, Stefano Crespi, and Ben L. Feringa*

*Rijksuniversiteit Groningen, Stratingh Institute for Chemistry, Groningen, The Netherlands*

## 11.1 Introduction

Photoswitches are molecules able to undergo a reversible transformation between different isomeric forms upon light absorption [1]. The photoisomerization of azo, imine, or alkene double bonds is one of the most widely used reactions in photoswitches. The application of light as the external trigger promoting the photochemical isomerization has several distinct advantages. Light stands out as a quintessential stimulus, which can be precisely tuned in space, time, intensity, wavelength, and polarization. Furthermore, the photon is the ideal traceless reagent that does not add or remove any mass from a closed system [2].

In alkene-based photoswitches (Scheme 11.1), the fixed geometry at the two $sp^2$ centers gives rise to two configurations indicated *E* and *Z* (*Entgegen/Zusammen)* or *trans* and *cis*. Irradiation of the photoswitch leads to a $\pi \rightarrow \pi^*$-transition, promoting an electron from a $\pi$-bonding to a $\pi^*$-antibonding orbital. In this excited state, the increased single-bond character allows isomerization between the two stereoisomers by rotation around its C=C axis. Switching in the reverse direction can be achieved via another photochemical isomerization. With sufficient irradiation, the system reaches an equilibrium between the photochemical forward and backward reactions, i.e. the so-called photostationary state (PSS). At a given wavelength, the equilibrium ratio depends on the respective absorptivity of the isomers involved and the quantum yields of the forward and backward photochemical steps.

For some photoswitches, such as stilbene **1** in Scheme 11.1a, a thermal *E/Z*-isomerization is also possible, where the higher-energy *Z*-stilbene can interconvert into the lower-energy *E* isomer [3]. Furthermore, *Z*-stilbene can undergo a photocyclization [4, 5] which will not be discussed further in this chapter. Stilbene represents the archetype of a class of widely studied alkene photoswitches [4, 6] and many of the structures discussed in this chapter have a stilbene-like photoswitching motif. Other fascinating switches sharing a similar mode of action have been developed, such as the imine-based motors by Lehn and Greb [7] or the hemithioindigo motors by the group of Dube [8]. These systems are the subject

*Molecular Photoswitches: Chemistry, Properties, and Applications*,
First Edition. Edited by Zbigniew L. Pianowski.


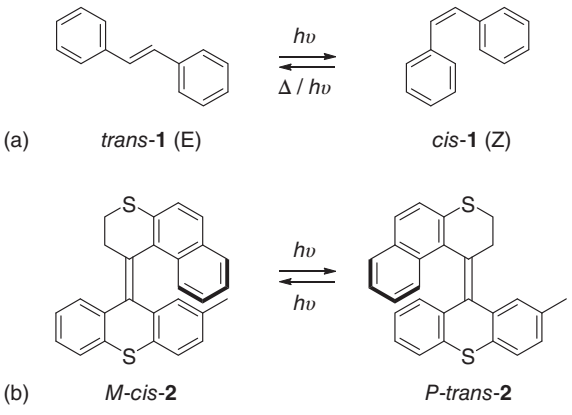


**Scheme 11.1** (a) Stilbene photoswitch, (b) Overcrowded alkene-based chiroptical molecular switch.

of other sections of this book. This chapter will focus on alkene-based chiroptical switches and molecular rotary motors. For extensive discussions on other classes of photoswitches, the reader is referred to specific chapters in this volume, and additional books and reviews [1, 4, 6, 9–14].

Chiroptical switches (e.g. *M-cis*-**2** in Scheme 11.1b) are overcrowded alkene-based chiral molecules with an intrinsic stilbene-type chromophore that can be isomerized from one stereoisomer to another (*P-trans*-**2** in Scheme 11.1b). These switches typically change helicity while preserve chiral information within the operating conditions, without racemization even after performing multiple switching cycles; hence, fatigue resistance is a prerequisite for this class of molecules [1]. This class owes its name to the possibility to study them with chiroptical techniques, i.e. involving anisotropic radiation [15]. The photochemical control of chiral information provides unique opportunities toward application of these molecules in many fields where chirality is of utmost importance [16–18].

## 11.2 From Helical Overcrowded Alkenes to Unidirectional Rotary Molecular Motors

The first light-driven rotary molecular motor was reported in 1999 by Feringa and coworkers [19]. Since then, molecular motors [20–22] have been extensively studied and further developed, making them a class of versatile nanoscale machines [9–12]. In this section, we will first briefly discuss the relevant chiroptical molecular switches from which the motors have evolved and continue with the research toward overcrowded alkene-based molecular rotary motors. Figure 11.1 provides a timeline with an overview of alkene-based chiroptical switches (**3** and **4**) and molecular rotary motors (**5**–**7**).

Unidirectional rotary molecular motors are generally classified by their generation, based on the number of stereogenic centers present in the molecule. The first

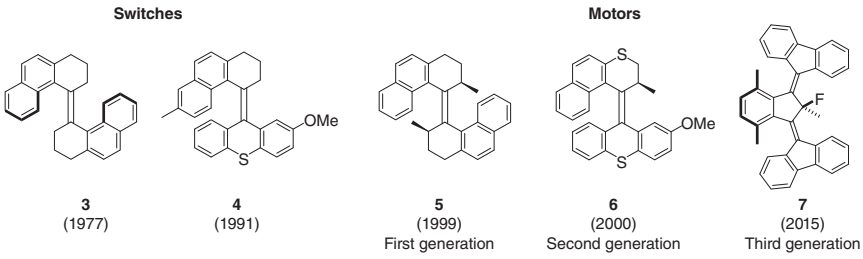


**Figure 11.1** Timeline with illustrative examples of molecular switches toward first-, second-, and third-generation molecular motors. Sources: Koumura et al. [19]; Feringa et al. [23]; Feringa et al. [24]; Kistemaker et al. [25]; Koumura et al. [26].

generation (Figure 11.1, compound **5**) is $C_2$-symmetric over the central alkene bond and has two stereogenic centers, one in each half. The second-generation motor **6** has only one stereogenic center in its rotor half. Finally, the third-generation molecular motor **7** is a meso-compound, with a pseudo-asymmetric center that drives its unidirectionality.

### 11.2.1 Chiroptical Molecular Switches

In 1977 Feringa and Wynberg reported an inherently chiral overcrowded alkene (Figure 11.1, Scheme 11.2, compound **3**) [23, 27]. The steric hindrance between the naphthalene- and the cyclohexane units causes the molecule to adopt a helical conformation in both the *cis*- and *trans* configurations. This feature leads to torsion around the central C=C axle. Four isomers (*P,P*)-*E*, (*M,M*)-*E*, (*P,P*)-*Z*, (*M,M*)-*Z* (Scheme 11.2) were isolated by chiral High Pressure Liquid Chromatography (HPLC) and analyzed by UV–vis and circular dichroism (CD) spectroscopy, as well as X-ray crystallography [28]. A crucial discovery was the room-temperature racemization of the (*M,M*)-*Z* isomer. CD and NMR spectroscopy and additional theoretical analysis [29, 30] revealed the purely thermal nature of the process, which inverts the helicity of *Z*-**3** with a barrier of $\Delta G^{\ddagger} = 90\,\text{kJ mol}^{-1}$ (Scheme 11.2). No thermal *E*/*Z*-isomerization or radical processes are involved in this racemization mechanism. In a similar way, the *E*-isomer racemized at elevated temperatures with a barrier of $\Delta G^{\ddagger} = 105\,\text{kJ mol}^{-1}$ [30]. This thermal helix inversion (THI) is a fundamental step inherent to this type of chiroptical switch, and its rationalization is a milestone for the development of unidirectional rotation in molecular motors.

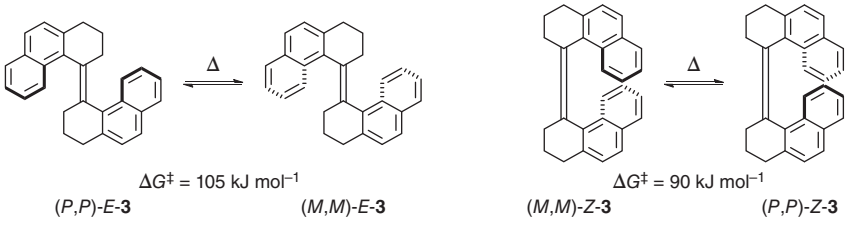


**Scheme 11.2** Stereoisomers of chiroptical switch **3** and their thermal helix inversions.

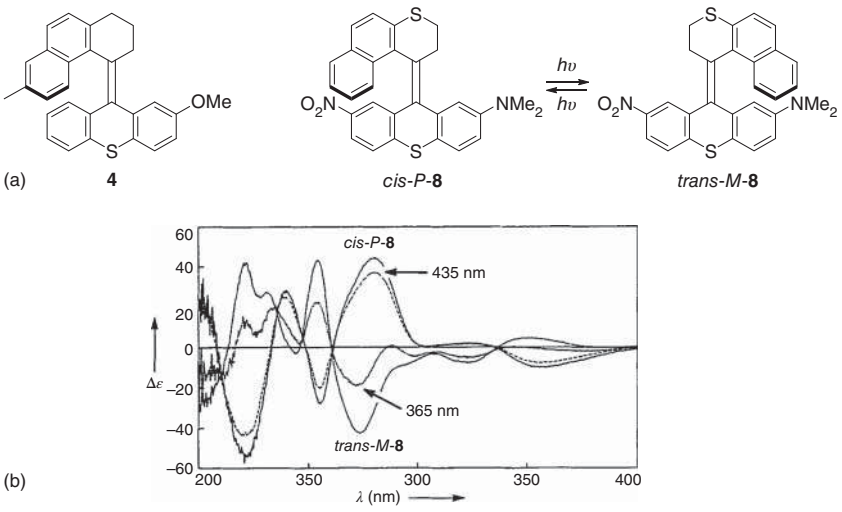


**Figure 11.2** (a) Non-symmetrical chiroptical switches and (b) CD spectra of *cis-P*-**8**, *trans-M*-**8**, and the PSS mixtures obtained by their irradiation with 365 and 435 nm light, respectively [24, 31, 32]. Source: Jager et al. [32].

A different class of chiroptical switches has a non-symmetric structure with respect to the central overcrowded alkene motif (Figure 11.2a). These switches are characterized by a relatively high barrier for helix inversions, which means that isolated enantiomers do not racemize under ambient conditions. On the other hand, the helicity of the initial state can be inverted by photochemical *E*/*Z*-isomerization. This process can be readily followed by optical rotatory dispersion (ORD) and CD (Figure 11.2b), as the pseudo-enantiomers *cis-P*-**8** and *trans-M*-**8** possess an inherent dissymmetric helical chromophore and show strong and approximately mirror-image CD spectra.

By irradiating with different wavelengths of light, different PSS mixtures can be obtained in an altered ratio of pseudo-enantiomers [24]. For compound **4** (Figure 11.2a), irradiation of the *M-cis* isomer with 300 nm led to a PSS of 64 : 35 (*M-cis*:*P-trans*), and subsequent irradiation of this mixture with 250 nm light modified the PSS to 68 : 32 [33]. By installing a dimethylamino and a nitro substituent in **8**, a donor/acceptor system was introduced, which red-shifted the operational irradiation wavelengths to 365 and 435 nm [32]. Protonation of the amine functionality stopped the photoswitching in both directions forming a proton-gated chiroptical photoswitch that could be read out by fluorescence or ORD spectroscopy [34].

### 11.2.2 First- and Second-Generation Molecular Motors

The addition of methyl groups to both cyclohexane rings of **3** introduced stereogenic centers to determine the absolute configuration of the molecule, which led to the synthesis of the overcrowded alkene **5** (Figure 11.3) [35]. The additional methyl groups imposed a further element of asymmetry to the system, also providing

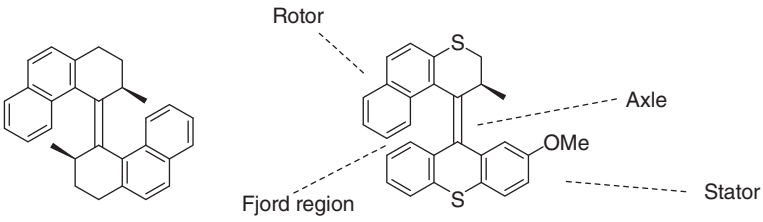


**Figure 11.3** First- and second-generation molecular motors. Sources: Koumura et al. [19]; Koumura et al. [36].

improved PSS ratios for the photochemical *E*/*Z*-isomerizations and directional THIs. By demonstrating the individual steps in the isomerization sequence, **5** was identified as the first artificial molecule to perform photochemical-driven unidirectional rotary motion [19].

First-generation molecular motors are $C_2$-symmetrical across the central axis of rotation, and both halves contain a stereogenic center. Their symmetry provides relatively straightforward synthetic options, such as reductive dimerization of ketones by McMurry coupling [37] to obtain the central overcrowded alkene. Forging the sterically congested, tetra-substituted double bond is often the crucial step in the synthesis of many switches and motors described in this chapter [38].

Second-generation molecular rotary motors are non-symmetrical over the central double-bond axis and are similar to the previously described unsymmetrical chiroptical switches, with an additional stereogenic center at the allylic position [26]. These structures (**6**, Figure 11.3) have only one stereogenic center in their *rotor* (or upper) half, while the lower half – the *stator* – typically consists of a fluorenyl or tricyclic motif [36]. The stereogenic carbon in the *rotor* governs the unidirectional rotation with respect to the *stator* around the *axle* of rotation. The sterically congested space between the aromatic parts of the *rotor* and the *stator* is called the *fjord-region*.

The Barton–Kellogg reaction is commonly used to form the unsymmetrical overcrowded alkene motif of the second-generation motors. A thioketone and a diazo compound react in a 1,3-dipolar cycloaddition followed by nitrogen evolution. The obtained thiirane is subsequently desulfurized to provide the overcrowded non-symmetrical alkenes [36, 39].

For both first- and second-generation molecular motors, the combination of helical chirality and point chirality due to the aforementioned stereogenic elements allows access to multiple diastereomers.

### 11.2.3 Fundamental Rotational Steps

First- and second-generation overcrowded alkene-based molecular motors undergo rotation, populating four distinct isomers sequentially, as illustrated in Schemes 11.3 and 11.4 [20, 36, 41, 42], via a combination of photochemical and thermal reactions [43].

Rotary molecular motor **9** (Scheme 11.3) is $C_2$-symmetrical over the central double-bond axis and contains two naphthalene units, which introduce helical

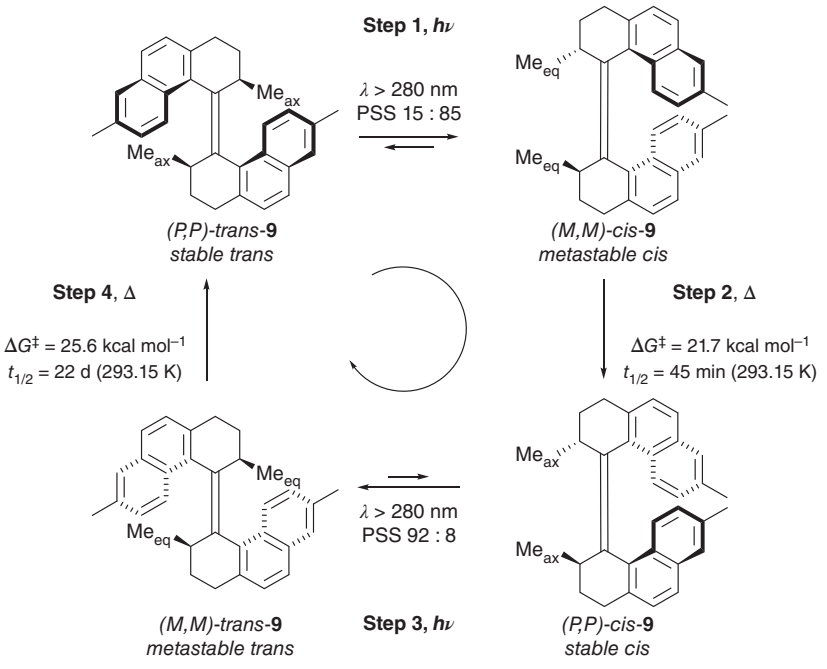


**Scheme 11.3** Rotation cycle for first-generation molecular motor **9**. Source: Ter Wiel et al. [40].

chirality and two stereogenic methyl substituents that determine the directionality of rotation. These stereogenic elements are the cause for the diastereomers and their distinct energies involved in this rotational cycle [43].

Following the rotational direction, the fundamental steps involved are as follows. The energetically lowest stereoisomer *(P,P)-trans*-**9**, known as the *stable trans* isomer, undergoes photochemical *E*/*Z*-isomerization (step 1) to the *metastable cis* isomer upon irradiation with the appropriate wavelength of light. This new configuration is energetically less favorable because of increased steric hindrance. Note that the stereogenic methyl substituents are now in a pseudo-equatorial position. From the metastable isomer, THI occurs, inverting the helicity of the molecule leading to a *stable cis* isomer (step 2). The THI step is discussed in further detail in Section 11.3.1.

After this 180° rotation, the *stable cis* isomer undergoes another photochemical *E*/*Z*-isomerization (step 3) to obtain the *metastable trans* isomer. A THI step again inverts the helicity (step 4), completing the 360° unidirectional rotation. The rates for the two THI steps are significantly different for first-generation molecular motors, as the metastable isomers experience a notably different steric hindrance (as an example, for motor **9** $t_{1/2} = 45$ minutes and 22 days for step 2 and 4 at 293.15 K, respectively) [41].

For second-generation molecular rotary motors, the fundamental steps of photochemical isomerization are comparable to the ones observed for the first generation, as illustrated in Scheme 11.4. Upon irradiation at the appropriate wavelength, the energetically most stable isomer *trans-M*-**6** (*stable trans*) undergoes

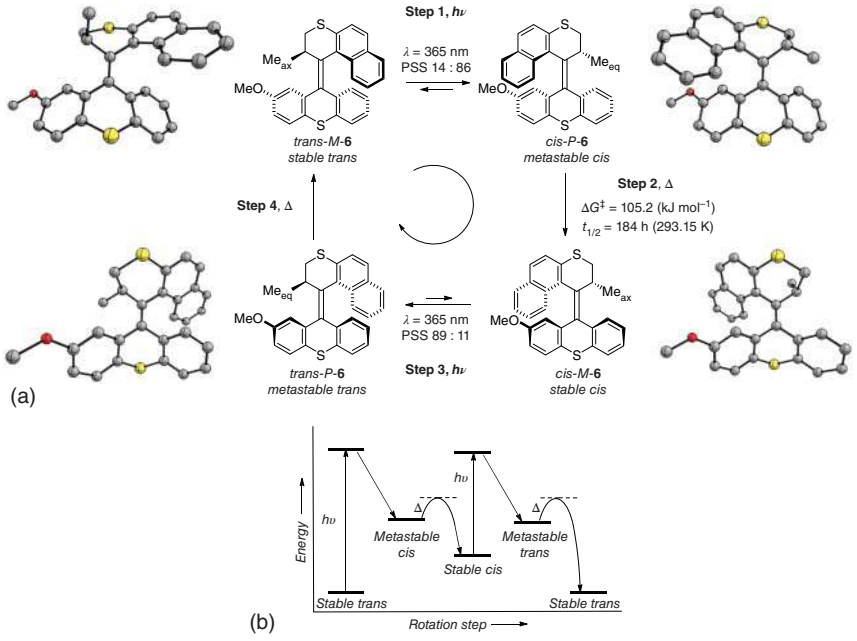


**Scheme 11.4** (a) Rotation cycle for a second-generation molecular motor **6**, including 3D representations and (b) corresponding energy diagram. Source: Koumura et al. [36] and Pollard et al. [41].

a photochemical *E*/*Z*-isomerization of the central double bond to form *cis-P*-**6** (step 1). In this step, the naphthalene motif of the rotor (for rotor, axle, stator nomenclature, see Section 11.2.2) remains on the same side with respect to the stator (i.e. above the plane of the paper). The photoisomerization leads to an inversion of helicity (*M*- to *P*-helicity) and a pseudo-equatorial orientation of the stereogenic methyl group. This metastable state is energetically unfavored because of increased steric repulsion between both halves, raising the ground-state energy level [44, 45].

From the metastable state, a THI occurs (step 2) to a more favored orientation, nearly identical to the initial geometry, but distinguishable by the relative *cis*-orientation of the rotor with respect to the methoxy substituent that desymmetrizes the stator. A repetition of the same sequence of photochemical *E*/*Z*-isomerization (step 3) and THI (step 4) completes the full 360° cycle, returning to the original state. As the extent of steric hindrance in both metastable states and both stable states is nearly identical, the energetic landscape for THI and the respective barriers in steps 2 and 4 are practically the same.

Overall, the 360° rotation of molecular motors is non-reciprocal motion; hence, the molecule has performed work. The complex combination of conformational and configurational changes of the intermediates influences the dynamics of the individual steps. The relative energies of each "station" of the motor relate to the rigidity and steric hindrance of rotor and stator halves. There are general trends and rules for

the dynamics of molecular motors, which are not ubiquitous. This will be discussed in further detail in Section 11.3.1. The full mechanistic details of all known variations of molecular rotary motors are intricate and not always fully unraveled [45]. However, the thorough study on the motion of various molecular motors allows an increasingly more precise picture of each step of their cycle, which will be discussed further in Section 11.3 of this chapter.

### 11.2.4 Third-Generation Rotary Molecular Motors

The previously mentioned motors have an element of point chirality as a characteristic feature controlling unidirectional rotation. A further challenge was to demonstrate the possibility of directional rotary motion in achiral systems. With one stereocenter with point chirality fewer than the second-generation molecular motors, the third-generation molecular motors achieve this goal. These meso-compounds differ from previous motor generations by having one central stator core, two axles, and two rotors (Figure 11.4).

In 2015, Feringa and coworkers showed that the use of a pseudo-asymmetric carbon atom was sufficient for directional rotary motion around two axles [25]. Using a central stator with a pseudo-asymmetric center and two identical fluorenyl rotors (Figure 11.4, compound **7**), it was demonstrated that a directional disrotatory motion occurs upon irradiation. Both stators are influenced by a different face of the pseudo-asymmetric center, which provides a bias for the direction of *E*/*Z*-photoisomerization. This preference originates from the size difference in the doubly allylic position (e.g. motor **10**, $R_1$ and $R_2$), where the larger substituent takes a "pseudo-axial" orientation. The presence of this pseudo-asymmetric center is essential for the occurrence of any directionality [46]. Unidirectionality was proven using desymmetrized rotor motifs by the introduction of a methoxy group (R in motor **7**, $R_3$ in motor **10**) and analysis of the products of each step of the photochemical and thermal isomerizations [25, 46].

The size of the core unit (Figure 11.4, compound **10**, $R_4$) is the main factor influencing the speed of rotation for these motors. A smaller core unit leads to lower barriers for THI [46]. By modification of the bridgehead groups (Figure 11.4, compound **10**, $R_1$ and $R_2$), the direction of rotation could be precisely controlled. Interestingly, a reversal of directionality occurs when $R_1$ = Me, $R_2$ = *i*-Pr are substituted

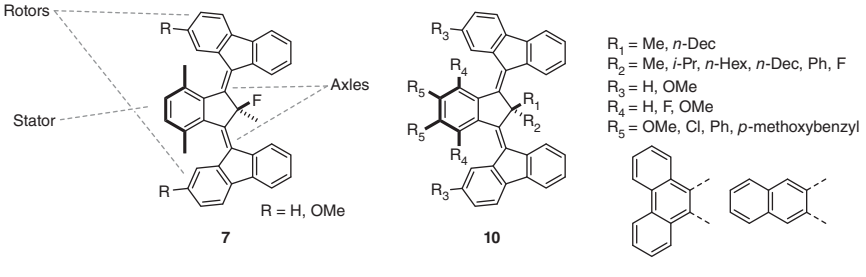


**Figure 11.4** Third-generation molecular motors. Sources: Kistemaker et al. [47]; Kistemaker et al. [46]; Berrocal et al. [47].

with $R_1 = H$, $R_2 = F$ [46]. The distal side of the core unit ($R_5$) can be modified in a modular synthesis route [47]. These modifications can increase the solubility and red-shift the absorption wavelength. Importantly, distal functionalization provides opportunities for further functionalization and future application in molecular cargo transport.

## 11.3 Dynamics and Kinetics of Molecular Motors

### 11.3.1 Thermal Isomerization

For molecular motors in general, the extent of unidirectionality depends on a combination of all steps in the rotary cycle, but can be fully dominated by the directionality of a single step. In practically all of the overcrowded alkene-based molecular motors, such as the motors developed by Feringa and coworkers, the energetic difference of the metastable- and stable states of the THI step drives the unidirectionality of the motors. For fully photochemically driven molecular motors, such as motors introduced in Sections 11.3.5 and 11.3.6, the quantum yields of individual forward and backward photoisomerization steps are crucial for unidirectionality.

For some structures, a step in the opposite rotational direction such as a thermal *E*/*Z*-isomerization can readily occur [48]. Usually, for molecular motors, as for structurally similar stilbenes, the barrier for thermal *E*/*Z*-isomerization is high (commonly exceeding 150 kJ $mol^{-1}$) [49]. Some molecular motors have a more favorable thermal *E*/*Z*-isomerization than THI, albeit only when barriers for THI are notably high [49]. This distinct thermal behavior is undesired for unidirectional rotation.

There are good indications that the extent of accommodation of folding in the rings adjacent to the central double bond is a crucial factor in the energetic profiles of THI, where more flexibility with respect to folding leads to a more facile slipping of the rotor over the stator [45]. A striking example is represented by the mechanistic pathways for THI for second-generation molecular motors, which involve a ring flip of the rotor followed by a slipping of the rotor over the stator and a ring flip of the stator. The structure of the molecular motor determines the stability of the intermediates and transition states and can therefore influence the most likely pathway for THI as well as the speed of the overall process [45].

An additional factor to be taken into consideration is the nature of the solvent. Many solvent parameters were investigated to probe the influence of the medium on the kinetics of molecular motors [50]. Most molecular motors are apolar and do not interact strongly with the solvent. THI rates are reduced in the presence of hydrogen bonding or π–π interactions between the motor and the solvent. The main kinetic effect of the medium was found to stem from the rearrangement of the solvent shell. Indeed, viscosity has a strong influence on the rate of THI [50]. A study of first-generation molecular motors with varying lengths of rigid "stirrer" substituents further shows the strong viscosity dependence. This effect increases with higher solvent displacement caused by longer substituents [51].

### 11.3.2 Tuning the Speed of Rotation

Understanding the factors that regulate the speed of rotation of molecular motors is crucial to apply or study these molecules. The speed of each individual step composing the rotational cycle determines the overall rate on a molecular level. Additionally, for an ensemble of molecules, the speed is influenced by the input of energy. As both thermal and photochemical steps are involved, external factors such as the temperature, photon flux, and absorption have the potential to be the determining factor to the overall speed.

For an individual molecule of a molecular motor, the THI is by far the slowest step. For an ensemble of molecular motors, there are two rate-limiting regimes. Motors with a high barrier for THI are *thermally rate limited*, meaning the speed of rotation, or frequency of rotational events, is mostly governed by the temperature [44].

For motors with a low energetic barrier for THI, the rotation process can become *photochemically rate limited* at common experimental conditions. At these conditions, the quantum yield for isomerization and absorptivity of the motor become more influential to the overall rotational frequency. The strongest influence in this regime becomes the light intensity of the irradiation source, and it is expected that under common experimental conditions (irradiation intensity of $20\,W\,cm^{-2}$), a speed of up to $\sim 10^2$ Hz is achievable [44]. Solution-based molecular motors with a speed for THI at room temperature in orders of magnitude ranging from $10^{-11}$ to $10^8$ Hz have been reported [44, 52].

As alkene photoisomerization of stilbenes and motors occurs within picoseconds after photon absorption (for a more detailed discussion see Section 11.3.3) [53], the rate-limiting step on a molecular level is the THI (a detailed overview on THI is presented in Schemes 11.3 and 11.4, Section 11.2.3 and additional discussion of this step can be found in Section 11.3.1). For example, for motor **6** (Figure 11.5), discussed earlier in Section 11.2.3, Eyring analysis by means of $^1$H-NMR spectroscopy provided a THI activation barrier of $105.2\,kJ\,mol^{-1}$ [41]. Being characterized by first-order kinetics, this barrier corresponds to a half-life of 7.6 days at 293.15 K (or a frequency of 1.51 μHz). The THI is, consequently, the rate-limiting step of the rotational cycle of the motors. Hence, it is used as the descriptor of the motor speed in terms of activation energy, half-life, or frequency. For a clear comparison of the rotary speed, in this section the half-life at 293.15 K is used.

In first-generation molecular motors, the two THI steps differ greatly in the *cis*- and *trans*-isomers (Section 11.2.3, Scheme 11.3). As a result of this asymmetry, structural modifications on first-generation molecular motors have an independent influence on both THI steps, where an increase in speed in one THI step can lead to a decrease in speed for the other THI step [58, 59].

Figure 11.5 illustrates a non-exhaustive selection of second-generation molecular motors, highlighting trends generally observed in the speeds of THI steps. Many additional factors than the ones described in this section have been shown to influence the THI rates [52]. For example, changing the nature of the heteroatom in

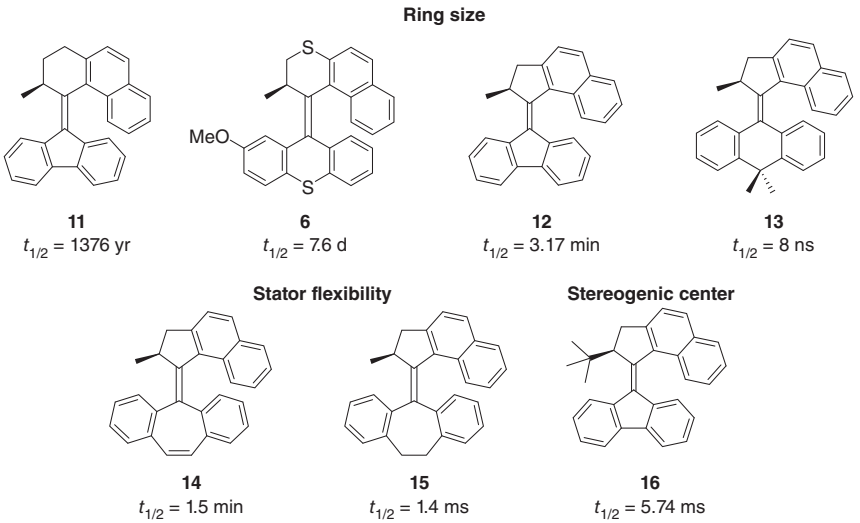


**Figure 11.5** Selected examples of various speeds, indicated by the half-life at 293.15 K, for second-generation molecular motors. Sources: Pollard et al. [41]; Bauer et al. [52]; Vicario et al. [54]; Vicario et al. [55]; Klok et al. [56]; Klok [57].

the rings adjacent to the central double bond [60] or introducing a donor–acceptor motif in conjugation with the double bond, changing the single-bond character of the alkene group [61]. Estimating THI rates *a priori* is a non-trivial task, where careful experimental and theoretical investigations are necessary for all new motor scaffolds.

The size and flexibility of the rings linked to the C=C axle and the size of the allylic substituent affect the THI half-lives significantly, so there is a delicate balance of steric and conformational effects. The most commonly used second-generation molecular motors have 5- or 6-membered rings connected to the axle. With a 6-membered ring in the rotor and a 5-membered ring in the stator, motor **11** (Figure 11.5) has relatively low steric hindrance in the fjord-region. However, this motor shows a remarkable low speed for rotation with a half-life of more than a thousand years [57]. Motor **6**, containing two 6-membered rings, has a slightly higher amount of steric hindrance in the fjord region, but a much faster THI, likely caused by more facile ring folding of the stator part [45].

When both rings adjacent to the C=C axle are 5-membered rings, such as in fluorenyl-based motor **12**, the speed is higher than the previously mentioned examples with 6-membered rotors. With 5-membered rings, conformational flexibility is lost. Consequently, the metastable states are most likely further destabilized, as steric hindrance cannot be accommodated by ring folding. With a higher-energy level of the metastable state compared to the energetic barrier of THI, the speed of this step increases [58].

The fastest overcrowded alkene-based motors reported to date are found in motors containing a 5-membered ring in the rotor and a 6-membered ring in the stator, as illustrated in motor **13** with a half-life of only 8 ns [52].

The significant difference in speed between the more rigid stator of **14** and the more flexible stator of **15** (half-lives of 1.5 minutes and 1.4 ms, respectively) shows that ring flexibility is a major contributor to the overall speed of THI. The considerable difference in speed between *tert*-butyl functionalized motor **16** and motor **12** (half-lives of 5.74 ms and 3.17 minutes, respectively) is illustrative of the strong influence of the allylic stereogenic group. This speed increase is caused by the relative rise in the energy level of the metastable state [55, 62].

### 11.3.3 Photoisomerization

The study of the excited-state photochemistry of overcrowded alkene-based molecular motors represents a more significant challenge, compared to the ground-state chemistry of the thermal isomerization steps. Absorption spectroscopy allows following the steady-state photochemical *E*/*Z*-isomerization with relative ease. The irradiation of a molecular motor in its stable state leads to a more strained, red-shifted, and higher-energy metastable state in a unimolecular process. However, as these processes occur in a picosecond timescale [53], ultrafast transient spectroscopy is required to record experimental data on the mechanisms during photoisomerization [63]. Alternatively, theoretical studies have shown to be a useful tool for the understanding of the photochemical pathways [64].

In the most commonly described situation for molecular motors (Figure 11.6), after absorption of a photon of the appropriate wavelength, an $S_1 \leftarrow S_0$ excitation, corresponding to a $\pi \rightarrow \pi^*$ transition, occurs [64], which leads to a reduced double-bond character and elongation of the axle olefinic bond [66]. This excitation is a vertical transition starting from the stable state of the motor to a Frank–Condon (FC) state. The initial excited state is a bright, fluorescent state that is limitedly affected by solvent polarity. This finding suggests the absence of significant change in dipole moment of the molecule upon light absorption and that charge transfer is not a key driving force for this excitation [67].

As it is typical in alkene photochemistry [68], conical intersections (CIs) play a central role in the photoisomerization mechanism of molecular motors [64, 69]. Transient spectroscopy, supported by calculations, indicates that the sloped topology of the excited-state potential energy surface for molecular motors shows a preference for unidirectional rotation in the photochemical step [70]. The twisted nature of the central double-bond axle, caused by the chirality of the molecular rotary motors, plays a crucial part in the motion during photorearrangement [64, 71].

In the excited state, the motor undergoes a barrierless, ultrafast relaxation toward a CI or an $S_1$ minimum in the order of 100 fs [63]. This process is likely a volume-conserved structural change as shown in ultrafast absorption studies revealing that this process is solvent friction independent [67]. It is confirmed that at the CI, a moderate twisting of the central olefinic axis occurs with increased pyramidalization of the stator axle carbon atom [72]. This mechanism of photoisomerization with pyramidalization and twisting is similar to other known stilbene photoisomerization dynamics [63, 73]. The pyramidalization and twist describe an inherently asymmetrical potential energy surface that leads to rotation around the axle in the excitation-relaxation step [53].

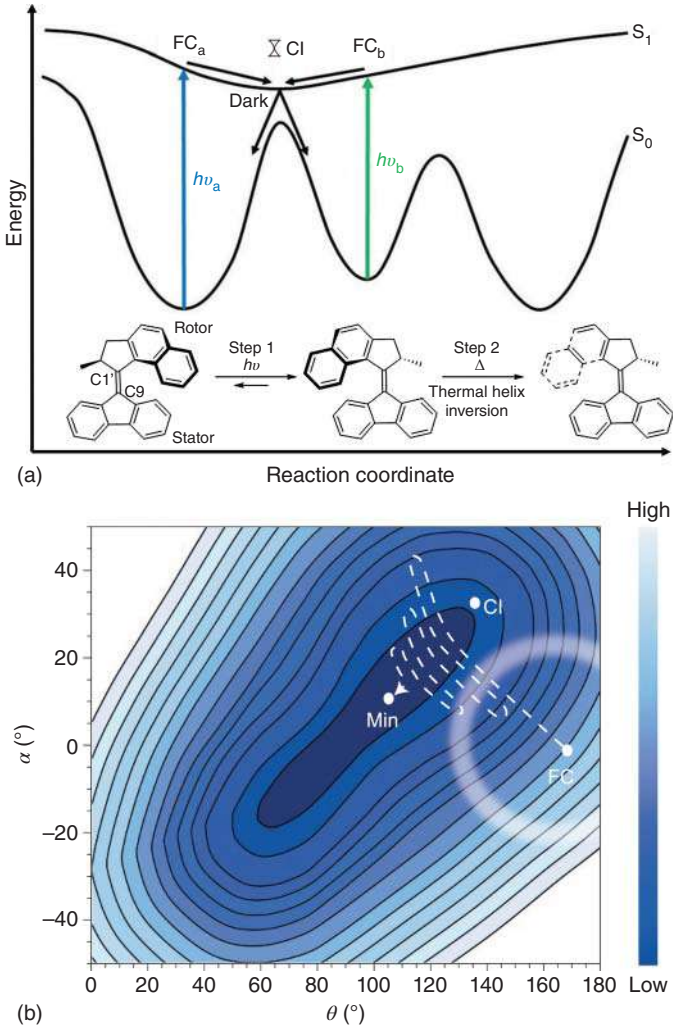


**Figure 11.6** (a) Schematic one-dimensional potential energy surface for a second-generation molecular motor. Source: Hall et al. [65]. (b) Schematic representation of the primary dynamics on the excited-state surface along the central double-bond dihedral angle ($\theta$) and C9-pyramidalization (α). Source: Conyard et al. [63].

It is interesting to notice that the region where the $S_0/S_1$ CIs and $S_1$ minimum are located, which is populated after the ultrafast relaxation from the bright Frank–Condon (FC) state, is a dark state. The lack of radiative relaxation is consistent with the relatively long lifetime of the dark state [72]. The exact nature and structure of this dark state is crucial for a full understanding of the photodynamics, but remains a topic of debate [66]. An $S_2$ excited state, reached via excitation to $S_1$ and an $S_1/S_2$ CI, has been suggested to be the dark state [74].

A fingerprint of the excited state of first- and second-generation molecular rotary motors can be obtained using ultrafast spectroscopic measurements, in the form

of an oscillation superimposed on the emission decay profile [63, 66, 67, 74–76]. This oscillation is reported to be caused by coherently excited vibrational modes in the excited state [63, 75]. Additionally, similar oscillations have been observed in the transient absorption spectra of both the bright and dark states [66]. These observed vibrations survive the structural relaxation starting from the FC to the dark state [66, 67]. An alternative explanation for the oscillations is the involvement of a dark $S_2$ excited state and repopulation of the bright $S_1$ excited state [74]. Other multistate models have been proposed for the excited-state dynamics of molecular motors [70].

From the CI between the excited and ground state, there is a "dark" relaxation that involves a large structural change within the molecule, consistent with the completion of the rotation around the central double-bond axis [67]. This transition to the ground state leads to a vibrationally hot ground state where the motor can continue the pathway of rotation to the metastable state [74]. This excess energy relaxes first via ultrafast intramolecular vibrational redistribution and is subsequently released to the environment [66].

Excitation of the stable state can also result in a relaxation pathway back to the initial state via radiative or non-radiative relaxation through CI or energetically lower-lying excited states. The reverse photoreaction that is from the metastable to the stable state can occur when the metastable state is irradiated. The pathway for reverse photoisomerization is distinct from the forward reaction and proceeds through a different CI [65].

The overall "efficiency" of the photochemical step can be expressed with the ratio of the isomers in the PSS, where the rates of the forward and reverse photoreaction are equal. The PSS is dependent on the quantum yield of either step and the absorptivity of each isomer. Consequently, the PSS is wavelength-dependent [75]. Because of the wavelength dependence of absorption and quantum yields, a favorable PSS can be obtained by selective irradiation where the stable state absorbs considerably more than the metastable state [67]. However, there often is significant overlap in absorption spectra of the stable and metastable isomers.

Quantum yields for helical overcrowded alkene molecular motor isomerization range from low to moderately high (experimentally determined in the range of 0.55–20%) [45, 63, 67, 77]. The electronic nature of a substituent that is not involved in the thermal steps can have a pronounced effect in the excited-state potential energy landscape and substituent-dependent quantum yields of isomerization have been reported [67].

A number of different effects and processes have been described or suggested in additional studies focusing on the details of the photochemical steps of various molecular motors. For a second-generation motor with a xanthylidene stator, the data were consistent with an initial fast relaxation to a local minimum on the $S_1$ excited-state energy surface [53]. A motor with rigid substituents was used to show that the movement during the photochemical step is mainly localized on the core structure of the motor, rather than the outer substituents [75]. For first-generation molecular motors, a similar twisting/pyramidalization mechanism for photoisomerization occurs and comparable involvement of CIs and ultrafast

initial relaxation steps. Notable differences are a longer-lived excited state, a red-shifted emissive state, and overall higher quantum yields [70, 76].

### 11.3.4 Tuning the Absorption Wavelength

A significant amount of work in the field of molecular motors and other photoswitches [78] has been performed into the tuning of the excitation wavelength. For the use of molecular motors in soft materials and biomedical applications, the ability to function without the use of UV irradiation would be highly beneficial. For biological or medicinal uses, an excitation wavelength inside the "therapeutic window" of 600–1200 nm is desired to avoid cell damage and have sufficient tissue penetration of light [79, 80].

A number of common strategies for red-shifting chromophores, such as the introduction of donor-acceptor motifs, the extension of the π-system, metal complexation, and intramolecular energy transfer, have been applied to molecular motors. A few examples are illustrated in Figure 11.7. In this section, all the PSS ratios of metastable:stable state are reported at the indicated wavelengths.

The introduction of a dimethylamino- and a nitro-substituent on the stator half of second-generation motor **17** shows the versatility of a donor–acceptor motif. A red-shift to an operational irradiation wavelength of 435 nm (PSS 90 : 10) compared to the parent motor (312 nm, PSS 92 : 8) was achieved [45, 81]. Further development of donor–acceptor motifs in molecular motors has led to absorbance up to 505 nm (PSS 24 : 76) for motor **18** [77].

Molecular motor **19** uses the strategy of extension of the π-system with a new, larger aromatic core in the stator. This synthetic modification has led to a red-shift of the operational wavelength up to 490 nm with a quite low PSS, but a commonly acceptable PSS of 76 : 24 at 420 nm. The parent motor with a fluorenyl stator has a PSS of 75 : 25 at 365 nm [82, 83].

Metal complexes have been used both directly conjugated to the C=C axle and connected via a linker. Molecular motor **20**, containing a 4,5-diazofluorenyl motif, was used as a ligand in a Ru(II) complex, leading to a shift in absorption spectrum up to 450 nm (PSS 36 : 64) [84]. By linking a palladium porphyrin complex to motor **21** as a "visible light antenna," molecular rotational motion was achieved with irradiation up to 532 nm (PSS 33 : 67) by absorption at the palladium porphyrin sensitizer and subsequent energy transfer to the motor core [85].

Using an organic two-photon absorber as a sensitizer linked to a second-generation molecular motor (**22**) allows using near-infrared light with an intensity and wavelength compatible with in vivo studies. It operates by two-photon excitation of the sensitizer and resonance energy transfer to the molecular rotary motor [86].

Finally, another strategy to achieve absorption wavelength alteration is to use a different photochromic core. Oxindole-based molecular motor **23** is functioning via the same fundamental steps as second-generation molecular motors, but has a significantly different, non-symmetric stator. This introduces a difference for both *E*/*Z*-photoisomerizations and both THIs akin to first-generation motors. The motor

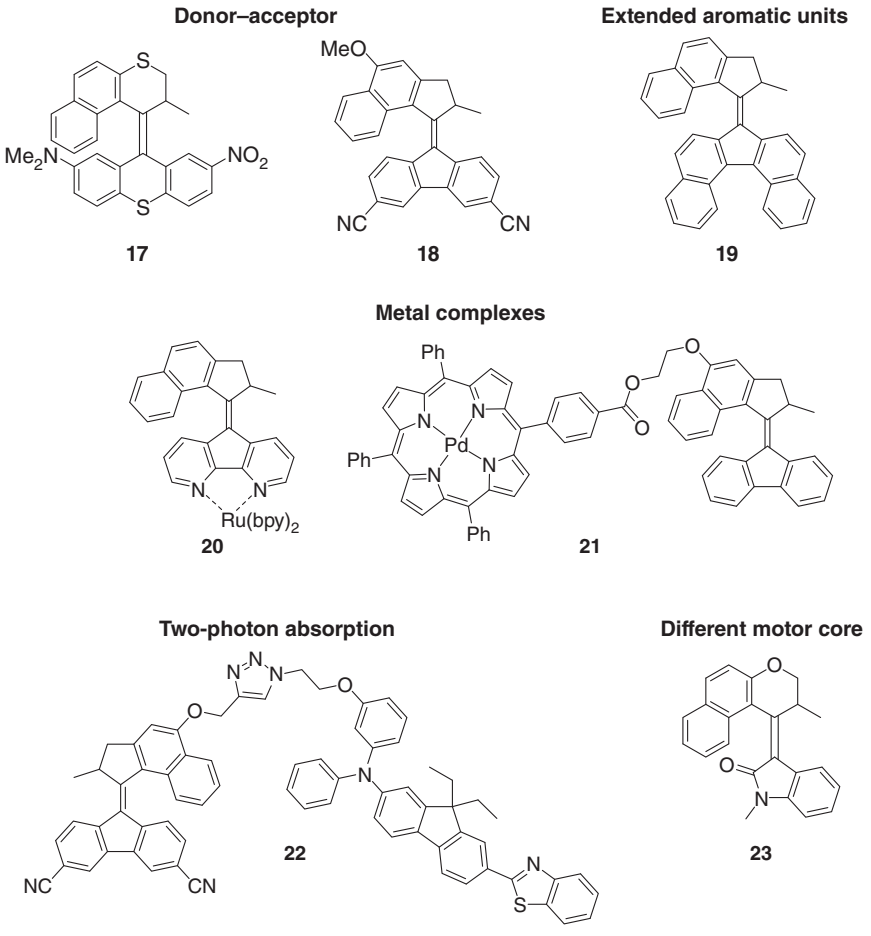


**Figure 11.7** Different strategies for red-shifted photon absorption to the visible light-driven molecular motors.

operates with an irradiation wavelength of 420 nm (PSS 94 : 6 and 62 : 38 for *Z* and *E*, respectively) [87].

### 11.3.5 Photochemical Motors

Some molecular rotary motors are based on purely photochemical steps such as the hemithioindigo-based motor developed by Dube and coworkers, which will be discussed in Chapter 13 [88]. In a recent example, Feringa and coworkers reported an overcrowded alkene-based molecular rotary motor based on only photochemical isomerizations (Scheme 11.5, **24**). This all-photochemical-driven, second-generation molecular motor with a phosphorous center in the stator can be converted into the four diastereomers by irradiation. A "shortcut" for rotation involving only three steps was achieved by thermal phosphine inversion [89].

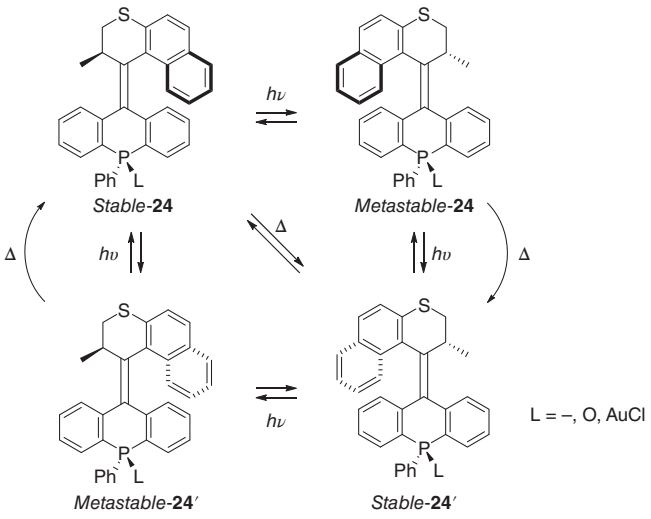


**Scheme 11.5** All-photochemical molecular motor. Source: Boursalian et al. [89].

### 11.3.6 Novel Motor Core Designs

The expansion of computational studies into molecular rotational motion in recent years has shown to be a powerful tool for new motor designs and study of the analytically challenging photochemical steps. Several structures have been proposed and investigated, mainly based on theoretical and computational studies (Figure 11.8). In many of these novel motor designs, the main challenges addressed are the improvement of quantum yields of the photochemical steps, fast photochemical steps, and the removal of thermal steps in the rotation mechanism. As the thermal steps in the rotary mechanism are rate-limiting for the rotation, a fully photochemical motor could be faster and temperature-independent. The thermal step is no longer the main ratchet and driving force for unidirectionality. Instead, unidirectionality is governed solely by the photochemical steps.

Olivucci and coworkers reported light-activated molecular motors based on a biomimetic indanylidene-pyrrolinium (IP) framework [71, 90, 91] inspired by natural photoswitchable molecules, such as rhodopsin, that operate in a unidirectional rotational way with high quantum yields [92]. In minimalistic IP **25**, the allylic methyl group only provides a small pretwisting of approximately 2° for the rotation axle, but this is sufficient to show rotational directionality of photoisomerization

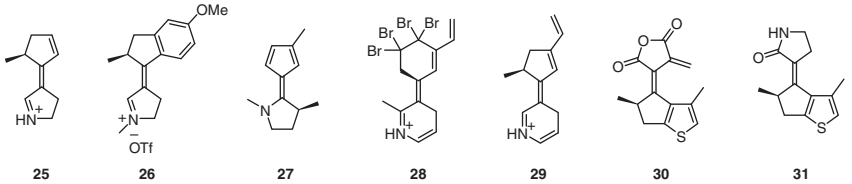


**Figure 11.8** Novel motor core designs.

[90]. In the further development using the same framework, the computational [71] and experimental [91] studies show that IP **26** could in principle work as a fast light-driven unidirectional molecular motor. The *Z*-to-*E* photoisomerization shows full clockwise unidirectional rotation. However, the unidirectionality of the *E*-to-*Z* isomerization is lacking. Indeed, a different degree of planarization and steric repulsion induce both clockwise and anticlockwise rotation.

Bicyclic enamine motor **27** was designed by Durbeej and coworkers and evaluated in molecular dynamics simulations and quantum chemical calculations as a fully photochemical molecular motor [93, 94]. The theoretical research into this motor shows unidirectional rotation for both *Z*-to-*E* and *E*-to-*Z* photoisomerization. These enamine motors could have relatively high quantum yields because the formation of excited-state aromaticity drives their rotation.

Durbeej and coworkers further designed visible light absorbing conjugated imine-based molecular motors such as **28** and **29**. Theoretical investigations predict high quantum yields and fast photoisomerizations for these type of motors [95, 96].

From quantum chemical calculations and molecular dynamics simulations, Filatov and coworkers showed that motors **30** and **31**, based on fulgide motifs, have the characteristics to operate as rotational molecular motors with high quantum yields and fast photochemical dynamics [97, 98].

These novel motor core designs can serve as an attractive stepping stone for mechanistic further understanding of photochemically driven molecular rotation and the development of motors with new properties.

## 11.4 Applications

As already predicted by Lehn in 2002 [99], the past decades have seen a general movement of the chemical sciences into the supramolecular realm. Some of the most promising applications for chiroptical molecular switches and motors, toward out-of-equilibrium and autonomous dynamic behavior in particular, are based on organized systems [100] and complex systems featuring collective action [101]. This field has now blossomed to such an extent that an entirely different chapter is justified. Therefore, supramolecular systems and smart materials such as responsive polymers [102], gels and liquid crystals [103] will be discussed elsewhere. In such a thriving field, there also remains much to discover for applications at the single molecular level [104].

### 11.4.1 Transfer of Chirality

The inherent ability to change stereochemical information by inverting helicity in both photochemical and thermal steps is a unique property of chiroptical molecular switches and motors that has found some fascinating applications in the previous decade. The chiral information stored in a chiroptical molecular motor or switch can be transferred to a second system, such as a newly formed stereogenic center or complex (*vide infra*). However, in contrast to commonly used chiral auxiliaries, the

absolute chirality can be inverted by a fast and highly efficient helix inversion. Since this inversion is induced by a simple stimulus such as light (stable to metastable) and/or temperature (metastable to stable), the process is orthogonal to many chemical reactions and (supra)molecular interactions, which means that in situ switching is often possible in reaction mixtures and complex systems.

The ability of a molecular motor to transfer chiral information at the single molecular level was first demonstrated in 2011 [105]. A first-generation xylene-based molecular motor **32** (Figure 11.9) with a highly efficient rotation cycle was functionalized with 4-dimethylaminopyridine (DMAP) and thiourea groups, and can cooperate to form a bifunctional organocatalyst [106]. In both *trans* isomers, these moieties are remote, but in the *cis* isomers, they are in close proximity. Moreover, the relative spatial orientation of the DMAP and thiourea groups adopts the helicity of the motor backbone. The ability of **32** to function as an enantioselective organocatalyst was demonstrated in an organocatalytic Michael addition of 2-methoxythiophenol to cyclohexenone (Figure 11.9c). In the presence of stable (2*R*,2′*R*)-(*P*,*P*)-*trans*-**32**, the racemic thiol product was formed slowly

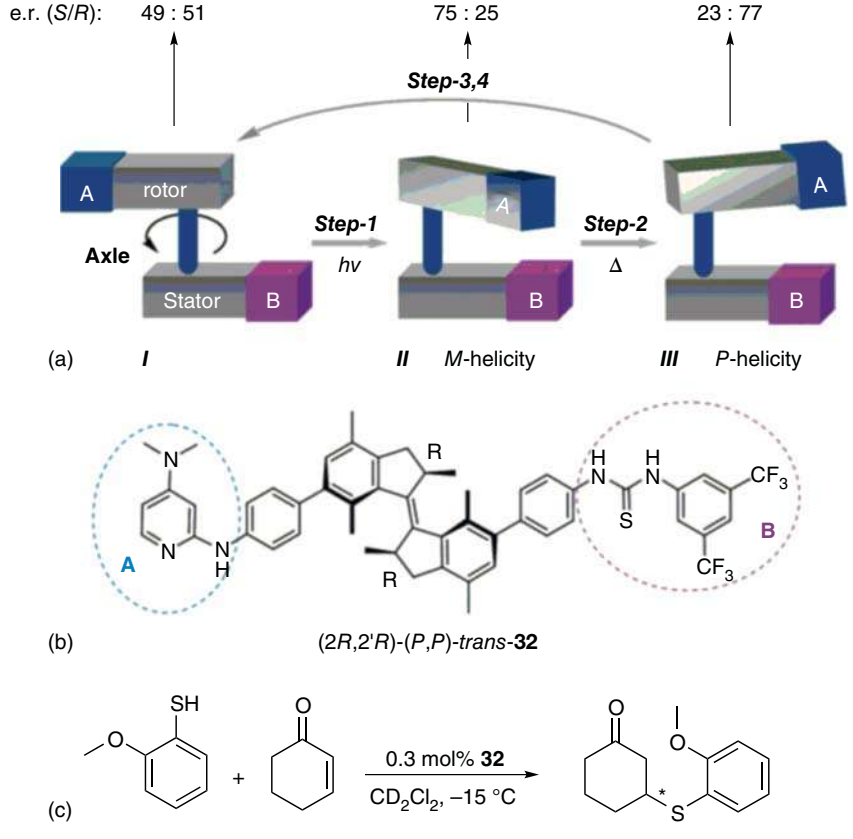


**Figure 11.9** Photoswitchable asymmetric catalysis. (a) Conceptual overview, (b) molecular structure of catalytic motor **32**, (c) Michael addition of 2-methoxy thiophenol to cyclohexanone. Source: Wang and Feringa [105].

as the DMAP and thiourea groups cannot cooperate, while the rate could be significantly enhanced by using either *cis* isomer. Remarkably, using the metastable (2*R*,2′*R*)-(*M*,*M*)-*cis* ligand led to selective formation of the (*S*)-enantiomer of the product (e.r. (*S*/*R*) 75 : 25), while using the stable (2*R*,2′*R*)-(*P*,*P*)-*cis* ligand inverted the enantioselectivity of the reaction (e.r. (*S*/*R*) 23 : 77). Photochemical isomerization from stable *trans*-**32** to metastable *cis*-**32**, i.e. switching from stage *I* to stage *II* of the catalyst (Figure 11.9), is highly efficient (>99%). By heating the catalyst at 70 °C for 40 minutes, the metastable stage *II*, *M*-helical catalyst could be converted to the stable stage *III*, *P*-helical catalyst. By irradiating stable *trans*-**32** in the presence of the reagents, the asymmetric Michael addition could be "switched on" in situ, leading to a comparable enantioselectivity and a slightly diminished reaction rate compared to the isolated metastable *cis* isomer.

Following this successful example, the same principle was applied to various molecular motors, reactions, and substrates [107]. Highlights include switchable, motor-based phosphine ligands, which have been used in asymmetric palladium catalysis [108] (Figure 11.10, **33**) and anion-binding catalysis (Figure 11.10, **34**) [110]. In a recent example, a photoresponsive phosphoramidite ligand based on bistable chiroptical switch **35** (Figure 11.10) was successfully used to tune the rate and stereochemical outcome of a copper-catalyzed conjugate addition [109]. In this complex, chiral information is transferred over five stereochemical elements: the fixed stereogenic carbon center of the switch, the helicity of the overcrowded alkene, the dynamic helical geometry and axial chirality of the attached biaryl unit and stereogenic phosphorous center, which is thermally stable at room temperature. In Figure 11.10b, the schematic overview shows the coupled inversion of helical and axial chirality. A maximum *ee* of 97% and maximum Δ*ee* of 106% were achieved for the copper-catalyzed addition of diethyl zinc to cyclohexanone.

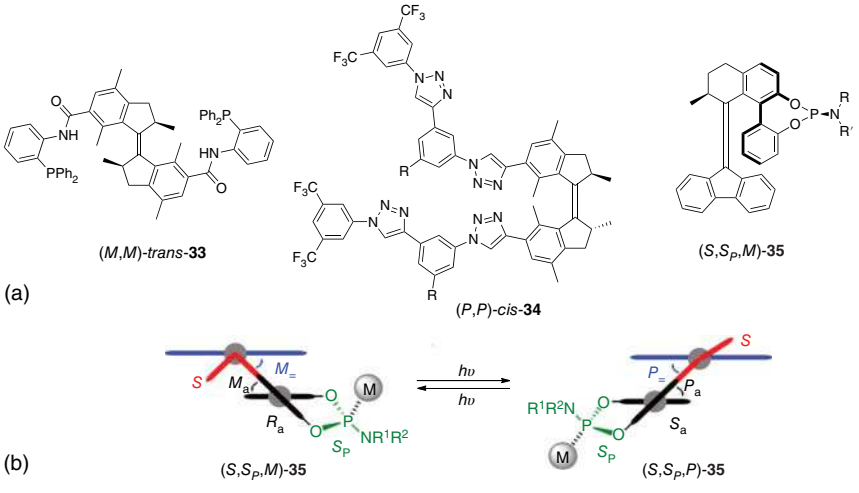


**Figure 11.10** (a) Several molecular motor-based photoswitchable catalysts and (b) a schematic top-down view of the switching of motor **35** upon metal complexation. Source: Modified from Pizzolato et al. [109].

While such results are not yet able to compete with traditional (non-responsive) phosphoramidite ligands, this particular example beautifully demonstrates the possibility of transferring the chiral information of a chiroptical switch or motor not simply from one molecule to the other, but across an intricate network of dynamic elements.

In the field of catalysis, future applications of photoresponsive systems may include in situ switching of selectivity and activity for sequential synthesis. Moreover, the transfer of chirality from chiroptical motors or switches to other responsive systems may prove a cornerstone in the design of more sophisticated molecular machinery or complex systems. Initial efforts toward dynamic transfer of chiral information focused on larger systems such as polymers and liquid crystalline materials. Such applications are discussed elsewhere (see Chapter 26). On a molecular scale, the principle was recently demonstrated using a short double-stranded helical copper complex (Figure 11.11) [111]. Taking inspiration from Lehn's supramolecular double helicates [112], a first-generation molecular motor was functionalized with two bipyridine ligands, which upon complexation to $Cu^+$ form a double helix. The stable (*P*,*P*′)-*trans* isomer forms oligomers in which the copper-complexed ligands adopt a defined *P* helical chirality. By irradiation with 312 nm light and subsequent heating the metastable (*M*,*M*′)-*cis* and stable (*P*,*P*′)-*cis* isomers, respectively, can be generated, which both form a dinuclear complex. CD spectroscopy was used to demonstrate that the THI is accompanied by an inversion of helical chirality. While this double helical system is relatively small, related work by Clayden and coworkers [113] and Feringa and Pijper [114], among others, already shows that chiral information may be transferred across single strands at multiple length scales.

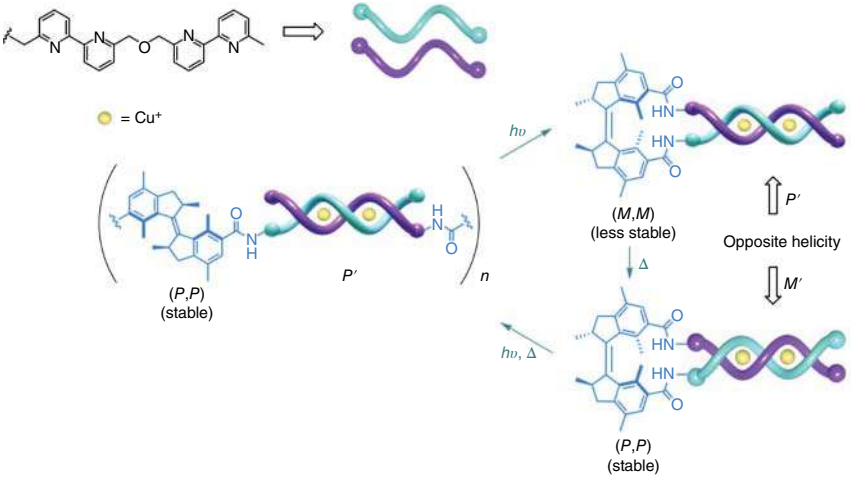


**Figure 11.11** Schematic overview of the switching of the helicity of oligomeric metal–ligand complexes. The switching of the helicity is governed by the motor core structure. Source: Zhao et al. [111].

## 11.4.2 Transfer of Motion

### 11.4.2.1 Coupled Rotary Systems

Much like the machines of the macroscopic world are fueled by motors via a complex network of cogwheels, ratchets, and pulleys, there is a sincere hope that one day, molecular motion on the single molecular scale may be transferred and amplified to fuel the nanomachinery of the future. The regulation and transfer of rotary motion are of essential importance to such systems, and the unidirectional rotation cycle of a light-driven molecular motor is perfectly suited to drive any envisioned machine on the nanoscale. Even so, early explorations toward controlling rotary motion using overcrowded alkenes precede the development of the molecular motor. In 1997, an overcrowded alkene-based chiroptical switch was functionalized with a xylene rotor (Figure 11.12a, **36**) [115]. Exchange Specstroscopy (EXSY)–NMR spectroscopy was used to investigate the rate of rotation around the biaryl axis of the xylene unit. Unexpectedly, the *trans* isomer has a higher barrier ($\Delta\Delta G_{303K}^{\ddagger} = 2.9\ \text{kJ mol}^{-1}$) than the *cis* isomer for xylene rotation. This design provided a starting point for the development of a range of more advanced coupled rotary systems, several of which are depicted in Figure 11.12. In the motor-based molecular "gearbox"

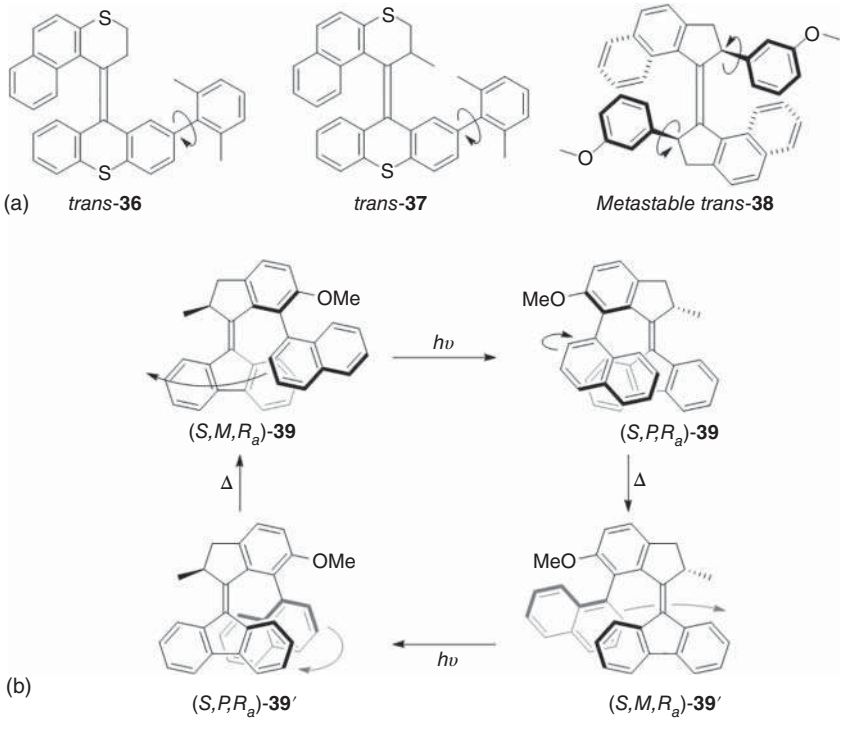


**Figure 11.12** (a) Several coupled rotary systems and (b) overview of the rotary cycle of locked synchronous motion of motor **39**.

**37** the *cis* isomers have a faster xylene biaryl rotation than the *trans* isomers, akin to **36**. Additionally, the *stable* isomers show faster xylene rotation than the respective *metastable* isomers, attributed to increased steric hindrance enforced by the pseudo-equatorial orientation of the rotor methyl substituents [116]. In first-generation motor-based coupled rotary system **38** (Figure 11.12a), rotation of the anisyl substituents was unhindered in three out of four of the isomers in the rotary cycle, but significantly slowed down in the metastable *trans* isomer [117].

While the speed of rotation of a secondary rotor may be regulated by the systems described above, there is no directionality. The molecular motors incorporated in structures **37** and **38** (Figure 11.12a) effectively function as four state switches. An important step in the direction of truly coupled rotary systems was achieved with the development of a second-generation motor functionalized with a naphthyl rotor (**39**), which displays a locked, synchronous rotary motion (Figure 11.12b) [118]. The design of **39** perfectly balances the barriers for motor and rotor rotation. Random thermal rotation around the biaryl axis is effectively blocked at the operating temperature. Instead, the rotor follows the rotation of the motor in a sequence of rotating and sliding motions, ensuring that the naphthyl unit always faces the motor with the same side. As the authors remark, this locked synchronous rotation is reminiscent of the rotation of the moon around the earth, and brings us a step closer to the design of more sophisticated geared molecular systems.

#### 11.4.2.2 Translation of Motion

While coupled rotary systems may, one day, drive complex artificial molecular machines, the direct conversion of unidirectional rotary motion to translational motion has already yielded impressive results. Nanocars are molecules consisting of wheels on a chassis, which were designed with the objective of moving them across a surface [119]. The first nanocar (Figure 11.13, **40**) was reported by Tour and coworkers and consisted of a central frame connecting four fullerene "wheels," which could be rolled across a flat gold surface by pulling with a Scanning Tunneling Microscopy (STM) tip [120]. Shortly thereafter, the group proposed a design for a motorized nanocar, containing a single light-driven rotary motor in the center of the chassis [121]. Further studies revealed that this design would not move on a copper surface, neither upon irradiation of the motor unit nor via STM tip pulling [122]. It was argued that the surface interactions for this particular nanocar were simply too high to allow for lateral movement. In the meantime, successful motorized motion on a surface had been demonstrated by Feringa and coworkers [123]. In this design **41** (Figure 11.13), four molecular motors were incorporated, functioning as the wheels. This design significantly reduces surface interactions, as the motor "paddlewheels" are both small and distorted. Electric pulses applied by the STM tip were used to fuel the nanocar on a 10-step, 6 nm long linear trajectory across the copper surface. Although motor rotation upon application of a voltage is thought to proceed *via* the same mechanism as light-induced rotation, movement of nanocar **41** across a surface upon irradiation has not yet been demonstrated. Recently, Tour, Grill, and coworkers reported light-induced translation across a surface for their "nanoroadster" **42** (Figure 11.13), thus demonstrating that overcrowded

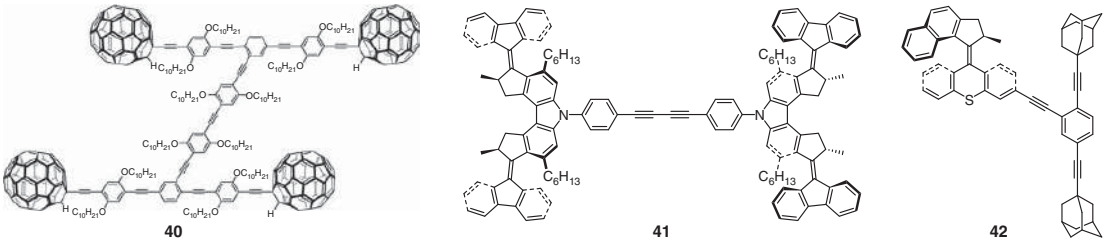


**Figure 11.13** Non-motorized (left), electrically driven (middle), and light-driven (right) nanovehicles. Source: Shirai et al. [120].

alkene-based molecular motors may be rotated by UV light while adsorbed on a surface [124]. While directional movement could not be observed, rotation of the motor led to an increased rate of diffusion across the copper surface.

Important steps for the future of nanoscale machinery and nanocars are to further develop the directional motion. Where nature has developed kinesin "walkers" to transport cargo in a guided unidirectional way [125], artificial molecular nanocars can strive to get closer to the level of control that nature has.

#### 11.4.2.3 Control Over Motion

Fueling nanomachines is on its own a challenge that will occupy chemists for years to come, but to perform complex operations, we will also need to exercise some degree of control over this motion. Feringa and coworkers have developed two different gated systems, which both have the power to reversibly halt rotation and thus act like brakes. These systems each comprise a second-generation molecular motor functionalized with either a pseudorotaxane [126] or a dithienylethene switch [127]. In each case, the "braking" functionality is turned on and off with a trigger that is orthogonal to the light used to rotate the motor, i.e. acid/base and higher wavelength light, respectively. In addition, the group reported a molecular motor in which the direction of rotation could be changed by a base-mediated epimerization of the asymmetric center responsible for determining the direction of rotation [128].

### 11.4.3 Biological Applications

The ability to switch a molecular structure and therefore its function using a trigger orthogonal to most processes in the cell, e.g. light, offers tremendous opportunities for biological applications [129, 130]. Containing an aromatic system at their core, overcrowded alkene-based molecular motors and switches are inherently hydrophobic, making applications in an aqueous environment challenging. The four-state switching cycle and unidirectional rotation of a molecular motor may be applied to create intriguing responsive systems with mechanical properties, hitherto impossible to achieve using two-state switches, such as azobenzenes, diarylethenes, or spiropyrans.

The use of chiroptical switches and molecular motors in an aqueous environment using aggregated systems, such as amphiphiles [131], is outside of the scope of this section and will be discussed elsewhere. For applications of molecular motors on the single molecular scale, solubilization using hydrophilic substituents has proven to be a largely successful strategy. Addition of two choline moieties to a first- or second-generation molecular motor was proven to be sufficient to completely dissolve the motors at concentrations up to 0.1 mM [132]. While first-generation motor **43** (Figure 11.14) suffered from minor degradation upon irradiation, most likely due to photoinduced water addition to the central double-bond, second-generation motor **44** (Figure 11.14) remained stable upon prolonged irradiation [132]. Notably, the solubilization of **44** was achieved by functionalizing only the lower half of the motor, leaving the possibility to further functionalize the top half for potential future application.

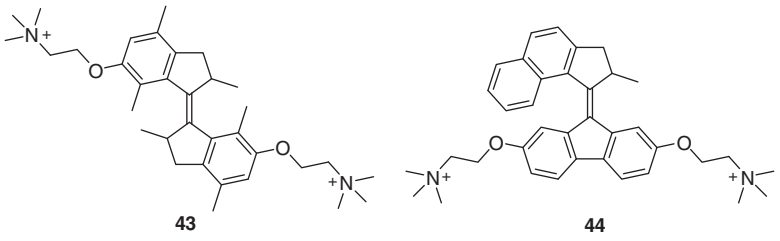


43 44

**Figure 11.14** Water-soluble light-driven molecular motors.

The hydrophobic nature of molecular motors can also be circumvented by incorporation into a much larger biomolecule. First-generation molecular motors were successfully adapted into building blocks for both peptides and oligonucleotides. In both cases, it was demonstrated that the large geometrical change associated with *trans*-to-*cis* isomerization of the relatively small motor unit could reversibly modify the secondary structure of the larger biohybrid system. For a motor-functionalized peptide, the *trans* isomer exists in a monomeric state, while isomerization to the *cis* isomer induces formation of a β-hairpin structure (see Figure 11.15) [133]. In an 8 base pair-long motor-functionalized oligonucleotide, both *cis* and *trans* isomers form a hairpin structure [134]. Isomerization of the motor proceeds despite its incorporation in a highly stable hybridized (double stranded) system, and a remarkable difference in duplex stability is observed upon 180° rotation.

In the non-aqueous parts of biological systems, the use of molecular motors is much more straightforward. Despite the limited amount of free space, both photochemical and thermal isomerization processes occur readily in aggregated systems such as nanofibers, nanotubes, and artificial muscles [135–137], making molecular motors ideal candidates for application in non-aqueous environments, such as cell membranes. Tour and coworkers loaded second-generation molecular motors modified with fluorescent tags in the cell membrane, and demonstrated that these are non-toxic [138]. They found that upon UV irradiation, the motors move across the membrane. As expected, exposure to UV light caused cell death, but the authors demonstrated that apoptosis was accelerated by more than 50% in the presence of molecular motors. This effect was attributed to disruption of the membrane by motor rotation. By modification of the motors with short peptides, specific cells could be targeted. In follow-up research, the group demonstrated that cell death can also be induced using molecular motors that rotate through two-photon excitation in the near-infrared domain, thus eliminating the need for damaging UV irradiation [139]. Finally, in vivo studies showed that light-activated molecular motors can cause severe damage in small eukaryotes, i.e. increased mortality in invertebrates such as *C. Elegans* and *Daphnia*, and skin lesions in hairless mice [140].

In a recent example, molecular rotary motion from motors attached to a glass surface was used to dynamically alter a surface, mediating a protein adhesion layer. This ultimately directed the fate of human bone-marrow-derived mesenchymal stem cells. The dynamic motor surface led to an increased differentiation into osteoblasts, while a non-rotating surface maintained higher multipotency [141].

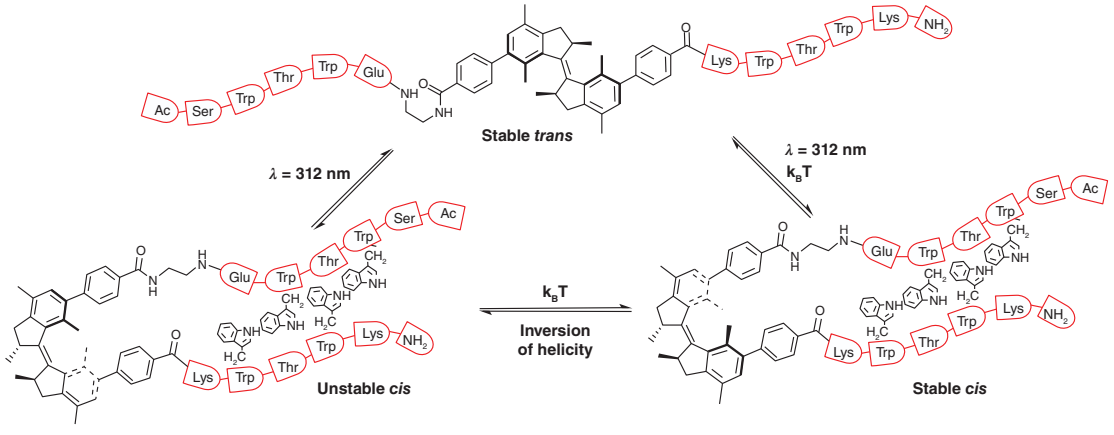


**Figure 11.15** First-generation molecular motor forming a β-hairpin structure. Source: Poloni et al. [133]. Licensed under CC BY-3.0.

Due to their conceptual similarity with biological molecular motors, application of artificial molecular motors in biological nanotechnology intuitively feels obvious. However, major challenges remain. While the possibility to target specific cells for cell death is certainly appealing, it needs to be determined whether the implied apoptosis will be an inevitable side effect to other in vivo applications. Meanwhile, solubility and stability remain an issue in aqueous environments.

### 11.4.4 Other Applications

The vast majority of research into chiroptical molecular switches and motors takes place in solution, where molecules are randomly oriented and continuously moving due to Brownian motion. As such, taking full advantage of their properties is challenging. Unidirectional rotation or chiral information can be easily transferred within the single molecule or complex, but to create an effect at larger length scales, orientational order needs to be imposed.

Surface functionalization is a straightforward method of creating large two-dimensional arrays of identically ordered molecules. Molecular motors have been functionalized to be attached to surfaces while ensuring enough free space around the motor to allow for unidirectional rotation [142, 143]. Taking inspiration from the landmark experiment of Kinosita and coworkers, in which rotation of a single ATPase protein motor was visualized on a surface [144], Cockroft, Feringa, Hofkens, and coworkers collaborated to visualize single molecular artificial motor rotation on a surface, using a tetrapodal second-generation molecular motor functionalized with a perylene diimide fluorophore, which is attached to the glass surface via electrostatic interaction [104, 145]. Using wide-field defocused fluorescence microscopy, the diffraction limit could be circumvented and the behavior of the motors upon irradiation with UV light could be observed. Although rotation was observed, it appeared that during the THI, the entire molecule was rotating with respect to the surface. This unexpected behavior was attributed to transient dissociation and reassociation of the surface attachment "feet". Covalent attachment of the legs to the surface is expected to solve this issue.

The evolution of data storage is a continuous story of shrinking bits into smaller spaces. Soon after the initial development of chiroptical molecular switches, optical data storage came to mind as an attractive potential application [32, 146]. A single bistable molecular switch could function as a bit, and a functionalized surface would possess tremendous storage capacity. For four-state rotary motors, the effect could be even more dramatic. Although such applications have not yet been realized using chiroptical switches and motors, synthesis of large, ordered arrays of photoswitches and motors is easily achieved in two or three dimensions [100], while the advance of nanophotonics has opened opportunities for overcoming the diffraction limit and enabling light–matter interactions at the nanoscale [147].

## 11.5 Perspective and Outlook

Chiroptical switches based on overcrowded alkenes have slowly been surpassed by rotary molecular motors, both in terms of understanding and applications. A molecular motor is undoubtedly the more versatile photoactive molecule of the two, but is also more complex to synthesize and to study. While the most exciting innovations may require to exploit the full potential of rotary molecular motors, it is beneficial to have tailor-made molecular switches or motors for the envisioned use.

Considering the broad scope of molecular motors available, the current research into new motors and the increasing insights in the fundamental processes of molecular motion, a myriad of robust tools for the selection and design of functional motors now exists. The development of new core designs, such as oxindole- or pyrrolinium-based systems, has the potential to evolve into new families of motors with unique properties.

The full understanding of the details of the photochemical steps in molecular motors is challenging, but has seen impressive progress taking advantage of ultrafast spectroscopy and theoretical chemistry. This knowledge has facilitated in the design of more and more efficient molecular unidirectional rotary motors. The tuning of the operational irradiation wavelengths opens up new possibilities for application, notably in biological systems and smart materials. The continually improving insight into motor photochemistry will advance new designs, widening the potential applications and tuning the motors to their specific applications.

The addressability of specific stereochemical information in molecular motors, which can be amplified or used in supramolecular systems or catalytic reactions, has been shown to be a powerful principle. This can serve as an interesting starting point for selectively modifying the chiral information present in molecular systems for information storage or using it in more complex programmable (supra-)molecular systems.

The application of chiroptical switches and motors in catalysis has as of yet seen several promising studies, but there is still significant potential for future investigation. Different states of the molecular motor can be used to tune the chirality of the motor and its environment specifically. The prospect of these catalytic motors to be applied in situ has already been demonstrated, leaving the door wide open for the development of highly efficient, green, photoswitchable catalytic systems, e.g. multitasking catalysis or sequential asymmetric synthesis.

Many reported and envisioned applications of motors require the translation of motion from the nano- to the meso- or macroscale, which needs amplification or coordination of the molecular machinery. The use of motors in supramolecular or multicomponent systems is a significant step into bridging the length scales where we can develop responsive systems and interactive materials. Overcoming the Brownian storm, increasing the quantum yields, as nature has done and developing tools to prove nanoscale motion in detail are challenges that remain. Rotary molecular motors are among the most exciting candidates for applications in nanotechnology. Several proof-of-principle coupled rotary systems have already been reported. The motorized directional motion of a nanocar across a surface and the unidirectional

rotation of a micro rod on a soft, liquid crystal surface, have demonstrated just how far a combination of synthetic experience, fundamental knowledge, and imagination can take us.

While molecular motors are unique in their unidirectional rotational motion, there have been limited direct uses of this type of motion. There are ample opportunities to take advantage of the fact that molecular motors are excellent to achieve rotary motion and can serve a crucial role in devices of the future based on nanoscale machines.

## References


1 Feringa, B.L. and Browne, W.R. (2011). *Molecular Switches*, vol. 1 & 2. Weinheim, DE: Wiley-VCH.
2 Albini, A. and Fagnoni, M. (2008). 1908: Giacomo Ciamician and the concept of green chemistry. *ChemSusChem* 1 (1): 63–66.
3 Bortolus, P. and Cauzzo, G. (1970). Thermal isomerization of stilbene and styrylpyridines in the liquid state. *Trans. Faraday Soc.* 66: 1161–1164.
4 Waldeck, D.H. (1991). Photoisomerization dynamics of stilbenes. *Chem. Rev.* 91 (3): 415–436.
5 Mallory, F.B. and Mallory, C.W. (1984). Photocyclization of stilbenes and related molecules. In: *Organic Reactions*, vol. 30 (ed. W.G. Dauben), 1–151. Wiley.
6 Villarón, D. and Wezenberg, S.J. (2020). Stiff-stilbene photoswitches: from fundamental studies to emergent applications. *Angew. Chem. Int. Ed.* 59 (32): 13192–13202.
7 Greb, L. and Lehn, J.-M. (2014). Light-driven molecular motors: imines as four-step or two-step unidirectional rotors. *J. Am. Chem. Soc.* 136 (38): 13114–13117.
8 Guentner, M., Schildhauer, M., Thumser, S. et al. (2015). Sunlight-powered kHz rotation of a hemithioindigo-based molecular motor. *Nat. Commun.* 6: 8406.
9 Kassem, S., Van Leeuwen, T., Lubbe, A.S. et al. (2017). Artificial molecular motors. *Chem. Soc. Rev.* 46 (9): 2592–2621.
10 Sauvage, J.P. (2017). From chemical topology to molecular machines (Nobel lecture). *Angew. Chem. Int. Ed.* 56 (37): 11080–11093.
11 Qiu, Y., Feng, Y., Guo, Q.H. et al. (2020). Pumps through the ages. *Chem* 6 (8): 1952–1977.
12 Baroncini, M., Silvi, S., and Credi, A. (2020). Photo- and redox-driven artificial molecular motors. *Chem. Rev.* 120 (1): 200–268.
13 Sauvage, J.P. and Gaspard, P. (eds.) (2010). *From Non-Covalent Assemblies to Molecular Machines*. Weinheim, DE: Wiley-VCH.
14 Burns, C.J. and Fraser Stoddart, J. (eds.) (2016). *The Nature of the Mechanical Bond: From Molecules to Machines*. Hoboken, NJ, USA: Wiley.
15 Moss, G.P. (1996). In: *Basic Terminology of Stereochemistry (IUPAC Recommendations 1996)*, *Pure & Appl. Chem.* 68 (12): 2193–2222.
16 Mason, S. (1988). Biomolecular homochirality. *Chem. Soc. Rev.* 17: 347–359.


**17** Crick, F. (1981). *Life Itself*. London, UK: McDonald & Co.

**18** Eliel, E.L. and Wilen, S.H. (1994). *Stereochemistry of Organic Compounds*. New York, NY, USA: Wiley.

**19** Koumura, N., Zijlstra, R.W.J., Van Delden, R.A. et al. (1999). Light-driven monodirectional molecular rotor. *Nature* 401: 152–155.

**20** Browne, W.R. and Feringa, B.L. (2006). Making molecular machines work. *Nat. Nanotechnol.* 1: 25–35.

**21** Feringa, B.L. (2007). The art of building small: from molecular switches to molecular motors. *J. Org. Chem.* 72 (18): 6635–6652.

**22** Feringa, B.L. (2017). The art of building small: from molecular switches to motors (Nobel lecture). *Angew. Chem. Int. Ed.* 56 (37): 11060–11078.

**23** Feringa, B.L. and Wynberg, H. (1977). Torsionally distorted olefins. Resolution of *cis*- and *trans*-4,4′-Bi-1,1′,2,2′,3,3′-hexahydrophenanthrylidene. *J. Am. Chem. Soc.* 99 (2): 602–603.

**24** Feringa, B.L., Jager, W.F., De Lange, B., and Meijer, E.W. (1991). Chiroptical molecular switch. *J. Am. Chem. Soc.* 113 (14): 5468–5470.

**25** Kistemaker, J.C.M., Štacko, P., Visser, J., and Feringa, B.L. (2015). Unidirectional rotary motion in achiral molecular motors. *Nat. Chem.* 7: 890–896.

**26** Koumura, N., Geertsema, E.M., Meetsma, A., and Feringa, B.L. (2000). Light-driven molecular rotor: unidirectional rotation controlled by a single stereogenic center. *J. Am. Chem. Soc.* 122 (48): 12005–12006.

**27** Biedermann, P.U. and Agranat, I. (2014). Stereochemistry of bistricyclic aromatic enes and related polycyclic systems. *Top. Curr. Chem.* 350: 177–278.

**28** Harada, N., Saito, A., Koumura, N. et al. (1997). Chemistry of unique chiral olefins. 1. Synthesis, enantioresolution, circular dichroism, and theoretical determination of the absolute stereochemistry of trans- and cis-1,1′,2,2′,3,3′,4,4′-Octahydro-4,4′- biphenanthrylidenes. *J. Am. Chem. Soc.* 119 (31): 7241–7248.

**29** Zijlstra, R.W.J., Jager, W.F., De Lange, B. et al. (1999). Chemistry of unique chiral olefins. 4. Theoretical studies of the racemization mechanism of trans- and cis-1,1′,2,2′,3,3′,4,4′-octahydro-4,4′- biphenanthrylidenes. *J. Org. Chem.* 64 (5): 1667–1674.

**30** Harada, N., Saito, A., Koumura, N. et al. (1997). Chemistry of unique chiral olefins. 2. Unexpected thermal racemization of cis-1,1′,2,2′,3,3′,4,4′-octahydro-4,4′- biphenanthrylidene. *J. Am. Chem. Soc.* 119 (31): 7249–7255.

**31** Feringa, B.L., Huck, N.P.M., and Van Doren, H.A. (1995). Chiroptical switching between liquid crystalline phases. *J. Am. Chem. Soc.* 117 (39): 9929–9930.

**32** Jager, W.F., De Jong, J.C., De Lange, B. et al. (1995). A highly stereoselective optical switching process based on donor – acceptor substituted dissymetric alkenes. *Angew. Chem. Int. Ed.* 34 (3): 348–350.

**33** Meijer, E.W. and Feringa, B.L. (1993). Chirality in nonlinear optics and optical switching. *Mol. Cryst. Liq. Cryst.* 235: 169–180.

**34** Huck, N.P.M. and Feringa, B.L. (1995). Dual-mode photoswitching of luminescence. *J. Chem. Soc., Chem. Commun.*: 1095–1096.


**35** Harada, N., Koumura, N., and Feringa, B.L. (1997). Chemistry of unique chiral olefins. 3. Synthesis and absolute stereochemistry of trans- and cis-1,1′,2,2′,3,3′,4,4′-octahydro-3,3′-dimethyl-4,4′- biphenanthrylidenes. *J. Am. Chem. Soc.* 119 (31): 7256–7264.

**36** Koumura, N., Geertsema, E.M., Van Gelder, M.B. et al. (2002). Second generation light-driven molecular motors. Unidirectional rotation controlled by a single stereogenic center with near-perfect photoequilibria and acceleration of the speed of rotation by structural modification. *J. Am. Chem. Soc.* 124 (18): 5037–5051.

**37** McMurry, J.E. (1989). Carbonyl-coupling reactions using low-valent titanium. *Chem. Rev.* 89 (7): 1513–1524.

**38** Feringa, B.L. (2001). In control of motion: from molecular switches to molecular motors. *Acc. Chem. Res.* 34 (6): 504–513.

**39** Ter Wiel, M.K.J., Vicario, J., Davey, S.G. et al. (2005). New procedure for the preparation of highly sterically hindered alkenes using a hypervalent iodine reagent. *Org. Biomol. Chem.* 3: 28–30.

**40** Ter Wiel, M.K.J., Van Delden, R.A., Meetsma, A., and Feringa, B.L. (2005). Light-driven molecular motors: stepwise thermal helix inversion during unidirectional rotation of sterically overcrowded biphenanthrylidenes. *J. Am. Chem. Soc.* 127 (41): 14208–14222.

**41** Pollard, M.M., Klok, M., Pijper, D., and Feringa, B.L. (2007). Rate acceleration of light-driven rotary molecular motors. *Adv. Funct. Mater.* 17 (5): 718–729.

**42** Klok, M., Janssen, L.P.B.M., Browne, W.R., and Feringa, B.L. (2009). The influence of viscosity on the functioning of molecular motors. *Faraday Discuss.* 143: 319–334.

**43** Astumian, R.D. (2017). How molecular motors work – insights from the molecular machinist's toolbox: the Nobel prize in chemistry 2016. *Chem. Sci.* 8 (2): 840–845.

**44** Klok, M., Browne, W.R., and Feringa, B.L. (2009). Kinetic analysis of the rotation rate of light-driven unidirectional molecular motors. *Phys. Chem. Chem. Phys.* 11 (40): 9124–9131.

**45** Cnossen, A., Kistemaker, J.C.M., Kojima, T., and Feringa, B.L. (2014). Structural dynamics of overcrowded alkene-based molecular motors during thermal isomerization. *J. Org. Chem.* 79 (3): 927–935.

**46** Kistemaker, J.C.M., Štacko, P., Roke, D. et al. (2017). Third-generation light-driven symmetric molecular motors. *J. Am. Chem. Soc.* 139 (28): 9650–9661.

**47** Berrocal, J.A., Pfeifer, L., Heijnen, D., and Feringa, B.L. (2020). Synthesis of core-modified third-generation light-driven molecular motors. *J. Org. Chem.* 85 (16): 10670–10680.

**48** Kuwahara, S., Suzuki, Y., Sugita, N. et al. (2018). Thermal E/Z isomerization in first generation molecular motors. *J. Org. Chem.* 83 (8): 4800–4804.

**49** Kistemaker, J.C.M., Pizzolato, S.F., Van Leeuwen, T. et al. (2016). Spectroscopic and theoretical identification of two thermal isomerization pathways for bistable chiral overcrowded alkenes. *Chem. Eur. J.* 22 (38): 13478–13487.


**50** Lubbe, A.S., Kistemaker, J.C.M., Smits, E.J., and Feringa, B.L. (2016). Solvent effects on the thermal isomerization of a rotary molecular motor. *Phys. Chem. Chem. Phys.* 18: 26725–26735.

**51** Chen, J., Kistemaker, J.C.M., Robertus, J., and Feringa, B.L. (2014). Molecular stirrers in action. *J. Am. Chem. Soc.* 136 (42): 14924–14932.

**52** Bauer, J., Hou, L., Kistemaker, J.C.M., and Feringa, B.L. (2014). Tuning the rotation rate of light-driven molecular motors. *J. Org. Chem.* 79 (10): 4446–4455.

**53** Augulis, R., Klok, M., Feringa, B.L., and Van Loosdrecht, P.H.M. (2009). Light-driven rotary molecular motors: an ultrafast optical study. *Phys. Status Solidi C* 6 (1): 181–184.

**54** Vicario, J., Meetsma, A., and Feringa, B.L. (2005). Controlling the speed of rotation in molecular motors. Dramatic acceleration of the rotary motion by structural modification. *Chem. Commun.*: 5910–5912.

**55** Vicario, J., Walko, M., Meetsma, A., and Feringa, B.L. (2006). Fine tuning of the rotary motion by structural modification in light driven unidirectional molecular motors. *J. Am. Chem. Soc.* 128 (15): 5127–5135.

**56** Klok, M., Boyle, N., Pryce, M.T. et al. (2008). MHz unidirectional rotation of molecular rotary motors. *J. Am. Chem. Soc.* 130 (32): 10484–10485.

**57** Klok, M. (2009). Motors for use in molecular nanotechnology. PhD thesis. University of Groningen.

**58** Roke, D., Wezenberg, S.J., and Feringa, B.L. (2018). Molecular rotary motors: unidirectional motion around double bonds. *Proc. Natl. Acad. Sci. U.S.A.* 115 (38): 9423–9431.

**59** Pollard, M.M., Meetsma, A., and Feringa, B.L. (2008). A redesign of light-driven rotary molecular motors. *Org. Biomol. Chem.* 6 (3): 507–512.

**60** Cnossen, A., Browne, W.R., and Feringa, B.L. (2014). Unidirectional light-driven molecular motors based on overcrowded alkenes. *Top. Curr. Chem.* 354: 139–162.

**61** Pijper, D., Van Delden, R.A., Meetsma, A., and Feringa, B.L. (2005). Acceleration of a nanomotor: electronic control of the rotary speed of a light-driven molecular rotor. *J. Am. Chem. Soc.* 127 (50): 17612–17613.

**62** Klok, M., Walko, M., Geertsema, E.M. et al. (2008). New mechanistic insight in the thermal helix inversion of second-generation molecular motors. *Chem. Eur. J.* 14 (35): 11183–11193.

**63** Conyard, J., Addison, K., Heisler, I.A. et al. (2012). Ultrafast dynamics in the power stroke of a molecular rotary motor. *Nat. Chem.* 4: 547–551.

**64** Kazaryan, A., Kistemaker, J.C.M., Schäfer, L.V. et al. (2010). Understanding the dynamics behind the photoisomerization of a light-driven fluorene molecular rotary motor. *J. Phys. Chem. A* 114 (15): 5058–5067.

**65** Hall, C.R., Browne, W.R., Feringa, B.L., and Meech, S.R. (2018). Mapping the excited-state potential energy surface of a photomolecular motor. *Angew. Chem. Int. Ed.* 57 (21): 6203–6207.

**66** Hall, C.R., Conyard, J., Heisler, I.A. et al. (2017). Ultrafast dynamics in light-driven molecular rotary motors probed by femtosecond stimulated Raman spectroscopy. *J. Am. Chem. Soc.* 139 (21): 7408–7414.


**67** Conyard, J., Cnossen, A., Browne, W.R. et al. (2014). Chemically optimizing operational efficiency of molecular rotary motors. *J. Am. Chem. Soc.* 136 (27): 9692–9700.

**68** Levine, B.G. and Martínez, T.J. (2007). Isomerization through conical intersections. *Annu. Rev. Phys. Chem.* 58: 613–634.

**69** Kazaryan, A., Lan, Z., Schäfer, L.V. et al. (2011). Surface hopping excited-state dynamics study of the photoisomerization of a light-driven fluorene molecular rotary motor. *J. Chem. Theory Comput.* 7 (7): 2189–2199.

**70** Liu, F. and Morokuma, K. (2012). Computational study on the working mechanism of a stilbene light-driven molecular rotary motor: sloped minimal energy path and unidirectional nonadiabatic photoisomerization. *J. Am. Chem. Soc.* 134 (10): 4864–4876.

**71** Filatov, M. and Olivucci, M. (2014). Designing conical intersections for light-driven single molecule rotary motors: from precessional to axial motion. *J. Org. Chem.* 79 (8): 3587–3600.

**72** Pang, X., Cui, X., Hu, D. et al. (2017). "Watching" the dark state in ultrafast nonadiabatic photoisomerization process of a light-driven molecular rotary motor. *J. Phys. Chem. A* 121 (6): 1240–1249.

**73** Takeuchi, S., Ruhman, S., Tsuneda, T. et al. (2008). Spectroscopic tracking of structural evolution in ultrafast stilbene photoisomerization. *Science* 322 (5904): 1073–1077.

**74** Amirjalayer, S., Cnossen, A., Browne, W.R. et al. (2016). Direct observation of a dark state in the photocycle of a light-driven molecular motor. *J. Phys. Chem. A* 120 (43): 8606–8612.

**75** Conyard, J., Štacko, P., Chen, J. et al. (2017). Ultrafast excited state dynamics in molecular motors: coupling of motor length to medium viscosity. *J. Phys. Chem. A* 121 (10): 2138–2150.

**76** Sardjan, A.S., Roy, P., Danowski, W. et al. (2020). Ultrafast excited state dynamics in a first generation photomolecular motor. *ChemPhysChem* 21 (7): 594–5990.

**77** Pfeifer, L., Scherübl, M., Fellert, M. et al. (2019). Photoefficient 2nd generation molecular motors responsive to visible light. *Chem. Sci.* 10: 8768–8773.

**78** Hansen, M.J., Lerch, M.M., Szymanski, W., and Feringa, B.L. (2016). Direct and versatile synthesis of red-shifted azobenzenes. *Angew. Chem. Int. Ed.* 55 (43): 13514–13518.

**79** Kalka, K., Merk, H., and Mukhtar, H. (2000). Photodynamic therapy in dermatology. *J. Am. Acad. Dermatol.* 42 (3): 389–413.

**80** Broichhagen, J., Frank, J.A., and Trauner, D. (2015). A roadmap to success in photopharmacology. *Acc. Chem. Res.* 48 (7): 1947–1960.

**81** Van Delden, R.A., Koumura, N., Schoevaars, A. et al. (2003). A donor-acceptor substituted molecular motor: unidirectional rotation driven by visible light. *Org. Biomol. Chem.* 1: 33–35.

**82** Van Leeuwen, T., Pol, J., Roke, D. et al. (2017). Visible-light excitation of a molecular motor with an extended aromatic core. *Org. Lett.* 19 (6): 1402–1405.


**83** Pollard, M.M., Wesenhagen, P.V., Pijper, D., and Feringa, B.L. (2008). On the effect of donor and acceptor substituents on the behaviour of light-driven rotary molecular motors. *Org. Biomol. Chem.* 6: 1605–1612.

**84** Wezenberg, S.J., Chen, K.Y., and Feringa, B.L. (2015). Visible-light-driven photoisomerization and increased rotation speed of a molecular motor acting as a ligand in a ruthenium(II) complex. *Angew. Chem. Int. Ed.* 54 (39): 11457–11461.

**85** Cnossen, A., Hou, L., Pollard, M.M. et al. (2012). Driving unidirectional molecular rotary motors with visible light by intra- and intermolecular energy transfer from palladium porphyrin. *J. Am. Chem. Soc.* 134 (42): 17613–17619.

**86** Pfeifer, L., Hoang, N.V., Scherübl, M. et al. (2020). Powering rotary molecular motors with low intensity near-infrared light. *Sci. Adv.* 6 (44): eabb6165.

**87** Roke, D., Sen, M., Danowski, W. et al. (2019). Visible-light-driven tunable molecular motors based on oxindole. *J. Am. Chem. Soc.* 141 (18): 7622–7627.

**88** Gerwien, A., Mayer, P., and Dube, H. (2018). Photon-only molecular motor with reverse temperature-dependent efficiency. *J. Am. Chem. Soc.* 140 (48): 16442–16446.

**89** Boursalian, G.B., Nijboer, E.R., Dorel, R. et al. (2020). All-photochemical rotation of molecular motors with a phosphorus stereoelement. *J. Am. Chem. Soc.* 142 (39): 16868–16876.

**90** Marchand, G., Eng, J., Schapiro, I. et al. (2015). Directionality of double-bond photoisomerization dynamics induced by a single stereogenic center. *J. Phys. Chem. Lett.* 6 (4): 599–604.

**91** Schapiro, I., Gueye, M., Paolino, M. et al. (2019). Synthesis, spectroscopy and QM/MM simulations of a biomimetic ultrafast light-driven molecular motor. *Photochem. Photobiol. Sci.* 18: 2259–2269.

**92** Strambi, A., Durbeej, B., Ferré, N., and Olivucci, M. (2010). Anabaena sensory rhodopsin is a light-driven unidirectional rotor. *Proc. Natl. Acad. Sci. U.S.A.* 107 (50): 21322–21326.

**93** Wang, J., Oruganti, B., and Durbeej, B. (2019). A straightforward route to aromatic excited states in molecular motors that improves photochemical efficiency. *ChemPhotoChem* 3 (6): 450–460.

**94** Oruganti, B., Wang, J., and Durbeej, B. (2017). Excited-state aromaticity improves molecular motors: a computational analysis. *Org. Lett.* 19 (18): 4818–4821.

**95** Wang, J. and Durbeej, B. (2018). Toward fast and efficient visible-light-driven molecular motors: a minimal design. *ChemistryOpen* 7 (8): 583–589.

**96** Wang, J. and Durbeej, B. (2019). Molecular motors with high quantum efficiency and visible-light responsiveness: meeting two challenges in one design. *Comput. Theor. Chem.* 1148: 27–32.

**97** Filatov, M., Paolino, M., Min, S.K., and Kim, K.S. (2018). Fulgides as light-driven molecular rotary motors: computational design of a prototype compound. *J. Phys. Chem. Lett.* 9 (17): 4995–5001.

**98** Filatov, M., Paolino, M., Min, S.K., and Choi, C.H. (2019). Design and photoisomerization dynamics of a new family of synthetic 2-stroke light driven molecular rotary motors. *Chem. Commun.*: 5247–5250.


**99** Lehn, J.-M. (2002). Toward complex matter: supramolecular chemistry and self-organization. *Proc. Natl. Acad. Sci. U.S.A.* 99 (8): 4763–4768.

**100** Danowski, W., Van Leeuwen, T., Abdolahzadeh, S. et al. (2019). Unidirectional rotary motion in a metal–organic framework. *Nat. Nanotechnol.* 14: 488–494.

**101** Eelkema, R., Pollard, M.M., Vicario, J. et al. (2006). Nanomotor rotates microscale objects. *Nature* 440: 163.

**102** Van Leeuwen, T., Heideman, G.H., Zhao, D. et al. (2017). In situ control of polymer helicity with a non-covalently bound photoresponsive molecular motor dopant. *Chem. Commun.*: 6393–6396.

**103** Bosco, A., Jongejan, M.G.M., Eelkema, R. et al. (2008). Photoinduced reorganization of motor-doped chiral liquid crystals: bridging molecular isomerization and texture rotation. *J. Am. Chem. Soc.* 130 (44): 14615–14624.

**104** Krajnik, B., Chen, J., Watson, M.A. et al. (2017). Defocused imaging of UV-driven surface-bound molecular motors. *J. Am. Chem. Soc.* 139 (21): 7156–7159.

**105** Wang, J. and Feringa, B.L. (2011). Dynamic control of chiral space in a catalytic asymmetric reaction using a molecular motor. *Science* 331 (6023): 1429–1432.

**106** Doyle, A.G. and Jacobsen, E.N. (2007). Small-molecule H-bond donors in asymmetric catalysis. *Chem. Rev.* 107 (12): 5713–5743.

**107** Dorel, R. and Feringa, B.L. (2019). Photoswitchable catalysis based on the isomerisation of double bonds. *Chem. Commun.*: 6477–6486.

**108** Zhao, D., Neubauer, T.M., and Feringa, B.L. (2015). Dynamic control of chirality in phosphine ligands for enantioselective catalysis. *Nat. Commun.* 6: 6652.

**109** Pizzolato, S.F., Štacko, P., Kistemaker, J.C.M. et al. (2020). Phosphoramidite-based photoresponsive ligands displaying multifold transfer of chirality in dynamic enantioselective metal catalysis. *Nat. Catal.* 3: 488–496.

**110** Dorel, R. and Feringa, B.L. (2020). Stereodivergent anion binding catalysis with molecular motors. *Angew. Chem. Int. Ed.* 59 (2): 785–789.

**111** Zhao, D., Van Leeuwen, T., Cheng, J., and Feringa, B.L. (2016). Dynamic control of chirality and self-assembly of double-stranded helicates with light. *Nat. Chem.* 9: 250–256.

**112** Krämer, R., Lehn, J.-M., and Marquis-Rigault, A. (1993). Self-recognition in helicate self-assembly: spontaneous formation of helical metal complexes from mixtures of ligands and metal ions. *Proc. Natl. Acad. Sci. U.S.A.* 90: 5394–5398.

**113** Brown, R.A., Diemer, V., Webb, S.J., and Clayden, J. (2013). End-to-end conformational communication through a synthetic purinergic receptor by ligand-induced helicity switching. *Nat. Chem.* 5: 853–860.

**114** Pijper, D. and Feringa, B.L. (2007). Molecular transmission: controlling the twist sense of a helical polymer with a single light-driven molecular motor. *Angew. Chem. Int. Ed.* 46 (20): 3693–3696.

**115** Schoevaars, A.M., Kruizinga, W., Zijlstra, R.W.J. et al. (1997). Toward a switchable molecular rotor. Unexpected dynamic behavior of functionalized overcrowded alkenes. *J. Org. Chem.* 62 (15): 4943–4948.


**116** Ter Wiel, M.K.J., Van Delden, R.A., Meetsma, A., and Feringa, B.L. (2005). Control of rotor motion in a light-driven molecular motor: towards a molecular gearbox. *Org. Biomol. Chem.* 3: 4071–4076.

**117** Lubbe, A.S., Ruangsupapichat, N., Caroli, G., and Feringa, B.L. (2011). Control of rotor function in light-driven molecular motors. *J. Org. Chem.* 76 (21): 8599–8610.

**118** Štacko, P., Kistemaker, J.C.M., Van Leeuwen, T. et al. (2017). Locked synchronous rotor motion in a molecular motor. *Science* 356 (6341): 964–968.

**119** Shirai, Y., Morin, J.-F., Sasaki, T. et al. (2006). Recent progress on nanovehicles. *Chem. Soc. Rev.* 35: 1043–1055.

**120** Shirai, Y., Osgood, A.J., Zhao, Y. et al. (2005). Directional control in thermally driven single-molecule nanocars. *Nano Lett.* 5 (11): 2330–2334.

**121** Morin, J.F., Shirai, Y., and Tour, J.M. (2006). En route to a motorized nanocar. *Org. Lett.* 8 (8): 1713–1716.

**122** Chiang, P.T., Mielke, J., Godoy, J. et al. (2012). Toward a light-driven motorized nanocar: synthesis and initial imaging of single molecules. *ACS Nano* 6 (1): 592–597.

**123** Kudernac, T., Ruangsupapichat, N., Parschau, M. et al. (2011). Electrically driven directional motion of a four-wheeled molecule on a metal surface. *Nature* 479: 208–211.

**124** Saywell, A., Bakker, A., Mielke, J. et al. (2016). Light-induced translation of motorized molecules on a surface. *ACS Nano* 10 (12): 10945–10952.

**125** Xie, P. (2020). Theoretical analysis of dynamics of Kinesin molecular motors. *ACS Omega* 5 (11): 5721–5730.

**126** Qu, D.H. and Feringa, B.L. (2010). Controlling molecular rotary motion with a self-complexing lock. *Angew. Chem. Int. Ed.* 49 (6): 1107–1110.

**127** Roke, D., Stuckhardt, C., Danowski, W. et al. (2018). Light-gated rotation in a molecular motor functionalized with a dithienylethene switch. *Angew. Chem. Int. Ed.* 57 (33): 10515–10519.

**128** Ruangsupapichat, N., Pollard, M.M., Harutyunyan, S.R., and Feringa, B.L. (2011). Reversing the direction in a light-driven rotary molecular motor. *Nat. Chem.* 3: 53–60.

**129** Szymański, W., Beierle, J.M., Kistemaker, H.A.V. et al. (2013). Reversible photocontrol of biological systems by the incorporation of molecular photoswitches. *Chem. Rev.* 113 (8): 6114–6178.

**130** Lerch, M.M., Hansen, M.J., Van Dam, G.M. et al. (2016). Emerging targets in photopharmacology. *Angew. Chem. Int. Ed.* 55 (37): 10978–10999.

**131** Chen, S., Costil, R., Leung, F.K.-C., and Feringa, B.L. (2020). Self-assembly of photoresponsive molecular amphiphiles in aqueous media. *Angew. Chem. Int. Ed.* 60 (21): 11604–11627.

**132** Lubbe, A.S., Böhmer, C., Tosi, F. et al. (2018). Molecular motors in aqueous environment. *J. Org. Chem.* 83 (18): 11008–11018.

**133** Poloni, C., Stuart, M.C.A., Van der Meulen, P. et al. (2015). Light and heat control over secondary structure and amyloid-like fiber formation in an overcrowded-alkene-modified Trp zipper. *Chem. Sci.* 6: 7311–7318.

**134** Lubbe, A.S., Liu, Q., Smith, S.J. et al. (2018). Photoswitching of DNA hybridization using a molecular motor. *J. Am. Chem. Soc.* 140 (15): 5069–5076.

**135** Coleman, A.C., Beierle, J.M., Stuart, M.C.A. et al. (2011). Light-induced disassembly of self-assembled vesicle-capped nanotubes observed in real time. *Nat. Nanotechnol.* 6: 547–552.

**136** Franken, L.E., Wei, Y., Chen, J. et al. (2018). Solvent mixing to induce molecular motor aggregation into bowl-shaped particles: underlying mechanism, particle nature, and application to control motor behavior. *J. Am. Chem. Soc.* 140 (25): 7860–7868.

**137** Chen, J., Leung, F.K.-C., Stuart, M.C.A. et al. (2018). Artificial muscle-like function from hierarchical supramolecular assembly of photoresponsive molecular motors. *Nat. Chem.* 10: 132–138.

**138** García-López, V., Chen, F., Nilewski, L.G. et al. (2017). Molecular machines open cell membranes. *Nature* 548: 567–572.

**139** Liu, D., García-López, V., Gunasekera, R.S. et al. (2019). Near-infrared light activates molecular nanomachines to drill into and kill cells. *ACS Nano* 13 (6): 6813–6823.

**140** Gunasekera, R.S., Galbadage, T., Ayala-Orozco, C. et al. (2020). Molecular nanomachines can destroy tissue or kill multicellular eukaryotes. *ACS Appl. Mater. Interfaces* 12 (12): 13657–13670.

**141** Zhou, Q., Chen, J., Luan, Y. et al. (2020). Unidirectional rotating molecular motors dynamically interact with adsorbed proteins to direct the fate of mesenchymal stem cells. *Sci. Adv.* 6 (5): eaay2756.

**142** Chen, K.-Y., Ivashenko, O., Carroll, G.T. et al. (2014). Control of surface wettability using tripodal light-activated molecular motors. *J. Am. Chem. Soc.* 136 (8): 3219–3224.

**143** Chen, K.-Y., Wezenberg, S.J., Carroll, G.T. et al. (2014). Tetrapodal molecular switches and motors: synthesis and photochemistry. *J. Org. Chem.* 79 (15): 7032–7040.

**144** Adachi, K., Yasuda, R., Noji, H. et al. (2000). Stepping rotation of F1-ATPase visualized through angle-resolved single-fluorophore imaging. *Proc. Natl. Acad. Sci. U.S.A.* 97 (13): 7243–7247.

**145** Chen, J., Vachon, J., and Feringa, B.L. (2018). Design, synthesis, and isomerization studies of light-driven molecular motors for single molecular imaging. *J. Org. Chem.* 83 (11): 6025–6034.

**146** Feringa, B.L., Huck, N.P.M., and Schoevaars, A.M. (1996). Chiroptical molecular switches. *Adv. Mater.* 8 (8): 681–684.

**147** Gu, M., Li, X., and Cao, Y. (2014). Optical storage arrays: a perspective for future big data storage. *Light Sci. Appl.* 3 (5): e177.

## 12 Stilbenes Revisited: Understanding the Mechanism of Mechanochemical Coupling

Robert T. O'Neill and Roman Boulatov

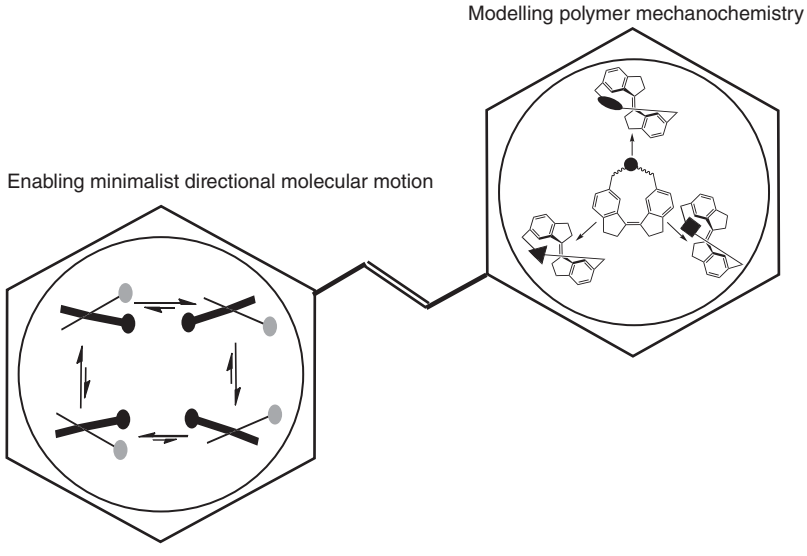


**Characteristic Features**

Modeling polymer mechanochemistry, enabling minimalist directional molecular motion.

**Key References**

Koumura, N. et al. (1999). Light-driven monodirectional molecular rotor. *Nature* 401: 152–155.

Yang, Q.Z. et al. (2009). A molecular force probe. *Nat. Nanotechnol.* 4: 302–306.

Akbulatov, S. et al. (2017). Experimentally realized mechanochemistry distinct from force-accelerated scission of loaded bonds. *Science* 357: 299–303.

# 12

# Stilbenes Revisited: Understanding the Mechanism of Mechanochemical Coupling

*Robert T. O'Neill*[1] *and Roman Boulatov*[1,2]

[1] *University of Liverpool, Department of Chemistry, Crown St., Liverpool, L69 7ZD, UK*
[2] *State Key Laboratory of Supramolecular Structure and Materials, College of Chemistry, Jilin University, Changchun, 130012, P. R. of China*

## 12.1 Introduction

Stilbene, or 1,2-diphenylethylene, exists in two forms, *Z* (or *cis*) and *E* (or *trans*) (Figure 12.1). The physical and chemical properties of *Z* and *E* stilbene differ widely, exemplified by their 120 °C difference in melting point (*Z* 5–6 °C, *E* 125 °C). The *Z* isomer is less stable than the *E* because of the unfavorable steric interactions between the *ortho, ortho′* hydrogens of its phenyl groups [1]. Many variations on the basic skeleton of stilbene exist, [2] (Figure 12.1) such as stiff stilbene which is widely used in supramolecular chemistry and bioactive stilbenes such as resveratrol, produced by some plants in response to pathogens and found in red wine, coming from the skin of red grapes [3].

The name stilbene derives from the Greek word *stilbos* that means shining, a reference to the bright colors of certain stilbene derivatives and to the relevance of light in its chemistry. The two isomers of many stilbenes interconvert readily upon exposure to UV or visible light. Photoisomerization proceeds via two mechanisms: the simultaneous rotation of the double bond and the adjacent single bond of the "hula-twist" mechanism means that only a single vinyl proton rotates out of the plane Figure 12.2. The "one-bond twist" mechanism requires rotation around the isomerizing C=C bond, with concomitant out-of-plane displacement of one Ph ring, whose motion during isomerization traces the surface of a cone [4, 5]. Which mechanism is favored depends on the stilbene structure and the surrounding environment. For example, the hula-twist path is favored by stilbenes in restricted environments [5] thanks to its low volume of activation but is blocked by the fused five membered rings in stiff stilbene. In addition to photoisomerization, *Z* stilbene is susceptible to photochemical ring closing to dihydrophenanthrene, whose spontaneous aerobic oxidation produces phenanthrene. This cyclization is impossible in stiff stilbene, making it better suited for applications in supramolecular chemistry [6]. The central C=C bond of stilbene is susceptible to oxidation, reduction, and electrocyclic additions [2].

*Molecular Photoswitches: Chemistry, Properties, and Applications*,
First Edition. Edited by Zbigniew L. Pianowski.


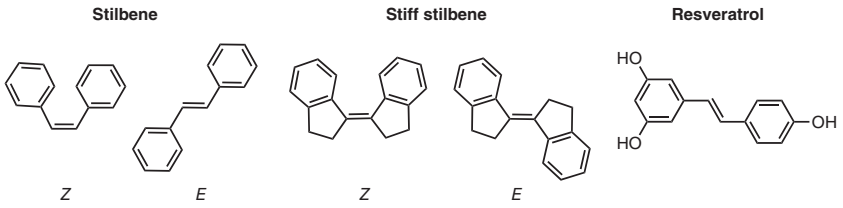


**Figure 12.1** Stilbene and its derivatives. The isomers of stilbene and several of its relevant derivatives.

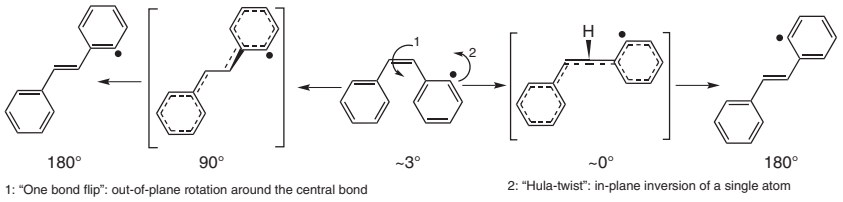


**Figure 12.2** Two mechanisms of thermal *Z*–*E* isomerization in stilbene. Path 2 is precluded by linking vinyl and aromatic C atoms, as in stiff stilbene, resulting in markedly different isomerization properties.

In the past decade, at least 10 reviews were published annually in which stilbene derivatives feature prominently, even excluding the innumerable reviews of resveratrol and related bioactive stilbenes [7]. This prominence attests to the importance of stilbene derivatives in diverse fields of natural sciences. Extensively reviewed early seminal studies of stilbene photochemistry and photophysics [8–11] have now been complemented by numerous reviews of the use of stilbenes in understanding subtle aspects of chemical bonding [12, 13] and energy flows in chemical reactions [14, 15] and in diverse applications in organic synthesis and catalysis [16, 17], material science [2, 18], biological studies [19–21], metrology [22, 23], and energy storage and conversion [2, 18, 24, 25]. The driving force behind much of this interest has been an increased demand for, and greater understanding of, the reliable photochemical switching that some stilbenes exhibit [6, 26–29].

Rather than add to this plentiful literature, we aim to highlight in this review the critical role that stilbene derivatives have so far played in advancing our fundamental understanding of an emerging area of intense contemporary interest at the interface of chemistry, material science, physics, and technology: coupling between mechanical motion and chemical reactions. Two broad and complementary manifestations of this coupling are generally recognized: mechanochemistry and molecular actuation. Both cover very diverse range of phenomena: in the former, directional motion at micro- to macroscale accelerates chemical reactions [30, 31]; in the latter, localized chemical reactions affect directional motion at micro- to macroscale [32]. While numerous reviews of both fields are available, the contribution of stilbene derivatives in uncovering the conceptual foundation of mechanochemical energy coupling, particularly in the form of polymer mechanochemistry and molecular motors, has been largely overlooked. We hope that an analysis of the approaches underlying the use

of stilbenes in these fields would yield insights that extend the specific experiments and would enable a wider adoption of the strategies.

## 12.2 Stiff Stilbene as a Molecular Force Probe

### 12.2.1 Introduction to Polymer Mechanochemistry

Polymer mechanochemistry studies how stretching a polymer chain changes the kinetic and thermodynamic stabilities of its constituent monomers. The field aims to utilize this knowledge in advancing our fundamental understanding of chemical reactivity and in developing new devices and materials [33–44]. The extreme aspect ratios of polymer chains predispose them to getting stretched in response to mechanical loads, making mechanochemistry important in almost any polymer application. A common example of mechanochemistry is the breaking of a stretched elastic band that requires fragmentation of polymer chains by scission of covalent C—C, S—S, and C—S bonds. Left undisturbed at room temperature, these bonds, the polymer chains they make and the elastic band would be stable for many years, suggesting that simply stretching a macroscopic object can accelerate certain reactions of its constituent molecules enormously. An overarching goal of mechanochemistry is therefore to develop a quantitative conceptual framework that describes the intricate sequence of physical processes which translate mechanical motion into such dramatic changes of chemical reactivity [40]. The framework must answer such questions as what is the minimum information about a polymer required to accurately predict its response to stretching? And how does the extent of stretching and stretching rate affect this?

No such framework currently exists and the questions such as those stated above can only be answered semi-quantitatively and in limited scenarios [33]. This lack of understanding has not precluded the identification of reactions that are accelerated by force, with over 30 examples reported in the last decade [34, 43]. This search has been guided by the qualitative considerations of how molecular strain affects chemical reactivity, informed largely by the increased reactivity of strained molecules developed by organic chemists over the last century [45]. This qualitative view is less well suited to designing more complex mechanochemical reaction sequences needed for practical applications of polymer mechanochemistry [46–48] and cannot guide the development of a conceptual framework needed to make polymer mechanochemistry a rigorous discipline.

The quantitative relationship between molecular strain and reaction rates in physical organic chemistry is based on the idea of strain energy, i.e. the difference in the free energy of the strained molecule compared to its strain-free analog [40, 45]. This strain-energy approach fails for polymers because energy is extensive [49, 50]. It increases with the size of the polymer whereas the reactivity of a monomer does not (i.e. reactivity is size-independent).

As a result, the modern quantitative understanding of polymer mechanochemistry relies on replacing strain energy with its gradient, force, along a specific molecular

axis. Force has two key properties that make it well suited for use in mechanochemical kinetics. First, it is intensive (size-independent) and thus applicable to quantifying the effect of molecular strain on the kinetic stability of a monomer that is a part of a strained molecule of any size, be it a long polymer, a short oligomer or even a small macrocycle of a certain molecular architecture. Second, it is a vector, allowing the distinct mechanochemical responses of a reactive site to stretching vs. compression to be captured [40].

The activation energy that determines the rate of a reaction in a molecule under force $f$ is treated as comprised of two contributions: those of the reacting molecule and of the complex and often difficult-to-identify set of physical processes that generate this force, often called "constraining potential." The former energy contribution reflects changes in chemical bonding and electronic structure of the reacting molecule. The change in the energy of the constraining potential captures evolution of the surroundings of the reacting molecule during the reaction. If the constraining potential is very soft (i.e. it accommodates changes in the molecular structure with minimal changes in its own physical behavior), the difference of its energy when coupled to the reactant or the transition state is the product of the force, $f$, and the change in the separation of the two atoms of the reacting molecule across which the force is assumed to act, $\langle \Delta q \rangle$, again between the two states that govern the reaction kinetics. Both are signed quantities, and their product can be negative, corresponding to reactions that are inhibited by tensile (stretching) force, positive (tensile-force accelerated reaction) or 0 (force-independent kinetics). In other words, a tensile force inhibits a reaction whose transition state is shorter than the reactant ($\langle \Delta q \rangle < 0$) and compressive force inhibits a reaction whose transition state is longer than the reactant ($\langle \Delta q \rangle > 0$). The reverse is true for accelerated reactions [37].

### 12.2.2 The Importance of Model Studies in Polymer Mechanochemistry

Fundamental understanding of polymer mechanochemistry requires experimental means to measure the kinetics and determine the mechanisms of diverse reactions as a function of force. The existing techniques, such as single-molecule force spectroscopy (SMFS) [51] and ultrasonication [33], fall short in three aspects. First, they allow either control over the applied force OR spectroscopic characterization of product structure but not both. Second, only reactions accelerated by force are observable. Third, inferring reaction kinetics requires multiple assumptions of unknown validity [33].

For example, SMFS allows a single macromolecule to be stretched and its length to be measured as a function of the applied force. Because physical quantities other than the applied force and chain extension are not quantifiable in such experiments, a change in the shape of the force/extension curve is the only indication of a reaction occurring in a stretched chain. Consequently, only reactions that either fracture the chain, or increase its contour length by many times the magnitude of thermal fluctuations are detectable. Conversely, sonication of polymer solutions provides a means of transiently stretching multiple chains at a time, at the expense of eliminating any

means of quantifying, much less controlling, the stretching force, stretching rate, and the duration of stretching. While spectroscopic analysis of sonicated solutions allows determination of the reaction products and estimate of the rate at which they appear, these rates do not reflect the microscopic reaction probabilities (as they normally do in chemical kinetics). Instead, they represent a complex convolution of multiple microscopic probabilities, including that for a chain to become trapped in the elongational flow and for a stretched chain to react before the flow disappears. As a result, molecular interpretations of sonication experiments are largely impossible. Reactions in melts and bulk solids under load are even less tractable. Consequently, these techniques yield a view of polymer mechanochemistry that is not simply qualitative, but exclusive of any but a very particular mechanochemical response.

Because of these limitations, fundamental studies of the effect of restoring force on localized reactivity (i.e. reactions that involve rearrangements of only a few covalent bonds) require studying small tractable model systems. The benefits of such models include the wider range of spectroscopic and computational tools suitable to study them compared to polymers and the ability to affect and quantify the full range of mechanochemical responses, instead of only accelerated fragmentation of chemical bonds that is currently observable in stretched polymers. The main drawback is the maximum restoring force generated in the reactive site by these model systems is fundamentally limited by the stabilities of covalent bonds comprising the rest of the molecule, to a value considerably lower the >5 nN limit routinely accessible experimentally by stretching polymers.

Early students of polymer mechanochemistry considered the ability to reproduce some of the unique reactivity of strained chains somewhat fantastical. The view probably reflected the gap between the attributes of known strained molecules and those needed to reproduce the strain of a monomer of a stretched macromolecule in a non-polymeric molecule. First, the majority of strained organic molecules manifest compressive strain, as evidenced, for example, by the contraction of bond angles in such molecules, relative to their strain-free analogs, whereas polymer mechanochemistry reflects tensile molecular strain. Second, the reliance on small rings and steric repulsion also means that no molecular fragment is strained predominantly along a single molecular axis.

The latter explains why early attempts to quantify kinetically significant molecular strain in many nonpolymeric strained molecules as restoring force rather than the strain energy were unproductive. The very large aspect ratio of macromolecules creates a molecular axis along which dimensional changes affect the molecular strain energy of a stretched macromolecule particularly strongly. As a result, variations in macromolecular strain energy due to even complex changes in molecular geometry associated with a localized reaction are approximated with useful accuracy from the energy gradient along this single axis (i.e. restoring force). In contrast, the vast majority of organic strained molecules lack such a privileged molecular axis. Quantum-chemical methods allow simple estimates of how accurately a restoring force of a strained molecule captures its kinetically significant strain. For a molecule in a stationary state, the restoring forces of all its internal coordinates are related by, in the harmonic limit, its compliance matrix [50].

Comparing the ratios of the restoring forces of key internal coordinates of the same reactive site in a strained molecule and when coupled to a harmonic spring yields an estimate of how closely the distribution of molecular strain within the reactive site in a strained nonpolymeric molecule reproduces that in a stretched polymer and hence how well force describes strain-induced reaction rates.

The ability to reproduce the molecular strain experienced by a monomer of a stretched polymer in a nonpolymeric molecule is a necessary but insufficient requirement to enable systematic model studies of polymer mechanochemistry. This strain must be imposed rapidly, varied systematically, and be amenable to reasonably accurate quantitation by calculations. For reactions that are accelerated by force, the rate at which the strain is imposed must compete with the rate of the mechanochemical reaction: once the latter exceeds the former, the restoring force cannot be increased further because the reactant would disappear [52]. The ability to vary the forces incrementally over a wide range and for diverse monomers is necessary to access reactivity and mechanisms that are qualitatively different from those of a strain-free reactant and to identify reliably trends between force, molecular structure, reactivity, and mechanisms. Lastly, one cannot study quantitatively the rate as a function of force if the value of the force is unknown [27].

### 12.2.3 Stiff Stilbene Is an Effective Molecular Force Probe

The only molecular architecture known so far to meet these criteria are macrocycles of stiff stilbene (Figure 12.3a). In these macrocycles, stiff stilbene is a molecular equivalent of the AFM in SMFS wherein a single polymer chain bridging an AFM tip and a glass slide (Figure 12.3b) is stretched. Instead of macromolecules, stiff stilbene acts as a molecular force probe to strain individual monomers in a manner reproducing the strain imposed by stretching a polymer chain. Stiff stilbene allows measurements of "intrinsic" mechanochemical reactivity, i.e. the dependence of the reaction rate on the stretching force experienced by the reacting moiety [54]. In contrast, SMFS measures apparent reactivity, which reflects the complex and incompletely understood relationship between the force responsible for the deflection of the AFM cantilever and the force experienced by the reacting moiety [55, 56].

Stiff stilbene can be used as a molecular force probe because, like most stilbene derivatives, its two isomers, *E* and *Z* differ significantly in their C6–C6′ separation (marked with * in Figure 12.3a). By connecting the C6, C6′ atoms with an appropriately sized molecular strap, i.e. one that is longer than the equilibrium C6, C6′ distance in *Z* but shorter than that in *E,* strained *E* macrocycles can be generated. A macroscopic analogy to a molecular force probe is a semi-rigid rod which bends when connected at both ends by a tether shorter than the rod itself. The rod exerts tensile force on the tether – the shorter the tether the higher the tensile force. Incorporating the same reactive group into varying-size linkers or "tethers" produces a series of *E* macrocycles in which the restoring force on the reactive moiety varies over 600 pN in 30–50 pN increments (Figure 12.4) [27].

Stiff stilbene is an effective molecular probe because of the combination of its high barrier of thermal isomerization (43 kcal $mol^{-1}$), rapid and efficient

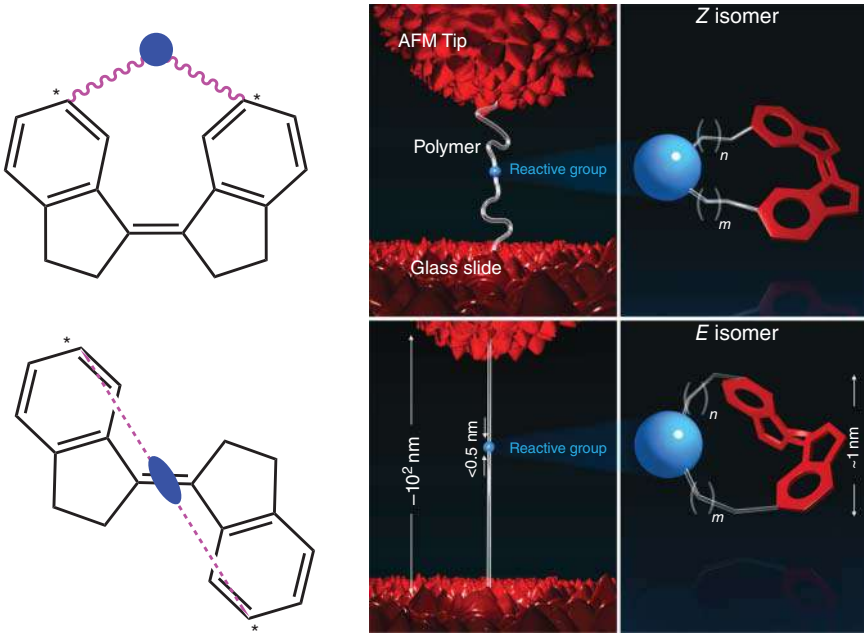


**Figure 12.3** Stiff stilbene as a force probe. (a) Shows how an appropriately sized linker containing a reactive group (blue circle) can be stretched by isomerization of the stilbene moiety. (b) Shows the difference between a macroscopic and a molecular force probe. Source: Yang et al. [53]/Reproduced with permission from Springer Nature.

photoisomerization and the significantly greater extinction coefficient of *Z* stiff stilbene compared to the *E* isomer at wavelengths above 360 nm [52]. These properties ensure that even highly strained *E* macrocycles needed to impose high forces on diverse monomers are sufficiently stable toward thermal relaxation, generated fast enough, and present in sufficient fraction in the photostationary state to enable detailed characterization of mechanochemical reactivity [27].

Compared to stilbene and its azo analogs, the C6, C6′ distance of stiff stilbene has much lower compliance because the additional rings eliminate rotations of the phenyl rings that allow stilbene and its azo analogs to relieve strain. As a result, macrocycles containing *E* stiff stilbene are considerably more strained that those containing *E* stilbene or *E* azobenzene of the same size.

### 12.2.4 How Intrinsic Mechanochemical Reactivity Is Measured with Stiff Stilbene

Four steps are required to quantify intrinsic mechanochemical reactivity of a monomer using stiff stilbene:

1. synthesize a series of increasingly large strain-free macrocycles containing *Z* stiff stilbene and the monomer;

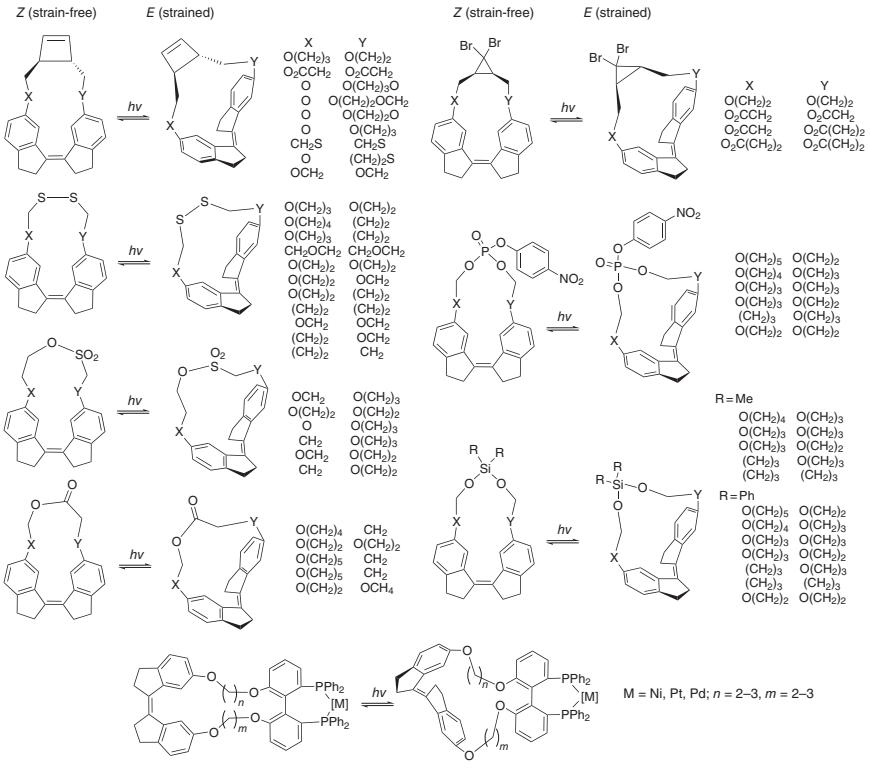


**Figure 12.4** The reported stiff stilbene macrocyclic series for model studies of covalent mechanochemistry. The variety of possible linker compositions allow a range of restoring force to be imposed on the functional group. The syntheses, characterizations, and reactivities of these macrocycles are reported in cyclobutenes [52, 53], disulfides [57–59], sulfonates [60], esters [61], dibromocyclopropane [62], phosphates and siloxanes [63], and metal complexes [64, 65]. Source: Modified from Huang and Boulatov [27].

2. generate strained *E* macrocycles by photoisomerization of *Z* stiff stilbene;
3. measure the reaction kinetics in each macrocycle, with *Z* macrocycles serving as strain-free reference for the *E* analogs, and
4. estimate the restoring force in each macrocycle by quantum-chemical calculations.

Below we briefly discuss each step.

A molecular force probe would be of limited impact in polymer mechanochemistry unless series of macrocycles of varying size are readily accessible synthetically for diverse reactive moieties. The ability to construct stiff stilbene from a pair of indanones by McMurry coupling, which tolerates a wide range of functional groups [66] contribute considerably to making stiff stilbene such an attractive force probe (Figure 12.5). Because McMurry reactions are often thermodynamically controlled, selective synthesis of *Z* macrocycles must rely on intramolecular coupling of two indanones connected with a linker which is too short to form strain-free *E* macrocycles. Otherwise, the more stable *E* isomer is generated preferentially. The required

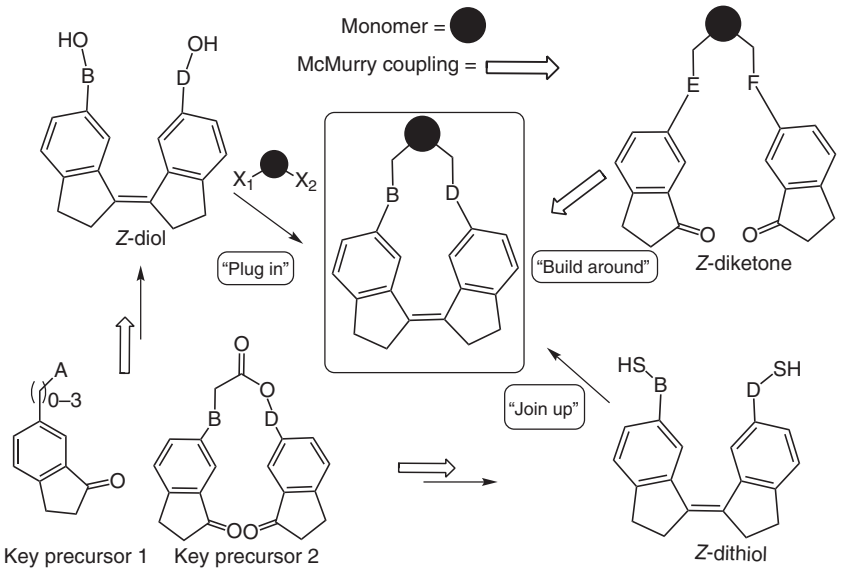


**Figure 12.5** The three established methods of synthesizing stiff stilbene macrocycles. Key precursor 1 generates both the *Z*-diketone and key precursor 2, which yields the *Z*-diol by a sequence of McMurry coupling and reduction with $LiAlH_4$. *Z*-dithiol is available from *Z*-diol. A = OH or $CO_2$. B, D, E, and F are made up of S, O, $CH_2$, and $CO_2$ moieties.

linker can be sacrificial to yield *Z* stiff stilbene diols for subsequent bridging by diverse monomers that do not withstand McMurry coupling, or it could already contain the monomer whose mechanochemistry is to be measured.

Commercial availability of six-substituted indanones, particularly hydroxyl and alkyl carboxy derivatives, accounts for the fact that only C6–C6′ constrained stiff stilbenes have been used in all model studies of mechanochemistry. Generation of *E* macrocycles by photoisomerization disfavors the use of carboxy stiff stilbenes because they are susceptible to yielding triplet states, which generates by-products upon irradiation.

*E* stiff stilbenes with C6, C6′ atoms bridged by fewer than 7 atoms are too strained to be studied by conventional techniques of chemical kinetics [52, 57], whereas 13+ atoms in the strap allow *E* stiff stilbene to adopt its minimum energy planar structure, resulting is strain-free macrocycles [27, 29]. All monomers studied to date contributed four to five atoms, although calculations suggest that monomers of up to seven atoms long [54] would still be compatible with a series of macrocycles across which the restoring force would vary by up to 600 pN. *E* stiff stilbene itself contributes eight atoms to the ring. The linkers connecting the monomer and stiff stilbene therefore can contribute between three and eight atoms, or ∼30% of the macrocycle size.

A perfect linker connecting the monomer to stiff stilbene would have no conformational preferences of its own, so that the compressive force of the C6, C6′ distance of stiff stilbene would equal the tensile force acting on the monomer. Such a linker does not exist. As a result, a fraction of tensile force generated by *E* stiff stilbene is

dissipated to strain molecular coordinates of the linker and the force transmitted to the monomer depends on the length of the linker, its composition and the position of heteroatoms relative to the C6, C6′ atoms of stiff stilbene. Linkers comprised of $sp^3$ atoms (e.g. aliphatic ethers and thioethers) appear to be closest to a perfect linker, whereas $sp^2$ atoms (e.g. esters) considerably reduce the fraction of transmitted force [53]. These dependences have been exploited to achieve the sub-100 pN increment in the force experienced by the monomer across a series of macrocycles of only five sizes. The capacity to vary the transmitted force by controlling the composition of the linkers in addition to the number of atoms they contribute to the macrocycle size justify the additional synthetic steps sometimes required to use carboxy indanones in the preparation of stiff stilbene macrocycles.

Three strategies for efficient macrocyclization of *Z* stiff stilbenes have been described, referred to as "plug in," "join up" or "build around" (Figure 12.5). The first combines *Z* stiff stilbene diols with the monomer. Its advantage is generality: once a diverse collection of *Z* stiff stilbene diols is synthesized, multiple sets of macrocycles containing different monomers become readily accessible. Its disadvantage is the need for careful optimization of macrocyclization conditions by sequential $SN_2$ displacement. This method has been applied to monomers that are not compatible with McMurry coupling, such as phosphate esters and siloxanes. In the "build-around" approach the formation of Z stiff stilbene also yields the macrocycle, benefiting from the known capacity of McMurry coupling to yield large strain-free macrocycles. Consequently, macrocycles of different sizes and containing different monomers are accessible under similar conditions. The "join up" approach was used for the preparation of disulfide macrocycles.

Syntheses of strained *E* macrocycles exploit the efficient photoisomerization of *Z* stiff stilbene under irradiation at ~400 nm. Because the absorption spectrum of *Z* stiff stilbenes is bathochromically shifted relative to the *E* isomer, photostationary states enriched with *E* macrocycles are readily accessible. In all but the shortest macrocycles, *E* isomers were sufficiently stable to be isolated and studied independently of the *Z* analogs. However, since the determination of force-dependent kinetics requires the difference in the apparent activation free energy of the two isomers, $\Delta\Delta G^{\ddagger}$, rather than the absolute values, kinetic measurements on photostationary mixtures are preferred [63] because such competition experiments usually yield more accurate estimates of $\Delta\Delta G^{\ddagger}$ than those obtained from the difference of activation energies measurement individually.

Importantly, a fairly straightforward method has been developed for obtaining kinetics of substrate reactions in *E* macrocycles that are too labile to isolate or even to be present in spectroscopically detectable steady-state concentrations [52]. This scenario is only relevant for the smallest, and hence most strained, macrocycles, with at least two of the following three factors contributing to the low steady state concentration. First, the quantum yield of $Z \rightarrow E$ photoisomerization tends to decrease as the strain of the *E* macrocycle increases, although the origin of the effect remains unknown [29]. Second, the activation barrier of thermal $E \rightarrow Z$ isomerization decreases with strain, as expected. Third, substrate reactions that are accelerated by tensile load reduce lifetime of *E* macrocycle. If the substrate

reaction is irreversible, continuous irradiation of a solution of *Z* macrocycle results in substrate reaction, occurring in the strained *E* macrocycle, even if it is present at undetectable concentrations.

Regardless of whether the kinetic measurements are carried out on an isolated *E* macrocycle, the photostationary state or under continuous irradiation needed to maintain a steady-state concentration of a highly labile *E* macrocycle, the substrate kinetics is determined solely by the geometry of the *E* macrocycle and not by how it was generated. In other words, electronic excitation resulting from photon absorption, whether or not it yields the other isomer, does not contribute to the substrate reaction. The alternative, whereby the substrate reaction occurs before the newly formed *E* macrocycle dissipates excess energy resulting from photon absorption (so-called "hot ground state reactivity") has been shown [53, 67] to be inconsistent with the known dynamics of intermolecular vibrational relaxation which occurs on the timescale $>10^6$ times shorter than the fastest substrate reaction observed in stiff stilbene macrocycles. This conclusion is broadly consistent with the acceptance of the fact that hot ground state reactivity is largely impossible in condensed phases.

Multiple methods have been used to measure substrate kinetics in stiff stilbene macrocycles, including high performance liquid chromatography (HPLC), UV–vis, and NMR spectroscopies. Unlike reactions in stretched polymers, temperature-dependent kinetics and kinetic orders have been reported for all reactions in stiff stilbene macrocycles and in some [63] the computed reaction mechanisms were confirmed experimentally. These data allow a far more detailed analysis of the effect of tensile force on chemical reactivity than has been possible so far with polymeric reactants.

Once the kinetics of the substrate reaction is measured, it needs to be correlated with the restoring force of the strained monomer to derive intrinsic mechanochemical reactivity. No experimental method exists to measure the monomer-level restoring force in any molecule, whether a polymer chain strained in SMF experiment or a strained macrocycle. Instead, the force is estimated from quantum-chemical calculations that are validated against experimentally measured physical observables, such as activation free energies or force/extension curves [46, 47, 62, 68]. This approach assumes that if the calculations reproduce the measured activation free energies accurately, they also accurately reflect the molecular distortions responsible for the variation in reaction kinetics across the series of macrocycles. Thus, unlike most computations of polymer mechanochemistry, [69, 70] the force/rate correlations derived from stiff stilbene macrocycles are fully benchmarked against the experiment.

Multiple molecular coordinates (i.e. internuclear distances, bond angle, and torsions) of the monomer in an *E* macrocycle deviate from the equivalent molecular coordinates of the *Z* analog. Each of these coordinates has a restoring force. Some are better suited for analysis of force/rate relationships both because they are sufficiently different between the two macrocycles to allow accurate quantitation of the restoring force and because they support intuitive interpretation of the mechanochemical kinetics.

### 12.2.5 How Stiff Stilbene Advanced Our Understanding of Mechanochemistry

The key contributions of model studies to our current fundamental understanding of polymer mechanochemistry are validation of (i) the foundational assumption of mechanochemical kinetics, i.e. that the restoring force of a stretched monomer predicts its reactivity independent of how the force is generated, [62] (ii) a simple model of mechanochemistry kinetics of multistep reactions [59], and (iii) experimental demonstrations of force/rate correlations beyond accelerated molecular fragmentations [63] that constitute mechanochemistry in polymers.

#### 12.2.5.1 The Restoring Force of a Stretched Monomer Predicts Its Reactivity Independent of How the Force Is Generated

Predicting the mechanochemical behavior of a polymer from the properties of a single monomer has been a longstanding goal in mechanochemistry because it would greatly accelerate the search of new materials with useful and exploitable responses to mechanical loads [38, 39]. While in theory restoring force enables such predictions, their accuracy remained unknown until its validation on mechanochemical isomerization of *cis*-dialkyldibromocyclopropane (DBC) using a series of stiff stilbene macrocycles (Figure 12.6) [62]. Subsequently, the same experimentally validated computational method was applied successfully to three other mechanochemically active polymers [46, 47, 68].

The studies approach was to demonstrate that the force-dependent activation free energies, $\Delta G^{\ddagger}(f)$ of DBC isomerization, derived from a series of increasingly strained stiff stilbene macrocycles accurately predicted the previously measured

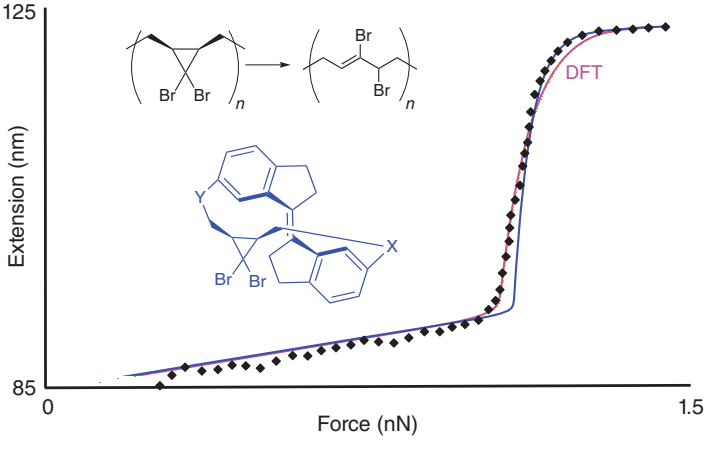


**Figure 12.6** Experimental verification that restore force is size independent. The experimental force extension curve of a polymer of DBC (black diamonds and structure) agrees well with force/extension curves predicted from force/rate correlations measured in a series of stiff stilbene macrocycles (blue line and structure) and that calculated quantum-chemically for a single DBC coupled to a virtual spring (magenta line). The abrupt elongation of the polymer at 1.2 nN reflects rapid isomerization of DBC to the longer olefin at this force. Linkers X and Y are defined in Figure 12.4. Source: Adopted from Wu et al. [71].

[71] force/extension curve of a polymer of DBC by SMFS. It used a series of five macrocycles of different size, which allowed the restoring force of the DBC moiety to be varied systematically from 0 to 400 pN. DBC in the smaller, more strained *E* macrocycles isomerized faster than those in their strain-free *Z* analogs, or in larger, less strained *E* congeners. The difference in the activation free energies within each *Z*/*E* pair of macrocycles, $\Delta\Delta G^{\ddagger}$, was correlated with the difference of the restoring forces and extrapolated to 1–2 nN range of SMFS measurements.

Both the macrocycles and direct quantum-chemical calculations of activation free energy of isomerization of *cis*-dimethyl-DBC with tensile force applied directly to the terminal C atoms yield energy as a function of the restoring force of an internal coordinate of the DBC moiety. In contrast, in SMFS only force acting at the ends of a μm-long chain is measured. The two forces are not generally identical because unlike temperature, which spreads uniformly over all molecular degrees of freedom in ensemble, microscopic force partitions among different degrees of freedom unequally [38]. The fraction of the force applied to the ends of a stretched chain that is transmitted to an internal coordinate (e.g. an internuclear distance), called mechanochemical coupling coefficient, is extrapolated from calculations on homologous series of increasingly long segments of the stretched chain. This coupling coefficient increases with applied force: at low force (<1 nN), only a small fraction of the force is transmitted to the individual monomer. At higher forces, the backbone increasingly resembles a perfect force transducer and the mechanochemical coupling coefficient approaches 1 [50, 55].

Once the mechanochemical coupling coefficient was estimated for the specific polymer measured by SMFS, its measured ensemble average force/extension curves were reproduced with startling accuracy (Figure 12.6) using both the extrapolated experimental $\Delta\Delta G^{\ddagger}$ and $\Delta G^{\ddagger}(f)$ calculated directly. Subsequent applications of this approach revealed the complex effect of single-molecule statistics in determining force/extension curves, [47] which were neglected in this first effort, suggesting that the excellent agreement between the predicted ensemble-average curves and measured stochastic ones may be fortuitous or reflects some cancelation of errors, or both. A proper statistical analysis of the experimental set of force/extension curves may have revealed up to 150 pN variance between the observed and predicted plateau forces, which, however, does not negate the primary finding of this study that force captures the effect of molecular strain a $10^{10}$–$10^{6}$ range of length scales and $10^{11}$-fold variation in reaction half-lives. This validation would be impossible unless the strain distribution of a monomer in a stretched macromolecule could be reproduced without the stretched polymer. More broadly, it illustrates the capacity of force to bridge the continuum and atomistic descriptions of matter, which is essential for detailed molecular understanding of the behavior of soft matter under macroscopic loads [39].

#### 12.2.5.2 Experimental Validation of a Simple Model of Mechanochemical Kinetics Over Complex Energy Landscapes

Most discussions of mechanochemical kinetics, including the most commonly used quantitative ansatzes, treat mechanochemical reactions as elementary, i.e. a

single energy barrier separating a reactant from its product(s). Yet, most reactions are complex, i.e. the reactant traverse multiple energy barriers to the product(s). Each barrier is changed by force differently, with two implications. First, accurate predictions of mechanochemical reactivity must explicitly account for force dependence of activation barriers that are not rate determining in strain-free reactions [63]. Distinct dependences of individual barriers on force make it likely that the nature of the rate determining step (RDS) is also force dependent, affecting not only the kinetics but also the product distribution and the capacity to exploit the underlying mechanochemistry. Second, measurements of mechanochemical kinetics offer an opportunity to characterize some of these kinetically invisible barriers. Nonrate-determining energy barriers are of interest because they can affect the distribution of the reaction products in strain-free reactions and are often critical in differentiating competing mechanistic hypotheses.

That a force/rate correlation of a multistep reaction allows accurate estimate of the height of a barrier that is kinetically invisible in a strain-free reaction was demonstrated experimentally on example of a two-step reduction of macrocyclic stiff-stilbene disulfides by phosphines (Figure 12.7) [59], in which the reversible formation of a zwitterionic intermediate is followed by its irreversible hydrolysis. The rate of this reaction is governed by the activation energy of the 2nd transition state (TS2) at force <0.2 nN but by the energy of TS1 at higher force. In this reaction, the 2nd barrier is force independent as the intermediate and TS2 are stabilized by force to the same extent. Yet, because at any force this stabilization exceeds that of TS1, at >0.2 nN TS1 becomes rate limiting. Although the reaction is accelerated by force of any magnitude, the slope of its $\Delta G^{\ddagger}$ vs. force dependence is different below and above 0.2 nN. Importantly, extrapolating $\Delta G^{\ddagger}(f)$ in the high-force regime yields the height of the first barrier. This fact was proven by estimating the TS1 energy independently by measuring the strain-free kinetics of reduction of the *Z* macrocycles as a function of $[H^+]$ (Figure 12.7). Because reversible protonation of the intermediate competes with its irreversible hydrolysis, the reaction rate in the presence of acid depends on both barriers.

Changes in the nature of the rate-determining barrier with force appear quite common in mechanochemical reactions, having been identified computationally in cycloreversions of cyclobutanes [46, 47] and maleimide/anthracene adducts [33, 48, 63]. A particularly interesting example of changing contributions of different barriers and competing reaction paths is offered by solvolysis of siloxanes, which is inhibited by tensile force of <0.15 nN and accelerated by larger force, as discussed in the Section 12.2.5.3.

#### 12.2.5.3 The Diversity of Force–Reactivity Relationships

All reactions demonstrated in stretched polymer chains for which the mechanochemical kinetics and mechanisms have been reported are dissociations of one or two backbone bonds that are accelerated $5.3 \pm 0.7$ fold per 0.1 nN of the restoring force of the scissile bond, despite their diverse molecular structures and reaction mechanisms. Detailed studies with the stiff stilbene molecular force probe demonstrate that this uniformity is not a fundamental aspect of polymer

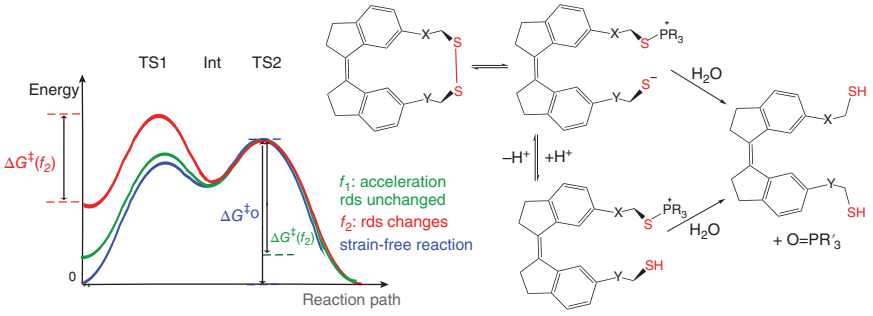


**Figure 12.7** Force-induced mechanistic cross over in a multibarrier reaction. Left, the energy change along the reaction pathway for a hypothetical reaction at various forces. The energy is referenced to that of the 2nd transition state (TS2) because it is unaffected by force. Right, the reaction used to verify the model energy profile. Competition between protonation of the intermediate and its reversal to the reactant was used to estimate the height of the inner barrier (defined by TS1), which it is not rate determining in strain-free macrocycles and kinetically invisible in neutral solution. Linkers X and Y are defined in Figure 12.4.

mechanochemistry by providing counterexamples of mechanochemical covalent bond dissociations that are (i) inhibited, (ii) unaffected, and (iii) accelerated by tensile force just within a single type of nucleophilic displacement reactions (Figure 12.8).

Despite their diversity, all experimental $\Delta G^{\ddagger}(f)$ correlations documents in stiff stilbene macrocycles are readily rationalized by comparing the molecular structures of the reactant and the rate-limiting transition states (Figure 12.9). As expected, the scissile bond elongates in the transition states of all reactions. The lack of the correlation between this elongation and the rate dependence reflects the local nature of the scissile bond: its elongation does not capture the structural differences between the two states that determines if stretching a reactant increases, decreases, and does not affect the height of the rate-determining barrier. For example, in phosphate hydrolysis force accelerates dissociation of the P—O bond orthogonal to the pulling axis because the reacting molecule elongates the most along the axis orthogonal to this bond even though the scissile bond contributes nothing to this elongation. In siloxanes, a similar elongation of the scissile S—O bond is more than offset by the contraction of the O–Si–O angle, leading to a net shortening of the molecule along the pulling axis. The same pair of countervailing structural changes occurs during sulfonate hydrolysis and thiol/disulfide exchange. In the former, bond elongation prevails and the reaction is accelerated by force; in the latter, the two balance each other almost precisely, resulting in a negligible force dependence of the reaction rate.

Later or loose transition states, which correspond to a greater elongation of the scissile bond and shorter bonds to the spectator ligands, would favor force-accelerated scission of backbone bonds, i.e. bonds approximately aligned with the pulling axis. Reactions proceeding through early or tight rate-determining transition states may even be inhibited by tensile force, despite resulting in chain fracture, because the scissile bond elongates too little to compensate for the

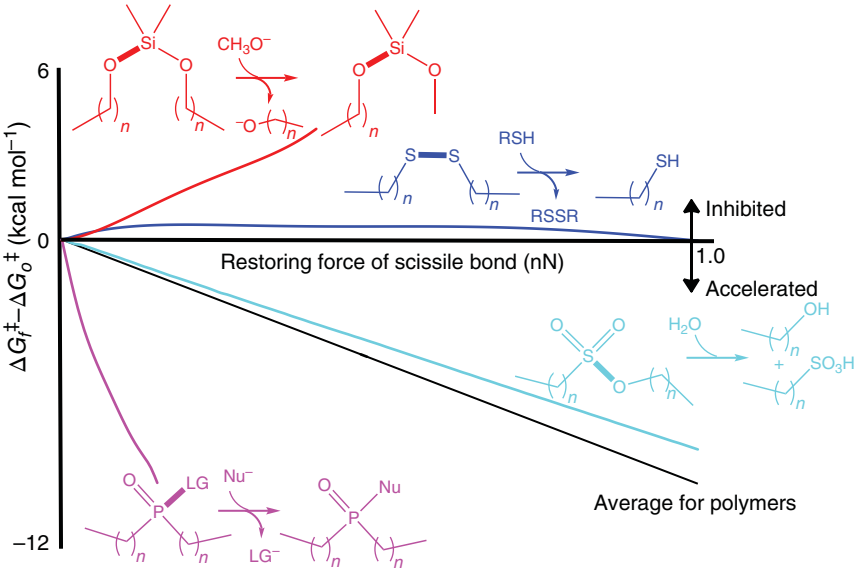


**Figure 12.8** The diversity of observable force–reactivity relationships in mechanochemical models compared to polymers. All known mechanochemical reactions in polymers are accelerated, on average 5.3 ± 0.7 fold per 0.1 nN of the restoring force of the scissile bond, whereas the full range of mechanochemical responses (accelerated, inhibited, or unaffected by tensile load) is experimentally observable using stiff stilbene as a molecular force probe. The force is applied at the methyl groups of the aliphatic, $(CH_2)_n$, chains. The data are plotted as a function of the restoring force of the scissile bond rather than the applied force to enable comparisons across structurally diverse reactants. Source: Kucharski et al. [58], Kucharski et al. [60], Akbulatov et al. [63].

contraction of the bond angles (Figure 12.10a). Conversely, force always accelerates nucleophilic displacement of groups orthogonal to the pulling axis (Figure 12.10b). Polymers containing electrophilic backbone atoms thus may be expected to manifest rich mechanochemical behavior in the presence of nucleophiles, driven by a competition between nucleophile-assisted fracture of a stretched backbone and dissociation of a side chain instead of the simple chain fracture characterizing most polymers. This richness could be potentially exploited, for example, for load-dependent delivery of molecular cargo (such as pharmaceuticals) or load-dependent dissolution of sacrificial scaffolds or encapsulants.

Static SMFS of proteins containing buried S—S bonds in the presence of nucleophilic reductants, such as dithiothreitol, suggested that force accelerates thiol/disulfide exchange [72], in seeming contradiction to the finding of practically force-insensitive kinetics in macrocyclic disulfides and in quantum-chemical calculations [58] (see [73] for a different perspective). The most plausible explanation in the increased accessibility of S—S bonds, which were buried within hydrophobic protein matrix to water-soluble thiol reactants, a biological mechanotransduction mechanism based on “cryptic sides” that is well established [74]. Likewise, expansive literature illustrates that small-molecule disulfides are considerably more

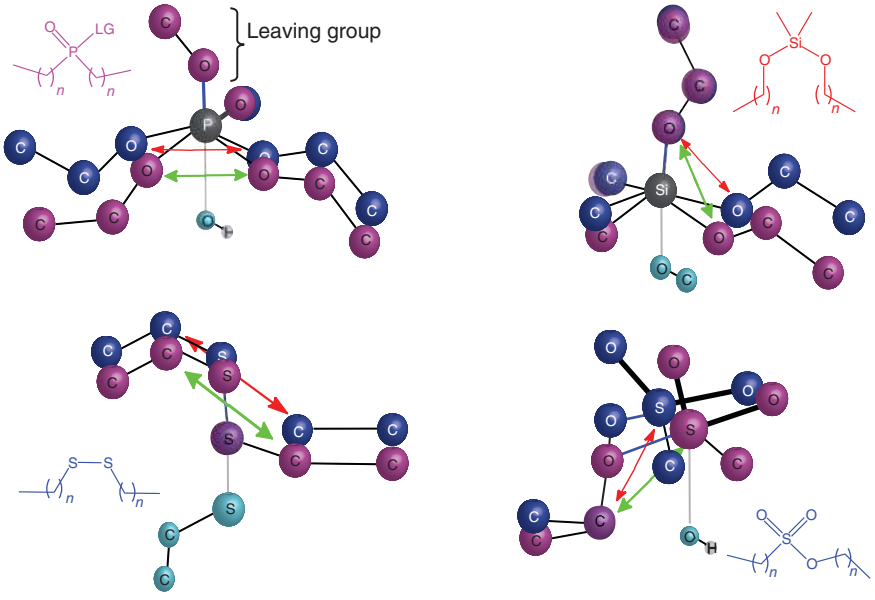


**Figure 12.9** The structural differences between the reactant and the rate-determining transition states that account for the diverse force-dependent kinetics of $S_N2$ reactions at P, Si, or S. All transition state structures are blue, reactant structures are magenta, and incoming nucleophile is cyan. H atoms are omitted for clarity. The tensile force is applied across the terminal C atoms: reactions in which this C· · ·C separation increases in the transition state (phosphate and sulfonate hydrolyses) are accelerated. Source: Kucharski et al. [58], Kucharski et al. [60], Akbulatov et al. [63].

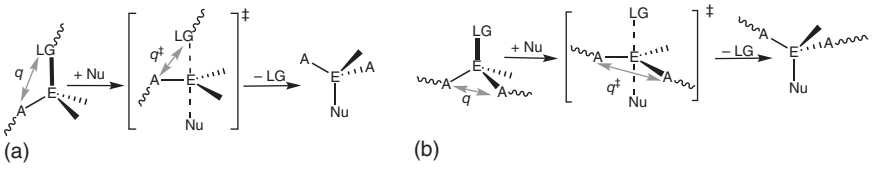


**Figure 12.10** An intuitive model of estimating mechanochemical kinetics of $S_N2$ reactions at an electrophilic atom, E, of a polymer backbone (wavy lines). Nu is a nucleophile and LG is the leaving group which may be either a part of the backbone (a) or a side chain (b). Force-dependent change in the activation barrier is estimated with useful accuracy as $f(q^{‡} - q)$, with the $q^{‡} - q$ difference reflecting changes in the bond angles and bond distances around the electrophilic atom.

reactive toward aqueous reductants than the S—S bonds in proteins, which has been exploited [75]. In contrast to reductive nucleophile-mediated cleavage, S—S bond homolysis is accelerated by force [76, 77].

The diversity of experimentally realized force/rate correlations in stiff stilbene macrocycles offered unique opportunity to test the validity of empirical models of mechanochemical kinetics. The simplest such model predicts that the change in the activation barrier is proportional to force but is silent on the nature of the proportionality constant. All $\Delta\Delta G^{‡}$ values measured in macrocycles change

approximately linearly with the restoring force. For all nucleophilic displacement reactions, using the change in the distance of the two atoms connecting the electrophilic center to the backbone (e.g. O· · ·O in phosphate or siloxane solvolysis, C· · ·O in sulfonate or ester hydrolysis, and S· · ·C in thiol/disulfide exchange, green and red arrows in Figure 12.8) yields estimates of $\Delta G^{\ddagger}(f)$ within a factor of 2 of the measured values (up to 0.5 nN) [63]. Subsequent computations indicated that for other reaction mechanisms, including unimolecular isomerizations of cyclobutene and DBC (Figure 12.8), a local coordinate exists that yields usefully accurate approximations of $\Delta G^{\ddagger}(f)$ [55, 78]. It also demonstrated that estimated $\Delta G^{\ddagger}(f)$ are highly sensitive to the choice of the local coordinate. However, with the exception of nucleophilic displacements, no general rules have emerged to identify such coordinates prior to detailed quantum-chemical calculations. Consequently, usefully accurate quantitative predictions of mechanochemical kinetics based on the activation parameters of strain-free reactions are not yet possible for the most common types of mechanochemical reactions.

Force-inhibited kinetics of siloxane solvolysis illustrated the importance of considering competing reaction mechanisms in extrapolating force-dependent kinetics from strain-free one. Whereas the dominant strain-free mechanism of solvolysis is inhibited by force, a higher energy path, which contributes negligible to strain-free kinetics, is stabilized by force. This results in a mechanistic turnover with the reaction mechanism changing at ∼1.6 nN (basic solvolysis) or ∼0.1 nN (neutral solvolysis) (Figure 12.11). As a result, the reaction is inhibited by force below these forces and is accelerated above. Such mechanistic crossovers are probably a common phenomenon in polymer mechanochemistry, but they are largely undetectable in stretched polymers.

## 12.3 Stilbenes in Fundamental Studies of Energy Transduction by Molecular Motors

### 12.3.1 Introduction to Molecular Machines

A molecular machine is a nanometer scale system designed to respond to an energy input with controlled motion of one component relative to another. A molecular motor is a subset of molecular machines capable of converting input energy into useful work, such as transporting molecules against a concentration gradient. Life would be impossible without the complex interactions of diverse molecular scale machines, which use chemical fuels to drive many life-enabling processes away from their thermodynamic equilibria [79]. The rich variety of biological tasks performed by the carefully controlled molecular motion of millions of such machines suggests fantastic rewards if scientists could reproduce these effects abiologically. The basic physics of creating useful work at the molecular scale was established more than half a century ago but for a long time insufficient synthetic knowledge prevented attempts at their synthesis, confining molecular machines to thought experiments [80]. Only in the last few decades have the synthetic and analytical tools developed

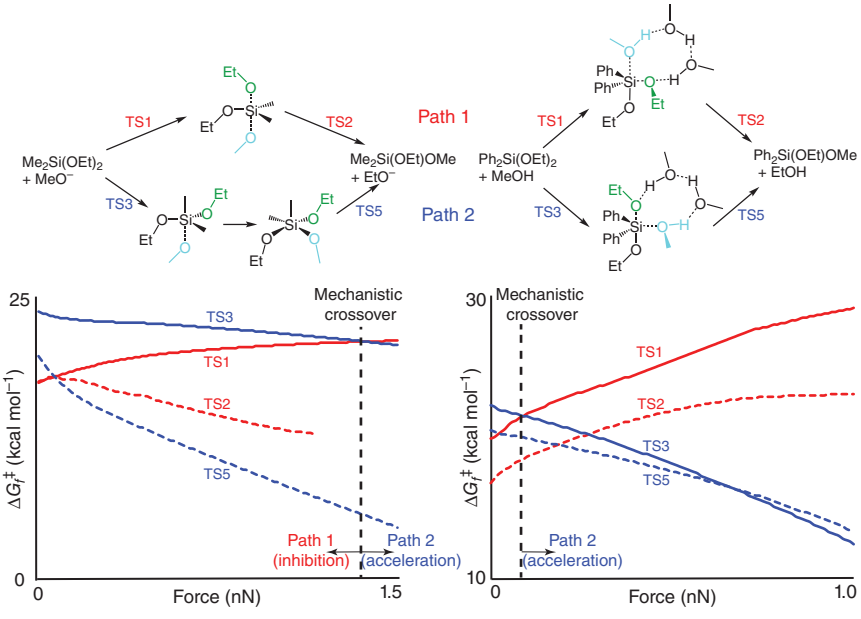


**Figure 12.11** The effect of competing reaction paths on the mechanochemical kinetics of nucleophilic displacement. The paths that dominate solvolysis of siloxanes in the absence of force (path 1, red) are destabilized by tensile force, resulting in increased kinetic stabilities of siloxanes under tensile load. However, as the force increases, the kinetics switches to the expected force-dependent acceleration because alternative reaction paths (path 2, blue), which are too high in energy to contribute to strain-free kinetics, become predominant, producing mechanistic crossover. These effects are thought to be general, illustrating the complexities of extrapolating mechanochemical behavior from the observed kinetics in the absence of force. TS2 for basic methanolysis of siloxanes disappears at 1.1 nN, with path 1 becoming single barrier. TS4 is present only in basic methanolysis and is not kinetically significant at any force. Source: Data from Akbulatov et al. [63].

enough to make substantive attempts at implementing these ideas and take the first steps toward creating complex useful molecular machines.

Designing molecular machines requires a fundamentally distinct approach from the one that governs the engineering of macroscopic motion because the forces that dominate at the corresponding scales are so different. Macroscopic motion is deterministic, dominated by inertia and gravity. In contrast, at the molecule level, motion is stochastic, driven by continuous fluctuations in energy and momentum (Brownian motion), while gravity is inconsequential [80, 81]. Despite the many advances in the field of molecular machines, the lack of an example that performs a demonstrably useful task, much less a practically useful implementation, attests to the complexity that such devices must possess, at least based on our knowledge of the biological systems [82].

Two distinct approaches to designing useful molecular machines are frequently articulated [82, 83]: one, referred to as bioinspiration, aims to reproduce the design features of biological machines free from the constraints faced by natural systems such as bioavailability of elements, mostly aqueous aerobic medium and narrow

temperature and pressure operating regimes. This approach is exemplified by the various reported molecular walkers [84, 85]. The second approach is to reproduce the pattern of motion of existing macroscopic machines at the molecular scale, exemplified by the molecular "car" [86] or "elevator" [82, 87]. The utility of the first approach increasingly becomes clear [83]. The stark difference in physical laws at the two length scales seems to have limited the second approach to reproducing something esthetic rather than functional from a macroscopic equivalent.

### 12.3.2 Minimalist Design of a Molecular Rotor Realized Using Stilbenes

A key question in designing a practical molecular motor is the minimum level of complexity required to convert input energy to useful work. The question attracted remarkably little attention in the literature. Biological motors are incredibly complex. For example, ATP synthase is a transmembrane enzyme that operates as a directional rotary molecular motor to couple exergonic relaxation of a transmembrane proton gradient to endergonic synthesis of a nearly universal biological fuel, ATP [88]. How much of its intricate structure and the enormous size, which exceeds 500 kDa, reflects the complexity required for directional rotation and how much is needed to achieve its other functions is unknown. So far, the structurally and operationally simplest abiological molecular motors capable of generating useful work under continuous energy input are based on stilbene derivatives, [79, 89] which operate by directional rotation around a molecular axis defined by the isomerizable C=C bond.

A motor driven solely by photoisomerization of a C=C bond and consuming no chemical fuel will produce work only if it completes the 360° rotation of a single cycle in at least four steps. For a stilbene derivative, the four isomers connected by these steps are usually defined by both the absolute value and the sign of the torsion angle of the isomerizable C=C bond (Figure 12.12a). The larger the difference in properties of the four states of the motor comprising the cycle, particularly their free energies of formation, absorption spectra and photoisomerization dynamics, the larger the efficiency of converting input energy into work. The reason is that this efficiency depends on the ratios of the forward and reverse rate constants of individual steps [90]. To a useful approximation, the higher the individual ratios, the higher efficiency of energy transduction. Conversely, no work is generated when the product of the ratios is 1.

The optomechanical cycle of a stilbene-based motor comprises alternating photochemical (*E*/*Z* conversion, red arrows in Figure 12.12a) and thermal (M/P conversion, black arrows) steps. The ratios of forward and reverse rate constants of the photoisomerization steps depend on the ratio of the extinction coefficients of the two isomers (e.g. *M*,*Z* vs. *M*,*E* and *P*,*Z* vs. *P*,*E*) and the respective quantum yields, whereas the ratios of the rate constants for thermal inversion of the helical chirality (black arrows) reflect the relative free energies of the formation of the two pairs of stereoisomers (*M*,*E* vs. *P*,*E* and *M*,*Z* vs. *P*,*Z*). These requirements mean that the motor will rotate directionally only if its M and P stereoisomers are distinct, i.e. they

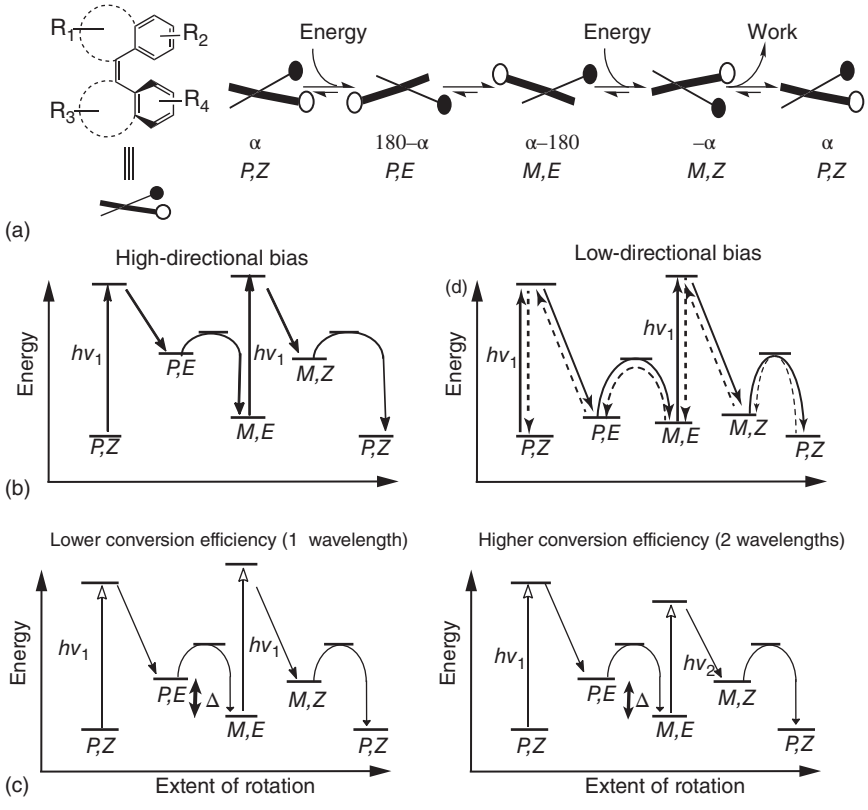


**Figure 12.12** The basic principles of operating molecular motor based on directional rotation of the C=C bond in stilbenes. (a) The simplest single work-producing cycle requires four steps to complete a single 360° rotation, usually by a combination of photochemical (red arrows) and thermal (black arrows) interconversions of four diastereomers, *M,Z*; *M,E*; *P,E*; and *P,Z*. These diastereomers are uniquely defined by the torsion of their isomerizable C=C bond: α, 180 − α, α − 180, −α. (b) Unlike a macroscopic motor, the two directions of rotation always compete in a molecular motor. Fast and highly favorable thermal isomerization steps (left diagram) bias the rotation in favor of one direction by minimizing the steady-state concentrations of (in this example) *P,E* and *M,Z* diastereomers, thus minimizing the probability of unproductive *P,E*→*P,Z* and *M,Z*→*M,E* photoisomerizations (dashed arrows, right diagram). Unfortunately, sufficiently large differences are difficult to achieve in practice, and the existing motors appear to manifest only modest energy differences (the right diagram) and hence modest preference for one direction of rotation over the other. (c) One strategy to improve the efficiency of mechanochemical energy conversion by a molecular motor is to maximize the fraction of photon energy that is converted into the energy difference between the pairs of diastereomers connected thermally, Δ. This strategy is most effective in the (less practical) stepwise implementation, whereby distinct wavelengths are used for *Z/E* and *E/Z* isomerizations.

are must be at least diastereomers. In other words, a molecular motor based on stilbene must have at least 2 chiral elements, one being the isomerizable C=C bond and the other either a chiral atom or another chiral axis. The latter type of motor will produce work even if one intermediate state is meso [91]. Conversely, isomerization of a stilbene lacking a second chiral element consists of interconversion of two pairs of enantiomers (M/P,E and M/P,Z), whose identical free energies, spectra, and photo dynamics mean that the product of the ratios of the rate constants is 1.

These general principles have been implemented in diverse molecular motors based on stilbene. Fused rings are added to the stilbene scaffold to deplanarize the *E* isomer (which is planar for parent stilbene and stiff stilbene) by creating steric crowding on both faces of the isomerizable C=C bond (dashed circle, Figure 12.12), and to inhibit epimerization of the *Z* isomer (in stiff stilbene, the barrier separating M,Z and P,Z diastereomers is $<5\ \text{kcal mol}^{-1}$ [54]). Aromatic substituents have been exploited to modify the composition of photostationary states by maximizing either photochromism of the isomers or the ratio of the quantum yields. Finally, nonaromatic substituents ($R_1$ and $R_3$, Figure 12.12) are used to introduce point chirality and maximize the energy difference, and hence the ratios of the forward and reverse rate constants, between diastereomers containing the same configuration of the isomerizable bond.

Far less data exist on strategies to maximize energy conversion efficiencies of molecular motors, but the maximum achievable efficiency is likely to be <1% for three reasons. First, photoisomerization of C=C bonds is intrinsically energy inefficient: only a small fraction of the energy deposited by photon absorption is captured as the excess free energy of the product. [24, 25, 29] Increasing the latter (by creating a photoproduct, e.g. M,E, which is more strained than the reactant, e.g. M,Z) increases the efficiency if it also increases the driving force of the subsequent thermally activated step (inversion of axial chirality), but this approach is limited by the concomitant increase in the rate of thermal relaxation of the strained isomer (e.g. M,E → M,Z or P,E → P,Z in this example), which lowers the efficiency. Second, under continuous irradiation, the ratios of the forward-to-backward rates of the two photoisomerization steps are inversely related, which limits how much the product of the ratios for all four steps can be modified, unless the two diastereomers (e.g. P,Z and M,E) are highly photochromic, which has been difficult to achieve in practice. This limitation does not exist if the cycle is affected stepwise, which allows photons of different frequency to be used for the two photoisomerization steps, without the need to rely on photochromism of the two isomers. However, such stepwise implementations lack practical utility. Finally, the quantum yields of E/Z isomerizations of C=C bonds appear to be inversely correlated with the increase in the strain energy of the product relative to the reactant [52]. Consequently, unlike motor proteins, molecular motors based on photoisomerization of a C=C bond in stilbene derivatives likely become less efficient and the higher the external load they operate against.

## 12.4 Summary

Historically, detailed studies of isomerization of stilbene made key contributions to our understanding of how energy flows in a chemical reaction, including nonadiabatic photochemical reactions. Recently, stilbene derivatives have played increasingly central role in yielding fundamental insights into two areas of intense contemporary interest: coupling of atomic motion that comprises chemical reactions to directional motion at micro- to macroscopic scales. The two manifestations of this coupling that have attracted particular interest among chemists are molecular motors [26, 79] and polymer mechanochemistry [30, 31]. In the former, thermodynamically favorable (exergonic) chemical reactions power translation of macroscopic objects in functional analogy to the operation of motor proteins. Stilbene derivatives yielded the first and some of the more remarkable examples of molecules capable of continuous directional rotation, including under conditions that result in motion of macroscopic objects. In polymer mechanochemistry, macroscopic motion powers chemical reactions within macroscopically strained materials or isolated polymer chains. Stilbene derivatives enable model studies of such reactions by allowing the unusual molecular strains responsible for reactions in stretched polymers to be generated without the intractable complexities of coupled macroscopic motion.

## References


1 Ziaullah and H.P.V. Rupasinghe, Application of NMR Spectroscopy in Plant Polyphenols Associated with Human Health. Applications of NMR Spectroscopy, Vol 2, 2015. 2: p. 3–92.

2 Likhtenshtein, G. (2010). *Stilbenes: Applications in Chemistry, Life Sciences and Materials Science*. Weinheim: Wiley-VCH.

3 Baur, J.A. and Sinclair, D.A. (2006). Therapeutic potential of resveratrol: the in vivo evidence. *Nat. Rev. Drug Discovery* 5 (6): 493–506.

4 Fuss, W., Kosmidis, C., Schmid, W., et al. (2004). The photochemical cis-trans isomerization of free stilbene molecules follows a hula-twist pathway. *Angew. Chem. Int. Ed.* 43 (32): 4178–4182.

5 Gerwien, A., Schildhauer, M., Thumser, S., et al. (2018). Direct evidence for hula twist and single-bond rotation photoproducts. *Nat. Commun.* 9, 2510.

6 Villaron, D. and Wezenberg, S. (2020). Stiff-stilbene photoswitches: from fundamental studies to emergent applications. *Angew. Chem. Int. Ed.* 59: 13192–13202.

7 Shen, T., Wang, X.N., and Lou, H.X. (2009). Natural stilbenes: an overview. *Nat. Prod. Rep.* 26 (7): 916–935.

8 Waldeck, D.H. (1991). Photoisomerization dynamics of stilbenes. *Chem. Rev.* 91 (3): 415.

9 Saltiel, J., Sears, D. F., Jr., Ko, Dong-Hoon, et al. (ed.) (1995). *Cis-Trans Isomerization of Alkenes*, 3. CRC Press.


**10** Dugave, C. and Demange, L. (2003). *Cis*-trans isomerization of organic molecules and biomolecules: implications and applications. *Chem. Rev.* 103 (7): 2475–2532.

**11** Muszkat, K.A., Castel, N., Jakob, A., et al. (1991). Photophysics and photochemistry of ring-fluorinated stilbenes. *J. Photochem. Photobiol., A* 56 (2, 3): 219–226.

**12** Durbeej, B., Wang, J., and Oruganti, B. (2018). Molecular photoswitching aided by excited-state aromaticity. *ChemPlusChem* 83 (11): 958–967.

**13** Rosenberg, M., Kilsaa, K., Dahlstrand, C., et al. (2014). Excited state aromaticity and antiaromaticity: opportunities for photophysical and photochemical rationalizations. *Chem. Rev.* 114 (10): 5379–5425.

**14** Peters, K.S. (2007). Nature of dynamic processes associated with the SN1 reaction mechanism. *Chem. Rev.* 107 (3): 859–873.

**15** Kumpulainen, T., Lang, B., Arnulf, R., et al. (2017). Ultrafast elementary photochemical processes of organic molecules in liquid solution. *Chem. Rev.* 117 (16): 10826–10939.

**16** Dorel, R. and Feringa, B.L. (2019). Photoswitchable catalysis based on the isomerisation of double bonds. *Chem. Commun.* 55 (46): 6477–6486.

**17** Molloy, J.J., Morack, T., and Gilmour, R. (2019). Positional and geometrical isomerisation of alkenes: the pinnacle of atom economy. *Angew. Chem. Int. Ed.* 58 (39): 13654–13664.

**18** Papper, V. and Likhtenshtein, G.I. (2001). Substituted stilbenes: a new view on well-known systems – new applications in chemistry and biophysics. *J. Photochem. Photobiol., A* 140 (1): 39–52.

**19** Krawczyk, H. (2019). The stilbene derivatives, nucleosides, and nucleosides modified by stilbene derivatives. *Bioorg. Chem.* 90: 103073.

**20** Albert, L. and Vazquez, O. (2019). Photoswitchable peptides for spatiotemporal control of biological functions. *Chem. Commun.* 55 (69): 10192–10213.

**21** Szymanski, W., Beierle, J., Kistemaker, H., et al. (2013). Reversible photocontrol of biological systems by the incorporation of molecular photoswitches. *Chem. Rev.* 113 (8): 6114–6178.

**22** Becchetti, F.D., Raymond, R., Torres-Isea, R., et al. (2017). Recent developments in deuterated scintillators for neutron measurements at low-energy accelerators. *Nucl. Instrum. Methods Phys. Res., Sect. A* 874: 72–78.

**23** Buckup, T. and Leonard, J. (2018). Multidimensional vibrational coherence spectroscopy. *Top. Curr. Chem.* 376 (5): 1–39.

**24** Sun, C.-L., Wang, C., and Boulatov, R. (2019). Applications of photoswitches in the storage of solar energy. *ChemPhotoChem* 3 (6): 268–283.

**25** Kucharski, T.J., Tian, Y., Akbulatov, S., et al. (2011). Chemical solutions for the closed-cycle storage of solar energy. *Energy Environ. Sci.* 4(Copyright (C) 2012 American Chemical Society (ACS). All Rights Reserved.): 4449–4472.

**26** van Leeuwen, T., Lubbe, A., Stacko, P., et al. (2017). Dynamic control of function by light-driven molecular motors. *Nat. Rev. Chem.* 1, 0096.

**27** Huang, Z. and Boulatov, R. (2010). Chemomechanics with molecular force probes. *Pure Appl. Chem.* 82 (4): 931–951.


**28** Bleger, D. and Hecht, S. (2015). Visible-light-activated molecular switches. *Angew. Chem. Int. Ed.* 54 (39): 11338–11349.

**29** Kucharski, T.J. and Boulatov, R. (2012). Fundamentals of molecular photoactuation. In: *Optical Nano and Micro Actuator Technology* (ed. G.K. Knopf), 83–106. CRC Press.

**30** Ghanem, M.A. et al. (2020). The role of polymer mechanochemistry in responsive materials and additive manufacturing. *Nat. Rev. Mater.* 6, 84–98.

**31** O'Neill, R.T. and Boulatov, R. (2021). The many flavours of mechanochemistry and its plausible conceptual underpinnings. *Nat. Rev. Chem.* 5, 148–167.

**32** Lancia, F., Ryabchun, A., and Katsonis, N. (2019). Life-like motion driven by artificial molecular machines. *Nat. Rev. Chem.* 3 (9): 536–551.

**33** Akbulatov, S. and Boulatov, R. (2017). Experimental polymer mechanochemistry and its interpretational frameworks. *ChemPhysChem* 18 (11): 1422–1450.

**34** Black, A.L., Lenhardt, J.M., and Craig, S.L. (2011). From molecular mechanochemistry to stress-responsive materials. *J. Mater. Chem.* 21 (6): 1655–1663.

**35** Chen, Y.L., Spiering, A., Karthikeyan, S., et al. (2012). Mechanically induced chemiluminescence from polymers incorporating a 1,2-dioxetane unit in the main chain. *Nat. Chem.* 4 (7): 559–562.

**36** Cravotto, G. and Cintas, P. (2012). Harnessing mechanochemical effects with ultrasound-induced reactions. *Chem. Sci.* 3 (2): 295–307.

**37** Ribas-Arino, J. and Marx, D. (2012). Covalent mechanochemistry: theoretical concepts and computational tools with applications to molecular nanomechanics. *Chem. Rev.* 112 (10): 5412–5487.

**38** Boulatov, R. (2013). Demonstrated leverage. *Nat. Chem.* 5 (2): 84–86.

**39** Boulatov, R. (2017). The challenges and opportunities of contemporary polymer mechanochemistry. *ChemPhysChem* 18 (11): 1419–1421.

**40** Anderson, L. and Boulatov, R. (2018). Polymer mechanochemistry: a new frontier for physical organic chemistry. *Adv. Phys. Org. Chem.* 52: 87–143.

**41** Bowser, B.H. and Craig, S.L. (2018). Empowering mechanochemistry with multi-mechanophore polymer architectures. *Polym. Chem.* 9 (26): 3583–3593.

**42** Willis-Fox, N., Rognin, E., Aljohani, T., et al. (2018). Polymer mechanochemistry: manufacturing is now a force to be reckoned with. *Chem* 4 (11): 2499–2537.

**43** Izak-Nau, E., Campagna, D., Baumann, C., et al. (2020). Polymer mechanochemistry-enabled pericyclic reactions. *Polym. Chem.* 11 (13): 2274–2299.

**44** Boulatov, R. (ed.) (2015). *Polymer Mechanochemistry. Topics in Current Chemistry*, vol. 369. Switzerland: Springer International Publishing.

**45** Stirling, C.J.M. (1985). Evaluation of the effect of strain upon reactivity. *Tetrahedron* 41 (9): 1613–1666.

**46** Wang, J.P., Kouznetsova, T., Boulatov, R., et al. (2016). Mechanical gating of a mechanochemical reaction cascade. *Nat. Commun.* 7, 13433.

**47** Zhang, H., Li, X., Lin, Y. J., et al. (2017). Multi-modal mechanophores based on cinnamate dimers. *Nat. Commun.* 8, 1147.


**48** Pan, Y., Zhang, H., Xu, P., et al. (2020). A mechanochemical reaction cascade for controlling load-strengthening of a mechanochromic polymer. *Angew. Chem. Int. Ed.* 50: 21980–21985.

**49** Boulatov, R. (2011). Reaction dynamics in the formidable gap. *Pure Appl. Chem.* 83(Copyright (C) 2012 American Chemical Society (ACS). All Rights Reserved.): 25–41.

**50** Kucharski, T.J. and Boulatov, R. (2011). The physical chemistry of mechanoresponsive polymers. *J. Mater. Chem.* 21(Copyright (C) 2012 American Chemical Society (ACS). All Rights Reserved.): 8237–8255.

**51** Garcia-Manyes, S. and Beedle, A.E.M. (2017). Steering chemical reactions with force. *Nat. Rev. Chem.* 1 0083.

**52** Huang, Z., Yang, Q., Khvostichenko, D., et al. (2009). Method to derive restoring forces of strained molecules from kinetic measurements. *J. Am. Chem. Soc.* 131(Copyright (C) 2012 American Chemical Society (ACS). All Rights Reserved.): 1407–1409.

**53** Yang, Q.Z., Huang, Z., Kucharski, T. J., et al. (2009). A molecular force probe. *Nat. Nanotechnol.* 4 (5): 302–306.

**54** Hermes, M. and Boulatov, R. (2011). The entropic and enthalpic contributions to force-dependent dissociation kinetics of the pyrophosphate bond. *J. Am. Chem. Soc.* 133(Copyright (C) 2012 American Chemical Society (ACS). All Rights Reserved.): 20044–20047.

**55** Tian, Y. and Boulatov, R. (2012). Quantum-chemical validation of the local assumption of chemomechanics for a unimolecular reaction. *ChemPhysChem* 13(Copyright (C) 2012 American Chemical Society (ACS). All Rights Reserved.): 2277–2281.

**56** Craig, S.L. (2012). A tour of force. *Nature* 487 (7406): 176–177.

**57** Huang, Z., Yang, Q., Kucharski, T., et al. (2009). Macrocyclic disulfides for studies of sensitized photolysis of the S–S bond. *Chem. Eur. J.* 15(Copyright (C) 2012 American Chemical Society (ACS). All Rights Reserved.): 5212–5214, S5212/1-S5212/19.

**58** Kucharski, T.J., Huang, Z., Yang, P., et al. (2009). Kinetics of thiol/disulfide exchange correlate weakly with the restoring force in the disulfide moiety. *Angew. Chem. Int. Ed.* 48 (38): 7040–7043.

**59** Tian, Y.C., Kucharski, T. J., Yang, Q., et al. (2013). Model studies of force-dependent kinetics of multi-barrier reactions. *Nat. Commun.* 4.

**60** Kucharski, T.J., Yang, Q., Tian, T., et al. (2010). Strain-dependent acceleration of a paradigmatic $S_N2$ reaction accurately predicted by the force formalism. *J. Phys. Chem. Lett.* 1(Copyright (C) 2012 American Chemical Society (ACS). All Rights Reserved.): 2820–2825.

**61** Akbulatov, S., Tian, Y., Kapustin, E., et al. (2013). Model studies of the kinetics of ester hydrolysis under stretching force. *Angew. Chem. Int. Ed.* 52 (27): 6992–6995.

**62** Akbulatov, S., Tian, Y.C., and Boulatov, R. (2012). Force-reactivity property of a single monomer is sufficient to predict the micromechanical behavior of its polymer. *J. Am. Chem. Soc.* 134 (18): 7620–7623.


**63** Akbulatov, S., Tian, Y., Huang, Z., et al. (2017). Experimentally realized mechanochemistry distinct from force-accelerated scission of loaded bonds. *Science* 357 (6348): 299–303.

**64** Kean, Z.S., Akbulatov, S., Tian, T., et al. (2014). Photomechanical actuation of ligand geometry in enantioselective catalysis. *Angew. Chem. Int. Ed.* 53 (52): 14508–14511.

**65** Wang, L., Yu., Y., Razgoniaev, A., et al. (2020). Mechanochemical regulation of oxidative addition to a palladium(0) bisphosphine complex. *J. Am. Chem. Soc.* 17714–177720.

**66** Mcmurry, J.E. (1989). Carbonyl-coupling reactions using low-valent titanium. *Chem. Rev.* 89 (7): 1513–1524.

**67** Tian, Y. and Boulatov, R. (2016). Comment on "Stiff-stilbene photoswitch ruptures bonds not by pulling but by local heating". *Phys. Chem. Chem. Phys.* 18: 26990–26993.

**68** Tian, Y., Xiaodong, C., Li, X., et al. (2020). A polymer with mechanochemically active hidden length. *J. Am. Chem. Soc.* 142 (43): 18687–18697.

**69** Stauch, T. and Dreuw, A. (2016). Advances in quantum mechanochemistry: electronic structure methods and force analysis. *Chem. Rev.* 116 (22): 14137–14180.

**70** Kochhar, G.S., Heverly-Coulson, G.S., and Mosey, N.J. (2015). Theoretical approaches for understanding the interplay between stress and chemical reactivity. *Top. Curr. Chem.* 369: 37–96.

**71** Wu, D., Lenhardt, J., Black, A., et al. (2010). Molecular stress relief through a force-induced irreversible extension in polymer contour length. *J. Am. Chem. Soc.* 132 (45): 15936–15938.

**72** Ainavarapu, S.R.K., Wiita, A., Dougan, L., et al. (2008). Single-molecule force spectroscopy measurements of bond elongation during a bimolecular reaction. *J. Am. Chem. Soc.* 130 (20): 6479–6487.

**73** Dopieralski, P., Ribas-Arino, J., Anjukandi, P., et al. (2017). Unexpected mechanochemical complexity in the mechanistic scenarios of disulfide bond reduction in alkaline solution. *Nat. Chem.* 9 (2): 164–170.

**74** Vogel, V. (2006). Mechanotransduction involving multimodular proteins: converting force into biochemical signals. *Annu. Rev. Biophys. Biomol. Struct.* 35: 459–488.

**75** Biswas, S., Yashin, V.V., and Balazs, A.C. (2020). Harnessing biomimetic cryptic bonds to form self-reinforcing gels. *Soft Matter* 16 (22): 5120–5131.

**76** Lebedeva, N.V., Nese, A., Sun, F., et al. (2012). Anti-Arrhenius cleavage of covalent bonds in bottlebrush macromolecules on substrate. *Proc. Natl. Acad. Sci. U.S.A.* 109 (24): 9276.

**77** Lee, B., Zhenbin, N., Wang, J., et al. (2015). Relative mechanical strengths of weak bonds in sonochemical polymer mechanochemistry. *J. Am. Chem. Soc.* 137 (33): 10826–10832.

**78** Tian, Y. and Boulatov, R. (2013). Comparison of the predictive performance of the Bell–Evans, Taylor-expansion and statistical-mechanics models of mechanochemistry. *Chem. Commun.* (49): 4187–4189.


**79** Kassem, S., Van Leeuwen, T., Lubbe, A., et al. (2017). Artificial molecular motors. *Chem. Soc. Rev.* 46 (9): 2592–2621.

**80** Kay, E.R., Leigh, D.A., and Zerbetto, F. (2007). Synthetic molecular motors and mechanical machines. *Angew. Chem. Int. Ed.* 46 (1–2): 72–191.

**81** Astumian, R.D. (1997). Thermodynamics and kinetics of a Brownian motor. *Science* 276 (5314): 917–922.

**82** Sluysmans, D. and Stoddart, J.F. (2018). Growing community of artificial molecular machinists. *Proc. Natl. Acad. Sci. U.S.A.* 115 (38): 9359–9361.

**83** Zhang, L., Marcos, V., and Leigh, D.A. (2018). Molecular machines with bio-inspired mechanisms. *Proc. Natl. Acad. Sci. U.S.A.* 115 (38): 9397–9404.

**84** Leigh, D.A. et al. (2014). Synthetic molecular walkers. In: *Molecular Machines and Motors: Recent Advances and Perspectives* (Eds. Alberto Credi, Serena Silvi, Margherita Venturi), vol. 354, 111–138, Springer.

**85** von Delius, M., Geertsema, E.M., and Leigh, D.A. (2010). A synthetic small molecule that can walk down a track. *Nat. Chem.* 2 (2): 96–101.

**86** Kudernac, T., Ruangsupapichat, N., Parschau, M., et al. (2011). Electrically driven directional motion of a four-wheeled molecule on a metal surface. *Nature* 479 (7372): 208–211.

**87** Badjic, J.D., Balzani, V., Credi, A., et al. (2004). A molecular elevator. *Science* 303 (5665): 1845–1849.

**88** Okuno, D., Iino, R., and Noji, H. (2011). Rotation and structure of FoF1-ATP synthase. *J. Biochem.* 149 (6): 655–664.

**89** Koumura, N. et al., Zijlstra, R., Van Delden, R., (1999). Light-driven monodirectional molecular rotor. *Nature* 401 (6749): 152–155.

**90** Astumian, R.D., Mukherjee, S., and Warshel, A. (2016). The physics and physical chemistry of molecular machines. *ChemPhysChem* 17 (12): 1719–1741.

**91** Kistemaker, J.C.M., Stacko, P., Visser, J., et al. (2015). Unidirectional rotary motion in achiral molecular motors. *Nat. Chem.* 7 (11): 890–896.


# 13 Indigoid Photoswitches

Thomas Bartelmann and Henry Dube

**Photochromism**

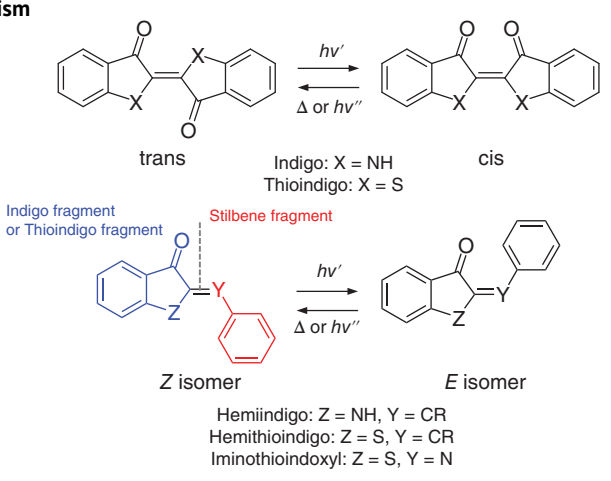


**Characteristic Features**

Visible light-range photochromism, long lived metastable isomers, rigid geometry changes, applications in molecular machinery, biological chemistry, and supramolecular assemblies.

**First Reported**

**(Hemi)indigo**: Baeyer, A. (1883). *Ber. Dtsch. Chem. Ges.* 16: 2188–2204.

**(Hemi)thioindigo**: Friedländer, P. (1906). *Chem. Ber*. 39: 1060–1066.

**Iminothioindoxyl**: Bezdrik, A., Friedländer, P., and Koeniger, P. (1908). *Chem. Ber*. 41: 227–242.

**Oxindole**: Baeyer, A. (1878). *Ber. Dtsch. Chem. Ges.* 11: 582–584.

**Key References**

**Indigo**: Weinstein, G.M. (1956). Wyman, *JACS* 78: 4007–4010.
Huang, C.-Y. and Hecht, S. (2017). *JACS* 139: 15205–15 211.
Huber, L.A., Mayer, P., and Dube, H. (2018). *ChemPhotoChem* 2: 458–464.

**Thioindigo**: Wyman, G. M. and Brode, W. R. (1951). *JACS* 73: 1487–1493.
Vlahakis, J. Z., Wand, M. D., and Lemieux, R. P. (2003). *JACS* 725: 6862–6863.

**Hemiindigo**: Ikegami, M. and Arai, T. (2003) *Bull. Chem. Soc. Jpn.* 76: 1783–1792.
Petermayer, C. and Dube, H. (2017) *JACS* 139: 15060–15 067.
Petermayer, C. and Dube, H. (2018). *JACS* 140: 13558–13 561.

**Hemithioindigo**: Izmail'skii, V.A. and Mostoslavski, M.A. (1961). *Ukr. Khem. Zh.* 27: 234–237.
Cordes, T. and Rück-Braun, K. (2008). *J. Phys. Chem. A* 112: 581–588.
Guentner, M. and Dube, H. (2015). *Nat. Commun.* 6: 8406.
Wiedbrauk, S. and Dube, H. (2016). *JACS* 138: 12219–12227.
Gerwien, A. and Dube, H. (2018). *Nat. Commun.* 9: 2510.

**Iminothioindoxyl**: Hoorens, M.W.H., Feringa, B.L., Buma, W.J., and Szymanski, W. (2019). *Nat. Commun.* 10: 2390.

**Oxindoles**: Roke, D., Wezenberg, S.J., and Feringa, B.L. (2019). *JACS* 141: 7622–7627.

# 13

# Indigoid Photoswitches

*Thomas Bartelmann*[1] *and Henry Dube*[2]

[1] *Ludwig-Maximilians-Universität München, Department of Chemistry and Center for Integrated Protein Science CIPSM, Butenandtstr. 5–13, 81377 München, Germany*
[2] *Friedrich-Alexander-Universität Erlangen-Nürnberg, Department of Chemistry and Pharmacy, Nikolaus-Fiebiger-Str. 10, 91058 Erlangen, Germany*

## 13.1 Indigo

Indigo is a naturally occurring dye, whose molecular structure was first elucidated and synthesized by *Adolf von Baeyer* more than 100 years ago [1]. Known for its high photostability, it is mainly used as a robust deep-blue dye with exceptionally high stability against photobleaching. The reason for this high photostability is a very efficient excited-state proton transfer (ESPT) deexcitation pathway [2]. After excitation, at least one N—H proton is transferred to its neighboring carbonyl group, leading to the enol form and instant thermal deexcitation. Since ESPT is also very fast, light-induced *trans* to *cis* isomerization cannot compete with it in N-unsubstituted indigo. ESPT can be prevented by N—H substitution, which leads to occurrence of photoswitching instead as first evidenced by *Wyman* and later also by others [3]. However, up to now, applications of N-substituted indigo photoswitches were largely hampered by low thermal stability of the metastable *cis* isomers - an exception being some acylated macrocyclic versions [4a]. Recent progress by the groups of *Hecht* [4b] and *Dube* [5] has addressed this issue delivering N-substituted derivatives with significantly greater thermal stabilities while maintaining red light responsiveness. Interestingly, mono N—H substitution is sufficient to enable photoisomerization despite the presence of competing ESPT (Figure 13.1) [5].

Substituted indigos are synthetically accessible by one or two step reaction pathways starting from indigo **1** (Figure 13.2). Through *Chan–Lam*-type coupling reactions, aryl substitution is possible. Alkylation can be achieved by nucleophilic substitution reactions and thereby mono-, double-, and mixed-substituted indigos are readily accessible [4b, 5].

By excluding ESPT, it is possible to photoisomerize the central double bond upon red light illumination and accumulate up to 80% of the *cis*-isomer depending on the substituents at the nitrogen atom. N-arylation is stabilizing the metastable *cis*-isomer, which results in much higher energy barriers for thermal *cis*-to-*trans*

*Molecular Photoswitches: Chemistry, Properties, and Applications*,
First Edition. Edited by Zbigniew L. Pianowski.


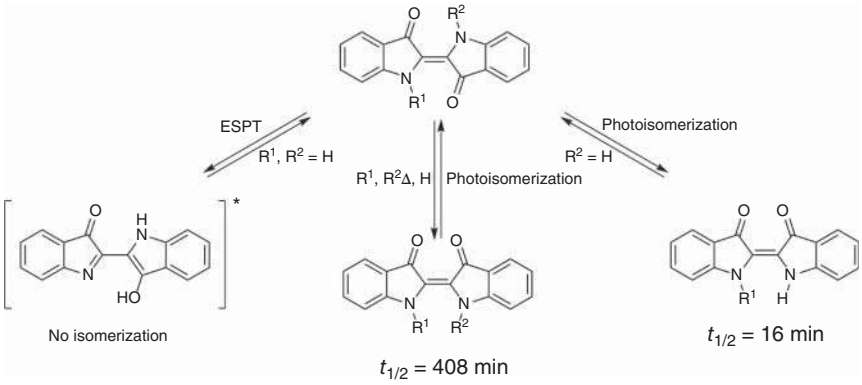


**Figure 13.1** Possible deexcitation pathways of indigos depending on the N—H substitution pattern. In unsubstituted indigo ESPT is the dominant pathway, while in mono- and double N-substituted indigos double-bond photoisomerization is accessible.

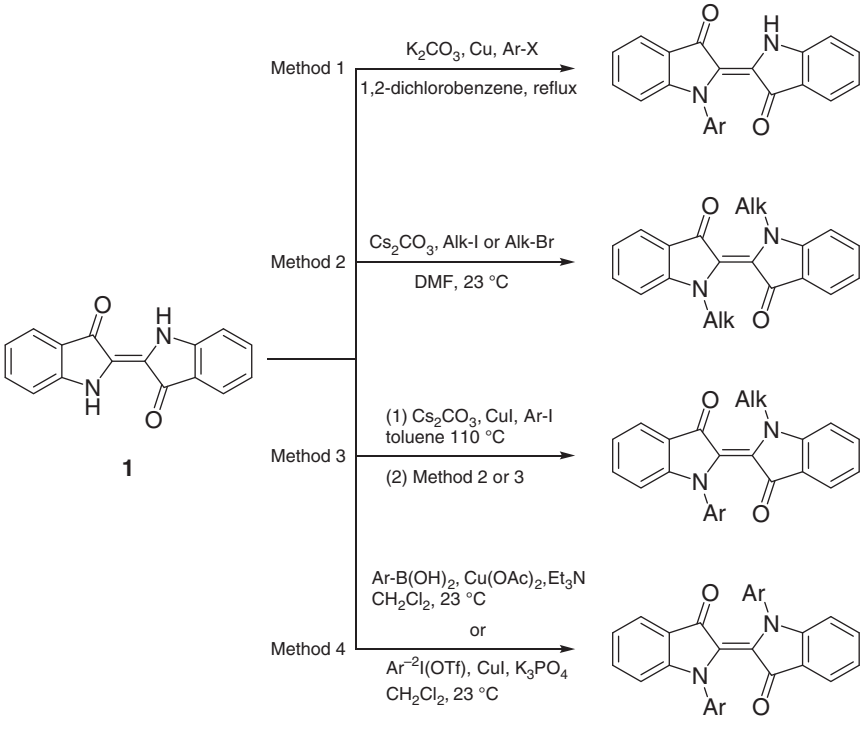


**Figure 13.2** Four different methods for N—H arylation or alkylation of indigo. Both mono- and double N-substitution of indigo is possible as well as combinations of alkyl and aryl substitutions. Source: Based on Huber et al. [5].

isomerization in contrast to doubly alkylated indigos. For the latter a maximum thermal half-life of 2.8 minutes at 22 °C is observed, in contrast to arylated indigos, where thermal half-lives of up to 408 minutes can be reached at 22 °C [4b]. Hammett analysis of substituent effects shows a clear trend correlating electron-withdrawing substituents with longer thermal half-lives. In this way, easily accessible and red-light responsive photoswitches are now available for a variety of applications.

Another interesting possibility is photoisomerization of mono-arylated indigos, where an ESPT is still possible. With mono-tolyl substitution, a *cis* isomer content of up to 38% can be reached after irradiation with light of 635 nm wavelength [5]. The low *cis* isomer yield shows that ESPT is still a dominant pathway. Mono-arylated indigos possess thermal half-lives of up to 16 minutes at ambient temperature, which are however highly dependent on the water content of the solution. This behavior suggests an intermolecular interaction between $H_2O$ and indigo influencing the thermal isomerization. Consequently, an acceleration of the thermal *cis* to *trans* isomerization rate by a factor of up to 300 is possible, rendering mono-arylated indigos as potential water sensors, with sensitivities possibly reaching below 1 ppm.

## 13.2 Thioindigo

Thioindigo is the sulfur derivative of indigo and has been synthesized for the first time by *Friedländer* in 1906 (in the same work hemithioindigo (HTI) is first described) [6]. Already in 1942, it was recognized by *Stearns* that thioindigo is photochromic (negative photochromism) [7], which could be assigned to light-induced *trans* to *cis* isomerization by *Wyman* and *Brode* as early as 1951 [8]. In the latter work, a variety of chlorinated and methylated derivatives were scrutinized for their photoisomerization properties demonstrating proficient photoswitching with visible light. In 1977, *Kirsch* and *Wyman* reported on the importance of triplet formation in the photoisomerization mechanism of thioindigo [9]. A later study by *Memming* and *Kobs* confirmed both singlet and triplet states to be mechanistically important [10]. Almost a decade later, in 1985, *Irie* et al. reported on photoresponsive thioindigo-based cation binders possessing two polyethylene glycol (PEG) chains on opposite sides of the central double bond [11]. Accumulation of up to 82% of the *cis* isomer was estimated from absorption values after irradiation with 550 nm light. The opposing *cis* to *trans* photoisomerization could be effected quantitatively with 450 nm light. Cation-binding regulation in a reversible ON/OFF manner as well as transport through liquid membranes via alternate irradiation with 550 and 450 nm light was demonstrated. This work was followed up in the 1990s by *Fukunishi* and coworkers who prepared PEG-substituted thioindigos as well as crown-ether motives and also demonstrated light modulation of cation binding, extraction, and transport through liquid membranes [12]. In the same decade, *Lemieux* and coworkers started to use thioindigo derivatives incorporating chiral branched alkoxy substituents as dopants to successfully alter the polarization of liquid crystals with visible light [13]. Lately, *Koeppe* and *Römpp* have reported on the photoswitching ability of a water-soluble thioindigo derivative bearing permanently charged sulfonate groups [14]. Up to 65% of the *cis* isomer could

be accumulated and thermal half-lives of up to several hours were observed. In another recent work by the same group, a thioindigo photoswitch possessing very different p$K_a$ values in the two different isomeric forms was reported [15]. Such property is of high interest for light control of acidity of a medium. Interestingly, thioindigo photoswitching can be aborted by the conscious implementation of ESPT as shown recently by *Zinth*, *Engelhard*, and coworkers [16]. Different to indigo, however, ESPT occurs not across the central double bond but within the two thioindigo fragments. To this end, hydroxy substituents were introduced in the *ortho*-positions of the carbonyl functions. Such substitution approach is highly interesting to stabilize chromophores against photodegradation, albeit currently at the expense of photoisomerization capacity.

## 13.3 Hemiindigo

Hemiindigo (HI) was first described and synthesized by *Adolf von Baeyer* in his seminal article "Ueber die Verbindungen der Indigogruppe" [1] about indigoid molecules. It is a molecular photoswitch with unique potential for medical applications and material science, due to its outstanding switching performance in the visible region of the electromagnetic spectrum combined with very high thermal bistability.

HI is easily accessible and can be synthesized by condensation reactions of indoxyl acetates with benzaldehyde derivatives (Figure 13.3). Besides the stilbene and indigo fragments, the indoxyl nitrogen atom can be used as a third vector point for introducing substituents and function into the molecule. The nitrogen

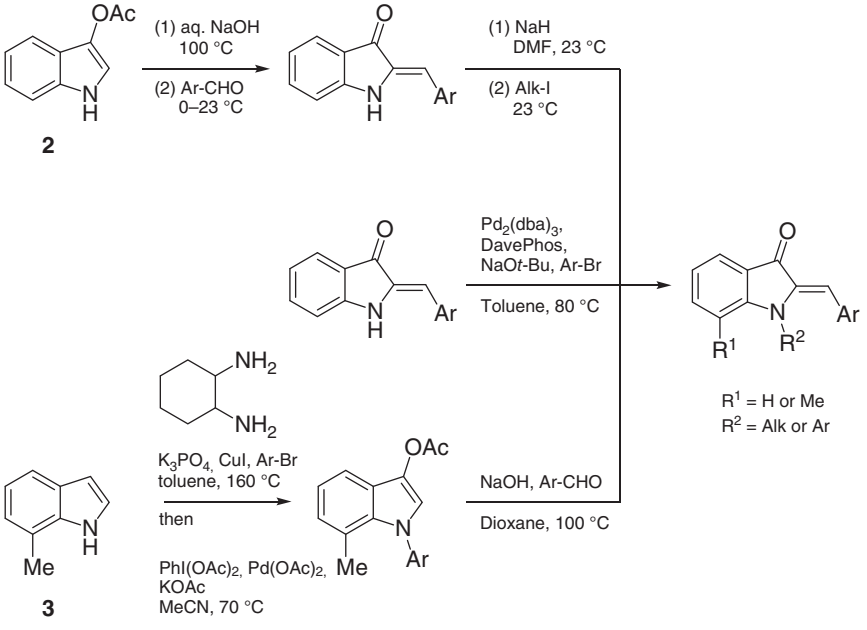


**Figure 13.3** Synthetic pathways for hemiindigos with different substitution patterns.

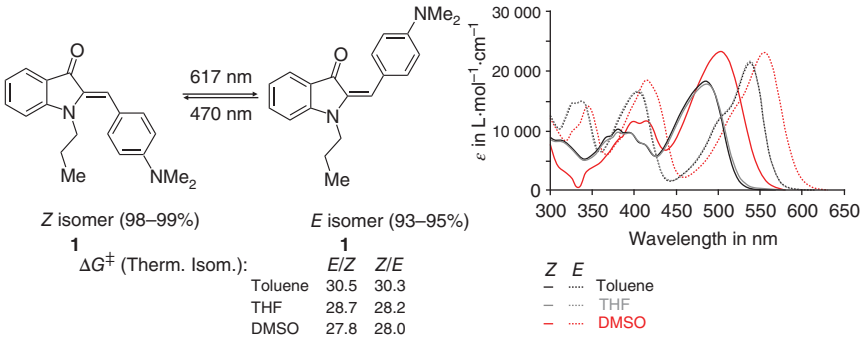


**Figure 13.4** Left: visible-light-induced isomerization of dHI **4** and free activation enthalpies for thermal isomerization in different solvents. Right: UV/vis spectra of HI **4** in different solvents showing the solvatochromism of HI **4**.

atom can be substituted with alkyl and aryl moieties by nucleophilic substitution or *Buchwald–Hartwig* coupling, respectively, in a late-stage functionalization of HI. Aryl substitution of the nitrogen is also possible prior to the condensation reaction of indoxyl acetate with aldehydes. This approach enables introduction of sterically demanding aryl substituents, which is not possible via late-stage functionalization.

*Mostoslavski* was most likely the first to describe the possibility of photoisomerization of the central double bond when studying a *para*-nitro-substituted derivative in 1970 [17]. In 1999, *Arai* and *Ikegami* explored heterocyclic HI derivatives that still required partially UV light for the switching [18]. The *Dube* group has shown that (photo)physical properties of HIs bearing strong electron donors at the stilbene fragment (dHI) possess highly advantageous properties as photoswitches (Figure 13.4). Exceptionally high yields of *Z* and *E* isomers are obtained in the respective photostationary states (PSS) and are accompanied by very high barriers for thermal double-bond isomerizations (DBIs) (life-times of up to several thousand years for individual isomers at ambient temperatures) [19].

*Z* to *E* photoisomerization of dHIs can typically be triggered by light of 470–505 nm wavelengths, *E* to *Z* photoisomerization by irradiation wavelengths >600 nm. This makes dHIs ideally suitable for biological applications [20], due to the possibility of switching in the bio-optical window without using harmful UV irradiation. The isomeric yields of dHIs in the PSSs vary depending on the substitution pattern from 81% to 95% for the *Z* to *E* isomerization direction and from 93% to 99% for the *E* to *Z* direction. Solvent polarity has only minor effects on the isomeric yields, which differ within a maximum of 8% when going from non-polar toluene to DMSO. Even in water, with a few drops of DMSO added for solubility, dHIs still produce high isomeric yields for both photoisomerization directions. Permanently charged dHIs do however not photoisomerize visibly in pure water at ambient temperatures, a situation that can be alleviated by replacing strong donating amine substituents by methoxy groups at the stilbene fragment. The latter derivatives have been used as fluorescence reporting HIV-1 RNA binders [20]. Permanently charged dHIs are nevertheless proficient photoswitches in media other than pure water and

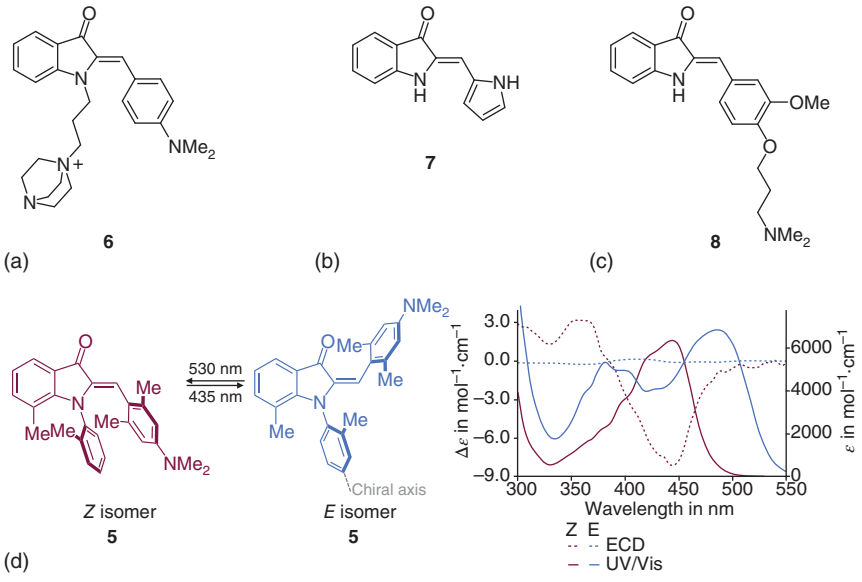


**Figure 13.5** Applications of HI photoswitches. (a) Permanently charged dHI **6** used for studies in the gas phase. (b) HI **7** switchable in the presence of bovine serum albumin. (c) HI **8** used as a binder for HIV-1 RNA. (d) Chiroptical dHI photoswitches. Left: visible-light-induced isomerization of dHI **5**. Right: UV/vis and ECD spectra of HI **5**, showing the possibility to switch between an ECD silent *E*-isomer and a *Z*-isomer with pronounced ECD signal. Source: (a) Based on Carrascosa et al. [21]; (b) Based on Masashi et al. [22]; (c) Based on Berdnikova [20]; (d) Based on Petermayer and Dube [23].

additionally are ideally suited for gas-phase experiments, as recently shown by reversible photoswitching of isolated dHIs (Figure 13.5a) [21]. Photoisomerization quantum yields in solution are consistently higher for the *Z* to *E* photoisomerization direction (in the range of 20%) than for the *E* to *Z* direction (up to 11%), rendering HIs quite efficient photoswitches overall. A few biological applications of HIs have been reported, first in 2005 by *Ikegami* and *Arai* who showed fluorescence modulation of pyrrole-HI derivative **7** upon photoswitching in the presence of bovine serum albumin (Figure 13.5b) [22]. In 2019, *Berdnikova* demonstrated a related fluorescence modulation of HI **8** upon photoswitching, while binding to HIV-1 RNA remains intact (Figure 13.5c) [20]. Such switchable emission responses in a biological context offer interesting prospects in bioimaging applications and real-time monitoring of dynamic processes.

A special feature of HIs arises from the additional possibility to introduce substituents at the nitrogen atom of the indoxyl fragment. The *Dube* group introduced axial chirality into HI photoswitches by substitution with an *ortho*-tolyl group at this position. Combined with a bulky substitution pattern on the stilbene fragment, it is possible to obtain asymmetric photoswitches with highly unusual chiroptical photoresponses (Figure 13.5d) [23].

These axially chiral dHIs (such as **5** depicted in Figure 13.5d) show a pronounced electronic circular dichroism (ECD) signal in the *Z*-isomeric state but almost no ECD

signal in the corresponding *E*-isomeric state. Thus, reversible photoisomerization results in a pronounced ON/OFF response of the ECD signal. In contrast to other ECD photoswitches, where the ON/OFF change in the ECD signal originates from the existence or absence of the corresponding absorption intensity, in axially chiral dHIs the ECD signal modulations occur despite the presence of high absorption intensities in both switching states. With such disentanglement of absorption and ECD changes upon photoswitching, interesting applications in, e.g. absolute asymmetric synthesis, smart filters, or molecular memories, can be expected in the future.

## 13.4 Hemithioindigo

Similar to HI, HTI is a photoswitch that photoisomerizes its central double bond upon visible light irradiation. It offers a rigid molecular structure with limited degrees of freedom for tight control of molecular geometry and, similar to HI, high thermal bistability of the switching states.

HTI was synthesized for the first time by *Friedländer* in 1906 [6]. The HTI core chromophore is accessible by simple condensation reactions of benzothiophenones and benzaldehydes, but also a variety of other methods have been reported so far (Figure 13.6) [24]. With increasing steric demand of introduced substituents, reactions become more and more inefficient and harsher conditions like Lewis acid activation with $BCl_3$ must be applied [25]. However, this approach is only successful to a certain extent of steric hindrance.

To generate sterically strongly hindered HTI derivatives, a gradual increase of steric constraints can be used, as reported by *Huber* et al. in a novel multistep synthesis [26]. As key step, a previously unknown ring-closing reaction of sulfonium chlorides is used. Another efficient approach for the synthesis of fourfold double-bond-substituted HTIs enables rapid structural diversification via a simple 3-step scheme. C—C cross-coupling reactions or nucleophilic substitutions at the chlorinated double bond serve as key diversification step in this synthesis [27].

The photophysical properties of HTIs have been studied in some detail and offer rare features. It is a great advantage of this chromophore that photoisomerization can be induced by visible-light irradiation in both switching directions (typically blue light (around 420 nm wavelength) is used for the *Z* to *E* direction and blue-green light (505 nm and longer) for the *E* to *Z* direction). However, for many applications, especially in a biological context, it is desirable to shift the switching wavelengths into the bio-optical window (starting approx. at 650 nm). For HTI, this is possible by introducing strong electron-donor substituents in the *para*-position of the stilbene fragment. In this way, the donor-acceptor character (the carbonyl group serves as acceptor) across the central double bond of HTI is increased, and photoisomerization can be triggered with yellow to red light. However, with this approach, the energy barrier for thermal *E*/*Z* isomerization is significantly lowered from 31 kcal $mol^{-1}$ in unsubstituted HTI to 21.4 kcal $mol^{-1}$ when introducing julolidine as the stilbene fragment. As a result, the thermal half-life of the *E* isomer is reduced from years to mere minutes at ambient temperatures. This problem can be circumvented by placing strong donor substituents at the thioindigo fragment in *para*-position of

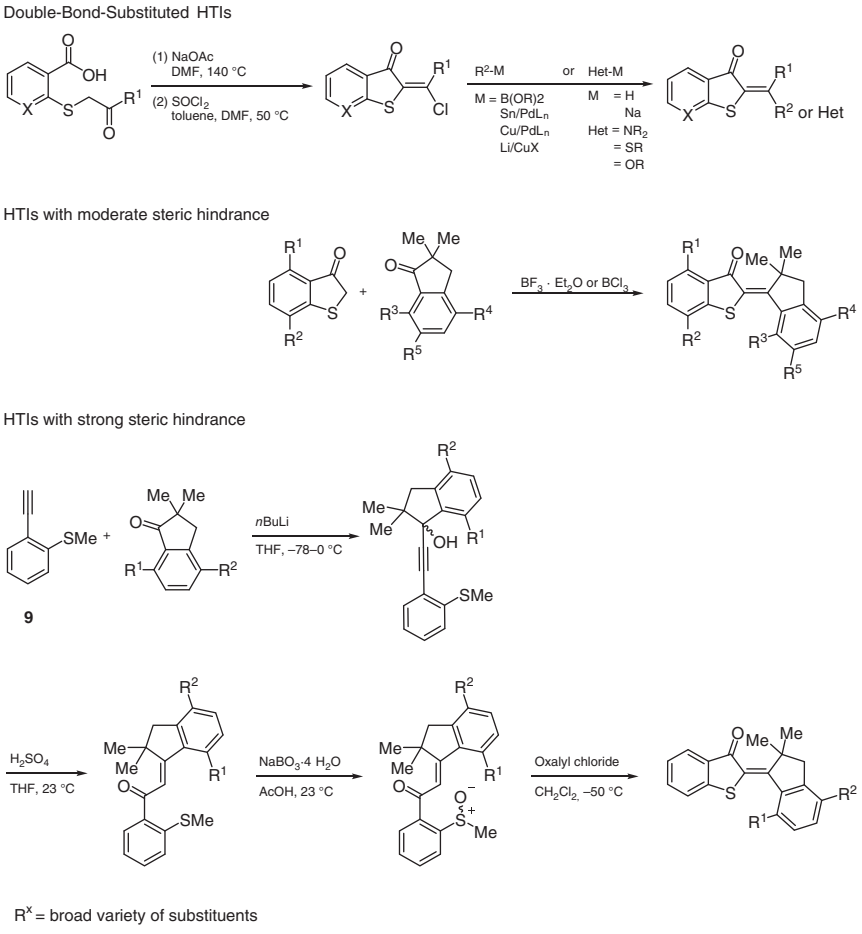


**Figure 13.6** Three pathways for the synthesis of HTIs with different degrees of structural elaboration and steric hindrance. Double-bond-substituted HTIs are obtained by transition-metal-catalyzed cross-coupling with a chlorinated precursor or a condensation reaction between benzothiophenone and ketones. Increasing steric hindrance is achieved by a stepwise synthesis, including a novel ring-closing reaction. Source: Based on Refs. [21, 24].

the sulfur atom instead. With this substitution pattern, a favorable redshift of the photoisomerization wavelengths is achieved without sacrificing thermal bistability [28]. By exchanging the phenyl ring of the stilbene fragment with a pyrrole moiety, bearing itself donor-substituted phenyl rings, a considerable bathochromic shift of the absorption can be achieved as a result of a combination of push-pull effects and intramolecular hydrogen bonding. At the same time, enhanced photochromism is observed resulting in very high isomeric yields in the respective PSSs while also thermal bistability is improved [29].

After *Mostoslavski* and coworkers recognized the photoisomerization capacity of HTI in 1961 [30], the group of *Ichimura* corroborated its extraordinary photofatigue resistance in the early 1990s [31]. Seminal studies on the excited-state mechanism of HTI photoisomerization were done by the groups of *Zinth*, *de Vivie-Riedle*, and

*Rück-Braun* in the early 2000s [32]. These works delivered important insights into the electronic and geometrical changes taking place in the excited state. At the same time, substituent effects on excited-state life-times were elucidated establishing that donor substituents lead to shorter life-times following linear Hammett correlations (see HTIs **10**–**15** in Figure 13.8a) [32c]. When introducing very strong electron-donor substituents, the *Dube* group in collaboration with the groups of *de Vivie-Riedle* and *Zinth* observed an interesting change of excited-state mechanism that leads to the opposite Hammett correlation. As a result, a maximum behavior for the photoisomerization rate was established for the electronic effects of substituents at the stilbene fragment [33].

When considering HTI double-bond photoisomerization, there is no inherent directionality in the planar core chromophore and both clockwise and anticlockwise rotation is equally likely. However, directionality can be introduced by alteration of the basic structure in three crucial ways: (i) introduction of stable asymmetry close to the rotating double bond via sulfur oxidation to the sulfoxide, (ii) rigidifying the stilbene fragment by ring fusion to the double bond, and (iii) increasing steric hindrance resulting in preferred helicity of the molecular structure. In this way, it was possible to generate HTI-based molecular motors that can be powered exclusively with visible light to perform fast and efficient unidirectional rotations (see Figure 13.7 for molecular motors **16**–**24**) [34].

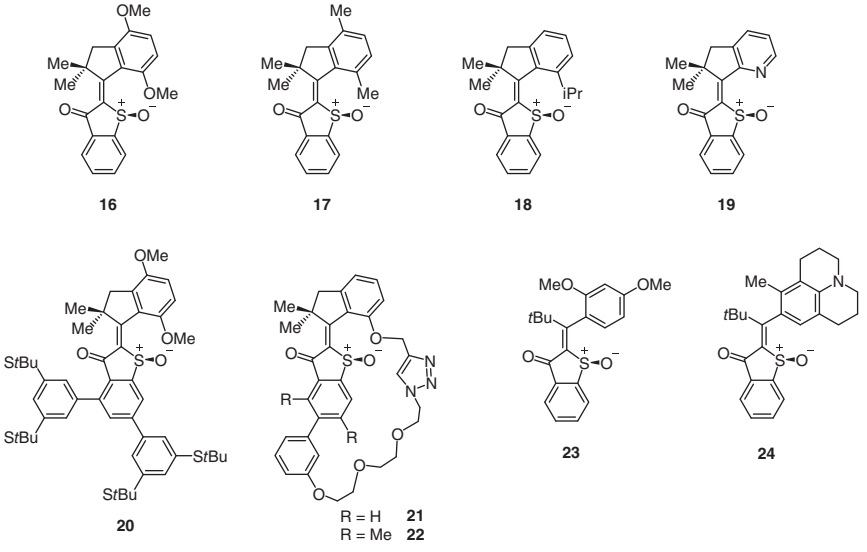


**Figure 13.7** Visible-light-driven molecular motors based on the HTI chromophore. **16**: First HTI molecular motor. **17**, **18**: Slow molecular motors for elucidation of the rotation mechanism. **19**: Prospective ultrafast molecular motor. **20**: Molecular motor for attachment on surfaces. **21**, **22**: Molecular machines transmitting and accelerating unidirectional motor motion to an attached remote biphenyl axis, respectively. **23**: Photon-only molecular motor with reverse-temperature dependency of its efficiency. **24**: Molecular motor performing an eight-shaped unidirectional motion. Source: Based on Refs. [34a, 34b].

More recently, these molecular motors were integrated into more complex molecular machines allowing to transfer the light-powered unidirectional motions of their double bond to remote and passive single-bond rotations (SBRs) (motor **21** in Figure 13.7) [25]. The passive SBRs can even be accelerated by several orders of magnitude upon action of the light-powered molecular motor entity, demonstrating how potential energy can be transferred in integrated nanomachines in an unidirectional manner (molecular motor **22** in Figure 13.7) [35]. More recent developments in the *Dube* group have brought forward the first photon-only powered molecular motor [36] and another setup that allows to produce a figure-eight-shaped unidirectional motion powered by green light (see structures **23** and **24**, respectively, in Figure 13.7 and more details in the text below) [37].

Besides the central double bond, the adjacent single bond connecting to the stilbene fragment is the only other option for bond rotation in HTI. When steric hindrance (via *ortho*-substitution) at the stilbene fragment is combined with strong electron donors (e.g. HTI **25**), rotation around this single bond can be evoked via formation of a twisted intramolecular charge transfer (TICT) state (Figure 13.8b). This highly polar state is populated by such pre-twisted HTIs only in polar solvents and then competes effectively with photoisomerization. In the TICT state, a partial charge separation takes place combined with rotation of the single bond to a 90° dihedral angle, which electronically decouples the stilbene and thioindigo fragments.

In apolar solvents the TICT state is not accessible, due to its slight energetic stabilization by the solvent and photoisomerization of the double bond is the predominant deexcitation pathway. As a consequence, it is possible to alter the motion that HTI **25** performs after photoexcitation by simply changing the solvent polarity. In apolar solvents the double bond rotates, whereas in polar solvents the single bond is rotated (Figure 13.8b) [38]. It should be noted at this point, however, that SBR via TICT state formation in twisted HTIs is not a full 180° rotation around this bond as opposed to the double-bond rotation.

After considering single- and double-bond rotations separately as deexcitation pathways of HTIs there is another option, which has been discussed for more than 30 years in the literature. This is the famous Hula twist photoreaction proposed first by *Liu* and *Asato* in 1985 to explain the ultrafast photoisomerization in the chromophore of vision retinal [39]. The Hula twist photoreaction as initially envisioned comprises a concerted coupled motion of a double bond and the adjacent single bond leading to deexcitation. This reaction has remained elusive for a long time and because of the lack of direct and unambiguous experimental evidences has been the center of much debate in the literature [40]. In unsubstituted HTI, it is not possible to discern such mechanism and distinguish between photoproducts of simple double-bond and Hula twist rotations. However, introducing an *ortho*-methoxy substituent on the stilbene fragment establishes atropisomers at the SBR axis. After increasing steric demand on the central double bond of such asymmetric HTI (by replacing the hydrogen atom by a *tert*-butyl group), the atropisomers become thermally stable. Oxidation of the sulfur atom to the corresponding sulfoxide (HTI **26**) results in four thermally stable diastereomers that can be separated and

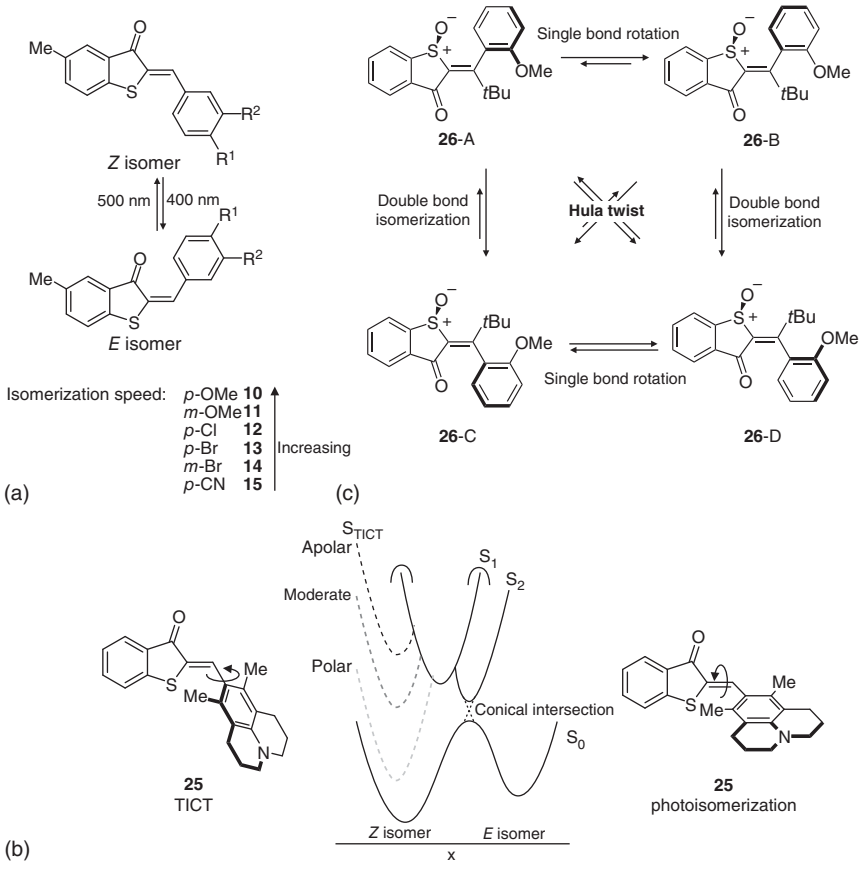


**Figure 13.8** Different light-induced motions in HTI. (a) Hammett correlation in a series of substituted HTIs **10–15** shows an accelerating photoisomerization speed with increasingly electron-donating substituents at the stilbene fragment. (b) Energy diagram for the solvent-dependent rotations within pre-twisted donor-substituted HTI **25**. With increasing polarity of the solvent, the energy level of the $S_{TICT}$ state becomes more accessible, enabling TICT formation as competition for photoisomerization. (c) Different photoinduced bond rotations were directly experimentally evidenced for HTI **26** (single-bond rotation (SBR), double-bond isomerization (DBI), and Hula twist).

are easily distinguished with conventional spectroscopy. Two atropisomers are obtained for the *Z* isomeric double-bond configuration and two atropisomers for the *E* isomeric one (Figure 13.8c). The atropisomers are interconverted at high temperatures (>80 °C) selectively without other bond rotations occurring. With this asymmetric molecular setup, it was possible to inter alia deliver direct experimental evidence for the formation of Hula twist photoproducts [41]. To this end, the photoisomerization reactions were followed for each of the four diastereomers separately. The photoreactions of the two different *Z* configured isomers were much more efficient than the ones of the *E* isomers and were thus analyzed in more detail. In general, sole DBI was found to be in competition with mainly one other

photoreaction, either 180° SBR (i.e. atropisomerization) or Hula twist, depending on the individual *Z*-atropisomer. The relative efficiencies of these photoreactions could be changed either by adjusting solvent polarity or much more significantly by temperature and rigidity of the solvent. Hula twist could be preferred up to 80% over DBI in cold but liquid polar solvents. DBI could be preferred >90% by freezing the solvent to an ice for the same isomer. The corresponding competition between SBR and DBI in the other isomer could only be altered between 40% (polar solvent, 22 °C) SBR and >90% DBI (solvent ice, −196 °C). By introducing a further *para*-methoxy substituent on the stilbene fragment of the same molecular setup, it was possible to alter the photoisomerization behavior such that only one specific sequence of isomer interconversion is observed under continuous light irradiation in a unidirectional manner (Figure 13.7, molecule **23**). In this sequence an SBR is followed by a Hula twist motion, which is then followed by a DBI to reestablish the original state. As a remarkable feature of this novel molecular motor system, it needs to be emphasized that the motion is driven by light exclusively omitting thermal steps in the working mechanism. Therefore, this motor becomes more efficient by temperature reduction [36] as opposed to conventional molecular motors that stop working and become switches at low temperature instead.

When the molecular setup of HTI **23** is altered by replacing its stilbene fragment with an *ortho*-methyl-substituted julolidine moiety, an entirely different type of molecular motor is obtained (Figure 13.7, molecular motor **24**). HTI **24** performs a four-step cycle, in which two photoinduced DBI steps are separated by two thermal Hula twist isomerization steps. Such thermal Hula twist reactions were not known before and effectively ratchet the reversibility in the working cycle of this molecular machine. The result is a significantly more complex directional trajectory than could be achieved with molecular motors before. Instead of a directional linear or circular motion, a crossing point is introduced into the trajectory and a figure-eight-shape motion results [37].

Conscious substitution of the HTI core chromophore also allows applications of this photoswitch as receptor in the field of supramolecular chemistry [42]. The earliest supramolecular applications have been reported by *Tanaka* in the early 2000s using benzoyl- or pyridine-containing HTIs as photoswitchable guest molecules in porphyrin receptors. In the latter case, a light-induced shuttling of the photoresponsive HTI guest **27** between two different and specifically designed porphyrin receptors was induced by photoisomerization (Figure 13.9a) [43]. Later it was shown that HTI can be used as photoswitchable guest molecule inside molecular capsules or cavitands [44] enabling for example multi-photonic control of guest exchanges and assembly formation in solution (HTI **28** in Figure 13.9b and **29** in Figure 13.9c) [44b].

By attaching an electron-rich biaryl moiety to each fragment of the HTI chromophore, it is possible to bring these in close proximity or separate them from each other by irradiation with light of a certain wavelength. In the resulting light-responsive molecular tweezers HTI **30,** the biaryl moieties are aligned parallel to each other at a distance of 7 Å in the *Z* isomeric state (Figure 13.9e). In this alignment, electron-deficient aromatic guest molecules can be bound via polar aromatic interactions. By simple light irradiation *Z* to *E* photoisomerization

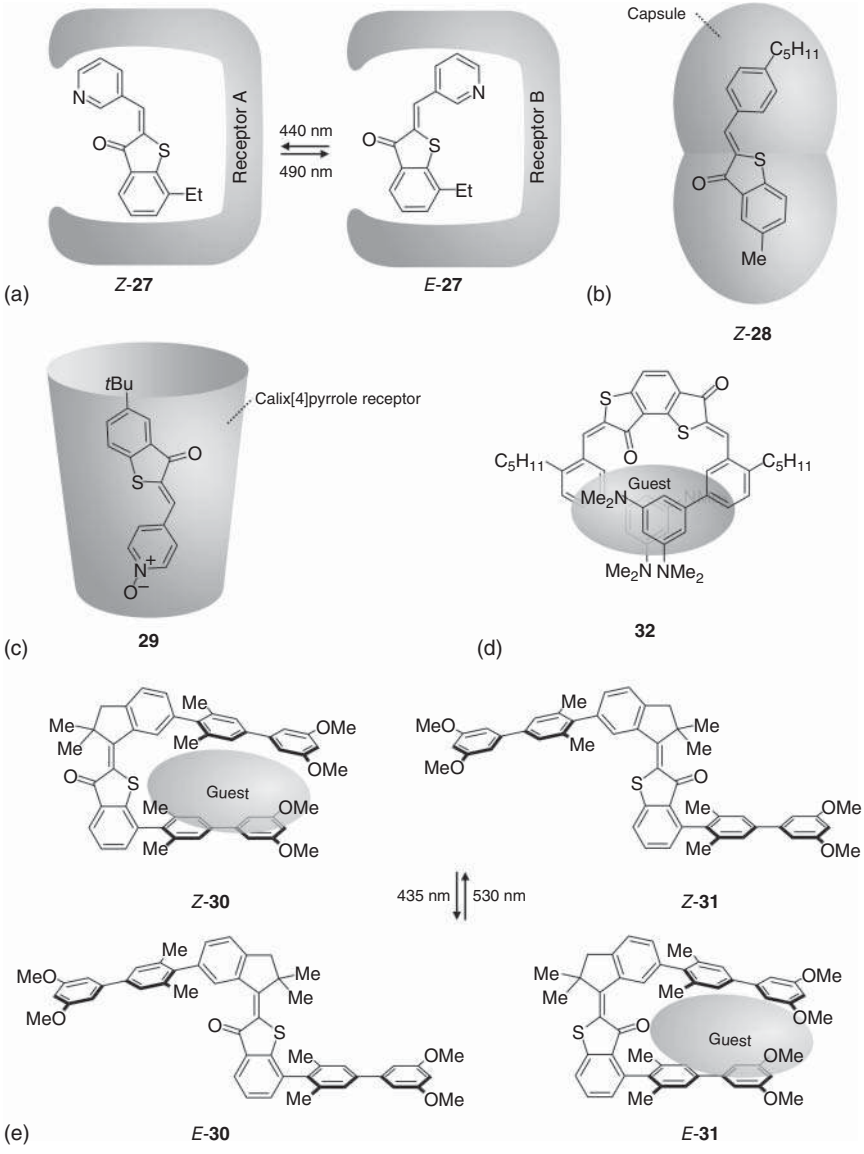


**Figure 13.9** (a) HTI guest molecule **27** can be shuttled between two different porphyrine receptors depending on its isomeric form. (b) HTI guest molecule **28** shows isomer-dependent binding and release within a molecular capsule. (c) N-oxide HTI **29** is a guest for a calix[4]pyrrole receptor, with equal binding constants for its isomeric forms. (d) Molecular tweezers **32** is based on a *bis*-HTI photoswitch and binds aromatic guest molecules within its helical structure. (e) Molecular tweezers **30** and **31** incorporate HTI as central switching unit for light-induced catch and release of guest molecules. The high-affinity forms of molecular tweezers **30** and **31** are in opposite isomeric states to each other, which enables reversible guest relocation from one binding site to another after application of a reduced set of only two external light stimuli. Source: (a) Based on Refs. [43a, 43b]; (b,c) Based on Dube and Rebek [44b]; (d) Based on Refs. [42a, 42b].

takes place, the two biaryls are separated spatially, and the guest molecule is released.

By altering the attachment point of one of the biaryl-binding sites on the thioindigo fragment another molecular tweezers receptor HTI **31** can be realized, but with opposite binding affinities for the respective isomeric forms (Figure 13.9e). Whereas tweezers **31** can bind aromatic molecules in their *E* form, tweezers **30** bind in their *Z* form. Both tweezers still use the same wavelengths of light to trigger DBI, rendering them into a complementarily responding receptor pair. Irradiation with one wavelength converts tweezers **30** from their binding into the non-binding form and tweezers **31** vice versa. Thereby, a significantly reduced set of visible light signals (explicitly two instead of four to address individual receptors) is used to shuttle a guest molecule between two receptors [45]. Another possibility is to affect binding affinity by controlling the folding state of a *bis*-HTI receptor motive (**32**) by visible light and thus alter capture and release of electron-deficient guest molecules (Figure 13.9d) [42].

Applications of HTIs in the field of chemical biology have been mainly developed in the laboratory of *Rück-Braun* in collaboration with the group of *Zinth* focusing on HTI-containing amino acids or peptides and the photoswitching of secondary structures such as β-sheets (see HTI **33** in Figure 13.10a) [46]. By employing time-resolved

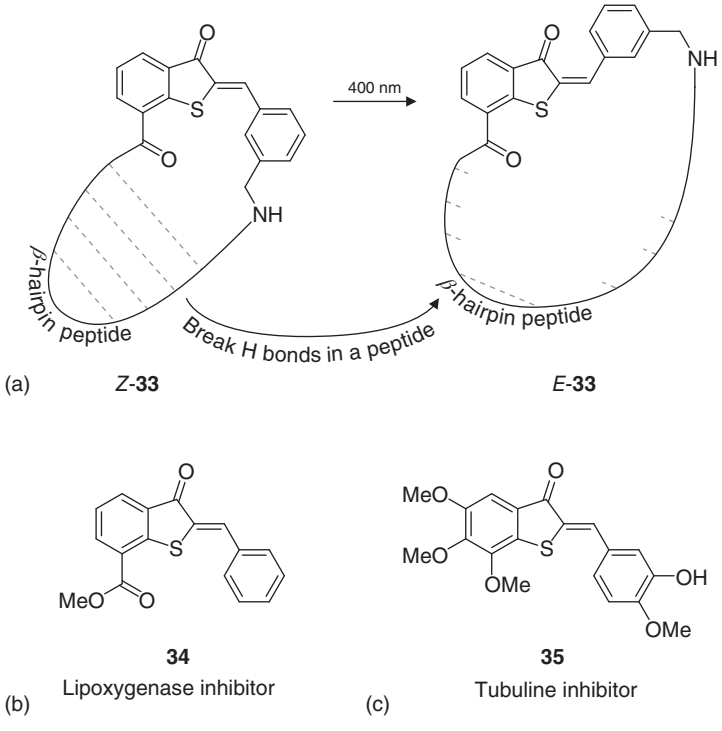


**Figure 13.10** Biological applications of HTIs. (a) HTI switch **33** operating in a β-hairpin peptide enabling photoinduced structural changes via breaking of H-bonding in the peptide. (b) HTI **34** is a photocontrollable lipoxygenase inhibitor with varying affinity depending on its isomeric form. (c) HTI **35** acts as visible-light-responsive tubuline inhibitor. Source: (a) Based on Refs. [46a, 46b]; (b) Based on Herre et al. [47]; (c) Based on Sailer et al. [48].

methods, individual structural responses on different time scales could be resolved. These studies delivered important insights into the nature and sequence of events following, e.g. photoexcitation in peptidic photoswitches. Together with the group of *Kuhn*, the first photopharmacology application was published in 2006, reporting on an HTI-based photoswitchable inhibitor of the 12/15 lipoxygenase pathway [47] (HTI **34** in Figure 13.10b). In the early 2000s, HTI was also introduced into gramicidin channels to photomodulate ionic currents across membranes [49] and into photoswitchable lipids [50]. These efforts have been furthered more recently by the development of HTI-based inhibitors for tubuline, which allow to photocontrol mitosis with visible light in vivo (HTI **35** in Figure 13.10c) [48]. It should be emphasized that biological applications are highly promising for HTIs because of their favorable visible-light responsiveness and thermal bistability. More progress in this regard is certainly expected in the near future.

## 13.5 Iminothioindoxyls

Iminothioindoxyls (ITIs) were first described as dyes more than 100 years ago [51]. The synthesis of ITIs can be achieved easily by a condensation reaction of benzothiophenone and nitrosobenzene derivatives [52] or a [4+1] cycloaddition of isocyanides with 2-mercaptobenzaldehydes (Figure 13.11) [53]. In 2019 *Szymanski*, *Buma*, *Feringa*, and coworkers investigated the photoswitching abilities of ITIs **36**–**41** by low-temperature Nuclear magnetic resonance (NMR) studies and

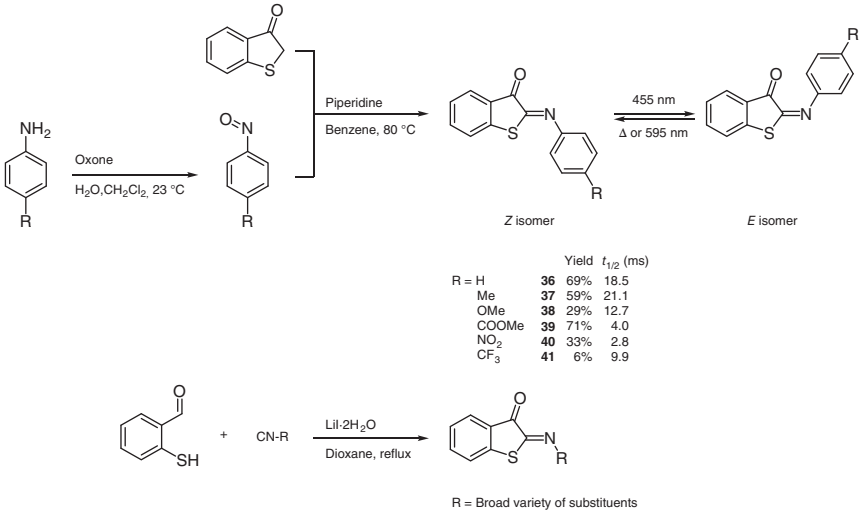


**Figure 13.11** Synthesis of ITIs **36**–**41** via a condensation reaction of benzothiophenone and a nitrosobenzene derivatives or a [4+1] cycloaddition reaction between isocyanides and 2-mercaptobenzaldehydes. Photoisomerization can be triggered with 455 nm light in the *Z*/*E* direction and 595 nm light in the *E*/*Z* direction. Thermal *Z*/*E* isomerization proceeds quickly on ms time scales, the corresponding half-lives of the metastable *E*-isomers at room temperature are indicated. Source: Based on Soeta et al. [53].

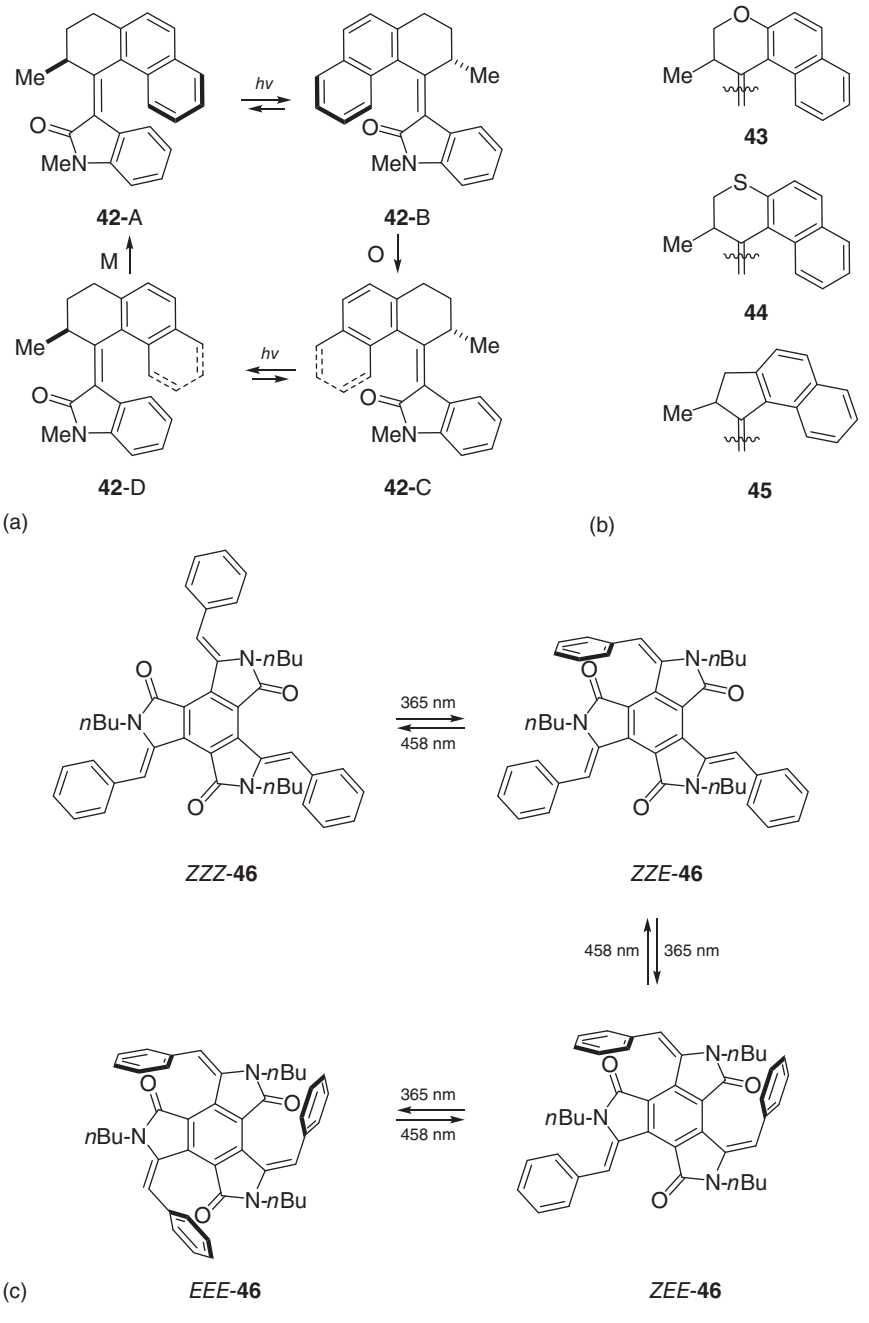


**Figure 13.12** (a) Rotation mechanism of motor **42** that can be powered with 422 nm light and operates via two photoisomerization and two thermal ratcheting steps. The speed of the thermal steps can be adjusted by different upper halves. (b) Molecular motors **43**–**45** based on oxindole. (c) Four-state photoswitch **46** based on isoindolinone.

time-resolved UV/vis measurements on the ms time scale [54]. ITIs are photoswitches that can, like the other indigoid switches, be isomerized between *E* and *Z* isomers with visible light exclusively. An exceptional feature of ITIs is their large band separation of the UV/vis maxima of about 100 nm, which results in particularly strong photochromism. After irradiation of ITIs with light of 455 nm wavelength up to 83% of the *E*-isomer were obtained in the PSS, with the photoisomerization being a fast process on the ps time scale. The thermal back isomerization (*E* to *Z* direction) is an ms process at ambient temperature, preventing bistable switching. Such thermal lability however can be a desired feature in specific applications that require fast OFF rates of molecular functions.

## 13.6 Oxindoles and Isoindolinones

Oxindole represents a constitutional isomer of indoxyl and has recently been used for the construction of visible-light-responsive molecular motors **42**–**45** by the groups of *Feringa* and *Wezenberg* [55]. In these motors, one half of the classical *Feringa* motor is replaced by oxindole resulting in a significant bathochromic shift of the absorption, which allows using visible light as power source. The working mechanism comprises four steps alternating photoisomerization of the central double bond with thermally induced helix inversions (Figure 13.12). Easy synthetic access by a *Knoevenagel*-type condensation reaction enables facile structural alterations. Different upper halves were used for instance to significantly alter kinetics of the thermal ratcheting steps. In this way, the maximum attainable rotation speeds of these motors can be tuned to specific applications in a straight-forward manner.

Isonindolinones were only recently introduced as photoswitching motives [56]. In the group of *Eisler*, multi-switching units were synthesized based on this structural motive and scrutinized for their photoisomerization behavior. These novel photoswitch systems are thermally stable and provide interesting possibilities for multi-state switching systems. For example, a four-state switching system **46** was reported in 2013 where different isomer mixtures are obtained under different irradiation and heating conditions [57].

## References


**1** Baeyer, A. (1883). *Ber. Dtsch. Chem. Ges.* 16: 2188–2204.

**2** (a) Iwakura, I., Yabushita, A., and Kobayashi, T. (2010). *Chem. Phys. Lett.* 484: 354–357. (b) Pina, J., Sarmento, D., Accoto, M. et al. (2017). *J. Phys. Chem. B* 121: 2308–2318.

**3** (a) Weinstein, J. and Wyman, G.M. (1956). *JACS* 78: 4007–4010. (b) Wyman, G.M. and Zenhäusern, A.F. (1965). *J. Org. Chem.* 30: 2348–2352. (c) Farka, D., Scharber, M., Głowacki, E.D., and Sariciftci, N.S. (2015). *J. Phys. Chem. A* 119: 3563–3568.


**4** (a) Omote, Y., Tomotake, A. , Aoyama, H., Nishio, T., Kashima, C. (1984). *Bull. Chem. Soc. Jpn.* 57: 470–472. (b) Huang, C.-Y., Bonasera, A., Hristov, L. et al. (2017). *JACS* 139: 15205–15211.

**5** Huber, L.A., Mayer, P., and Dube, H. (2018). *ChemPhotoChem* 2: 452–452.

**6** Friedlaender, P. (1906). *Chem. Ber.* 39: 1060–1066.

**7** Stearns, E.I. (1942). *J. Opt. Soc. Am.* 35: 282–284.

**8** (a) Wyman, G.M. and Brode, W.R. (1951). *JACS* 73: 1487–1493. b) Rogers, D.A., Margerum, J.D., and Wyman, G.M. (1957). *JACS* 79: 2464–2468.

**9** Kirsch, A.D. and Wyman, G.M. (1977). *J. Phys. Chem.* 81: 413–420.

**10** Memming, R. and Kobs, K. (1981). *Ber. Bunsen-Ges. Phys. Chem* 85: 238–242.

**11** Irie, M. and Kato, M. (1985). *JACS* 107: 1024–1028.

**12** (a) Rahman, S.M.F.-U., Shahjin, F., and Fukunishi, K. (2014). *J. Bangladesh Acad. Sci.* 37: 219–229. (b) Fatah-ur Rahman, S.M. and Fukunishi, K. (1994). *J. Chem. Soc., Chem. Commun.* 917–918.

**13** (a) Vlahakis, J.Z., Wand, M.D., and Lemieux, R.P. (2003). *JACS* 125: 6862–6863. (b) Dinescu, L. and Lemieux, R.P. (1997). *JACS* 119: 8111–8112. (c) Dinescu, L. and Lemieux, R.P. (1996). *Liq. Cryst.* 20: 741–749.

**14** Koeppe, B. and Römpp, F. (2018). *Chem. Eur. J.* 24: 14382–14386.

**15** Koeppe, B., Rühl, S., and Römpp, F. (2019). *ChemPhotoChem* 3: 71–74.

**16** Dittmann, M., Graupner, F.F., Maerz, B. et al. (2014). *Angew. Chem. Int. Ed.* 53: 591–594.

**17** Mostoslavskii, M.A., Kravchenko, M.D., and Shevchuk, I.N. (1970). *Zh. Fiz. Khim.* 44: 1008–1012.

**18** Arai., T., Ikegami, M., (1999). *Chem. Lett.* 28: 965–966.

**19** Petermayer, C., Thumser, S., Kink, F. et al. (2017). *JACS* 139: 15060–15067.

**20** Berdnikova, D.V. (2019). *Chem. Commun.* 55: 8402–8405.

**21** Carrascosa, E., Petermayer, C., Scholz, M.S. et al. (2020). *ChemPhysChem* 21: 680–685.

**22** Ikegami, M. and Arai, T. (2005). *Chem. Lett.* 34: 492–493.

**23** Petermayer, C. and Dube, H. (2018). *JACS* 140: 13558–13561.

**24** (a) Konieczny, M.T. and Konieczny, W. (2005). *Heterocycles* 65: 451–464. (b) Wiedbrauk, S. and Dube, H. (2015). *Tetrahedron Lett.* 56: 4266–4274.

**25** Uhl, E., Thumser, S., Mayer, P., and Dube, H. (2018). *Angew. Chem. Int. Ed.* 57: 11064–11068.

**26** Huber, L.A., Hoffmann, K., Thumser, S. et al. (2017). *Angew. Chem. Int. Ed.* 14536–14539.

**27** Gerwien, A., Reinhardt, T., Mayer, P., and Dube, H. (2018). *Org. Lett.* 20: 232–235.

**28** Kink, F., Collado, M.P., Wiedbrauk, S. et al. (2017). *Chem. Eur. J.* 23: 6237–6243.

**29** Zweig, J.E. and Newhouse, T.R. (2017). *JACS* 139: 10956–10959.

**30** Izmail'skii, V.A. and Mostoslavskii, M.A. (1961). *Ukr. Khem. Zh.* 27: 234–237.

**31** Ichimura, K., Seki, T., Tamaki, T., and Yamaguchi, T. (1990). *Chem. Lett.* 9: 1645–1646.

**32** (a) Nenov, A., Cordes, T., Herzog, T.T. et al. (2010). *J. Phys. Chem. A* 114: 13016–13030. (b) Cordes, T., Heinz, B., Regner, N. et al. (2007). *ChemPhysChem*


8: 1713–1721. (c) Cordes, T., Schadendorf, T., Priewisch, B. et al. (2008). *J. Phys. Chem. A* 112: 581–588.
**33** Maerz, B., Wiedbrauk, S., Oesterling, S. et al. (2014). *Chem. Eur. J.* 20: 13984–13992.
**34** (a) Guentner, M., Schildhauer, M., Thumser, S. et al. (2015). *Nat. Commun.* 6: 8406. (b) Wilcken, R., Schildhauer, M., Rott, F. et al. (2018). *JACS* 140: 5311–5318.
**35** Uhl, E., Mayer, P., and Dube, H. (2020). *Angew. Chem. Int. Ed.* 59: 5730–5737.
**36** Gerwien, A., Mayer, P., and Dube, H. (2018). *JACS* 140: 16442–16445.
**37** Gerwien, A., Mayer, P., and Dube, H. (2019). *Nat. Commun.* 10: 4449.
**38** Wiedbrauk, S., Maerz, B., Samoylova, E. et al. (2016). *JACS* 138: 12219–12227.
**39** Liu, R.S. and Asato, A.E. (1985). *Proc. Natl. Acad. Sci. U.S.A* 82: 259–263.
**40** (a) Redwood, C., Bayda, M., and Saltiel, J. (2013). *J. Phys. Chem. Lett.* 4: 716–721. (b) Kaila, V.R.I., Schotte, F., Cho, H.S. et al. (2014). *Nat. Chem.* 6: 258–259. (c) Jung, Y.O., Lee, J.H., Kim, J. et al. (2014). *Nat. Chem.* 6: 259–260.
**41** Gerwien, A., Schildhauer, M., Thumser, S. et al. (2018). *Nat. Commun.* 9: 2510.
**42** Guentner, M., Uhl, E., Mayer, P., and Dube, H. (2016). *Chem. Eur. J.* 22: 16433–16436.
**43** (a) Tanaka, K., Taguchi, K., Iwata, S., and Irie, T. (2005). *Supramol. Chem.* 17: 637–642. (b) Tanaka, K., Kohayakawa, K., Iwata, S., and Irie, T. (2008). *J. Org. Chem.* 73: 3768–3774.
**44** (a) Moncelsi, G., Escobar, L., Dube, H., and Ballester, P. (2018). *Chem. Asian J.* 13: 1632–1639. (b) Dube, H. and Rebek, J. Jr., (2012). *Angew. Chem. Int. Ed.* 51: 3207–3210.
**45** Wiedbrauk, S., Bartelmann, T., Thumser, S. et al. (2018). *Nat. Commun.* 9: 1456.
**46** (a) Regner, N., Herzog, T.T., Haiser, K. et al. (2012). *J. Phys. Chem. B* 116: 4181–4191. (b) Steinle, W. and Rück-Braun, K. (2003). *Org. Lett.* 5: 141–144.
**47** Herre, S., Schadendorf, T., Ivanov, I. et al. (2006). *ChemBioChem* 7: 1089–1095.
**48** Sailer, A., Ermer, F., Kraus, Y. et al. (2019). *ChemBioChem* 20: 1305–1314.
**49** Lougheed, T., Borisenko, V., Hennig, T. et al. (2004). *Org. Biomol. Chem.* 2: 2798–2801.
**50** Eggers, K., Fyles, T.M., and Montoya-Pelaez, P.J. (2001). *J. Org. Chem.* 66: 2966–2977.
**51** Bezdrik, A., Friedländer, P., and Koeniger, P. (1908). *Ber. Dtsch. Chem. Ges.* 41: 227–242.
**52** Pummerer, R. (1910). *Ber. Dtsch. Chem. Ges.* 43: 1370–1376.
**53** Soeta, T., Shitaya, S., Okuno, T. et al. (2016). *Tetrahedron* 72: 7901–7905.
**54** Hoorens, M.W.H., Medved', M., Laurent, A.D. et al. (2019). *Nat. Commun.* 10: 2390.
**55** Roke, D., Sen, M., Danowski, W. et al. (2019). *JACS* 141: 7622–7627.
**56** (a) Cameron, D. and Eisler, S. (2018). *J. Phys. Org. Chem.* 31: e3858. (b) Lawson, M. and Eisler, S. (2012). *Org. Biomol. Chem.* 10: 8770–8773. (c) Belluau, V., Noeureuil, P., Ratzke, E. et al. (2010). *Tetrahedron Lett.* 51: 4738–4741.
**57** Estey, P., Bubar, A., Decken, A. et al. (2013). *Chem. Eur. J.* 19: 16204–16208.

# 14 Donor–Acceptor Stenhouse Adducts

Friedrich Stricker, Serena Seshadri, and Javier Read de Alaniz

## Photochromism

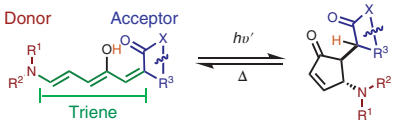


## Characteristic Features

Visible to near-IR range photochromism, negatively photochromic, applications in drug delivery, sensing and actuation.

## Synthetic Methods

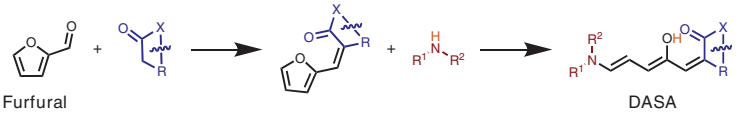


1st generation

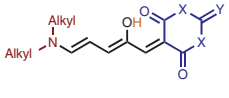

Meldrums acid: X: –O; Y: –$(Me)_2$
Barbituric acid: X: –NMe; Y: O

$\lambda_{max}$ ~ 500 nm

- Control of dark equilibrium
- Limited solent switchability
- Limited wavelength tuneability

2nd generation

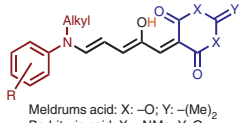

Meldrums acid: X: –O; Y: –$(Me)_2$
Barbituric acid: X: –NMe; Y: O

$\lambda_{max}$ ~ 400–700 nm

- Enhanced switching properties
- *Solid-state switching*
- Thermodyn. equi. favors closed

3rd generation

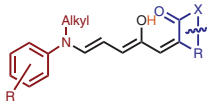

$\lambda_{max}$ ~ 400–700 nm

- Control of dark equilibrium
- Enhanced switching properties
- *Solid-state switching*

## First Reported

Helmy, S., Leibfarth, F.A., Oh, S., et al. (2014). Photoswitching using visible light: a new class of organic photochromic molecules. *J. Am. Chem. Soc.* 136: 169–172.

## Key References

Hemmer, J.R., Page, Z.A., Clark, K.D., et al. (2018). Controlling dark equilibria and enhancing donor-acceptor stenhouse adduct photoswitching properties through carbon acid design. *J. Am. Chem. Soc.* 140: 10425–10429.

Lerch, M.M., Szymanski, W. and Feringa, B.L. (2018). *Chem. Soc. Rev.* 47: 1910–1937.

# 14

# Donor–Acceptor Stenhouse Adducts

*Friedrich Stricker, Serena Seshadri, and Javier Read de Alaniz*

*University of California at Santa Barbara, Department of Chemistry and Biochemistry, Santa Barbara CA 93106, USA*

## 14.1 Introduction

Photochromism – the property to undergo a light-induced reversible change of color based on a chemical reaction – was first reported by Fritzsche in 1867 [1]. From this initial discovery, many new classes of photochromic molecules such as photoswitches, which undergo a reversible conversion between their stable and (meta)stable isomers triggered by light, have been discovered. Not surprisingly, each photoswitch has its own advantageous properties and drawbacks, which have been significantly optimized in the past 30 years. Wide-ranging applications that leverage photoswitching molecules, such as drug delivery, sensing, photopatterning, and actuation, are likewise impressive. It is important to note, however, that the initial discovery of numerous classes of "modern" photochromic molecules actually dates back to the 1800s and early 1900s when these molecules were being investigated for their dye properties.

This chapter summarizes an emerging class of negatively photochromic photoswitches discovered in our group in 2014 (Figure 14.1) [2] termed donor–acceptor Stenhouse adducts (DASAs), whose history dates back to a structurally related red dye initially reported by J. Stenhouse in 1850 [3]. In this lecture, Stenhouse disclosed that skin, paper, white velvet, canvas, or cotton fabric treated with furfural slowly changes to roseate with the addition of a few drops of aniline. In 1887, Schiff accurately determined the structure of the red dye as a five-carbon cyanine dye with a hydroxyl substituent at the second carbon, commonly referred to as a Stenhouse salt [4]. Despite these pioneering reports, it would take nearly a century before their photochromic properties were investigated. In 1982, Honda reported the photochromic behavior of more than 10 Stenhouse salts [5]. Although the product of the visible-light-driven photochromic reaction was not identified, through retrospective mechanistic analysis we now know that the product was a colorless 4,5-diaminocyclopentenone adduct.

*Molecular Photoswitches: Chemistry, Properties, and Applications*,
First Edition. Edited by Zbigniew L. Pianowski.


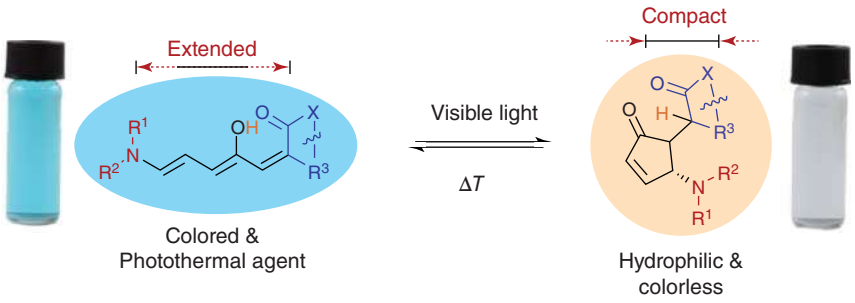


**Figure 14.1** DASAs, a new platform of visible light organic photoswitches.

It was the synthesis of 4,5-disubstituted cyclopentenone adducts that lead to our serendipitous discovery of DASA-based photoswitches. Motivated to replace multistep chemical synthesis of biologically active cyclopentenone scaffolds, we were drawn to the Piancatelli rearrangement [6]. In 1976, Piancatelli and co-workers reported a new method for the synthesis of 4-hydroxycyclopentenone derivatives by an acid-catalyzed rearrangement of furylcarbinols [7]. Inspired by this work, in 2010 we developed an efficient aza-Piancatelli rearrangement of furylcarbinols using aniline-based nucleophiles [8–11]. The overall transformation proceeds through a cascade sequence that terminates with a 4π electrocyclic ring closure of a pentadienyl cation; a step that is analogous to the ring-closing step of DASAs. In an effort to expand the generality of this new methodology to aliphatic amines, we turned our attention to a preliminary study by Safar and coworkers on the rearrangement of activated furans with cyclic secondary aliphatic amines [12]. In contrast to traditional Stenhouse salts that proceeded through imine/iminium activation, this system leveraged the electron-withdrawing nature of Meldrum's acid to facilitate the furan-ring-opening reaction to generate what we later coined as DASAs. Guided by our interest in cascade rearrangements of furfural-derived materials, we hypothesized that the photochromic behavior observed by Honda was due to a light-driven isomerization of the Stenhouse salt triene, which led to the key intermediate for the subsequent 4π electrocyclization and the formation of the closed 4,5-aminocyclopentenone (Figure 14.2). With these considerations in mind, we initiated our preliminary studies on the photochromic properties of DASAs and launched a new period in our research group. Herein, we describe the evolution of DASAs, their photophysical properties and highlight a range of applications that have already been demonstrated since their initial report in 2014.

## 14.2 DASA Synthesis

### 14.2.1 Molecular Photoswitch

DASA-based photochromes all share a general architecture with a triene backbone bearing a hydroxy group in the C2-position, an electron-withdrawing carbon acid acceptor, and an electron-donating secondary amine at the terminal end (Figure 14.3a). These structural properties are derived from furfural, which serves

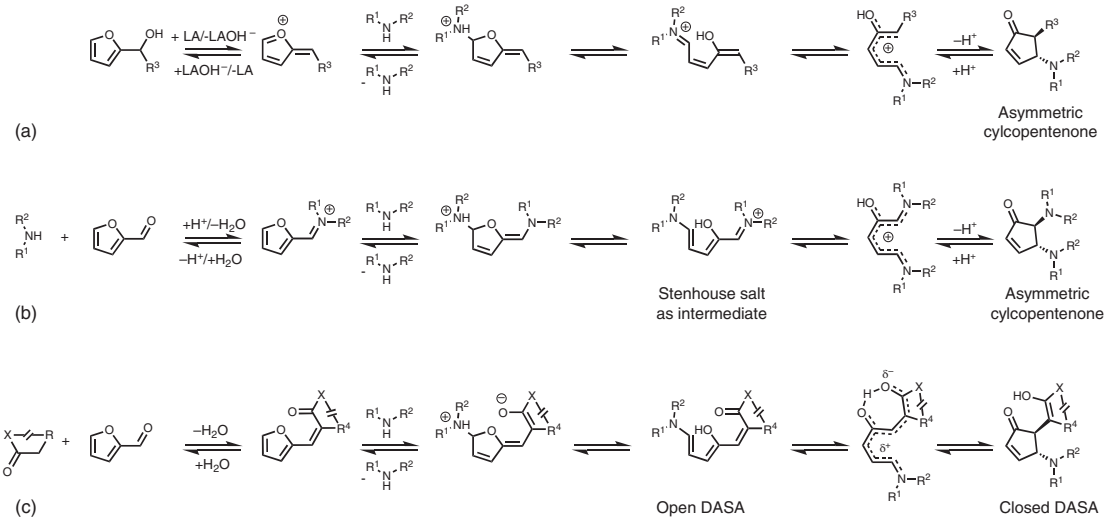


**Figure 14.2** Schematic representation of (a) aza-Piancatelli rearrangement, (b) Stenhouse salt synthesis, and (c) DASA synthesis.

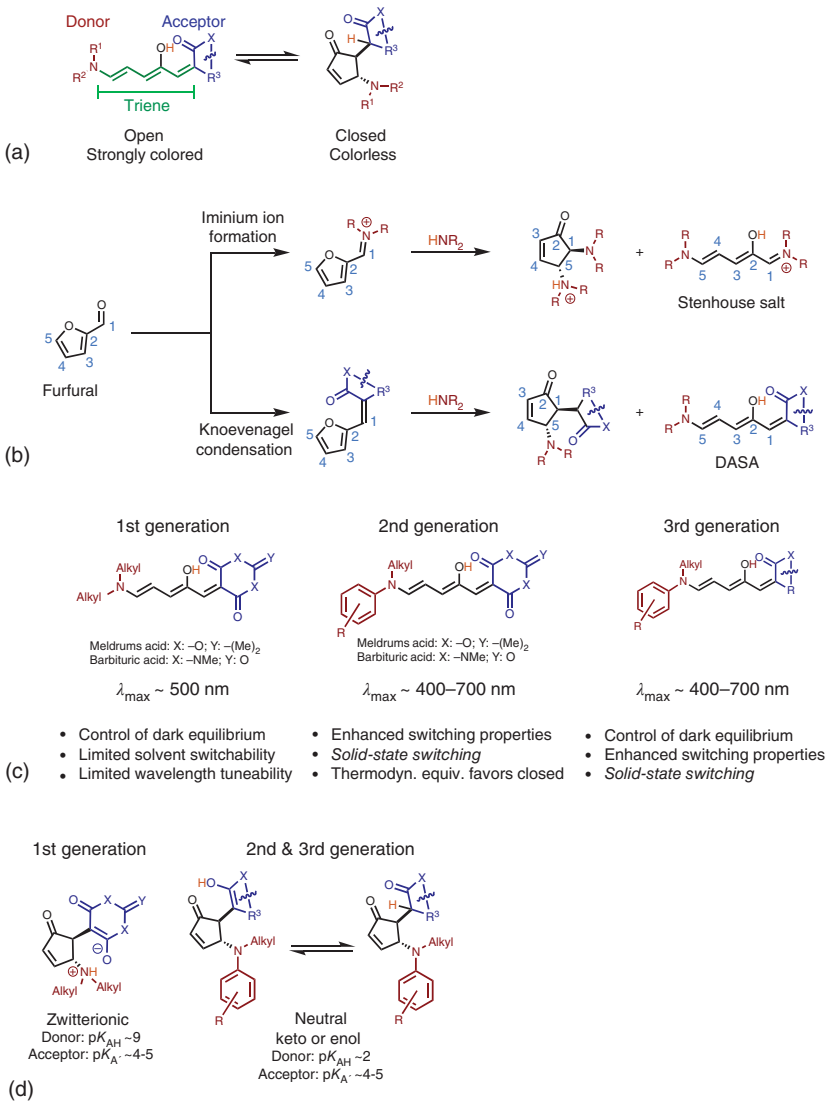


**Figure 14.3** Structure and modular synthesis of donor–acceptor Stenhouse adducts. (a) General structure of DASA photochromes. (b) Modular synthesis of DASA photochromes and Stenhouse salts. (c) Synthetic evolution through three generations of DASA photochromes. (d) Closed-form isomers of DASA photochromes [2, 14, 15].

as the precursor to the triene bridge with the furan oxygen providing the hydroxy group in the final architecture. Using a modular two-step synthesis, furfural is activated with readily available carbon acid acceptor moieties via a Knoevenagel condensation. Subsequently, a secondary amine nucleophile initiates a ring-opening reaction of the activated furan core, resulting in the visible-light-responsive DASA photochrome. This modularity allows straightforward design of DASA photochromes and has played a major role in the rapid exploration of this new class

of photochromic material. The original discovery of DASA photochromes in 2014 was based on dialkylamine donors and acceptors derived from either Meldrum's acid or barbituric acid. This first generation was based on the strongly nucleophilic dialkylamines and relatively weak electron-withdrawing acceptor groups, but suffered from a number of drawbacks discussed in Section 14.3 [2, 13].

Due to the strong donating character of the dialkylamines, these compounds show a high bond length alternation (BLA) suggesting a zwitterionic open form, which is supported by theoretical calculations [16, 17].

In 2016, arylamines (*N*-methylaniline and indoline derivatives) were introduced independently by Read de Alaniz [15] and Beves [16] as a second-generation DASA, which employed weaker electron-donating amines to address a range of shortcomings of the first generation. These derivatives show less BLA suggesting a more hybrid open form triene structure. Although the weakly donating amines provided improved photoswitching properties, it also introduced several drawbacks, most notably compromised thermodynamic equilibria meaning high amounts of closed form in the dark [15]. As a result, a third generation was developed in 2018, which introduced new classes of more electron-withdrawing acceptor moieties to overcome drawbacks while maintaining the improvements of the second generation [14]. More recently, improved photochromic performance of first-generation DASA has been achieved by modifying the steric properties of the donor sidechains using asymmetric alkylamines [18].

When evaluating the effects of the donor and acceptor groups on DASA-based photochromes, the closed-form derivative that results from irradiation also plays a significant role. DASA has been reported to form a zwitterionic closed form as the kinetic product, in which the acceptor is deprotonated by the amine donor to form an enolate, as well as a thermodynamic ketone form with an enol as the intermediate. More basic donors like alkylamines in the first generation have been reported to exclusively form the zwitterionic intermediate, while the less basic arylamines in generations 2 and 3 have been reported to form a mixture of the neutral keto and enol acceptors (Figure 14.3d) depending on the substitution pattern on the aryl moiety [15, 16, 18, 19]. The closed-form derivatives can also be trapped by the addition of nucleophiles into the Michael acceptor of the cyclopentenone making it possible to drain the equilibrium while also limiting the compatibility with strong nucleophiles [20].

### 14.2.2 Photoswitches in Macromolecules

To apply DASA into functional materials, multiple groups have explored ways of conjugating DASA photochromes with polymeric systems [13, 21–24]. However, the presence of radicals or strong nucleophiles in common polymerization methods leads to undesired side reactions with DASA; as a result, only post-polymerization functionalization methods have proven successful to date.

The most common pathway involves the introduction of the donor or acceptor moiety onto a polymer backbone and utilizing the DASA-forming reaction as the final functionalization step. Wang and coworkers demonstrated in 2017 the use of a polyethylenimine network to directly form DASA photochromes on

a polymeric system (Figure 14.4a (**1**)) [24]. Two research groups have demonstrated two additional ways of including amines as donor groups by utilizing acrylate or methacrylate polymers. Beves and coworkers copolymerized a protected alkylamine acrylate or methacrylate derivative, which was unmasked post-polymerization (Figure 14.4a (**2**)) [22]. Read de Alaniz and coworkers employed an activated pentafluorophenolacrylate to functionalize the backbone

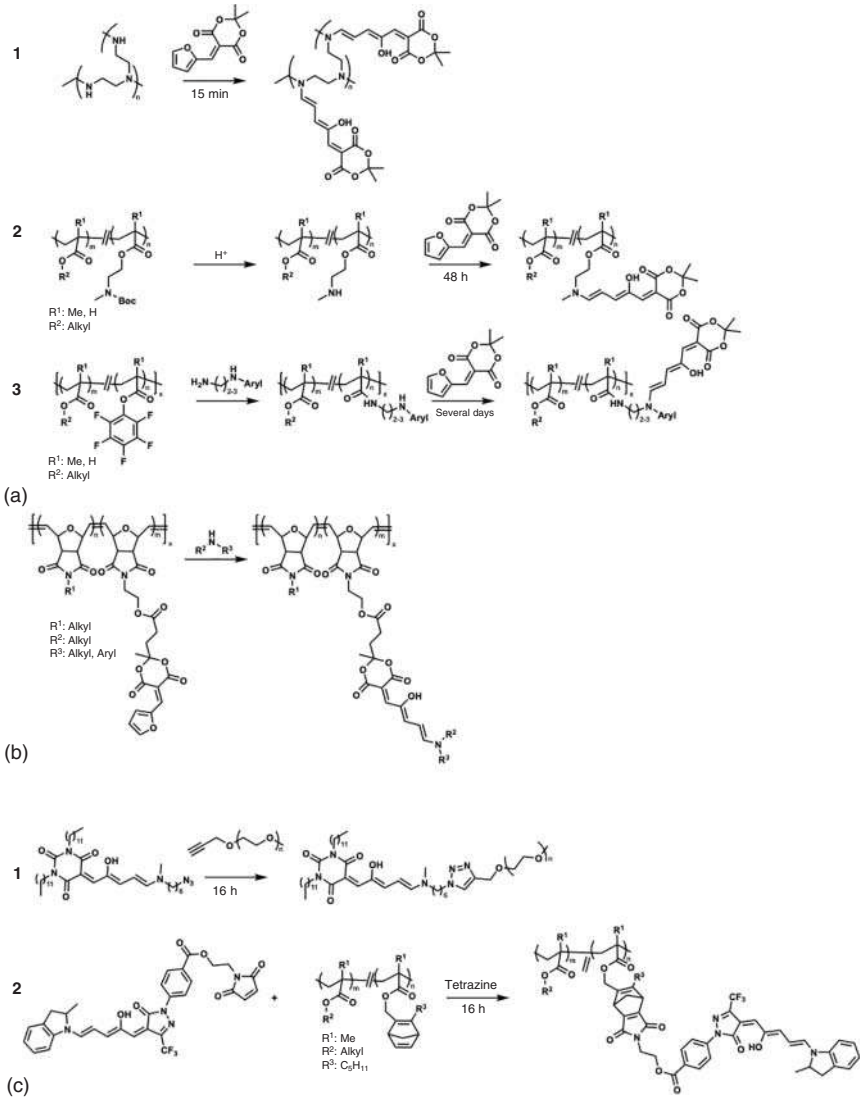


**Figure 14.4** Structure of donor–acceptor Stenhouse adducts polymer conjugates. (a) Examples of backbone functionalization with amines [21, 22, 24]. (b) Examples of backbone functionalization with an acceptor [25]. (c) Click Chemistry approaches toward functionalization with DASA photochromes [23, 26].

with a primary amine using either an indoline or *N*-methylaniline pendant group. The subsequent DASA-forming reaction allows for second- and third-generation DASA functionalization (Figure 14.4a (**3**)) [21].

To introduce an acceptor unit onto a polymer backbone, Read de Alaniz and coworkers developed a synthetic pathway in which a furan adduct acceptor unit is attached to an oxa-norbornene derivative and subsequently polymerized through ROMP. The DASA-forming reaction was then performed with either dialkyl- or arylamines (Figure 14.4b) [25].

The main challenge with relying on the DASA-forming reaction, either from polymer bearing an amine donor or an activated furan, is the slow reaction kinetics when deactivated amines with more desirable photophysical properties are used. One strategy to address this limitation is to rely on "click" chemistry to introduce the DASA photochrome onto the polymer backbone. Here, Read de Alaniz and coworkers demonstrated that a first-generation DASA carrying an azide moiety on the donor alkyl chains could be efficiently conjugated with an alkyne-functionalized polyethyleneglycol in a copper azide click reaction (Figure 14.4c (**1**)) [26]. More recently, they developed a metal-free click method to conjugate third-generation DASA using Diels–Alder cycloaddition (Figure 14.4c (**2**)) [23].

Additionally, DASA photochromes have been attached to more complicated architectures like nanoparticle (NP) surfaces in several fashions. Schober and coworkers utilized a polyethyleneimine-functionalized surface to directly react a first-generation DASA onto the surface [27]. In another approach, the synthesis of a catechol-functionalized secondary amine was utilized to form a DASA molecule. Upon mixing the catechol-derived DASA with iron(II,III)oxide, NP-functionalized particles can be obtained; however, reversible photoswitching was not observed from this system [28]. Reliable, general, and fast polymer conjugation still remains a challenge in the field due to the slow reaction kinetics of less activated donor amines especially in sterically hindered systems. Novel methods of DASA synthesis reducing necessary reaction time of the DASA formation from days to hours would be highly beneficial toward easily accessible DASA-functionalized materials.

## 14.3 Photoswitching Properties

### 14.3.1 Mechanism

The underlying mechanism of DASA photochromes is rather complicated and has been extensively studied by Feringa and coworkers [29–33]. The currently proposed mechanism consists of an actinic step followed by a series of thermal steps to fully transition from the colored open form to the colorless closed isomer. Through irradiation, the DASA transitions from the original extended open form **A** through an *E*/*Z*-isomerization around the α-C2 bond next to the hydroxy group to the first isomer **A′** (Figure 14.5) This actinic step is a key intermediate since its photostationary state drives the overall forward reaction [32]. However, this step can also be driven backwards through irradiation, since **A′** exhibits a red-shifted absorption

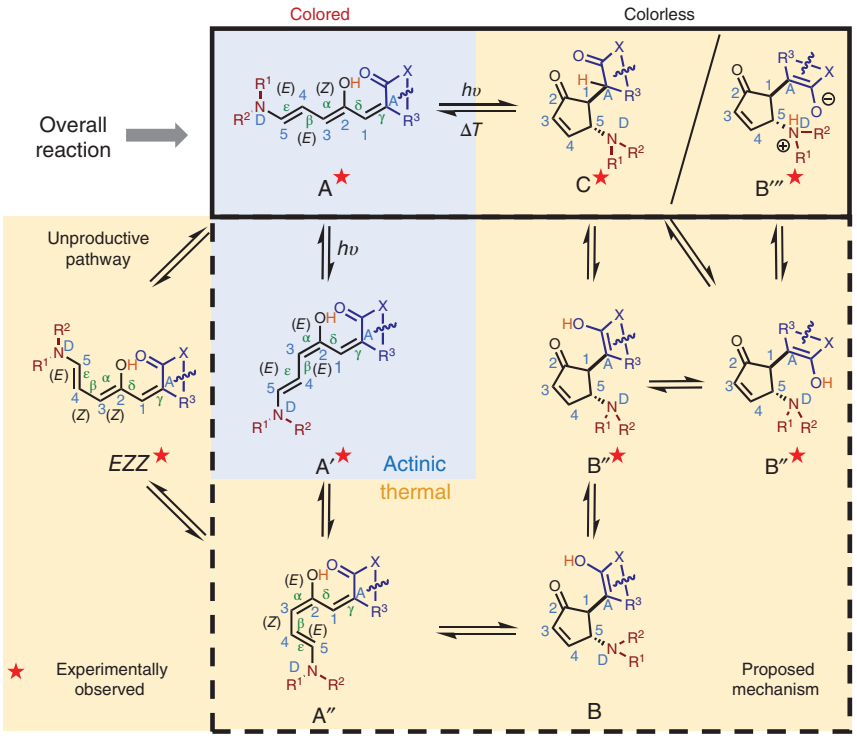


**Figure 14.5** Proposed photoswitching mechanism of donor–acceptor Stenhouse adducts [29].

spectrum [30]. The hydrogen bond between the acceptor and the hydroxy group on the triene is responsible for the directionality of the isomerization and is necessary for DASA to form the closed isomer [31]. After this actinic step, a thermal bond rotation from **A′** to **A″** around the β-bond is proposed to set up the molecule for the subsequent 4π electrocyclization, which converts the molecule from the colored isomers to the first closed isomer **B** that is colorless [29, 32]. From **B** the compound can be further stabilized by undergoing an inversion on the donor nitrogen atom to **B′**, followed by either a bond rotation around the γ-bond to form **B″** or a direct tautomerization to the thermodynamic product **C**. Intermediate **B″** either undergoes a proton transfer step toward the kinetic zwitterionic product **B‴**, or can form **C** through tautomerization [29]. Beyond this productive pathway, there are several unproductive pathways, which hinder the overall reaction productivity [29]. Most of these seem not to be prominent; however, the stability of the isomer *EZZ* (which can be formed from **A** and **A″**) has been experimentally shown to significantly impact the overall yield of the photoreaction. This is due to the conversion of **A″** into *EZZ* instead of converting into the overall products [29]. The mechanism is rather complex with a number of steps making a thorough investigation difficult; however, its complexity also offers opportunity to gain additional control by manipulating the energy landscape of each intermediate [29]. To accomplish this will require a

detailed understanding of the factors that influence each intermediate and their corresponding energy barriers. Currently proposed improvements include increasing the stability and lifetime of **A′** and **A″**, elimination of *EZZ* formation, *and* optimizing the energy barrier of the key 4π electrocyclization to improve quantum yield and forward kinetics. For overall equilibrium and recovery rates understanding what governs the stability of the closed isomers **B″**, **B‴**, and **C** seems to be key.

### 14.3.2 The Absorption Properties

One of the most promising properties of DASA photochromes is their activation by visible light. The benign properties of long wavelength light make this especially desirable for biomedical and material applications. This low-energy activation is due to a strong push–pull system through the triene backbone, which results in a π–π* transition similar to merocyanine dyes. The absorbance profile for the open isomer **A** ranges from a absorption maximum ($\lambda_{max}$) around 500 nm for dialkylamines with Meldrum's acid acceptors into the near IR region at 700 nm by extending the conjugation [13–15]. The closed isomers depend on the carbonyl structure but typically have some absorbance around 250 nm. Extending the conjugation of the open isomers is highly dependent on the planarity of the attached π-system. An inclusion of an indoline ($\Phi_{D\text{-}T} = 0°$) donor increases the absorbance compared to a methylaniline ($\Phi_{D\text{-}T} = 39°$) by 30 nm purely due to a lower dihedral angle and better overlap [15].

The $\lambda_{max}$ can be further increased using electron-donating substituents on the arylamines such as amino or methoxy groups [14, 15]. The introduction of donor groups which possess even larger conjugated systems, such as carbazole or indole, has not been successful due to the lack of nucleophilicity of the amines in the DASA-forming reaction, but this remains a significant goal. Increased conjugation on the acceptor group can also significantly shift the absorption band, as the introduction of an hydroxypyridone-derived acceptor increases the $\lambda_{max}$ with significant shoulders over 700 nm [14]. The introduction of additional conjugated acceptors is of high interest for DASA photoswitches, to expand the absorption further into the IR regions.

### 14.3.3 Dark Equilibria

Another important characteristic for T-type photoswitches is thermodynamic equilibrium, which depends on the stability of the open isomer **A** and the closed isomers **B‴** and **C**. High thermodynamic equilibrium (i.e. increased percent of open form) can be observed with a strongly donating dialkylamine due to the formation of the less stable kinetic product **B‴** as well as a stronger push–pull system stabilizing the open form (Figure 14.6b) [2]. Utilizing a weaker amine, like indoline or an aniline derivative, leads to the formation of a weaker push–pull system and the formation of **C**; the resulting thermodynamic equilibrium is compromised and more closed form is observed (Figure 14.6d) [15, 16]. However, this trend can be reversed by combining a weak donor with a stronger electron-withdrawing carbon acid acceptor [14]. This combination stabilizes the open form and results in high content of the open form **A** under thermodynamic equilibrium [13–16, 18].

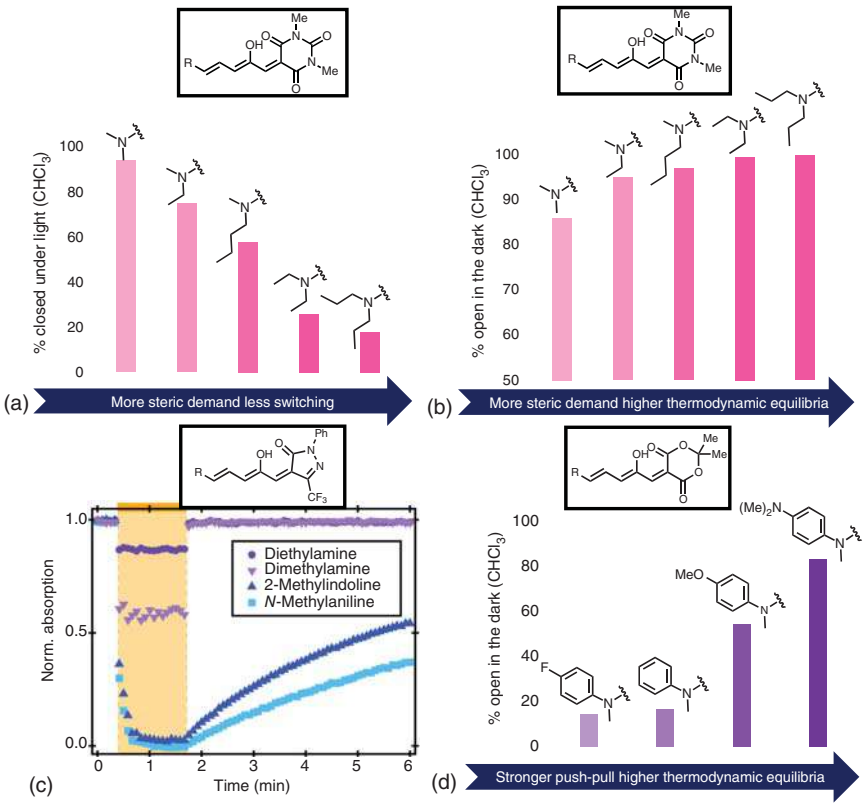


**Figure 14.6** Effects of donor and acceptor groups on photoswitching properties and open-closed equilibria in the dark (thermodynamic equilibria). (a) Photothermal stationary state of DASA photochromes with differing steric demand on the donor side [18]. (b) Percentage of the open form under thermodynamic equilibrium with differing steric demand on the donor group [18]. (c) Influence of electronics of both the forward light-driven reaction as well as the recovery of the open form of DASA photochromes. Time-dependent UV–vis spectra measured at 10 μM of DASA in toluene with irradiation with a 617 nm ThorLabs LED. Absorption was measured at the respective $\lambda_{max}$ of each compound. (d): Percentage of open form under thermodynamic equilibrium of DASA photochromes with differing electronic properties [16].

### 14.3.4 Cyclization Efficiency Under Illumination

In literature, the efficiency of photoswitches is described by the quantum yield of the actinic step. However, quantum yield measurements for DASA photochromes are particularly challenging because the actinic step is coupled with thermal bond rotation and subsequent 4π-electrocyclizations all of which contribute to the overall mechanism. To more accurately describe the efficiency of DASA, extended analyses of cyclization efficiencies under illumination have been performed. These consider the thermal steps of both the forward and back reaction while also accounting for the overall stability of the metastable product isomers **B‴** and **C**. This efficiency also depends on a number of external effects such as solvent, pH, and concentration.

Understanding each of these effects is vital for designing a tailored DASA for specific applications. Here we provide a short summary of each contributing factor [13–15, 29–34].

### 14.3.5 Electronic Effects

The strengths of both donor and acceptor have a direct influence on the actinic step and the amount of DASA, which can be cyclized under irradiation. By comparing a diethylamine donor to a *p*-methoxyindoline donor, Feringa and coworkers show that the lifetime of the excited step increased from 2 to 24 ps [32]. This does not fully explain the different behavior of these two DASA photoswitches, which is due to the complicated thermal steps that are involved in the overall mechanism and are also influenced by the push–pull system. Generally, a stronger push–pull system favors the open form in the DASA energy landscape, as seen with strong donors in the first generation and strong acceptors in the third generation. This results in high photothermal equilibria (open form under irradiation) and low closed isomer half-lives in the dark (Figure 14.6c) [2, 13]. On the other hand, introducing more electron-poor amines or electron-rich acceptors leads to longer half-life for the closed form and a larger amount of closed form. This pattern is widely observed in the second-generation derivatives [15, 16]. Additionally, the resulting closed-form derivative is different from the strongly donating alkyl amines, which are basic enough to easily deprotonate the acceptor proton. This basicity results in the formation of the kinetic zwitterionic product **B‴**, while less basic amines like aniline and indoline derivatives mostly form the enol product **B‴** and the thermodynamic keto product **C** [13–16].

### 14.3.6 Steric Effects

Another important factor influencing the overall energy landscape and photoswitching efficiency is the steric demand of both the donor and acceptor. Triene substitutions are also important to consider but have not yet been fully explored. The acceptor side has been minimally studied, but similar compounds such as dimethylbarbituric acid acceptors and dioctylbarbituric acid acceptors show very similar behavior [13, 15]. At a minimum, this suggests that steric demand on acceptor that is distal from the triene does not directly interfere with the photoswitching efficiency. On the donor side, Beves and coworkers published an in-depth study on dialkylamine donors with asymmetric substituents (Figure 14.6a-b) [18]. It was demonstrated that increasing the size of both sidechains favors the open form and results in faster recovery rates. Interestingly, increasing the sidechain of one of the substituents has a smaller effect on the photoswitching properties of DASA [13, 15]. This is due to the linear orientation to the open form, which allows for the larger substituents to be oriented away from the triene. However, an increase in both sidechains presumably interacts with the closed-form acceptor unit while also destabilizing **A′** due to an $A^{1,3}$ strain with the hydrogen on the triene. Both of these

effects shift the overall energy landscape to the closed form while also destabilizing the key intermediate **A′**, promoting the back reaction to **A** over the forward reaction to **A″**. Taken together, these results demonstrate that the photoswitching efficiency can be tuned through both electronic and steric modifications [16, 18].

### 14.3.7 Solvent Effects

One of the biggest developments of DASA over the years is improved solvent compatibility. The first-generation publications only showed formation of the closed isomers in significant amounts in apolar aromatic solvents such as toluene and benzene. However, this limitation was also due to the use of diethylamine and similarly sterically hindered dialkylamine donors. Beves and coworkers showed in 2018 that using dimethylamine instead enabled reasonable switching in chlorinated solvents like chloroform. Introducing an aryl amine as the donor results in weakening the triene push–pull system and disfavors the open form, allowing for switching at higher concentrations in more polar solvents like ethyl acetate and acetonitrile in addition to apolar and chlorinated solvents [13–16, 18]. This expansion of compatible solvents is presumably due to a more stable **A′** isomer, allowing for a longer lifetime resulting in the reaction to the closed form in weaker push–pull systems. This can also be seen in the subsequent introduction of stronger acceptors increasing the strength of the push–pull system in 2018 [14]. These novel acceptors enabled the same solvent compatibility while increasing the thermodynamic equilibrium and while decreasing the closed form half-live. To this date, there has been no DASA reported, which is capable of switching reversibly in the presence of protic solvents. Presumably this is due to a lowering in the activation energy of the thermal back reaction from **A′** to **A** combined with a spectral overlap of both isomers compromising the photostationary state of the actinic step [33]. Additionally, over time, the closed isomer is formed even in the dark in these solvents, which is assumed to be due to the hydrogen-bonding ability of these solvents stabilizing the closed isomers [35]. Identification of a system that enables reversible switching in protic media such as water will greatly expand the potential of DASA-based photochromes and enable their use in biological applications that would benefit from their wavelength tunability.

### 14.3.8 Concentration Effects

Interestingly, another factor influencing the efficiency of DASA photoswitches is their concentration, as shown by Bardeen and Read de Alaniz in 2019. The thermal back reaction rate was shown to greatly increase at higher concentration with a derivative based on an indoline donor with a pyrazolone acceptor bearing a $CF_3$ moiety. The quantum yield was also significantly lowered [36]. This effect is highly interesting and warrants further investigation. However, there is no direct evidence for aggregation explaining these results and potentially long-range coulombic interactions are at play.

### 14.3.9 Cyclization Under Exclusion of Light

In addition to a light-driven isomerization, a slower purely thermal isomerization from the open form to the closed form (especially in polar, protic solvents) can be observed for DASA. While the actual mechanism is unclear, the DASA photoswitches depend heavily on the relative energy of both the thermodynamic stable isomer **A** and the two metastable isomers **B‴** and **C** for cyclization both under light and in the dark. Depending on the structure of the molecule the thermodynamic equilibrium can shift from fully open to fully closed, similar to stenhouse salt derivatives. This equilibrium can be shifted significantly in favor of the closed form with either solvents or substitutions. Decreasing the overall strength of the push–pull system leads to an increase in the formation of the closed isomer [13–16, 18].

### 14.3.10 Role of Water and Substituents on Cyclization and Ring Opening

Water and other protic solvents drive the overall equilibrium toward the closed isomers. Presumably this is due to the stabilization of the isomers through hydrogen bonding, which shifts the overall equilibrium toward the products and water-assisted hydrogen transfer facilitating the 4π electrocyclization. Furthermore, a slow complex formation of the closed form with up to five water molecules is reported to help stabilize the closed form to fully compromise the equilibrium in favor of the closed isomers **B‴** and **C** [35].

Interestingly, the effect of the backbone substitution was investigated before DASA compounds were found to have photochromic properties. Safar and coworkers investigated in 2000 the aza- Piancatelli rearrangements of compounds using acyclic secondary amine donors and Meldrum's acid acceptors [12]. In this study, they explored a number of derivatives bearing substitutions (Br, Me, SMe, $N_3$) at the 3-position of the triene unit. These derivatives resulted directly form the closed adduct with no report of them being in equilibrium with the open form, which is in contrast to unsubstituted triene derivatives. Presumably, the equilibrium shifts to the closed form due to an $A^{1,3}$ strain that arises in the open triene as a result of the sterically demanding substitution (Br, Ph).

## 14.4 Illustrative Applications

DASA's unique photoswitching properties enable a range of applications primarily based on properties such as high degree of polarity change, wide range of wavelength tunability, high extinction coefficients as well as a large change in spectral absorption. The property changes enabled by this highly tunable and visible-light triggered photoswitch make it a unique and ideal candidate for a range of applications, including drug delivery, wettability, photopatterning, sensing, microfluidics, and actuation. Applications of DASAs have been further fueled by the fact that they are highly tunable and easily functionalizable in both solution and solid state.

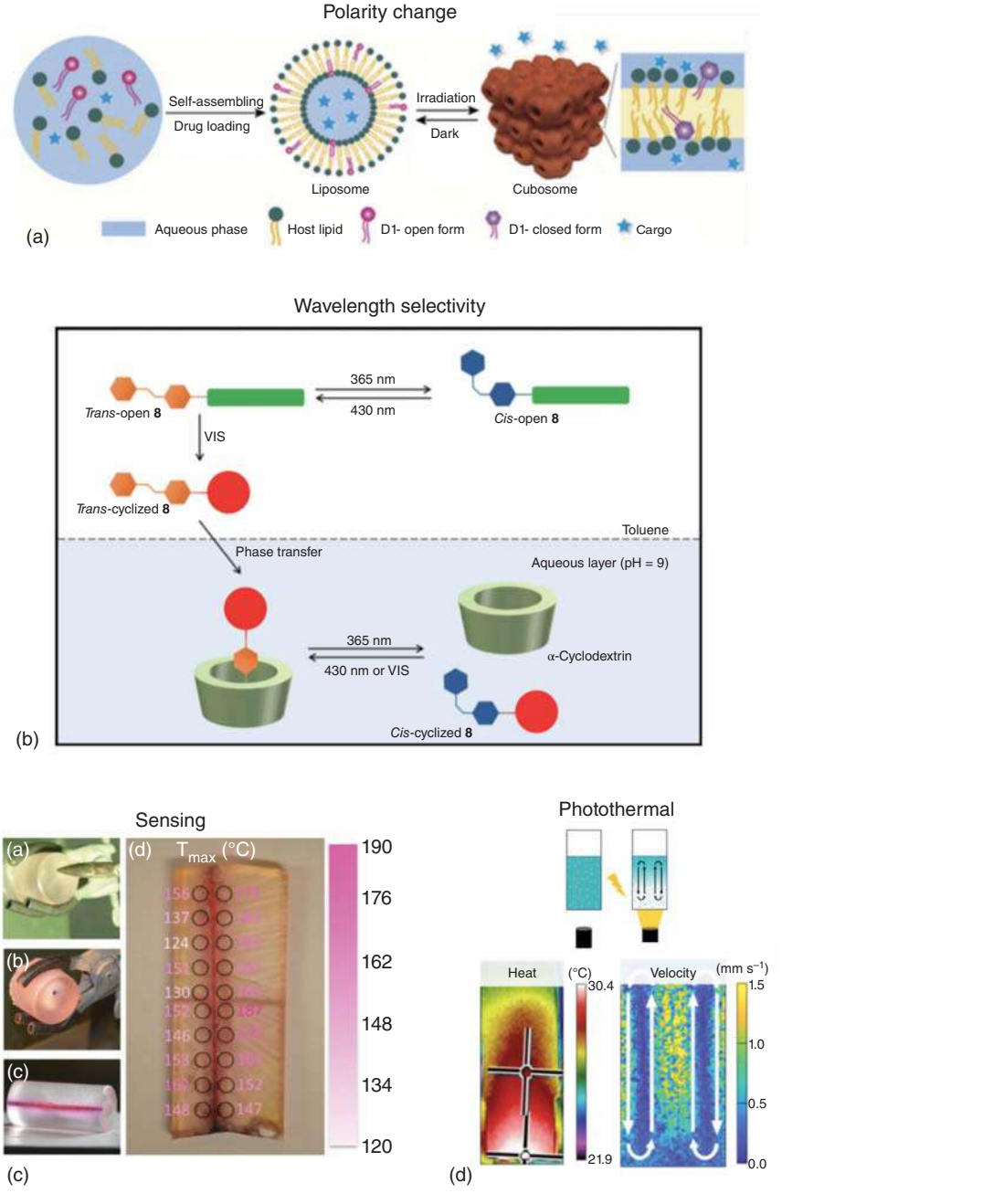


**Figure 14.7** Illustrative applications that leverage the photophysical properties of DASA. DASA is shown in these examples in (A) liquid crystal nanocarriers used for drug delivery. Source: Reproduced with permission from *Journal of Colloid and Interface Science* Jia et al. [37]. (B) orthogonal wavelength selective molecular systems. Source: Reproduced with permission from *Nature Communication* Lerch et al. [38], (C) thermochromic sensors for temperature mapping. Source: Reproduced with permission from *Applied Physics Letters* Mason et al. [39], and (D) self-regulated photothermal fluid actuators. Source: Reproduced with permission from *Nature Communication* Seshadri et al. [40].

### 14.4.1 Polarity Change

The conformational change of DASA from an open form that is neutral or slightly polar to a highly polar, often zwitterionic closed form upon irradiation leads to a drastic and reversible polarity change, which is promising for a range of applications such as drug delivery, desorption, and surface wettability. So far groups have shown DASA in this capacity for drug delivery and surface wettability. The light-induced polarity change has been utilized to drive a hydrophilic to hydrophobic transition that enables the disassembly of a drug carrier as demonstrated by Read de Alaniz and coworkers using a micellar system [26]. Upon irradiation, the hydrophilic character of the DASA leads to a partitioning into the aqueous phase and a release of the hydrophobic cargo. This was demonstrated as a means of delivering a chemotherapeutic agent to MCF-7 human breast cancer epithelial cells. Drug delivery via polarity change is also accomplished by doping DASA into liquid crystalline nanoparticles for encapsulated cargo release [37, 41, 42] as well as appended on to polymer nanoparticles [43] for triggered release (Figure 14.7a). In each case, DASA presents a non-invasive, facile form of remote drug release that allows for improved efficiency and minimizes toxicity due to its visible light activation.

In addition to drug delivery, the polarity change of DASA has been used to control surface wettability in polymer films and substrates. Triggered change in surface wettability is an exciting application of photoswitches that provides an on–off switch for adhesion. Attaching a DASA adduct has been shown to lead to de-adhesion of a polystyrene film off of a glass substrate [44]. Photoresponsive DASA nanoparticles immobilized on a glass substrate have also been used to control the wettability and contact angle hysteresis with green light and, reversibly, with heat [45]. The thermal reversibility of DASA allows for an additional handle on control of adhesive surfaces by providing both light- and heat-driven routes to control adhesion via different kinetic processes. Polarity change presents one of the primary properties of DASA that has been harnessed for practical applications as the control of wettability has potential practical applications in stimuli-responsive materials and the ability to selectively direct adhesion and deadhesion.

### 14.4.2 Wavelength Selectivity

The synthetic ability to tune DASA's response in the visible range has made it possible to achieve wavelength selectivity with multiple DASA derivatives or combined with other photoswitches to access a wide range of applications as controlled phase transfer. These applications allow for photopatterning to be accomplished, as well as the use of multiple photochromes that respond to unique sources of light and additionally as a means of drug delivery. Feringa and coworkers have demonstrated that combining DASA and azobenzene enables directed phase transfer and binding using three unique wavelengths to trigger each step of the release process (Figure 14.7b) [38]. This robust and flexible design provides a model for other potential two-switch systems [46] and allows for ease of control over drug delivery. Bruns and coworkers have developed a polymerosome nanoreactor system that utilizes a cascade reaction initiated by irradiation with multiple wavelengths [47]. These DASA

polymerosomes allow for the potential for triggered pharmacological applications that rely on precise spatial and temporal delivery.

In addition to utilizing the wavelength selectivity of DASA for drug delivery, applications involving selective photopatterning have been explored. Read de Alaniz and coworkers demonstrated that the synthesis of DASA polymer conjugates enables the selective switching in thin films. Taking advantage of the synthetic modularity, range of absorption spectrum of DASA and ease of spin coating enable the potential for data storage or sensing [21]. Other groups have similarly utilized DASA pendant groups [27, 48, 49] as well as in conjunction with azobenzene moieties [50] for wavelength selective photo-printing. These photosensitive polymer surfaces offer a range of opportunities for applications given the large change in properties of the patterned regions, thus opening up the space for the development of smart, multi-responsive materials. Many of these materials alter the glass transition temperature ($T_g$), conductivity, wettability, and color upon irradiation making DASA a promising, highly versatile photochrome for responsive materials.

### 14.4.3 Sensing

Deriving from DASA's high extinction coefficient and colorimetric response, many applications have sought to use DASA as a sensing agent. This sensing work has been used to detect salts, amines, and heat changes and thus offers a versatile sensor. Some early work is the result of the highly activated furan group's uncatalyzed reaction with amines. In work done by Read de Alaniz and coworkers, chemical and thermal sensors were developed from activated furan conjugated polymers, which generated DASA upon amine exposure [25, 51]. Because of differing reactivity of primary and secondary amines, this colorimetric sensor provides easy visible detection of ppm quantities of secondary amines [25, 51] and, additionally, after subsequent closing of the newly formed DASA photochromes changes in temperature, which trigger the reverse reaction to the open form. Temperature sensing using DASA has been similarly explored with work done in collaboration with Hooper and US Navy in which DASA serves as a thermochromic molecular sensor dispersed as the closed derivative within a crosslinked polyurethane elastomer. The rapid and confined response of DASA to colored open form triggered by instantaneous changes in temperature allows the mapping of heat changes in materials due to high strain impact for example by penetrating bullets (Figure 14.7c) [39] DASA has also been conjugated to polymers to detect nerve agent mimics in vapor state [52] as well as highly charged Lewis Acids by utilizing a ligating donor group [53]. The creation of DASA functionalized polymer dots responds to the presence of acid and alkali metals making it a rapid chemosensor for iron and copper ions in aqueous solutions [24]. The ability of DASA to detect salts, acids, and amines enables its use as a rapid response colorimetric detector for a range of applications that benefit from the high molar absorptivity that can be easily seen by eye.

In a related system, DASA has additionally been used in conjunction with fluorophores; this unique combination of a fluorescent chemosensor and DASA provides the possibility for creation of unique logic gates [54]. Studies have shown

that DASA can be used to develop novel visible-light-triggered aggregation-induced emission compounds whose presence in fluorescent materials additionally enables applications in sensing [55, 56].

### 14.4.4 Photothermal

Most recently, the spectral change of DASA has been utilized to elicit a photothermal gradient for the purpose of actuation. This has been studied in both fluid systems as well as in thin films and is being explored as a means of generating mechanical force through light. Recent work by Read de Alaniz, Valentine and coworkers demonstrates the photothermal capacity of DASA to generate and direct fluid flow. DASA 3.0 is utilized in this study because of its drastic change in spectral absorption and molar absorptivity upon irradiation leading to immense heat generation and subsequent loss. By altering the solvent, concentration, and light intensity, these studies demonstrate the ability to use DASA to generate and control convective fluid flow in solution at rates of mm/s. This behavior is self-regulated as a result of the balance between the forward and backward reaction of DASA and the stabilization of a thermal gradient (Figure 14.7d) [40]. Similarly, the photothermal capacity of DASA is utilized to create self-actuating materials. Valentine and Read de Alaniz have also demonstrated the synthetic formation of chemically conjugated DASA-PHMA(poly(hexyl methacrylate)) bilayer actuator that can lift weight against gravity, as well as a simple light-powered crawler, which exploits photothermal energy conversion. Control of the magnitude of actuation is achieved by slowly converting a high-absorbing DASA photochrome into a non-absorbing form upon irradiation [23]. These examples are the first uses of DASA toward photothermal actuation and invite further investigation into other applications.

## 14.5 Conclusion

In conclusion, the modular two-step synthesis and negative photochromic properties of DASAs have enable the rapid development of this emerging photoswitch. DASAs have a range of advantageous properties such as wavelength tunability, large geometry change, significant change of polarity, and high molar absorptivity. Through careful choice of the donor and acceptor groups, the wavelength, thermodynamic stability, and solvent switching properties can be precisely controlled. Furthermore, DASA's tunability and unique photoswitching properties enable a range of applications, such as drug delivery, sensing, photopatterning, and actuation.

Mechanistically, DASA's photoswitching consists of an actinic step followed by a series of thermal steps to fully transition from the colored open form to the colorless closed isomer. Structural features have a tremendous influence on the photoswitching efficiency and going forward a better understanding of how to modify the overall energy landscape will be essential for overcoming current limitations. Beyond this,

there are still a myriad of challenges to address before DASA-based photoswitches can realize their full potential. For example, we envision advances that enable photoswitching in an aqueous media will open up new opportunities in photopharmacology and medical applications. Furthermore, applications that leverage the large geometry change upon irradiation with visible light hold tremendous potential for soft robotics that can be powered by sunlight. Given the rapid development of this class of photoswitches and the possibilities offered for specifying complex spatiotemporal responses through the use of visible light, we are hopeful that this emerging class of photochromic material with a rich history will continue to facilitate new discoveries.

## References


1 Fritzsche, M. (1867). Note sur les carbures d'hydrogene solides, tires du goudron de houille. *C. R. Acad. Sci.* 69: 1035.
2 Helmy, S., Leibfarth, F.A., Oh, S. et al. (2014). Photoswitching using visible light: a new class of organic photochromic molecules. *J. Am. Chem. Soc.* 136 (23): 8169–8172.
3 Stenhouse, J. (1850). Ueber die Oele, die bei der Einwirkung der Schwefel. *Justus Liebigs Ann. Chem.* 74 (April): 278–297.
4 Schiff, H. (1887). Ueber Farbstoff basen. *Justus Liebigs Ann. Chem.* 239: 349–385.
5 Honda, K., Komizu, H., and Kawasaki, M. (1982). Reverse photocharomism of stenhouse salts. *J. Chem. Soc. Chem. Commun.* 4: 253–254.
6 Palmer, L.I. and Read de Alaniz, J. (2014). Lewis acid catalyzed rearrangement of furylcarbinols: the aza- and oxa-piancatelli cascade reaction. *Synlett* 25 (1): 8–11.
7 Piancatelli, G., Scettri, A., and Barbadoro, S. (1976). A useful preparation of 4-substituted 5-hydroxy-3-oxocyclopentene. *Tetrahedron Lett.* 13 (1976): 3555–3558.
8 Veits, G.K., Wenz, D.R., and Read de Alaniz, J. (2010). Versatile method for the synthesis of 4-aminocyclopentenones: dysprosium(III) triflate catalyzed aza-piancatelli rearrangement. *Angew. Chem. Int. Ed.* 49 (49): 9484–9487.
9 Veits, G.K., Wenz, D.R., Palmer, L.I. et al. (2015). Cascade rearrangement of furylcarbinols with hydroxylamines: practical access to densely functionalized cyclopentane derivatives. *Org. Biomol. Chem.* 13 (31): 8465–8469.
10 Palmer, L.I. and Read de Alaniz, J. (2011). Direct and highly diastereoselective synthesis of azaspirocycles by a dysprosium(III) triflate catalyzed aza-piancatelli rearrangement. *Angew. Chem. Int. Ed.* 50 (31): 7167–7170.
11 Wenz, D.R. and Read de Alaniz, J. (2013). Aza-piancatelli rearrangement initiated by ring opening of donor-acceptor cyclopropanes. *Org. Lett.* 15 (13): 3250–3253.
12 Šafář, P., Považanec, F., Prónayová, N. et al. (2000). Dichotomy in the ring opening reaction of 5-[(2-furyl)methylidene]-2,2-dimethyl-1,3-dioxane-4,6-dione with cyclic secondary amines. *Collect Czechoslov. Chem. Commun.* 65 (12): 1911–1938.


**13** Helmy, S., Oh, S., Leibfarth, F.A. et al. (2014). Design and synthesis of donor-acceptor stenhouse adducts: a visible light photoswitch derived from furfural. *J. Org. Chem.* 79 (23): 11316–11329.

**14** Hemmer, J.R., Page, Z.A., Clark, K.D. et al. (2018). Controlling dark equilibria and enhancing donor-acceptor Stenhouse adduct photoswitching properties through carbon acid design. *J. Am. Chem. Soc.* 140 (33): 10425–10429.

**15** Hemmer, J.R., Poelma, S.O., Treat, N. et al. (2016). Tunable visible and near infrared photoswitches. *J. Am. Chem. Soc.* 138 (42): 13960–13966.

**16** Mallo, N., Brown, P.T., Iranmanesh, H. et al. (2016). Photochromic switching behaviour of donor-acceptor Stenhouse adducts in organic solvents. *Chem. Commun.* 52 (93): 13576–13579.

**17** Laurent, A.D., Medved', M., and Jacquemin, D. (2016). Using time-dependent density functional theory to probe the nature of donor–acceptor Stenhouse adduct photochromes. *ChemPhysChem*: 1846–1851.

**18** Mallo, N., Foley, E.D., Iranmanesh, H. et al. (2018). Structure-function relationships of donor-acceptor Stenhouse adduct photochromic switches. *Chem. Sci.* 9 (43): 8242–8252.

**19** Mallo, N., Tron, A., Andréasson, J. et al. (2020). Hydrogen-bonding donor-acceptor Stenhouse adducts. *ChemPhotoChem* 4 (6): 407–412.

**20** Alves, J., Wiedbrauk, S., Gräfe, D. et al. (2020). It's a trap: thiol-Michael chemistry on a DASA photoswitch. *Chem. A Eur. J.* 26 (4): 809–813.

**21** Ulrich, S., Hemmer, J.R., Page, Z.A. et al. (2017). Visible light-responsive DASA-polymer conjugates. *ACS Macro Lett.* 6 (7): 738–742.

**22** Yap, J.E., Mallo, N., Thomas, D.S. et al. (2019). Comparing photoswitching of acrylate or methacrylate polymers conjugated with donor-acceptor Stenhouse adducts. *Polym. Chem.* 10 (47): 6515–6522.

**23** Lee, J., Sroda, M.M., Kwon, Y., et al. (2020) Programmable bilayer actuator driven by visible light using donor–acceptor Stenhouse adducts. *ACS Appl. Mater. Interfaces.* 12 (48): 54075–54082.

**24** Zhong, D., Cao, Z., Wu, B. et al. (2018). Polymer dots of DASA-functionalized polyethyleneimine: synthesis, visible light/pH responsiveness, and their applications as chemosensors. *Sensors Actuators, B* 254: 385–392.

**25** Chen, Q., Diaz, Y.J., Hawker, M.C. et al. (2019). Stable activated furan and donor-acceptor Stenhouse adduct polymer conjugates as chemical and thermal sensors. *Macromolecules* 52 (11): 4370–4375.

**26** Poelma, S.O., Oh, S.S., Helmy, S. et al. (2016). Controlled drug release to cancer cells from modular one-photon visible light-responsive micellar system. *Chem. Commun.* 52 (69): 10525–10528.

**27** Singh, S., Mai, P., Borowiec, J. et al. (2018). Donor-acceptor Stenhouse adduct-grafted polycarbonate surfaces: selectivity of the reaction for secondary amine on surface. *R. Soc. Open Sci.* 5: 180207.

**28** Ahrens, J., Bian, T., Vexler, T., and Klajn, R. (2017). Irreversible bleaching of donor-acceptor Stenhouse adducts on the surfaces of magnetite nanoparticles. *ChemPhotoChem* 1 (5): 230–236.


**29** Zulfikri, H., Koenis, M.A.J., Lerch, M.M. et al. (2019). Taming the complexity of donor-acceptor stenhouse adducts: infrared motion pictures of the complete switching pathway. *J. Am. Chem. Soc.* 141 (18): 7376–7384.

**30** Lerch, M.M., Wezenberg, S.J., Szymanski, W., and Feringa, B.L. (2016). Unraveling the photoswitching mechanism in donor-acceptor Stenhouse adducts. *J. Am. Chem. Soc.* 138 (20): 6344–6347.

**31** Lerch, M.M., Medved, M., Lapini, A. et al. (2018). Tailoring photoisomerization pathways in donor-acceptor Stenhouse adducts: the role of the hydroxy group. *J. Phys. Chem, A.* 122 (4): 955–964.

**32** Di Donato, M., Lerch, M.M., Lapini, A. et al. (2017). Shedding light on the photoisomerization pathway of donor-acceptor Stenhouse adducts. *J. Am. Chem. Soc.* 139 (44): 15596–15599.

**33** Lerch, M.M., Di Donato, M., Laurent, A.D. et al. (2018). Solvent effects on the actinic step of donor–acceptor Stenhouse adduct photoswitching. *Angew. Chem. Int. Ed.* 57 (27): 8063–8068.

**34** Dolinski, N.D., Page, Z.A., Eisenreich, F. et al. (2017). A versatile approach for in situ monitoring of photoswitches and photopolymerizations. *ChemPhotoChem.* 1 (4): 125–131.

**35** Wang, D., Zhao, L., Zhao, H. et al. (2019). Inducing molecular isomerization assisted by water. *Commun. Chem.* 2 (1): 118.

**36** Lui, B.F., Tierce, N.T., Tong, F. et al. (2019). Unusual concentration dependence of the photoisomerization reaction in donor-acceptor Stenhouse adducts. *Photochem. Photobiol. Sci.* 18 (6): 1587–1595.

**37** Jia, S., Tan, A., Hawley, A. et al. (2019). Visible light-triggered cargo release from donor acceptor Stenhouse adduct (DASA)-doped lyotropic liquid crystalline nanoparticles. *J. Colloid Interface Sci.* 548: 151–159.

**38** Lerch, M.M., Hansen, M.J., Velema, W.A. et al. (2016). Orthogonal photoswitching in a multifunctional molecular system. *Nat. Commun.* 7: 12054.

**39** Mason, B.P., Whittaker, M., Hemmer, J. et al. (2016). A temperature-mapping molecular sensor for polyurethane-based elastomers. *Appl. Phys. Lett.* 108 (4): 041906.

**40** Seshadri, S., Gockowski, L.F., Lee, J. et al. (2020). Self-regulating photochemical Rayleigh-Bénard convection using a highly-absorbing organic photoswitch. *Nat. Commun.* 11: 2599.

**41** Jia, S., Du, J.D., Hawley, A. et al. (2017). Investigation of donor-acceptor Stenhouse adducts as new visible wavelength-responsive switching elements for lipid-based liquid crystalline systems. *Langmuir* 33 (9): 2215–2221.

**42** Chen, Y., Li, Z., Wang, H. et al. (2018). Visible light-controlled inversion of pickering emulsions stabilized by functional silica microspheres. *Langmuir* 34 (8): 2784–2790.

**43** Senthilkumar, T., Zhou, L., Gu, Q. et al. (2018). Conjugated polymer nanoparticles with appended photo-responsive units for controlled drug delivery, release, and imaging. *Angew. Chem. Int. Ed.* 57 (40): 13114–13119.


**44** Mostafavi, S.H., Li, W., Clark, K.D. et al. (2019). Photoinduced deadhesion of a polymer film using a photochromic donor-acceptor Stenhouse adduct. *Macromolecules* 52 (16): 6311–6317.

**45** Zhao, H., Wang, D., Fan, Y. et al. (2018). Surface with reversible green-light-switched wettability by donor–acceptor Stenhouse adducts. *Langmuir* 34 (50): 15537–15543.

**46** Li, M., Yang, S., Liang, W. et al. (2019). A novel multiphotochromic system with orthogonal light excitations. *Dye Pigm.* 16: 239–244.

**47** Rufaie-Gragan, O., Ulrich, S., Galensowske, N.F.B. et al. (2018). *J. Am. Chem. Soc.* 140: 8027–8026.

**48** Sinawang, G., Wu, B., Wang, J. et al. (2016). Polystyrene based visible light responsive polymer with donor–acceptor Stenhouse adduct pendants. *Macromol. Chem. Phys.* 217 (21): 2409–2414.

**49** Singh, S., Friedel, K., Himmerlich, M. et al. (2015). Spatiotemporal photopatterning on polycarbonate surface through visible light responsive polymer bound DASA compounds. *ACS Macro Lett.* 4 (11): 1273–1277.

**50** Tang, F.Y., Hou, J.N., Liang, K.X. et al. (2017). A facile way to achieve all-photonic logic functions and photo-printing based on a donor-acceptor Stenhouse adduct. *New J. Chem.* 41 (14): 6071–6075.

**51** Diaz, Y.J., Page, Z.A., Knight, A.S. et al. (2017). A versatile and highly selective colorimetric sensor for the detection of amines. *Chem. A Eur. J.* 23 (15): 3562–3566.

**52** Balamurugan, A. and Lee, H.I. (2016). A visible light responsive on-off polymeric photoswitch for the colorimetric detection of nerve agent mimics in solution and in the vapor phase. *Macromolecules* 49 (7): 2568–2574.

**53** De Cai, Y., Chen, T.Y., Chen, X.Q., and Bao, X. (2019). Multiresponsive donor-acceptor Stenhouse adduct: opportunities arise from a diamine donor. *Org. Lett.* 21 (18): 7445–7449.

**54** Yang, S., Liu, J., Cao, Z. et al. (2018). Fluorescent photochromic donor-acceptor Stenhouse adduct controlled by visible light. *Dye Pigm.* 148: 341–347.

**55** Wu, B., Xue, T., Wang, W. et al. (2018). Visible light triggered aggregation-induced emission switching with a donor-acceptor Stenhouse adduct. *J. Mater. Chem. C.* 6 (31): 8538–8545.

**56** Yan, Q., Li, C., Wang, S. et al. (2020). Visible light responsive donor-acceptor stenhouse adducts with indoline-tri/tetra-phenylethylene chromophore: synthesis, aggregation-induced emission, photochromism and solvent dependence effect. *Dye Pigm.* 178: 108352.

# 15 Imines as Threefold Functional Devices: Motional, Photochemical, Constitutional

Lutz Greb, Ghislaine Vantomme, and Jean-Marie Lehn

### Photo/Thermochromism and Constitutional Dynamics

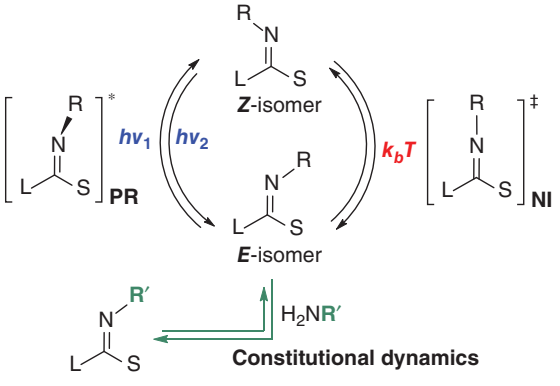


### Characteristic Features

Thermal *E/Z*-isomerization barrier mainly controlled by nitrogen residue. High-energy light required for *E/Z*-photoisomerization of pure C=N bond. Features for molecular motors inherent in chiral imines. Can be coupled with constitutional dynamics.

### Synthetic Methods

Condensation of carbonyl compounds with primary amines; oxidation of secondary amines.

### First Reported

Fischer, E. and Frei, Y. (1957). Photoisomerization equilibria involving the C=N double bond. *J. Chem. Phys.* 27: 808–809.

### Key References

Lehn, J.-M. (2006). Conjecture: imines as unidirectional photodriven molecular motors – motional and constitutional dynamic devices. *Chem. Eur. J.* 12: 5910–5915.

Greb, L. and Lehn, J.-M. (2014). Light-driven molecular motors: imines as four-step or two-step unidirectional rotors. *J. Am. Chem. Soc.* 136: 13114–13117.

Vantomme, G. and Lehn, J.-M. (2013). Photo- and thermoresponsive supramolecular assemblies: reversible photorelease of $K^+$ ions and constitutional dynamics. *Angew. Chem. Int. Ed.* 52: 3940–3943.

# 15

# Imines as Threefold Functional Devices: Motional, Photochemical, Constitutional

*Lutz Greb[1], Ghislaine Vantomme[2], and Jean-Marie Lehn[3]*

[1] *Universität Heidelberg, Anorganisch-Chemisches Institut, Im Neuenheimer Feld 270, 62210 Heidelberg*
[2] *Eindhoven University of Technology, Institute for Complex Molecular Systems, Eindhoven, 5612 AZ, The Netherlands*
[3] *Université de Strasbourg, Institut de Science et d' Ingénierie Supramoléculaires (ISIS), 8 allée Gaspard Monge, 67000 Strasbourg*

## 15.1 Introduction

Imines, $R^1R^2C{=}NR^3$, can be considered as the chimera of olefins and azo compounds. For olefins and azo compounds, the *E*/*Z*-photoisomerization is well established (see Chapters 12 and 3 of this book). Hence, it is of no surprise that imines can display a similar type of reactivity. However, beyond this relationship and in view of their hybrid nature, they combine the switching features of an olefin with the stereochemical and coordinative flexibility inherent to a nitrogen atom. Despite the omnipresence and straightforward synthetic access of imines, their implementation as strategic photoswitches in molecules and materials, as will be covered in the present chapter, is only at its beginnings. Since the imine functional group embraces sub-types such as oximes, hydrazones, and acylhydrazones, which present specific ground-state and excited-state properties, the present chapter will also include selected work on such units performed by our group as well as others.

## 15.2 Imine Photoswitches

### 15.2.1 Electronic Spectra and Photochemical *E*/*Z*-Isomerization of Imines

Simple alkyl-substituted imines show a strong π–π* ($S_0 \rightarrow S_2$, <200 nm) and a much weaker, symmetry forbidden n–π* ($S_0 \rightarrow S_1$, ≈240 nm) transition [1–4]. For imines with aromatic substituents, the two bands occur at >240 and >290 nm, but an unequivocal assignment can be difficult due to the participation of charge transfer [1, 4, 5]. Appropriate electronic perturbation can be used for effective red-shifting of the bands [6]. After excitation, the *E*/*Z*-photoisomerization is the

*Molecular Photoswitches: Chemistry, Properties, and Applications*,
First Edition. Edited by Zbigniew L. Pianowski.


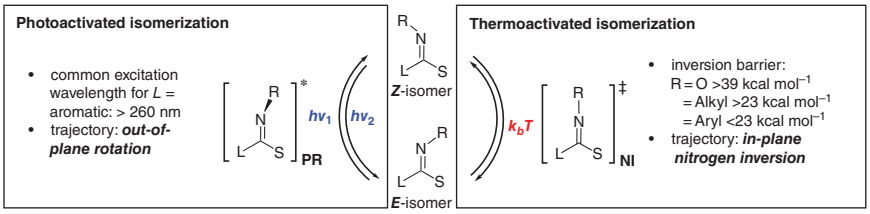


**Figure 15.1** Photo- and thermoactivated *E*/*Z*-isomerization of imines with its energetic and trajectorial characteristics. L = large substituent; S = small substituent.

most likely event to happen (Figure 15.1a) [7–12]. This isomerization is the major reason for the high rate and efficiency of non-radiative decay of the excited states and accounts for the lack of other photoreactivity with simple imines [13]. Indeed, for the configurationally most stable aldoximes, *E*/*Z*-photoisomerization was described already in 1903 by Ciamician [14]. The photoisomerization involving common C=N—R (R = Ph) double bonds was made observable by low-temperature UV/vis-spectroscopy in 1957 [15], and later on reproduced by several groups [16–18], among other studies. For several cases, the absorption properties of the *E* and the *Z*-isomers differ substantially, conferring P-type and, depending on the thermal stability, T-type photochromism to imines [19]. In the absence of heavy atoms, the *E*/*Z*-isomerization occurs more likely via the lowest singlet state, but in the presence of heavy atoms or photosensitizers, isomerization via the triplet state can contribute [13, 17, 20]. Important within the context of molecular motors (see Section 15.5), theoretical studies concluded that the *E*/*Z*-photoisomerization proceeds via out-of-plane rotation (***PR***), independent of the spin state (Figure 15.1a) [8–10, 12, 21–29]. Of course, the complexity brought about by differing excited states, adiabatic or diabatic nature, the influence of substituents, and solvent effects make more general statements about the photochemical isomerization process difficult but require experimental and theoretical effort for each specific case.

### 15.2.2 Thermal *E*/*Z*-Isomerization of Imines

Multiple investigations on the thermal isomerization of the C=N double bond revealed a remarkable sensitivity to the attached nitrogen substituents, R (Figure 15.1b) [30–33]. For instance, with benzophenone-derived imines, isomerization rates spanning 14 orders of magnitude are covered by choice of R [32, 34]. *N*-heteroatom-substituted derivatives (i.e. oxime ethers and hydrazones) have very high inversion barriers and show marked configurational stability even at elevated temperature ($\Delta G^{\ddagger} > 39\,\text{kcal mol}^{-1}$), followed by *N*-alkyl imines ($\Delta G^{\ddagger} > 23\,\text{kcal mol}^{-1}$) and *N*-aryl imines as the least stable ($\Delta G^{\ddagger} < 23\,\text{kcal mol}^{-1}$) [33, 35, 36]. Experimental [37–45] and theoretical [22, 46–53] studies revealed that the thermal isomerization proceeds by an in-plane nitrogen inversion (***NI***), through a lateral shift transition state (Figure 15.1b). The thermal rotational process is substantially higher in energy. However, if the substituents at the carbon atoms

are prone to deprotonation, also tautomerization pathways can come into play [54]. If heteroatoms are directly attached to the imine carbon atom (cf. guanidines or ureas), rotational barriers might be lowered, but the inversion remains the preferred pathway [1, 33, 55].

### 15.2.3 Imines as Photoswitches

Although every previously studied photochemical *E*/*Z*-isomerization of imines *a priori* described a switching, the deliberate coupling of this event with other molecular functions was considered only recently. One of the first reports described the photoinduced switching of an intramolecular hydrogen bond between an amide NH and carboxylate anion (Figure 15.2a) [56]. It was proposed that the hydrogen bond donor might be used to modify the nucleophilicity of the hydrogen bond acceptor anion for controlled reactivity. The photoisomerization and the formation of an intramolecular hydrogen bonding were verified by in situ irradiation in low-temperature NMR conditions and the back-reaction was analyzed kinetically. Unfortunately, the low thermal stability of *N*-aryl imines prevented the permanent stability of the *Z*-state and thus any follow-up application. In further studies, benzil α-bisimines were applied as photoswitches for the speed regulation of internal C—C bond rotation rates (Figure 15.2b) [57]. Therein, *N*-alkyl-C-aryl imines were chosen as suitable candidates since they combine good absorption characteristics with thermal *E*/*Z*-configurational stability that warrant thermal back-reaction rates at convenient time scales. A variety of photo-induced approaches for the slowing down or stopping of intramolecular single-bond rotations have been described earlier [58–64]. However, this study addressed the challenge of motional *acceleration* by application of an external stimulus [65–68]. In the benzil α-bisimines, three different states were accessible, for which light irradiation enabled a 2-step acceleration of the internal single bond rotation rates across 12 orders of magnitude.

More recently, the photochemical *E*/*Z*-switching of imines was used as a mechanistic tool to unravel the asymmetric Brønsted acid-catalyzed reduction of imines and to alternate product selectivity [69]. Later on, the photoisomerization of azomethine phthalimides was applied to alter the fluorescence properties, wherein unusual thermal $Z \rightarrow E$ back-reactions were found depending on the nature of the D-A system [70].

The transfer of imines as photoswitches in materials has also been explored. For instance, 4-methoxy-*N*-Benzylideneaniline units were used as photosensitive side chain groups in liquid crystalline poly(methyl methacrylates) to obtain optical anisotropies by using linearly polarized light on spin-coated films (Figure 15.3a) [71, 72]. Photoinduced molecular reorientation and surface relief gratings comparable to those of polymers with azobenzene side groups were accomplished. However, prolonged light exposure of the films resulted in other photoreactions such as photocleavage and photocrosslinking. The advantage of these materials over azobenzene switchable units resides in their transparency in the visible region, making those compounds applicable to birefringent films and diffraction devices for display applications.

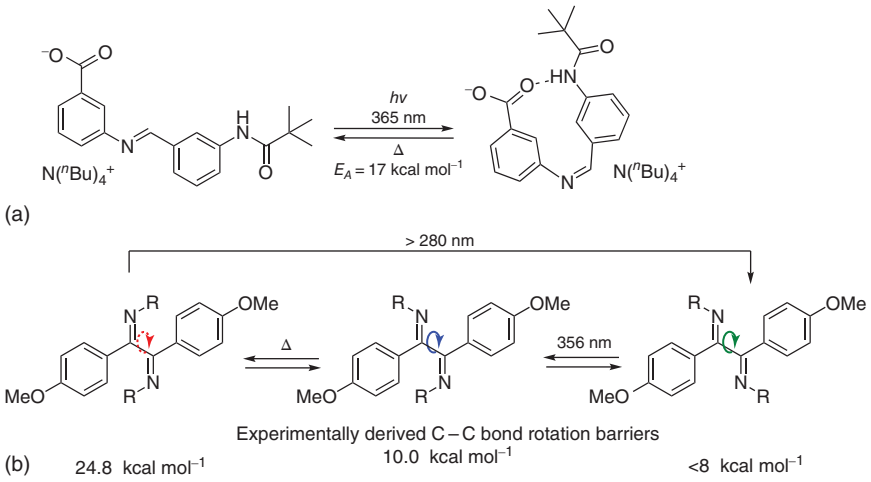


**Figure 15.2** Imines as molecular photoswitches for the control of (a) intramolecular hydrogen bonding and (b) of the rates of internal C—C bond rotation.

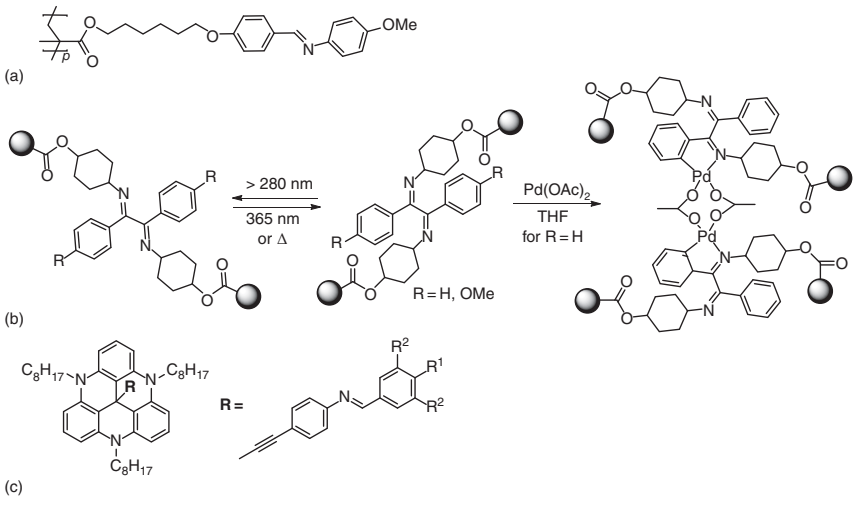


**Figure 15.3** Imines in (a) polymethyl methacrylate for axis selective *E*/*Z*-isomerization; (b) ADMET-polymers for light- and metallo responsiveness; (c) The triazatriagulenium platform for imine switching on surfaces.

Besides this side-chain imine decoration of polymers, imines incorporated in the polymeric main chain have also been studied (Figure 15.3b) [73]. This strategy enabled a dual-controlled change in the shape of single-chain nanoparticles (SCNPs) by either light- or metallo-stimulation. Symmetric α,ω-diene monomers with internal *Z*/*Z*-bisimine units were polymerized by acyclic diene metathesis polymerization (ADMET), yielding polymers with $M_n$ of up to 11 kDa and PDIs of 1.7. In these SCNPs, the apparent molecular weight decreased from 11 to 5 kDa after UV-light *Z*/*E*-photoisomerization of the C=N double bonds, as determined by

size-exclusion chromatography (SEC). The process was found to be fully reversible either by thermal back-reaction or by irradiation with light of another wavelength, thus imparting dual-gated light control for the return to its original size value. The shape switching was further corroborated by dynamic light scattering (DLS) and DOSY–NMR analyses, showing a reduced hydrodynamic diameter from 5.1 to 3.3 nm and an increased diffusion coefficient. Although one would expect an increase of polymer size due to the geometrical change of the bisimine units (*Z*/*E*), the observed size decrease was rationalized by increased flexibility due to the less hindered internal C—C bond rotation (cf. Figure 15.2b).

Besides light, $Pd(OAc)_2$-mediated *ortho*-CH functionalization under mild conditions was used as an orthogonal stimulus for the SCNP size control of the material (Figure 15.3b). The reaction was supported by infrared (IR) and NMR measurements of the metallo-treated polymeric material and by single X-ray diffraction analysis of a twofold C—H activated metallacyle of a monomeric unit. In the future, the double-stimuli responsiveness in these polymers might be coupled with the inherent dynamic covalent features of imines or olefins (via dynamic metathesis) as a valuable tool for advanced functional materials.

The use of imines as photoswitches was meanwhile extended also to immobilized states, by using imine-functionalized triazatriangulenium platforms for highly ordered, self-assembled monolayers of imines on Au(111) surfaces (Figure 15.3c) [74]. Several conditions for maximum power transmission to eventual load transport by light energy were discussed: (i) The imines have to be immobilized as an array with sufficient free volume for switching. (ii) The orientation of the switching units should be vertical and free standing. (iii) The imines have to be electronically decoupled from the metal surface to prevent alternative decay pathways. Successful photoisomerization and a swift thermal back reaction at the surface were observed. Thus, this work represents a vital step toward an artificial ciliated epithelium.

As can be seen from the previous paragraph, although the potential of imines for photoswitching in molecules and materials is undoubtedly given, there is plenty untapped work to be done, like the shifting of absorption into the visible range or the coupling with more sophisticated function. By all means, the ease of synthesis of imines should make such endeavors straightforward and rewarding.

### 15.2.4 Imines as Light-Driven Molecular Motors

Based on the distinct trajectories in thermal and photochemical *E*/*Z*-imine isomerization (Figure 15.1), a combination of light and thermal energy on chiral imines was proposed for the particularly simple realization of a molecular motor [75]. In principle, directionally preferred light-driven rotation stores energy, which is released by the orthogonal in-plane thermal nitrogen inversion. The preferred directionality is made plausible by the asymmetry of the excited-state force field, as was corroborated in unpublished computational work (J. Gálvez, L. Greb, J.-M. Lehn) and more recent results (*vide infra*). This concept differs from the other double-bond motors, as the directionality is induced in the photochemical step, rather than in the thermal isomerization.

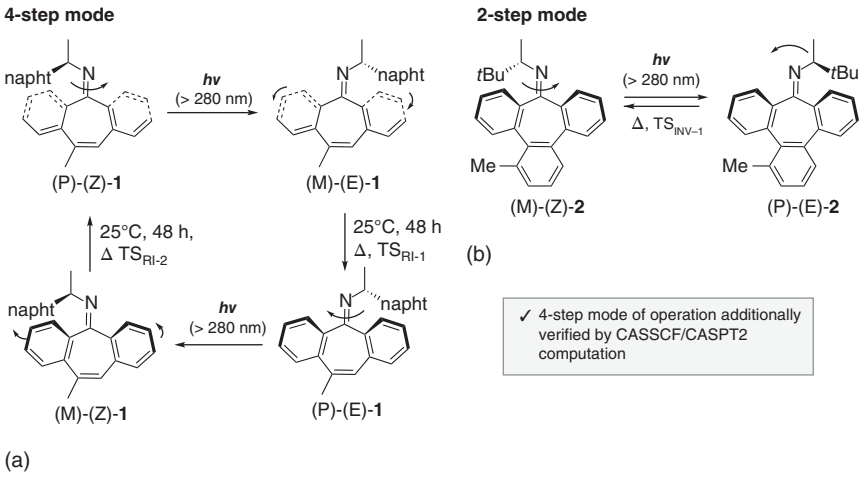


**Figure 15.4** Imine-based molecular motor operation in (a) 4-step mode or in (b) 2-step mode via a single atom-centered back-stroke.

The first realization of an imine-based molecular motor was reported in 2014 based on the diaryl-*N*-alkyl imine **1** (Figure 15.4a) [76]. In a first design, the above-described imine specific principle was not followed, but rather the well-established 4-step operation of Feringa's overcrowded olefins was emulated [77]. The interconversion of the four possible diastereomers of **1** was achieved by the alternating application of light and heat, as followed by NMR-spectroscopy. The thermodynamically favored (P)-(Z)-**1** was transformed to the metastable (M)-(E)-**1** form by photoisomerization with light of >280 nm. Subsequent thermal relaxation via ring inversion (RI) converted the (M)-(E)-**1** enriched mixture to a (P)-(E)-**1** enriched state. The second photoisomerization led to the (M)-(Z)-**1** state by another half-rotation around the double bond, and a final ring inversion step closed the 360° cycle around the C=N axis. Although the energetic bias of the different states is not very pronounced, these observations verified that molecules of type **1** indeed behave as 4-step unidirectional rotors. In the same study, the energy barrier for helix inversion of the stator part was controlled by annealing an aromatic ring the heptenyl core in **2** (Figure 15.4b). Now, the barrier for helix inversion was increased above nitrogen inversion, and the photochemical C=N bond rotation combined with the thermal in-plane nitrogen inversion process. Hence, essential achievements for the field of molecular motors were made by exploiting the specific characteristics of the C=N double bond: (i) The combination of photo-induced rotation with *two* independent and orthogonal thermal processes, in-plane nitrogen inversion (NI) and ring inversion (RI), conferred triple motional dynamics to the imine – based system. (ii) By adjustment of the conformational flexibility of the "stator," the *mode of operation* can be either 2-step (light power stroke and thermal relaxation via NI) or 4-step (alternating light power stroke and thermal relaxation via RI). (iii) Ultimately, in-plane nitrogen inversion allowed for a motor stroke by a *single atom* centered process.

The full operation cycle of the 4-step mode of a derivative of **1** was subsequently studied by complete active space self-consistent field (CASSCF) and second-order perturbation theory (CASPT2) [78]. First of all, the study verified that the photochemical (P)-(M) C=N-bond isomerization is a barrierless and directional rotary process, with a large initial force that leads to the release of the substantial steric hindrance between the rotor and the stator in the (P)-states. The $S_1$ state trajectory leads via a conical intersection to the $S_0$ state without the requirement of vibrational modes other than the C=N bond torsion, ideally keeping the directionality of the rotation. Importantly, the energy difference between the highest point ($\Theta = 0°$) and the lowest point ($\Theta = 90°$) on the energy profile of the $S_1$ state (25.3 kcal mol$^{-1}$) is more significant than that of overcrowded-alkene-based motors (8.9 kcal mol$^{-1}$). Thus, the work not only confirmed the experimental findings and hypotheses but indicated that this particular type of imine-based molecular motor might indeed be *more* directional than some overcrowded-alkene-based motors in the photoisomerization process.

To substantiate the 2-step mode operation of imines in a more general sense, camphorquinone imines **3** were synthesized in a follow-up experimental study (Figure 15.5) [79]. First of all, those imines were shown to undergo effective photoswitching upon irradiation with UV-light, transforming the almost pure *E* ground-state isomer to an *E*/*Z* distribution of 21 : 79 in the photostationary state (PSS). Due to the asymmetry of the rigid stator camphorquinone, the excited-state force field should be asymmetric and bias the directionality during the photochemical C=N bond rotation. Indeed, this picture was supported by a diastereoselective radical trapping experiment. Excitation of an *N*-cyclopropyl derivative with light of 254 nm caused the opening of the cyclopropyl ring and the formation of a biradical species. This intermediate underwent a rearrangement to two diastereomeric products, wherein a preferred rotational pathway on the excited-state surface should be reflected in the ratio of exo- and endo-trapped states. Indeed, a significant difference in the yields of both diastereomers indicated the preference of one over the other trajectory, which might also reflect a preferred directionality of the *E*/*Z*-isomerization. Although the rotational preference in the biradical $S_2$ state could differ from the pure rotation observed in the $S_1$ state, this result was the first experimental indication for the unidirectional rotation of chiral imines.

The switching states of the camphorquinone imine **3** (R = $^t$Bu) were later on verified by a combination of matrix-isolation and vibrational circular dichroism [80]. This study revealed that both isomers could be obtained photochemically even at cryogenic temperatures (22 K) and fully confirmed the original experimental findings. The theoretical proof of the proposed 2-step working mechanism within such compounds was provided in a recent CASSCF/CASPT2 study [81]. It was found that **3** (R = $^t$Bu) reaches the $S_1$ ($n_N \rightarrow \pi^*$) state upon irradiation and relaxes by rotation with preferred directionality to a perpendicular state, which may reach the ground state via a conical intersection while maintaining the directionality of C=N bond rotation.

Overall, this combination of experimental and computational studies suggests that every imine with a chiral center in sufficient proximity could behave as a

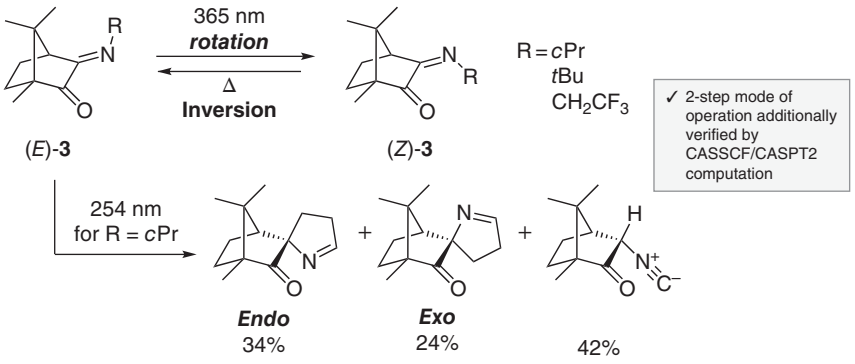


**Figure 15.5** Realization of the simplest molecular motor and experimental indication of preferred directionality of the photochemical out-of-plane rotation.

rotary motor driven by light and thermal energy. One of the significant advantages of imine-based molecular motors is their effortless accessibility in one-step condensation procedures, potentially from commercially available precursors. It offers a straightforward means to fine-tune the speed of these motors via the barrier for thermal N-inversion. Finally, the dynamic covalent features of imines offer the intriguing possibility to merge motional dynamics with constitutional dynamics, thus giving, in principle, access to motional dynamic libraries of a variety of molecular motors turning at different speeds.

## 15.3 Acylhydrazone and Hydrazone Photoswitches

### 15.3.1 The Triple Dynamics of Imine-Based Photoswitches

Imines, acylhydrazones, and hydrazones have the interesting characteristic of being triple dynamic entities [82] able to undergo: (i) constitutional dynamics, by exchange of amine or carbonyl compounds, (ii) conformational dynamics, by shape switching upon coordination with a cation and (iii) configurational dynamics, by photochemical and thermal *E*/*Z*-isomerization (Figure 15.6). These constitution, coordination, and configuration dynamics are all reversible, operate through orthogonal processes, and occur on different time scales. The triple dynamics of imine-based photoswitches have been extensively studied as versatile tools to demonstrate a variety of concepts, in catalysis, sensing, and adaptation. In this section, after a detailed analysis of the dynamic characteristics of these motifs, we present a selection of seminal examples combining these dynamics in responsive systems.

(i) The constitutional dynamics play a major role in processes where components exchange generates new molecules at rates that can be chemically controlled [83–85]. The imine bond C=N is particularly interesting because the reversibility can be triggered under mild conditions [86–88]. Hydrazones are kinetically inert under neutral conditions, due to the C=N—N conjugation, which decreases the electrophilicity of the C=N bond, making them more

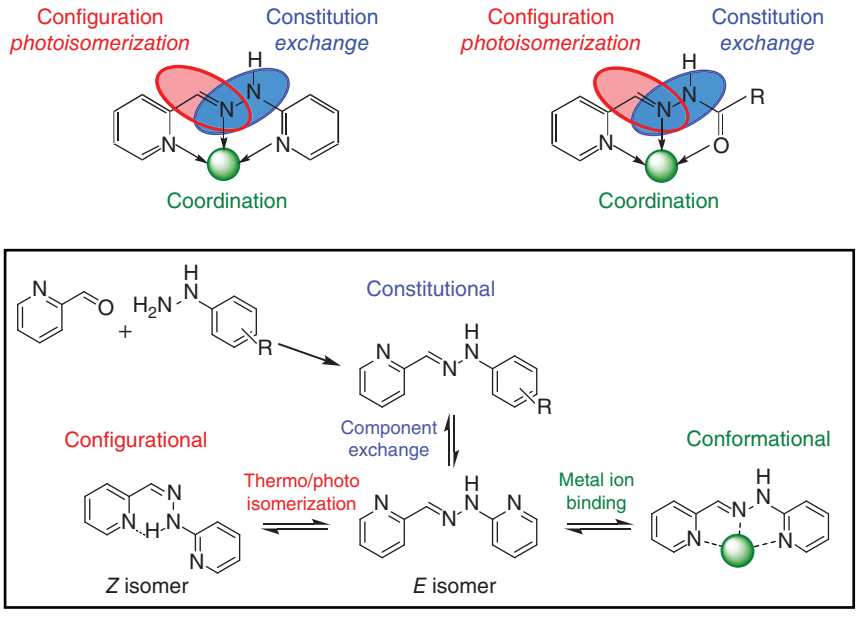


**Figure 15.6** Pyridyl-hydrazone and pyridyl-acylhydrazone as triple dynamic switches (top). The three types of reversible dynamic processes are: constitutional by component exchange (middle), conformational by coordination with a metal cation (right), and configurational by photo- and thermo-isomerization (left). Source: Modified from Chaur et al. [82].

stable against hydrolysis or exchange. Such exchange however becomes fast for compounds having electron-withdrawing groups, or in presence of catalyst [89, 90]. In between imines and hydrazones, acylhydrazones are easily exchanged because the conjugation of the nitrogen site of acylhydrazone on the carbonyl group decreases conjugation with the C=N bond, which makes acylhydrazones more reactive to attack by nucleophiles. Constitutional exchange dynamics of acylhydrazone compounds have been widely studied under Brønsted acid catalysis conditions [91–94].

(ii) The conformational dynamics of hydrazones and acylhydrazones are observed by complexation with metal cations. In the case of pyridyl derivatives, the presence of a tridentate coordination site (NNN and NNO) allows the formation of stable complexes with transition metals [95–99].

(iii) As described in the first part of this chapter, the configurational dynamics of imines, acylhydrazones, and hydrazones arise from the *E*/*Z*-isomerization of the C=N bond under light irradiation [1, 2, 100]. In the case of pyridyl-hydrazones and pyridyl-acylhydrazones, the *Z* isomer is stabilized by the formation of an intramolecular hydrogen bond linked to the pyridine unit [101–104]. These studies have also been extended to bis-hydrazone and bis-acylhydrazone switches, in which the controlled movement of each arm can be independently operated between three isomeric states [105, 106].

In addition to light, it has been shown that *E*/*Z*-isomerizations of hydrazones can also be induced by pH changes [107–109].

The multi-dynamic entities exhibit three levels of information control and can be used to switch different physical properties (e.g. spectroscopic, absorption, fluorescence) [110–112]. They thus represent compounds for the design of systems with greater degrees of complexity and can be used for the modulation of properties in supramolecular assemblies [113–116]. These C=N units are also candidates for the development of molecular information storage and training systems [82, 117]. Indeed, constitutional and configurational dynamics represent long- and short-term information storage, respectively. Constitutional dynamics generate new molecules by component exchange and represent a long-term molecular storage (memory), whereas configurational dynamics bring structural variation to the molecule and represent a short-term storage of molecular information. Conformational dynamics represent a locking process where the presence of metal ions controls the locking and unlocking of interconversion between the different states.

### 15.3.2 The Consequences of Pyridyl-Hydrazones Shape Switching

The configurational and conformational changes of the pyridyl-hydrazones and pyridyl-acylhydrazones have been used as shape switches. The *E*/*Z*-photoisomerization of the C=N bond and the coordination to metal ion [118] induce a geometric change of the core, which can be implemented as ON/OFF switch to control molecular functions and as a trigger to command a cascade of molecular events. The following section gives an overview of the fields of research where the shape switching of pyridyl-hydrazones has been coupled to molecular functions.

#### 15.3.2.1 Photo-Responsive Receptor

A major area in which pyridyl-acylhydrazone and -hydrazone have been employed is in the design of photoswitchable monotopic [119] and ditopic receptors [120]. As explained earlier, the presence of a tridentate coordination site (NNN and NNO) allows the formation of complexes with a large variety of cations. Photo-irradiation of the complex induces a cascade of events: *E*/*Z*-photoisomerization of the imine unit, stabilization of the *Z* isomer by formation of intramolecular hydrogen bond, and concomitant release of the ionic species in solution. The release of the cation has been used for example to trigger phase separation in acetonitrile/water binary mixture (Figure 15.7) [119]. Herein, upon irradiation, the responsive complex [*E*-bis-pyridyl-hydrazone/$CaCl_2$] undergoes *E*/*Z*-isomerization, release of calcium cations in solution, and macroscopic phase separation of the binary mixture. Interestingly, although the association constant between the bis-pyridyl-hydrazone ligand and the calcium cation is weak, an ionic threshold of the cation concentration free in solution is reached during irradiation. This cation release translates into a separation of the single acetonitrile/water phase visible at the macroscopic scale. This system demonstrates that minor molecular events can be translated into major macroscopic changes in synthetic molecular processes. Using similar binding units,

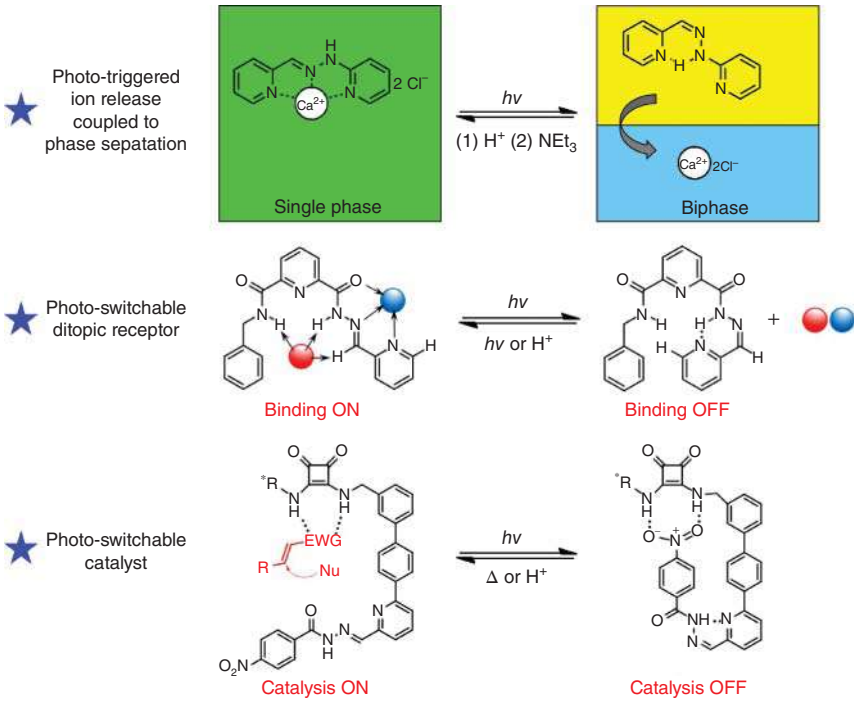


**Figure 15.7** The consequences of pyridyl-hydrazones and -acylhydrazones shape switching to light-induce binary phase separation [119], to make photoswitchable heteroditopic ion-pair receptor [120], and to develop photo-responsive catalysts (with R* a chiral group) [121]. Source: Refs. [119–121].

Chmielewski and coworker designed a heteroditopic ion-pair receptor combining the binding sites of the ion-pair and the photoswitchable imine unit (Figure 15.7) [120]. This receptor has been reported as the first photoswitchable ion-pair receptor in which both cation- and anion-binding sites are simultaneously and reversibly switched OFF and ON by a single photoswitch.

### 15.3.2.2 Switchable Catalysis

The shape switching of the pyridyl-acylhydrazone was also used to control catalyst activity and stereoselectivity. A complementary pair of enantioselective switchable organocatalysts was designed to catalyze Michael addition with chalcones (Figure 15.7) [121, 122]. The catalyst contains a bifunctional cinchona alkaloid-squaramide motif as the active site and a pyridyl-acylhydrazone arm decorated with the hydrogen bond acceptor nitrobenzene as an additional potentially inhibiting unit. The *E*/*Z*-isomerization of the pyridyl-acylhydrazone unit controls the activity of the catalyst. In the *E* form, the pyridyl-acylhydrazone arm stands away from the catalytic site and the catalyst is active. However, upon light irradiation, the pyridyl-acylhydrazone arm switches to the *Z* isomer and the shape change brings the nitro substituent in proximity to the squaramide active site, which renders the catalyst inactive. By changing the position of the substituents on

the squaramide core, two enantiomeric catalysts were obtained and demonstrated complementarity in their activity.

#### 15.3.2.3 Control of Supramolecular Polymerization

Recently, the acylhydrazone photoswitch was incorporated into benzene-1,3,5-tricarboxamide (BTA) supramolecular polymers to control their structure and morphology [116]. These BTA monomers self-assemble cooperatively into one-dimensional aggregates stabilized by threefold helical intermolecular hydrogen bonding. A chiral BTA monomer was functionalized with an acylhydrazone unit and used as an additive to control the polymerization of alkyl BTA monomers. In the *E* form, the chiral additive intercalates into BTA stacks and biases the helicity of the aggregates. Photoisomerization from the *E* to the *Z* isomer transforms the intercalator into a chain capper, resulting in the shortening of the BTA supramolecular polymers. The chain-capping effect was explained by the shape switching of the acylhydrazone from the planar E isomer to the non-planar *Z* isomer, which induces steric hindrance on one face of the monomer and prevents the polymer for further growth.

#### 15.3.2.4 The Dynamics of Molecular Movements

The multiple dynamics of hydrazones and acylhydrazones can be used to control molecular motion in the area of molecular machines [123–125]. For example, Leigh and coworkers have reported a rotaxane and a molecular shuttle built from a pyridyl-acylhydrazone unit [126]. The pyridyl-acylhydrazone is used as the axle of the rotaxane and acts as a hydrogen bonding template to direct the assembly with a macrocycle. Photoswitching the hydrazone from the *E* to the *Z* isomer blocks the formation of the rotaxane because of the disruption of the hydrogen bonding template by intramolecular stabilization. Implemented in a molecular shuttle containing two possible binding sites, pyridyl-acylhydrazone and succinic amide ester, the position of the macrocycle on the binding sites was controlled by light irradiation and heating cycles.

#### 15.3.2.5 Adaptation

Pyridyl-acylhydrazones and -hydrazones are attractive tools to design dynamic molecular systems responsive to multiple stimuli and to study the adaptation of chemical systems to their environment [127, 128]. A W-shaped pyridyl-hydrazone decorated with aldehydes in the 6-position of the pyridine units undergoes preferentially polycondensation with α,ω-diamines to form linear dynamic oligomers or polymers (Figure 15.8). Irradiation of this switch and formation of the stable Z-isomer interconvert the W-shaped core into a U-shaped one. As a result, the dialdehyde functions are held closer to each other in space, thus favoring the formation of a macrocycle when reacting with a suitable diamine. Reversible switching between polymeric and macrocyclic states takes place upon *E*/*Z* interconversion. Moreover, the same photoswitch can also undergo conformational W to U switching upon metal ion binding [130, 131]. It was demonstrated the possibility to achieve switching of adaptation in response to two orthogonal

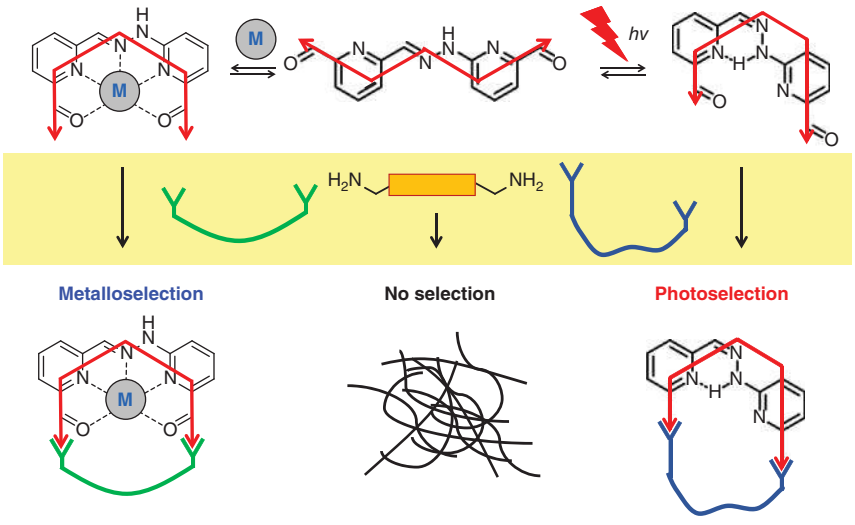


**Figure 15.8** Constitutional adaptation. The initial W-shape hydrazone switch (center) forms polymers by non-selective condensation with α,ω-diamines. Switching of the hydrazone by coordination with a metal ion (left side) or by light irradiation (right side) induces selective reaction with a diamine. Source: Vantomme et al. [128].

external agents (light and metal ion) through component selection on reaction with different α,ω-diamines. The morphological information borne by the switch is thus transferred into the constitutional space involving the formation of different species with component selection. Thus, the morphological photoswitching process results in a constitutional adaptation behavior induced by light.

Exploring similar principles, Otto and coworkers reported the redox control over *E*/*Z* photoisomerization of acylhydrazone to generate diversity in an acylhydrazone-based dynamic combinatorial library [132]. Specifically, the *Z* to *E* back-isomerization of the acylhydrazone is triggered with aromatic thiols by nucleophilic catalysis. The *E*/*Z* isomerization rate of the acylhydrazone photoswitch is controlled by the oxidation state of the thiols, oxidized into catalytically inactive disulfides. The dynamic combinatorial library is composed of macrocycles isomers of the acylhydrazone switch and undergoes adaptation to the redox state of the thiols, translated to the *E*/*Z* isomerization state of the acylhydrazone photoswitch. These results describe constitutional adaptation in a triple chemical system: thiol/disulfide chemistry, nucleophilic catalysis of *Z* to *E* isomerization, and photochemical *E* to *Z* isomerization.

## 15.3.3 Constitutional Dynamic Networks

### 15.3.3.1 Photoswitching of Constitutional Dynamic Networks

In the progress toward chemical systems with higher levels of complexity [133–135], constitutional dynamic chemistry generates chemical diversity in constitutional dynamic libraries (CDLs) by constitutional exchange. In response to an external

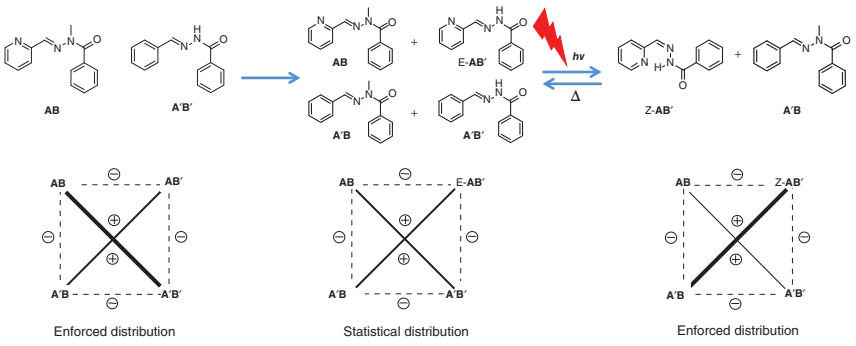


**Figure 15.9** Adaptation of the constitutional dynamic network of four acylhydrazones **AB**, **A′B**, **AB′**, and **A′B′** upon equilibration followed by light irradiation (top). Weighted graph representation of the square CDN of the acylhydrazones **AB**, **A′B**, **AB′**, and **A′B′** (bottom). Source: Vantomme et al. [129].

input, the constitutional dynamics within the CDL allows for variation in the system and operates selection and amplification mechanisms to achieve adaptation. The set of interconnected compounds of a CDL forms a constitutional dynamic network (CDN). It can be represented in a schematic way by a weighted graph, where the connections between the compounds describe the correlation between the members of a set, their agonistic or antagonistic relationships, as well as their relative amounts. The simplest network is that of four constituents located at the corners of a square, where the edges connect antagonistic and the diagonals agonistic constituents (Figure 15.9). Upon application of external stimuli, the CDL distribution changes by amplification of the responsive constituent and its agonist and by down-regulation of the antagonists. CDNs are adaptive systems as the weights of the networks change in response to external stimuli. Based on their triple dynamics, imines-based switches represent powerful tools to explore the adaptation of CDNs. Figure 15.9 illustrates the adaptation to light of a CDN of acylhydrazones. Two acylhydrazones **AB** and **A′B′** generate four acylhydrazones **AB**, **A′B**, **AB′,** and **A′B′** by reversible C=N exchange. Upon light irradiation, **AB′** undergoes *E*/*Z*-isomerization, and the *E* isomer is stabilized by formation of an intramolecular hydrogen bond [129]. The distribution of the constituents reaches a new equilibrium with an amplification of the stabilized **AB′** constituent as well as of its antagonist **A′B** and a down-regulation of the constituents **AB** and **A′B′**. The concept of CDNs has recently been extended to systems of increasing complexity implementing [3X3] networks [136], responsive to multiple adaptation [137] as well as chrono-switching between kinetic and thermodynamic distributions of constituents [138]. A very intriguing feature of linked constituents in a network is the concept of agonist amplification, whereby the perturbation (e.g. amplification) of one member of a pair of agonists enforces a modification in the same direction of its agonistially linked partner. Such behaviors are of broad significance and extend to other fields of science.

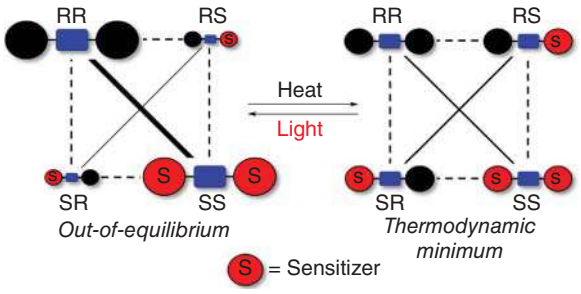


**Figure 15.10** Photochemically and thermally switchable dynamic covalent reaction network consisting of sensitized (SS) and nonsensitized (RR) alkoxyamines (AOAs). Starting from RR and SS, heat induces formation of the mixed derivatives (RS and SR) and thus equilibration of the network toward the thermodynamic minimum. On the other hand, selective photoactivation of sensitized AOAs SS, RS, and SR with light and the resulting enrichment of the nonsensitized analogue RR drives it back to the initial out-of-equilibrium state. Source: Herder and Lehn [139].

#### 15.3.3.2 Photoswitching in Dynamic Covalent Chemistry: The Photodynamic Covalent Bond

The development of constitutional dynamic chemistry has been very actively pursued especially on the covalent level in dynamic covalent chemistry (DCC), making use of different types of reversible covalent bonds. Photochemically driven DCC processes have already been mentioned above. A case in point is that of photoswitching a dynamic covalent library (DCL) from one constitutional state to another one by implementation of a photodynamic covalent bond. Such a process can be photo-induced by means of a reversible photocleavable bond such as the N—O bond of alkoxyamines (AOAs). Indeed, photocleavage of suitably designed light-sensitized AOAs has been shown to allow for the reversible switching of AOA DCLs between two constitutional states on light irradiation and thermal back reaction. Light induces the formation of an out-of-equilibrium state of higher energy that reverts to thermodynamic equilibrium on thermal-energy dissipation. The process represents a reversible light-induced switching of a photo-driven CDN. It is schematically represented in Figure 15.10 [139].

## 15.4 Conclusion

Imine-based photoswitches have proven to be versatile tools to reach functions of higher level of complexity and to develop innovative proof-of-concept processes in molecular systems. They also form an attractive class of compounds thanks to their ease of synthesis, their stability, and their modularity. Without doubt, imine-based photoswitches have still bright days ahead of them.

## References


1 Padwa, A. (1977). Photochemistry of the carbon-nitrogen double bond. *Chem. Rev.* 77 (1): 37–68.
2 Pratt, A.C. (1977). The photochemistry of imines. *Chem. Soc. Rev.* 6 (1): 63–81.
3 Vocelle, D., Dargelos, A., Pottier, R., and Sandorfy, C. (1977). Photoelectron and far-ultraviolet absorption spectra of nonaromatic azomethine compounds. *J. Chem. Phys.* 66 (7): 2860–2866.
4 Paetzold, R., Reichenbächer, M., and Appenroth, K. (1981). Die Kohlenstoff-Stickstoff-Doppelbindung: Spektren, Struktur, thermische und photochemische E/Z-Isomerisierung. *Z. Chem.* 21 (12): 421–430.
5 Jacquemin, D., Laurent, A.D., Perpète, E.A., and André, J.-M. (2009). An ab initio simulation of the UV/visible spectra of *N*-benzylideneaniline dyes. *Int. J. Quantum Chem.* 109 (15): 3506–3515.
6 Smith, W.F. (1963). Application of molecular orbital theory to the electronic absorption spectra of Schiff bases. *Tetrahedron* 19 (3): 445–454.
7 Russegger, P. (1978). Photoisomerization about carbon—nitrogen double bonds. I. Kinetic and potential energy for ground and excited states of methylenimine. *Chem. Phys.* 34 (3): 329–339.
8 Osamura, Y., Yamabe, S., and Nishimoto, K. (1980). MO study of the photochemical behavior of the imine bond. *Int. J. Quantum Chem.* 18 (2): 457–462.
9 Russegger, P. (1980). Theoretical investigation of the triplet to ground state photoisomerization of imines. *Chem. Phys. Lett.* 69 (2): 362–366.
10 Bonacic-Koutecky, V. and Persico, M. (1983). CI study of geometrical relaxation in the ground and excited singlet and triplet states of unprotonated Schiff bases: allylidenimine and formaldimine. *J. Am. Chem. Soc.* 105 (11): 3388–3395.
11 Bonacic-Koutecky, V. and Michl, J. (1985). Photochemical syn-anti isomerization of a Schiff base: a two-dimensional description of a conical intersection in formaldimine. *Theor. Chim. Acta* 68 (1): 45–55.
12 Tavernelli, I., Röhrig, U.F., and Rothlisberger, U. (2005). Molecular dynamics in electronically excited states using time-dependent density functional theory. *Mol. Phys.* 103 (6–8): 963–981.
13 Uraguchi, D., Tsuchiya, Y., Ohtani, T. et al. (2020). Unveiling latent photoreactivity of imines. *Angew. Chem. Int. Ed.* 59 (9): 3665–3670.
14 Ciamician, G. and Silber, P. (1903). Chemische Lichtwirkungen. *Ber. Dtsch. Chem. Ges.* 36 (4): 4266–4272.
15 Fischer, E. and Frei, Y. (1957). Photoisomerization equilibria involving the C=N double bond. *J. Chem. Phys.* 27 (3): 808–809.
16 Anderson, D.G. and Wettermark, G. (1965). Photoinduced isomerizations in anils. *J. Am. Chem. Soc.* 87 (7): 1433–1438.
17 Padwa, A. and Albrecht, F. (1974). Photochemical syn-anti isomerization about the carbon-nitrogen double bond. *J. Am. Chem. Soc.* 96 (15): 4849–4857.


**18** Maeda, K. and Fischer, E. (1977). Photoformation of "Z" (cis) isomers in diaryl- and triaryl- azomethines, part II.[1] Electronic and NMR spectra of methyl derivatives of benzylideneaniline (C6H5—CH=N—C6H5). *Isr. J. Chem.* 16 (4): 294–298.

**19** Luo, Y., Utecht, M., Dokić, J. et al. (2011). Cis–trans isomerisation of substituted aromatic imines: a comparative experimental and theoretical study. *ChemPhysChem* 12 (12): 2311–2321.

**20** Herkstroeter, W.G. (1976). Excited-state multiplicity for the direct photochemical isomerization of azomethine dyes. *J. Am. Chem. Soc.* 98 (20): 6210–6218.

**21** Mitric, R., Werner, U., and Bonacic-Koutecky, V. (2008). Nonadiabatic dynamics and simulation of time resolved photoelectron spectra within time-dependent density functional theory: ultrafast photoswitching in benzylideneaniline. *J. Chem. Phys.* 129 (16): 164118.

**22** Gálvez, J. and Guirado, A. (2010). A theoretical study of topomerization of imine systems: inversion, rotation or mixed mechanisms? *J. Comput. Chem.* 31 (3): 520–531.

**23** Al-Ansari, I.A.Z. (2018). Role of solvent polarity and hydrogen-bonding on excited-state fluorescence of 3-[(E)-{4-[Dimethylamino]benzylidene}amino]-2-naphthoic acid (DMAMN): isomerization vs rotomerization. *J. Phys. Chem. A* 122 (7): 1838–1854.

**24** Herkstroeter, W.G. (1976). A model for the triplet state photochemical isomerization of azomethine dyes. *J. Am. Chem. Soc.* 98 (2): 330–336.

**25** Russegger, P. (1979). Vibrational wavefunctionals for the thermal and photochemical syn—anti isomerization of imines. *Chem. Phys.* 41 (3): 299–317.

**26** Osamura, Y., Kitaura, K., Nishimoto, K., and Yamabe, S. (1979). An MO study of methylenimine in the lowest excited state. Comparison with CH2=CH2, NH=NH and CH2=O. *Chem. Phys. Lett.* 63 (2): 406–410.

**27** Segawa, K., Kikuchi, O., Arai, T., and Tokumaru, K. (1995). Photochemical EZ isomerization of aryl-substituted methanimines. AM1-CI potential energy curves along the CN double bond twisting and the N atom in-plane inversion. *J. Mol. Struct. THEOCHEM* 343 (0): 133–140.

**28** Arai, T., Furuya, Y., and Tokumaru, K. (1996). Photochemical isomerization around the C=N double bonds of N-methoxy-1-(1-pyrenyl)methanimine in the excited state. *J. Photochem. Photobiol., A* 97 (3): 133–138.

**29** Gaenko, A., Devarajan, A., Gagliardi, L. et al. (2007). Ab initio DFT study of Z–E isomerization pathways of N–benzylideneaniline. *Theor. Chem. Acc.* 118 (1): 271–279.

**30** Curtin, D.Y. and Hausser, J.W. (1961). Effects of structural changes on the interconversion of stereoisomeric imines. Isoelectronic models for vinyl anions[1]. *J. Am. Chem. Soc.* 83 (16): 3474–3481.

**31** Curtin, D.Y. and McCarty, C.G. (1962). Configuration stability at the carbon-nitrogen double bond. *Tetrahedron Lett.* 3 (26): 1269–1274.

**32** Curtin, D.Y., Grubbs, E.J., and McCarty, C.G. (1966). Uncatalyzed syn-anti isomerization of imines, oxime ethers, and haloimines[1]. *J. Am. Chem. Soc.* 88 (12): 2775–2786.


**33** Lehn, J.M. (1970). Nitrogen inversion. In: *Topics in Current Chemistry* (Eds. A. Davison, M. J. S. Dewar, K. Hafner, E.Heilbronner, U. Hofmann, K. Niedenzu, Kl. Schäfer, G. Wittig), 311–377. Berlin, Heidelberg: Springer.

**34** Cook, R.J. and Mislow, K. (1971). Barrier to planar inversion in an N-germyl imine. *J. Am. Chem. Soc.* 93 (24): 6703–6704.

**35** Alkorta, I. (2009). Barriers about double carbon-nitrogen bond in imine derivatives. *Croat. Chem. Acta* 82 (1): 173–183.

**36** McCarty, C.G. (2010). Syn-anti isomerizations and rearrangements. In: *Carbon–Nitrogen Double Bonds (Ed. S. Patai) (1970)*, 363–464. Wiley.

**37** Reiker, A. and Kessler, H. (1967). NMR-studien an chinonanilen: Der einfluss paraständiger substituenten im phenylring auf die thermische isomerisierung. *Tetrahedron* 23 (9): 3723–3732.

**38** Wurmb-Gerlich, D., Vögtle, F., Mannschreck, A., and Staab, H.A. (1967). Untersuchungen über Schiffsche Basen, VI. Protonenresonanz-Untersuchungen zur syn-anti-Isomerisierung von Iminen. *Justus Liebigs Ann. Chem.* 708 (1): 36–50.

**39** Kessler, H. (1968). Nachweis innermolekularer beweglichkeit durch nmr-spektrometrie-III: Magnetische nichtäquivalenz geminaler gruppen durch rotationshinderung in achiralen molekülen. *Tetrahedron* 24 (4): 1857–1867.

**40** Kessler, H. and Leibfritz, D. (1970). Nachweis innermolekularer beweglichkeit durch NMR-spektroskopie, XIX magnetische nichtäquivalenz als beweis für die inversion am stickstoff in iminen. *Tetrahedron Lett.* 11 (17): 1423–1426.

**41** Kessler, H. and Leibfritz, D. (1971). Nachweis innermolekularer Beweglichkeit durch NMR-Spektroskopie, XXIII. Mechanismus der syn-anti-Isomerisierung in Iminen. Diastereotopie und Enantiotopie. *Chem. Ber.* 104 (7): 2143–2157.

**42** Jennings, W.B. and Boyd, D.R. (1972). Mechanism of interconversion of (Z)-and (E)-ketimines. *J. Am. Chem. Soc.* 94 (20): 7187–7188.

**43** Kessler, H. (1974). Thermal isomerization about double bonds: rotation and inversion. *Tetrahedron* 30 (13): 1861–1870.

**44** Jennings, W.B., Al-Showiman, S., Boyd, D.R., and Campbell, R.M. (1976). Dynamic stereochemistry of imines and derivatives. Part IX. The mechanism of E-Z isomerization in *N*-alkylimines. *J. Chem. Soc. Perkin Trans.* 2 (13): 1501–1506.

**45** Knorr, R., Ruhdorfer, J., Mehlstäubl, J. et al. (1993). (E, Z)1-Equilibria, 17 demonstration of the nitrogen inversion mechanism of imines in a Schiff Base model. *Chem. Ber.* 126 (3): 747–754.

**46** Lehn, J.M. and Munsch, B. (1968). An ab initio SCF-LCAO-MO study of the nitrogen inversion barriers in methylenimine, diimide and carbodiimide. *Theor. Chim. Acta* 12 (1): 91–94.

**47** Lehn, J.M., Munsch, B., and Millie, P. (1970). Analyse conformationnelle théorique. *Theor. Chim. Acta* 16 (5): 351–372.

**48** Kerek, F., Ostrogovich, G., and Simon, Z. (1971). Mechanism of the uncatalysed syn-anti-isomerization of imine systems. Part IV. A theoretical study of the influence of substituents. *J. Chem. Soc. B Phys. Org.*: 541–544.


**49** Weiss, K., Warren, C.H., and Wettermark, G. (1971). Cis-trans isomerization about the carbon-nitrogen double bond. Structures of the isomers of N-benzylideneaniline. *J. Am. Chem. Soc.* 93 (19): 4658–4663.

**50** Jennings, W.B. and Worley, S.D. (1980). Inversion at trivalent nitrogen: application of the MNDO and MINDO/3 semiempirical molecular orbital methods. *J. Chem. Soc. Perkin Trans.* 2 (10): 1512–1515.

**51** Hofmann, H.-J., Asano, T., and Cimiraglia, R. (1991). On the conformation of the inversion state in the thermal E,Z isomerization of aromatic azomethines. *J. Chem. Soc., Chem. Commun.* (5): 295–296.

**52** Yamataka, H., Ammal, S.C., Asano, T., and Ohga, Y. (2005). Thermal isomerization at a C=N double bond: how does the mechanism vary with the substituent? *Bull. Chem. Soc. Jpn.* 78 (10): 1851–1855.

**53** He, S., Tan, Y., Xiao, X. et al. (2010). Substituent effects on electronic character of the CN group and trans/cis isomerization in the C-substituted imine derivatives: a computational study. *J. Mol. Struct. THEOCHEM* 951 (1–3): 7–13.

**54** Landge, S.M., Tkatchouk, E., Benítez, D. et al. (2011). Isomerization mechanism in hydrazone-based rotary switches: lateral shift, rotation, or tautomerization? *J. Am. Chem. Soc.* 133 (25): 9812–9823.

**55** Kutsik-Savchenko, N.V., Lebed, O.S., and Prosyanik, A.V. (2015). The effect of C-substituents on the topomerization mechanism, inversion barriers and electronic character of CN bond in *N*-alkylimines: a theoretical study. *Comput. Theor. Chem.* 1072: 15–20.

**56** Matsuhira, T., Yamamoto, H., Onoda, A. et al. (2006). Photoinduced switching of intramolecular hydrogen bond between amide NH and carboxyl oxygen. *Org. Biomol. Chem.* 4 (7): 1338–1342.

**57** Greb, L., Eichhöfer, A., and Lehn, J.-M. (2016). Internal C–C bond rotation in photoisomers of α-bisimines: a light-responsive two-step molecular speed regulator based on double imine photoswitching. *Eur. J. Org. Chem.* 2016 (7): 1243–1246.

**58** Schoevaars, A.M., Kruizinga, W., Zijlstra, R.W.J. et al. (1997). Toward a switchable molecular rotor. Unexpected dynamic behavior of functionalized overcrowded alkenes. *J. Org. Chem.* 62 (15): 4943–4948.

**59** Jog, P.V., Brown, R.E., and Bates, D.K. (2003). A redox-mediated molecular brake: dynamic NMR study of 2-[2-(methylthio)phenyl]isoindolin-1-one and S-oxidized counterparts. *J. Org. Chem.* 68 (21): 8240–8243.

**60** Yang, J.-S., Huang, Y.-T., Ho, J.-H. et al. (2008). A pentiptycene-derived light-driven molecular brake. *Org. Lett.* 10 (11): 2279–2282.

**61** Hirose, K. (2010). Molecular brake systems controlled by light and heat. *J. Inclusion Phenom. Macrocyclic Chem.* 68 (1–2): 1–24.

**62** Sun, W.-T., Huang, S.-L., Yao, H.-H. et al. (2012). An antilock molecular braking system. *Org. Lett.* 14 (16): 4154–4157.

**63** Jye-Shane, Y. and Wei-Ting, S. (2014). Light- and electricity-gated internal rotation of molecular rotors: toward artificial molecular machines. In: *Organic Structures Design* (Ed. T. J. Chow), 137–183. Stanford: Pan.

**64** Tan, W.S., Chuang, P.-Y., Chen, C.-H. et al. (2015). Light-gated molecular brakes based on pentiptycene-incorporated azobenzenes. *Chem. Asian J.* 10 (4): 989–997.

**65** Alfonso, I., Burguete, M.I., and Luis, S.V. (2006). A hydrogen-bonding-modulated molecular rotor: environmental effect in the conformational stability of peptidomimetic macrocyclic cyclophanes. *J. Org. Chem.* 71 (6): 2242–2250.

**66** Welch, C.J., Biba, M., Pye, P. et al. (2008). Serendipitous discovery of a pH-dependant atropisomer bond rotation: toward a write-protectable chiral molecular switch? *J. Chromatogr. B* 875 (1): 118–121.

**67** Dial, B.E., Rasberry, R.D., Bullock, B.N. et al. (2011). Guest-accelerated molecular rotor. *Org. Lett.* 13 (2): 244–247.

**68** Dial, B.E., Pellechia, P.J., Smith, M.D., and Shimizu, K.D. (2012). Proton grease: an acid accelerated molecular rotor. *J. Am. Chem. Soc.* 134 (8): 3675–3678.

**69** Renzi, P., Hioe, J., and Gschwind, R.M. (2017). Decrypting transition states by light: photoisomerization as a mechanistic tool in brønsted acid catalysis. *J. Am. Chem. Soc.* 139 (19): 6752–6760.

**70** Georgiev, A., Yordanov, D., Dimov, D. et al. (2020). Azomethine phthalimides fluorescent E→Z photoswitches. *J. Photochem. Photobiol., A* 393: 112443.

**71** Kawatsuki, N., Matsushita, H., Kondo, M. et al. (2013). Photoinduced reorientation and polarization holography in a new photopolymer with 4-methoxy-*N*-benzylideneaniline side groups. *APL Mater.* 1 (2): 22103.

**72** Kawatsuki, N., Matsushita, H., Washio, T. et al. (2014). Photoinduced orientation of photoresponsive polymers with N-benzylideneaniline derivative side groups. *Macromolecules* 47 (1): 324–332.

**73** Greb, L., Mutlu, H., Barner-Kowollik, C., and Lehn, J.-M. (2016). Photo- and metallo-responsive *N*-alkyl α-bisimines as orthogonally addressable main-chain functional groups in metathesis polymers. *J. Am. Chem. Soc.* 138 (4): 1142–1145.

**74** Hammerich, M., Rusch, T., Krekiehn, N.R. et al. (2016). Imine-functionalized triazatriangulenium platforms: towards an artificial ciliated epithelium. *ChemPhysChem* 17 (12): 1870–1874.

**75** Lehn, J.-M. (2006). Conjecture: imines as unidirectional photodriven molecular motors—motional and constitutional dynamic devices. *Chem. Eur. J.* 12 (23): 5910–5915.

**76** Greb, L. and Lehn, J.-M. (2014). Light-driven molecular motors: imines as four-step or two-step unidirectional rotors. *J. Am. Chem. Soc.* 136 (38): 13114–13117.

**77** Koumura, N., Zijistra, R.W.J., Van Delden, R.A. et al. (1999). Light-driven monodirectional molecular rotor. *Nature* 401 (6749): 152–155.

**78** Li, Y., Wang, W., and Liu, F. (2019). Exploring the mechanism of a chiral *N*-alkyl imine-based light-driven molecular rotary motor at MS-CASPT2//CASSCF and MS-CASPT2//(TD) DFT levels. *Chem. Eur. J.* 25 (16): 4194–4201.


**79** Greb, L., Eichhofer, A., and Lehn, J.M. (2015). Synthetic molecular motors: thermal N inversion and directional photoinduced C=N bond rotation of camphorquinone imines. *Angew. Chem. Int. Ed.* 54 (48): 14345–14348.

**80** Pollok, C.H., Riesebeck, T., and Merten, C. (2017). Photoisomerization of a chiral imine molecular switch followed by matrix-isolation VCD spectroscopy. *Angew. Chem. Int. Ed.* 56 (7): 1925–1928.

**81** Su, Q., Li, Y., Wang, B. et al. (2017). Combining the advantages of alkene and azo E–Z photoisomerizations: mechanistic insights into ketoimine photoswitches. *J. Phys. Chem. A* 121 (13): 2588–2596.

**82** Chaur, M.N., Collado, D., and Lehn, J.-M. (2011). Configurational and constitutional information storage: multiple dynamics in systems based on pyridyl and acyl hydrazones. *Chem. Eur. J.* 17 (1): 248–258.

**83** Lehn, J.M. (2002). Toward complex matter: supramolecular chemistry and self-organization. *Proc. Natl. Acad. Sci. U.S.A.* 99 (8): 4763–4768.

**84** Cousins, G.R.L., Poulsen, S.A., and Sanders, J.K.M. (2000). Molecular evolution: dynamic combinatorial libraries, autocatalytic networks and the quest for molecular function. *Curr. Opin. Chem. Biol.* 4 (3): 270–279.

**85** Lehn, J.M. (2012). Constitutional dynamic chemistry: bridge from supramolecular chemistry to adaptive chemistry. *Top. Curr. Chem.* 322: 1–32.

**86** Giuseppone, N., Schmitt, J.L., Schwartz, E., and Lehn, J.M. (2005). Scandium(III) catalysis of transimination reactions. Independent and constitutionally coupled reversible processes. *J. Am. Chem. Soc.* 127 (15): 5528–5539.

**87** Giuseppone, N. and Lehn, J.-M. (2006). Protonic and temperature modulation of constituent expression by component selection in a dynamic combinatorial library of imines. *Chem. Eur. J.* 12 (6): 1715–1722.

**88** Ciaccia, M., Cacciapaglia, R., Mencarelli, P. et al. (2013). Fast transimination in organic solvents in the absence of proton and metal catalysts. A key to imine metathesis catalyzed by primary amines under mild conditions. *Chem. Sci.* 4 (5): 2253–2261.

**89** Nguyen, R. (2003). Optimizing the reversibility of hydrazone formation for dynamic combinatorial chemistry. *Chem. Commun.* 8 (8): 942–943.

**90** Yuen, L.H., Saxena, N.S., Park, H.S. et al. (2016). Dark hydrazone fluorescence labeling agents enable imaging of cellular aldehydic load. *ACS Chem. Biol.* 11 (8): 2312–2319.

**91** Ingerman, L.A. and Waters, M.L. (2009). Photoswitchable dynamic combinatorial libraries: coupling azobenzene photoisomerization with hydrazone exchange. *J. Org. Chem.* 74 (1): 111–117.

**92** Klein, J.M., Saggiomo, V., Reck, L. et al. (2012). Dynamic combinatorial libraries for the recognition of heavy metal ions. *Org. Biomol. Chem.* 10 (1): 60–66.

**93** Bhat, V.T., Caniard, A.M., Luksch, T. et al. (2010). Nucleophilic catalysis of acylhydrazone equilibration for protein-directed dynamic covalent chemistry. *Nat. Chem.* 2 (6): 490–497.

**94** Higgs, P.L., Ruiz-Sanchez, A.J., Dalmina, M. et al. (2019). Enhancing the kinetics of hydrazone exchange processes: an experimental and computational study. *Org. Biomol. Chem.* 17 (12): 3218–3224.

**95** Lions, F. and Martin, K.V. (1958). Sexadentate chelate compounds. X. *J. Am. Chem. Soc.* 80 (15): 3858–3865.

**96** Lions, F., Dance, I.G., and Lewis, J. (1967). Mono-chelate complexes of pyridine-2-aldehyde 2′-pyridylhydrazone. *J. Chem. Soc. A Inorg. Phys. Theor. Chem.* 0 (0): 565–572.

**97** Bell, C.F., Mortimore, G.R., and Reed, G.L. (1976). The 1H NMR spectra of zinc complexes of pyridine-2-carbaldehyde 2′-pyridylhydrazone. *Org. Magn. Reson.* 8 (1): 45–48.

**98** Ainscough, E.W., Brodie, A.M., Ingham, S.L., and Waters, J.M. (1996). Synthesis and structural characterisation of a pair of linkage isomers of copper(I) pyridine-2-carbaldehyde 2′-pyridylhydrazone complexes. *Inorg. Chim. Acta* 249 (1): 47–55.

**99** Stadler, A.M. and Harrowfield, J. (2009). Bis-acyl-/aroyl-hydrazones as multidentate ligands. *Inorg. Chim. Acta* 362 (12): 4298–4314.

**100** Van Dijken, D.J., Kovaříček, P., Ihrig, S.P., and Hecht, S. (2015). Acylhydrazones as widely tunable photoswitches. *J. Am. Chem. Soc.* 137 (47): 14982–14991.

**101** Courtot, P., Pichon, R., and Le Saint, J. (1976). Photochromisme par isomerisation syn-anti de phenylhydrazones-2- de tricetones-1,2,3 et de dicetones-1,2 substituees. *Tetrahedron Lett.* 17 (15): 1181–1184.

**102** Pichon, R., Le Saint, J., and Courtot, P. (1981). Photoisomerisation d′arylhydrazones-2 de dicetones-1,2 substituees en 2. Mecanisme d′isomerisation thermique de la double liaison CN. *Tetrahedron* 37 (8): 1517–1524.

**103** Wong, J.L. and Zady, M.F. (1975). Photochromism of quinolylhydrazones. III. The mechanism of isomerization of the photocolored α-quinolylimino-(Z)-hydrazone to the α-quinolylamino-(E)-hydrazone. *J. Org. Chem.* 40 (17): 2512–2516.

**104** Syakaev, V.V., Podyachev, S.N., Buzykin, B.I. et al. (2006). NMR study of conformation and isomerization of aryl- and heteroarylaldehyde 4-tert-butylphenoxyacetylhydrazones. *J. Mol. Struct.* 788 (1–3): 55–62.

**105** Ratjen, L. and Lehn, J.M. (2014). Reversible photo-, metallo- and thermo-induced morphological dynamics of bis-acylhydrazones. *RSC Adv.* 4 (92): 50554–50557.

**106** Gordillo, M.A., Soto-Monsalve, M., Carmona-Vargas, C.C. et al. (2017). Photochemical and electrochemical triggered bis(hydrazone) switch. *Chem. Eur. J.* 23 (59): 14872–14882.

**107** Ray, D., Foy, J.T., Hughes, R.P., and Aprahamian, I. (2012). A switching cascade of hydrazone-based rotary switches through coordination-coupled proton relays. *Nat. Chem.* 4 (9): 757–762.

**108** Foy, J.T., Ray, D., and Aprahamian, I. (2015). Regulating signal enhancement with coordination-coupled deprotonation of a hydrazone switch. *Chem. Sci.* 6 (1): 209–213.


**109** Shao, B. and Aprahamian, I. (2019). Induced fluorescence and thermal relaxation rate modulation in a hydrazone photoswitch. *ChemPhotoChem* 3 (6): 361–364.

**110** Hall, K.C., Franks, A.T., McAtee, R.C. et al. (2017). Metal-binding hydrazone photoswitches for visible light reactivity and variable relaxation kinetics. *Photochem. Photobiol. Sci.* 16 (11): 1604–1612.

**111** Coman, A.G., Paun, A., Popescu, C.C. et al. (2018). Conformation-induced light emission switching of: N -acylhydrazone systems. *New J. Chem.* 42 (17): 14111–14119.

**112** Franks, A.T., Peng, D., Yang, W., and Franz, K.J. (2014). Characterization of a photoswitching chelator with light-modulated geometric, electronic, and metal-binding properties. *Inorg. Chem.* 53 (3): 1397–1405.

**113** Goulet-Hanssens, A., Eisenreich, F., and Hecht, S. (2020). Enlightening materials with photoswitches. *Adv. Mater.*: 32:1905966.

**114** Vantomme, G. and Lehn, J.-M. (2013). Photo- and thermoresponsive supramolecular assemblies: reversible photorelease of $K^+$ ions and constitutional dynamics. *Angew. Chem. Int. Ed.* 52 (14): 3940–3943.

**115** Vantomme, G., Gelebart, A.H., Broer, D.J., and Meijer, E.W. (2017). A four-blade light-driven plastic mill based on hydrazone liquid-crystal networks. *Tetrahedron* 73 (33): 4963–4967.

**116** Weyandt, E., ter Huurne, G.M., Vantomme, G. et al. (2020). Photodynamic control of the chain length in supramolecular polymers: switching an intercalator into a chain capper. *J. Am. Chem. Soc.* 142 (13): 6295–6303.

**117** Holub, J., Vantomme, G., and Lehn, J.M. (2016). Training a constitutional dynamic network for effector recognition: storage, recall, and erasing of information. *J. Am. Chem. Soc.* 138 (36): 11783–11791.

**118** Ulrich, S. and Lehn, J.M. (2009). Adaptation to shape switching by component selection in a constitutional dynamic system. *J. Am. Chem. Soc.* 131 (15): 5546–5559.

**119** Vantomme, G., Hafezi, N., and Lehn, J.M. (2014). A light-induced reversible phase separation and its coupling to a dynamic library of imines. *Chem. Sci.* 5 (4): 1475–1483.

**120** Kokan, Z. and Chmielewski, M.J. (2018). A photoswitchable heteroditopic ion-pair receptor. *J. Am. Chem. Soc.* 140 (47): 16010–16014.

**121** De Bo, G., Leigh, D.A., McTernan, C.T., and Wang, S. (2017). A complementary pair of enantioselective switchable organocatalysts. *Chem. Sci.* 8 (10): 7077–7081.

**122** Beswick, J., Blanco, V., De Bo, G. et al. (2015). Selecting reactions and reactants using a switchable rotaxane organocatalyst with two different active sites. *Chem. Sci.* 6 (1): 140–143.

**123** Kassem, S., Van Leeuwen, T., Lubbe, A.S. et al. (2017). Artificial molecular motors. *Chem. Soc. Rev.* 46 (9): 2592–2621.

**124** Aprahamian, I. (2020). The future of molecular machines. *ACS Cent. Sci.* 6 (3): 347–358.

**125** Heard, A.W. and Goldup, S.M. (2020). Simplicity in the design, operation, and applications of mechanically interlocked molecular machines. *ACS Cent. Sci.* 6 (2): 117–128.

**126** Leigh, D.A., Marcos, V., Nalbantoglu, T. et al. (2017). Pyridyl-acyl hydrazone rotaxanes and molecular shuttles. *J. Am. Chem. Soc.* 139 (20): 7104–7109.

**127** Lehn, J.-M. (2015). Perspectives in chemistry-aspects of adaptive chemistry and materials. *Angew. Chem. Int. Ed.* 54 (11): 3276–3289.

**128** Vantomme, G. and Lehn, J.-M. (2014). Reversible adaptation to photoinduced shape switching by oligomer-macrocycle interconversion with component selection in a three-state constitutional dynamic system. *Chem. Eur. J.* 20 (49): 16188–16193.

**129** Vantomme, G., Jiang, S., and Lehn, J.M. (2014). Adaptation in constitutional dynamic libraries and networks, switching between orthogonal metalloselection and photoselection processes. *J. Am. Chem. Soc.* 136 (26): 9509–9518.

**130** Ulrich, S. and Lehn, J.-M. (2008). Reversible switching between macrocyclic and polymeric states by morphological control in a constitutional dynamic system. *Angew. Chem. Int. Ed.* 47 (12): 2240–2243.

**131** Ulrich, S., Buhler, E., and Lehn, J.M. (2009). Reversible constitutional switching between macrocycles and polymers induced by shape change in a dynamic covalent system. *New J. Chem.* 33 (2): 271–292.

**132** Cvrtila, I., Fanlo-Virgós, H., Schaeffer, G. et al. (2017). Redox control over acyl hydrazone photoswitches. *J. Am. Chem. Soc.* 139 (36): 12459–12465.

**133** Grzybowski, B.A. and Huck, W.T.S. (2016). The nanotechnology of life-inspired systems. *Nat. Nanotechnol.* 11 (7): 585–592.

**134** Merindol, R. and Walther, A. (2017). Materials learning from life: concepts for active, adaptive and autonomous molecular systems. *Chem. Soc. Rev.* 46 (18): 5588–5619.

**135** Ashkenasy, G., Hermans, T.M., Otto, S., and Taylor, A.F. (2017). Systems chemistry. *Chem. Soc. Rev.* 46 (9): 2543–2554.

**136** Men, G. and Lehn, J.M. (2017). Higher order constitutional dynamic networks: [2×3] and [3×3] networks displaying multiple, synergistic and competitive hierarchical adaptation. *J. Am. Chem. Soc.* 139 (6): 2474–2483.

**137** Men, G. and Lehn, J.M. (2019). Multiple adaptation of constitutional dynamic networks and information storage in constitutional distributions of acylhydrazones. *Chem. Sci.* 10 (1): 90–98.

**138** He, M. and Lehn, J.M. (2019). Time-dependent switching of constitutional dynamic libraries and networks from kinetic to thermodynamic distributions. *J. Am. Chem. Soc.* 141 (46): 18560–18569.

**139** Herder, M. and Lehn, J.M. (2018). The photodynamic bond: sensitized alkoxyamines as a tool to shift reaction networks out-of-equilibrium using light energy. *J. Am. Chem. Soc.* 140: 7647–7657.

# 16 Norbornadiene/Quadricyclane (NBD/QC) and Conversion of Solar Energy

Jessica Orrego-Hernández, Helen Hölzel, Zhihang Wang, Maria Quant, and Kasper Moth-Poulsen

**Photochromism**

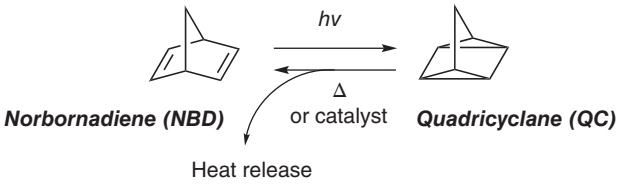


**Characteristic Features**

High energy storage density, long energy storage periods (months or years), application as MOST system

**Synthetic Methods**

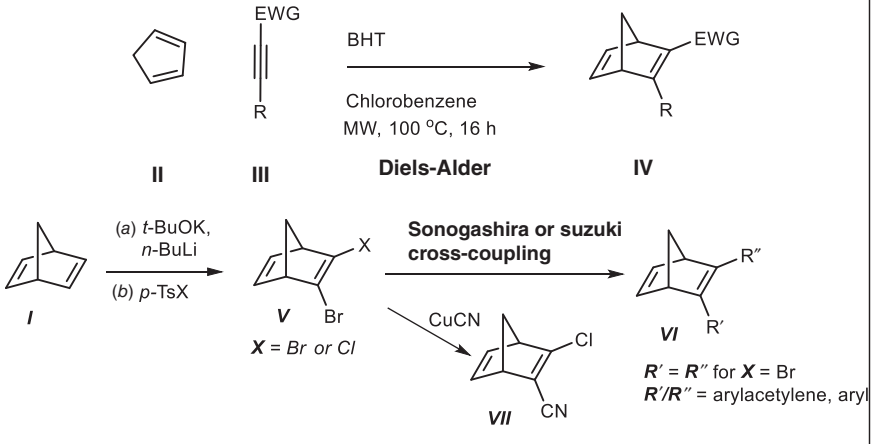


**First reported synthesis (NBD)**

Hyman, I. (1951). *BE 498176*.

**Key References**

Orrego-Hernández, J., Dreos, A., and Moth-Poulsen, K. (2020). Engineering of norbornadiene-quadricyclane photoswitches for molecular solar thermal energy storage applications. *Acc. Chem. Res.* 53: 1478–1487.

Wang, Z., Roffey, A., Losantos, R., et al. (2019). Macroscopic heat release in a molecular solar thermal energy storage system. *Energy Environ. Sci.* 12: 187–193.

# 16

# Norbornadiene/Quadricyclane (NBD/QC) and Conversion of Solar Energy

*Jessica Orrego-Hernández, Helen Hölzel, Zhihang Wang, Maria Quant, and Kasper Moth-Poulsen*

*Chalmers University of Technology, Department of Chemistry and Chemical Engineering, 41286 Gothenburg, Sweden*

## 16.1 Introduction

Bicyclo[2.2.1]hepta-2,5-diene, also known as norbornadiene **1** (NBD), is a bicyclic ring system containing two double bonds (Scheme 16.1). The name norbornadiene comes from the island Borneo since it shares a common core structure with the natural product borneol found in trees (*Dryobalanops camphora*) [1]. However, NBD is not a natural product, and it was first synthesized in the 1950s by condensation of cyclopentadiene with acetylene under pressure [2].

The photoisomer of NBD, quadricyclane **2** (QC), is a highly strained and metastable molecule meaning that the conversion from NBD to QC has a high capacity of storing energy ($\Delta H = 89$ kJ mol$^{-1}$) [3]. QC can be obtained by irradiating NBD with an appropriate light source. The light may induce a [2+2] cycloaddition reaction, breaking the two $\pi$-bonds of NBD **1** and forming two new $\sigma$ carbon-carbon bonds to obtain QC **2**. This reaction is reversible, and by applying heat or a catalyst, QC **2** can convert back to NBD **1**, releasing energy as heat [4]. Unsubstituted QC **2** can be obtained by irradiation of NBD **1** [5] or by the use of photosensitizers [6], e.g. benzophenones [7] or acetophenone [8], and photocatalysts [9–11].

The unsubstituted NBD/QC couple is featured by a low quantum yield of photoisomerization ($\Phi = 0.05$), an onset of absorption ($\lambda_{onset}$) around 300 nm, and a thermally stable QC form ($t_{1/2} = 14$ h at 140 °C) [3]. Modifications to the system via substitution have been shown to have pronounced effects on the absorption of the light that triggers the conversion, the half-life ($t_{1/2}$) of quadricyclane, and the quantum yield of the photoisomerization reaction ($\Phi$). Interestingly, the external environment also has a high impact on the NBD/QC system. The polarity of the solvent has a significant effect on the absorption of some NBD systems ($\lambda_{max}$), the quantum yield of the reaction ($\Phi$), and the half-life ($t_{1/2}$) of quadricyclanes [12]. As solvent polarity increases, the light absorption of NBD derivatives is red-shifted, while the quantum

*Molecular Photoswitches: Chemistry, Properties, and Applications*,
First Edition. Edited by Zbigniew L. Pianowski.


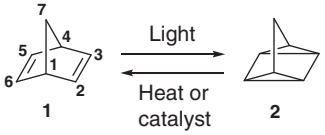


**Scheme 16.1** Norbornadiene **1** and its light-induced photoisomerization to quadricyclane **2** along with the back-conversion reaction.

yield of NBD to QC reaction is drastically diminished. Also, the half-life of QC is significantly reduced in non-polar solvents [12].

The NBD/QC system is widely studied in many different applications such as molecular solar thermal-energy storage (MOST) [13, 14], molecular logic [15, 16], optical devices [17–20], and molecular electronics [21–23]. The molecular features of the NBD/QC system in different applications can be tuned by structural functionalization of NBD [3, 14], by incorporating this photoswitch into materials such as polymers [17, 24] and fullerenes [25, 26], or by complexing with metal ions [27, 28]. MOST is the application that has been studied more intensively in recent years, motivated by a desire to create emission-free energy-storage systems. Due to the broad and high impact of NBD/QC systems in the conversion of solar energy, a major part of this chapter will involve MOST. This book chapter will divide into five main sections: (i) general synthesis of different NBD systems, (ii) molecular engineering of NBD photoswitches and their contribution in MOST applications, (iii) hybrid photoswitches based on NBD, (iv) development of devices, and finally (v) the use of NBD in other applications.

## 16.2 Synthesis

### 16.2.1 Norbornadiene (NBD)

A convenient way for synthesizing NBDs is a one-step Diels–Alder reaction between acetylene and cyclopentadiene. In many cases, this reaction can be scaled-up and carried out without a solvent, which is also beneficial from environmental aspects. By introducing electron-withdrawing substituents on the alkyne substrates, NBD derivatives can be obtained with high yields. An example of an NBD synthesis through the Diels–Alder reaction is illustrated in Scheme 16.2, where 2-cyano-3-(4-nitrophenyl)norbornadiene **5** is formed by reacting cyclopentadiene **3** with 3-(4-nitrophenyl)propiolonitrile **4** [29]. Historically, the Diels–Alder

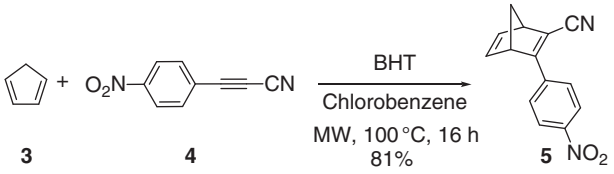


**Scheme 16.2** Synthesis of NBD **5** through the Diels–Alder reaction. Source: Modified from Jevric et al. [29].

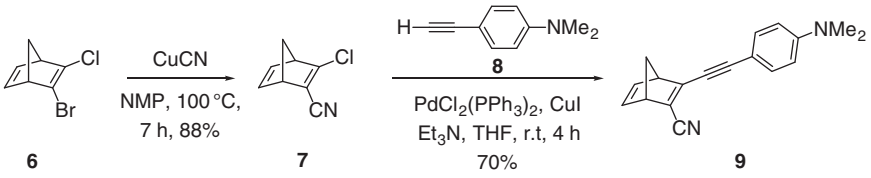


**Scheme 16.3** Stepwise synthesis of NBD **9** starting with the formation of intermediate **7** assisted by CuCN followed by a Sonogashira cross-coupling catalyzed by palladium complex catalyst. Source: Modified from Quant et al. [30].

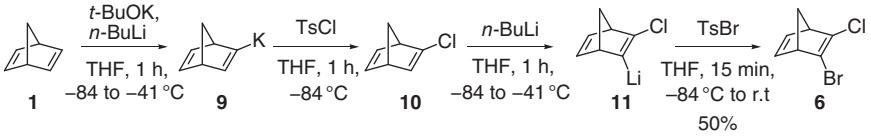


**Scheme 16.4** One-pot synthesis of 2-bromo-3-chloronorbornadiene **6**. Source: Modified from Lennartson et al. [31].

reaction has been the most common way to obtain NBDs. However, the reaction scope is limited since it typically requires electron-deficient alkynes or electron-rich cyclopentadienes.

Consequently, other synthetic methods have been developed, and an alternative is using a halogenated NBD, such as 2-bromo-3-chloronorbornadiene (**6**). This halogenated compound can be functionalized with different substituents via catalytic cross-coupling reactions. An example is illustrated in scheme 16.3, where after copper cyanide (CuCN) addition, a nitrile group substitutes a bromide group in the NBD **6** to afford the intermediate **7**. Then, a second substituent is introduced via Sonogashira cross-coupling reaction with a palladium complex catalyst between phenylacetylene derivative **8** with NBD **7** to get 2-cyano-3-((4(dimethylamino) phenyl)ethynyl)norbornadiene **9** [30].

The dihalogenated NBD **6** can be synthesized in a one-pot procedure using *p*-toluenesulfonyl bromide (TsBr) and *p*-toluenesulfonyl chloride (TsCl) (Scheme 16.4) [31]. The reaction starts with deprotonation of NBD using a mixture of potassium *tert*-butoxide (*t*-BuOK) and *n*-butyllithium (*n*-BuLi). After that, TsCl is added to introduce the first halogen. Further deprotonation is carried out using *n*-BuLi followed by the addition of TsBr to afford the desired product 2-bromo-3-chloronorbornadiene **6** with a yield of 50% after purification by distillation [31].

Several successful examples using cross-coupling reactions have been carried out to get substituted NBDs that were not accessible through the Diels–Alder reaction. The approach mentioned above represents a good alternative, however, requires expensive noble metals such as palladium. Although metals are used in catalytic amounts, scaling up the synthesis of NBDs can increase costs and be more tedious than the Diels–Alder reaction. Additionally, since halogenated NBDs are required as starting material in cross-coupling reactions, the synthesis of halogenated compounds like NBD **6** needs to be optimized.

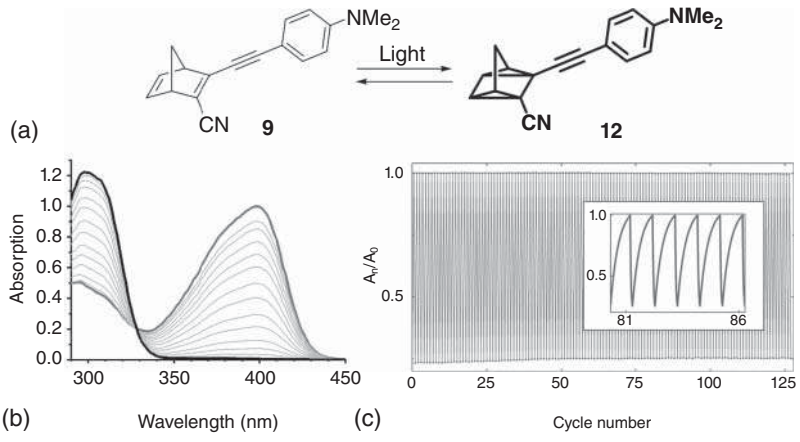


**Figure 16.1** (a) The photoisomerization reaction of a norbornadiene **9** toward a quadricyclane **12** monitored by UV/vis. (b) The gray and black lines represent the absorption of NBD **9** and QC **12**, respectively. (c) Cyclability test of NBD/QC system, photoconversion followed by thermal back reaction at 60 °C for 127 cycles [30]. Source: (b) Quant et al. [30]. (c) Source: Dreos et al. [32]. Licensed under CC BY-3.0

### 16.2.2 Quadricyclane (QC)

As described in the introduction, quadricyclanes can be synthesized by exposing NBD to light (Scheme 16.1). The reaction can be monitored by UV/Vis spectroscopy, e.g. Figure 16.1 illustrates the conversion of NBD **9** toward the corresponding QC **12**. The gray and black lines represent the absorption spectra of **9** and **12**, respectively [30]. As seen in Figure 16.1, a typical feature of the NBD/QC systems is that the absorption spectrum of the NBD derivative is red-shifted, resulting from the conjugation through the double bonds, compared to the QC isomer, in which the conjugation is broken. Also, the photoisomerization and the conversion back reaction of the NBD/QC system operate with high cyclability.

## 16.3 Molecular Engineering of the Norbornadiene/Quadricyclane Photoswitch Toward MOST Application

MOST has been studied using different photoswitches. These molecules can be either in liquid or solid form, depending on the application. For example, for possible future bulk heating applications, a fluid MOST system that can dissolve in water or non-toxic solvents may be attractive. In other applications, a solid MOST system may be coated onto or integrated into windows or fabrics for heating purposes. For MOST use, the NBD/QC photoswitch is one of the most promising systems, and their molecular properties have extensively been investigated in recent decades. The molecular photoswitch needs to fulfill a number of molecular requirements to be a functional system in MOST application (Figure 16.2) [3, 13, 33, 34]:

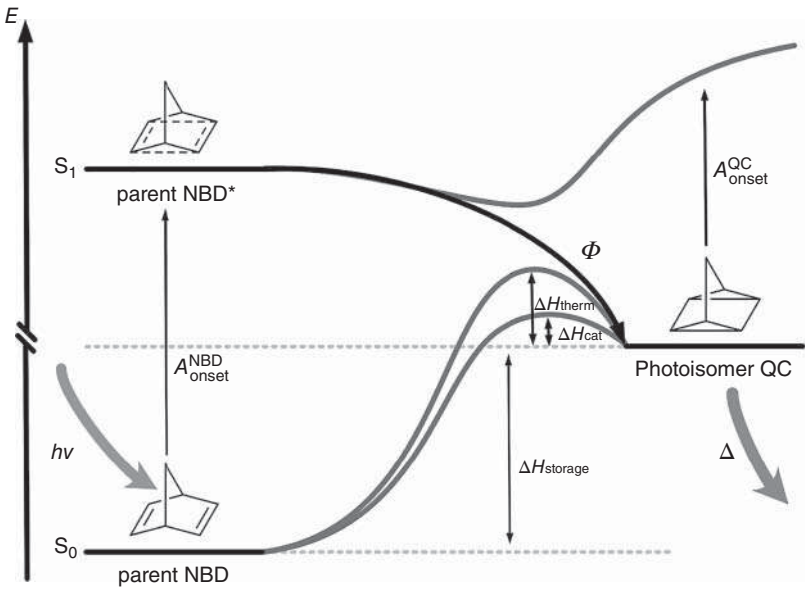


**Figure 16.2** Energy diagram for the conversion of NBD to QC and the respective back reaction. The parent NBD can firstly absorb light to an excited state of NBD*, then photoisomerizes to QC (high-energy metastable intermediate) with a photoisomerization quantum yield $\Phi$. The $\Delta H_{thermal}$ and $\Delta H_{cat}$ are the back-conversion barriers with thermal and catalytic methods, respectively. The enthalpy difference between parent and photoisomer is noted with $\Delta H_{storage}$ in the figure.

(i) The absorption ($A_{onset}$) of the NBD systems should overlap efficiently with the solar spectrum between 300 and 800 nm to cover the visible light range. According to the air mass solar irradiation spectrum (AM 1.5), more than 50% of the oncoming photons need to be located in the aforementioned range. At the same time, the cross-section of QC in the absorption profile ($A_{onset}$) should have minimal overlap with the NBD absorption profile. This condition reduces competition for photons between NBD and the metastable QC photoisomer. In case the absorption profile of NBD does not fit well with the required spectral range, a photosensitizer can be used for enhanced conversion to QC. Herein it should be considered that QC is not quenching the photosensitizer.

(ii) The photoisomer QC should have a high-energy difference to the parent NBD molecule and a long enough half-life ($t_{1/2}$) at ambient conditions to ensure an application-relevant storage period. Further for efficient solar charging, the photoisomerization quantum yield ($\Phi_{iso}$) should be close to 1.

(iii) Previous literature notes that the energy difference for MOST systems should be at least higher than the heat-storage capacity of salt hydrates ($\Delta H_{storage} > 0.25\ MJ\ g^{-1}$). Thus, molecular weight should be kept relatively low to ensure a high-energy density of the photoisomerization pair.

(iv) For a liquid MOST system, in which the molecules are once charged, the normal thermal dynamic back conversion is usually not convenient to release the stored heat on demand. Thus, a heterogeneous catalyst is necessary to ensure a fast energy-release process. For an optimal operation, the catalyst should operate without any depletion.
(v) As a new type of solar battery, the MOST system should operate for an infinite or large number of cycles over the charging and discarding process.
(vi) The synthesis of an ideal MOST system should be easy and cheap, even on an industrial scale. For sustainability concerns, such a system should be ideally environmentally non-toxic with additional straightforward recovery.

### 16.3.1 Molecular Engineering Strategies for Optimization of MOST Properties in NBD/QC Systems

Several attempts have been made to investigate and develop the NBD/QC pair as an efficient MOST system throughout the years. Three different approaches were generally considered to achieve this goal (Figure 16.3) [14]. First, via the introduction of four substituents (in positions 2, 3, 5, and 6) to the parent molecular NBD unit, where donor and acceptor moieties should interact through space with each other (so-called homoconjugation). Consequently, using this approach, the absorption profile is red-shifted and matches better to the solar spectrum [33, 35, 36]. Nevertheless, it comes with increased molecular weight and reduced energy density, and usually also reduced energy-storage time [3, 14]. A second approach is to extend the π-conjugation, mainly with electron-donating and -withdrawing groups on a single double bond (2 and 3 positions) to generate a push–pull system. Herein, the reduction in energy density is less pronounced, whereas energy-storage times typically are reduced and generally also comes along with reduced quantum yields [3, 29, 30, 37–45]. The third and more recent approach is to generate NBD dimers or even multiple NBD systems. This strategy allows the possibility of engineering the stability of the photoisomer by introducing in one molecule two or more photoswitches moieties with independent thermal-energy conversion barriers resulting in higher-energy heat release and different discharge times [44, 46–48].

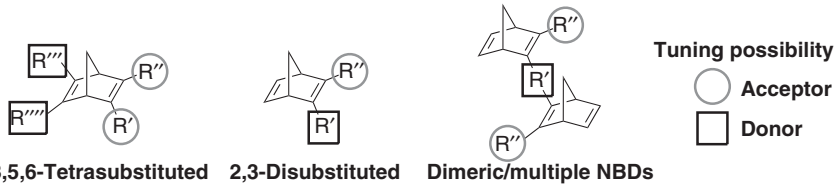


**Figure 16.3** Depiction of three different approaches for optimizing the NBD/QC couple for MOST applications. Source: Orrego-Hernández et al. [14]. Licensed under CC BY-4.0.

### 16.3.2 2,3,5,6-Tetrasubstituted NBDs (Donor–Acceptor Systems – Through-Space)

One of the first attempts to modify the parent system efficiently was to synthesize tetrasubstituted NBDs with the main introduction of donor and acceptor groups (so-called donor–acceptor systems) for developing a through-space interaction. In this context, in 1985, the synthesis and investigation of systems carrying two nitrile units on one of the NBD double bonds and methyl substituents on the other, which causes a new absorption band to arise at around 338 nm, were reported. Changing the methyl groups for two aryl substituents resulted in the best-performing system in this study: the *p*-methoxyphenyl derivative **13** with an absorption onset of 557 nm [33]. In 1999 and 2001, it was found that 2,3-di(trifluoromethyl)-5,6-diaryl-NBDs **14** shows an absorption onset up to 580 nm with the use of 4-$Me_2$NPh **15** and 2-benzofuryl substituents at positions 5 and 6, respectively [35]. The QC isomer's stability at room temperature could be increased by changing the substituents with the 4-MeOPh group **16**. Further, it was found that several numbers of charge–discharge cycles can be applied, but depending on the substituents, it comes along with gradual degradation [36]. Within the type of tetrasubstituted NBDs, the methyl ester derivative **17** substituted at position 7 (e.g. H, Me, or *i*Pr) presented slightly red-shifted absorption onset, higher quantum yield, and longer half-life when the substituent was bulkier (Figure 16.4) [49].

### 16.3.3 2,3-Substituted NBDs (Push–Pull Systems Through One Double Bond)

The approach of 2,3-substituted NBDs brought a plethora of different systems to life. In 1982, water-soluble systems with amide and carboxylic acid functionalities **18** were reported (Figure 16.5) that afford stable QC isomers. This photoisomer can quantitatively be converted back to the parent NBD **18** using cobalt hematoporphyrin as a catalyst at room temperature with heat release during the process [45].

Further, it was found that aroyl and aryl substituents at the 2 and 3-positions **19** gave conversion quantum yields of reaction in a range of 0.3–0.6. The

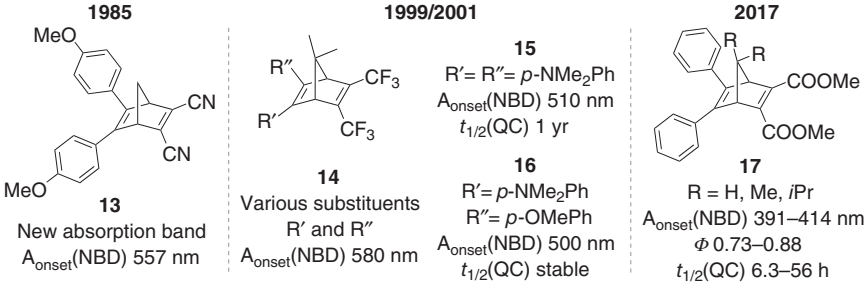


**Figure 16.4** Examples of NBD structure engineering in 2, 3, 5, and 6 positions and the systems' resulting features [33, 35, 36, 49]. Source: Modified from Jorner et al. [49].

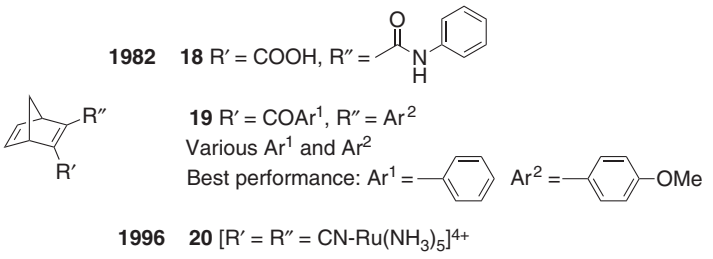


**Figure 16.5** Examples for early reported 2,3-substituted NBDs. Sources: Takashi et al.[37]; Kazuhiro et al.[45]; Lainé et al. [37, 45, 50].

**Figure 16.6** Differences between dicyanovinyl derivatives NBD **21-** and NBD **22-**substituted with a donor (*p*-phenylamine) group and an acceptor (*p*-nitrophenyl) group, respectively. Source: Dubonosov et al. [54].

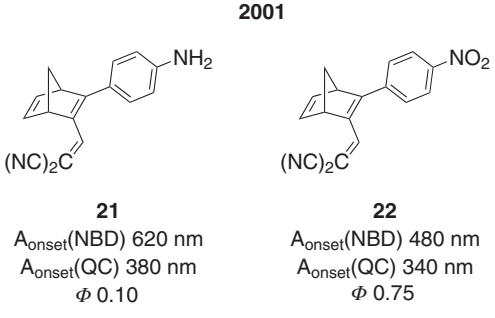


*p*-methoxyphenyl- and phenyl-substituted system with an absorption up to 400 nm afforded the highest quantum yield ($\Phi = 0.91$) from this library of compounds [37].

Other NBD derivatives were studied to evaluate the photoisomerization to QC in protic solvents using aryl and imine substituents [51] or the effect of cationic species that resulted in an absorption onset of 580 nm with degradation caused by small impurities of moisture [52]. Photoisomerization of NBD derivatives to QC was later reported for phenyl and different ester functionalities with quantum yields between 0.25 and 0.36 and absorption onsets between 340 and 355 nm [19, 36]. The highest absorption onset of 700 nm was achieved with a 2,3-dicyano-substituted bis-ruthenium complex **20**, where a low quantum yield was experimentally determined ($\Phi = 0.000\,83$ at 500 nm excitation wavelength) [50].

Several different functionalities have been studied during the last years [3, 29, 30, 38–44, 53]. Two interesting examples have been reported in 2001 [54]. The first one is the NBD derivative **21** substituted at 2,3-positions with phenylamine (donor) and dicyanovinyl (acceptor) groups (Figure 16.6). This compound showed a red-shifted absorption onset up to 620 nm, while the corresponding photoisomer QC derivative showed an absorption onset of 380 nm, thus leaving an excellent spectral window of 240 nm. NBD **21** has a relatively low quantum yield of only 0.10. The second example, NBD **22**, achieved the highest quantum yield in this study (0.75%) using an acceptor nitrophenyl group. NBD **22** had an absorption onset of up to 480 nm and the corresponding photoisomer QC has an absorption onset (340 nm) having a spectral window of 140 nm [54].

In 2014, 2,3-diaryl-substituted NBDs **23–25** with different donor and acceptor groups at the *p*-positions (push–pull systems) were synthesized. These substituents cause a significant bathochromic shift of the absorption onset up to 462 nm with varying half-life times and quantum yields (Table 16.1) [38]. Despite the redshift, absorptions were achieved with this approach, the molecular weight was increased, affecting the energy density of these systems.

For this reason, further investigations in 2016, in which the goal was to keep the molecular weight low featuring an electron-withdrawing moiety directly attached to a side of the double bond (position 2) and using acetylene-phenyl donor groups at 3-position, shows that it is possible to tune the desired variables. Within this series of molecules, the best results were obtained for a 2-phenyl-3-(*p*-$NMe_2$-)phenyl-ethynyl-substituted derivative **26** with an energy-storage density of 103 kJ $mol^{-1}$; however, this energy-density storage was still lower than the 2-cyano-3-phenyl-substituted NBD **27** (122 kJ $mol^{-1}$) [30].

Later, energy-storage density was increased up to 152 kJ $mol^{-1}$ by changing the cyano-substituent for a $COCF_3$ group in NBD **28**. This compound also kept the absorption onset (426 nm) and the quantum yield in the same range to **27**, but with a significant reduction of the half-life of the photoisomer QC (72 hours). A variation of this $COCF_3$ derivative with a methyl group in position 7, NBD **29**, was investigated, resulting in a good half-life and absorption onset, but at the same time, a decrease in energy-storage density was observed compared with the analog **28** [40].

The half-life time was drastically improved by introducing heterocycles (triazoles) and *p*-methoxyphenyl or phenyl substituents at the 2,3-positions [41]. Also, these compounds kept a broad spectral window between the onset absorption of NBD and QC isomer. However, parameters such as energy-storage density, quantum yield, and absorption were not significantly improved compared with analogs **26–29** [41]. Besides, the NBD **30** was initially a precursor in the synthetic pathway to affording the triazole-NBD systems. This derivative **30** with acetyl and *p*-methoxy-phenyl substituents performed quite well except for a low quantum yield ($\Phi = 0.28\%$) [41].

In 2018, it was investigated how rotational hindrance on the substituents of NBD/QC systems influences the back conversion of QC to NBD by preparation of a series of 2-cyano-3(*o*-functionalized)phenyl-NBD derivatives **31**. Also, a group of NBDs carrying asymmetric side groups (**32–33**) was synthesized. Herein, the so-called high-performers **31–33** outperformed the so far investigated systems in parameters such as half-life, quantum yields, absorption onset of NBD/QC system, and the spectral window between both isomers (Table 16.1) [29].

Nevertheless, the excellent performance was also obtained using the cyano and *p*-methoxyphenyl groups at the 2 and 3 positions (**34**) [39]. This molecule resulted in a high photoisomerization quantum yield, a long half-life, high solubility, and robustness in solution, important features for real MOST applications [42].

From the examples mentioned above, it was observed that NBDs with high conjugation through the double bond displayed a bathochromic shift with absorption up to 427 nm resulting in a shorter half-life (down to less than one minute). In contrast, modifications with bulkier groups in position 7, with, e.g. an acetyl (**35**) or ethylene

**Table 16.1** According to the substituents, recently studied NBD systems show different photophysical variables (onset of absorption, half-life, quantum yield, energy-storage density, and a spectral window between NBD and QC absorption) [29, 30, 38–41, 44].

| | | | | | $A_{onset}$ (NBD) (nm) | $t_{1/2}$ | $\Phi$ (%) | Energy Storage density (kJ mol$^{-1}$) | Spectral window (NBD-QC) (nm) |
|---|---|---|---|---|---|---|---|---|---|
| 2014  diaryl–approach | **23** | $Ar^1 = Ar^2 =$ 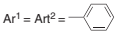 | | | 389 | 42.9 d | 60.2 | | |
| | **24** | $Ar^1 =$  OMe $Ar^2 =$  $CF_3$ | | | 414 | 2.9 d | 75.5 | | |
| | **25** | $Ar^1 =$  $NMe_2$ $Ar^2 =$  $CF_3$ | | | 462 | 1.9 h | 45.8 | | |
| 2016-2019 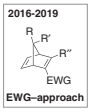 EWG–approach | **26** | EWG = CN | R = R′ = H | R″ = 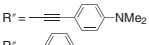 $NMe_2$ | 456 | 5.05 h | 28 | 103 | |
| | **27** | EWG = CN | R = R′ = H | R″ =  | 358 | 1320 h | 58 | 122 | |
| | **28** | EWG = $COCF_3$ | R = R′ = H | R″ =  | 426 | 72 h | 53 | 152 | |
| | **29** | EWG = $COCF_3$ | R = R′= $CH_3$ | R″ =  | 439 | 84 h | 55 | 49 | |
| | **30** | EWG = $COCH_3$ | R = R′ = H | R″ =  OMe | 412 | 524 d | 30 | 114 | **46** |
| | **31** | EWG = CN | R = R′ = H | R″ =  MeO OMe<br>R″ = 1-naphthyl<br>R″ = 2-naphthyl | 385 | 2971 d | 79 | | **79** |
| | **32** | EWG = CN | R = R′ = H | R″ = 1-naphthyl | 373 | 6729 d | 59 | | **48** |
| | **33** | EWG = CN | R = R′ = H | R″ = 2-naphthyl | 384 | 212 d | 60 | | **41** |
| | **34** | EWG = CN | R = R′ = H | R″ =  OMe | 380 | 30 d | 61 | 88 | **35** |
| | **35** | EWG = CN | R = H, R′ = $COCH_3$ | R″ =  OMe | **384** | **79 d** | **64** | | **55** |
| | **36** | EWG = $COCF_3$ | R = R′ = H | R″ =  OMe<br>R″ = 1-naphthyl | **475** | **6.6 h** | **68** | | **55** |
| | **37** | EWG = $COCF_3$ | R = R′ = H | R″ = 1-naphthyl | **439** | **10 mo** | **46** | | **98** |

Source: Based on Lennartson et al. [38].

glycol protecting group, gave longer half-life times and may be used for implementation into polymers [39].

The use of strong electron-withdrawing groups like $COCF_3$ afforded strong push–pull NBDs systems. Among these compounds, the NBD **36** (Table 16.1) leads to a redshift of the absorption profile, which comes along with shortened half-life times, resulting in possible day-to-day applications in MOST systems. Interestingly, using a bulky group like 1-naphthyl group in the NBD **37** increased the half-life up to 10 months and broadened the spectral window drastically to 98 nm with a low photoisomerization quantum yield ($\Phi = 0.46$) [44].

During the last years, very successful approaches have already been made to approach some of the requirements for suitable MOST systems by small variations of the NBD systems. Nevertheless, it is still a challenge to simultaneously fulfill all aspects since the parameters are correlated with each other. A deeper understanding of structure–property relationships is certainly needed to be able to derive more efficient molecular designs.

### 16.3.4 Dimeric and Multiple Norbornadienes Systems

Dimeric and multiple NBD systems have been designed to improve the energy density and half-life of the respective photosiomer QC. This strategy has the advantage of enhancing the stability of the photoisomer QC by the connection of two or more photoswitches with individual energy thermal barriers (Figure 16.7). Additionally, the absorption onset of the dimeric NBD–NBD system could have a bathochromic shift compared to the corresponding monomeric NBD and a broad spectral window

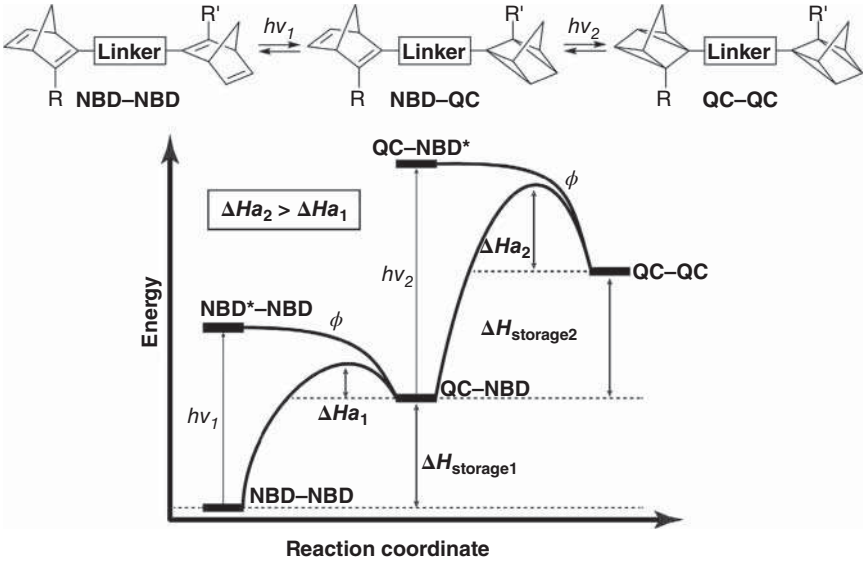


**Figure 16.7** Energy diagram for a dimeric NBD–NBD system and its different stages.

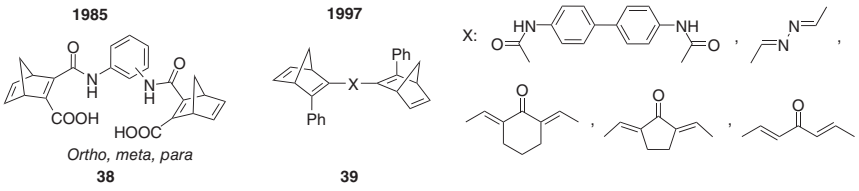


**Figure 16.8** Early examples for dimeric NBD systems with chromophoric linkers.

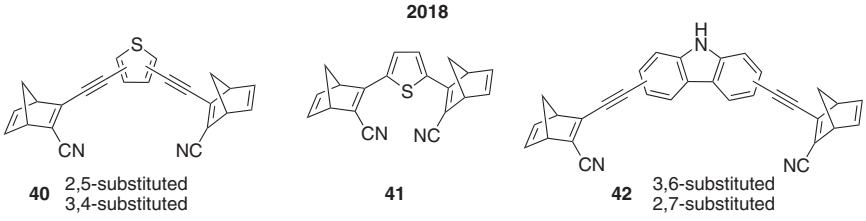


**Figure 16.9** Heterocycle-bridged NBD systems. Source: Mansø et al. [47].

with the corresponding photoisomer QC–QC. This section shows the design of different dimeric or multiple NBD systems using as strategy different linkers that tune the photophysical properties of these systems.

The first example of systems containing two NBD moieties in one molecule was reported in 1985. This dimeric system **38** has a phenylene-bis-carboxamide fragment as the connector between the two NBD units (Figure 16.8). The use of this chromophoric fragment favors a bathochromic shift ($\lambda$ = 316–460 nm at $\varepsilon$ = 35) but reduces the quantum yields ($\Phi$ = 0.004–0.09 at 360 nm excitation wavelength) and the energy stored due to the increased molecular weight [33]. The second generation of biphotochromic NBD **39** was reported in 1997, where π-conjugated molecules connect the NBD moieties (Figure 16.8). This approach also demonstrated good red-shift absorptions in the systems ($\lambda_{max}$ = 345–451 nm) with improved quantum yields ($\Phi$ = 0.011–0.029) [46]. These two examples have shown that dimeric NBDs linked with chromophoric linkers might harvest the solar spectrum in the MOST applications.

In 2019, dimeric NBD molecules **40–42** were synthesized using a heterocycle in the core like carbazole and thiophene linked by acetylene fragments (Figure 16.9). Similar to analogs **38** and **39**, the systems **40–42** show red-shifted absorption ($\lambda_{max}$ = 323–408 nm). Other properties like quantum yields ($\Phi$ = 0.44–0.70) and half-lives (from 43.8 seconds to 16.1 hours) have been improved compared to previous examples [47]. For MOST applications, these dimers are attractive in matching the solar spectrum and, in some examples, long storage time. Besides, the nature of the heterocycle tunes the optical absorption properties of the systems, opening opportunities in other applications such as photopharmacology [47].

Systems with two and three NBD moieties **43–44** were synthesized using phenylene and acetylene as a linker (Figure 16.10). Compared with previous analogs, the redshift in absorption was not significant ($\lambda_{max}$ = 308–362 nm) for these molecules due to the cross-conjugation and/or weaker donor character. Surprisingly, other

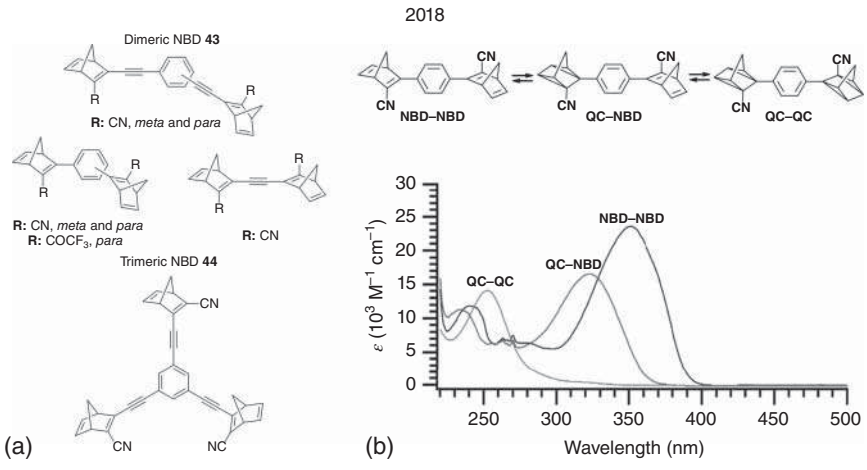


**Figure 16.10** (a) Examples for reported phenyl-spaced oligomeric NBD systems. (b) UV/vis spectra of dimeric an NBD–NBD system and the corresponding photoisomers [48]. Source: (c) Mansø et al. [48]. Licensed under CC BY-4.0.

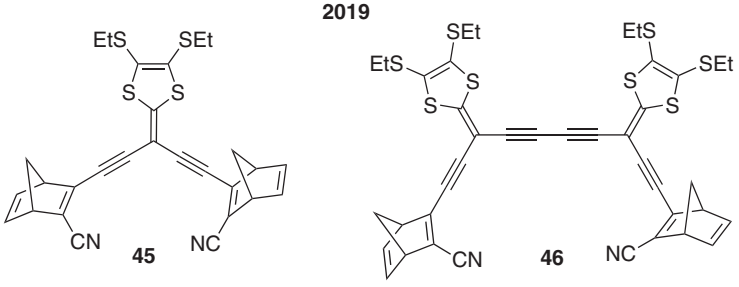


**Figure 16.11** Dithiafulvalene functionalized NBD structures. Source: Mansø et al. [55].

properties like quantum yields ($\Phi = 0.52–0.94$), half-life (for QC–QC from 4.3 hours to 48.5 days, and QC–NBD from 7.8 minutes to 2.1 days), and energy storage (from 98.7 to 172.5 kJ mol$^{-1}$) were significantly improved [44, 48]. Besides, the photoisomerization and conversion back reaction for these systems is a stepwise process with a robust synergistic stabilization in the QC–QC intermediate, prolonging the energy-storing time.

Dithiafulvene-functionalized NBDs **45–46** were designed (Figure 16.11), aiming for a synergistic effect of red-shift absorption of fulvalene with NBD photoswitching properties. These derivatives have shown a significantly red-shifted absorption ($\lambda_{max} = 387–475$ nm) compared to the parent molecules [55]. However, the dithiafulvene fragment affected the photoisomerization properties of the NBD moiety since this process was completely quenched [55].

## 16.4 Hybrid Photoswitch Systems Based on Norbornadiene

As mentioned in previous sections, dimeric or polymeric NBD systems presented improved energy densities, red-shifted absorption, and stepwise switching for MOST applications. Likewise, multimode switches have been designed to harvest broader range of UV-visible light. These hybrid MOST chromophore systems are created by the linkage of NBD and other photoswitches, such as 2-(*N*-Acyl-*N*-arylaminomethylidene)-1-benzothiophen-3(2*H*)-ones [46], dihydroazulene (DHA) [56], azo [54, 57], and diarylethene (DAE) [58].

The first example of an NBD hybrid photoswitch system was reported by using 2-(*N*-Acyl-*N*-arylaminomethylidene)-1-benzothiphen-3(2*H*)-ones as a second chromophore (Scheme 16.5) [46]. This second molecular switch has a Z/E-photoisomerization accompanied by thermal N → O acyl migration upon light irradiation, changing various physical properties like absorption [59]. The hybrid **47** was designed with three different substituents (4-MePh, 4-MeOPh, and 4-$NO_2$Ph), which *O*-acyl derivatives **48** are formed with a quantum yield of 0.05 ($\lambda_{exc} = 436$ nm) in isopropanol. The electron-donating-substituted NBD **48** undergoes a partial isomerization into quadricyclane derivative QC **49** at 365 nm. As an exception, the 4-$NO_2$Ph-substituted *O*-acyl isomer **48** is stable, and further photoisomerization is not observed. The back reactions to QC **49** to **47** were catalyzed with trifluoroacetic acid ($CF_3COOH$) at room temperature [46]. This NBD hybrid has independent absorption in each chromophoric unity. Hence, a stepwise photoswitch response undergoes first *Z*/*E*-isomerization accompanied by N → O acyl migration and, then, an isomerization to NBD to QC.

The NBD-DHA conjugate is the second hybrid example for multisystem photoswitches. This hybrid combines the traditional with negative photochromic functions and high-energy-storage capacities of these photoswitches (Figure 16.12). The NBD–DHA **50** system in Figure 16.12b was irradiated at 400 nm (absorption onset of DHA unit), having a total conversion of NBD–DHA **50** to NBD–vinylheptafulvene (VHF) **51** with an easy ring opening of the DHA scaffold. The irradiation at 330 nm of

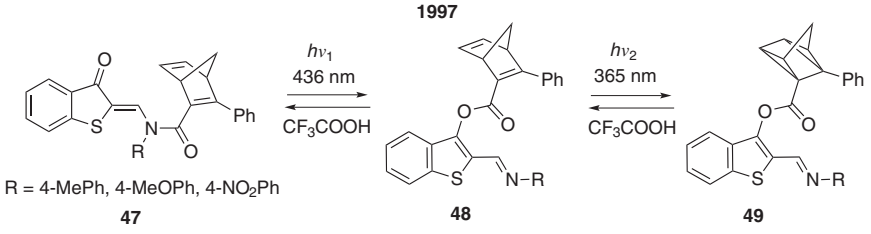


**Scheme 16.5** Switching modes of NBDs with 2-(*N*-Acyl-*N*-arylaminomethylidene)-1-benzothiphen-3(2*H*)-ones [46]. Source: Modified from Wang et al. [42].

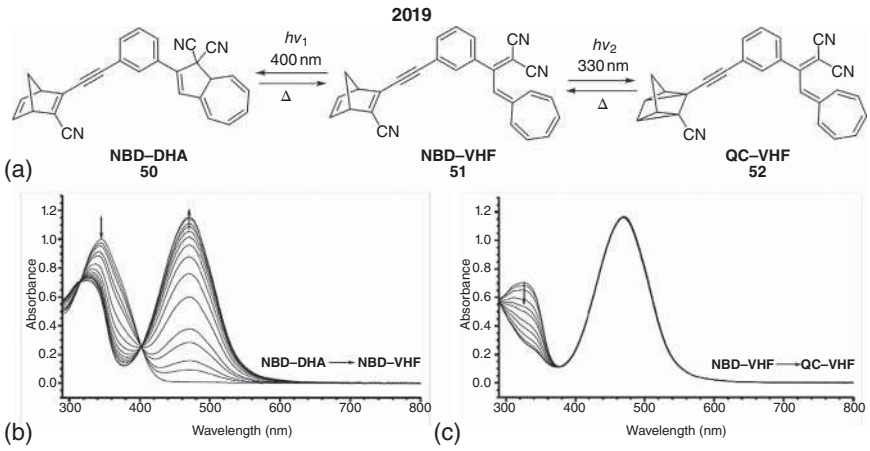


**Figure 16.12** (a) Switching modes of NBD–DHA hybrid **50**, (b) absorption profile change switching from NBD–DHA to NBD–VHF, (c) absorption profile change switching from NBD–VHF to QC–VHF [56]. Source: (b, c) Source: Modified from Kilde et al. [56].

compound NBD–VHF **51** allows a full transformation to the QC–VHF **52** photoisomer (Figure 16.12c) [56]. For analog compounds to NBD–DHA **50** (Figure 16.12), where the alkyne linker is placed on the phenyl ring, the isomerization to NBD to QC unities is entirely or partially afforded. On the contrary, this photoconversion is not observed for the analogs with the alkyne-linker on the seven-member ring resulting in the photodegradation of these systems [56]. The half-life of the QC moieties in this hybrid system is solvent-dependent from 11 minutes in toluene (50 °C) to 3 minutes in dichloromethane (25 °C) [56]. Computational studies of the isomerization QC–VHF revealed energy storage of 96–101 kJ $mol^{-1}$ exceeding the energy-storage capacity of the corresponding separate photochromic units [56].

Azobenzene is another photoswitch that has been used in the design of NBD hybrids. These systems have two types of photochemical processes: *E*/*Z*-isomerization at the azo group (N=N) and NBD to QC isomerization. Two examples of NBD-azobenzene systems are shown in Schemes 16.6 and 16.7. The first one is a trimodal NBD-azobenzene-NBD hybrid [54] (Scheme 16.6). In contrast, the second one explores the substitution effect in the azobenzene in bimodal NBD-azobenzene and trimodal azobenzene-NBD-azobenzene combinations [57] (Scheme 16.7).

The trimodal NBD-azo-NBD systems have *E*/*Z*-isomerization after irradiation of these compounds in toluene at 365 nm for 335 minutes to afford the NBD-(*Z*)azo-NBD and QC-(*Z*)azo-QC isomers, which can be reversible on heat to get the initial *E* isomers (Scheme 16.2a). The quadricyclane formation happens after irradiation at 436 nm with a low quantum yield ($\Phi = 0.025\%$). The QC-(*E*)azo-QC photoisomer can be converted to the initial NBD-(*E*)azo-NBD using molybdenum(VI) oxide ($MoO_3$) as a heterogeneous catalyst (Scheme 16.2a) [54]. These trimodal NBD-azo-NBD systems can be photoisomerized in four photochromic configurations.

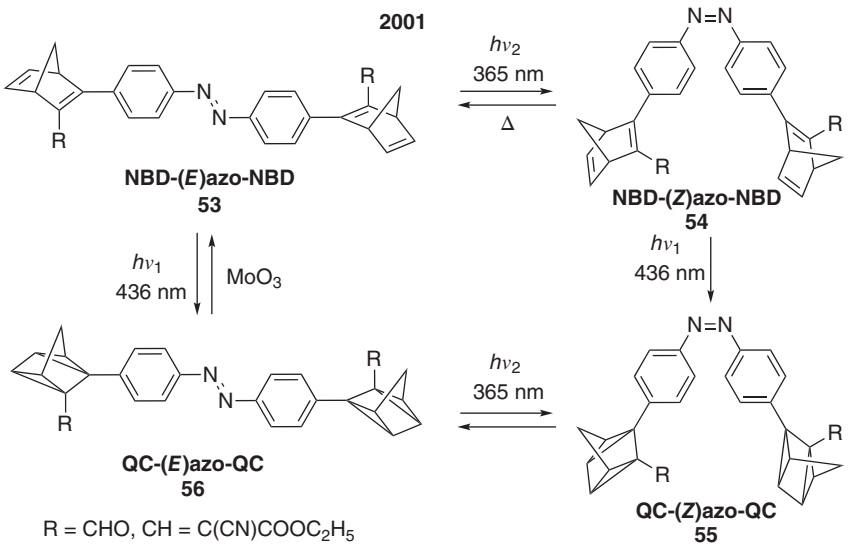


**Scheme 16.6** Trimodal NBD-azobenzene-NBD hybrids and their switching into four different photochromic configurations. Source: Modified from Dubonosov et al. [54].

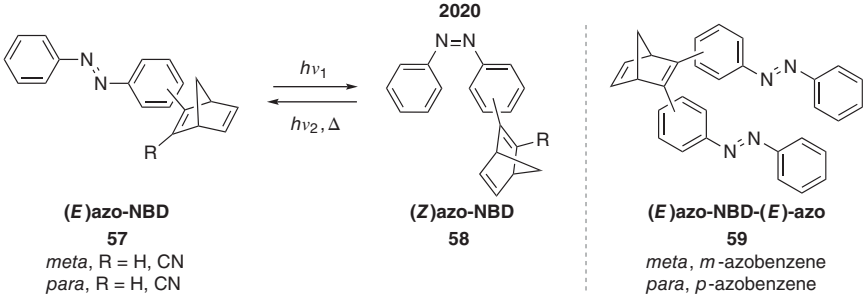


**Scheme 16.7** Bimodal and trimodal azo-NBD hybrids are switching between two photochromic forms. Source: Modified from Kunz and Wegner [57].

In contrast to the trimodal NBD-azo-NBD **53,** bimodal azo-NBD **57** and trimodal azo-NBD-azo **59** systems presented two photochromic forms corresponding to the *E/Z* isomerization in different solvents due to the NBD unit not photoisomerizes to QC (Scheme 16.7) [57].

The last example of hybrid systems is the NBD-DAE hybrid **60**. Photochromic compounds represented by **60** undergo a cyclization under ultraviolet (UV) irradiation that is reversible under visible light (vis) irradiation (Figure 16.13). A new absorption band at 500 nm is observed when NBD–DAE is irradiated at 300 nm in acetonitrile (Figure 16.13a). Also, the reversibility of these photoswitches was tested, having a good cyclability (Figure 16.13b). The isomerization of the NBD moiety to QC form was not observed, indicating that these NBD–DAE hybrids have photophysical properties that compete with the DAEs [58].

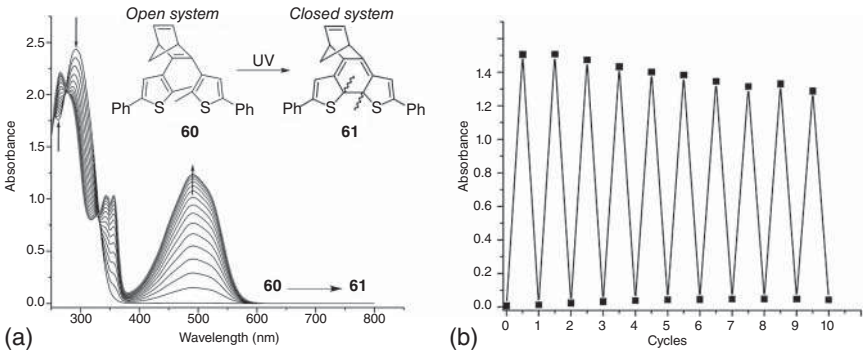


**Figure 16.13** Norbornadiene-diarylethene hybrids. (a) Absorption profiles and changes due to irradiation with UV light. (b) Cyclability testing for NBD–DAE hybrids [58]. Source: Modified from Büllmann and Jäschke [58].

In summary, a broad range of synthetic modifications have been applied to the NBD/QC couple. The modifications have led to the identification of the molecular design concepts that can enhance almost all of the relevant parameters of the systems, such as quantum yield, the onset of absorption, storage time, and energy density. One remaining challenge is to combine attractive functions in several of these design targets in a single functional system.

## 16.5 Use of Norbornadiene in Devices for MOST Applications

For practical applications, various strategies have been investigated to integrate NBD/QC couples into devices. As one of the significant demonstrations in 2019, NBD derivative **34** with the cyano group as acceptor unit and *p*-methoxy-phenyl group as donor unit was tested in an outdoor facility (Figure 16.14). This compound shows several attractive features. For instance, one advantage of this NBD is that the absorption profile is redshifted (with an onset of absorption at 380 nm and a high quantum yield of 0.61), at the same time keeping a high-energy-storage enthalpy of 88.5 kJ $mol^{-1}$. The experimental half-life of the QC was determined to 30 days at room temperature, making it suitable for outdoor testing. Therefore, the compound was later set up as an outdoor facility [42]. The experimental setup used a parabolic concentrator to focus the solar power (up to a maximum of 16 suns) and a double-layered glass tubing (Figure 16.14a). The outer layer was used to pass through the NBD solution, and the inner layer was used as a cooling layer to prevent the thermal back conversion caused by the focused light beam. With a 0.1 M concentration in toluene, the NBD solution was converted quantitatively to QC form with sunlight, achieving an energy-storage efficiency of up to 0.03% (Figure 16.14c) [42].

The NBD systems **23** and **26** have also been combined with the water-heating system (Figure 16.15a). Such a complex device contains two fluidic layers. The upper layer was used for flowing the NBD solution, while the bottom layer served to flow

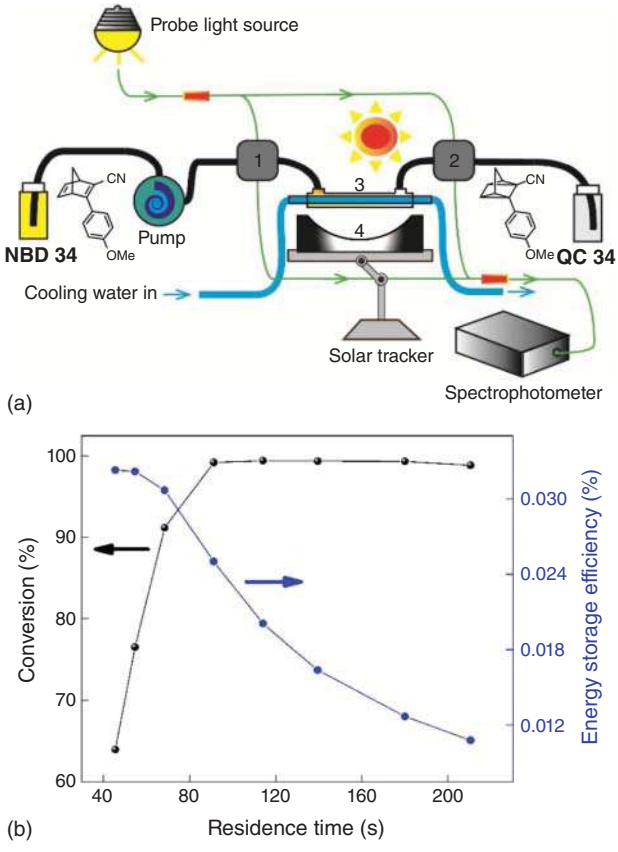


**Figure 16.14** (a) NBD **34** for outdoor tests. (b) outdoor conversion facility. 1 and 2 are the flow spectrometer. 3 is the double-layer glass tubing. 4 is the parabolic concentrator. (c) conversion percentage and energy-storage efficiency varied with a residence time of a 0.1 M NBD solution in toluene [42]. Source: Modified from Wang et al. [42].

water for additional solar water heating (Figure 16.15b). The most robust NBD **26** in this work finally provided a solar-energy-storage efficiency of 1.1% for MOST, and up to 80% of the solar spectrum can be utilized (Figure 16.15c) [32].

Another important parameter to be optimized is the release of stored energy. For that purpose, a heterogeneous catalyst triggers the conversion back reaction of QC to NBD, releasing heat during the process. During the last years, different catalysts have been designed for the conversion back reaction depending on the molecular features of NBD systems [60, 61]. As an example, the back reaction of the QC to the ethyl ester NBD (ethyl-3-phenylbicyclo[2.2.1]hepta-2,5-diene-2-carboxylate) was tested. This QC has a half-life of 450 days and can store a high amount of energy (88 kJ $mol^{-1}$). Using magnetic iron-oxide nanoparticles functionalized with CoSalphen catalyst, the back reaction from QC to NBD was performed efficiently [53].

In early 1988, cobalt(II) porphyrin derivatives supported on alumina beads were used to demonstrate the release of the stored energy from unsubstituted QC to NBD.

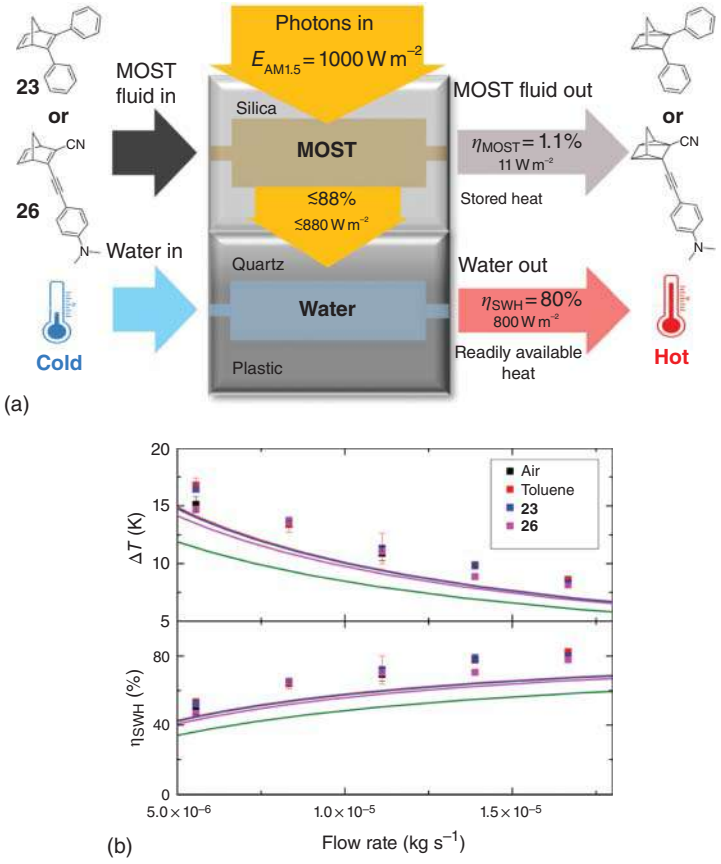


**Figure 16.15** (a) NBDs **23** and **26** for water-heating setup. (b) Scheme of the MOST-water-heating device. The MOST system can capture and store up to 1.1% solar energy. The residual energy can be captured by water on the bottom layer. (c) Temperature gradient and solar-water-heating efficiency in function of flow rate [32]. Source: Dreos et al. [32]. Licensed under CC BY-3.0.

Such catalyst was loaded on a 2 cm inner diameter, 70 cm long reactor with a total volume of 200 $cm^3$. Impressively, it was demonstrated that the charged QC solution with 1 M concentration could fully release a temperature gradient of up to 58.5 °C, successfully demonstrated the energy-storage potential of NBD/QC couple on MOST [62].

In the same year, alumina-anchored cobalt(II) Schiff base catalyst was also discovered to have a strong catalytic effect on the back conversion of QC photoisomer (88.7 kJ $mol^{-1}$) to its corresponding dicyano-substituted NBD derivative [63]. Same as previous work, the catalyst has been loaded into a similar reactor (4 cm inner diameter and 70 cm length). During experiments, the converted QC solution was pumped through the reactor with a flow speed of 0.0151 cm $s^{-1}$ over four to eight hours. Unfortunately, the maximum energy gradient with 1 M concentration was only 50.5 °C. However, the absorption profile of such used NBD can cover a

small part of the solar irradiation spectrum, thus can be considered one of the most significant early achievements on MOST concept [33, 63].

In later literature, cobalt(II) phthalocyanine (CoPc) was demonstrated as a catalyst. However, the catalyst reactivity remains relatively low, likely because of the π–π stacking of phthalocyanine units [13]. Hence, it was found that CoPc compounds physisorbed on the surface of activated carbon had increased activity. With NBD **34** in Figure 16.16a, theoretically, the maximum temperature gradient for the highest concentration in toluene can release up to 65 °C under adiabatic conditions. While experimentally, a maximum of 63 °C under vacuum conditions was finally demonstrated. At the same time, to be highlighted, the reactor size in this work was much smaller than previous examples; only 5 mg of the CoPc@C was loaded into a 5 cm long, ≈ 2 mm diameter Teflon tubing [42].

In addition to traditional catalytic conversions, it was recently found that QC can be converted to NBD electrochemically. Different electrodes have been used, including Pt (111) and highly oriented pyrolytic graphite (HOPG) electrodes. To be noticed, with the latter, reversibility of up to 99.8% can be achieved, showing new potential electro triggered back conversion for future applications [64, 65].

The integration of NBD into fabrics is another alternative to use this photoswitch in solid state. For that purpose, the monomeric and dimeric NBD derivatives have been incorporated into a polymer matrix (polystyrene) windows laminate applications. NBD derivatives like compound **36** were loaded into polystyrene (0.1–0.8 wt%). These composites presented fast conversion in the presence of sunlight, good cyclability of photoisomerization and conversion back reaction, and low decomposition after several cycles (Figure 16.17). These composites' material (0.8 wt% of NBD in polystyrene) presented a heat release in the range of 2.7–3.0 kJ $kg^{-1}$ [44].

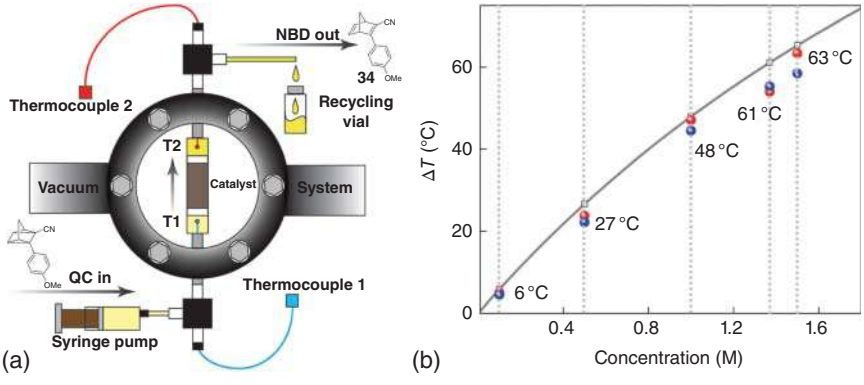


**Figure 16.16** (a) Macroscopic heat-release setup. The converted QC solution is pumped through the catalytic reaction in a vacuum chamber. The temperature gradient is monitored before and after the thermocouples. (b) The macroscopic heat-release measurements were achieved with different concentrations, corresponding well to the predicted simulation values [42]. Source: Wang et al. [42]. Licensed under CC BY-3.0.

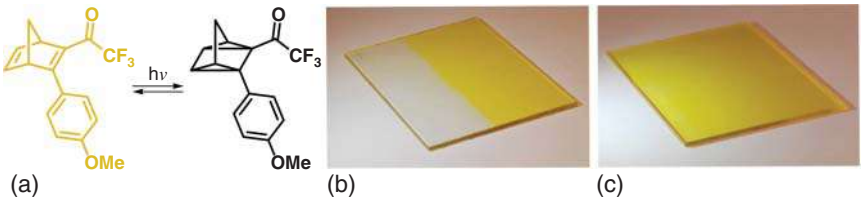


**Figure 16.17** (a) NBD **36** used for smart window demonstration. Glass coated with a composite of 0.8 wt% of NBD **36** into polystyrene where (b) half of the glass was exposed under sunlight and (c) the irradiation was interrupted favoring the back-conversion reaction [44]. Source: Reproduced with permission from Petersen et al. [44]. Copyright 2019 John Wiley and Sons.

## 16.6 Use of Norbornadiene Photoswitch in Other Applications

In addition to the application in MOST applications, NBD/QC systems have been investigated in other applied fields like molecular logic [8, 9], fluorescence readout [10–13], and molecular electronics [14–16]. This section will describe the NBD's molecular features' use in these applications.

Two approaches have been explored using NBD/QC photoswitch in molecular logic: first photon/acid–base chemistry [8] and second metallic chelation orthogonal photoswitching [16]. In the first approach, the NBD/QC photoswitch performs by three inputs acid, base, and light at 310 nm, where there is a unique input sequence that interconverts $QCH^+$ to $NBDH^+$ (Figure 16.18a). Thus, this NBD/QC system behaves as a three-input keypad lock function [15]. In the second approach, the NBD's functionalization with chelating groups allows the formation of metallic complexes that redshift the photoswitch's absorption. A mixture of an NBD-Pd(II) complex and uncomplexed NBD enables the formation of four NBD/QC states by an orthogonal photoswitching (Figure 16.18b) [16]. Hence, these two approaches have shown the concept of multimode switching systems that inspire the future design of more sophisticated logic functions.

In previous literature, few NBD/QC systems with fluorescence emissions have been reported [17–20]. One example is NBD **62** (Figure 16.19), where the structure of this compound is based on a linear conjugation through the alkynyl-phenyl bond. This structural feature favors a high fluorescence quantum yield ($\Phi = 0.49$) compared with cross-conjugated analogs that undergo a photoisomerization process. The irradiation of light (405 nm) to NBD affords the respective QC derivative allowing a turn-off of the fluorescence response. The fluorescence emission can be recovered by heating or irradiating light at 340 nm that induces the back isomerization from QC to NBD (Figure 16.19). The photoisomerization and back conversion to the NBD **62** operate fast with high fatigue resistance [20]. The molecular properties of NBD **62** are promising in optical memory storage and imaging application based on fluorescence readout [20].

Highly conjugated NBDs have been explored for molecular electronic applications [21–23]. The NBD **62** has been tested as a functional molecule in tuning molecular

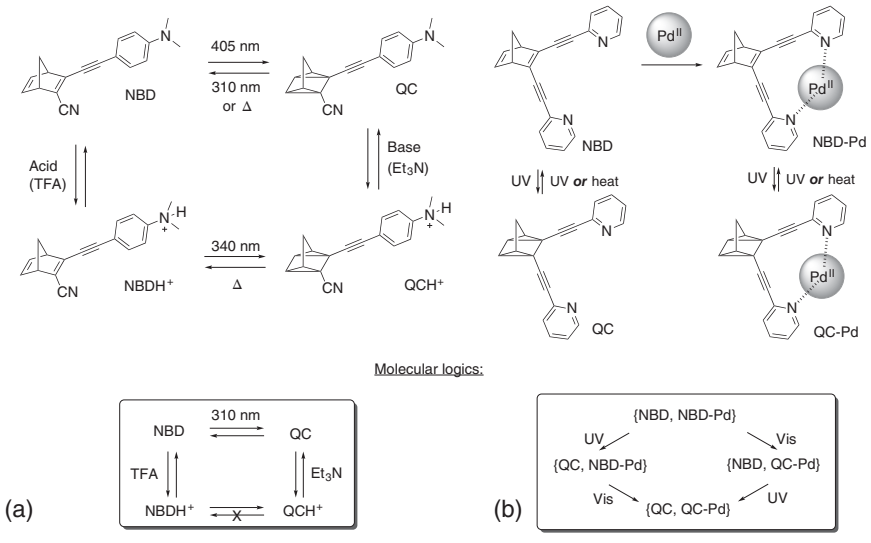


**Figure 16.18** Example of NBD/QC systems used in molecular logic. (a) photon/acid–base chemistry. Source: Dreos et al. [15] and (b) metallic chelation orthogonal photoswitching. Source: Drøhse Kilde et al. [16].

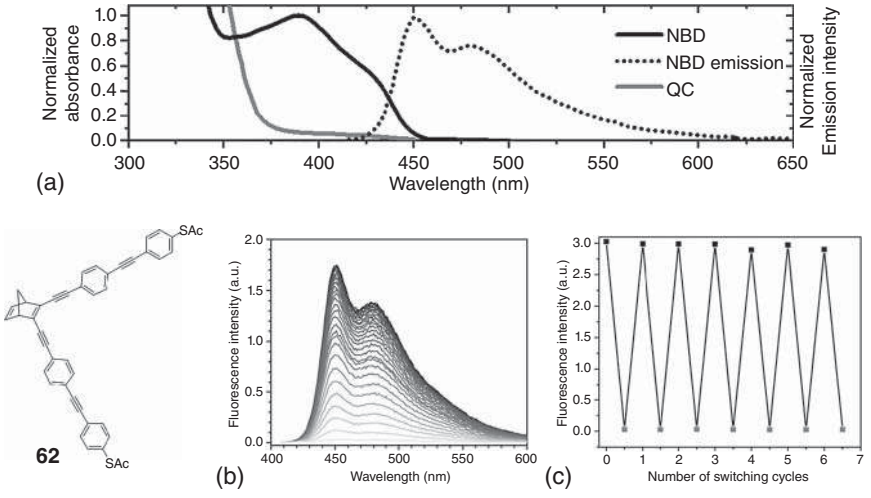


**Figure 16.19** Fluorescence emission for optical memory storage and imaging based on the emission of NBD **62** where (a) represents absorption spectra of NBD/QC system and fluorescence emission of NBD; (b) is the recovering back irradiation of NBD at 340 nm and (c) High fatigue resistance test of NBD 61 [20]. Source: Tebikachew et al. [20]Licensed under CC BY-3.0.

conductance [23] and molecular memristive devices [22]. In the first case, the NBD/QC system presents two conductive states (high at $1.2 \pm 0.1 \times 10^{-4}$ $G_0$ and low at $1.9 \pm 0.8 \times 10{-}5\,G_0$). It has a unique charge transport mechanism where the conductance is modulated by breaking the conjugation once the NBD is converted

to QC and taking the current through the QC's three-bond path [23]. In the second case, NBD **62** can be isomerized to QC using an electrical stimulus. The isomerization from NBD to QC is performed due to the local heating caused by current flow, and a single electron transfer (SET) process favors conversion back from QC to NBD. This manipulation of the isomerization indicates that this NBD/QC system can be used as an electrically controllable single-molecule memristive element [22].

## 16.7 Summary and Outlook

This chapter presented a detailed overview of the synthesis, the engineering of the NBD/QC isomerization pair as MOST system, the use in MOST devices, and the performance of hybrid NBD systems, The NBD/QC systems developed through last years have presented significant progress in different properties such as redshifting the absorption onset, high quantum yield (up to $\Phi = 0.94$), high-energy density (up to 0.9 MJ $kg^{-1}$), and tuning the storage time (from hours to years). The individual properties of NBD systems make it possible to suit different applications, such as liquid systems for the development of devices or solid materials for windows applications. Finally, examples of further applications such as molecular logics and molecular electronics were showed, giving suggestions and future development ideas.

## References


1 Lennartson, A., Roffey, A., and Moth-Poulsen, K. (2015). Designing photoswitches for molecular solar thermal energy storage. *Tetrahedron Lett.* 56 (12): 1457–1465.

2 Plate, A.F. and Pryanishnikova, M.A. (1956). Preparation of bicyclo[2.2.1]hepta-2,5-diene by the condensation of cyclopentadiene with acetylene. *Bull. Acad. Sci. USSR* 5 (6): 753–754.

3 Dubonosov, A.D., Bren, V.A., and Chernoivanov, V.A. (2002). Norbornadiene–quadricyclane as an abiotic system for the storage of solar energy. *Russ. Chem. Rev.* 71 (11): 917–927.

4 An, X.-w. and Y-d, X. (1993). Enthalpy of isomerization of quadricyclane to norbornadiene. *Thermochim. Acta* 220: 17–25.

5 Dauben, W.G. and Cargill, R.L. (1961). Photochemical transformations—VIII: the isomerization of $\Delta^{2,5}$-bicyclo[2.2.1]heptadiene to quadricyclo[2.2.1.$0^{2,6}$.$0^{3,5}$]heptane (quadricyclene). *Tetrahedron* 15 (1): 197–201.

6 Hammond, G.S., Turro, N.J., and Fischer, A. (1961). Photosensitized cycloaddition reactions 1. *J. Am. Chem. Soc.* 83 (22): 4674–4675.

7 Tatsuo, A., Takahisa, O., Toshio, W. et al. (1987). Mechanistic approach to the sensitization process of aromatic ketones in the isomerization between norbornadiene and quadricyclane. *Bull. Chem. Soc. Jpn.* 60 (8): 2937–2943.

8 Smith, C.D. (1971). Quadricyclane. *Org. Synth.* 51: 133.


9 Kazuhiro, M., Kazutoshi, T., Yoshinori, N., and Yoshinori, Y. (1980). Photoisomerization of norbornadiene to quadricyclane in the presence of copper(I)-nitrogen ligand catalyst. *Chem. Lett.* 9 (10): 1259–1262.

10 Maruyama, K., Terada, K., and Yamamoto, Y. (1981). Exploitation of solar energy storage systems. Valence isomerization between norbornadiene and quadricyclane derivatives. *J. Org. Chem.* 46 (26): 5294–5300.

11 Franceschi, F., Guardigli, M., Solari, E. et al. (1997). Designing copper(I) photosensitizers for the norbornadiene–quadricyclane transformation using visible light: an improved solar energy storage system. *Inorg. Chem.* 36 (18): 4099–4107.

12 Quant, M., Hamrin, A., Lennartson, A. et al. (2019). Solvent effects on the absorption profile, kinetic stability, and photoisomerization process of the norbornadiene–quadricyclanes system. *J. Phys. Chem. C* 123 (12): 7081–7087.

13 Bren, V.A., Dubonosov, A.D., Minkin, V.I., and Chernoivanov, V.A. (1991). Norbornadiene–quadricyclane – an effective molecular system for the storage of solar energy. *Russ. Chem. Rev.* 60 (5): 451–469.

14 Orrego-Hernández, J., Dreos, A., and Moth-Poulsen, K. (2020). Engineering of norbornadiene/quadricyclane photoswitches for molecular solar thermal energy storage applications. *Acc. Chem. Res.* 53 (8): 1478–1487.

15 Dreos, A., Wang, Z., Tebikachew, B.E. et al. (2018). Three-input molecular keypad lock based on a norbornadiene–quadricyclane photoswitch. *J. Phys. Chem. Lett.* 9 (21): 6174–6178.

16 Drøhse Kilde, M., Broløs, L., Mansø, M. et al. (2020). Orthogonal photoswitching with norbornadiene. *Chem. Eur. J.* 26 (21): 13429–13435.

17 Babudri, F., Bilancia, G., Cardone, A. et al. (2007). Photochemical tuning of light emission in a conjugated polymer containing norbornadiene units in the main chain. *Photochem. Photobiol. Sci.* 6 (4): 361–364.

18 Maafi, M., Lion, C., and Aaron, J.J. (1996). Electrosynthesis and photoisomerization of a new fluorescent aromatic polymer bearing a pendant substituted norbornadiene group. *Synth. Met.* 83 (2): 167–169.

19 Mounir, M., Jean-Jacques, A., and Claude, L. (1994). Direct valence isomerization of newly synthesized norbornadiene aromatic derivatives. A kinetic and photophysical study. *Chem. Lett.* 23 (10): 1865–1868.

20 Tebikachew, B.E., Edhborg, F., Kann, N. et al. (2018). Turn-off mode fluorescent norbornadiene-based photoswitches. *Phys. Chem. Chem. Phys.* 20 (36): 23195–23201.

21 Bonfantini, E.E. and Officer, D.L. (1994). The synthesis of orbornadienes conjugatively linked to tetraphenylporphyrin ad anthracene: towards a norbornadiene-derived molecular electronic device. *J. Chem. Soc., Chem. Commun.* (12): 1445–1446.

22 Li, H.B., Tebikachew, B.E., Wiberg, C. et al. (2020). A memristive element based on an electrically controlled single-molecule reaction. *Angew. Chem. Int. Ed.* 59 (28): 11641–11646.

23 Tebikachew, B.E., Li, H.B., Pirrotta, A. et al. (2017). Effect of ring strain on the charge transport of a robust norbornadiene–quadricyclane-based molecular photoswitch. *J. Phys. Chem. C* 121 (13): 7094–7100.


**24** Iizawa, T., Kurisu, T., Nakajima, K., and Nishikubo, T. (1998). Synthesis of poly(phenylene sulfide) containing pendant norbornadiene moieties and their valence isomerization. *Polym. J.* 30 (5): 446–449.

**25** Lorenz, P. and Hirsch, A. (2020). Photoswitchable norbornadiene–quadricyclane interconversion mediated by covalently linked $C_{60}$. *Chem. Eur. J.* 26 (23): 5220–5230.

**26** Akhmetov, A.R., Tuktarov, A.R., Sadretdinova, Z.R. et al. (2020). New norbornadiene-tethered fulleropyrrolidines. *Mendeleev Commun.* 30 (3): 352–354.

**27** Herges, R. and Reif, W. (1996). Photoresponsive carboxylic acids. *Liebigs Annalen* 1996 (5): 761–768.

**28** Winkler, T., Dix, I., Jones, P.G., and Herges, R. (2003). Synthesis, structure, and complexation properties of amide-substituted derivatives of norbornadiene and quadricyclane. *Angew. Chem. Int. Ed.* 42 (30): 3541–3544.

**29** Jevric, M., Petersen, A.U., Mansø, M. et al. (2018). Norbornadiene-based photoswitches with exceptional combination of solar spectrum match and long-term energy storage. *Chem. Eur. J.* 24 (49): 12767–12772.

**30** Quant, M., Lennartson, A., Dreos, A. et al. (2016). Low molecular weight norbornadiene derivatives for molecular solar-thermal energy storage. *Chem. Eur. J.* 22 (37): 13265–13274.

**31** Lennartson, A., Quant, M., and Moth-Poulsen, K. (2015). A convenient route to 2-bromo-3-chloronorbornadiene and 2,3-dibromonorbornadiene. *Synlett* 26 (11): 1501–1504.

**32** Dreos, A., Börjesson, K., Wang, Z. et al. (2017). Exploring the potential of a hybrid device combining solar water heating and molecular solar thermal energy storage. *Energy Environ. Sci.* 10 (3): 728–734.

**33** Yoshida, Z.-i. (1985). New molecular energy storage systems. *J. Photochem.* 29 (1): 27–40.

**34** Börjesson, K., Lennartson, A., and Moth-Poulsen, K. (2013). Efficiency limit of molecular solar thermal energy collecting devices. *ACS Sustainable Chem. Eng.* 1 (6): 585–590.

**35** Takabumi, N., Kazuhisa, F., Ikuko, T., and Miwa, S. (2001). Trifluoromethyl-substituted donor–acceptor norbornadiene, useful solar energy material. *Bull. Chem. Soc. Jpn.* 74 (9): 1673–1678.

**36** Nagai, T., Takahashi, I., and Shimada, M. (1999). Trifluoromethyl-substituted norbornadiene, useful solar energy material. *Chem. Lett.* 28 (9): 897–898.

**37** Takashi, T., Eietsu, H., Toshio, M. et al. (1982). Photochemical reaction of 2-aroyl-3-arylnorbornadienes. *Chem. Lett.* 11 (10): 1551–1554.

**38** Gray, V., Lennartson, A., Ratanalert, P. et al. (2014). Diaryl-substituted norbornadienes with red-shifted absorption for molecular solar thermal energy storage. *Chem. Commun.* 50 (40): 5330–5332.

**39** Jevric, M., Wang, Z., Petersen, A.U. et al. (2019). Tuning molecular solar thermal properties by modification of a promising norbornadiene photoswitch. *Eur. J. Org. Chem.* 2019 (13): 2354–2361.

**40** Dreos, A., Wang, Z., Udmark, J. et al. (2018). Liquid norbornadiene photoswitches for solar energy storage. *Adv. Energy Mater.* 8 (18): 1703401.


**41** Petersen, A.U., Jevric, M., and Moth-Poulsen, K. (2018). Triazole-functionalized norbornadiene-quadricyclane photoswitches for solar energy storage. *Eur. J. Org. Chem.* 2018 (32): 4465–4474.

**42** Wang, Z., Roffey, A., Losantos, R. et al. (2019). Macroscopic heat release in a molecular solar thermal energy storage system. *Energy Environ. Sci.* 12 (1): 187–193.

**43** Schuschke, C., Hohner, C., Jevric, M. et al. (2019). Solar energy storage at an atomically defined organic-oxide hybrid interface. *Nat. Commun.* 10 (1): 2384.

**44** Petersen, A.U., Hofmann, A.I., Fillols, M. et al. (2019). Solar energy storage by molecular norbornadiene–quadricyclane photoswitches: polymer film devices. *Adv. Sci.* 6 (12): 1900367.

**45** Kazuhiro, M. and Hitoshi, T. (1982). A water-soluble solar energy storage system. *Chem. Lett.* 11 (11): 1699–1702.

**46** Bren, V.A., Minkin, V.I., Dubonosov, A.D. et al. (1997). Biphotochromic norbornadiene systems. *Mo. Cryst. Liquid Cryst. Sci. Technol. Sec. A Mol. Cryst. Liq. Cryst.* 297 (1): 247–253.

**47** Mansø, M., Tebikachew, B.E., Moth-Poulsen, K., and Nielsen, M.B. (2018). Heteroaryl-linked norbornadiene dimers with redshifted absorptions. *Org. Biomol. Chem.* 16 (31): 5585–5590.

**48** Mansø, M., Petersen, A.U., Wang, Z. et al. (2018). Molecular solar thermal energy storage in photoswitch oligomers increases energy densities and storage times. *Nat. Commun.* 9 (1): 1945.

**49** Jorner, K., Dreos, A., Emanuelsson, R. et al. (2017). Unraveling factors leading to efficient norbornadiene–quadricyclane molecular solar-thermal energy storage systems. *J. Mater. Chem. A* 5 (24): 12369–12378.

**50** Lainé, P., Marvaud, V., Gourdon, A. et al. (1996). Electron transfer through norbornadiene and quadricyclane moieties as a model for molecular switching. *Inorg. Chem.* 35 (3): 711–714.

**51** Chernoivanov, V.A., Dubonosov, A.D., Minkin, V.I. et al. (1989). Photoisomerization of 3-phenylnorbornadiene-2-carbaldehyde and its imines. *Zhurnal Organicheskoi Khimii (Russ.).* 25: 443–444.

**52** Koblik, A.V., Murad'yan, L.A., Dubonosov, A.D., and Zolotovskova, G.P. (1990). Ethynyl carbonium ions. 3. Diene synthesis with 4-phenylethynylpyrylium salts. *Chem. Heterocycl. Compd.* 26 (3): 259–263.

**53** Luchs, T., Lorenz, P., and Hirsch, A. (2020). Efficient cyclization of the norbornadiene-quadricyclane interconversion mediated by a magnetic [$Fe_3O_4$−CoSalphen] nanoparticle catalyst. *ChemPhotoChem* 4 (1): 52–58.

**54** Dubonosov, A.D., Galichev, S.V., Chernoivanov, V.A. et al. (2001). Synthesis and photoinitiated isomerizations of 3-(4-nitrophenyl)-and 3-(4-aminophenyl)bicyclo[2.2.1]hepta-2,5-diene-2-carbaldehyde and -2-carboxylic acid derivatives. *Russ. J. Org. Chem.* 37 (1): 67–71.

**55** Mansø, M., Kilde, M.D., Singh, S.K. et al. (2019). Dithiafulvene derivatized donor–acceptor norbornadienes with redshifted absorption. *Phys. Chem. Chem. Phys.* 21 (6): 3092–3097.


**56** Kilde, M.D., Mansø, M., Ree, N. et al. (2019). Norbornadiene–dihydroazulene conjugates. *Org. Biomol. Chem.* 17 (33): 7735–7746.

**57** Kunz, A. and Wegner, H.A. (2020). 1+1≥2? Norbornadiene-azobenzene molecules as multistate photoswitches. *ChemSystemsChem* 2: e2000035.

**58** Büllmann, S.M. and Jäschke, A. (2020). Norbornadiene-bridged diarylethenes and their conversion into turn-off fluorescent photoswitches. *Chem. Commun.* 56 (52): 7124–7127.

**59** Minkin, V.I., Bren', V.A., Dubonosov, A.D., and Tsukanov, A.V. (2012). Acylotropic intramolecular rearrangements of keto enamines of benzo[*b*]-annelated heterocycles. *Chem. Heterocycl. Compd.* 48 (1): 107–116.

**60** Maruyama, K. and Tamiaki, H. (1986). Catalytic isomerization of water-soluble quadricyclane to norbornadiene derivatives induced by cobalt-porphyrin complexes. *J. Org. Chem.* 51 (5): 602–606.

**61** Maruyama, K., Tamiaki, H., and Kawabata, S. (1986). Exothermic isomerization of water-soluble quadricyclanes to norbornadienes by soluble and insoluble catalysts. *J. Chem. Soc. Perkin Trans.* 2 (4): 543–549.

**62** Miki, S., Asako, Y., Morimoto, M. et al. (1988). Alumina-anchored cobalt porphine catalysts for the conversion of quadricyclane to norbornadiene. *Bull. Chem. Soc. Jpn.* 61 (3): 973–981.

**63** Sadao, M., Toshiro, M., Toshinobu, O. et al. (1988). Alumina-anchored cobalt(II) schiff base catalyst for the isomerization of trimethyldicyanoquadricyclane to the norbornadiene. *Chem. Lett.* 17 (5): 861–864.

**64** Waidhas, F., Jevric, M., Fromm, L. et al. (2019). Electrochemically controlled energy storage in a norbornadiene-based solar fuel with 99% reversibility. *Nano Energy* 63: 103872.

**65** Waidhas, F., Jevric, M., Bosch, M. et al. (2020). Electrochemically controlled energy release from a norbornadiene-based solar thermal fuel: increasing the reversibility to 99.8% using HOPG as the electrode material. *J. Mater. Chem. A* 8 (31): 15658–15664.

# 17 Dihydroazulene/Vinylheptafulvene (DHA/VHF) and Molecular Electronics

Martina Cacciarini and Mogens B. Nielsen

## Photochromism

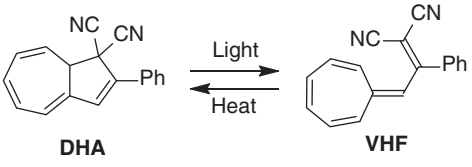


**DHA**

Dihydroazulene

**VHF**

Vinylheptafulvene

## Characteristic Features

Quantitative photoisomerization, quantitative thermal back-reaction in the dark with rate determined by solvent polarity, photo-/thermo-switch for conductance switching in molecular electronics.

## Synthetic Methods

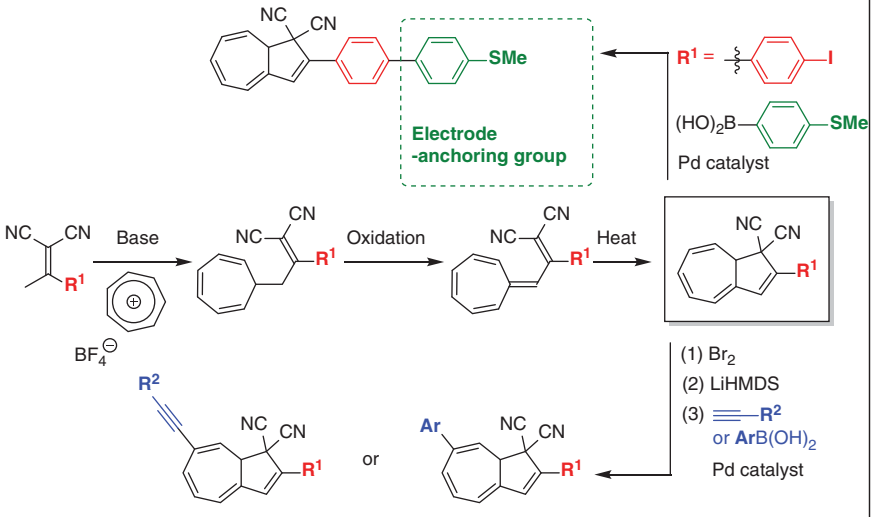


## First Reported

Daub, J., Knöchel, T., and Mannschreck, A. (1984). Photosensitive dihydroazulenes with chromogenic properties. *Angew. Chem. Int. Ed. Engl.* 23: 960–961.

## Key References

Broman, S.L., Lara-Avila, S., Thisted, C.L., et al. (2012). Dihydroazulene photoswitch operating in sequential tunneling regime: synthesis and single-molecule junction studies. *Adv. Funct. Mater*. 22: 4249–4258.

Huang, C., Jevric, M., Borges, A., et al. (2017). Single-molecule detection of dihydroazulene photo-thermal reaction using break junction technique. *Nat. Commun*. 8: 15436.

# 17

# Dihydroazulene/Vinylheptafulvene (DHA/VHF) and Molecular Electronics

*Martina Cacciarini*[1] *and Mogens B. Nielsen*[2]

[1] *University of Florence, Department of Chemistry "U. Schiff", Via della Lastruccia, 3-13 50019, Sesto Fiorentino (FI), Italy*
[2] *University of Copenhagen, Department of Chemistry, Universitetsparken 5, DK-2100, Copenhagen Ø, Denmark*

## 17.1 Introduction

Development of molecular components for the assembly of electronic devices is a wide and interdisciplinary area of research that evolves rapidly. It basically involves development at the molecular level of all kinds of electronic components that we know from the macroscopic world, such as wires, rectifiers, transistors, and advanced switches that can be used to perform computing operations [1]. Molecular photoswitches are particularly interesting in this field as they allow light stimuli to control the conductance along a π-conjugated molecular wire. Azobenzenes (AZBs) that undergo *cis*/*trans* photoisomerizations are particularly attractive when one aims for conductance switching based on geometrical changes of the molecular wire [2]. In contrast, dithienyl- and diarylethenes undergoing electrocyclic reactions are interesting when aiming at conductance switching as a consequence of alterations of the π-electron delocalization along the molecular wire [3]. Two fundamentally different kinds of conjugation exist in molecules as illustrated in Figure 17.1: linear and cross. Linear conjugation corresponds to alternating single and double bonds (or triple bonds), while cross-conjugation implies an $sp^2$ carbon whose double bond is branching off from the main chain. Thus, one double bond is a bifurcation point with one atom being geminally substituted [4]. When dithienylethenes (**DTE**s) are photoisomerized into dihydrodithienobenzenes (**DHDTB**s) (Figure 17.2), the conjugation along the molecule changes from a cross-conjugated arrangement of alternating double bonds (highlighted in red) to a linearly conjugated arrangement (highlighted in blue). From several experimental and theoretical studies, it has been shown that electron transport through a cross-conjugated structural element is less efficient than via a linearly conjugated one [5]. By sandwiching a DTE derivative (containing suitable electrode-anchoring groups) between electrodes or nanoparticles in various kinds of devices, reversible conductance switching between

*Molecular Photoswitches: Chemistry, Properties, and Applications*,
First Edition. Edited by Zbigniew L. Pianowski.



**Figure 17.1** Structural definitions of cross-conjugated and linearly conjugated double bonds.

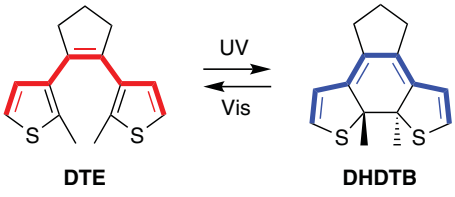


**Figure 17.2** Interconversion between dithienylethene (**DTE**) and dihydrodithienobenzene (**DHDTB**) using ultraviolet (UV) light in one direction and visible (vis) light in the other. Cross-conjugated and linearly conjugated pathways along the molecules are highlighted in red and blue colors, respectively.

a low-conducting, cross-conjugated DTE state (*off state*) and a high-conducting, linearly conjugated DHDTB state (*on state*) was observed [3].

In this chapter, we will focus on another class of photoswitches that has been explored in the field of molecular electronics, namely derivatives of the dihydroazulene (DHA) photoswitch. We will present an overview on its properties, its synthesis and relevant functionalization methods to introduce functional groups, such as electrode-anchoring groups (molecular "alligator clips") at specific positions to allow controlled anchoring of the molecule to electrodes. Then, we will provide examples of junction studies on DHA photoswitches. Thus, studies of the system will be covered, including studies of single-molecule junctions as well as of self-assembled monolayers. Finally, a few recent examples on how to employ the system for data-storage systems will be presented. Early studies in the field, pioneered by Daub and coworkers, used photomodulated amperometry to measure the current response upon subjecting DHA derivatives to a light stimulus. This work is summarized in Ref. [6] and will not be covered in this chapter. Optimization of the DHA/vinylheptafulvene (VHF) couple for molecular solar-thermal-energy storage (MOST) systems has also received significant attention, aiming at a large DHA–VHF energy difference and at the same time a long VHF lifetime (corresponding to a long-energy-storage time); Ref. [7] gives a recent overview of these efforts.

## 17.2 The Dihydroazulene/Vinylheptafulvene (DHA/VHF) Photo-/Thermo-Switch

The synthesis and properties of 2-phenylazulene-1,1(8a*H*)-dicarbonitrile (here referred to as parent **DHA**) were first reported by Daub and coworkers [8]. It is a photoactive molecule undergoing a light-induced electrocyclic ring-opening reaction to form a **VHF** as shown in Figure 17.3. It should be noted that **DHA** is

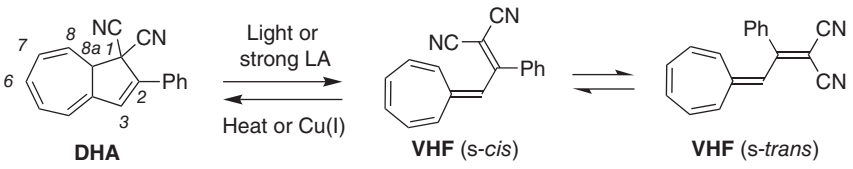


**Figure 17.3** Interconversion between parent dihydroazulene (**DHA**) and vinylheptafulvene (**VHF**). LA = Lewis acid.

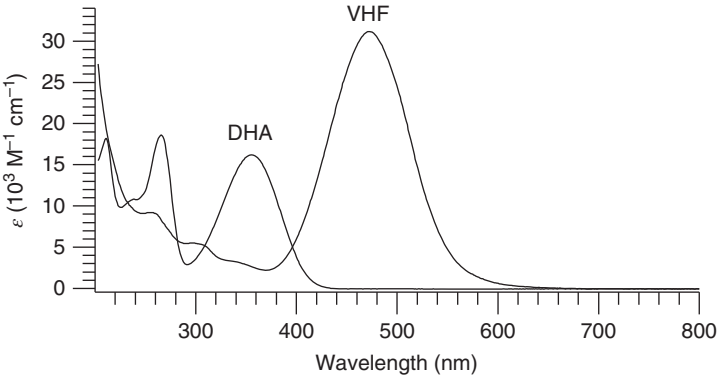


**Figure 17.4** UV–vis absorption spectra of the parent **DHA** and **VHF** in MeCN. Source: Nielsen [12b]. Licensed under CC BY-3.0.

chiral due to the stereocenter at C8a, and for this reason all structures shown in this chapter correspond to racemic mixtures. The quantum yield of photoisomerization is 55% in acetonitrile [8b]. This **VHF** is in equilibrium between s-*cis* and s-*trans* conformers, the latter usually being the most stable. The metastable **VHF** will via the s-*cis* conformer ultimately return thermally to the parent **DHA**. This ring-closure reaction is strongly dependent on the solvent polarity, and the parent system shown in Figure 17.3 is characterized by **VHF** half-lives that span from 202 minutes in ethanol to 2333 minutes in cyclohexane at 25 °C [9]. The reversible transformations can also be mediated by strong Lewis acids (LAs; such as $AlCl_3$, promoting DHA-to-VHF – no light involved) [10] or by copper(I) ions (promoting VHF-to-DHA) [11]. The parent **DHA** is a yellow-colored solid with absorption maximum at 353 nm in acetonitrile, while **VHF** has been isolated as green crystals and gives strongly orange/red solutions with an absorption maximum at 470 nm in acetonitrile [9]. The absorption spectra of the two isomers are shown in Figure 17.4.

One particular advantage of the system is that both the forward (DHA-to-VHF) and backward (VHF-to-DHA) conversions occur quantitatively. Thus, for the photoisomerization, there is no photostationary state – all DHA is ultimately photoisomerized into VHF. For fine-tuning the properties of the system, functionalizations at different positions of the original scaffold, both on the five-membered ring and/or on the seven-membered ring, have been developed within the last 15 years [12]. The thermal VHF-to-DHA conversion is most strongly influenced by replacing one of the two cyano groups for another group [13]; replacing it with a hydrogen atom results

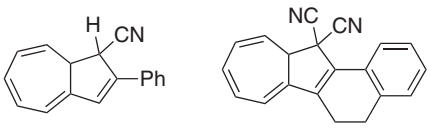


1 2

**Figure 17.5** Two structural modifications that have strong influence on the VHF lifetime: The VHF of **1** does not return to DHA (even at elevated temperature), while the VHF of **2**, locked in the s-*cis* conformation, "instantaneously" returns to DHA.

in a DHA (compound **1**; Figure 17.5) that is still photoactive, but the corresponding VHF has an infinite lifetime in regard to the ring-closure reaction [13a]. On the contrary, replacement of one nitrile with an acetyl group [13b], a primary amide [13b], secondary amides [13b], or differently functionalized benzothiazoles [13c] maintains the DHA photoactivity and induces a faster backward-switching event than for the parent system. In the context of MOST systems, the energy-storage density of the DHA/VHF couple of **1** was c. twice as high as that of the parent system. These properties are in principle attractive in the context of MOST systems, but, in contrast to the parent VHF, it was unfortunately not possible to trigger the energy-releasing back-reaction by various metal ions without decomposition. In contrast, locking the VHF in its reactive s-*cis* conformation as in the polycyclic DHA **2** (Figure 17.4) results in a VHF half-life of less than a second [14]. Also for this system, the energy-storage density was about doubled relative to the parent system [15], but here it comes with the drawback of a fast energy release. In the context of molecular electronics, a fast switching event may on the other hand be advantageous.

## 17.3 Synthesis and Functionalizations

### 17.3.1 Synthesis of DHA

The key intermediate in the synthetic preparation of DHAs with a substituent at position C2 ($R^1$) is the general structure **3** (Figure 17.6), which can be obtained in two different synthetic pathways. One possibility is by nucleophilic addition of the enolate of a ketone containing a substituent group $R^1$ (usually an acetophenone derivative) to a tropylium salt, followed by a Knoevenagel condensation with malononitrile [16]. The other possibility, depicted in Figure 17.6 and most widely utilized nowadays even in multigram scale, consists in an initial Knoevenagel condensation between the ketone and malononitrile [9, 16]. Then a deprotonation followed by a nucleophilic addition to freshly prepared tropylium tetrafluoroborate salt furnishes **3**. An oxidation ultimately gives the VHF derivative, which in the dark thermally isomerizes to the corresponding DHA. This strategy has today replaced the first procedure originally employed for the synthesis of DHAs, which consisted in a [8+2] cycloaddition reaction between 8-methoxyheptafulvene and the appropriate 1,1-dicyanoethylene intermediate, followed by elimination of methanol [8a]. Stoichiometric amounts of toxic mercury(II)acetate were necessary in the preparation

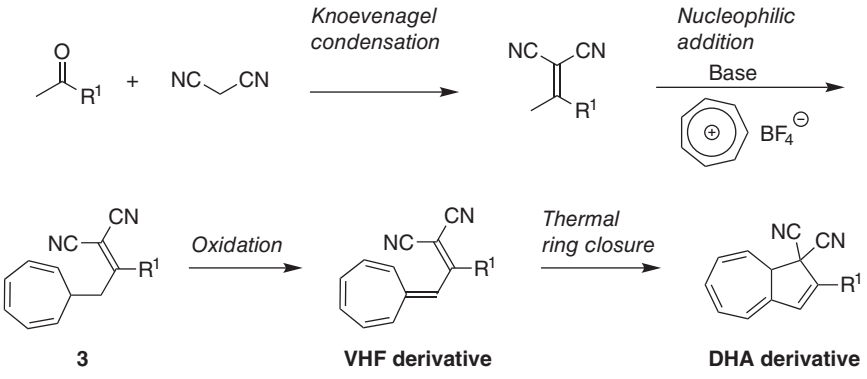


**Figure 17.6** General synthetic route to access a wide variety of 2-substituted DHA scaffolds. The substituent $R^1$ is usually an aryl.

of 8-methoxyheptafulvene and have been the driving force to develop and optimize the other strategy, which proceeds in high yields and large, multigram scale.

### 17.3.2 Functionalization of the DHA Scaffold

Regioselective functionalization of the seven-membered ring has been accomplished by a bromination–elimination – cross-coupling strategy allowing the introduction of aryl or arylethynyl groups at position C7 of DHA (by final Suzuki or Sonogashira coupling reactions) [17]. One such synthetic sequence of reactions is shown in Figure 17.7 [17c]. Treatment of **DHA** with 1 equiv of bromine gave the 7,8-dibromide **4** (containing three stereocenters, which are formed stereoselectively therefore giving a racemic mixture, not a mixture of diastereoisomers) [17c]. Regioselective elimination of HBr by treatment with the bulky base lithium

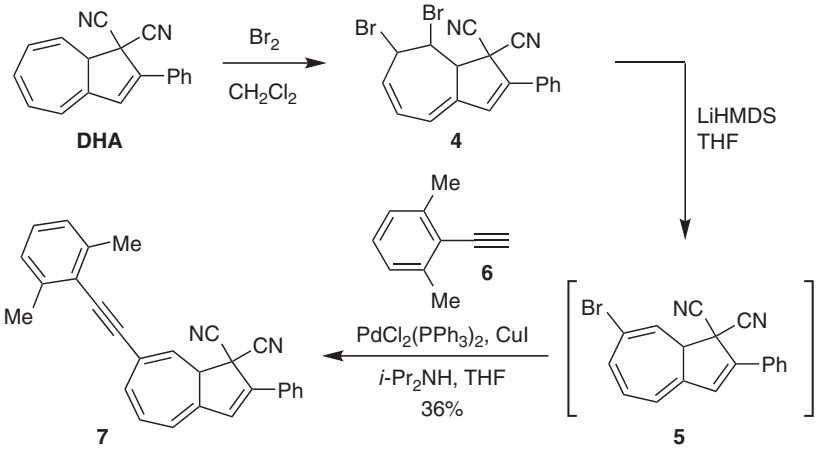


**Figure 17.7** Synthesis of arylethynyl-substituted DHA by bromination–elimination – cross-coupling protocol. Source: Modified from Broman et al. [17c].

hexamethyldisilazide (LiHMDS) gave the 7-bromo-substituted DHA **5**. The choice of this base and use of only one equivalent is crucial for the success of this elimination reaction as an additional elimination of HCN can readily occur, generating the fully unsaturated azulene. Compound **5** is a convenient building block for Pd-catalyzed coupling reactions. Thus, treating it with the terminal alkyne **6** under Sonogashira conditions gave the product **7**. This product was studied in a junction (*vide infra*). The next examples will show how a specific anchoring group (sulfur) can be introduced into the molecules to control the binding configuration in the junction.

A synthetic protocol for introducing a bromo substituent at position C3 has also been developed [18], but Pd-catalyzed coupling reactions at this position turned out more difficult. Yet, it has been possible to introduce a *p*-methoxyphenyl at this position in a Suzuki coupling, albeit in low yield [19].

### 17.3.3 Incorporation of Electrode-Anchoring Groups

DHA has been functionalized with sulfides and thioacetates to allow controlled anchoring of the molecule to silver or gold electrodes taking advantage of the strong affinity of sulfur for gold and silver [20]. For example, treating the iodophenyl-substituted DHA **8** with the boronic acid **9** in a Suzuki coupling provided the product **10** containing one sulfide-anchoring group ("alligator clip") as shown in Figure 17.8 [21].

Introduction of anchoring groups on both the five-membered ring side and on the seven-membered ring was accomplished according to Figure 17.9 [22]. Here compound **8** was first subjected to the bromination–elimination protocol to furnish the product **11**. A twofold Suzuki coupling with the boronic acid **12** then gave the product **13**. The two *tert*-butyl sulfides were finally converted into thioacetate groups by the action of boron tribromide and acetylchloride. This reaction gave a mixture of the two regioisomers **14** and **15**. This isomerization most likely proceeds via a VHF-like intermediate with DHA-to-VHF conversion being promoted by the $BBr_3$ Lewis acid (Figure 17.10). Rotation around the fulvene double bond followed by ring closure will give the other DHA isomer (namely isomer **15**). The pure 6-substituted isomer **15** was obtained by crystallization from toluene [23]. Conversely, the pure 7-substituted isomer **14** was obtained from another synthetic strategy in which the thioacetate was introduced directly, to avoid the use of a Lewis acid. Thus, subjecting the dihalo-substituted compound **11** to a twofold stannation reaction gave the

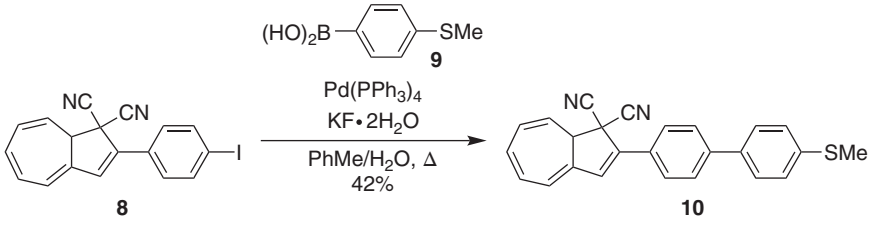


**Figure 17.8** Introduction of a sulfide-anchoring group. Source: Modified from Broman et al. [21].

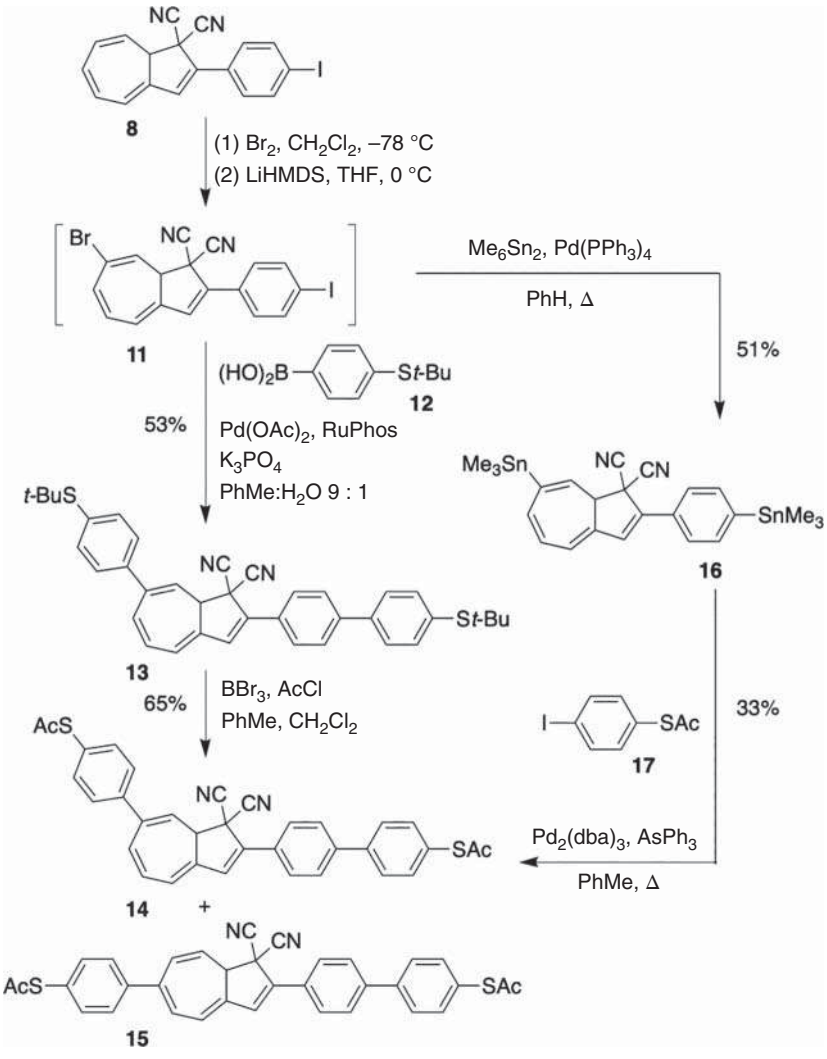


**Figure 17.9** Introduction of two thioacetate-anchoring groups. Source: Modified from Jevric et al. [22].

product **16** that was subsequently subjected to a Stille reaction with the aryl iodide **17** to give the desired product **14** [22]. Thioacetate handles have the advantage to be easily hydrolyzed, releasing the thiolate that will bind stronger to the gold or silver electrodes than an alkylsulfide.

## 17.4 Single-Molecule Conductance Measurements

### 17.4.1 Junction with No Controlled Anchoring

The first single-molecule conductance measurements on the DHA/VHF system in a junction were performed on DHA **7** (Figure 17.11) [24]. This relatively small

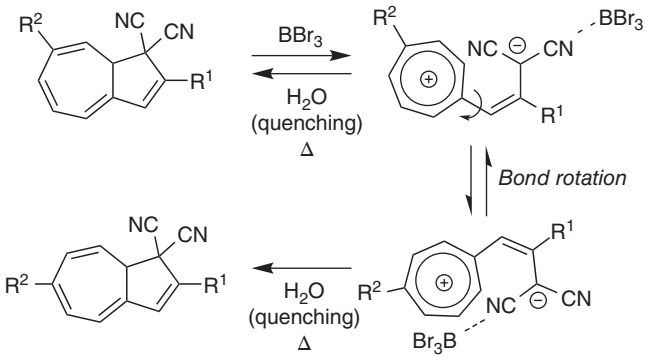


**Figure 17.10** Lewis-acid-induced isomerization between 7- and 6-substituted DHAs via a VHF intermediate having zwitterionic character.

molecule was evaporated onto a substrate with a pre-fabricated nanogap between silver electrodes (in a vacuum chamber). The silver source and drain electrodes were deposited onto a planar gate electrode made of aluminum metal covered with aluminum oxide that was prepared on a chip of oxidized silicon. A schematic representation of the sample geometry is shown in Figure 17.11b. Samples with a molecule trapped were studied at a temperature of 4 K. Experiments on four different samples showed no gate-induced conductance modulation or Coulomb blockade effects, and for different samples, the sample resistance varied from 20 MΩ to 20 GΩ. For these reasons, it was concluded that the DHA was well coupled to one electrode and separated by a tunneling gap from the other (but the actual orientation of the molecule in the gap is not known). Three out of four samples were found to respond to irradiation at 355 nm, triggering a switching event after 10–20 minutes of irradiation (from form **A** to form **B**). The new sample (**B**) showed a reduction of transport gap in tunneling density of states as shown in Figure 17.11c. After a few hours with no irradiation, the sample was found to reset to the original form **A**. Three such switching cycles between forms **A** and **B** could be obtained. The transport gap in tunneling density was reduced by 0.7–1 eV when converting form **A** into form **B**. This reduction agrees well with a reduced HOMO–LUMO gap of the corresponding VHF **18** relative to that of the DHA **7** based on optical and electrochemical studies in solution: reduction by c. 1.0 eV (based on cyclic voltammograms, see Figure 17.12) and by 0.7 eV (based on UV–vis absorption spectra). It is therefore reasonable to assign the two forms **A** and **B** to the DHA and VHF forms, respectively. The loss of photosensitivity after a few cycles is likely due to a rearrangement of the molecule-to-electrode interface, which ultimately reduces to the most favorable and therefore most strongly coupled geometry.

### 17.4.2 Junction Based on Sulfide Anchoring – Coulomb Blockade Regime

By placing DHA **10** containing a sulfide-anchoring group by sublimation in a similar nanogap as the one described above, a single-molecule device was obtained operating in the Coulomb blockade regime [21]. In this regime, electron transport

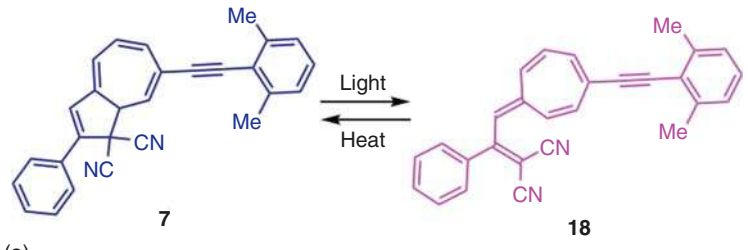


7 18

(a)

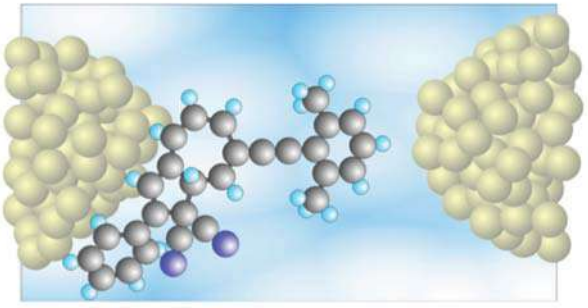

(b)

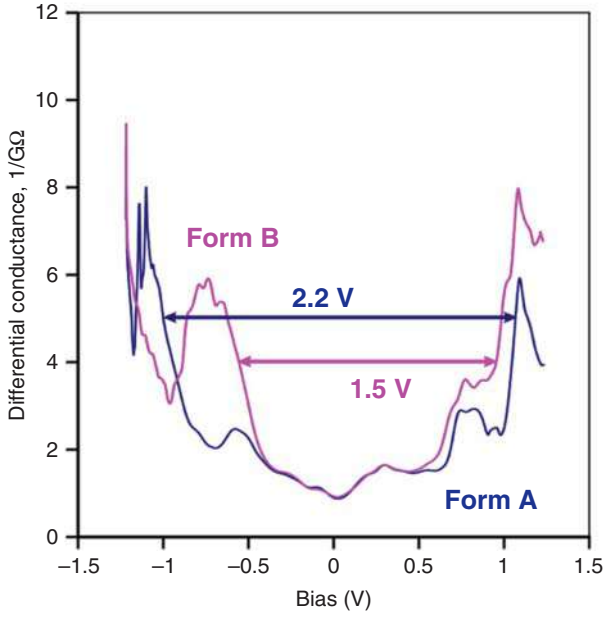


(c)

**Figure 17.11** (a) DHA/VHF system studied in nanogap. (b) Schematic representation of the sample geometry of **7** in a junction (the exact orientation is unknown). (c) Differential conductance plot for single-molecule DHA junction showing the tunneling density of states before (form **A**) and after (form **B**) irradiation. Source: Lara-Avila et al. [24].

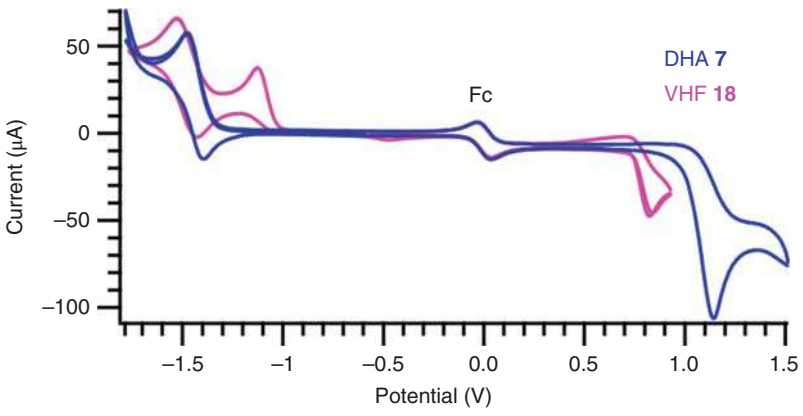


**Figure 17.12** Cyclic voltammograms of DHA **7** and VHF **18** in acetonitrile containing 0.1 M $Bu_4NPF_6$ as supporting electrolyte and ferrocene (Fc) as internal reference. Scan rate: 100 mV $s^{-1}$. Source: Lara-Avila et al. [24].

occurs via sequential tunneling; an electron "jumps" from one electrode to the molecule, resides there for a time, before "jumping" to the second electrode. Conductance measurements were performed at 4–25 K as a function of the gate voltage, irradiation, bias potential between source and drain, and temperature. Several switching processes were observed (Figure 17.13). First, at high bias voltages, switching from the DHA form characterized by a high resistivity (*off* state) to a more conducting VHF form (*on* state) was observed at a gate voltage of c. 3 V. At gate voltages not too far from this critical value, light sensitivity of the junction was obtained. Thus, photoisomerization of the DHA into its VHF was triggered by irradiating the sample for a few minutes by visual light. The sample stayed in the VHF form at low bias voltages, but at higher bias voltages, it would return to DHA within time. A light – high bias cycle could be repeated many times (20 *on–off* cycles were recorded) as shown in Figure 17.13a. Another way to trigger the conversion of the VHF into DHA was to increase the temperature up to 25 K, and several light – heat *on–off* cycles were recorded (Figure 17.13b). Thus, in this junction reversible switching between DHA (*off*) and VHF (*on*) was triggered by light, gate, and bias voltages, as well as by temperature.

The bias-induced conductance switching at high gate voltage ("dark photoswitching") was subjected to a theoretical study where theoretical Coulomb blockade diamonds were constructed for DHA **10** and its VHF isomer [25]. The quantum chemical calculations suggest that at the gate voltage where the switching occurs, the molecule has a net positive charge of +1. For charge states 0 and +1, the DHA has lower energy than the VHF, while the VHF form is less energetic for the +2 state. At the gate voltage corresponding to the +1 charge, there will at finite bias be a non-equilibrium population of the neighboring redox states corresponding to charge +2 and 0. Beyond a bias threshold, the population of the +2 state is significant, and the DHA will have time to relax to the less energetic VHF form – corresponding to the switching event.

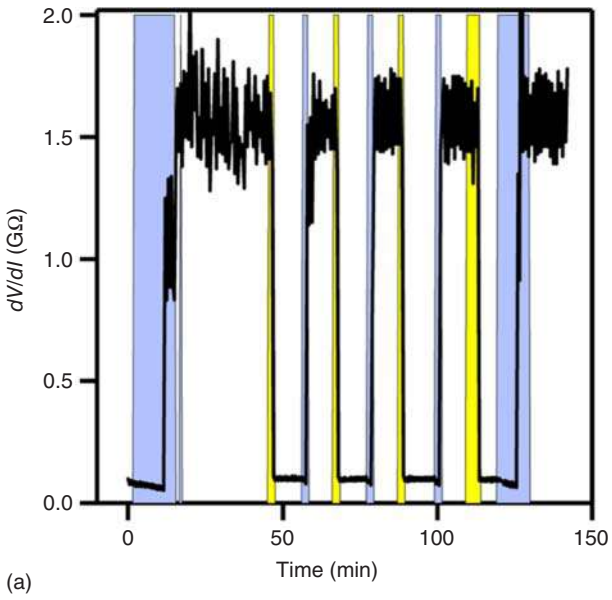


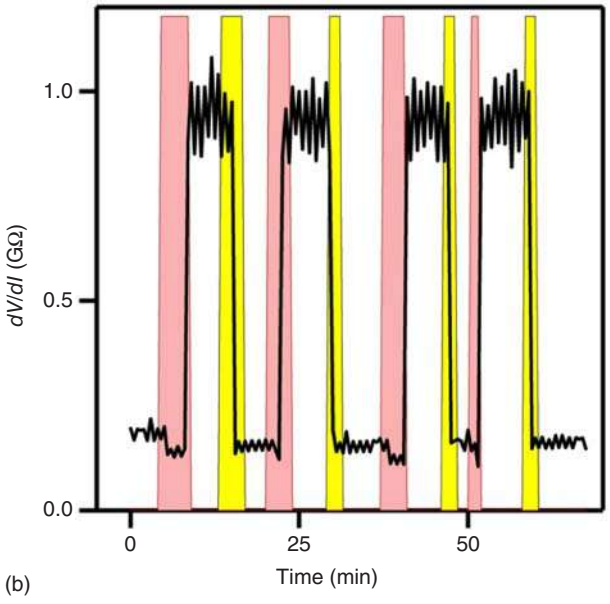


**Figure 17.13** Series of *on–off* switching with DHA **10** in junction. The differential resistance *dV/dI* was recorded at a bias voltage of 25 mV for both *on* (VHF) and *off* (DHA) states and shown vs. time as a result of different stimuli. Gate potential = 2.7 V. (a) Light and bias voltage control. The highlighted background indicates the time intervals when the sample was illuminated with light (yellow) or the bias voltage was increased to 80 mV (blue). (b) Light and temperature control. The highlighted background indicates the time intervals when the sample was subjected to light (yellow) or the temperature was increased from 4 to 25 K (rose). Source: Broman et al. [21].

### 17.4.3 Break-Junction Studies – Coherent Electron Transport

More recent studies have investigated the conductance properties of the two DHA isomers **14** and **15** and their corresponding VHFs (*E*/*Z* isomers) in devices with coherent electron transport by means of the mechanical break-junction technique, using gold electrodes and ambient conditions (Figure 17.14) [23]. The selected DHA candidates contain thioacetate-anchoring groups, which are assumed to be cleaved under the experimental conditions, forming Au—S bonds and therefore furnishing a direct control of the anchoring of the molecules. Under these conditions, light-induced conductance switching was also observed, with conductances that now depended on the conjugation through the molecules from one anchoring site to the other. At a fixed bias potential (100 mV), the current through the junction was measured. Irradiation of DHA **15** by UV light resulted in formation of a VHF characterized by a significantly reduced conductance. Upon heating to c. 60 °C, the VHF returned to the higher-conducting DHA state. These conversions were reversible over several cycles. Interestingly, DHA **14** was found to have a smaller conductance than the VHF **19**. The VHF returns to DHA **15** rather than to the original DHA **14**. This isomerization, when starting from DHA **14**, corresponds to a rotation around the exocyclic fulvene bond (see Figure 17.10). The one-dimensional conductance histograms are shown in Figure 17.14. The difference in conductances can be explained by the different conjugation pathways within the molecules. For DHA **15**, a linearly conjugated pathway can be drawn through the entire molecule from one sulfur to the other, while DHA **14** and the VHF **19** (*E*/*Z*) have one cross-conjugated element along the molecule as indicated in Figure 17.14a. According to X-ray crystallography, the π-system of DHA **14** also deviates significantly from planarity (Figure 17.15), rendering it the least conducting. The results were also supported by density functional theory (DFT) transport calculations. The less efficient π-electron delocalization in DHA **14** relative to that in DHA **15** is also reflected by their longest-wavelength absorption maxima: 372 nm (**14**) and 393 nm (**15**) in acetonitrile; thus, the absorption of **15** is redshifted by 21 nm relative to that of **14** [23].

### 17.4.4 Self-Assembled Monolayers

Light/heat controlled conductance switching was also achieved for DHA/VHF molecules **20**/**21** organized in a self-assembled monolayer between gold electrodes (source and drain) and a reduced graphene oxide transparent top contact that functions as the interfacial layer to top metal electrodes [26]. A schematic illustration of the molecular test bed is shown in Figure 17.16. Here anchoring to the gold source and drain substrates was realized via a thioacetate group sitting on the *meta* position of a phenyl substituent located at position C2 of the DHA. By alternating UV irradiation and heating, the conductance could be switched. The studies revealed a higher conductance for the DHA state relative to the VHF state. The break-junction experiments described above clearly showed how the position of anchoring plays an important role in regard to whether DHA or VHF

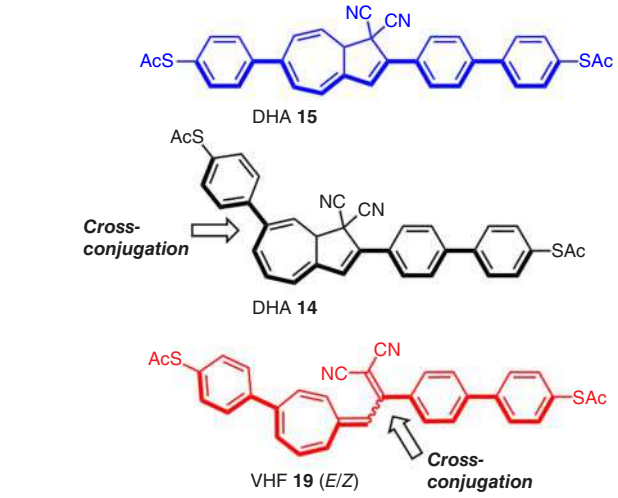


(a)

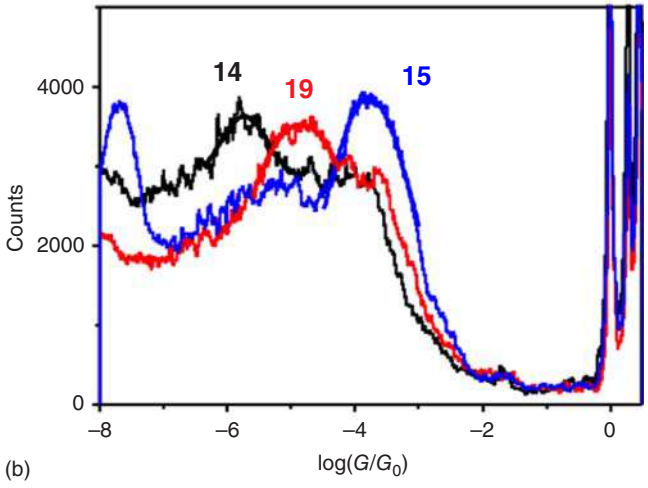


(b)

**Figure 17.14** (a) Different conjugation pathways along the molecules – pathway from one sulfur end group to the other is highlighted by thick bonds in each molecule. A linearly conjugated pathway exists for **15**, while **14** and **19** have one cross-conjugated segment. (b) One-dimensional conductance histograms for DHA **14** (black curve), VHF **19** (red curve), and DHA **15** (blue curve). Conductances $G$ are reported in units of the conductance quantum $G_0$. Source: Modified from Huang et al. [23]. Licensed under CC BY-4.0.

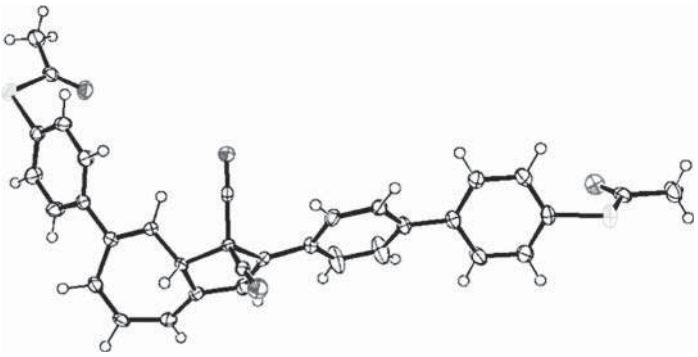

**Figure 17.15** Molecular structure of DHA **14** according to X-ray crystallographic analysis. Source: Huang et al. [23]. Licensed under CC BY-4.0.

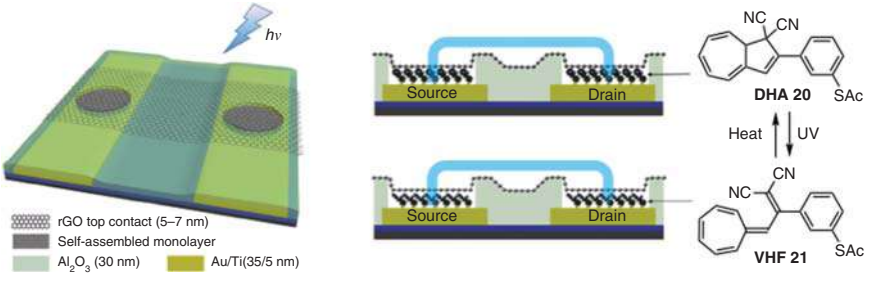


**Figure 17.16** Left: Illustration of junction based on a reduced graphene oxide thin film as top contact between two self-assembled molecular monolayers on source and drain gold substrates. Right: Illustration of cross-section of the molecular junction containing DHA/VHF molecules **20** and **21**. Source: Jevric et al. [26].

is most conducting for coherent charge transport. For the set-up in Figure 17.16, it is not possible to make conclusions rooted in cross-conjugation as the contact between the physisorbed top electrode and the molecules is not well defined; it is not known how the reduced graphene oxide electrode couples to the molecules (to either an atom of the seven-membered ring or possibly to one of the cyano groups for some conformations). We note that light-heat stimulated interconversion of a DHA derivative assembled on an Au(111) surface has also been studied by surface-enhanced Raman spectroscopy [27].

## 17.5 DHA in Combination with Other Functional Units

Here we shall show three examples of the combination of DHA with other functional units. The one example shows the combination of DHA with the Buckminsterfullerene ($C_{60}$) electron acceptor, while the two other examples show the combination of DHA with other photoswitches, AZB, and norbornadiene (NBD), respectively. These multimode photoswitch systems are of interest for the

development of advanced data-storage system. For other examples, we refer to references [6, 12b].

### 17.5.1 DHA–Fullerene Conjugates – Light-Induced Electron Transfer

The selection of DHA derivatives **22**–**26** (Figure 17.17) with $C_{60}$ linked to position C2 via molecular wires of different lengths has been reported [28]. Compounds **24** and **25** were prepared by first subjecting the aryl iodide **8** to a Sonogashira coupling reaction with the corresponding acetylenic linker scaffolds having a formyl end-group that was subsequently subjected to a Prato reaction, thereby introducing the $C_{60}$ unit. Compound **26** was instead prepared by forming the actual butadiyne bridge in the last step by either Glaser–Hay or Cadiot–Chodkiewicz coupling reactions, using two acetylenic coupling partners. Similarly, compound **24** was also prepared by connecting the units in a final Sonogashira coupling of suitable coupling partners. Buckminsterfullerene is known to act as an electrode-anchoring group to gold electrodes [29], but so far, these molecules have not been studied in molecular junctions, but only in solution. Figure 17.17 lists estimated ratios of quantum yields of photoisomerization (relative to the parent **DHA**) for these compounds in 1,2,-dichloroethane. It is clear that the photoactivity of the DHA is strongly reduced for short bridges. The quenching of photoactivity was explained by a light-induced electron transfer from the excited DHA to the $C_{60}$ electron acceptor.

Redox-controlled switching of DHA photoactivity was observed in other systems where either an electron donor or acceptor was introduced; examples include DHAs functionalized with ferrocene (DHA photochromism quenched by the ferrocene donor, but not for the corresponding ferrocenium) [30], anthraquinone (photochromism quenched by the anthracene-9,10-diol donor) [31], and tetrathiafulvalene (photochromism quenched by the tetrathiafulvalene dication acceptor) [32].

### 17.5.2 DHA–Azobenzene Conjugates – Data-Storage Systems

Molecular photoswitches are also interesting as data-storage systems. Here we shall present one example where the DHA photoswitch is used in combination with the AZB photoswitch. Thus, the macrocyclic system **27**/***trans*-AZB–DHA–DHA** consisting of two DHA units and one AZB unit was recently reported (Figure 17.18) [33]. Molecule **27** can potentially be interconverted between states by different light-heat stimuli (Figure 17.19); it was found that some of these states could be selectively activated. Calculations revealed a Gibbs free energy difference of c. 73 kJ mol$^{-1}$ between the lowest-energy isomer ***trans*-AZB–DHA–DHA** and the highest-energy isomer ***cis*-AZB–VHF–VHF**. If we label these two isomers by binary numbers ⟨**000**⟩ and ⟨**111**⟩, respectively, where the first number refers to AZB, *trans* (**0**) or *cis* (**1**), and the second and third numbers to DHA(**0**)/VHF(**1**), a large selection of isomeric states can be imagined (here we shall ignore additional stereoisomers on account of the DHA stereocenter at position C8a). The ⟨**001**⟩ and ⟨**010**⟩ states are degenerate in this labeling as are the ⟨**101**⟩ and ⟨**110**⟩

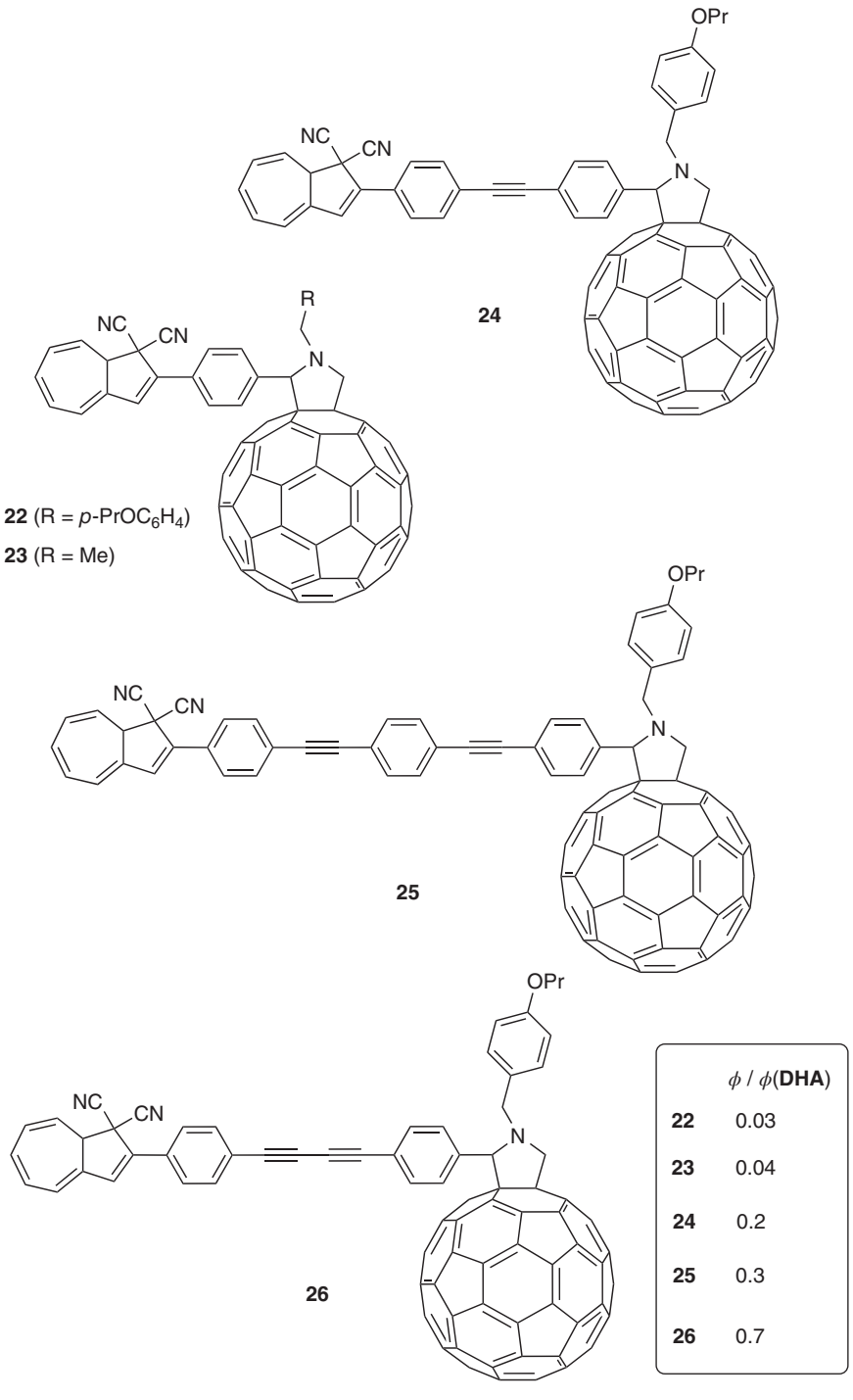


**Figure 17.17** DHA-$C_{60}$ conjugates. The estimated quantum yield ($\phi$) of photoisomerization relative to that of the parent **DHA** is listed for each compound.

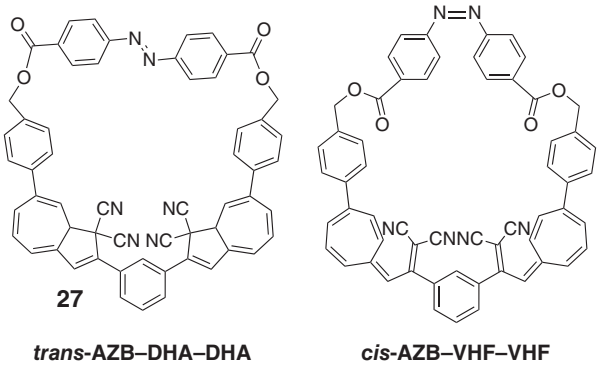


**Figure 17.18** Macrocycle **27** consisting of two DHA units and one *trans*-azobenzene unit (***trans*-AZB DHA–DHA**) and its fully isomerized isomer, ***cis*-AZB VHF–VHF**. Source: Modified from Vlasceanu et al. [33].

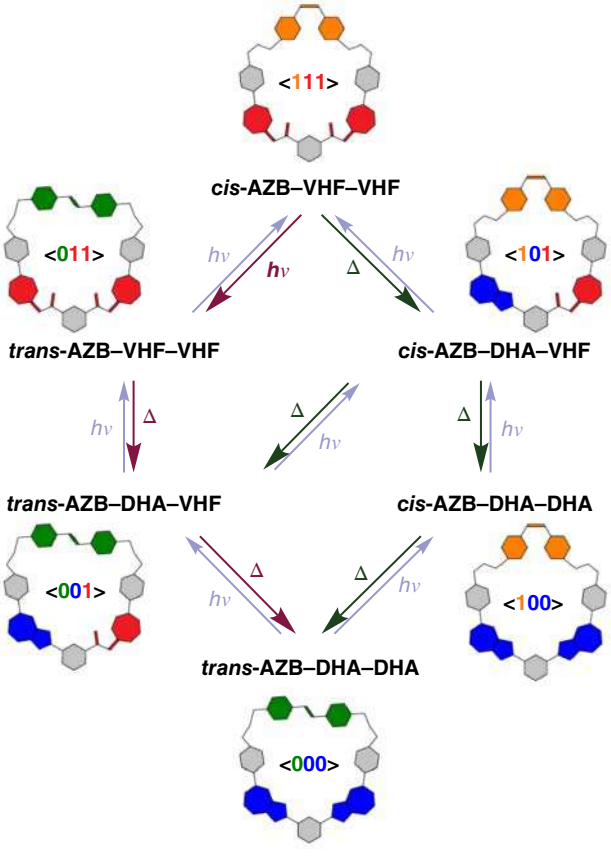


**Figure 17.19** Various states of macrocycle **27**. Binary numbers 1 and 0 are used to specify the individual DHA(**0**)/VHF(**1**) and *trans*-AZB(**0**)/*cis*-AZB(**1**) states. DHA and VHF are schematically shown in blue and red colors, respectively, while *trans*-AZB and *cis*-AZB are schematically shown in dark green and orange colors, respectively. Irradiation at 365 nm (light-blue arrows); irradiation at 410 nm (maroon arrow). Source: Vlasceanu et.al. 2018 [33] / with permission of John Wiley & Sons.

states. Irradiation of ***trans*-AZB–DHA–DHA** (⟨**000**⟩) with 365-nm light gave a simultaneous isomerization of *trans*-to *cis*-AZB as well as both DHAs to VHFs, leading to a state predominated by ***cis*-AZB–VHF–VHF** (⟨**111**⟩). This state may be formed from any of the paths highlighted by light-blue arrows in Figure 17.19. Subsequent irradiation at 410 nm stimulated the *cis*-AZB $n \rightarrow \pi^*$ transition, and a resulting photostationary state dominated by ***trans*-AZB–VHF–VHF** (⟨**011**⟩); corresponding to the maroon-colored reaction pathway at top left of Figure 17.19. The thermal isomerization of VHF–VHF to DHA–DHA could be initiated from one of the two starting points ***trans*-AZB–VHF–VHF** (⟨**011**⟩) (maroon-colored arrows) or ***cis*-AZB–VHF–VHF** (⟨**111**⟩) (dark green-colored arrows). In each case, the conversion occurred stepwise via an intermediate DHA–VHF. Thus, the relaxation of ***cis*-AZB–VHF–VHF** to ***trans*-AZB–DHA–DHA** initially proceeded via a fast decay (half-life of 36 minutes at 30 °C in MeCN) followed by a much slower process (half-life of 1900 minutes at 30 °C). In fact, conversion of half of the VHF species to DHA (one moiety per macrocycle) was observed before any significant switching of *cis*-AZB to *trans*-AZB. This first event was thus assigned to relaxation of ***cis*-AZB–VHF–VHF** (⟨**111**⟩) to ***cis*-AZB–DHA–VHF** (⟨**101**⟩). Relaxation of ***trans*-AZB–VHF–VHF** (⟨**011**⟩) to ***trans*-AZB–DHA–DHA** (⟨**000**⟩) also proceeded via a fast and a slow thermal decay process, which accounts for two VHF-to-DHA isomerizations, exhibiting half-lives of 31 and 620 minutes at 30 °C. When comparing the two pathways from ***cis*-AZB–VHF–VHF** to ***trans*-AZB–DHA–DHA**, one fully thermally activated and the other first light-activated and then thermally, the kinetics of the first VHF-to-DHA ring closure, $\langle \boldsymbol{x}\mathbf{11} \rangle \rightarrow \langle \boldsymbol{x}\mathbf{01} \rangle$, is unaffected by the state of AZB; $\boldsymbol{x} = \mathbf{1}$ (*cis*) or **0** (*trans*). The major effect of *cis*-/*trans*-AZB isomerization, however, is on the second VHF-to-DHA ring closure, $\langle \boldsymbol{x}\mathbf{01} \rangle \rightarrow \langle \boldsymbol{x}\mathbf{00} \rangle$.

### 17.5.3 DHA–Norbornadiene Conjugates

A selection of molecules where the DHA was connected to the NBD photoswitch, using Sonogashira couplings, has been reported [34]. NBD undergoes upon irradiation an intramolecular [2+2] cycloaddition to form a quadricyclane (QC) isomer that thermally returns to the more stable NBD. Compound **28** shown in Figure 17.20 presents one example of a DHA–NBD conjugate. This compound exhibits an absorption maximum at 392 nm, which is significantly red-shifted relative to that of the parent **DHA**. By first irradiating with 450-nm light and thereafter with 320-nm light, it was possible to stepwise convert the DHA and NBD units into VHF and QC units, respectively. It was, however, not possible to convert the NBD before the DHA by using lower-wavelength light (290 nm). Thus, orthogonal photoswitching was not obtained. The QC and VHF units were found to return to the original NBD and DHA units with estimated half-lives of 11 and 70 minutes, respectively, in toluene at 50 °C.

## 17.6 Conclusions

The ability to fully isomerize DHA into VHF by light and the quantitative thermally activated back reaction from VHF to DHA have made the DHA/VHF system

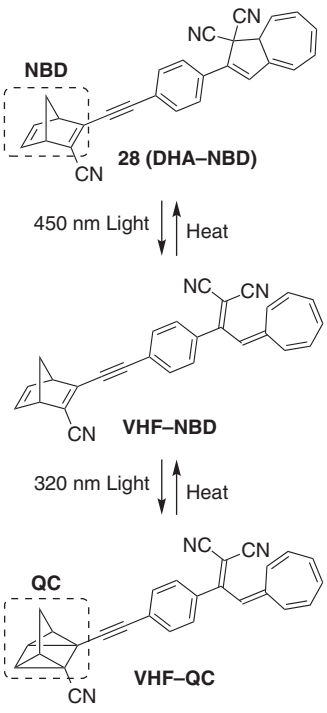


**Figure 17.20** Stepwise photoswitching of dihydroazulene–norbornadiene (DHA–NBD) conjugate.

an interesting photo-/thermo-switch for molecular electronics. Synthetic protocols were developed for regioselectively functionalizing DHA at positions C2 and C7, which have allowed introduction of electrode-anchoring groups. Depending on the character of these anchoring groups, a variety of switchable junctions have been obtained, all of which showed light-controlled conductance switching. For coherent electron transport, the conjugation along the molecular wire – cross-conjugation vs. linear conjugation – can be used as a guideline to predict low- and high-conducting isomers. The combination of DHA with other functional units, including other photoswitches or new hybrid switches, and controlled self-assembly of such systems, may provide more advanced functional devices in the future.

## References

**1** (a) Nielsen, M.B. (ed.) (2014). *Organic Synthesis and Molecular Engineering*. Wiley. (b) Moth-Poulsen, K. (ed.) (2016). *Handbook of Single-Molecule Electronics*. Jenny Stanford Publishing.

**2** Mativetsky, J.M., Pace, G., Elbing, M. et al. (2008). *J. Am. Chem. Soc.* 130: 9192–9193.

**3** (a) Kronemeijer, A.J., Akkerman, H.B., Kudernac, T. et al. (2008). *Adv. Mater.* 20: 1467–1473. (b) van der Molen, J.S., Liao, J., Kudernac, T. et al. (2009). *Nano Lett.* 9: 76–80.

**4** Hopf, H. and Sherburn, M.S. (eds.) (2016). *Cross-Conjugation: Modern Dendralene, Radialene and Fulvene Chemistry*. Wiley-VCH.

**5** (a) Mayor, M., Weber, H.B., Reichert, J. et al. (2003). *Angew. Chem. Int. Ed.* 42: 5834–5838. (b) Solomon, G.C., Andrews, D.Q., Van Duyne, R.P. et al. (2008). *J. Am. Chem. Soc.* 130: 7788–7789. (c) Solomon, G.C., Bergfield, J.P., Stafford, C.A. et al. (2011). *Beilstein J. Nanotechnol.* 2: 862–871. (d) Arroyo, C.R., Tarkuc, S., Frisenda, R. et al. (2013). *Angew. Chem. Int. Ed.* 52: 3152–3155.

**6** Mrozek, T., Ajayaghosh, A., and Daub, J. (2001). Optoelectronic Molecular Switches Based on Dihydroazulene-Vinylheptafulvene (DHA-VHF). *Molecular Switches* (ed. B.L. Feringa), 63–106. Weinheim, Germany: Wiley-VCH.

**7** Nielsen, M.B., Ree, N., Mikkelsen, K.V. et al. (2020). *Russ. Chem. Rev.* 89: 573–586.

**8** (a) Daub, J., Knöchel, T., and Mannschreck, A. (1984). *Angew. Chem. Int. Ed. Engl.* 23: 960–961. (b) Görner, H., Fischer, C., Gierisch, S. et al. (1993). *J. Phys. Chem.* 97: 4110–4117.

**9** Broman, S.L., Brand, S.L., Parker, C.R. et al. (2011). *Arkivoc* ix: 51–67.

**10** Parker, C.R., Tortzen, C.G., Broman, S.L. et al. (2011). *Chem. Commun.* 47: 6102–6104.

**11** Cacciarini, M., Vlasceanu, A., Jevric, M. et al. (2017). *Chem. Commun.* 53: 5874–5877.

**12** (a) Cacciarini, M., Broman, S.L., and Nielsen, M.B. (2014). *Arkivoc* i: 249–263. (b) Broman, S.L. and Nielsen, M.B. (2014). *Phys. Chem. Chem. Phys.* 16: 21172–21182.

**13** (a) Cacciarini, M., Skov, A.B., Jevric, M. et al. (2015). *Chem. Eur. J.* 21: 7454–7461. (b) Cacciarini, M., Jevric, M., Elm, J. et al. (2016). *RSC Adv.* 6: 49003–49010. (c) Andersen, D., Kilde, M.D., Kadziola, A. et al. (2018). *Helv. Chim. Acta* 101: e1800153.

**14** Broman, S.L., Kushnir, O., Rosenberg, M. et al. (2015). *Eur. J. Org. Chem.* 2015: 4119–4130.

**15** Skov, A.B., Broman, S.L., Gertsen, A.S. et al. (2016). *Chem. Eur. J.* 22: 14567–14575.

**16** Gobbi, L., Seiler, P., and Diederich, F. (2001). *Helv. Chim. Acta* 84: 743–776.

**17** (a) Petersen, M.Å., Kilså, K., Kadziola, A. et al. (2007). *Eur. J. Org. Chem.* 2007: 1415–1418. (b) Petersen, M.Å., Broman, S.L., Kadziola, A. et al. (2009). *Eur. J. Org. Chem.* 2009: 2733–2736. (c) Broman, S.L., Petersen, M.Å. et al. (2010). *J. Am. Chem. Soc.* 132: 9165–9174. (d) Kilde, M.D., Broman, S.L., Kadziola, A. et al. (2016). *Synlett* 27: 450–454.

**18** Mazzanti, V., Cacciarini, M., Broman, S.L. et al. (2012). *Beilstein J. Org. Chem.* 8: 958–966.

**19** Kilde, M.D., Hansen, M.H., Broman, S.L. et al. (2017). *Eur. J. Org. Chem.* 2017: 1052–1062.


**20** (a) Reed, M.A., Zhou, C., Muller, C.J. et al. (1997). *Science* 278: 252–254. (b) Xu, B. and Tao, N.J. (2003). *Science* 301: 1221–1223. (c) Ulrich, J., Esrail, D., Pontius, W. et al. (2006). *J. Phys. Chem. B* 110: 2462–2466.
**21** Broman, S.L., Lara-Avila, S., Thisted, C.L. et al. (2012). *Adv. Funct. Mater.* 22: 4249–4258.
**22** Jevric, M., Broman, S.L., and Nielsen, M.B. (2013). *J. Org. Chem.* 78: 4348–4356.
**23** Huang, C., Jevric, M., Borges, A. et al. (2017). *Nat. Commun.* 8: 15436.
**24** Lara-Avila, S., Danilov, A., Kubatkin, S. et al. (2011). *J. Phys. Chem. C* 115: 18372–18377.
**25** Olsen, S.T., Hansen, T., and Mikkelsen, K.V. (2015). *J. Phys. Chem. C* 119: 14829–14833.
**26** Li, T., Jevric, M., Hauptmann, J.R. et al. (2013). *Adv. Mater.* 25: 4164–4170.
**27** Pathem, B.K., Zheng, Y.B., Morton, S. et al. (2013). *Nano Lett.* 13: 337–343.
**28** Santella, M., Mazzanti, V., Jevric, M. et al. (2012). *J. Org. Chem.* 77: 8922–8932.
**29** Martin, C.A., Ding, D., Sørensen, J.K. et al. (2008). *J. Am. Chem. Soc.* 130: 13198–13199.
**30** Daub, J., Gierisch, S., and Salbeck, J. (1990). *Tetrahedron Lett.* 31: 3113–3116.
**31** Achatz, J., Fischer, C., Salbeck, J. et al. (1991). *J. Chem. Soc., Chem. Commun.*: 504–507.
**32** Petersen, M.Å., Andersson, A.S., Kilså, K. et al. (2009). *Eur. J. Org. Chem.* 2009: 1855–1858.
**33** Vlasceanu, A., Koerstz, M., Skov, A.B. et al. (2018). *Angew. Chem. Int. Ed.* 57: 6069–6072.
**34** Kilde, M.D., Mansø, M., Ree, N. et al. (2019). *Org. Biomol. Chem.* 17: 7735–7746.

# 18 Emerging Molecular Photoswitches

Peter Gödtel and Zbigniew L. Pianowski

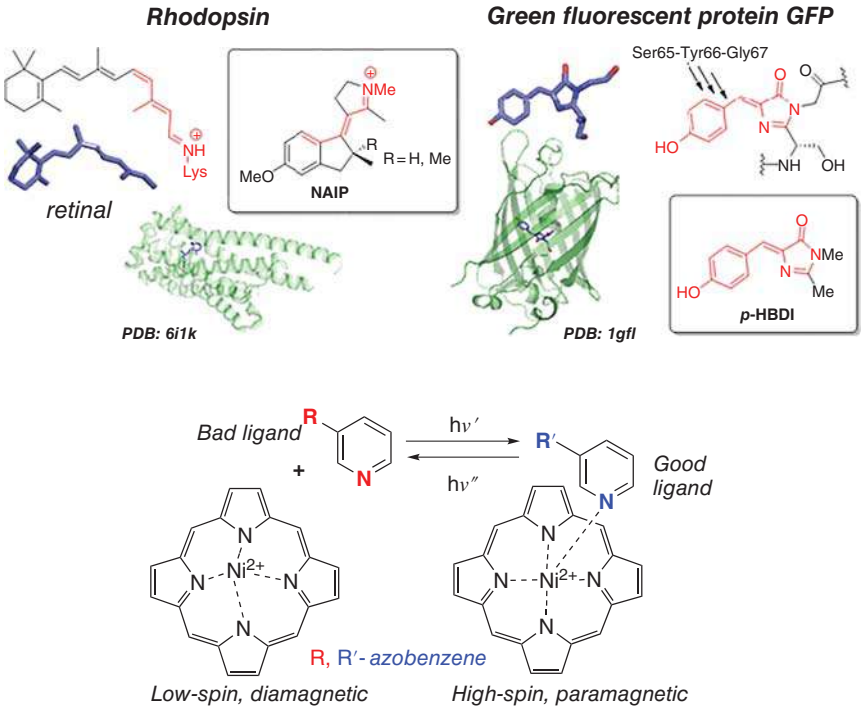


**Characteristic Features**

Apart from well-established classes of molecular photoswitches, like azobenzenes, diarylethenes, or spiropyrans, a number of novel photochromic motifs have been recently reported, often inspired by light-transforming systems that occur in nature. Several examples of such emerging photoswitches illustrated with selected applications, such as light-driven modulation of their bioactivity or magnetic properties, have been collected in this chapter.

**Key References**

Sampedro, D. et al. (2004). Design and photochemical characterization of a biomimetic light-driven *Z/E* switcher. *J. Am. Chem. Soc.* 126: 9349–9359.

Dong, J. et al. (2008). Isomerization in fluorescent protein chromophores involves addition/elimination. *J. Am. Chem. Soc.* 130: 14096–14098.

Lawson, M. and Eisler, S. (2012). Isoindolinone-based molecular switches. *Org. Biomol. Chem.* 10: 8770–8773.

Venkataramani, S., Jana, U., Dommaschk, M. et al. (2011). Magnetic bistability of molecules in homogeneous solution at room temperature. *Science* 331: 445–448.

# 18

# Emerging Molecular Photoswitches

*Peter Gödtel*[1] *and Zbigniew L. Pianowski*[1,2]

[1] *Karlsruhe Institute of Technology (KIT), Institute of Organic Chemistry IOC, Fritz-Haber-Weg 6, 76131, Karlsruhe, Germany*
[2] *Karlsruhe Institute of Technology (KIT), Institute of Biological and Chemical Systems – Functional Molecular Systems IBCS-FMS, Hermann-von-Helmholtz-Platz 1, 76344, Eggenstein-Leopoldshafen, Germany*

## 18.1 Introduction

Numerous classes of photochromic compounds – some established since decades, others reported relatively recently – have been individually described in preceding sections. However, novel types of chemical structures capable of reversible photoisomerization are reported every year. That includes not only previously unreported photochromic scaffolds [1] but also new application modes of existing photoswitches, like light-switchable molecular magnetism [2] or photoswitching in confined spaces [3]. Some of the new scaffolds are inspired by biological systems, others are designed, or unexpectedly discovered. Here we would like to focus on emerging photochromic residues, which were not covered by the previous chapters. Due to the broad variety of such reported systems, we have selected a few representative examples as an illustration of the more general phenomenon. We hope that this digest will inspire the readers to more detailed explorations.

## 18.2 Natural Chromophore Mimetics

### 18.2.1 Molecular Photoswitches Inspired by Retinal

Retinal is the most common light-receptive molecule in living organisms, e.g. as a component of the vertebrate visual pigment rhodopsin present in the human eye. Unsurprisingly, numerous researchers were motivated to analyze its photoisomerization mechanism [4] and to apply its principle in simplified photochromic systems with a variety of potential applications.

In 2004, the group of Olivucci reported [5] the computational design as well as the first synthesis and empirical characterization of the penta-2,4-dieniminium backbone containing protonated Schiff bases (PSBs) (Figure 18.1). This structural

*Molecular Photoswitches: Chemistry, Properties, and Applications*,
First Edition. Edited by Zbigniew L. Pianowski.


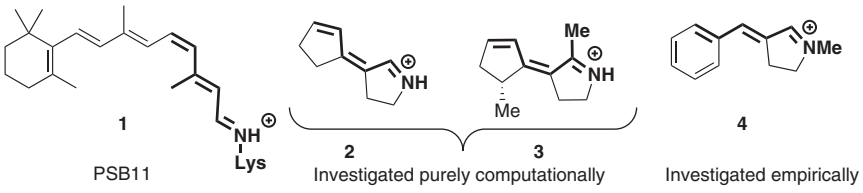


**Figure 18.1** PSB11 (left) inspired molecular PSB-photoswitches (right). While **2** and **3** were characterized purely computationally, **4** and several derivatives were synthesized and also investigated empirically.

motif was previously determined computationally to be a suitable analog to investigate the photophysical behavior of the 11-*cis*-retinal chromophore (PBS11) **1** of rhodopsin [6].

PSB11 is an exciting target for biomimetic photochromes, especially because of its high isomerization quantum yield (QY) of 0.67 while bound to rhodopsin (**Rh**), and its ultra-fast unidirectional switching mechanism, preserving vibrational coherence [7]. The excited state $S_1$, which is populated via a $\pi \rightarrow \pi^*$ transition, has a lifetime of about 150 fs and resolves into the all-*trans* isomer of Rh-bound retinal. In ethanolic solution, however, PSB11 exhibits a significantly lower QY of 0.25 and a longer lifetime of $S_1$, in the range of picoseconds [8]. It is therefore of great interest to design model systems of Rh-bound PSB11 which exhibit its highly favorable photophysical properties in a broader variety of solvents.

Further developments of PSBs were achieved with the support of *ab initio* calculations, using the complete active space self-consistent field (CASSCF) method and multiconfigurational second-order perturbation theory (CASPT2) [9]. In order to extend the π-system while keeping the number of possible torsional degrees of freedom equal to previous PSBs, the researchers concluded that annulation of a phenyl ring to the 4-(cyclo-pent-2-enylidene)-3,4-dihydro-2H-pyrrolinium cation (CPP) scaffold would constitute a logical synthetic target; the resulting photochromes were dubbed *N*-alkylated/-protonated indanylidene pyrroliniums (NAIPs/NHIPs). The NHIP photochrome **5** emerged out of the additional consideration of an incorporated methoxy group (Scheme 18.1). According to the researchers, installing this moiety in *para*-position to the 2*H*-pyrrolinium function would stabilize the benzyl-carbocation intermediate during synthesis and further promote the $S_0 \rightarrow S_1$ excitation through translocation of the delocalized positive charge of the iminium

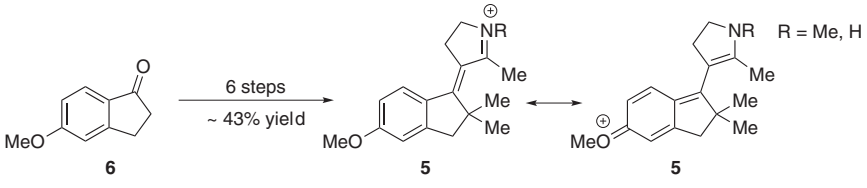


**Scheme 18.1** Commercially available precursor **6** for synthesis of NAIPs and NHIPs (left). Resonance structures, illustrating the charge translocation, promoting $S_0 \rightarrow S_1$ excitation (right) [10].

moiety. Indeed, simulations of **5** without the *p*-OMe function show a decreased change in dipole moment, as well as decreased charge translocation and $\lambda_{max}$ values [9, 10].

Through a series of further structural modifications, various NAIPs have been synthesized and characterized, which exhibit QYs of about 0.20 [11], values of 40%–60% of the native isomer in photostationary states (PSSs) [9, 11b], and sub-picosecond excited state lifetimes [12]. Introduction of a stereo center at the C2′ position (Scheme 18.2) led to predominantly unidirectional rotation during isomerization. First calculations of a few trajectories point towards favored rotations in opposite directions for each diastereoisomer, ***Z*-7** or ***E*-7**; the *Z*-isomer being more specific in its direction of rotation. At the current stage, however, these observations are purely of mechanistic and not statistical nature. Therefore, this system does not yet constitute a biomimetic molecular motor, although it is an important preliminary step for further optimization [11b].

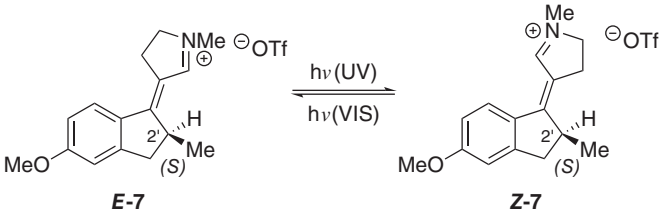


***E*-7** **Z-7**

**Scheme 18.2** *E/Z*-isomerization of the NAIP **7**, containing a stereo center at the 2′ position.

### 18.2.2 Molecular Photoswitches Inspired by the Green Fluorescent Protein (GFP)

Green fluorescent protein (GFP), originally found in the jelly fish *Aequorea victoria*, constitutes a widely employed biocompatible fluorescent probe, which can be genetically encoded and expressed in a broad spectrum of organisms, ranging from microbes to mammals [13]. The chromophore in GFP is formed through a post-translational autocatalytic cyclization of the three amino acids Ser65, Tys66, and Gly67, resulting in 4-(*p*-hydroxybenzylidene)-5-imidazole (*p*-HBI) **8** (Scheme 18.3). Interestingly, by mutagenesis and the resulting modifications of the

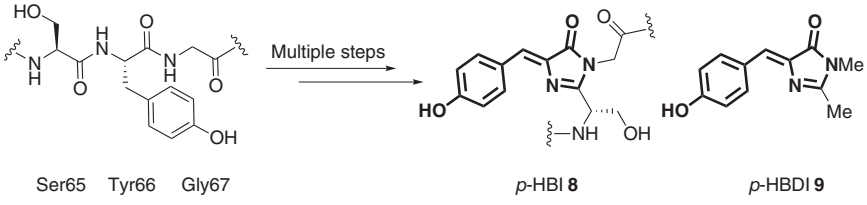


**Scheme 18.3** Schematic formation of the chromophore *p*-HBI **8** (highlighted in bold) in the wildtype of GFP over multiple steps, such as folding, cyclization, dehydration, and oxidation (left) [13]. General framework of the GFP chromophore, *p*-HBDI **9** (right).

amino acid's nature (and sometimes position), a whole palette of colors – from blue to deep red – can be obtained. Combinations of these GFP mutants often constitute genetically encoded FRET pairs, extensively used in molecular biology experiments worldwide [13].

The general, simplified framework of the GFP chromophore is often referred to as *para*-4-hydroxybenzylidene-2,3-dimethylimidazolone (*p*-HBDI) **9** [10, 14]. In GFP, this chromophore is located in a β-barrel cavity, which locks the double bond in place, resulting in a photochemically stable and very efficient fluorophore. In fact, *p*-HBDI exhibits a very pronounced loss of fluorescence in solution, which can be attributed to fast twisting of the central bond. This hypothesis is strongly supported by computational and empirical studies [15].

#### 18.2.2.1 Mechanistic Details of Thermal Relaxation

Benzylidine-2,3-dimethylimidazolones (BDI) with various substituents in the *para*-position were reported by the group of Tolbert in 2008. The native hydroxyl function was replaced with methoxy-, methyl-, chloride-, or hydrogen-substituents in the *para*-position, yielding a range of derivatives named *p*-XBDI (Figure 18.2) [16].

All *p*-XBDI derivatives undergo photoisomerization in a variety of solvents, with thermal back-isomerization occurring readily in DMSO-$d_6$. While thermal isomerization does not occur in pure benzene or acetonitrile, the addition of 1,4-diaza[2.2.2]octane (DABCO) results in a positive correlation of the reaction rate and the Hammett parameter σ for all but one *p*-XBDI. Furthermore, isomerization was observed to be linearly dependent on the base concentration over one order of magnitude. Therefore, the group proposed an addition–elimination mechanism for the reverse isomerization (Scheme 18.4).

Considering the well-established fluorescence blinking phenomenon in GFP [17], the addition–elimination mechanism might serve as one possible explanation for this peculiar behavior: as the crystal-structure of *mTFP0.7* shows, the glutamate

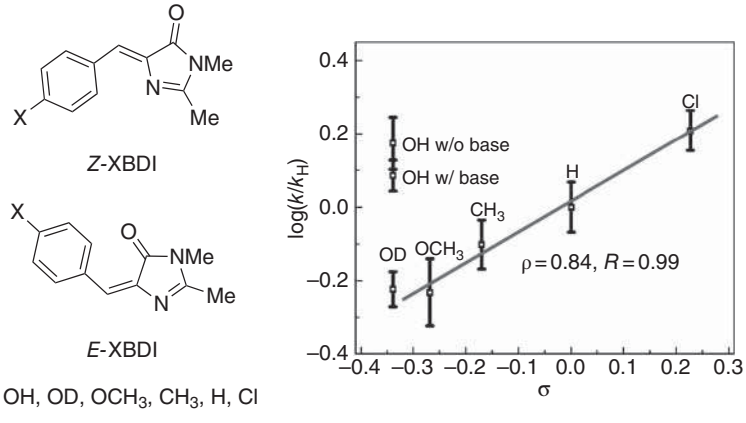


**Figure 18.2** Hammett σρ plot for *p-E*-XBDI thermal isomerization in $CD_3CN$ in the presence of 0.089 M DABCO; $k_H = 1.4\ 10^{-5}\ s^{-1}$. Source: Reproduced with permission from Dong et al. [16].

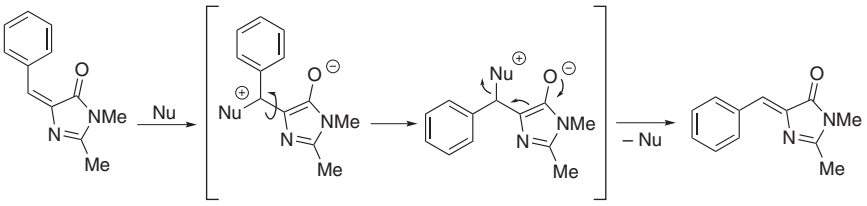


**Scheme 18.4** The addition–elimination mechanism involved in the thermal isomerization of *p*-XBDIs, as proposed by the Tolbert group [16].

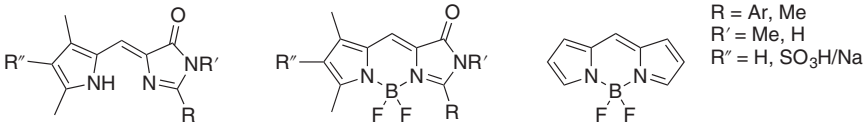


*Z*-**10** **11** **12**

**Figure 18.3** Nonfluorescent, heterocyclic analogs of *p*-HBDI *Z*-**10** become strong fluorophores upon $BF_3$ coordination (**11**) due to hampering of free rotation around the aryl-alkene bond. A similar process has been demonstrated for the well-known BODIPY fluorophores **12** [19].

residue Glu148 in close proximity to the chromophore coordinates a water molecule [18], which could serve as an appropriate nucleophile for the proposed mechanism. Thus, a back isomerization could be induced after *p*-HBDI **8** undergoes photoisomerization as a competitive process to its fluorescence.

Another evidence that free rotation around the aryl-alkene bond of the *p*-HBDI motif is responsible for the sharp decrease in fluorescence in vitro was delivered by Wu and Burgess. By complexing several nonfluorescent heterocyclic *p*-HBDI analogs *Z*-**10** with $BF_3$, they emulated the steric hindrance caused by the β-barrel of GFP. The resulting highly fluorescent complexes **11** (QY up to 0.89) were structurally analogous to the well-known BODIPY fluorophores **12** (Figure 18.3) [19]. Interestingly, the photoisomers *E*-**10**, formed upon UV-light irradiation (up to 75% *E*-**10** at $PSS_{365\,nm}$), also formed complexes with $BF_3$. However, their fluorescence was negligible, most likely due to the unfavorable geometry.

#### 18.2.2.2 Benzylidene–Oxazolones

Photoisomerization of unsaturated butyrolactones and analogs has already been reported over 50 years ago [20]. However, photochromism of structurally similar arylidene-substituted oxazolones, being synthetic intermediates on the way to *p*-HBDI, has been explored only in the last decade by the group of Sampedro [21]. The benzylidene-oxazolones **13** are readily prepared through a well-established oxazolone synthesis as pure *Z*-isomers in 30%–90% yields, depending on the aldehyde used (Scheme 18.5).

The same group studied these photochromes extensively regarding the relation of the substitution pattern with their photophysical properties. Oxazolones substituted with a heterocycle or a phenyl substituent containing an electron donating

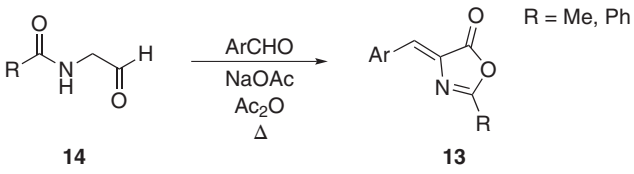


**Scheme 18.5** Schematic synthesis of GFP-inspired oxazolones **13**, as employed by the Sampedro group [21].

function, such as *p*-OMe, are reported to promote a shift in the *E*/*Z* isomer ratio in the $PSS_{UV(>290\ nm)}$ toward the *E*-isomer, while electron-withdrawing functions do not influence that ratio significantly. Furthermore, choosing an aromatic moiety as a substituent at the 2-position increases the ratio of *E*/*Z*-isomers significantly as well [21]. These photoswitches exhibit a QY of the *Z*→*E* photoisomerization of up to 0.25 and a QY of up to 0.11 for the reverse reaction (*E*→*Z*). Furthermore, isomer mixtures in the PSS are stable for several hours when heated to 50 °C. Only refluxing in toluene leads to a slow thermal isomerization to the thermodynamically favored *Z*-isomer [22].

Benzylidene–methyloxazolones (BMO) also exhibit aggregation-induced emission (AIE) with QYs of up to 0.50 and emission wavelengths of up to 635 nm in the solid state [14]. Restriction of intramolecular rotation and *Z*/*E*-isomerization in the crystalline phase leads to significant increases in QYs compared to the solution phase (QYs up to 0.004). Decreased torsional angles lead to increased planarity and thus the decay of $S_1$ through nonradiative processes like internal conversion is diminished. Furthermore, reduction of π–π interactions through bulky groups like tetraphenyl ethane (TPE) or triphenyl amine (TPA) inhibits excimer and exciplex formation, which in turn amplifies QYs (Figure 18.4).

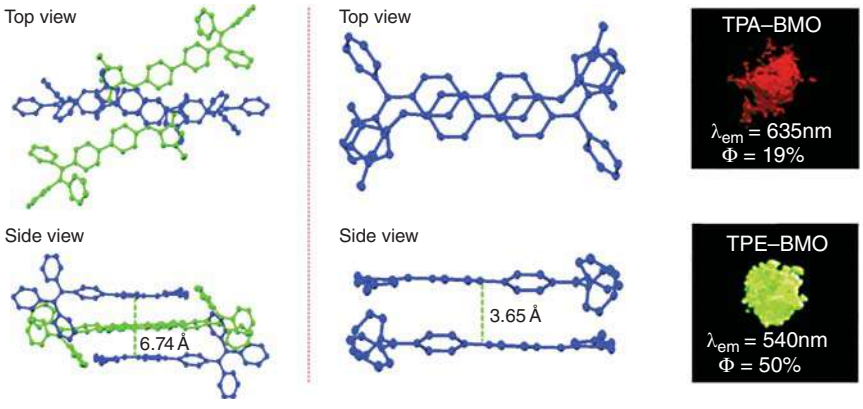


**Figure 18.4** Crystal structures of TPA-BMO and TPE-BMO, illustrating increased planarity, as well as reduced π−π interactions through introduction of bulky groups (left). Illuminated solid samples with their respective emission wavelength maxima and fluorescence QYs (right). Source: Reproduced from Jiang et al. [14], Figure 09, p 07/with permission of Royal Society of Chemistry.

### 18.2.2.3 Imidazolinone Derivatives

5-Arylhydantoins (5-AHT) can be synthesized by condensation of phenylpropynoic acid and urea, or by acid-catalyzed condensation of benzaldehydes with hydantoins, which in turn are obtained, e.g. by reaction of glyoxal with ureas. The latter method was employed by the Sampedro group to synthesize a range of 5-AHTs **15** with varying aryl substituents [23]. Methyl groups at the amidic nitrogen atoms increased solubility in common solvents and caused slight bathochromic shifts of the absorption maxima (Scheme 18.6).

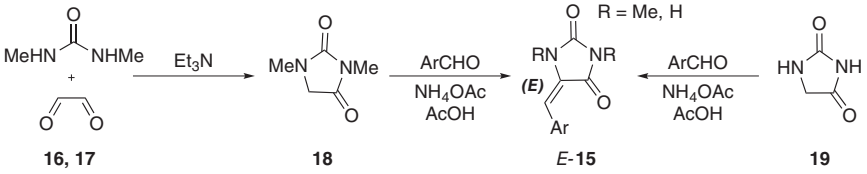


**Scheme 18.6** Schematic synthetic protocol for bis-*N*-methylated and non-*N*-substituted 5-AHTs **15**, by Martínez-López et al [23].

The thermodynamically stable *E*-isomers (depicted in Scheme 18.6) photoisomerize upon irradiation with UV light to mixtures with a ratio of the *Z*-photoisomers exceeding 60% in the PSSs in most cases. Some derivatives exhibit even quantitative $E \rightarrow Z$ switching. High thermal stability of the *Z*-isomers and photostability over multiple switching cycles were reported as well [23].

### 18.2.2.4 Photopharmacology of the Emerging Molecular Photoswitches

Photopharmacology is a rapidly growing area of application for molecular photoswitches [24]. Geometry changes of azobenzenes or flexibility differences in photoisomers of diarylethene have been broadly used to design systems with photoreversible changes of biological activity. Later, we want to demonstrate several examples of photopharmacological applications of emerging photochromic motifs, in particular photochromes that are based on the light-induced geometry reorientation of five-membered heterocyclic arylidene substituents.

An interesting application for switching antimicrobial activity was published by Contreras-García et al. Nalidixic acid and ciprofloxacin are quinolone-based gyrase inhibitors, the latter of which is being used clinically to treat a variety of grave bacterial infections. The researchers functionalized the antibiotic quinolones with 5-AHT (**20a**), or a phytochrome-derived unsaturated photochromic lactam (**20b**) (Figure 18.5a) [25].

All the phytochrome derivatives were thermally rather stable: heating to 110 °C over three days is required to completely revert the mixture to the native isomer, while the 5-AHT derivative **20a** decomposes over 70 °C. Additionally, solubility of the compounds in water is rather poor; however, compound **20b** could be rendered more water soluble by converting it to its sodium salt. Cytotoxicity against *Escherichia coli* (Minimum Inhibitory Concentration - MIC) was also found to differ up to twofold dilution between the native isomer **20b** and the isomer mixture in the

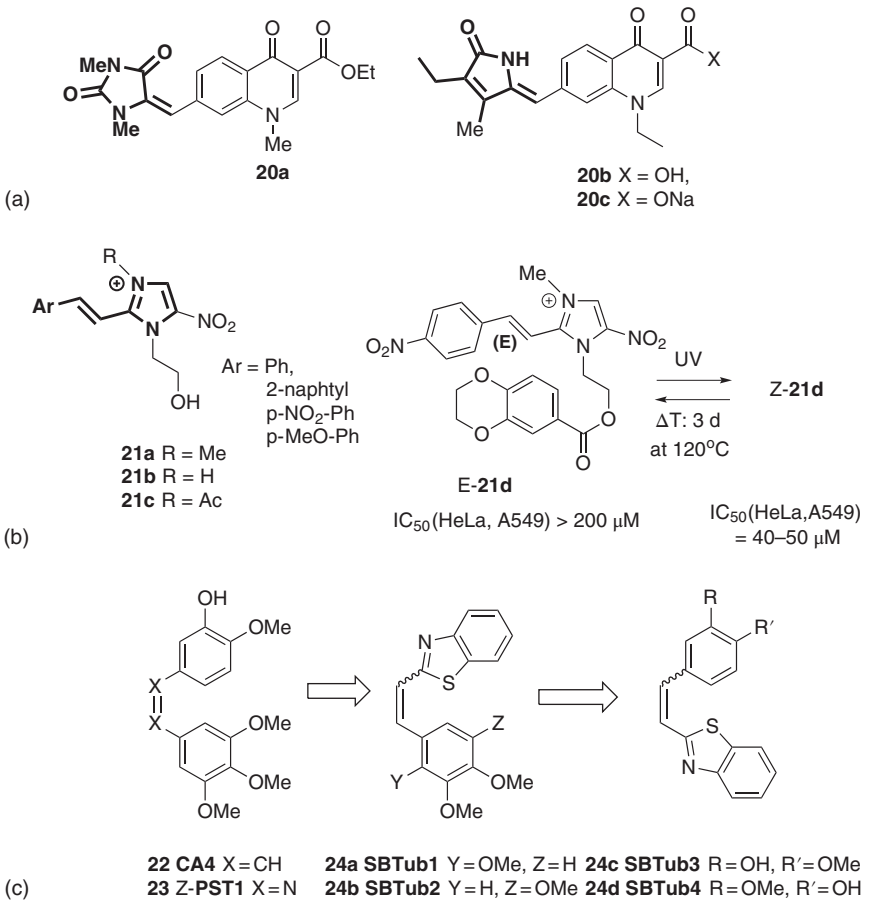


**Figure 18.5** Photopharmacological applications of the emerging switches. (a) 5-AHT containing quinolone **20a** and phytochrome-substituted quinolone as the protonated acid **20b** and the sodium salt **20c** were applied in photomodulation of antibacterial activity [25]; (b) imidazole-based metronidazole analogs **21a–d** – the compound **21d** exhibited significant difference in cytotoxicity against human cancer cells upon photoisomerization [26]; (c) photochromic inhibitors of microtubule dynamics **24a–d** based on the styrylbenzothiazole (SBT) photoswitch [27].

PSS (37% ***E*-20b**) (MIC (*Z*-isomer) = 16 mg $l^{-1}$/MIC (PSS) = 64 mg $l^{-1}$). While **20a** exhibits the highest reported PSS of 59% switched isomer, there is no discernible difference in MIC between the thermodynamically favored *E*-isomer and the isomer mixture in the PSS. The authors note, however, that the carboxylic function of ciprofloxacin and other drugs of the quinolone family has been shown to be crucial for appropriate efficacy.

Metronidazole is an antibiotic and antiprotozoan medication. The group of Sampedro functionalized it with arylidene residues [26]. The resulting photochromic imidazole derivatives **21a–d** (Figure 18.5b) demonstrated high photoisomerization efficiency under UV light irradiation. Interestingly, although

antimicrobial potency of the photoisomers was not determined, one of the derivatives (**21d**) exhibited a considerable difference in cytotoxicity against human cancer cell lines (HeLa, A549). Its thermally stable *E*-isomer did not elicit cytotoxicity at 200 μM concentration, while the equilibrium mixture (PSS) obtained upon UV light irradiation exhibited $IC_{50} = 44.06 \pm 2.52$ μM.

A series of combretastatin A-4 analogs with light-modulated cytotoxicity, based on the styrylbenzothiazole (SBT) photochrome, has recently been demonstrated by the group of Thorn-Seshold (Figure 18.5c) [27]. Combretastatin A-4 (CA4) **22** is a stilbene-based inhibitor of microtubule dynamics with low-nanomolar cytotoxic activity in its *Z*-configuration. By exchanging the central —C=C— to —N=N— bond, photochromic photostatins (PST) **23** have been previously designed as prospective light-activated anticancer photopharmacology agents [28]. In the current report, the azobenzene scaffold has been replaced by the rare photochromic motif of styrylbenzothiazoles (SBs). The resulting "SBTub" derivatives **24a–d** show longer thermal stability of the *Z*-photoisomer, and resistance against glutathione-driven reduction (or, more generally, intracellular reduction potential) as compared to the azobenzene-based PST. Moreover, the absorption peaks of **24a–d** do not overlap with the channel used for GFP visualization in biological systems, thus providing an orthogonal microtubule dynamics inhibitor.

#### 18.2.2.5 Boronated Acyl-Hydrazones

Another interesting class of heterocycle-bearing molecular photoswitches – boronated acyl-hydrazones (BOAHYs) – has recently been reported by Yu et al. [29]. These compounds exhibit aggregation-induced (AI) fluorescence in a very broad spectrum of emission wavelengths, tuneable by appropriate substituent choice. Equipping the arylhydrazone moiety with electron-donating functions causes larger bathochromic shifts of the emission band than substitution with the same functional group at the aldehyde moiety. All BOAHYs with electron-donating functions exhibited significant solvatochromism: an increased Stokes shift for an increase in polarity was observed, while the QYs decrease for an increasingly polar medium (0.72 in toluene to 0.03 in MeOH). Furthermore, AIE studies were performed, and the researchers were able to show up to 30-fold enhanced fluorescence in acetonitrile/water mixtures, at water fractions of $f_w = 95\%$. Additionally, PSSs were reported to be up to 60% switched *E*-isomer, and the thermal reverse reaction was found to occur in a matter of days at room temperature in $CDCl_3$. Interestingly, the isomer mixture of **25b** was shown to increase fluorescence intensity and the bathochromic shift of the emission maximum [29] (Scheme 18.7).

## 18.3 Isoindolinones

Multi-stable molecular photoswitches are described rather rarely, even though such systems would have great potential for applications in material sciences and information technology [30]. Isoindolinones (IINs) are one example of such multi-state photochromic molecules: obtained primarily in their thermodynamically *all-Z*-form

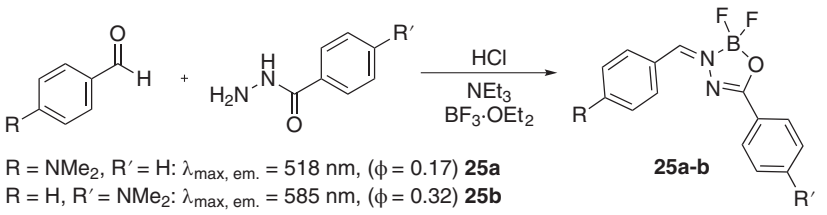


**Scheme 18.7** Schematic synthesis of BOAHYs **25a** and **25b** and their respective emission wavelength maxima, as well as the fluorescence QYs, illustrating the effect of varying the substituents R and R' [29].

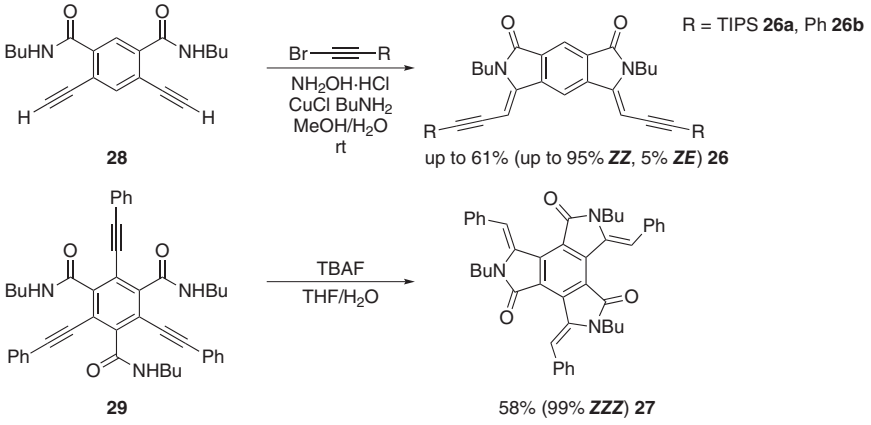


**Scheme 18.8** Schematic synthesis of bis- and trisalkene isoindolinones **26a,b** and **27**, as reported by the group of Eisler [31].

from amide-containing bis- or tris-alkynes (Scheme 18.8), these molecules exhibit several favorable switching properties [31].

Upon irradiation of compound **26a** in $CDCl_3$ with UV light of 365 nm for several hours, an isomer ratio of 50% ***EE*-26a**, 45% ***ZE*-26a**, and 5% ***ZZ*-26a** is detectable. Subsequent irradiation with blue light of 470 nm results in a high yielding isomerization to 95% ***ZE*-26a** and 5% ***ZZ*-26a**. This mixture can then be cycled between these two ratios, using 411 nm and 470 nm, respectively (Scheme 18.9). Thermally induced isomerization to the native **ZZ**-isomer **26a** was neither observed in $CDCl_3$ at ambient temperature nor at 60 °C, whereas heating in DMF to 120 °C induced minor decomposition [31a].

In their subsequent work, Eisler and her group reported a four-state switch based on the same design, yielding the propeller-shaped tris-IIN **27** (Scheme 18.10) [31b]. This system exhibits a remarkable temperature dependency of its equilibrium photoisomer ratio in the PSS: Irradiation with a wavelength of 365 nm at room temperature results in a ratio of 1.0 : 2.4 : 1.4 : 0.1 (**ZZZ**/**ZZE**/**ZEE**/**EEE-27**). These ratios increase in favor of the switched species up to 1.0 : 3.0 : 3.6 : 0.5 (**ZZZ**/**ZZE**/**ZEE**/**EEE-27**) at −40 °C. Although temperature-sensitive PSS photoisomer ratios are not surprising, considering that fast thermal relaxation can easily

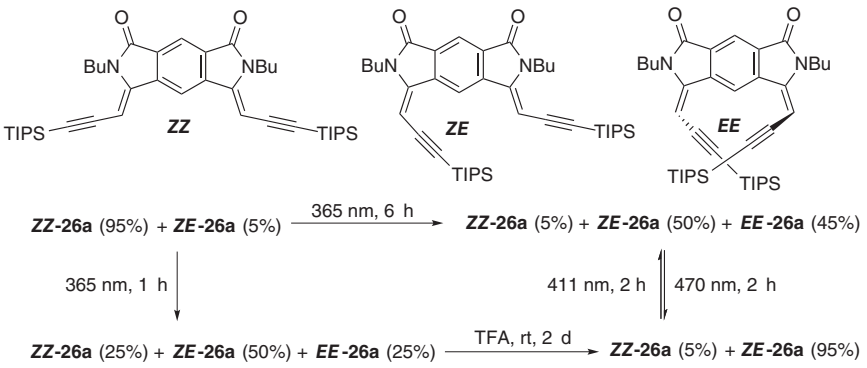


**Scheme 18.9** Switching scheme of compound **26a** between three isomeric mixtures. Source: Reproduced from Lawson and Eisler [31a] with permission from the Royal Society of Chemistry.

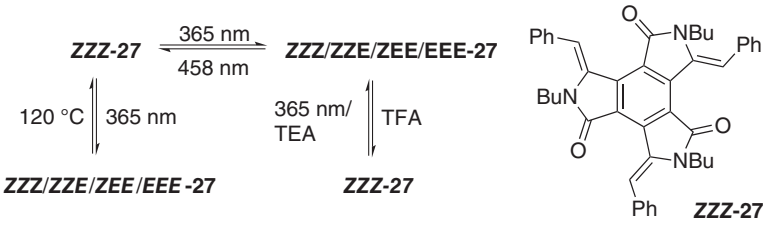


**Scheme 18.10** Switching scheme of tris-IIN **27** with light, temperature, and pH stimuli (TEA - triethylamine). Source: Figure adapted from Estey et al. [31b].

occur for numerous photoswitches at room temperature, the effect described here is rather unexpected: For the tris-IIN **27**, a change in the isomer ratio upon heating only occurs at temperatures over 120 °C, which is a proof of exceptional thermal stability. Back-switching to a ratio of 1.0 : 3.0 : 0.1 : 0.0 (**ZZZ**/**ZZE**/**ZEE**/**EEE-27**) occurs upon irradiation at 458 nm; complete conversion to the native ZZZ-isomer can be achieved with the addition of TFA to the isomer mixture.

A minor drawback of IINs, however, is their sensitivity toward oxygen upon prolonged irradiation with UV light, likely resulting in [2+2] cycloaddition products through the reaction of $^1O_2$ with the olefin functions. Prior purging of the solvents with $N_2$ allows for cycling through the PSSs without any observable degradation [31b].

## 18.4 Iminothioindoxyls

Another class of molecular photoswitches – iminothionidoxyls (ITIs) – arose from the desire to design molecular photoswitches that combine the favorable photophysical properties of azobenzenes and indigoid switches. These properties include large

band separation of the isomers, absorption of both isomers in the visible region, and improved solubility in water [32].

ITIs can be thought of as a blend of hemithioindigos (HTIs) and azobenzenes. They can be synthesized by condensation of nitrosobenzene and thioindoxyl, or by Passerini-type reaction (Scheme 18.11).

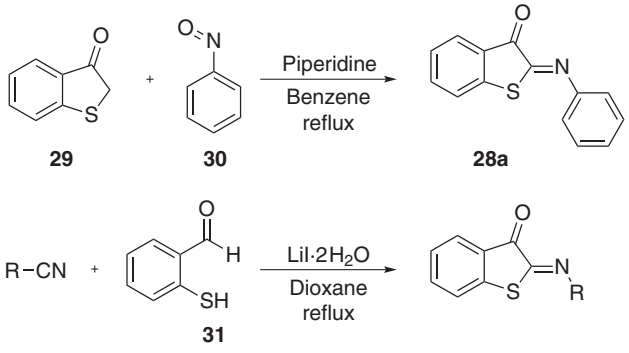


**Scheme 18.11** Synthethic routes to iminothioindoxyl (ITI) photoswitches [32].

Hoorens et al. [32] reported on ITIs with various electron-withdrawing and -donating substituents in the *para*-position with respect to the imine function. The large band separation of around 100 nm was observed in different solvents. Computational data indicate that this immense bathochromic shift is supposed to be observable due to a destabilization of the HOMO in the more twisted *E*-isomer and thus a diminished energy gap for a $\pi \rightarrow \pi^*$ transition.

Electron-donating groups (EDGs), such as *p*-OMe and *p*-Me, amplify this twisting around the N=C bond while simultaneously decreasing the twist of the C—N bond and thus planarizing the molecule. In combination, these effects can be interpreted as an explanation for the bathochromic shift of ITIs equipped with EDGs with respect to ITIs containing electron-withdrawing groups (EWGs).

The thermal half-life of ITIs at room temperature lies in the millisecond range, with a clear correlation between a decrease in half-life for increased solvent polarity. Comparison to the half-lifes of the *E*-isomers in the range of days or months observed for HTI suggests that, in the case of *E*-ITI, the nitrogen undergoes rapid inversion – an effect which also explains the thermal instability of *Z*-azobenzenes and *E*-imines. This was also corroborated by a very recent report, where protonation of this nitrogen atom increases thermal lifetime of the *E*-isomer up to 3 orders of magnitude, with concomitant bathochromic shift of the absorption (Figure 18.6) [33].

Reisomerization of the neutral *E*-**ITIs** can be promoted with irradiation using light of 595 nm wavelength. However, the fast thermal relaxation to the *Z*-isomer at room temperature overshadows this effect. Upon protonation, mutual switching with green (526 nm) and red (652 nm) light has been observed (Figure 18.6, bottom right).

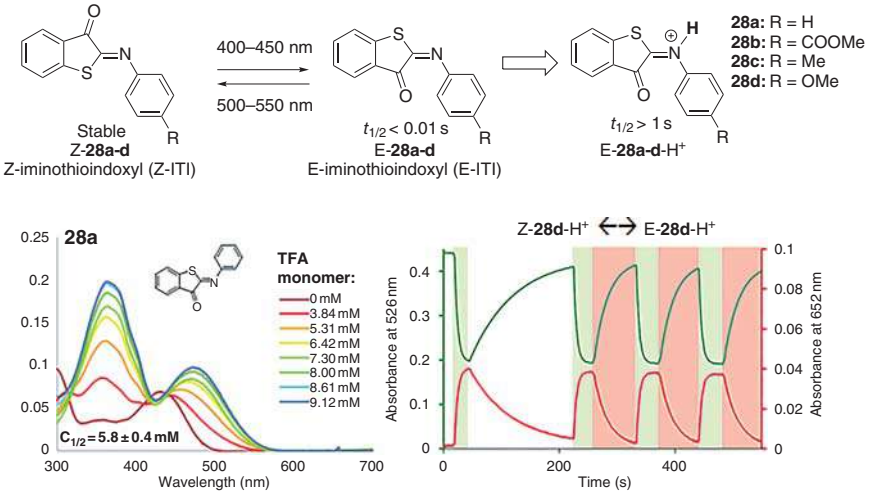


**Figure 18.6** Iminothioindoxyl (ITI) photoswitches as a structural blend between azobenzenes and indigoids. *Top*: Photoisomerization of the stable *Z*-**28** isomer with visible light results in short-living *E*-**28**. Protonation hampers the rapid nitrogen inversion and increases the lifetime of *E*-**28**-H$^+$ isomers by over three orders of magnitude; *Bottom left*: UV–vis spectrum of the unsubstituted ITI **28a** under neutral conditions and upon protonation; *Bottom right*: mutual photoisomerization of the protonated **28d**-H$^+$ with green (*Z*→*E*) and red (*E*→*Z*) light; Source: Medved et al. [33].

## 18.5 Photoswitching of Molecular Magnetism

The first part of this chapter described a selection of novel photochromic motifs, their properties, and prospective applications. In its final section, we will describe a novel paradigm for application of established azobenzene photoswitches as an emblematic

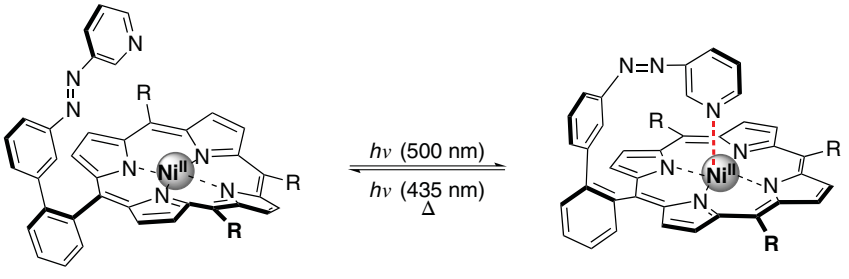


**Scheme 18.12** Photoinduced *E*-/*Z*-isomerization of the "record player" – azopyridine-substituted Ni$^{2+}$-tris(pentafluorophenyl)porphyrin **32**. The electron-withdrawing pentafluorphenyl groups have been chosen to ensure that spin-switching can occur with the coordination of only one additional axial ligand; Ni$^{2+}$ was employed since it is more stable under air than, i.e. Fe$^{2+}$, and can be simulated more precisely using DFT calculations [34]. Source: Figure adapted from Venkataramani et al. [2].

example of creating a new area of application from transforming light into an effect at the molecular level.

In 2011, the group of Herges reported on photo-controllable magnetism in homogenous solution: A $Ni^{2+}$-tris(pentafluorophenyl)porphyrin complex, equipped with an azopyridine functionality **32**, dubbed the "record player," allowed for reversible *E*-/*Z*-isomerization of the azo-bond using light of 500 and 435 nm, respectively (Scheme 18.12) [2]. Formation of the metastable *Z*-conformer leads to an increase in the coordination number of $Ni^{2+}$, from $n = 4$ of the square-planar complex to the $n = 5$ square-pyramidal complex of $Ni^{2+}$. This light-driven coordination-induced spin-state switching (LD-CISSS) allows for generation of an effective magnetic moment of $\mu_{eff} \approx 3\ \mu_B$ as well as turning off the effective magnetic moment completely. This reversible process is repeatable for more than 10 000 cycles without any signs of degradation, even at room temperature and irradiation under ambient air. The discovery of single-molecular manipulation regarding magnetic bistability broke down the notion that this behavior can only be found in bulk materials of transition metal complexes.

Thus far, there are two conceptual options for designing photo-sensitive molecular spin-switches:

Photodissociable Ligands (PDLs): Shortly after their initial discovery, the same group reported on a $Ni^{2+}$-tetrakis(pentafluorophenyl)porphyrin-complex, additionally coordinated with 3,3′-azopyridines bearing bulky substituents in the *para*-positions. Construction of the photochromic ligand causes significant differences in binding constants between photoisomers. This, in turn, leads to reversible switching of the magnetic properties upon alternate illumination with 365 and 455 nm light, resulting in 86% and 11% of the *Z*-isomer, respectively (Figure 18.7). This effect is, however, negligible in case of the respective 2,2′- and 4,4′-azopyridines, due to less favorable combination of particular steric and electronic effects [34].

An optimized ligand based on the phenylazoimidazole scaffold has been reported four years later (Figure 18.7) [35]. High basicity and nucleophilicity of the *N*-methylimidazole, as well as additional steric hindrance appended at the phenyl ring through *m*-$^t$Bu substituents, assure that binding to the porphyrin complex occurs almost exclusively in the *E*-isomer of the ligand **34**. The electron-donating *p*-OMe group improves the switching efficiency (up to 98% *Z*-isomer at 365 nm and 51% *E*-isomer at 525 nm, after 20 minutes irradiation). As a result, 19% of the paramagnetic $Ni^{2+}$ is generated in the PSS of 365 nm, and 89% of the same form is present in the PSS of 525 nm.

Tethered Ligands ("Record Players"): Examples of these species include **32**, the first photoresponsive spin-switch, and more recently reported *p*-substituted azopyridines, which achieve almost quantitative PSS for either isomer at wavelengths above 400 nm, as well as high conversion to >85% of the paramagnetic $Ni^{2+}$ upon irradiation [36]. Furthermore, no fatigue after 100 000 switching cycles and no degradation in the presence of glutathione were observed, which is a vital

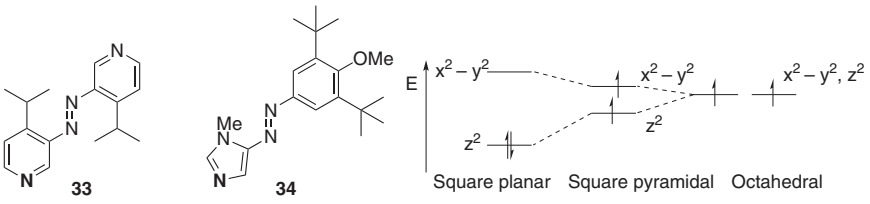


**Figure 18.7** Left: The most efficient photodissociable ligands (PDL) for spin-switching in $Ni^{2+}$-porphyrins based on the core of *E*-3,3′-azopyridine (**33**) or *E*-phenylazoimidazole (**33**) as their respective coordinating photoisomers; the coordinating nitrogen atom is highlighted in bold. Frontier orbitals of varying coordination geometries for $Ni^{2+}$ ions, resulting in a transition from low spin to high spin, are also depicted (right) [34, 35].

prerequisite for in vivo applications. While switching efficiency might generally be higher for the "record player" design and the thermal half-life of >1 year at room temperature surpasses that of PDLs, intermolecular coordination at large concentrations can occur and impede switchability [35].

### 18.5.1 Switching MRI Responsiveness

Besides $Ni^{2+}$, $Fe^{3+}$-porphyrin complexes also exhibit spin-switchability, while being neither oxygen nor water sensitive. These systems could be used to model the cytochrome P450 (CYP450), since this type of spin switching – induced through substrate binding – is the first step in the catalytic cycle of naturally occurring cytochrome enzymes [37]. Switching to the high spin state in the reported species (Figure 18.8) leads to a change in redox potential of c. 60 mV and an increase in spin–lattice relaxation time of water protons by a factor of 15. These properties point toward an application in (photo-switchable) catalysis [38].

Generally, these photoresponsive transition-metal porphyrin complexes exhibit exciting properties for the use of switchable MRI contrast agents. Photo-sensitive

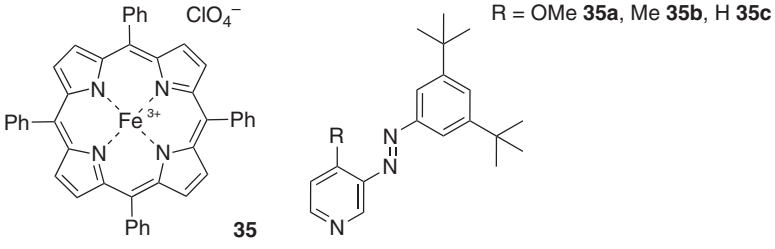


**Figure 18.8** $Fe^{3+}$-porphyrin complex and accompanying PDL in its coordinating E-form, responsible for light-driven spin-switching and the resulting change in redox potential [37].

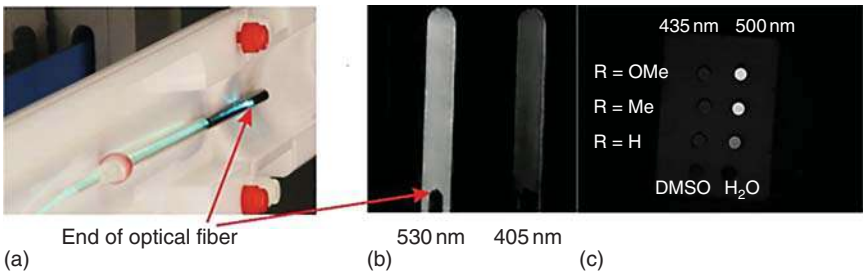


**Figure 18.9** Experimental setup for contrast switching in an MRI machine (a) and MRI images recorded after irradiation of **35a** with 530 and 405 nm, respectively (b). MRI-contrast comparison of varying substituents on the diazopyridine PDL, after irradiation with 435 and 500 nm in DMSO and water (c). Source: Dommaschk et al. [36], Figure 05,06, p 04/with permission of American Chemical Society.

$Gd^{3+}$ chelators in the form of spiropyrans had already been investigated prior to this discovery: these complexes exhibit a change of relaxivity of about 20% [39, 40]. However, a change from a completely MRI-silent diamagnetic to an MRI-responsive paramagnetic species, as reported by the Herges group, can provide a more efficient control: a change with a factor of up to 6.7 in relaxivity was determined upon irradiation with 435 and 500 nm of the porphyrin complexes, based on the "record player" design **32** (Scheme 18.12), as well as a visually clear contrast change observable through MRI measurements (Figure 18.9) [36].

## 18.6 Summary

In this chapter, we wanted to demonstrate selected examples of novel molecular photoswitches, which go beyond the established scaffolds and scope of applications. We have chosen bioinspired systems derived from the photoswitching of retinal in rhodopsin and from the fluorophore of GFP. The latter efficiently emits light upon steric congestion, and its nonradiative excitation decay in solutions inspired the design of a structurally related photoswitch. Further emerging photochromic motifs, mainly based on the *E/Z* photoisomerization of five-membered heteroaromatic arylidenes around the alkene bond, have been shown – together with applications in the photopharmacology area. Finally, we also decided to depict the idea of switching magnetic properties of single molecules using light via photochromic antenna. We believe that this digest provided readers with an interesting overview over the perspectives of design and applications of novel photochromic motifs and will be a good introduction to the following parts of this book (Table 18.1).

**Table 18.1** Summary Table of the different classes of photoswitches, discussed in this chapter.

| Thermodynamically Favored isomer | $\lambda_{irr.,\ forward}$ PSS[a] | $\lambda_{irr.,\ reverse}$ PSS[a] | Thermal $t_{1/2}$[a] | $QY_{iso.}$[a] | Special features |
|---|---|---|---|---|---|
| 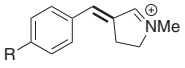 <br>***E***-Arylidene imines | 360 nm<br>R = *p*-$NO_2$, ***Z*** 60% [5] | 223 nm<br>R = *p*-$NO_2$, ***E*** 99% [5] | n/a, ***Z***-Isomers can be isolated [5] | $6 \times 10^{-3}$ (forward) [5] | • First iteration of a rhodopsin-bound 11-*cis*-retinal model system [5] |
| 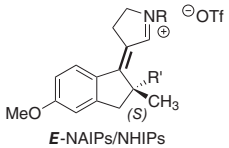 <br>***E***-NAIPs/NHIPs<br>(Note: for R′ = Me, the Z-isomer is thermodynamically favoured) | 440 nm<br>R = H, R' = Me, ***Z*** 60% [9]<br><br>387 nm<br>R = Me, R' = H, ***E*** 66% [11b] | 360 nm<br>R = H, R' = Me, ***E*** 78% [9]<br><br>428 nm<br>R = Me, R' = H, ***Z*** 72% [11b] | R = H, R' = Me:<br>n/a, Rapid isomerization at rt [9]<br><br>R = Me, R' = H:<br>n/a, No isomerization at rt [11b] | 0.20 (forward)<br>0.35 (reverse) [9] | • Ultrafast photoisomerization [12]<br>• Predominantly unidirectional rotation for chiral switches [11b] |
| 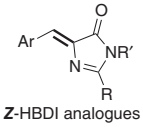 <br>***Z***-HBDI analogues | 365 nm<br>Ar = $Me_2$Pyrrole, R = PhI, R' = Me, ***E*** 75% [19] | n/a | n/a, Equilibrium reached after 51 h in DMSO-$d_6$ at 100 °C [19] | n/a | • Heteroaryl-substituted HBDIs can form fluorescent BODIPY-like complexes with $BF_3$ and high QYs [19] |
| 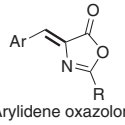 <br>***Z***-Arylidene oxazolones | 330 nm<br>Ar = Ph, R = Me, ***E*** 57% [21] | 370 nm<br>Ar = Ph, R = Me, ***Z*** 83% [21] | n/a, No isomerization after several hours in toluene-$d_6$ at 100 °C [21] | 0.25 (forward)<br>0.11 (reverse) [21] | • BMOs can exhibit fluorescence with QYs of up to 0.50 in the solid state [14] |

| | | | | | |
|---|---|---|---|---|---|
| 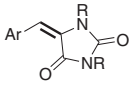 ***E***-5AHTs | >290 nm<br>Ar = *p*-OMePh, R = Me, ***Z*** 95% [23] | 350 nm<br>Ar = *p*-OMePh, R = Me, ***E*** 35% [23] | n/a, Some examples stable for several days over 100 °C [23] | 0.15 (forward) [23] | • Several examples with very high PSSs [23]<br>• Conjugation with the quinolone motif found in ciprofloxacin leads to photoswitchable anti-bacterial activity [25] |
| 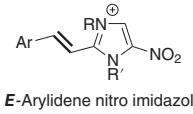 ***E***-Arylidene nitro imidazoles | 400 nm<br>***Z*** 88% [26] | n/a | n/a, Stable at rt over 3 d; Recovery of the pure ***E***-isomer required heating for 3 d at >120 °C [26] | 0.35 (forward) [26] | • Photoswitchable toxicity against human cancer cells (HeLa, A549) was demonstrated [26] |
| 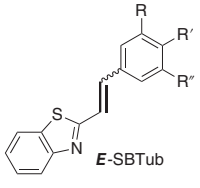 ***E***-SBTub | 360 nm<br>R = R' = R" = OMe<br>***Z*** 85% [27] | 260 nm<br>PSS n/a [27] | n/a, No isomerization in aqueous media at 25 °C and pH = 7 [27]; Full isomerization overnight in aqueous media at 50–60 °C [27] | n/a | • Thermally more stable than PSTs<br>• Stable against glutathione<br>• Switchable in aqueous media<br>• GFP orthogonal [27] |
| 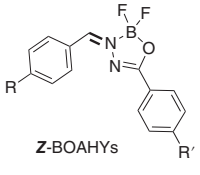 ***Z***-BOAHYs | 365 nm<br>***E*** 60% [29] | n/a | n/a, Almost complete isomerization after 5 d in $CDCl_3$ at rt [29] | n/a | • Photoswitchable fluorescence: Redshift upon photoisomerization [29] |

(*continued*)

**Table 18.1** (Continued)

| Thermodynamically Favored isomer | $\lambda_{irr.,\ forward}$ PSS[a] | $\lambda_{irr.,\ reverse}$ PSS[a] | Thermal $t_{1/2}$[a] | $QY_{iso.}$[a] | Special features |
|---|---|---|---|---|---|
| 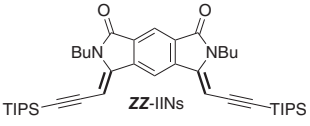 ***ZZ***-IINs | 411 nm<br>***ZE*** 45%, ***EE*** 50%<br>[31a] | 470 nm<br>***ZE*** 95%, ***EE*** 0%<br>[31a] | n/a,<br>Isomerization was not observed in $CDCl_3$ at rt or at 60 °C [31a] | n/a | • Remarkable thermal stability<br>• Stable over many switching cycles [31a] |
| 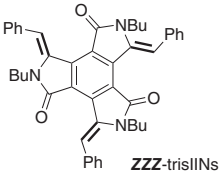 ***ZZZ***-trisIINs | 365 nm<br>***ZZE*** 37%<br>***ZEE*** 44%<br>***EEE*** 6%<br>(at -40 °C) [31b] | 458 nm<br>***ZZZ*** 25%<br>***ZZE*** 73%<br>***ZEE*** 2% [31b] | n/a,<br>Isomerization only occurs in DMF at >120 °C [31b] | n/a | • High thermal stability<br>• Reverse isomerization to the native isomer inducible by the addition of TFA [31b] |
| 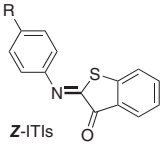 ***Z***-ITIs | 455 nm<br>***E*** 83%<br>(at -60 °C) [32] | 595 nm<br>+ very fast thermal relaxation<br>***Z*** 99% [32] | In the order of 10 ms [32]<br>In the order of 1 min in the protonated form [33] | 0.04–0.06 (forward, estimate) [32] | • Irradiation leads to 100 nm band separation between the isomers in aqueous media<br>• Very short thermal half-life<br>• Ultra-fast isomerization kinetics [32] |

| | | | | | |
|---|---|---|---|---|---|
| 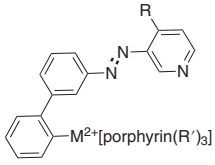 <br>***E***-Porphyrin tethered azopyridines | 500 nm<br>R = OMe<br>***Z*** > 85% [2] | 435 nm<br>***E*** > 95% [2] | >1 year at rt [2] | n/a | • First example of single-molecular manipulation of magnetic bistability<br>• High PSSs<br>• High SE<br>• High thermal stability<br>• No fatigue after >100 000 switching cycles<br>• No degradation with glutathione in MeCN/PBS buffer-mixture [2] |
| 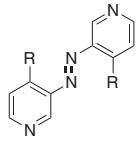 <br>***E***-3,3′-Bisazopyridenes | 365 nm<br>R = *i*-Pr<br>***Z*** 85% [34] | 455 nm<br>R = *i*-Pr<br>***Z*** 90% [34] | 1–2 wk at 25 °C [34] | n/a | • PDL for photo-sensitive bistable magnetic switches in $Ni^{2+}$-porphyrin complexes [34] |
| 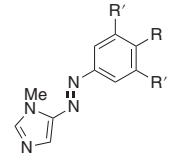 <br>***E***-Phenylazoimidazoles | 365 nm<br>R = OMe,<br>R' = H<br>***Z*** > 95% [35] | 525 nm<br>R = OMe,<br>R' = H<br>***E*** 85% [35] | 22 d at 25 °C [35] | n/a | • PDL for photo-sensitive bistable magnetic switching in $Ni^{2+}$ porphyrin switches<br>• Higher SE than 3–3′-bispyridines [35] |

Bonds that isomerize upon irradiation are highlighted in bold.

a) Values refer to selected examples.

## References


1 Harris, J.D., Moran, M.J., and Aprahamian, I. (2018). *Proc. Natl. Acad. Sci. U.S.A.* 115: 9414–9422.
2 Venkataramani, S., Jana, U., Dommaschk, M. et al. (2011). *Science* 331: 445–448.
3 Grommet, A.B., Lee, L.M., and Klajn, R. (2020). *Acc. Chem. Res.* 53: 2600–2610.
4 Gai, F., Hasson, K.C., McDonald, J.C., and Anfinrud, P.A. (1998). *Science* 279: 1886–1891.
5 Sampedro, D., Migani, A., Pepi, A. et al. (2004). *J. Am. Chem. Soc.* 126: 9349–9359.
6 Garavelli, M., Vreven, T., Celani, P. et al. (1998). *J. Am. Chem. Soc.* 120: 1285–1288.
7 Dartnall, H.J.A. (1968). *Vision Res.* 8: 339–358.
8 Becker, R.S. and Freedman, K. (1985). *J. Am. Chem. Soc.* 107: 1477–1485.
9 Lumento, F., Zanirato, V., Fusi, S. et al. (2007). *Angew. Chem. Int. Ed.* 46: 414–420.
10 Paolino, M., Gueye, M., Pieri, E. et al. (2016). *J. Am. Chem. Soc.* 138: 9807–9825.
11 (a) Gueye, M., Manathunga, M., Agathangelou, D. et al. (2018). *Nat. Commun.* 9: 313. (b) Schapiro, I., Gueye, M., Paolino, M. et al. (2019). *Photochem. Photobiol. Sci.* 18: 2259–2269. (c) Gueye, M., Paolino, M., Gindensperger, E. et al. (2020). *Faraday Discuss.* 221: 299–321.
12 Dunkelberger, A.D., Kieda, R.D., Shin, J.Y. et al. (2012). *J. Phys. Chem. A* 116: 3527–3533.
13 Tsien, R.Y. (2009). *Angew. Chem. Int. Ed.* 48: 5612–5626.
14 Jiang, M., He, Z., Zhang, Y. et al. (2017). *J. Mater. Chem. C* 5: 7191–7199.
15 (a) Olsen, S., Lamothe, K., and Martínez, T.J. (2010). *J. Am. Chem. Soc.* 132: 1192–1193. (b) Webber, N.M., Litvinenko, K.L., and Meech, S.R. (2001). *J. Phys. Chem. B* 105: 8036–8039. (c) Kummer, A.D., Kompa, C., Niwa, H. et al. (2002). *J. Phys. Chem. B* 106: 7554–7559.
16 Dong, J., Abulwerdi, F., Baldridge, A. et al. (2008). *J. Am. Chem. Soc.* 130: 14096–14098.
17 Dickson, R.M., Cubitt, A.B., Tsien, R.Y., and Moerner, W.E. (1997). *Nature* 388: 355–358.
18 Henderson, J.N., Ai, H.-w., Campbell, R.E., and Remington, S.J. (2007). *Proc. Natl. Acad. Sci. U.S.A.* 104: 6672–6677.
19 Wu, L. and Burgess, K. (2008). *J. Am. Chem. Soc.* 130: 4089–4096.
20 Ullman, E.F. and Baumann, N. (1970). *J. Am. Chem. Soc.* 92: 5892–5899.
21 Blanco-Lomas, M., Campos, P.J., and Sampedro, D. (2012). *Org. Lett.* 14: 4334–4337.
22 (a) Funes-Ardoiz, I., Blanco-Lomas, M., Campos, P.J., and Sampedro, D. (2013). *Tetrahedron* 69: 9766–9771. (b) Blanco-Lomas, M., Funes-Ardoiz, I., Campos, P.J., and Sampedro, D. (2013). *Eur. J. Org. Chem.* 2013: 6611–6618.
23 Martínez-López, D., Yu, M.-L., García-Iriepa, C. et al. (2015). *J. Org. Chem.* 80: 3929–3939.


**24** (a) Hüll, K., Morstein, J., and Trauner, D. (2018). *Chem. Rev.* 118: 10710–10747. (b) Lerch, M.M., Hansen, M.J., van Dam, G.M. et al. (2016). *Angew. Chem. Int. Ed.* 55: 10978–10999.
**25** Contreras-García, E., Martínez-López, D., Alonso, C.A. et al. (2017). *Eur. J. Org. Chem.* 2017: 4719–4725.
**26** Martínez-López, D., García-Iriepa, C., Piñeiro-Hermida, S. et al. (2019). *ChemPhotoChem* 3: 425–430.
**27** Gao, L., Meiring, J.C.M., Kraus, Y. et al. (2021). *Cell Chem. Biol.* 28: 228–241.e226.
**28** Borowiak, M., Nahaboo, W., Reynders, M. et al. (2015). *Cell* 162: 403–411.
**29** Yu, C., Hao, E., Fang, X. et al. (2019). *J. Mater. Chem. C* 7: 3269–3277.
**30** Szaciłowski, K. (2008). *Chem. Rev.* 108: 3481–3548.
**31** (a) Lawson, M. and Eisler, S. (2012). *Org. Biomol. Chem.* 10: 8770–8773. (b) Estey, P., Bubar, A., Decken, A. et al. (2013). *Chem. Eur. J.* 19: 16204–16208.
**32** Hoorens, M.W.H., Medved, M., Laurent, A.D. et al. (2019). *Nat. Commun.* 10: 2390.
**33** Medved, M., Hoorens, M.W.H., Di Donato, M. et al. (2021). *Chem. Sci.* 12: 4588–4598.
**34** Thies, S., Sell, H., Schütt, C. et al. (2011). *J. Am. Chem. Soc.* 133: 16243–16250.
**35** Schütt, C., Heitmann, G., Wendler, T. et al. (2016). *J. Org. Chem.* 81: 1206–1215.
**36** Dommaschk, M., Peters, M., Gutzeit, F. et al. (2015). *J. Am. Chem. Soc.* 137: 7552–7555.
**37** Shankar, S., Peters, M., Steinborn, K. et al. (2018). *Nat. Commun.* 9: 4750.
**38** Meunier, B., de Visser, S.P., and Shaik, S. (2004). *Chem. Rev.* 104: 3947–3980.
**39** Tu, C. and Louie, A.Y. (2007). *Chem. Commun.* 1331–1333.
**40** Tu, C., Osborne, E.A., and Louie, A.Y. (2009). *Tetrahedron* 65: 1241–1246.

# 19 Photochromism of Coordination Compounds

Nathan Man-Wai Wu, Chi-Chiu Ko, and Vivian Wing-Wah Yam

## Photochromism of Coordination Compounds

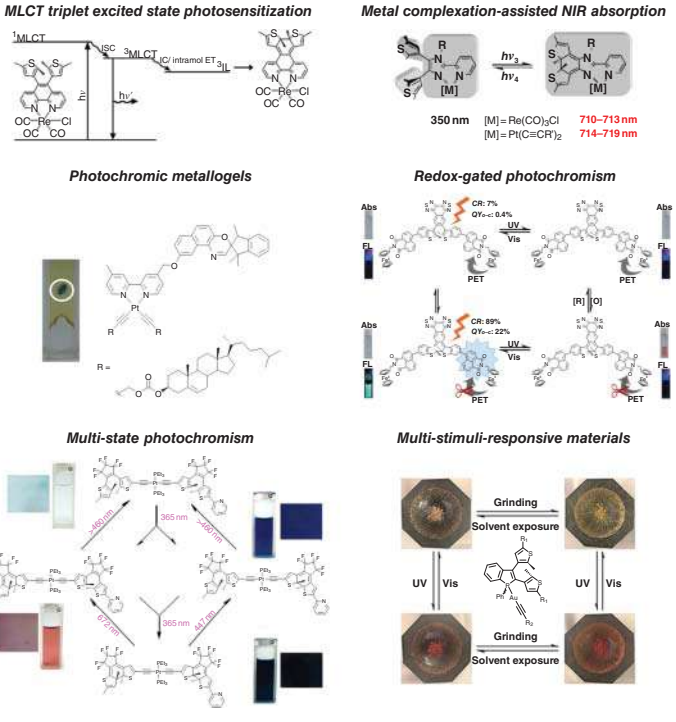


## Characteristic Features

Intramolecular metal-to-ligand charge-transfer (MLCT) triplet excited state photosensitization, metal complexation-assisted near-infrared (NIR) absorption, photochromic metallogels, redox-gated photochromism, multi-state photochromism, multi-stimuli-responsive materials. Source: Reproduced with the permission of Wiley-VCH from Ko et al. [1]; Reproduced with the permission of American Chemical Society from Lee et al. [2]; Reproduced with the permission of Wiley-VCH form Li et al. [3]; Reproduced with the permission of Wiley-VCH from Cai et al. [4]; Reproduced with the permission of American Chemical Society from Li et al. [5]; Reproduced with the permission of Wiley-VCH from Wu et al. [6].

## Key References

Ko, C.-C. and Yam, V.W.-W. (2010). Transition metal complexes with photochromic ligands – photosensitization and photoswitchable properties. *J. Mater. Chem.* 20: 2063–2070.

Ko, C.-C. and Yam, V.W.-W. (2018). Coordination compounds with photochromic ligands: ready tunability and visible light-sensitized photochromism. *Acc. Chem. Res.* 51: 149–159.

# 19

# Photochromism of Coordination Compounds

*Nathan Man-Wai Wu[1], Chi-Chiu Ko[2], and Vivian Wing-Wah Yam[1]*

*[1] The University of Hong Kong, Department of Chemistry, Pok Fu Lam, Hong Kong, People's Republic of China*
*[2] City University of Hong Kong, Department of Chemistry, 83 Tat Chee Ave, Kowloon Tong, Hong Kong, People's Republic of China*

## 19.1 Introduction

Photochromic coordination compounds are designed based on two different types of reversible photo-isomerization: (i) linkage isomerization that involves the rearrangements of the metal–ligand bonds (i.e. linkage isomerization); (ii) bond/conformational rearrangement within a ligand. For the former type, the design of ambidentate ligands with two or more donor atoms or moieties for the formation of different coordination modes is one of the crucial factors to achieve photochromism in the coordination compounds [7, 8]. In the latter type, the photochromism is derived from the ligand with well-reported organic photochromic moieties such as stilbenes, azobenzenes, spiropyrans, spirooxazines, diarylethenes, and others [9–12]. Therefore, ligand design plays an important role in the photochromic properties of the coordination compounds.

Although photoinduced linkage isomerizations and the realization of their photochromic behavior in coordination compounds with simple ambidentate ligands, such as NO, $NO_2$, and $SO_2$, have been reported for decades [13–15], research study on these coordination compounds as photochromic materials did not receive much attention because most of them exhibit photochromism only in their solid state at low temperature. In recent years, there has been growing attention on photochromic coordination complexes with organic ambidentate sulfoxide ligands, which display photochromism in the solution state at room temperature [16–20]. The challenges in systematic tuning of their photochromic properties render this type of photochromic transition metal complexes much less popular compared to those designed from the coordination of photochromic ligands [7, 8]. In contrast, the well-established knowledge on photochemistry and photophysics of the organic photochromic families [9–12] has provided an important foundation for designing photochromic ligands with more predictable and tunable properties. As a result, most of the photochromic coordination compounds are developed based

*Molecular Photoswitches: Chemistry, Properties, and Applications*,
First Edition. Edited by Zbigniew L. Pianowski.


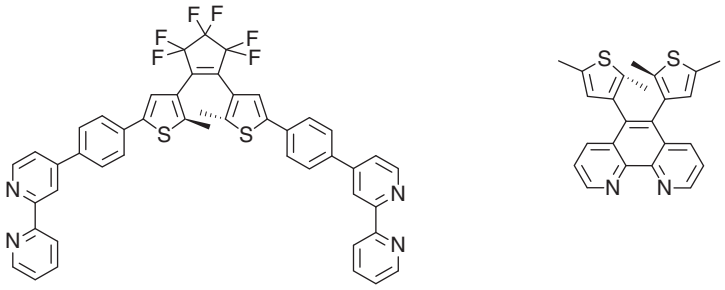


**Figure 19.1** Examples of photochromic diarylethene-containing ligands developed by (a) attachment of a diarylethene pendant to the bipyridine ligand and (b) incorporation of the phenanthroline ligand as the reactive part of the diarylethene. Source: Reproduced with the permission of American Chemical Society from Refs. [21, 22], respectively.

on this strategy. In this chapter, the design of photochromic ligands as well as the photochromism in their coordination compounds are discussed. The impacts of the photophysics, photochromic reactivity, and photoswitching properties upon coordination will also be described.

Most of the early reports on photochromic ligands were developed through the attachment of photochromic moiety as a pendant of the ligand (Figure 19.1a). In that design, the linkage between the photochromic moiety and ligand framework has been demonstrated to be important in governing the interaction between the coordination unit and the photochromic component in the ligand. As a result, the photochromic properties of many of these coordination compounds are similar to those of the ligands. Another approach to the design of photochromic ligands involves the ligand framework itself as the reactive part of the photochromic unit (Figure 19.1b). For this type of photochromic ligands, the photochromic properties are usually significantly perturbed or modified upon coordination, rendering a simple and effective strategy for the development of photochromic compounds with diverse and desirable properties.

## 19.2 Differences in Photochromic Reactivity and Photochromism upon Coordination

### 19.2.1 Photophysical Properties

Although many families of organic photochromic compounds operated by different reaction mechanisms, such as reversible photoinduced *trans*-to-*cis* isomerization, electrocyclic cyclization/cycloreversion, tautomerization, and bond dissociation, have been developed, these photochromic reactions are mainly initiated from $\pi\pi^*$ or $n\pi^*$ electronic excited states formed upon the absorption of light. This is because many of these compounds are $\pi$-conjugated systems with $\pi \rightarrow \pi^*$ or $n \rightarrow \pi^*$ electronic transitions as their lowest-energy absorptions. Therefore, modifications

of the photochromic properties of these compounds are mostly achieved by changing the π-conjugation of the reactive moiety.

After incorporation of the organic photochromic ligands into the transition metal complex systems, metal-based d orbitals are involved in the frontier molecular orbitals. This not only perturbs the electronic properties of the ligands due to metal–ligand interactions but also introduces various types of electronic transitions, such as metal-centered or ligand–field transition, metal-to-ligand charge transfer (MLCT) transition, ligand-to-metal charge transfer (LMCT) transition, and ligand-to-ligand charge transfer (LLCT) transition, in addition to the ligand-based $\pi \rightarrow \pi^*$ or $n \rightarrow \pi^*$ transitions [23]. Moreover, the presence of heavy metal atom in the coordination compounds also enhances spin–orbit coupling. Thus, spin-forbidden deactivation processes become more efficient and triplet excited states are more accessible. It also opens up photochromic reactivity from triplet excited states. Consequently, the excited-state dynamics and photochromism usually involve more excited states and are more complicated in coordination compounds with a photochromic ligand.

### 19.2.2 Photosensitized Photochromism

Despite the involvement of different types of excited states in the excited-state dynamics, reactive ligand-centered excited states ($^1$LC or $^3$LC) must be populated to initiate the photochromic reaction in photochromic coordination compounds. Therefore, the energy transfer processes between electronic excited states associated with the transition metal complexes and the reactive ligand-centered excited states play important roles in the photochromic reactions. By incorporation of photochromic ligands to transition metal complex systems with triplet excited states higher-lying than the reactive triplet ligand-centered ($^3$LC) states, photosensitization of the photochromic reaction via intramolecular triplet–triplet energy transfer from the triplet state of the transition metal complex to the $^3$LC state can be achieved [24, 25].

Photosensitization of the photochromic ligand was first demonstrated in Ru(II) bipyridine complex with 4-stibazole (stpy) ligand, $[Ru(bpy)_2(stpy)_2]^{2+}$ in 1973 [26]. Photoinduced *trans–cis* isomerization can be achieved by excitation into the MLCT absorption band of this complex. No mechanism for the photosensitization was postulated at that time. In 1990, intramolecular energy transfer from $^3$MLCT state to populate the reactive $^3$LC state for *trans–cis* isomerization was proposed based on the short-lived emission and the characterization of a much longer-lived transient absorption in mononuclear and dinuclear tris(bipyridyl)ruthenium(II) complexes with 1,4-divinylbenzene-bridged bipyridine ligand (Figure 19.2). The intramolecular energy transfer from the $^3$MLCT state to the reactive $^3$LC state for *trans*-to-*cis* isomerization has also been reported in tricarbonyl Re(I) bipyridine systems with azo- or stilbene-containing pyridine ligands [27, 28]. In these Re(I) complexes, efficient energy transfer from the $^3$MLCT state to the $^3$LC state occurs in the *trans*-isomer because the $^3$LC state is lower-lying in energy. As a result, the *trans*-isomer of these Re(I) complexes only show very weak MLCT phosphorescence. Upon photoisomerization to the *cis*-form, the $^3$LC

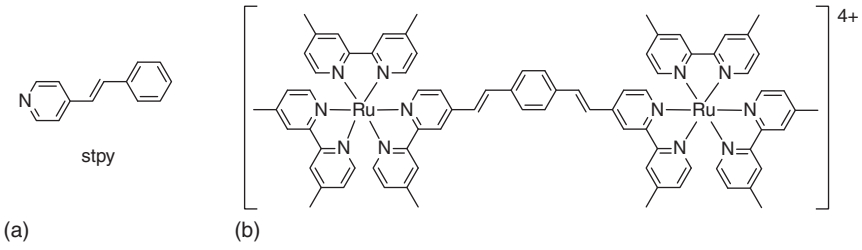


**Figure 19.2** Structures of (a) 4-stibazole (stpy) and (b) dinuclear tri(bipyridyl) Ru(II) complexes with 1,4-divinylbenzene-bridged bipyridine ligand. Source: Reproduced with the permission of American Chemical Society from Zarnegar et al. [26] and Royal Society of Chemistry from Yam et al. [27], respectively.

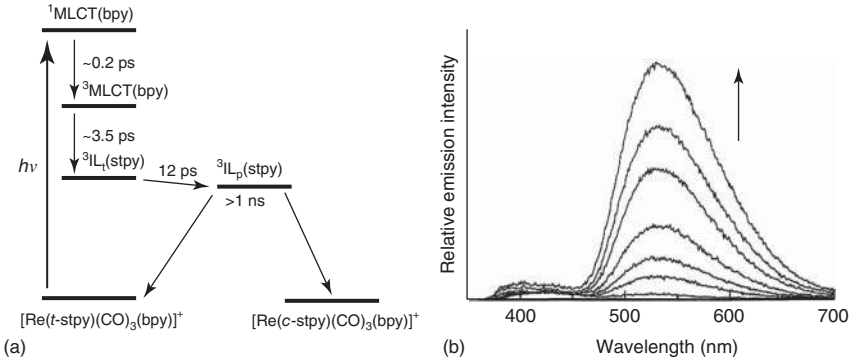


**Figure 19.3** (a) Excited-state dynamics of $[Re(CO)_3(bpy)(stpy)]^+$ determined by ultrafast transient absorption spectroscopic study ($^3IL_t$ and $^3IL_p$ denote triplet intraligand excited states of **stpy** with a *trans* geometry and a perpendicular geometry, respectively). Source: Reproduced with the permission of American Chemical Society from Busby et al. [29]. (b) Emission spectral changes of $[Re(CO)_3(phen)(NO_2\text{-stpy})]^+$ in $CH_2Cl_2$ upon 330-nm excitation. Source: Reproduced with the permission of Royal Society of Chemistry from Yam et al. [28].

state becomes higher-lying in energy, which blocks the energy transfer process, and as a result the MLCT phosphorescence is turned on (Figure 19.3). The detailed excited-state dynamics, including intersystem crossing and intramolecular triplet-triplet energy transfer in the $^3$MLCT-sensitized *trans*-to-*cis* isomerization in $[Re(CO)_3(bpy)(stpy)]^+$, have been later elucidated by ultrafast transient absorption and vibrational spectroscopy [29]. The MLCT-photosensitization strategy has been applied to design many transition metal complexes with many different *trans–cis* isomerizable pyridines, bipyridines, and other ligands [30–35]. Photosensitized photochromism of *trans–cis* isomerizable ligands can also be achieved by coordination to dithiolato-bipyridyl platinium(II) complexes with $^3$LLCT excited state [36].

Apart from *trans–cis* isomerization, photosensitization of ring-opening reaction of spirooxazine-containing pyridine ligand (**SOPY**) by the $^3$MLCT excited state has also been reported in tricarbonyl Re(I) bipyridine complexes, $[Re(CO)_3(N\text{–}N)(\mathbf{SOPY})]^+$ (N–N = $^t$Bu$_2$bpy, Me$_2$bpy, phen) (Figure 19.4) [37]. The photochromic ring-opening


**Figure 19.4** Photochromism of tricarbonyl Re(I) bipyridine complexes with spirooxazine-containing pyridine ligand (**SOPY**). Source: Reproduced with the permission of American Chemical Society from Yam et al. [37].

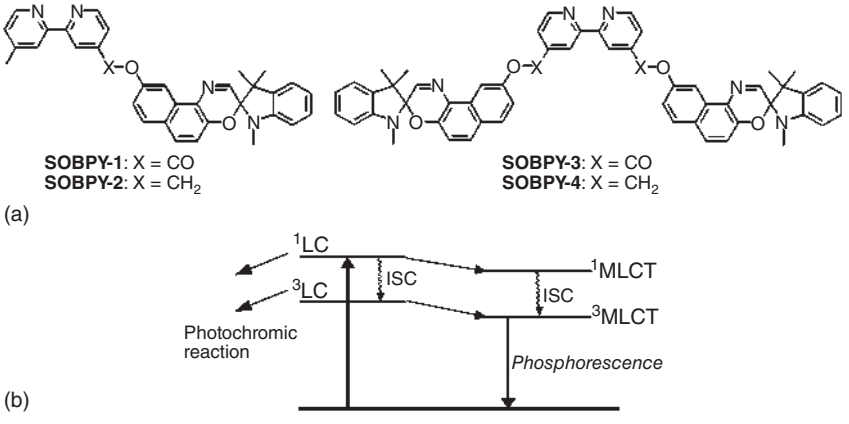


**Figure 19.5** (a) Structures of spirooxazine-containing bipyridine ligands (**SOBPY-n**). (b) Schematic diagram showing the quenching of the photochromic reaction by lower-energy MLCT excited state of [$Re(CO)_3$(**SOBPY-n**)Cl]. Source: Reproduced with the permission of Wiley-VCH from Ko et al. [38].

reaction of the **SOPY** in these complexes can be initiated by the excitation into the MLCT absorption band. As all these complexes exhibit $^3$LC phosphorescence instead of the commonly observed $^3$MLCT emission, an intramolecular energy transfer from the $^3$MLCT state to the $^3$LC state in the photosensitization was suggested.

To achieve photosensitization, the triplet state of the donor must be higher-lying than the reactive $^3$LC state. When a series of spirooxazine-containing bipyridine ligands (**SOBPY-n**) (Figure 19.5) was incorporated into the tricarbonyl Re(I) coordination unit [$Re(CO)_3$(**SOBPY-n**)Cl] with lower-energy $^3$MLCT state (166–188 kJ mol$^{-1}$), the photochromic reaction did not take place with MLCT excitation [38]. In these complexes, the photochromic reactions are quenched rather than photosensitized by the MLCT state. The quenching is further supported by the lower photochromic quantum efficiencies in these complexes compared to the free ligands. Moreover, the quantum efficiencies in these complexes follow the order of MLCT state energies [38]. By incorporating one of these spirooxazine-containing bipyridine ligands (**SOBPY-2**) into the alkynyl Pt(II) complexes with higher $^3$MLCT/$^3$LLCT energy, $^3$MLCT/$^3$LLCT-sensitized photochromism can be achieved [3].

Photosensitization of photochromic diarylethene-containing ligands (Figure 19.1) designed from two different approaches with the MLCT excited state has been demonstrated almost at the same time in 2004. Upon coordination of the diarylethene-containing bridging bipyridine ligand to two tris(bipyridyl)ruthenium(II) complex units, the photocyclization of the diarylethene in the dinuclear Ru(II) complex can be performed by excitation into the MLCT absorption [21] (Figure 19.6a). However, photosensitization of the photochromic reaction was not observed in the dinuclear tris(bipyridyl)osmium(II) complex with the same ligand. Instead, the quantum efficiency of the photocyclization is significantly reduced. This is due to the much lower-energy MLCT state in the Os(II) complex, which quenches the reactive $^3$LC state responsible for cyclization. On the other hand, the photocyclization of a diarylethene-containing phenanthroline ligand in its tricarbonyl Re(I) complex can be sensitized by excitation of the MLCT absorption [22]. In both systems, the intramolecular energy transfer from the $^3$MLCT state to the reactive $^3$LC state for cyclization was proposed. Subsequently, the proposed intramolecular energy transfer and the excited dynamics of the Re(I) complex have been elucidated by ultrafast transient absorption and time-resolved emission spectroscopic studies (Figure 19.6b) [1]. Successful photosensitization of the diarylethene-containing phenanthroline ligand by coordination to different metal complex systems has also been reported [39–41].

The effects of different ligand design on photosensitization have been gradually revealed as more studies on different diarylethene-containing ligands and their transition metal complexes have been reported. For ligands developed by the attachment of photochromic diarylethene as pendants, the linkage has been demonstrated to play an important role in governing the efficiency of the intramolecular energy transfer process between the triplet excited state of the transition metal complexes and the reactive $^3$LC state for photocyclization [42, 43]. As illustrated in diarylmaleimide-linked phenanthroline ligands with different linkage groups (Figure 19.7a), they can be photosensitized with $^3$MLCT state when coordinated to bis(bipyridyl)ruthenium(II) units [42]. The excited-state dynamics and the photosensitization mechanism have been studied by ultrafast transient absorption spectroscopy. The results show that the kinetics of energy transfer processes between $^1$MLCT and $^1$LC states (150 ps vs. 30 ps) as well as $^3$MLCT and $^3$LC states (40 ns vs. 1.5 ns) are significantly slower for the complex with additional non-conjugated methylene group in the linkage [42]. The decreased intramolecular energy transfer efficiency is also revealed in the terpyridylplatinum(II) complexes with diarylethene-containing alkynyl ligands separated by an additional non-conjugated spacer ($-CH_2OC_6H_4-$) [43]. This also resulted in the lowering of the quantum yield for MLCT-sensitized photochromism (Figure 19.7b).

For transition metal complexes containing diarylethene ligands with their frameworks involved as the photochromic reactive part, such as the diarylthenene-containing phenanthroline ligand (Figure 19.1b), there is minimum or almost no structural separation between the photosensitizing excited state of the transition metal complex and the reactive $^3$LC state. Moreover, coordination of this type of photochromic ligand to the transition metal complex would also lead to stronger

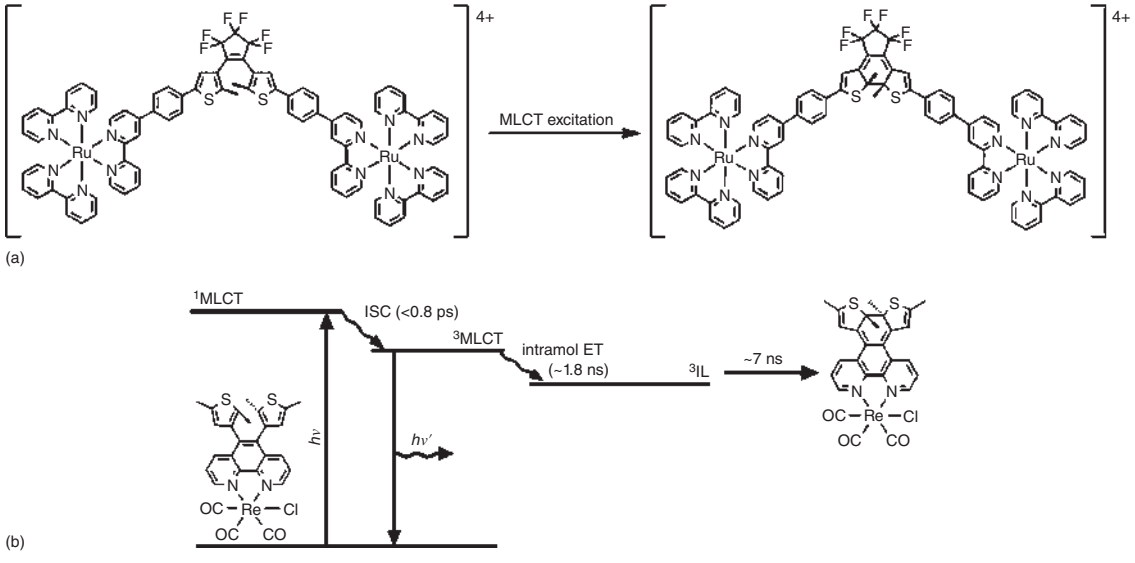


**Figure 19.6** (a) MLCT-photosensitized photochromism of diarylethene-containing bridging bipyridine ligand in its dinuclear Ru(II) complex. (b) Excited-state dynamics of the MLCT-photosensitized cyclization of diarylethene-containing phenanthroline ligand in its Re(I) complex. Source: Reproduced with the permission of American Chemical Society from Jukes et al. [21] and Wiley-VCH from Ko et al. [1], respectively.

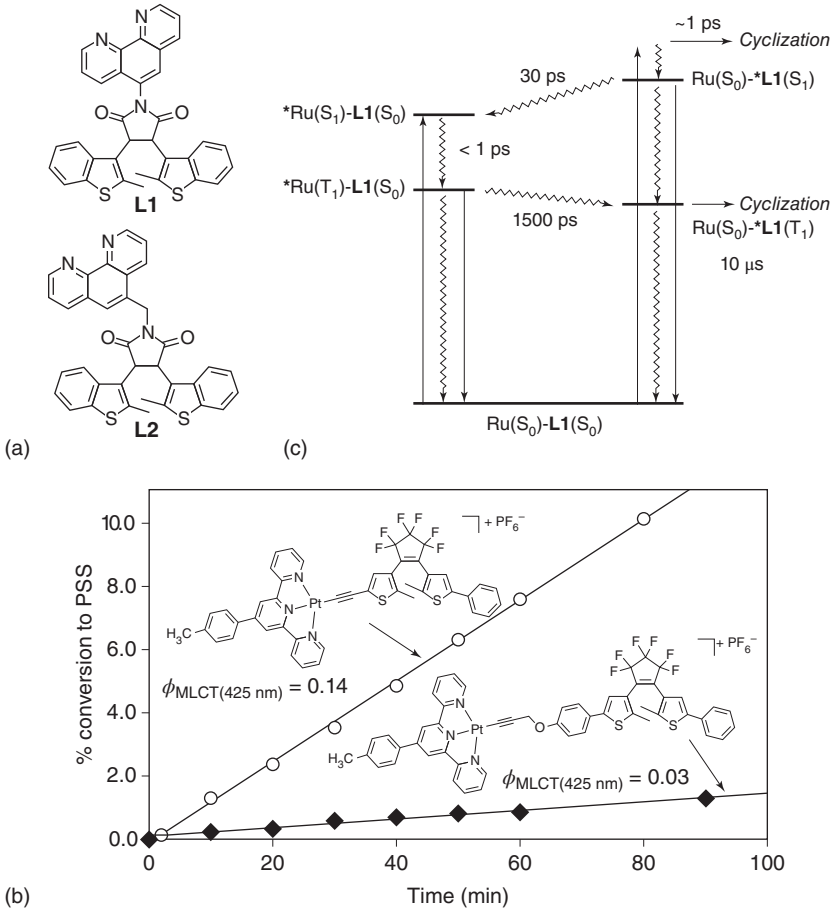


**Figure 19.7** (a) Structures of diarylmaleimide-linked phenanthroline ligands. (b) Percentage conversion to photostationary states of diarylethene-linked Pt(II) terpyridine complexes in acetonitrile solution at different irradiation times with wavelengths between 415 and 425 nm. (c) Excited-state dynamics of the photosensitization mechanism for the Ru(II) complex with diarylmaleimide-linked phenanthroline ligand. Source: Reproduced with the permission of American Chemical Society from Refs. [42, 43].

spin–orbit coupling. The strong spin–orbit coupling enhances the efficiency of the spin-forbidden processes, including higher triplet photocyclization kinetics from a few nanoseconds in the Re(I) complex (Figure 19.6b) [1] to a few microseconds in the Ru(II) complexes with diarylethene separated by a spacer (Figure 19.7c) [42, 43]. Successful photosensitization of many other photochromic ligands with triplet excited states of different transition metal complexes has been subsequently reported [2, 44–51].

Through triplet photosensitization, the excitation wavelength for the photochromic reactions can be extended from ligand-based absorption, usually in the UV region, to transition metal complex-based charge transfer transitions in the

visible region. Although triplet photosensitization can also be achieved through intermolecular energy transfer from organic triplet photosensitizers [52–54], the intersystem crossing and intramolecular energy transfer in transition metal complexes are more efficient. Even for intramolecular processes, the kinetics of triplet-state photochromic reactions also show strong dependence on the spacer between donor and acceptor moieties [2, 39, 43]. As a result, some of the triplet-state photochromic reactions are highly sensitive to oxygen [2, 43].

Detailed study revealed that prolonged high-energy UV excitation used in photocyclization of the photochromic diarylethene would also result in by-product formation [53]. This lowers the reversibility and the fatigue resistance of the photochromism. On the other hand, the use of lower-energy visible light in triplet-sensitized photochromic reaction in an anaerobic condition has been shown to significantly reduce or block the photochemical pathway to by-product formation [53]. Therefore, triplet photosensitized photochromism, together with the use of lower-energy excitation, provides an effective approach to improve the fatigue resistance.

### 19.2.3 Near-Infrared (NIR) Photochromism by Coordination-Induced Perturbation

Apart from triplet-state photosensitized photochromism, perturbation of the ligand-based orbitals and electronic transitions through metal coordination could also lead to a red shift of the absorption and the extension of excitation wavelength for photochromism. Strong perturbation is observed when the ligand framework is involved in the photochromic reactive moiety. This is first illustrated in the red shift of the photocyclized form absorption upon coordination of diarylethene-containing phenanthroline ligand to different transition metal complexes [1, 21, 39–41]. Amplification of this effect has been achieved by designing diarylethene-containing ligands with extended π-conjugation upon coordination. With dithineyl 2-(2-pyridyl)imidazole ligands, the lowest-energy absorption of their closed form can be significantly red-shifted from $\lambda_{abs}$: 580 nm to $\lambda_{abs}$: 710–730 nm in the near-infrared (NIR) region upon coordination to tricarbonyl Re(I) [2] and bis(alkynyl) Pt(II) complexes [44]. The significant red shift is due to the coordination-assisted planarization of the pyridine and imidazole moieties together with the metal perturbation of the ligand-based orbitals (Figure 19.8). This provides a simple approach for developing NIR photochromic compounds.

Using this design strategy, NIR photochromic transition metal complexes with diarylethene-containing cyclometalated ligands (Figure 19.9a) have also been developed [45–47]. In these cyclometalated transition metal complexes, they exhibit intraligand charge transfer (ILCT) and LLCT transitions in addition to LC $\pi \rightarrow \pi^*$ transitions. Apart from planarization and metal perturbation, the mixing of ILCT and LLCT transitions arisen from the coordination with the LC $\pi \rightarrow \pi^*$ transitions has also contributed to the bathochromic shift of the absorption maxima of the cyclized form. The contribution of the ILCT and LLCT transitions in the lowest-energy absorption of the closed form is supported by the strong sensitivity


**Figure 19.8** Photochromism and absorption maxima of diarylethene-containing 2-(2-pyridyl)imidazole ligands and their metal complexes. Source: Reproduced with the permission of American Chemical Society from Lee et al. [2].

of the absorption maxima to the substituents on the ancillary ligand as well as the pyridine ring of the cyclometalated ligand (Figures 19.9b and 19.9c).

NIR-active photochromic compounds can be developed by coordination of diarylethene-containing $\beta$-diketonate and $\beta$-ketoiminate ligands to boron(III) system ($BX_2$, X = F, $C_6H_5$, $C_6F_5$) [55–57]. As revealed from the density-functional theory (DFT) calculations, the strong perturbation and electron-accepting properties of B(III) center would introduce a low-energy lowest unoccupied molecular orbital (LUMO) localized on $\beta$-diketonatoborane or $\beta$-diketoiminatoborane moiety as well as an intramolecular donor–acceptor charge transfer transition. With these effects, the absorption of the closed form would be significantly red-shifted (Figure 19.10), rendering NIR-active photochromic behavior. The heavy involvement of the B(III) center in the electronic transition associated with the lowest energy absorption of the closed form can be reflected by the sensitivity of the absorption maximum to the nature of the substituent ($C_6F_5$ and F) on the B(III) center.

### 19.2.4 Gated Photochromism

Owing to the nondestructive readout for the potential applications in optical memory devices, gated photochromic materials have received considerable attention from academia over the past decades [12, 58]. As demonstrated in previous sections, the introduction of different electronic states upon coordination could lead to sensitization or quenching of the photochromic reactions. By incorporation of diarylethene into coordination systems with electronic states readily modified by an external stimulus, such as solvent, pH, redox, temperature, or chemicals, gated photochromic compounds, in which their photochromic reactivity can be locked or unlocked by an additional external stimulus, can be designed [58].

In a series of diarylethene-containing triarylborane complexes [59], they do not show any photochromic activity due to the presence of the highly emissive $\pi \rightarrow \pi^*/p_\pi(B)$ excited state that quenches the photochromic reactive excited state. They become photochromic active upon addition of tetra-*n*-butylammonium fluoride (TBAF) (Figure 19.11). This is due to the coordination of fluoride, which changes the boron(III) center from a trigonal planar to a tetrahedral geometry, which results in a hypsochromic shift of the lowest-energy absorption bands from c. 400 to 360 nm [59]. Moreover, the emission of the triarylboron(III) peaking at c. 465 nm would drop dramatically to almost non-emissive on binding a fluoride [59].

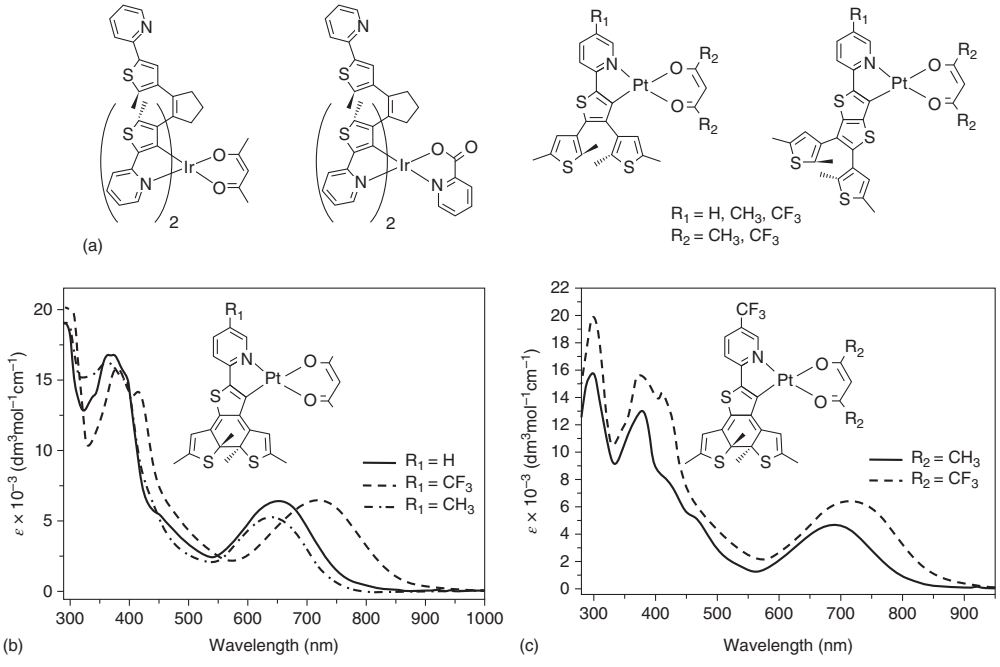


**Figure 19.9** (a) NIR photochromic diarylethene-containing cyclometalated transition metal complexes. (b) Overlaid UV–vis absorption spectra of the closed form of selected diarylethene-containing cyclometalated Pt(II) complexes. Source: Reproduced with the permission of American Chemical Society from Chan et al. [47].

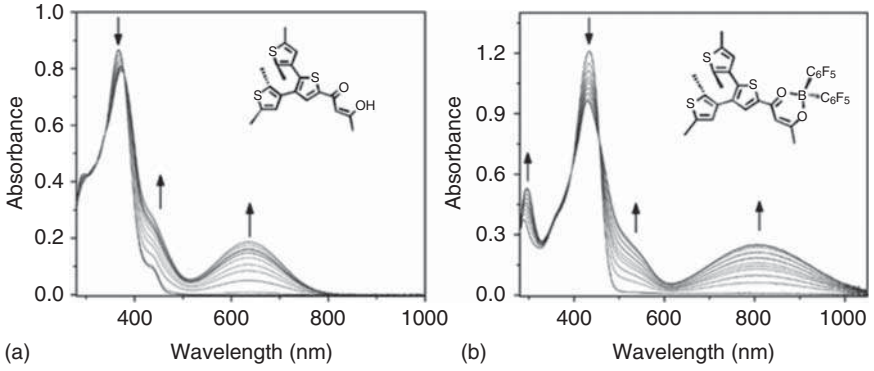


**Figure 19.10** UV–vis absorption spectral change of (a) diarylethene-containing $\beta$-diketonate and (b) its B(III) coordination compound. Source: Reproduced with the permission of American Chemical Society from Poon et al. [55].

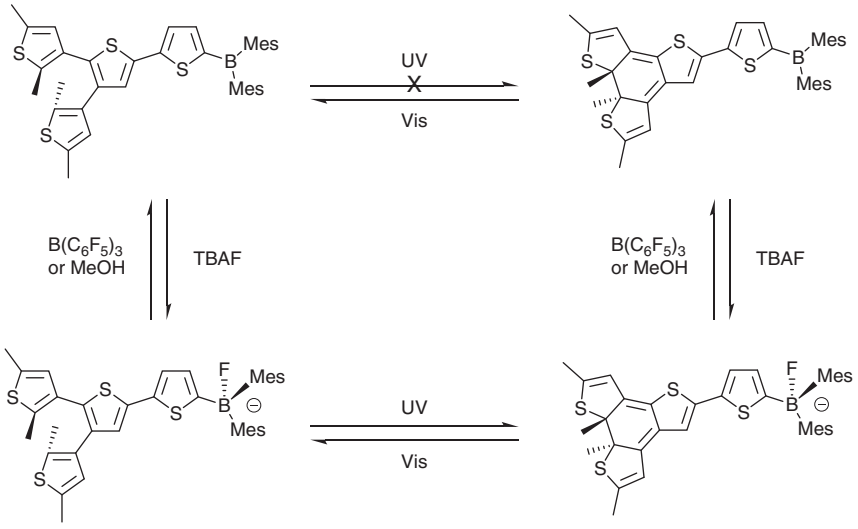


**Figure 19.11** Gated photochromic behavior of the diarylethene-containing boron(III) complex. Source: Reproduced with the permission of American Chemical Society from Poon et al. [59].

UV irradiation of the boron-fluoride adduct would induce photocyclization as confirmed by the evolution of the low-energy absorption bands at c. 560 nm. By abstraction of fluoride from the closed form of the boron–fluoride adduct via addition either of an excess amount of methanol or stronger Lewis acid of $[B(C_6F_5)_3]$, the closed form of the triarylboron(III) complex could be obtained [59]. A bathochromic shift of the lowest-energy absorption band from c. 560 to 600 nm was observed upon the dissociation of fluoride with boron-fluoride adduct. This is probably due to the extended π-conjugation over the condensed ring system with the boron $p_\pi$ orbital [59]. This represents a "lock–unlock" gated photochromic system operated by fluoride ion (Figure 19.11).

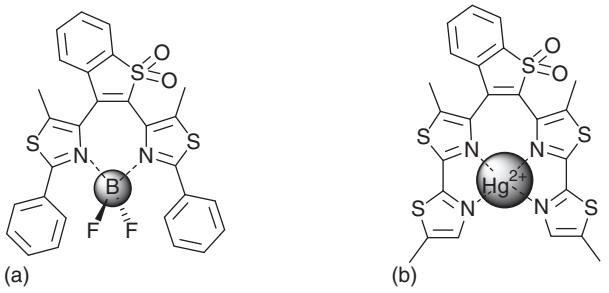


**Figure 19.12** Locking of photochemical inactive parallel conformation of thiazole-containing diarylethenes upon coordination to (a) boron(III) and (b) mercury(II) centers. Source: Reproduced with the permission of Royal Society of Chemistry from Refs. [60, 61], respectively.

Gated photochromic reactivity of dithiazolethene, in which the photochromic activity could be highly suppressed upon $BF_3$ coordination, has been reported [60]. The deactivation of the photochromism is due to the locking of the conformation in a photochemically inactive parallel configuration upon coordination with the thiazole moieties (Figure 19.12a) [60]. Upon UV irradiation, the dithiazolethene in acetonitrile solution shows a color change from colorless to red, with the evolution of a low-energy absorption band at c. 526 nm; whereas its coordination compound with $BF_3$ shows no obvious photoinduced coloration (locked state) [60]. The locked photochromism could be restored upon addition of $Et_3N$ with the release of the photoactive anti-parallel conformation of dithiazolethene [60]. With a similar design strategy, a gated photochromic system based on conformational locking with mercury coordination of a bithiazole-pendant-containing diarylethene (Figure 19.12b) was later reported [61]. In this system, the coordination of mercury(II) ion in the binding pocket of the two bithiazole units would lock it in a photochemically inactive parallel conformation [61]. The dissociation of the mercury(II) ion upon addition of ethylenediaminetetraacetic acid (EDTA) would result in a recovery of the photochromic activity [61].

Copper(II)-coordination-induced gated photochromic property of a star-shaped triamino-guanidinium-containing dithienylethene (Figure 19.13) has been recently reported [62]. The diarylethene in acetonitrile solution changes its color from colorless to yellow with the new emergence of the lowest-energy absorption band at c. 450 nm upon coordination with copper(II) [62]. The copper(II) complex shows no photochromic reactivity upon UV irradiation [62], while the organic counterpart (free ligand) would undergo photoinduced coloration from colorless to red in solution with the new absorption band at c. 533 nm, corresponding to the formation of the closed form. The photoinduced cycloreversion of the closed form could also be inhibited by coordination of copper(II) ion, which induced a color change from red to pewter with the new appearance of a broad absorption band tailing at c. 700 nm [62]. The inhibition of the photochemical reactivity was attributed to the perturbation of energy levels of the frontier molecular orbitals by copper coordination [62]. The photochromic reactivity could be restored by the

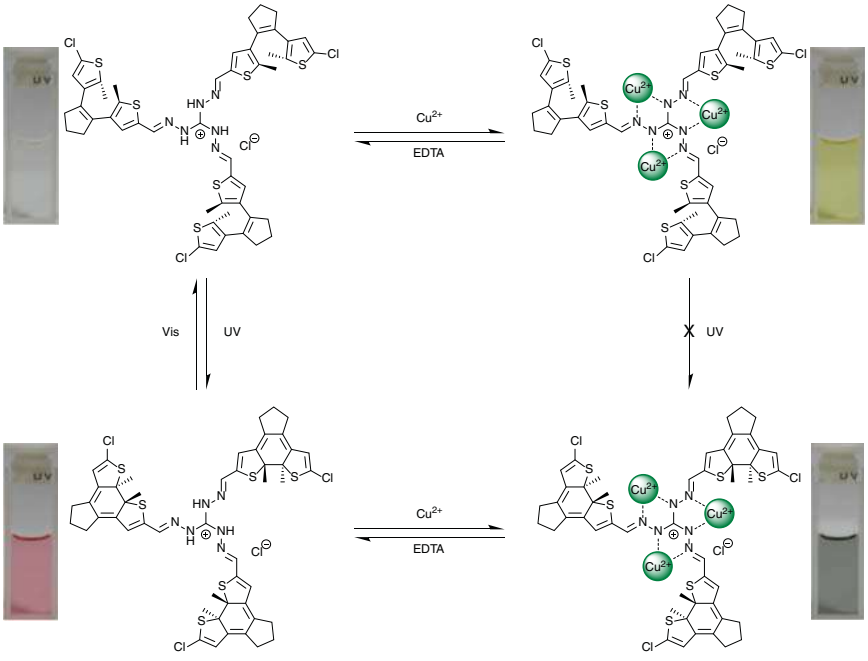


**Figure 19.13** Triamino-guanidinium-containing dithienylethene with copper(II)-induced gated photochromism. Source: Reproduced with the permission of Royal Society of Chemistry from Wang et al. [62].

addition of ethylenediaminetetraacetate (EDTA) to remove the copper(II) ion from the complex. Interestingly, the gated reactivity is highly selective for $Cu^{2+}$ ion and the photochromism would not be inhibited by other metal ions including $Ag^{+}$, $Al^{3+}$, $Ca^{2+}$, $Cd^{2+}$, $Co^{2+}$, $Cr^{3+}$, $Fe^{2+}$, $Hg^{2+}$, $K^{+}$, $Mg^{2+}$, $Mn^{2+}$, $Na^{+}$, $Ni^{2+}$, and $Zn^{2+}$ ions.

Apart from gated photochromic diarylethene systems by metal complexation, a rhodamine-containing azobenzene with photochemical reactivity controlled by iron(III) complexation has been developed (Figure 19.14) [63]. In the rhodamine-azobenzene system, there are two possible photochromic reactions, *trans–cis* isomerization of the azobenzene moiety and ring-opening reaction of the rhodamine. In the absence of the iron(III) ion, the azobenzene undergoes photochemical *trans–cis* isomerization reaction from the *trans*-isomer to the *cis*-isomer upon UV excitation. After adding iron(III) ion, the compound would undergo ring-opening reaction in the spirolactam ring of the rhodamine. As a result, the excited state of the iron(III) induced open form is lower-lying than that of the reactive excited state of the azobenzene for *trans–cis* isomerization. Thus, the photochemical *trans–cis* isomerization reaction of the azobenzene moiety is inhibited in the presence of iron(III) [63]. Decomplexation of the iron(III) ion from the rhodamine by adding fluoride would regenerate the closed form to restore the photoinduced *trans–cis* isomerization [63].

With redox-active ferrocene unit, redox-gated photochromic diarylethenes have been developed [4, 64]. In these ferrocene-coupled diarylethene systems, the

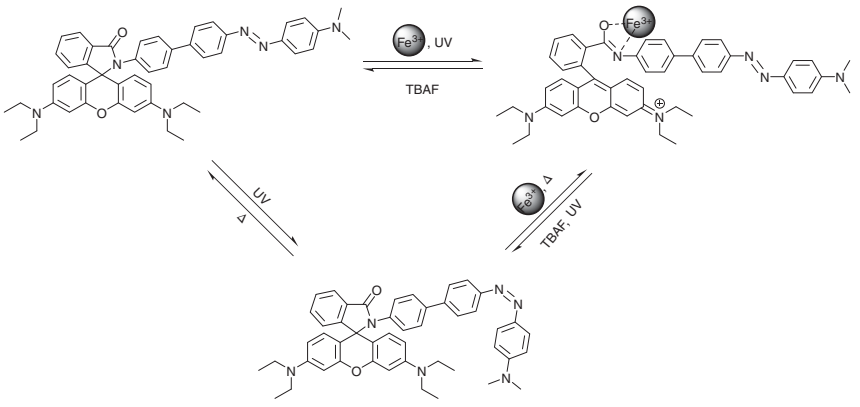


**Figure 19.14** Rhodamine-containing azobenzene with selective photoindued *trans–cis* isomerization or ring-opening reaction controlled by the iron(III) complexation. Source: Reproduced with the permission of Royal Society of Chemistry from Raman et al. [63].

photocyclization quantum yields of the Fe(II) state are much lower than those of the Fe(III) state (ferrocenium) due to the photoinduced electron transfer (PET) quenching process of the Fe(II) state. For naphthalimide-fused diarylethene [4], the photocyclization can be completely inhibited or locked by chemical oxidation of two thiophene units with excessive amounts of $Fe(ClO_4)_3$ (Figure 19.15a). For benzobisthiadiazole-fused diarylethene, the photochromism of the open form of Fe(II) state is almost suppressed with quantum yield $\phi$ of ~0.4% [4]. Its photochromism becomes unlocked by blocking the PET quenching process through the oxidation to the Fe(III) state ($\phi \sim 22\%$) (Figure 19.15b). In addition to unlocking the photocyclization through oxidation to ferrocenium state, the luminescence of the open form in both ferrocenium-coupled diarylethenes can also be switched on [4, 64]. The emission enhancement in the Fe(III) is consistent with the proposed blockage of the PET quenching process.

### 19.2.5 Multiple Addressable/Multi-State Photochromism

As coordination compounds usually contain more than one ligand, it enables the development of multi-addressable or multi-state photochromic compounds through the incorporation of other functional ligands in addition to a photochromic ligand [65]. By incorporation of two different azobenzene-containing ligands that undergo photoisomerization with different wavelengths of excitation into dithiolato Pt(II) bipyridine complex, a photochromic compound with three different states switchable by specific wavelengths of excitation (Figure 19.16) has been obtained [36].

The coordination of multiple diarylethene ligands to transition metal complexes such as those of Pt(II), Au(I), and Ru(II) metal centers to achieved multi-state photochromic behavior has been extensively investigated (Figures 19.17 and 19.18) [5, 66–69]. To achieve multi-state photochromism in the coordination compounds, the inhibition/suppression of intramolecular energy transfer between different photochromic units is required; otherwise, the reactive excited state of

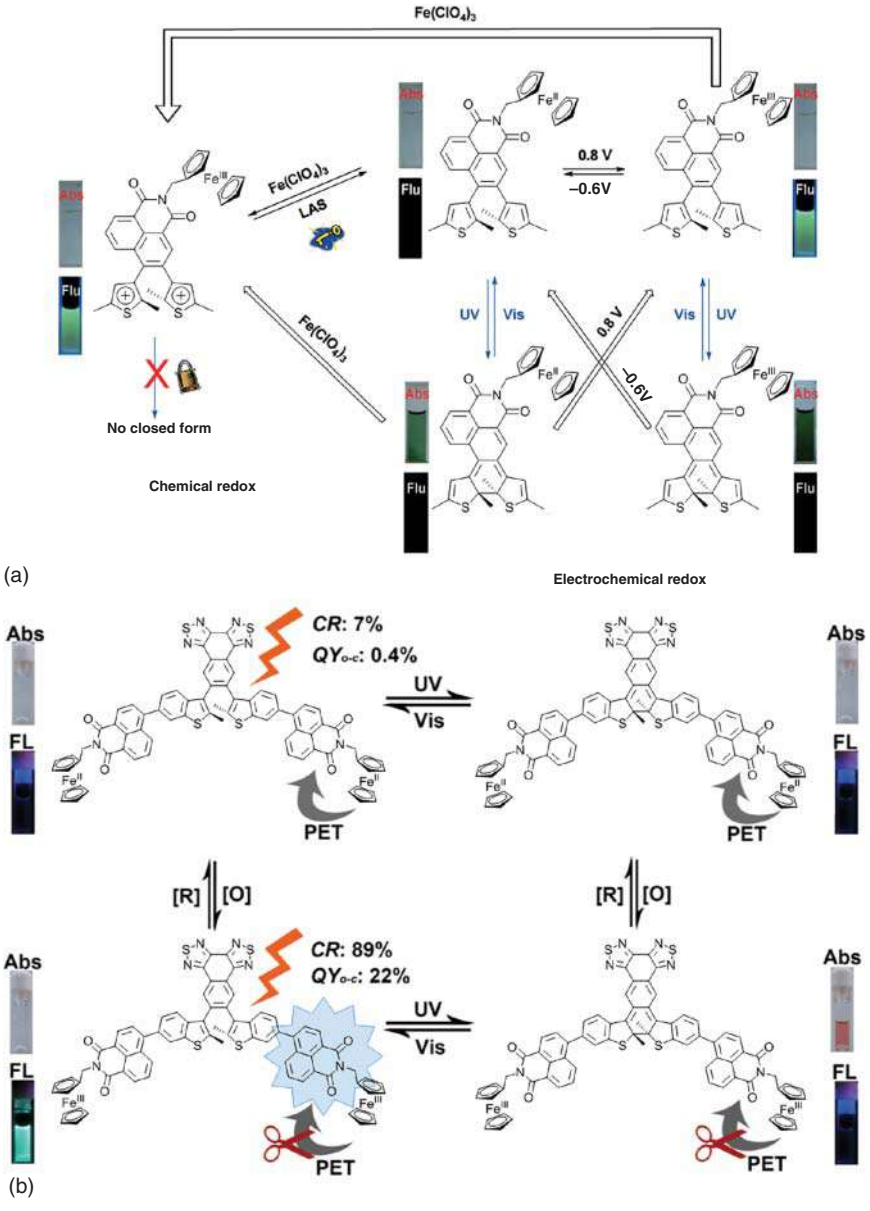


**Figure 19.15** Ferrocene-based (a) naphthalimide-fused and (b) benzobisthiadiazole-fused diarylethenes with redox-gated photochromic property. Source: (a, b) Reproduced with the permission of Wiley-VCH from Refs. [4, 64], respectively.

some of photochromic units would be quenched [65, 70]. Through systematic investigation of various transition metal complexes with multiple photochromic diarylethene units, the effects of linkages, backbones, or pendants between different diarylethene units on inhibiting the quenching pathway have been studied [70].

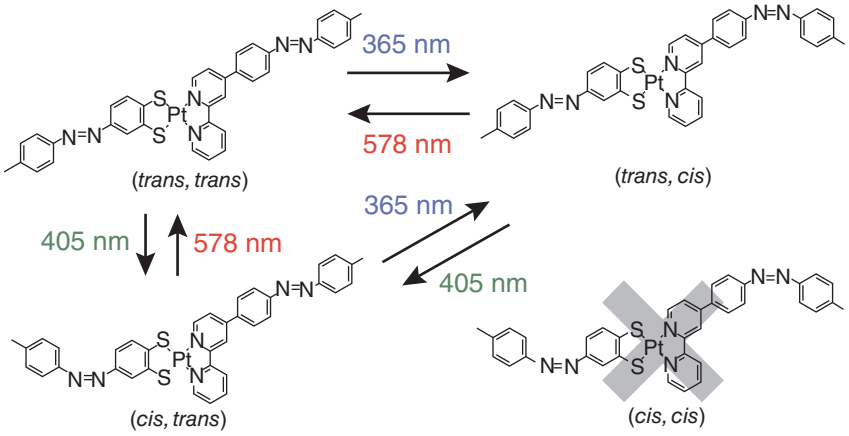


**Figure 19.16** Dithiolato Pt(II) bipyridine complex with photocontrolled multiple states. Source: Reproduced with the permission of Wiley-VCH from Sakamoto et al. [36].

Stepwise photochromism of two diarylethene-containing alkynyl ligands with three states (*open–open*, *open–closed*, *closed–closed*) in their *cis*- and *trans*- bis(phosphino) Pt(II) complexes was reported [5, 68]. For the *trans*-Pt(II) complexes, distinct stepwise photochromic reactions were observed because the first photocyclization (*open–open* to *open–closed*) was much more efficient than the second photocyclization (*open–closed* to *closed–closed*), due to the quenching of the reactive excited state by the lower-lying excited state in the cyclized diarylethene-containing ligand [5]. In the *cis*-isomer, the electronic interaction of the two diarylethene-containing acetylide ligands is much weaker, and thus the efficiency of the first and second photocyclizations in the complex is similar [5]. As a result, the *open–closed* in the *cis*-complex always exists as a minor component during the photocyclization process. Based on this result, the *trans*-diphosphino Pt(II) with two different diarylethene-containing alkynyl ligands was designed to achieve four different chromic states switchable by selective wavelength excitations (Figure 19.17a) [5].

On the other hand, intramolecular energy transfer between different photochromic ligands was found to be inefficient in a Au(I) complex [66]. Stepwise photocyclization of the Au(I) complex (*open–open–open* to *closed–open–closed*) occurred upon initial irradiation at c. 365 nm. Subsequent UV excitation at c. 254 nm resulted in complete photocyclization (*closed–open–closed* to *closed–closed–closed*). For the photocycloreversion of the fully closed form, selective stepwise ring-opening reaction (*closed–closed–closed* to *open–closed–open*) can also be achieved by photoirradiation at c. 672 nm. Eventually, the original state (*open–open–open*) can be obtained via the photocycloreversion upon irradiation at $\lambda > 460$ nm [66]. Therefore, in the dinuclear Au(I) complex with three diarylethene-containing ligands of two different types, four states (colorless, blue, reddish violet, and bluish violet) can be switched by different wavelengths of excitation (Figure 19.17b) [66].

When two diarylethene-containing alkynyl ligands were introduced into an electrochemically active Ru(II) system [67, 69], the resulting Ru(II) complexes also

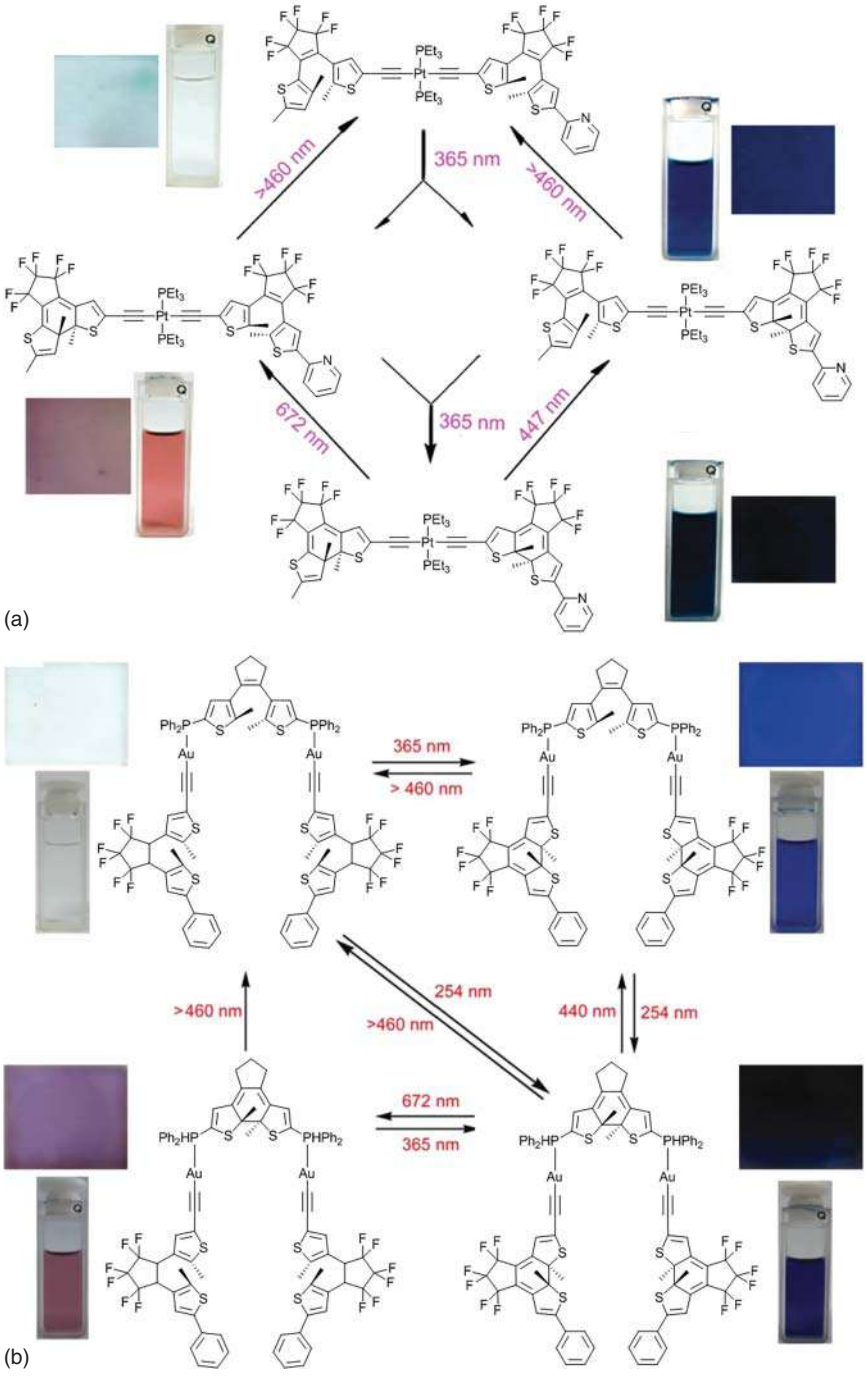


**Figure 19.17** (a) Pt(II) and (b) Au(I) complexes with multiple diarylethene units to show multiple photocontrolled states. Source: (a, b) Reproduced with the permission of American Chemical Society from Refs. [5, 66], respectively.

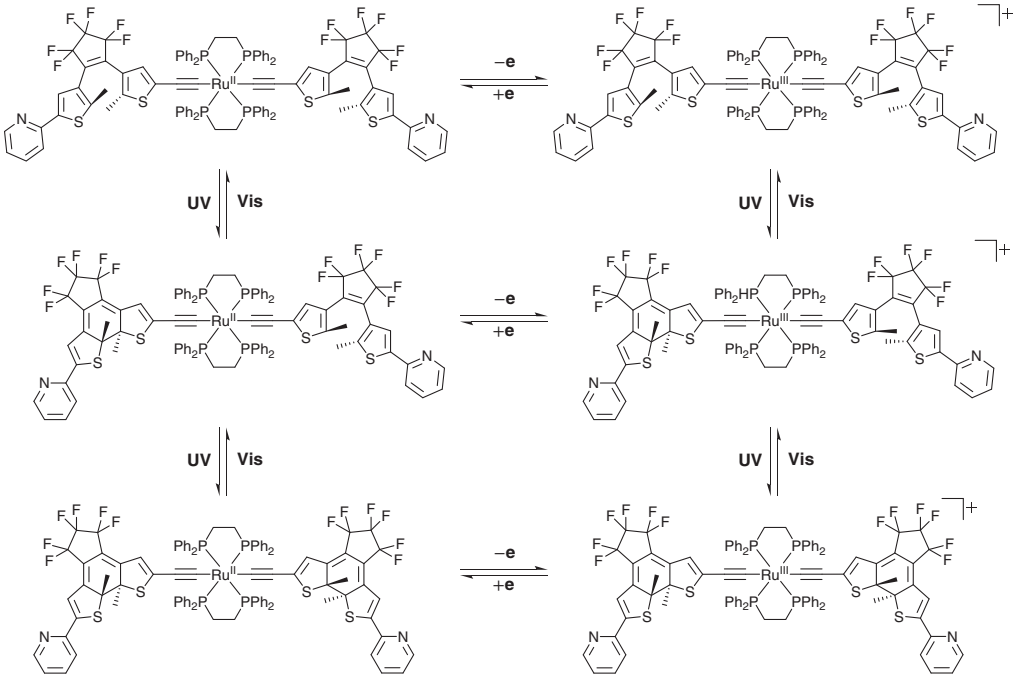


**Figure 19.18** Ru(II) complex with photochromic and electrochromic behaviors. Source: Reproduced with the permission of American Chemical Society from Li et al. [67].

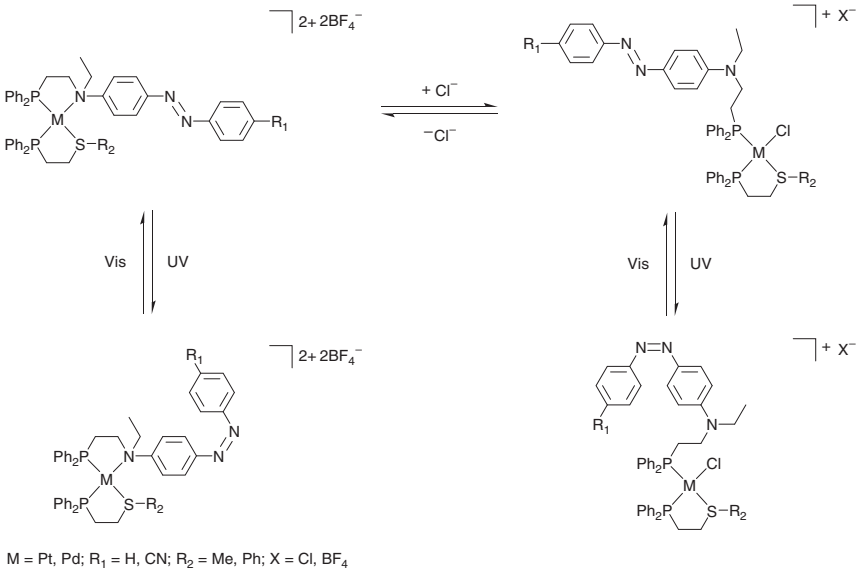


**Figure 19.19** Photochromic azobenzene-based phosphino-amino (P^N) platinum(II) and palladium(II) complexes with chloride-induced reversible chelation. Source: Reproduced with the permission of American Chemical Society from Park et al. [71].

display three-state stepwise photochromism with evolution of low-energy absorption bands peaking at c. 684–698 nm. In addition, coupling the photochromism with electrochromic properties of the Ru(II) complex, the three states were further extended to six states (Figure 19.18) with new low-energy NIR absorption band at c. 1263 nm, ascribable to the LMCT transitions [67].

Apart from combining photochromism with electrochromism, coupling of photochromic and coordination reactivity can also result in multi-state photochromic coordination compounds [71]. This is demonstrated by coordination of a series of photochromic azobenzene-based bidentate phosphine-amine ligands to platinum(II) and palladium(II) (Figure 19.19) [71]. As the bidentate ligand is hemilabile with the N atom of the tertary amine of the bidentate ligand readily de-coordinated, addition of chloride would change the ligating mode of the azobenezene-containing phosphine-amine ligands from a chelating to a monodentate mode. This extended the binary photochromic state to four states (Figure 19.19).

By coordination of diarylethene-containing phosphole ligands to triphenylamine-substituted alkynyl Au(I) system with mechanochromic behaviors, the solid state of these complexes exhibits multi-stimuli-responsive properties with four different states (Figure 19.20a) [6]. Similar to other photochromic diarylethene-containing phospholes [72–76], these Au(I) complexes are robust with high fatigue resistance and excellent thermal irreversibility with no apparent thermal backward reaction over 40 hours even at 60 °C [6]. Interestingly, the open forms of gold(I) complexes display color changes from pale yellow to yellow in solid samples upon grinding (Figure 19.20b) [6]. With the absence of short Au···Au

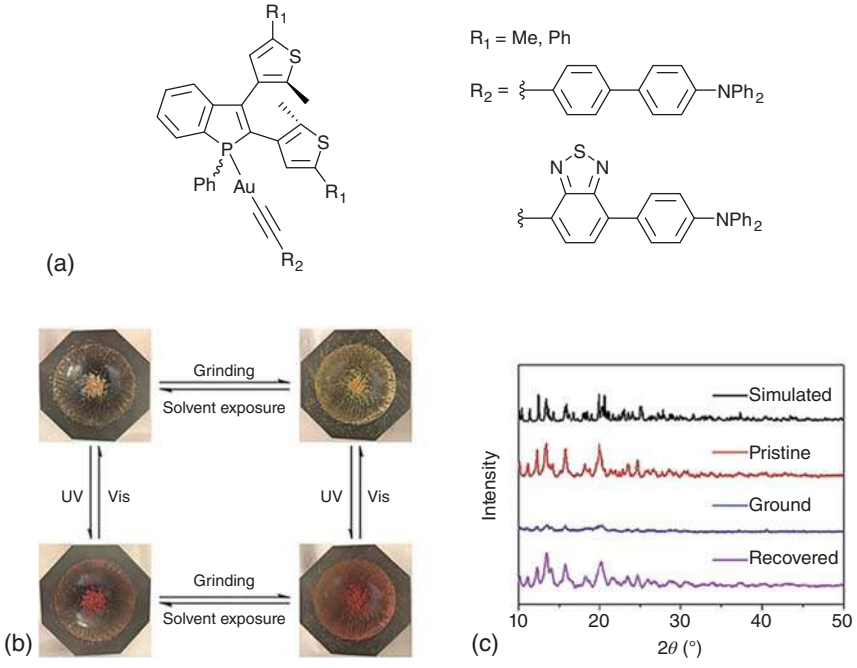


**Figure 19.20** (a) Chemical structures of benzo[*b*]phosphole alkynylgold(I) complexes. (b) Solid-state mechanochromism and photochromism of the gold(I) complex upon grinding and UV irradiation, respectively. (c) PXRD patterns of the gold(I) complex in various forms. Source: (b) Reproduced with the permission of Wiley-VCH from Wu et al. [6].

contacts in the X-ray structure, the mechanically induced bathochromic shifts were probably attributed to the planarization of the triphenylamine-containing alkynyl ligands instead of the changes in the Au···Au distance [6]. Powder X-ray diffraction (PXRD) analysis of the pristine and ground samples suggested that a well-ordered crystalline to random amorphous phase transition occurred during the grinding process (Figure 19.20c) [6]. The pristine sample showed sharp and intense diffraction peaks, well-matched with the simulated signals of the single crystal in the X-ray crystallographic analysis, whereas the ground sample displayed no characteristic signals. The mechanochromic shift could be reverted within several minutes of exposure to solvent vapor such as diethyl ether [6]. Hence, these Au(I) complexes exhibit reversible transformations among multiple states in the solid form arisen from the photochromic and mechanochromic behavior induced by light and mechanical stimuli, suggesting the important role of the metal center in isolating the different stimuli-responsive states through appropriate design.

Through coordination of an ancillary ligand with gelating functional properties into photochromic coordination compounds, solution-to-gel transformation can be introduced in addition to the photochromic transformation. This has been first demonstrated in spirooxazine-containing bipyridyl platinum(II) with cholesteryl-functionalized alkynyl ligands (Figure 19.21a) [3]. This platinum(II) complex exhibits photochromism in solution and gel states formed in various

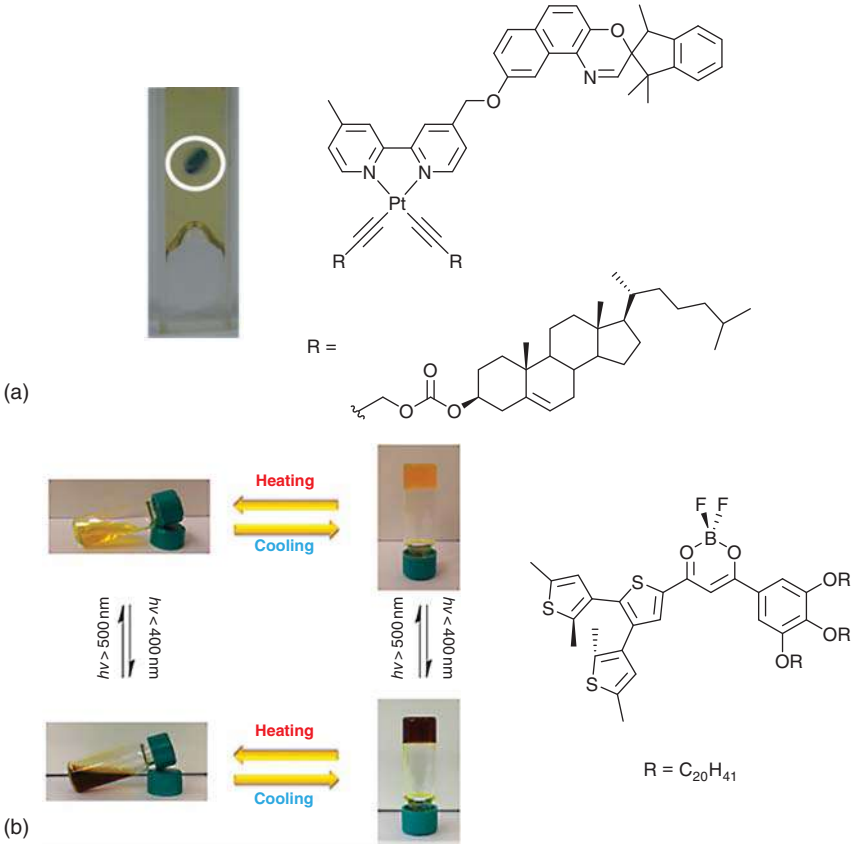


**Figure 19.21** (a) Photochromic Pt(II) complex and (b) B(III) complexes with gelation behavior. Source: (a) Reproduced with the permission of Wiley-VCH from Li et al. [3] and (b) American Chemical Society from Wong et al. [77], respectively.

aliphatic solvents, including heptane, octane, decane, and dodecane at room temperature [3]. By functionalization of the photochromic ligand with thermal-responsive gelation functional groups (icosyloxy chains), its boron(III) complex exhibits the sol–gel transition controllable by temperature and photochromism in both solution and gel states [77] (Figure 19.21b).

## 19.3 Conclusion

In summary, the reversible photo-reactions of the photochromic ligands could be perturbed significantly upon coordination despite the similarity in the chemical transformation. This can be mainly attributed to the perturbation of the molecular orbitals arising from the formation of coordination bonds and geometrical modification. This would introduce additional electronic transitions and excited states. As a result, reactive excited states for the photochromic reaction can be

photosensitized or quenched, depending on the energy levels of the characteristic excited states of the coordination units, by the intramolecular energy transfer processes. Moreover, the coordination of the photochromic ligands to heavy metal atom also strengthens the spin–orbital coupling, which opens up triplet-state-sensitized photochromic reactions. Through coordination to transition metal complex systems with high-lying triplet excited states, photosensitized photochromism from ligand-centered excited states can be achieved. In the examples described in this chapter, this strategy can extend the photochromism from UV excitation in the free ligands to visible excitation in their coordination compounds. However, coordination to systems with lower-lying excited states could also result in inhibition of the photochromic reaction due to the deactivation of the reactive excited state. Besides, perturbation of the molecular orbitals upon coordination represents an effective strategy to modify the energy of the electronic states of the photochromic moieties. This enables the modification of the absorption properties of the photochromic ligands through the incorporation into different coordination systems and leads to the development of near-IR photochromic compounds through simple coordination.

On the other hand, functionalization of the ancillary ligand in the photochromic coordination compounds offers a possibility to introduce other functional properties such as electrochemical, photochemical, mechanochemical, and gelation properties. This enables the design of multi-state, multiple-addressable, and gated photochromic coordination compounds. Parallel to the development of wide varieties of ligands with diverse functional properties and as demonstrated in the above examples, it would facilitate the expanding development of photochromic coordination compounds with novel multifunctional properties.

## References


1 Ko, C.C., Kwok, W.M., Yam, V.W.W. et al. (2006). Triplet MLCT photosensitization of the ring-closing reaction of diarylethenes by design and synthesis of a photochromic rhenium(I) complex of a diarylethene-containing 1,10-phenanthroline ligand. *Chem. Eur. J.* 12 (22): 5840–5848.

2 Lee, P.H.M., Ko, C.C., Zhu, N. et al. (2007). Metal coordination-assisted near-infrared photochromic behavior: a large perturbation on absorption wavelength properties of N, N-donor ligands containing diarylethene derivatives by coordination to the rhenium(I) metal center. *J. Am. Chem. Soc.* 129 (19): 6058–6059.

3 Li, Y.G., Tam, A.Y.Y., Wong, K.M.C. et al. (2011). Synthesis, characterization, and the photochromic, luminescence, metallogelation and liquid-crystalline properties of multifunctional platinum(II) bipyridine complexes. *Chem. Eur. J.* 17 (29): 8048–8059.

4 Cai, Y., Gao, Y., Luo, Q. et al. (2016). Ferrocene-grafted photochromic triads based on a sterically hindered ethene bridge: redox-switchable fluorescence and gated photochromism. *Adv. Opt. Mater.* 4 (9): 1410–1416.


5 Li, B., Wen, H.M., Wang, J.Y. et al. (2015). Multistate and multicolor photochromism through selective cycloreversion in asymmetric platinum(II) complexes with two different dithienylethene–acetylides. *Inorg. Chem.* 54 (23): 11511–11519.

6 Wu, N.M.W., Ng, M., and Yam, V.W.W. (2019). Photochromic benzo[*b*]phosphole alkynylgold(I) complexes with mechanochromic property to serve as multistimuli-responsive materials. *Angew. Chem. Int. Ed.* 58 (10): 3027–3031.

7 Nakai, H. and Isobe, K. (2010). Photochromism of organometallic compounds with structural rearrangement. *Coord. Chem. Rev.* 254 (21–22): 2652–2662.

8 Rack, J.J. (2009). Electron transferred sulfoxide isomerization in ruthenium and osmium complexes. *Coord. Chem. Rev.* 253 (1–2): 78–85.

9 Dürr, H. and Bous-Laurent, H. (1990). *Photochromism-Molecules and Systems*. Amsterdam (NL): Elsevier.

10 Crano, J.C. and Guglielmetti, R.J. (1999). *Organic Photochromic and Thermochromic Compounds, Vol. 1: Main Photochromic Families*. New York: Plenum Press.

11 Tian, H. and Zhang, J. (2016). *Photochromic Materials: Preparation, Properties and Applications*. Wiley-VCH: Weinheim.

12 Irie, M. (2000). Diarylethenes for memories and switches. *Chem. Rev.* 100 (5): 1685–1716.

13 Coppens, P., Novozhilova, I., and Kovalevsky, A. (2002). Photoinduced linkage isomers of transition-metal nitrosyl compounds and related complexes. *Chem. Rev* 102 (4): 861–883.

14 Bitterwolf, T.E. (2006). Photochemical nitrosyl linkage isomerism/metastable states. *Coord. Chem. Rev.* 250 (9–10): 1196–1207.

15 Kubas, G.J. (1994). Chemical transformations and facile disproportionation of sulfur dioxide on transition metal complexes. *Acc. Chem. Res.* 27 (7): 183–190.

16 Butcher, D.P., Rachford, A.A., Petersen, J.L. et al. (2006). Phototriggered S→O isomerization of ruthenium-bond chelating sulfoxide. *Inorg. Chem.* 45 (23): 9178–9180.

17 Rachford, A.A. and Rack, J.J. (2006). Picosecond isomerization in photochromic ruthenium-dimethyl sulfoxide complexes. *J. Am. Chem. Soc.* 128 (44): 14318–14324.

18 McClure, B.A. and Rack, J.J. (2009). Two-color reversible switching in a photochromic ruthenium sulfoxide complex. *Angew. Chem. Int. Ed.* 48 (45): 8556–8558.

19 Mockus, N.V., Rabinovich, D., Petersen, J.L. et al. (2008). Femtosecond isomerization in a photochromic molecular switch. *Angew. Chem. Int. Ed.* 47 (8): 1458–1461.

20 Sylvester, S.O., Cole, J.M., and Waddell, P.G. (2012). Photoconversion bonding mechanism in ruthenium sulfur dioxide linkage photoisomers revealed by in situ diffraction. *J. Am. Chem. Soc.* 134 (29): 11860–11863.

21 Jukes, R.T.F., Adamo, V., Hartl, F. et al. (2004). Photochromic dithienylethene derivatives containing Ru(II) or Os(II) metal units, sensitized photocyclization from a triplet state. *Inorg. Chem.* 43 (9): 2779–2792.


**22** Yam, V.W.W., Ko, C.C., and Zhu, N. (2004). Photochromic and luminescence switching properties of a versatile diarylethene-containing 1,10-phenanthroline ligand and its rhenium(I) complex. *J. Am. Chem. Soc.* 126 (40): 12734–12735.

**23** Vogler, A. and Kunkely, H. (2001). Luminescent metal complexes: diversity of excited states. *Top. Curr. Chem.* 213: 143–182.

**24** Ko, C.C. and Yam, V.W.W. (2010). Transition metal complexes with photochromic ligands – photosensitization and photoswitchable properties. *J. Mater. Chem.* 20: 2063–2070.

**25** Ko, C.C. and Yam, V.W.W. (2018). Coordination compounds with photochromic ligands: ready tunability and visible light-sensitized photochromism. *Acc. Chem. Res.* 51 (1): 149–159.

**26** Zarnegar, P.P., Bock, C.R., and Whitten, D.G. (1973). Photoreactions of transition metal complexes. Ligand reactivity as a prober for excited-state characterization. *J. Am. Chem. Soc.* 95 (13): 4367–4372.

**27** Yam, V.W.W., Lau, V.C.Y., and Cheung, K.K. (1995). Synthesis, photophysics and photochemistry of novel luminescent rhenium(I) photoswitchable materials. *J. Chem. Soc. Chem. Commun.*: 259–261.

**28** Yam, V.W.W., Lau, V.C.Y., and Wu, L.X. (1998). Synthesis, photophysical, photochemical and electrochemical properties of rhenium(I) diimine complexes with photoisomerizable pyridyl-azo, -ethenyl or -ethyl ligands. *J. Chem. Soc., Dalton Trans.*: 1461–1468.

**29** Busby, M., Matousek, P., Towrie, M. et al. (2005). Ultrafast excited-state dynamics preceding a ligand trans-cis isomerization of *fac*-[Re(Cl)$(CO)_3$(t-4-styrylpyridine$)_2$] and *fac*-[Re(t-4-styrylpyridine)$(CO)_3$(2,2′-bipyridine)]. *J. Phys. Chem. A.* 109 (13): 3000–3008.

**30** Lewis, J.D., Pertuz, R.N., and Moore, J.N. (2000). Proton-controlled photoisomerization: rhenium(I) tricarbonyl bipyridine linked to amine or azacrown ether groups by a styryl pyridine bridging ligand. *Chem. Commun.*: 1865–1866.

**31** Sun, S.S. and Lees, A.J. (2002). Synthesis, photophysical properties, and photoinduced luminescence switching of trinulear diimine rhenium(I) tricarbonyl complexes linked by an isomerizable stilbene-like ligand. *Organometallics.* 21 (1): 39–49.

**32** Wenger, O.S., Henling, L.M., Day, M.W. et al. (2004). Photoswitchable luminescence of rhenium(I) tricarbonyl diimines. *Inorg. Chem.* 43 (6): 2043–2048.

**33** Bossert, J. and Daniel, C. (2006). Trans-cis Photoisomerization of the styrylpyridine ligand in [Re$(CO)_3$(2,2′-bipyridine)(*t*-4-styrylpyridine)]$^+$: role of the metal-to-ligand charge-transfer excited states. *Chem. Eur. J.* 12 (18): 4835–4843.

**34** Tissot, A., Boillot, M.L., Pillet, S. et al. (2010). Unidirectional photoisomerization of styrylpyridine for switching the magnetic behavior of an iron(II) complex: a MLCT pathway in crystalline solids. *J. Phys. Chem. C.* 114 (49): 21715–21722.

**35** Hasegawa, Y., Takahashi, K., Kume, S. et al. (2011). Complete solid state photoisomerization of bis(dipyrazolylstyrylpyridine) iron(II) to change magnetic properties. *Chem. Commun.* 47 (24): 6846–6848.


**36** Sakamoto, R., Kume, S., Sugimoto, M. et al. (2009). Trans-cis photoisomerization of azobenzene-conjugated dithiolato-bipyridine platinum(II) complexes: extension of photoresponse to longer wavelengths and photocontrollable tristability. *Chem. Eur. J.* 15 (6): 1429–1439.

**37** Yam, V.W.W., Ko, C.C., Wu, L.X. et al. (2000). Synthesis, crystal structure, and photochromic properties of rhenium(I) complexes containing the spironaphthoxazine moiety. *Organometallics* 19 (10): 1820–1822.

**38** Ko, C.C., Wu, L.X., Wong, K.M.C. et al. (2004). Synthesis, characterization and photochromic studies of spirooxazine-containing 2,2′-bipyridine ligands and their rhenium(I) tricarbonyl complexes. *Chem. Eur. J.* 10 (3): 766–776.

**39** Lee, J.K.W., Ko, C.C., Wong, K.M.C. et al. (2007). A photochromic platinum(II) bis(alkynyl) complex containing a versatile 5,6-dithienyl-1,10-phenanthroline. *Organometallics* 26 (1): 12–15.

**40** Belser, P., de Cola, L., Hartl, F. et al. (2006). Photochromic switches incorporated in bridging ligands: a new tool to modulate energy-transfer processes. *Adv. Funct. Mater.* 16 (2): 195–208.

**41** Ngan, T.W., Ko, C.C., Zhu, N. et al. (2007). Synthesis, luminescence switching, and electrochemical studies of photochromic dithienyl-1,10-phenanthroline zinc(II) bis(thiolate) complexes. *Inorg. Chem.* 46 (4): 1144–1152.

**42** Indelli, M.T., Carli, S., Ghirotti, M. et al. (2008). Triplet pathways in diarylethene photochromism: photophysical and computational study of dyads containing ruthenium(II) polypyridine and 1, 2-bis(2-methylbenzothiophene-3-yl) maleimide units. *J. Am. Chem. Soc.* 130 (23): 7286–7299.

**43** Roberts, M.R., Nagle, J.K., Majewski, M.B. et al. (2011). Charge transfer and intraligand excited state interactions in platinum-sensitized dithienylethenes. *Inorg. Chem.* 50 (11): 4956–4966.

**44** Wong, H.L., Zhu, N., and Yam, V.W.W. (2014). Photochromic alkynylplatinum(II) diimine complexes containing a versatile dithienylethene-functionalized 2-(2′-pyridyl)imidazole ligand. *J. Organomet. Chem.* 751: 430–437.

**45** Tan, W., Zhang, Q., Zhang, J. et al. (2009). Near-infrared photochromic diarylethene iridium(III) complex. *Org. Lett.* 11 (1): 161–164.

**46** Tan, W., Zhou, J., Li, F. et al. (2011). Visible light-triggered photoswitchable diarylethene-based iridium(III) complexes for imaging living cells. *Chem. Asian J.* 6 (5): 1263–1268.

**47** Chan, J.C.H., Lam, W.H., Wong, H.L. et al. (2011). Diarylethene-containing cyclometalated platinum(II) complexes: tunable photochromism via metal coordination and rational ligand design. *J. Am. Chem. Soc.* 133 (32): 12690–12705.

**48** Zhong, Y.W., Vilà, N., Henderson, J.C. et al. (2009). Transition-metal tris-bipyridines containing three dithienylcyclopentenes: synthesis, photochromic, and electrochromic properties. *Inorg. Chem.* 48 (15): 7080–7085.

**49** Duan, G.P. and Yam, V.W.W. (2010). Syntheses and photophysical properties of N-pyridylimidazol-2-ylidene tetracyanoruthenates(II) and photochromic studies of their dithienylethene-containing derivatives. *Chem. Eur. J.* 16 (42): 12642–12649.

**50** Brayshaw, S.K., Schiffers, S., Stevenson, A.J. et al. (2011). Highly efficient visible-light driven photochromism: developments towards a solid-state


molecular switch operating through a triplet-sensitised pathway. *Chem. Eur. J.* 17 (16): 4385–4395.

**51** Wang, N., Ko, S.B., Lu, J.S. et al. (2013). Tuning the Photoisomerization of a N^C-chelate organoboron compound with a metal-acetylide unit. *Chem. Eur. J.* 19 (17): 5314–5323.

**52** Ryutaro, M., Tomoaki, Y., and Masanobu, W. (2011). Cyclization reaction of diarylethene through the triplet excited state. *Bull. Chem. Soc. Jpn.* 84 (12): 1336–1338.

**53** Herder, M., Schmidt, B.M., Grubert, L. et al. (2015). Improving the fatigue resistance of diarylethene switches. *J. Am. Chem. Soc.* 137 (7): 2738–2747.

**54** Zhang, Z., Zhang, J., Wu, B. et al. (2018). Diarylethenes with a narrow singlet–triplet energy gap sensitizer: a simple strategy for efficient visible-light photochromism. *Adv. Opt. Mater.* 6 (6): 1700847.

**55** Poon, C.T., Lam, W.H., Wong, H.L. et al. (2010). A versatile photochromic dithienylethene-containing $\beta$-diketonate ligand: near-infrared photochromic behavior and photoswitchable luminescence properties upon incorporation of a boron(III) center. *J. Am. Chem. Soc.* 132 (40): 13992–13993.

**56** Poon, C.T., Lam, W.H., and Yam, V.W.W. (2013). Synthesis, photochromic, and computational studies of dithienylethene-containing $\beta$-diketonate derivatives and their near-infrared photochromic behavior upon coordination of a boron(III) center. *Chem. Eur. J.* 19 (10): 3467–3476.

**57** Wong, C.L., Poon, C.T., and Yam, V.W.W. (2016). Photochromic dithienylethene-containing boron(III) ketoiminates: modulation of photo-responsive behavior through variation of intramolecular motion. *Chem. Eur. J.* 22 (36): 12931–12940.

**58** Irie, M., Fukaminato, T., Matsuda, K. et al. (2014). Photochromism of diarylethene molecules and crystals: memories, switches, and actuators. *Chem. Rev.* 114 (24): 12174–12277.

**59** Poon, C.T., Lam, W.H., and Yam, V.W.W. (2011). Gated photochromism in triarylborane-containing dithienylethenes: a new approach to a "lock-unlock" system. *J. Am. Chem. Soc.* 133 (49): 19622–19625.

**60** Wu, Y., Chem, S., Yang, Y. et al. (2012). A novel gated photochromic reactivity controlled by complexation/dissociation with BF3. *Chem. Commun.* 48 (4): 528–530.

**61** Wu, Y., Zhu, W., Wan, W. et al. (2014). Reversible photoswitching specifically responds to mercury(II) ions: the gated photochromism of bis(dithiazole)ethene. *Chem. Commun.* 50 (91): 14205–14208.

**62** Wang, S., Li, X., Zhao, W. et al. (2017). $Cu^{2+}$-selectivity gated photochromism in Schiff-modified diarylethenes with a star-shaped structure. *J. Mater. Chem. C.* 5 (2): 282–289.

**63** Raman, A., Augustine, G., Ayyadurai, N. et al. (2018). Gated photochromism in azobenzene-appended rhodamine cassette: through-bond energy transfer – a universal strategy towards "lock and unlock" system. *J. Mater. Chem. C.* 6 (39): 10497–10501.

**64** Zhu, W., Song, L., Yang, Y. et al. (2012). Novel bisthienylethene containing ferrocenyl-substituted naphthalimide: a photo- and redox multi-addressable molecular switch. *Chem. Eur. J.* 18 (42): 13388–13394.

**65** Fihey, A., Perrier, A., Browned, W.R. et al. (2015). Multiphotochromic molecular systems. *Chem. Soc. Rev.* 44 (11): 3719–3759.

**66** Li, B., Wu, Y.H., Wen, H.M. et al. (2012). Gold(I)-coordination triggered multistep and multiple photochromic reactions in multi-dithienylethene (DTE) systems. *Inorg. Chem.* 51 (3): 1933–1942.

**67** Li, B., Wang, J.Y., Wen, H.M. et al. (2012). Redox-modulated stepwise photochromism in a ruthenium complex with dual dithienylethene-acetylides. *J. Am. Chem. Soc.* 134 (38): 16059–16067.

**68** Li, B., Wen, H.M., Wang, J.Y. et al. (2013). Modulating stepwise photochromism in platinum(II) complexes with dual dithienylethene–acetylides by a progressive red shift of ring-closure absorption. *Inorg. Chem.* 52 (21): 12511–12520.

**69** Chen, J.X., Wang, J.Y., Zhang, Q.C. et al. (2017). Multiphotochromism in an asymmetric ruthenium complex with two different dithienylethenes. *Inorg. Chem.* 56 (21): 13257–13266.

**70** Fihey, A. and Jacquemin, D. (2016). How metals can help multiphotochromism: an ab initio study. *J. Phys. Chem. C* 120 (20): 11140–11150.

**71** Park, J.S., Lifschitz, A.M., Young, R.M. et al. (2013). Modulation of electronics and thermal stabilities of photochromic phosphino–aminoazobenzene derivatives in weak-link approach coordination complexes. *J. Am. Chem. Soc.* 135 (45): 16988–16996.

**72** Chan, J.C.H., Lam, W.H., Wong, H.L. et al. (2013). Tunable photochromism in air-stable, robust dithienylethene-containing phospholes through modifications at the phosphorus center. *Angew. Chem. Int. Ed.* 52 (44): 11504–11508.

**73** Chan, J.C.H., Wong, H.L., Wong, W.T. et al. (2015). Tunable photochromism in the robust dithienylethene-containing phospholes: design, synthesis, characterization, electrochemistry, photophysics, and photochromic studies. *Chem. Eur. J.* 21 (18): 6936–6948.

**74** Wu, N.M.W., Wong, H.L., and Yam, V.W.W. (2017). Photochromic benzo[*b*]phosphole oxide with excellent thermal irreversibility and fatigue resistance in the thin film solid state via direct attachment of dithienyl units to the weakly aromatic heterocycle. *Chem. Sci.* 8 (2): 1309–1315.

**75** Wu, N.M.W., Ng, M., Lam, W.H. et al. (2017). Photochromic heterocycle-fused thieno[*3,2-b*]phosphole oxides as visible light switches without sacrificing photoswitching efficiency. *J. Am. Chem. Soc.* 139 (42): 15142–15150.

**76** Wu, N.M.W. and Yam, V.W.W. (2019). Photochromic barbiturate pendant-containing benzo[*b*]phosphole oxides with co-assembly property and photoinduced morphological changes. *ACS Appl. Mater. Interfaces* 11 (43): 40290–40299.

**77** Wong, C.L., Poon, C.T., and Yam, V.W.W. (2017). Photoresponsive organogelator: utilization of boron(III) diketonate as a building block to construct multiresponsive materials. *Organometallics* 36 (14): 2661–2669.


## 20 Versatile Photoswitchable Molecules in Catalysis

Jie Li and Stefan Hecht

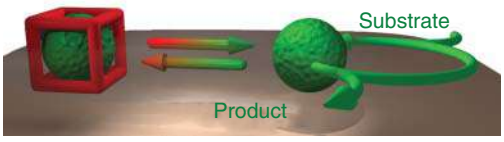


**Characteristic Features**

Remote-controlling chemical reactions with regard to activity and selectivity using: *E/Z*-photoisomerization, electrocyclic ring opening/closure, unidirectional rotation, helical chirality.

**First Reported**

Ueno, A., Takahashi, K., and Osa, T. (1981). Photocontrol of catalytic activity of capped cyclodextrin. *Chem. Soc. Chem. Commun.*: 94–96.

**Key References**

Stoll, R.S. and Hecht, S. (2010). Artificial light-gated catalyst systems. *Angew. Chem. Int. Ed*. 49: 5054–5075.

Göstl, R., Senf, A., and Hecht, S. (2014). Remote-controlling chemical reactions by light: toward chemistry with high spatio-temporal resolution. *Chem. Soc. Rev*. 43: 1982–1996.

Blanco, V., Leigh, D.A., and Marcos, V. (2015). Artificial switchable catalysts. *Chem. Soc. Rev*. 44: 5341–5370.

Vlatkovic, M., Collins, B.S., and Feringa, B.L. (2016). Dynamic Responsive Systems for Catalytic Function. *Chem. Eur. J.* 22: 17080–17111.

Ihrig, S.P., Eisenreich, F., and Hecht, S. (2019). Photoswitchable polymerization catalysis: state of the art, challenges, and perspectives. *Chem. Commun.* 55: 4290–4298.

# 20

# Versatile Photoswitchable Molecules in Catalysis

*Jie Li*[1] *and Stefan Hecht*[1,2,3]

[1] *DWI – Leibniz Institute for Interactive Materials, Forckenbeckstr. 50, 52074 Aachen, Germany*
[2] *RWTH Aachen University, Institute of Technical and Macromolecular Chemistry, Worringer Weg 2, 52074 Aachen, Germany*
[3] *Humboldt-Universität zu Berlin, Department of Chemistry & IRIS Adlershof, Brook-Taylor-Str. 2, 12489 Berlin, Germany*

## 20.1 Introduction

The field of catalysis has gained significant attention over decades in both industrial and academic areas, with the aim to enable chemical reactions associated with high activation barriers and converting reactants selectively into desired products [1, 2]. Over the past decades, a variety of metal-based as well as purely organic catalysts have been developed to enable and facilitate specific synthetic transformations with high degrees of chemo-, regio-, and stereoselectivity. In strong contrast to such traditional somewhat "one-dimensional" catalysts, the field of switchable catalysis has been emerging and received increasing interest in recent years due to its promise to locally and temporarily control (bio)chemical processes for example through the use of allosteric effects and feedback loops in cell [3–6]. Thus, significant research activities have been dealing with catalysts incorporating units that respond to external stimuli such as temperature [7], chemical regents [8–11], mechanical force [12], or light [13–15]. Among the various available stimuli, light offers some exceptional advantages, including superior spatial and temporal resolution, precise energy (wavelength and intensity) input, traceless non-invasive nature, and ease of handling [16]. To harness full control over catalytic activity and selectivity, a reversible toggling process is necessary, and thus a photoswitchable catalyst is typically composed of a photochromic unit able to regulate a nearby catalytically active site. Here, we first discuss general design strategies for photoswitchable catalysts and afterwards detail particular catalytic transformations over which control has been achieved.

*Molecular Photoswitches: Chemistry, Properties, and Applications*,
First Edition. Edited by Zbigniew L. Pianowski.


## 20.2 Design Strategy of Photoswitchable Catalysts

Upon analyzing the various examples described in the literature, several strategies appear to be useful in the design of the "ideal" photoswitchable catalyst. First and foremost, a high efficiency of the photochemical transformation associated to forward (and backward) switching is essential and is typically reflected by high photoconversion and associated strongly different composition of the photostationary states (PSSs) upon irradiation at the specific switching wavelength(s). Clearly, a relatively high PSS ratio change upon switching is imperative since the activity/selectivity difference between both switching states is typically limited. To maximize the latter, a significant alteration of the geometric/electronic properties of the catalyst upon illumination is necessary. It is the tradeoff between maximizing these two effects – photoswitching and inherent reactivity differences – that in the end will determine the overall ability to control the desired chemical transformation by light.

To date, a variety of photoswitchable catalysts based on versatile photochromic units such as azobenzenes, diarylethenes (DAEs), spiropyrans, among others, has been developed and found applications in diverse chemical transformations. Based on the type of photoreaction involved, photoswitchable molecules can be classified into two groups: molecules with *E/Z* isomerization or electrocyclization (Scheme 20.1).

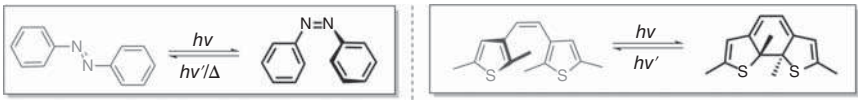


**Scheme 20.1** Light-induced reversible changes of the molecular structure upon either *E/Z*-isomerization of azobenzenes (left) or electrocyclization of diarylethenes (right).

### 20.2.1 Photoswitchable Catalysts Based on *E/Z* Isomerization

Photochromic unit with double bonds, such as stilbenes, azobenzenes, acylhydrazones, among others, can result in large changes of the molecular geometry via *E/Z* isomerization, leading to significant variation of the distance between two terminal (het)aryl moieties and attached substituents [17, 18]. Geometrical changes of catalysts can ultimately give rise to HIGH/LOW or even ON/OFF switching of a reaction through steric and possibly cooperative effects. Steric effects refer to large geometrical changes that block access to the active site in one switching state of the catalyst. Different approaches have been reported to achieve steric switching, such as the use of bulky groups, host–guest binding, and hydrogen bonding, respectively, to shield or de-shield the catalytically active site. Cooperative effects can occur when two or more catalytically active sites work together in a synergistic fashion, typically by modulating their relative distance or orientation.

### 20.2.2 Photoswitchable Catalysts Based on Electrocyclization

Changes in electronic properties can be caused via electrocyclic ring-closing/ring-opening reactions of conjugated systems of which DAE and spiropyran

derivatives are the most popular photochromic families based on electrocyclization [19]. Upon illumination, the molecular geometry of DAEs barely changes, whereas electronic changes can be significant resulting in large variations of the energy levels for the highest occupied molecular orbital (HOMO) and lowest unoccupied molecular orbital (LUMO) between the open and closed isomers. The light-induced valence tautomerization can be followed by thermal (keto-enol) tautomerization [20] to effectively remove the essential part of the catalytic system and thereby control its activity [21].

## 20.3 Formation of Carbon–Carbon Bonds

Formation of carbon–carbon bonds is arguably one of the most fundamental chemical reactions to master to construct complex molecules and involves prototypical transformations, such as the aldol and the related Henry reaction as well as the Michael addition. In this section, we summarize recent advances in controlling the formation of carbon–carbon bonds by photoswitchable catalysts employing various photochromic motifs.

### 20.3.1 Michael Addition

An azobenzene-based photoswitchable catalyst, incorporating a thiourea as hydrogen-bond donor and a nitro group as hydrogen-bond acceptor, has been developed by the group of Pericas to catalyze the Michael addition to a nitro olefin (Scheme 20.2) [22]. In this example, the accessible thiourea active site in *E*-**1** catalyzes the reaction of acetylacetone and *m*-bromonitrostyrene. However, when the azobenzene moiety undergoes *E/Z* isomerization induced by 365 nm light, the nitro group in the thus formed *Z*-**1** intramolecularly blocks the thiourea active site and inhibits catalytic activity. Thus, in the presence of the *E*-configured photoswitchable thiourea organocatalyst, the reaction rate for the Michael addition is much higher as compared to the one in the presence of the photogenerated *Z*-form. However, an inevitable disadvantage in this design is that a true in situ

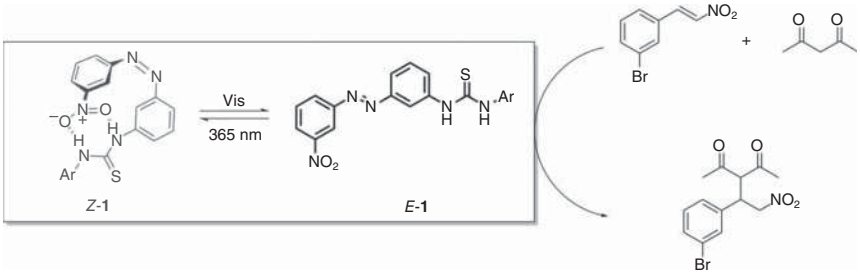


**Scheme 20.2** *E/Z* photoisomerization of azobenzene-based organocatalyst **1** controls the intramolecular interaction of a nitro group and its nearby thiourea unit and thereby its catalytic activity. Source: Based on Osorio-Planes et al. [22].

ON/OFF switching cannot be really achieved. According to the aforementioned description, a true OFF state can be achieved only when the PSS is extremely high. In this particular case, the PSS is composed of 56% *Z*-**1** after 2.5 hours of irradiation, which means nearly half of the catalyst remains active for the transformation and as a result, the reaction was still observed due to the presence of 44% *E*-**1**. The same thiourea organocatalyst **1** was reported to facilitate the ring-opening polymerization of lactide as well [23].

A complementary pair of enantioselective photoswitchable pyridyl-acyl hydrazones has been shown to act as organocatalysts in enantioselective Michael additions (Scheme 20.3) [24]. The catalysts **2**/**3** comprised an active site based on a bifunctional hydrogen-bonding cinchona alkaloid-squaramide motif and a nitrobenzene group, which serves as an inhibiting unit. Similar to the previous strategy outlined for catalyst **1**, *E/Z* isomerization of double bonds forcing the inhibiting nitro group close or away from the squaramide active site leads to catalytically inactive OFF or active ON states. In this case, an *E*:*Z* ratio of 21 : 79 can be reached by irradiation of *E*-**2** or *E*-**3** with 395 nm light. Surprisingly, the PSS *E*:*Z* ratio could be promoted to 5 : 95 by treatment with $CF_3CO_2H$ in $CHCl_3$ in the case of *E*-**3**, while for *E*-**2** this improvement did not work. Both catalysts **2** and **3** mediated Michael additions of carbon or sulfur nucleophiles with electron-deficient olefins in good yields and stereoselectivity. The simultaneous use of the catalyst pair in the same reaction vessel, however, was not possible since the OFF state of one catalyst inhibits the ON state of the other one and vice versa.

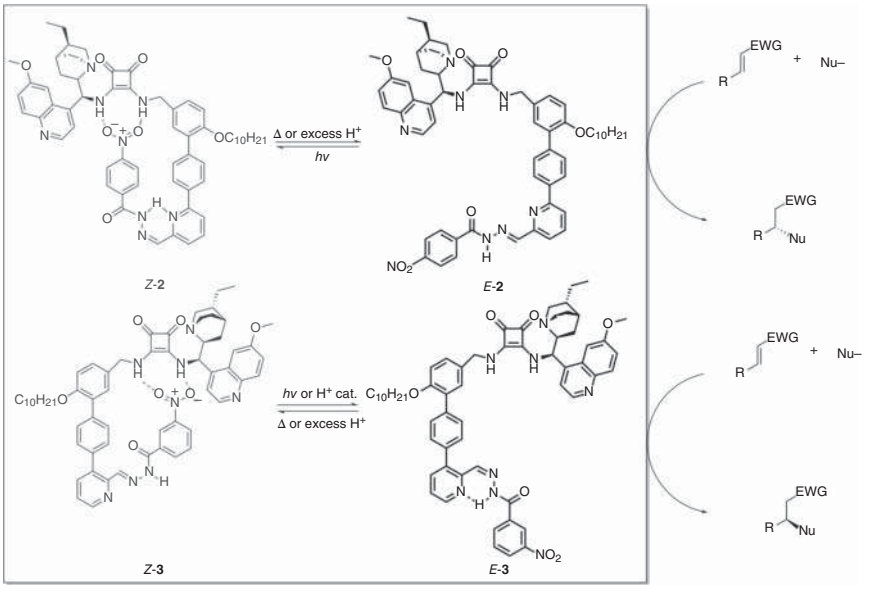


**Scheme 20.3** A pair of photoswitchable bifunctional organocatalysts **2** and **3** employed in enantioselective Michael addition reactions. Source: Based on De Bo et al. [24].

In addition to the aforementioned photoswitchable organocatalysts, bifunctional molecular switches based on a photoresponsive tetrasubstituted alkene

core were explored in Michael additions between (*E*)-acetylacetone and 3-bromo-β-nitrostyrene as reported by Feringa and coworkers (Scheme 20.4) [25]. Incorporation of a hydrogen-bonding thiourea moiety and a basic dimethylamino group in the upper and lower halves of an overcrowded alkene scaffold provided a means to photochemically alter the reaction rate. When (*P*)-*E*-**4** was used as catalyst, the reaction rate was higher as compared to the one in the presence of (*M*)-*Z*-**4** obtained by irradiation by 312 nm light (PSS ratio (*M*)-*Z*-**4**:(*P*)-*E*-**4** = 80 : 20). Contrarily, (*P*)-*Z*-**5** was more active in facilitating the reaction than (*M*)-*E*-**5** under the same reaction. Therefore, the higher activity of (*P*)-*E*-**4** and (*P*)-*Z*-**5** compared to (*M*)-*Z*-**4** and (*M*)-*E*-**5** cannot be simply attributed to intramolecular hydrogen bonding between the thiourea and dimethylamino groups [22] or simple shielding of the reactive site [13]. Thus, the rationale for the deactivation of these photoswitches upon irradiation and interactions between two catalytically active centers remains unclear and, moreover, further studies are necessary to create true ON/OFF photoswitches.

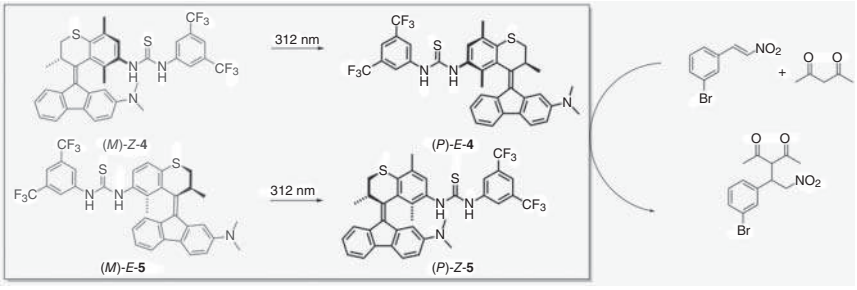


**Scheme 20.4** Bifunctional molecular photoswitches based on overcrowded alkenes enables dynamic control over catalytic activity in Michael addition reactions. Source: Based on Pizzolato et al. [25].

### 20.3.2 Henry Reaction

About 15 years ago, our group developed a photoswitchable Brønsted base catalyst **6** derived from a conformationally restricted N-alkylated piperidine and able to promote the Henry reaction of 4-nitrobenzaldehyde with nitroethane (Scheme 20.5) [13]. The catalytically active lone pair of the N-alkylated piperidine can reversibly be shielded or deshielded by *E/Z* isomerization of an orthogonally fused photochromic azobenzene moiety carrying a bulky azo fragment. Upon irradiation with 365 nm light, the catalytically active *Z*-**6** with significantly increased basicity was accessible (PSS ratio *Z*-**6**:*E*-6 > 95 : 5) and exhibited a more than 35-fold rate increase as compared to inactive *E*-**6**. Contrarily, irradiation of visible light induces back isomerization to *E*-**6** (PSS ratio *E*-**6**:*Z*-6 > 90 : 10) and thus catalytic deactivation. In a subsequent study, the photoswitchable catalyst could successfully be immobilized on silica gel [26].

In another example of photoswitchable catalysis, Feringa and coworkers developed a novel dynamic organocatalyst based on a molecular motor core for the

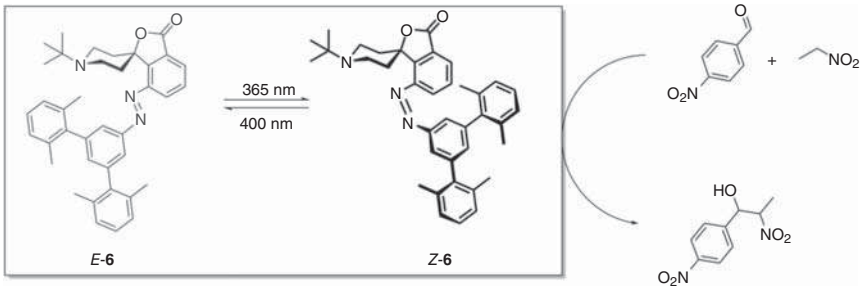


**Scheme 20.5** *E/Z* photoisomerization of the photoswitchable organocatalyst **6** leads to deshielding or shielding of the active site of a general base catalyst, enabling its selective activation and deactivation, respectively. Source: Based on Peters et al. [13].

enantioselective Henry reaction of nitromethane with α,α,α-trifluoroketones (see Section 20.4.1) [27].

### 20.3.3 Morita–Baylis–Hillman Reaction

A photoswitchable cooperative acid catalyst based on an azobenzene-tethered bis-(trityl alcohol) has been reported by Imahori et al. and was found to be highly efficient in catalyzing the Morita–Baylis–Hillman reaction (Scheme 20.6) [28]. In their design, an intramolecular hydrogen bond between two hydroxyl groups can only be formed in the Z-isomer and thus regulated by *E/Z* isomerization of the photochromic azobenzene bridge. The enhanced acidity resulting from this intramolecular hydrogen bond leads to an approximately 86-fold rate acceleration (comparing extrapolated "pure" *Z*-**7** with *E*-**7**) for the phosphine-catalyzed Morita–Baylis–Hillman reaction of 2-cyclopenten-1-one and 3-phenylpropanal. Despite the large reactivity difference of the isolated catalysts, a significant disadvantage arises from the fact that photochemical back isomerization to the less active *E*-isomer is rather inefficient (PSS ratio *E*-**7**:*Z*-7 = 48 : 52), preventing a reversible in situ modulation of catalytic activity with this catalyst system.

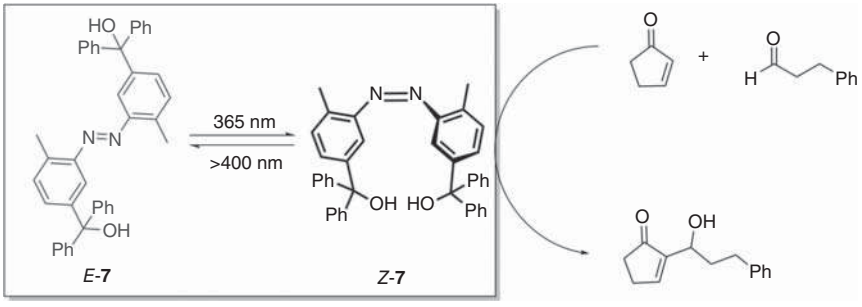


**Scheme 20.6** *E/Z* photoisomerization leads to formation of an intramolecular hydrogen bond in bifunctional azobenzene catalyst *Z*-**7** and thereby enables the effective modulation of its acidity and catalytic activity in a Morita–Baylis–Hillman reaction. Source: Based on Imahori et al. [28].

### 20.3.4 Asymmetric Heck Reaction

The groups of Craig, Boulatov, and Widenhoefer reported a novel photoswitchable catalyst bearing a stiff stilbene and a chiral biaryl bisphosphine ligand backbone, enabling asymmetric Heck arylations and Trost allylic alkylations in the presence of palladium (Scheme 20.7) [29]. The irradiation of *Z*-**8** with UV light (365 nm) in dichloromethane led to the formation of a PSS mixture containing 23% *E*-**8** as well as 9% *E*′-**8**. After isolation of the ligands by liquid chromatography, they were tested independently in asymmetric Heck arylations and Trost allylic alkylations, where *Z*-**8** exhibited higher enantioselectivity when compared to *E*-**8** under the same reaction condition. Though this catalyst showed excellent activity and enantioselectivity in mediating asymmetric Heck reactions independently, the relatively low PSS prohibits in situ ON/OFF switching in these chemical transformations.

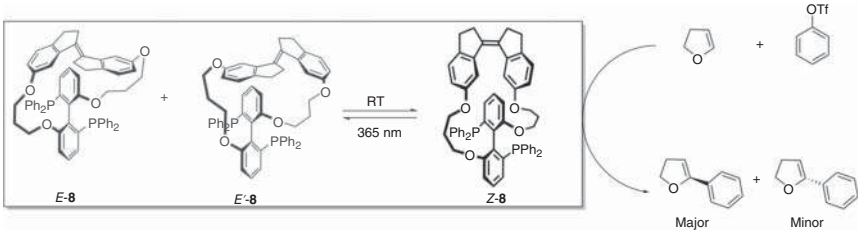


**Scheme 20.7** *E/Z* photoisomerization of a stiff stilbene unit switches axially chiral biaryl bis(phosphine) ligand **8**, which in the *Z* isomer (*Z*-**8**) displays higher activity and enantioselectivity in Heck reactions. Source: Based on Kean et al. [29].

### 20.3.5 Steglich Rearrangement

The chiral dibenzosuberane-based helicene **9** containing a 4-aminopyridine as catalytically active moiety has been developed by Chen et al. (Scheme 20.8) [30]. Due to the *E/Z* photoisomerization of the stilbazole core leading to a change in the helical chirality, the chiral environment of the 4-aminopyridine unit and therefore its catalytic activity and selectivity should be modulated by light. Notably, upon irradiation with 290 nm light, *P*-**9** almost completely isomerizes to *M*-**9** (PSS ratio *M*-**9**:*P*-**9** > 99 : 1) and the latter efficiently switches back to *P*-**9** (PSS ratio

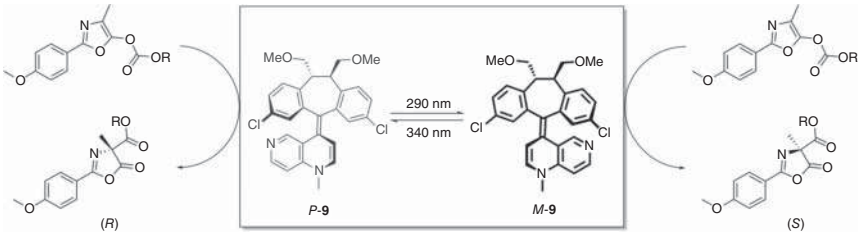


**Scheme 20.8** *E/Z* photoisomerization of dibenzosuberane-based helicene catalyst **9** enables control over an enantiodivergent Steglich rearrangement. Source: Based on Chen et al. [30].

*M*-**9**:*P*-**9** = 9 : 91) with 340 nm light. The two pseudo-enantiomers catalyzed the enantiodivergent Steglich rearrangement of O- to C-carboxylazlactones with enantioselectivities of up to 91% *ee* (*R*) and 94% *ee* (*S*), respectively.

### 20.3.6 Stereoselective Cyclopropanation Reaction

The first example of in situ photoswitching of stereoselective catalysis has been reported by Branda and coworkers, who reported the cyclopropanation of styrene with ethyl diazoacetate mediated by the dithienylethene (DTE)-bridged chiral bis(oxazoline) ligand **10** back in 2005 (Scheme 20.9) [31]. The catalyst in the open form **10o** is able to chelate to the catalytically active copper(I) center, allowing for a flexible chiral environment around the copper center that is essential for the stereoselective cyclopropanation reaction to occur. By contrast, the closed-form **10c** does not allow for chelation and provides a rigid chiral environment around the copper center. As a consequence, moderate enantioselectivities (30–50% *ee*) were found when using **10o**, whereas a very low 5% *ee* was observed with **10c**. The modulation of enantioselectivity is offset by the low switching efficiency since the PSS upon irradiation with 313 nm light contained only 23% of **10c**.

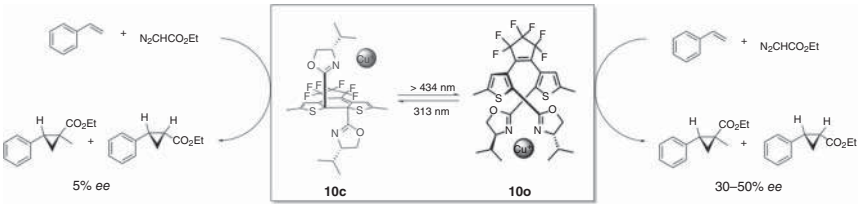


**Scheme 20.9** Photoswitchable chiral bis(oxazoline) catalyst **10** with a dithienylethene (DTE) bridge enables photocontrol over the level of enantioselectivity in the cyclopropanation of styrene. Source: Based on Sud et al. [31].

### 20.3.7 Ring-Closing Metathesis and Ring-Opening Metathesis Polymerization of Cyclic Olefins

Bielawski and coworkers reported a DTE-functionalized *N*-heterocyclic carbene (NHC) as a ligand and explored the catalytic performance of the corresponding ruthenium complex **11** in ring-closing metathesis (RCM) as well as ring-opening metathesis polymerization (ROMP) of olefins (Scheme 20.10) [32]. Exposure of NMR samples to 313 nm light for 120 minutes led to effective ring closure (PSS ratio **11c**:**11o** = 80 : 20), whereas irradiation with visible light (>500 nm) for 60 minutes induced nearly quantitative back switching. In the presence of **11c** as the catalyst, an enhanced RCM activity ($k_{\mathbf{11c}}$:$k_{\mathbf{11o}}$ = 1.4–1.7) was found while the opposite effect was observed for ROMP ($k_{\mathbf{11c}}$:$k_{\mathbf{11o}}$ = 0.56–0.66). Moreover, in situ photoirradiation enabled to tune the reaction rate during RCM and ROMP reactions. Although the system allows for an elegant reactivity tuning by affecting both the electron-donating capability of the NHC ligand as well as its steric constraints, the system suffers from long times switching times required due to the relatively high

catalyst loadings and thus optical densities as well as less efficient photochemistry and catalytic activity thereby limiting the obtainable temporal resolution.

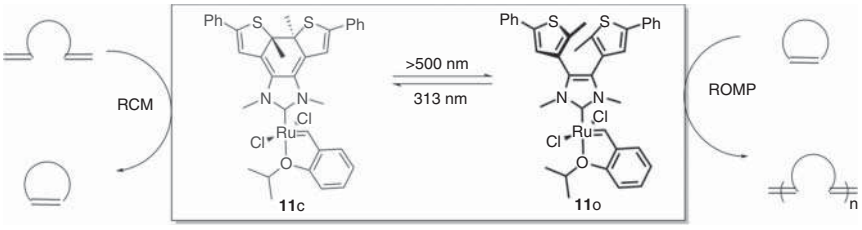


**Scheme 20.10** A DTE-based NHC-Ru(II) complex displays opposite activity differences for the RCM and ROMP of olefins. Source: Teator et al. [32] / American Chemical Society.

### 20.3.8 Enantioselective Dialkylzinc Addition Reactions

A photoswitchable axially chiral catalyst **12** resembling the bis(2-naphthol) moiety was designed by the group of Feringa and used to modulate the enantioselectivity in the organozinc addition to aromatic aldehydes (Scheme 20.11) [33]. The catalytically relevant bi(2-phenol) axial chirality was affected by a light-controlled change in the helicity of Feringa's overcrowded olefin motor. For example, upon irradiation with 365 nm light ($R$,$P$,$S_a$)-**12** can efficiently be converted to ($R$,$M$,$R_a$)-**12** (PSS ratio ($R$,$M$,$R_a$)-**12**:($R$,$P$,$S_a$)-**12** = 83 : 17), while the back switching with 420 nm light is less efficient (PSS ratio ($R$,$P$,$S_a$)-**12**:($R$,$M$,$R_a$)-**12** = 50 : 50). As a consequence, the enantioselectivity addition of diethylzinc to aromatic aldehydes could successfully be demonstrated by the observed opposite enantioselectivity, i.e. with 68% ($R$) product in the presence of ($R$,$P$,$S_a$)-**12** as opposed to 55% ($S$) product after irradiation with 365 nm light.

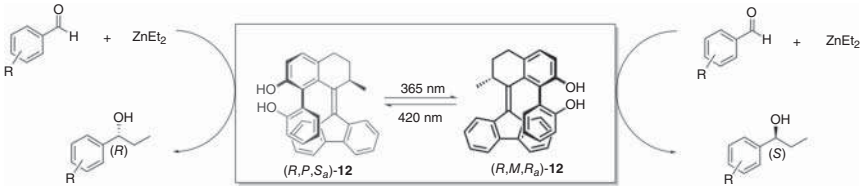


**Scheme 20.11** Photoswitchable 1,1′-bi-2-naphthol (BINOL)-type catalyst **12** enables enantioselective addition of organozinc to aromatic aldehydes. Source: Based on Pizzolato et al. [33].

## 20.4 Formation of Carbon–Heteroatom Bonds

The formation of carbon–heteroatom bonds (heteroatom = O, S, N, P) often happens in nucleophilic processes, such as substitution or addition to C=C or C=O double bonds, which is of importance for the synthesis of both natural products as well as the polymer materials. In this section, photoswitchable catalysts mediating formation of C—O, C—S, and C—N bonds are discussed in detail.

### 20.4.1 Asymmetric Thio-Michael Reaction

The light-driven molecular motor **13** based on a stiff stilbene photochromic unit was demonstrated to efficiently control both stereoselectivity and catalytic activity of thio-Michael additions (Scheme 20.12) [34]. The cooperative organocatalytic 4-dimethylaminopyridine (DMAP) and thiourea moieties were incorporated into the helical geometry of the motor, which undergoes light-driven unidirectional rotation cycles. The (*P,P*)-*E*-**13** exhibited low catalytic activity in the Michael addition of 2-methoxylthiophenol to cyclohexenone since the DMAP and thiourea groups are far apart and their cooperative action is precluded. Thus, under these conditions, a slow reaction rate (7% conversion in 15 hours) to racemic product was observed. Upon irradiation with 312 nm UV light leading to formation of (*M,M*)-*Z*-**13**, a significant enhanced reaction rate (40% conversion in 15 hours) and stereoselectivity (*er* 75 : 25 *S:R*) was observed. Heating to 70 °C caused transformation to (*P,P*)-*Z*-**13**, which displays an even higher catalytic activity (83% yield in 15 hours) yet inverse enantioselectivity (*er* 23 : 77 *S:R*). The chirality of the product is therefore determined by the relative helical orientation of two cooperating, catalytically active groups, which is dictated by the helical configuration of the motor. This very elegant photoswitchable catalyst with an integrated unidirectional light-driven molecular motor is exceptional as it allows to control both the rate as well as the stereochemical outcome of a chemical reaction in a reversible and sequential manner by light and heat.

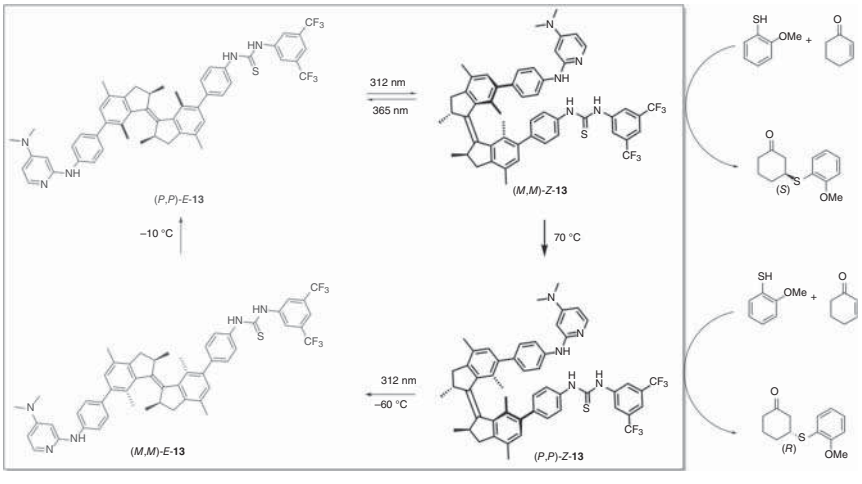


**Scheme 20.12** Light-driven molecular motor **13** enables dynamic control over catalytic activity and enantioselectivity in thio-Michael additions. Source: Based on Wang et al. [34].

Photoswitchable catalyst **14** was designed by omitting the phenylene spacer present in **13** and was used in Henry reactions to construct carbon–carbon bonds (Scheme 20.13) [27]. (*P,P*)-*E*-**14** exhibited low catalytic activity and provided racemic products for the reaction of nitromethane with α,α,α-trifluoroketones. In contrast, UV-light-induced formation of (*M,M*)-*Z*-**14** afforded an enantio-enriched product

mixture (*er* up to 86 : 14 *R:S*) with higher reaction rate. Upon heating to 60 °C and conversion to (*P,P*)-*Z*-**14**, the opposite enantioselectivity (*er* up to 79 : 21 *S:R*) was obtained.

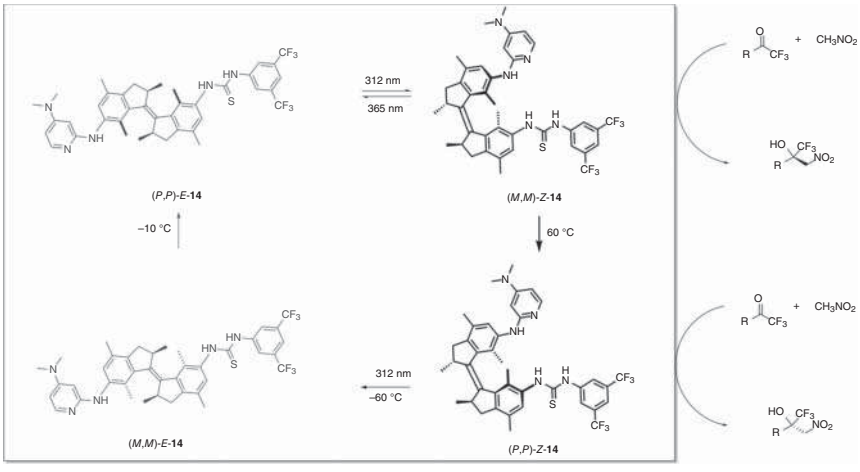


**Scheme 20.13** Light-driven molecular motor **14** enables dynamic control over catalytic activity and enantioselectivity in Henry reaction. Source: Based on Vlatkovic et al. [27].

## 20.4.2 Asymmetric Allylic Alkylation Reaction

Similar to the aforementioned photoswitchable axially chiral organocatalysts, related bidentate phosphorus ligands can also be attached to the motor core to provide ligand **15**, which has been used to control the desymmetrization of *meso*-cyclopent-2-en-1,4-diol bis(carbamate) in a Pd-catalyzed reaction (Scheme 20.14) [35]. The stepwise control over spatial distance between the two phosphine donors and the helicity of the bisphosphine ligand were once again realized via successive

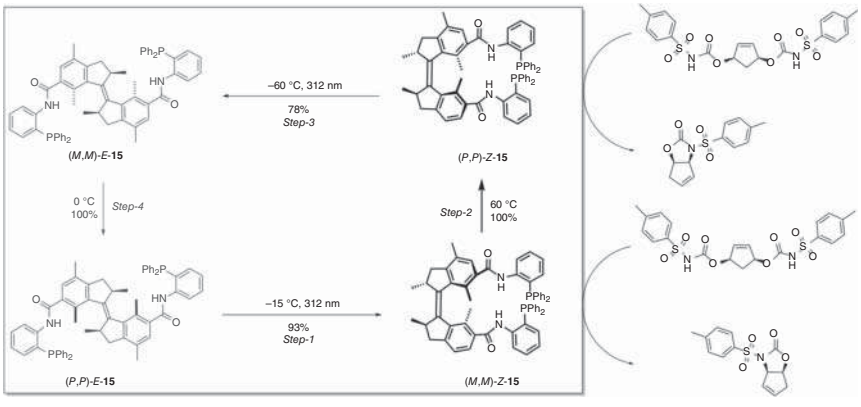


**Scheme 20.14** Light-driven molecular motor **15** enables dynamic control over enantioselectivity in desymmetrization reactions. Source: Based on Zhao et al. [35].

photochemical and thermal isomerization providing unidirectional rotation. In the presence of (*P,P*)-*Z*-**15**, an enantiomeric ratio of 94 : 6 in favor of the (3*S*,4*R*)-configuration was realized, whereas the opposite (3*R*,4*S*)-configuration (*er* 93 : 7) could also be achieved in the presence of (*M,M*)-*Z*-**15**. Although the levels of enantioselectivity that can be achieved using these bisphosphine ligands in Pd-catalyzed desymmetrization reactions are exquisite, in situ switching could not be realized due to the limited stability of the catalysts under UV irradiation and heating.

### 20.4.3 Hydrolysis of Esters and Glycosides

As early as 1981, Ueno et al. reported the first photoswitchable catalyst system featuring a 4,4′-biscarboxyazobenzene and a β-cyclodextrin and used it to control the hydrolysis of *p*-nitrophenyl benzoates (Scheme 20.15) [36]. In their design, *E*-**16** exhibited a lower activity due to the internal shallow cavity, which blocked one end of the β-cyclodextrin and prevented the binding of *p*-nitrophenyl benzoate. However, a fivefold increase in reaction rate was realized upon irradiation with UV light, leading to formation of 38% of *Z*-**16**, in which the extended cavity of β-cyclodextrin promoted substrate binding and accelerated the rate of hydrolysis.

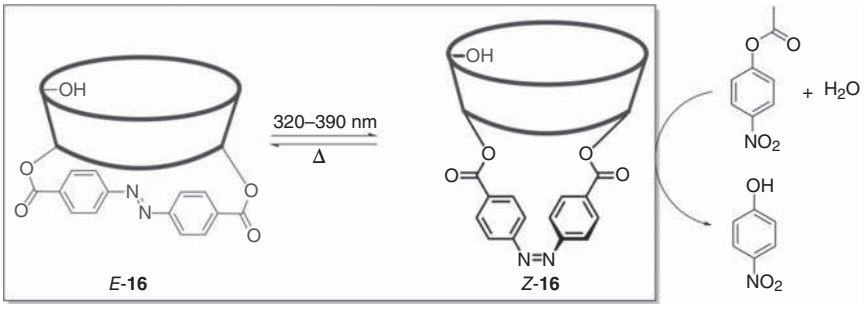


**Scheme 20.15** Azobenzene-capped β-cyclodextrin **16** enables dynamic control over substrate binding and thus catalytic activity in the hydrolysis of *p*-nitrophenyl benzoate. Source: Based on Ueno et al. [36].

Subsequently, the same authors designed a catalyst with a histidine spacer connecting the azobenzene moiety to the β-cyclodextrin to promote hydrolysis of various esters, including *p*-nitrophenyl acetate and *Boc*-alanine-*p*-nitrophenyl ester [37]. In this case, the linked *E*-azobenzene is blocking the internal cavity but upon UV-induced switching to the *Z*-isomer, it cannot bind to the cavity any longer therefore giving rise to substrate binding and subsequent catalysis.

A photoresponsive azobenzene 3,3′-dicarboxylic acid catalyst using cooperative effects for the hydrolysis of glycoside has been reported by Bandyopadhyay et al. (Scheme 20.16) [38]. It was found that the deprotonation of both carboxylic acid groups takes place at the same pH of 4.4 in *E*-**17**, whereas in *Z*-**17** obtained by irradiation with 360 nm light (PSS ratio *Z*-**17**:*E*-**17** = 70 : 30) deprotonation occurs

stepwise associated with two distinct p$K_a$ values at 4.7 and 6.5. Therefore, at pH = 5.8 where only *Z*-**17** is deprotonated and thus catalytically active, a rate enhancement of six orders of magnitude was observed for the hydrolysis of 4-nitrophenyl-β-D-glucopyranoside when comparing *Z*-**17** with *E*-**17**. Moreover, the authors demonstrated reversible ON–OFF switching of their glycosidase mimic with light.

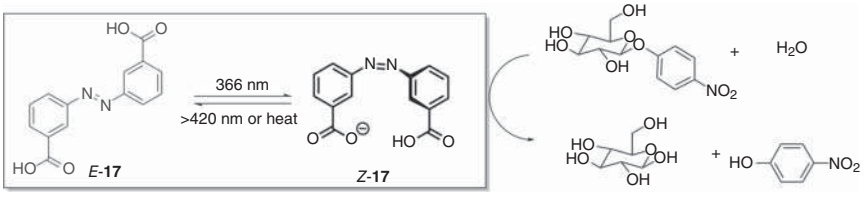


**Scheme 20.16** *E/Z* Photoisomerization of organocatalyst **17** allows for acidity tuning and thus switching of the catalytic activity for 4-nitroxyphenyl-β-D-glucopyranoside hydrolysis. Source: Based on Samanta et al. [38].

### 20.4.4 Ethanolysis of Tertiary Anilides, Transesterification, and Amidation Reactions

A photoswitchable bifunctional cooperative catalyst **18** for the ethanolysis of tertiary anilides has been devised by Cacciapaglia et al. (Scheme 20.17) [39] inspired by a bimetallic reaction mechanism in which one barium center activates the amide electrophile and the other activates the nucleophilic ethoxide and delivers it to the carbonyl group of the acetanilide. The catalyst, therefore, features a dinuclear barium complex of a symmetrically crown ether appended photochromic azobenzene, which in the *Z*-configuration presents the two barium centers at the optimal distance to cooperate. As expected, only low catalytic activity was observed in the presence of *E*-**18**. Upon irradiation with 370 nm UV light leading to near-quantitative switching (PSS ratio *Z*-**18**:*E*-**18** = 95 : 5), a more than fivefold increase in reaction rate was observed. At late stages of the reaction, however, notable product inhibition resulting from carboxylate binding to the catalyst was observed and hampered overall catalyst performance.

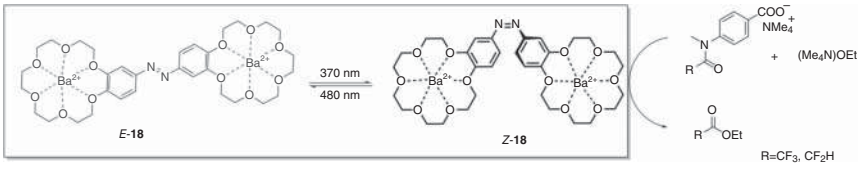


**Scheme 20.17** Photoswitchable cooperative catalyst **18** allows to control the ethanolysis of tertiary anilides. Source: Based on Cacciapaglia et al. [39].

The first example of a photoswitchable bifunctional cooperative catalyst dates back to work by Würthner and Rebek, who reported compound **19** to catalyze

amidation reactions only in its bent *Z*-configuration presenting both adenine receptors at close proximity (Scheme 20.18) [40]. In the extended *E*-isomer, there is almost no reaction due to the large distance of the two substrate-binding sites. However, upon exposure to 366 nm UV light, one half of the catalyst is isomerized (PSS ratio *Z*-**19** : *E*-**19** = 50 : 50) leading to a nearly ninefold enhancement in reaction rate when compared to the catalyst in the dark state (pure *E*-**19**). While the preorganization of the substrates in the Z-configured catalyst leads to this significant rate enhancement, the design suffers from product inhibition as the formed amide has a high (multivalent) binding affinity for the catalyst.

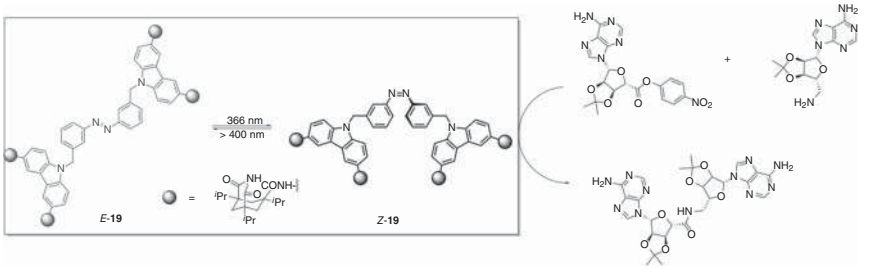


**Scheme 20.18** Photoswitchable cooperative catalyst **19** to control amide bond formation between preorganized amines and activated esters. Source: Based on Würthner and Rebek [40].

The above examples rely on the *E/Z* photoisomerization of a double bond to modulate the relative orientation of two catalytically interacting/cooperating units. One notable exception has been described by Bielawski and coworkers and consists of the DTE-based photoswitch **20** (Scheme 20.19) [41]. As described in Section 20.3.7, the electron density at the carbene center of an NHC can be modulated by incorporating a DTE into the imidazole framework. Upon exposure to 313 nm UV light, the open imidazolium salt could efficiently be ring-closed (PSS ratio **20c**·$HPF_6$:**20o**·$HPF_6$ = 88 : 12) and quantitatively ring-opened with >500 nm visible light. In the presence of a base, imidazolium salt **20o**·$HPF_6$ forms the corresponding NHC **20o**, which serves as efficient nucleophilic catalyst in the transesterification of vinylacetate with allyl alcohol and in the amidation of ethyl acetate with 2-aminoethanol. In contrast, after being exposed to UV light,

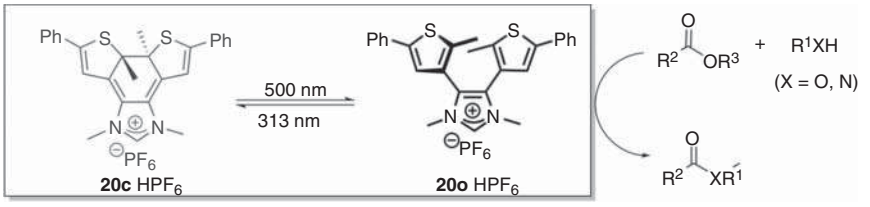


**Scheme 20.19** Photoswitchable NHC organocatalyst **20** enables modulation of nucleophilicity at the carbene center and hence switches catalytic activity in transesterification and amidation reactions. Source: Based on Neilson et al. [41].

significantly decreased rates both for the transesterification ($k_{vis}/k_{UV} = 12.5$) and the amidation ($k_{vis}/k_{UV} = 100$) were observed due to the variation of electron density at the carbene center. Although the modulation of catalytic activity is significant and the switching efficiency is very good, the catalyst undergoes substantial side reactions (13% byproduct formation) and thus repetitive ON–OFF switching is limited to few cycles.

### 20.4.5 Cycloaddition Reactions of $CO_2$ and Epoxides

More than two decades ago, Inoue and coworkers reported the photoswitchable catalyst system **21** for chemical $CO_2$ fixation by reacting it with epoxides and converting them into cyclic carbonates (Scheme 20.20) [42]. The system consists of an aluminum porphyrin complex and a cleverly designed photoswitchable axial stilbazole ligand, which reversibly binds to the aluminum depending on it switching state. While the *E*-isomer cannot bind due its steric bulk, the *Z*-isomer can coordinate to the aluminum and thereby activates it to catalyze the conversion of $CO_2$ and propylene oxide to propylene carbonate. Therefore, low conversion (2% over 18 hours) was observed in the thermal resting state *E*-**21**, whereas UV light–induced formation of *Z*-**21** led to an acceleration. Switching back to *E*-**21** again slows down the reaction. Despite the elegant design and efficient remote control by alternating UV or visible light exposure, the relatively low catalytic activity (turnover frequency) constitutes the main drawback of this catalyst system.

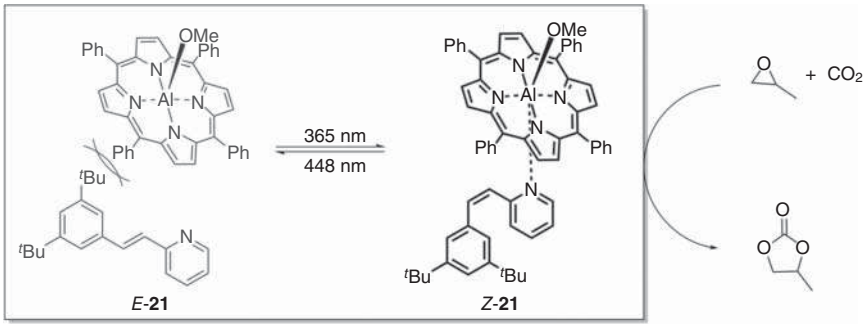


**Scheme 20.20** Photoswitchable catalyst system **21** provides remote control over $CO_2$ fixation. Source: Based on Hiroshi et al. [42].

### 20.4.6 Alkene and Alkyne Hydroboration

The DTE-based NHC ligand discussed in Section 20.3.7 has also been used to prepare the photoswitchable Rh-NHC complex **22** to catalyze alkene and alkyne hydroboration (Scheme 20.21) [43]. The ring-open Rh-catalyst **22o** efficiently catalyzed the reaction of terminal olefins and acetylenes with pinacolborane. Irradiation with 313 nm UV light induced ring-closure (PSS ratio **22c**:**22o** = 62 : 38), whereas irradiation with >500 nm visible light led to 98% recovery of the initial ring-open state **22o**. Comparing the rates of catalysts irradiated prior to adding the

substrate provided differences ($k_{vis}$:$k_{UV}$ = 2.4–9.2) reaching almost one order of magnitude for hydroboration of styrene. The observed rate difference was attributed to the inhibition of the rate-limiting reductive elimination step in **22c** due to the decreased electron-donating ability of the ring-closed DTE-NHC ligand.

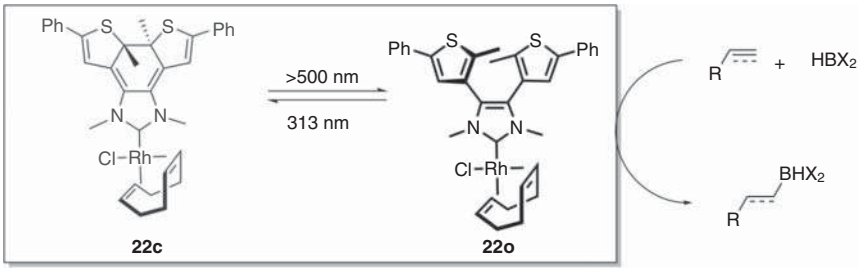


**Scheme 20.21** Photoswitchable rhodium catalyst **22** to control alkene and alkyne hydroboration. Source: Based on Neilson and Bielawski [43].

### 20.4.7 Ring-Opening Polymerization of Lactones

Using the same DTE-based NHC ligand **20** as organocatalyst, the group of Bielawski was able to control the ring-opening polymerization of lactones (Scheme 20.22) [44]. As expected on the basis of the activity of these nucleophilic organocatalysts in trans-esterification/amidation reactions (see Section 20.4.4), the polymerization rate of δ-valerolactone in the presence of the ring-open NHC was much higher as compared to the ring-closed tautomer ($k_{vis}$:$k_{UV}$ = 59).

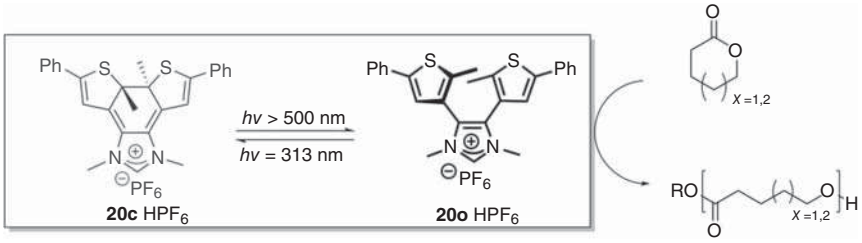


**Scheme 20.22** Photoswitchable DTE-based NHC organocatalyst **20** to remote control the ring-opening polymerization of lactones. Source: Based on Neilson and Bielawski [44].

Boyer and coworkers demonstrated the spiropyran-merocyanine pair **23** to be an efficient photoswitchable catalyst for the ring-open polymerization of lactones (Scheme 20.23) [45]. Their work is based on the use of the protonated merocyanine **23o** as a photoswitchable acid, which upon 460 nm blue light induced cyclization to spiropyran **23c** releases a proton that initiates the ring-opening polymerization. Interestingly, the spiropyran form **23c** thermally reverts to the more stable **23o** to recapture the proton and pause the polymerization. Therefore, polymerization only takes place in the presence of blue light. Moreover, the authors merged their system with the photoinduced radical polymerization of methyl acrylate as another

light-controlled orthogonal polymerization and were able to prepare block and graft copolymers in one pot through switching the polymerization between them.

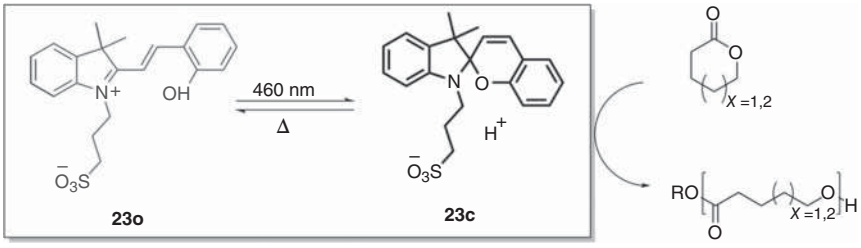


**Scheme 20.23** Photoswitchable acid catalyst **23** to control the ring-opening polymerization of lactones. Source: Based on Fu et al. [45].

Our own group has developed DAE **24** as photoswitchable organocatalyst to control the polymerization of L-lactide and copolymerization of δ-valerolactone and trimethylene carbonate (Scheme 20.24) [21]. Upon 365 nm UV irradiation, ring closure breaks the aromaticity of **24o** and thereby drives tautomerism of the enol to the ketone **24c**. This mechanism allows to toggle between the H-bond-accepting ketone **24c** and the H-bond-donating phenol **24o**. The latter is catalytically active and enables the polymerization of L-lactide in the presence of a tertiary amine cocatalyst. The favorable and robust switching behavior of **24** in the presence of the amine cocatalyst allowed for the first time true ON–OFF control of a living polymerization in situ by light.

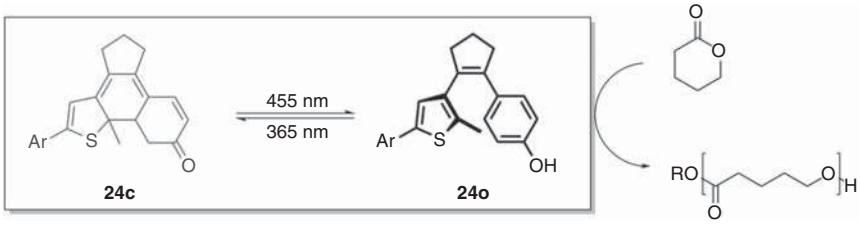


**Scheme 20.24** Photoswitchable DAE-catalyst **24** enables in situ control over living ring-opening polymerization and copolymerization of lactones and cyclic carbonates. Source: Based on Eisenreich et al. [21].

## 20.5 Formation of Carbon–Hydrogen/Deuterium Bonds

In this last section, we want to cover the use of photoswitches to control the exchange of C—H/C—D bonds and thus racemization/epimerization processes.

### 20.5.1 Racemization of α-Amino Acids

Wilson and Branda developed a photoswitchable catalyst for the racemization of alanine by exploiting the significant electronic difference between the two isomers

of DTE **25** (Scheme 20.25) [46]. Inspired by the fact that the activity of pyridoxal 5-phosphate in the racemization of alanine depends on the electronic connection of the aldehyde and pyridinium functional groups, the authors devised **25** as a photoresponsive pyridoxal 5-phosphate mimic. Indeed, in the presence of ring open **25o**, L-alanine did not racemize. However, upon nearly quantitative 365 nm UV light-induced formation of the ring-closed **25c** (PSS ratio **25c**:**25o** = 97 : 3), L-alanine racemization took place due to the presence of a fully π-conjugated structure facilitating deprotonation of the aldimine α-hydrogen. Irradiation with >490 nm visible light led to quantitative ring opening and turned off the catalyst. The authors demonstrated successive ON–OFF switching by alternating exposure to UV and visible light.

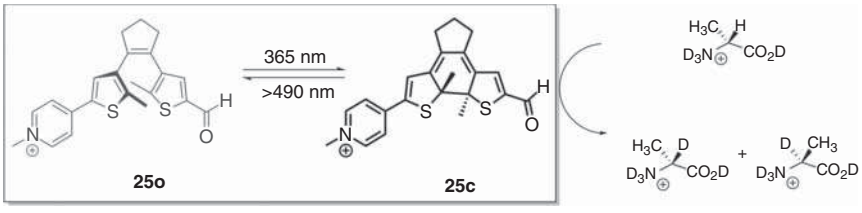


**Scheme 20.25** Photoswitchable catalyst **25** to control the racemization of L-alanine [46] wavelengths. Source: Based on Wilson and Branda [46].

## 20.6 Conclusion and Outlook

Over the past four decades, photoswitchable catalysis has developed from an intellectual intricacy to a topic with great potential and increasing activity, in particular in recent years due to the advent of light-based additive manufacturing techniques [47], such as xolography [48], Moreover, the potential for controlling living polymerization processes to harvest the high spatial and temporal control in polymer science is undeniable [49]. But also for small-molecule catalysis, the control over biochemical pathways, concentration of cellular messengers, and others is certainly an appealing tool for chemical biology. This chapter illustrates the breadth of the work that has been carried out over the years and highlights the different conceptual approaches. Without doubt, remarkable progress has been made and various feasible solutions have been developed to reversibly control reaction rates and/or (enantio)selectivities with light. On the one hand, geometrical variation of catalysts based on *E/Z* isomerization of photochromic motifs (such as azobenzene, stilbenes, and others) has taken advantage of switching catalytic activity and/or (enantio)selectivity through cooperative or steric effects. On the other hand, catalytic systems with photochromic diarylethene or spiropyran moieties allow to toggle between vastly different electronic properties of catalysts.

Yet although significant advances have been made in the area, several challenges remain to be addressed to harness the true potential of photoswitchable catalysts as optical remote control over chemistry. Clearly, there is a demand for more

efficient and more versatile photoswitchable catalysts. While the majority of the aforementioned examples targets the control of catalytic activity, only a modest activity modulation is often observed. Moreover, only a small number of transformations have been reported to date and catalysts for a wider range of chemical processes are needed. This, of course, also necessitates more chemically robust and fatigue-resistant photoswitchable catalysts. In addition, there are lots of technical issues that await clever practical solution, for example concerning clever ways to address the photoswitchable catalysts with light precisely and efficiently. Although it remains challenging to devise photoswitchable catalysts systems and thereby take advantage of the unique features of light to control chemistry in space and time, we are convinced that this research will lead to new methodologies and disruptive technologies.

## References


1 van Leeuwen, P.W.M.N. (2004). *Homogeneous Catalysis: Understanding the Art*. Dordrecht: Kluwer.
2 Hagen, J. (2006). *Industrial Catalysis: A Practical Approach*, 2e. Weinheim: Wiley-VCH.
3 Traut, T.W. (2008). *Allosteric Regulatory Enzymes*. New York, NY: Springer.
4 Blanco, V., Leigh, D.A., and Marcos, V. (2015). *Chem. Soc. Rev.* 44: 5341–5370.
5 Vlatkovic, M., Collins, B.S., and Feringa, B.L. (2016). *Chem. Eur. J.* 22: 17080–17111.
6 Van Dijk, L., Tilby, M.J., Szpera, R. et al. (2018). *Nat. Rev. Chem.* 2: 0117.
7 Olsen, P., Odelius, K., Keul, H., and Albertsson, A.C. (2015). *Macromolecules* 48: 1703–1710.
8 Balof, S.L., P'Pool, S.J., Berger, N.J. et al. (2008). *Dalton Trans.* 2008: 5791–5799.
9 Blanco, V., Carlone, A., Hanni, K.D. et al. (2012). *Angew. Chem. Int. Ed.* 51: 5166–5169.
10 Yoon, H.J., Kuwabara, J., Kim, J.H., and Mirkin, C.A. (2010). *Science* 330: 66–69.
11 Wei, J. and Diaconescu, P.L. (2019). *Acc. Chem. Res.* 52: 415–424.
12 Karthikeyan, S., Potisek, S.L., Piermattei, A., and Sijbesma, R.P. (2008). *J. Am. Chem. Soc.* 130: 14968–14969.
13 Peters, M.V., Stoll, R.S., Kühn, A., and Hecht, S. (2008). *Angew. Chem. Int. Ed.* 47: 5968–5972.
14 Neilson, B.M. and Bielawski, C.W. (2013). *ACS Catal.* 3: 1874–1885.
15 Göstl, R., Senf, A., and Hecht, S. (2014). *Chem. Soc. Rev.* 43: 1982–1996.
16 Stoll, R.S. and Hecht, S. (2010). *Angew. Chem. Int. Ed.* 49: 5054–5075.
17 Berkovic, G., Krongauz, V., and Weiss, V. (2000). *Chem. Rev.* 100: 1741–1754.
18 Dorel, R. and Feringa, B.L. (2019). *Chem. Commun.* 55: 6477–6486.
19 Zhang, J. and Tian, H. (2018). *Adv. Opt. Mater.* 6: 1701278.
20 Yamaguchi, T., Kamihashi, Y., Ozeki, T. et al. (2014). *Bull. Chem. Soc. Jpn.* 87: 528–538.
21 Eisenreich, F., Kathan, M., Dallmann, A. et al. (2018). *Nat. Catal.* 1: 516–522.


**22** Osorio-Planes, L., Rodriguez-Escrich, C., and Pericas, M.A. (2014). *Org. Lett.* 16: 1704–1707.

**23** Dai, Z., Cui, Y., Chen, C., and Wu, J. (2016). *Chem. Commun.* 52: 8826–8829.

**24** De Bo, G., Leigh, D.A., McTernan, C.T., and Wang, S. (2017). *Chem. Sci.* 8: 7077–7081.

**25** Pizzolato, S.F., Collins, B.S.L., Van Leeuwen, T., and Feringa, B.L. (2017). *Chem. Eur. J.* 23: 6174–6184.

**26** Stoll, R.S. and Hecht, S. (2009). *Org. Lett.* 11: 4790–4793.

**27** Vlatkovic, M., Bernardi, L., Otten, E., and Feringa, B.L. (2014). *Chem. Commun.* 50: 7773–7775.

**28** Imahori, T., Yamaguchi, R., and Kurihara, S. (2012). *Chem. Eur. J.* 18: 10802–10807.

**29** Kean, Z.S., Akbulatov, S., Tian, Y. et al. (2014). *Angew. Chem. Int. Ed.* 53: 14508–14511.

**30** Chen, C.T., Tsai, C.C., Tsou, P.K. et al. (2017). *Chem. Sci.* 8: 524–529.

**31** Sud, D., Norsten, T.B., and Branda, N.R. (2005). *Angew. Chem. Int. Ed.* 117: 2055–2057.

**32** Teator, A.J., Shao, H., Lu, G. et al. (2017). *Organometallics* 36: 490–497.

**33** Pizzolato, S.F., Stacko, P., Kistemaker, J.C.M. et al. (2018). *J. Am. Chem. Soc.* 140: 17278–17289.

**34** Wang, J. and Feringa, B.L. (2011). *Science* 331: 1429–1432.

**35** Zhao, D., Neubauer, T.M., and Feringa, B.L. (2015). *Nat. Commun.* 6: 6652.

**36** Ueno, A., Takahashi, K., and Osa, T. (1981). *Chem. Soc. Chem. Commun.* 1981: 94–96.

**37** Lee, W.S. and Ueno, A. (2001). *Macromol. Rapid Commun.* 22: 448–450.

**38** Samanta, M., Krishna, V.S.R., and Bandyopadhyay, S. (2014). *Chem. Commun.* 50: 10577–10579.

**39** Cacciapaglia, R., Di Stefano, S., and Mandolini, L. (2003). *J. Am. Chem. Soc.* 125: 2224–2227.

**40** Würthner, F. and Rebek, J. (1995). *Angew. Chem. Int. Ed.* 34: 446–448.

**41** Neilson, B.M. and Bielawski, C.W. (2012). *J. Am. Chem. Soc.* 134: 12693–12699.

**42** Hiroshi, S., Kimura, T., and Inoue, S. (1999). *J. Am. Chem. Soc.* 121: 2325–2326.

**43** Neilson, B.M. and Bielawski, C.W. (2013). *Organometallics* 32: 3121–3128.

**44** Neilson, B.M. and Bielawski, C.W. (2013). *Chem. Commun.* 49: 5453–5455.

**45** Fu, C., Xu, J., and Boyer, C. (2016). *Chem. Commun.* 52: 7126–7129.

**46** Wilson, D. and Branda, N.R. (2012). *Angew. Chem. Int. Ed.* 51: 5431–5434.

**47** Jung, K., Corrigan, N., Ciftci, M. et al. (2019). *Adv. Mater.* 31: 1903850.

**48** Regehly, M., Garmshausen, Y., Reuter, M. et al. (2020). *Nature* 588: 620–624.

**49** Ihrig, S.P., Eisenreich, F., and Hecht, S. (2019). *Chem. Commun.* 55: 4290–4298.


# Section III

# Materials Based on Molecular Photoswitches

# 21 Multinary Photoswitches

Andreas H. Heindl and Hermann A. Wegner

**Multinary Photoswitches**

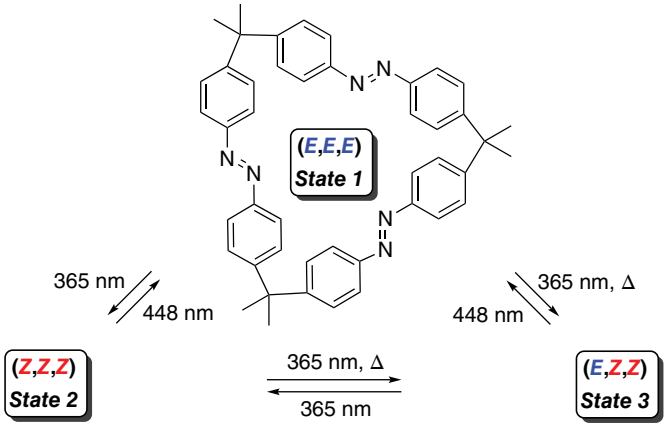


**Characteristic Features**

Multinary photoswitches expand the possibilities and properties of single photochromic compounds to a higher level. Constructing compounds of multiple switching units, a large number of potential tasks, e.g. multiple catalytic functions or information storage, can be ideally achieved. The precise photocontrol of the multiple states and interactions of the subunits with each other represent the major challenging task in this highly interesting field.

**Key Publications**

Uchida, K., Masuda, G., Aoi, Y. et al. (1999). *Chem. Lett*. 28: 1071–1072.

Lerch, M.M., Hansen, M.J., Velema, W.A. et al. (2016). *Nat. Commun*. 7: 12054.

Higashiguchi, K., Matsuda, K., Tanifuji N., and Irie, M. (2005). *J. Am. Chem. Soc*. 127: 8922–8923.

# 21

# Multinary Photoswitches

*Andreas H. Heindl*[1,2] *and Hermann A. Wegner*[1,2]

[1]*Justus Liebig University, Institute of Organic Chemistry, Heinrich-Buff-Ring 17, 35392 Giessen, Germany*
[2]*Justus Liebig University, Center for Material Research (ZfM/LaMa), Heinrich-Buff-Ring 16, 35392 Giessen, Germany*

## 21.1 Introduction

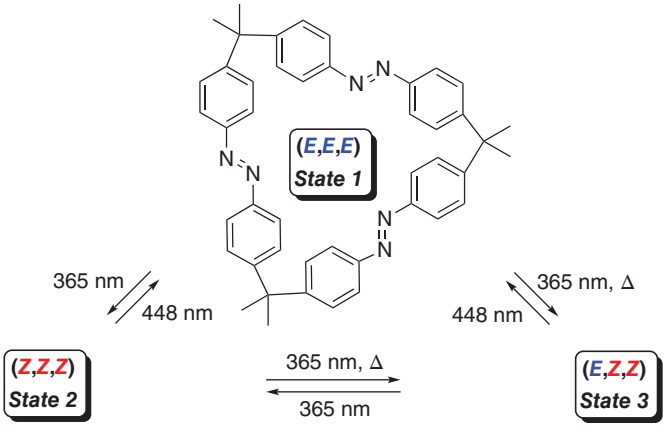


Multinary photoswitches [1] expand the possibilities and properties of single photochromic compounds to a higher level. Constructing compounds of multiple switching units, a large number of potential tasks, e.g. multiple catalytic functions [2] or information storage [3], can be ideally achieved. The precise photocontrol of the multiple states and interactions of the subunits with each other represents the major challenging task in this highly interesting field.

*Molecular Photoswitches: Chemistry, Properties, and Applications*,
First Edition. Edited by Zbigniew L. Pianowski.

## 21.2 Multinary Photoswitches

All photoswitches represent two-state logical units with simple "on–off" or "0/1" behavior that can be read out, e.g. by measuring their absorbance at a certain wavelength which differs in the two states. Integrating more than one photoswitchable unit in a single compound opens the possibility to store larger amount of information or to perform multiple tasks. For example, an acyclic multiphotochromic compound with $n$ photoswitching units can principally isomerize to $2^n$ states, forming a highly complex molecular logical unit. With a library of the different known photoswitches, the design of multistate logical units can be divided in two strategies: first, multinary photoswitches can be constructed by combining units of the same photochrome, which can lead to higher symmetry and more straight-forward syntheses of the corresponding multiswitches. Second, photoswitches of different kinds can be combined, utilizing the unique advantages and properties of each type [4]. In this book chapter, we will focus on molecular multiphotochromic systems excluding polymers. Furthermore, we do not attempt to completely review the literature, but show selected examples that demonstrate the achievements and challenges in the design of multinary photoswitches.

### 21.2.1 Basic Concepts in the Design of Multiphotoswitches

The major challenge in the design of multinary photoswitches lies in retaining the switching behavior of its components, while generating new properties by favorable connection of multiple switches. Depending on the chemical linkage of the subunits, the isomerization state of one unit can influence the other, e.g. by electronic communication. However, strong conjugation can inhibit multistate switching due to energy transfer between the subunits. Furthermore, linkers that completely prevent electronic coupling lead to systems that behave like the sum of independent, isolated switches.

In general, if a single chromophore absorbs a photon with matching energy $\Delta E$, it can be excited from its electronic ground state (GS) to its excited state (ES). In this process, the electron density distribution changes and creates an instantaneous dipole, the transition dipole moment $\mu$. Classically, it is described by a vector, depending on the direction of the electron density change and the intensity of the transition. If multiple chromophores are in spatial proximity in a multiphotoswitch, the electronic excitation becomes delocalized over the entire molecule, which is termed exciton coupling, introduced by Kasha [5]. If one considers a molecule composed of two chromophores, two nondegenerate ESs are the result of the linear combination of the individual, unperturbed ESs. Depending on the orientation of the chromophores A and B, the transition dipoles can be orientated in parallel or colinear fashion (Figure 21.1) [6].

If $\mu_A$ and $\mu_B$ are orientated in an antiparallel fashion, a net dipole moment of zero results for ES′ and thus this transition is forbidden. As a result, the higher energy state ES″ with a positive net transition dipole moment represents the allowed transition and a blue-shift compared to the unperturbed chromophore is the result

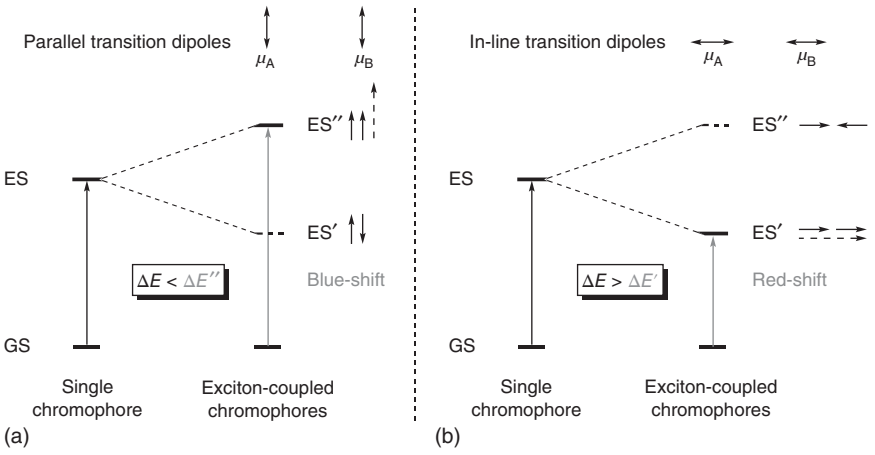


**Figure 21.1** Two nondegenerate excited states (ES′, ES″) are the result of excitonic coupling of two chromophores. (a) In a pair of chromophores with parallel transition dipole moments, ES′ has zero net transition dipole moment and is therefore a forbidden transition. (b) Colinear transition dipole moments result in a lower-energy transition to ES′ in the head-to-tail case with nonzero magnitude. Source: Modified from Kasha et al. [6].

(Figure 21.1a). On the other hand, the transition dipole moments can be orientated in a colinear fashion. In this case, the lower energy excited state ES′ becomes the favored transition and is therefore red-shifted compared to the unperturbed chromophore. Note that in most cases the transition dipole moments of two coupled chromophores are not in perfect parallel or colinear orientation. For more detailed information, see references cited above. In the case of multiphotoswitches, excitonic coupling can lead to completely different behavior of the subunits compared to their monomer behavior. For example, energy transfer from one to another subunit can prevent a second isomerization event or photoisomerization is completely deactivated.

Furthermore, geometrical constraints can be of importance in the design of multiphotoswitches. For example, steric or macrocyclic strain can make photoisomerizations unfavorable and, therefore, change the photochromic property of a switch. Regarding multiphotoswitches, even sterically noncrowded subunits may prevent isomerization to all possible states due to strain in a resulting geometry with multiple isomerized subunits (Figure 21.2c). In contrast, close proximity of certain groups in one photoisomer may not destabilize the corresponding state. For example, attractive noncovalent interactions, such as London dispersion, can have a significant stabilizing effect on the photoswitch (Figure 21.2d) [7].

Additionally, macrocyclic arrangements of multiple photoisomers strongly influence the isomerization behavior of the system. For example, photoswitches that undergo drastic geometrical changes during isomerization may become highly strained in a cyclic arrangement. This can even lead to reversed stabilities of the subunits (Figure 21.2e). All in all, the delicate balance of these effects is still the major challenge in the design of effective multiresponsive photoswitches. In

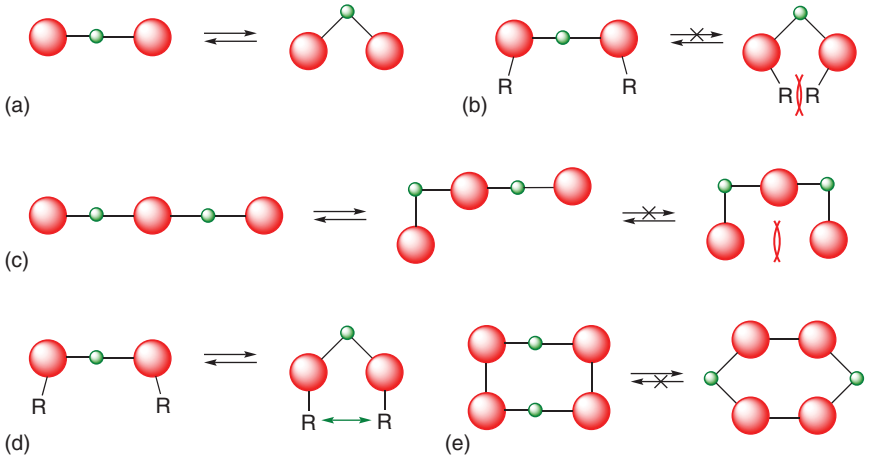


**Figure 21.2** Exemplary representation of the effect of sterics by combining two photoswitches. (a) Photoisomerization process of a hypothetical single photoswitch. (b) Photoisomerization can be prevented by steric constraints in a photoswitching system. (c) Dimers of photoswitches may undergo one photoisomerization, but a second can be prevented by geometric constraints or repulsion. (d) Attractive interactions of substituents can also stabilize photoisomers. (e) Macrocyclic strain in multiphotoswitches strongly influences their isomerization properties.

the next paragraphs, some examples of multinary photoswitches and the typical difficulties in their design will be introduced.

## 21.3 Dithienylethene Multiphotoswitches

One of the most used scaffolds for the construction of multiphotochromic compounds are dithienylethenes (DTEs) which can be reversibly isomerized to a closed form with UV- and to the open form with visible light. The first dimer of two DTE units was reported in 1999 [1], having two switches connected by a tetrathiafulvalene unit (Scheme 21.1a, **1**). Upon irradiation with 254 nm light, the closure of one DTE subunit was detected. However, prolonged irradiation did not yield the fully closed isomer, which was rationalized by electronic conjugation of the photochromes. In the singly closed isomer **1′**, energy transfer from the excited open moiety to the previously closed subunit via the double bond linkage prevents full photoisomerization in the DTE dimer. The compact dimer **2** (Scheme 21.1b) was one of the first three-state switches presented, although the fully closed isomer was not detected [8]. Due to the asymmetry of **2**, both the closed-open (**2a**) and open-closed (**2b**) isomers were distinguishable in solution. However, the selective generation of the two different isomers was not possible. Furthermore, the absence of a fully closed isomer was rationalized by high amount of steric stress on the open DTE units in **2a**,**b** after the first closing. A second photocyclization would lead to a thermodynamically unstable product, which prevents the second closure [9].

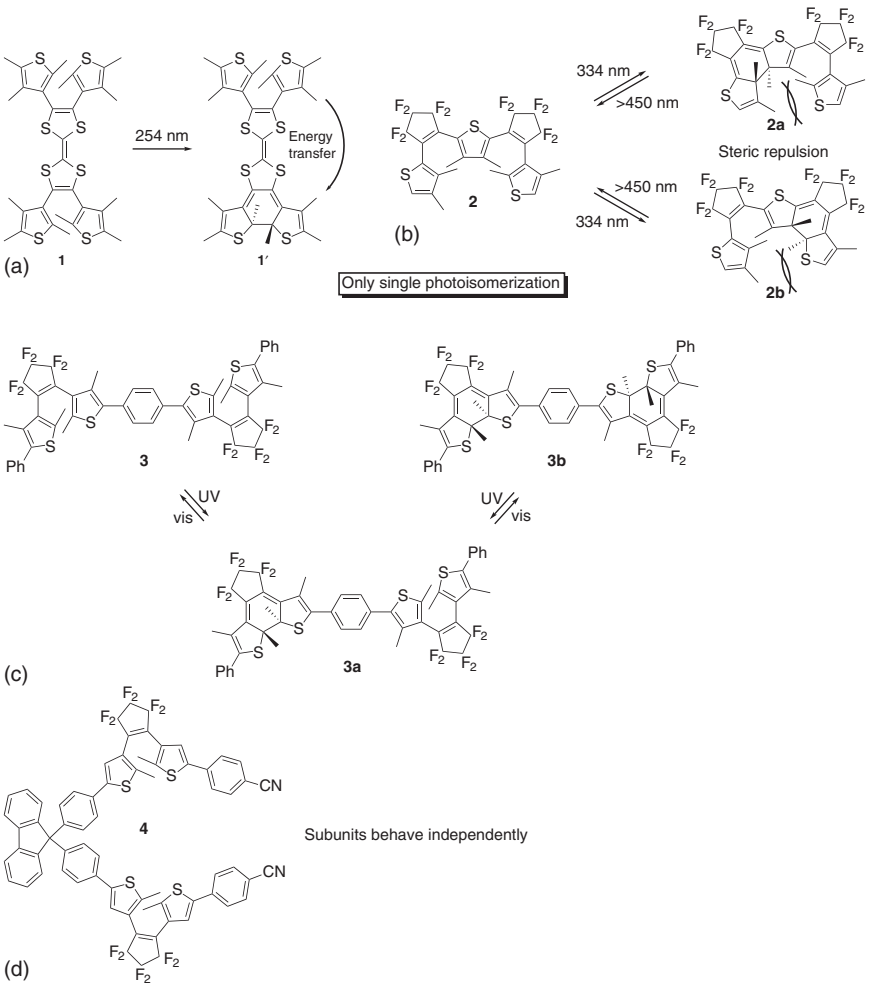


**Scheme 21.1** (a) The dimeric DTE photoswitch **1** only cyclizes once due to energy transfer from the open to the closed DTE unit in **1′** after photoexcitation. (b) Thiophene-bridged dimer **2** isomerizes to the two different singly closed isomers **2a**,**b**, respectively, and cannot cyclize completely. (c) Phenyl-linked DTE dimer **3** showed total and stepwise photoisomerization. (d) Alkyl connection in compound **4** prevents communication between the DTE subunits.

When extending the spatial separation of two DTEs using conjugated aromatic linkers, also, only singly closing photoswitches could be obtained. In all cases, energy transfer from the excited open DTE moiety to the previously closed unit quenches the second cyclization [10]. The first DTE dimer with full reversible photochromism of all units was presented by Kobatake and Irie in 2003. Herein, the photochromes are connected with a phenyl linker at the α positions of the two thiophene moieties (Scheme 21.1c, **3**) [11]. Upon irradiation with UV light (313 nm), **3** isomerizes stepwise to **3a** and **3b**, respectively. Furthermore, the initial open-open-isomer **3** can be regenerated by irradiation with visible light. Changing the aromatic or $sp^2$ nature

of the linker to $sp^3$, the communication between the DTE units is almost lost and the systems behave like a sum of the properties of the individual subunits without addressable selectivity (**4**, Scheme 21.1d) [12].

There are some examples showing multiple selectively addressable states by using light of different wavelengths. In fused asymmetric DTE trimer **5** (Scheme 21.2), five of the hypothetical eight isomers can be generated by using combinations of different wavelengths or UV light only [3]. In the system, the states change their color from the colorless, fully open "000" state over blue "010," red "100," yellow "001," to orange "101." Again, steric stress has been put forward as the reason by the authors [3], which prohibits cyclization of two neighboring, fused DTE units, leaving the hypothetical remaining states not accessible.

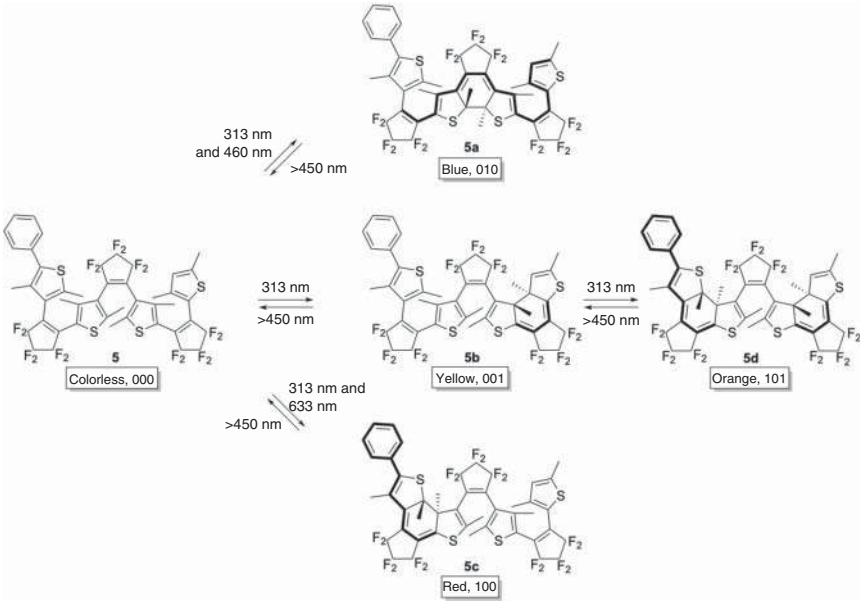


**Scheme 21.2** Fused DTE trimer **5c** can selectively be switched to five different states.

## 21.4 Azobenzene Multiphotoswitches

### 21.4.1 Acyclic Oligoazobenzenes

The general versatility of the azobenzene (AB) photoswitch, proven by a vast number of studies and applications reported, makes this scaffold highly interesting for the design of multinary photoswitches [4, 13]. Acyclic oligo-ABs promise straight-forward preparation of potentially highly efficient multinary photoswitches [14]. A systematic study on the electronic coupling in *para*-bis-ABs was reported by Hecht and coworkers (Scheme 21.3a) [16]. By changing the dihedral biphenyl angle by *ortho* methyl substitution, the conjugation between both AB units could

be reduced and the content of (*Z*,*Z*) isomer in the photo stationary states (PSSs) could be increased from 3% in **6** up to 95% in **8**. Based on this principle, Bléger and coworkers reported the asymmetric AB dimer **9** capable of selective four-state switching using light and electrocatalytic isomerization (Scheme 21.3b) [15].

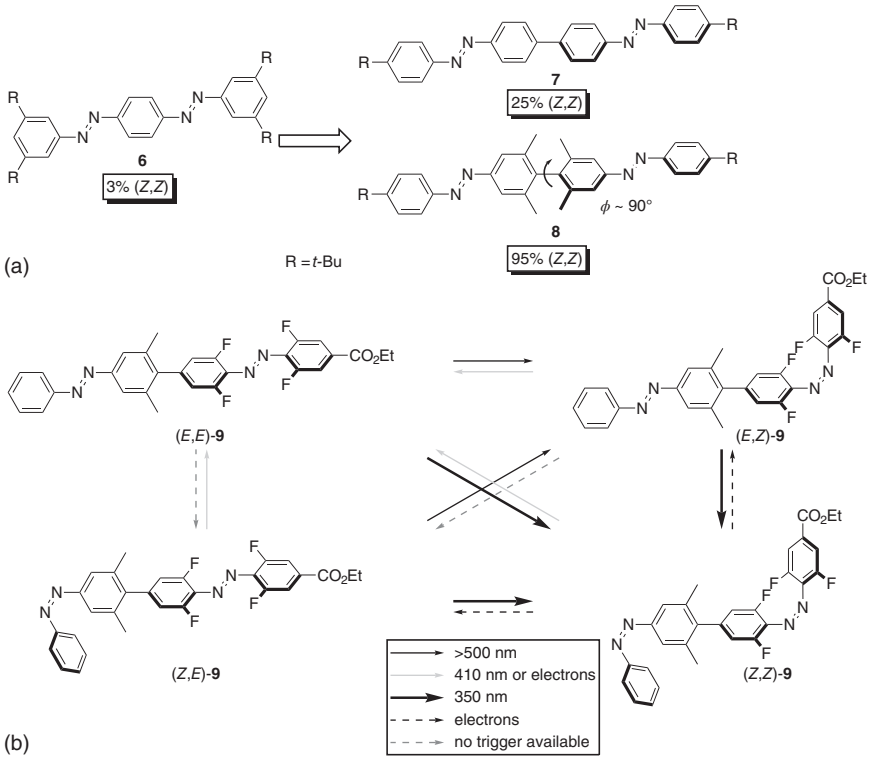


**Scheme 21.3** (a) Increasing the biphenyl torsion angle $\phi$ lowers the electronic $\pi$-conjugation and enables efficient photoswitching of both subunits in bis-ABs. (b) Using the latter principle in asymmetric bis-AB **9** enables effective four-state switching. Source: Zhao et al. [15a]; Goulet-Hanssens et al. [15b].

In a similar, trimeric *meta*-AB derivative **10** with a central benzene core, $\pi$-conjugation between the switches was limited and, therefore, all three azo arms could be isomerized independently (Scheme 21.4) [17]. The same was proposed for azo dendrimer **11** with a 1,3,5-tricarboxamide core in a theoretical study [18].

The photochemical properties of *ortho*-, *meta*-, and *para*-AB dimers sharing one phenyl ring differ drastically depending on their connectivity pattern (Scheme 21.5, **12–14**) [19, 20]. While the spectral properties and quantum yield of photoisomerization are similar to the parent AB in *ortho*-bis-AB (**12**), its (*Z*) → (*E*) thermal relaxation occurs on the millisecond range due to strong intramolecular excitonic coupling between the AB subunits. *Para*-connected derivative **14** shows extremely high π-conjugation, very low isomerization quantum yield (∼1%), and a bathochromically shifted absorption spectrum. *Meta*-bis-AB (**13**), though, behaves

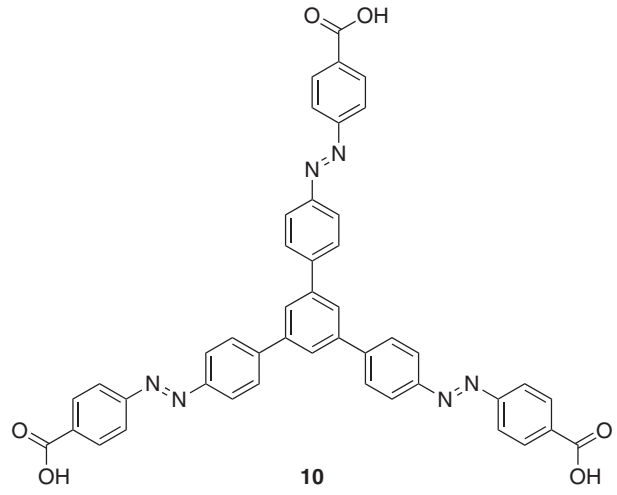


**10**

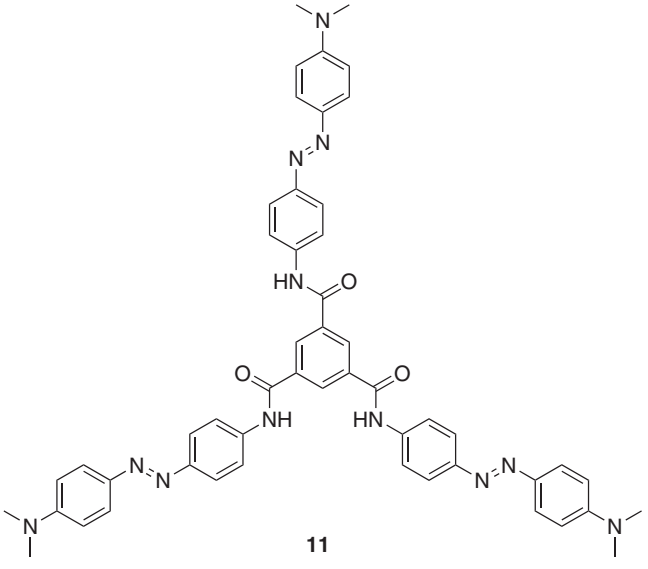


**11**

**Scheme 21.4** Due to low π-conjugation between the azo arms, compounds **10** and **11** show independent isomerization of the subunits.

almost like two independent AB switches and can be isomerized in a stepwise fashion ("*meta*-rule").

In order to increase the functionality of single molecules even further, more than just two AB subunits can be fused together [21]. Expanding the advantages of highly dense bis-ABs, Cho and coworkers reported the synthesis of 1,3,5-tris-ABs in 2004 (Scheme 21.6, **15**) [22]. The group prepared a series of symmetrically substituted derivatives and isolated them as (*E*,*E*,*E*)-**15** from mixtures of all isomers, with a composition of 70 : 20 : 7 : 3 [(*E*,*E*,*E*):(*E*,*E*,*Z*):(*E*,*Z*,*Z*):(*Z*,*Z*,*Z*)] in

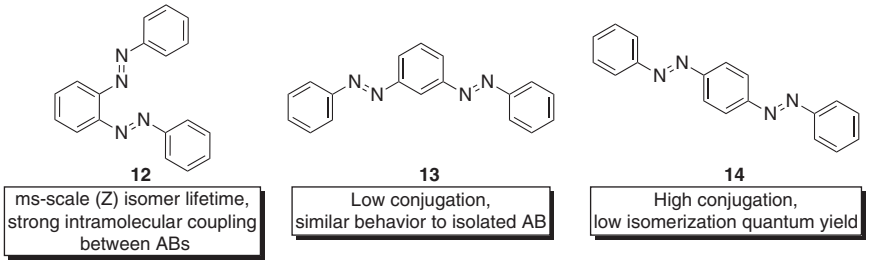


**Scheme 21.5** The properties of bisazobenzenes strongly depend on their connectivity pattern. Source: Slavov et al. [19] and Cisnetti et al. [19].

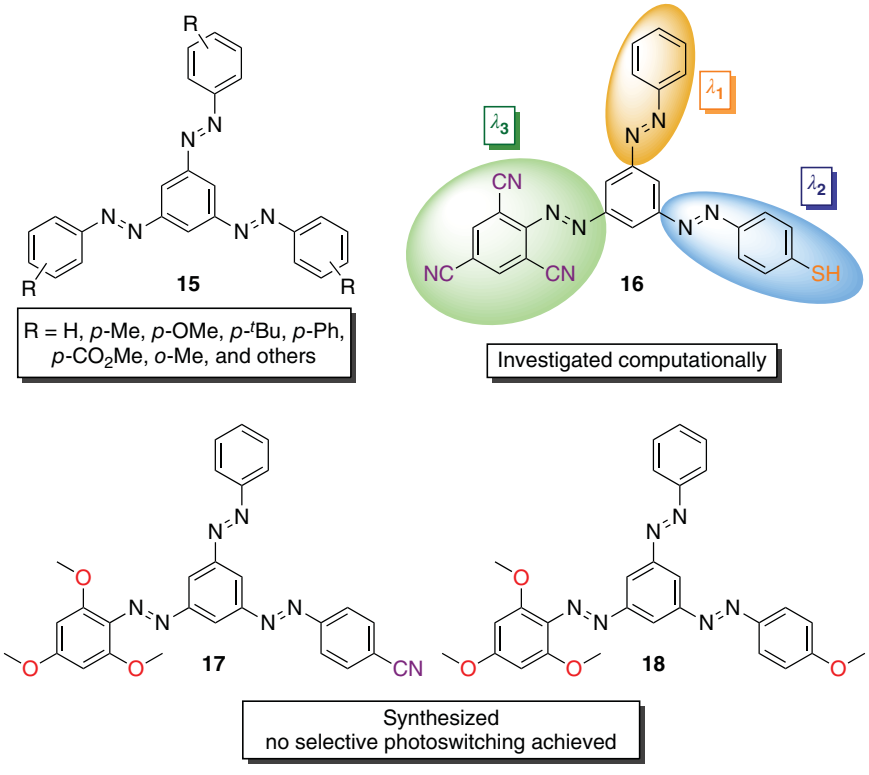


**Scheme 21.6** AB trimers **15** were introduced by Cho and coworkers in 2004. Dreuw and coworkers investigated asymmetric derivative **16** toward the application as multinary switch. A synthetic strategy for the preparation of asymmetric starazos **17** and **18** was developed. However, no selective photoswitching could be achieved.

the unsubstituted case. However, the authors did not perform any studies on the photophysical properties of these interesting compounds. In 2018, Dreuw and coworkers published a computational study on tuning the AB subunits by suitable substitution toward achieving selective multistate photoswitching [23]. As a result,

"starazo" **16** was found to feature spectrally separated absorption maxima of all AB branches that would in theory allow wavelength-selective photoisomerization. Analogous to *meta*-bis-ABs, the three AB subunits were found to be electronically decoupled, despite the spatial overlap. Shortly after that, a synthetic route toward the asymmetric starazos **17** and **18** was presented (Scheme 21.6) [24]. In preliminary isomerization studies, both **17** and **18** showed complex mixtures of isomers in their PSSs without the ability of selective isomerization. However, the synthesis of starazo **16** is still elusive to validate the proposed selective multiple photoswitching.

### 21.4.2 Macrocyclic Azobenzenes

As it is the case for acyclic ABs, also AB macrocycles can be connected either using conjugating or nonconjugating linkers. Furthermore, there are many examples of nonconjugated macrocyclic ABs in the literature that are significantly influenced by macrocyclic ring strain [25]. All in all, the type of linkage in the AB multinary switches determines their photochromic, photo-, and thermal isomerization behavior and thus opens great versatility in the design of multiaddressable AB-based systems. The compound class was introduced by Rau and coworkers in 1982 (Scheme 21.7a, **19**) [27]. In their study, macrocycle **19** isomerized upon irradiation with 366 nm to the corresponding (*E*,*Z*) and (*Z*,*Z*) isomers in a stepwise mechanism [28]. Regarding the thermal back-reaction, one would expect the (*Z*,*Z*) isomer to be the least and (*E*,*Z*)-**19** to be the second most stable isomer due to the general lower stability of (*Z*)-ABs. However, macrocyclic strain destabilizes (*E*,*Z*)-**19**, resulting in a lifetime of only approximately six minutes. In contrast, the (*Z*,*Z*) isomer showed a rather long half-life of ∼5 days, caused by strain that has to be built up in the (*Z*,*Z*) → (*E*,*Z*) thermal isomerization step.

After this initial discovery of the important influence of ring strain on azobenzophanes, a more rigid malonic ester bridged derivative was presented (Scheme 21.7a, **20**). As expected, the half-live of the (*Z*,*Z*) and (*E*,*Z*) isomers dramatically increased to ∼400 days for the former and decreased to ∼9 μs for the latter, respectively, making **20** a thermally bistable system [26].

Further research on macrocyclic ABs was done by the groups of Tamaoki and Norikane. They reported electronically decoupled *meta*- and *para*-alkyl linked structures showing stepwise isomerization behavior [29–31]. A *meta*-methylene-linked bis-AB dimer was found to be able to isomerize selectively either to a PSS with excess of (*Z*,*Z*) or a slight excess of (*E*,*Z*) isomers, depending on the irradiation wavelength (Scheme 21.7b, **21**). When the linkers are removed completely, and thus even more ring strain is incorporated in the macrocycle, *meta*-connected cyclobis-AB **22** (Scheme 21.7b) was the first example of an AB with reversed thermodynamic stability [32]. The most stable isomer is (*Z*,*Z*)-**22**, and photoisomerization was only possible after intense irradiation with a Hg high pressure lamp or a laser. Due to extremely high ring strain, the (*E*,*Z*) isomer was found to be rather unstable ($t_{1/2} = 1$ s), whereas the (*E,E*) isomer showed a prolonged half-life (20 days), which is comparable to the examples reported by Rau.

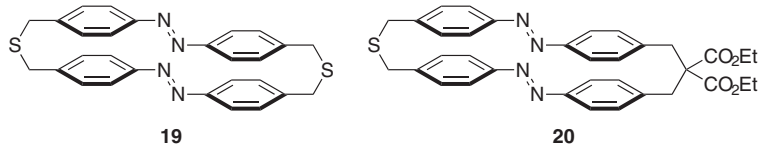

19 20

(a)

| Thermal isom. step | $t_{1/2}$ 19 | 20 |
|---|---|---|
| (*Z*,*Z*) → (*E*,*Z*) | 5 d | ~400 d |
| (*E*,*Z*) → (*E*,*E*) | 6.25 min | ~9 μs[a] |

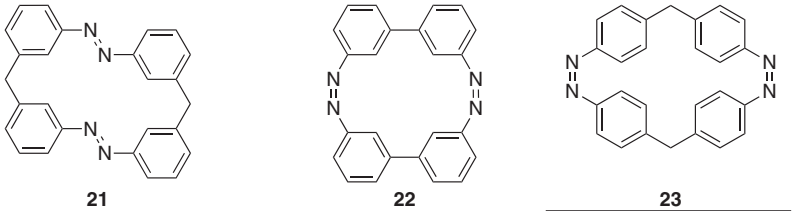

21 22 23

366 nm → 87% (*Z*,*Z*), 29% (*E*,*Z*)
436 nm → 49% (*E*,*Z*), 45% (*E*,*E*)

(b)

$t_{1/2}$[(*E*,*E*) → (*E*,*Z*)] = 20 d
$t_{1/2}$[(*E*,*Z*) → (*Z*,*Z*)] = 1 s

*Only switching to (E,Z) back-reaction in ms range*

(c)

**Scheme 21.7** (a) The stabilities of different isomers of azobenzophanes **19** and **20** strongly depend on macrocyclic ring strain. (b) *Meta*-methylene-linked **19** can be isomerized selectively to some extent. Large ring strain inverts the thermodynamic isomer stability of **22** and (c) **23** and thus makes the (*Z*,*Z*) isomers the most stable conformations. [a]Half-life calculated from the *k* value given in ref. [26].

Increasing the macrocyclic ring strain to extreme, our group has reported the synthesis of (*Z*,*Z*)-stable *para*-methylene connected bis-AB **23** (Scheme 21.7c) [33]. The structure was confirmed by single crystal X-ray analysis, and irradiation did not lead to any spectral change, indicating that the highly strained compound was not capable of photoisomerization. Only ultrafast spectroscopy revealed that in **23** one AB unit can isomerize to the corresponding (*E*,*Z*) isomer [34]. Detailed computational analysis revealed extreme strain in (*E*,*Z*)-**23** to be responsible for fast (*E*,*Z*) → (*Z*,*Z*) thermal isomerization in the millisecond range.

A series of ethylene-bridged macrocycles by Tamaoki et al. showed photoisomerization to all possible isomers (Scheme 21.8) [29, 30]. The thermal half-lives of the corresponding (*Z*) isomers were comparable to linear AB because the relatively flexible ethylene connection prevents the build-up of macrocyclic strain.

Mayor and coworkers reported hinge-like bisazo macrocycles **26** (Scheme 21.8) and only observed the symmetric (*E*,*E*) and (*Z*,*Z*) isomers during isomerization experiments [35]. In contrast to the alkyl-linked examples shown before, the rigid *meta*-terphenyl units generated large amounts of strain in the hypothetical (*E*,*Z*) isomer, resulting in half-lives too short for $^1$H NMR spectroscopy. Further studies on macrocyclic ring strain and its influence on the isomerization behavior in *para*-dimethyl(methylene) linked macrocycles were carried out in our group (Scheme 21.9) [36]. Azobenzophane **28** was found to be an effective three-state

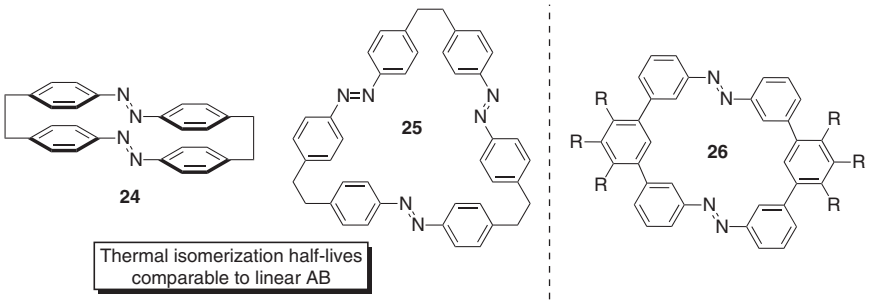


**Scheme 21.8** Macrocycles **24** and **25** are almost uninfluenced by ring strain and show comparable behavior to linear AB. In contrast, the hinge-like macrocycles **26** did not show the mixed (*E*,*Z*) isomers, but only (*E*,*E*) and (*Z*,*Z*).

photoswitch, where light of different wavelengths and temperature could be used as inputs to obtain PSSs containing more than 75% of three out of the four possible isomers. Detailed NMR spectroscopy and computational analyses revealed that macrocyclic ring strain in the right amount is responsible for this unique behavior.

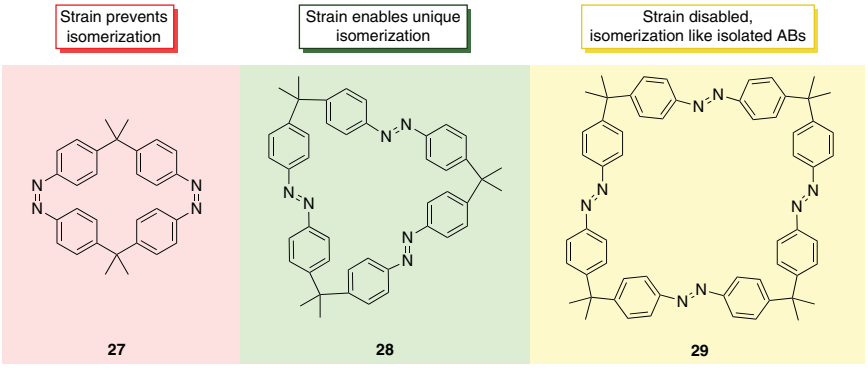


**Scheme 21.9** The AB macrocyles **27–29** revealed that the right amount of ring strain is necessary to enable unique isomerization properties to create the effective three-state switch **28**.

Alternatively, also AB units can be directly connected in a macrocyclic fashion without linker groups. The smallest possible, directly fused azobenzophane containing more than two azo units is cyclotris-AB (Scheme 21.10, **30a**) [37]. No studies on the compounds spectral properties were reported in the initial publication by Dreiding and coworkers. Therefore, our group re-synthesized the compound among some other derivatives [38] and revealed the absence of photoisomerization due to the structural constraints in this highly rigid system [39]. Further research focused on creating multiadressability in cyclotrisazobiphenyl (CTB) (Scheme 21.10, **31**), which could be isomerized to different PSSs with every possible isomer as the main component in slight excess, depending on the irradiation wavelength [40]. Introducing chirality to the CTB system by

changing one biphenyl to a bimesityl unit (**32**), three different outputs could be created by using 302, 365 nm, or visible light irradiation. The states could be read out by circular dichroism (CD) spectroscopy at 275 nm, leading to a positive, negative, or no signal originating from different mixtures of all possible isomers [41].

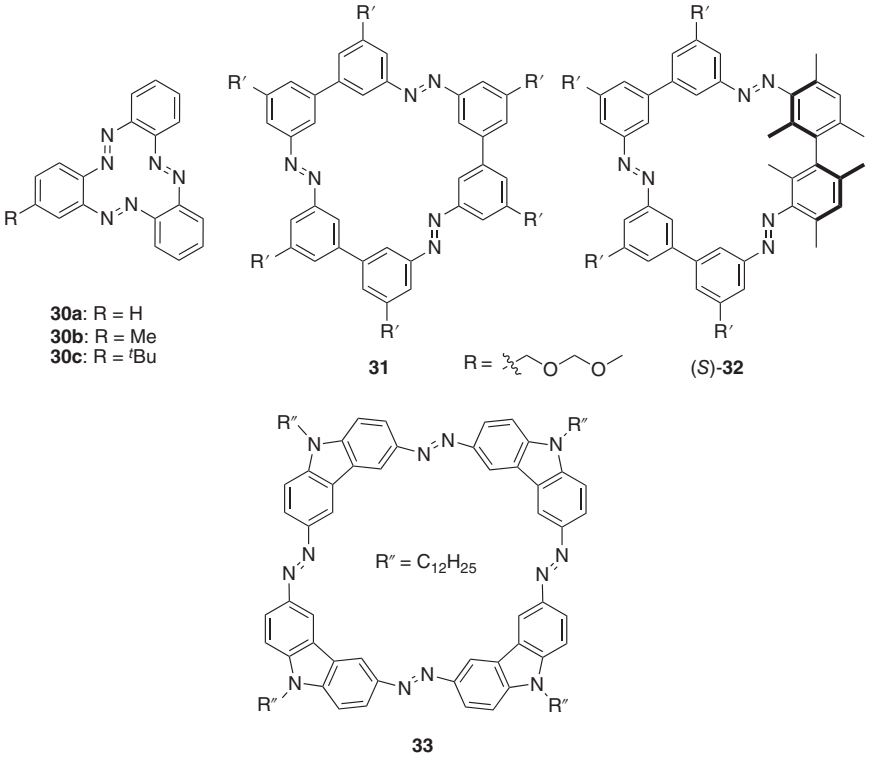


**Scheme 21.10** Cyclic AB trimer **30** shows no photoswitching, while **31** isomerizes to different PSSs depending on the irradiation wavelength. Chiral **32** can be switched between three different isomeric compositions, which can be read out by circular dichroism (CD) spectroscopy. The more rigid tetraazocarbazole **33** was demonstrated as a logic gate with three inputs: UV light, acid, and temperature.

To get deeper understanding of the isomerization behavior of azobenzophanes, tetraazocarbazole **33** was prepared. The compound showed potential as a logic gate with UV light, acid, and temperature as inputs by reading out the absorbance at 570 nm [42]. Furthermore, the compound was used to investigate the effect of symmetry during isomerization. Detailed NMR spectroscopic and computational analysis revealed that the mixed (*E*,*Z*,*E*,*Z*) isomer showed higher thermal stability than (*E*,*E*,*Z*,*Z*)-**33** caused by higher ring strain. However, during photoisomerization, the (*E*,*E*,*Z*,*Z*) isomer is preferred over the (*E*,*Z*,*E*,*Z*) in the corresponding PSS [43].

## 21.5 Multiphotoswitches Composed of Different Photoswitches

An alternative approach toward multinary switches is the combination of the advantages of two or more different photochromic systems. Especially considering effective spectral separation, which ensures multiaddressability of the system, the use of alternating switching units can be a powerful strategy. The first example of a hybrid photoswitch was presented by Daub and coworkers, who combined a DTE and a dihydroazulene–vinylheptafulvene (DHA/VHF) unit, linked by a shared double bond (Scheme 21.11) [44]. Upon irradiation wit UV light (254–366 nm), both the DTE cyclizes to **34b** and the DHA unit opens to VHF **34c**. However, the VHF is thermally not stable, while the closed DTE is. Therefore, the PSS composition depends on the quantum yields of the DHA/VHF ring opening and the DTE cyclization, as well as on the duration of irradiation. The hypothetical closed-DTE/VHF isomer **34d** could not be observed.

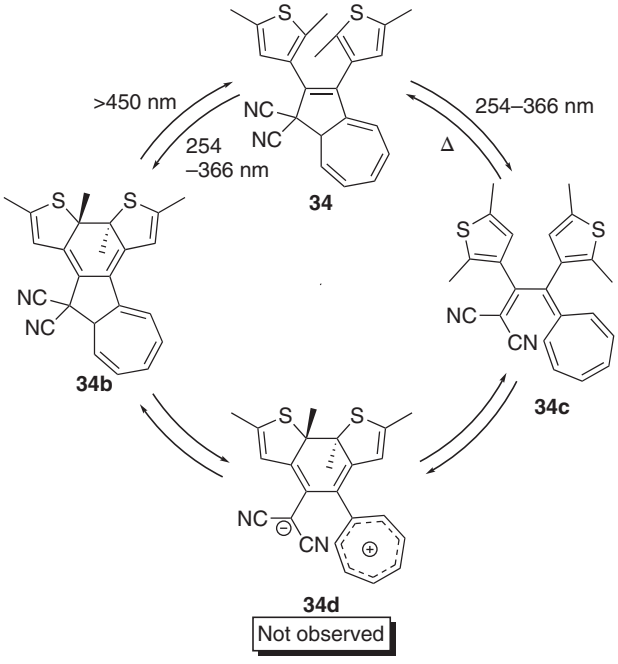


**Scheme 21.11** The fused DTE/DHA hybrid dimer **34** can be switched between three of the possible four states. Source: Mrozek et al. [44a]; Mrozek et al. [44b].

A combination of a DTE and two identical fulmigide (FG) photoswitches connected by a bis-phenyl ethynylene bridge capable of effective multinary photoswitching was reported by Gust and coworkers (Scheme 21.12, **35**) [45]. FGs, like DTEs, belong to the class of electrocyclization-based photoswitches that can be reversibly closed using UV light and reopened with visible light [46]. Due to the identical FG

units in **35**, the molecule features four possible isomerization states. All states can be addressed selectively with light of different wavelengths or wavelength combinations. Compound **35** was used as a logic gate and could perform operations such as "AND," "exclusive OR," and even arithmetic operations using several absorption and emission wavelengths as readouts.

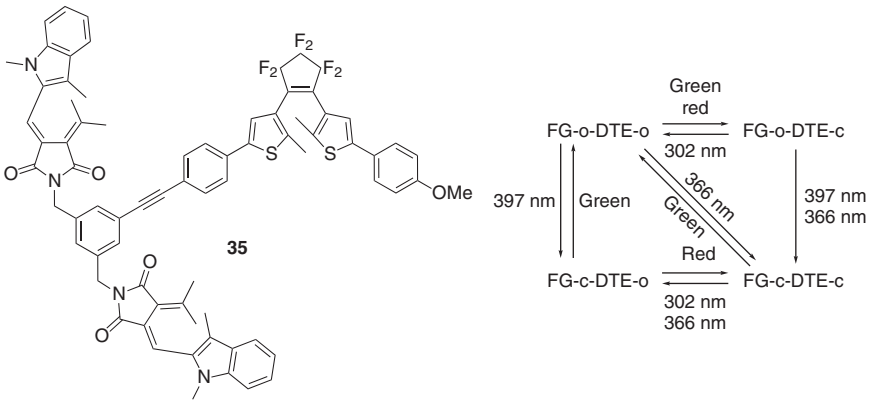


**Scheme 21.12** Bis-fulmigide-DTE hybrid system **35** can be selectively addressed with light of different wavelengths and was successfully used as a logic gate (o: open subunit, c: closed subunit). Source: Andréasson et al. [45a]; Andréasson et al. [45b].

Feringa and coworkers presented a highly effective, multiaddresable hybrid switch bearing a donor–acceptor–Stenhouse adduct (DASA) and an AB moiety as switching units [2]. Their design utilized the complementary absorptions of AB in the 300–500 nm range and those of the DASAs that do not absorb in this region. In compounds **36** and **37**, where both photochromes were connected with alkyl linkers of different chain lengths, the degree of coupling between the photoswitches could be tuned (Scheme 21.13a). In the shorter-linked hybrid switch **36**, 370 nm irradiation did not only affect the AB but also to some extent the DASA subunit. Using a longer linker, an orthogonal switchable system could be constructed. The large change in polarity from the open to the closed DASA unit was utilized to create a molecular machine that is capable of photoresponsive phase transition between an organic and an aqueous layer (Scheme 21.13b). While the AB unit can reversibly isomerize in toluene, phase transition to the aqueous layer ($pH \geq 9$) is triggered when the DASA subunit closes photochemically with visible light. In addition to that, the AB moiety can bind to water-soluble α-cyclodextrin (CD) in its ($E$) state. Upon photochemical $(E) \rightarrow (Z)$ isomerization, the AB guest leaves the CD host, which in principal can be used for the control of catalytic activity in phase-transfer catalysis. Finally, upon phase separation and re-extraction of the aqueous layer with dichloromethane, both the DASA and AB subunits relax thermally to the initial state. Based on these insights, light responsive phase-transfer catalytic systems that would allow catalyst recycling could be designed.

Another successful combination of a first-generation DASA with another photoswitch was recently presented by Qu and coworkers [47]. In their approach, a

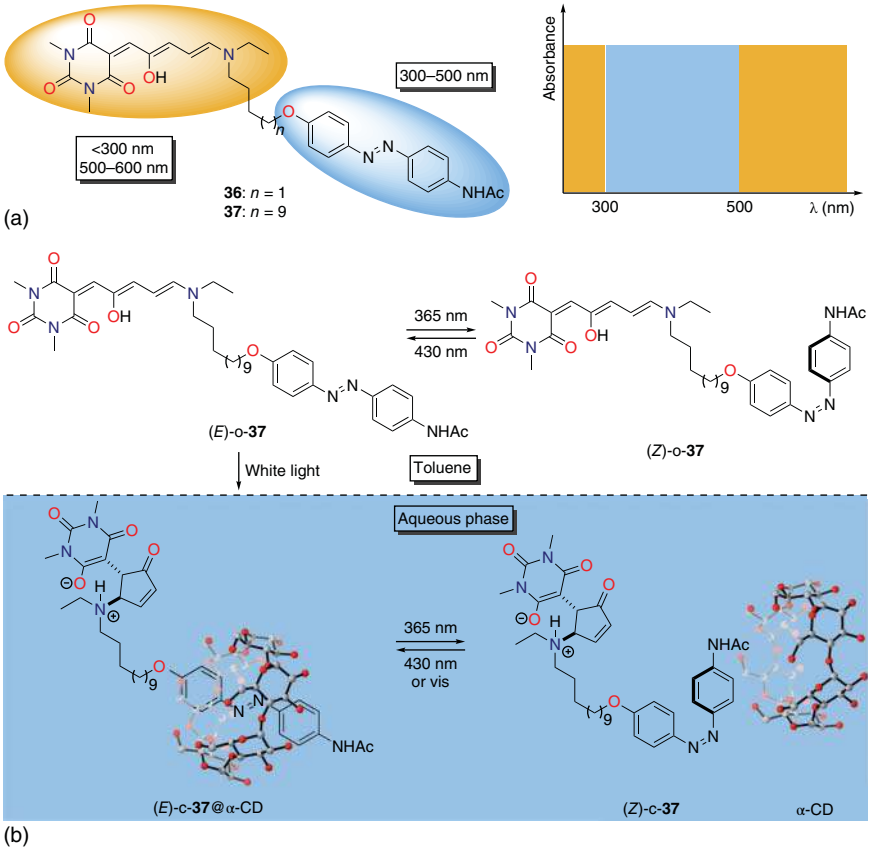


**Scheme 21.13** (a) DASA-AB heteroswitches **36** and **37** show complementary absorption of their subunits. (b) Isomerization of the DASA unit in **37** was used for photoresponsive phase transition, while the AB isomerization was applied for host–guest binding to α-cyclodextrin in the aqueous phase.

DASA was combined with an aurone moiety, allowing selective, orthogonal photoswitching (Scheme 21.14). All four possible states of compound **38** could be accessed using light of 365 nm for the aurone *trans*→*cis* isomerization and 430 nm for the reverse reaction. By using 585 nm, the DASA cyclization could be induced, and the cycloreversion was achieved by heating to 40 °C or keeping the sample in the dark ($t_{1/2}$ = 41 s).

## 21.6 Conclusion

In summary, the examples shown above outline the challenges in the design of selectively addressable multiphotoswitches. On the one hand, conjugated linkage of the subunits can lead to new properties in photoswitching due to communication of the photoswitches with each other. On the other hand, strong electronic communication

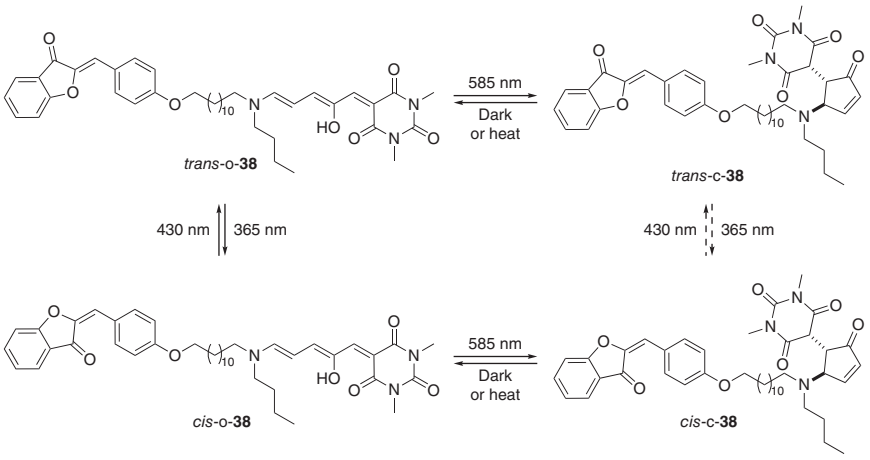


**Scheme 21.14** The combination of a 1st generation DASA and an aurone led to orthogonal, selective photoswitching.

between the switching units can even prevent multiple photoswitching. Furthermore, geometrical strain can also prevent the formation of certain states, as it was found in some DTE multiswitches. Additionally, ring strain enables new properties, such as reversed thermodynamic stability of the photoisomers, especially in the case of macrocyclic ABs.

Additionally, photoswitches can be connected by electronically decoupling linkers, such as simple alkyl branches. This enables multistate switching, but often a loss of selectivity is the drawback when systems of equal photochromes are designed.

A promising approach toward effective multinary photoswitches is the combination of different classes of switches with orthogonal absorption behavior. Again, communication between the subunits is a major challenge that must be overcome to create selectively addressable multinary switches.

A delicate balance between all those concepts is necessary and is still one of the most challenging tasks in the field of multiphotoswitches. In the future, the combination of favorable properties of different classes of photoswitching units represents a promising approach toward highly functional molecules and materials. Many impressive examples have already been reported, and future research can now apply these fundamental insights to create multifunctionality for example in catalysis, photobiology, material science or information processing and molecular computing.

## References

**1** Uchida, K., Masuda, G., Aoi, Y. et al. (1999). *Chem. Lett.* 28: 1071–1072.
**2** Lerch, M.M., Hansen, M.J., Velema, W.A. et al. (2016). *Nat. Commun.* 7: 12054.
**3** Higashiguchi, K., Matsuda, K., Tanifuji, N., and Irie, M. (2005). *J. Am. Chem. Soc.* 127: 8922–8923.

**4** Fihey, A., Perrier, A., Browne, W.R., and Jacquemin, D. (2015). *Chem. Soc. Rev.* 44: 3719–3759.

**5** Kasha, M. (1959). *Rev. Mod. Phys.* 31: 162–169.

**6** Kasha, M., Rawls, H.R., and Ashraf El-Bayoumi, M. (1965). *Pure Appl. Chem.* 11: 371–392.

**7** Schweighauser, L., Strauss, M.A., Bellotto, S., and Wegner, H.A. (2015). *Angew. Chem. Int. Ed.* 54: 13436–13439.

**8** Higashiguchi, K., Matsuda, K., Matsuo, M. et al. (2002). *J. Photochem. Photobiol. A* 152: 141–146.

**9** Perrier, A., Maurel, F., and Jacquemin, D. (2011). *J. Phys. Chem. C* 115: 9193–9203.

**10** (a) Kawai, T., Sasaki, T., and Irie, M. (2001). *Chem. Commun.* 711–712. (b) Saita, S., Yamaguchi, T., Kawai, T., and Irie, M. (2005). *ChemPhysChem* 6: 2300–2306. (c) Wong, H.-L., Ko, C.-C., Lam, W.H. et al. (2009). *Chem. Eur. J.* 15: 10005–10009.

**11** Kobatake, S. and Irie, M. (2003). *Tetrahedron* 59: 8359–8364.

**12** (a) Kobatake, S., Kuma, S., and Irie, M. (2004). *Bull. Chem. Soc. Jpn.* 77: 945–951. (b) Jung, I., Choi, H., Kim, E. et al. (2005). *Tetrahedron* 61: 12256–12263. (c) Liu, H.-h. and Chen, Y. (2011). *J. Mater. Chem.* 21: 1246–1249.

**13** (a) Nie, H., Self, J.L., Kuenstler, A.S. et al. (2019). *Adv. Optical Mater.* 7: 1900224. (b) Goulet-Hanssens, A., Eisenreich, F., and Hecht, S. (2020). *Adv. Mater.* 32: 1905966.

**14** Merino, E. (2011). *Chem. Soc. Rev.* 40: 3835–3853.

**15** (a) Zhao, F., Grubert, L., Hecht, S., and Bléger, D. (2017). *Chem. Commun.* 53: 3323–3326. (b) Goulet-Hanssens, A., Utecht, M., Mutruc, D. et al. (2017). *J. Am. Chem. Soc.* 139: 335–341.

**16** Bléger, D., Dokić, J., Peters, M.V. et al. (2011). *J. Phys. Chem. B* 115: 9930–9940.

**17** Galanti, A., Santoro, J., Mannancherry, R. et al. (2019). *J. Am. Chem. Soc.* 141: 9273–9283.

**18** Koch, M., Saphiannikova, M., Santer, S., and Guskova, O. (2017). *J. Phys. Chem. B* 121: 8854–8867.

**19** Slavov, C., Yang, C., Schweighauser, L. et al. (2016). *Phys. Chem. Chem. Phys.* 18: 14795–14804.

**20** Cisnetti, F., Ballardini, R., Credi, A. et al. (2004). *Chem. Eur. J.* 10: 2011–2021.

**21** (a) Bellotto, S., Reuter, R., Heinis, C., and Wegner, H.A. (2011). *J. Org. Chem.* 76: 9826–9834. (b) Reuter, R. and Wegner, H.A. (2012). *Beilstein J. Org. Chem.* 8: 877–883.

**22** Lim, Y.-K., Choi, S., Park, K.B., and Cho, C.-G. (2004). *J. Org. Chem.* 69: 2603–2606.

**23** Yang, C., Slavov, C., Wegner, H.A. et al. (2018). *Chem. Sci.* 9: 8665–8672.

**24** Heindl, A.H. and Wegner, H.A. (2020). *Beilstein J. Org. Chem.* 16: 22–31.

**25** (a) Wagner-Wysiecka, E., Łukasik, N., Biernat, J.F., and Luboch, E. (2018). *J. Incl. Phenom. Macrocycl. Chem.* 90: 189–257. (b) Reuter, R. and Wegner, H.A. (2011). *Chem. Commun.* 47: 12267–12276.

**26** Röttger, D. and Rau, H. (1996). *J. Photochem. Photobiol. A* 101: 205–214.


**27** Gräf, D., Nitsch, H., Ufermann, D. et al. (1982). *Angew. Chem. Int. Ed.* 21: 373–374.

**28** Rau, H. and Lueddecke, E. (1982). *J. Am. Chem. Soc.* 104: 1616–1620.

**29** Tamaoki, N., Koseki, K., and Yamaoka, T. (1990). *Tetrahedron Lett.* 31: 3309–3312.

**30** Tamaoki, N., Ogata, K., Koseki, K., and Yamaoka, T. (1990). *Tetrahedron* 46: 5931–5942.

**31** (a) Norikane, Y., Kitamoto, K., and Tamaoki, N. (2002). *Org. Lett.* 4: 3907–3910. (b) Norikane, Y., Kitamoto, K., and Tamaoki, N. (2003). *J. Org. Chem.* 68: 8291–8304.

**32** Norikane, Y., Katoh, R., and Tamaoki, N. (2008). *Chem. Commun.* 1898–1900.

**33** Heindl, A.H., Schweighauser, L., Logemann, C., and Wegner, H. (2017). *Synthesis* 49: 2632–2639.

**34** Slavov, C., Yang, C., Heindl, A.H. et al. (2018). *J. Phys. Chem. Lett.* 9: 4776–4781.

**35** Müri, M., Schuermann, K.C., de Cola, L., and Mayor, M. (2009). *Eur. J. Org. Chem* 2562–2575.

**36** Heindl, A.H., Becker, J., and Wegner, H.A. (2019). *Chem. Sci.* 10: 7418–7425.

**37** Hilpert, H., Hoesch, L., and Dreiding, A.S. (1985). *Helv. Chim. Acta* 68: 325–333.

**38** Reuter, R., Hostettler, N., Neuburger, M., and Wegner, H.A. (2009). *Eur. J. Org. Chem.* 5647–5652.

**39** Slavov, C., Yang, C., Schweighauser, L. et al. (2017). *ChemPhysChem* 18: 2137–2141.

**40** Reuter, R. and Wegner, H.A. (2011). *Chem. Eur. J.* 17: 2987–2995.

**41** Reuter, R. and Wegner, H.A. (2011). *Org. Lett.* 13: 5908–5911.

**42** Schweighauser, L. and Wegner, H.A. (2013). *Chem. Commun.* 49: 4397–4399.

**43** Schweighauser, L., Häussinger, D., Neuburger, M., and Wegner, H.A. (2014). *Org. Biomol. Chem.* 12: 3371–3379.

**44** (a) Mrozek, T., Daub, J., and Görner, H. (1999). *Chem. Commun.* 1487–1488. (b) Mrozek, T., Görner, H., and Daub, J. (2001). *Chem. Eur. J.* 7: 1028–1040.

**45** (a) Andréasson, J., Pischel, U., Straight, S.D. et al. (2011). *J. Am. Chem. Soc.* 133: 11641–11648. (b) Andréasson, J., Straight, S.D., Moore, T.A. et al. (2008). *J. Am. Chem. Soc.* 130: 11122–11128.

**46** (a) Santiago, A. and Becker, R.S. (1968). *J. Am. Chem. Soc.* 90: 3654–3658. (b) Yokoyama, Y. (2000). *Chem. Rev.* 100: 1717–1740.

**47** Li, M., Yang, S., Liang, W. et al. (2019). *Dyes Pigm.* 166: 239–244.


# 22 Photoinduced Reversible Solid-to-Liquid Transitions of Photochromic Materials

Chengwei Liu, Shaodong Sun, and Si Wu

## Photoisomerization

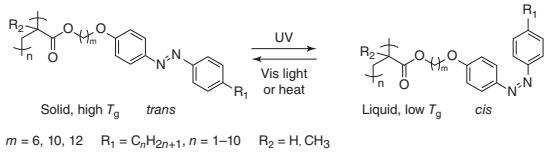


## Characteristic Features

Photoinduced reversible solid-to-liquid transitions, photoswitchable glass transition temperature ($T_g$), applications in switchable adhesives and healable coatings

## Synthetic Methods

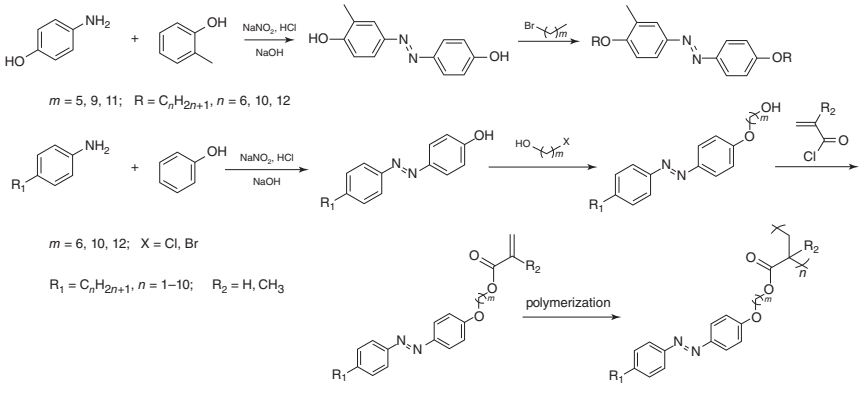


## First Reported

Akiyama, H.; Yoshida, M., Photochemically Reversible Liquefaction and Solidification of Single Compounds Based on a Sugar Alcohol Scaffold with Multi Azo-Arms. *Adv. Mater*. **2012,** *24*, 2353-2356.

## Key References

Norikane, Y., Uchida, E., Tanaka, S. et al. Photoinduced Crystal-to-Liquid Phase Transitions of Azobenzene Derivatives and Their Application in Photolithography Processes through a Solid–Liquid Patterning. *Org. Lett*. **2014,** *16*, 5012-5015.

Zhou, H., Xue, C., Weis, P. et al. Photoswitching of glass transition temperatures of azobenzene-containing polymers induces reversible solid-to-liquid transitions. *Nat. Chem*. **2017**, *9*, 145-151.

# 22

# Photoinduced Reversible Solid-to-Liquid Transitions of Photochromic Materials

*Chengwei Liu, Shaodong Sun, and Si Wu**

*CAS Key Laboratory of Soft Matter Chemistry, Department of Polymer Science and Engineering, University of Science and Technology of China, 96 Jinzhai Road, Hefei 230026, China*

## 22.1 Introduction

Reversible solid–liquid transitions such as ice–water transition, which are induced thermally, are a common phenomenon. In contrast, reversible switching chemical structures using chemical reactions may change melting points ($T_m$*s*) or glass transition temperatures ($T_g$*s*), which may also result in reversible solid-to-liquid transitions.

Isomerization is a chemical process by which a compound is transformed into any of its isomeric forms, i.e. forms with the same chemical composition but with a different structure or configuration [1]. Consequently, isomers in different forms possess different physical properties. For instance, oleic acid in *cis* form is liquid and its melting point is at 12.82 °C, while elaidic acid in *trans* form is solid and its melting point is at 43.35 °C. [2]. Usually, they cannot interconvert into each other under mild conditions [3]; otherwise, reversible solid-to-liquid transitions can occur.

Azobenzene is a photochromic compound that shows reversible photoisomerization [4]. UV light induces *trans*-to-*cis* isomerization, while visible light or heat induces *cis*-to-*trans* isomerization. It is well known that $T_m$*s* or $T_g$*s* are generally affected by chemical structures. So, *cis-trans* photoisomerization of azobenzene results in drastic changes of molecular shape, which may induce reversible solid-to-liquid transitions. Recently, a few groups, including our group, developed some novel azobenzene compounds that exhibit photoinduced reversible solid-to-liquid transitions [5–8]. Here, we discuss materials that present photoinduced reversible solid-to-liquid transitions and introduce their potential applications in solar thermal fuels [9], gas separation [10], healable coatings [11], transfer printing [11], switchable adhesives [12], lithography [13], and actuators [14].

*Senior author of this chapter

*Molecular Photoswitches: Chemistry, Properties, and Applications*,
First Edition. Edited by Zbigniew L. Pianowski.


## 22.2 Melting Points of Azobenzene Small Molecules in *Trans* and *Cis* Form

The temperature at which a substance transforms from solid to liquid is defined as the melting point $T_m$. $T_m$s of crystalline azobenzene compounds in *trans* and *cis* configurations are different. We summarized $T_m$s of *trans* and *cis* azobenzene compounds to get some hints on how to design azobenzene compounds for photoinduced reversible solid-to-liquid transitions [7]. We found that $T_m$s of *cis* azobenzene compounds are rarely reported. The possible reasons are: (i) *Cis* azobenzene compounds are generally produced by exposing their *trans* isomers to UV light. However, half-lives of many cis azobenzene compounds are too short for isolating them from trans/cis mixtures. (ii) *Trans* azobenzene compounds are in thermodynamically stable state, while *cis* azobenzene compounds are in thermodynamically metastable state. Heat-induced *cis*-to-*trans* isomerization may occur when $T_m$s of *cis* azobenzene compounds are measured.

Samples with 100% *cis* azobenzene isomers are difficult to obtain. The ratio of *cis* and *trans* isomers affects $T_m$ of their mixtures. When Hartley discovered *cis* azobenzene and measured its $T_m$ in 1937, he observed that consecutive measurements on *cis* azobenzene initially gave lower and lower $T_m$ value, then passing through a minimum at about 35 °C, and finally rising to 68 °C [4a]. This is mainly because a proportion of *cis* azobenzene was converted back to *trans* azobenzene thermally during the measurement. Consequently, what he determined were $T_m$s of mixtures of *trans* and *cis* isomers. To understand this phenomenon, Galashin et al. and Eligehausen et al. measured $T_m$s of *trans* and *cis* azobenzenes and their mixtures with different ratios [15]. Galashin et al. reported that the azobenzene mixtures showed a eutectic temperature of 40 °C at $X_{trans}$ (proportion of *trans* isomer) = 0.4 [15b]. Eligehausen et al. found that the azobenzene mixtures possessed two eutectic temperatures at 36.7 and 41.4 °C, respectively [15a]. Though the eutectic temperatures measured by different groups are slightly different, these results indicate that $T_m$s of *trans*/*cis* azobenzene mixtures are lower than pure *trans* or *cis* azobenzene. So, as long as ambient temperature is higher than the eutectic temperature, it is feasible to realize photoinduced solid-to-liquid transition even though $T_m$s of both *trans* and *cis* azobenzene compounds are above room temperature.

## 22.3 Photoinduced Reversible Solid-to-Liquid Transitions of Azobenzene Small Molecules

We introduce azobenzene small molecules that exhibit photoinduced reversible solid-to-liquid transitions in this section. It was well known that certain *trans* azobenzene compounds are solid and their *cis* isomers are oil already several decades ago. However, photoinduced solid-to-liquid transition was not developed. It is probably because azobenzene small molecules are prone to crystallize and

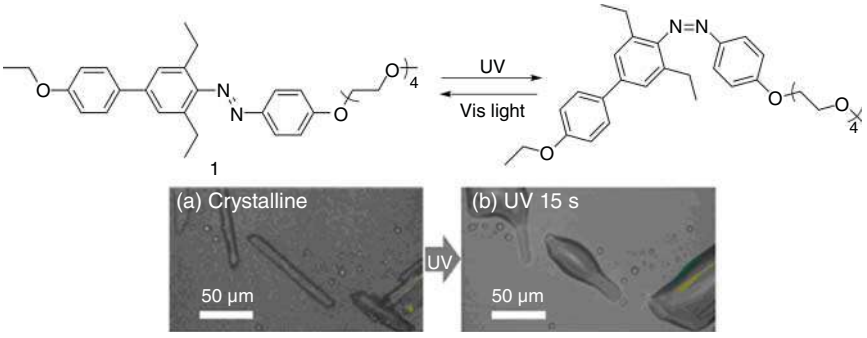


**Figure 22.1** (Upper panel) Chemical structure and reversible photoisomerization of **1**. (Lower panel) Optical microscopy (OM) images of liquefaction of **1** caused by UV light. (a) Before and (b) after irradiation with UV light at room temperature. Source: Adapted from Okui and Han [17].

the crystal packing prevents photoisomerization of azobenzene molecules in crystals [16]. Photoisomerization at the surface of crystalline samples is possible, but isomerization in such a thin layer might be ignored by researchers.

In 2012, Okui and Han observed photomelting of azobenzene compound **1** using optical microscopy (OM) (Figure 22.1) [17]. They interpreted that the low-phase transition temperature from crystalline to isotropic state was caused by weaker intermolecular π–π stacking interactions between *trans* **1** due to the distorted *ortho*-alkylated azobenzene group [17]. The authors did not delve further into this phenomenon.

In 2012, reversible photochemical liquefaction and solidification of sugar alcohol derivatives with multi azo-arms was reported by Akiyama and Yoshida [12a]. Then, they systematically investigated a series of sugar alcohols with multi azo-arms (Figure 22.2a,b) [12a, b, d]. For compounds **2** and **3**, there was no color or shape change under UV irradiation, suggesting that the crystalline solids did not exhibit photoisomerization due to lack of free volumes. Compounds **4** and **5** showed a change in color from yellow to orange while retaining solid after irradiation with UV light, indicating *trans*-to-*cis* photoisomerization took place in **4** and **5** and both *trans* and *cis* isomers were solid. Photoinduced reversible solid-to-liquid transitions could also take place in the compounds **6–12**. They summarized that the following features indicate that reversible photochemical liquefaction and solidification can occur in their azobenzene derivatives: (i) The molecular weights probably critical for differentiating between liquid and solid at ambient temperature are in the range of a few thousand Daltons; (ii) the azo-arms at each carbon in the sugar alcohol main chain are jammed in a molecular center, likely to cause more disordered crystal structure; and (iii) a homogeneous molecular structure with no polydispersity facilitates sharp transition to the single molecule [12a].

In addition, they exhibited the application of their azobenzene molecules as photo-controllable reworkable adhesives (Figure 22.2c,d). The adhesion strength of azobenzene compounds weakened sharply after irradiation with UV light and recovered after subsequent visible light irradiation.

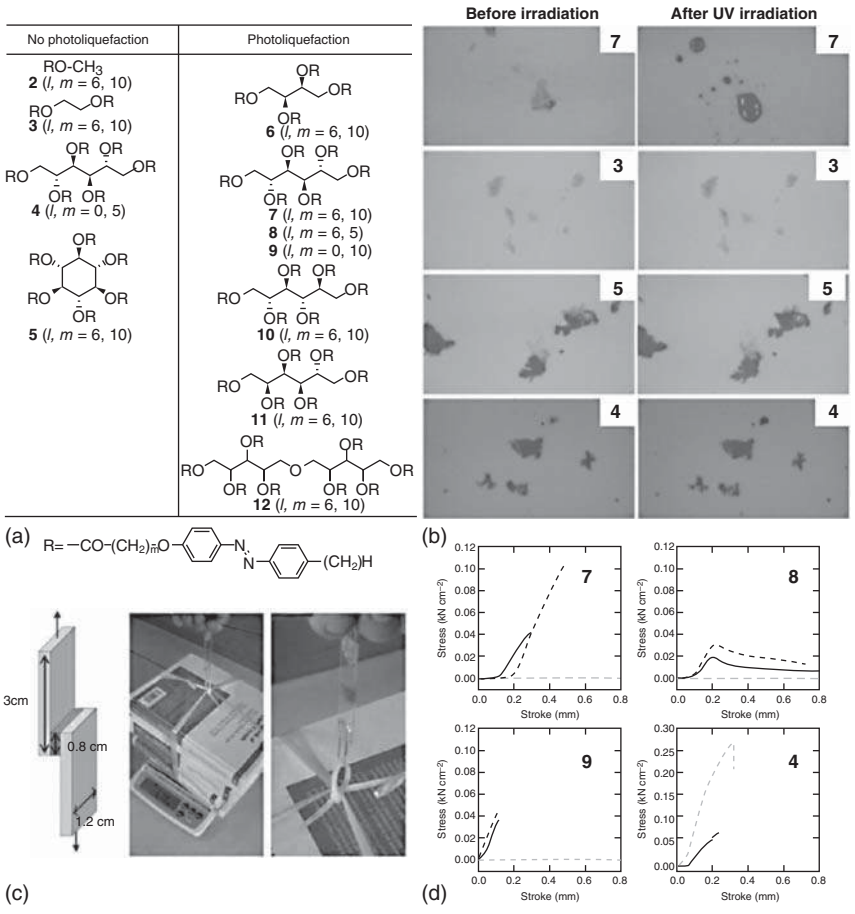


**Figure 22.2** (a) Chemical structures of compounds **2–12**. (b) Appearances of **3, 4, 5**, and **7** before irradiation (left) and after irradiation (right) with 365 nm UV light (40 mW $cm^{-2}$, one hour). Size: $1.3 \times 0.72$ $mm^2$. (c) The use of **7** as an adhesive. (d) Stress–strain curves of **4**, **7**, **8**, and **9** before (solid line) irradiation and after (gray dashed line) 365 nm UV light irradiation and subsequent 525 nm light irradiation (dashed line). Source: Panels (a), (b), and (d) are adapted from Akiyama et al. [12b]. Copyright 2014 American Chemical Society. Panel (c) is adapted from Akiyama and Yoshida [12a]. Copyright 2012 Wiley-VCH Verlag GmbH & Co. KGaA, Weinheim.

The above-mentioned azobenzene compounds have complicated multi-arm structures. It is highly desirable to design azobenzene compounds with simple structures, which still exhibit photoinduced reversible solid-to-liquid transitions. Norikane et al. reported some simple azobenzene compounds that presented photoinduced solid-to-liquid transition in 2014 (Figure 22.3a–c) [13]. Upon UV irradiation, compounds **13**, **14**, **18**, and **19** retained solid and compounds **15**–**17** were converted to liquids. $T_m$*s* of the *cis* isomers decreased extremely because the methyl group in **15**–**17** could destroy the tight packing of the crystal structures. The use of a methyl group to break the packing symmetry illustrates a simple and valuable

strategy for developing azobenzene compounds with photoinduced solid-to-liquid transition. An environment-friendly photoresist prepared from compound **17** was used for photolithography (Figure 22.3d). A solid/liquid pattern of **17** on a copper substrate was obtained through masked UV irradiation. Liquefied **17** was washed off using propanol. Then, the bare copper substrate was subjected to an aqueous solution of $FeCl_3$ to realize selective etching. Afterwards the unexposed **17**, which lay on the unetched copper substrate, was removed by rinsing with water and acetone.

The study of photoinduced reversible solid-to-liquid transitions of compounds **13**–**19** indicated that the photoinduced phase transition behavior could be significantly changed by introducing a methyl group on a rod-shaped azobenzene molecule [13]. Inspired by this strategy, a series of rod-shaped azobenzene compounds **20-n** containing a methyl group at 3-position and alkoxy groups with various chain lengths ($n$ = 1–18) at 4- and 4′-positions were synthesized by Norikane and coworkers (Figure 22.3a) [18]. The authors investigated how alkyl chain length influenced photoinduced solid-to-liquid transition (Figure 22.3e). Relatively fast photoinduced solid-to-liquid transition occurred in the compounds with medium alkyl chain length ($n$ = 6–10) (Figure 22.3f).

Using the above-mentioned strategy, Yu reported an azobenzene small molecule **21** possessing an ethyl group at 3-position in 2018. Compound **21** showed photoinduced solid-to-liquid transition (Figure 22.3g) [19]. A photo-actuator was prepared by annealing **21** on a rubbed low-density polyethylene (LDPE). The photo-actuator bent to the azobenzene layer and performed diverse deformations upon UV irradiation (Figure 22.3h). The authors attributed this phenomenon to synergistic interactions generated by photoinduced asymmetric contraction stress [19]. Interestingly, the photo-actuator could grasp objects (prey) upon UV irradiation, just like the way of pythons' predation (Figure 22.3i–l).

There are some other azobenzene small molecules with different chemical structures, which show photoinduced reversible solid-to-liquid transitions (Figure 22.4). These compounds include macrocyclic compound **22** [20–22], rod-shaped azobenzene derivatives **23**–**27** [23–27], tetra (azobenzene)methane compounds **28**–**30** [10], and cationic azobenzene derivatives **31(n,m)-X** [9]. These compounds have potential applications in solar–thermal fuels, gas separation, and lithography.

## 22.4 Photoinduced Reversible Solid-to-Liquid Transitions of Polymers Based on Photoswitchable Glass Transition Temperatures

As described in the introduction, isomerization has enormous influences on properties of the substance. In particular, *trans* and *cis* configurations do not only influence properties of small molecules, but also influence properties of polymers. There are many examples of *trans* and *cis* configurations on polymer backbone influences transitions and mechanical properties of polymers in textbook. How do *trans* and *cis*

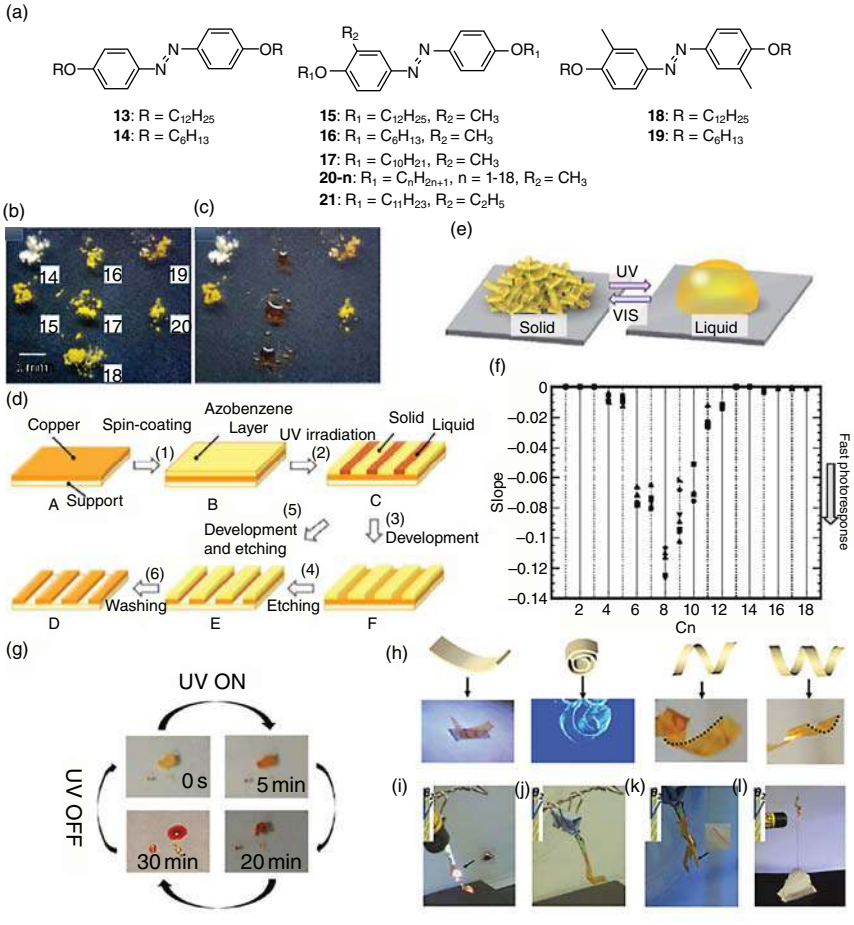


**Figure 22.3** (a) Chemical structures of compounds **13–21** and images of these compounds (b) before and (c) after irradiation with 365 nm UV light (100 mW cm$^{-2}$, 30 minutes). (d) Photolithographic process using **17**. (e) Schematic diagram of photoinduced reversible solid-to-liquid transitions of **20-n**. (f) Relative photoresponse of **20-n**. (g) Reversible photoinduced solid-to-liquid transitions of **21** upon irradiation with UV at 30 mW cm$^{-2}$. (h) Photo-actuators fabricated using **21** carried out on various deformations, which ranged from arc (UV light at 30 mW cm$^{-2}$, size: 15 mm × 6 mm × 25 mm), and coil (UV light >100 mW cm$^{-2}$, size: 15 mm × 3 mm × 25 mm) to left-handed or right-handed helices (UV light >100 mW cm$^{-2}$, size: 20 mm × 3 mm × 25 mm). (i–l) The use of actuators to mimic the prey of pythons. (i, j) The photo-actuator caught a sheet of metal under UV irradiation and subsequently let it out after moving away the light source. (k) The photo-actuator captured and released a wood stick. (l) The photo-actuator mimicked the python perching on a tree by twisting around one slender rod. (The left-handed helix film with $\theta_2 = 30°$. Size: 20 mm × 3 mm × 25 mm, UV light >100 mW cm$^{-2}$.) Source: Panels (a)–(d) are adapted from Norikane et al. [13]. Copyright 2014 American Chemical Society. Panels (e) and (f) are adapted from Norikane et al. [18]. Copyright 2016 SPST. Panels (g)–(l) are adapted from Hu et al. [19] with permission from The Royal Society of Chemistry 2018.

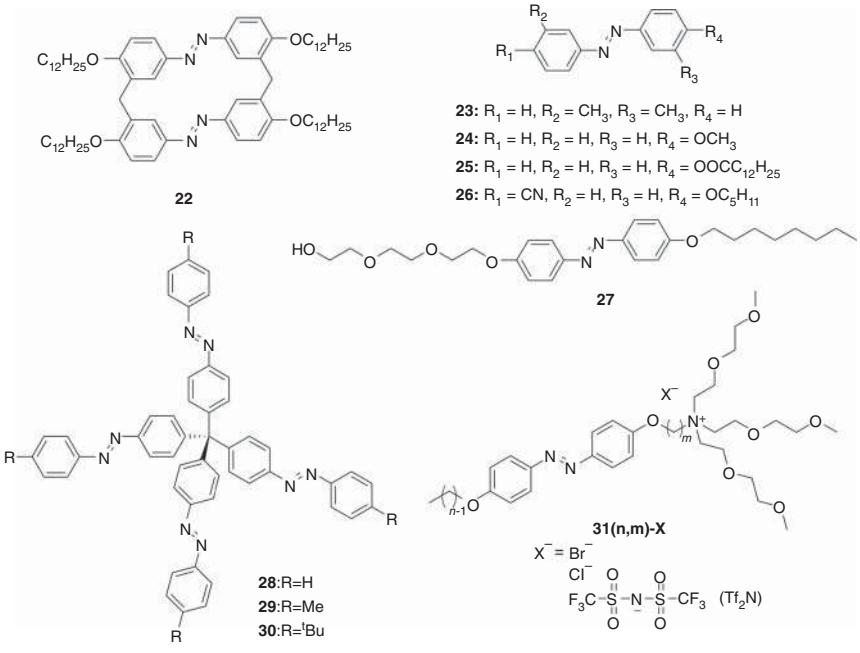


**Figure 22.4** Chemical structures of compounds **22–31(n,m)-X**.

configurations on polymer side chains affect polymer properties was not clear. So, we introduced *trans* and *cis* configurations into polymer side chains.

Our group synthesized two methacrylate polymers **32** with *cis* double bonds and *trans* double bonds in the polymer side chain, respectively (Figure 22.5a) [28]. We obtained optimized monomer configurations of *cis* **I** and *trans* **I** by DFT calculations (Figure 22.5b), which indicated the angle resulting from parts of the side group unfolded to the left and to the right of the double bond caused a weaker ability of packing for polymers with the *cis* form in their side group [28]. Then, we demonstrated the segmental dynamics could be affected by this structural characteristic. *Trans* I displayed three different processes ($\alpha_1$, $\alpha_2$, and $\beta$), in which $\alpha_1$ and $\alpha_2$ showed Vogel–Fulcher–Tammann (VFT) T-dependence and $\beta$ represented Arrhenius T-dependence. In contrast, *cis* I contained three processes ($\alpha_1$, $\alpha_2$, and $\alpha_3$) all with a VFT T-dependence (Figure 22.5c,d). Combined with analysis of temperature-modulated differential scanning calorimetry (TM-DSC), we found that the synthesized polymers **32** showed a difference in transition temperatures between the two conformers. Furthermore, the *cis* polymer **32** was an amorphous polymer with two glass transitions at −86 and −26 °C. The *trans* polymer **32** was a semicrystalline polymer with a $T_g$ at −40 °C and a $T_m$ at −15 °C (Figure 22.5e,f). We also demonstrated that the effects of *trans* and *cis* configurations on $T_g$ exist in a wide range of molecular weights (Figure 22.5g).

The above-mentioned results show that *trans* and *cis* configurations can affect the $T_g$ and $T_m$ of polymers. So, photoinduced reversible solid-to-liquid transitions

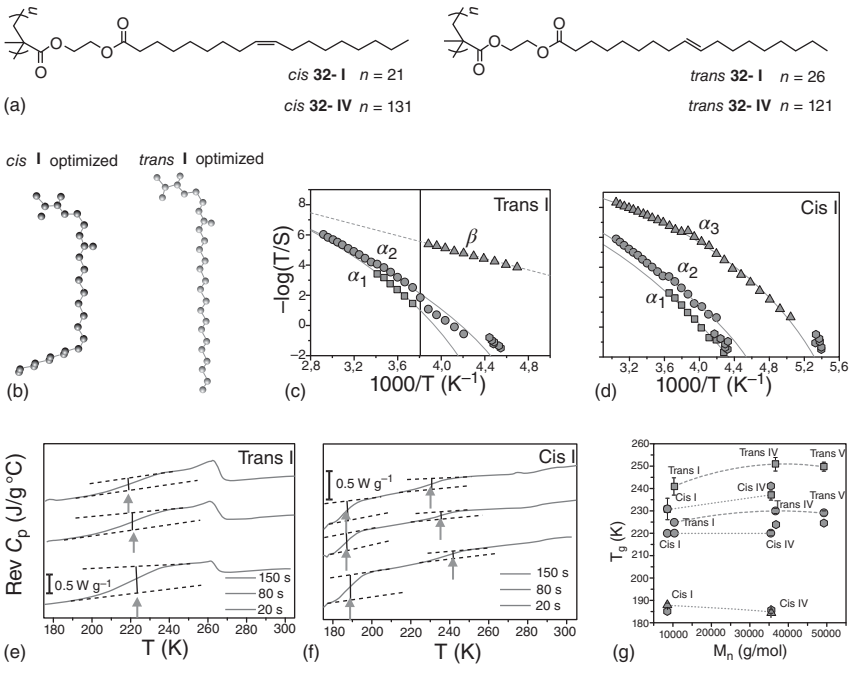


**Figure 22.5** (a) Chemical structures of *cis* **32** and *trans* **32**. (b) Optimized monomer configurations of *cis* **32-I** and *trans* **32-I**. Activation diagram of the different processes in (c) *trans* **32-I** and (d) *cis* **32-I**. The dashed and solid lines stand for the fitting of the Arrhenius equation and Vogel–Fulcher–Tammann (VFT), respectively. The vertical line in (c) shows the $T_m$ of *trans* **32-I**. The different periods of modulation indicate heat capacity of *trans* **32-I** (e) and *cis* **32-I** (f) is reversed. Vertical arrows in (e) and (f) indicate respective $T_g$*s*. (g) The relation of $T_g$ obtained from DSC (polygons) and DS with molecular weight.
Source: Adapted from Ref. [28]. Copyright 2018 American Chemical Society.

of azobenzene-containing polymers (azopolymers) can be achieved by rational designs. Meanwhile, we suppose that photoinduced reversible solid-to-liquid transitions are more likely to occur in polymers than in small molecules. Different from small molecules that easily crystallize, polymers generally crystallize partly or are even completely amorphous. Thus, the amorphous structures provide azopolymers with enough free volume for photoisomerization in solid. Solid-to-liquid transition could happen in polymers. Next, we will discuss general design principles and applications of azopolymers with photoinduced solid-to-liquid transitions.

Recently, our group reported photoinduced reversible solid-to-liquid transitions of azopolymers based on photoswitching of glass transition temperatures ($T_g$*s*) (Figure 22.6a,b) [11]. The *trans* azopolymer **33** is a solid with $T_g$ of 48 °C, while *cis* **33** is a liquid with $T_g$ of −10 °C. Alternate UV and visible light irradiation on **33**, **34**, and **35** induced reversible *cis–trans* isomerization photoinduced reversible solid-to-liquid transitions. Our recent studies indicated that only azopolymers with suitable substituent, spacer, and chain architecture show photoinduced reversible solid-to-liquid transitions.

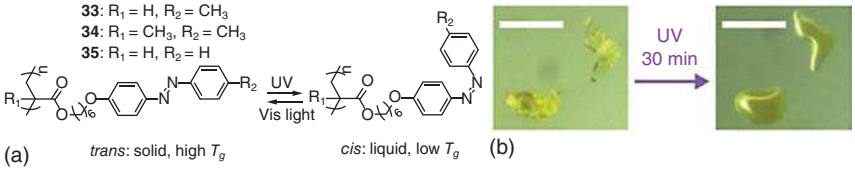
33: R1 = H, R2 = CH3
34: R1 = CH3, R2 = CH3
35: R1 = H, R2 = H
UV
Vis light
UV
30 min
(a)
trans: solid, high Tg
cis: liquid, low Tg
(b)

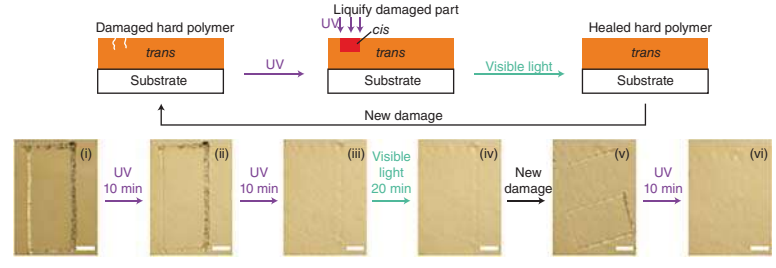
Damaged hard polymer
Liquify damaged part
Healed hard polymer
trans
cis
Substrate
UV
Visible light
New damage
(i)
(ii)
(iii)
(iv)
(v)
(vi)
UV 10 min
UV 10 min
Visible light 20 min
New damage
UV 10 min
(c)

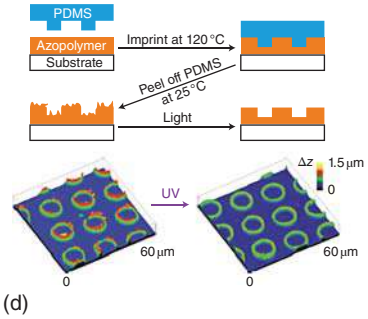
PDMS
Azopolymer
Substrate
Imprint at 120 °C
Peel off PDMS at 25 °C
Light
UV
Δz
1.5 μm
0
60 μm
60 μm
0
0
(d)

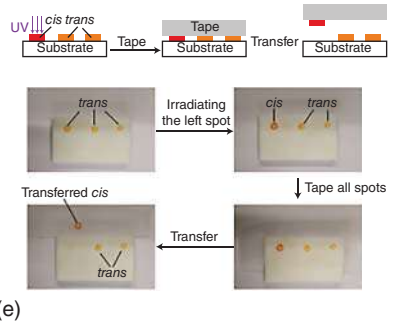
UV
cis trans
Substrate
Tape
Tape
Substrate
Transfer
Substrate
trans
Irradiating the left spot
cis
trans
Transferred cis
Tape all spots
Transfer
trans
(e)

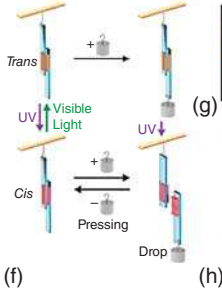
Trans
UV
Visible Light
Cis
UV
Pressing
Drop
(f)

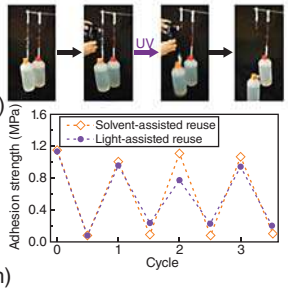
UV
(g)
Adhesion strength (MPa)
Solvent-assisted reuse
Light-assisted reuse
Cycle
(h)

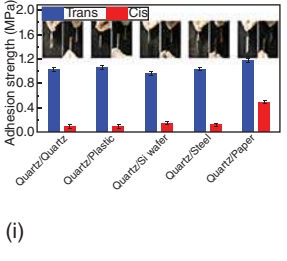
Trans
Cis
Adhesion strength (MPa)
Quartz/Quartz
Quartz/Plastic
Quartz/Si wafer
Quartz/Steel
Quartz/Paper
(i)

**Figure 22.6** (a) Chemical structures and reversible photoisomerization of azopolymers **33**, **34**, and **35**. The *trans* form of these polymers with $T_g$*s* higher than room temperature is in solid state, whereas the *cis* form with $T_g$*s* lower than room temperature is in liquid state. (b) OM images of **33** before irradiation and after irradiation with 365 nm UV light at 67 mW cm$^{-2}$. The scale bars represent 20 μm. (c) Using light to heal scratches on **33**. Schematic diagram (top) of the healing process. OM images (bottom) exhibiting repeated healing of **33** by alternating 365 nm UV light at 67 mW cm$^{-2}$ and 530 nm visible light at 5 mW cm$^{-2}$. (d) Photoinduced reduction of surface roughness. Schematic diagram (top) of this process. Confocal microscopy images (bottom) of patterned P1 before and after 365 nm UV light irradiation at 20 mW cm$^{-2}$ for 30 minutes. (e) Schematic diagram (top) and images (bottom) of transfer printing supported by photoinduced solid-to-liquid transition. Using 365 nm UV light at 67 mW cm$^{-2}$ irradiated spot on the left side for 20 minutes. (f) Schematic illustration of the application of **33** as photoswitchable adhesive. (g) Snapshots present the adhesion strength controlled by UV light. *Trans* **33**-glued quartz substrates on the left could sustain a bottle of water weighing about 500 g. After irradiation with UV light, the bottle quickly dropped. A control experiment on the right indicating that the **33**-glued substrates without UV irradiation can hold the bottle of water. (h) The reusing of the adhesive assisted by light and solvent. (i) Photoswitchable adhesion of different **33**-glued substrates. The insets are images of various substrates adhered with *trans* **33** and separated after UV irradiation. Source: Panels (a)–(e) are adapted from Zhou et al. [11]. Copyright 2016 Springer Nature. Panels (f)–(i) are adapted from Zhou et al. [29]. Copyright 2019 American Chemical Society.

Photoinduced reversible solid-to-liquid transitions provide an innovative strategy for designing healable polymers with high $T_g$*s* and allow the control of mechanical properties of polymers with high spatiotemporal resolution [11]. Numerous potential applications can be developed based on photoinduced reversible solid-to-liquid transitions.

First, healable coatings can be prepared using azopolymers (Figure 22.6c). The damaged coating can be repaired by liquefying the damaged area upon UV irradiation. The scratch could be filled by flow of polymer chains. Then, healing could be achieved by solidification under the following visible light irradiation. In addition, this healing process can be repeated multiple times. Different from conventional healable polymers such as polymer gels and elastomers, which are intrinsically soft due to their low $T_g$*s*, our healable azopolymers are inherently hard due to their high $T_g$*s*. It is a challenge to design healable polymers with high $T_g$ [30]. Our *trans* azopolymers are healable polymers that are hard and have $T_g$*s* higher than room temperature.

Second, light can reduce surface roughness of materials composed of azopolymers (Figure 22.6d). We fabricated microstructures using the azopolymer **33**. The microstructure became smoother after UV irradiation by eliminating harsh sharp edges due to solid-to-liquid transition.

Third, transfer printing was developed using the azopolymer **33** as ink (Figure 22.6e). On a Teflon substrate, we prepared three spots of **33**, one of which was liquefied by UV irradiation. Then, we pressed a tape on all three spots. Only the liquefied spot was transferred to the tape. Compared with commercial technique based on thermal processes, our transfer printing based on a photo process possesses higher spatiotemporal resolution.

Fourth, light-switchable adhesives have been developed using azopolymers (Figure 22.6f–i) [29]. Solid *trans* **33** exhibited insufficient chain mobility so that two substrates could be bonded tightly using *trans* **33**. Liquid *cis* **33** generated by UV irradiation possessed sufficient chain mobility. So, adhesion strength was weak for separating glued surfaces. Meanwhile, *trans* **33** can be regenerated by visible light irradiation (Figure 22.6f,g). Moreover, our adhesive was reusable and the efficiency of light-assisted reuse was comparative with solvent-assisted reuse (Figure 22.6h). We also demonstrated that our adhesive can be applied to different substrates, including quartz, plastic, wafer, steel, and paper (Figure 22.6i).

Besides our work about photoswitchable azopolymer adhesives, Akiyama et al. investigated adhesion of azopolymers **36–44** with different spacers and alkyl tails (Figure 22.7a–c) [12c]. All of these azopolymers exhibited photoinduced reversible solid-to-liquid transitions except for **36** and **37,** which have short spacers and alkyl tails. They measured the adhesion strengths of thermosetting and photosettting azopolymers before and after light irradiation. In photosetting samples, azopolymers that possess longer alkyl chains presented stronger adhesion (Figure 22.7c).

Ito et al. also reported polymethacrylate and polyacrylate azopolymers (**45** and **46**) that worked as reworkable adhesives (Figure 22.7a,d–g) [31]. Their azopolymers exhibited photoinduced reversible solid-to-liquid transitions. Upon UV irradiation, storage moduli (G′) of azopolymers decreased within one minute. Continuous exposure caused loss moduli (G″) finally surpassed storage moduli (G′), suggesting that the light transformed solids into liquids (Figure 22.7d,e). Adhesion strength decreased drastically by solid-to-liquid transition (Figure 22.7f,g). Meanwhile, the isomerization rate of **46** was faster than that of **45,** which indicated that the azo polyacrylate exhibited faster photoresponsive rate than the azo polymethacrylate.

Light cannot penetrate deeply in azopolymers nor liquefy thick azopolymer sample because of the strong absorption of azobenzene chromophore. This effect is weak when azopolymers with low contents of azobenzene moieties are used. ABA-type triblock copolymers (**47** and **48**) containing a none-azobenzene B block were synthesized by Ito et al. (Figure 22.8a) [32]. So, they have a lower content of azobenzene moieties than homopolymers. The authors demonstrated their polymers exhibited photoinduced reworkable adhesion. Firstly, the azopolymers were used to glue glass substrates. Then, debonding of azopolymer-glued glass substrates induced by UV irradiation and rebonding assisted by green light irradiation can occur (Figure 22.8b). G′ and G″ of **47** and **48** decreased rapidly in one minute upon UV irradiation (Figure 22.8c,d). After irradiation G′ values remained above G″ values, suggesting that UV irradiation softened the azopolymers. UV light did not liquefy the polymer or UV light only liquefied the surface but not the bottom layer. They also demonstrated repeatable bonding and debonding (Figure 22.8e). The adhesion strengths of photochemically bonded samples showed almost a constant value of 1.7 MPa. When exposed to UV light, it decreased quickly to 0.08 MPa.

In 2019, Braun et al. reported switching of thermal conductivity of azopolymer **49** based on photoinduced reversible solid-to-liquid transitions (Figure 22.9a) [33]. **49** was anisotropic solids. Spherulites in the film disappeared after irradiation with UV light and reappeared after irradiation with green light (Figure 22.9b). Next, the

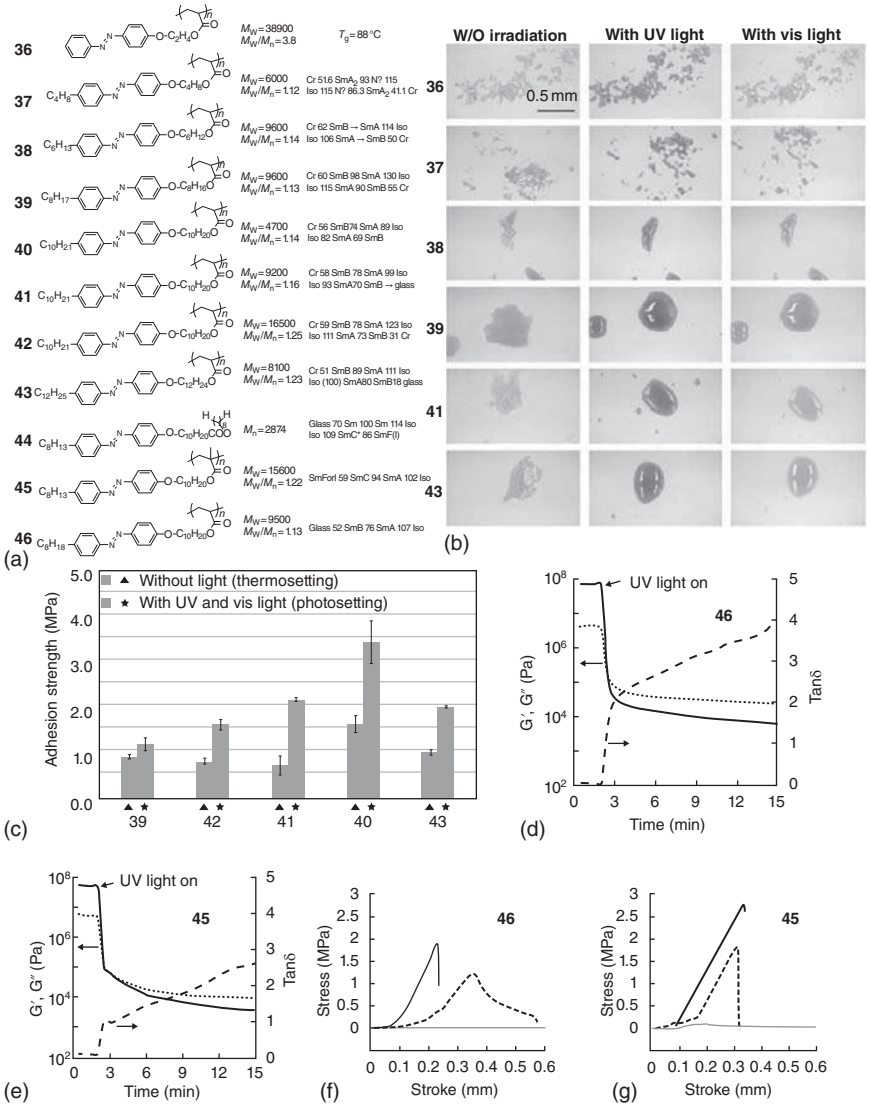


**Figure 22.7** (a) Chemical structures and physical properties of azopolymers **36**–**46**. (b) Photographs of azopolymers (left) before and (center) after irradiation with 365 nm UV light irradiation at 20 mW cm$^{-2}$ for two hours and (right) after subsequent irradiation with 520 nm visible light at 15 mW cm$^{-2}$ for 20 minutes. (c) Adhesion strengths of thermosetting and photosettting polymers **39**–**43**, respectively. Time-dependent changes of storage moduli (G′, solid line), loss moduli (G″, dotted line), and loss tangent (tan δ, dashed line) of (d) **46** and (e) **45** under 365 nm UV light irradiation at 30 °C. The UV light intensity is 100 mW cm$^{-2}$. Stress and strain curves of (f) **46** and (g) **45** for (solid line) photochemically bonded samples, (dashed line) thermally bonded samples and (gray solid line) photochemically bonded samples under irradiation with UV light for 15 seconds. Source: Panels (a)–(c) are adapted from Akiyama et al. [12c]. Copyright 2017 Taylor & Francis. Panels (d)–(g) are adapted from Ito et al. [31]. Copyright 2018 American Chemical Society.

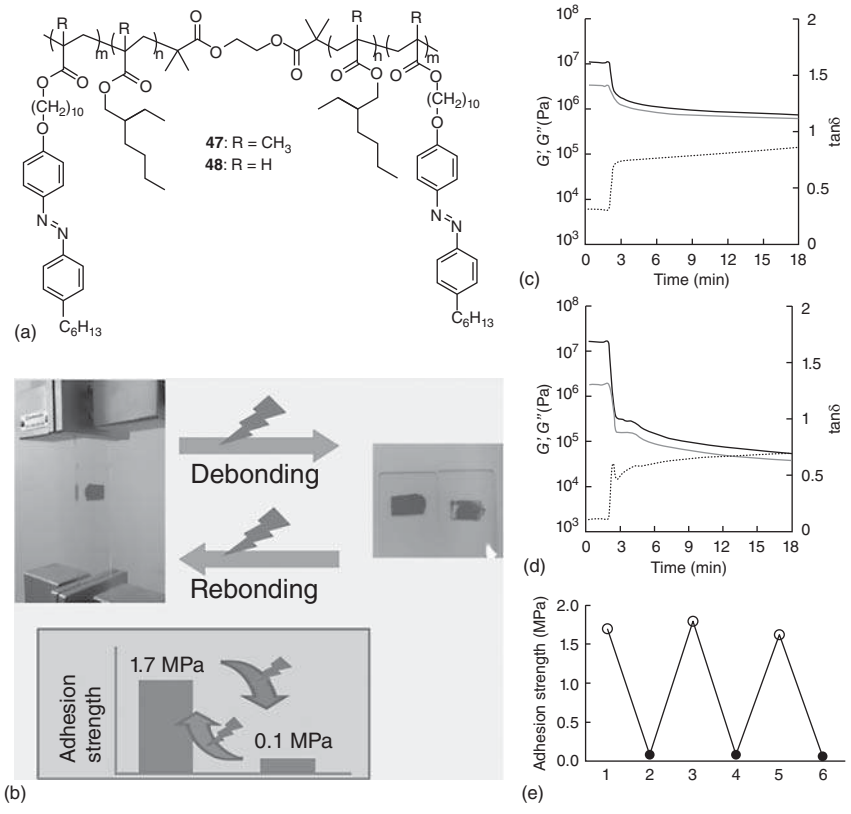


**Figure 22.8** (a) Chemical structures of ABA-type triblock copolymers **47** and **48**. (b) Light-assisted debonding and rebonding. The varieties of storage moduli (G′, solid line), loss moduli (G″, gray line), and loss tangent (tan δ, dotted line) of (c) **47** and (d) **48** under irradiation with 365 nm UV light at 100 mW $cm^{-2}$ at 30 °C. The start time of UV irradiation is two minutes. (e) Photoinduced repeatable bonding and debonding using **47**. Source: Adapted from Ito et al. [32]. Copyright 2018 American Chemical Society.

authors demonstrated the changes in thermal conductivity when the crystal changed to liquid via light irradiation (Figure 22.9c). The change of thermal conductivity was associated with the crystal-to-liquid transition of **49**. The longer lifetimes and stronger dispersion of vibrational modes resulting from the out-of-plane orientation of side chains with planar azobenzene groups caused the higher thermal conductivity of crystalline *trans* azopolymer [33]. They also demonstrated rationality of the rapid melting and crystallization within 10s.

To investigate how chemical structures affect photoinduced reversible solid-to-liquid transitions of azopolymers, our group synthesized azopolymers **50–54** (Figure 22.10a) [34]. We found that **52** and **53** presented photoinduced reversible solid-to-liquid transitions, while **50**, **51**, and **54** with a short or long spacer did not show photoinduced solid-to-liquid transitions at room temperature (Figure 22.10b). In general, spacers are used to supply sufficient flexibility for the motions of azobenzene group [35]. For **54**, the spacer was too long that

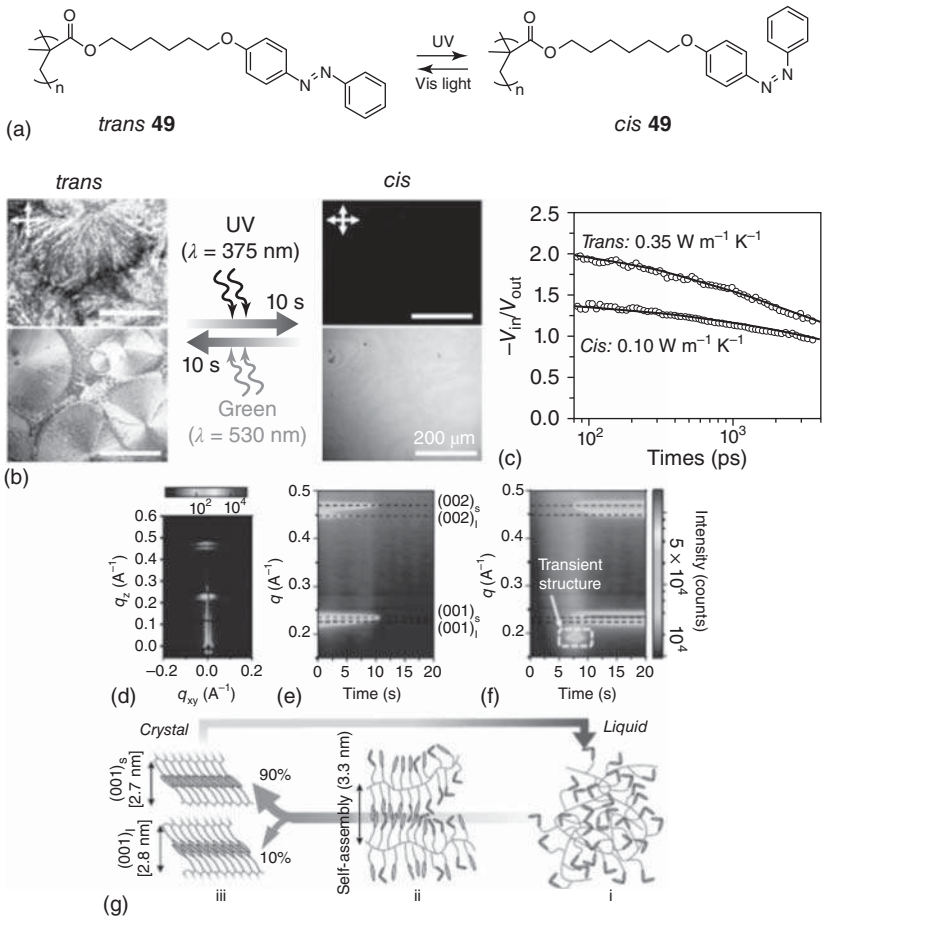


**Figure 22.9** (a) The chemical structure and photoisomerization of **49.** (b) Photographs of *trans* **49** and *cis* **49** films under polarized optical microscopy (upper) and optical microscopy under constant irradiation with UV and green light (lower). The scale bars represent 200 μm. (c) Measured and fitted time-domain thermoreflectance (TDTR) data for *trans* **49** and *cis* **49** films after irradiation with UV and green light, respectively. (d) 2D GISAXS diffraction pattern of the *trans* **49** film. Azimuth integrated in situ transmission small-angle X-ray scattering (SAXS) intensity of **49** upon (e) UV light irradiation and (f) green light irradiation. (g) Schematic indicating the crystallization pathway upon irradiation with green light (right to left). Source: Adapted from Shin et al. [33]. Copyright 2019 National Academy of Sciences.

the interactions between the spacers resulted in crystallization, which hindered photoinduced liquefaction.

Photoinduced reversible solid-to-liquid transitions were also used for photo-actuators. Usually, photo-actuators are prepared by introducing photoswitchable chromophores like azobenzene into networks of liquid crystal (LC) polymers [36]. Photo-actuators based on crosslinked networks are difficult to repair and reprocess. Very recently, our group reported the applications of entangled linear azopolymers that showed photoinduced reversible solid-to-liquid transitions

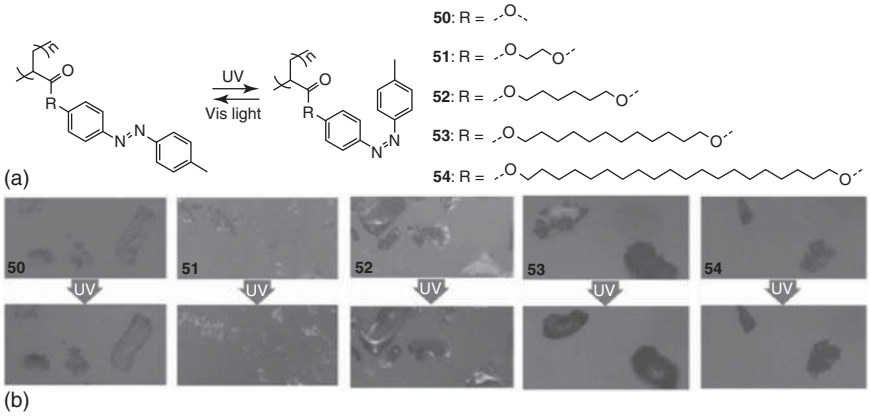


**Figure 22.10** (a) Chemical structures and reversible photoisomerization of azopolymers **50–54**. (b) OM images (260 × 130 μm) of **50–54** before and after irradiation with 365 nm UV light at 20 mW cm$^{-2}$ for eight minutes. Source: Adapted from Weis et al. [34]. Copyright 2019 Wiley-VCH Verlag GmbH & Co. KGaA, Weinheim.

as healable and reprocessable photo-actuators (Figure 22.11) [14]. Both the low-molecular-weight azopolymer **55** and high-molecular-weight azopolymer **56** exhibited photoinduced reversible solid-to-liquid transitions (Figure 22.11a,b). Entangled high-molecular-weight azopolymer **56** was better suited for fabricating photo-actuators than low-molecular-weight azopolymer **55** due to their outstanding mechanical properties and processability (Figure 22.11c). The azopolymer photo-actuators showed light-induced bending. Our azopolymer photo-actuators can be healed by locally liquefying and solidifying damaged area with UV and visible light irradiation (Figure 22.11d). Moreover, we cut azopolymer actuators into halves and welded the actuators by UV and visible light irradiation (Figure 22.11e). The welded actuator also presented light-induced bending (Figure 22.11f). We also showed a simple way to fabricate microstructured photo-actuators based on the photoresponsiveness (Figure 22.11g–j).

Yu's group also demonstrated photoinduced healing of azopolymers. They prepared light-powered bilayer photo-controllable flexible microtubes (PFMs) using copolymer polycyclooctene **57**. The ratios of biphenyl side chains and azobenzene side chains are 2 : 1, which showed photoinduced reversible solid-to-liquid transitions (Figure 22.12a) [37]. The authors demonstrated the healable property of the PFM (Figure 22.12b). **57** with *trans* azobenzene owned a $T_g$ of 57 °C, whereas *cis* **57** owned a $T_g$ of 28 °C. Meanwhile, during the healing process, the authors observed that the temperature of **57** rose to around 40 °C, indicating that the achievement of self-healing process was caused by both the photothermal effect and photoswitchable $T_g$.

Very recently, a convenient yet versatile strategy, which combined athermal nanoimprint lithography (AT-NIL) and photolithography to prepare multiple nanopatterns on flexible azopolymer **58** substrate, was reported by Yu and coworkers (Figure 22.13a) [38]. *Trans* **58** was a typical glassy plastic with $T_g$ = 76 °C

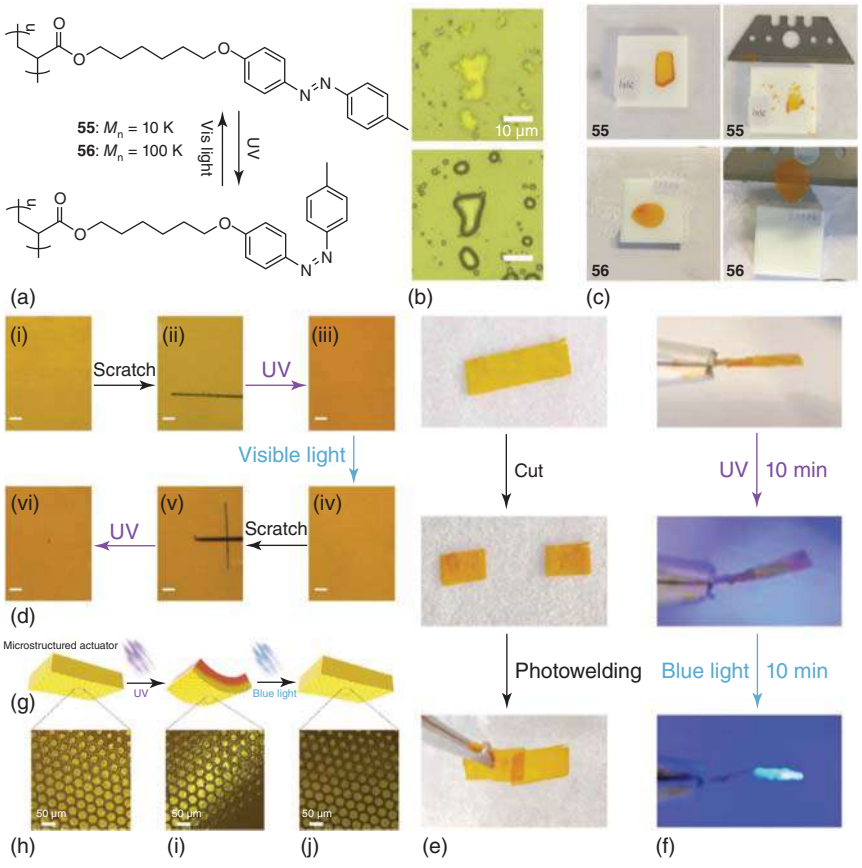


**Figure 22.11** (a) The chemical structures and reversible photoisomerization of **55** and **56**. (b) OM images of **55** and **56** before and after 365 nm UV light. (c) The azopolymer films **55** and **56** stripped from Teflon substrates. The stripping of a freestanding film of **56** was achieved straightforward, but a freestanding film of **55** did not form due to the lack of polymer chain entanglement. (d) Using light to heal scratches on a **56** film. The scale bars represent 20 μm. (e) The photowelding of two pieces of actuator. (f) The light-induced bend of the photowelded actuator under irradiation with 365 nm UV light at 51 mW $cm^{-2}$ for 10 minutes and 470 nm blue light at 9 mW $cm^{-2}$ for 10 minutes. (g) Schematic diagram of utilizing light to prepare actuator containing microstructure. OM image of the actuator containing microstructure before irradiation (h), after irradiation with UV light (i), and after following irradiation with blue light (j). Source: Adapted from Chen et al. [14]. Copyright 2019 The Authors. Published by Wiley-VCH Verlag GmbH & Co. KGaA, Weinheim.

(Figure 22.13b), while *cis* **58** exhibited $T_g$ of 3 °C, which showed obvious viscoelastic deformation (Figure 22.13c). Next, the authors demonstrated the AT-NIL process for gradually preparing multiple nanopatterns by choosing **58** as the NIL resist. The azopolymer on polyethylene terephthalate (PET) substrates was irradiated with UV light (Figure 22.13d). Then, an exterior mechanical stress was pressed with a pre-designed poly(dimethylsiloxane) (PDMS) mold onto the film. Microarrays of the molds filled with ductile azopolymer **58** by flowing (Figure 22.13e). Subsequently,

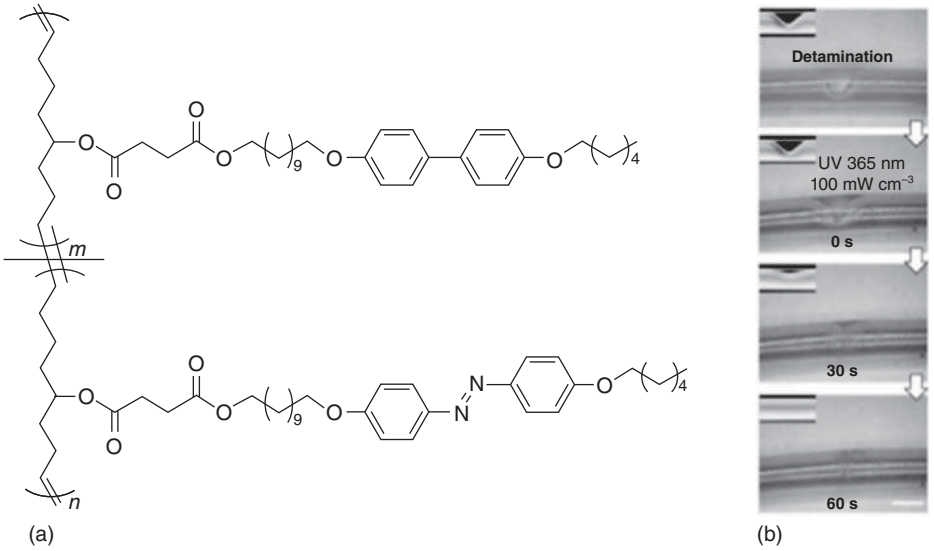


**Figure 22.12** (a) Chemical structure of **57**. (b) Light-induced self-healing of the microtube with **57** as the inner layer. The scale bar represents 500 μm. Source: Adapted from Xu et al. [37]. Copyright 2019 Wiley-VCH Verlag GmbH & Co. KGaA, Weinheim.

the negative pattern of the mold was duplicated by solidifying the azopolymer **58** with visible light (Figure 22.13f). So, with the assistance of a mask, the multiple nanopatterns with regioselectivity could be obtained by more AT-NIL iterations (Figure 22.13g–i). In addition, the thermally caused shrinkage could be avoided by such an athermal process.

Azobenzene groups in the polymers mentioned above are in polymer side chains. So far, main-chain-type azopolymers only showed photoswitchable $T_g$ but no photoinduced reversible solid-to-liquid transitions [39]. Except for main-chain and side-chain-type azopolymers, polymers with azo end groups were studied. Meijer's group reported siloxane oligomers with azobenzene termini (**60–64**) (Figure 22.14a) [40]. A waxy solid compound **60** with a $T_m$ at 46.2 °C changed to a red oil after UV irradiation, which owned a $T_m$ lower than −60 °C (Figure 22.14b,c). Crystal–isotropic–crystal transition of **60** via UV and visible light irradiation was demonstrated by the disappearance and reappearance of birefringence (Figure 22.14d–f). The nanostructure of *trans* **60** was composed of spaced crystalline azobenzene monolayers in regular arrangement of amorphous oligo(dimethylsiloxane) exfoliation (Figure 22.14g). The bent *cis* configuration probably hindered crystallization of the azobenzene and prevented phase segregation. G′ of *trans* **60** dropped to 1.5 MPa upon UV irradiation and decreased continuously until turning off the UV light. Then, G′ increased significantly and recovered the initial value upon irradiation with visible light (Figure 22.14h).

Different from polymers with covalently linked azobenzene groups, Yamamoto et al. demonstrated photoswitchable $T_g$*s* of photo-inactive poly(methyl methacrylate) (PMMA) doped with photoresponsive liquid crystal (LC) plasticizers. The

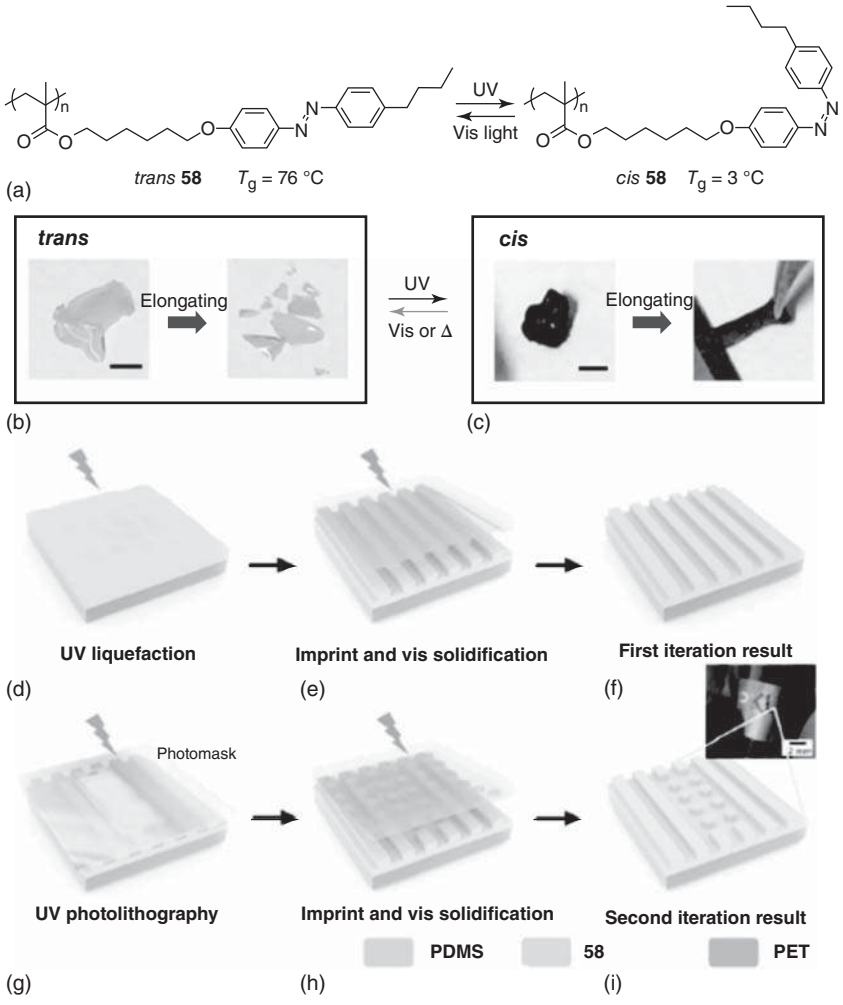


**Figure 22.13** (a) The chemical structure and reversible photoisomerization of **58.** Appearance of *trans*-rich **58** (b) and *cis*-rich **58** (c). Schematic illustration of multiple nanopatterning fabrication: The first imprint iteration contains: (d) liquefying by irradiation with UV light, (e) imprinting with predesigned PDMS and solidifying by irradiation with visible light, (f) the appearance of the first imprint iteration. The second imprint iteration contains: (g) Using a photomask to assist UV photolithography, (h) imprinting with predesigned PDMS and solidifying by irradiation with visible light, (i) the appearance of the second imprint iteration. Source: Adapted from Yang et al. [38]. Copyright 2019 Wiley-VCH Verlag GmbH & Co. KGaA, Weinheim.

plasticizers were composed of an LC compound **65** and azobenzene compound **66** (Figure 22.15a) [41]. The ratio of the plasticizer to PMMA resulted in different composites **C-30**, **C-40**, **C-50**, **C-60**, and **C-70** (Figure 22.15b). At 20 °C, all composites were glassy. **C-60** exhibited birefringence, while **C-40** did not. The phase separation of azo-doped LC in **C-60** resulted in the birefringence. Upon UV irradiation, the birefringence of **C-60** disappeared. Softening and re-hardening of **C-60** were

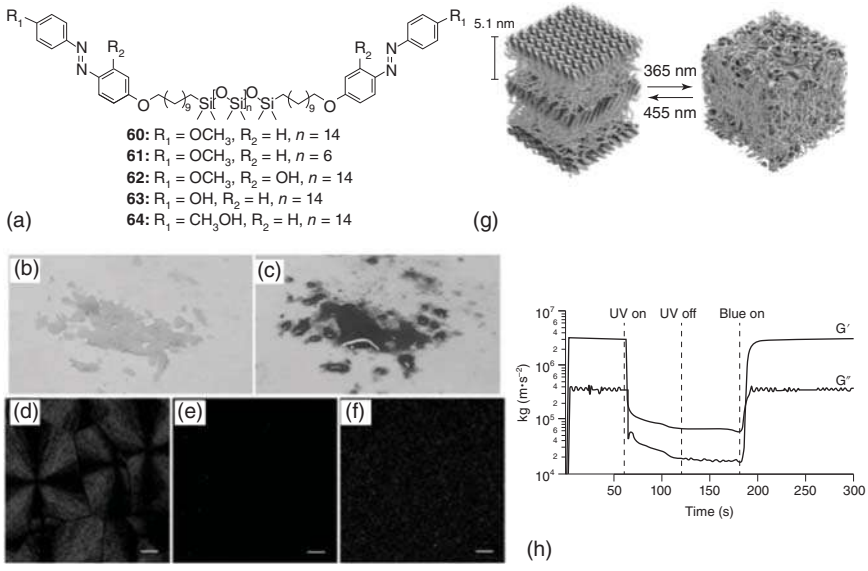


**Figure 22.14** (a) Chemical structures of siloxane oligomers with azobenzene termini **60–64**. Photographs of *Trans* **60** before (b) and after irradiation (c) with 365 nm light. POM of *trans* **60** thin films at room temperature (d), after irradiation (d) with 365 nm light and following irradiation (f) with 455 nm light. Scale bars are 50 μm. (g) Schematic diagram showing the change of morphology upon alternate irradiation with 365 nm light and 455 nm light. (h) Oscillatory shear rheology of **60**, showing decrease in moduli within five seconds during irradiation with 365 nm light. Then after irradiation with 455 nm light, moduli restored totally within 20 seconds. Source: Adapted from Zha et al. [40]. Copyright 2017 Wiley-VCH Verlag GmbH & Co. KGaA, Weinheim.

induced by alternate irradiation with UV and visible light (Figure 22.15g). The authors summarized $T_g$ values of the composites, which were measured before and after irradiation with UV light (Figure 22.15h). **C-70** exhibited the largest decrease of $T_g$, suggesting that the degree of photoplasticization was related to the ratio of LC in the composites.

## 22.5 The Mechanism of Photoinduced Reversible Solid-to-Liquid Transitions of Azopolymers

As described in Section 22.4, the critical factor for photoinduced reversible solid-to-liquid transitions of azopolymers is photoswitchable $T_g$. Why *cis*-to-*trans* photoisomerization can change $T_g$*s* of polymers? It is well known that $T_g$*s* of polymers are significantly affected by *trans* and *cis* forms [42]. The reduction of energy barrier for rotation of adjacent bond in polymers can be achieved by introducing *cis* double bonds, which can soften the chain and further reduce $T_g$ [43]. The results of the model polymers **32** with *trans* and *cis* side chains indicate that side-chain-type polymers in *trans* and *cis* forms have different $T_g$*s* because different packing of side chains has different free volumes (Figure 22.5) [28]. So, these consequences

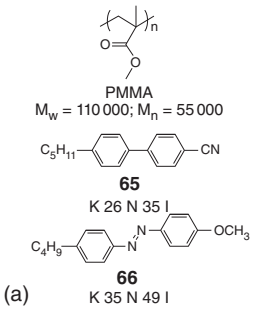


| Composites | Azo-doped LC (wt%) | PMMA (wt%) | 66 in azo-doped LC (mol%) |
|---|---|---|---|
| C-30 | 30 | 70 | 5 |
| C-40 | 40 | 60 | 5 |
| C-50 | 50 | 50 | 5 |
| C-60 | 60 | 40 | 5 |
| C-70 | 70 | 30 | 5 |

(b)

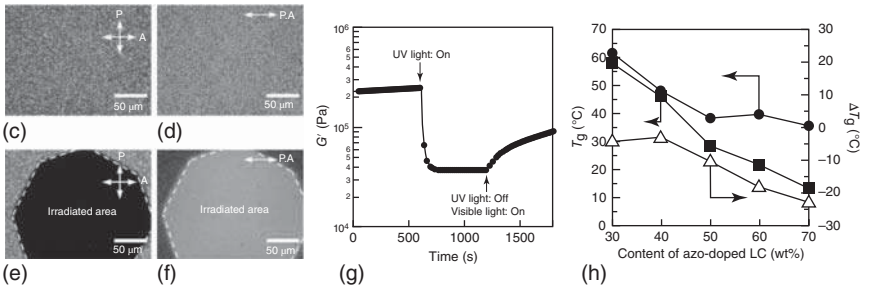


**Figure 22.15** (a) Chemical structures and corresponding physical properties of **PMMA**, **65**, **66**. (b) The chart of the composites about their nomenclature and composition. (c)–(f) POM of **C-60** film of 10 μm thickness: (c) cross-polarized mode, before 365 nm UV irradiation; (d) parallel-polarized mode, before the photoirradiation; (e) cross-polarized mode, during photoirradiation; (f) parallel-polarized mode, during photoirradiation. A and P represent analyzer and polarizer, respectively. The intensity of UV irradiation is 50 mW cm$^{-2}$. (g) Exposing **C-60** to irradiation with 365 nm UV light at 130 mW cm$^{-2}$ and 450 nm visible light at 30 mW cm$^{-2}$ to soften and re-harden at 30 °C. (h) Summarizing the change of $T_g$ of the composites: circle, $T_g$ before irradiation with UV light; square, $T_g$ during irradiation with UV light; triangle, degree of light-induced decrease in $T_g$ ($\Delta T_g$). Source: Adapted from Yamamoto et al. [41]. Copyright 2017 The Chemical Society of Japan.

can explain the photoswitchable $T_g$ of side-chain-type azopolymers. *Trans* and *cis* configurations in polymer back bone also influence $T_g$. For example, *trans* and *cis* polybutadienes have very different $T_g$s [42, 44]. *Trans* and *cis* configurations of polybutadienes disclose why main-chain-type azopolymers own switchable $T_g$ [39]. In addition, compared with conjugated *trans* isomers, the distorted *cis* isomers possess poorer intermolecular π–π stacking interactions, causing the decrease of the transition temperatures [7].

## 22.6 Comparison of Reversible Solid-to-Liquid Transitions with Directional Photofluidization

There is another phenomenon called directional photofluidization. Karageorgiev et al. and Wang et al. reported directional photofluidization of azopolymers, which was different from photoinduced reversible solid-to-liquid transitions [45, 46].

Directional photofluidization is a phenomenon where certain azopolymers can "flow" along the light polarization direction upon polarized light irradiation. Although its mechanism still is under debate, it is probably based on light-induced *trans–cis–trans* cycling [6, 47]. What we would like to emphasize is that photoinduced solid-to-liquid transitions and directional photofluidization are two phenomena. We have discussed this difference in detail in our recent reviews that the type of azobenzene groups, isomerization processes, irradiation wavelengths, and flow directions of directional photofluidization and photoinduced reversible solid-to-liquid transitions are different [6, 7].

## 22.7 Summary and Outlook

In conclusion, photoinduced reversible solid-to-liquid transitions based on photoswitching of $T_m$ or $T_g$ are introduced. The design strategies for azobenzene small molecules and polymers are also discussed. Moreover, we demonstrate potential applications of photoinduced reversible solid-to-liquid transitions. We believe that many potential applications have not been exploited. Some remaining challenges in this field include: (i) The flowability of *cis* samples should be improved for fast processing. The improvement can facilitate processing azobenzene materials in *cis* forms. (ii) UV light, as light source, may damage organic and polymeric materials and reduce their lifetimes. Reducing photodamage is important.

## Conflicts of Interest

The authors declare no conflict of interest.

## Acknowledgments

S.W. acknowledges National Natural Science Foundation of China (NSFC, No. 52120105004 and 52073268), Hefei Municipal Natural Science Foundation (No. 2021013), Fundamental Research Funds for the Central Universities (WK3450000006 and WK2060190102), and Anhui Provincial Natural Science Foundation (No. 1908085MB38) for financial support.

## References

1 IUPAC (2006). *Compendium of Chemical Terminology*, 2e. (the "Gold Book") (**1997**). Online corrected version: (**2006**–) "isomerization". doi:https://doi.org/10.1351/goldbook.I03295.
2 Knothe, G. and Dunn, R.O. (2009). J. Am. Oil Chem. Soc. 86: 843–856.

3 Litchfield, C., Lord, J.E., Isbell, A.F., and Reiser, R. (1963). J. Am. Oil Chem. Soc. 40: 553–557.
4 a) Hartley, G.S. (1937). *Nature* 140: 281–281. b) Bandara, H.M.D. and Burdette, S.C. (2012). *Chem. Soc. Rev.* 41: 1809–1825.
5 Weis, P. and Wu, S. (2018). *Macromol. Rapid Commun.* 39: 1700220.
6 Weis, P., Tian, W., and Wu, S. (2018). *Chem. Eur. J.* 24: 6494–6505.
7 Xu, W.C., Sun, S., and Wu, S. (2019). *Angew. Chem. In. Ed.* 58: 9712–9740.
8 Yamamoto, T., Norikane, Y., and Akiyama, H. (2018). *Polym. J.* 50: 551–562.
9 Ishiba, K., Morikawa, M., Chikara, C. et al. (2015). *Angew. Chem. In. Ed.* 54: 1532–1536.
10 Baroncini, M., d'Agostino, S., Bergamini, G. et al. (2015). *Nat. Chem.* 7: 634–640.
11 Zhou, H., Xue, C., Weis, P. et al. (2017). *Nat. Chem.* 9: 145–151.
12 a) Akiyama, H. and Yoshida, M. (2012). *Adv. Mater.* 24: 2353–2356. b) Akiyama, H., Kanazawa, S., Okuyama, Y. et al. (2014). *ACS Appl. Mater. Interfaces* 6: 7933–7941. c) Akiyama, H., Fukata, T., Yamashita, A. et al. (2017). *J. Adhes.* 93: 823–830. d) Akiyama, H., Kanazawa, S., Yoshida, M. et al. (2014). *Mol. Cryst. Liq. Cryst.* 604: 64–70.
13 Norikane, Y., Uchida, E., Tanaka, S. et al. (2014). *Org. Lett.* 16: 5012–5015.
14 Chen, M.S., Yao, B.J., Kappl, M. et al. (2019). *Adv. Funct. Mater.* 30: 1906752.
15 a) Eligehausen, S., Sarge, S., Öhlschläger, G. et al. (1989). *J. Therm. Anal. Calorim.* 35: 515–526. b) Galashin, A.E. and Yakovlev, V.B. (1979). *Vestn. Mosk. Univ. Ser. 2 Khim.* 20: 439–441.
16 Koshima, H. and Ojima, N. (2012). *Dyes Pigments* 92: 798–801.
17 Okui, Y. and Han, M. (2012). *Chem. Commun.* 48: 11763–11765.
18 Norikane, Y., Uchida, E., Tanaka, S. et al. (2016). *J. Photopolym. Sci. Technol.* 29: 149–157.
19 Hu, J., Li, X., Ni, Y. et al. (2018). *J. Mater. Chem. C* 6: 10815–10821.
20 Uchida, E., Sakaki, K., Nakamura, Y. et al. (2013). *Chem. Eur. J.* 19: 17391–17397.
21 Norikane, Y., Hirai, Y., and Yoshida, M. (2011). *Chem. Commun.* 47: 1770–1772.
22 Hoshino, M., Uchida, E., Norikane, Y. et al. (2014). *J. Am. Chem. Soc.* 136: 9158–9164.
23 Uchida, E., Azumi, R., and Norikane, Y. (2015). *Nat. Commun.* 6: 7310.
24 Norikane, Y., Tanaka, S., and Uchida, E. (2016). *CrystEngComm* 18: 7225–7228.
25 Han, G.G.D., Li, H., and Grossman, J.C. (2017). *Nat. Commun.* 8: 1446.
26 Hao, Y., Huang, S., Guo, Y. et al. (2019). *J. Mater. Chem. C* 7: 503–508.
27 Kim, D.-Y., Lee, S.-A., Kim, H. et al. (2015). *Chem. Commun.* 51: 11080–11083.
28 Pipertzis, A., Hess, A., Weis, P. et al. (2018). *ACS Macro Lett.* 7: 11–15.
29 Zhou, Y., Chen, M., Ban, Q. et al. (2019). *ACS Macro Lett.* 8: 968–972.
30 Yang, Y. and Urban, M.W. (2013). *Chem. Soc. Rev.* 42: 7446–7467.
31 Ito, S., Yamashita, A., Akiyama, H. et al. (2018). *Macromolecules* 51: 3243–3253.
32 Ito, S., Akiyama, H., Sekizawa, R. et al. (2018). *ACS Appl. Mater. Interfaces* 10: 32649–32658.
33 Shin, J., Sung, J., Kang, M. et al. (2019). *Proc. Natl. Acad. Sci. U.S.A.* 116: 5973–5978.
34 Weis, P., Hess, A., Kircher, G. et al. (2019). *Chem. Eur. J.* 25: 10946–10953.


**35** Menzel, H., Weichart, B., Schmidt, A. et al. (1994). *Langmuir* 10: 1926–1933.
**36** a) Yu, Y.L., Nakano, M., and Ikeda, T. (2003). *Nature*: 425. b) Lv, J.A., Liu, Y., Wei, J. et al. (2016). *Nature* 537: 179. c) Liu, Y.Y., Xu, B., Sun, S.T. et al. (2017). *Adv. Mater.* 29: 1604792.
**37** Xu, B., Zhu, C., Qin, L. et al. (2019, 2019). Small. 15: 1901847.
**38** Yang, B., Cai, F., Huang, S. et al. (2020). *Angew. Chem. In. Ed.* 59: 4035–4042.
**39** Appiah, C., Woltersdorf, G., Pérez-Camargo, R.A. et al. (2017). *Eur. Polym. J.* 97: 299–307.
**40** Zha, R.H., Vantomme, G., Berrocal, J.A. et al. (2018). *Adv. Funct. Mater.* 28: 1703952.
**41** Yamamoto, T., Hasegawa, R., Kawata, Y. et al. (2018). *Chem. Lett.* 47: 272–275.
**42** Andrews, R.J. and Grulke, E.A. (1999). *Polymer Handbook*, *4*e (Eds: J. Brandrup, E.H. Immergut and E.A. Grulke), VI 193–VI 278. New York, NY: Wiley.
**43** Ebewele, R.O. (2000). *Polymer Science and Technology CRC press*, 99. New York, NY: Boca Raton.
**44** Takeda, M., Tanaka, K., and Nagao, R. (1962). *J. Polym. Sci.* 57: 517–528.
**45** Karageorgiev, P., Neher, D., Schulz, B. et al. (2005). *Nat. Mater.* 4: 699–703.
**46** Li, Y., He, Y., Tong, X. et al. (2005). *J. Am. Chem. Soc.* 127: 2402–2403.
**47** Lee, S., Kang, H.S., and Park, J.-K. (2012). *Adv. Mater.* 24: 2069–2103.

# 23 *En Route* to Ultrafast Switchable Azo Dyes

Jaume Garcia-Amorós and Dolores Velasco

**Photochromism**

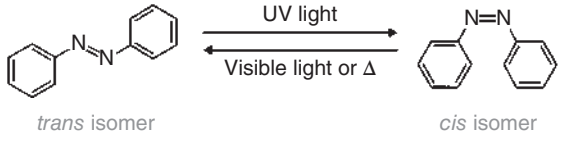


Design of novel azo derivatives with potential applicability in real-time information transmission.

**Characteristic Features**

Visible light-range photochromism, ultrafast isomerization rate in the picosecond time scale, potential applicability in real-time information transmission

**Design Schemes**

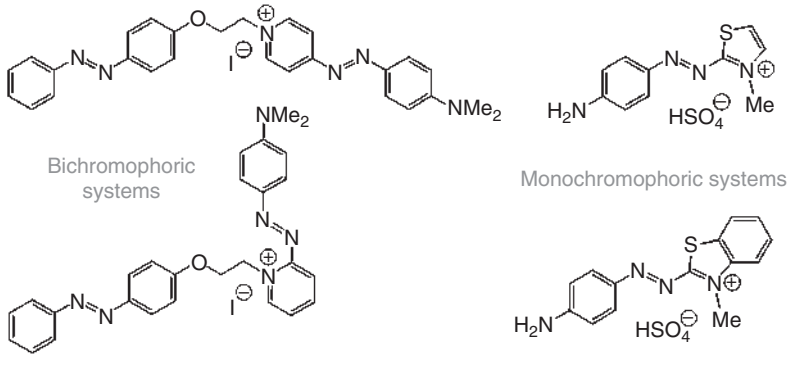


**First Reported**

Hartley, G. S. (1938). The *cis*-form of azobenzene and the velocity of the thermal *cis*→*trans*-conversion of azobenzene and some derivatives. *J. Chem. Soc*. 633–642.

**Key References**

Garcia-Amorós, J., Cuadrado, A., Reig, M., et al. (2015). Spatially close azo dyes with sub-nanosecond switching speeds and exceptional temporal resolution. *Chem. Eur. J*. 21: 14292–14296.

Garcia-Amorós, J., Maerz, B., Reig, M., et al. (2019). Picosecond switchable azo dyes. *Chem. Eur. J*. 25: 7726–7732.

# 23

# *En Route* to Ultrafast Switchable Azo Dyes

*Jaume Garcia-Amorós and Dolores Velasco*

*Universitat de Barcelona, Grup de Materials Orgànics, Institut de Nanociència i Nanotecnologia (IN$^2$UB), Departament de Química Inorgànica i Orgànica (Secció de Química Orgànica), Martí i Franquès 1, E-08028, Barcelona, Spain*

## 23.1 Light and Photoresponsive Materials

Chemical compounds exhibit a wide palette of beautiful colors depending on the range of wavelengths of the electromagnetic spectrum they absorb. They range from the well-known blue of copper(II) sulfate pentahydrate, by the green of nickel(II) chloride, to the red of Sudan Red G, a food colorant. In addition, some inorganic and organic compounds absorb light of a particular wavelength and exploit it to alter significantly their chemical structures [1, 2]. The photoinduced structural changes at the atomic, molecular, and supramolecular scale results in a complete modification of many macroscopic features of the system, such as its luminescence [3–7], electric conductivity [8–10], and hydrophilicity [11–13]. Along the years, scientists have learnt how to take advantage from such phenomena to create and envision new smart materials with remarkable abilities.

Light is a ubiquitous, cheap, and ecofriendly energy source, which permits fine-tuning the performance and functionality of biological systems and engineered materials on demand. Furthermore, light can be delivered non-invasively with high spatial definition, enabling, moreover, the in situ monitoring of the whole operation in real time. All these features have led photoresponsive materials to be the top ones among those now being researched worldwide and to play a key role in current science and technology.

Photoresponsive materials can be classified into two main groups (Figure 23.1) [14]:

- Photoswitchable non-deformable materials, i.e. small molecules or supramolecular constructs that use light to swap reversibly between two distinct states (*ON* and *OFF*) of the system. Photoswitchable materials have found application in diverse areas, ranging from information processing technology to the biomedical field [15–22].

*Molecular Photoswitches: Chemistry, Properties, and Applications*,
First Edition. Edited by Zbigniew L. Pianowski.


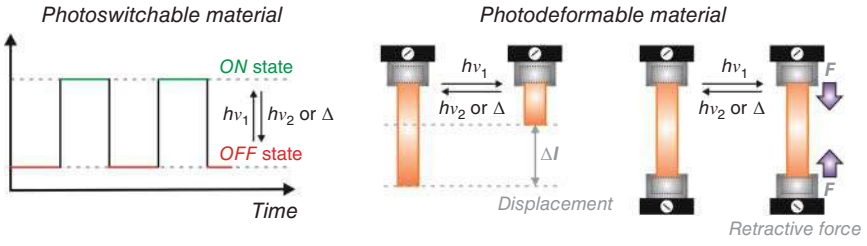


**Figure 23.1** Schematic illustration of photoswitchable and photodeformable materials. Source: Garcia-Amorós and Velasco [14].

- Photodeformable materials, i.e. materials that use light as a fuel to produce a mechanical action (displacement or force). In these materials, a dramatic change in the geometry of the chromophore occurs upon irradiation. Such feature results in a variation of the macroscopic dimensions of the material, thereby producing the displacement or force observed. Photodeformable materials have attracted great interest in robotics [23–27].

## 23.2 Photoswitchable Azo Dyes for Real-Time Information Transmission

The development of modern society demands more than ever the rapid transmission and processing of a large amount of data. As a result, current science and technology is heading to the miniaturization of switchable components all the way down to the molecular level. In this context, molecular (and supramolecular) chromophores, i.e. light-sensitive systems that change their color or absorbance when they are illuminated with light of the appropriate wavelength, emerge as valuable candidates for this purpose thanks to their nanometer size, their ability to shift reversibly between the *ON* and *OFF* states of the system, and their distinct absorption profiles upon irradiation.

Azobenzenes are ideal organic chromophores for such a task since they show two distinct configurational isomers, *trans* and *cis*, with different stability [28]. The *trans* isomer is thermodynamically stable and, generally, it is the predominant form under ambient conditions. Irradiation of the system with UV light starts the *trans*-to-*cis* isomerization and generates a photostationary state enriched in *cis* isomer (*ON* state). The photo-generated *cis* isomer can be reverted to the *trans* isomer upon irradiation with visible light. It should be noticed that the precise wavelength required to trigger the forward and reverse isomerization of the azo chromophore depends on its exact chemical structure. The metastable *cis* isomer can also relax back to the initial *trans* isomer spontaneously in the dark. In this way, the *OFF* state of the material can be restored either photochemically or thermally. However, a thermal reverse switching is generally preferred since it avoids the use of a second external stimulus and diminishes the complexity of the final material.

For a rapid transmission and processing of information to be achieved, the "forward switching (data writing) – data reading – reverse switching (data erasing)"

cycle should be completed in a very short time. Therefore, the corresponding photoswitch should swap between the *ON* and *OFF* states of the system as fast as possible. While the photochemical *trans*-to-*cis* isomerization can be performed in a few femtoseconds, depending on the intensity of the light source, the rate at which the thermal *cis*-to-*trans* isomerization occurs depends mainly on the chemical architecture of the azo chromophore. In other words, the speed of the thermal back reaction and, in turn, the response time of the final material, can be tuned by means of subtle and rational structural modifications of the azobenzene platform at the required positions. In this regard, the development of novel azo compounds that exhibit ultrafast isomerization kinetics under ambient conditions is continuing at the forefront of new research not only in synthetic organic chemistry but also in materials science and related disciplines. Therefore, it is the main aim of this chapter to present the reader the most recent progress made in the design of new azo dyes potentially suitable for information transmission in real time, that is, the realization of novel azo derivatives exhibiting very fast thermal isomerization kinetics, spanning from the millisecond to the picosecond time scale, under ambient conditions.

## 23.3 The Starting Grid: Toward the Millisecond Timescale

Azobenzene and 4,4′-dialkoxysubstituted azo dyes exhibit slow thermal isomerization kinetics. As representative examples, 4,4′-dimethoxyazobenzene (**1**) and 4,4′-di-(5-hexenyloxy)azobenzene (**2**) display relaxation times ($\tau$ in Figure 23.2; $\tau = 1/k$, where $k$ is the first-order rate constant for the thermal *cis*-to-*trans* isomerization) of 15 and 12 hours in ethanol at 25 °C (Figure 23.2) [29]. The solvent polarity does not exert a noticeable effect on the rate of the process ($\tau$ values of 15 and 14 hours for **1** and **2** in toluene, respectively). Although the thermal isomerization rate of these azo dyes can be accelerated when integrated into liquid-crystalline matrices, their switching speed is still too slow for optical information transmission [29, 30]. Nevertheless, azo compound **2** has been successfully introduced into liquid single-crystal elastomers to produce efficient artificial muscle-like actuators [31]. It should be emphasized, however, that very slow thermally isomerizing azo compounds can become handy for optically controlled information storage devices. For instance, 2,2′,6,6′-tetrafluorosubstituted azo derivatives, exhibiting unprecedented relaxation times up to two years, have been reported, which could be extremely valuable for this purpose [32]. During recent years, this type of fluorinated azo compounds has been intensively investigated for other uses as well, e.g. adaptable metal organic frameworks (MOFs) [33], photocontrollable bioactive molecules (in this case, 2,2′,6,6′-tetramethoxysubstituted azo dyes have been used) [34] and chaotic self-oscillating actuators [35].

The substitution of one of the alkoxyl chains of **2** by an electron-withdrawing group results in an acceleration of the thermal isomerization process. Indeed, while *cis*-**2** shows a relaxation time of 12 hours in ethanol at 25 °C, its cyano- (**3**) and nitro- (**4**)

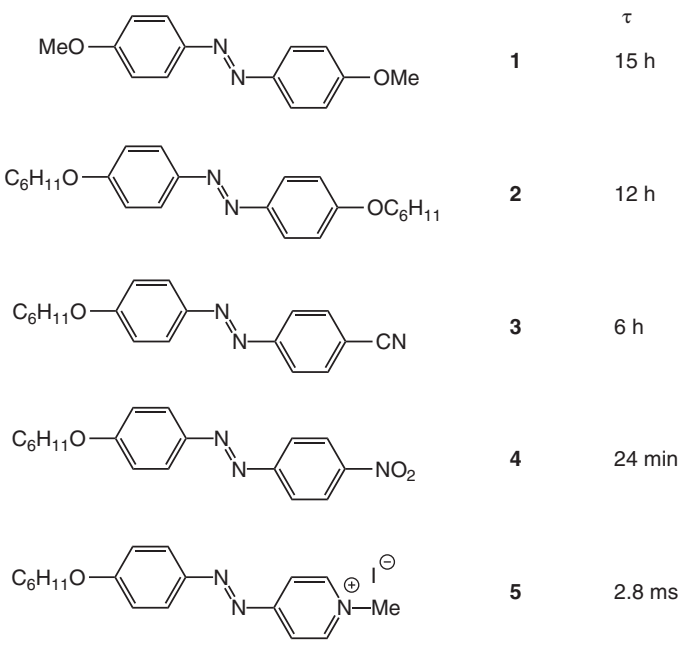


**Figure 23.2** Chemical structure and relaxation time, $\tau$, in ethanol for azo compounds **1**–**5**.

substituted counterparts display $\tau$ values of 6 hours and 24 minutes, respectively, under the same experimental conditions (Figure 23.2) [36, 37].

The replacement of one of the benzene rings of the azo dye by a pyridine heterocycle allows the introduction of permanent positive charges in the form of pyridinium salts, which exhibit a much more electron-withdrawing character than the cyano and nitro functional groups. This structural modification results into a remarkable acceleration of the isomerization reaction, thereby reaching switching speeds within the millisecond time window (for example, $\tau = 2.8$ ms for the azopyridinium salt **5** in ethanol at 25 °C, Figure 23.2) [38]. For the sake of comparison, at the time when azo compound **5** was published, the fastest known azo dye was 4-*N*,*N*-dimethylamino-4′-nitroazobenzene (DNAB), which showed relaxation times ranging from 21 to 122 ms in alcoholic solutions [39, 40].

Two different mechanisms have been established for the thermal *cis*-to-*trans* isomerization kinetics of azo dyes (Figure 23.3): inversional (involving an in-plain lateral shift of one of the nitrogen atoms of the azo function and a rehybridized linear transition state) and rotational (implying a rotation around the N—N bond) [42–46]. Azobenzene and azo derivatives **1**–**3** isomerize through the inversional mechanism [29]. The faster isomerization kinetics observed for azo compounds **4** and **5** is the result of a changeover in the reaction mechanism from inversion to rotation. It is well known that the combination of electron-donating and electron-withdrawing groups in the positions 4 and 4′ of an azobenzene causes the azo bond to adopt a more single bond character, which enables the operation of the rotational path and speeds up the thermal isomerization step [47].

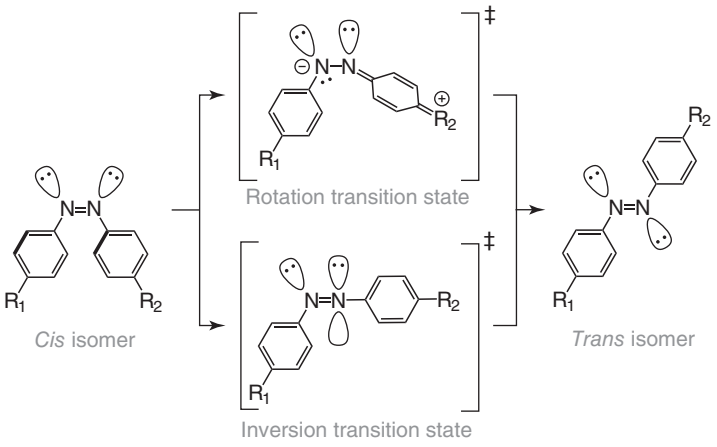


**Figure 23.3** Transition states for the mechanisms (rotation and inversion) of the *cis*-to-*trans* thermal isomerization occurring on azo derivatives. Source: Garcia-Amorós et al. [41].

Besides endowing the azo dye with a push–pull electronic configuration, another powerful strategy to reach millisecond isomerization speeds is to take advantage from the keto-enol tautomerism. 4-(5-Hexenyloxy)azobenzene (**6**), as its 4,4′-dialkoxysubstituted analogues **1** and **2**, exhibits a very slow thermal isomerization at room temperature ($\tau$ = 70 hours in ethanol, Figure 23.4). The replacement of the alkoxyl chain of **6** by a free hydroxyl group results in a dramatic acceleration of the thermal isomerization kinetics of the chromophore. Indeed, 4-hydroxyazobenzene (**7**), the simplest azophenol, shows a relaxation time of only 205 ms in ethanol solution (Figure 23.4) [48]. As a whole, azophenols are an interesting type of azo derivatives for real-time information transmission because they display a fast thermal *cis*-to-*trans* isomerization under ambient conditions.

The switching speed for azophenols depends on the solvent where they are dissolved. The fast isomerization kinetics observed in ethanol can be explained in terms of the azo compound undergoing a solvent-assisted azo-hydrazone tautomeric equilibrium. This dynamic process enables the N—N bond to adopt a partially single bond nature and promotes the operation of the rotational mechanism, which accelerates the isomerization process. This tautomeric equilibrium can also occur in non-protic solvents like toluene. In this instance, the azo-hydrazone tautomerism is established through intermolecular hydrogen bonding between two molecules of azophenol [49]. As a consequence, a much slower isomerization is detected ($\tau$ = 32 minutes for *cis*-**7** in toluene, Figure 23.4) [48]. Recent kinetico-mechanistic studies, based on the analysis of the thermal and pressure activation parameters for the isomerization reaction, have corroborated the operation of the rotational mechanism both in protic and aprotic solvents for azophenols [50].

The isomerization kinetics of azophenols is also strongly influenced by the number of hydroxyl groups the molecule contains and their exact location within the azobenzene platform. This is an important fact since it means that

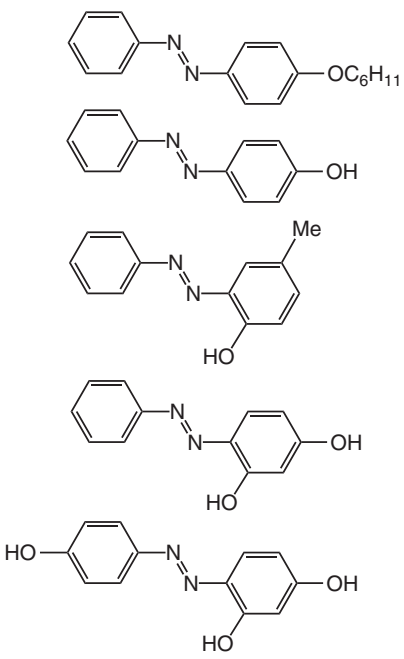


**Figure 23.4** Chemical structure and relaxation time, $\tau$, in ethanol for azo compounds **6**–**10**. Source: Modified from Garcia-Amorós et al. [48].

the thermal relaxation time of the azo chromophore can be modulated by placing the hydroxyl groups in precise positions of the molecule. In this regard, 2-hydroxy-5-methylazobenzene (**8**) exhibits a relaxation time of 399 and 650 ms in ethanol and toluene, respectively (Figure 23.4). In this type of azophenols, intramolecular hydrogen bonding can occur independent of the solvent nature and, therefore, a fast isomerization is detected in both protic and aprotic solvents. In addition, the combination of two hydroxyl groups in the *ortho* and *para* positions of the same benzene ring in the shape of **9** produces a significant acceleration of the process ($\tau$ = 12 ms for *cis*-**9** in ethanol, Figure 23.4). This effect is not observed when the two hydroxyl groups are located in the positions 2 and 4′ of the azobenzene platform ($\tau$ = 175 ms for 2,4′-dihydroxy-5-methylazobenzene). Finally, the poly-hydroxy-substitution of the azobenzene core, such as in 2,4,4′-trihydroxyazobenzene (**10**), decreases the relaxation time of the photoswitch to a few milliseconds (6 ms in ethanol, Figure 23.4) [48].

The fast isomerization of azophenols can also be observed in liquid-crystalline and polymeric materials in the absence of a protic environment [51]. This fact has allowed to conceive artificial muscle-like actuators with fast responses (c. 1 second, Figure 23.5) based on these azo derivatives [52]. In these completely aprotic media, intramolecular hydrogen bonding can be efficiently established between two azophenol molecules, due to their spatial proximity, although their concentration within the host matrix is relatively small. It is noteworthy that polyazophenolic networks have been applied recently as vapor and humidity sensors [53].

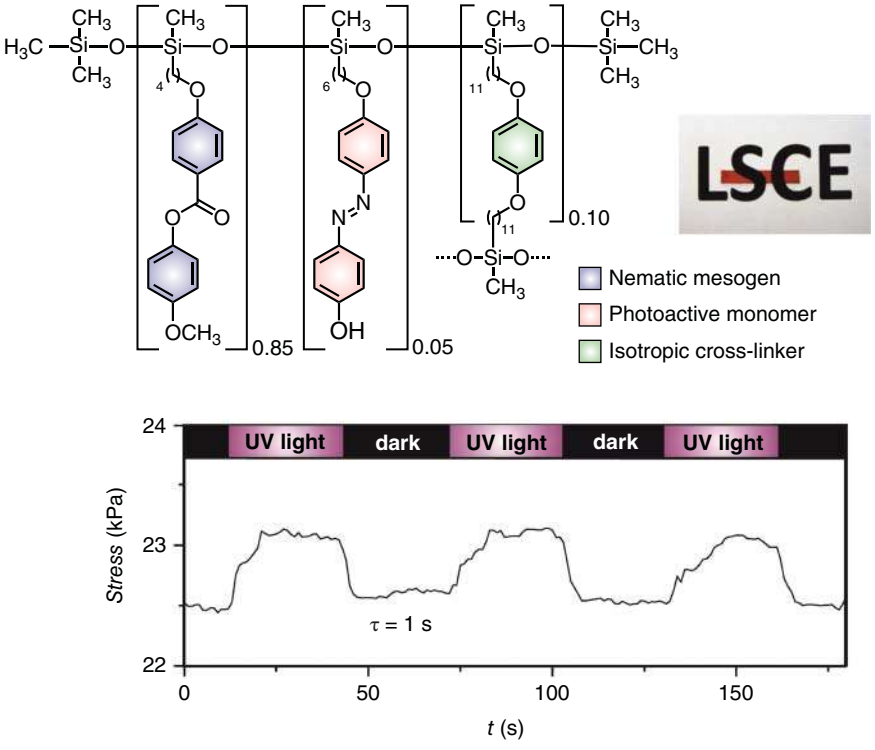


**Figure 23.5** Chemical composition of an azophenol-containing liquid single crystal elastomer and its opto-mechanical response upon irradiation at $\lambda_{Ex}$ = 380 nm. Source: Modified from Garcia-Amorós et al. [52].

## 23.4 The Race Continues: The Micro- and Nanosecond Timescale

Even though the azo chromophores that we have seen in the previous section exhibit a fast thermal isomerization, it is still too slow for their potential use for real-time information transmission. During the last decade, enormous effort has been put forth to design novel azo dyes displaying switching speeds within the micro- and nanosecond temporal domains.

A pivotal strategy for this goal to be achieved comes from the combination into the very same azo chromophore of electron-withdrawing and electron-donating groups, placed in such a way that the system obtained is endowed with a strong push–pull electronic configuration, and functional groups that promote tautomeric equilibria. Individually, these two approaches have allowed access to azo compounds that isomerize in a few milliseconds but when combined the resulting chromophores exhibit improved isomerization kinetics, elapsing within the microsecond and even the nanosecond timescale.

The first attempt to shift the relaxation time of the azo dye beyond the millisecond temporal domain resulted from the combination of a hydroxyl group, an

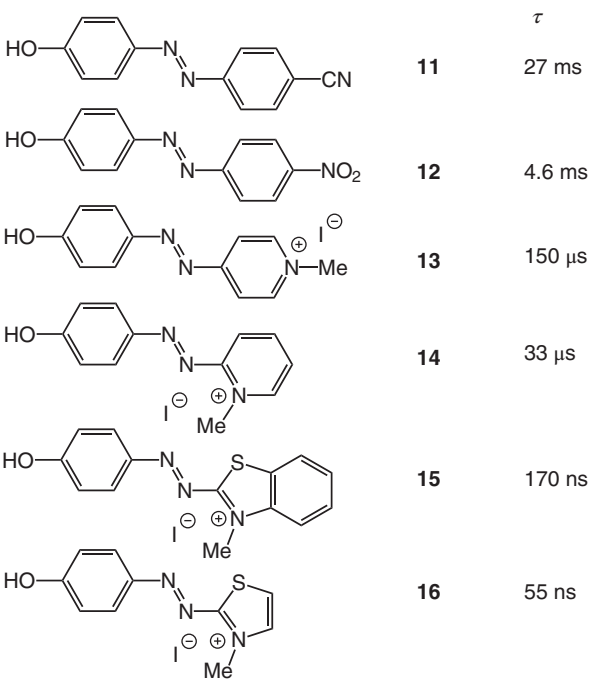


**Figure 23.6** Chemical structure and relaxation time, $\tau$, in ethanol for azo compounds **11**–**16**. Source: Modified from Garcia-Amorós et al. [54].

azo-hydrazone tautomerism promoter, with the strong electron-withdrawing cyano and nitro functional groups, which were located at the position 4′ with respect to the phenol function. This design scheme yielded azo compounds **11** and **12**, which displayed $\tau$ values of 27 and 4.6 ms in ethanol, respectively (Figure 23.6) [54]. As it has been already mentioned, the substitution of one of the benzene rings of the azo dye by a pyridine heterocycle, with a permanent positive charge in its nitrogen atom, increases significantly the push–pull electronic distribution of the chromophore and improves its switching speed. Indeed, phenolic azopyridinium salts **13** and **14** exhibit $\tau$ values of only 150 and 33 μs in ethanol at room temperature (Figure 23.6) [54].

This methodology has been extended further by changing the nature of the electron-withdrawing heterocycle. Specifically, the substitution of the pyridinium moiety of **13** and **14** by a positively charged benzothiazole (**15**) and thiazole ring (**16**) accelerates the thermal isomerization of the chromophore from the microsecond to the nanosecond timescale (170 and 55 ns for **15** and **16** in ethanol, respectively, Figure 23.6) [55].

Azo dyes **15** and **16** have been also physically incorporated into microcrystalline cellulose (MCC) to produce solid materials (**15-MCC** and **16-MCC** in Figure 23.7) with fast switching speeds. MCC is a widely used biorenewable material for many applications. In addition, it is a particularly attractive solid support to integrate these azo compounds due to its highly hydroxylated structure. In this solid environment, the azo dye can establish an efficient hydrogen bonding with the hydroxyl groups of MCC, which promotes the azo-hydrazone tautomerism. As a

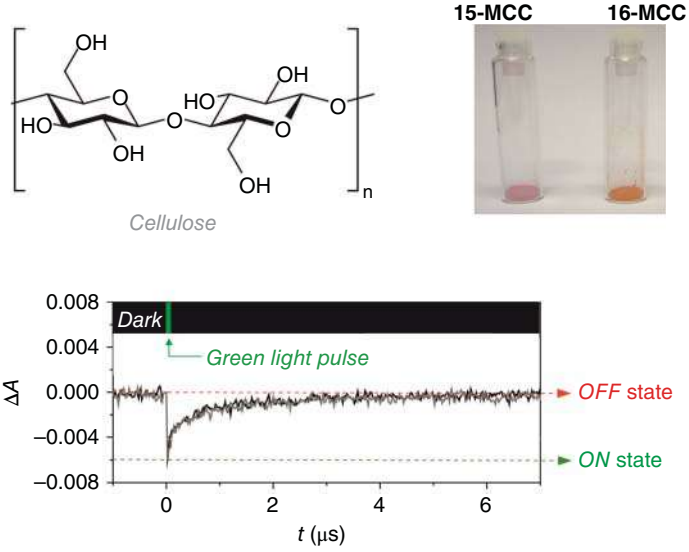


**Figure 23.7** Chemical structure of cellulose and pictures of the solid cellulose-based materials **15-MCC** and **16-MCC**. Transient absorption generated by irradiation at $\lambda_{Ex}$ = 532 nm ($\lambda_{Obs}$ = 570 nm) for the material **16-MCC** in toluene suspension at 25 °C. Source: Modified from Garcia-Amorós et al. [55]. Reproduced with permission of the Royal Society of Chemistry.

result of this intermolecular tautomeric equilibrium, the thermal back reaction for **15-MCC** and **16-MCC** occurs in the solid state within the same timescale (540 and 380 ns, respectively) as for the unsupported molecules in ethanol solution. However, the restricted medium imposed by MCC delays the whole isomerization process, originating a slow temporal component of 23 and 3.4 μs, respectively [55]. This sophisticated kinetic behavior is related to the presence of two distinct populations of azo moieties in the composite, while some of the azo chromophores are encapsulated in the inner cavities of MCC, the others are freely adsorbed on its surface. In this case, and for a better temporal characterization of the final photoactive materials, the corresponding half-lives, i.e. the time needed for the material to recover the 50% of its initial absorbance value, is considered. Half-lives of 570 and 260 ns have been found for **15-MCC** and **16-MCC** at 298 K, respectively. Remarkably, these light-sensitive solid systems have been the first all-organic solid azobenzene-containing materials exhibiting thermal isomerization kinetics within the nanosecond temporal domain.

4-(Benzo[d]thiazol-2-yldiazenyl)phenol and 4-(thiazol-2-yldiazenyl)phenol (**17** and **18** in Figure 23.8, respectively) thermally isomerize within the millisecond time scale (6 and 15 ms in ethanol, respectively, Figure 23.8) [55]. The donor part of **17** can be replaced by the electron-donating *Tph–Tph–Pyr* triad (*Tph* = thiophene and *Pyr* = pyrrole) to furnish azo compound **19** (Figure 23.8). Importantly, this structural modification has allowed access to the first neutral azo dye displaying a relaxation time within the microsecond time scale ($\tau$ = 70 μs for *cis*-**19** in ethanol at 25 °C, Figure 23.8) [56].

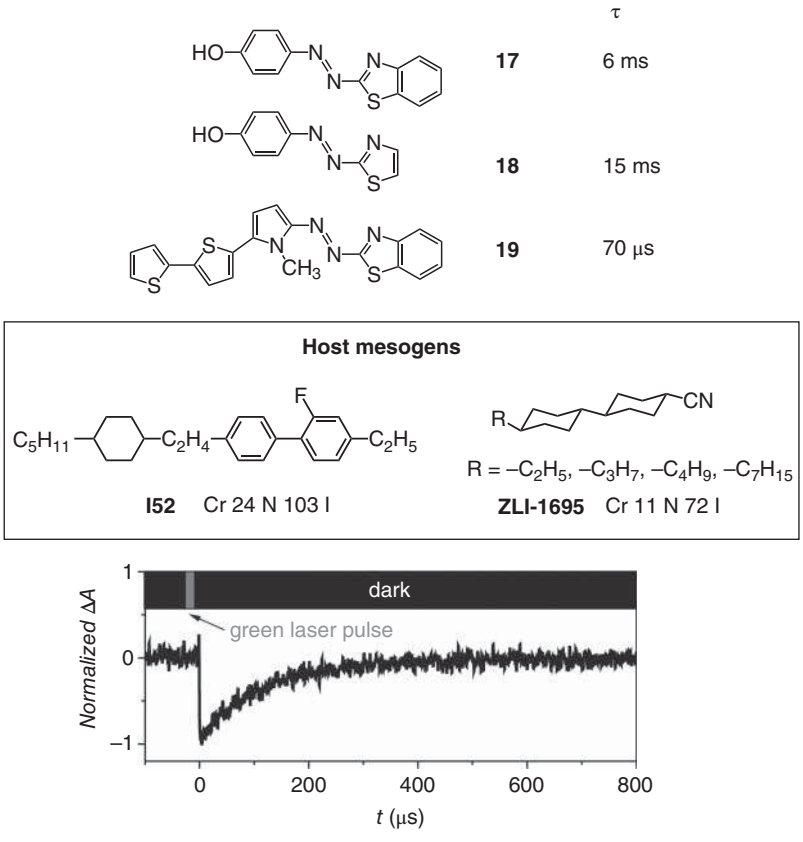


**Figure 23.8** Chemical structure of azo compounds **17**–**19** and the nematic mesogens **I52** and **ZLI-1695**. The phase transformation temperatures for the different liquid crystals are given in Celsius (Cr = crystalline, N = nematic, I = isotropic). Relaxation time, $\tau$, for azo compounds **17**–**19** in ethanol. Transient absorption change photo-induced by laser pulse irradiation ($\lambda_{Ex}$ = 532 nm, $\lambda_{Obs}$ = 500 nm) for azo dye **19** in mesogen **I52**. Source: Garcia-Amorós et al. [56].

Azo compound **19** has been introduced into liquid-crystalline matrices to produce solid switchable components with fast responses. When azo dyes that isomerize through the inversional mechanism are introduced into nematic liquid crystals, a modest acceleration of their isomerization reaction is observed with respect to that in a solvent of an identical polarity (see above). This enhancement results from the tendency of the mesogen molecules to quickly recover their pre-irradiation orientation along the nematic director once the illumination of the sample is stopped [29, 30, 57, 58]. Remarkably, *cis*-**19** isomerizes c. 160 times faster in the nematic phase of mesogen **I52** ($\tau$ = 130 μs, Figure 23.8) than in toluene ($\tau$ = 21 ms). In fact, it isomerizes in the nematic environment almost as fast as in ethanol, a polar protic solvent [56]. It should be stressed out that for those azo dyes that follow the rotational pathway, like compound **19**, the relaxation time falls within the same timescale as that for the reorganization of the host mesogens toward the director

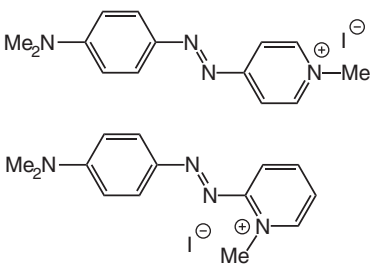


| | $\tau$ |
|---|---|
| **20** | 329 ns |
| **21** | 368 ns |

**Figure 23.9** Chemical structure and relaxation time, $\tau$, in ethanol for azo compounds **20** and **21**.

direction. As a consequence, the dynamics of the host liquid-crystalline matrix plays a key role in the thermal isomerization kinetics of the azo dye. The dynamics of the host nematic mesophase is characterized by its viscoelastic coefficient ($K_{11}/\gamma_1$), where $K_{11}$ and $\gamma_1$ stand for the deformation elastic constant and the rotational viscosity, respectively [59, 60]. *Cis*-**19** isomerizes slower in the nematic mesogen **ZLI-1695** (1.2 ms, Figure 23.8) than in **I52** (130 μs). Mesogen **I52** shows a larger $K_{11}/\gamma_1$ ratio ($5.21 \times 10^{-10}$ m$^2$ s$^{-1}$) than **ZLI-1695** ($1.22 \times 10^{-10}$ m$^2$ s$^{-1}$). The shorter viscoelastic coefficient of **ZLI-1695** implies that this mesogen requires a longer time to recover its initial orientation along the director than **I52**. This fact explains the faster thermal isomerization of *cis*-**19** when it is dissolved in the latter mesogen.

To finish the discussion on azo dyes displaying thermal isomerization rates within the micro- and nanosecond temporal windows, we cannot forget to mention those azo dyes resulting from the combination of the strong electron-withdrawing character of pyridinium salts and the electron-donating nature of amines, which are also capable to establish the well-known amino-imino tautomerism. This design scheme permitted to obtain positively charged azo compounds displaying very short thermal relaxation times, falling within the nanosecond temporal domain. Indeed, *N*,*N*-dimethylamino-substituted azopyridinium salts **20** and **21** exhibit $\tau$ values of 329 and 368 ns in ethanol, respectively (Figure 23.9). The relaxation time of these azo derivatives is strongly solvent-dependent, as it has been widely described for rotationally isomerizing azo compounds on countless occasions. In fact, their isomerization kinetics is up to $10^4$-times slower in the non-polar solvent 1,2-dimethoxyethane (1.9 and 9.7 ms for *cis*-**20** and *cis*-**21**, respectively) [61].

## 23.5 Pressing Down the Throttle: Beyond the Nanosecond Timescale

Currently, the most challenging task in the area of azo compounds for real-time information transmission is the design of new azobenzene-based molecular switches showing thermal isomerization speeds in the subnanosecond timescale. To the best of our knowledge, only two examples have been reported heretofore [62, 63]. Such extremely fast thermal relaxation of the metastable *cis* isomer has been achieved by two completely different approaches.

Azo dyes combining electron-withdrawing thiazole or benzothiazole heterocycles and electron-donating amino groups within the very same covalent skeleton (**22** and

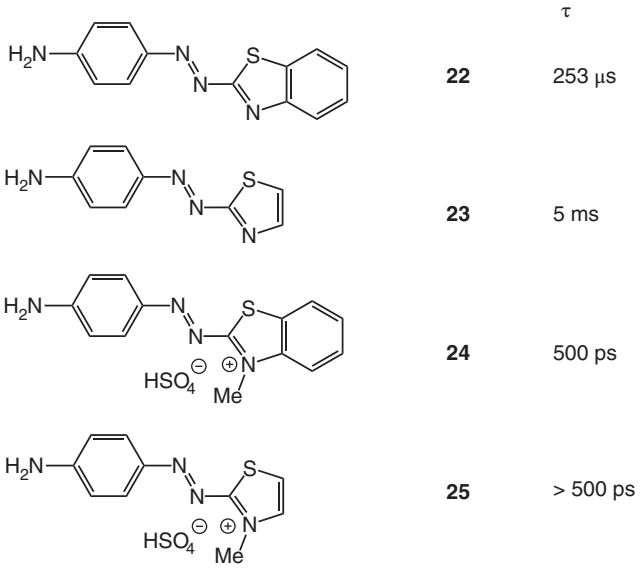


**Figure 23.10** Chemical structure and relaxation time, $\tau$, in ethanol for azo compounds **22**–**25**. Source: Modified from Garcia-Amorós et al. [62].

**23** in Figure 23.10) display relaxation times for the *cis*-to-*trans* isomerization within the milli- and microsecond timescales at room temperature (253 μs and 5 ms for **22** and **23** in ethanol at 25 °C, Figure 23.10) [62]. The thermal back reaction for these two azo dyes can be drastically accelerated by methylating the nitrogen atom of their heterocycles, i.e. synthesizing the corresponding benzothiazolium and thiazolium salts (compounds **24** and **25** in Figure 23.10). For these two azo dyes, the reverse isomerization occurs much faster, within the picosecond temporal domain, than for their non-methylated analogues. Indeed, compounds **24** and **25** are the first azo chromophores capable of reversible switching between their *trans* and *cis* isomers in a subnanosecond timescale under ambient conditions.

The kinetics of the thermal *cis*-to-*trans* isomerization process for the benzothiazolium and thiazolium salts **24** and **25** was analyzed by means of the nanosecond flash photolysis technique. However, no thermal back reaction was detected within this temporal window, indicating that *cis*-**24** and *cis*-**25** live less than one nanosecond under ambient conditions. On this basis, their thermal back isomerization was monitored by means of ultrafast spectroscopy. The photodynamics of the excited state has multiple time constants within the shorter timescale (< 20 ps): one of approximately 0.1 ps ($\tau_1$), another between 0.5 and 1.2 ps ($\tau_2$), a third around 3 ps ($\tau_3$), and a fourth around 15 ps ($\tau_4$) [62]. The shortest time constant, $\tau_1$, is ascribed to the $S_2 \rightarrow S_1$ decay, i.e. to the switch from the $\pi\pi^*$ to the $n\pi^*$ state. After this decay, one part of the excited chromophores isomerize to the *cis* isomer, while another returns to the *trans* configuration. These processes yield time constants $\tau_2$ and $\tau_3$. The time constant $\tau_4$ corresponds to the vibrational cooling of the hot ground state formed during the decay. A similar complex dynamics with three to four time constants

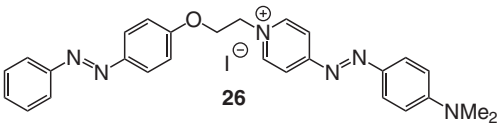


26

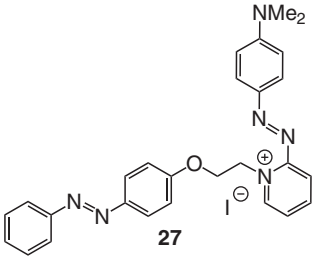


27

**Figure 23.11** Chemical structure of azo compounds **26** and **27**.

in the femto- and picosecond time window has been reported for other push–pull azo dyes [64–68]. The longer timescale (20 ps to 3 ns) is dominated by the thermal *cis*-to-*trans* isomerization of the dye. On this timescale, a slowly decaying absorption can be detected and fitted with a time constant $\tau_5$ of approximately 500 ps for both molecules in different solvents (ethanol, acetonitrile, and water) with the exception of compound **24** in ethanol, for which the decay is slower but still in the picosecond range. Such ultrafast *cis*-to-*trans* isomerization is consistent with calculations on the ground-state isomerization carried out at the PCM-MP2/cc-pVTZ level (including solvation) [62]. The absence of sizeable barriers along the reaction path explains the fast decay times that are determined experimentally. In this way, and owing to their very strong push–pull electronic configuration, these systems are not only the fastest molecular azo dyes heretofore described in the literature but are also capable of completing a full switching cycle within the picosecond timescale.

Another, and less conventional, strategy to achieve optical switching within the subnanosecond timescale arises from the juxtaposition of two azo moieties within the very same molecular construct. Although systems containing two or more azo units in their chemical structures have been widely reported, they have been mostly built up by repeating the very same motif. In that situation, the distinct azo units isomerize synchronously and, therefore, the resulting material can only perform one task at a time [69–74].

Bis-azo compounds **26** and **27** (Figure 23.11) were prepared to get optical switches exhibiting two light-responsive units with a very high spatiotemporal resolution. These bichromophoric systems combine in the same molecular entity a slow (a 4-alkoxysubstituted azobenzene) and a fast (an aminoazopyridinium salt) azo compound. The slow fragment isomerizes in several days, regardless of whether it is isolated or part of the bichromophoric material. On the other hand, the fast fragment returns to the thermodynamically stable *trans* form within the nanosecond timescale when it is isolated (see compounds **20** and **21** in Figure 23.9). Surprisingly, when the azo compound is covalently connected to the slow fragment through a flexible spacer, its thermal isomerization is greatly enhanced (c. $10^3$-fold faster), elapsing within the picosecond time window ($\tau$ values of

670 and 305 ps for the fast fragments of **26** and **27**) [63]. These bifunctional azo chromophores are currently under extensive investigation to unravel the origin of the unusually accelerated thermal isomerization of their fast fragment. Indeed, these azo derivatives can be extremely useful within photonics for applications where simultaneous optical switching will be required within two very different timescales. Moreover, the possibility to orthogonally switch the two azo platforms might allow access to applications that would be otherwise impossible to achieve with their monochromophoric counterparts.

## References


**1** Bouas-Laurent, H. and Dürr, H. (2001). *Pure Appl. Chem.* 73: 639–665.
**2** Dürr, H. and Bouas-Laurent, H. (2003). *Photochromism – Molecules and Systems*. Amsterdam: Elsevier.
**3** Thapaliya, E.R., Captain, B., and Raymo, F.M. (2014). *J. Org. Chem.* 79: 3973–3981.
**4** Zhang, Y., Tang, S., Thapaliya, E.R. et al. (2018). *Chem. Commun.* 54: 8799–8809.
**5** Sansalone, L., Tang, S., Garcia-Amorós, J. et al. (2018). *ACS Sens.* 3: 1347–1353.
**6** Qi, Q., Li, C., Liu, X. et al. (2017). *J. Am. Chem. Soc.* 139: 16036–16039.
**7** Hou, L., Zhang, X., Cotella, G.F. et al. (2019). *Nat. Nanotechnol.* 14: 347–353.
**8** Orgiu, E., Crivillers, N., Herder, M. et al. (2012). *Nat. Chem.* 4: 675–679.
**9** El Gemayel, M., Börjesson, K., Herder, M. et al. (2015). *Nat. Commun.* 6: 6630.
**10** Rekab, W., Leydecker, T., Hou, L. et al. (2020). *Adv. Funct. Mater.* 30: 1908944.
**11** Demirel, G.B., Dilsiz, N., Çakmak, M. et al. (2011). *J. Mater. Chem.* 21: 3189–3196.
**12** Wagner, N. and Theato, P. (2014). *Polymer* 55: 3436–3453.
**13** Kwon, G., Panchanathan, D., Mahmoudi, S.R. et al. (2016). *Nat. Commun.* 8: 14968.
**14** Garcia-Amorós, J. and Velasco, D. (2016). *Tautomerism – Concepts and Applications in Science and Technology* (ed. L. Antonov) Chapter 11. Weinheim: Wiley-VCH, 253–271.
**15** Raymo, F.M. and Giordani, S. (2001). *Org. Lett.* 3: 1833–1836.
**16** Raymo, F.M. and Giordani, S. (2002). *Proc. Natl. Acad. Sci. U.S.A* 99: 4941–4944.
**17** Andréasson, J. and Pischel, U. (2015). *Chem. Soc. Rev.* 44: 1053–1069.
**18** Andréasson, J. and Gust, D. (2012). *Molecular and Supramolecular Information Processing: From Molecular Switches to Logic Systems* (ed. E. Katz) Chapter 4. Weinheim: Wiley-VCH, 53–78.
**19** Morstein, J., Dacheux, M.A., Norman, D.D. et al. (2020). *J. Am. Chem. Soc.* 142: 10612–10616.
**20** Borowiak, M., Küllmer, F., Gegenfurtner, F. et al. (2020). *J. Am. Chem. Soc.* 142: 9240–9249.
**21** Reis, J.M., Xu, X., McDonald, S. et al. (2018). *ACS Synth. Biol.* 7: 2355–2364.
**22** Frank, J.A., Moroni, M., Moshourab, R. et al. (2015). *Nat. Commun.* 6: 7118.


**23** Yamada, M., Kondo, M., Mamiya, J.-I. et al. (2008). *Angew. Chem. Int. Ed.* 47: 4986–4988.

**24** Yu, Y. and Ikeda, T. (2005). *Macromol. Chem. Phys.* 206: 1703554.

**25** Zeng, H., Wasylczyk, P., Wiersma, D.S. et al. (2018). *Adv. Mater.* 30: 1705–1708.

**26** Chen, M., Wang, X., Xing, X. et al. (2011). *J. Mech. Eng. Res.* 3: 114–119.

**27** Camacho-López, M., Finkelmann, H., Palffy-Muhoray, P. et al. (2004). *Nat. Mater.* 3: 307–310.

**28** Rau, H. (1990). *Photochemistry and Photophysics*, vol. 2, Chapter 4. Stockholm: CRC Press.

**29** Garcia-Amorós, J., Martínez, M., Finkelmann, H. et al. (2010). *J. Phys. Chem. B* 114: 1287–1293.

**30** Garcia-Amorós, J., Finkelmann, H., and Velasco, D. (2011). *Phys. Chem. Chem. Phys.* 13: 11233–11238.

**31** Garcia-Amorós, J., Finkelmann, H., and Velasco, D. (2011). *J. Mater. Chem.* 21: 1094–1101.

**32** Knie, C., Utrecht, M., Zhao, F. et al. (2014). *Chem. Eur. J.* 20: 16492–16501.

**33** Castellanos, S., Goulet-Hanssens, A., Zhao, F. et al. (2016). *Chem. Eur. J.* 22: 746–752.

**34** Yasuike, N., Backlock, K.M., Lu, H. et al. (2019). *ChemPhotoChem* 3: 431–440.

**35** Kumar, K., Knie, C., Bléger, D. et al. (2016). *Nat. Commun.* 7: 11975.

**36** Garcia-Amorós, J., Martínez, M., Finkelmann, H. et al. (2014). *Phys. Chem. Chem. Phys.* 16: 8448–8454.

**37** Garcia-Amorós, J., Finkelmann, H., and Velasco, D. (2011). *Chem. Eur. J.* 17: 6518–6523.

**38** Garcia-Amorós, J., Massad, W.A., Nonell, S. et al. (2010). *Org. Lett.* 12: 3514–3517.

**39** Wildes, P.D., Pacifici, J.G., Irick, G. et al. (1971). *J. Am. Chem. Soc.* 93: 2004–2008.

**40** Baba, K., Ono, H., Itoh, E. et al. (2006). *Chem. Eur. J.* 12: 5328–5333.

**41** Garcia-Amorós, J., Martínez, M., and Velasco, D. (2019). *J. Phys. Chem. C* 123: 30578–30585.

**42** Talaty, E.R. and Fargo, J.C. (1967). *Chem. Commun.*: 65–66.

**43** Binenboym, J., Burcat, A., Lifshitz, A. et al. (1966). *J. Am. Chem. Soc.* 88: 5039–5041.

**44** Schulte-Frohlinde, D. (1958). *Justus Liebigs Ann. Chem.* 612: 138–152.

**45** Le Fevre, R.J.W. and Northcott, J. (1953). *J. Chem. Soc.*: 867–870.

**46** Bandara, H.M.D. and Burdette, S.C. (2012). *Chem. Soc. Rev.* 41: 1809–1825.

**47** Asano, T. and Okada, T. (1984). *J. Org. Chem.* 49: 4387–4391.

**48** Garcia-Amorós, J., Sánchez-Ferrer, A., Massad, W.A. et al. (2010). *Phys. Chem. Chem. Phys.* 12: 13238–13242.

**49** Kojima, M., Nebashi, S., Ogawa, K. et al. (2005). *J. Phys. Org. Chem.* 18: 994–1000.

**50** Garcia-Amorós, J., Stopa, G., Stochel, G. et al. (2018). *Phys. Chem. Chem. Phys.* 20: 1286–1292.


**51** Garcia-Amorós, J. and Velasco, D. (2014). *Phys. Chem. Chem. Phys.* 16: 3108–3114.

**52** Garcia-Amorós, J., Piñol, A., Finkelmann, H. et al. (2011). *Org. Lett.* 13: 2282–2285.

**53** Poutanen, M., Ahmed, Z., Rautkari, L. et al. (2018). *ACS Macro Lett.* 7: 381–386.

**54** Garcia-Amorós, J., Nonell, S., and Velasco, D. (2011). *Chem. Commun.* 47: 4022–4024.

**55** Garcia-Amorós, J., Bucinskas, A., Reig, M. et al. (2014). *J. Mater. Chem. C* 2: 474–480.

**56** Garcia-Amorós, J., Reig, M., Castro, M.C.R. et al. (2014). *Chem. Commun.* 50: 6704–6706.

**57** Sung, J.H., Hirano, S., Tsutsumi, O. et al. (2002). *Chem. Mater.* 14: 385–391.

**58** Garcia-Amorós, J., Szymczyk, A., and Velasco, D. (2009). *Phys. Chem. Chem. Phys.* 11: 4244–4250.

**59** Wu, S.-T., Neubert, M.E., Keast, S.S. et al. (2000). *Appl. Phys. Lett.* 77: 957–959.

**60** Gauza, S., Wang, H., Wen, C.-H. et al. (2003). *Jpn. J. Appl. Phys.* 42: 3463–3466.

**61** Garcia-Amorós, J., Nonell, S., and Velasco, D. (2012). *Chem. Commun.* 48: 3421–3423.

**62** Garcia-Amorós, J., Maerz, B., Reig, M. et al. (2019). *Chem. Eur. J.* 25: 7726–7732.

**63** Garcia-Amorós, J., Cuadrado, A., Reig, M. et al. (2015). *Chem. Eur. J.* 21: 14292–14296.

**64** Simeth, N.A., Crespi, S., Fagnoni, M. et al. (2018). *J. Am. Chem. Soc.* 140: 2940–2946.

**65** Hoffman, D.P. and Mathies, R.A. (2012). *Phys. Chem. Chem. Phys.* 14: 6298–6306.

**66** Wang, Y., Zhang, S., Sun, S. et al. (2015). *J. Photochem. Photobiol. A* 309: 1–7.

**67** Nançoz, C., Licari, G., Beckwith, J.S. et al. (2018). *Phys. Chem. Chem. Phys.* 20: 7254–7264.

**68** Lygo, O.N., Khodot, E.N., Ogurtsov, V.A. et al. (2014). *High Energy Chem.* 48: 325–329.

**69** Vapaavuori, J., Goulet-Hanssens, A., Heikkinen, I.T.S. et al. (2014). *Chem. Mater.* 26: 5089–5096.

**70** Bléger, D., Liebig, T., Thiermann, R. et al. (2011). *Angew. Chem. Int. Ed.* 50: 12559–12563.

**71** Yu, Z. and Hecht, S. (2013). *Angew. Chem. Int. Ed.* 52: 13740–13744.

**72** Yu, Z., Weidner, S., Risse, T. et al. (2013). *Chem. Sci.* 4: 4156–4167.

**73** Weber, C., Liebig, T., Gensler, M. et al. (2015). *Macromolecules* 48: 1531–1537.

**74** Nagamani, S.A., Norikane, Y., and Tamaoki, N. (2005). *J. Org. Chem.* 70: 9304–9313.


# 24 Photoswitchable Ion Receptors

Alketa Lutolli and Amar H. Flood

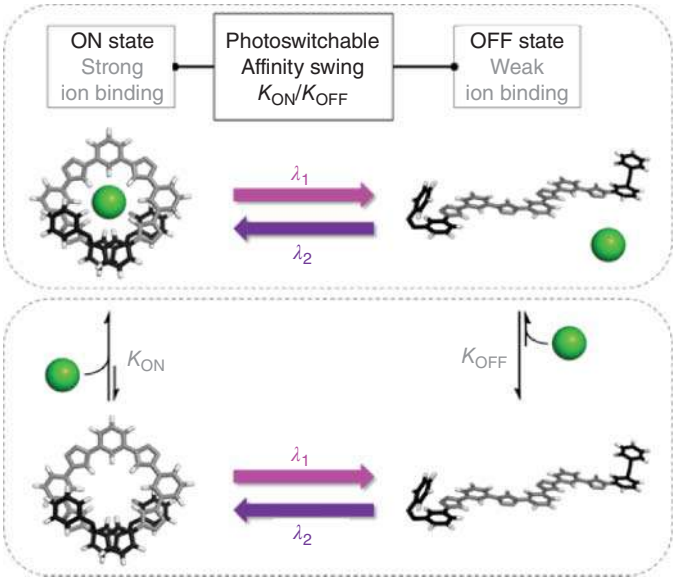


**Characteristic Features**

Photoswitchable ion receptors contain two states of higher (ON-state) and lower (OFF-state) affinity to produce an affinity swing for binding and releasing ions.

**Key References**

Kokan, Z. and Chmielewski, M.J. (2018). A photoswitchable heteroditopic ion-pair receptor. *J. Am. Chem. Soc.* 140: 16010–16014.

Li, R.-J., Holstein, J.J., Hiller, W.G. et al. (2019). Mechanistic interplay between light switching and guest binding in photochromic [$Pd_2$Dithienylethene$_4$] coordination cages. *J. Am. Chem. Soc.* 141: 2097–2103.

de Jong, J., Feringa, B.L., and Wezenberg, S.J. (2019). Light-modulated self-blockage of a urea binding site in a stiff-stilbene based anion receptor. *ChemPhysChem* 20: 3306–3310.

Chi, X., Cen, W., Queenan, J.A., et al.(2019). Azobenzene-bridged expanded "Texas-sized" box: a dual-responsive receptor for aryl dianion encapsulation. *J. Am. Chem. Soc.* 141: 6468–6472.

Parks, F.C., Liu, Y., Debnath, S., et al. (2018). Allosteric control of photofoldamers for selecting between anion regulation and double-to-single helix switching. *J. Am. Chem. Soc.* 140: 17711–17723.

# 24

# Photoswitchable Ion Receptors

*Alketa Lutolli and Amar H. Flood*

*Indiana University, Department of Chemistry, 800 E. Kirkwood Avenue, Bloomington, IN 47405, USA*

## 24.1 History, Development, and Concepts

### 24.1.1 The First Synthetic Photoswitchable Ion Receptor

Nature was the first to use photocontrol for ion regulation. An example of such can be seen in halorhodopsin, which is a photodriven chloride pump containing an iminium-tether capable of *trans-cis* isomerization for pumping anions across membranes [1]. Shinkai designed the first synthetic photoresponsive ion receptor in 1979, which consisted of an azobenzene-bridged azacrown ether [2]. He evolved this design in 1980 into an azobenzene-fused-bis crown ether with light-driven butterfly motions capable of capturing and releasing alkali metals (Figure 24.1) [3–5]. It was discovered that the alkali metals influenced photoisomerization and the thermal (*cis* to *trans*) isomerization by stabilizing the *cis*-isomer with the following order of stability: $Rb^+ > Cs^+ > K^+ > Na^+$. The conformational changes between the *cis* and *trans*-isomer were expected, and found, to alter guest binding affinities as well as the putative mode of complexation. Rank orders of binding affinities were estimated. Transport studies were conducted using U-tube apparatus in which alkali cations were transported from one water phase to the other through an intervening organic solution containing the receptor. Shinkai found that the order of extractability varied with each isomer; the *cis*-isomer showed $Rb^+ > Cs^+ > K^+ > Na^+$, whereas the *trans*-isomer preferred $Na^+ > Rb^+ > Cs^+ > K^+$. These results demonstrate light-driven ion transport across immiscible phases, which resembles ion transport across lipid membranes.

Shinkai's work was the first to illustrate the ability of photoresponsive ion receptors to switch between a stronger binding state (referred to as the ON-state) and a weaker binding OFF-state. Under continuous irradiation with a 500-W high-pressure Hg lamp, he showed selective transport of $K^+$ in the U-tube experiments. Shortly after, Shinkai and others began to design new photoresponsive receptors to evaluate guest recognition, improve affinity swings, and explore new functionalities.

*Molecular Photoswitches: Chemistry, Properties, and Applications*,
First Edition. Edited by Zbigniew L. Pianowski.


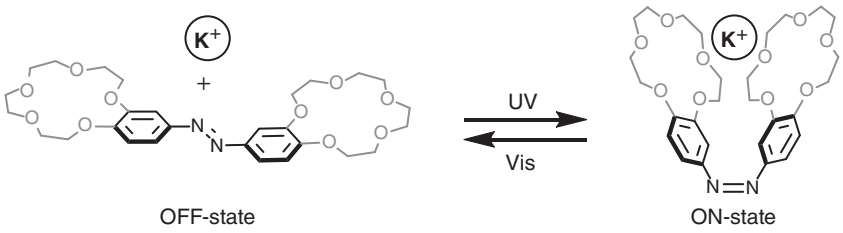


**Figure 24.1** An azobenzene-appended-bis-crown ether capable of alkali metal capture and release. The receptor in the *trans* azobenzene state displays weaker binding (OFF-state) relative to the *cis* (ON-state). Sources: Shinkai et al. [3–5].

### 24.1.2 Ion Receptors

Shinkai's photoresponsive receptors make use of crown ethers, discovered in 1967 to bind alkali cation. While working for DuPont, C.J. Pedersen synthesized the first crown ethers and studied their complexation with various salts [6]. A year after, in 1968, Parks and Simmons designed a macrocyclic amine capable of capturing halides [7]. These two discoveries led to the rise of supramolecular chemistry and the exploration of ion receptors.

### 24.1.3 Photoswitches Develop Along with Molecular Machines

Around the same time as Shinkai's photoresponsive macrocycles began to emerge, so did other types of artificial molecular machines. In 1983, Dietrich-Buchecker and Sauvage designed Cu(I)-directed metallo-catenanes [8]. These interlocked molecules rely on the use of recognition motifs (electron donors) commonly used for metal coordination. Sauvage later used electrochemical oxidation from Cu(I) to Cu(II), as well as KCN as a chemical agent to remove Cu(I) and eventually obtain a metal-free catenane receptor [9]. Control over complexation led to catenanes and their analogs, rotaxanes, being used for switches and motors [10]. During the same period, the cross-fertilization of ideas occurred. It is no coincidence, therefore, that the recent 2016 Nobel was shared by Sauvage, Stoddart, and Feringa on molecular machines spanning interlocked molecular machines and photodriven rotary motors.

### 24.1.4 From Receptor- and Guest-Driven Design to Photoswitchable Receptors

The recognition of ions can be achieved by using either a receptor- or guest-driven design approach, though it is often the receptor that is modified to control ion binding with light. Pederson's crown ethers were easy to make and modify, which helped motivate the broad exploration of their recognition chemistry through the 1970s. At the same time, a guest-driven approach emerged in which ion receptors were designed for binding specific guests using the principles of complementarity and preorganization. Irrespective of whether the emphasis was placed on either

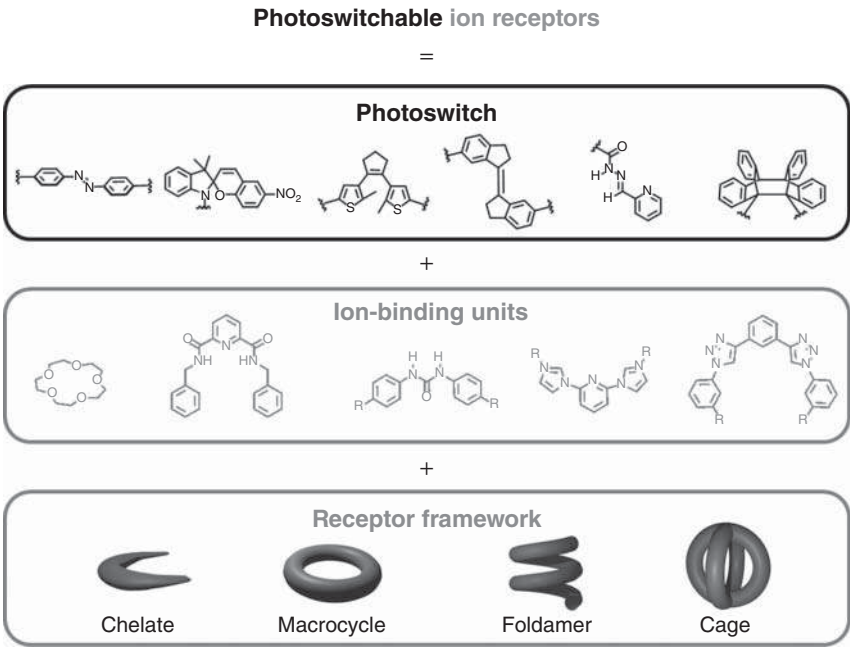


**Figure 24.2** Summary of the design elements needed for photoswitchable ion receptors.

the receptor- or guest-driven design approach, synthetic elaboration was key to understanding ion recognition at a comprehensive level. This deep connection to synthesis paved the way for the facile incorporation of other functionalities, such as photoswitches, into ion-binding receptors.

One way to look at the design of photoswitchable ion receptors (Figure 24.2) is the unification of a photoswitch with ion-binding units inside a specific receptor framework. The range of photoswitches is broad and is laid out across the various chapters in this book. The ion-binding units are identified according to the dictates of the ion being bound. The selection of a receptor framework requires an awareness of how the photoswitch can alter the ion-binding strength of the entire system.

To switch the binding affinities of ion receptors, a photoswitch is incorporated strategically within the structure. Irradiating the photoswitch to toggle it between its two photostationary states (PSSs) produces receptor structures with different supramolecular profiles. These altered profiles can lead to differences in the binding units (e.g. neutral/charged, Figure 24.3a), shape and size (e.g. Figure 24.3b), preorganization, complementarity, or cooperativity.

The photodriven changes in structure (Figure 24.4a) therefore produce differences in binding affinities between the ON-state ($K_{ON}$) and OFF-state ($K_{OFF}$). Most of the studies in this area have explored different ways to alter the supramolecular profiles resulting in measurable affinity swings ($K_{ON}/K_{OFF}$). In addition, the swings in the affinity ratios between states that were initially measured (Figure 24.4b) can be enhanced (Figure 24.4c–e) by either making the ON-state stronger, the OFF-state

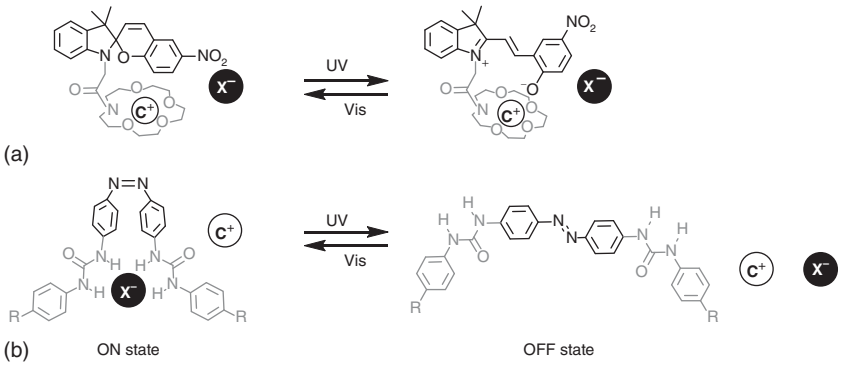


**Figure 24.3** (a) A crown ether is appended onto a spiropyran for photoswitchable metal recognition. (b) Urea-appended azobenzene for anion capture and release. Source: Based on Choi et al. [11].

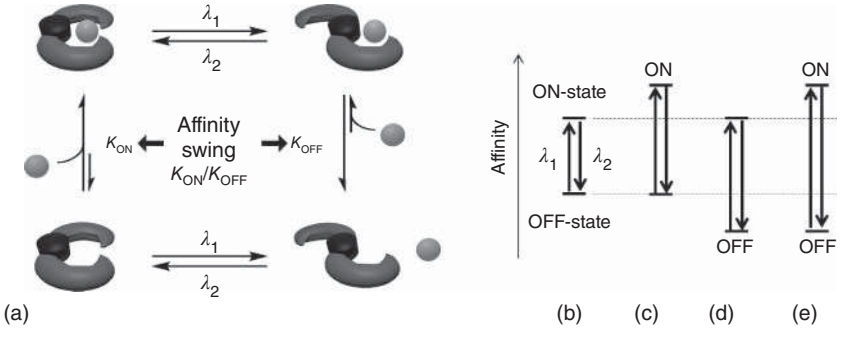


**Figure 24.4** (a) Photoswitchable ion receptors have a high binding ON-state (at left) that can be switched with light into a low binding OFF-state (at right). The ratio of affinities define the affinity swing. (b) Initial swings can be enhanced by (c) enhancing the ON-state, (d) weakening the OFF-state, or (e) strengthening the ON-state and weakening the OFF-state.

weaker, or a combination of the two. Optimizing the behavior of one or both states is challenging. As a result, only a few case studies have emerged, and thus understanding how to control the underlying chemistry of both molecular switching and ion recognition remains outstanding. Examples of these approached have been undertaken (*vide infra*) [12, 13].

Many photoresponsive receptors used for cation recognition consist of macrocycles (e.g. crown ethers and azomacrocycles) and chelates containing electron donors [14–18]. The aforementioned examples can be found in Kitao's [19, 20] (Figure 24.3a), Yokoyama's [21] crown ether appended spiropyrans, Kawai's [22] and Irie's [23, 24] use of crown ether diarylethenes, Valtancoli's azobenzene azomacrocycles [25], and Kato's thioindigo ethylenedioxy chelate [26]. Historically, the extensive work done on cation recognition was followed by a substantial growth of interest from 2010 onwards on photoswitchable anion receptors. As a consequence, these studies constitute the major topic of this chapter.

Capturing anions is more challenging than cations. Contrary to cations, which are generally spherical in size, show high charge densities and can support bonds with partial covalency, anions vary greatly in size and shape, are charge diffuse, can be pH sensitive, and rarely display covalency [27]. To overcome the greater challenges for recognition posed by anions, strong hydrogen-bond donors, such as the NH groups in urea, are commonly incorporated into receptors [28–30] (e.g. Figure 24.3b [11]). While OH hydrogen-bond donors from alcohols are typically stronger than NH donors, their use is rare [31]. Non-traditional CH hydrogen bonding, e.g. from 1,2,3-triazoles [32], and halogen bonding [33] have emerged recently. Electrostatics have also been used from the early days. All of these motifs are available for strategic incorporation of photoswitches.

### 24.1.5 Motivations and Applications: Demonstrations Vs. Real-World Application

Ions play critical roles in our environment: cesium-137 is a major byproduct of uranium fission in radioactive waste [34], nitrates and phosphates enhance crop growth while their overuse also leads to eutrophication [35], and salt water covers nearly 71% of our planet with the amount of drinkable water at 1% and shrinking [36]. Therefore, there is a strong need to bind, sense, and manipulate ions for the sustainable maintenance and growth of the quality of life of the global community. Applications for cation capture emerged in the 1970s with crown ethers. With the slower growth of anion recognition, their applications are only now starting to get more attention [37]. The promise of photoresponsive receptors for cations or anions to have an impact in real-world applications is high owing to the clean, controllable, tunable, and non-byproduct generating character of light. This promise has led to proof-of-concept investigations of photoswitchable ion sensing [38, 39], exchange [40, 41], and transport [11].

## 24.2 Classes of Photoswitchable Receptors

### 24.2.1 Photoswitchable Chelates for Anion Binding

Ion recognition receptors come in the four broad classes: chelates, macrocycles, foldamers, and cages (Figure 24.2). Incorporation of a photoswitch into these receptors leads to tunable binding and selectivity. This chapter covers all four of these receptor classes and will include their combination with a wide range of photoswitches, including stiff-stilbene, azobenzene, spiropyran, dithienylethene, and acylhydrazone to name a few.

The first anion recognition photoresponsive chelate did not emerge until 2007 in which Shimaski and Shimmyozu designed a dihydroxy-binaphththyl-appended stiff-stilbene capable of binding chloride and dihydrogen phosphate [31]. However, it was not until 2010 that photoswitchable anion recognition receptors began to grow and with it came an interest in quantifying changes in selectivity and affinity swings (defined as the ratio of affinities for the ON and OFF states).

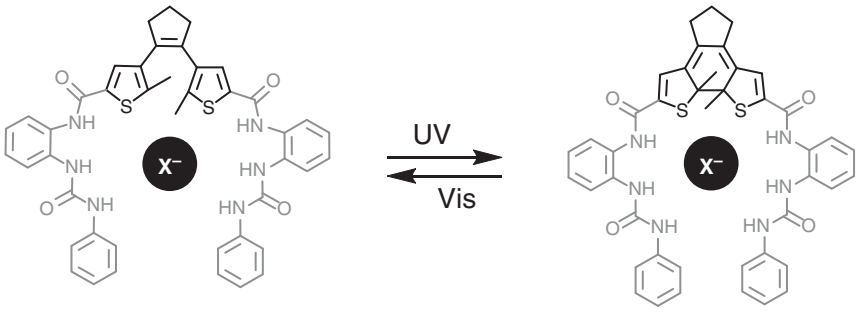


**Figure 24.5** An amide-urea-functionalized dithienylethene receptor for halide capture and release. Source: Li et al. [42].

In 2010, Li and Liu designed a urea-functionalized dithienylethene receptor for halide anion capture (Figure 24.5) [42]. The open-ring isomer forms a 1 : 1 complex with chloride and bromide with binding affinities of 68 and 14 $M^{-1}$, respectively. Irradiation with UV light causes the open-ring isomer to photocyclize to the closed-ring isomer with a 34% conversion yield. Energy minimization of the structures revealed that the closed-ring isomer had a larger cavity. This structural difference produced a modest decrease in halide binding from 68 to 58 $M^{-1}$ for chloride and 14 to 13 $M^{-1}$ for bromide. The anion-bound isomers can be photoisomerized to change binding affinity over 10 cycles without degradation. However, the affinity swings were modest at 1.2 and 1.1 for chloride and bromide, respectively.

To achieve higher-affinity swings compared to Li and Liu, Wezenberg and Feringa designed a photoswitch that upon irradiation changes the number of hydrogen-bonding contacts. Urea groups are recognized as strong NH hydrogen-bond donors for anion recognition, and their geometries offer shape-selective binding that is complementary to phosphates and acetates. Starting in 2014, Wezenberg and Feringa incorporated these recognition motifs into a photoswitchable stiff-stilbene chelate, which changes the number of NH$\cdots$$X^-$ contacts (Figure 24.6a) [43]. Affinity ratios of the stronger binding *cis*-isomer over the weaker binding *trans*-isomer were reported for tetrabutylammonium ($TBA^+$) salts of dihydrogen phosphate and acetate. The affinity ratios were 58 (7500 $M^{-1}$/130 $M^{-1}$) for dihydrogen phosphate and 18 (1300 $M^{-1}$/71 $M^{-1}$) for acetate in dimethyl sulfoxide (DMSO)-$d_6$/0.5% $H_2O$. Subsequent studies of the stiff-stilbene urea chelates investigated chiral phosphate recognition [44], the binding of three differently shaped anions ($Cl^-$, $H_2PO_4^-$, and $NO_3^-$) [45], and the control of rotary motion using chiral guests [46].

In 2019, Wezenberg and Feringa showed the use of intramolecular self-blockage within a stiff-stilbene urea chelate (Figure 24.6b) [13]. This work was undertaken to probe strategies to improve the affinity swings (Figure 24.4b–e). This elegant design contains a urea for NH$\cdots$$X^-$ hydrogen bonding on one end of the stiff-stilbene and a phosphate for intramolecular self-blockage of the binding site on the other. The anion-binding characteristics of the (*E*)-isomer, with R = Et and OEt, was

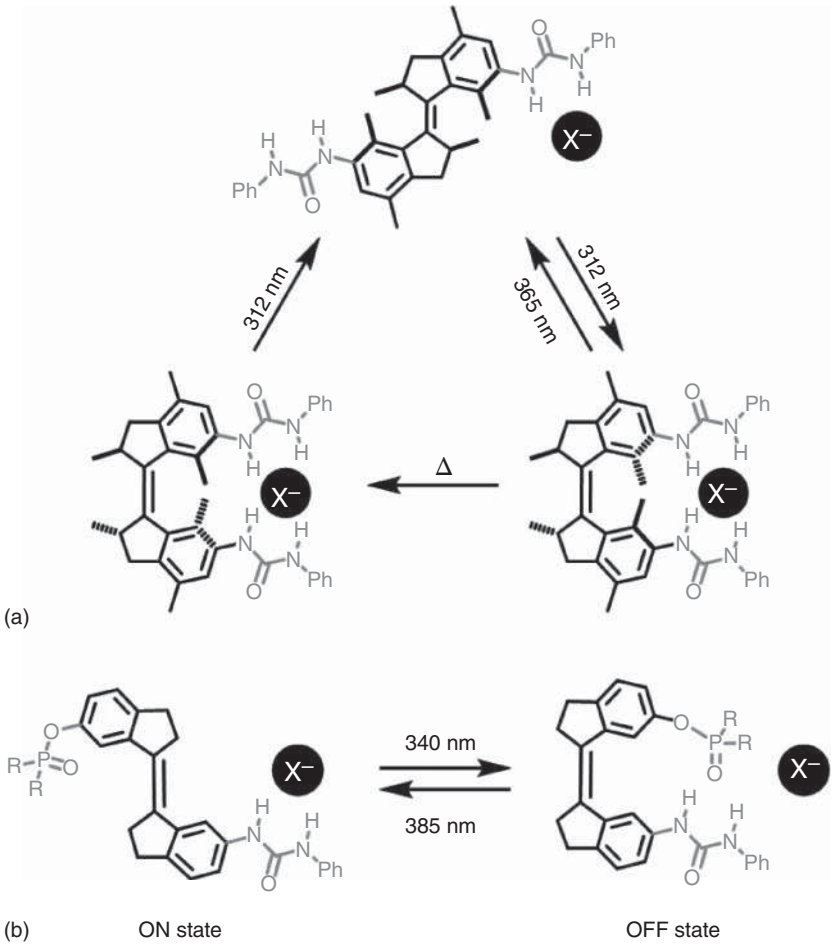


**Figure 24.6** (a) A light- and heat-responsive bis-urea-stiff-stilbene chelate for anion recognition. (b) A photoresponsive intramolecular self-blockage bis-urea chelate (R = Et and OEt). Source: (a) Wezenberg et al. [43], (b) de Jong et al. [13].

tested with $TBA^+$ salts of acetate, dihydrogen phosphate, and chloride. These guests showed binding affinities when R = Et of $K$ = 1500, 620, and 32 $M^{-1}$ and when R = OEt of $K$ = 1400, 720, and 30 $M^{-1}$, respectively in 0.5% $H_2O$ in DMSO. Irradiation of the (*E*)-isomer at 340 nm results in *E*/*Z* PSS ratios of 47 : 53 and 42 : 58 for R = Et and OEt. The corresponding anion affinities of the (*Z*)-isomer toward acetate, dihydrogen phosphate, and chloride were estimated to be 1200, 310, and 22 $M^{-1}$ (R = Et) and 840, 290, and 18 $M^{-1}$ (R = OEt). These modest changes in binding affinities result in low-affinity swings for acetate, dihydrogen phosphate, and chloride with ratios of 1.3, 2, and 1.5 (when R = Et), and 1.6, 2.5, and 1.7 (when R = OEt). Although the phosphate intramolecular self-blockage did not result in

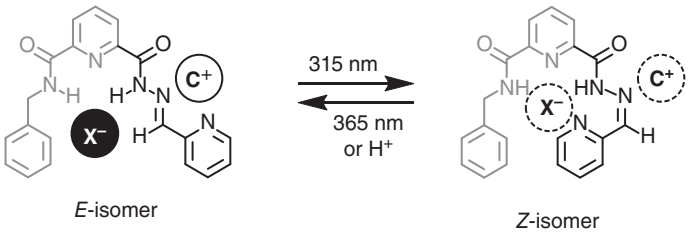


**Figure 24.7** A heteroditopic acylhydrazone chelate with anion and cation binding with the *E*-isomer and a weaker anion- and cation-binding site with the *Z*-isomer.

large affinity ratios, this self-blockage receptor is the first photoresponsive receptor to incorporate intramolecular competitive binding modulated by light.

Most ion chelates designed have been specific for either cations or anions. Kokan and Chmielewski [47] developed a system for generating switchable heteroditopic ion recognition. This was achieved using a 2-pyridyl acylhydrazone photoswitch and a bisamide for anion binding that is appended on a pyridine (Figure 24.7). Ion-pair binding of the (*E*)-isomer was tested using a combination of salts based on $TBA^+$, $Li^+$, $Na^+$, and $K^+$ paired with $Ph_4B^-$, $Cl^-$, $Br^-$, and $I^-$. Binding constants in acetonitrile (MeCN) revealed that binding strengths favored smaller cations ($Li^+ > Na^+ > K^+ > TBA^+$) and smaller anions ($Cl^- > Br^- > I^- > Ph_4B^-$) with LiCl having a large binding constant of $\sim 1\,700\,000\ M^{-1}$. Strong cooperativity between cation- and anion-binding events was observed. Irradiation with UV light results in the pyridine to change position and occupy the anion-binding pocket and to create a weaker cation-binding site (Figure 24.7). The modulation in the binding pocket is reminiscent of the self-blockage mode of affinity switching. Binding constants for the *Z*-isomer could not be determined on account of negligible chemical shift changes, and therefore no affinity ratios are reported. Reversible switching of *E* to *Z* using 315 nm irradiation followed by acid-catalyzed back isomerization showed improved switching cycles with near-quantitative conversion. This acylhydrazone provides a new class of reversible photoswitching chelate that can switch between the weaker binding OFF-state and stronger binding ON-state that is selective for size-matched ion pairs.

### 24.2.2 Transition-Metal Complexes as Chelates

Most photodriven changes leverage photoswitches that toggle between a stable state and a long-lived metastable state that is characterized by a change in structure. Less attention has been given to short-lived metastable states such as those that emerge using from photoinduced electron transfer. Inspired by seminal work in the 1970s that focused on the photorelease of chloride from platinum complexes [48] and photochemical release of ligands from chromium complexes [49, 50], Turlington and Meyer designed a transition-metal complex (Figure 24.8) that displays ligand-controlled chloride photorelease [51]. Here, the anion-binding chelate is defined by amides NH donors, bipyridine CH donors, and the proximal dicationic charge. When the complex is irradiated, the metal-to-ligand charge-transfer

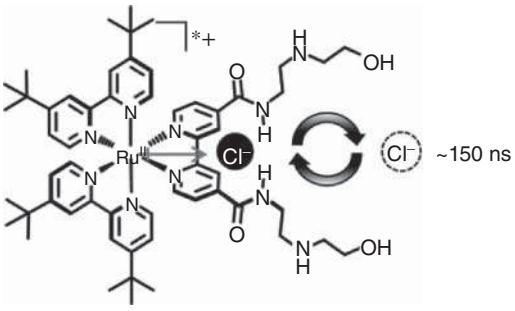


**Figure 24.8** Proposed excited-state structure of chromophore with dipole orientation pointed toward chloride.

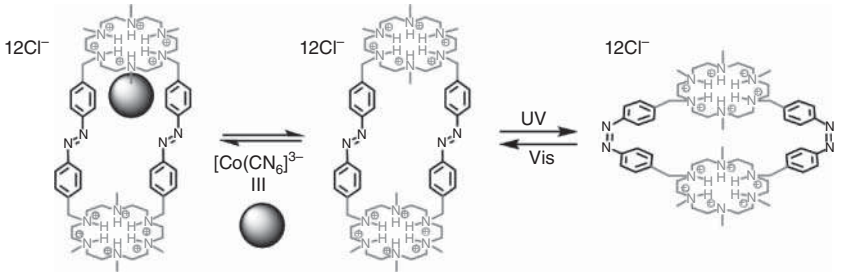


**Figure 24.9** A cylindrical macrocycle capable of binding $[Co(CN)_6]^{3-}$ and photoisomerizing between states. Source: Modified from Bencini et al. [53].

excited-state dipole is directed toward the binding site, resulting in an excited-state chloride release. Equilibrium constants between the ground and excited state varied by a factor of about 22 ($3\,900\,000\,M^{-1}/170\,000\,M^{-1}$) and led to a rapid photorelease and return of chloride in about 150 ns.

### 24.2.3 Macrocyclic Receptors

Macrocyclic receptors offer stronger binding compared to their more flexible chelate counterparts [52]. As a result, photoswitchable macrocycles for cation recognition dominated the field up to the early 2000s [2–5, 17–25]. Photoresponsive anion-binding macrocycles appeared with Bencini's cylindrical receptor in 2001, which contained two azocrown macrocycles appended onto two azobenzene motifs (Figure 24.9) [53]. Although anion capture and release was not tested, the free macrocycle was capable of photoisomerization from the *trans-trans* to *cis-trans* and *cis-cis* state as well as binding $[Co(CN)_6]^{3-}$. A few years later, macrocycles developed with the aid of guest-driven and receptor-driven design approaches. For guest-driven design, macrocycles were created to test the capture and release of larger anions, e.g. bis-carboxylates [54] and diaryl anions [55]. For receptor-driven design, anthracene was incorporated into an anion recognition receptor motif to alternate between a chelate and a macrocycle [56].

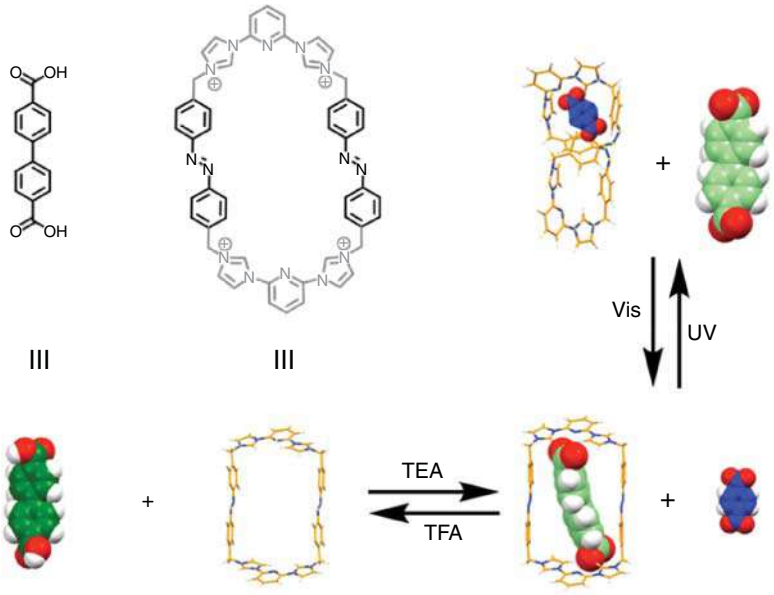


**Figure 24.10** An azobenzene-based Texas-sized box selective for large aryl dicarboxylates capable of guest capture and release via light, pH, and anion-responsiveness. Source: Chi et al. [55].

Most photoresponsive anion recognition motifs have involved selective binding to smaller spherical anions such as chloride or to anions as large as acetate and dihydrogen phosphate. Chi and Sessler designed a photoswitchable macrocycle that is selective for large organic anions (Figure 24.10) [55]. The azobenzene-based "Texas-sized box" is capable of binding diaryl dicarboxylates and releasing them upon photoirradiation, pH changes, or competitive titration with tetrabutylammonium chloride (TBACl). When the *trans-trans* isomer is irradiated with UV light, its cavity size gets smaller and the large dicarboxylate guest is expelled in favor of smaller aryl dicarboxylates (Figure 24.10). The guest can also be released by addition of trifluoroacetic acid, as well as by subsequent titration using excess TBACl. Anion recognition by this Texas-sized box can be controlled by two stimuli: light and chemical. It should be noted that reversible photoisomerization with UV light in DMSO to drive the *E* to *Z* conversion generates three isomers: *trans-trans*, *cis-trans*, and *cis-cis* in a 15%, 41%, and 44% ratio, respectively. This conversion is lower than the typical 80% seen for azobenzene [57]. Density functional theory (DFT) calculations reveal that the conversion is affected by the high stability of the *trans-trans* isomer.

Photoswitches, such as diarylethenes and spiropyrans, are most commonly incorporated into ion receptors on account of their near-quantitative conversions between open- and closed-ring isomers, their stability, and modular synthesis [58, 59]. Inspired by these photocyclizations, Rahaman and Bandyopadhyay created a photoresponsive ion receptor using bis-anthracene, which is known to undergo a reversible [4+4] photocyclization (Figure 24.11) [56]. The binding strength of the

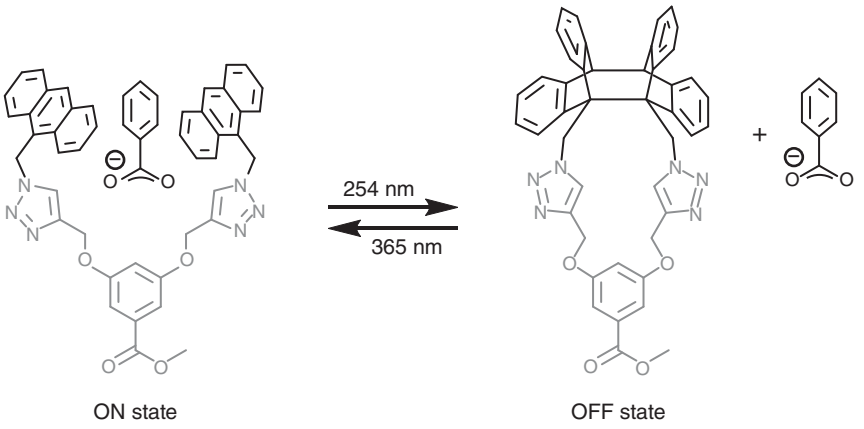


**Figure 24.11** Bis-anthracene receptor for benzoate capture and release. Source: Rahaman et al. [56].

open-ring receptor to various $TBA^+$ salts was tested, and it was discovered that the anthracene receptor had the strongest binding for benzoate ($K = 28\,600\ M^{-1}$, MeCN) in a 1 : 1 complexation. Furthermore, fluorescent quenching with benzoate caused a 13-fold reduction in emission intensity, the largest amongst the anions tested. When irradiated with UV light, a [4+4] cyclization of the bis-anthracene occurs. The cyclization lowers the flexibility of the receptor to create a more rigid cavity, and it also destroys the 14π system of the open-ring isomer. These changes in cavity size and electronic environment lead to a significantly lower binding constant for benzoate ($K = \ll 1\ M^{-1}$). The large differences in the binding affinities between the open and closed isomers result in a large affinity ratio of 1000 for benzoate. This receptor highlights the ability to switch between a flexible and rigid recognition motif.

### 24.2.4 Photoswitchable Foldamers

Photofoldamers are of interest because of their shape dynamic characteristics, allowing them to access either organized states with larger binding affinities or more flexible states with weaker binding. Incorporation of a photoswitchable motif into a helical foldamer bearing overlapping end groups was investigated by Khan and Hecht in 2006. They demonstrated that phenylene-ethynylene oligomers with a central azobenzene unit undergo conformational changes between a helix and random coil when irradiated with UV and visible light [60, 61]. A year after Hecht's azobenzene foldamers, Yashima designed a *para*-substituted azobenzene oligomer that assembles into a double helix by forming self-complementary amidinium-carboxylate hydrogen bonding (Figure 24.12) [62]. They observed 48% conversion of the *trans* to *cis* under light irradiation with complete recovery of the *trans* conformation by back isomerization. The demonstration of switchable helices provides a basis to translate this structural change into functions.

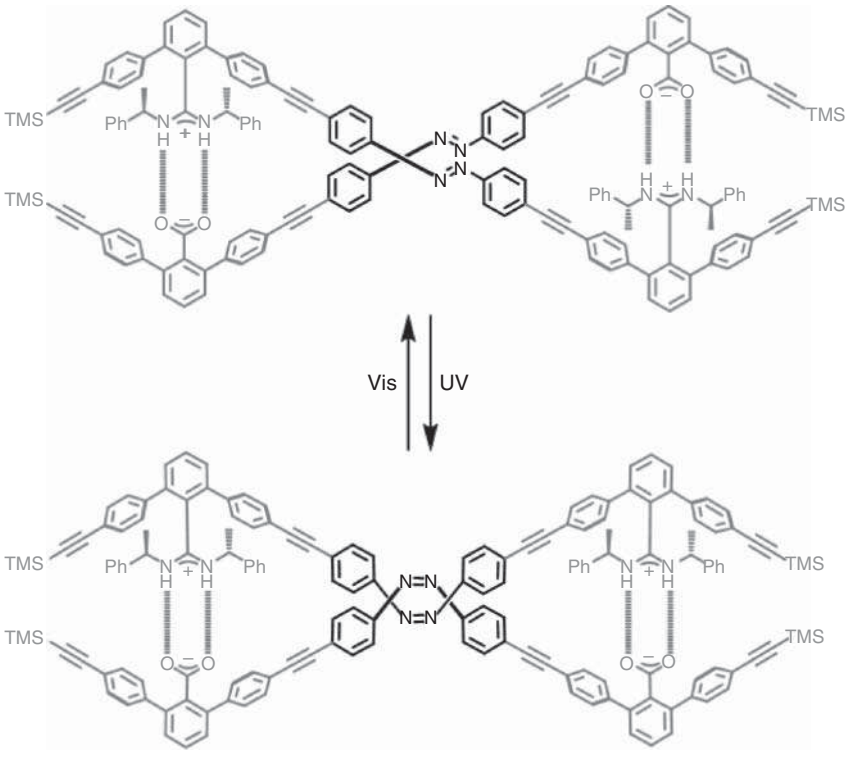


**Figure 24.12** Helical self-assembly of a chiral amidine-carboxylate-linked azobenzene oligomer. Source: Furusho et al. [62].

Wang and Jiang synthesized an aryl-triazole dimer bearing a central azobenzene motif. The oligomer uses CH···$X^-$ hydrogen bonding to stabilize anions (Figure 24.13) [63]. Anion-binding affinities were ranked $Cl^- > HSO_4^- > Br^- > I^- \approx NO_3^-$ for the *cis*-isomer. Affinity swings were found to be around two for $HSO_4^-$ and $NO_3^-$, around three for $I^-$, and four $Cl^-$ and $Br^-$. These swings are attributed to the change from a better-fitting cavity in the *cis*-isomer to a larger cavity in the *trans*-form.

In 2010 Hua and Flood designed a photoresponsive aryl-triazole photofoldamer with two azobenzene units at the ends of the oligomer (Figure 24.14a) [64]. In the visible PSS, stacking of three π units helps stabilize the helical conformation by solvophobic effects to enhance the chloride binding affinity. In the UV PSS, however, the foldamer adopts a random-coil conformation, weakening chloride binding (Figure 24.14b). An affinity swing of eightfold was recorded in acetonitrile. Cycling between visible and UV light allows for the capture and release of chloride over multiple cycles as evaluated in the conductivity of an electrolyte solution.

Modifications were undertaken to enhance affinity swings by using extended π surfaces and terminal hydrogen-bonding contacts to help create β-sheet-like hydrogen bonds within the photofoldamer (Figure 24.14c,d) [12]. Helical propensity in the ON-state was greatly increased with increasing the number of π contacts from

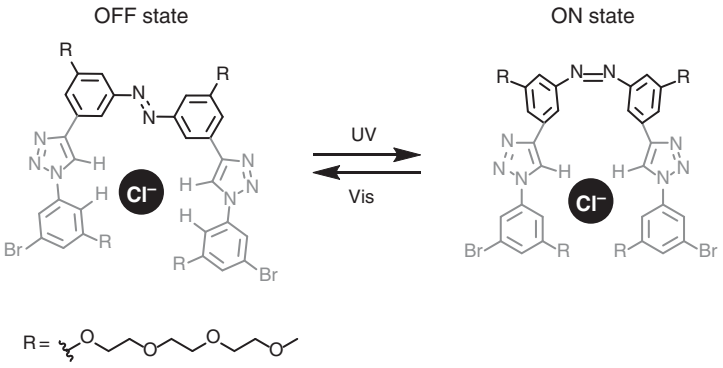


**Figure 24.13** Aryl-triazole photoresponsive foldamer capable of binding and releasing chloride. Source: Modified from Wang et al. [63].

three to five and using the interlocking hydrogen-bonding units. Enhanced helical stability was found to correlate with chloride binding strength. The anion-binding strength in 50% MeCN/THF was increased from 40 300 $M^{-1}$ for the original photofoldamer with three π–π stacks (Figure 24.14d, left), to 126 000 $M^{-1}$ for the photofoldamer with five π–π stacks (Figure 24.14d, middle), and 970 000 $M^{-1}$ for the β-sheet foldamer (Figure 24.14d, right). Helical organization of the anion-free foldamer was also enhanced using the β-sheet photofoldamer. Unsurprisingly, affinity swings were increased from 8-fold, to 17-fold, and up to 84-fold. This work shows how knowledge of the mechanism of affinity switching can be used as a tool to optimize the performance of the photoswitchable ion receptor. Herein, the stability of the ON-state was enhanced while the OFF-state was largely unchanged after the fashion of Figure 24.4c.

In a study of solvent effects, *ortho*-substituted azobenzene caps were used on an aryl-triazole foldamer to help create a solvent-excluded binding pocket for chloride (Figure 24.15a) [65]. Hydrophobic interactions were found to stabilize double-helix formation creating a putative solvent-free microenvironment inside the anion-bound cavity, helping enhance the chloride affinities; $6 \times 10^{13}\ M^{-2}$ in MeCN (Figure 24.15a). The double-helix stability was found to increase when water content was increased up to 50% $H_2O$ in MeCN and strong binding strength was retained ($\beta_2 = 9 \times 10^{12}\ M^{-2}$ in 50% $H_2O$). In this case, the extent of photoisomerization was poor.

More recently, Parks and Flood studied the recognition behavior of aryl-triazole photofoldamers with smaller and larger anions (Figure 24.15b) [66]. Smaller anions (<45 Å) were seen to produce single helices for the binding and release of anions. With larger anions (>45 Å), however, a chiral double-helical complex was formed that converts reversibly into an achiral single helix with UV light (Figure 24.15b). Size matching presumably occurs, whereby the foldamer will expand to accommodate larger anions resulting in a destabilizing of the single helix relative to the duplex. The OFF-state of the foldamer formed upon UV light irradiation resembles a random coil and, surprisingly, it showed no anion selectivity.

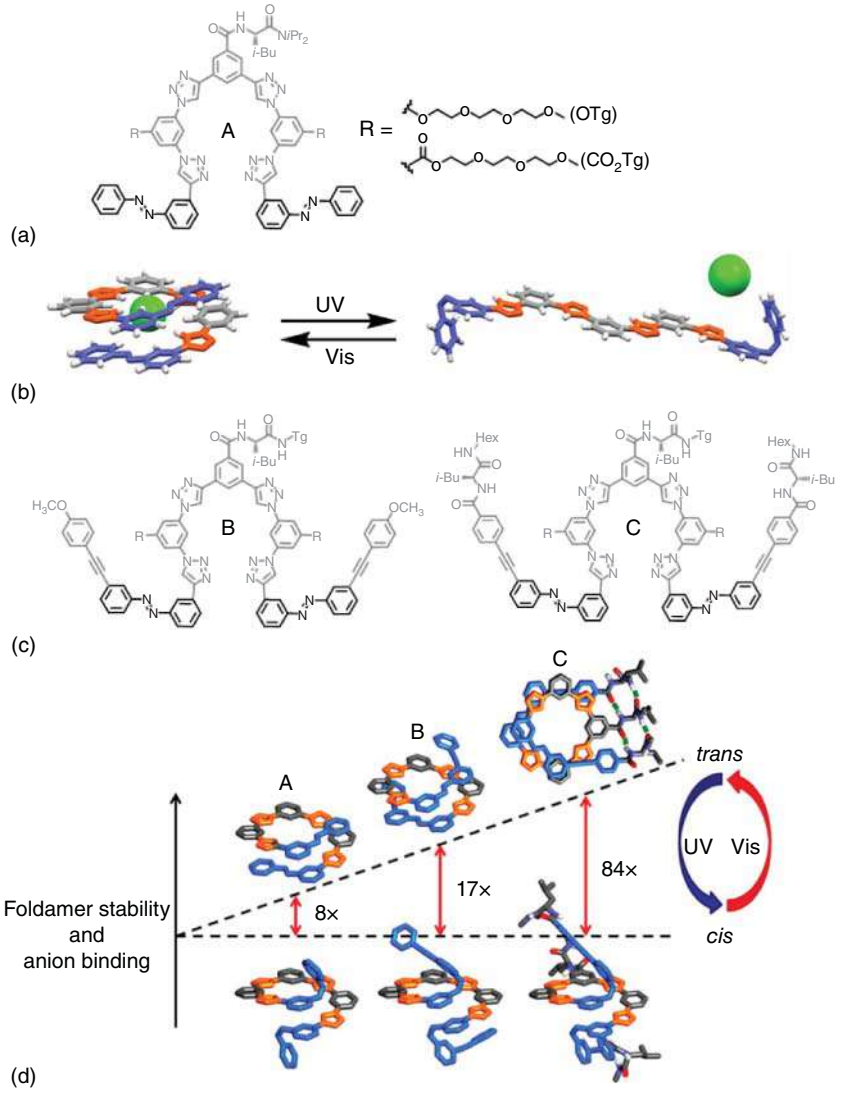


**Figure 24.14** (a) Aryl-triazole photofoldamer with terminal azobenzenes. (b) Photofoldamer for chloride capture and release. (c) Series of photofoldamers designed to enhance the affinity of the ON-state to produce larger affinity swings. (d) Interlocking hydrogen-bonding units and increasing π contacts strengthen foldamer stability and anion binding resulting in enhanced affinity swings. Source: (a) Hua and Flood [64], (c, d) Lee et al. [12].

Taken all together, the studies on these foldamer frameworks demonstrate the power of receptor-driven design. They also provide a growing understanding of the effects of the primary foldamer sequence, solvent, and anion size on the structures and binding strengths of switchable, anion-binding photofoldamers.

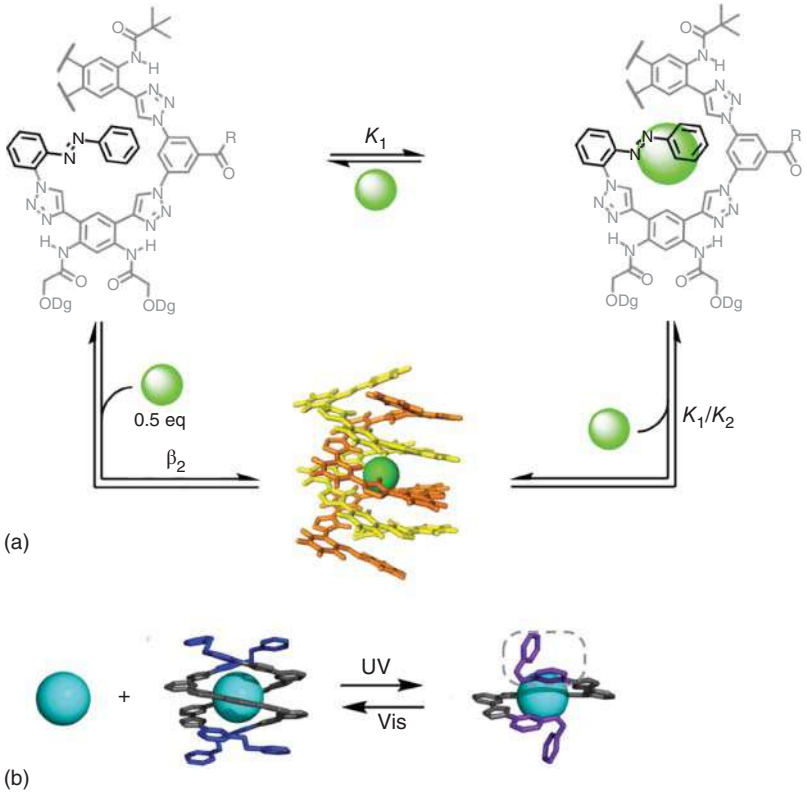


**Figure 24.15** (a) Equilibria associated with single and double-helix formation around chloride using a solvent-capped photofoldamer. (b) Anion recognition behavior of photofoldamers: double-to-single helix switching. Source: (a) Hua et al. [65], (b) Parks et al. [66].

Another interesting facet of photofoldamers is their chirality. Analogous to proteins and DNA, foldamers with chiral moieties in their backbones can form enantiomeric helices. To study photo-switchable chirality, Zhao and Feringa designed stiff-stilbene appended oligobipyridyl ligands (L, Figure 24.16) capable of photoresponsive self-assembly into a double helicate in the presence of copper [67]. The (*P*,*P*)-*trans*-isomer of the rotary motor forms an oligomeric array (*P/M* for plus/minus helical twist sense). Irradiation with UV light results in the (*M*,*M*)-*cis*-isomer where the oligobipyridine ligands are brought into close proximity leading to *P′* double-helicate formation with copper. Conversion of the (*P*,*P*)-*trans* to the (*M*,*M*)-*cis* form occurs with high selectivity (>90%). Helical inversion is dependent on the rotary motion of the stiff-stilbene rotary switch, which is also the determinant of chirality for the helicate. The less stable (*M*,*M*)-*cis* form is then converted to the stable (*P*,*P*)-*cis* isomer that creates an *M′* helicate in a >90/10 ratio. Understanding the mechanisms of assembly/disassembly and attaining photochemical control of chirality is important for use of ion receptors for chiral guest recognition, catalysis, and as molecular motors.

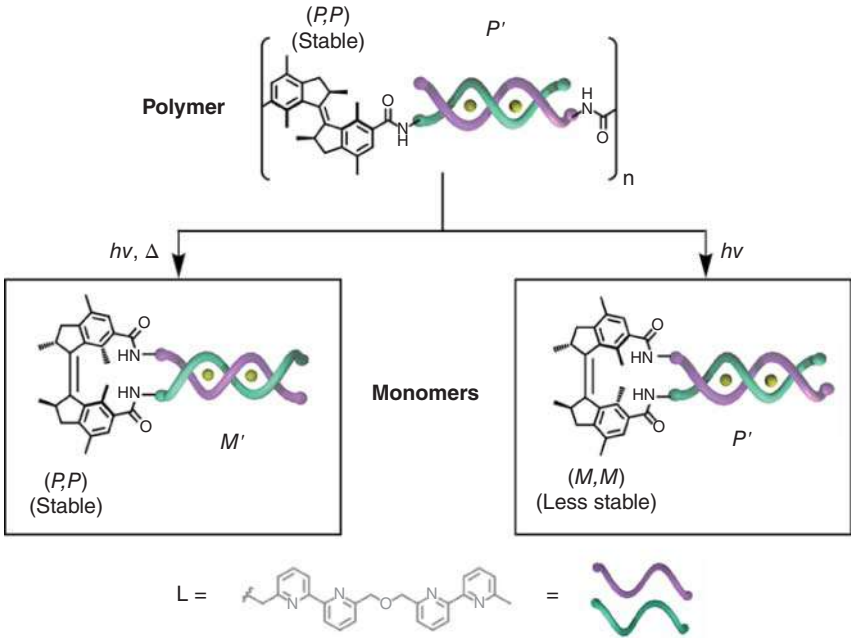


**Figure 24.16** Stiff-stilbene helicate that displays chiral inversion with cation binding.

### 24.2.5 Photoactive Cages

Among the wide range of photoresponsive chelates, macrocycles, and foldamers, there exists only a few photoswitchable cages [68]. Although three-dimensional ion receptors have existed since the early days of supramolecular chemistry, it was not until 2010 that Liu and Huang designed the first photoresponsive cage using an azobenzene-bridged cryptand (Figure 24.17) [69]. In a solution of MeCN, the thermodynamically stable *trans*-isomer is preferred in a 78:22 *trans*-to-*cis* ratio. When the cation-free receptor is irradiated with UV light for one minute, the ratio changes to 57 : 43 (*trans*/*cis*). However, when a solution of the *trans*-cryptand cage with the guest 2,7-diazapyrenium ($DAP^{2+}$) is photoisomerized, the *trans*/*cis* ratio is enhanced to 48 : 52. The *trans*–isomer is unable to bind $DAP^{2+}$; therefore, the binding gets turned on by formation of the *cis*–isomer. The bigger cavity shows an affinity of 330 000 $M^{-1}$ (MeCN) as a result of better π–π stacking between the host and guest. Since $DAP^{2+}$ is fluorescent, photocontrolled host–guest behavior can be correlated to restoration of the fluorescence upon formation of the *trans*–isomer and free $DAP^{2+}$. Fluorescence is then decreased in the *cis* isomer, with emergence of a charge-transfer transition between host and guest. Several cycles of this fluorescence switching experiment can be done to visually observe the ON/OFF states.

Li and Clever designed a photoresponsive coordination cage capable of chiral guest–host induction (Figure 24.18) [70]. The palladium-driven dithienylethene coordination cage $[Pd_2L_4]$ self-assembles without a guest. As a result, the cage can be studied both with and without anionic guests. When an achiral anion is

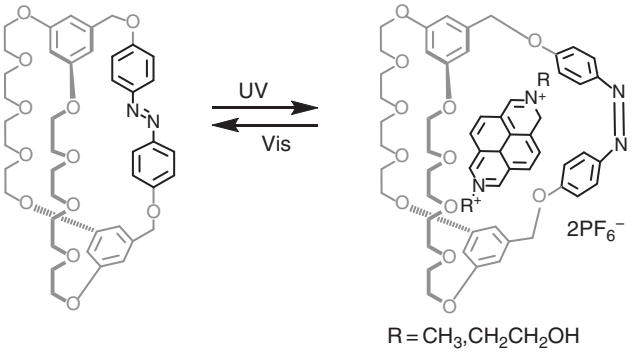


**Figure 24.17** Azobenzene-bridged cryptand cation recognition cage. Source: Liu et al. [69].

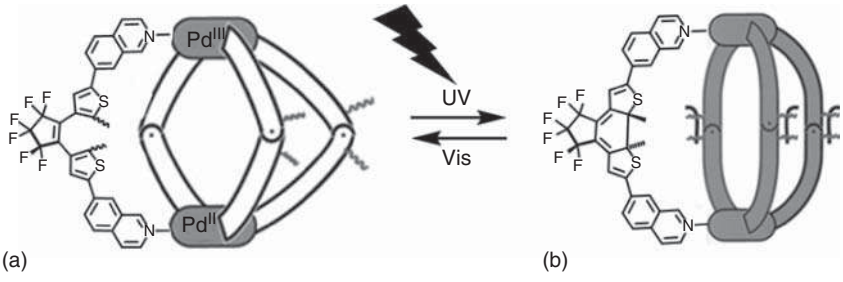


**Figure 24.18** (a) The open form of the cage involves coordination by four dithienylethene-based ligands. It can bind anionic guests, and upon irradiation with UV light it produces (b) cages constituted by dithienylethene-based ligands in their closed states. Encapsulation of a chiral guest with the open cage induces *P* or *M* helical chirality, which is retained after irradiation with UV light. This photoswitching produces a conformational change to the cage's shape and exclusion of guest. Source: Li et al. [70].

added to the cage composed of the open form of the dithienylethene photoswitch, equal amounts of *M* and *P* diastereomers are observed at ambient temperature. Conversion between the open and closed forms of the photoswitchable cage can occur by UV irradiation of the dithienylethene ligand with or without the bound anion. Upon addition of the chiral camphor sulfonate anion as guest to the open form of the cage, a Cotton effect is observed indicating chiral induction from the guest to the host. In this case, binding affinities were unable to be determined. The degree of chiral information transfer was found to be dependent on the temperature and guest's concentration. When the anion-bound and open-form of the cage is irradiated with UV light or a nonchiral benzene-1,4-disulfonate guest is added, the chiral anionic guest is expelled. Interestingly, chiral information is still retained in the guest-free closed-form cage with enantiomeric excess of around 25%.

## 24.3 Conclusions

The field of photoresponsive ion receptors has seen substantial growth since Shinkai's early butterfly crown ethers, particularly in the recent exploration of

photoswitchable anion recognition. Receptor-driven design of these functional molecules has led to a formative understanding of the possible mechanisms that enhance affinity swings. These have included conformational changes, changes in the size of the binding cavity, use of intramolecular self-blockage, changes to terminal hydrogen bonding, use of allosteric control over binding-site preorganization, and distal photocyclization to compress binding pockets. These efforts have also provided insights into helical self-assembly, chiral induction, the capture of larger anions derived from aromatic subunits, heteroditopic ion-pair binding, and solvent exclusion. Despite these advances, the field is still in its infancy. More work is needed to help establish the design principles that can produce the specific binding affinities in either of the two ON/OFF states, to achieve target affinity swings $K_{ON}/K_{OFF}$, and to develop a means to optimize these properties across a homologous series of receptors. Photoresponsive ion receptors have seen proof-of-concept demonstrations of sensing and ion transport with many more areas of potential application in the future, such as ion remediation, catalysis, and optogenetics.

## Acknowledgments

We appreciate and acknowledge support by the Chemical Sciences, Geosciences, and Biosciences Division of the Basic Energy Sciences Program of the U.S. Department of Energy Office of Science (DE-FG02-09ER16068).

## References

1 Schobert, B. and Lanyi, J.K. (1982). Halorhodopsin is a light-driven chloride pump. *J. Biol. Chem.* 257: 306–313.
2 Shinkai, S., Ogawa, T., Nakaji, T. et al. (1979). Photocontrolled extraction ability of azobenzene-bridged azacrown ether. *Tetrahedron Lett.* 20: 4569–4572.
3 Shinkai, S., Shigematsu, K., Kusano, Y., and Manabe, O. (1981). Photoresponsive crown ethers. Part 3. Photocontrol of ion extraction and ion transport by several photofunctional bis(crown ethers). *J. Chem. Soc. Perkin Trans.* 1: 3279–3283.
4 Shinkai, S., Nakaji, T., Ogawa, T. et al. (1981). Photoresponsive crown ethers. 2. Photocontrol of ion extraction and ion transport by a bis(crown ether) with a butterfly-like motion. *J. Am. Chem. Soc.* 103: 111–115.
5 Shinkai, S., Nakaji, T., Nishida, Y. et al. (1980). Photoresponsive crown ethers. 1. *Cis-trans* isomerism of azobenzene as a tool to enforce conformational changes of crown ethers and polymers. *J. Am. Chem. Soc.* 102: 5860–5865.
6 Pedersen, C.J. (1967). Cyclic polyethers and their complexes with metal salts. *J. Am. Chem. Soc.* 89: 7017–7036.
7 Park, C.H. and Simmons, H.E. (1968). Macrobicyclic amines. III. Encapsulation of halide ions by in,in-1,(k + 2)-diazabicyclo[k.l.m.]alkane ammonium ions. *J. Am. Chem. Soc.* 90: 2431–2432.

**8** Dietrich-Buchecker, C.O., Sauvage, J.P., and Kintzinger, J.P. (1983). Une Nouvelle Famille de Molecules: Les Metallo-catenanes. *Tetrahedron Lett.* 24: 5095–5098.

**9** Dietrich-Buchecker, C.O., Sauvage, J.P., and Kern, J.M. (1984). Templated synthesis of interlocked macrocyclic ligands: the catenands. *J. Am. Chem. Soc.* 106: 3043–3045.

**10** Collin, J.-P., Kern, J.-M., Raehm, L., and Sauvage, J.-P. (2008). Metallo-rotaxanes and catenanes as redox switches: towards molecular machines and motors. In: *Molecular Switches* (Eds. Ben L. Feringa and Wesley R. Browne), 249–280.

**11** Choi, Y.R., Kim, G.C., Jeon, H.-G. et al. (2014). Azobenzene-based chloride transporters with light-controllable activities. *Chem. Commun.* 50: 15305–15308.

**12** Lee, S., Hua, Y., and Flood, A.H. (2014). β-sheet-like hydrogen bonds interlock the helical turns of a photoswitchable foldamer to enhance the binding and release of chloride. *J. Org. Chem.* 79: 8383–8396.

**13** de Jong, J., Feringa, B.L., and Wezenberg, S.J. (2019). Light-modulated self-blockage of a urea binding site in a stiff-stilbene based anion receptor. *ChemPhysChem* 20: 3306–3310.

**14** Tsien, R.Y. and Zucker, R.S. (1986). Control of cytoplasmic calcium with photolabile tetracarboxylate 2-nitrobenzhydrol chelators. *Biophys. J.* 50: 843–853.

**15** Kaplan, J.H. and Ellis-Davies, G.C. (1988). Photolabile chelators for the rapid photorelease of divalent cations. *Proc. Natl. Acad. Sci. U.S.A.* 85: 6571–6575.

**16** Collins, G.E., Choi, L.-S., Ewing, K.J. et al. (1999). Photoinduced switching of metal complexation by quinolinospiropyranindolines in polar solvents. *Chem. Commun.* (4): 321–322.

**17** Pipoosananakaton, B., Sukwattanasinitt, M., Jaiboon, N. et al. (2000). Preparation of new azobenzene crown ether *p-tert*-butylcalix[4]arenes and their roles as switchable ionophores for Na+ and K+ ions. *Tetrahedron Lett.* 41: 9095–9100.

**18** Fedorova, O.A., Gromov, S.P., Pershina, Y.V. et al. (2000). Novel azacrown ether-containing spiro[indoline-2,3′-naphthoxazines]: design, synthesis and cation-dependent photochromism. *J. Chem. Soc. Perkin Trans.* 2: 563–570.

**19** Inouye, M., Ueno, M., Tsuchiya, K. et al. (1992). Alkali-metal cation recognition induced isomerization of spirobenzopyrans and spironaphthoxazins possessing a crown ring as a recognition site: multifunctional artificial receptors. *J. Org. Chem.* 57: 5377–5383.

**20** Inouye, M., Ueno, M., Kitao, T., and Tsuchiya, K. (1990). Alkali metal recognition induced isomerization of spiropyrans. *J. Am. Chem. Soc.* 112: 8977–8979.

**21** Kimura, K., Yamashita, T., and Yokoyama, M. (1992). Syntheses, cation complexation, isomerization and photochemical cation-binding control of spirobenzopyrans carrying a monoazacrown moiety at the 8-position. *J. Chem. Soc. Perkin Trans.* 2: 613–619.

**22** Kawai, S.H. (1998). Photochromic bis(monoaza-crown ether)s. alkali-metal cation complexing properties of novel diarylethenes. *Tetrahedron Lett.* 39: 4445–4448.

**23** Takeshita, M. and Irie, M. (1998). Photoresponsive cesium ion tweezers with a photochromic dithienylethene. *Tetrahedron Lett.* 39: 613–616.


**24** Takeshita, M. and Irie, M. (1998). Photoresponsive tweezers for alkali metal ions. Photochromic diarylethenes having two crown ether moieties. *J. Org. Chem.* 63: 6643–6649.

**25** Bencini, A., Alexandra Bernardo, M., Bianchi, A. et al. (1998). Modulation of the ligational properties of a new cylindrical macrotricycle by coupling of photochemical- and pH-switching properties. *J. Chem. Soc. Perkin Trans.* 2: 413–418.

**26** Irie, M. and Kato, M. (1985). Photoresponsive molecular tweezers. Photoregulated ion capture and release using thioindigo derivatives having ethylenedioxy side groups. *J. Am. Chem. Soc.* 107: 1024–1028.

**27** Beer, P.D. and Gale, P.A. (2001). Anion recognition and sensing: the state of the art and future perspectives. *Angew. Chem. Int. Ed.* 40: 486–516.

**28** Dąbrowa, K., Niedbała, P., and Jurczak, J. (2014). Anion-tunable control of thermal Z→E isomerisation in basic azobenzene receptors. *Chem. Commun.* 50: 15748–15751.

**29** Dąbrowa, K. and Jurczak, J. (2017). Tetra-(*meta*-butylcarbamoyl)azobenzene: a rationally designed photoswitch with binding affinity for oxoanions in a long-lived Z-state. *Org. Lett.* 19: 1378–1381.

**30** Dąbrowa, K., Niedbała, P., and Jurczak, J. (2016). Engineering light-mediated bistable azobenzene switches bearing urea *d*-aminoglucose units for chiral discrimination of carboxylates. *J. Org. Chem.* 81: 3576–3584.

**31** Shimasaki, T., Kato, S.-i., Ideta, K. et al. (2007). Synthesis and structural and photoswitchable properties of novel chiral host molecules: axis chiral 2,2′-dihydroxy-1,1′-binaphthyl-appended stiff-stilbene1. *J. Org. Chem.* 72: 1073–1087.

**32** McDonald, K.P., Hua, Y., and Flood, A.H. (2010). 1,2,3-Triazoles and the expanding utility of charge neutral CH···anion interactions. In: *Anion Recognition in Supramolecular Chemistry* (eds. P.A. Gale and W. Dehaen), 341–366. Berlin Heidelberg: Springer.

**33** Brown, A. and Beer, P.D. (2016). Halogen bonding anion recognition. *Chem. Commun.* 52: 8645–8658.

**34** Rauwel, P. and Rauwel, E. (2019). Towards the extraction of radioactive cesium-137 from water via graphene/CNT and nanostructured prussian blue hybrid nanocomposites: a review. *Nanomaterials* 9: 682.

**35** Chouyyok, W., Wiacek, R.J., Pattamakomsan, K. et al. (2010). Phosphate removal by anion binding on functionalized nanoporous sorbents. *Environ. Sci. Technol.* 44: 3073–3078.

**36** Al-Abri, M., Al-Ghafri, B., Bora, T. et al. (2019). Chlorination disadvantages and alternative routes for biofouling control in reverse osmosis desalination. *npj Clean Water* 2: 2.

**37** Busschaert, N., Caltagirone, C., Van Rossom, W., and Gale, P.A. (2015). Applications of supramolecular anion recognition. *Chem. Rev.* 115: 8038–8155.

**38** Sumiya, S., Doi, T., Shiraishi, Y., and Hirai, T. (2012). Colorimetric sensing of cyanide anion in aqueous media with a fluorescein–spiropyran conjugate. *Tetrahedron* 68: 690–696.


**39** Lee, G.W., Kim, N.-K., and Jeong, K.-S. (2010). Synthesis of biindole–diazo conjugates as a colorimetric anion receptor. *Org. Lett.* 12: 2634–2637.

**40** Mistlberger, G., Xie, X., Pawlak, M. et al. (2013). Photoresponsive ion extraction/release systems: dynamic ion optodes for calcium and sodium based on photochromic spiropyran. *Anal. Chem.* 85: 2983–2990.

**41** Soberats, B., Uchida, E., Yoshio, M. et al. (2014). Macroscopic photocontrol of ion-transporting pathways of a nanostructured imidazolium-based photoresponsive liquid crystal. *J. Am. Chem. Soc.* 136: 9552–9555.

**42** Li, Z., Zhang, C., Ren, Y. et al. (2011). Amide- and urea-functionalized dithienylethene: synthesis, photochromism, and binding with halide anions. *Org. Lett.* 13: 6022–6025.

**43** Wezenberg, S.J., Vlatković, M., Kistemaker, J.C.M., and Feringa, B.L. (2014). Multi-state regulation of the dihydrogen phosphate binding affinity to a light- and heat-responsive bis-urea receptor. *J. Am. Chem. Soc.* 136: 16784–16787.

**44** Vlatkovic, M., Feringa, B.L., and Wezenberg, S.J. (2016). Dynamic inversion of stereoselective phosphate binding to a bisurea receptor controlled by light and heat. *Angew. Chem. Int. Ed.* 55: 1001–1004.

**45** Wezenberg, S.J. and Feringa, B.L. (2017). Photocontrol of anion binding affinity to a bis-urea receptor derived from stiff-stilbene. *Org. Lett.* 19: 324–327.

**46** Wezenberg, S.J. and Feringa, B.L. (2018). Supramolecularly directed rotary motion in a photoresponsive receptor. *Nat. Commun.* 9: 7.

**47** Kokan, Z. and Chmielewski, M.J. (2018). A photoswitchable heteroditopic ion-pair receptor. *J. Am. Chem. Soc.* 140: 16010–16014.

**48** Wright, R.C. and Laurence, G.S. (1972). Production of platinum(III) by flash photolysis of $PtCl_6^{2-}$. *J. Chem. Soc. Chem. Commun.* (3): 132–133.

**49** Wong, C. and Kirk, A. (1974). Chloride quantum yields from photolysis of chloropentammine and chloropentakisalkylamino chromium(III) complexes. *Can. J. Chem.* 52: 3384–3386.

**50** Adamson, A.W. (1967). Photochemistry of complex ions. IV. Role of quartet excited states in the photochemistry of chromium(III) complexes. *J. Phys. Chem.* 71: 798–808.

**51** Turlington, M.D., Troian-Gautier, L., Sampaio, R.N. et al. (2018). Ligand control of supramolecular chloride photorelease. *Inorg. Chem.* 57: 5624–5631.

**52** Hua, Y., Ramabhadran, R.O., Karty, J.A. et al. (2011). Two levels of conformational pre-organization consolidate strong CH hydrogen bonds in chloride–triazolophane complexes. *Chem. Commun.* 47: 5979–5981.

**53** Bencini, A., Bianchi, A., Giorgi, C. et al. (2001). Photochemical- and pH-switching properties of a new photoelastic ligand based upon azobenzene. Basicity and anion binding. *Supramol. Chem.* 13: 277–285.

**54** Cafeo, G., Kohnke, F.H., Mezzatesta, G. et al. (2015). Host–guest chemistry of a bis-calix[4]pyrrole derivative containing a *trans*/*cis*-switchable azobenzene unit with several aliphatic bis-carboxylates. *Chem. Eur. J.* 21: 5323–5327.

**55** Chi, X., Cen, W., Queenan, J.A. et al. (2019). Azobenzene-bridged expanded "Texas-sized" box: a dual-responsive receptor for aryl dianion encapsulation. *J. Am. Chem. Soc.* 141: 6468–6472.


**56** Rahaman, S.A., Hossain, M.S., Baburaj, S. et al. (2019). A phototunable anion receptor for C–H· · ·X interactions with benzoate anions. *Org. Biomol. Chem.* 17: 5153–5160.

**57** Bandara, H.M.D. and Burdette, S.C. (2012). Photoisomerization in different classes of azobenzene. *Chem. Soc. Rev.* 41: 1809–1825.

**58** Fukaminato, T., Ishida, S., and Métivier, R. (2018). Photochromic fluorophores at the molecular and nanoparticle levels: fundamentals and applications of diarylethenes. *NPG Asia Mater.* 10: 859–881.

**59** Klajn, R. (2014). Spiropyran-based dynamic materials. *Chem. Soc. Rev.* 43: 148–184.

**60** Khan, A., Kaiser, C., and Hecht, S. (2006). Prototype of a photoswitchable foldamer. *Angew. Chem. Int. Ed.* 45: 1878–1881.

**61** Khan, A. and Hecht, S. (2006). Towards photocontrol over the helix–coil transition in foldamers: synthesis and photoresponsive behavior of azobenzene-core amphiphilic oligo(*meta*-phenylene ethynylene)s. *Chem. Eur. J.* 12: 4764–4774.

**62** Furusho, Y., Tanaka, Y., Maeda, T. et al. (2007). Photoresponsive double-stranded helices composed of complementary strands. *Chem. Commun.* (30): 3174–3176.

**63** Wang, Y., Bie, F., and Jiang, H. (2010). Controlling binding affinities for anions by a photoswitchable foldamer. *Org. Lett.* 12: 3630–3633.

**64** Hua, Y. and Flood, A.H. (2010). Flipping the switch on chloride concentrations with a light-active foldamer. *J. Am. Chem. Soc.* 132: 12838–12840.

**65** Hua, Y., Liu, Y., Chen, C.-H., and Flood, A.H. (2013). Hydrophobic collapse of foldamer capsules drives picomolar-level chloride binding in aqueous acetonitrile solutions. *J. Am. Chem. Soc.* 135: 14401–14412.

**66** Parks, F.C., Liu, Y., Debnath, S. et al. (2018). Allosteric control of photofoldamers for selecting between anion regulation and double-to-single helix switching. *J. Am. Chem. Soc.* 140: 17711–17723.

**67** Zhao, D., van Leeuwen, T., Cheng, J., and Feringa, B.L. (2017). Dynamic control of chirality and self-assembly of double-stranded helicates with light. *Nat. Chem.* 9: 250–256.

**68** Wezenberg, S.J. (2020). Light-switchable metal-organic cages. *Chem. Lett.* 49: 609–615.

**69** Liu, M., Yan, X., Hu, M. et al. (2010). Photoresponsive host–guest systems based on a new azobenzene-containing crytpand. *Org. Lett.* 12: 2558–2561.

**70** Li, R.-J., Holstein, J.J., Hiller, W.G. et al. (2019). Mechanistic interplay between light switching and guest binding in photochromic [Pd2Dithienylethene4] coordination cages. *J. Am. Chem. Soc.* 141: 2097–2103.


# 25 Molecular Switches in Light-Responsive Liquid-Crystalline Polymer Actuators

Albert P. H. J. Schenning, Hong Yang, Sebastian Fredrich, and Li Liu

**Photochromism**

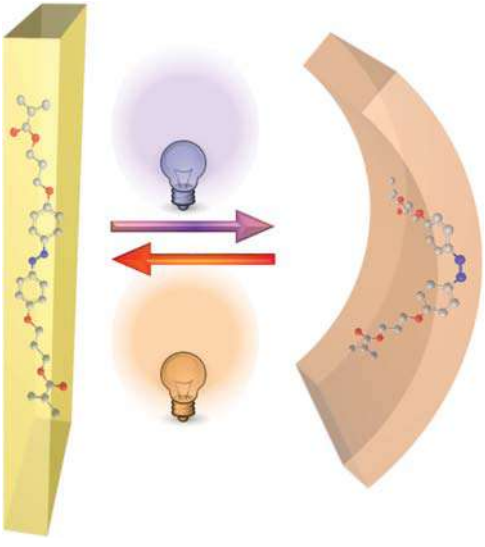

**Characteristic Features**

Deformation of polymer upon irradiation into various programmable shapes in soft actuators.

**Synthesis – Preparation of the Materials**

Polymerization by

- Photopolymerization
- Oligomerization via aza-Michael addition, thiol-acrylate Michael addition reaction

Alignment by

- Surface-induced alignment
- External stress alignment
- Inkjet and 3D printing
- Photoalignment
- External (magnetic/electric) field alignment

**First Reported**

de Gennes, P.-G. (1975). Réflexions sur un type de polymères nématiques. *C. R. Acad. Sci. Paris, Ser. B* 281: 101.

**Key References**

Pianowski, Z.L. (2019). Recent Implementations of molecular photoswitches into smart materials and biological systems. *Chem. Eur. J.* 25 (20): 5128–5144.

White, TJ. (2017). *Photomechanical Materials, Composites, and Systems: Wireless Transduction of Light Into Work*. Wiley.

# 25

# Molecular Switches in Light-Responsive Liquid-Crystalline Polymer Actuators

*Albert P. H. J. Schenning[1,2], Hong Yang[3], Sebastian Fredrich[1], and Li Liu[1,3]*

*[1] Eindhoven University of Technology, Stimuli-responsive Functional Materials and Devices, Department of Chemical Engineering and Chemistry and Institute for Complex Molecular Systems, Eindhoven 5600 MB, The Netherlands*
*[2] South China Normal University, SCNU-TUE Joint Laboratory of Device Integrated Responsive Materials (DIRM), Guangzhou 510006, China*
*[3] Southeast University, Institute of Advanced Materials, School of Chemistry and Chemical Engineering, Jiangsu Province Hi-Tech Key Laboratory for Biomedical Research, State Key Laboratory of Bioelectronics, Nanjing 211189, China*

## 25.1 Light-Responsive Soft Actuators

Soft actuators responding to external stimuli are receiving much attention nowadays [1, 2]. Their flexibility affords touching, lifting, and transportation of fragile objects of arbitrary shape, and they are therefore discussed as bionic compartments. Accordingly, pneumatically, electrically, light-, and hydraulically responsive soft materials have been designed and fabricated. Among them, light-responsive soft actuators are particularly interesting for their remote-controlled motion and precise addressability. The introduction of photoswitches enables light-induced generation of at least two distinct deformation states. As a result, photoswitches have been employed in various functional polymers, such as shape-memory materials, hydrogels, and liquid-crystal polymers (LCPs) [3]. Among these smart materials, LCPs with the anisotropic character of liquid crystals (LCs) and the elasticity of rubber provide the possibility of fast, directed, and reversible actuation upon irradiation in both a dry and aqueous environment. The photoswitches enable the transformation of collective motions from the molecular scale to the macroscopic level in a programmable way.

## 25.2 Liquid-Crystal-Based Polymers in Light-Responsive Soft Actuators

LCs have been recognized as fourth state of matter between the anisotropic crystal and the isotropic liquid state (Figure 25.1a). The simultaneous presence of order and

*Molecular Photoswitches: Chemistry, Properties, and Applications*,
First Edition. Edited by Zbigniew L. Pianowski.


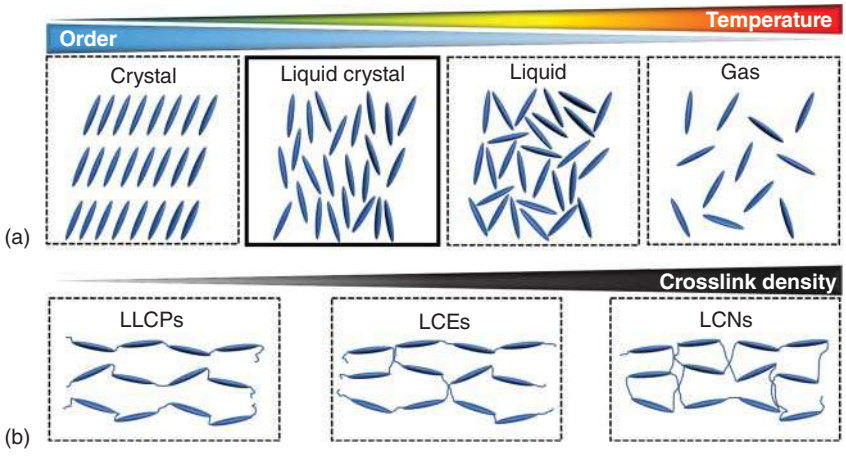


**Figure 25.1** (a) Phase behavior of matter, including the liquid-crystal phase. (b) The classification of liquid-crystal polymers.

mobility renders LCs promising responsive functionalities for diverse applications. Except their most prevalent applications in LC displays, they have increasingly emerged as outstanding materials in soft actuators allowing for the combination of properties and retaining the ordered state over a large temperature range. LCPs can be divided into main chain and side chain as well as linear LCPs (LLCPs) and crosslinked LCPs. Especially crosslinked LCPs, including liquid-crystal polymer networks (LCNs) and liquid-crystal elastomers (LCEs), are attractive for reversible and repeatable actuation. The differences between LCNs and LCEs are illustrated in Figure 25.1b. Multifunctional monomers, i.e. reactive mesogens, which are capable of self-assembling in the LC phase, were employed to prepare a moderately or densely crosslinked network in LCNs. LCEs are formed from main-chain oligomers and polymers having a low crosslink density.

In LCPs-based actuators, defined macroscopic alignment of LCs is crucial for developing reversible and programmed shape morphing. Two processing strategies, i.e. polymer surface- and external stress-induced alignment, are widely adopted. In the first method, a polyimide (PI) layer is commonly utilized to induce planar or homeotropic alignment in the monomer mixture (Figure 25.2a,b), which is subsequently polymerized by excitation of dissolved photoinitiators. The resulting film contracts along the molecular director and expands in all other directions at elevated temperatures (Figure 25.2). This response process is caused by a reversible decrease of the local molecular order. Splay and twisted alignment result in three-dimensional deformation, such as bending (Figure 25.2c). In the other alignment strategy, LC oligomers and polymers are aligned along the direction of exerted stress.

Recently, a series of new fabrication techniques such as inkjet printing, three-dimensional (3D) printing, and photoalignment have been developed. Inkjet printing technology facilitates the deposition of LC materials on a planar substrate in a single step as shown by van Oosten et al. who fabricated photoresponsive cilia

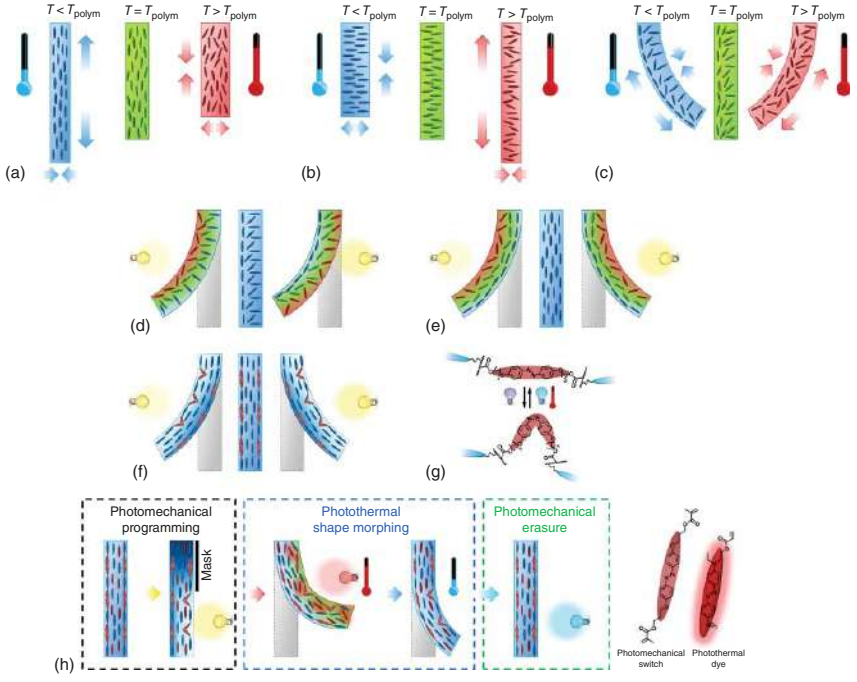


**Figure 25.2** Thermal deformation of LCPs with (a) planar alignment, (b) homeotropic alignment, (c) splay alignment. Photothermal deformation of an LCP film with (d) splay alignment, (e) planar alignment. Bending of (f) planar-aligned LCP films containing (g) photoswitches upon irradiation toward the light due to network contraction. (h) Light-induced shape programming. No or minor deformation is observed under mild intensity irradiation to pattern parts of the photomechanical switch. Photothermally induced heat is releasing the stress leading to stable bending of the isomerized areas, which can be erased irradiating the *cis*-isomer.

with an inkjet printer (Figure 25.3c) [6]. 3D printing oligomers and subsequently crosslinking into an LC network allow for mesogenic orientation via elongational flow along the printing path in high resolution [8]. Prior oligomerization by chain-extension reactions, such as aza-Michael addition, thiol-acrylate Michael addition reaction, etc. [9–12], is crucial for obtaining suitable viscosity of the ink. Lewis et al. developed LCE-based actuators with programmed director alignment showing reversible and complex shape-morphing at elevated temperatures [13]. Another common technique to control the LC orientation is photoalignment. To create a photosensitive layer, often azobenzenes with a short lifetime of the *cis*-isomer are used, which show a strong dichroism meaning that the absorbance is highly orientation dependent [14]. If the alignment layer is irradiated with polarized light, only those molecules oriented in the polarization direction isomerize and thermally return to their *trans*-state. However, after this isomerization cycle, the addressed molecules are randomly aligned, and therefore the overall ratio of azobenzenes aligned with the polarization decreases. Under constant irradiation, this process (so-called Weigert effect) is leading to almost perfect alignment of the azobenzenes perpendicular to the polarization direction. Upon using photomasks and variable polarization directions, a precise and high-resolution alignment pattern can be induced into the spatial control LCs. The development of various photoaligning materials and mechanisms has stimulated the complex shape morphing [15, 16]. The flow-induced mesogenic alignment was also applied to fabricate cilia-like structures through drop-casting technique [4]. Fibers from viscous LC oligomers were formed from drawing droplets, and photopolymerized to lock the mesogenic alignment (Figure 25.3a,b). Finally, magnetic-field-assisted mesogenic alignment has been introduced for developing LCP microactuators with highly controlled molecular anisotropy [17].

## 25.3 Photoswitches in Light-Responsive Soft Actuators

Analogous to the thermally induced macroscopic deformation of LCPs by bulk heating/cooling, a shape change can also be induced by light, if absorbing molecules are incorporated into the network [18, 19]. First, a so-called photothermal dye molecule is considered, which does not disturb the liquid-crystal phase. Upon irradiation, the absorbed light energy is converted into heat via thermal relaxation resulting in the same effect as observed for purely thermal deformation (Figure 25.2a–c). The group of Yang demonstrated a uniaxially aligned LCEs-based soft actuator functionalized with a near-infrared chromophore [20]. Owing to the high content of photothermal reagents and the main-chain end-on structure of the network, the strip finished one contraction/expansion cycle with 110% contraction ratio in ca. 7s. If the dye is homogeneously distributed in the polymer film, it causes an absorbance gradient across its thickness. Therefore, most of the incident light is absorbed on the exposed side. The inhomogeneous absorption and heat dissipation in the material might thus cause it to bend even in the absence of an alignment gradient (Figure 25.2d,e). This effect is more pronounced for strongly absorbing

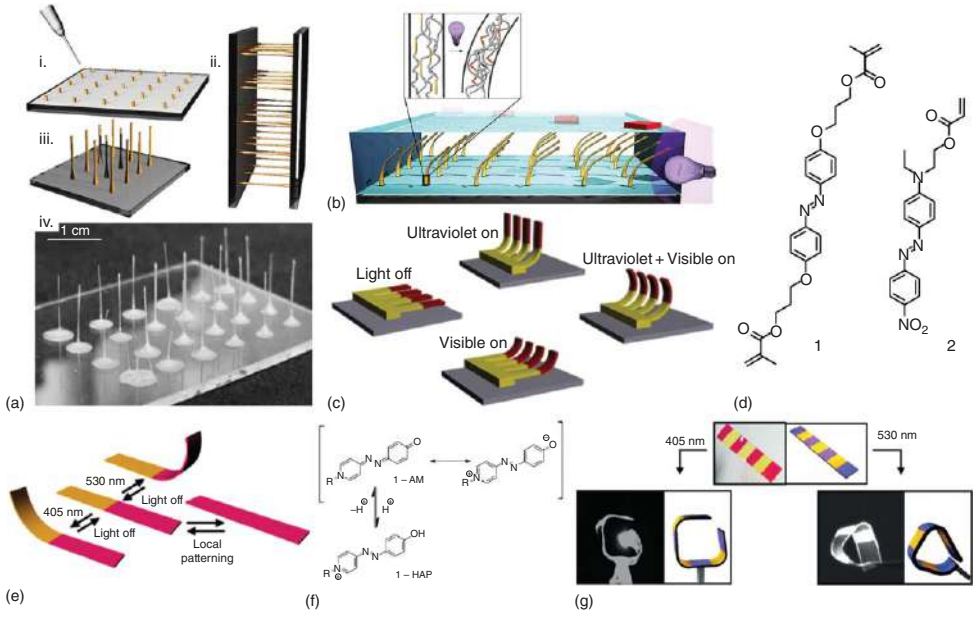


**Figure 25.3** (a) Scheme of the drop-casting technique. (i) Droplets are placed onto a glass plate, (ii) fibers are formed by pulling apart two glass plates, and (iii/iv) after polymerization and cutting at one side, the array is obtained. (b) Scheme of the collective bending leading to directional transportation. (c) Light-driven cilia produce an asymmetric motion controlled by wavelength of the light. (d) azobenzenes used in (c). (e) Scheme of a reprogrammable and rewritable polymer actuator. The yellow regions contain 1-HAP (hydroxyazopyridinium) and the magenta regions contain 1-AM (azomerocyanine). (f) Molecular changes upon acid and base treatment of 1-AM. (g) Bending of a patterned film. The same film is exposed with 405 nm (left) and 530 nm (right) light. Source: (a, b, d) Gelebart et al. [4, 5], (c) van Oosten et al. [6], (e–g) Gelebart et al. [7].

or highly concentrated dyes as dopants, but also in layered structures. Long-term irradiation leads to uniform heating and back-binding of a planar-aligned film as depicted in Figure 25.2a–c.

The photothermal effect is usually dependent on the light intensity and sample thickness. Although gradually heating up the sample gives a correlated motion, overcoming the glass transition temperature $T_g$ (photosoftening) or the liquid crystalline to isotropic transition temperature $T_{LC\text{-}iso}$ boosts the extent of deformation. Fast recovery of the initial shape is usually obtained by ceasing the irradiation. However, reached temperature, surrounding medium, and transition temperatures influence the speed of back-folding.

If the photothermal dye is exchanged by a photoswitchable molecule, the isomerization can lead to photomechanical actuation [2, 21]. In contrast to the photothermal effect, the orientation, compatibility, location, and connection of photoswitch and LCP are crucial for efficient actuation. Significant actuation is obtained by a change of the order. Specifically, the stable form of the photoswitch has to be compatible to co-align, whereas the other isomer must not. Thus, miscibility and alignment with the monomeric LC is important. Along with the compatibility goes the geometric change upon isomerization. A large macroscopic shape change is obtained, if the molecular shape change is equally significant. A cooperative effect of the photoswitches is observed depending on the connection with the polymer. The distance between the substitution with polymerizable groups defines the contraction or expansion (stress release) modes of the photoswitch. Only if both ends of the molecule are connected to the network, the photomechanical effect contributes to the macroscopic deformation.

Azobenzenes are the most employed photoswitches in LC actuators due to their linear arrangement of the *trans*-isomer compatible with the LC alignment, whereas the *cis*-form is not. The easy availability of derivatives with distinct colors and thermal half-lives makes them suitable for various light responses. Substitutions and upconversion mechanisms were employed to adjust the excitation wavelength in LCPs [22, 23]. UV-induced degradation of the polymer and competitive absorption of the photoinitiator make a red-shifting of the excitation wavelength particularly appealing. Donor–acceptor-substituted azobenzenes are thus used as red-shifted photoswitches with short half-life (as compound 2, Figure 25.3d), whereas fluorinated azobenzene derivatives are used for bistable, visible-light-addressable components [23]. Protonation and deprotonation of an azomerocyanine or hydroxyazopyridinium (HAP) even gave rise to a pH-switchable addressable wavelength (Figure 25.3e–g) [5]. Also other classes of photoswitches are employed such as hydrazones [24, 25] again exploiting the order–disorder effect of a *cis-trans*-isomerization, but also diarylethenes, fulgides, or spiropyrans [26, 27]. The latter ones are rather integrated for other purposes than the actuation, but for sensing or decoration (Figure 25.4). It needs to be emphasized that photoswitchable molecules might also act as photothermal agents. Only a small part of the light energy is converted to the isomerization and stored in the molecule, but most is immediately released in form of heat. Therefore, the photothermal behavior is superposed with any effect of the isomerization.

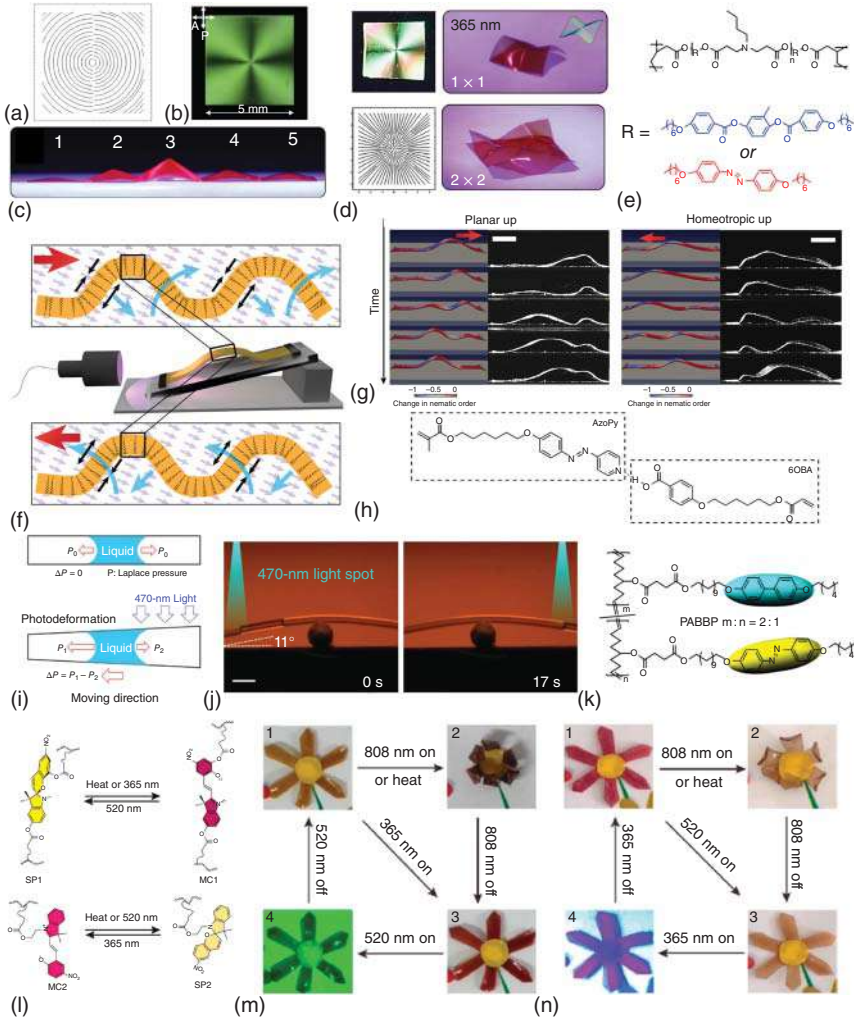


**Figure 25.4** (a) Illustration of programmed photoalignment. (b) Photograph of an azo-LCE taken between crossed polarizers. (c) The five azo-LCE films show photomechanical deformation upon 365 nm irradiation; (d) Both single (1 × 1) and array (2 × 2) of topological patterns (e) structure of the azobenzene functionalized LCE polymer. (f) Schematic set-up, showing a polymeric film constrained at both ends upon irradiation. Blue arrows show the film deformation, while red ones indicate the propagation direction of the wave. (g) Comparison of simulation (left) and experimental (right) data for planar-up and homeotropic-up configurations. (h) Structure of the used azopyridine complex. (i) Mechanism of light-directed liquid transport in an LCP tube upon 470 nm light irradiation. (j) Photographs of the light-directed motion of an isopropanol slug climbing over a slope of 11°. The scale bar is 2 mm. (k) Structure of the uncrosslinked LCP. (l) Two spiropyran derivatives with different functionalization positions show the same photochromic performances but different thermochromic properties. LCE with (m) SP1 and (n) SP2 flowers blooming and unblooming by photothermal effect, the color was modulated by light with different wavelength. Source: (a–e) Ahn et al. [28], (f–h) Gelebart et al. [7], (i–k) Xu et al. [29], (l-n) Zuo et al. [26].

If the photochromic molecule comprises a short lifetime in the thermodynamically disfavored state, it acts similar to a photothermal dye [21, 30]. A linearly aligned LCP film having a relatively high dye concentration is bending toward the light source upon irradiation and as soon as the light is switched off, photoswitch and macroscopic shape are converted back to their initial state (compare Figure 25.2d,e) [31]. However, also bending away from the light can be observed in an LCP layer when combined with a passive layer. The bending is ascribed to the generation of free volume during isomerization in the LCP layer. After removing the light, the network adapts to the stable isomer and reduces its volume again. Therefore, this process requires constant isomerization by photoswitching in one direction and simultaneous thermal or light-induced back reaction [32].

A benefit of a photoswitch compared to photothermal dyes in an LC network is achieved with compounds comprising a long half-life, which makes it possible to obtain a stable deformation after irradiation [28]. The geometric change of azobenzenes leads to a contraction of the photoswitch and the polymer network in alignment direction upon photoisomerization (Figure 25.2f,g). However, this is only relevant, if both sides of the contracting photoswitch are connected to the network. Just one covalent linkage or linkage in other than the *para*-positions does not lead to a significant contraction of the network. Representative examples exploiting this behavior include an azobenzene-functionalized LCP-based actuator with splay alignment across the strip thickness reported by Schenning and coworkers [33]. This amplified actuation in the films containing side-chain azobenzenes based on photothermal effect. Yu's group reported on manipulating the bending direction of photoactuators via controlling alignment [34]. When mesogens were aligned with a smectic A phase, the *trans*-to-*cis* isomerization caused bending toward light, whereas films containing mesogens with a smectic C phase bent away from light due to the surface expansion. Wu et al. demonstrated healable and reprocessable photoactuators with reversible bending [35].

The contribution of photomechanical effects to the overall shape change of the LCPs can be determined individually from the photothermal effect if the generated heat is immediately released to the surrounding medium [33]. While cooling of the LCPs in air is relatively slow, water has a high thermal conductivity and can thus instantly absorb the heat from the film, which makes the photothermal effect negligible. LCN films proofed to bend under water only if crosslinking azobenzenes are incorporated and the photomechanical effect is operative. The photothermal effect can also be estimated from the difference between the hot bright state and the dark photochemically induced stable state. Sometimes, the $T_g$ has to be overcome photothermally to facilitate the photomechanical deformation, or local photomechanical modification leads to an inhomogeneous $T_g$ and therefore a programmable (photo)thermal response of the LCP (Figure 25.2h). For medium thermally labile photoswitches, their conversion in the photostationary state is dependent on the induced heat and thus intensity of the light. Considerable thermal bistability could be achieved in actuators using fluorinated azobenzenes [36] or hydrazones [24].

The crosslinking density of LCPs plays a crucial role for their static and photoinduced properties. Photoreversible dimerization, e.g. of substituted anthracenes can

be exploited to photocrosslink those materials [37]. The stiffness is considerably increasing with dimerization. This is interesting for light-responsive shape-memory materials and programming of complex motions.

## 25.4 Light-Responsive Soft Actuators and Their Applications

Exploiting different deformation modes of LCPs offers a wide variety of applications [2, 21]. Various elaborate designs make use of simple deformations [38, 39], but also programming shapes (Figure 25.4), lift objects, transport cargo. The materials show large strain deformations resembling the behavior of muscles. The addressability by light as remote-controlled motion in an untethered way avoiding cables, enables use in medical fields, manufacturing, or logistics. Converting light into mechanical and subsequently into electric energy can be furthermore considered to directly use sunlight as resource [23].

Only some illustrative examples can present the potential applications of light-responsive actuators in this scope. A self-propelled strip driven by light has been reported by Broer's group [7]. Azobenzenes with short *cis* life time were incorporated into a splay-aligned LCN to induce the photothermal effect. When the two ends of strip were fixed, a continuous traveling wave was generated upon light irradiation (Figure 25.4f,g). The used azopyridine (Figure 25.4h) comprised a short lifetime due to complexation. More recently, Yang et al. have demonstrated sustained oscillators composed of splay-aligned LCNs and a polydopamine (PDA) coating layer [40]. The programmability of the PDA layer allows local and repeated adjustment of the oscillating behaviors of the strip. Oscillatory motions are often reported and mostly rely on the photothermal effect and self-shadowing of the irradiated films upon bending [39]. The bent tip of the film is covering the rest from light upon bending leading to cooling and recovery of the initial shape. Variations of this can also be used to create rotary motions as in a motor [5, 25].

Actuation is not only observed in films, but also in surface coatings [28], switching the roughness, porosity, or surface tension. Recently, also the flow within microfluidic devices could be controlled by light using LCPs [29, 34]. Thereby, the expansion or shrinkage of tubular LCPs by the Weigert effect in the uncrosslinked polymer was exploited to direct droplets of fluid (Figure 25.4i-k). Coating of LCPs on nonresponsive substrates such as textile fibers could render them smart giving woven cloth with adaptive ventilation [41].

Various examples are reported on light conversion into mechanical energy or motion, fueling a motor or directly move in a crawling [42], rolling, jumping, or swimming way. Whereas terrestrial walkers mostly rely on the stepwise light-induced bending and shape recovery in the dark upon cooling [7], swimmers or divers need the crosslinked photoswitches to show locomotion [33]. Many motions are also inspired by nature (Figure 25.4l-n) [43, 44], not only resembling animal movement of caterpillars [42] or beetles, but also carnivorous plants [45] or tendrils in response to sunlight [46].

## 25.5 Conclusion and Outlook

The incorporation of photoswitches and photothermal dyes into LCPs enables various light-addressable shape changes. The anisotropic structure of the LCPs matrix allows for a translation of the change in molecular geometry into macroscopic motion. Precise control of intensity and spatial resolution offers a large toolkit in fabrication, product design, sensors, or medical protheses. Lifting objects by light-responsive actuators in a non-destructive way renders the use of cable connections redundant. Whereas photothermal dyes show a fast and reversible response, the great advantage of using photoswitches in photoactuators becomes substantive when thermally bistable deformations, underwater applications, or deformation programming are required. Although self-shadowing is often used in sophisticated modulations, it restricts the further development of those materials almost exclusively to thin films and narrow structures without effect to the bulk material. Current attempts try to increase the transformation efficiency of light into mechanical energy to harvest sunlight directly or indirectly for subsequent conversion into electricity. Further trends are going for increased bistability and robustness avoiding the use of UV-light excitation in favor of visible or even infrared light instead. Another challenge is the upscaling of small film actuators and microrobots via developing cheap and easy methods of processing.

Photoswitches furthermore improved the versatility and resolution of precise LC aligning by using photoalignment layers. Thus, the advantage of applying photochromic compounds is not limited to the direct incorporation into the materials, and their exploitation for sophisticated material production is expected to rise in the future.

## References


1 Li, Q. (2018). *Photoactive Functional Soft Materials: Preparation, Properties, and Applications*. Wiley.

2 White, T.J. (2017). *Photomechanical Materials, Composites, and Systems: Wireless Transduction of Light Into Work*. Wiley.

3 Pianowski, Z.L. (2019). Recent implementations of molecular photoswitches into smart materials and biological systems. *Chem. Eur. J.* 25 (20): 5128–5144.

4 Gelebart, A.H., Mc Bride, M., Schenning, A.P.H.J. et al. (2016). Photoresponsive fiber array: toward mimicking the collective motion of cilia for transport applications. *Adv. Funct. Mater.* 26 (29): 5322–5327.

5 Gelebart, A.H., Mulder, D.J., Vantomme, G. et al. (2017). A rewritable, reprogrammable, dual light-responsive polymer actuator. *Angew. Chem. Int. Ed.* 56 (43): 13436–13439.

6 van Oosten, C.L., Bastiaansen, C.W.M., and Broer, D.J. (2009). Printed artificial cilia from liquid-crystal network actuators modularly driven by light. *Nat. Mater.* 8 (8): 677–682.


7 Gelebart, A.H., Mulder, D.J., Varga, M. et al. (2017). Making waves in a photoactive polymer film. *Nature* 546 (7660): 632–636.

8 Gantenbein, S., Masania, K., Woigk, W. et al. (2018). Three-dimensional printing of hierarchical liquid-crystal-polymer structures. *Nature* 561 (7722): 226–230.

9 Ambulo, C.P., Burroughs, J.J., Boothby, J.M. et al. (2017). Four-dimensional printing of liquid crystal elastomers. *ACS Appl. Mater. Interfaces* 9 (42): 37332–37339.

10 López-Valdeolivas, M., Liu, D., Broer, D.J., and Sánchez-Somolinos, C. (2018). 4D printed actuators with soft-robotic functions. *Macromol. Rapid Commun.* 39 (5): 1700710.

11 Saed, M.O., Ambulo, C.P., Kim, H. et al. (2019). Molecularly-engineered, 4D-printed liquid crystal elastomer actuators. *Adv. Funct. Mater.* 29 (3): 1806412.

12 Ren, L., Li, B., He, Y. et al. (2020). Programming shape-morphing behavior of liquid crystal elastomers via parameter-encoded 4D printing. *ACS Appl. Mater. Interfaces* 12 (13): 15562–15572.

13 Kotikian, A., Truby, R.L., Boley, J.W. et al. (2018). 3D printing of liquid crystal elastomeric actuators with spatially programed nematic order. *Adv. Mater.* 30 (10): 1706164.

14 Liu, Q., Zhan, Y., Wei, J. et al. (2017). Dual-responsive deformation of a crosslinked liquid crystal polymer film with complex molecular alignment. *Soft Matter* 13 (36): 6145–6151.

15 Guin, T., Settle, M.J., Kowalski, B.A. et al. (2018). Layered liquid crystal elastomer actuators. *Nat. Commun.* 9 (1): 2531.

16 De Haan, L.T., Gimenez-Pinto, V., Konya, A. et al. (2014). Accordion-like actuators of multiple 3D patterned liquid crystal polymer films. *Adv. Funct. Mater.* 24 (9): 1251–1258.

17 Yao, Y., Waters, J.T., Shneidman, A.V. et al. (2018). Multiresponsive polymeric microstructures with encoded predetermined and self-regulated deformability. *Proc. Natl. Acad. Sci. U.S.A* 115 (51): 12950–12955.

18 Dong, L. and Zhao, Y. (2018). Photothermally driven liquid crystal polymer actuators. *Mater. Chem. Front.* 2 (11): 1932–1943.

19 Ge, F. and Zhao, Y. (2020). Microstructured actuation of liquid crystal polymer networks. *Adv. Funct. Mater.* 30 (2): 1901890.

20 Liu, L., Liu, M.-H., Deng, L.-L. et al. (2017). Near-infrared chromophore functionalized soft actuator with ultrafast photoresponsive speed and superior mechanical property. *J. Am. Chem. Soc.* 139 (33): 11333–11336.

21 Pang, X., Lv, J., Zhu, C. et al. (2019). Photodeformable azobenzene-containing liquid crystal polymers and soft actuators. *Adv. Mater.* 31 (52): 1904224.

22 Jiang, Z., Xu, M., Li, F., and Yu, Y. (2013). Red-light-controllable liquid-crystal soft actuators via low-power excited upconversion based on triplet–triplet annihilation. *J. Am. Chem. Soc.* 135 (44): 16446–16453.

23 Kumar, K., Knie, C., Bléger, D. et al. (2016). A chaotic self-oscillating sunlight-driven polymer actuator. *Nat. Commun.* 7 (1): 11975.

24 Ryabchun, A., Li, Q., Lancia, F. et al. (2019). Shape-persistent actuators from hydrazone photoswitches. *J. Am. Chem. Soc.* 141 (3): 1196–1200.


**25** Vantomme, G., Gelebart, A.H., Broer, D.J., and Meijer, E.W. (2017). A four-blade light-driven plastic mill based on hydrazone liquid-crystal networks. *Tetrahedron* 73 (33): 4963–4967.

**26** Zuo, B., Wang, M., Lin, B.-P., and Yang, H. (2018). Photomodulated tricolor-changing artificial flowers. *Chem. Mater.* 30 (21): 8079–8088.

**27** Wani, O.M., Verpaalen, R., Zeng, H. et al. (2019). An artificial nocturnal flower via humidity-gated photoactuation in liquid crystal networks. *Adv. Mater.* 31 (2): 1805985.

**28** Ahn, S., Ware, T.H., Lee, K.M. et al. (2016). Photoinduced topographical feature development in blueprinted azobenzene-functionalized liquid crystalline elastomers. *Adv. Funct. Mater.* 26 (32): 5819–5826.

**29** Xu, B., Zhu, C., Qin, L. et al. (2019). Light-directed liquid manipulation in flexible bilayer microtubes. *Small* 15 (24): 1901847.

**30** Zuo, B., Wang, M., Lin, B.-P., and Yang, H. (2019). Visible and infrared three-wavelength modulated multi-directional actuators. *Nat. Commun.* 10 (1): 4539.

**31** Pilz da Cunha, M., Foelen, Y., van Raak, R.J.H. et al. (2019). An untethered magnetic- and light-responsive rotary gripper: shedding light on photoresponsive liquid crystal actuators. *Adv. Opt. Mater.* 7 (7): 1801643.

**32** Ma, S., Li, X., Huang, S. et al. (2019). A light-activated polymer composite enables on-demand photocontrolled motion: transportation at the liquid/air interface. *Angew. Chem. Int. Ed.* 131 (9): 2655–2659.

**33** Pilz da Cunha, M., van Thoor, E.A.J., Debije, M.G. et al. (2019). Unravelling the photothermal and photomechanical contributions to actuation of azobenzene-doped liquid crystal polymers in air and water. *J. Mater. Chem. C*. 7 (43): 13502–13509.

**34** Liu, Q., Liu, Y., Lv, J. et al. (2019). Photocontrolled liquid transportation in microtubes by manipulating mesogen orientations in liquid crystal polymers. *Adv. Intell. Syst.* 1 (6): 1900060.

**35** Chen, M., Yao, B., Kappl, M. et al. (2020). Entangled azobenzene-containing polymers with photoinduced reversible solid-to-liquid transitions for healable and reprocessable photoactuators. *Adv. Funct. Mater.* 30 (4): 1906752.

**36** Donovan, B.R., Matavulj, V.M., Ahn, S. et al. (2019). All-optical control of shape. *Adv. Mater.* 31 (2): 1805750.

**37** Jiang, Z.-C., Xiao, Y.-Y., Tong, X., and Zhao, Y. (2019). Selective decrosslinking in liquid crystal polymer actuators for optical reconfiguration of origami and light-fueled locomotion. *Angew. Chem. Int. Ed.* 58 (16): 5332–5337.

**38** Okihara, T., Kawaguchi, A., Ohara, M., and Katayama, K. (1990). Subcell-matched epitaxy of normal long chain compounds on polyethylene: I. On the (110) plane. *J. Cryst. Growth* 106 (2): 318–332.

**39** Sol, J.A.H.P., Peeketi, A.R., Vyas, N. et al. (2019). Butterfly proboscis-inspired tight rolling tapered soft actuators. *Chem. Commun.* 55 (12): 1726–1729.

**40** Lan, R., Sun, J., Shen, C. et al. (2020). Near-infrared photodriven self-sustained oscillation of liquid-crystalline network film with predesignated polydopamine coating. *Adv. Mater.* 32 (14): 1906319.


**41** Ohzono, T., Saed, M.O., Yue, Y. et al. (2020). Dynamic manipulation of friction in smart textile composites of liquid-crystal elastomers. *Adv. Mater. Interfaces* 7 (7): 1901996.

**42** Zeng, H., Wani, O.M., Wasylczyk, P., and Priimagi, A. (2018). Light-driven, caterpillar-inspired miniature inching robot. *Macromol. Rapid Commun.* 39 (1): 1700224.

**43** Shang, Y., Wang, J., Ikeda, T., and Jiang, L. (2019). Bio-inspired liquid crystal actuator materials. *J. Mater. Chem. C* 7 (12): 3413–3428.

**44** Koshima, H. (2019). Mechanically responsive materials for soft robotics. Wiley.

**45** Wani, O.M., Zeng, H., and Priimagi, A. (2017). A light-driven artificial flytrap. *Nat. Commun.* 8 (1): 15546.

**46** Aßhoff, S.J., Lancia, F., Iamsaard, S. et al. (2017). High-power actuation from molecular photoswitches in enantiomerically paired soft springs. *Angew. Chem. Int. Ed.* 56 (12): 3261–3265.

# 26 Molecular Photoswitches in Liquid Crystals

Alexander Ryabchun and Nathalie Katsonis

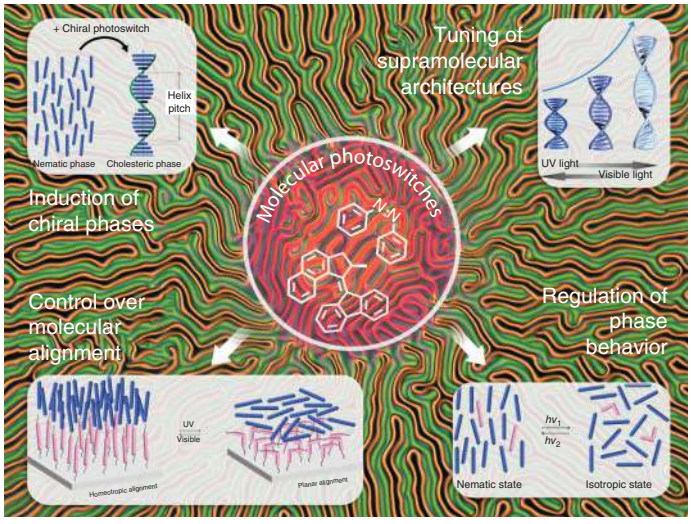


**Characteristic Features**

The long range order of liquid crystals can transduce, and sometimes amplify molecular shape changes, up to the macroscopic length scale. Therefore, the nanoscale operation of molecular photoswitches is known to effectively regulate the organisation of liquid crystal systems and materials.

**Key References**

Amrutha, A.S., Achalkumar, A.S., and Li, Q. (2019). Light-driven phase transitions in liquid crystals and their applications. In: *Photoactive Functional Soft Materials: Preparation, Properties, and Applications*. Weinheim: Wiley.

Lancia, F., Ryabchun, A., and Katsonis, N. (2019). Life-like motion driven by artificial molecular machines. *Nat Rev Chem* 3: 536–551.

Katsonis, N., Lacaze, E., and Ferrarini, A. (2012). Controlling chirality with helix inversion in cholesteric liquid crystals. *J. Mater. Chem.* 22: 7088–7097.

# 26

# Molecular Photoswitches in Liquid Crystals

*Alexander Ryabchun and Nathalie Katsonis*

*University of Groningen, Stratingh Institute for Chemistry, Faculty of Science and Engineering, Nijenborgh 8, 9747 AG, Groningen, The Netherlands*

## 26.1 Introduction

Light-driven processes are ubiquitus and light also sustains many living systems, either directly or indirectly. The scientific community has thus strived to investigate and understand how to harvest, transmit, store, and use light. One effective strategy to transmit light energy into a relevant molecular operation is to use molecular photoswitches as nanoscale transducers of light energy into movement. By absorbing light photons, these molecules are able to perform large molecular rearrangements, and thus they also change colour. While the dramatic color change of such compounds is fascinating, a more important aspect is that these molecular rearrangements can be harnessed to modulate various macroscopic properties of the materials, which can become relevant for practical applications. Harnessing the molecular operation of these molecular photoswitches requires amplifying their motion across multiple length scales. The development of strategies and approaches to achieve such an amplification remains a major current challenge. A key and highly promising approach is the integration of molecular photoswitches into liquid crystal materials which act as amplifying media [1, 2]. In this chapter, we will discuss the main strategies for coupling molecular photoswitches with liquid crystals - we will focus primarily on small molecule liquid crystals as liquid crystalline polymer systems will be considered in Chapter 25 (Section III). The chapter consists of a brief general introduction to liquid crystals, followed by three sections devoted to molecular photoswitches which can (i) regulate the phase behavior of liquid crystals, (ii) regulate the orientation of liquid crystals, and (iii) modify the expression of chirality in liquid crystals.

*Molecular Photoswitches: Chemistry, Properties, and Applications*,
First Edition. Edited by Zbigniew L. Pianowski.


## 26.2 Liquid Crystals

Liquid crystallinity is characterized by both the fluidity inherent to conventional liquids and the long-range molecular orientation typical for crystals [3–5]. Liquid crystal phases can appear in a range of aqueous concentrations (lyotropic phases) [6] or as bulk materials, in a given range of temperatures (thermotropic phases) [7]. Here, we focus only on the thermotropic liquid crystalline state, which exists in the temperature interval between the solid crystalline state with perfect positional order of molecules and the isotropic state, in which molecules are distributed randomly. The liquid crystalline state is often referred to as the mesophase, and molecules composing it are called mesogens. Liquid crystallinity can appear as a result of non-covalent interactions (e.g. dipolar, π–π interactions, metal coordination, hydrogen and halogen bonds, etc.) between the molecular components, with the key distinctive feature of these components being shape anisotropy. For lyotropic phases, shape anisotropy is provided by lamellar or columnar organization of amphiphilic molecules, while for thermotropic ones by anisotropy of molecular shape. Molecular shape geometry is another way to classify liquid crystals into: (i) calamitic liquid crystals formed by rod-like molecules; (ii) discotic liquid crystals formed by disc shaped molecules, and (iii) bend-core liquid crystals formed by banana-like molecules. Sofar, most host matrices for photoswitches have been calamitic liquid crystals.

Nematic, smectic, and cholesteric liquid crystals are the most frequently used calamitic liquid crystals (Figure 26.1). In the nematic phase, the centers of mass of mesogens are distributed randomly but the long axes of the mesogens align on average in preferential direction referred as the director **n** [8]. The smectic phase exhibits a higher degree of ordering: apart from alignment of long axes, the centers of mass of the mesogens lie in the planes forming the smectic layers. The common types of smectic phases are smectic A and C, where the liquid crystal director is, respectively, perpendicular or tilted in respect to smectic layer. In

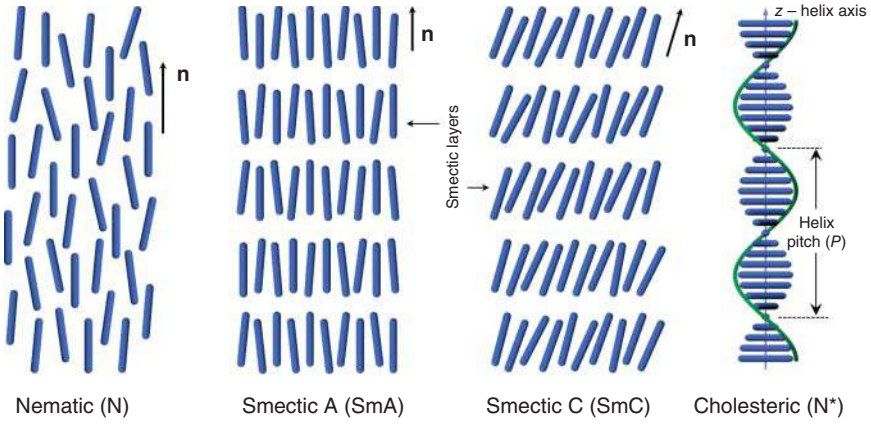


**Figure 26.1** Main classes of calamitic liquid crystals. **n** refers to liquid crystal director.

contrary to crystals, smectic layers can slide over one another in a manner similar to that of soap. Another liquid crystalline phase possessing a set of unique optical properties is the cholesteric (or chiral nematic) phase, where the molecules are organized into a supramolecular helix. The centers of mass of mesogens forming the cholesteric mesophase are randomly distributed; however, the long molecular axes twist, which defines a supramolecular helix with a given handedness and pitch. Cholesteric liquid crystals are considered as one-dimensional photonic crystals, due the periodicity of the helix which reflects light of a given wavelength and circular polarization.

Due to the anisotropic character of their optical properties and their high responsiveness to external stimuli, liquid crystals find practical applications, typically in liquid crystal display devices. However, there are many applications beyond the displays, such as tunable optical devices (retarders, filters, diffraction gratings, lenses, lasers, etc.), sensors and soft actuators, to name only a few [9–12]. We refer the reader to the literature for in-depth information on liquid crystals, also including their applications [3–5, 9, 10, 12].

## 26.3 Photochromic Switches Can Regulate Phase Behavior

Liquid crystals can accomodate a variety of "guest" molecules, such as photochromic switches. Upon light-induced rearrangement, the photochromic switches modify their interaction with the liquid crystal, and this leads to a change in the phase behaviour of the liquid crystal material [13, 14].

The best candidates to tune the phase behavior of liquid crystals are rigid rod-like molecules that experience *E*/*Z* isomerization in response to light. Examples are azobenzenes (see also Chapter 3 in Section II), stilbenes (Chapter 12 in Section II), and alkenes [15–22]. The typical operation of these molecules in liquid crystals can be explained by the example of azobenzene, which is undoubtedly the most widely used photochrome due to its fast, efficient, and fully reversible photoisomerization. The initial *E* isomer of azobenzene has a rod-like molecular shape which is usually compatible with liquid crystal molecules and does not interfere with molecular ordering. On the contrary, the *Z*-isomer has a bent shape, so it interferes with the liquid crystalline order substantially. With azobenzene, the large change in molecular geometry can lead to the complete loss of liquid crystallinity (Figure 26.2a), i.e. to isotropization under illumination. Studies in which nematic liquid crystals were doped with azobenzene (**1**) (Scheme 26.1) have revealed that on the macroscopic level light-induced isotropization starts with formation of isotropic domains which expand upon further illumination, as evidenced by the growth of "dark" areas observed between crossed polarizers (Figure 26.2b). Since the decrease in liquid crystal order, and consequent isotropization, is associated with accumulation of the

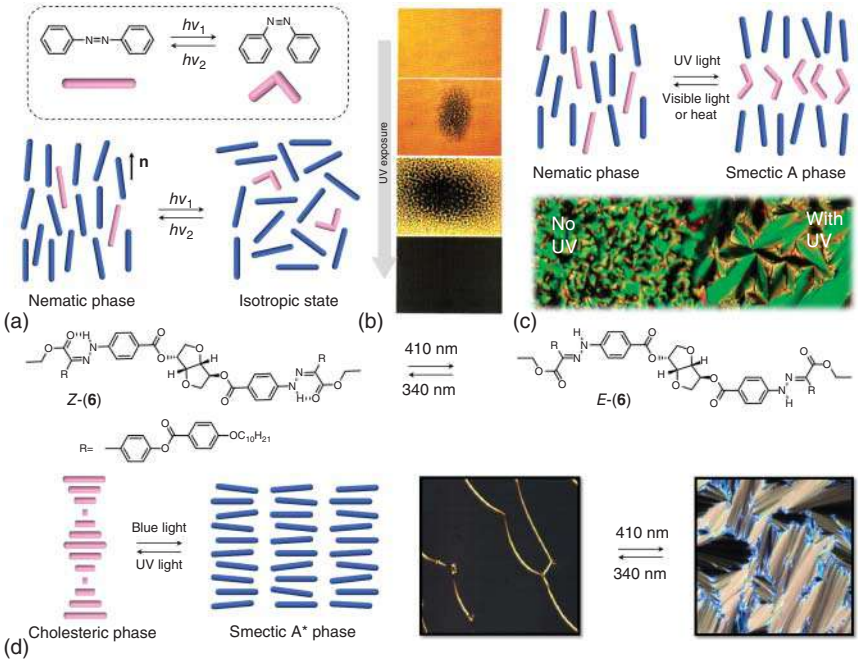


**Figure 26.2** (a) The light-induced isotropization of a nematic liquid crystal is caused by the operation of an azobenzene. (b) Polarized optical microscopy (POM) images of light-induced phase transition. Source: Reproduced with permission from Sung et al. [19], Figure 04, p 03/with permission of American Chemical Society. (c) Light-driven nematic to smectic A phase transition and corresponding polarized optical microscopy images (at the bottom). Source: Prasad et al. [23], Figure 05, p 04/with permission of American Chemical Society. (d) Cholesteric to chiral smectic A* transition due to photoisomerization of chiral hydrazone *Z*-(**6**). Corresponding microscopy images are at the right. Source: Reproduced with permission from Moran et al. [24], Figure 03, p 05/with permission of American Chemical Society.

*Z*-isomer, the phase transition from isotropic back to liquid crystalline state can be initiated by visible light illumination or heating, which accelerates the *Z*-to-*E* isomerization. Besides azobenzenes, light-induced isotropization was observed for liquid crystals doped with chlorostilbenes (**2**) [15] and butadienes (**3**) [20, 21]. There are other examples of phase transitions in liquid crystals accompanied by reduction of molecular order, such as smectic to cholesteric and cholesteric (or smectic) to isotropic state observed in cholesterol-based azobenzene (**4**) [17, 18].

Phase transitions can also be induced in the direction of an increase in molecular order [23–27]. The use of an azobenzene (**5**) doped nematic liquid crystal allowed it to reach the smectic A phase under UV light exposure (Figure 26.2c) [23]. The mechanism of that transition is based on the segregation of the low compatible *Z*-form of azo compound with formation of layered smectic structure as

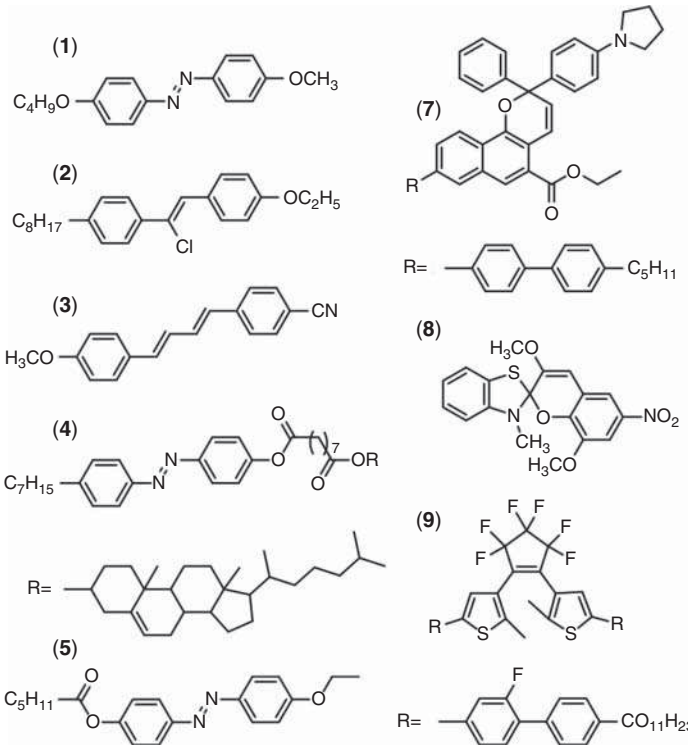


**Scheme 26.1** Chemical structures of molecular photoswitches that can interfere with the phase behavior of liquid crystals.

schematically depicted in Figure 26.2c. Another order-increase light-driven phase transition has been recently demonstrated for a negative photochrome based on hydrazone (see Chapter 6 in Section II) [24]. Exposure of the initial nematic host doped with chiral hydrazone (**6**) in the Z-state to blue light yields the stable E-state of hydrazone (half-life time exceeds thousand years) facilitating the formation of chiral smectic A phase (Figure 26.2d).

The use of photochromic switches capable of performing an *E*/*Z* photoisomerization is dictated by the required large change in molecular shape in order to tune (disrupt or enhance) the mesomorphic properties of liquid crystals. There are, however, also a few examples where light-driven pericyclic reactions can interfere with the organization of liquid crystals [27, 28]. The light-induced ring-opening of a naphthopyrane-based dopant (**7**) enhances the anisometric character of the molecule, thus facilitating the liquid crystal ordering. Reversible isothermal phase transitions from isotropic state to nematic and from nematic to smectic phase were achieved in liquid crystal mixtures doped with (**7**) under the action of light [27]. A similar isothermal phase transition from isotropic to nematic state was reported for spiropyranes, e.g. (**8**) (see also Chapter 7 in Section II) where illumination results in a ring-opening reaction yielding the merocyanine form, disrupting the liquid crystalline order in less extent compared with initial form [28].

It should be stressed that not all photochromes are embeddable within liquid crystals and can influence their phase behavior. The standard approach to overcome this compatibility issue is a coupling photochromic molecules with mesogenic fragments [29]. The approach is versatile and widely used, especially in designing chiral photochromic dopants for liquid crystals (see Section 26.5) and allows fine adjustment properties by tuning multiple structural parameters. This strategy has been applied to create photochromic liquid crystalline spironaphthoxazines [30], biindenylidenedione [31], and dithienylcyclopentenes [32, 33]. The latter ones, e.g. (**9**), demonstrate a reduction of the stability of the liquid crystal phase in response to light, due to ring-closing photoreaction resulting in the loss of flexibility of the photochromic core.

There are two major ways to exploit the modulation of liquid crystalline phases. The first one involves systems demonstrating a light-driven transition between a liquid crystalline phase and an isotropic state. The liquid crystalline phase is characterized by a high optical anisotropy associated with birefringence: $\Delta n = n_e - n_o$, where $n_e$ and $n_o$ are the extraordinary refractive index and the ordinary refractive index, respectively. The refractive index of the isotropic state ($n$) is considerably lower than $n_e$ and slightly higher than $n_o$, $n_e > n > n_o$. Consequently, the isothermal phase transition between liquid crystalline and isotropic states generates a remarkable difference in refractive index which can be used for optical imaging [15, 34], lasers [35], holographic data recording and patterning [13, 36, 37]. The second way involves a light-induced transition between two liquid crystalline phases. Since each phase has its own optical texture (footprint), the light-induced phase transition is able to switch between different textures, e.g. between transparent and opaque states, which can find applications as smart windows and optical shutters [14, 24, 34].

## 26.4 Photochromic Switches Can Regulate Molecular Alignment

In the absence of any specific treatment, liquid crystal materials display a multidomain structure, where each domain has a preferential direction of molecular orientation, but this direction is different from the next domain. Therefore, on the macroscopic level the "useful" anisotropy of physical properties averages out. However, for practical applications, the liquid crystals have tp be aligned in homogeneous domains – e.g. planar, homeotropic, splay, or twist alignement, which can be imposed by interfacial interactions. Planar and homeotropic alignment are where long axis of liquid crystal molecules is parallel and perpendicular to the confining surface, respectively. Homogeneous planar alignment can be either random or unidirectional when liquid crystal molecules orient along one direction. There are many ways to achieve a certain type of alignment, both physical (rubbing or structuring of the surface) and chemical (surfactants, surface modification) [3, 4]. Commonly, these techniques have limitations in terms of spatial resolution and create a stable alignment which cannot be modified further. However, it has been discovered that some photochromic compounds are able to guide liquid crystals

and this guidance can be spatially and temporally controlled by light [38–40]. This phenomenon is usually called "photoalignment" and the photoaligning layers "command layers" [41–44]. The driving force for liquid crystals to "follow" command layers is their anisotropic interactions with the photochromic switches of the command layer, which originates from their anisometric molecular shapes.

It has been shown by Ichimura et al. that azobenzene (**10**) attached to the substrate promotes vertical (homeotropic) orientation of liquid crystals (Figure 26.3a) [41]. On the other hand, UV light generates the bent *cis*-isomer of azobenzene which promotes random planar alignment. Hence, UV–Vis exposure cycles enable the reversible switching between planar and homeotropic alignment of liquid crystals. Only a monolayer of such azobenzenes is able to drive the alignment of a whole thin layer of liquid crystal of several microns of thickness, which justifies its "command" layer name.

The isomerization of azobenzenes has been later exploited in optically switchable devices based on the realignment of LCs from the azo-modified surface of gold nanoparticles homogeneously mixed with liquid crystal (Figure 26.3b) [45]. When the shell of nanoparticles is in the *trans*-state, they do not promote any specific alignment; however, when exposed to UV light the azobenzene groups orient along the direction of light propagation thereby functionalized nanoparticles start serving as distributed seeds for homeotropic alignment as schematically shown in Figure 26.3b. It is likely that these seeds are adsorbed at the confining substrates because enhanced interactions with polar *cis*-state of azobenzene, similar to "bulk alignment" in dye-doped liquid crystals [46–48]. In the latter case, the alignment is promoted by the photoisomerized azobenzene molecule adsorbed at the surface.

Photoalignment of liquid crystals can also be achieved using azobenzene dyes [38, 49, 50] such as (**11**) shown in Figure 26.3c. Here, the phenomenon of "photo-orientation/photo-reorientation" (widely used in azobenzene-containing polymer systems [13, 40, 51, 52]) of azo-dyes upon polarized light exposure plays a main role. When the azo-dye (**11**) is exposed to linearly polarized UV light, it reorients in such a way that the long molecular axis becomes perpendicular to the light polarization. The uniaxial orientation of azo-dye molecules generates anisotropy of surface energy which results in the alignment of liquid crystals as schematically shown in Figure 26.3c. This approach allows creating complex liquid crystal molecular alignment patterns such as the ones used in the production of various q-plates (Figure 26.3d) [44]. Apart from azo-dyes, a variety of polymers bearing azobenzene, cinnamate, and coumarine fragments can also be used as command layers for the alignment of liquid crystals. In the case of cinnamate and coumarine photochromes, the required anisotropy of surface energy comes from the [2+2]-photocycloaddition reaction. A comprehensive overview of photoalignment approaches and materials can be found in [38, 40, 42, 43]. The main features of the photoalignment technique which makes it very appealing to industry are that it is contactless and clean, allows for fine adjustment of pretilt angles and

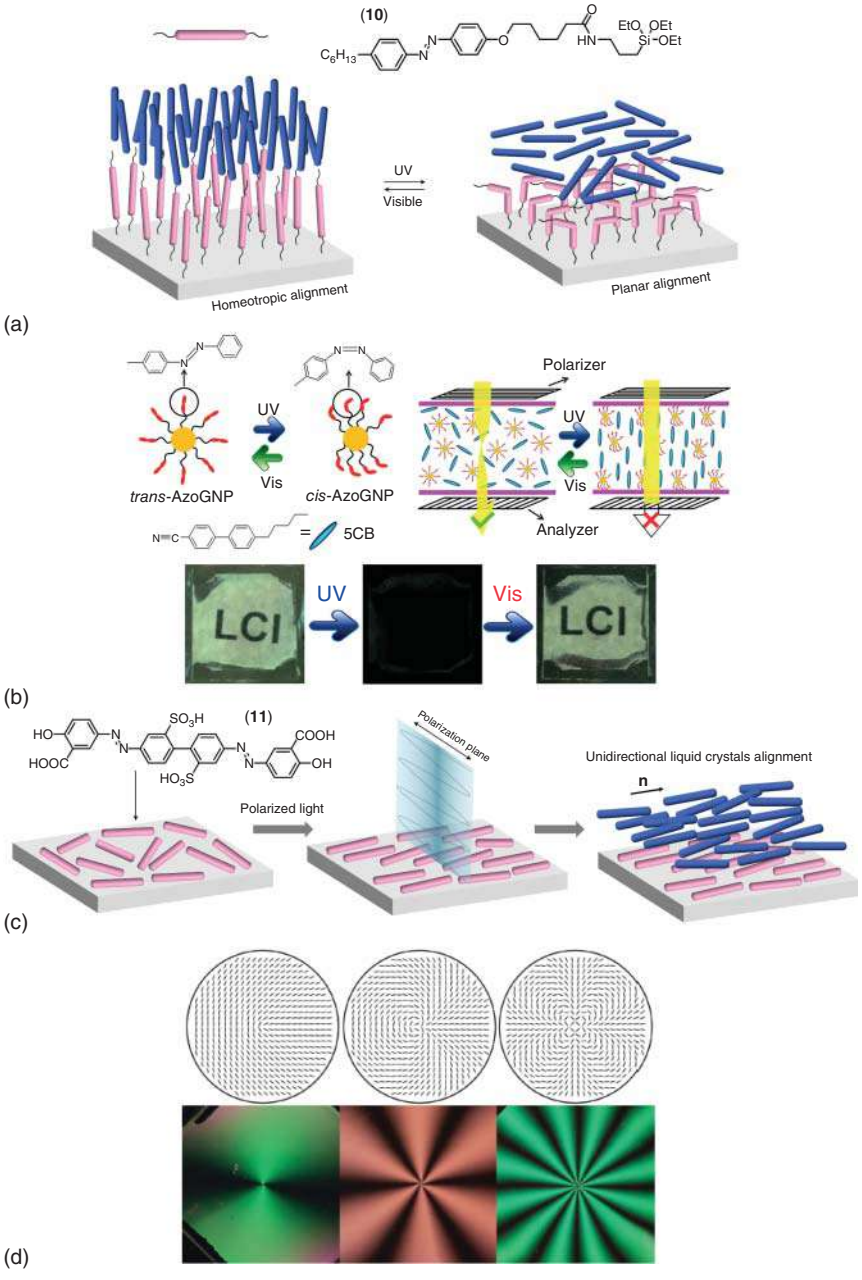


**Figure 26.3** (a) The switch from homeotropic (vertical) to planar (horizontal) alignment of the liquid crystal is induced by E to Z photoisomerization of azobenzene (**10**) attached to a substrate. (b) Modulation of liquid crystal alignment by azobenzene-functionalized nanoparticles embedded in the liquid crystal. Example of reversible optical information recording (bottom). Source: Reproduced with permission from Xue et al. [45], Figure 03,p 03/with permission of Wiley-VCH. (c) Schematic representation of photoalignment of liquid crystals with azobenzene dye (**11**). (d) Alignment patterns (top) and POM images (bottom) of optical q-plates produced by photoalignment technique. Source: Slussarenko et al. [44], Figure 02, p 04/with permission of The Optical Society.

anchoring energy, and the possibility to reversibly create alignment patterns of high complexity and on non-flat surfaces which is not possible with conventional rubbing techniques.

Of all the examples of the application of photochromic molecules for liquid crystals discussed in this chapter, photoalignment is the most promising and widely used. For example, the Sharp corporation launched on the market novel large liquid crystal screens fabricated by exploiting photoalignment [53]. Moreover, photoalignment has been used to produce diffraction gratings, tunable optical retarders, photonic components, switchable lenses, laser, and optical rewritable displays [38, 48, 54–56].

## 26.5 Photochromic Switches Can Engineer Helical Organizations in Cholesteric Liquid Crystals

Here we introduce cholesteric mesophases in more detail. The cholesteric liquid crystalline phase is often called the chiral nematic phase since the most common way to achieve it is to add small amount of chiral molecules (dopant) to a nematic liquid crystal (Figure 26.4a) which causes a twisting of the liquid crystalline director into a supramolecular helix. All chiral dopants can be characterized by their helical twisting power (HTP), a phenomenological parameter defining how strong the dopant can twist the nematic director, and can be calculated as HTP $= p^{-1}/c$, where $p$ is cholesteric pitch and $c$ is concentration. The HTP value is mostly determined by chemical structure of the chiral dopant and by its interaction with liquid crystal molecules. One of the outstanding properties of the cholesteric mesophase is a capability to selectively reflect circularly polarized light due to Bragg diffraction. The wavelength of the reflected light ($\lambda_{max}$) is directly connected with the periodicity of the helical structure (or helix pitch) according to equation: $\lambda_{max} = np$, where $n$ is average refractive index. Thus, the color of the cholesteric layer is a "structural color" and fully depends on HTP (at constant concentration of chiral dopant). If the chiral dopant is coupled with a molecular photoswitch, or if the molecular photoswitch is chiral itself, one can expect that its HTP would be modified upon photochemical conversion. Indeed, changes in the geometry of the molecular photoswitch modify the HTP and consequently also the pitch and color of the thin film of liquid crystal are modified [13, 58]. The tunability of the pitch (Figure 26.4b) is a key to numerous applications of cholesteric materials in optics, photonics, and sensorics.

There is a great variety of different chiral photochromic dopants for liquid crystals [13, 58–63]. Here, we highlight a number of them and distinguish them in two categories based on type of chirality they can translate to liquid crystalline media: (i) dopants build by coupling stereocenter-based chirality with photochromic unit(s), and (ii) photochromic dopants having axially chiral fragments. The first type includes dopants based on menthone (**12**) (Scheme 26.2) [64, 65], cholesterol (**13**) [66], and sorbitol (**14**,**15**) [67–69] chiral cores which can be coupled with

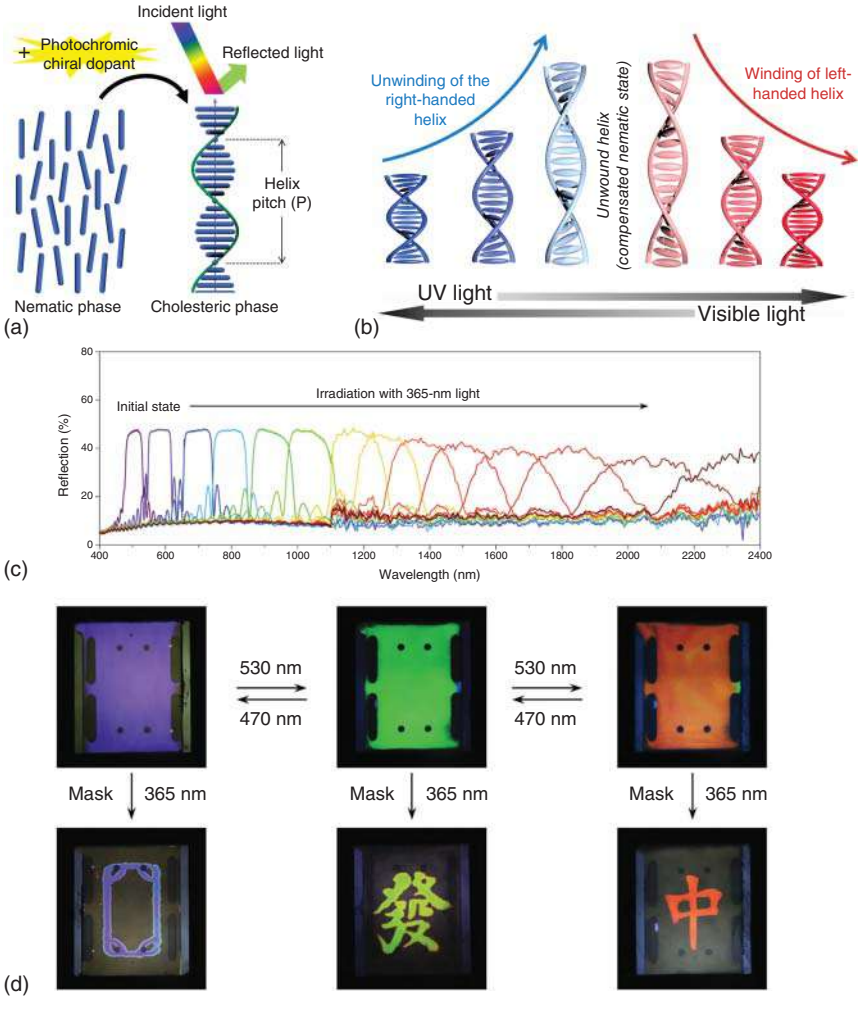


**Figure 26.4** (a) Induction of cholesteric phase by doping a nematic liquid crystal with chiral molecules. (b) Dynamic tuning of the cholesteric helix accompanied by inversion of handedness. (c) Wide-range variation of reflection colors achieved using photochromic chiral dopant (**18**). The colors are stable allowing optical information recording (d). Source: Qin et al. [57], Figure 05, p 07/with permission of Wiley-VCH.

photochromes experiencing *E*/*Z* photoisomerization of C=C or N=N double bonds. The sorbitol chiral core substituted with rod-like photochromes demonstrates the highest values of HTP and its variation upon exposure to light. Alternatively, using spirooxazine-based photochromes usually leads to low modulation of HTP [70]. An analysis of structure–property relationships of stereocenter-based photochromic chiral dopants can be found in [71, 72].

Attachment of photochromes to an axially chiral binaphthyl group (**16**–**18**) yields dopants with moderate and high HTP values, therefore enabling a wide range of

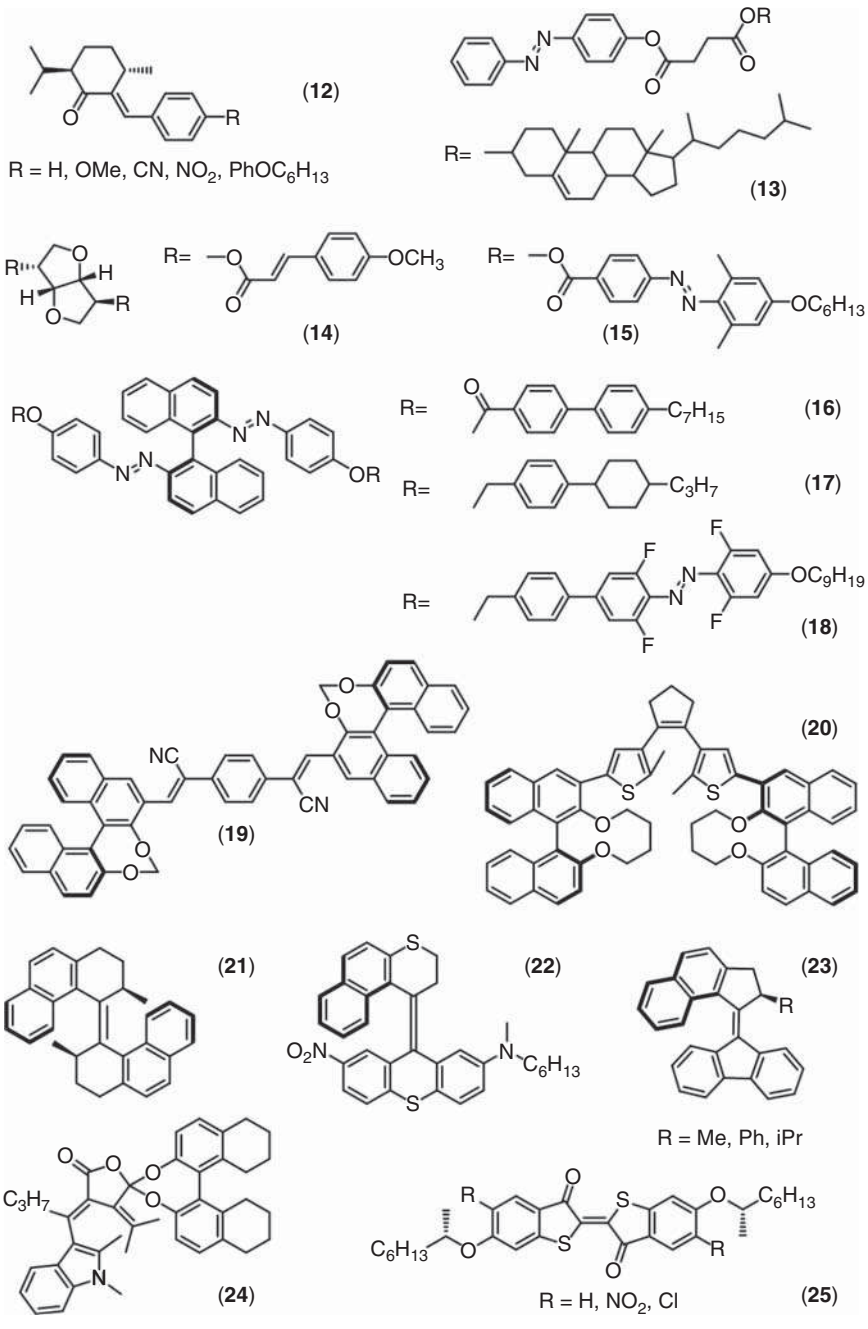


**Scheme 26.2** Chemical structure of artificial molecular motors and switches used to modulate properties of liquid crystal materials.

tunability of optical properties [73–75]. One specific example is a binaphthyl-based chiral dopant functionalized with two azobenzene moieties (**18**) [57]. The authors reached a wide range of tunable and stable structural colors by the design of azobenzene lateral fragments substituted in the *ortho*-position with fluorine atoms which makes the *cis*-isomer considerably thermally stable (Figure 26.4c,d). Overall, the tunability of selective reflection has been extensity exploited for optical information recording and patterning [57, 73, 75], for tunable lasers, filters, gratings [76–78], and optical displays [79, 80]. Besides controlling colors of thin films of liquid crystals, other functionalities can be encoded by combining molecular photoswitches with liquid crystals, which we will focus on further to give a broader perspective of the field.

The chiral photochromic dopant based on dicyanodistyrylbenzene and two bridged binaphthol chiral units (**19**) is characterized by vivid emission colors and remarkable variation of HTP upon irradiation [81]. The chiral photoswitch experiences irreversible *E*/*Z* photoisomerization responsible for tuning fluorescence and reflection colors of cholesteric materials over a 1500 nm spectral range. It was demonstrated that such chiral photochromic compounds can be used in fabrication of reflective-photoluminescent dual-mode liquid crystal devices where recorded optical information can be visualized in reflected and emitted light (Figure 26.5a).

The light-induced transformation of the switches can either wind or unwind the cholesteric helix, and sometimes the structural rearrangements are so large that they can even invert the handedness of helices (Figure 26.4B) [82, 84, 85]. However, inversion of cholesteric handedness is typically acheived by co-doping nematic liquid crystals with two chiral dopants of opposite chirality [59–61, 68]. If one chiral dopant is non-photochromic, having a constant HTP value, and the other one is photochromic and provides a substantial range of pitch variation, then by mixing them in a proper ratio, one can engineer light-responsive cholesteric helices, that also feature light-driven helix inversion. In this system, the decreasing HTP value of the photochromic dopant upon illumination is eventually overcome by the contribution of the non-photochromic dopant of opposite chirality. The liquid crystalline materials with light-induced helix inversion enable a number of unique phenomena occurring at macroscopic scale, as shown hereafter.

Cholesteric helices that feature a light-driven handedness inversion (see Figure 26.4b) allowed managing supramolecular helices in two and three dimensions [68, 82]. In [82], the inversion was induced by a dopant consisting of a dithienylcyclopentene photochromic core coupled with two axially chiral binaphthol fragments (**20**). The light-activated ring-closing reaction results in transition from initial right-handed helical structure to a completely unwound state and then further to a left-handed helical organization. These light-induced transitions are accompanied by realignment of the helical axis, from a standing helix (axis is perpendicular to the plane) to a lying helix (axis is parallel to the plane). The lying helix was used as a diffraction grating to steer light beam in two-dimensions (Figure 26.5b). In [68], a co-doping strategy was used to create a cholesteric liquid crystal that inverts handedness in response to light. A pair of chiral dopants: a sorbitol based azobenzene switch with stable *cis*-form (**15**) and a non-photochromic

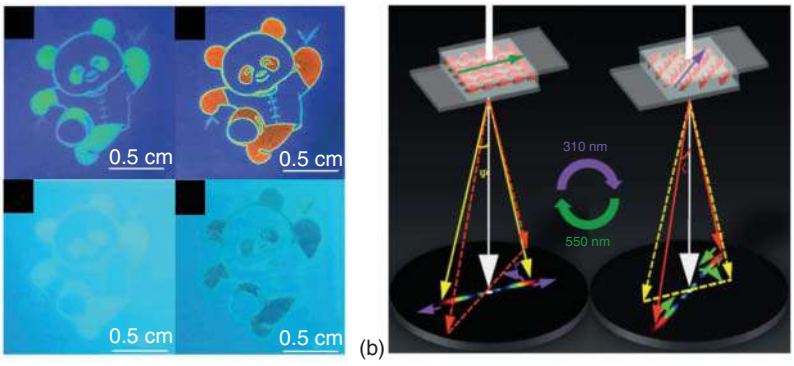
(a)
0.5 cm
0.5 cm
0.5 cm
0.5 cm
(b)
310 nm
550 nm

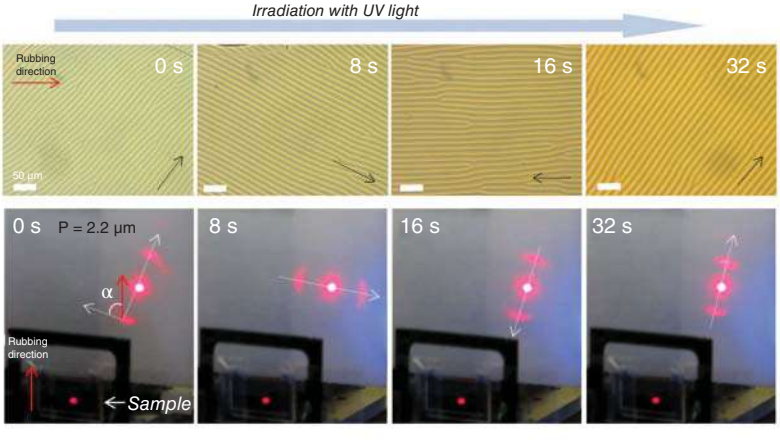
Irradiation with UV light
Rubbing direction
0 s
8 s
16 s
32 s
50 µm
0 s P = 2.2 µm
α
Rubbing direction
Sample
8 s
16 s
32 s
(c)

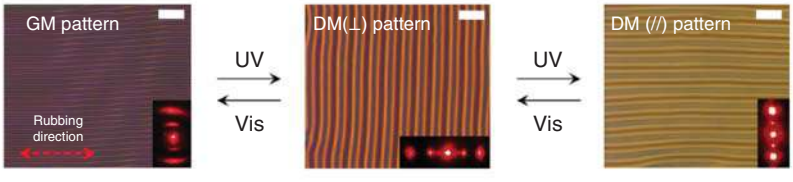
GM pattern
Rubbing direction
UV
Vis
DM(⊥) pattern
UV
Vis
DM (//) pattern
(d)

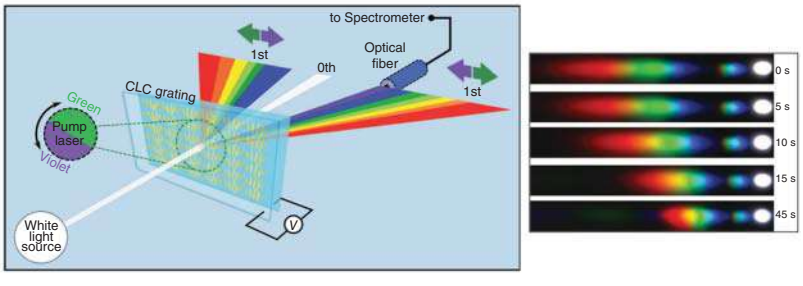
to Spectrometer
1st
0th
Optical fiber
1st
CLC grating
Green
Pump laser
Violet
White light source
V
0 s
5 s
10 s
15 s
45 s
(e)

**Figure 26.5** (a) Optical patterns observed in reflection (top) and by fluorescence (bottom) in a cholesteric liquid crystal doped with switch (**19**). Source: Li et al. [81], Figure 08, p 08/with permission of Wiley-VCH. (b) Steering a white light beam in two dimensions by light-induced structural changes of chiral switch (**20**). Source: Zheng et al. [82], Figure 02, p 03/with permission of Nature Publishing Group. (c) Light-induced rotation of striped cholesteric pattern acting as optical diffraction grating. Source: Ryabchun et al. [68], Figure 02,03, p 03,04/with permission of Wiley-VCH. (d) Light-switchable diffraction grating formed in cholesteric layer-based azobenzene chiral dopant (**15**) under weak electric field applied. Source: Ryabchun et al. [61], Figure 03, p 04/with permission of American Chemical Society. (e) Schematic representation of a cholestericbased beam steering device used in spectrum scanning system. Source: Reproduce with permission from Jau et al. [83], Figure 04, p 04/with permission of Wiley-VCH.

chiral dopant of opposite chirality were used. A hybrid-aligned (homo-planar) layer of this liquid crystal forms regular structures that act as an optical diffraction grating. Large continuous rotation of gratings was demonstrated upon irradiation with light, both clockwise and counterclockwise (Figure 26.5c). A similar photo-responsive liquid crystal was used to create a switchable and tunable electro-induced diffraction grating. In the latter case, a weak electric field applied to the cholesteric layer generated a regular pattern of stripes (grating), while light was used for switching between different orthogonal gratings and to tune their pitch (Figure 26.5d) [61]. These kinds of photo-responsive liquid crystals can find application in non-mechanical light beam steering and for spectrum scanning systems, as was demonstrated in [83] (Figure 26.5e).

## 26.6 Liquid Crystals Amplify the Motion of Molecular Switches Across Length Scales

Clearly, the operation of molecular photoswitches, often combined to a chiral character, enables the field of tunable diffraction optics [86–89]. There are, however, a number of other interesting and recently explored phenomena that reach beyond liquid crystals and displays. These phenomena and related emergent functionalities are associated with the unique operation of molecular motors that rotate unidirectionally in response to light (see Chapter 11 in Section II). Next, we discuss a few examples in which the molecular motion of light-driven molecular motors is transmitted across length scales, into macroscopic movement.

Molecular rotary motors based on overcrowded alkenes were first designed and synthesized by Ben Feringa, and subsequently studied in last decade [90, 91]. These motors (**21**–**23**) twist the liquid crystal phase effectively, due to their strong axial chirality, which inverts two times per molecular rotation cycle and thus allows switching the handedness of cholesteric liquid crystals reversibly, and tuning their pitch [85, 92–95].

The unidirectional light-driven molecular rotation of a motor was translated to the rotation of microscopic glass rod (Figure 26.6a) [96, 99, 100]. A cholesteric layer doped with molecular motor (**23**, R = Ph) and cast on a substrate promoting planar alignment forms regular patterns (polygonal fingerprint texture, similar to one in Figure 26.5c) that are mirrored in the surface corrugation. In response to light, the unwinding and rewinding of the cholesteric helix drives the rotation of the pattern

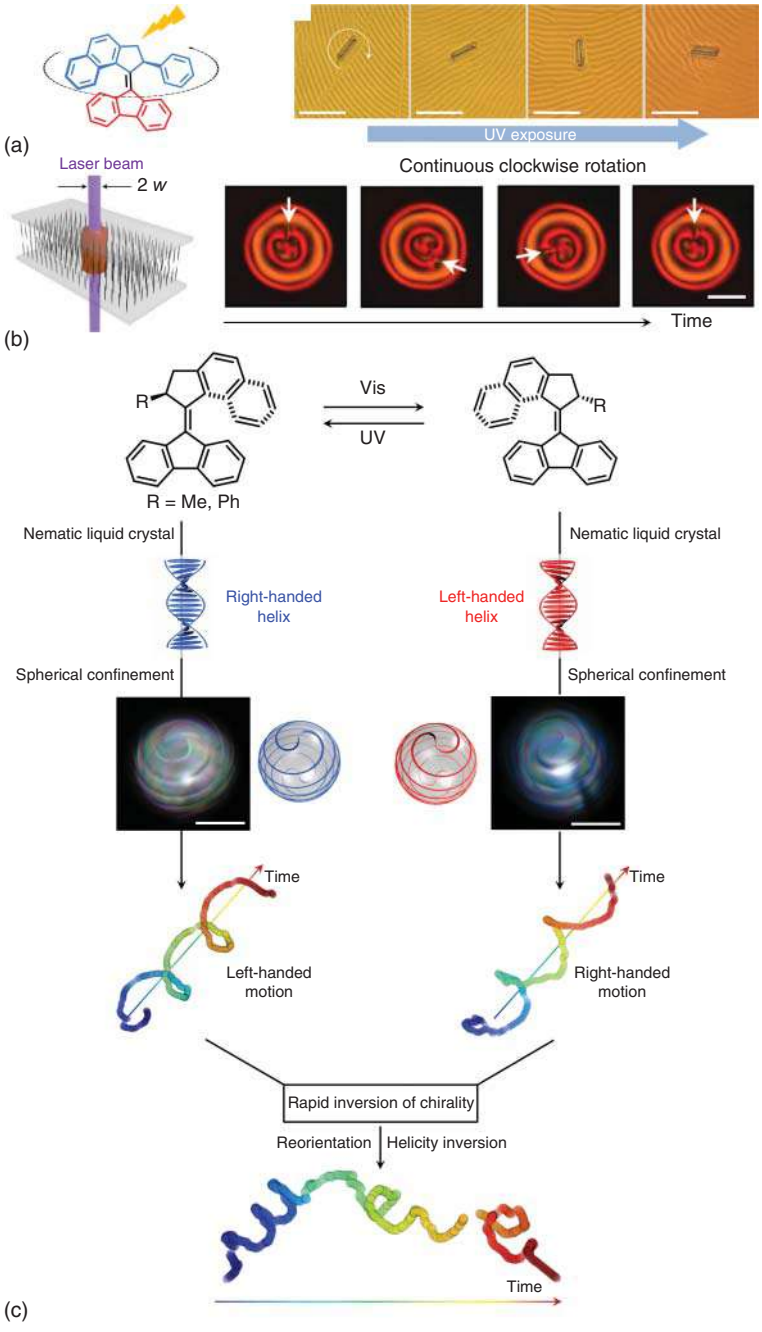
(a)
UV exposure
Laser beam
2 w
Continuous clockwise rotation
Time
(b)
R
Vis
UV
R
R = Me, Ph
Nematic liquid crystal
Nematic liquid crystal
Right-handed helix
Left-handed helix
Spherical confinement
Spherical confinement
Time
Time
Left-handed motion
Right-handed motion
Rapid inversion of chirality
Reorientation
Helicity inversion
Time
(c)

and that of objects placed on top of the liquid crystal thin film. Similar rotation of macroscopic objects was later observed for cyclic azobenzene-based chiral dopants [101, 102].

In the example above, the rotation of the micro-rod is limited by the establishment of a photo-stationary state. Next, a system featuring the continuous rotation of microscopic structures was designed (Figure 26.6b) [97]. A cholesteric liquid crystal was prepared by co-doping of a nematic liquid crystal with molecular motors (**23**) and a non-photochromic chiral dopant of opposite chirality in order to achieve helix inversion of long pitch initial state followed by helix winding. This light-responsive liquid crystal was sandwiched between two glass slides that were spaced apart just enough so that the interfacial interactions unwind the cholesteric helix. When the layer was exposed to a focused laser beam, a topological structure was formed locally, akin to a vortex. Upon longer irradiation times, the vortex starts rotating unidirectionally, and it keeps rotating for as long as the laser light is on, as a result of the delicate interplay between chiral torque, diffusion of chiral species, and the circular boundary conditions.

Complementary to the ability to control rotational motion on macroscopic scale, molecular motors can also tune translational motion. Recently, we have shown that molecular motors operating in liquid crystals can steer the movement of droplets (Figure 26.6c) [98]. Cholesteric liquid crystal materials doped with molecular motor (**23**) were confined in spherical geometry – microscopic droplets, which revealed a double helix spiral structure of the droplets. When the droplets were introduced into soapy water, they started self-propelling in a helical fashion due to micellar solubilization of liquid crystals and induced Marangoni flow [103]. The handedness of propulsion is fully determined by the handedness of cholesteric helix so that a left-handed helix promotes right-handed propulsion and vice versa. When the handedness of spiral droplets is rapidly inverted by exposure to light of high intensity, the direction (and handedness) of helical propulsion changes by the angle which is defined by the confinement of cholesteric helix. So, the operation of the molecular motor was transmitted to control the direction of propulsion of the microswimmers.

In addition to the series of molecular photoswitches and motors we discussed above, chiral fulgides (see also Chapter 9 in Section II) and thioindigos (see also Chapter 13 in Section II) should be mentioned in the context of light-responsive

**Figure 26.6** (a) The rotation of a molecular motor is transduced into the rotational motion of a microscopic glass rod through a helical architecture of cholesteric liquid crystals. Source: Reproduced with permission from Eelkema et al. [96], Figure 01, p 01/with permission of Nature Publishing Group. (b) A focused laser beam can generate a topological structure, here a vortex-like structure, in a frustrated cholesteric layer doped with a molecular motor (**23**). The vortex rotates continuously and unidirectionally upon constant light exposure. Source: Reproduced with permission from Orlova et al. [97], Figure 02, p 02/with permission of Nature Publishing Group. (c) The helix inversion promoted by artificial molecular motors can redirect the trajectory of chiral droplets. Source: Reproduced with permission from Lancia et al. [98], Figure 01, p 02/Nature Publishing Group/CC BY 4.0.

liquid crystals. Fulgide-based switches such as (**24**) were developed to modify the cholesteric pitch in a wide optical range solely by UV or visible light since the product of photo-cyclization reaction is thermally stable [104]. Photo-addressable thin films of cholesteric liquid crystals were developed based on these molecular photoswitches. Chiral thioindigo-based dopants (**25**) were used to dope ferroelectric liquid crystals [105]. Light-induced *E*/*Z* isomerization of the thioindigo molecular core results in increased polarity and a transverse dipole moment which was used to enhance the spontaneous polarization of ferroelectric liquid crystals [106]. Light-driven inversion of the sign of spontaneous polarization was achieved by later achieved also [107].

## 26.7 Conclusion

In this chapter, we have chartered recent advances in establishing a synergy between light-responsive molecular motors and switches, and their liquid crystal environment. We have shown that the light-induced rearrangements of these artificial molecular switches can be coupled with the self-assembling properties of liquid crystals in such a way as to translate these molecular rearrangements (change in molecular shape, polarity, flexibility, etc.) into new functionalities at the macroscopic level. The photochromic molecules are a highly versatile tool to control the phase behavior and molecular alignment of liquid crystals, to twist helical structures made of molecules, and to control motile behavior with light (see also Chapter 25 in Section III).

The field had witnessed great progress in utilizing achiral molecular switches in low molar mass and polymeric liquid crystal materials, and, in the future, we believe that the full complexity of light-induced molecular movement might be achieved in chiral systems. Overall the coupling of supramolecular architectures (soft matter with hierarchical organization) with chiral photochromic molecules can potentially bring the system to operate out-of-equilibrium upon action of light which would allow synthetic materials to adapt to their environmental conditions. We envision that future efforts will be focused on the synthesis of novel chiral photoswitches and molecular motors, on strategies to couple their operation with soft matter, and on setting up feedback loops toward new "intelligent" materials.

## References


1 Goodby, J.W., Saez, I.M., Cowling, S.J. et al. (2008). Transmission and amplification of information and properties in nanostructured liquid crystals. *Angew. Chem. Int. Ed.* 47: 2754.

2 Lancia, F., Ryabchun, A., and Katsonis, N. (2019). Life-like motion driven by artificial molecular machines. *Nat. Rev. Chem.* 3: 536.

3 Kelker, H. and Hatz, R. (1980). *Handbook of Liquid Crystals*. Verlag Chemie: Weinheim.


4 Collings, P.J. and Goodby, J.W. (2019). *Introduction to Liquid Crystals: Chemistry and Physics*. Boca Raton, FL: CRC Press.

5 Andrienko, D. (2018). Introduction to liquid crystals. *J. Mol. Liq.* 267: 520.

6 Petrov, A.G. (1999). *The Lyotropic State of Matter: Molecular Physics and Living Matter Physics*. Amsterdam: Gordon & Breach Science Pub.

7 Ramamoorthy, A. (ed.) (2007). *Thermotropic Liquid Crystals: Recent Advances*. Dordrecht: Springer.

8 Oswald, P. and Pieranski, P. (2005). *Nematic and Cholesteric Liquid crystals: Concepts and Physical Properties Illustrated by Experiments*. Boca Raton, FL: CRC Press.

9 Li, Q. (2012). *Liquid Crystals Beyond Displays: Chemistry, Physics, and Applications*. New Jersey: Wiley.

10 Shen, Y. and Dierking, I. (2019). Perspectives in liquid-crystal-aided nanotechnology and nanoscience. *Appl. Sci.* 9: 2512.

11 Kim, Y.K., Noh, J., Nayani, K., and Abbott, N.L. (2019). Soft matter from liquid crystals. *Soft Matter* 15: 6913.

12 Lagerwall, J.P. and Scalia, G. (2012). A new era for liquid crystal research: applications of liquid crystals in soft matter nano-, bio-and microtechnology. *Curr. Appl Phys.* 12: 1387.

13 Bisoyi, H.K. and Li, Q. (2016). Light-driven liquid crystalline materials: from photo-induced phase transitions and property modulations to applications. *Chem. Rev.* 116: 15089.

14 Amrutha, A.S., Achalkumar, A.S., and Li, Q. (2019). Light-driven phase transitions in liquid crystals and their applications. In: *Photoactive Functional Soft Materials: Preparation, Properties, and Applications*. Weinheim: Wiley.

15 Haas, W.E., Nelson, K.F., Adams, J.E., and Dir, G.A. (1974). UV imaging with nematic chlorostilbenes. *J. Electrochem. Soc.* 121: 1667.

16 Yang, R., Zhao, D., Dong, G. et al. (2018). Synthesis and characterization of photo-responsive thermotropic liquid crystals based on azobenzene. *Crystals* 8: 147.

17 Mallia, V.A. and Tamaoki, N. (2003). Photochemically driven smectic–cholesteric phase transition in an inherently photoactive dimesogen. *Chem. Mater.* 15: 3237.

18 Tamaoki, N., Aoki, Y., Moriyama, M., and Kidowaki, M. (2003). Photochemical phase transition and molecular realignment of glass-forming liquid crystals containing cholesterol/azobenzene dimesogenic compounds. *Chem. Mater.* 15: 719.

19 Sung, J.H., Hirano, S., Tsutsumi, O. et al. (2002). Dynamics of photochemical phase transition of guest/host liquid crystals with an azobenzene derivative as a photoresponsive chromophore. *Chem. Mater.* 14: 385.

20 Das, S., Varghese, S., and Kumar, N.S. (2010). Butadiene-based photoresponsive soft materials. *Langmuir* 26: 1598.

21 Davis, R., Mallia, V.A., and Das, S. (2003). Reversible photochemical phase transition behavior of alkoxy-cyano-substituted diphenylbutadiene liquid crystals. *Chem. Mater.* 15: 1057.


**22** Legge, C.H. and Mitchell, G.R. (1992). Photo-induced phase transitions in azobenzene-doped liquid crystals. *J. Phys. D: Appl. Phys.* 25: 492.

**23** Prasad, S.K., Nair, G.G., and Hegde, G. (2007). Nonequilibrium liquid crystalline layered phase stabilized by light. *J. Phys. Chem. B* 111: 345.

**24** Moran, M.J., Magrini, M., Walba, D.M., and Aprahamian, I. (2018). Driving a liquid crystal phase transition using a photochromic hydrazone. *J. Am. Chem. Soc.* 140: 13623.

**25** Prasad, S.K. and Nair, G.G. (2001). Effects of photo-controlled nanophase segregation in a re-entrant nematic liquid crystal. *Adv. Mater.* 13: 40.

**26** Prasad, S.K., Nair, G.G., and Hegde, G. (2005). Dynamic self-assembly of the liquid-crystalline smectic A phase. *Adv. Mater.* 17: 2086.

**27** Kosa, T., Sukhomlinova, L., Su, L. et al. (2012). Light-induced liquid crystallinity. *Nature* 485: 347.

**28** Kurihara, S., Ikeda, T., Tazuke, S., and Seto, J.E. (1991). Isothermal phase transition of liquid crystals induced by photoisomerization of doped spiropyrans. *J. Chem. Soc., Faraday Trans.* 87: 3251.

**29** Morimoto, M., Kobatake, S., Irie, M. et al. (2016). Photochromic Bulk Materials. In: *Photochromic Materials: Preparation, Properties and Applications*. Weinheim: Wiley.

**30** Shragina, L., Buchholtz, F., Yitzchaik, S., and Krongauz, V. (1990). Searching for photochromic liquid crystals spironaphthoxazine substituted with a mesogenic group. *Liq. Cryst.* 7: 643.

**31** Han, J., Li, Y.X., Pang, M.L. et al. (2007). A novel photochromic liquid crystal system based on biindenylidenedione derivatives. *New J. Chem.* 31: 543.

**32** Frigoli, M. and Mehl, G.H. (2004). Modulation of the absorption, fluorescence, and liquid-crystal properties of functionalised diarylethene derivatives. *Chem. - Eur. J.* 10: 5243.

**33** Frigoli, M., Welch, C., and Mehl, G.H. (2004). Design of mesomorphic diarylethene-based photochromes. *J. Am. Chem. Soc.* 126: 15382.

**34** Ikeda, T. (2003). Photomodulation of liquid crystal orientations for photonic applications. *J. Mater. Chem.* 13: 2037.

**35** Lisinetskii, V., Ryabchun, A., Bobrovsky, A., and Schrader, S. (2015). Photochromic composite for random lasing based on porous polypropylene infiltrated with azobenzene-containing liquid crystalline mixture. *ACS Appl. Mater. Interfaces* 7: 26595.

**36** Sobolewska, A., Bartkiewicz, S., Mysliwiec, J., and Singer, K.D. (2014). Holographic memory devices based on a single-component phototropic liquid crystal. *J. Mater. Chem. C* 2: 1409.

**37** Ryabchun, A., Raguzin, I., Stumpe, J. et al. (2016). Cholesteric polymer scaffolds filled with azobenzene-containing nematic mixture with phototunable optical properties. *ACS Appl. Mater. Interfaces* 8: 27227.

**38** Chigrinov, V.G., Kozenkov, V.M., and Kwok, H.S. (2008). *Photoalignment of Liquid Crystalline Materials: Physics and Applications*. Chichester: Wiley.


**39** Seki, T., Nagano, S., and Hara, M. (2013). Versatility of photoalignment techniques: from nematics to a wide range of functional materials. *Polymer* 54: 6053.

**40** Ichimura, K. (2000). Photoalignment of liquid-crystal systems. *Chem. Rev.* 100: 1847.

**41** Ichimura, K., Suzuki, Y., Seki, T. et al. (1988). Reversible change in alignment mode of nematic liquid crystals regulated photochemically by command surfaces modified with an azobenzene monolayer. *Langmuir* 4: 1214.

**42** Yaroshchuk, O. and Reznikov, Y. (2012). Photoalignment of liquid crystals: basics and current trends. *J. Mater. Chem.* 22: 286.

**43** Priimagi, A., Barrett, C.J., and Shishido, A. (2014). Recent twists in photoactuation and photoalignment control. *J. Mater. Chem. C* 2: 7155.

**44** Slussarenko, S., Murauski, A., Du, T. et al. (2011). Tunable liquid crystal q-plates with arbitrary topological charge. *Opt. Express* 19: 4085.

**45** Xue, C., Xiang, J., Nemati, H. et al. (2015). Light-driven reversible alignment switching of liquid crystals enabled by azo thiol grafted gold nanoparticles. *ChemPhysChem* 16: 1852.

**46** Ouskova, E., Reznikov, Y., Shiyanovskii, S.V. et al. (2001). Photo-orientation of liquid crystals due to light-induced desorption and adsorption of dye molecules on an aligning surface. *Phys. Rev. E* 64: 051709.

**47** West, J.L., Su, L., and Reznikov, Y. (2001). Photo-alignment using adsorbed dichroic molecules. *Mol. Cryst. Liq. Cryst. Sci. Technol., Sect. A* 364: 199.

**48** Schaal, F., Rutloh, M., Weidenfeld, S. et al. (2018). Optically addressed modulator for tunable spatial polarization control. *Opt. Express* 26: 28119.

**49** Akiyama, H., Kawara, T., Takada, H. et al. (2002). Synthesis and properties of azo dye aligning layers for liquid crystal cells. *Liq. Cryst.* 29: 1321.

**50** Pan, S., Ho, J.Y., Chigrinov, V.G., and Kwok, H.S. (2018). Novel photoalignment method based on low-molecular-weight azobenzene dyes and its application for high-dichroic-ratio polarizers. *ACS Appl. Mater. Interfaces* 10: 9032.

**51** Bobrovsky, A., Ryabchun, A., and Shibaev, V. (2011). Liquid crystals photoalignment by films of side-chain azobenzene-containing polymers with different molecular structure. *J. Photochem. Photobiol., A* 218: 137.

**52** Ryabchun, A., Bobrovsky, A., Chun, S.H., and Shibaev, V. (2013). A novel generation of photoactive comb-shaped polyamides for the photoalignment of liquid crystals. *J. Polym. Sci., Part A: Polym. Chem.* 51: 4031.

**53** Miyachi, K., Kobayashi, K., Yamada, Y., and Mizushima, S. (2010). The World's First Photo Alignment LCD Technology Applied to Generation Ten Factory. *Dig. Tech. Pap. - Soc. Inf. Disp. Int. Symp.* 41: 579.

**54** Chigrinov, V.G. (2013). Photoaligning and photopatterning—a new challenge in liquid crystal photonics. *Crystals* 3: 149.

**55** Zarins, E., Balodis, K., Ruduss, A. et al. (2018). Molecular glasses of azobenzene for holographic data storage applications. *Opt. Mater.* 79: 45.

**56** Lin, T.H., Huang, Y., Zhou, Y. et al. (2006). Photo-patterning micro-mirror devices using azo dye-doped cholesteric liquid crystals. *Opt. Express* 14: 4479.


**57** Qin, L., Gu, W., Wei, J., and Yu, Y. (2018). Piecewise phototuning of self-organized helical superstructures. *Adv. Mater.* 30: 1704941.

**58** Kim, Y. and Tamaoki, N. (2019). Photoresponsive chiral dopants: light-driven helicity manipulation in cholesteric liquid crystals for optical and mechanical functions. *ChemPhotoChem* 3: 284.

**59** Qiao, J., Lin, S., Li, J. et al. (2019). Reversible chirality inversion of circularly polarized luminescence in a photo-invertible helical cholesteric superstructure. *Chem. Commun.* 55: 14590.

**60** Bisoyi, H.K. and Li, Q. (2016). Light-directed dynamic chirality inversion in functional self-organized helical superstructures. *Angew. Chem. Int. Ed.* 55: 2994.

**61** Ryabchun, A., Yakovlev, D., Bobrovsky, A., and Katsonis, N. (2019). Dynamic diffractive patterns in helix-inverting cholesteric liquid crystals. *ACS Appl. Mater. Interfaces* 11: 10895.

**62** Wang, Y. and Li, Q. (2012). Light-driven chiral molecular switches or motors in liquid crystals. *Adv. Mater.* 24: 1926.

**63** Zheng, Z.G., Lu, Y.Q., and Li, Q. (2020). Photoprogrammable Mesogenic Soft Helical Architectures: A Promising Avenue toward Future Chiro-Optics. *Adv. Mater.* 1905318.

**64** Lub, J., Hoeve, W.T., Nijssen, W.P.M. et al. (2002). The effect of the position of the methyl group on the helical twisting powers of aldol condensation products of methyl cyclohexanones. *Liq. Cryst.* 29: 995.

**65** Yarmolenko, S.N., Kutulya, L.A., Vashchenko, V.V., and Chepeleva, L.V. (1994). Photosensitive chiral dopants with high twisting power. *Liq. Cryst.* 16: 877.

**66** Kim, Y. and Tamaoki, N. (2016). Asymmetric dimers of chiral azobenzene dopants exhibiting unusual helical twisting power upon photoswitching in cholesteric liquid crystals. *ACS Appl. Mater. Interfaces* 8: 4918.

**67** Bobrovsky, A., Ryabchun, A., Cigl, M. et al. (2014). New azobenzene-based chiral-photochromic substances with thermally stable Z-isomers and their use for the induction of a cholesteric mesophase with a phototunable helix pitch. *J. Mater. Chem. C* 2: 8622.

**68** Ryabchun, A., Bobrovsky, A., Stumpe, J., and Shibaev, V. (2015). Rotatable diffraction gratings based on cholesteric liquid crystals with phototunable helix pitch. *Adv. Opt. Mater.* 3: 1273.

**69** Lub, J., Nijssen, W.P.M., Wegh, R.T. et al. (2005). Synthesis and properties of photoisomerizable derivatives of isosorbide and their use in cholesteric filters. *Adv. Funct. Mater.* 15: 1961.

**70** Jin, L.M., Li, Y., Ma, J., and Li, Q. (2010). Synthesis of novel thermally reversible photochromic axially chiral spirooxazines. *Org. Lett.* 12: 3552.

**71** Zahangir Alam, M., Yoshioka, T., Ogata, T. et al. (2007). The influence of molecular structure on helical twisting power of chiral azobenzene compounds. *Liq. Cryst.* 34: 1215.

**72** Eelkema, R. (2011). Photo-responsive doped cholesteric liquid crystals. *Liq. Cryst.* 38: 1641.


**73** Li, Q., Green, L., Venkataraman, N. et al. (2007). Reversible photoswitchable axially chiral dopants with high helical twisting power. *J. Am. Chem. Soc.* 129: 12908.

**74** Huang, H., Orlova, T., Matt, B., and Katsonis, N. (2018). Long-lived supramolecular helices promoted by fluorinated photoswitches. *Macromol. Rapid Commun.* 39: 1700387.

**75** Ma, J., Li, Y., White, T. et al. (2010). Light-driven nanoscale chiral molecular switch: reversible dynamic full range color phototuning. *Chem. Commun.* 46: 3463.

**76** Kong, X., Wang, X., Luo, T. et al. (2017). Photomanipulated architecture and patterning of azopolymer array. *ACS Appl. Mater. Interfaces* 9: 19345.

**77** Chen, L., Li, Y., Fan, J. et al. (2014). Photoresponsive monodisperse cholesteric liquid crystalline microshells for tunable omnidirectional lasing enabled by a visible lightdriven chiral molecular switch. *Adv. Opt. Mater.* 2: 845.

**78** Mykytiuk, T.V., Ilchishin, I.P., Yaroshchuk, O.V. et al. (2014). Rapid reversible phototuning of lasing frequency in dye-doped cholesteric liquid crystal. *Opt. Lett.* 39: 6490.

**79** Li, Q., Li, Y., Ma, J. et al. (2011). Directing dynamic control of red, green, and blue reflection enabled by a light-driven self-organized helical superstructure. *Adv. Mater.* 23: 5069.

**80** Venkataraman, N., Magyar, G., Montbach, E. et al. (2009). Thin flexible photosensitive cholesteric displays. *J. Soc. Inf. Disp.* 17: 869.

**81** Li, J., Zhang, Z., Tian, J. et al. (2017). Dicyanodistyrylbenzene-based chiral fluorescence photoswitches: an emerging class of multifunctional switches for dual-mode phototunable liquid crystals. *Adv. Opt. Mater.* 5: 1700014.

**82** Zheng, Z.G., Li, Y., Bisoyi, H.K. et al. (2016). Three-dimensional control of the helical axis of a chiral nematic liquid crystal by light. *Nature* 531: 352.

**83** Jau, H.C., Li, Y., Li, C.C. et al. (2015). Light-driven wide-range nonmechanical beam steering and spectrum scanning based on a self-organized liquid crystal grating enabled by a chiral molecular switch. *Adv. Opt. Mater.* 3: 166.

**84** Katsonis, N., Lacaze, E., and Ferrarini, A. (2012). Controlling chirality with helix inversion in cholesteric liquid crystals. *J. Mater. Chem.* 22: 7088.

**85** Ryabchun, A., Lancia, F., Chen, J. et al. (2020). Helix inversion controlled by molecular motors in multistate liquid crystals. *Adv. Mater.* 32: 2004420.

**86** Ryabchun, A. and Bobrovsky, A. (2018). Cholesteric liquid crystal materials for tunable diffractive optics. *Adv. Opt. Mater.* 6: 1800335.

**87** Yuan, C.L., Huang, W., Zheng, Z.G. et al. (2019). Stimulated transformation of soft helix among helicoidal, heliconical, and their inverse helices. *Sci. Adv.* 5: eaax9501.

**88** Fan, J., Li, Y., Bisoyi, H.K. et al. (2015). Light-directing omnidirectional circularly polarized reflection from liquid-crystal droplets. *Angew. Chem. Int. Ed.* 54: 2160.

**89** Wang, H., Bisoyi, H.K., McConney, M.E. et al. (2019). Visible light induced self organized helical superstructure in orientationally ordered fluids. *Adv. Mater.* 31: 1902958.


**90** Browne, W. and Feringa, B. (2006). Making molecular machines work. *Nat. Nanotechnol.* 1: 25.

**91** van Leeuwen, T., Lubbe, A.S., Štacko, P. et al. (2017). Dynamic control of function by light-driven molecular motors. *Nat. Rev. Chem.* 1: 0096.

**92** Sleczkowski, P., Zhou, Y., Iamsaard, S. et al. (2018). Light-activated helical inversion in cholesteric liquid crystal microdroplets. *Proc. Natl. Acad. Sci. U.S.A.* 115: 4334.

**93** Aβhoff, S.J., Sukas, S., Yamaguchi, T. et al. (2015). Superstructures of chiral nematic microspheres as all-optical switchable distributors of light. *Sci. Rep.* 5: 14183.

**94** Orlova, T., Aßhoff, S.J., Yamaguchi, T. et al. (2015). Creation and manipulation of topological states in chiral nematic microspheres. *Nat. Commun.* 6: 7603.

**95** Aßhoff, S.J., Iamsaard, S., Bosco, A. et al. (2013). Time-programmed helix inversion in phototunable liquid crystals. *Chem. Commun.* 49: 4256.

**96** Eelkema, R., Pollard, M.M., Vicario, J. et al. (2006). Nanomotor rotates microscale objects. *Nature* 440: 163.

**97** Orlova, T., Lancia, F., Loussert, C. et al. (2018). Revolving supramolecular chiral structures powered by light in nanomotor-doped liquid crystals. *Nat. Nanotechnol.* 13: 304.

**98** Lancia, F., Yamamoto, T., Ryabchun, A. et al. (2019). Reorientation behavior in the helical motility of light-responsive spiral droplets. *Nat. Commun.* 10: 1.

**99** Eelkema, R., Pollard, M.M., Katsonis, N. et al. (2006). Rotational reorganization of doped cholesteric liquid crystalline films. *J. Am. Chem. Soc.* 128: 14397.

**100** Bosco, A., Jongejan, M.G., Eelkema, R. et al. (2008). Photoinduced reorganization of motor-doped chiral liquid crystals: bridging molecular isomerization and texture rotation. *J. Am. Chem. Soc.* 130: 14615.

**101** Thomas, R., Yoshida, Y., Akasaka, T., and Tamaoki, N. (2012). Influence of a change in helical twisting power of photoresponsive chiral dopants on rotational manipulation of micro-objects on the surface of chiral nematic liquid crystalline films. *Chem. - Eur. J.* 18: 12337.

**102** Mafy, N.N., Kim, Y., Thomas, R. et al. (2019). Molecular crankshaft effect converting piston-like molecular motion to continuous rotation of macro objects. *ACS Appl. Mater. Interfaces* 11: 15097.

**103** Yamamoto, T. and Sano, M. (2017). Chirality-induced helical self-propulsion of cholesteric liquid crystal droplets. *Soft Matter* 13: 3328.

**104** Janicki, S.Z. and Schuster, G.B. (1995). A liquid crystal opto-optical switch: nondestructive information retrieval based on a photochromic fulgide as trigger. *J. Am. Chem. Soc.* 117: 8524.

**105** Maly, K. and Lemieux, R. (1999). Design of photonic liquid crystal materials: synthesis and evaluation of new chiral thioindigo dopants designed to photomodulate the spontaneous polarization of ferroelectric liquid crystals. *J. Mater. Chem.* 9: 1679.


**106** Lemieux, R.P. (2005). Photoswitching of ferroelectric liquid crystals using photochromic dopants. *Soft Matter* 1: 348.

**107** Vlahakis, J.Z., Wand, M.D., and Lemieux, R.P. (2003). Photoinduced polarization inversion in a ferroelectric liquid crystal using an ambidextrous chiral thioindigo dopant. *J. Am. Chem. Soc.* 125: 6862.

# 27 Photoswitchable Fluorophores for Super-Resolution Optical Microscopy

Kakishi Uno, Vladimir N. Belov, and Mariano L. Bossi

**Fluorescent Molecular Switches**

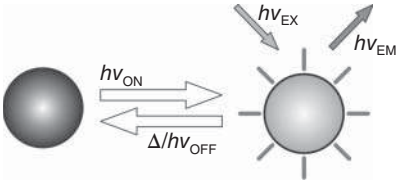


Switching between two distinct molecular states, a fluorescent and a dark one, is the common feature of all fluorescence nanoscopies, and the key to breaking the diffraction barrier.

**Characteristic Features**

High brightness, outstanding fatigue resistance, high contrast between molecular states, and tunable *on*- and *off*- rates. Photochromic compounds offer a great synthetic flexibility to design molecular switches with tailored and optimized properties.

**Main Core Structures**

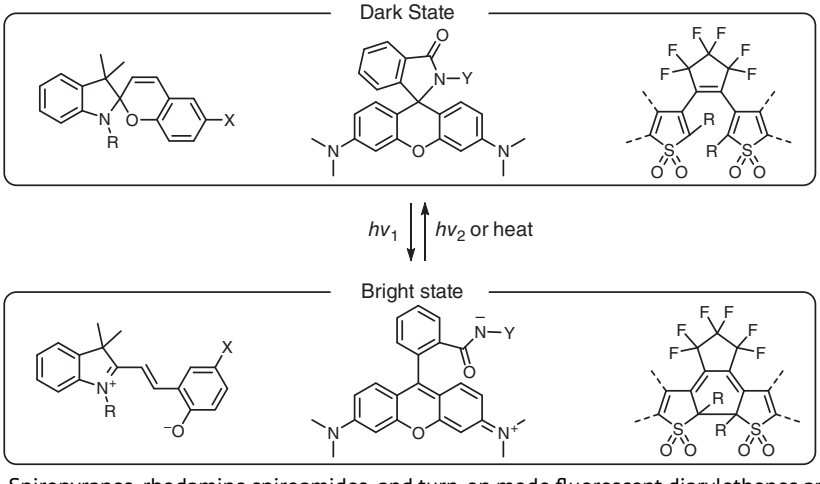


Spiropyranes, rhodamine spiroamides, and turn-on mode fluorescent diarylethenes are the most popular classes of photochromic compounds used to design photo-switchable fluorescent markers for super-resolution microscopies.

**Key References**

Lee, M., Rai, P., Williams, J. et al. (2014). Small-molecule labeling of live cell surfaces for three-dimensional super-resolution microscopy. *J. Am. Chem. Soc*. 136: 14003–14006.

Roubinet, B., Bossi, M.L., Alt, P., et al. (2016). Carboxylated photoswitchable diarylethenes for biolabeling and super-resolution RESOLFT microscopy. *Angew. Chem. Int. Ed*. 55: 15429–15433.

Nevskyi, O., Sysoiev, D., Dreier, J., et al. (2018). Fluorescent diarylethene photoswitches – a universal tool for super-resolution microscopy in nanostructured materials. *Small* 14: 1703333.

# 27

# Photoswitchable Fluorophores for Super-Resolution Optical Microscopy

*Kakishi Uno, Vladimir N. Belov, and Mariano L. Bossi*

*Department of NanoBiophotonics, Max Planck Institute for Multidisciplinary Sciences, Am Fassberg 11, 37077 Göttingen, Germany*

## 27.1 Introduction: Targeted and Stochastic Methods of Optical Super-Resolution

Super-resolution fluorescence microscopies have radically transformed optical imaging in the life and material sciences over the past two decades [1–6]. As a result, objects and structural features at distances on the (bio)macromolecular scale, i.e. far below the diffraction limit, can be resolved. The key feature of all optical nanoscopies is the ability to discern densely packed fluorescent emitters, by establishing the position of a marker while silencing all neighboring ones. A simple game with two molecular states is essential for breaking the diffraction barrier: molecules are transiently transferred to a fluorescent (*on*) state for registration while keeping all adjacent ones in a dark (*off*) state [1]. In addition to this requirement (sequential fluorescence *on*/*off* switching), it is necessary to find the position of the active markers (those in the *on* state). This can be done by applying various strategies that can be grouped in two main families: coordinate-targeted methods (STED and RESOLFT) with (stimulated emission depletion (STED) and reversible saturable optical fluorescence transitions (RESOLFT)), and coordinate-stochastic methods (photo-activated localization microscopy (PALM), stochastic optical reconstruction microscopy (STORM), points accumulation for imaging in nanoscale topography (PAINT); see below for abbreviations). These methods improve the spatial resolution by at least one order of magnitude compared to conventional ones and deliver routinely ~20–50 nm. The most recent MINFLUX nanoscopy, based on a synergistic combination of the previous two approaches, has extended nanoscopy to molecular sizes (~1 nm) [7].

Coordinate-targeted methods (STED [8], RESOLFT [9], GSD [10]) rely on an illumination pattern, featuring a zero-intensity point, that forces all the molecules to transition to their dark states, except those that are in or quite near the nodal point. Although the spot with molecules *initially* switched-on (and excited) is relatively large (limited by light diffraction), only a group in a sub-diffraction spot is observed

*Molecular Photoswitches: Chemistry, Properties, and Applications*,
First Edition. Edited by Zbigniew L. Pianowski.


*upon application of the illumination pattern*. Their position is predefined and known, by the geometry of this off-switching pattern. Sequentially, the process consists of two steps: driving a set of molecules to the *on* state within a diffraction limited spot (on-switching), followed by application of a co-centered depletion beam, which switches off (to the dark state) only the emitters on the periphery. Finally, the emission of the molecules remaining in the *on* state, at the very center of the depletion "doughnut," is measured (Scheme 27.1). The emission is recorded in a confocal, point-like detector, and the image is formed by repetition and raster-scanning this pulse sequence of beams, similar to a confocal microscope. It is important to notice that, at a certain position of the beams, all fluorophores in the areas of excitation, on-switching, and off-switching beams will be "active." That means, they will be forced to switch on and off regardless of whether they are observed or not. The consequence is that they need to repeat their performance, once the beams scan their position highlighting them on the "scene." In fact, they need to "silently switch" at least hundreds or thousands of times per "observed switch." A failure to fulfil this condition (e.g. due to photobleaching) results in a massive loss of the image quality and resolution.

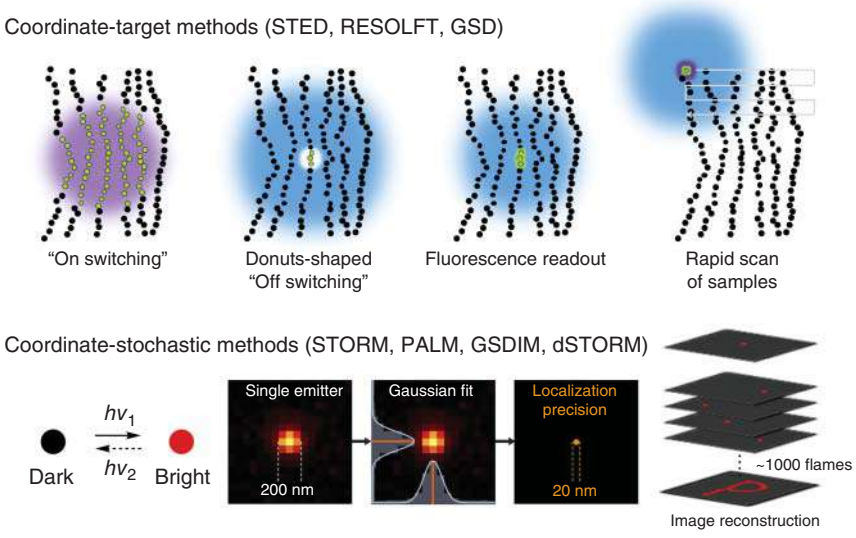


**Scheme 27.1** Schematic representation of fluorescence nanoscopy schemes: coordinate-targeted (top) and coordinate-stochastic (bottom) methods. States and transitions involved are also shown. Source: Hell [11], Jimenez et al. [12].

The first and now widely established targeted method is STED microscopy. The off- and on-states are the ground and the first excited singlet, respectively. Excitation is the on-switching transition, and stimulated emission is the off-switching one. The competing spontaneous decay depopulates the *on* state, and the whole process (on/off-switching, excitation, and detection) must be completed within the lifetime of the singlet state ($\tau_{S1}$, a few nanoseconds). Thus, the light intensities are kept high (depletion ~100 MW cm$^{-2}$) [4] and laser pulses short (100–600 ps), resulting

in potentially high photo-toxicity and photo-damage; moreover, more expensive laser sources are required. In contrast, RESOLFT methods use ground states as the on- and off-states [1, 9]. The light intensities decrease proportional to $\tau_{nr}/\tau_{S1}$ (with respect to STED), where $\tau_{nr}$ is the lifetime ($1/k$) of any thermal reaction inducing the on–off transition (with rate $k$) and competing with the photoinduced ones. In a bi-stable system (e.g. *P*-type photochrome), the intensities used are typically in the order of $10\,W\,cm^{-2}$–$100\,kW\,cm^{-2}$, for practical (speed) reasons [4].

In coordinate-stochastic methods (STORM [13], PALM [14], GSDIM [15], dSTORM [16]), the vast majority of the fluorophores must be brought into the off-state, leaving only a small and sparse fraction of them in the on-state at a time, at random unknown positions. The markers that are simultaneously in the *on* state must be separated by distances large enough (i.e. the diffraction limit) to attribute the emitted photons to single emitters. Importantly, coordinate-stochastic approaches require the detection of fluorophores at the single-molecule (SM) level. A fluorescence wide-field image is recorded at a camera, and the positions of the emitters are estimated from the centroids of the patterns they produced in the image. The precision of this localization process improves with the number of photons collected from each marker (Scheme 27.1). Then, the molecules whose positions had been recorded are switched off, and the process is repeated: a new sparse subset of molecules is switched on, and a new frame is recorded (wide-field image). New positions are calculated and added to a list that keeps track of localized single molecules, from typically (few) tens of thousands of frames [12]. The super-resolution image is constructed as a 2D histogram of a multitude of positions, with a spatial resolution equal to the localization accuracy, provided the localization density is high enough to meet the sampling requirements.

The crucial factor for breaking the diffraction barrier is how the transition between molecular states is induced, controlled, and detected. The nature of the states of the fluorescent markers, as well as their photophysical and photochemical properties, are of paramount relevance. Fortunately, the synthetic organic chemistry allows creating "tailor-made" compounds with desired features. Therefore, it is not surprising that super-resolution techniques renewed interest in switchable fluorescent probes. Indeed, the new molecular photoswitches with outstanding properties set the pace, to a large extent, for the progress in all research fields of optical super-resolution [6, 11, 17–21].

## 27.2 Specific Properties Required for Optimal Performance

Modern nanoscopies demand fluorescent dyes that can be reversibly switched between emissive (*on*) and non-emissive (*off*) states by irradiation with focused light (Scheme 27.2). Super-resolution microscopes are built with state-of-the-art optics and light sources. High-quality, aberration-corrected lenses with large numerical apertures (1.35–1.45) exist only in the visible range, with some extensions to ~355 nm. This limits the shortest wavelengths available for *on*/*off* switching ($\lambda_{on}/\lambda_{off}$) to a region >355 nm. However, longer wavelengths (preferable

532–640 nm) are desirable for applications in which living specimens are involved, because UV and violet light elicits higher autofluorescence in living cells and tissues, is potentially phototoxic, and highly dispersed and thus penetrates less into the sample. Other general requirements for the reversible markers include a large spectral separation between states to minimize cross-talk, significant signal contrast between states (i.e. difference in the fluorescence efficiency), as well as a reliable control of the switching processes and rates (preferably all-optically addressable).

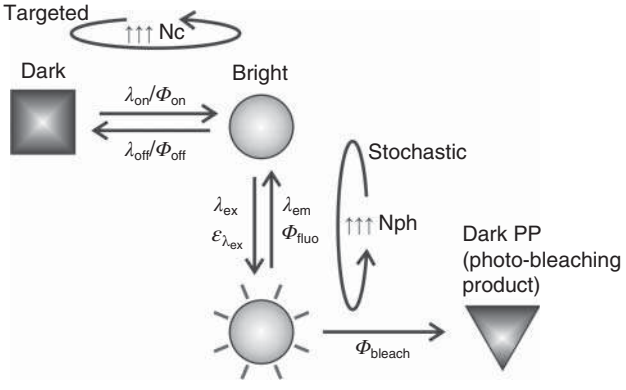


**Scheme 27.2** Major states and transitions in targeted and stochastic optical nanoscopies. *Dark* – non-fluorescent state. *Bright* – fluorescent state (ground and excited one), Nc – number of (photoinduced) *on–off* cycles, Nph – number of emitted photons, *PP* – (dark) photoproduct; $\Phi$ – quantum yields; $\varepsilon$–extinction coefficients; $\lambda$ – wavelengths of the photoinduced transitions between states.

In addition to requirements and limitations posed on wavelengths inducing transitions between states, each technique has its own demands regarding the photophysical properties of the markers and the states involved. A good **brightness** (product of the fluorescence quantum yield $\Phi_{fluo}$ and extinction coefficient at the excitation wavelength $\lambda_{EX}$) is in principle required in all methods, but clearly more critical for stochastic ones. Improving the spatial resolution to 20–30 nm requires detection of $10^2$–$10^3$ photons. If we consider a typical collection efficiency of 10% for a good microscope, we need $10^3$–$10^4$ emitted photons per incursion into a fluorescent state ($Nph \approx \Phi_{fluo}/\Phi_{off}$). For a perfect fluorophore ($\Phi_{fluo} \approx 1$), this imposes a value of $\Phi_{off} \approx 10^{-3}$–$10^{-4}$. The reason for the low value is that both reactions, emission and off-switching, compete for the same excited state. **Conversion** in the photo-stationary state ($\alpha_{PSS} = [dark]/C_0$) is also critical in stochastic methods; these techniques require high labeling density combined with sparse activation (*off* → *on* switching) to ensure meaningful images and single-molecule detection. A 10-fold resolution enhancement in 2D requires a density of over 1000 molecules in a diffraction-limited spot. Thus, to start an image acquisition, one must reach the photo-stationary state with an ensemble conversion to the dark species of over 99.9%. Consequently, the ratio of the ***on*- and *off*-rates** (~the duty cycle) must be kept $<10^{-3}$ during the whole measurement. This is not so critical in coordinate-targeted methods, as they can better tolerate a higher background [1, 4];

high conversion is still desired there, but such extreme values are unnecessary. **Fatigue resistance**: the targeted strategies need as many *on*/*off* cycles (Nc) as possible, with a reasonable photon yield per burst; while stochastic ones need few on/off cycles (or even one), but as many photons per burst Nph (as many excitation/emission cycles), as possible. "Burst" in this context means incursion into a bright "*on*" state. As a result, the preferable *off*-switching quantum yields ($\Phi_{off}$) required for target methods are in the range $10^{-2}$–$10^{-3}$ (to provide reasonable imaging speed), and for stochastic ones $<10^{-4}$. The photobleaching quantum yields ($\Phi_{bleach}$) for the most photostable fluorescent dyes are $10^{-6}$–$10^{-7}$ [22]. Thus, when $\Phi_{off}$ reaches that order of magnitude, the photochromic compounds (PC) that switch reversibly under low irradiation (in an ensemble experiment, in a cuvette), in a microscope under single-molecule observation, are likely to undergo only "a half cycle" and bleach from the *on* state (*off* → *on* → *bleached*). This is not critical for stochastic methods, which tolerate such a "caged-fluorophore" behavior. Nevertheless, though reversibility is not mandatory for stochastic methods, it is desired nevertheless. Switchable dyes (even if Nc∼10 cycles) [23] are advantageous over the "single-use" photoactivatable (caged) dyes, because more localizations improve the image quality and facilitate time-lapse imaging.

## 27.3 Design of Photoswitchable Fluorescent Compounds

A combination of photoswitching and fluorescence is not a common feature, let alone a probe also fulfills all requirements mentioned above. Nevertheless, a few strategies have been successful and provided fluorescence switching in super-resolution microscopies. Photoswitchable and photoactivatable fluorescent proteins are widely used in both targeted (RESOLFT) [24] and stochastic (PALM) [25] methods. Despite substantial improvements, their fatigue resistance is in general inferior to organic dyes [5]. The so-called blinking fluorophores are applicable in stochastic methods (STORM, GSDIM, dSTORM) [15, 17, 23]. Relying on long-living photophysical states, they need relatively high irradiation powers to initially pump to and keep the markers in the dark state. The actual mechanism is not always fully understood, with an exception of cyanines [26]. Cyanines require special "blinking buffers" containing an enzymatic system for oxygen removal, high thiol content, or redox agents [18, 23, 26]. Such cocktail is strongly disfavored in live cell studies; however, intracellular glutathione (a thiol) may support blinking [27]. These limitations have been overcome with xanthene dyes bearing an intramolecular nucleophile and existing in thermal equilibrium between a fluorescent "open" form and a non-fluorescent spirocyclic form, interconverting via intramolecular spirocyclization reaction [28]. Unfortunately, this equilibrium is strongly pH sensitive and lacks any photo-control over the blinking statistics.

Alternatively, photochromic organic compounds offer great synthetic freedom and flexibility as scaffolds to achieve the desired goals: independence from any chemical additives, a known and accessible mechanism, reliable photochemical control over the *on* and *off* reactions, extremely long-living metastable states involved or even bi-stability. So far, several fluorescent switches from various

families of photochromic compounds have been used in imaging with super-resolution in targeted and stochastic methods. The most prominent examples belong to spiropyranes, diarylethenes (DAEs), and photoswitchable spiroamides, and will be discussed in the following section.

As most photochromic compounds (PCs) have non-fluorescent isomeric states, early approaches toward fluorescence switching were based on binding a photochromic compound with a fluorescent one, in a dyad style (Scheme 27.3). The switching usually results from Förster resonance energy transfer (FRET) (though other mechanisms are possible) from the fluorophore (donor) selectively to one isomer of the photochromic part (acceptor) with an absorption band overlapping with the emission band of the fluorophore. This strategy has some disadvantages. First, the large molecular size may result in low solubility and insufficient cell permeability (important for live-cell applications), to say nothing about the multistep synthesis. Second, the initial (stable) isomer is usually a bright one (with spiropyranes and diarylethenes as acceptors), and it is not always possible to drive the system quantitatively to the dark state. Third, photobleaching is favored for the PC leaving the system in a constantly bright state (bright photoproduct). Fourth, the readout may be destructive, as it results in the PC in the excited state. On the other hand, the advantage is that practically any PC can be used, as long as a matching fluorophore is available. Its choice is rather simple: high emission efficiency, photostability, a binding site, and an emission overlapping with the absorption band of one of the PC's isomers.

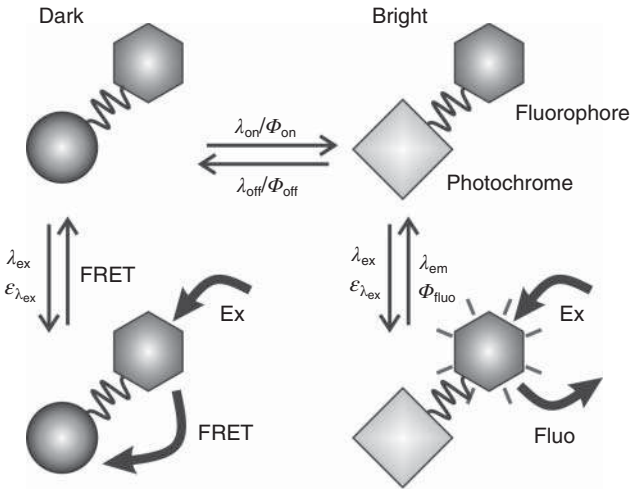


**Scheme 27.3** Fluorescence modulation based on FRET involves a photochromic compound (PC) bound with a fluorophore forming a dyad.

More recently, the development of new photochromic compounds, such as diarylethenes with "oxidized" benzothiophene units [29], or rhodamine spiroamides with one emissive isomer, was a breakthrough, as it removed the necessity of "pairing" a fluorophore. Spiropyranes represent a special case, because

their merocyanine (MC) photo-isomers are (in practice) only fluorescent in highly non-polar solvents. Thus, spiropyranes are usually combined with fluorescent dyes in assemblies when applied in aqueous or polar environments, but can be used alone in material chemistry, e.g. in hydrophobic block copolymers. Recent developments have shown that the emission of the MC isomer can also be enhanced upon binding a biopolymer (e.g. e protein), which provides a hydrophobic environment.

## 27.4 Examples

### 27.4.1 Spiropyranes and Spironaphthoxazines

Spiropyranes are photochromic compounds responsive to different stimuli, such as temperature, pH, redox potential, and, importantly, light (Scheme 27.4) [30]. Most applications involve 6-nitro ($X = NO_2$) derivatives, because the presence of a nitro group facilitates the reaction via the triplet state and improves the ring-opening quantum efficiency. This advantage is in part opposed by a concomitant photodegradation caused by the reaction with molecular oxygen, which reduces the fatigue resistance. While the merocyanine isomers produced upon UV irradiation are poorly fluorescent in water, emission is enhanced in organic solvents and hydrophobic environments, or by the steric hindrance (the presence of a bulky substituent $R \gg Me$) [30]. Thus, the use of spirocompounds in super-resolution applications has been initially limited to material science, and the samples were, for example, polymeric nanoparticles (NPs) [31] or self-assembled block-copolymer fibers (Figure 27.1a) [32], where the emission of the MC was sufficient for SM observation. Recently, Zhang and coworkers [33] observed a substantial fluorescence enhancement of the MC upon binding to tubulin filaments in living cells (Figure 27.1b), demonstrating the importance of a combined design of the molecular switch and its matching with a targeting object. Compound **2** in Figure 27.1 contains a colchicine as the recognition unit selective for tubuline. In a similar way, Chai et al. [34] presented a multiresponsive system (compound **3**) containing a locked spyropirane that becomes photochromic upon release of galactose in the presence of β-galactosidase (Figure 27.1c). The system contained a naphthalimide dye (similar to Lucifer yellow) that binds with HSA (human serum albumin) and provides a green emission as a reference signal (non-switchable). The probe/protein hybrid was water-soluble and cell-permeable, and the hydrophobic pocket in HSA enhanced the emission efficiency of the merocyanine isomer. In these three examples, stochastic-coordinate

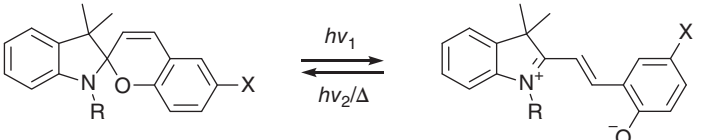


**Scheme 27.4** Photochromic reaction of a spiropyrane. Source: Modified from Kortekaas and Browne [30].

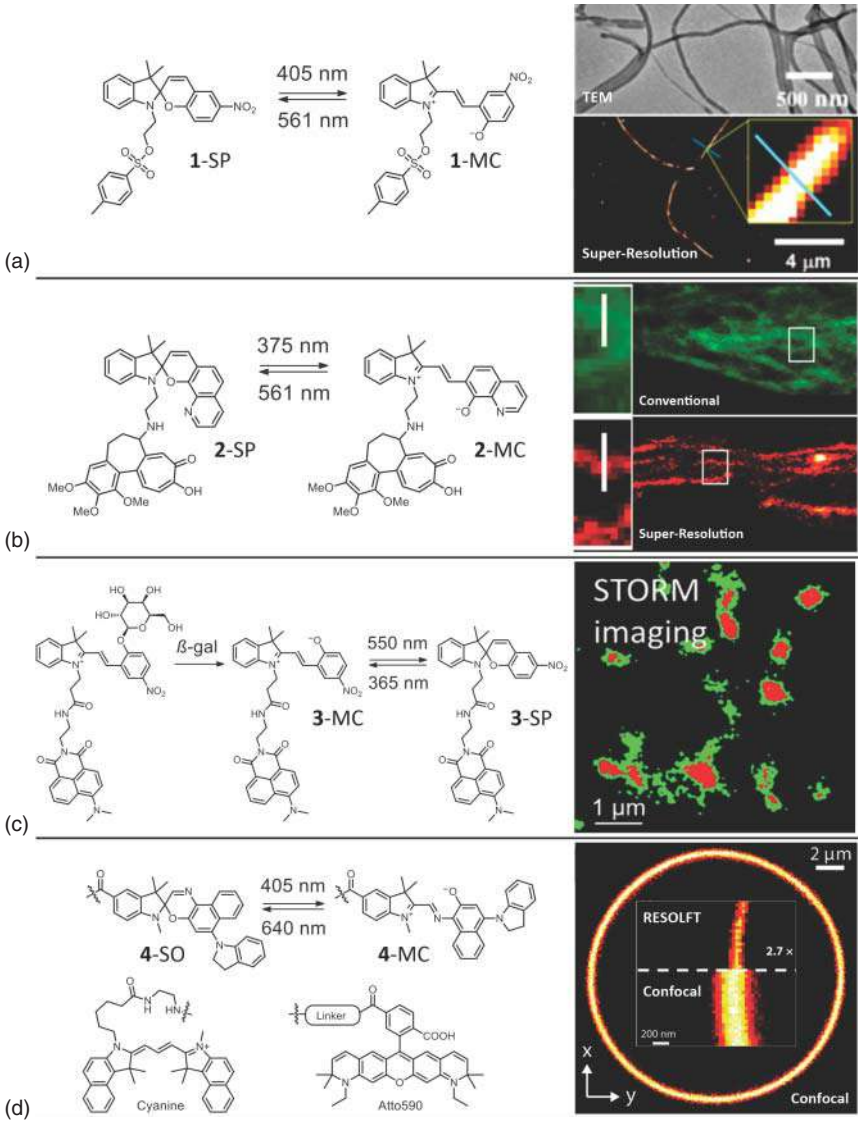


**Figure 27.1** Applications of spiropyranes in stochastic and targeted nanoscopies. Source: (a) Yan et al. [32], (b) Zhang et al. [33], (c) Chai et al. [34], (d) Frawley et al. [35].

methods were used. A green 561 nm laser provided excitation and off-switching, while low-power 405 nm light switched on the markers (SP → MC), with frame integration times being in the range of 20–60 ms.

Alternatively, spiropyranes are often used in FRET assemblies (Scheme 27.3) with green-emitting fluorescent dyes. The emission of the fluorophore (FRET donor) is efficiently quenched by the merocyanine isomer, provided that the emission band overlaps with the MC absorption, and the distance between them is shorter than

the Förster radius. For example, Frawley and coworkers coupled a spironaphtooxazine (structurally similar to spiropyranes) with a fluorescent cyanine dye (Cy3.5) or spectrally similar rhodamine (compound **4**), to modulate their emission. Despite a theoretical FRET efficiency of ≥99%, a signal quenching of ca. 80% was observed in the microscope. The dyad was used for RESOLFT microscopy (Figure 27.1d) of giant unilamellar vesicles (GUVs) [35]. Excitation with 594 nm light elicits the emission of the molecules in the *on* state. Irradiation with 405 nm light shifts the equilibrium toward the *off* state (MC isomer) with ca. 90% conversion. The *off* markers return back to the *on* state thermally, but for imaging purposes, the back reaction (*off–on*) is accelerated with 640 nm light. The achieved resolution was limited by the motion of the markers in the vesicle membrane, as well as photofatigue. The latter was observed as a loss of signal or reduced contrast after tens of cycles, indicating photobleaching of the fluorescent dye or degradation of the photochrome, so that it was no longer able to quench the emission efficiently. This illustrates typical drawbacks of FRET-based dyads.

### 27.4.2 Photoactivatable Spiroamides

Colorless and non-fluorescent spiroamides (Scheme 27.5) and spirocyclic compounds, in general, are easily prepared from fluorescent rhodamines and xanthene dyes. The spiro-form, colorless and non-fluorescent due to the broken π-conjugation in xanthene chromophore, converts to a colored and fluorescent open-ring isomer upon UV irradiation. This form cyclizes spontaneously back into the "dark" form (T-type photochromism) [36]. For this reason, rhodamine spiroamides have been widely used in stochastic super-resolution microscopies [37–40]. Due to simple switching mechanism, there is no need for special "blinking buffers" or imaging conditions. Spiroamides do not need the exclusion of oxygen or the presence of any other additives (thiols, redox buffers). Due to the absence of the photoinduced back reaction (*off*-switching), the average *on*-times are few (tens of) milliseconds [36], with high photon extraction rates (high yields of Nph) typical from robust rhodamine dyes. Photophysical properties can be tailored by careful selection of the residue (Z) connected to the amide nitrogen. The electronic properties as well as the bulkiness of this substituent influence the switching rates. It is also common to attach a chromophore to amide nitrogen, to red-shift the absorption and thus

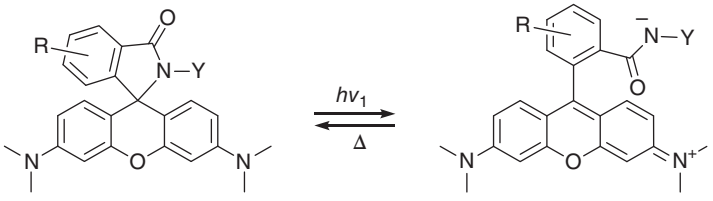


**Scheme 27.5** T-type photochromism of rhodamine spiroamides.

the *on*-switching wavelength to the visible range [41, 42]. The *on*-switching with powerful red light (>650 nm) through a two-photon absorption process is also possible, with appropriate molecular design [43, 44]. Avoiding UV irradiation considerably decreases photodamage and provides (axial) optical sectioning.

In addition to the photo-induced ring-opening reaction, protonation is also possible (if proton donors are available), resulting in a similar *on/off* spontaneous switching (blinking). By tailoring the donor and acceptor properties of the nucleophile (N in amides or $CH_2NH_2$; $CH_2OH$ or $CH_2SH$ groups, if these residues are present instead of CONZ) and electrophile (the chromophore ring), it is possible to select the pH range suitable for blinking, or even avoid photo-switching completely (i.e. image only with the spontaneous, thermal blinking) [28]. This is usually the case with spiroamides prepared from aliphatic amines, as well as rhodamines and silicon-rhodamines having spiro-cyclic ether, thioether, and amine residues. These compounds incorporate no light antenna (Z = alkyl, H or absent), and thus the photoinduced reaction is only practical with short UV-light (c. <320 nm). Thus, the pH-induced blinking becomes the only practical option.

The rhodamine scaffold, with its well-known chemistry, can be tailored for multicolor applications (Figure 27.2a). Indeed, this was early achieved by simple variations in the chromophore (compounds **4–6**). This shifts the absorption and emission bands predictably, but hardly changes the switching kinetics, so that three colors can be recorded simultaneously with a single excitation (532 nm) and activation laser (375 nm) [45]. Compounds **4–6** were covalently incorporated in silica nanoparticles, and conjugated to secondary antibodies. Lee et al. [41] shifted the absorption of a rhodamine B spirolactam **7** to the visible range (Figure 27.2b) by iterative synthesis to optimize the lactam substituent (Z). The reduced photodamage allows for imaging in three dimensions the surface of live bacteria *Caulobacter crescentus*, a model organism for asymmetric cell division. Emitters were activated with low-intensity 405 nm light (18 W $cm^{-2}$). The authors assumed that the reactive group of compound **7** was covalently attached to amino groups forming an S-layer composed of a semi-crystalline matrix of a protein called RsaA, on the cell surface. Modifications in the Z substituent have also been used to extend the *on*-time (reduce the *off*-switching rate). In another series of spiroamides, Ye et al. [46] introduced a carboxyl group close to the lactam (a glycine/RhB adduct **8-Gly**) to impose an intramolecular acidic environment, stabilizing the zwitterionic on-state. The *on*-time along with the photons per cycle (Nph) is doubled for Rh-Gly with respect to a methyl ester analog. As a side effect, the average number of *on/off* cycles was reduced from ~10 to ~8. This suggests the photobleaching rate is similar for both compounds, and so the total number of emitted photons (excitation/emission cycles). As a consequence, the same total photons are spread in fewer cycles (Nc), but each one with higher Nph. A further modification with a HaloTag® ligand (**8-Gly-Halo**) enabled to get super-resolution images of histone H2B proteins, fused with the Halo-Tag protein, in living HeLa cells (Figure 27.2c). The *on*-switching was performed with 375 nm light, but the low doses resulting from short pulses and the low intensity of 2 W $cm^{-2}$ caused no apparent cell damage.

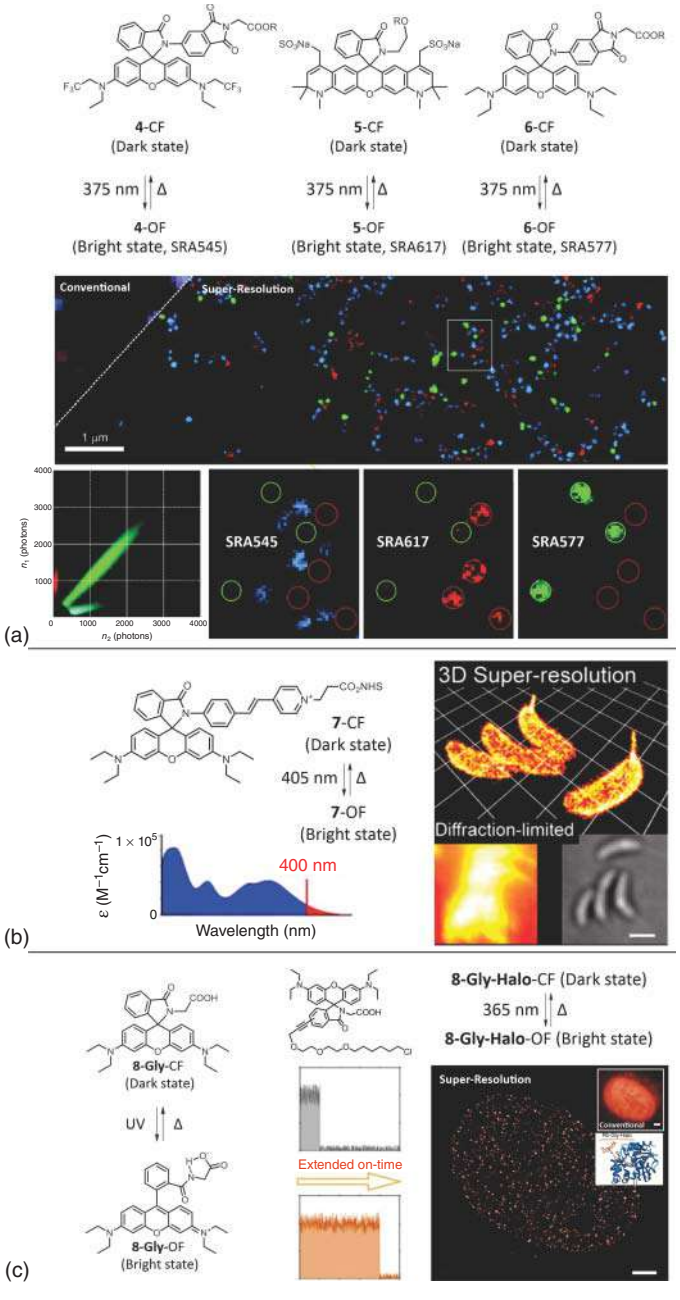


**Figure 27.2** Applications of rhodamine spiroamides in stochastic nanoscopies. Source: Bossi et al. (a) [45], (b) Lee et al. [41], and (c) Ye et al. [46].

### 27.4.3 Photochromic and Fluorescent Diarylethenes

Due to their unique properties, diarylethenes (DAEs) represent an extremely versatile platform for constructing optical and functional materials [47]. Specifically, they feature fast photoisomerization (in the picoseconds range), outstanding fatigue resistance, and complete thermal stability of both isomers (a P-type photochromism). Moreover, isomerization quantum yields can be tuned by molecular design to span almost six orders of magnitude (from nearly unit to $10^{-6}$). DAEs undergo reversible photoinduced reaction between a colorless open form and a colored closed form (Scheme 27.6). The unsubstituted OF have absorption maxima around 300 nm, but extending the conjugation by attaching aromatic groups to the core structure shown in Scheme 27.6 enables to perform the ring-closing reaction with 350–375 nm light. To overcome the lack of emission of diarylethenes with X = S, they were bound with bright fluorophores forming dyads (Scheme 27.7). For instance, compound **9** [48], containing a DAE and a fluorescent rhodamine 101, was incorporated in 30 nm silica nanoparticles through an amino reactive linker. Super-resolution images were acquired in a RESOLFT microscope with 375 nm and 671 nm lasers to switch *off* and *on* the emission, respectively, and a 543 nm laser for excitation. However, the resolution enhancement was limited to one dimension due to the relatively low fatigue resistance of the photochromic unit. In another example, Li et al. [49] incorporated compound **10**, containing a photochromic DAE and a pH-sensitive fluorescent naphthalimide, into a water-soluble and thermoresponsive poly(*N*-isopropylacrylamide). The obtained copolymer was cell-permeable and accumulated in lysosomes. The acidity of these organelles (pH ≈ 4.5–5.0) enhanced the emission of naphthalimide dye, by protonating the remote (aliphatic) nitrogen atom of the piperazine ring. In a non-protonated state, the emission was partially quenched by electron transfer. The super-resolution PALM imaging of lysosomes in live HeLa cells was demonstrated by applying alternating 405 nm laser pulses for excitation, and 302 nm light from a UV lamp to switch off the emission.

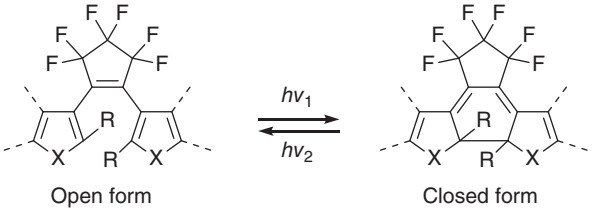


**Scheme 27.6** Photoisomerization of a non-fluorescent (X = S) or fluorescent (X = $SO_2$) diarylethene, with a perfluorocyclopentene bridge.

The applications in material science often require the incorporation of fluorescent or photoswitchable markers into the solid state or aggregate materials (e.g. organic polymers). The aggregation-induced quenching may weaken the emission, reducing the amount of active markers and thus the total signal. To overcome these limitations, Li et al. [50] combined a fluorophore having a well-known

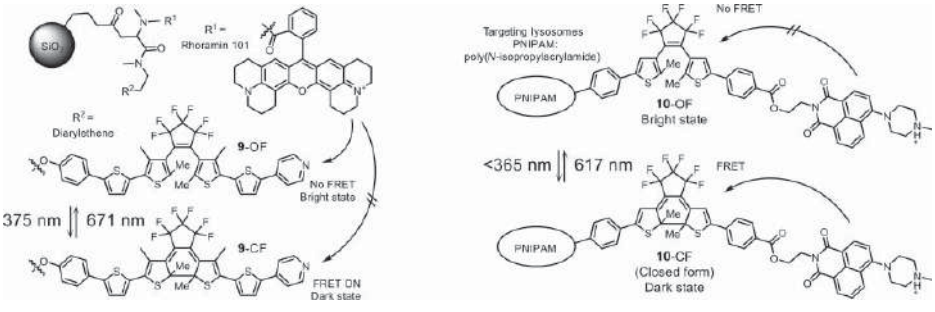


**Scheme 27.7** Reversible fluorescence modulation via FRET of Rhodamine 101 (left) and 1,8-naphthalimide-4-(*N*-piperazine) (right) with photochromic DAEs. Compounds **9** and **10** were used in RESOLFT and PALM nanoscopy, respectively.

aggregation-induced emission (a tetraarylethene, TPE or OTPE) with two DAEs to modulate the emission signal by FRET (Figure 27.3a). Despite the absorption maximum of the DAE units is around 310 nm, the off-switching was induced with 405 nm light to a conversion in the photo-stationary state of 40–50% (a mixture of TPE-2DTE-oc and -cc). The presence of two photochromes enhanced the intramolecular quenching effect and compensated for the incomplete conversion. Additional intermolecular quenching is present in the solid state, and the overall ON/OFF emission ratio amounts to ~1000–2000. Taking advantage of such high modulation, super-resolution images of cylindric micelles of an amphiphilic block copolymer were recorded by a stochastic method. A 405 nm laser was kept *on* all the time for excitation and off-switching, and intermittently a 561 nm laser was used for *on*-switching.

Recently, *turn-on* mode fluorescent diarylethenes (fDAEs) bearing two benzothiophene-1,1-dioxide residues attached to perfluorocyclopentene ring (Scheme 27.8, **11**) have been discovered [29]. Since then, they have attracted a great interest in the field of super-resolution microscopy, and triggered a great effort to improve the photochemical and photophysical properties [55]. Compounds with optimized structures present fluorescence quantum yields larger than 0.8, fatigue resistance of thousands cycles, cyclization wavelengths in the visible range (>405 nm), and tunable cycloreversion quantum yields.

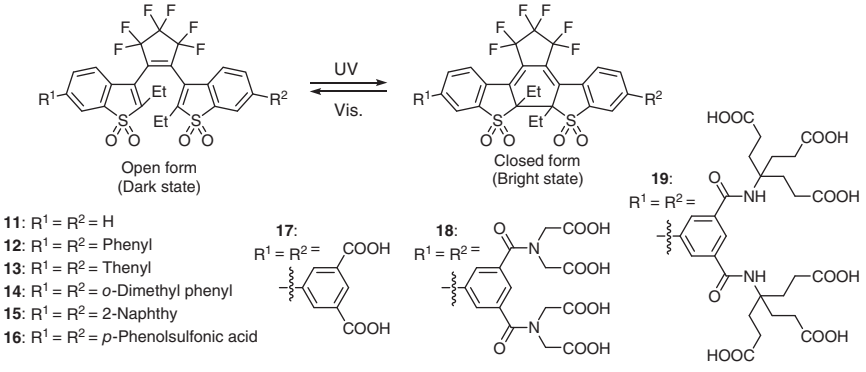


**Scheme 27.8** DAEs with fluorescent closed forms (*turn-on* fDAEs) used in super-resolution microscopies.

Most of fDAEs with oxidized benzothiophene units are highly hydrophobic. This is an advantage for applications in polymer and material science, in particular, for the non-invasive super-resolution imaging of the nanostructured soft materials. Wöll and coworkers [56, 57] prepared non-polar fDAE derivatives (Scheme 27.8, **15**), studied their switching in polymers with different density and glass transition temperature, and applied STORM imaging in soft matter (amphiphilic block copolymers) for the first time. The markers incorporated themselves into the core of the fibers by hydrophobic affinity. Interestingly, a fraction of fDAEs did not switch in rigid polymers and have to be bleached prior to imaging. In another study, Qiang et al. [51]

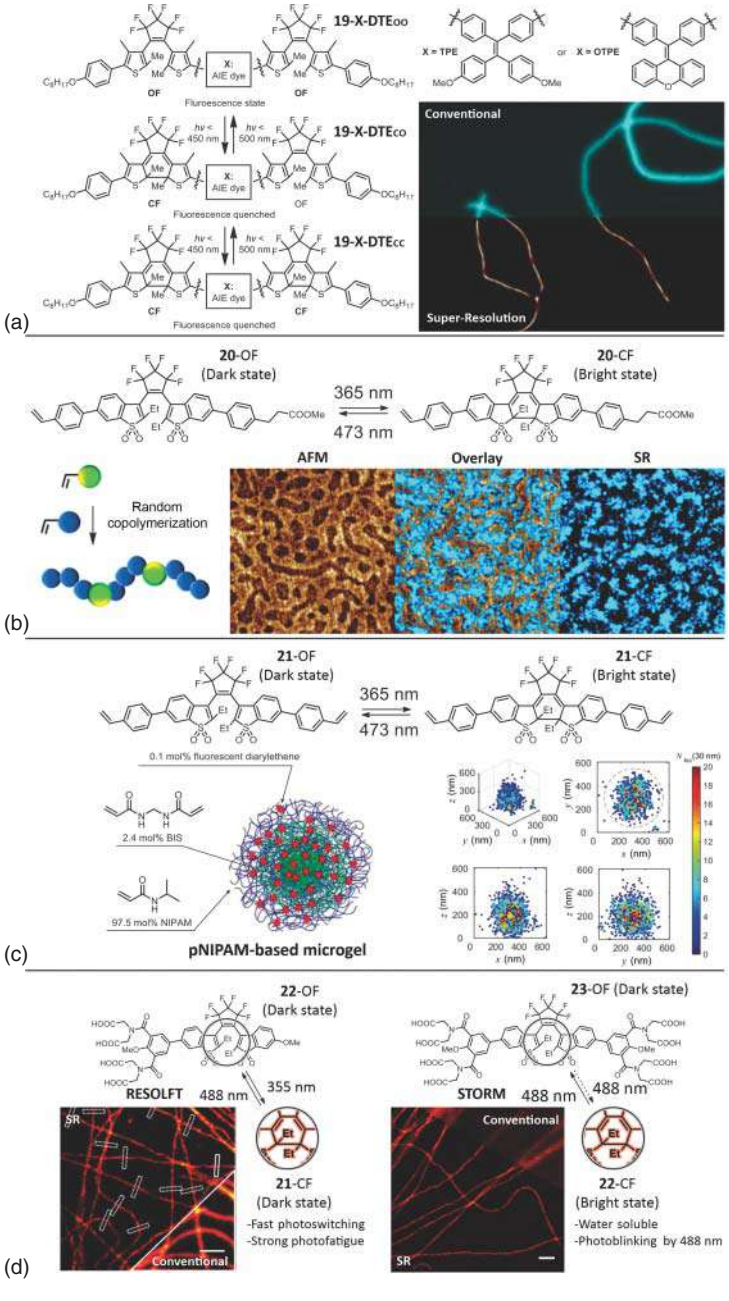


**Figure 27.3** Applications of DAEs in in stochastic and targeted nanoscopies. Source: (a) Li et al. [50], (b) Qiang et al. [51], (c) Siemes et al. [52], and (d) Uno et al. [53], Roubinet et al. [54].

introduced a vinyl-terminated fDAE (**20**) that was copolymerized with styrene to a random distribution of fluorophores inside the polymer backbones. This strategy provides a simple and effective way to adjust and control the amount of a switchable reporter incorporated into a polymer, and was applied for super-resolution imaging of nanostructures in self-assembled polymeric blends (Figure 27.3b), using a stochastic method (PALM). Siemes et al. [52] designed and prepared a polymerizable fDAE with two styrene residues (**21**). The incorporation into microgels allowed the nanoscopic visualization of single cross-linking sites in the polymer network (Figure 27.3c).

In contrast, applications in biology and life science require hydrophilic or even water-soluble probes. Moreover, the outstanding photophysical properties must be retained for super-resolution imaging. Eventually, the water-soluble fDAEs decorated with numerous carboxylic acid residues were reported, and their applications in RESOLFT [53, 58] and STORM [54] nanoscopies were demonstrated. The fast-switching RESOLFT probes were based on phenylated fDAEs with asymmetric tetra-acid (Figure 27.3d, **21**) [53] and symmetric tetra- and octa-acid substitution patterns (Scheme 27.8, **17**–**18**) [58]. The off-switching was slowed down by electron-donating 4-methoxyphenyl group(s), which reduced the quantum yield of the ring-opening reaction, but increased the number of photons per burst (Nph) in stochastic methods (STORM) [54]. Amino reactive *N*-hydroxysuccinimidyl esters were generated, coupled with secondary antibodies, and used in immunofluorescence imaging of tubuline filaments and nuclear pore complexes (Figure 27.3d, **23**).

Low photostability in aqueous solutions remained the main drawback of fDAEs (the same is true for many other synthetic photochromic families). Even the most promising photochromes (fDAEs decorated with eight carboxylic acid groups) tolerated only several tens of switching cycles in aqueous solutions, due to a loss of solubilizing carboxylates, cleavedoff photochemically. To solve this problem, alternative branching patterns in the solubilizing side-groups were designed [59]. Replacement of the reactive centers with *N*-(tert-alkyl) branching points suppressed photo-cleavage and improved the fatigue resistance drastically. Compound **19** endured over a thousand switching cycles (Nc) in aqueous buffers (under 365/470nm irradiation), without exclusion of oxygen (outperforming the photoswitchable and fluorescent protein Dreiklang, having comparable spectra and switching parameters). This is the first example of a (f)DAE displaying a better fatigue resistance in aqueous media than in organic solvents. Carboxylates are ionized near neutral pH, found in biological systems, but they are protonated under acidic conditions. To improve the solubility and stabilize the properties in a broader pH range, Um et al. [60] prepared a water-soluble fDAE decorated with two sulfonic acid residues as solubilizing groups (Scheme 27.8, **16**). An alternative strategy is based in their incorporation into biocompatible polymer nanoparticles (NPs) having hydrophobic cores of poly(caprolactone), and a hydrophilic surface stabilized with a surfactant (Pluronic F-68) [61]. Their efficient intracellular endocytosis allowed to visualize NPs by means of super-resolution PALM microscopy in the cytosol of RAW264.7 macrophage cells. The size of the NPs, with a hydrodynamic radius of

ca. 60 nm, limited the spatial resolution. This example demonstrates an alternative strategy to make fDAEs biocompatible without substitution.

Another drawback of fDAEs, also common to most photochromic compounds, is the need of irradiation with high-energy UV light. This is undesired for biological applications in living organisms. The synthesis provided compounds which switching under irradiation with 405 nm light [62]. However, in some cases even this light may be phototoxic, particularly at high doses or in long-lasting imaging experiments. The electronic nature of the molecular states in most photochromic families makes shifting of the switching wavelengths far from the UV unlikely. Fortunately, Irie and coworkers have recently reported that the so-called "Urbach tail effect" [63] allows the cyclization of fDAEs by irradiation in the off-resonance region (hot bands) of the absorption tails of the OF at room temperature. The molecular design can enhance this effect and provide fDAEs with on- and off- switching only with visible light (470/530 nm), possible even in ensemble experiments [64]. In addition, many fDAEs have shown sufficient on-switching with visible light at the single-molecule level, through the Urbach tail effect, to keep a sparse population of the molecules in the on-state required for imaging in PALM/STORM nanoscopies [52, 54, 57, 65]. While in most applications a single 473–488 nm laser was used for excitation and activation, compound **13** can be switched at the single-molecule level with a 532 nm laser [65]. Recently, theinyl group bearing multi-carboxylic acids were prepared and applied in STORM super-resolution microscopy on biological samples with a single 562 nm laser [66].

## 27.5 Conclusions and Outlook

Super-resolution microscopes use standard optics (lenses) and light sources (lasers) that are well developed. Instrumental improvements contribute to the constant refinement of super-resolution techniques (e.g. speeding them up). However, the diffraction barrier was surpassed by a clever use of molecular states and transitions. Thus, key improvements came from molecular design, which is ultimately a chemistry task. Photochromic compounds can help to keep up with further progress in the super-resolution methods, and indeed, they have demonstrated good performance in the short but successful history of optical nanoscopies. Transition rates (*on* and *off*), excitation and emission colors, and specific molecular properties must be carefully tuned to achieve the best possible results. The success of any fluorescence nanoscopy technique, i.e. the image quality and spatial resolution, depends on these aspects much more than on the instrumental equipment. Organic photochromic compounds offer a unique platform to produce fluorescent molecular switches matching the ever-demanding conditions of existing and emerging super-resolution techniques, as well as the broad and expanding palette of applications. Along with the systems discussed in this chapter, we foresee many others to appear in the near future. Specific characteristics of the fluorescent markers must be constantly improved and adapted to keep pace with the developments on established and future nanoscopies, as well as the broad and expanding palette of applications.

## References


1 Hell, S.W. (2007). Far-field optical nanoscopy. *Science* 316: 1153–1158.
2 Hell, S.W. (2009). Microscopy and its focal switch. *Nat. Methods* 6: 24–32.
3 Betzig, E. (2015). Single molecules, cells, and super-resolution optics (Nobel lecture). *Angew. Chem. Int. Ed.* 54: 8034–8053.
4 Sahl, S., Hell, S.W., and Jakobs, S. (2017). Fluorescence nanoscopy in cell biology. *Nat. Rev. Mol. Cell Biol.* 18: 685–701.
5 Sigal, Y., Zhou, R., and Zhuang, X. (2018). Visualizing and discovering cellular structures with super-resolution microscopy. *Science* 361: 880–887.
6 Möckl, L. and Moerner, W.E. (2020). Super-resolution microscopy with single molecules in biology and beyond—essentials, current trends, and future challenges. *J. Am. Chem. Soc.* 142: 17828–17844.
7 Balzarotti, F., Eilers, Y., Gwosch, K. et al. (2017). Nanometer resolution imaging and tracking of fluorescent molecules with minimal photon fluxes. *Science* 355: 606–612.
8 Hell, S.W. and Wichmann, J. (1994). Breaking the diffraction resolution limit by stimulated emission: stimulated-emission-depletion fluorescence microscopy. *J. Opt. Lett* 19: 780–782.
9 Hofmann, M., Eggeling, C., Jakobs, S., and Hell, S.W. (2005). *Proc. Natl. Acad. Sci. U.S.A* 102: 17565–17569.
10 Hell, S.W. and Kroug, M. (1995). Ground-state-depletion fluorescence microscopy: a concept for breaking the diffraction resolution limit. *Appl. Phys. B* 60: 495–497.
11 Hell, S.W. (2015). Nanoscopy with focused light (Nobel lecture). *Angew. Chem. Int. Ed.* 54: 8054–8066.
12 Jimenez, A., Friedl, K., and Leterrier, C. (2020). About samples, giving examples: optimized single molecule localization microscopy. *Methods* 174: 100–114.
13 Rust, M., Bates, M., and Zhuang, X. (2006). Sub-diffraction-limit imaging by stochastic optical reconstruction microscopy (STORM). *Nat. Methods* 3: 793–795.
14 Betzig, E., Patterson, G.H., Sougrat, E. et al. (2006). Imaging intracellular fluorescent proteins at nanometer resolution. *Science* 313: 1642–1645.
15 Folling, J., Bossi, M., Bock, H. et al. (2008). Fluorescence nanoscopy by ground-state depletion and single-molecule return. *Nat. Methods* 5: 943–945.
16 Heilemann, M., van de Linde, S., Schuttpelz, M. et al. (2008). Subdiffraction-resolution fluorescence imaging with conventional fluorescent probes. *Angew. Chem. Int. Ed.* 47: 6172–6176.
17 Fernández-Suárez, M. and Ting, A. (2008). Fluorescent probes for super-resolution imaging in living cells. *Nat. Rev. Mol. Cell Biol.* 9: 929–943.
18 Heilemann, M., Dedecker, P., Hofkens, J., and Sauer, M. (2009). Photoswitches: key molecules for subdiffraction-resolution fluorescence imaging and molecular quantification. *Laser Photonics Rev.* 3: 180–202.
19 Wöll, D. and Flors, C. (2017). Super-resolution fluorescence imaging for material science. *Small Methods* 1: 1700191.


**20** Fukaminato, T., Ishida, S., and Metivier, R. (2018). Photochromic fluorophores at the molecular and nanoparticle levels: fundamentals and applications of diarylethenes. *NPG Asia Mater.* 10: 859–881.

**21** Li, H. and Vaughan, J.C. (2018). Switchable fluorophores for single-molecule localization microscopy. *Chem. Rev.* 118: 9412–9454.

**22** Eggeling, C., Widengren, J., Rigler, R., and Seidel, C.A.M. (1998). Photobleaching of fluorescent dyes under conditions used for single-molecule detection: evidence of two-step photolysis. *Anal. Chem.* 70 (13): 2651–2659.

**23** Dempsey, G., Vaughan, J., Chen, K. et al. (2011). Evaluation of fluorophores for optimal performance in localization-based super-resolution imaging. *Nat. Methods* 8: 1027–1036.

**24** Jensen, N.A., Jansen, I., Kamper, M., and Jakobs, S. (2020). Reversibly switchable fluorescent proteins for RESOLFT nanoscopy. In: *Nanoscale Photonic Imaging*, Topics in Applied Physics, vol. 134 (eds. T. Salditt, A. Egner and D. Luke). Cham: Springer https://doi.org/10.1007/978-3-030-34413-9_9.

**25** Shcherbakova, D., Sengupta, P., Lippincott-Schwartz, J., and Verkhusha, V. (2014). Photocontrollable fluorescent proteins for superresolution imaging. *Annu. Rev. Biophys.* 43: 303–329.

**26** Gidi, Y., Payne, L., Glembockyte, V. et al. (2020). Unifying mechanism for thiol-induced photoswitching and photostability of cyanine dyes. *J. Am. Chem. Soc.* 142: 12681–12689.

**27** Morozumi, A., Kamiya, M., Uno, S. et al. (2020). Spontaneously blinking fluorophores based on nucleophilic addition/dissociation of intracellular glutathione for live-cell super-resolution imaging. *J. Am. Chem. Soc.* 142: 9625–9633.

**28** Uno, S., Kamiya, M., Yoshihara, T. et al. (2014). A spontaneously blinking fluorophore based on intramolecular spirocyc-lization for live-cell super-resolution imaging. *Nat. Chem.* 6: 681–689.

**29** Jeong, Y., Yang, S., Ahn, K., and Kim, E. (2005). Highly fluorescent photochromic diarylethene in the closed-ring form. *Chem. Commun.*: 2503–2505.

**30** Kortekaas, L. and Browne, W. (2019). The evolution of spiropyran: fundamentals and progress of an extraordinarily versatile photochrome. *Chem. Soc. Rev.* 48: 3406–3424.

**31** Hu, D., Tian, Z., Wu, W. et al. (2008). Photoswitchable nanoparticles enable high-resolution cell imaging: PULSAR microscopy. *J. Am. Chem. Soc.* 130: 15279–15281.

**32** Yan, J., Zhao, L., Li, C. et al. (2015). Optical nanoimaging for block copolymer self-assembly. *J. Am. Chem. Soc.* 137 (7): 2436–2439.

**33** Zhang, H., Wang, C., Jiang, T. et al. (2015). Microtubule-targetable fluorescent probe: site-specific detection and super-resolution imaging of ultratrace tubulin in microtubules of living cancer cells. *Anal. Chem.* 87: 5216–5222.

**34** Chai, X., Han, H.H., Sedgwick, A.C. et al. (2020). A photochromic fluorescent probe strategy for the super-resolution imaging of biologically important biomarkers. *J. Am. Chem. Soc.* 142: 18005–18013.


**35** Frawley, A., Wyciks, V., Xiong, Y. et al. (2020). Super-resolution RESOLFT microscopy of lipid bilayers using a fluorophore-switch dyad. *Chem. Sci.* 11: 8955–8960.

**36** Knauer, K. and Gleiter, R. (1977). Photochromism of rhodamine derivatives. *Angew. Chem. Int. Ed.* 16: 113.

**37** Belov, V., Bossi, M., Fölling, J. et al. (2009). Rhodamine spiroamides for multicolor single-molecule switching fluorescent nanoscopy. *Chem. Eur. J.* 15: 10762–10776.

**38** Aoki, H., Mori, K., and Ito, S. (2012). Conformational analysis of single polymer chains in three dimensions by super-resolution fluorescence microscopy. *Soft Matter* 8: 4390–4395.

**39** Roberti, M., Fölling, J., Celej, M. et al. (2012). Imaging nanometer-sized a-synuclein aggregates by superresolution fluorescence localization microscopy. *Biophys. J.* 102: 1598–1607.

**40** Belov, V.N. and Bossi, M.L. (2013). Photoswitching emission with rhodamine spiroamides for super-resolution fluorescence nanoscopies. *Isr. J. Chem.* 53: 267–279.

**41** Lee, M., Rai, P., Williams, J. et al. (2014). Small-molecule labeling of live cell surfaces for three-dimensional super-resolution microscopy. *J. Am. Chem. Soc.* 136: 14003–−14006.

**42** Qi, Q., Chi, W., Li, Y. et al. (2019). A H-bond strategy to develop acid-resistant photoswitchable rhodamine spirolactams for super-resolution single-molecule localization microscopy. *Chem. Sci.* 10: 4914–4922.

**43** Fölling, J., Belov, V., Kunetsky, R. et al. (2007). Photochromic rhodamines provide nanoscopy with optical sectioning. *Angew. Chem. Int. Ed.* 46: 6266–6270.

**44** Fölling, J., Belov, V., Riedel, D. et al. (2008). Fluorescence nanoscopy with optical sectioning by two-photon induced molecular switching using continuous-wave lasers. *ChemPhysChem* 9: 321–326.

**45** Bossi, M., Fölling, J., Belov, V. et al. (2008). Multicolor far-field fluorescence nanoscopy through isolated detection of distinct molecular species. *Nano Lett.* 8: 2463–2468.

**46** Ye, Z., Yu, H., Yang, W. et al. (2019). Strategy to lengthen the on-time of photochromic rhodamine spirolactam for super-resolution photoactivated localization microscopy. *J. Am. Chem. Soc.* 141: 6527–6536.

**47** Irie, M., Fukaminato, T., Matsuda, K., and Kobatake, S. (2014). Photochromism of diarylethene molecules and crystals: memories, switches, and actuators. *Chem. Rev.* 114: 12174–−12277.

**48** Fölling, J., Polyakova, S., Belov, V. et al. (2008). Synthesis and characterization of photoswitchable fluorescent silica nanoparticles. *Small* 4: 134–142.

**49** Li, C., Hu, Z., Aldred, M. et al. (2014). Water-soluble polymeric photoswitching dyads impart super-resolution lysosome highlighters. *Macromolecules* 47: 8594–8601.

**50** Li, C., Xiong, K., Chen, Y. et al. (2020). Visible-light-driven photoswitching of aggregated-induced emission-active diarylethenes for super-resolution imaging. *ACS Appl. Mater. Interfaces* 12: 27651.


**51** Qiang, Z., Shebek, K., Irie, M., and Wang, M. (2018). A polymerizable photoswitchable fluorophore for super-resolution imaging of polymer self-assembly and dynamics. *ACS Macro Lett.* 7: 1432–1437.

**52** Siemes, E., Nevskyi, O., Sysoiev, D. et al. (2018). Nanoscopic visualization of cross-linking density in polymer networks with diarylethene photoswitches. *Angew. Chem. Int. Ed.* 57: 12280–12284.

**53** Uno, K., Bossi, M.L., Konen, T. et al. (2019). Asymmetric diarylethenes with oxidized 2-alkylbenzothiophen-3-yl units: chemistry, fluorescence, and photoswitching. *Adv. Opt. Mater.* 7: 1801746–1801746.

**54** Roubinet, B., Weber, M., Shojaei, H. et al. (2017). Fluorescent photoswitchable diarylethenes for biolabeling and single-molecule localization microscopies with optical superresolution. *J. Am. Chem. Soc.* 139: 6611–6620.

**55** Irie, M. and Morimoto, M. (2018). Photoswitchable turn-on mode fluorescent diarylethenes: strategies for controlling the switching response. *Bull. Chem. Soc. Jpn.* 91: 237–250.

**56** Nevskyi, O., Sysoiev, D., Oppermann, A. et al. (2016). Nanoscopic visualization of soft matter using fluorescent diarylethene photoswitches. *Angew. Chem. Int. Ed.* 55: 12698–12702.

**57** Nevskyi, O., Sysoiev, D., Dreier, J. et al. (2018). Fluorescent diarylethene photoswitches – a universal tool for super-resolution microscopy in nanostructured materials. *Small* 14: 1703333.

**58** Roubinet, B., Bossi, M.L., Alt, P. et al. (2016). Carboxylated photoswitchable diarylethenes for biolabeling and super-resolution RESOLFT microscopy. *Angew. Chem. Int. Ed.* 55: 15429–15433.

**59** Uno, K., Bossi, M.L., Irie, M. et al. (2019). Reversibly photoswitchable fluorescent diarylethenes resistant against photobleaching in aqueous solutions. *J. Am. Chem. Soc.* 141: 16471–16478.

**60** Um, S., Kimb, H., Kim, D. et al. (2018). Highly fluorescent and water soluble turn-on type diarylethene for super-resolution bioimaging over a broad pH range. *Dyes Pigm.* 158: 36–41.

**61** Kim, D., Jeong, K., Kwon, J. et al. (2019). Dual-color fluorescent nanoparticles showing perfect color-specific photoswitching for bioimaging and super-resolution microscopy. *Nat. Commun.* 10: 3089.

**62** Sumi, T., Kaburagi, T., Morimoto, M. et al. (2015). Fluorescent photochromic diarylethene that turns on with visible light. *Org. Lett.* 17: 4802–4805.

**63** Kashihara, R., Morimoto, M., Ito, S. et al. (2017). Fluorescence photoswitching of a diarylethene by irradiation with single-wavelength visible light. *J. Am. Chem. Soc.* 139: 16498–16501.

**64** Schleper, A.L., Bossi, M.L., Belov, V.N., and Hell, S.W. (2019). Mono- and bithiophene-substituted diarylethene photoswitches with emissive open or closed forms. *Beilstein J. Org. Chem.* 15: 2344–2354.

**65** Arai, Y., Ito, S., Fujita, H. et al. (2017). One-colour control of activation, excitation and deactivation of a fluorescent diarylethene derivative in super-resolution microscopy. *Chem. Commun.* 53: 4066–4069.

**66** Uno, K., Aktalay, A., Bossi, M.L. et al. (2021). PNAS 118:e2100165118.


## 28 Photochromic Nanoparticles: From Fluorescence to Assembly

Rémi Métivier, Nicolas Fabre, Ashkan Mokhtar, and Tuyoshi Fukaminato

**Photochromic Nanoparticles: From Fluorescence to Assembly**

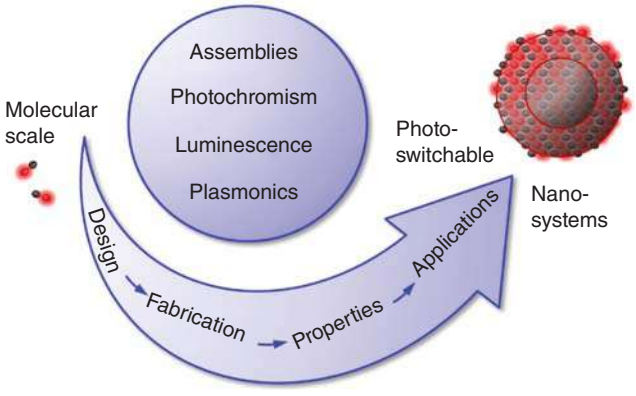


**Characteristic Features**

Luminescence, plasmonic, conductance, or assembly photoswitching with photochromic nanosystems; design of molecular and hybrid photochromic nanomaterials; amplification effects, enhancement phenomena; controllable emission color or excitation wavelength; applications to optical data storage, optoelectronics, imaging, and medicine.

**Key References**

Lim, S.J., An, B.K., Jung, S.D. et al. (2004). Photoswitchable organic nanoparticles and a polymer film employing multifunctional molecules with enhanced fluorescence emission and bistable photochromism. *Angew. Chem. Int. Ed*. 43: 6346–6350.

Klajn, R., Wesson, P.J., Bishop, K.J. et al. (2009). Writing self-erasing images using metastable nanoparticle "inks". *Angew. Chem. Int. Ed*. 48: 7035–7039.

Diaz, S.A., Gillanders, F., Jares-Erijman, E.A. et al. (2015). Photoswitchable semiconductor nanocrystals with self-regulating photochromic Forster resonance energy transfer acceptors. *Nat. Commun.* 6: 6036.

Su, J., Fukaminato, T., Placial, J.P. et al. (2016). Giant amplification of photoswitching by a few photons in fluorescent photochromic organic nanoparticles. *Angew. Chem. Int. Ed*. 55: 3662–3666.

Zhao, T., Wang, P., Li, Q. et al. (2018). Near-Infrared Triggered Decomposition of Nanocapsules with High Tumor Accumulation and Stimuli Responsive Fast Elimination. *Angew. Chem. Int. Ed*. 57, 2611–2615.

Mokhtar, R. Morinaga, Y. Akaishi, M. et al. (2020). Reversible luminescence photoswitching of colloidal $CsPbBr_3$ nanocrystals hybridized with a diarylethene photoswitch, *ACS Mater. Lett*. 2: 727–735.

# 28

# Photochromic Nanoparticles: From Fluorescence to Assembly

*Rémi Métivier[1], Nicolas Fabre[1], Ashkan Mokhtar[2], and Tuyoshi Fukaminato[2]*

[1] *Université Paris-Saclay, ENS Paris-Saclay, CNRS Photophysique et Photochimie Supramoléculaires et Macromoléculaires, 4 Avenue des Sciences, 91190, Gif-sur-Yvette, France*
[2] *Department of Applied Chemistry and Biochemistry, Kumamoto University, 2-39-1 Kurokami, Chuo-ku, Kumamoto 860-8555, Japan*

## 28.1 Introduction

Recently, various types of organic, inorganic, or hybrid nanomaterials come to be commercially available and contribute to the development of a variety of industrial applications. It becomes now crucial to consider the advances of nanomaterials from the viewpoint of the design of functional nanosystems with specific optical, optoelectronic, magnetic, catalytic, and mechanical properties. In this context, photoresponsive nanoparticles (NPs) that can exhibit changes of several attributes in response to external light stimuli have been attracting an increasing attention in a wide range of research fields. In the past two decades, many research groups have been dedicated to the development of photoresponsive nanoparticles based on organic photochromic molecules and, as a result, various applications on smart optical materials have been established with tremendous progress. Photochromic molecules typically exist in two isomers, and switching from one isomer to the other is activated upon irradiation with appropriate wavelengths of light. This phototransformation phenomenon can affect a variety of physicochemical properties such as dielectric constant, geometric structure, chirality, or fluorescence. When nanoparticles are coupled to or made from photochromic molecules, smart organic and inorganic nanosystems with photoactivation or photomodulation effects can be prepared and implemented in different media.

Spiropyran (SP), azobenzene, and diarylethene (DAE) derivatives are the most commonly used photochromic molecules in this research field. On one side, the very large conformational changes of SP and azobenzene derivatives upon light exposure, associated with a drastic modification of their molecular dipole or charge distribution, are particularly appealing. On the other side, the DAE compounds constitute a promising family of photochromic molecules owing to their large spectral shift, excellent thermal stability, and high-fatigue resistance.

*Molecular Photoswitches: Chemistry, Properties, and Applications*,
First Edition. Edited by Zbigniew L. Pianowski.


DAEs can be reversibly switched between two conformations: a closed-ring isomer upon UV irradiation and an open-ring isomer upon visible light irradiation, by either breaking or forming a chemical bond through cyclization or cycloreversion reactions. In this chapter, therefore, a progress overview on photoresponsive optical nanomaterials is provided, mostly based on the abundant literature on DAE, but also interesting reports related to other photochromic compounds. According to the classes of the nanomaterials, we categorize our discussions into the following subtopics: (nonfluorescent) photochromic nanoparticles (Section 28.2), photoresponsive fluorescent organic nanosystems (Section 28.3), photoresponsive nanosystems involving inorganic emitters (Section 28.4), and metallic (plasmonic) nanomaterials combined with photochromic compounds (Section 28.5). In Section 28.2, we describe the synthesis and preparation methods of several photochromic nanomaterials such as nanospheres, nanorods, or nanowires and introduce their specific photochromic properties compared to the solution and bulk solid state.

Photoswitchable luminescent devices are highly desirable for advanced technologies, when high sensitivity together with spatial and temporal control of the optical state are required, e.g. for reversible optical data storage and new high-resolution imaging techniques. At the molecular scale, the design of photoswitchable systems relies on the association of two components: (i) a luminescent material (either organic or inorganic) and (ii) a photochromic dye, the latter operating the switch of the luminescence of the first. Preparation strategies of several types of fluorescent photoswitchable organic nanoparticles and their applications are described in Section 28.3. Whereas many nanosystems based on organic molecules are described, the luminescence photocontrol of inorganic nanoparticles by organic photochromic derivatives is still in its infancy. The continuous improvements of synthesis protocols have given access to a wide variety of inorganic nanoparticles with narrow and symmetric emission spectra, multiple bright colors, and excellent photostability compared to small organic dyes. In Section 28.4, we discuss photoswitchable inorganic emitters hybridized with photochromic compounds. The covered content extends from conventional semiconducting quantum dots to most advanced perovskite lead halide nanocrystals in addition to other attractive materials such as carbon dots (CDs) and upconverting nanoparticles (UCNPs). Finally, we focus on hybrid nanosystems based on metallic nanoparticles coupled to photochromic compounds. Several unique photoswitching properties of metallic nanoparticles functionalized with photochromic molecules are introduced in Section 28.5, such as plasmonic–photochromic interactions giving rise to mutual enhancements, light-responsive assembly–disassembly phenomena of suprastructures made of metallic nanoparticles, or conductance photoswitching with photochromic-metallic nano-networks.

Due to length constraints, the content of this chapter cannot include all achievements related to this research field and therefore, the most important and recent developments will be described by selecting representative examples. Many other excellent review papers can advantageously help to cover the wide variety of recent results reported in this area [1–7].

## 28.2 Photochromic Nanoparticles

The attractive characteristics of nanomaterials, especially colloidal suspensions of nanoparticles or nanoparticles-doped thin films, with improved optical or photochemical properties compared to the solution or solid states, have triggered the fabrication of a variety of photochromic nanosystems [2]. The synthesis and investigation of crystalline or amorphous nanospheres, nanorods, or nanowires have been described, mostly based on SPs (or spirooxazines), and DAEs, with a special emphasis on their photochromic properties compared to the solution and bulk solid state counterparts.

Among the "top-down" approaches to prepare nanoparticles in colloidal suspension, the laser ablation (or photo-fragmentation) method is extremely efficient. The organic powder of pure photochromic materials can be directly converted into a stable suspension in water, with good optical quality (low scattering) [8]. The tunability of such a technique, via the laser wavelength, laser fluence, or pulse width, can provide different sizes or morphologies, in a controllable manner. For instance, the photo-fragmentation of a photochromic salicylidene-aminopyridine crystalline powder by laser ablation was demonstrated to yield molecular nanorods with dimensions of ~300–800 nm in length and ~70–200 nm in width [9]. The photochromic properties of such nanomaterials were investigated, displaying intermediate properties of the keto-to-enol thermal back reaction between solution and solid state. The determination of quantum yields was achieved for the suspension of nanoparticles, which is usually considered to be challenging for this class of protochromic compounds, with quantum yields for the enol→keto reaction estimated at $0.22 \pm 0.02$ and almost unity for the keto→enol reaction. DAE nanoparticles can be prepared by this technique as well. The first example by Piard et al. [10] showed that small isotropic nanoparticles ($25 \pm 10$ nm) of a DAE compound were a good trade-off between the solution (photochromic, but weakly fluorescent) and the solid state (fluorescent, but not photochromic), combining advantageously both properties at appreciable levels. A more sophisticated laser ablation method was described with another DAE compound, taking part of the photochromic nature of the material. This version was called "cw-light-assisted" photo-fragmentation method, using continuous irradiation of the sample during the laser ablation, shifting the laser wavelength to the red, in the absorption band of the closed-ring isomer of the DAE, as represented in Figure 28.1a [11]. This strategy reduces significantly the photodegradation side effects during the laser application. Interestingly, the photoreactivity in nanoparticles was found to increase by a factor two compared to that in solution due to the overall antiparallel conformation of the DAE molecules in the crystal lattice of the NPs. The photochromic properties were demonstrated down to the nanoscale with single-particle spectroscopy under dark-field microscope.

The simplest "bottom-up" approach to yield organic nanoparticles consists in the dispersion of the concentrated organic solution containing the hydrophobic photochromic molecule into stirred water, namely the reprecipitation method [14]. In 2003, Sun et al. [15] reported that nano-aggregation can be achieved with a DAE compound in a simple THF/water mixture, yielding NPs in the range of 100–200 nm

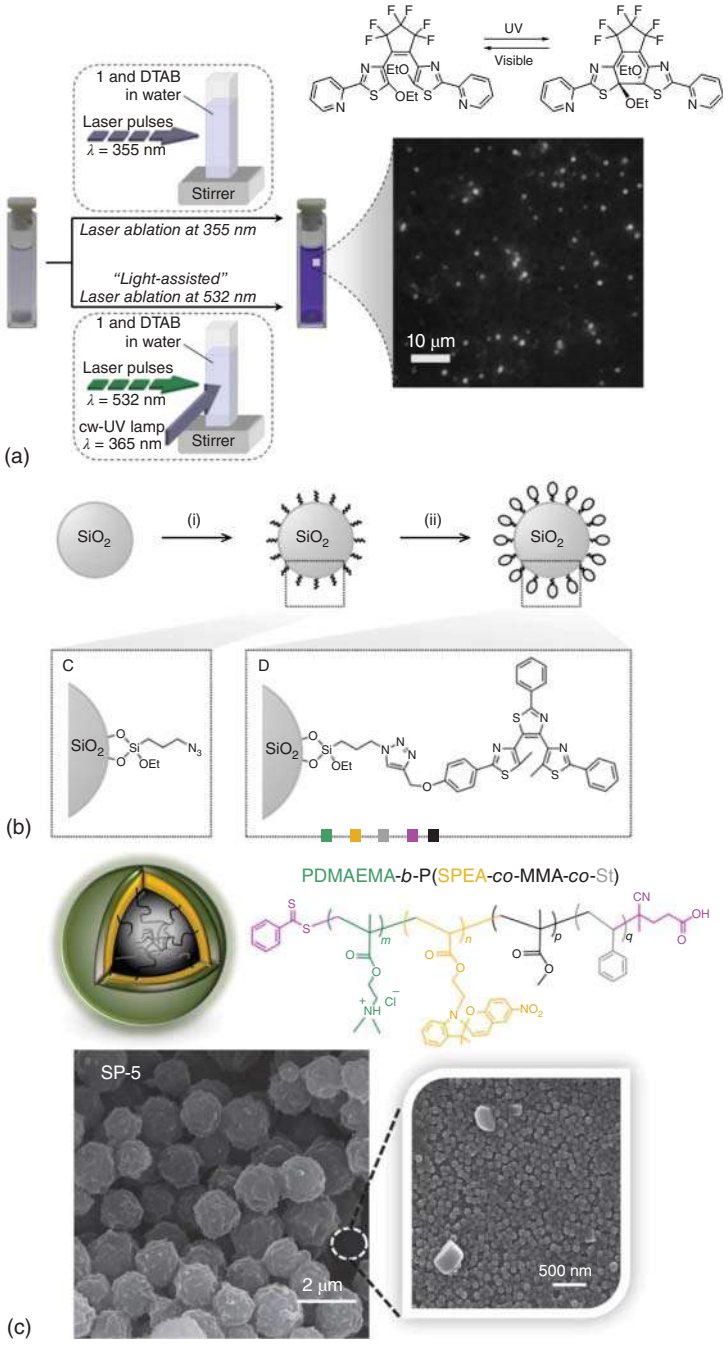


**Figure 28.1** (a) Laser ablation of DAE in a water surfactant medium by nanosecond laser pulses, following a "cw-light-assisted" procedure, to produce a colloidal suspension of photochromic nanoparticles. Source: Spangenberg et al. [11]/with permission of Wiley-VCH. (b) DAE-functionalized silica NPs via click chemistry. Source: Ouhenia-Ouadahi et al. [12]/with permission of American Chemical Society. (c) Latex nanoparticles including a SP molecule grafted to the polymer backbone, through polymerization-induced self-assembly. Source: Khakzad et al. [13]/with permission of Elsevier.

in diameter. The absorption blue-shift of the spectra as well as the reduced photocyclization quantum yields in NPs compared to the corresponding molecule in solution was ascribed to intra- and intermolecular effects induced by the aggregation. Then, Tagawa et al. [16] demonstrated that the nanocrystallization of DAE under the reprecipitation condition was explained by a cluster model. Crystallinity and photochromism of the NPs were evidenced and different ways to control the process was investigated, such as microwave irradiation after the reprecipitation step to promote the crystallization and evaporate the THF, or starting from an initial solution of DAE in the closed form [17]. The addition of sodium dodecyl sulfate (SDS) surfactant in an acetone/water mixture was shown to be an effective factor to yield photochromic micro-rods of DAE (length ~5 μm), whereas only rectangular nanocrystals were obtained in absence of SDS [18]. Such molecular DAE nanocrystals can be advantageously encapsulated with a polystyrene shell, using a soap-free emulsion polymerization technique, to enhance the cohesion of the nanosystem, provide an attractive protection and maintain its photochromic properties [19]. More recently, suspensions of SP nanocrystals were successfully prepared by the reprecipitation method. Their behavior after irradiation revealed a slower biexponential kinetics of the merocyanine (MC)→SP reaction, compared to a faster and monoexponential kinetics in acetonitrile solution [20]. The specific properties of SP NPs can be interpreted by the presence of several conformations of the MC form which cannot interconvert each other due to the crystal lattice constraints. These hypotheses were further confirmed by nanosecond transient spectroscopy, demonstrating that nanocrystals suspensions provide an ideal medium for studying photochromic reactions and spectroscopic characteristics in the solid state, without the drawback of multiphotonic effects usually encountered with conventional macroscopic solid samples [21]. Specific processes in nanoparticles were also reported for DAE systems. Enhanced photoinduced cycloreversion reaction of DAE nanoparticles subjected to nanosecond laser pulses was notably evidenced by Ishibashi et al. [22]. This amplification effect was ascribed to a laser heating model, in which the excitation of the first DAE molecule during the laser pulse contributes to the local rise of temperature in the nanoparticle which facilitates the cycloreversion transformation of the neighboring molecules that are excited by the next photons. More sophisticated reprecipitation methods were also described. An intriguing procedure, involving supramolecular stacking of DAE in nanofibers, aligned hydrodynamically upon exposure to audible sound (120 Hz) was evoked by Hotta et al. [23], as evidenced by linear dichroism experiments. Another phenomenon, based on the different solubility of the DAE in the open form (higher solubility) and in the closed form (lower solubility), was implemented by Patra et al. [24] in order to control the nano-aggregation of the photochromic molecules in colloidal suspension by light. Indeed, light-induced precipitation, at 405 nm, of the DAE molecule in an aqueous medium containing a surfactant could efficiently produce nanorods, which were redissolved under visible light, at 546 nm, and further yielded very long nanowires after the second cycle of irradiation at 405 nm. Finally, an elegant demonstration of the applicability of photochromic nano-aggregates in biology was given by Tong et al. [25]. Stable colloidal NPs were prepared by mixing a SP molecule bearing a long hydrophobic alkyl chain

(SP-C9) in an ethanolic solution containing lecithin and a lipid-polyethylene glycol (DSPE-PEG) under sonication. The NPs were determined to be monodisperse with an average hydrodynamic diameter of ~140 nm (SP $NP_H$). Under illumination in the UV, the hydrophobic SP was fully converted to the amphiphilic MC form (MC-C9), accompanied by a drastic reduction of size of the NPs down to ~50 nm (MC $NP_H$). This remarkable light-triggered shrinkage of the NPs size was used to encapsulate guest molecules and enable the release of drugs or fluorescent markers into cells upon light illumination. The enhanced diffusive transport under light through dense collagen gel was demonstrated, to carry and deliver therapeutics across the cornea.

Several examples of incorporation of photochromic molecules or nano-aggregates to silica matrices are reported and belong to the "bottom-up" category as well. For instance, photochromic thin films of an organo-silicate sol–gel film were prepared by spin coating in a single step with an organic SP molecule and the sol–gel precursors, simultaneously achieving inorganic polymerization and molecular nanocrystallization. The SP nanocrystals were formed and embedded into the pores of the sol–gel matrix. The photochromic properties of the resulting nanocrystals were found to be different from the microcrystalline material obtained by slow evaporation, with slower thermal back reaction from the MC to the SP form [26]. The same process was also used to produce sol–gel thin films containing DAE nanocrystals, preserving the photochromic properties of the molecules and improving their stability [27]. Another approach is the fabrication of functionalized silica nanoparticles. Indeed, as shown in Figure 28.1b, silica nanobeads (mean diameter 80 nm) were synthesized and decorated at their surface with DAE molecules through click chemistry, producing photochromic nanoparticles with advantages of both components [12]. Their properties were studied by fluorescence correlation spectroscopy, showing that such nanomaterials are suitable to probe not only the dynamics of conformational interconversion but also the photochromic reactions induced by light, on timescales which are usually inaccessible with the simple DAE molecule dissolved in solution, thanks to the slow diffusion of the larger nano-objects. Chen et al. [28] reported a preparation procedure of mesoporous silica nanoparticles modified by grafting a random copolymer with pendent SP molecules, via surface-initiated atom transfer radical polymerization and chemical hydrolysis. The resulting system showed an interesting photoresponsive behavior, changing the hydrophilicity of the nanoparticle upon light illumination. Consequently, drugs can be loaded to the mesopores, then released at will by light or pH stimulation, providing great premises toward the control of drug delivery to complex environments.

Fabrication of polymer nanoparticles represents the last category of "bottom-up" techniques to produce photochromic nanomaterials. Most of the reported examples involve SP or spirooxazine photochromes. The first straightforward one-step mini-emulsion procedure was achieved to prepare polymeric nanoparticles incorporating a SP photochrome in water, displaying excellent photochromic properties [29]. Poly(methyl methacrylate) (PMMA) or ethyl cellulose nanocapsules containing spirooxazine dyes were synthesized by the same type of mini-emulsion method [30], with improved fatigue resistance when photostabilizer additives are

included in the polymer [31]. However, dye-doped polymeric nanoparticles generally suffer from the disadvantage of leakage, since the photochromic molecules are simply entrapped into the nanobeads by weak interactions. In this regard, a direct access to polymeric vesicles with SP molecules covalently attached to the polymer chains was demonstrated via reversible addition-fragmentation chain transfer (RAFT) dispersion polymerization [32]. The photochromic behavior of the vesicles showed better reversibility and stability than the polymer chains solubilized in solution. Similarly, the RAFT polymerization was employed to fabricate latex nanoparticles including a SP grafted to the polymer backbone, through polymerization-induced self-assembly (Figure 28.1c) [13]. These polymeric NPs represent excellent candidates for imaging applications. SP-doped polymeric NPs were actually used to generate photochromic nanosystems with UV-induced fluorescence activation, taking advantage of the bright fluorescence of the MC form. On–off fluorescence switching in human breast cancer cells was achieved upon alternate 780-nm irradiation, to induce both two-photon SP→MC photoconversion and fluorescence excitation, and 488 nm irradiation to promote the one-photon MC→SP reaction [33].

Few other alternative procedures based on physical principles were developed to prepare photochromic nanomaterials as well. For instance, vapor deposition of photochromic molecules such as salicylidene-anilines or DAE derivatives under vacuum was shown to lead to nanocrystals directly spread onto surfaces and dry substrates, without any intermediate step of colloidal suspension [34]. Another strategy was exemplified by Tong et al. [35], with the fabrication of molecular nanowires by a template method. With this method, the nanomaterials were directly grown by slow solvent annealing in a porous anodic aluminum oxide template, which was dissolved in acid medium in the second step, liberating the nanowires that could be dispersed in an aqueous suspension or deposited on a substrate to investigate their photochromic and photomechanical properties.

## 28.3 Nanosystems Involving Photochromic Molecules and Organic Fluorophores

Fluorescence photoswitchable molecular systems are very attractive due to their potential applications in various fields such as bio-imaging, optoelectronics, and super-resolution microscopy. Several possibilities to combine photochromism and fluorescence can be envisaged [3]. One option consists in using intrinsically fluorescent photochromic derivatives, emissive in one form and non-emissive in the other isomer. The second strategy involves the coupling of a photochromic molecule to a fluorophore using a nonconjugated linker, i.e. photochromic–fluorescent dyads. In this case, the fluorescence modulation can be achieved via energy transfer processes, especially Förster resonance energy transfer (FRET). The fluorophore must be selectively quenched by only one isomer of the photochromic unit, usually the colored form, showing an appropriate spectral overlap between the donor (fluorophore) and the acceptor (colored form of the photochromic molecule) [36]. In some cases,

photoinduced electron transfer (PET) processes can also be at the origin of fluorescence photoswitching in molecular dyads [37]. However, the synthesis of covalently linked photochromic–fluorescent dyads suffers from a lack of versatility, and the development of more flexible preparation methods are desired to produce bright photoswitchable nanomaterials. An attractive strategy consists in gathering several complementary photoactive molecules, namely photochromic and fluorescent moieties, into nanoparticles (NPs) [4]. Several designs can be found to fabricate such nanosystems: the photochromic and fluorescent molecules can be simply mixed to generate nano-aggregates, hosted in a polymer matrix, or embedded in silica beads. Moreover, these preparation methods of organic NPs can also be employed by using covalently linked photochromic–fluorescent dyads to enhance the FRET processes that occur between the two moieties. Each possible strategy, namely silica based nanoparticles, emissive polymer nanoparticles and molecular nano-aggregates show some respective advantages and drawbacks, as described in this section.

## 28.3.1 "ON-OFF" Photoswitchable Fluorescent Nanoparticles

### 28.3.1.1 Silica Nanoparticles Embedding Photochromic and Fluorescent Dyes

Silica nanobeads are great host platforms for photochromic and fluorescent molecules. They display advantages since they are easy to functionalize, they can be used for biological applications, and they have appreciable optical properties to prepare smart functionalized NPs [38]. The organic compounds are loaded into the silica or attached to the surface. Folling et al. [39] reported a photoswitchable fluorescent silica NPs in which the photochromic compound (DAE) was covalently linked to a Rhodamine 101 fluorophore and then covalently attached to the silica network as shown in Figure 28.2a. The fluorescence photoswitching was demonstrated: in dilute solution, the quenching of the photochromic–fluorescent dyad was linearly dependent on the conversion yield of DAE whereas in the NPs state, the quenching was much more efficient, displaying a clear deviation from linearity. However, this method is difficult to utilize for general (non-synthetic) researchers due to the hard synthetic steps, the DAE and the fluorophore have to be linked together and then connected to silica to generate the NPs. Jung et al. [42] described the one-pot synthesis of silica NPs. This straightforward method does not require that the photochromic compound, here a DAE, and the fluorophore one, a Cy3, are attached together. DAE and Cy3 were first functionalized with triethoxysilane and then simply mixed together with vinyltriethoxysilane to generate, by copolymerization, the embedded NPs. This procedure does not require difficult synthesis and can achieve tunable fluorescence photoswitching. The system is fluorescent under irradiation at 510 nm. While the silica beads were irradiated with UV light, the DAE in the closed form quenched the fluorescence of Cy3 by FRET. The authors demonstrated the fluorescence photoswitching of NPs internalized on living HeLa cells. Unfortunately, a complete fluorescence photoswitching could not be reached. Another possibility is to dope the core of the silica nanoparticles with fluorophores and incorporate photochromic compounds in the outer shell, as proposed by Genovese et al. [40]. In this case, the silica NPs were prepared from micelles of

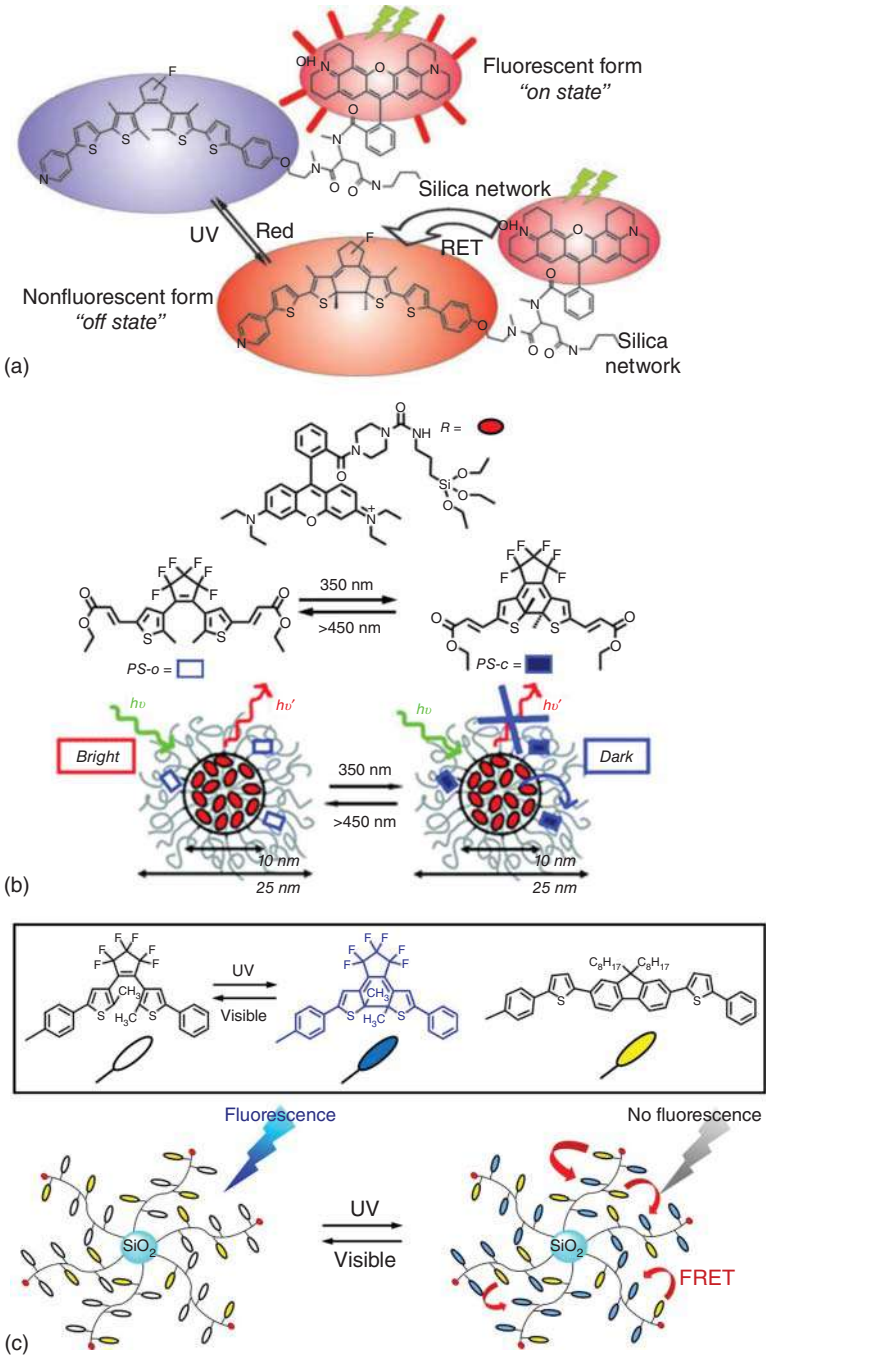


**Figure 28.2** (a) Molecular structure of the DAE and Rhodamine 101 attached to silica. Under green light excitation, the rhodamine emits red light when the DAE is in its open form, and FRET occurs when the DAE is in its closed. Source: Folling et al. [39]/with permission of John Wiley & Sons. (b) Representation of the core–shell silica NPs and molecular structures of the rhodamine B and DAE used for FRET. Source: Genovese et al. [40]/with permission of Royal Society of Chemistry. (c) Silica nanoparticles functionalized with copolymers of DAE and fluorene derivatives. Source: Shimizu et al. [41]/with permission of John Wiley & Sons.

Pluronic F127 in water. The NPs were covalently doped with Rhodamine, and the photochromic DAE molecules were then positioned in the outer shell, outside but close enough to the Rhodamine dyes to allow FRET to occur and perform fluorescence photoswitching. A schematic representation of such a system appears in Figure 28.2b. Once again, a complete fluorescence quenching could not be reached. Alternatively, the silica NPs can be just employed as nanoplatforms and functionalized by polymer chains bearing the photochromic derivatives. Indeed, Shimizu et al. [41] designed silica NPs covered by a random copolymer consisting of fluorene derivatives and DAE compounds. The molecular structures are shown in Figure 28.2c. Such a system showed more efficient fluorescence photoswitching than the simple random copolymer. Similar strategies have also been reported to build up photoswitchable fluorescent silica NPs using DAEs [43, 44] or SPs [45, 46].

#### 28.3.1.2 Photochromic–Fluorescent Polymer Nanoparticles

As silica nanobeads, polymeric nanoparticles are suitable for biological application and generally have high brightness. Conjugated polymer nanoparticles, called polymer dots (P-dots), are excellent candidates, usually prepared with the following procedure: a water-miscible organic solution of a conjugated polymer is injected into water. Quick injection in water leads to a decrease of solvent and appearance of nano-aggregates of polymers [47]. The size can be controlled through the concentration of polymer solution [48]. Davis et al. [49] reported P-dots doped with a DAE molecule and a perylenebisimide (PBI) dye. Fluorescence photoswitching was successfully obtained in colloidal suspension in water and also at the single-particle level under microscope. The fluorescence of the PBI is quenched by the closed form of the DAE by FRET. Osakada et al. [50, 51] and Kuo et al. [52] reported DAE-doped P-dots dedicated to biological imaging. These P-dots were prepared by a reprecipitation method, mixing into water a THF solution containing the PFBT (poly(fluorene-*alt*-benzothiadiazole)) fluorescent polymer, the photochromic DAE, and an amphiphilic polymer having hydrophilic side chains terminated with carboxylic groups. The DAE and PFBT are also amphiphilic and trapped with the amphiphilic polymer and the hydrophilic side chains are at the outside in contact with water. Moreover, the surface can be functionalized by streptavidin as represented in Figure 28.3a. Repeatable fluorescence photoswitching was demonstrated in a fixed cell and also in a macrophage one [50, 51]. The photoswitching of P-dots in fixed BHK cells is exhibited in Figure 28.3b. Under UV light, the fluorescence of the cell is almost completely turned off and recovered with visible light. This can also be used for "optical painting" to select targeted cells from tissue in order to label and cure them from genetic analysis [52]. The P-dots were linked to streptavidin and biotinylation took place to tag cells. After irradiation with a laser, the cells were "painted" and easily observable under microscope, and then a sorting step was performed. This method can be applied for DNA sequencing and mRNA extraction. The authors were able to sequence an oncogene after applying the painting and sorting method. They also checked the impact of the method on mRNA and no damages were caused by the method.

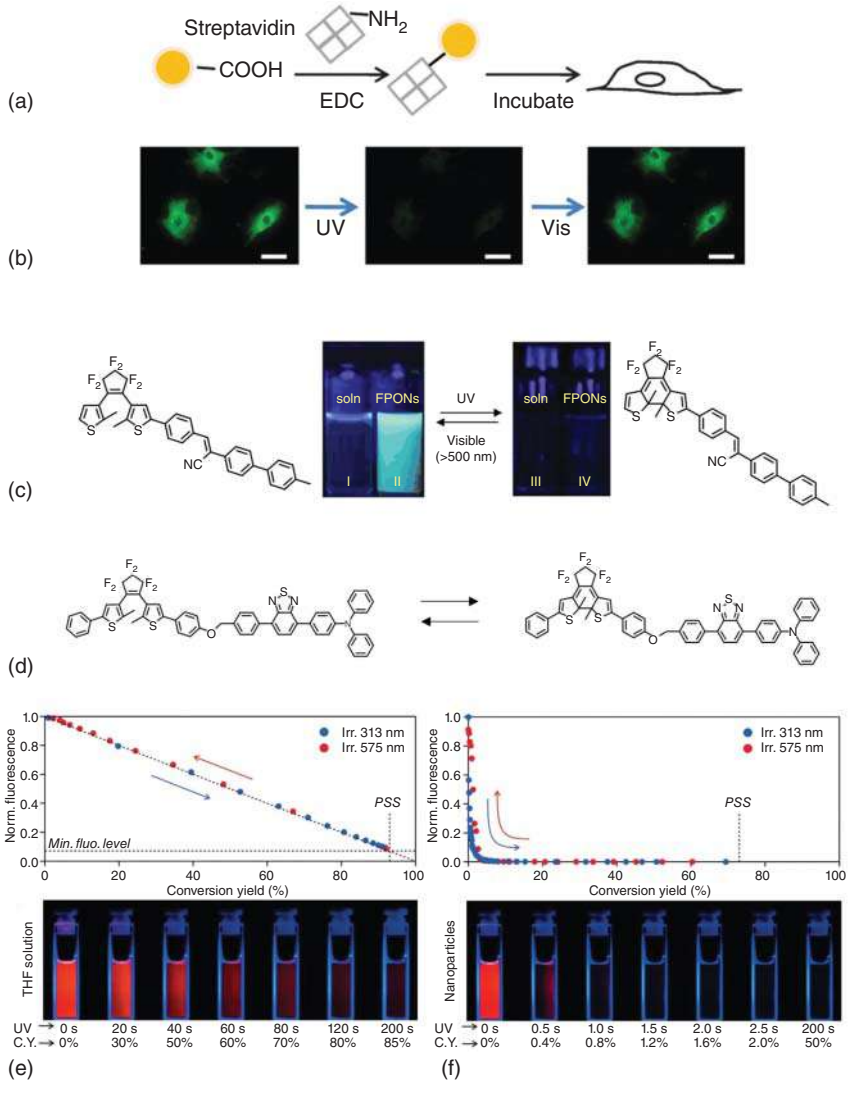


**Figure 28.3** (a) Schematic representation for functionalization of the P-dots. (b) Photoswitching of P-dots in fixed BHK (Baby hamster kidney) cells (left: before UV irradiation, middle: after UV irradiation and right: after visible light irradiation, scale bar = 50 μm). Source: Osakada et al. [50]/with permission of Royal Society of Chemistry. (c) Molecular structure of DAE showing AIEE effect. Picture in THF (tetrahydrofuran) solution (soln) and colloidal suspension (FPONs) in the open form (left) and the closed form (right). Source: Lim et al. [53]/with permission of Wiley-VCH. (d) Molecular structure of the DAE-BTD dyad, corresponding fluorescence vs. conversion yield correlation plots, and photographs of the samples in (e) THF solution (at $10^{-6}$ M in THF solution) and (f) NPs colloidal suspension (at $10^{-5}$ M in $H_2O$/THF 80 : 20 solution). Source: Su et al. [54]/with permission of Wiley-VCH.

The preparation of polymer micelles to trap photochromic and fluorescent compound can be a smart strategy as well. Yildiz et al. [55] combined an amphiphilic copolymer with a hydrophilic one to obtain polymer micelles. They encapsulated SPs as photochromic moieties with boron dipyrromethene (BODIPY). A fluorescence modulation was described in colloidal suspension in PBS media and also at the intracellular level. The assembly demonstrated its capability to be used for super-resolution imaging, with noncytotoxic properties. Moreover, Liu et al. [56] prepared conjugated fluorescent polymer nanoparticles and doped them with polyhedral oligomeric silsesquioxane core where eight DAE are attached. A fluorescence modulation was achieved for example with the F8BT (poly(9,9-dioctylfluorene-*alt*-benzothiadiazole)) fluorophore. The yellow fluorescence of the NPs was quenched under UV irradiation and could be recovered with visible light. By combing P-dots of F8BT, PFO (poly(9,9-di-*n*-octylfluorenyl-2,7-diyl)) and MEH-PPV (poly(2-methoxy-5-(2-ethylhexyloxy)-1,4-phenylenevinylene)) doped with silica-DAE core, a white emission of fluorescence was observed. This fluorescence was almost completely turned off under UV and turned on with visible light. However, the size of the prepared NPs are generally larger than the Förster radius and most of the time, the fluorescence photoswitching is incomplete [56]. An elegant way to overcome this issue was found by Trofymchuk et al. [57]. The authors took advantage of the exciton diffusion occurring over multi-chromophoric assemblies to enhance the fluorescence photoswitching. Rhodamine cationic fluorescent dyes were encapsulated into polymeric nanoparticles with various bulky counter anions, together with a DAE molecule acting as the fluorescence quencher. The bulky counter anions allow to avoid the self-quenching of the Rhodamine dyes but keep them at such short distance to enable homo-FRET. The amount of photochromic quenchers within the NPs was investigated, and switching efficiency higher than 98% was obtained with polymer NPs containing 0.3 wt% of DAE. Fluorescence photoswitching of single NPs was also demonstrated under wide-field microscopy.

Zhang et al. [58] reported a very interesting system using an unconventional spirooxazine and fluorescent-conjugated polymer. P-dots (based on fluorenyl-benzothiadiazole) were prepared and doped with spirooxazines. The spirooxazine stable state is the MC form, leading to doped P-dots which are initially nonfluorescent. Under visible illumination, the MC was converted to the spiro form and a green fluorescence signal appeared. When visible light irradiation was stopped, the fluorescence spontaneously disappeared, since the MC form was thermally regenerated. If the power of the irradiation light is too high, a photoproduct can be generated. Such a system is very sensitive to the irradiation power applied to induce the photoconversion.

#### 28.3.1.3 Photochromic and Fluorescent Nano-Aggregates

Gathering organic fluorophores into nanoparticles can affect negatively their fluorescence properties, decreasing their emission quantum yield. This phenomenon is called "aggregation-caused-quenching" (ACQ) and has to be taken into account in the design of emissive molecular nano-objects, consisting of aggregated

fluorophores. On the other hand, molecules that are brighter in the condensed state compared to the solution state can be designed, based on a phenomenon named "aggregation-induced emission" (AIE) or "aggregation-induced enhanced emission" (AIEE). Lim et al. [53] synthetized a DAE molecule that displays such an AIEE effect. The introduction of 1-cyano-*trans*-1,2-bis-(4′-methylbiphenyl)ethylene unit makes this DAE derivative nonfluorescent ($\Phi_F < 0.000\,02$) in both forms in THF solution. But when this compound was condensed into NPs, the open form became emissive ($\Phi_F = 0.05$) and an efficient fluorescence photoswitching was achieved between the bright open isomer and the quenched closed one. In that case, the quenching occurs in not only an intramolecular but also an intermolecular level, because the molecules are closely packed within the nano-aggregate. The Figure 28.3c illustrates this interesting behavior by means of photographs of dilute THF solution and colloidal suspension of NPs of this DAE molecule. The fluorescence enhancement of the DAE derivative in open form can be clearly observed in colloidal suspension of NPs, as well as the complete fluorescence quenching under UV light. The size distribution of the prepared nano-aggregates was broadly dispersed between 40 and 275 nm, to be further employed for fluorescence imaging. Recently, Chen et al. [59] reported a new AIE-active DAE molecule covalently linked to two quinolinemalonitrile. The fluorescence can be turned on and off in the NPs state depending on the isomer of DAE. Moreover, the photochromic activity of DAE can be controlled by the aggregation state during the AIE process. A recent review by Yan and Wang [60] summarizes the photochromic compounds displaying AIE or AIEE effects.

An interesting effect of fluorescence photoswitching in molecular nanoparticles was reported by Su et al. [54], with a DAE derivative covalently linked to a benzothiadiazole (BTD) dye, as shown in Figure 28.3d. BTD is a well-known fluorophore that can emit fluorescence in dilute solution and solid state. The DAE-BTD dyad is strongly emissive in its open form in dilute solution ($\Phi_F = 0.67$) as well as in colloidal suspension of NPs ($\Phi_F = 0.65$), but not in its closed form. The photophysical properties (absorption spectra, maximum of fluorescence emission, and fluorescence lifetime) of the DAE-BTD are comparable in the solution and NPs states. The main difference concerns its fluorescence photoswitching behavior upon increasing irradiation time. In dilute solution, the fluorescence emission linearly decreases with the number of dyads in the closed form, and only 85% of the initial fluorescence is quenched at the photostationary state (PSS) (Figure 28.3e). For the NPs, a "giant amplification effect of fluorescence photoswitching" was evidenced. Interestingly, only few photons were required to totally quench the fluorescence of the nano-aggregates. For only 1% of closed-ring isomer, 90% of the initial fluorescence was turned off, and a full quenching was reached for a conversion yield of 5%, as depicted in Figure 28.3f. Intramolecular FRET is responsible for the linear relationship between the emission and the conversion yield in dilute solution, whereas in colloidal NPs, this "giant amplification effect of fluorescence photoswitching" can be assigned to a very efficient intermolecular FRET process occurring within NPs. Experimental estimations and theoretical calculations concluded that a single closed-ring DAE isomer can quench more than 400 BTD neighboring fluorophores

located in the Förster sphere. In the same line, very recently, Ikariko et al. [61] reported a similar system using a PBI fluorophore attached to a DAE molecule instead of the BTD. To overcome the ACQ phenomenon relative to the PBI in solid state, the bay position was substituted with bulky substituents, allowing a suitable fluorescence quantum yield in the nano-aggregates to be reached ($\Phi_F = 0.23$) and exhibiting the same "giant amplification of fluorescence photoswitching" effect, associated with a higher photostability than DAE-BTD. It is worth noting that such amplification of fluorescence photoswitching can be observed at different levels in a wide variety of systems, like molecular nano-aggregates [62, 63], silica nanobeads [39], and polymer nanoparticles [57] as mentioned previously, but also in macroscopic molecular crystals [64] and polymer matrices [65–67].

### 28.3.2 Nanoparticles with Fluorescence Color Modulation

The nanosystems described previously can perform "ON-OFF" fluorescence photoswitching. However, the design and synthesis of nano-objects with the ability to trigger multiple emission colors are very attractive, with perspectives for new full-color displays, lighting sources, and biological imaging in order to sort simultaneous phenomena [47]. Many systems with phototunable fluorescence colors have been developed in the recent years, mixing at least two fluorescent dyes with photochromic components, allowing the control of the fluorescence intensity of each fluorophore.

In 2012, Kim et al. [68] reported dual-color photoswitchable NPs. Two fluorophores displaying AIEE with high brightness in the NPs state were designed, and then mixed with a DAE to yield NPs which behave as red emitters when the DAE is in open form and turn to blue-greenish emitters after UV irradiation. This dual fluorescence photoswitching was totally reversible and demonstrated in polymer films as well [68, 69]. Multi-stimulus fluorescence patterning and nondestructive fluorescence readout of the fluorescence signal were also achieved.

P-dots that can perform dual-color photoswitchable fluorescence were designed by Kim and Lee [70]. These NPs are composed of DAE and a conjugated polymer functionalized with a BTD fluorophore (green emitter) and a phenylene unit (blue emitter). When the DAE is in its open isomer, the P-dots exhibit a green fluorescence as shown in Figure 28.4a despite the blue emission of phenylene. Upon UV exposure, the closed isomer of DAE is generated and the P-dots emission changes from green to blue. Such emission color change is due to an efficient FRET phenomenon between the BTD fluorophores and the photochromic DAE molecules in their closed-ring isomers. The overlap between the absorption spectrum of DAE closed-ring isomer and emission spectrum of BTD is much larger than the one with the emission spectrum of the phenylene unit. Therefore, an efficient FRET occurs only between the BTD and the DAE moieties. A demonstration for biological application was also achieved. P-dots were loaded into a living zebrafish, and fluorescence color photoswitching was carried out. Without UV irradiation, a strong fluorescence was detected form the zebrafish in emission channel of blue and green. No difference in the shape

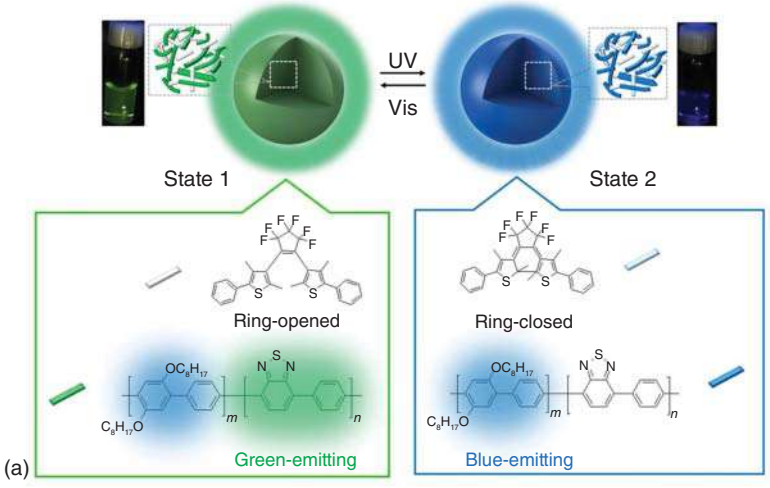
UV
Vis
State 1
State 2
Ring-opened
Ring-closed
Green-emitting
Blue-emitting
(a)

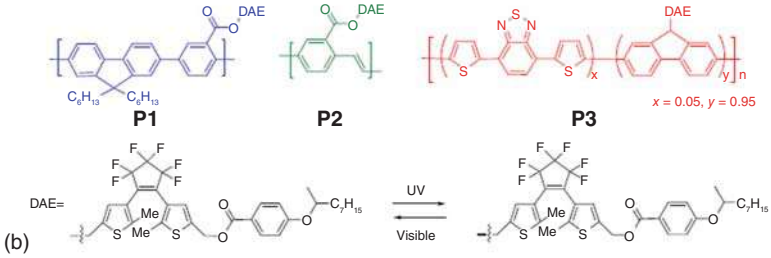
DAE
P1
P2
P3
x = 0.05, y = 0.95
DAE=
UV
Visible
(b)

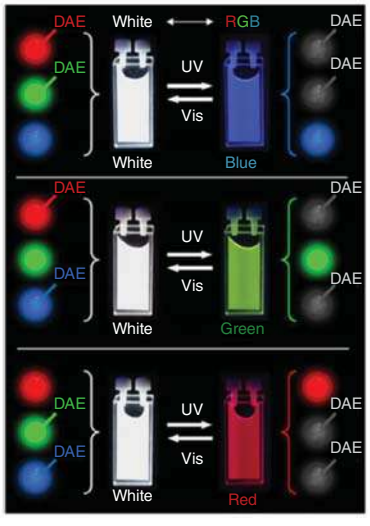
DAE
White
RGB
UV
Vis
Blue
Green
Red
(c)

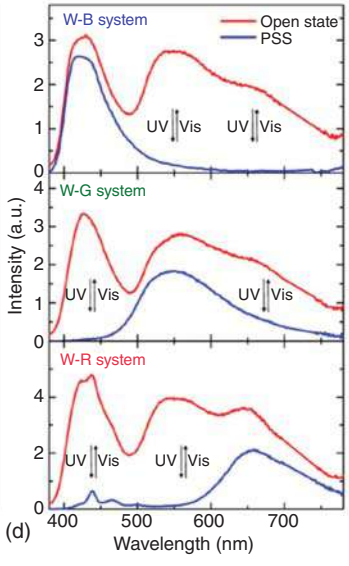
W-B system
W-G system
W-R system
Open state
PSS
UV
Vis
Intensity (a.u.)
Wavelength (nm)
400
500
600
700
(d)

**Figure 28.4** (a) Fluorescence color photoswitching of P-dots containing DAE and a conjugated polymer doped with two emitters. Source: Kim et al. [70]/with permission of American Chemical Society. (b) Molecular structures of polymers P1, P2, and P3. (c) Photographs of the photoswitchable samples between white and RGB fluorescence. One of the three nanospheres was replaced by a non-photoresponsive one (no DAE on the side chain) to achieve fluorescence color photoswitching. (d) Fluorescence emission spectra for the white-to-blue (W-B), white-to-green (W-G), and white-to-red (W-R) systems under UV or visible light irradiation (from top to bottom). Source: Bu et al. [71]/with permission of Springer Nature.

of zebrafish was reported. When the zebrafish was irradiated with UV light, the green fluorescence was quenched, but the blue emission remained. This kind of dual-color fluorescence change can find useful application in biology to obtain accurate analysis of biological events by fluorescence microscopy. In the same perspective, Chen et al. [72] prepared polymeric nanoparticles with a PMMA core and a PEO (poly(ethylene oxide)) shell containing a yellow fluorescent BODIPY and a photochromic SP that display dual-color photoswitching. The resulting nanoparticles were shown to emit a yellow fluorescence, which becomes red under UV irradiation. In this case, SP is converted to its merocyanine form, leading to BODIPY quenching and red emission of the merocyanine. These nanosystems were used to obtain confocal images of living cells. Very recently, Kim et al. [73] reported the preparation of polymeric nanoparticles having specific dual-color fluorescence photoswitching and employed them for super-resolution microscopy.

Although many systems with photoinduced fluorescence color modulation have been reported, they are mainly based on a ratiometric change between two colors, leading to a limited space for the color change. To obtain a full-color fluorescence control, a combination of a red (R), green (G), and blue (B) emitters is required. A dedicated methodology to obtain RGB fluorescence photoswitchable P-dots using various fluorescent species and several photochromic molecules was described by Bu et al. [71] First, R, G, and B fluorescent-conjugated polymers bearing DAE molecules on their side chains (P1, P2, and P3) were synthesized, as shown in Figure 28.4b, and photoresponsive P-dots were prepared. Non-photoresponsive nanoparticles were also fabricated, using R-, G-, and B-conjugated polymers without DAE (P1′, P2′, and P3′). Several combinations of P-dots were obtained: P1′, P2, and P3 for white to blue fluorescence, P1, P2′, and P3 for white to green fluorescence, and P1, P2, and P3′ for white to red fluorescence, each system being composed of two photoresponsive and one non-photoresponsive P-dots, mixed in the appropriate ratio to generate white light fluorescence. Upon UV irradiation, the DAE is converted to its closed form and energy transfer can occur, leading to the fluorescence quenching of the photoresponsive nanospheres, while the fluorescence of the non-photoresponsive nanoparticles remains unchanged. Therefore, the white fluorescence switches to B, R, and G for the white-to-blue, white-to-red, and white-to-green systems, respectively, by UV light. This color change is depicted in Figure 28.4c. The white fluorescence can be recovered for each nanosystem upon visible irradiation, as shown by the spectra displayed in Figure 28.4d. Such multicolor fluorescence photoswitching is very promising, but the tunability of the

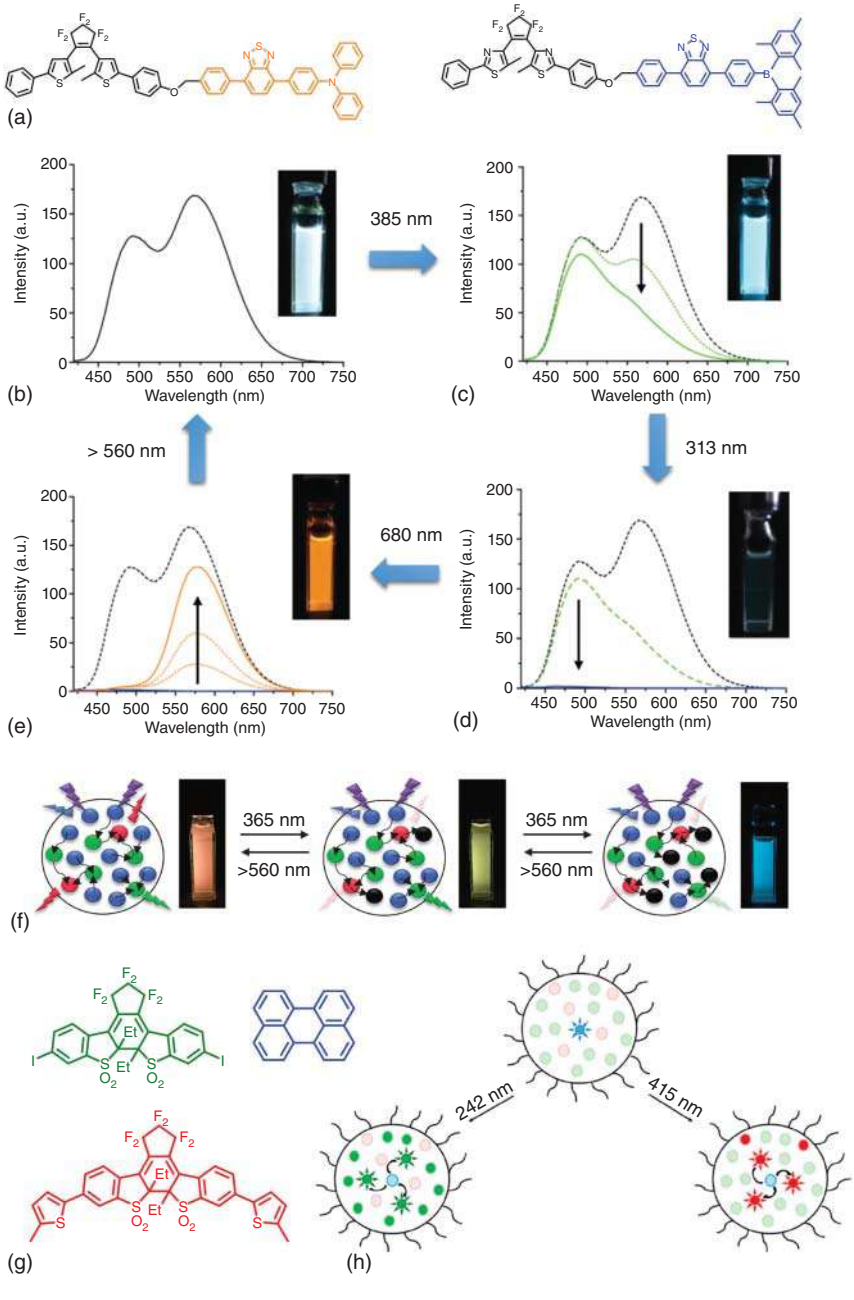
(a)
(b)
(c)
(d)
(e)
(f)
(g)
(h)
Intensity (a.u.)
Wavelength (nm)
385 nm
313 nm
680 nm
> 560 nm
365 nm
>560 nm
365 nm
>560 nm
242 nm
415 nm

**Figure 28.5** (a) Molecular structures of the DAE-BTD dyads used for fluorescence photoswitching. (b–e) Emission spectra and photographs of cuvette of colloidal suspension containing NPs (b) before irradiation, white emission, (c) after irradiation at 385 (nm), cyan emission, (d) after irradiation at 313 nm, total quenching, and (e) after irradiation at 680 nm, orange emission. White fluorescence is restored after irradiation at 640 nm. Source: Ishida et al. [75]/with permission of Royal Society of Chemistry. (f) Schematic representation of reversible RGB color photoswitching upon UV irradiation and visible irradiation. Blue, green, and red dots correspond to blue, green, and red emitters, respectively, whereas black dots are quenched species [74]. (g) Molecular structures of the three components used to design "cocktail" micelles and (h) schematic principle of RGB fluorescence photoswitching. Source: Ishida et al. [76]/with permission of The Chemical Society of Japan.

color strongly depends on the composition of the initial mixture of P-dots, which limits the accessible variation of color change. Selective photoswitching of each fluorescent molecules and high contrast without interactions between them would be required to obtain an ideal multicolor fluorescence photoswitching, which turns to be challenging due to the broad absorption band of the photochromic derivatives and the difficulty to convert them entirely to their quenching state.

To overcome this drawback, Ishida et al. [74, 75] ingeniously employed the "giant amplification effect of fluorescence photoswitching." The authors synthetized two different photochromic–fluorescent dyads, composed of a DAE linked to BTD fluorophores emitting either in the orange or cyan regions, as represented in Figure 28.5a. As expected, the NPs composed of only one type of dyads show an efficient nonlinear quenching of the fluorescence under UV irradiation. Interestingly, a wavelength dependence of the fluorescence photoswitching was discovered. Upon irradiation at 385 nm, due to different molar absorption coefficients, the fluorescence intensity of the first dyad is preferentially turned off while the fluorescence signal of the second dyad remains at 60% of its initial level. Oppositely, under irradiation at 313 nm, the second dyad can be completely switched off. To recover the fluorescence, irradiation in the visible is used: at 680 nm, the first dyad returns back to its initial state whereas the second dyad remains nonfluorescent, the latter being fully restored at 560 nm. Based on this irradiation selectivity, a mixed colloidal suspension NPs of both dyads displayed multicolor photoswitching with very high contrast. Indeed, when the two kinds of dyad NPs were mixed into appropriate proportion, the sample could generate white light fluorescence emission, covering the whole visible region. Upon irradiation with 385-nm light, the orange emission was turned off, leading to cyan fluorescence. After subsequent irradiation at 313 nm, the cyan emission was quenched and the system was fully quenched. To recover the fluorescence, the system was first irradiated with 680-nm light to allow the bright orange emission to appear, and then exposed to 560-nm light to restore the white emission. These steps are represented in Figure 28.5b–e. A sequential R-G-B fluorescence photoswitching was also achieved, gathering a single photoswitchable DAE-BTD dyad (blue-emissive) with two BTD fluorophores (green- and red-emissive) into NPs [74]. When mixed together, the colloidal NPs showed a red emission which was sequentially changed to green and then blue fluorescence under irradiation at 365 nm. This behavior was totally reversible when

exposed to 560-nm light. The Figure 28.5f describes the different emission state, as illustrated by the sample pictures.

Very recently, Naren et al. [76] succeeded to obtain a fully controllable RGB fluorescence photoswitching system. Two DAE molecules were synthesized, showing fluorescence in their closed form: one in the green and the other in the red. These two components were mixed with a perylene (playing the role of blue emitter) into polymer micelles, as mentioned previously [55]. The molecular structures of the compounds are represented in Figure 28.5g. These "cocktail" nanosystems showed initially the blue fluorescence of perylene. Under irradiation at 242 nm, the emission turned green since the green-emissive DAE was converted to the closed form and quenched the fluorescence of perylene. Alternately, when the "cocktail" micelles were exposed to a 415-nm light, the blue fluorescence was quenched by the red-emissive DAE in the closed form, and the whole system was switched to red emission. The principle of such a RGB fluorescence photoswitching is schematized in Figure 28.5h. Smart combinations of 242-nm and 415-nm light doses may give access to various colors of emission, as depicted by the CIE coordinates of the "cocktail" micelles [76].

## 28.4 Nanosystems Involving Photochromic Molecules and Inorganic Emitters

Hybrid organic–inorganic luminescent materials are an interesting class of functional materials that have attracted wide attention. Inorganic materials benefit from various properties that are often difficult to achieve in organic systems. Examples of such properties include robustness against harsh environmental conditions and irradiation of light, narrow, and symmetric emission bands that offer high color purity and ready tunability of optoelectronic properties such as emission wavelength or bandgap adjustment. However, a major challenge is faced upon when one wants to add functionality of organic molecules such as photoswitches to inorganic materials. Synthesis of such materials requires precise design of both the organic and inorganic components to achieve the desired affinity. High functionality of inorganic materials, especially nanoparticles, has gathered a great amount of researchers with their efforts focused on architecting organic–inorganic hybrids.

Inorganic nanoparticles that have recently become of particular interest are semiconductor quantum dots (QDs), CDs, and UCNPs. Each class of materials shows a distinct function that when coupled with an organic photoswitch can give birth to even more advanced nanomaterials for applications such as high-density optical memories displays with high color purity and high-resolution fluorescence microscopy. In this section, some cutting-edge recent advances in photoswitchable hybrid nanoparticles incorporating both organic photochromic species and inorganic nanoemitters are introduced, with the main focus being on the control of their photoluminescence (PL) properties.

### 28.4.1 Photochromic Nanoparticles Based on Quantum Dots (QDs) Emitters

One of the highly studied classes of inorganic nanoparticles are semiconductor quantum dots. The most interesting properties of semiconductor quantum dots relies in tunability of their optoelectronic properties. Bandgap and therefore the PL from these semiconductor quantum dots can be tuned by both their chemical composition and their size. By decreasing the particle size to nearly less than 20 nm, the bandgap of these structures differ from the bulk material and becomes dependent on particle size where upon decreasing the size, the bandgap becomes larger. Therefore, one can tune the emission wavelength by precisely controlling the particle size [77–79].

CdSe/ZnS or CdSe/CdS/ZnS core–shell structures are a class of QDs that have become a research target worldwide. One of such targets has been to achieve photoswitchable quantum dots by hybridizing the inorganic nanoparticles with photochromic molecules such as SPs, azobenzenes, or DAEs. During the past decade, hybrids of CdSe/ZnS QDs with different DAEs have been developed. Such hybrids are usually achieved through surface coating or by direct coordination of the organic photoswitch.

One of the early attempts on photoswitchable CdSe/ZnS QDs was done by designing an amphiphilic polymer with long alkyl chains and hydrophobic DAE photoswitches [80]. The strategy included introduction of alkyl amines and DAEs having an amine group into polyisobutylene-*alt*-maleic anhydride (PMA) polymer chains. Upon reaction of amine with the maleic anhydride groups, hydrolysis yields a polymer chain with one side having hydrophilic carboxylic acid groups and the other side having hydrophobic alkyl chains and DAE photoswitches. Because most inorganic QDs benefit from surface ligands with long alkyl chains as capping reagents, such photoswitchable polymers can wrap their hydrophobic side around the QDs. This surface modification yields water-soluble hybrids of QDs which are of special importance in bio-imaging. The photoswitchable QDs showed modulation of fluorescence between ON and OFF states with 40% fluorescence quenching in the OFF state based on FRET. As this strategy offers the adjustment of length between the DAE moiety and the QDs by simply adjusting the length of the linker between the DAE backbone and the amine group, formulation of FRET equations became possible in later studies (Figure 28.6a) [81].

Integration of DAE into PMA has also been used in dual-color photoswitching systems. One way is addition of the second organic dye as FRET donor for both QDs and DAE [83, 84]. Hydrophilic lucifer yellow (LY) was introduced together with DAE into PMA. Upon excitation with blue light, both LY and QDs are excited. Upon induction of photocyclization of DAE, the closed-ring isomer of DAE acts as a FRET acceptor and quenches the fluorescence of both LY and QDs, however, each with a different degree of modulation. The emission of LY is quenched to a much greater degree than QDs, and therefore the emission ratio of QDs to LY is dramatically different when the closed-ring isomer of DAE is present [83]. The reverse version of

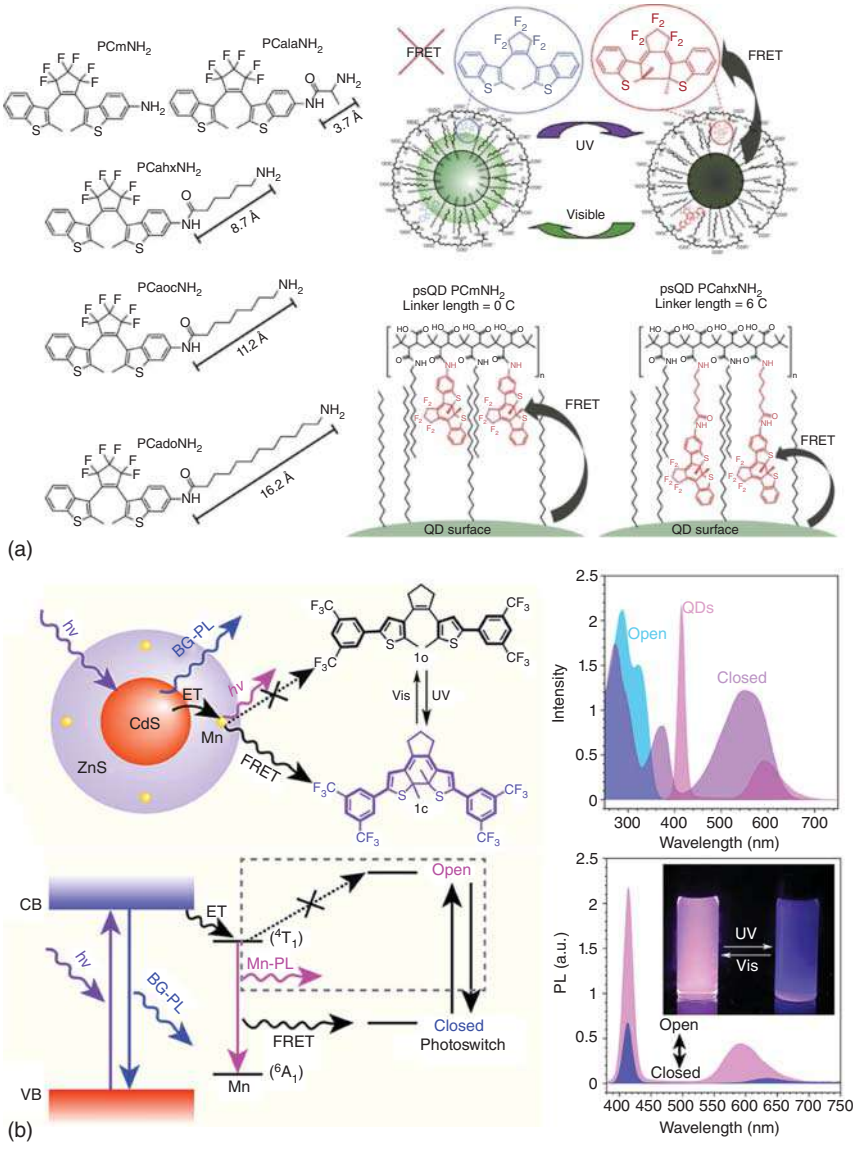


**Figure 28.6** (a) Photoswitchable QDs with variable separation of the photochromic DAE FRET acceptors. Source: Diaz et al. [81]/with permission of Springer Nature. (b) Proposed mechanism for the selective Mn-PL quenching between Mn-doped CdS/ZnS core–shell QDs and DAE molecules and its PL photoswitching behavior. Source: Yuan et al. [82]/with permission of Frontiers Media S.A.

this dual-color system was also introduced by coupling green-emissive QDs and a red-emissive organic dye (Alexa Fluor647 cadaverine) where only the emission of QDs was modulated along with the photochromic reactions of DAE [84].

Upon development of DAEs during the past decade, turn-on fluorescent DAEs have also been coupled with QDs for dual-color photoswitching systems. Such DAEs remove the need for a fluorescent dye such as LY because the DAE emission is mainly

observed in the closed-ring isomer. An example is the introduction of a turn-on fluorescent DAE into PMA and coating of ZnS/ZnSe QDs with the polymer. By using two different wavelengths for excitation, the resulting hybrid showed a very high modulation of emission ratio in each state. Such high change in emission ratio is possible because the respective emissions change in the reverse manner along with the photochromic reactions of DAE [85].

Photoswitchable dual-color QDs systems have also been demonstrated by modification of the QDs. For example in a study by Yuan et al. [82], Mn-oped CdS/ZnS QDs were used which show a narrow emission band centered at 413 nm originated from the bandgap of QDs and a broad emission band centered at 592 nm originating from Mn impurities. They used a DAE derivative with large spectral overlap between the absorption of the closed-ring isomer and the PL from Mn. The spectral overlap with the emission at 413 nm was small. Upon alternate irradiation with UV and visible light, the PL from Mn undergoes dramatic decrement as a result of FRET, while the PL from QDs shows relatively small change (Figure 28.6b). Such dual-emissive photoswitchable nanomaterials are good candidates for monitoring biological events as a function of time.

The second main approach to hybridization of QDs with photochromic materials is direct coordination of the photochromic compound onto the surface of QDs. In contrast with the coating approach, direct coordination offers higher control over the distance between the photochromic acceptor and the QDs donor. The earliest attempt on direct coordination of photochromic DAE onto QDs was achieved through a pyridinium group containing ligand [86]. Hybridization was attempted from the closed-ring isomer of DAE. After the coordination of the photochromic ligand, the QDs hybrids were in OFF state. Upon irradiation of visible light, the emission intensity from QDs increased to three times the initial OFF state, but it was much lower than the emission intensity of QDs alone. Based on cyclic voltammetry studies, the authors revealed that an electron transfer mechanism is responsible for quenching and slow degradation of QDs and DAEs in the hybrid system.

In a different study, the authors attached a tripod-like DAE having a carboxylic acid group in each leg (Figure 28.7a) [87]. Such carboxylic acid groups can coordinate to the surface of QDs through a chelate-type binding and having three anchoring groups per molecule ensures strong interaction with the QDs. The system showed reversible photoswitching upon alternate irradiation of UV and visible light. However, the system showed a loss in PL intensity during each photoswitching cycle. Based on time-resolved PL spectroscopy, the authors stated that an increase in non-radiative trap states upon coordination of DAE is responsible for the decrease in the PL intensity.

Very recently, a highly robust photoswitchable CdSe/ZnS QDs system with DAE ligands was reported (Figure 28.7b) [88]. The authors took advantage of thiol (SH)-containing DAE ligands having a methyl spacer between the -SH group and the DAE backbone to reduce the possibility of electron transfer between QDs and DAE. Their system showed complete and reversible ON/OFF switching of fluorescence from QDs upon irradiation of incident light. The system showed

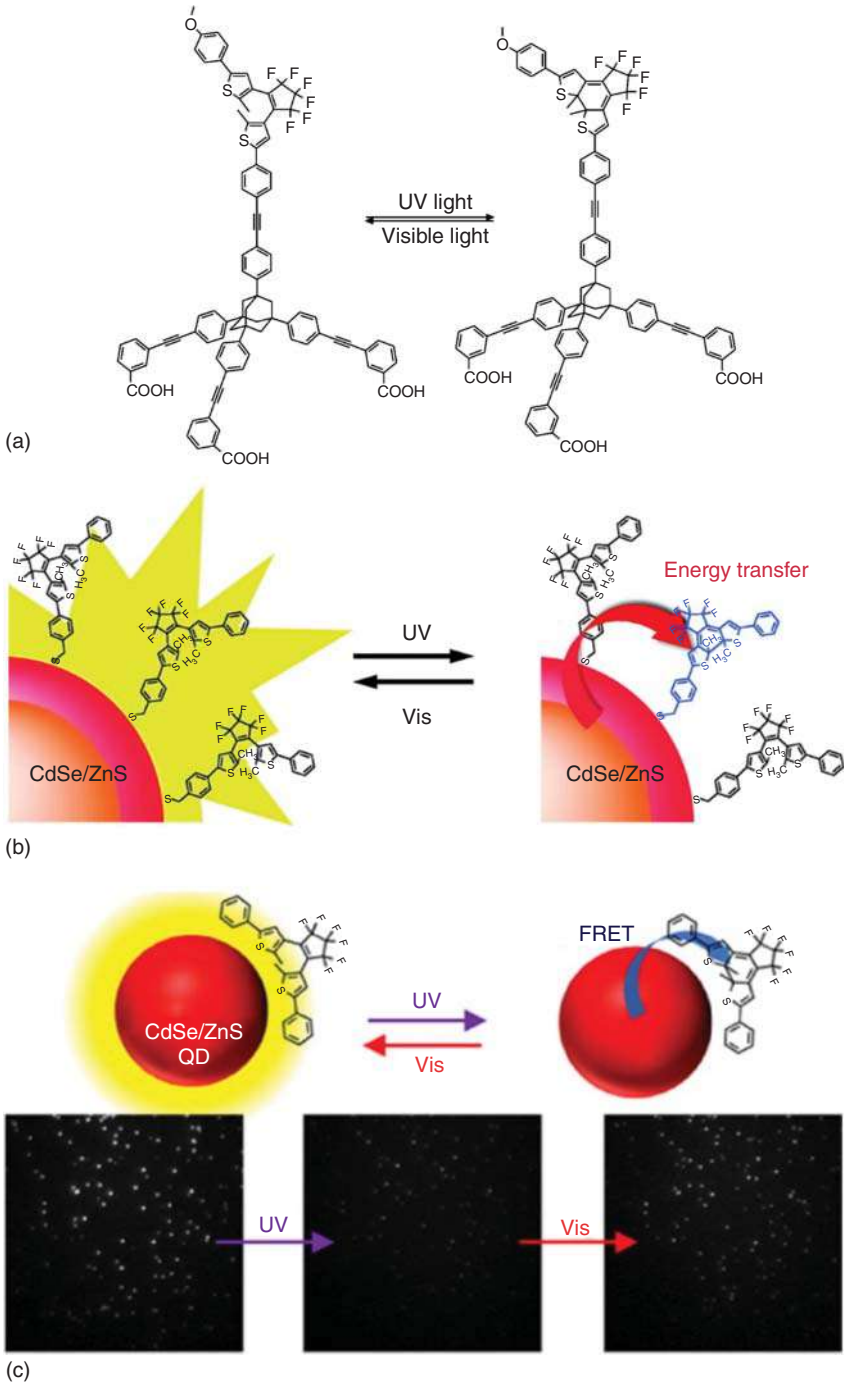


**Figure 28.7** (a) Molecular structure of the tripod-like DAE derivative. Source: Dworak et al. [87]/with permission of Royal Society of Chemistry. (b) Schematic illustration of photoluminescence ON/OFF switchable quantum dot coated with DAE ligands. Source: Seto et al. [88]/with permission of The Chemical Society of Japan. (c) PL photoswitching of single CdSe/ZnS QDs dispersed in a PMMA thin film with DAE upon alternate irradiation with UV and visible light. Source: Yano et al. [89]/with permission of American Chemical Society.

only 5% loss in intensity after 30 ON/OFF switching cycles. In a later work, the same group reported single-particle photoswitching of CdSe/ZnS QDs in a thin film (Figure 28.7c) [89]. QDs mixed with PMMA and a DAE derivative at different concentrations were coated on a glass substrate. The distance between QDs particles and DAE molecules can be adjusted by varying the concentration. This strategy gives control over uniformity of QDs and DAE molecules compared to direct coordination because in contrast to coordinated DAEs, there exists no equilibrium of coordination on the surface. QDs having photochromic ligands are known to show an increase in non-radiative trap states as a result of ligand loss which is especially easy to occur at low concentrations needed for single-particle microscopy. Hence, complication of the system is greatly reduced for studying FRET-based photoswitching. Photoswitching in single particles was demonstrated with FRET efficiency of up to 80%. However, the system underwent loss of luminescence and degradation in each photoswitching cycle.

Great contribution in studies on Cd- and Zn-based QDs has made them a matured class of research subject. Introduction of a new family of QDs in 2015 [90] directed the attention of many researchers toward them. All inorganic perovskite lead halide QDs ($CsPbX_3$; X = Cl, Br, I) are a replacement for organic–inorganic hybrid QDs ($MAPbX_3$; MA = methyl ammonium) and are synthesized through a conventional hot injection method. Replacement of MA with Cs greatly improved the stability of the perovskite QDs and offered much wider material processing techniques. Taking advantage of a metal such as Cs opened doors to a broader temperature range during the hot injection process. Perovskite QDs are one of the hottest topics of research because of their prominence for application in a wide range of fields, from solar cells to fluorescence probes. An interesting feature of this class of QDs is in easy adjustment of their emission color. They show change in bandgap (and therefore color of emission) not only based on quantum size effect but also by changing the composition of the halide ion. Composites of "Cl" show the widest bandgap (blue emission), "I" composites show the narrowest bandgap (red emission), and "Br" QDs have an intermediate bandgap (green emission). Near unity photoluminescence quantum yields and very narrow full width at half maximum (12–42 nm) of emission result in a very bright luminescence with pure color. Unfortunately, the biggest barrier standing in the way of their application is their low stability.

Since their introduction, various groups have attempted to add a luminescence switching capability to these QDs. Switching by addition of chemical reagents is the conventional way and only few reports exist on modulation of their luminescence by light. Photoswitching of luminescence has been achieved by three methods so far: (i) creation of a noble metal (Au or Ag) energy state upon irradiation with light [91], (ii) phase transition by irradiation-induced heat [92], and (iii) photoswitching by photochromic (SPs or DAEs) molecules. The first example based on photochromic materials was through integration of photochromic SPs into a thin film of $MAPbBr_3$ quantum dots and PMMA [93]. The authors took a simple approach of blade-coating a solution of PMMA, a carboxylic acid derivative of SP and QDs. Upon irradiation of UV light, the MC isomer of SP is generated which shows spectral overlap with the emission

of QDs. The authors demonstrated that the photoluminescence can be almost completely quenched at this state. However, typical of SP systems, thermal conversion of SP to its initial SP isomer resulted in rapid restoration of PL. The authors attempted to slow this restoration process down by addition of Zn ions so that the carboxylic acid group coordinates with the metal and therefore prevent thermal recovery of the SP isomer. This approach slowed the recovery of PL from 3 seconds to 20 minutes; however, a loss of PL occurred in each photoswitching cycle.

The next successful example on photoswitching of perovskite QDs was achieved by simply mixing DAE and $CsPbBr_3$ QDs in a toluene solution [94]. The system showed reversible switching of PL in all blue-, green-, and red-emissive QDs upon alternate irradiation of UV and visible light. Green- and red-emissive QDs showed 90% quenching of the emission light. The stability of the system, however, was low and part of luminescence was lost in each cycle. By coating the surface of QDs using silica, the stability was greatly improved while the quenching ratio remained the same although a relatively thick silica layer existed on the surface of QDs. These results showed highly efficient FRET-based energy transfer in systems containing DAE and perovskite QDs. This remarkable contrast between ON and OFF states indicates the prominence of the system for application in fluorescence probes and optical memories (Figure 28.8a). Soon after, Mokhtar et al. [95] reported successful synthesis and photoswitching of luminescence in hybrids of green-emitting QDs ($CsPbBr_3$) and a derivative of DAE with the same backbone as the previous study. Hybridization was achieved by addition a triethoxysilane terminal to the DAE compound so that DAE can be embedded into the silica layer when coating the surface with silica through conventional methods. DAE successfully underwent silane-coupling reaction, and the final hybrid was characterized as a silica-coated QDs system with DAE molecules in the coat layer. The system showed 90% quenching of PL both in dispersed state and in solid state with high stability during multiple cycles (Figure 28.8b).

### 28.4.2 Photochromic Nanoparticles Based on Carbon Dots (CDs) Emitters

During the past decade, carbon-based nanomaterials or CDs have also been in the spotlight of many researches. The reason that makes these materials interesting compared to semiconductor QDs is their nontoxic composition (being made mainly of C, H, O, and N) and bio-compatibility. These materials can be synthesized by top-down or bottom-up synthetic methods and exhibit different optical properties depending on the starting material and synthetic methods [96]. However, in contrast with QDs, their emission bands are broad, similar to organic fluorescent dyes. In addition, the mechanism of their photoluminescence is not well understood. Further improvement of CDs with narrow emission bands and high PL quantum yields in the future will make them a major candidate for photoswitchable materials. Even though only few examples of CDs with narrow emission exists [97, 98], it has not stopped researchers from developing photoswitchable systems based on CDs.

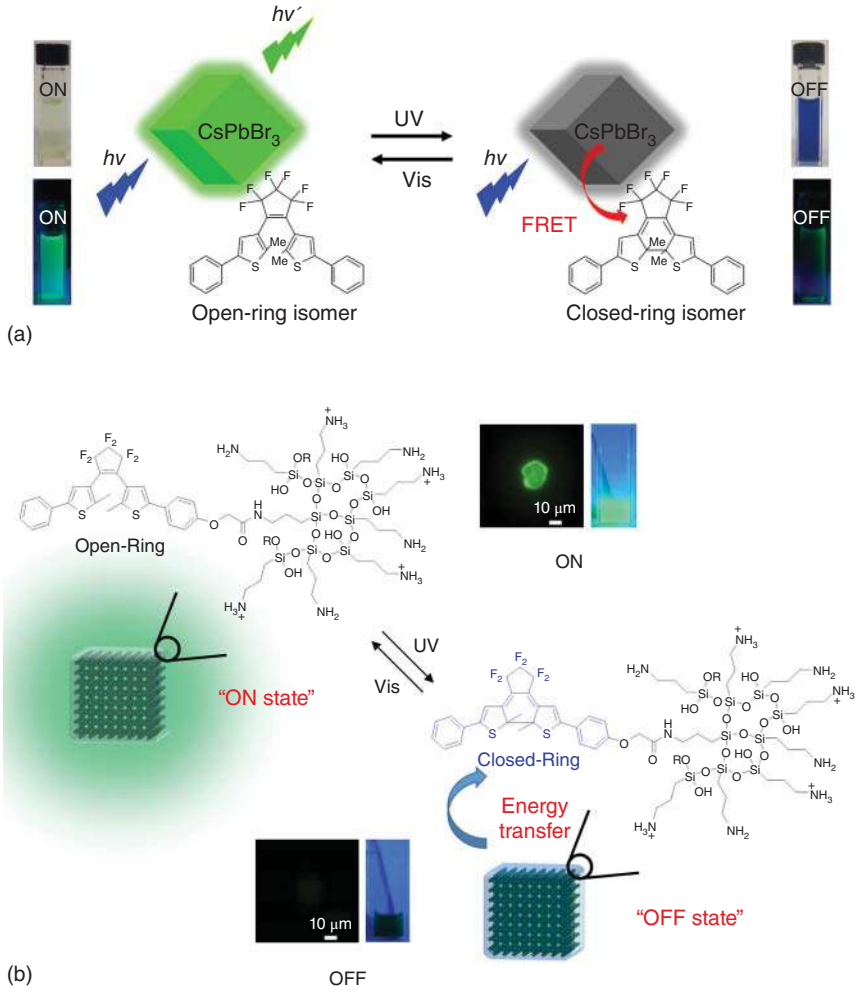


**Figure 28.8** Schematic illustration of the PL photoswitching in (a) a mixture of $CsPbBr_3$ nanocrystals and DAE molecules Source: Akaishi et al. [94]/with permission of Royal Society of Chemistry. (b) Colloidal $CsPbBr_3$ nanocrystals hybridized with a DAE photoswitch. Source: Mokhtar et al. [95]/with permission of American Chemical Society.

The surface hydroxyl, amine, or carboxylic acid groups of CDs and their relatively high stability have made the process of hybridization of these materials with functional molecules more straightforward. The first report on photoswitching of PL in CDs was fabricated with a SP on the surface of these nanomaterials [99]. The authors used a conventional method for modification of CDs surface by introducing ethylenediamine on the surface of CDs to create terminal amines. Consecutively, a carboxylic acid derivative of a photochromic SP was introduced by amide bonds (Figure 28.9a). The SP molecule is stable in its spiro-isomer which upon irradiation of UV, photoisomerizes to a fluorescent MC form. The absorption of the spiro-isomer of SP has no overlap with the emission of CDs. On the contrary, upon irradiation of

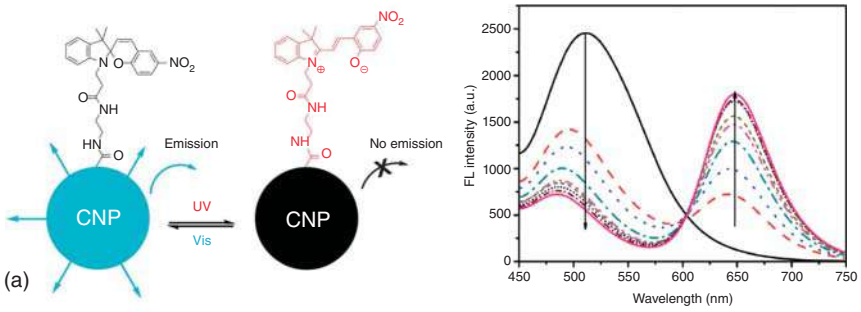


**Figure 28.9** (a) Fluorescence photoswitching of the SP-functionalized CNPs. Source: Liao et al. [99]/with permission of Royal Society of Chemistry and (b) schematic illustration of the in situ multicolor luminescence photoswitching of a supramolecular assembly. Source: Wu et al. [100]/with permission of American Chemical Society.

the hybrids with UV light, the population of MC isomers increases and an absorption band which overlaps with the emission of CDs emerges. Upon excitation of the hybrids in this state, a FRET process from the CDs to the MC isomer of SPs causes the quenching of CDs emission and appearance of a red emission from MC. The emission of CDs was quenched to nearly 80% and the process was reversible for at least 20 cycles upon consecutive irradiation with UV and visible light. Later on, Liao et al. [101] took a different approach to synthesize SP-functionalized CDs. They grafted the surface of CDs through copolymerization with styrene and SP monomers. The resulting hybrids showed a similar photoswitching behavior and could be observed in solution, film, and electrospun nanofibers. In a different study by Jin et al. [102], SP molecules were introduced to a cationic cellulose backbone and were then coated on the surface of CDs through electrostatic interactions. The hybrids which were synthesized through this method were applicable to photoswitchable papers and anti-counterfeiting.

SPs are very often applied to photoswitching systems because of their ease of synthesis, however, suffer from thermal reversibility and low fatigue resistance. DAEs are therefore one of the best candidates because of their excellent thermal stability in both isomers and high-fatigue resistance. Wu et al. [100] reported a supramolecular assembly of a DAE derivative and CDs in aqueous solution that show dual-color switching with white emission at the proper condition (Figure 28.9b). They demonstrated that by using a styrylpyridinium-modified DAE together with cucurbit[8]uril, a supramolecular nanofiber assembly is constructed. This assembly showed enhanced fluorescence properties compared to solutions of the DAE derivative alone. Since this assembly was cationic in nature, upon titration of a solution of the DAE assembly to a solution of CDs, nanoparticles of up to 700 nm in size were produced. These nanoparticles showed dual-colored emission with bands centered at 582 nm (yellow) and 458 nm (blue). Upon irradiation with UV light, the yellow emission of the DAE fluorophore was selectively quenched and the process was reversible where upon alternate irradiation with visible light (>600 nm), the yellow emission was recovered. The white light emission from the nanoparticles could be achieved by either controlling the ratio of the DAE assembly to CDs or by photoswitching.

### 28.4.3 Photochromic Nanoparticles Based on Upconversion Nanoparticles (UCNPs)

Inorganic materials also play an important role in the field of photon upconversion. Upconversion nanoparticles (UCNPs) have the potential for application in a variety of fields such as solar cells, drug delivery systems, or fluorescence switching systems [103]. Low-energy photons in the near-infrared (NIR) region can be converted to higher energy photons in the UV or visible light region. A typical upconversion system uses lanthanide-doped materials [103] or a triplet-triplet annihilation process [104]. Through development of colloid-based inorganic nanoparticle synthesis methods, lanthanide-doped inorganic nanoparticles have gained interest in luminescence photoswitching systems. Construction of state-of-the-art core/multishell structures allows various optical responses from the same type of nanoparticle. UCNPs are especially of interest in bio-applications because of high tissue permeability and low toxicity to cells or low auto-fluorescence from cells.

SPs and azobenzenes are of special interest in drug delivery systems where on-demand drug release is needed upon irradiation of NIR light. Photochromic SPs and azobenzenes undergo a relatively big structural change upon photoreactions where the molecular volume or charge distribution within the molecule can be greatly altered. Such properties enable destruction of drug-containing nanocarriers at the location of interest and therefore selective delivery of the drug to the targeted cells becomes possible. A recent example is a study by Rojas-Gutierrez et al. [105] where they encapsulated $Yb^{3+}$ and $Tm^{3+}$ doped $LiYF_4$ UCNPs with an azobenzene-containing lipid bilayer together with a model drug (Nile red, a fluorescent dye). Upon irradiation with 980 nm, UV light emission from the nanoparticles causes *cis* to *trans* photoisomerization of the azobenzene moiety.

The resulting steric hindrance causes Nile red molecules to be released at the location of interest. They reached 50% drug release after one hours of irradiation with NIR. A very interesting study by Zhao et al. [106] demonstrated selective drug release near the tumor cells in mice using UCNPs. Nanoparticles of 100–200 nm in size are known to be good nanocarriers for drug delivery to tumors because of long circulation and high tumor accumulation. However, such big nanoparticles are not easily discarded by living organisms after use. Hence, it is important to have 100–200 nm photoresponsive carriers that can be decomposed to smaller compartments after drug release. To this aim, the authors used a template of $SiO_2$ nanoparticles and coated them with consecutive cationic polymers and anionic azobenzene-containing polymers. Anionic UCNPs were sandwiched between two cationic polymer layers. After etching of the silica template, a photoresponsive nanocapsule remains for the drug delivery purpose. The nanoparticles used in the study were core/multishell upconverting-downconverting nanostructures (U/DCNPs) that emit upconverted UV emission (excitation wavelength: 980 nm) and downconverted 1060-nm emission (excitation wavelength: 808 nm). Screening the emission at 1060 nm allows the observation of the location of the carriers, while excitation with 980 nm induces drug release. Upon irradiation of the tumor location with 980-nm light, drug-loaded capsules are destructed to 20-nm U/DCNPs and the coating polymers while releasing the drug to the tumor (Figure 28.10A).

DAEs can also be indirectly used in drug delivery by controlling the release of singlet oxygen. Mi et al. [107] reported a system of $Yb^{3+}$ and $Er^{3+}$ doped UCNPs coated with mesoporous silica. A photosensitizer (PS) that releases singlet oxygen upon excitation was embedded within the pores of the silica coat layer together with a DAE derivative having an absorption tail (in the closed-ring isomer) within the NIR region. Upon excitation of UNCPs (excitation wavelength: 980 nm), green upconverted emission from the particles excites the PS and causes the release of cytotoxic singlet oxygen. However, when DAE is in its closed-ring isomer, energy transfer from UCNPs to DAE prevents the excitation of PS and as a result, production of singlet oxygen does not occur (Figure 28.10B). Therefore, such modified UCNPs can be used in drug delivery systems starting with the closed-ring isomer to induce the release of toxic singlet oxygen upon irradiation with 808-nm NIR light (photocycloreversion reaction).

Although combination of DAE with UCNPs can be used in drug delivery, the main application remains in bio-imaging and switching systems for memories. There have been many reports over the years in the development of DAE-UCNPs hybrids. Strategies similar to those used to make hybrids of DAE and QDs (surface coating with polymers or direct coordination) are often employed. Boyer et al. [109] reported a core/multishell UCNPs system with the ability of undergoing both the photocyclization and photocycloreversion reactions of DAE upon irradiation with stimuli light of the same wavelength (980 nm) but different intensities. Appropriate separation of core and shells consisting of different lanthanides ($Tm^{3+}$ and $Yb^{3+}$ for UV light emission, $Er^{3+}$ and $Yb^{3+}$ for green light emission) causes this multi-response in UCNPs because of the difference in the number of photons needed for different emissions. Development of such systems contributes

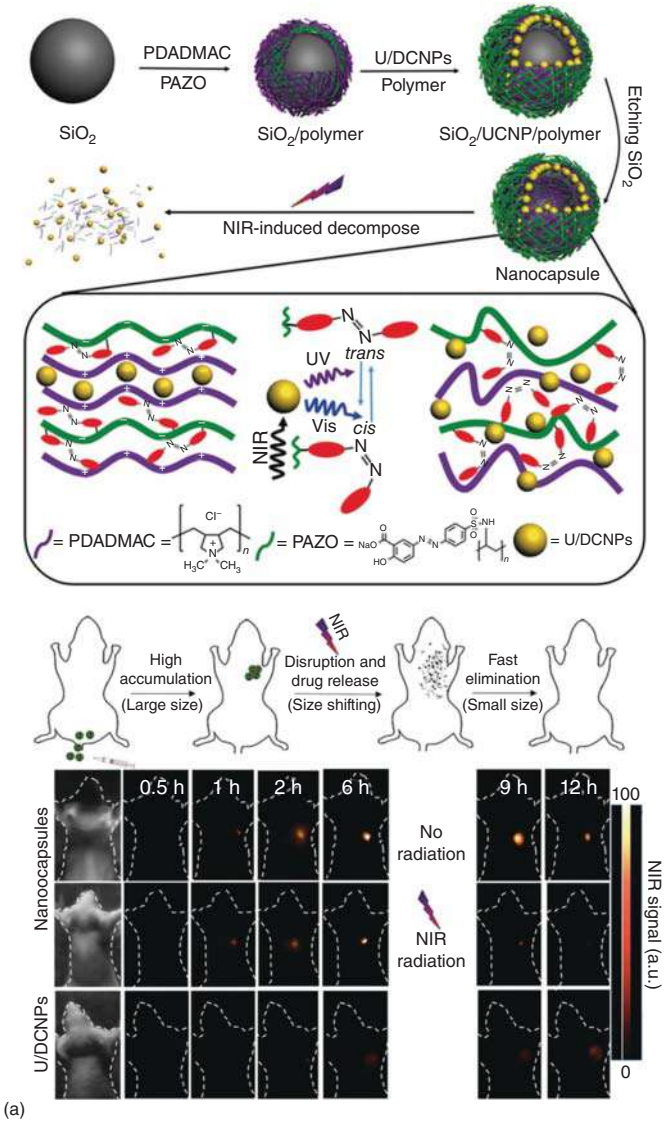


**Figure 28.10** Schematic illustrations of (a) the fabrication of the up/down conversion nanoparticle (U/DCNP) functionalized hollow polymer nanocapsules and its decomposing process induced by the near-infrared (NIR) light irradiation in the in vivo study. Source: Zhao et al. [106]/with permission of Wiley-VCH. (b) The 980-nm NIR light photosensitized UCNP-DAE nano-construct and the photoswitching of $^1O_2$ generation capability upon 808-nm NIR light irradiation. Source: Mi et al. [107]/with permission of Royal Society of Chemistry. (c) The self-assembled nanosystem containing an amphiphilic polymer wrapped around the lanthanide-doped UCNPs with encapsulated DAE chromophores and fluorescence microscopy images of a representative *Caenorhabditis elegans* under several excitation conditions. Source: Wu et al. [108]/with permission of Royal Society of Chemistry.

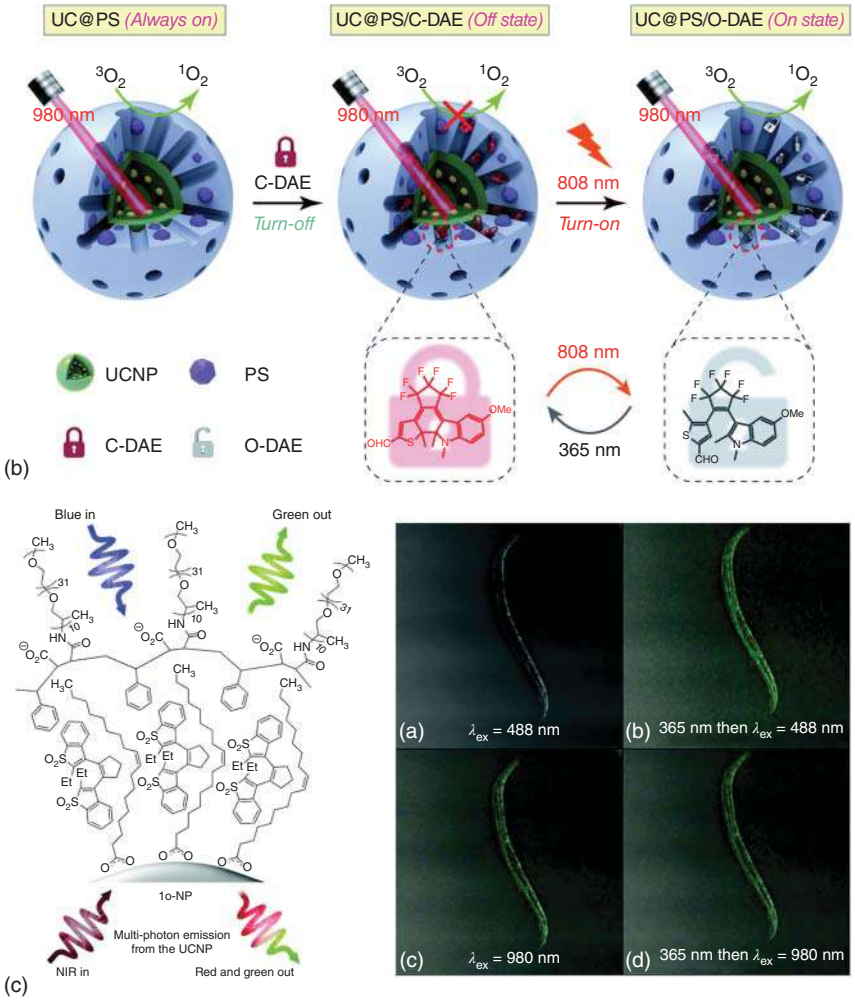


**Figure 28.10** (*Continued*)

to simplification of the instrument used for bio-imaging applications. Later on, hybrids of UCNPs and a turn-on fluorescence DAE were used to demonstrate two-color fluorescence imaging in *Caenorhabditis elegans* nematodes [108]. $Er^{3+}$ and $Yb^{3+}$ doped $NaYF_4$ nanoparticles show distinctive upconverted emissions at 504–568 nm and 627–684 nm upon excitation with NIR light (980 nm). On the other hand, the DAE molecules which were sandwiched between the surface ligands of the UCNPs and a polymer do not show any emission under irradiation of NIR light (DAE molecules have no absorption in this region). The DAE counterpart shows fluorescence only in the closed-ring isomer under excitation with 488-nm light. Therefore, by monitoring emissions caused by photon upconversion and selective induction of fluorescence from the closed-ring isomer of DAE, a time component can be added to the observations of the living organisms (Figure 28.10C).

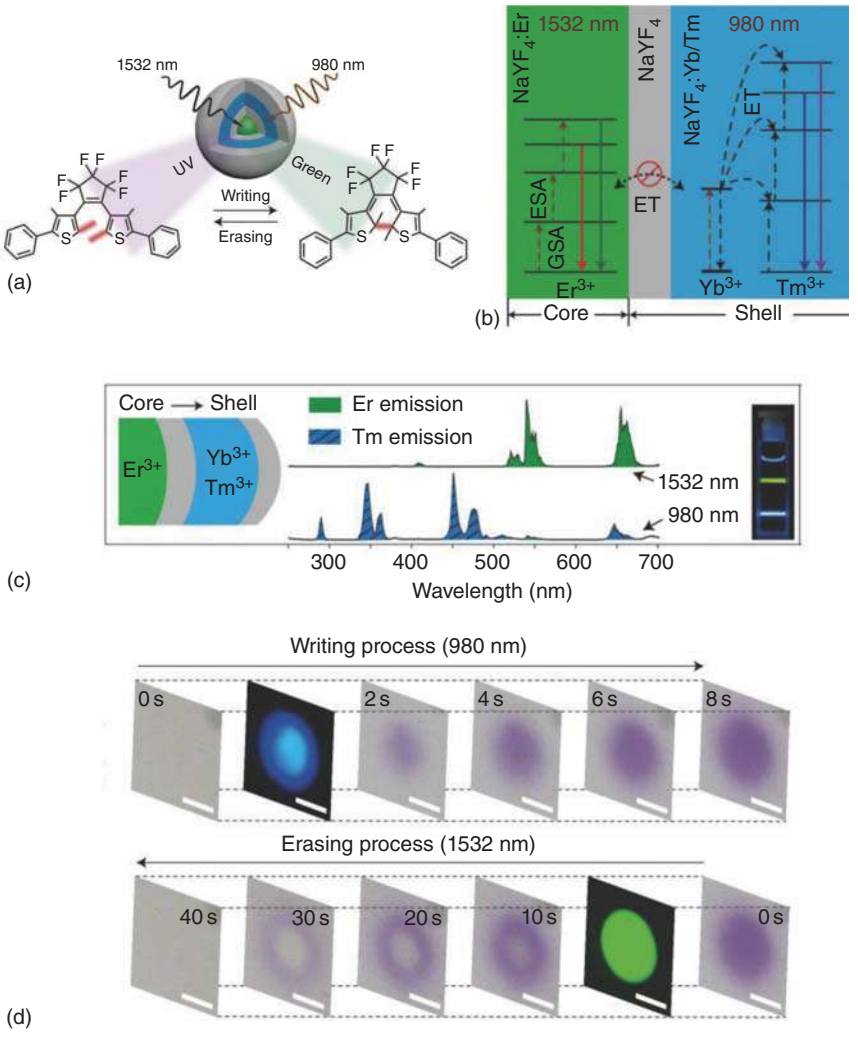


**Figure 28.11** (a) Schematic illustration of rewritable optical memory using core–shell upconversion nanoparticles combined with diarylethene molecules. The ultraviolet emission of the nanoparticles upon 980-nm excitation can be used to activate the cyclization reaction of DAE, while the green emission from the nanoparticles under 1532-nm irradiation can lead to the reversal ring-closure reaction of the DAE molecule. (b) Proposed energy transfer pathways between the lanthanide dopants under 980- and 1532-nm excitation, respectively. (c) Upconversion luminescence profiles of $NaYF_4$:Er@$NaYF_4$@$NaYF_4$:Yb/Tm@$NaYF_4$, $NaYF_4$:Yb/Er/Tm@$NaYF_4$, and $NaYF_4$:Er@$NaYF_4$:Yb/Tm@$NaYF_4$ nanoparticles upon excitation at 980 and 1532 nm, respectively, and (d) images showing time-dependent color changes (for data writing and erasing process, respectively) of a PMMA film containing a hybrid of UCNP-DAE upon excitation at 980 and 1532 nm, respectively. Scale bars: 50 μm. Source: Zheng et al. [110]/with permission of Wiley-VCH.

For memory applications, fluorescent ON/OFF photoswitching systems that respond in only one direction (ON→OFF or OFF→ON) to NIR incident light are well known. However, photoswitchable UCNPs that respond in both ways are more difficult to construct. For example, Zheng et al. [110] demonstrated core/multishell $NaYF_4$ UCNPs with $Er^{3+}$ doped to the core and $Yb^{3+}$ and $Tm^{3+}$ doped in a shell layer. A neutral separating $NaYF_4$ existed between the doped layers and at the outermost layer of the UCNPs. Upon excitation with 980-nm laser, $Er^{3+}$ doped core layer emits visible upconverted light at around 545 nm. In contrast, excitation with 1532-nm laser induces emission of UV and blue light from the $Yb^{3+}$ and $Tm^{3+}$ doped shell. These NIR excitation lasers were successfully used to induce selectively the photocyclization and photocycloreversion reactions of a DAE derivative (Figure 28.11).

## 28.5 Nanoassemblies Involving Photochromic Molecules and Metallic Nanoparticles

### 28.5.1 Metallic Nanoparticles Functionalized by Photochromic Molecules

A large number of hybrid nanosystems based on metallic nanoparticles (mostly gold or silver) coupled to photochromic materials, with the aim of favoring the interactions between the surface plasmon resonance (SPR) of the metallic nanoparticles and the photoresponsive molecules, have been designed over the past 15 years [5]. Gold nanoparticles (Au-NPs) or silver nanoparticles (Ag-NPs) functionalized with DAE molecules bearing a thiol functional group were first described, showing unaltered [111, 112] or partially deactivated photochromic reactivities due to the presence of the metallic NPs [113], depending on the linker length and nature. More sophisticated functionalization of the Au-NPs with DAE polymers were then reported [114], demonstrating the complex interactions between the two components. The photochromic reaction can influence the SPR band through the change of refractive index under illumination [115], but the SPR has also a strong effect on the photochromic reactivity for the molecules located at a short distance from the interface [116]. Opposite design of hybrid systems were reported as well, such as large azobenzene-based molecular nanoparticles decorated by a dense shell of smaller Au-NPs [117]. Some attempts to obtain metallic nanoparticles functionalized with photochromic–fluorescent ligands showed the difficulty of this task: the excited state of the photochromic and/or fluorescent molecules are easily quenched by the metallic center [118]. In this regard, promising results were obtained with silica-coated gold nanorods (Au-NRs) functionalized with a photochromic–fluorescent DAE, providing an accurate control of the distance between the metallic core and the photoactive organic counterparts, and evidence of plasmon–photochromism coupling on one side and plasmon–fluorescence interaction on the other side [119]. Au-NRs capped by DAE-based polymers were also described and studied, showing a fluorescence quenching but on the other hand, a significant enhancement of the cycloreversion reaction of the DAE by the Au-NRs [120].

## 28.5.2 Metallic Nanoassemblies Modulated by Photochromic Molecules

### 28.5.2.1 Assembly–Disassembly of Metallic Nanoparticles by Photochromic Molecules

Diverse approaches have been developed recently to assemble metallic nanoparticles using photochromic molecules in order to trigger the self-assembly morphology or the inter-particle communication, either by decorating the nanoparticles with photochromic monolayers or by using the photochromic molecules in the surrounding medium to change the pH [6, 7]. The applicability of such photoswitchable nanoassemblies is extremely promising in many perspectives, with the development of new concepts related to reversible data storage, drug delivery, or nanoelectronics.

The simplest way to induce nanoassembly of metallic NPs by light is to functionalize their surface with photochromic ligands. Azobenzene molecules terminated with thiol groups mixed with dodecylamine were designed by Klajn et al. [121] to coat the surface of Au-NPs and Ag-NPs (5–6 nm diameter). The principle of the method is based on the nonpolar nature of the *E* (*trans*) isomer of the azobenzene derivatives, which is converted to the polar *Z* (*cis*) isomer under UV irradiation, as illustrated in Figure 28.12a [123]. Therefore, the NPs decorated with (*E*) azobenzene ligands are initially stable and well soluble in hydrophobic solvents, giving a deep-red (resp. yellow) color to the suspension of Au-NPs (resp. Ag-NPs), due to the SPR of isolated metallic nanoparticles. Upon UV light exposure, the metallic nanoparticles lose their colloidal stability and spontaneously assemble into large ordered suprastructures ("supraspheres") [124] with diameters in the 50–300 nm range, made of hundreds to millions of NPs. The aggregation process of the metallic nanoparticles is associated with a red-shift and broadening of the SPR band, leading to a significant color change of the suspension. As expected, the spontaneous $E \rightarrow Z$ thermal back-reaction of the azobenzene makes the assembly metastable, leading to a gradual disassembly process in absence of UV light. Hundreds of assembly–disassembly cycles can be performed without noticeable change of properties. The authors showed that the metallic NPs could be dispersed in a thin film of syndiotactic poly(methylmethacrylate) (sPMMA) organogel. The films doped with nanoparticle "inks" were brightly colored even at low concentration and could serve as rewritable materials with self-erasable properties: when exposed to UV light, the Au-NPs inks turned gradually from red to pale blue, whereas the Ag-NPs evolved from yellow to violet [121]. Masks can be applied to create high-contrast patterns (Figure 28.12a), whose lifetime before fading can be adjusted through the fractional coverage of azobenzene ligands on the surface of the metallic NPs: higher concentration of photochromic moieties makes stronger inter-particle interactions, yielding more persistent images. In another example from the same group, a comparable approach was followed using thiolated SP molecule instead of the azobenzene as a ligand at the surface of Au-NPs and Ag-NPs [125]. Similarly, the NPs efficiently assemble upon UV exposure and disassemble spontaneously in absence of light, up to 30 cycles before photodegradation occurs.

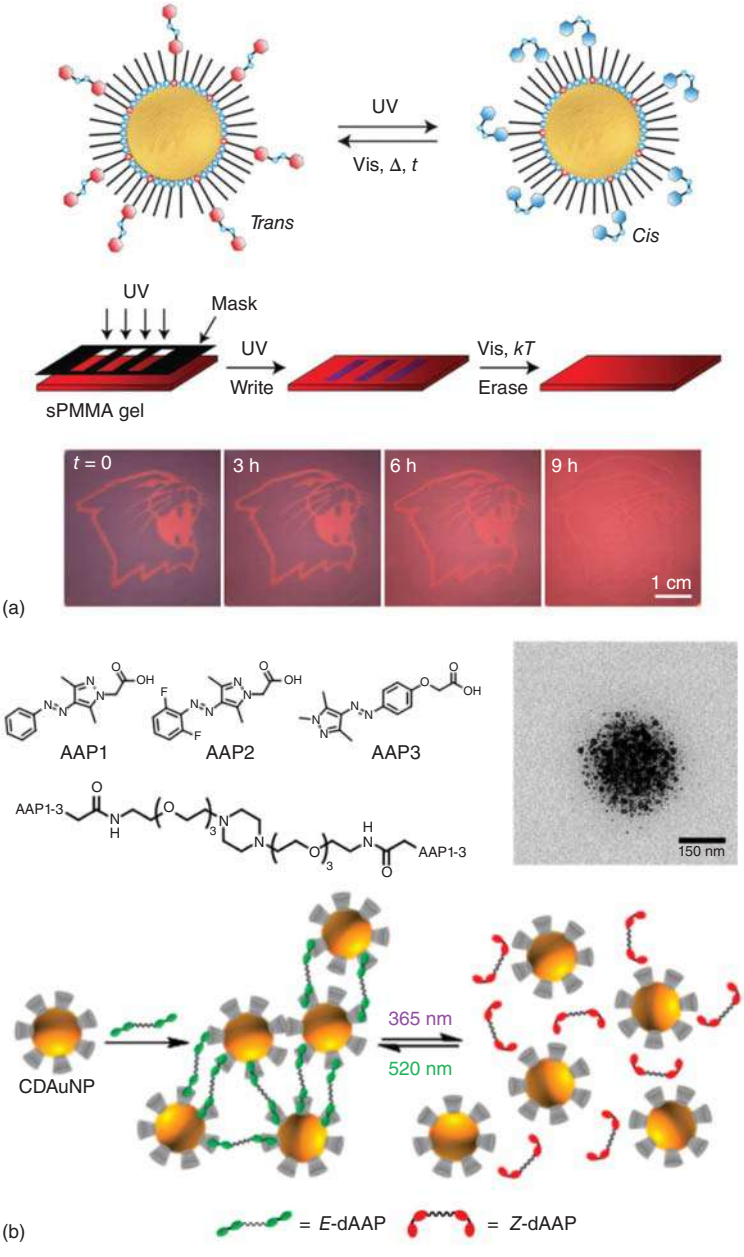


**Figure 28.12** (a) Schematic representation of the $E \rightarrow Z$ photochromic reaction of azobenzene-functionalized Au-NPs, inducing a dramatic change of polarity at their surface and triggering the nanoassembly (top). Once incorporated in an organogel thin film, a rewritable/self-erasable material was obtained (bottom). Source: Klajn et al. [121]/with permission of Wiley-VCH. (b) Bis-arylazopyrazole (bis-AAP) derivatives used to interconnect β-cyclodextrin-functionalized Au-NPs via light-responsive host–guest interactions, allowing photoswitchable assembly–disassembly of the hybrid nanosystem under visible and UV light, respectively. Source: Stricker et al. [122]/with permission of American Chemical Society.

Alternately, another group showed that the assembly could be induced by a photoswitchable electrostatic interaction between cationic Au-NPs and hydrophobic SP molecules, initially non-covalently attached to the NPs [126]. More sophisticated light-responsive metallic nanoassemblies were further developed, functionalizing several populations of Au-NPs by ligands holding different azobenzene derivatives, making the system responsive to multiple irradiation wavelengths with orthogonal self-assembly processes [127].

An alternative strategy to the covalent functionalization of photochromic molecules involves host–guest inclusion complexes with cyclodextrins on the nanoparticle surface. In this perspective, Stricker et al. [122] proposed to decorate metallic nanoparticles with heptathiolated β-cyclodextrins (β-CD). Since arylazapyrazole (AAP) molecules are a family of photochromic derivatives with attractive properties compared to azobenzenes (distinct absorption band in their two forms, higher thermal stability of the *Z* isomer, quantitative conversion under illumination) and particularly suitable to form inclusion complexes with β-CD, the authors designed a series of bis-AAP divalent linkers to mediate and control attractive interactions between the Au-NPs. When the photoswitchable linker is introduced in the solution, the metallic NPs spontaneously assemble into suprastructures (∼200-nm diameter), which disassemble upon UV light and reassemble under 520-nm irradiation, for several cycles, as represented in Figure 28.12b. The host–guest interaction and the assembly characteristics are strongly dependent on the AAP molecular structure (AAP1 > AAP2, AAP3). The same AAP-β-CD interaction has been applied to gold nanorods to control reversibly their end-to-end assembly [128]. In this case, the heptathiolated β-CD was preferentially attached at the tips of the Au-NRs, where the surfactant (cetyltrimethylammonium bromide, CTAB) has weaker interaction with the gold surface. After β-CD functionalization and proper CTAB removal, the nanosystem could assemble and disassemble in the presence of bis-AAP linker, under UV/green light.

Photoacids or photobases can conveniently and reversibly change the solution pH in a transient way, upon exposure to light. They actually represent a straightforward strategy to induce the assembly or disassembly of a large number of metallic NPs dispersed in colloidal suspension, which does not require the particles to be functionalized with light-responsive ligands. In this context, SP-derived photoacids are particularly interesting, for their unique combination of photochromic and acidochromic properties. The light-induced proton capture and release associated with the spiropyran (SP) ↔ merocyanine ($MCH^+$) interconversion could be coupled to deprotonation and protonation of the ligands which are present at the surface of the NPs. A beautiful demonstration of this principle has been provided by Kundu et al. with Au-NPs functionalized with monolayers of 11-mercaptoundecanoic acid (MUA), forming insoluble nanoassemblies in polar, nonaqueous solvents [129]. The authors introduced a $MCH^+$ molecule in the solution which, upon exposure to blue light, was converted to the SP form to a sufficient extent. It allows the protonation of the MUA ligands and solubilizes the Au-NPs, changing the suspension color to deep-red corresponding to the free Au-NPs. When the light is switched off, the photochromic molecules return to their $MCH^+$ form, and the system reverts to its

initial state (Figure 28.13a). More than 100 cycles of disassembly–assembly could be performed in a virtually fatigue-free fashion, owing to the nonaggressive visible light which was employed to trigger the system. Interestingly, this photon-induced dynamic nanoassembly process could be employed to trap and release reversibly some specific third-party molecular targets which, for instance, could display a strong affinity to aggregated NPs. It is worth noting that the opposite phenomenon could occur when the same MUA-capped Au-NPs were placed in water, in presence of a water-soluble version of the photoacid [131]. In this case, the Au-NPs were initially well dispersed in water, and their nanoassembly was initiated upon visible irradiation. However, in this latter situation, the number of assembly–disassembly cycles was limited to ~20.

Another approach was developed by Liu et al. with Au-NPs functionalized with SP-terminated thiol ligands, water-soluble in both SP and MC forms [132]. When the MC isomer of the ligand is mixed with copper ions, it forms a 2 : 1 complex, involving two MC ligands for one $Cu^{2+}$ cation. Consequently, when the functionalized Au-NPs are either UV-illuminated or introduced in a solution of copper ions, the suspension stays unaffected with a red color typical of well-dispersed Au-NPs. But when both light trigger (UV) and chemical stimulus (cations) were applied simultaneously, the self-assembly was initiated, even at very low concentrations of $Cu^{2+}$. This phenomenon can be used as an ultra-sensitive detection technique: the simple monitoring of the color of the suspension from red to purple is sufficient to identify the presence of low levels of metallic cations in water.

Light-triggering assembly of amphiphilic Au-NPs was further achieved by Zhang et al. by means of co-functionalization of the surface by two different ligands: a hydrophylic poly(ethylene glycol) (PEG) and a hydrophobic photoswitchable polymethacrylate (PSPMA) containing a SP unit [130]. The resulting Au-NPs were soluble in polar solvents. Under UV illumination, the SP was converted to the MC form, with planar-conjugated zwitterionic structure, promoting the aggregation between MC moieties from adjacent Au-NPs, through molecular π–π stacking and electrostatic interactions. This led to the formation of self-assembled Au-NPs oligomers, made of a small number of individual Au-NPs (2–5 on average), as shown in Figure 28.13b. Interestingly, this reversible nanoassembly–disassembly has been used to tune the surface-enhanced Raman scattering (SERS) effects, which usually occur when "hot spots" appear in hybrid systems allowing contacts between metallic nanoparticles. A Raman probe molecule (4-mercaptopyridine) was used to quantify the enhancement efficiency in different assembly–disassembly stages, which turned to be significantly higher in aggregated Au-NPs compared to non-aggregated ones, demonstrating the formation of "hot spots" within the oligomers produced by UV light [130].

Such light-controlled metallic nanoassemblies can be exploited to build up attractive "photoresponsive nanoreactors," with the objective to manipulate the course of a chemical reaction. As illustrated in Figure 28.13d, Au-NPs functionalized with azobenzene ligands were employed to modify the chemical behavior of molecules entrapped in the confined inter-space between Au-NPs of the nanoassembly [133]. A variety of polar molecules can be trapped from the surrounding bulk solution into

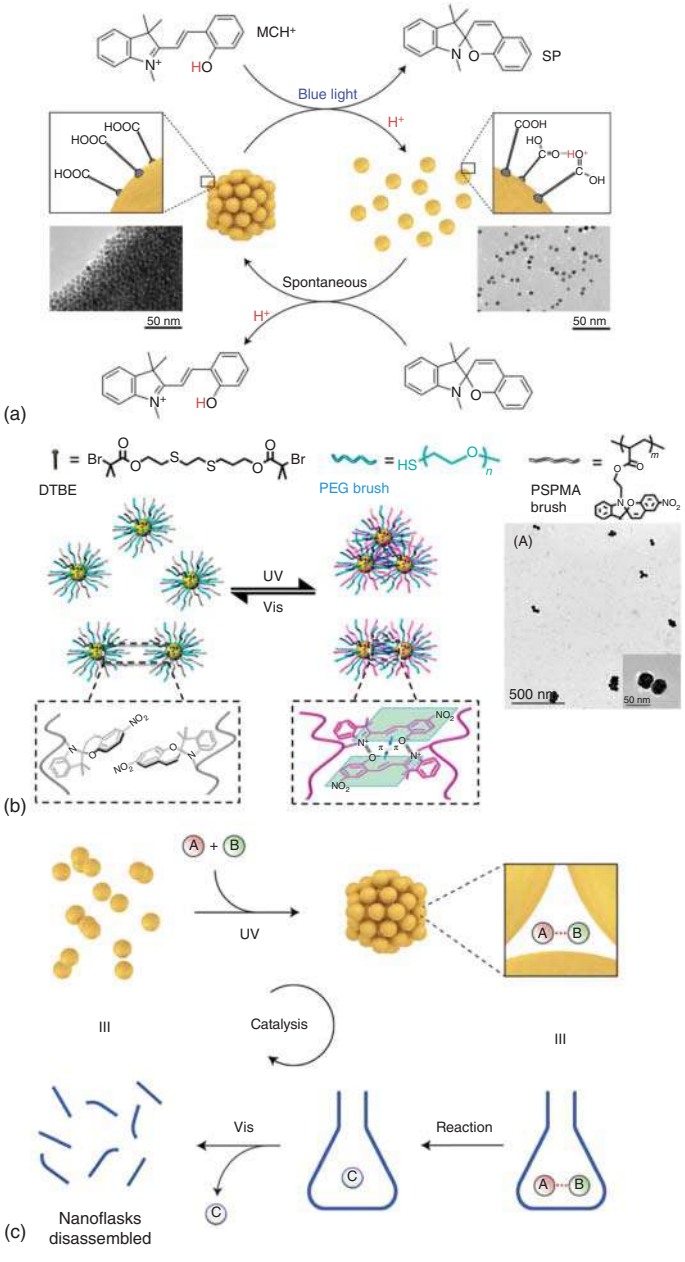


**Figure 28.13** Schematic representations of photoswitchable nanoassemblies involving spiropyran-merocyanine photochromic molecules and Au-NPs. (a) The use of a protonated merocyanine ($MCH^+$) induces a reversible disassembly of Au-NPs coated with 11-mercaptoundecanoic acid in a polar solvent. Source: Kundu et al. [129]/with permission of Springer Nature. (b) Amphiphilic Au-NPs bearing spiropyran ligands aggregate into oligomers via merocyanine interactions and create "hot spots" for surface-enhanced Raman scattering (SERS). Source: Zhang et al. [130]/with permission of American Chemical Society. (c) "Photoresponsive nanoreactors" in the confined space between Au-NPs in nanoassemblies allow specific chemical reactions to occur. Source: Zhao et al. [6]/with permission of Royal Society of Chemistry.

the self-assembled nano-pores and then undergo chemical reactions with increased rates or modified stereoselectivities compared to the standard conditions. A typical example was obtained with the dimerization of 9-(hydroxymethyl)-anthracene, which yields a majority of *syn* products in the "nanoreactors," to be compared to the exclusive *anti* isomer produced in bulk solution, demonstrating the specific substrate preorganization in the confined space of the nanoassembly. The light-responsive dynamic nature of these "nanoreactors" paves the way to a fully controllable reaction: after trapping the molecules of interest, the reaction proceeds and the products can be released in solution upon visible light illumination, and the catalytic cycle can proceed again applying UV light to the system (Figure 28.13c). This sequence can be repeated multiple times to transform larger amounts of material.

#### 28.5.2.2 Conductance Photoswitching of Photochromic-Metallic Nano-Networks

Molecular nanoelectronics is a rapidly expanding field of research. The control of the flow of electrical signals at the nanoscale with activatable molecules represents a challenge for photochemists and photophysicists. Photochromic molecules can play a great role in this domain, taking advantage of their large change of electronic conjugation between their isomeric forms, translating into variable conductance properties between electrodes. In this regard, Matsuda et al. have demonstrated the first convincing example of reversible conductance photoswitching with a network composed of gold nanoparticles covered with DAE derivatives, located in the gap between gold electrodes, as schematized in Figure 28.14a [135]. For this purpose, diarylethene dithiophenols were synthesized and reacted with previously prepared Au-NPs with 3–4 nm diameter to produce the photochromic-metallic network. The photochromic properties of grafted DAE was successfully preserved, with a bathochromic shift of the absorption spectrum after grafting, revealing the perturbation of its electronic structure by the Au-NPs. The extended nanoparticles network was deposited in the interdigitated nanogapped (5 μm) gold electrode, and conductance measurements could be performed under light illumination (Figure 28.14b). Upon irradiation with UV (290–400 nm), the conductance increased significantly, while the conductance decreased back to its initial level upon irradiation in the visible (>560 nm). The maximum ratio of the conductance between the high and low conductance states was found to reach 25 for the DAE molecule with the highest quantum yields of both cyclization and cycloreversion reactions, allowing complete reversibility of the system (Figure 28.14c) [134]. The switching behavior of the DAE/Au-NPs network is attributed to the change of the π-conjugation length of the molecule. Furthermore, a series of DAE with thiol groups located at different positions has been investigated, leading to opposite direction of conductance photoswitching [136]. As a conclusion, the topology of π-conjugation of the DAE between Au-NPs that connects the electrodes represents one of the most decisive factors in the photoswitchable conductance of Au-NPs networks. In cases where the DAE photocyclization reaction is quenched by the Au-NPs, a combination of conductance switching by chemical oxidation for the cyclization and photoirradiation for the cycloreversion can be achieved [137]. In similar systems, other groups

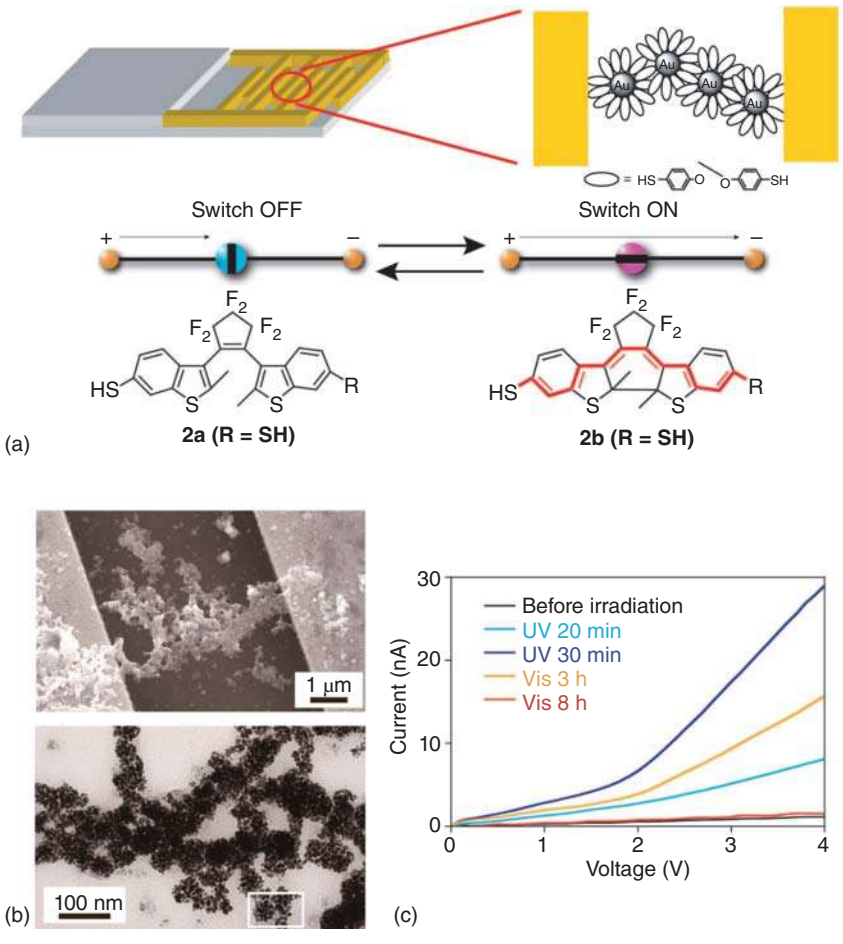


**Figure 28.14** (a) Schematic representation, (b) electronic microscopy images, and (c) *I*–*V* curves of a network of Au-NPs decorated with DAE molecules, deposited on an interdigitated nanogapped gold electrode, demonstrating the conductance photoswitching properties of photochromic-metallic nanoassemblies. Source: Matsuda et al. [134]/with permission of American Chemical Society.

confirmed this appealing phenomenon [138]. The reversible change of conductance levels under light stimuli was also related to the change of SPR of the network, which confirms that the molecular isomerization is the origin of conductance switching of the nanoassemblies.

## 28.6 Conclusion

In this chapter, the most recent developments in the design, fabrication, and implementation of photoresponsive nanoparticles, based on photochromic compounds and their applications have been presented. Photochromic dyes have long been

studied at the molecular scale, but the preparation of nanomaterials enables their dispersion in more diverse media, reaching intrinsic photochromic properties and a variety of combinations with additional photoactive units that were previously inaccessible. The advent of photochromism into the world of nanoscience has been a major breakthrough in the field, associated with tremendous phenomena such as giant amplification effect of fluorescence photoswitching, bright and controllable multicolor emission, upconverted all-visible photo-actuation, simultaneous imaging and drug-release, photoswitchable plasmonic or conductance enhancement, and reversible photo-triggered assembly, to name just a few. All in all, the design of photoresponsive nanosystems and nano-assemblies, organic or hybrid, with emissive or plasmonic properties, opens up virtually unlimited perspectives in the field of photoactive functional materials. Beyond the main typical applications of photochromic nanoparticles, such as optical data storage, optoelectronic devices, information encoding, bio-imaging, or drug photorelease, several new areas are expected to serve as new playgrounds for photochromic nanosystems in the future. For instance, one can foresee an increasing demand in the field of solar energy storage, photocontrolled catalysis, tamper-proof security systems, or four-dimensional photoprinting, with exciting challenges to meet, from both fundamental and practical points of view. Photochromic nanosystems will have a major role to play on these aspects, integrating several properties within smart nano-objects, to achieve new capabilities which would be unreachable with conventional materials. The topics mentioned above are only representative examples of unlimited research opportunities that will be probably exploited with photoresponsive nanomaterials in the near future. Given the number of conceivable applications of such nanoparticles in chemistry, physics, materials, biology, and computing sciences, it is presumptuous to make general recommendations but we hope that our readers will find the content of this chapter helpful when designing their future research, selecting the fabrication method of their photoactive nanosystems, considering their expected characteristics. The great diversity of designs, properties, and applications of photochromic nanomaterials makes them excellent candidates to develop novel molecular nano-constructs with unexplored behaviors, and we anticipate this field to continue its rapid progress over the next decade.

## References


1 Wang, L. and Li, Q. (2018). Photochromism into nanosystems: towards lighting up the future nanoworld. *Chem. Soc. Rev.* 47: 1044–1097.

2 Feczko, T. and Voncina, B. (2013). Organic nanoparticulate photochromes. *Curr. Org. Chem.* 17: 1771–1789.

3 Fukaminato, T., Ishida, S., and Métivier, R. (2018). Photochromic fluorophores at the molecular and nanoparticle levels: fundamentals and applications of diarylethenes. *NPG Asia Mater.* 10: 859–881.

4 Zhang, Y., Zhang, K., Wang, J. et al. (2015). Photoswitchable fluorescent nanoparticles and their emerging applications. *Nanoscale* 7: 19342–19357.


5 Laurent, G., Maurel, F., Asahi, T. et al. (2017). Photoswitchable hybrid nanosystems based on diarylethene molecules and gold nanoparticles. In: *Photon-working switches* (ed. Y. Yokoyama and K. Nakatani), 443–464. Springer.

6 Grzelczak, M., Liz-Marzan, L.M., and Klajn, R. (2019). Stimuli-responsive self-assembly of nanoparticles. *Chem. Soc. Rev.* 48: 1342–1361.

7 Bian, T., Chu, Z., and Klajn, R. (2020). The many ways to assemble nanoparticles using light. *Adv. Mater.* 32: e1905866.

8 Asahi, T., Sugiyama, T., and Masuhara, H. (2008). Laser fabrication and spectroscopy of organic nanoparticles. *Acc. Chem. Res.* 41: 1790–1798.

9 Patra, A., Métivier, R., Piard, J., and Nakatani, K. (2010). SHG-active molecular nanorods with intermediate photochromic properties compared to solution and bulk solid states. *Chem. Commun.* 46: 6385–6387.

10 Piard, J., Métivier, R., Giraud, M. et al. (2009). Photoswitching in diarylethene nanoparticles, a trade-off between bulk solid and solution: towards balanced photochromic and fluorescent properties. *New J. Chem.* 33: 1420–1426.

11 Spangenberg, A., Métivier, R., Gonzalez, J. et al. (2009). Multiscale approach of photochromism: synthesis and photochromic properties of a diarylethene in solution, in nanoparticles, and in bulk crystals. *Adv. Mater.* 21: 309–313.

12 Ouhenia-Ouadahi, K., Laurent, G., Barrez, E. et al. (2018). Spectroscopic investigation of diarylethene photochromes linked to silica nanoparticles. *J. Phys. Chem. C* 122: 6984–6995.

13 Khakzad, F., Mahdavian, A.R., Salehi-Mobarakeh, H., and Sharifian, M.H. (2018). A step-wise self-assembly approach in preparation of multi-responsive poly(styrene-co-methyl methacrylate) nanoparticles containing spiropyran. *J. Colloid Interface Sci.* 515: 58–69.

14 Kasai, H., Nalwa, H.S., Oikawa, H. et al. (1992). A novel preparation method of organic microcrystals. *Jpn. J. Appl. Phys., Part 2* 31: L1132–L1134.

15 Sun, F., Zhang, F., Zhao, F. et al. (2003). Preparation and photochromic properties of diarylethene nanoparticles. *Chem. Phys. Lett.* 380: 206–212.

16 Tagawa, N., Masuhara, A., Onodera, T. et al. (2011). Nanocrystallization process of diarylethene. *Mol. Cryst. Liq. Cryst.* 539: 45/[385]–349/[389].

17 Tagawa, N., Masuhara, A., Kasai, H. et al. (2010). Nanocrystallization of diarylethene and photochromic properties. *Cryst. Growth Des.* 10: 2857–2859.

18 Tagawa, N., Masuhara, A., Okada, S. et al. (2013). Diarylethene nanorods: preparation, crystal structure, and photochromic properties. *Chem. Lett.* 42: 636–637.

19 Tagawa, N., Masuhara, A., Onodera, T. et al. (2011). Polystyrene-encapsulated diarylethene nanocrystals by soap-free emulsion polymerization. *J. Mater. Chem.* 21: 7892–7894.

20 Breslin, V.M. and Garcia-Garibay, M.A. (2017). Transmission spectroscopy and kinetics in crystalline solids using aqueous nanocrystalline suspensions: the Spiropyran-Merocyanine photochromic system. *Cryst. Growth Des.* 17: 637–642.

21 Breslin, V.M., Barbour, N.A., Dang, D.K. et al. (2018). Nanosecond laser flash photolysis of a 6-nitroindolinospiropyran in solution and in nanocrystalline


suspension under single excitation conditions. *Photochem. Photobiol. Sci.* 17: 741–749.

**22** Ishibashi, Y., Nakai, S., Masuda, K. et al. (2020). Nanosecond laser photothermal effect-triggered amplification of photochromic reactions in diarylethene nanoparticles. *Chem. Commun.* 56: 7088–7091.

**23** Hotta, Y., Fukushima, S., Motoyanagi, J., and Tsuda, A. (2015). Photochromism in sound-induced alignment of a diarylethene supramolecular nanofibre. *Chem. Commun.* 51: 2790–2793.

**24** Patra, A., Métivier, R., Brisset, F., and Nakatani, K. (2012). Photochromic one-dimensional nanostructures based on dithienylethene: fabrication by light-induced precipitation and reversible transformation in the nanoparticle state. *Chem. Commun.* 48: 2489–2491.

**25** Tong, R., Hemmati, H.D., Langer, R., and Kohane, D.S. (2012). Photoswitchable nanoparticles for triggered tissue penetration and drug delivery. *J. Am. Chem. Soc.* 134: 8848–8855.

**26** Spagnoli, S., Block, D., Botzung-Appert, E. et al. (2005). Photochromism of spiropyran nanocrystals embedded in sol-gel matrices. *J. Phys. Chem. B* 109: 8587–8591.

**27** Sanz-Menez, N., Monnier, V., Colombier, I. et al. (2011). Photochromic fluorescent diarylethene nanocrystals grown in sol–gel thin films. *Dyes Pigm.* 89: 241–245.

**28** Chen, S., Hu, J., Wang, F., and Liu, H. (2019). Preparation and drug release application of pH and light dual-stimuli- responsive nanocarrier based on mesoporous silica nanoparticles. *J. Dispersion Sci. Technol.* 40: 1725–1735.

**29** Su, J., Chen, J., Zeng, F. et al. (2008). Synthesis and photochromic property of nanoparticles with spiropyran moieties via one-step miniemulsion polymerization. *Polym. Bull.* 61: 425–434.

**30** Feczkó, T., Varga, O., Kovács, M. et al. (2011). Preparation and characterization of photochromic poly(methyl methacrylate) and ethyl cellulose nanocapsules containing a spirooxazine dye. *J. Photochem. Photobiol., A* 222: 293–298.

**31** Feczkó, T., Kovács, M., and Voncina, B. (2012). Improvement of fatigue resistance of spirooxazine in ethyl cellulose and poly(methyl methacrylate) nanoparticles using a hindered amine light stabilizer. *J. Photochem. Photobiol., A* 247: 1–7.

**32** Huang, C.Q., Wang, Y., Hong, C.Y., and Pan, C.Y. (2011). Spiropyran-based polymeric vesicles: preparation and photochromic properties. *Macromol. Rapid Commun.* 32: 1174–1179.

**33** Zhu, M.Q., Zhang, G.F., Li, C. et al. (2011). Reversible two-photon photoswitching and two-photon imaging of immunofunctionalized nanoparticles targeted to cancer cells. *J. Am. Chem. Soc.* 133: 365–372.

**34** Spangenberg, A., Brosseau, A., Métivier, R. et al. (2007). Fabrication of nanoscale photochromic materials by vapor deposition method. *J. Phys. Org. Chem.* 20: 985–991.

**35** Tong, F., Kitagawa, D., Dong, X. et al. (2018). Photomechanical motion of diarylethene molecular crystal nanowires. *Nanoscale* 10: 3393–3398.

**36** Irie, M., Fukaminato, T., Sasaki, T. et al. (2002). Organic chemistry: a digital fluorescent molecular photoswitch. *Nature* 420: 759–760.

**37** Fukaminato, T., Doi, T., Tamaoki, N. et al. (2011). Single-molecule fluorescence photoswitching of a diarylethene-perylenebisimide dyad: non-destructive fluorescence readout. *J. Am. Chem. Soc.* 133: 4984–4990.

**38** Bonacchi, S., Genovese, D., Juris, R. et al. (2011). Luminescent silica nanoparticles: extending the frontiers of brightness. *Angew. Chem. Int. Ed.* 50: 4056–4066.

**39** Folling, J., Polyakova, S., Belov, V. et al. (2008). Synthesis and characterization of photoswitchable fluorescent silica nanoparticles. *Small* 4: 134–142.

**40** Genovese, D., Montalti, M., Prodi, L. et al. (2011). Reversible photoswitching of dye-doped core-shell nanoparticles. *Chem. Commun.* 47: 10975–10977.

**41** Shimizu, K. and Kobatake, S. (2017). Synthesis and optical properties of fluorescent switchable silica nanoparticles covered with copolymers consisting of diarylethene and fluorene derivatives. *ChemistrySelect* 2: 5445–5452.

**42** Jung, H.Y., You, S., Lee, C. et al. (2013). One-pot synthesis of monodispersed silica nanoparticles for diarylethene-based reversible fluorescence photoswitching in living cells. *Chem. Commun.* 49: 7528–7530.

**43** Jeong, J., Yun, E., Choi, Y. et al. (2011). Photoreversible cellular imaging using photochrome-conjugated fullerene silica nanoparticles. *Chem. Commun.* 47: 10668–10670.

**44** Edelsztein, V.C., Jares-Erijman, E.A., Müllen, K. et al. (2012). A luminescent steroid-based organogel: ON–OFF photoswitching by dopant interplay and templated synthesis of fluorescent nanoparticles. *J. Mater. Chem.* 22: 21857–21861.

**45** May, F., Peter, M., Hutten, A. et al. (2012). Synthesis and characterization of photoswitchable fluorescent $SiO_2$ nanoparticles. *Chem. Eur. J.* 18: 814–821.

**46** Achilleos, D.S., Hatton, T.A., and Vamvakaki, M. (2016). Photoreponsive hybrid nanoparticles with inherent FRET activity. *Langmuir* 32: 5981–5989.

**47** Wu, C., Bull, B., Szymanski, C. et al. (2008). Multicolor conjugated polymer dots for biological fluorescence imaging. *ACS Nano* 2: 2415–2423.

**48** Wu, C. and Chiu, D.T. (2013). Highly fluorescent semiconducting polymer dots for biology and medicine. *Angew. Chem. Int. Ed.* 52: 3086–3109.

**49** Davis, C.M., Childress, E.S., and Harbron, E.J. (2011). Ensemble and single-particle fluorescence photomodulation in diarylethene-doped conjugated polymer nanoparticles. *J. Phys. Chem. C* 115: 19065–19073.

**50** Osakada, Y., Hanson, L., and Cui, B. (2012). Diarylethene doped biocompatible polymer dots for fluorescence switching. *Chem. Commun.* 48: 3285–3287.

**51** Osakada, Y., Fukaminato, T., Ichinose, Y. et al. (2017). Live cell imaging using photoswitchable diarylethene-doped fluorescent polymer dots. *Chem. Asian J.* 12: 2660–2665.

**52** Kuo, C.T., Thompson, A.M., Gallina, M.E. et al. (2016). Optical painting and fluorescence activated sorting of single adherent cells labelled with photoswitchable Pdots. *Nat. Commun.* 7: 11468.

**53** Lim, S.J., An, B.K., Jung, S.D. et al. (2004). Photoswitchable organic nanoparticles and a polymer film employing multifunctional molecules with enhanced


fluorescence emission and bistable photochromism. *Angew. Chem. Int. Ed.* 43: 6346–6350.

**54** Su, J., Fukaminato, T., Placial, J.P. et al. (2016). Giant amplification of photoswitching by a few photons in fluorescent photochromic organic nanoparticles. *Angew. Chem. Int. Ed.* 55: 3662–3666.

**55** Yildiz, I., Impellizzeri, S., Deniz, E. et al. (2011). Supramolecular strategies to construct biocompatible and photoswitchable fluorescent assemblies. *J. Am. Chem. Soc.* 133: 871–879.

**56** Liu, R., Yang, Y., Cui, Q. et al. (2018). A diarylethene-based photoswitch and its photomodulation of the fluorescence of conjugated polymers. *Chem. Eur. J.* 24: 17756–17766.

**57** Trofymchuk, K., Prodi, L., Reisch, A. et al. (2015). Exploiting fast exciton diffusion in dye-doped polymer nanoparticles to engineer efficient photoswitching. *J. Phys. Chem. Lett.* 6: 2259–2264.

**58** Zhang, X., Kurimoto, A., Frank, N.L., and Harbron, E.J. (2018). Controlling photoswitching via pcFRET in conjugated polymer nanoparticles. *J. Phys. Chem. C* 122: 22728–22737.

**59** Chen, S., Li, W., Li, X., and Zhu, W.-H. (2017). Aggregation-controlled photochromism based on a dithienylethene derivative with aggregation-induced emission. *J. Mater. Chem. C* 5: 2717–2722.

**60** Yan, Q. and Wang, S. (2020). Fusion of aggregation-induced emission and photochromics for promising photoresponsive smart materials. *Mater. Chem. Front.* 4: 3153–3175.

**61** Ikariko, I., Deguchi, S., Fabre, N. et al. (2020). Highly-stable red-emissive photochromic nanoparticles based on a diarylethene-perylenebisimide dyad. *Dyes Pigm.* 180: 108490.

**62** Nakahama, T., Kitagawa, D., Sotome, H. et al. (2018). Fluorescence on/off switching in nanoparticles consisting of two types of diarylethenes. *ACS Omega* 3: 2374–2382.

**63** Sasaki, S., Watanabe, T., Ishibashi, Y. et al. (2018). Giant fluorescence modulation induced by UV–vis excitation of benzothiadiazole nanoparticles doped with diarylethene derivatives. *Chem. Lett.* 47: 163–166.

**64** Ishida, S., Kitagawa, D., Kobatake, S. et al. (2019). Efficient "turn-off" fluorescence photoswitching in a highly fluorescent diarylethene single crystal. *Chem. Commun.* 55: 5681–5684.

**65** Shimizu, K., Métivier, R., and Kobatake, S. (2020). Synthesis and fluorescence on/off switching of hyperbranched polymers having diarylethene at the branching point. *J. Photochem. Photobiol., A* 390: 112341.

**66** Nakahama, T., Kitagawa, D., Sotome, H. et al. (2017). Fluorescence on/off switching in polymers bearing diarylethene and fluorene in their side chains. *J. Phys. Chem. C* 121: 6272–6281.

**67** Métivier, R., Badré, S., Méallet-Renault, R. et al. (2009). Fluorescence photoswitching in polymer matrix: mutual influence between photochromic and fluorescent molecules by energy transfer processes. *J. Phys. Chem. C* 113: 11916–11926.

**68** Kim, S., Yoon, S.J., and Park, S.Y. (2012). Highly fluorescent chameleon nanoparticles and polymer films: multicomponent organic systems that combine FRET and photochromic switching. *J. Am. Chem. Soc.* 134: 12091–12097.

**69** Kim, D., Kwon, J.E., and Park, S.Y. (2016). Is color-specific photoswitching in dual-color fluorescence systems possible? Manipulating intermolecular energy transfer among two different fluorophores and one photoswitch. *Adv. Optical Mater.* 4: 790–797.

**70** Kim, D. and Lee, T.S. (2016). Photoswitchable emission color change in Nanodots containing conjugated polymer and photochrome. *ACS Appl. Mater. Interfaces* 8: 34770–34776.

**71** Bu, J., Watanabe, K., Hayasaka, H., and Akagi, K. (2014). Photochemically colour-tuneable white fluorescence illuminants consisting of conjugated polymer nanospheres. *Nat. Commun.* 5: 3799.

**72** Chen, J., Zhong, W., Tang, Y. et al. (2015). Amphiphilic BODIPY-based photoswitchable fluorescent polymeric nanoparticles for rewritable patterning and dual-color cell imaging. *Macromolecules* 48: 3500–3508.

**73** Kim, D., Jeong, K., Kwon, J.E. et al. (2019). Dual-color fluorescent nanoparticles showing perfect color-specific photoswitching for bioimaging and super-resolution microscopy. *Nat. Commun.* 10: 3089.

**74** Ishida, S., Fukaminato, T., Kim, S. et al. (2017). Sequential red-green-blue (RGB) fluorescence color photoswitching in multicomponent photochromic fluorescent nanoparticles. *Chem. Lett.* 46: 1182–1185.

**75** Ishida, S., Fukaminato, T., Kitagawa, D. et al. (2017). Wavelength-selective and high-contrast multicolour fluorescence photoswitching in a mixture of photochromic nanoparticles. *Chem. Commun.* 53: 8268–8271.

**76** Naren, G., Hsu, C.W., Li, S. et al. (2019). An all-photonic full color RGB system based on molecular photoswitches. *Nat. Commun.* 10: 3996.

**77** Brus, L. (1986). Electronic wave functions in semiconductor clusters: experiment and theory. *J. Phys. Chem.* 90: 2555–2560.

**78** Michalet, X., Pinaud, F.F., Bentolila, L.A. et al. (2005). Quantum dots for live cells, in vivo imaging, and diagnostics. *Science* 307: 538–544.

**79** Alivisatos, A.P. (1996). Semiconductor clusters, nanocrystals, and quantum dots. *Science* 271: 933–937.

**80** Diaz, S.A., Menendez, G.O., Etchehon, M.H. et al. (2011). Photoswitchable water-soluble quantum dots: pcFRET based on amphiphilic photochromic polymer coating. *ACS Nano* 5: 2795–2805.

**81** Diaz, S.A., Gillanders, F., Jares-Erijman, E.A., and Jovin, T.M. (2015). Photoswitchable semiconductor nanocrystals with self-regulating photochromic Forster resonance energy transfer acceptors. *Nat. Commun.* 6: 6036.

**82** Yuan, Y., Zhu, H., Nagaoka, Y. et al. (2019). Reversible photo-switching of dual-color fluorescent Mn-doped CdS-ZnS quantum dots modulated by diarylethene molecules. *Front. Chem.* 7: 145.

**83** Diaz, S.A., Giordano, L., Azcarate, J.C. et al. (2013). Quantum dots as templates for self-assembly of photoswitchable polymers: small, dual-color


nanoparticles capable of facile photomodulation. *J. Am. Chem. Soc.* 135: 3208–3217.

**84** Diaz, S.A., Giordano, L., Jovin, T.M., and Jares-Erijman, E.A. (2012). Modulation of a photoswitchable dual-color quantum dot containing a photochromic FRET acceptor and an internal standard. *Nano Lett.* 12: 3537–3544.

**85** Diaz, S.A., Gillanders, F., Susumu, K. et al. (2017). Water-soluble, thermostable, photomodulated color-switching quantum dots. *Chem. Eur. J.* 23: 263–267.

**86** Erno, Z., Yildiz, I., Gorodetsky, B. et al. (2010). Optical control of quantum dot luminescence via photoisomerization of a surface-coordinated, cationic dithienylethene. *Photochem. Photobiol. Sci.* 9: 249–253.

**87** Dworak, L., Reuss, A.J., Zastrow, M. et al. (2014). Discrimination between FRET and non-FRET quenching in a photochromic CdSe quantum dot/dithienylethene dye system. *Nanoscale* 6: 14200–14203.

**88** Seto, Y., Yamada, R., Kitagawa, D. et al. (2019). Photoluminescence ON/OFF switching of CdSe/ZnS core/shell quantum dots coated with diarylethene ligands. *Chem. Lett.* 48: 1394–1397.

**89** Yano, N., Yamauchi, M., Kitagawa, D. et al. (2020). Photoluminescence on/off switching of a single colloidal quantum dot using photochromic diarylethene. *J. Phys. Chem. C* 124: 17423–17429.

**90** Protesescu, L., Yakunin, S., Bodnarchuk, M.I. et al. (2015). Nanocrystals of cesium Lead halide perovskites ($CsPbX_3$, X = Cl, Br, and I): novel optoelectronic materials showing bright emission with wide color gamut. *Nano Lett.* 15: 3692–3696.

**91** Li, P., Yang, D., Zhong, Q. et al. (2019). Photoreversible luminescence switching of CsPbI3 nanocrystals sensitized by photochromic AgI nanocrystals. *Nanoscale* 11: 3193–3199.

**92** Zou, C., Zheng, J., Chang, C. et al. (2019). Nonvolatile rewritable photomemory arrays based on reversible phase-change perovskite for optical information storage. *Adv. Optical Mater.* 7: 1900558.

**93** Kim, S.-H., Yun, S., Choi, J., and Kim, J.H. (2018). High contrast fluorescence switching based on $CH_3NH_3PbBr_3$ perovskite nanoparticles in photochromic composites. *J. Photochem. Photobiol., A* 353: 279–283.

**94** Akaishi, Y., Pramata, A.D., Tominaga, S. et al. (2019). Reversible ON/OFF switching of photoluminescence from $CsPbX_3$ quantum dots coated with silica using photochromic diarylethene. *Chem. Commun.* 55: 8060–8063.

**95** Mokhtar, A., Morinaga, R., Akaishi, Y. et al. (2020). Reversible luminescence photoswitching of colloidal $CsPbBr_3$ nanocrystals hybridized with a diarylethene photoswitch. *ACS Mater. Lett.* 2: 727–735.

**96** Anwar, S., Ding, H., Xu, M. et al. (2019). Recent advances in synthesis, optical properties, and biomedical applications of carbon dots. *ACS Appl. Bio Mater.* 2: 2317–2338.

**97** Yuan, F., Yuan, T., Sui, L. et al. (2018). Engineering triangular carbon quantum dots with unprecedented narrow bandwidth emission for multicolored LEDs. *Nat. Commun.* 9: 2249.

**98** Liu, J., Geng, Y., Li, D. et al. (2020). Deep red emissive carbonized polymer dots with unprecedented narrow full width at half maximum. *Adv. Mater.* 32: e1906641.

**99** Liao, B., Long, P., He, B. et al. (2013). Reversible fluorescence modulation of spiropyran-functionalized carbon nanoparticles. *J. Mater. Chem. C* 1: 3716–3721.

**100** Wu, H., Chen, Y., Dai, X. et al. (2019). In situ photoconversion of multicolor luminescence and pure white light emission based on carbon dot-supported supramolecular assembly. *J. Am. Chem. Soc.* 141: 6583–6591.

**101** Liao, B., Wang, W., Long, P. et al. (2015). The carbon nanoparticles grafted with copolymers of styrene and spiropyran with reversibly photoswitchable fluorescence. *Carbon* 91: 30–37.

**102** Jin, K., Ji, X., Yang, T. et al. (2021). Facile access to photo-switchable, dynamic-optical, multi-colored and solid-state materials from carbon dots and cellulose for photo-rewritable paper and advanced anti-counterfeiting. *Chem. Eng. J.* 406: 126794.

**103** Zhou, J., Liu, Q., Feng, W. et al. (2015). Upconversion luminescent materials: advances and applications. *Chem. Rev.* 115: 395–465.

**104** Singh-Rachford, T.N. and Castellano, F.N. (2010). Photon upconversion based on sensitized triplet–triplet annihilation. *Coord. Chem. Rev.* 254: 2560–2573.

**105** Rojas-Gutierrez, P.A., Bhuckory, S., Mingoes, C. et al. (2018). A route to triggered delivery via photocontrol of lipid bilayer properties using lanthanide upconversion nanoparticles. *ACS Appl. Nano Mater.* 1: 5345–5354.

**106** Zhao, T., Wang, P., Li, Q. et al. (2018). Near-infrared triggered decomposition of nanocapsules with high tumor accumulation and stimuli responsive fast elimination. *Angew. Chem. Int. Ed.* 57: 2611–2615.

**107** Mi, Y., Cheng, H.B., Chu, H. et al. (2019). A photochromic upconversion nanoarchitecture: towards activatable bioimaging and dual NIR light-programmed singlet oxygen generation. *Chem. Sci.* 10: 10231–10239.

**108** Wu, T., Johnsen, B., Qin, Z. et al. (2015). Two-colour fluorescent imaging in organisms using self-assembled nano-systems of upconverting nanoparticles and molecular switches. *Nanoscale* 7: 11263–11266.

**109** Boyer, J.C., Carling, C.J., Gates, B.D., and Branda, N.R. (2010). Two-way photoswitching using one type of near-infrared light, upconverting nanoparticles, and changing only the light intensity. *J. Am. Chem. Soc.* 132: 15766–15772.

**110** Zheng, K., Han, S., Zeng, X. et al. (2018). Rewritable optical memory through high-registry orthogonal upconversion. *Adv. Mater.* 30: e1801726.

**111** Matsuda, K., Ikeda, M., and Irie, M. (2004). Photochromism of diarylethene-capped gold nanoparticles. *Chem. Lett.* 33: 456–457.

**112** Yamaguchi, H., Ikeda, M., Matsuda, K., and Irie, M. (2006). Photochromism of diarylethenes on gold and silver nanoparticles. *Bull. Chem. Soc. Jpn.* 79: 1413–1419.

**113** Kudernac, T., van der Molen, S.J., van Wees, B.J., and Feringa, B.L. (2006). Uni- and bi-directional light-induced switching of diarylethenes on gold nanoparticles. *Chem. Commun.* 3597–3599.


**114** Nishi, H. and Kobatake, S. (2008). Photochromism and optical property of gold nanoparticles covered with low-polydispersity diarylethene polymers. *Macromolecules* 41: 3995–4002.

**115** Nishi, H., Asahi, T., and Kobatake, S. (2009). Light-controllable surface Plasmon resonance absorption of gold nanoparticles covered with photochromic diarylethene polymers. *J. Phys. Chem. C* 113: 17359–17366.

**116** Nishi, H., Asahi, T., and Kobatake, S. (2012). Plasmonic enhancement of gold nanoparticles on photocycloreversion reaction of diarylethene derivatives depending on particle size, distance from the particle surface, and irradiation wavelength. *Phys. Chem. Chem. Phys.* 14: 4898–4905.

**117** Snell, K.E., Mevellec, J.Y., Humbert, B. et al. (2015). Photochromic organic nanoparticles as innovative platforms for plasmonic nanoassemblies. *ACS Appl. Mater. Interfaces* 7: 1932–1942.

**118** Yamaguchi, H., Matsuda, K., and Irie, M. (2007). Excited-state behavior of a fluorescent and photochromic diarylethene on silver nanoparticles. *J. Phys. Chem. C* 111: 3853–3862.

**119** Ouhenia-Ouadahi, K., Yasukuni, R., Yu, P. et al. (2014). Photochromic-fluorescent-plasmonic nanomaterials: towards integrated three-component photoactive hybrid nanosystems. *Chem. Commun.* 50: 7299–7302.

**120** Noda, S., Hasegawa, S., Hamada, H. et al. (2019). Plasmon enhanced optical responses of diarylethene molecules adsorbed on gold nanorods. *Chem. Lett.* 48: 537–540.

**121** Klajn, R., Wesson, P.J., Bishop, K.J., and Grzybowski, B.A. (2009). Writing self-erasing images using metastable nanoparticle "inks". *Angew. Chem. Int. Ed.* 48: 7035–7039.

**122** Stricker, L., Fritz, E.C., Peterlechner, M. et al. (2016). Arylazopyrazoles as light-responsive molecular switches in cyclodextrin-based Supramolecular systems. *J. Am. Chem. Soc.* 138: 4547–4554.

**123** Klajn, R., Bishop, K.J., and Grzybowski, B.A. (2007). Light-controlled self-assembly of reversible and irreversible nanoparticle suprastructures. *Proc. Natl. Acad. Sci. U.S.A.* 104: 10305–10309.

**124** Klajn, R., Bishop, K.J., Fialkowski, M. et al. (2007). Plastic and moldable metals by self-assembly of sticky nanoparticle aggregates. *Science* 316: 261–264.

**125** Kundu, P.K., Das, S., Ahrens, J., and Klajn, R. (2016). Controlling the lifetimes of dynamic nanoparticle aggregates by spiropyran functionalization. *Nanoscale* 8: 19280–19286.

**126** Zhang, H., Muhammad, J., Liu, K. et al. (2019). Light-induced reversible hydrophobization of cationic gold nanoparticles via electrostatic adsorption of a photoacid. *Nanoscale* 11: 14118–14122.

**127** Manna, D., Udayabhaskararao, T., Zhao, H., and Klajn, R. (2015). Orthogonal light-induced self-assembly of nanoparticles using differently substituted azobenzenes. *Angew. Chem. Int. Ed.* 54: 12394–12397.

**128** Niehues, M., Tegeder, P., and Ravoo, B.J. (2019). Reversible end-to-end assembly of selectively functionalized gold nanorods by light-responsive arylazopyrazole-cyclodextrin interaction. *Beilstein J. Org. Chem.* 15: 1407–1415.

**129** Kundu, P.K., Samanta, D., Leizrowice, R. et al. (2015). Light-controlled self-assembly of non-photoresponsive nanoparticles. *Nat. Chem.* 7: 646–652.

**130** Zhang, L., Dai, L., Rong, Y. et al. (2015). Light-triggered reversible self-assembly of gold nanoparticle oligomers for tunable SERS. *Langmuir* 31: 1164–1171.

**131** Samanta, D. and Klajn, R. (2016). Aqueous light-controlled self-assembly of nanoparticles. *Adv. Optical Mater.* 4: 1373–1377.

**132** Liu, D., Chen, W., Sun, K. et al. (2011). Resettable, multi-readout logic gates based on controllably reversible aggregation of gold nanoparticles. *Angew. Chem. Int. Ed.* 50: 4103–4107.

**133** Zhao, H., Sen, S., Udayabhaskararao, T. et al. (2016). Reversible trapping and reaction acceleration within dynamically self-assembling nanoflasks. *Nat. Nanotechnol.* 11: 82–88.

**134** Matsuda, K., Yamaguchi, H., Sakano, T. et al. (2008). Conductance photoswitching of diarylethene–gold nanoparticle network induced by photochromic reaction. *J. Phys. Chem. C* 112: 17005–17010.

**135** Ikeda, M., Tanifuji, N., Yamaguchi, H. et al. (2007). Photoswitching of conductance of diarylethene-Au nanoparticle network. *Chem. Commun.* 1355–1357.

**136** Toyama, T., Higashiguchi, K., Nakamura, T. et al. (2016). Photoswitching of conductance of diarylethene-gold nanoparticle network based on the alteration of pi-conjugation. *J. Phys. Chem. Lett.* 7: 2113–2118.

**137** Yamaguchi, H. and Matsuda, K. (2009). Photo- and electrochromic switching of diarylethene–gold nanoparticle network on Interdigitated electrodes. *Chem. Lett.* 38: 946–947.

**138** van der Molen, S.J., Liao, J., Kudernac, T. et al. (2009). Light-controlled conductance switching of ordered metal-molecule-metal devices. *Nano Lett.* 9: 76–80.

# 29 Photomechanical Performance of Diarylethene Single Crystals

Masakazu Morimoto

**Photomechanical Performance of Diarylethene Single Crystals**

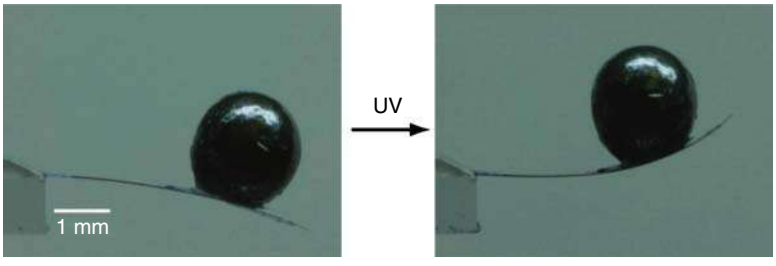


**Characteristic Features**

Photochromic diarylethene crystals show reversible shape changes upon photoirradiation and perform macroscopic mechanical work.

**Key References**

Irie, M., Kobatake, S., and Horichi, M. (2001). *Science* 291: 1769.

Kobatake, S., Takami, S., Muto, H. et al. (2007) *Nature* 446: 778.

Morimoto, M. and Irie, M. (2010). *J. Am. Chem. Soc*. 132: 14172.

Terao, F., Morimoto, M., and Irie, M. (2012). *Angew. Chem. Int. Ed*. 51: 901.

# 29

# Photomechanical Performance of Diarylethene Single Crystals

*Masakazu Morimoto*

*Rikkyo University, Department of Chemistry and Research Center for Smart Molecules, 3-34-1 Nishi-Ikebukuro, Toshima-ku, Tokyo 171-8501, Japan*

## 29.1 Introduction

It is a long-standing ambition for scientists to construct molecular systems that exhibit mechanical movement based on geometrical structure changes of individual molecules induced by external stimuli, such as chemicals, photons, or electrons (or holes), and have the systems perform macroscopic mechanical work [1]. In biological systems, sliding movements of actin-myosin proteins at the molecular level are successfully transformed to a directional force and macroscopic motion of muscles [2]. Various types of artificial molecular machines [3], such as molecular shuttles [4], molecular muscles [5, 6], molecular elevators [7], molecular rotors [8–10], and nano-cars [11–13], have been elaborately designed and synthesized. Although their machine-like motions are characterized by nuclear magnetic resonance (NMR) spectroscopy and other experiments, attempts to link the molecular-scale motions of these artificial nano-devices to macroscopic movements of materials are limited. As an outstanding example, it has been reported that microcantilever beams coated on one side with a monolayer of bistable rotaxane molecules reversibly bend by contracting and expanding motions of the rotaxane upon addition of chemical oxidants and reductants [6]. At the present stage, however, any certain strategy for rationally assembling the molecular machines to perform macroscopic mechanical work has not yet been developed. Although various types of polymers, gels, and carbon nanotubes have been reported to transfer molecular-scale phenomena into macroscopic movements of the materials [14–20], the movements rely not on individual molecular behavior but on the response of bulk materials. For example, the photoinduced contraction of liquid-crystal elastomers is ascribed to order–disorder phase transition of the liquid crystals [14–18].

In order to link molecular-scale motions of molecular machines to macroscopic mechanical works, it is essential to construct precisely organized structures of the molecules. A possible method is to use molecular crystals. Molecular crystals can be considered one of ideal self-assembled structures, in which component molecules

*Molecular Photoswitches: Chemistry, Properties, and Applications*,
First Edition. Edited by Zbigniew L. Pianowski.


are densely and regularly aligned. Unlike the amorphous polymer systems, even a slight change in the geometrical structures of the molecules packed in the crystals is expected to generate mechanical stress and induce the shape change of the bulk crystals. This chapter describes photoinduced deformation and mechanical performance of photochromic diarylethene single crystals and their potential applicability to light-driven actuators.

## 29.2 Single-Crystalline Photochromism of Diarylethene

Diarylethene derivatives undergo reversible isomerization reactions between colorless open-ring and colored closed-ring isomers upon irradiation with ultraviolet (UV) and visible light [21, 22]. They show photochromism not only in solution but also in the single-crystalline phase [23, 24]. Figure 29.1 shows color changes of diarylethene single crystals. Upon irradiating the colorless crystals with UV light, diarylethene molecules in the crystals undergo cyclization reactions to form closed-ring isomers and the crystals turn yellow, red, blue, or green, depending on the chemical structures of the molecules. The photogenerated colors are thermally stable in the dark and are completely bleached by irradiation with visible light. The diarylethene single crystals also show excellent resistance against photofatigue. It has been demonstrated that the coloration and decoloration processes can be repeated more than 30 000 times by alternate irradiation with UV and visible light [25]. Photoreactivity of the diarylethene crystal depends on the molecular conformation in the crystal. The requirement for the photocyclization reaction to take place in the crystalline state is that diarylethene molecules are fixed in an antiparallel type conformation with $C_2$ symmetry and the distance between the reactive carbon atoms is less than 0.42 nm [26, 27]. When these conditions are fulfilled, the photocyclization reaction proceeds with high quantum yield closed to unity. Time-resolved absorption spectroscopy [25] and electron diffraction [28, 29] have revealed that the cyclization reaction of diarylethene in the crystalline state is completed within a few picoseconds after photoexcitation.

Photoisomerization of the diarylethene molecule in the single-crystalline phase was observed by *in situ* X-ray crystallographic analysis [30]. X-ray analysis was carried out on a UV-irradiated single crystal of diarylethene **1** shown in Figure 29.2. Photogenerated closed-ring isomer in the crystal was observed as a disordered structure. Figure 29.2a illustrates the molecular structures of the open-ring and closed-ring isomers in the crystal. The sulfur and reactive carbon atoms in the thiophene rings significantly move during the cyclization process, while the other atoms remain at almost the original positions. This small structure change allows the diarylethene molecule to undergo the photoisomerization reaction in the crystal lattice. Figure 29.2b,c show the structural difference between the open- and closed-ring isomers in more detail. The shape of the diarylethene molecule is represented as a triangle connecting the three carbon atoms in the central hexafluorocyclopentene ring and the two methyl groups at both ends. The top

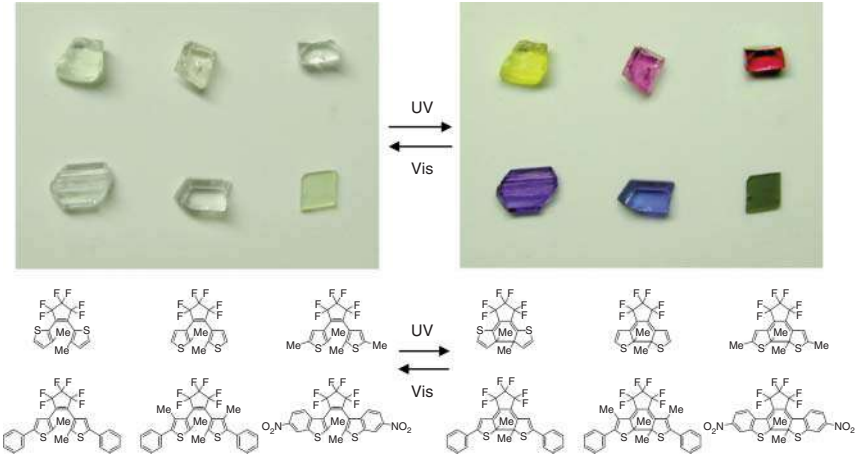


**Figure 29.1** Photochromism of diarylethene single crystals. Source: Irie et al. [22]/American Chemical Society.

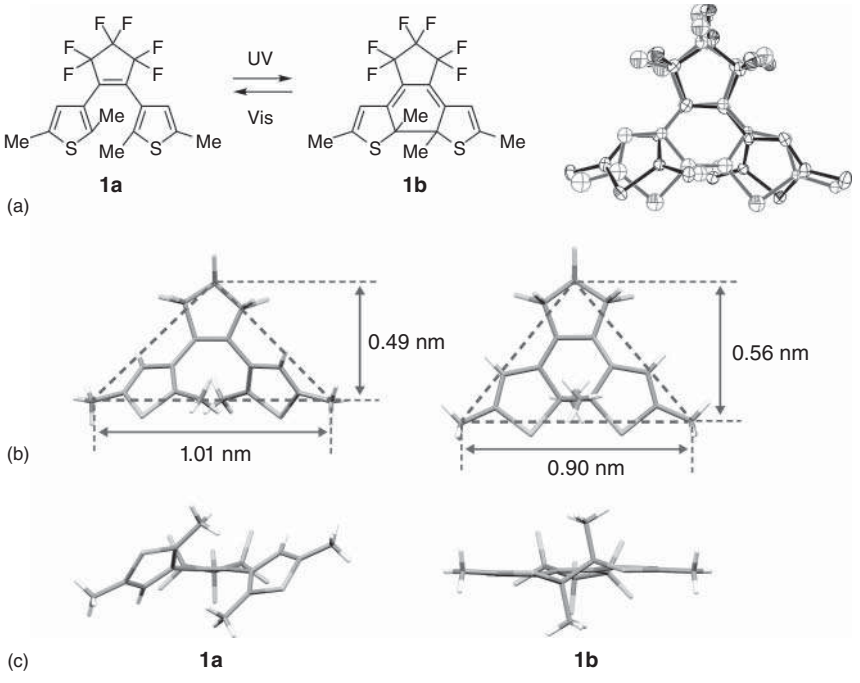


**Figure 29.2** (a) Chemical structures of open-ring isomer **1a** and closed-ring isomer **1b** of 1,2-bis(2,5-dimethyl-3-thienyl)perfluorocyclopentene. Oak Ridge thermal-ellipsoid plot (ORTEP) drawings of the photoirradiated crystal **1**. Black and gray lines show the open- and closed-ring isomers, respectively. (b and c) Molecular structures of **1a** and **1b** in crystals (b: top view, c: side view). The two isomers were isolated and independently recrystallized. Source: Reproduced from Morimoto and Irie [24].

view (Figure 29.2b) indicates that the base width of the triangle (the long axis of the molecule) decreases from 1.01 to 0.90 nm upon photocyclization, while the height (the short axis) increases from 0.49 to 0.56 nm. The side view (Figure 29.2c) shows that the thickness of the molecule becomes thinner. Such a small but distinct change of the molecular geometry upon photoisomerization induces shape changes of bulk single crystals, as described later.

## 29.3 Photoinduced Surface Morphology Change of a Diarylethene Single Crystal

Densely packed molecular alignment in single crystals enables geometrical structure changes of component molecules induced by photoisomerization to be linked to shape changes of the bulk crystals. The photomechanical effect of diarylethene single crystals was observed for the first time as photoinduced nanometer-scale morphology change on the crystal surface [31]. Diarylethene **2** (Figure 29.3) shows photochromism in the single-crystalline phase. Upon irradiation with UV light, the diarylethene molecule undergoes the cyclization reaction and the colorless crystal turns blue. Then, upon irradiation with visible light, the blue-colored crystal returns to the original colorless state. The morphology change of the crystal surface upon

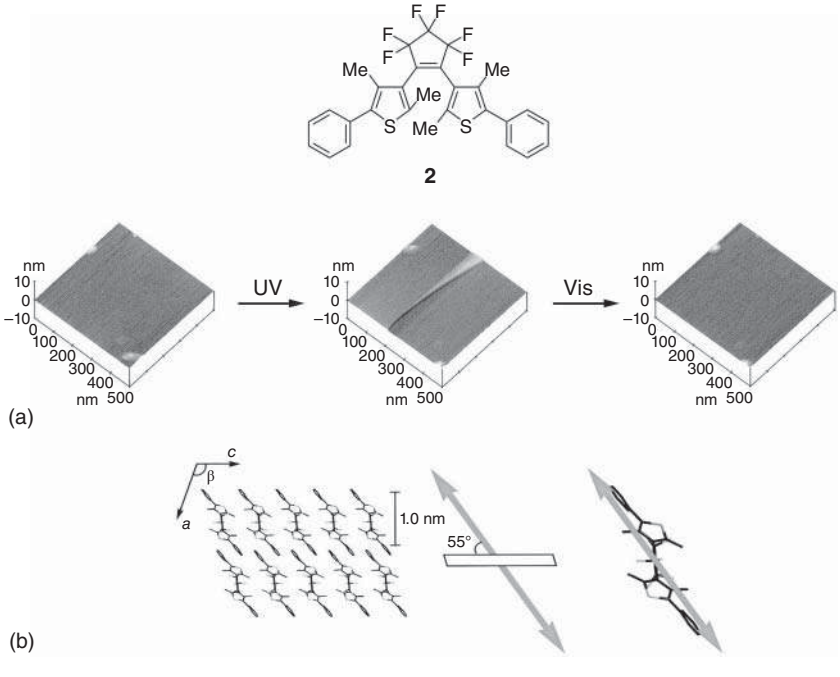


**Figure 29.3** (a) AFM images of (100) crystal surface of diarylethene **2** before photoirradiation, after irradiation with UV light, and after irradiation with visible light. (b) Molecular packing of **2** in the crystal. Source: Irie et al. [31]/AAAS.

photoirradiation was observed by atomic force microscopy (AFM). Figure 29.3a shows an AFM image of the (100) surface of the single crystal of **2**. Upon UV irradiation, a new step appears on the crystal surface. The step disappears when irradiated with visible light. The height of the step is c. 1 nm, which corresponds to the thickness of one layer of the diarylethene molecules in the crystal, as shown in Figure 29.3b. The morphology change of the crystal surface is ascribed to reversible contraction and expansion of the diarylethene molecules along their long axes during the photoisomerization reactions. Upon irradiation with UV light, the long axis of the diarylethene molecule is shrunk by the cyclization reaction. As the photoreaction proceeds, geometrical structure changes of the molecules are accumulated in the crystal. The resulting void inside the crystal is filled by the displacement of the molecular layers, creating the step on the crystal surface. Upon irradiation with visible light, the long axis of the molecule returns to its original length and the step disappears. This result indicates that the geometrical structure change of the diarylethene molecule upon photoisomerization leads to the macroscopic shape change of the bulk crystal.

## 29.4 Photoinduced Shape Changes of Diarylethene Single Crystals

Diarylethene single crystals change not only the surface morphology at the nanometer scale but also the entire shape of the bulk crystal [32–34]. Microcrystals with a size of c. 10 μm, which are prepared by sublimation, undergo reversible deformation upon photoirradiation. Figure 29.4a shows photoinduced deformation of a microcrystal of diarylethene **3** [32]. When the colorless crystal is irradiated with UV light, it turns blue and deforms from a rectangle to a parallelogram. The corner angles change from 88° and 92° to 82° and 98°. Upon irradiation with visible light, the blue color is bleached and the crystal returns to the original shape. The deformation of the crystal can be explained by the geometrical structure change of the diarylethene molecule and the molecular packing structure in the crystal. Figure 29.4b shows the crystal structure of **3**. The deformation of the plate crystal from the rectangle to the parallelogram upon irradiation with UV light corresponds to the elongation of the *b*-axis and the contraction of the *c*-axis. X-ray analysis of the crystal before and after the photocyclization reaction revealed that the length of the *b*-axis was expanded from 10.971 to 11.026 Å, while the *c*-axis was contracted from 10.585 to 10.542 Å. As shown in Figure 29.2, the diarylethene molecule changes its geometrical structure upon photoisomerization. When the diarylethene molecule undergoes the photocyclization reaction, the short axis of the molecule (the height of the triangle) becomes longer, inducing the expansion of the *b*-axis. In addition, the molecule becomes thinner upon photocyclization. The cofacial packing of the diarylethene molecules along the *c*-axis indicates that the thin layers of closed-ring isomers allow the molecules to be stacked one-by-one, resulting in the contraction along the *c*-axis. Thus, the geometrical structure change of the diarylethene molecule upon photoisomerization induces the anisotropic deformation of the crystal lattice and the shape change of the bulk crystal.

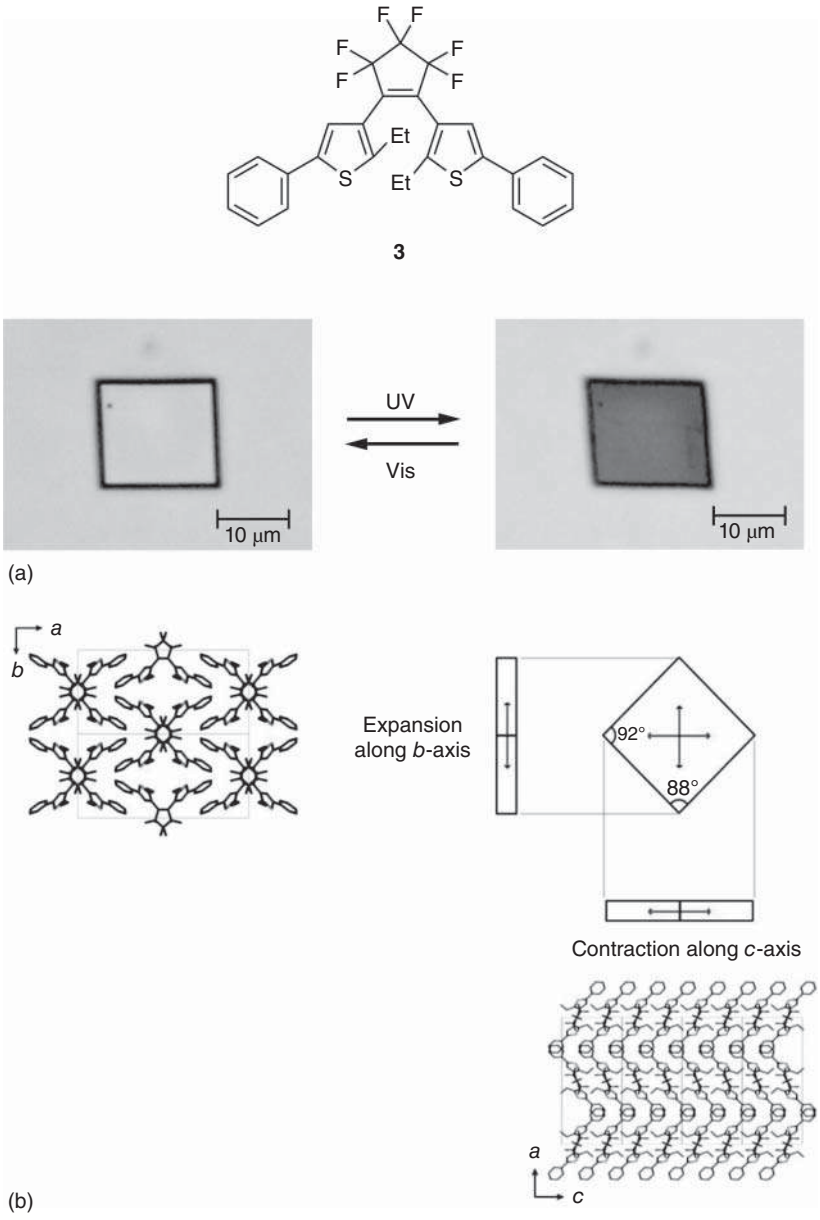


**Figure 29.4** (a) Photoinduced deformation of a single crystal of diarylethene **3**. (b) Molecular packing of **3** in the single crystal. Source: Adapted with permission from Kobatake et al. [32].

Figure 29.5a shows photoinduced deformation of a plate-like microcrystal of diarylethene **4** having thiazole rings [32]. Upon irradiation with UV light, the crystal turns violet and the length of the crystal is shrunk by about 7% along the long axis. Upon irradiation with visible light, the violet color is bleached and the crystal recovers the original length. Diarylethene **4** also forms rod-like crystals with a high aspect ratio by changing the crystal preparation condition. Upon irradiation with UV light, the rod-like crystal bends toward the direction of incident UV light, as shown in Figure 29.5b. This bending deformation is due to the gradient in the extent of the photoisomerization from the surface caused by the high optical absorption of the crystal in the UV-wavelength region. The contraction of the irradiated part of the crystal leads to the bending as observed in a bimetal. The crystal returns to the original straight shape by irradiating with visible light.

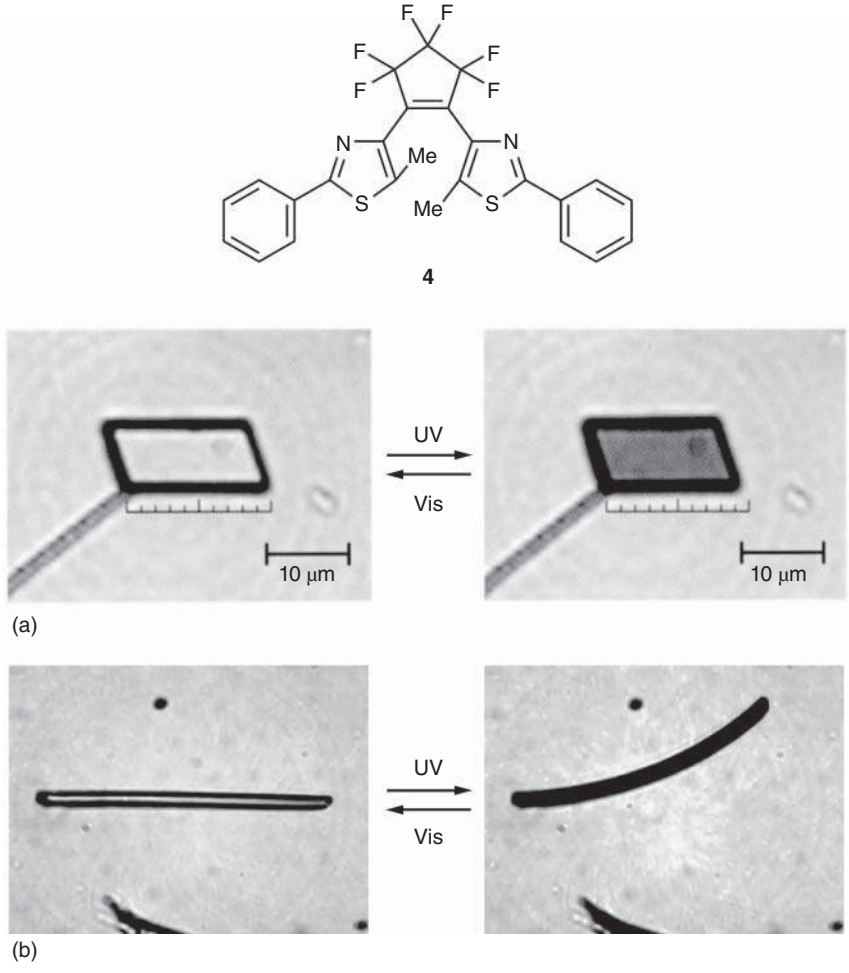


**Figure 29.5** Photoinduced deformation of (a) plate-like and (b) rod-like single crystals of diarylethene **4**. Source: Kobatake et al. [32]/Springer Nature.

## 29.5 Light-Driven Molecular Crystal Actuators

In order to use photochromic molecular crystals as light-driven actuators, the crystals are required to have high durability and mechanical properties. Two-component mixed crystals composed of diarylethenes **5** and **6** shown in Figure 29.6 were found to have excellent fatigue resistance [35]. Upon alternate irradiation with UV and visible light, the rod-like mixed crystal shows reversible bending deformation. The deformation can be repeated more than 1000 cycles. The melting point of the mixed crystal is lower than those of the single-component crystals of **5** and **6**. The low melting point suggests that intermolecular interaction among the component molecules is weakened in the mixed crystal. The weakened intermolecular interaction is considered to favor the macro-scale mechanical movement and improve the durability of the crystal. As shown in Figure 29.6a, the rod-like crystal bends with a large curvature into a hairpin shape by irradiation with UV light. The crystal can also bend toward any direction by changing the direction of the incident UV light. When the direction and intensity of UV and visible light are precisely controlled, the edge of the rod-like crystal exhibits rotation movement. A gearwheel with a diameter of 3.2 mm can be rotated by utilizing the photoinduced bending of the rod-like crystal, as shown in Figure 29.6b. Such molecular crystals that show various motions have a potential for the application in micro- and nano-mechanics, such as micro actuators and micro robotic arms, which can be remotely controlled by light illumination.

Diarylethene **7** and octafluoronaphthalene ($\mathbf{Np^F}$) shown in Figure 29.7 form two-component cocrystals with a ratio of 1 : 2, and the rectangular plate-like crystals also show photoinduced reversible bending deformation [36]. Upon irradiation with UV light, the colorless thin-plate crystal turns blue and bends moving away from the UV light source. Upon irradiation with visible light, the blue color disappears and the crystal recovers the original straight shape. The bending deformation away from the UV source indicates that the crystal surface irradiated with UV light is elongated. X-ray crystallographic analysis revealed that the deformation of the crystal is ascribed to the anisotropic deformation of the crystal lattice induced by the geometrical structure change of the diarylethene molecule upon photoisomerization. The bending deformation of the crystal occurs within 5 μs after irradiation with UV pulsed laser light (8 ns pulse width), as observed by a high-speed camera. The cocrystal also shows the reversible bending deformation upon irradiation with UV and visible light at extremely low temperature of 4.7 K. The photoinduced bending deformation of the cocrystal can be used to perform actual mechanical work. The rectangular plate-like crystal was fixed at the edge of a glass plate to prepare a cantilever arm and a lead ball was loaded onto the crystal, as shown in Figure 29.7. Upon irradiation with UV light from below, the crystal cantilever arm (0.17 mg) lifted up the lead ball (46.77 mg), where the weight of the lead ball is 270 times heavier than that of the crystal. The Young's modulus of the crystal determined by beam bending tests was about 11 GPa. The modulus is larger than those of polymer materials and gels. The stress generated by photoisomerization was estimated to be about 44 MPa by the analysis of the photoinduced deformation based on structural mechanics. This stress is about 100

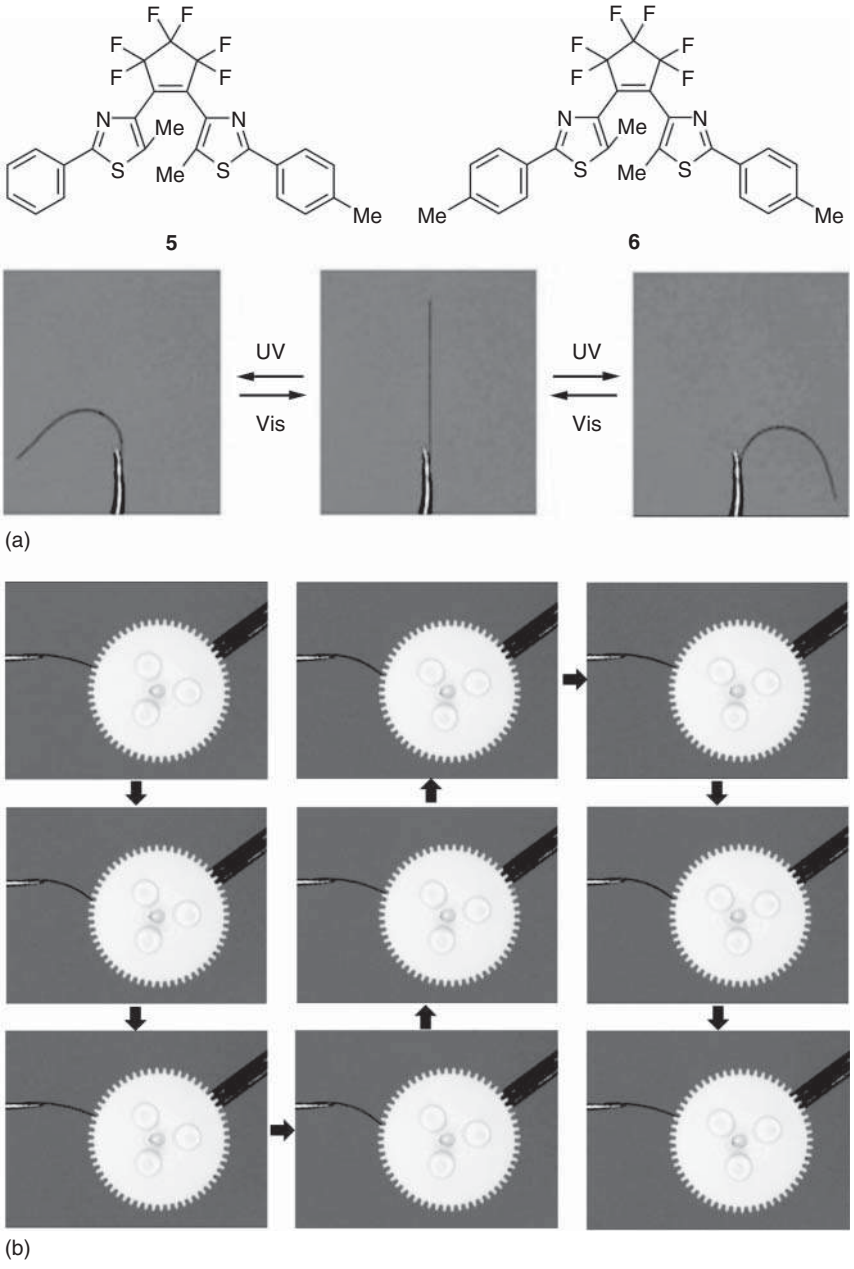


**Figure 29.6** (a) Photoinduced bending of a rod-like mixed crystal containing diarylethenes **5** and **6**. (b) Gearwheel rotation operated by a light-driven molecular crystal actuator. The two-component mixed crystal containing **5** and **6** was fixed on the tip of a metal needle. The gear (diameter: 3.2 mm) was rotated by the crystal, which showed reversible bending upon alternate irradiation with UV and visible light. Source: Terao et al. [35]/WILEY-VCH Verlag GmbH & Co. KGaA, Weinheim.

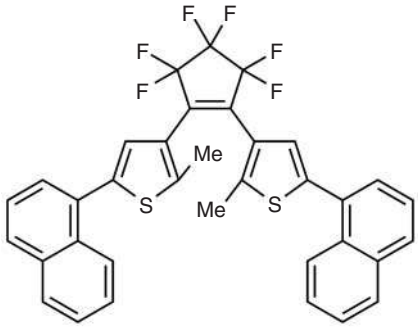


**7**

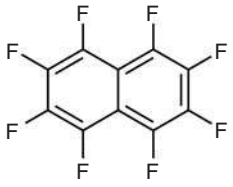


**Np$^F$**

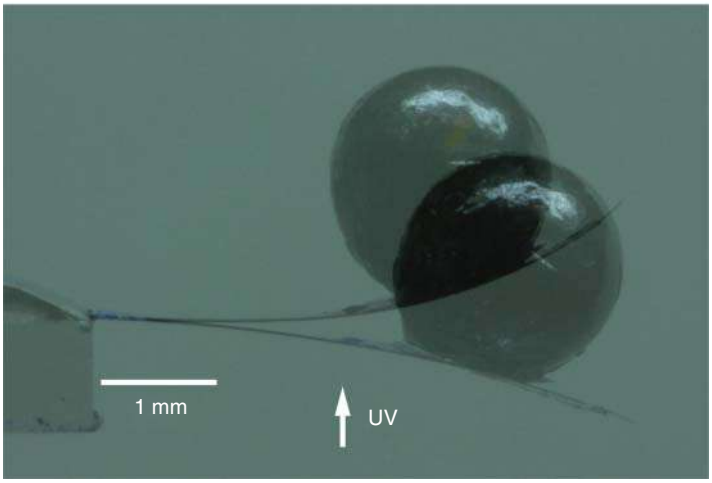


**Figure 29.7** Photomechanical work of a molecular crystal cantilever made of a cocrystal of **7** and perfluoronaphthalene (**Np$^F$**). Illumination of light was carried out below the crystal. The weights of the lead ball and the crystal cantilever were 46.77 and 0.17 mg, respectively. Source: Morimoto and Irie [36]/American Chemical Society.

times higher than that of biological muscles and comparable to that of piezoelectric materials.

In addition to the contraction/expansion and bending deformations described earlier, several crystals show unusual deformation upon photoirradiation. As shown in Figure 29.8, a thin ribbon-like crystal of diarylethene **8** turns blue upon UV irradiation and twists into a helical shape [37]. When the twisted crystal is irradiated with visible light, the blue color is bleached and the crystal returns to the original shape. The reversible twisting deformation can be repeated more than 30 times by alternate irradiation with UV and visible light. Such twisting deformation can also be explained on the basis of the mechanism in which the crystal lattice is deformed by geometrical structure change of the diarylethene molecule during photoisomerization. It has also been reported that another diarylethene crystal shows photoinduced twisting deformation and changes the helical pitch depending on the irradiation direction [38].

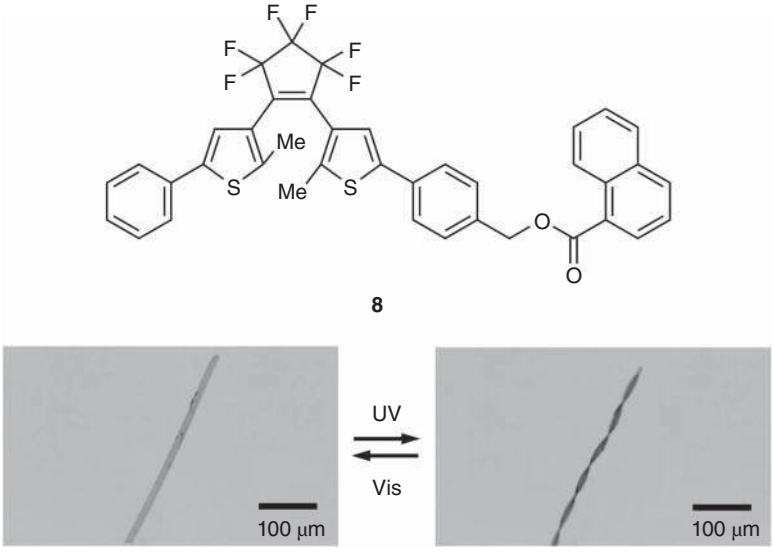


**Figure 29.8** Photoinduced twisting of a single crystal of diarylethene **8**. Source: Kitagawa et al. [37]/WILEY-VCH Verlag GmbH & Co. KGaA, Weinheim.

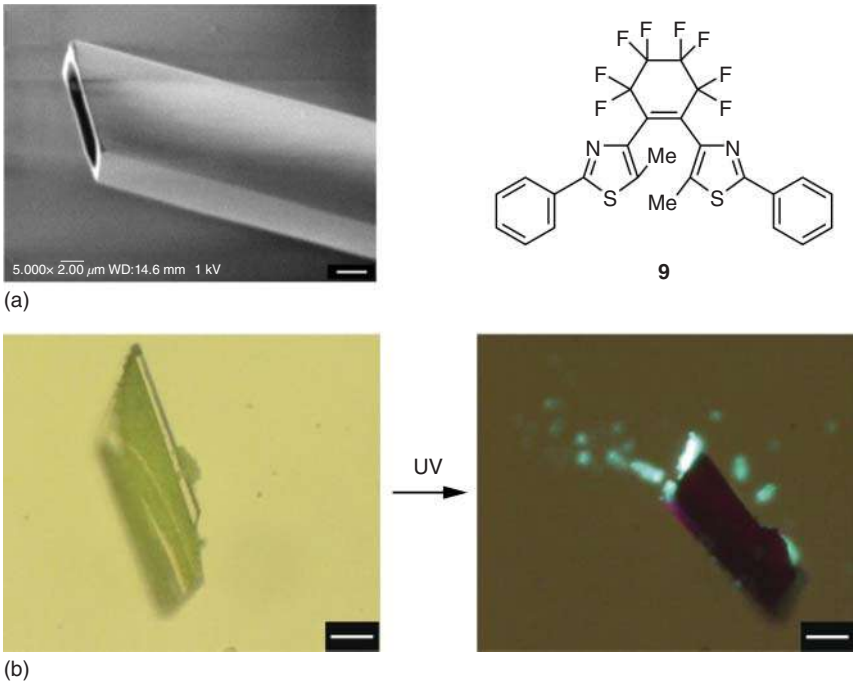


**Figure 29.9** (a) A scanning electron microscopy image of a hollow crystal of diarylethene **9** (scale bar: 2.0 μm). (b) Photosalient effect of a hollow crystal, mimicking *Impatiens*. UV irradiation to a hollow crystal of **9**, into which small fluorescent beads (1-μm diameter) were inserted, causes deformation and bursting of the hollow structure and the fluorescent beads are scattered (Scale bars: 20 μm). Source: Hatano et al. [42]/WILEY-VCH Verlag GmbH & Co. KGaA, Weinheim.

The scattering phenomenon of molecular crystals by light stimuli is called the photosalient effect [39, 40]. Single crystals of diarylethene **9** having an octafluorocyclohexene ring exhibit a remarkable photosalient effect [41, 42]. Upon UV irradiation, the crystals show remarkable photosalient phenomena and scatter into small pieces. The photosalient effect is attributed to the structural changes during photoisomerization from the open- to closed-ring isomer in the crystal as well as the existence of two conformers with different photoconversions. Interestingly, diarylethene **9** was found to form hollow crystals by sublimation, as shown in Figure 29.9a. Small fluorescent beads (1-μm diameter) were inserted into the hollow crystal. UV irradiation to the crystal caused deformation and bursting of the hollow structure, and scattering of the beads inserted was observed, as shown in Figure 29.9b. This phenomenon is unique to hollow crystals and is similar to the behavior of hollow-structured *Impatiens* in nature.

## 29.6 Summary and Outlook

Photochromic diarylethene crystals show reversible shape changes upon irradiation with UV and visible light. This phenomenon originates from the geometrical structure change of the diarylethene molecule in the crystal, which leads to the anisotropic deformation of the crystal lattice and the shape change of the bulk crystal. The photomechanical effect of the diarylethene crystals occurs over a wide temperature range (4–350 K) and exhibits excellent fatigue resistance and rapid response. The crystals can generate a large amount of stress upon photoirradiation and perform macroscopic mechanical work, such as rotating a tiny gearwheel, lifting up a heavy metal object, and so on. Such molecular crystals with excellent photomechanical performance have potential applications as light-driven actuators in micro- and nano-mechanics. Other photoreactive molecular crystals, such as azobenzene [43–45], salicylideneaniline [46], furyl fulgide [47], and anthracene derivatives [48–50], have also been reported to show photoinduced deformation. These results suggest that fabrication of single-crystalline assemblies is a promising approach to integrate stimuli-responsive molecules into macroscopic materials that perform significant mechanical work.

## References


**1** Merian, E. (1966). *Tex. Res. J.* 36: 612.
**2** Whittaker, M., Wilson-Kubalek, E.M., Smith, J.E. et al. (1995). *Nature* 378: 748.
**3** Balzani, V., Credi, A., and Venturi, M. (2008). *Molecular Devices and Machines: Concepts and Perspectives for the Nanoworld*. Weinheim: Wiley-VCH.
**4** Anelli, P.L., Spencer, N., and Stoddart, J.F. (1991). *J. Am. Chem. Soc.* 113: 5131.
**5** Jiménez, M.C., Dietrich-Buchecker, C., and Sauvage, J.-P. (2000). *Angew. Chem. Int. Ed.* 39: 3284.
**6** Liu, Y., Flood, A.H., Bonvallet, P.A. et al. (2005). *J. Am. Chem. Soc.* 127: 9745.


**7** Badjić, J.D., Balzani, V., Credi, A. et al. (2004). *Science* 303: 1845.
**8** Koumura, N., Zijlstra, R.W.J., van Delden, R.A. et al. (1999). *Nature* 401: 152.
**9** van Delden, R.A., ter Wiel, M.K.J., Pollard, M.M. et al. (2005). *Nature* 437: 1337.
**10** Kelly, T.R., De Silva, H., and Silva, R.A. (1999). *Nature* 401: 150.
**11** Morin, J.F., Shirai, Y., and Tour, J.M. (2006). *Org. Lett.* 8: 1713.
**12** Sasaki, T. and Tour, J.M. (2008). *Org. Lett.* 10: 897.
**13** Kudernac, T., Ruangsupapichat, N., Parschau, M. et al. (2011). *Nature* 479: 208.
**14** Jiang, H.Y., Kelch, S., and Lendlein, A. (2006). *Adv. Mater.* 18: 1471.
**15** Ikeda, T., Mamiya, J., and Yu, Y. (2007). *Angew. Chem. Int. Ed.* 46: 506.
**16** Finkelmann, H., Nishikawa, E., Pereira, G.G., and Warner, M. (2001). *Phys. Rev. Lett.* 87: 015501.
**17** Yu, Y., Nakano, M., and Ikeda, T. (2003). *Nature* 425: 145.
**18** Yamada, M., Kondo, M., Mamiya, J. et al. (2008). *Angew. Chem. Int. Ed.* 47: 4986.
**19** Juodkazis, S., Mukai, N., Wakaki, R. et al. (2000). *Nature* 408: 178.
**20** Aliev, A.E., Oh, J., Kozlov, M.E. et al. (2009). *Science* 323: 1575.
**21** Irie, M. (2000). *Chem. Rev.* 100: 1685.
**22** Irie, M., Fukaminato, T., Matsuda, K., and Kobatake, S. (2014). *Chem. Rev.* 114: 12174.
**23** Kobatake, S. and Irie, M. (2004). *Bull. Chem. Soc. Jpn.* 77: 195.
**24** Morimoto, M. and Irie, M. (2005). *Chem. Commun.* 3895.
**25** Jean-Ruel, H., Cooney, R.R., Gao, M. et al. (2011). *J. Phys. Chem. A* 115: 13158.
**26** Shibata, K., Muto, K., Kobatake, S., and Irie, M. (2002). *J. Phys. Chem. A* 106: 209.
**27** Kobatake, S., Uchida, K., Tsuchida, E., and Irie, M. (2002). *Chem. Commun.* 2804.
**28** Jean-Ruel, H., Gao, M., Kochman, M.A. et al. (2013). *J. Phys. Chem. B* 117: 15894.
**29** Miller, R.J.D. (2014). *Science* 343: 1108.
**30** Yamada, T., Kobatake, S., and Irie, M. (2000). *Bull. Chem. Soc. Jpn.* 73: 2179.
**31** Irie, M., Kobatake, S., and Horichi, M. (2001). *Science* 291: 1769.
**32** Kobatake, S., Takami, S., Muto, H. et al. (2007). *Nature* 446: 778.
**33** Irie, M. (2008). *Bull. Chem. Soc. Jpn.* 81: 917.
**34** Kuroki, L., Takami, S., Yoza, K. et al. (2010). *Photochem. Photobiol. Sci.* 9: 221.
**35** Terao, F., Morimoto, M., and Irie, M. (2012). *Angew. Chem. Int. Ed.* 51: 901.
**36** Morimoto, M. and Irie, M. (2010). *J. Am. Chem. Soc.* 132: 14172.
**37** Kitagawa, D., Nishi, H., and Kobatake, S. (2013). *Angew. Chem. Int. Ed.* 52: 9320.
**38** Kitagawa, D., Tsujioka, H., Tong, F. et al. (2018). *J. Am. Chem. Soc.* 140: 4208.
**39** Naumov, P., Chizhik, S., Panda, M.K. et al. (2015). *Chem. Rev.* 115: 12440.
**40** Naumov, P., Sahoo, S.C., Zakharov, B.A., and Boldyreva, E.V. (2013). *Angew. Chem. Int. Ed.* 52: 9990.
**41** Hatano, E., Morimoto, M., Hyodo, K. et al. (2016). *Chem. Eur. J.* 22: 12680.
**42** Hatano, E., Morimoto, M., Imai, T. et al. (2017). *Angew. Chem. Int. Ed.* 56: 12576.
**43** Koshima, H., Ojima, N., and Uchimoto, H. (2009). *J. Am. Chem. Soc.* 131: 6890.


**44** Bushuyev, O.S., Tomberg, A., Friščić, T., and Barrett, C.J. (2013). *J. Am. Chem. Soc.* 135: 12556.
**45** Nath, N.K., Pejov, L., Nichols, S.M. et al. (2014). *J. Am. Chem. Soc.* 136: 2757.
**46** Koshima, H., Takechi, K., Uchimoto, H. et al. (2011). *Chem. Commun.* 47: 11423.
**47** Koshima, H., Nakaya, H., Uchimoto, H., and Ojima, N. (2012). *Chem. Lett.* 41: 107.
**48** Al-Kaysi, R.O., Müller, A.M., and Bardeen, C.J. (2006). *J. Am. Chem. Soc.* 128: 15938.
**49** Al-Kaysi, R.O. and Bardeen, C.J. (2007). *Adv. Mater.* 19: 1276.
**50** Zhu, L., Al-Kaysi, R.O., and Bardeen, C.J. (2011). *J. Am. Chem. Soc.* 133: 12569.

# 30 Light-Responsive Metal–Organic Frameworks Based on Photochromic Molecules

Zejun Zhang, Yunzhe Jiang, Peng Qin, and Lars Heinke

**Light-Responsive Metal–Organic Frameworks Based on Photochromic Molecules**

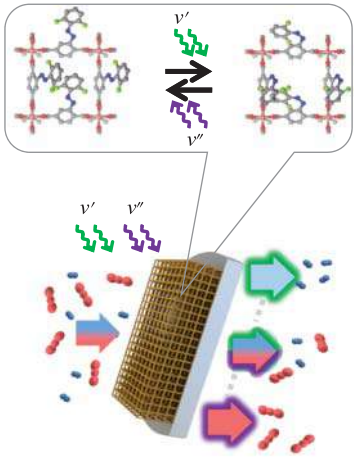


**Characteristic Features**

Nanoporous crystalline materials with incorporated photochromic moieties. The macroscopic properties are governed by the switching on the molecular level.

**First Reported**

Ohara, K., lnokuma, Y., and Fujita, M. (2010). The catalytic Z to E isomerization of stilbenes in a photosensitizing porous coordination network. *Angew. Chem. Int. Ed*. 49: 5507–5509.

Modrow, A., Zargarani, D., Herges, R., Stock, N. (2011). The first porous MOF with photoswitchable linker molecules. *Dalton Trans*. 40: 421–74222.

**Key References**

- **$CO_2$ adsorption switching**: Park, J., Yuan, D. Q., Pham, K. T. et al. (2012). *J. Am. Chem. Soc*. 134: 99–102.
- **Photoswitchable membrane separation**: Wang, Z., et al. (2016). *Nat. Commun*. 7: 13872.
- **Photomodulated energy transfer**: Park, J., et al. (2015). *Angew. Chem. Int. Ed*. 54: 430–435.
- **Proton conduction switching**: Müller, K., et al. (2018). *Adv. Mater*. 30: 1706551.
- **Electronic properties modulation**: Garg, S., et al. *Angew. Chem. Int. Ed*. 58: 1193–1197.

# 30

# Light-Responsive Metal–Organic Frameworks Based on Photochromic Molecules

*Zejun Zhang, Yunzhe Jiang, Peng Qin, and Lars Heinke*

*Karlsruhe Institute of Technology (KIT), Institute of Functional Interfaces (IFG), Hermann-von-Helmholtz-Platz 1, 76344 Eggenstein-Leopoldshafen, Germany*

## 30.1 Introduction

Among the great challenges in material science is the preparation of smart solids based on photochromic molecules where the molecular functionality multiplies to macroscopic properties of the material. A material class, which allows the realization of such solids, is based on metal–organic frameworks, MOFs [1]. MOFs have a crystalline nanoporous structure, composed of metal nodes connected by multitopic organic ligands, also referred to as linker molecules. The MOF structure and properties can be tuned and designed by the choice of appropriate components, allowing the fabrication of designer materials with regular pores and large internal surface areas. While conventional solvothermal MOF synthesis results in crystalline powders, using the material in the form of thin films is often beneficial. This is particularly true for focusing on the interaction with light, whose penetration depth in MOF materials is typically in the order of a 1 μm. Among the various methods for fabricating thin film, the layer-by-layer MOF synthesis resulting in surface-mounted metal–organic frameworks (SURMOFs) [2], is attractive, Figure 30.1. SURMOFs are often suited as well-defined model systems, e.g. for uptake and diffusion studies. In addition, the homogeneous SURMOF morphology with a small surface roughness and a low defect density enables spectroscopic investigation of the MOF material in transmission mode. This allows to avoid complex methods like the investigation of the UV–vis absorption in MOF powders by integrating spheres.

Here, we review the state of the art of MOF materials with incorporated photoswitchable molecules. Since light is a simple and practical stimulus, this is a straightforward approach for realizing materials whose properties can be remote-controlled in a fast and clean manner. Generally, there are three methods for integrating photoswitchable molecules in the MOF material: (i) as guests embedded in the pores;

*Molecular Photoswitches: Chemistry, Properties, and Applications*,
First Edition. Edited by Zbigniew L. Pianowski.


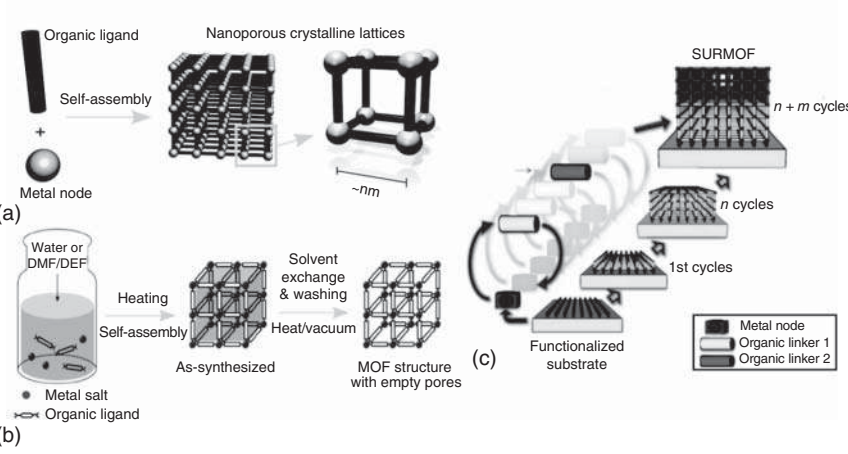


**Figure 30.1 MOF synthesis**. (a) MOFs are ordered scaffolds built from metal nodes (spheres) connected by organic ligands or linker molecules (sticks). (b) Conventional solvothermal synthesis of MOF particles and powders. (c) Sketch of the layer-by-layer SURMOF synthesis. The exchange of the organic linker solution and/or of the metal node solution during the synthesis allows the heteroepitaxial growth of SURMOFs with multilayered structures. Source: Reproduced with permission from refs. [2, 4].

(ii) as functional side group pendant to the linker; (iii) as part of the linker backbone, Figure 30.2 [3]. The opportunities of such photoswitchable MOF materials are discussed.

### 30.1.1 Photochromic Molecules as Guests in the Pores

Numerous photochromic molecules have been explored for immobilization in MOFs. A straightforward method for incorporating photoswitches in MOFs is by simply embedding them as guest molecules inside the pores, often denoted as photoswitch@MOF. In this approach, the major requirement for integration is that the MOF pores be large enough to host the photoswitches [6]. Since several (plain) photoswitches are commercially available, it avoids complex organic syntheses, in contrast to the other approaches.

The embedment of azobenzene (AB) but also of spiropyran (SP), diarylethene (DAE) and stilbene was demonstrated for different MOF structures [5a, 6, 7]. The switching can be verified by UV–vis spectroscopy, using integrating spheres for powder or in transmission mode for thin films, Figure 30.2d. Applying infrared spectroscopy allows the quantification of the switching performance. The photostationary state (PSS) can be determined from the vibration bands, which are typically separate for the different isomers, Figure 30.2e.

The embedment of photoswitches like AB in rigid MOF structures allows the control of the material properties, like the adsorption capacity, see below. Using flexible MOF structures may result in an amplification of the changes caused by the molecular isomerization, as demonstrated for AB embedded in a flexible MOF. The *cis–trans* isomerization of AB by light and heat triggered reversible structural transformations

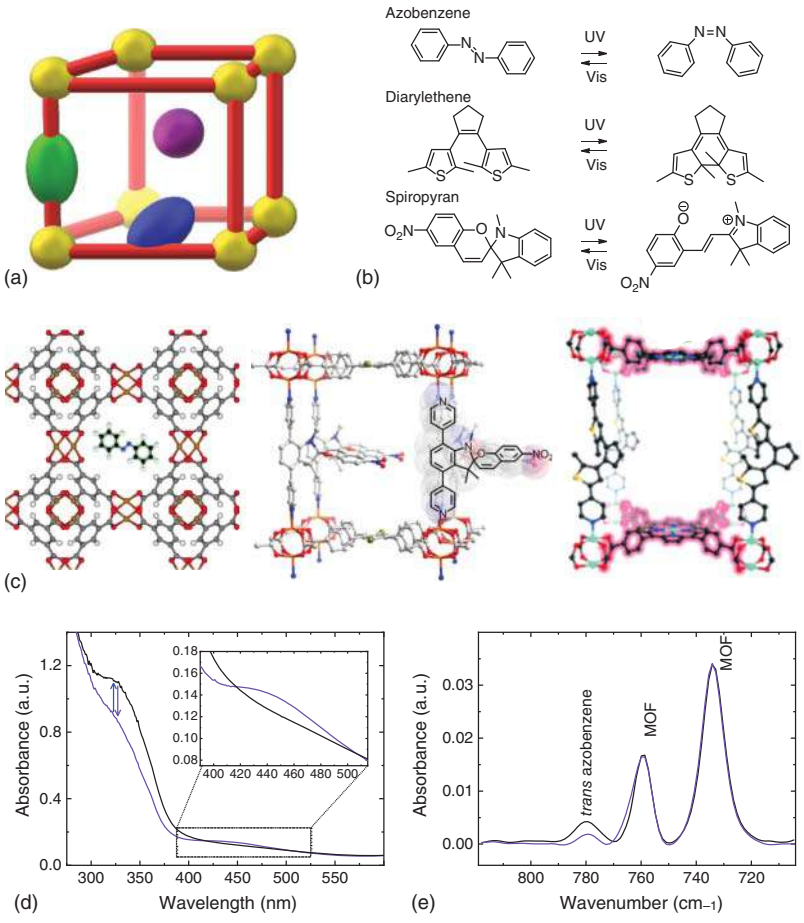


**Figure 30.2 Photoswitches in MOFs**. (a) Schematic representation of photochromic moieties integrated as a guest molecule in the pores (violet), as a side group (blue), and in the framework backbone (green). (b) Three prototype photochromic molecules used for light-responsive MOFs. (c) Three MOF structures with photoswitchable molecules: azobenzene embedded in the pores of MOFs referred to as HKUST-1, spiropyran as side group, and diarylethene incorporated in the linker backbone. The UV–vis (d) and infrared (e) spectra of the HKUST-1 SURMOF with embedded azobenzene. The spectra of the pristine sample with 100% *trans* isomers are shown in black, the violet spectra are obtained after irradiation with UV light, resulting in *trans*-to-*cis* isomerization. Source: (e) Reproduced with permission from Müller et al. [5a]/Royal Society of Chemistry. (c [middle]) Reproduced with permission from Dolgopolova et al. [5b]/American Chemical Society. (c [right]) Reproduced with permission from Park et al. [5c]/John Wiley & Sons.

of the crystalline host framework, resulting in a drastic switching of the adsorption behavior of the porous material (Figure 30.3). Nitrogen adsorption measurements showed the adsorption amount of the composite materials dramatically increased after the UV-induced *trans*-to-*cis* isomerization.

Spiropyran (SP) can undergo reversible isomerization between the colorless "closed" spiropyran and colored "open" merocyanine (MC) form. Because of the

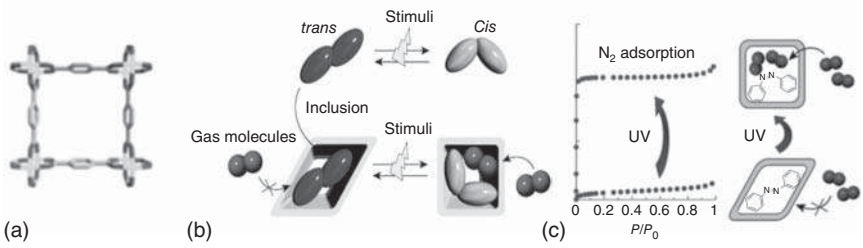


**Figure 30.3 Photoswitch embedded in flexible MOF structure**. (a) MOF referred to as $Zn_2(bdc)_2(dabco)$, which shows structural changes, in particular the angle between two adjacent linkers at one metal node varies, as response to the embedment of different molecules. (b) Schematic illustration of guest-to-host structural transmission. The conformational change in the AB guest molecule by UV light and thermal relaxation triggers a structural transformation of the crystalline host framework. (c) Adsorption isotherms of $N_2$ at 77 K of the composite before and after UV irradiation. Source: (b, c) Reproduced with permission from Yanai et al. [7b]/American Chemical Society. (a) Reproduced with permission from Dybtsev et al. [8]/John Wiley & Sons.

large structural changes going along with the isomerization, the integration of photoswitchable SP in MOFs is difficult. On the other hand, the embedment of SP in the MOF pores is straightforward. A photochromic MOF film with a structure referred to as JUC-120 and SP embedded in the pores was prepared [9]. Attributed to the specific MOF–guest interactions, the open MC form was found to be stabilized in the pores and MC-to-SP isomerization was initiated by UV irradiation. In addition to AB- and SP-based compounds, many other light-responsive molecules like DAE [10], viologen [11], and anthracene [12] were embedded in the pores of MOFs to prepare functional materials. Noteworthy, the MOF hosts, which may have different polarities, can be considered as solid solvent for the photochromic guest molecules, influencing their absorption spectra [13].

### 30.1.2 Photochromic Groups Pendant to the Framework

Many photochromic molecules can be immobilized as side groups pendant to the MOF scaffold. Typically, functional linker molecules with photoswitchable side groups are used for the MOF synthesis [14]; however, the post-MOF-synthesis implementation is also possible. By functionalizing one of the AB phenyl rings with two carboxylic acid groups in *para* position, the molecule can be used as linker for the MOF synthesis resulting in scaffolds with attached AB side groups. Such MOF thin films or powder have proven to allow the photoswitching of various functionalities, see below.

DAE derivatives are attractive photoresponsive moieties integrated into MOFs because of their large changes of the electronic properties, their excellent thermal stability, large fatigue-resistant photochromic performance, and rapid responses in the solid state. A DAE-based MOF, referred to as PSZ-1, showed a reversible photoisomerization between the UV-absorbing open conformation (PSZ-1-open) and the visible-light-absorbing closed conformation (PSZ-1-closed). This MOF was applied

for the separation of aromatic hydrocarbons, including toluene, naphthalene, and pyrene [15].

### 30.1.3 Photoswitchable Moieties in the MOF Backbone

The incorporation of light-responsive moiety in the backbone of the MOF is principally possible. However, the rigidity of the framework often sterically hinders the photoisomerization, in particular when the isomerization goes along with large structural changes. On the other hand, photochromic moieties like DAE, naphthalenediimide (NDI), and viologen, which leads to only small structural changes, can be switched when incorporated in the MOF backbone.

To coordinatively immobilize DAE in the framework backbone of a MOF, the DAE core is modified with anchors such as pyridyl or carboxylic acid groups, which enable coordination to the metal nodes. The DAE photoisomerization process occurs without significant disruption of the framework integrity. Viologen compounds and NDI undergo photoinduced electron transfer, associated with only minute structural changes. Three viologen-based MOFs exhibited reversible photochromism through radical formation caused by photoinduced electron transfer and the potential application of these MOFs as inkless and erasable printing media is suggested [16]. Moreover, due to the drastic color change and photoluminescence quenching accompanied by the photoisomerization process, a porous photochromic Mg-MOF using NDI linkers was used for effective amine detection [17].

## 30.2 Photoswitchable Host–Guest Interaction

Due to the high porosity and well-defined structure, MOFs are among the most promising materials in the field of storage and separation of molecules and molecular mixtures [18]. Moreover, the pores and windows in MOFs offer excellent space for immobilizing photoswitchable molecules allowing the modulation of the mass transfer. Azobenzene (AB) is the most widely investigated photoswitchable molecule for this application. Upon *trans* to *cis* isomerization, a significant structural change occurs, thereby changing the adsorption and diffusion capabilities of the MOF [5d]. Calculation showed that isomerization can also lead to a blocking of the attractive adsorption sites at the metal nodes [19]. In addition to structural changes, the polarity of AB varies, which influences the interaction between the MOF host and polar guest molecules such as $CO_2$ [20] and alcohols [21]. For spiropyran, considering the flexible structure in MC form and the large dipole moment change during SP-MC isomerization, the change of polarity as part of the host–guest interaction is usually the main reason for affecting the MOF adsorption performance and steric effects are believed to have only a minor influence [22]. DAE shares a similar polarity-change-based mechanism with SP [23].

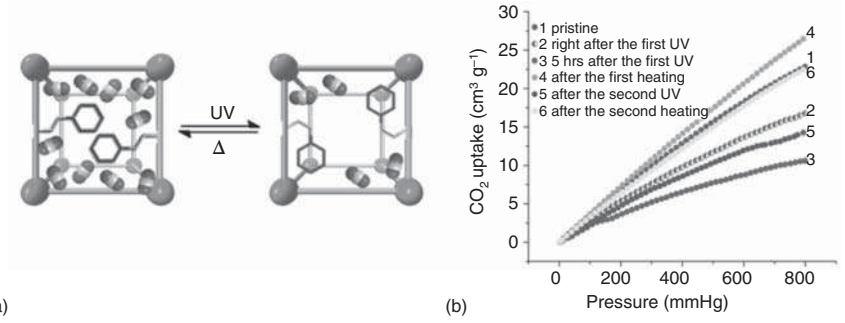


**Figure 30.4 Photoswitchable $CO_2$ adsorption**. (a) AB side groups in the MOF termed PCN-123. While the AB groups in *trans* state allow $CO_2$ adsorption at the metal nodes (right), these adsorption sites are blocked by *cis* AB (left). The adsorption of $CO_2$ is sketched. (b) $CO_2$ adsorption isotherms of the pristine *trans* sample and upon UV-irradiation and thermal relaxation, see legend. Source: Reproduced with permission from Park et al. [25]/American Chemical Society.

### 30.2.1 Photoswitching the Uptake and Release

One of the promising applications of photoswitchable MOFs is to use them as smart adsorbents, with the aim of energy saving and easy handling. Photoswitchable $CO_2$ storage was intensively investigated for its significance in environment protection [24]. A MOF with AB side group was reported to show a $CO_2$ uptake decrease by 26.6% after one hour of UV irradiation, and returned to its original state after thermal relaxation, Figure 30.4. The change of adsorption ability was attributed to the isomerization of the azobenzene to the *cis* form, which blocks the $CO_2$ adsorption sites at the metal nodes [25]. In following works, SP was grafted onto MOF-808 by post-synthetic modification and the $CO_2$ capacity increased by 17.1% upon UV irradiation [26]. A DAE MOF was reported with a $CO_2$ adsorption capacity increase of factor four under UV irradiation, which is the largest on–off ratio presented to date [23].

Controllable adsorption and release of large molecules were investigated with the focus in the application of drug delivery. As an example, light-induced release of propidium iodide using MOFs with one-dimensional pores and AB side groups was demonstrated by irradiation with light of a wavelength close to the isosbestic point, resulting in simultaneous *trans*-to-*cis* and *cis*-to-*trans* isomerizations [27]. Using a nontoxic Zr-MOF with AB in the linker backbone shows photodegradation upon UV-irradiation, causing *trans*-to-*cis* isomerization destroying the scaffold. The controlled light-induced MOF destruction is used to demonstrate the controlled release of Nile Red in HeLa cells [28].

Another application is photoswitchable resolution of chiral compounds. To this end, a MOF with chiral and photoswitchable linkers, namely with D-camphorate and with AB side groups, was prepared, which shows enantioselective adsorption of (*S*)- and (*R*)-phenylethanol. The enantioselective adsorption can be substantially

photomodulated; this means the calculated enantioselective excess (*ee*) can be switched between approximately 7% for the AB *cis* state and 49% for *trans*, although the chirality of the MOF material is not affected [29].

### 30.2.2 Photoswitching the Diffusion in the Pores

The mass transfer of guest molecules in the MOF pores is pivotal for applications in molecular separation and catalysis [30]. The control of the diffusion in photoswitchable MOFs with AB side groups was demonstrated for a two-layered thin film: A two-component SURMOF where the bottom layer is a photo-inactive container layer with a photoswitchable layer on top was prepared, and the uptake of butanediol as probe molecule was measured using a quartz crystal microbalance (QCM). It was found that the diffusion coefficient decreases by a factor 15 when switching the AB groups from *trans* to *cis*. The mechanism is explained by the larger AB dipole moment in the *cis* state that interacts more strongly with butanediol than in *trans* state, slowing down the diffusion [31]. The switching of the diffusion coefficient results in the modification of the permeability of the top layer. This allows to demonstrate the remote-controlled release of molecules from a nanoporous container using the 2-layered-SURMOF.

The mechanics of the diffusion switching was also investigated for MOF powders with AB side groups. It was found for $CO_2$ that the switching of the diffusion rate is caused by changes in the polar interaction, rather than steric effect [32]. The polarity change was also visualized by sensitive probe molecules in the pores.

### 30.2.3 Photoswitching the Membrane Permeation and Separation

As a highly efficient and energy-saving method, membrane separation of liquid or gas mixtures is an attractive research field and has been widely applied in industry. MOFs are seen to be one of the best candidates in this field for their high porosity, uniform but tunable pore sizes, and well-defined molecular adsorption sites [33]. The performance of membrane separation is determined by two factors: selectivity (also called separation factor) and permeability (representing the flux). It was demonstrated that controllable separation can be realized by photoswitchable MOF membranes to change the adsorption/diffusion ability or permeability of one (or more) component in the mixture [20]. A SURMOF membrane with AB side groups was used for photoswitchable separation of $H_2/CO_2$, where the separation factor was photomodified between 3 in *trans* state to 8 in *cis* state. By adjusting the relative intensities of ultraviolet and visible light, the *cis*/*trans* ratio can be precisely controlled, leading to an adjustable selectivity between 3 and 8, Figure 30.5.

For industrial applications, large-area, pinhole-free membranes are required, which are difficult to prepare with the common MOF approaches. A promising solution is mixing photoswitchable MOF with polymers to make mixed-matrix membranes (MMMs), which are easy to fabricate and convenient to scale up. For example, two MMMs with 15 wt% AB-based MOF were reported to show a 5–8% decrease after irradiating with UV light [34].

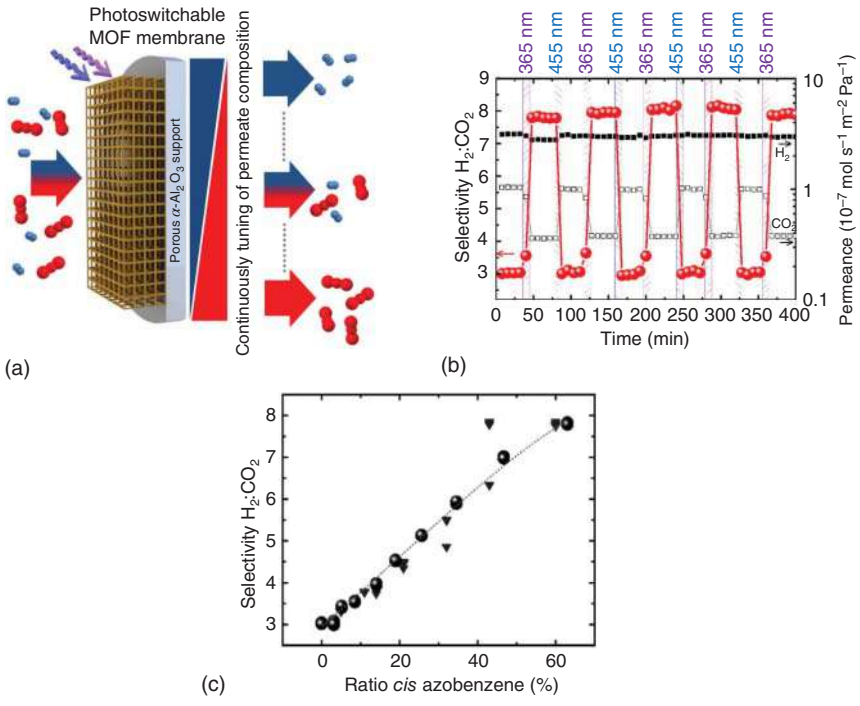


**Figure 30.5 Photoswitchable membrane separation**. (a) Schematic illustration of tunable, remote-controllable molecular selectivity by a photoswitchable MOF membrane. (b) Separation performance of $H_2/CO_2$. (c) The $H_2/CO_2$ separation factor vs. the ratio of *cis* azobenzene, showing the tunability of the separation process.

### 30.2.4 Photoswitching Energy Transfer and Catalysis

Controlled singlet oxygen ($^1O_2$) generation is a widely studied process, attractive for the $^1O_2$ importance in pollution treatment as well as in photochemical synthesis and medical care, like in photo-dynamic therapy. Efficient singlet oxygen generation can be realized by porphyrins. The remote control of the generation rate can be achieved by combining porphyrin with photochromic molecules. It was demonstrated in solution that the closed form of DAE can quench the photoexcitation in Zn-porphyrin, suppressing its catalytic ability of producing $^1O_2$, while the open form shows no effect [35]. This idea was used in photoswitchable MOFs made of DAE and Zn-porphyrin, where the $^1O_2$ generation rate in closed-form DAE is decreased by 30% compared to the open state [5c]. This effect was further applied in photooxidation of 2,7-dihydroxynaphthalene [5c] and photodynamic therapy in melanoma cells [36].

Another example of photomodulated energy transfer in MOFs is demonstrated by loading DAE in luminescent MOF for reversible visible/invisible information transformation. The emission band of $Eu^{3+}$ has spectral overlap with the absorption band of DAE in its closed form, while there is no spectral overlap with the open form. As result, photoswitchable fluorescence resonance energy transfer (FRET) can be

obtained between $Eu^{3+}$ and DAE. So, MOFs made of $Eu^{3+}$ and DAE change their color to blue when switching to the closed form of DAE by UV irradiation, while under daylight they turn back to red, which is the color of $Eu^{3+}$. This MOF was suggested for potential application in security protection [37].

## 30.3 Conduction Photoswitching

The high porosity of MOFs combined with the wide variety of MOF materials as well as the option of designed chemical functionalization and strong chemical stability of several MOF structures have resulted in the exploration of MOFs as functional proton-conducting materials [38]. The implementation of organic (semi-) conducting molecules yields MOF materials with electronic conductivity. The usage of MOF materials as advanced semiconductors has been extensively researched, with numerous electronically conductive MOFs [39].

### 30.3.1 Photoswitching Electronic Conduction

Since the first report on electronically conductive MOFs in 2009 [40], the conductivity of the MOF material was continuously increased, now showing excellent electronic conductivity of more than $10^{-1}\,S\,m^{-1}$ [39a]. In 2018, the first realization of MOF material with photomodulated electronic conductivity was realized based on (somewhat conducting) SP embedded in nonconducting MOF films, Figure 30.6a [41]. As result of UV-light-induced SP-to-MC isomerization, the current increased by a factor 10, Figure 30.6b. Advanced density-functional theory (DFT) calculations show that the conduction occurs via charge hopping between the HOMOs (highest occupied molecular orbitals) of SP and MC. The electronic coupling, and thus the charge-hopping rate and conductivity, dramatically decreases when increasing the molecular SP or MC distance by 1 nm, Figure 30.6c. The plot shows that the electronic coupling is significantly stronger between adjacent SP than between adjacent MC molecules for all molecular distances. The calculation also unveils that the change of electronic coupling is a result of two effects: the molecular length is approximately 0.2 nm longer and the frontier orbitals are significantly more delocalized in MC compared to SP. Both effects result in a higher electronic coupling of MC.

By immobilization of SP at the MOF scaffold, the conduction of a MOF material in the form of powder pressed in pellets can also be modified and a conduction change of approximately 5% was realized [5b]. DAE molecules also show a tremendous modification of the electronic structure upon photomodulation and were used for the photomodulation of the MOF properties [5b].

### 30.3.2 Photoswitchable Protonic Conduction

Proton conduction is fundamental in nature and is pivotal in many technical processes, like in proton-exchange membranes used in fuel cells [42] or sensors [43].

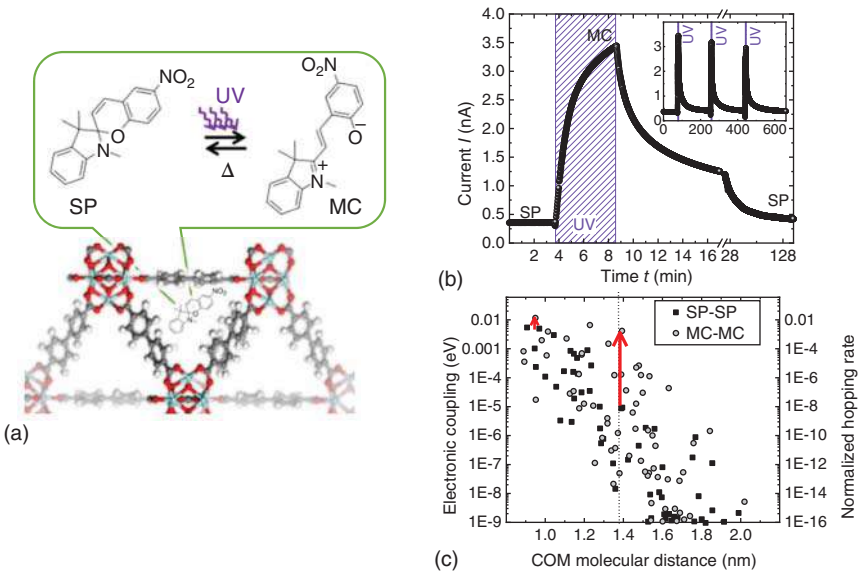


**Figure 30.6** (a) MOF film with a structure referred to as UiO-67 and embedded photoswitchable SP. (b) Current at a DC voltage of +1 V. The sample was irradiated with 365 nm UV light for five minutes, resulting in SP-to-MC isomerization and subsequent thermal MC-to-SP back-isomerization. (c) Calculated electronic coupling between the HOMOs of two molecules in the SP (solid squares) or MC (open spheres) forms as a function of the center-of-mass (COM) molecular distance. The scale on the right-hand-side shows the normalized hoping rate, calculated from the electronic coupling. Source: (a, b) Reproduced with permission from Garg et al. [41].

The application of MOFs as efficient proton conductors has been widely studied, and proton conductivities of up to $10\,S\,m^{-1}$ have been realized. [38]

In the first realization of nanoporous materials with photomodulated proton conductivity, nonconducting SURMOFs with fluorinated AB side groups were used [44]. The pores were loaded with alcohol and triazole as efficient proton conductors, Figure 30.7a. By *trans*-to-*cis* azobenzene photoisomerization, the proton conductivity decreases, for example the proton conductivity of triazole in the MOF pores decreases from $1.2\times10^{-4}\,S\,m^{-1}$ to $7.9\times10^{-5}\,S\,m^{-1}$. Quantum chemical calculations and infrared spectroscopy revealed that in the *cis* state the hydrogen bridge between the azo nitrogen and the guest molecule is stronger compared to the *trans* state, thereby immobilizing the guest molecules. The study showed that the switching is based on the dipole moment change.

To further increase the switching effect, in particular the on–off ratio, photochromic molecules with large dipole moment changes are required, like SP where the dipole moment changes from about 5 D (SP form) to about 16 D (MC form). By anchoring SP to the MOF structure via post-synthetic modifications, a photoswitchable MOF film with large dipole-moment changes was realized. The proton conductivity of the guest, here water, ethanol, and methanol, was photomodulated by up to two orders of magnitude. [45]

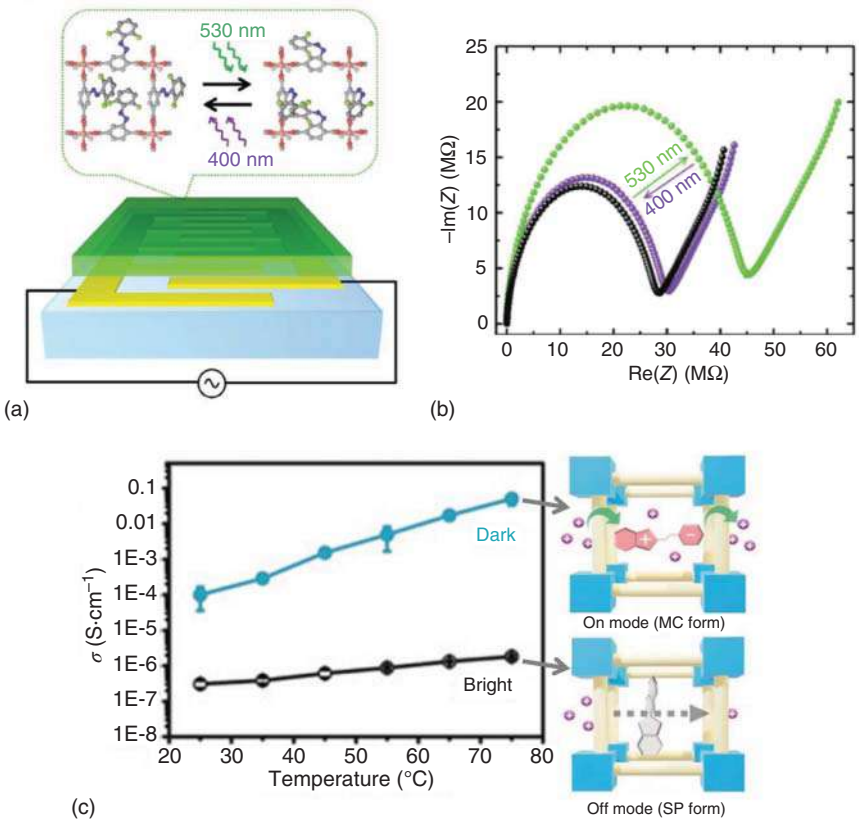


**Figure 30.7 Photoswitchable proton conduction**. (a) Sketch of the SURMOF film (green) on the interdigitated gold electrodes (yellow) on quartz (light blue) substrate. This setup allows the measurement of the proton conductivity of various guest molecules. (b) Nyquist plot of the impedance *Z* of triazole in the SURMOF with azobenzene side groups. The black data are measured for the pristine sample (*trans*), green after irradiation with green light (*cis*), and violet after irradiation with violet light (*trans*). (c) Proton conductivities of the SSP@ZIF-8 membrane in the dark and under irradiation with white light as a function of temperature. On the right-hand side, an SSP in the open MC form (on) and closed SP form (off) in the pore is sketched. Source: Reproduced with permission from Refs. [44, 46]/John Wiley & Sons.

By embedding sulfonated spiropyran (SSP) in the pores of a MOF membrane with ZIF-8 structure, a light-responsive nanoporous membrane working in aqueous solution was obtained, [46] Figure 30.7c. Due to the polar environment, the thermodynamically stable form is the open MC form with mobile acid protons. Upon UV irradiation, SSP is switched to the closed SP form and a dramatic decrease of proton conductivity was observed, Figure 30.7c.

## 30.4 Conclusions

In the last decade, various nanoporous MOFs with different photochromic molecular components, in particular azobenzene, DAE, and spiropyran, have been

presented. These responsive components can be incorporated by embedment in the pores, by attachment as side group or included in the linker backbone. Such MOF materials were used for demonstrating a number of different light-triggered functionalities. The adsorption and diffusion properties were photomodulated, which can be governed either by steric changes in the pore structure or by changes of the electronic structure affecting the host–guest interaction. Based on this, the performance of membranes separating molecular mixtures can be switched and continuously tuned. By controlling the energy transfer in the MOF, the singlet oxygen generation and fluorescence can be affected by light. Photoswitching the functional moieties between isomers with different extensions and energy levels of the frontier orbitals results in a control of the electronic properties of the material. The proton conduction of the guest molecules in the MOF material was modulated over many orders of magnitude by photoswitching the polar interaction in the material. It should be stressed that some functionalities, like the photomodulation of the proton conduction as well as the membrane separation, are novel and have not yet been presented before in any other class of photoswitchable materials. We are convinced that further unprecedented functionalities follow.

For further improvements of the device performance, a better understanding of the switching behavior is crucial. For example, although the PSS, quantifying the maximum switching yield, can be determined for instance by infrared spectroscopy for thin MOF films [5d, 20] or by nuclear magnetic resonance (NMR) or chromatography for MOF powders [47], the PSS is not addressed in many proof-of-principle demonstrations. Due to the strong light absorption by the photochromic molecules and their high density on the MOF material, the light penetration depth is typically in the order of 1 μm. As a result, the entire illumination of powder MOF materials is often not given. Since thin MOF films guarantee the illumination of the entire material as well as the option to prepare such films on essentially all substrates required for detailed investigations and device implementations, we believe that thin well-defined MOF films, like SURMOFs, are an excellent choice for studying the properties of photoswitchable nanoporous materials as well as for exploring their functionalities.

## References


**1** a) Kaskel, S. (2016). *The Chemistry of Metal-Organic Frameworks: Synthesis, Characterization, and Applications*. Wiley. b) Yaghi, O.M., Kalmutzki, M.J., and Diercks, C.S. (2019). *Introduction to Reticular Chemistry: Metal-Organic Frameworks and Covalent Organic Frameworks*. Wiley. c) Furukawa, S., Reboul, J., Diring, S. et al. (2014). *Chem. Soc. Rev.* 43: 5700–5734.

**2** Wang, Z.B., Weidler, P.G., Azucena, C. et al. (2016). *Microporous Mesoporous Mater.* 222: 241–246.

**3** Rice, A.M., Martin, C.R., Galitskiy, V.A. et al. (2019). *Chem. Rev.*

**4** a) Lee, Y.R., Kim, J., and Ahn, W.S. (2013). *Korean J. Chem. Eng.* 30: 1667–1680. b) Forgan, R.S. (2019). *Dalton Trans.* 48: 9037–9042.


5 a) Müller, K., Wadhwa, J., Malhi, J.S. et al. (2017). *Chem. Commun.* 53: 8070–8073. b) Dolgopolova, E.A., Galitskiy, V.A., Martin, C.R. et al. (2019). *J. Am. Chem. Soc.* 141: 5350–5358. c) Park, J., Feng, D., Yuan, S., and Zhou, H.C. (2015). *Angew. Chem. Int. Ed.* 54: 430–435. d) Müller, K., Knebel, A., Zhao, F. et al. (2017). *Chem. Eur. J.* 23: 5434–5438.

6 Schwartz, H.A., Ruschewitz, U., and Heinke, L. (2018). *Photochem. Photobiol. Sci.* 17: 864–873.

7 a) Ohara, K., Inokuma, Y., and Fujita, M. (2010). *Angew. Chem. Int. Ed.* 49: 5507–5509. b) Yanai, N., Uemura, T., Inoue, M. et al. (2012). *J. Am. Chem. Soc.* 134: 4501–4504.

8 Dybtsev, D.N., Chun, H., and Kim, K. (2004). *Angew. Chem. Int. Ed.* 43: 5033–5036.

9 Zhang, F., Zou, X.Q., Feng, W. et al. (2012). *J. Mater. Chem.* 22: 25019–25026.

10 Walton, I.M., Cox, J.M., Coppin, J.A. et al. (2013). *Chem. Commun.* 49: 8012–8014.

11 Zeng, Y., Fu, Z.Y., Chen, H.J. et al. (2012). *Chem. Commun.* 48: 8114–8116.

12 Kitao, T., Hongu, R., Kitagawa, S., and Uemura, T. (2017). *Chem. Lett.* 46: 1705–1707.

13 Schwartz, H.A., Olthof, S., Schaniel, D. et al. (2017). *Inorg. Chem.* 56: 13100–13110.

14 Modrow, A., Zargarani, D., Herges, R., and Stock, N. (2011). *Dalton Trans.* 40: 4217–4222.

15 Furlong, B.J. and Katz, M.J. (2017). *J. Am. Chem. Soc.* 139: 13280–13283.

16 Shi, Q., Wu, S.Y., Qiu, X.T. et al. (2019). *Dalton Trans.* 48: 954–963.

17 Mallick, A., Garai, B., Addicoat, M.A. et al. (2015). *Chem. Sci.* 6: 1420–1425.

18 Li, H., Wang, K., Sun, Y. et al. (2018). *Mater. Today* 21: 108–121.

19 Yang, C.T., Kshirsagar, A.R., Eddin, A.C. et al. (2018). *Chem. Eur. J.* 24: 15167–15172.

20 Wang, Z., Knebel, A., Grosjean, S. et al. (2016). *Nat. Comm.* 7: 13872.

21 Wang, Z.B., Grosjean, S., Bräse, S., and Heinke, L. (2015). *Chemphyschem* 16: 3779–3783.

22 Haldar, R., Heinke, L., and Wöll, C. (2019). *Adv. Mater.* e1905227.

23 Luo, F., Fan, C.B., Luo, M.B. et al. (2014). *Angew. Chem. Int. Ed.* 53: 9298–9301.

24 Leung, D.Y.C., Caramanna, G., and Maroto-Valer, M.M. (2014). *Renewable Sustainable Energy Rev.* 39: 426–443.

25 Park, J., Yuan, D.Q., Pham, K.T. et al. (2012). *J. Am. Chem. Soc.* 134: 99–102.

26 Healey, K., Liang, W.B., Southon, P.D. et al. (2016). *Chem. A* 4: 10816–10819.

27 Brown, J.W., Henderson, B.L., Kiesz, M.D. et al. (2013). *Chem. Sci.* 4: 2858–2864.

28 Epley, C.C., Roth, K.L., Lin, S.Y. et al. (2017). *Dalton Trans.* 46: 4917–4922.

29 Kanj, A.B., Bürck, J., Grosjean, S. et al. (2019). *Chem. Commun.* 55: 8776–8779.

30 Heinke, L. (2017). *J. Phys. D: Appl. Phys.* 50: 193004.

31 Heinke, L., Cakici, M., Dommaschk, M. et al. (2014). *ACS Nano* 8: 1463–1467.

32 Huang, H.B., Sato, H., and Aida, T. (2017). *J. Am. Chem. Soc.* 139: 8784–8787.

33 Qiu, S., Xue, M., and Zhu, G. (2014). *Chem. Soc. Rev.* 43: 6116–6140.

34 Prasetya, N., Teck, A.A., and Ladewig, B.P. (2018). *Sci. Rep.* 8: 2944.


**35** Hou, L.L., Zhang, X.Y., Pijper, T.C. et al. (2014). *J. Am. Chem. Soc.* 136: 910–913.

**36** Park, J., Jiang, Q., Feng, D.W., and Zhou, H.C. (2016). *Angew. Chem. Int. Ed.* 55: 7188–7193.

**37** Li, Z., Wang, G., Ye, Y. et al. (2019). *Angew. Chem. Int. Ed.* 58: 18025–18031.

**38** a) Ramaswamy, P., Wong, N.E., and Shimizu, G.K. (2014). *Chem. Soc. Rev.* 43: 5913–5932. b) Taylor, J.M., Mah, R.K., Moudrakovski, I.L. et al. (2010). *J. Am. Chem. Soc.* 132: 14055–14057. c) Ye, Y., Guo, W., Wang, L. et al. (2017). *J. Am. Chem. Soc.* 139: 15604–15607. d) Yoon, M., Suh, K., Natarajan, S., and Kim, K. (2013). *Angew. Chem. Int. Ed.* 52: 2688–2700.

**39** a) Xie, L.S., Skorupskii, G., and Dincă, M. (2020). *Chem. Rev.* b) Stassen, I., Burtch, N., Talin, A. et al. (2017). *Chem. Soc. Rev.* 46: 3185–3241.

**40** Takaishi, S., Hosoda, M., Kajiwara, T. et al. (2009). *Inorg. Chem.* 48: 9048–9050.

**41** Garg, S., Schwartz, H., Kozlowska, M. et al. (2019). *Angew. Chem. Int. Ed.* 58: 1193–1197.

**42** Kreuer, K.-D. (1996). *Chem. Mater.* 8: 610–641.

**43** Korotcenkov, G., Do Han, S., and Stetter, J.R. (2009). *Chem. Rev.* 109: 1402–1433.

**44** Müller, K., Helfferich, J., Zhao, F.L. et al. (2018). *Adv. Mater.* 30: 1706551.

**45** Kanj, A.B., Chandresh, A., Gerwien, A. et al. (2020). *Chem. Sci.* 11: 1404–1410.

**46** Liang, H.Q., Guo, Y., Shi, Y. et al. (2020). *Angew. Chem. Int. Ed.* 59 (20): 7732–7737.

**47** a) Mutruc, D., Goulet-Hanssens, A., Fairman, S. et al. (2019). *Angew. Chem. Int. Ed.* b) Castellanos, S., Goulet-Hanssens, A., Zhao, F. et al. (2016). *Chem. Eur. J.* 22: 746–752. c) Danowski, W., van Leeuwen, T., Abdolahzadeh, S. et al. (2019). *Nat. Nanotec.* 14: 488–494.


## 31 Molecular Switches and Motors in 2-D

Jiří Kaleta

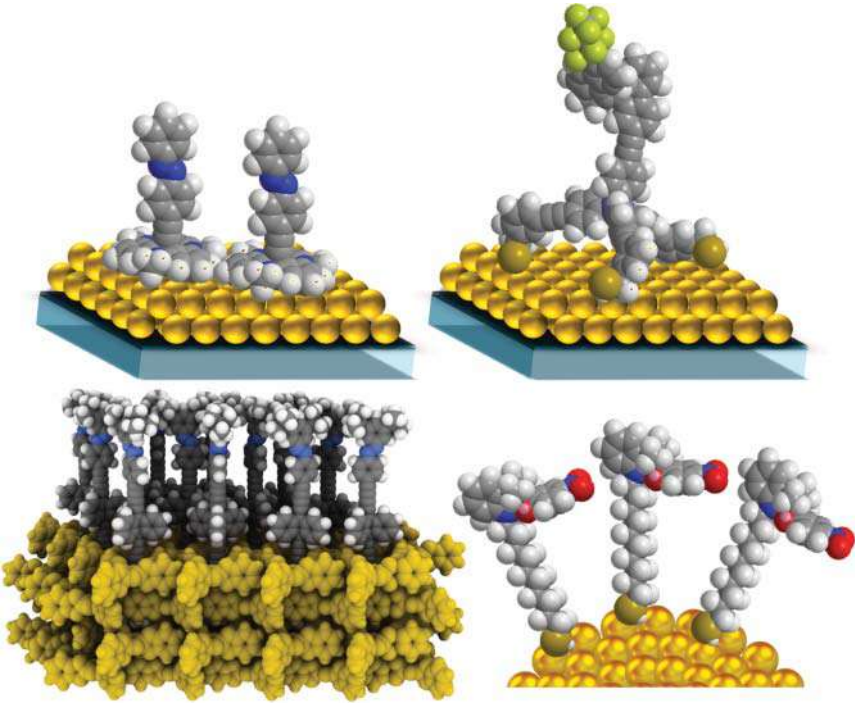

**Characteristic Features**

Two-dimensional self-assembled monolayers of molecular switches or motors on flat or curved surfaces. Structures of individual molecules in combination with the type of surface have a crucial impact on the structure of the film and functionality of the photoactive group.

**First Reported**

*Molecular switches on a flat Au(111) surface*:

Herr, B.R. and Mirkin, C.A. (1994). *J. Am. Chem. Soc*. 116: 1157–1158.

*Molecular motors on a flat and curved Au(111) surfaces*:

Carrol, G.T., Pollard, M.M., van Delden, R., and Feringa, B.L. (2010). *Chem. Sci*. 1: 97–101.

van Delden, R.A., Wiel, M.K.J., Pollard, M.M. et al. (2005). *Nature* 437: 1337–1340.

*Molecular switches and motor in TPP:*

Kaleta, J., Chen, J., Bastien, G., et al. (2017). *J. Am. Chem. Soc*. 139: 10486–10498.

Santos Hurtado, C., Bastien, G., Mašát, M. et al. (2020). *J. Am. Chem. Soc*. 142: 9337–9351.

**Key References**

Klajn, R. (2010). *Pure Appl. Chem*. 82: 2247–2279.

Corra, S., Curcio, M., Baroncini, M. et al. (2020). *Adv. Mater*. 32: 1906064.

García-López, V., Liu, D., and Tour, J.M. (2020). *Chem. Rev*. 120: 79–124.

# 31

# Molecular Switches and Motors in 2-D

*Jiří Kaleta*

*Institute of Organic Chemistry and Biochemistry of the CAS, Flemingovo nám. 542/2, 160 00 Prague 6, Czech Republic*

This chapter focuses on the preparation, formation, structure, and application of 2-D arrays of molecular machines on various surfaces. Self-assembled monolayers (SAMs) of simple organic molecules on mostly metallic surfaces have been known and widely studied for decades, as demonstrated by numerous extensive reviews and books [1–5].

During the last few years, a lot of effort has been also directed toward anchoring much more complex, light-driven molecular machines (switches and motors) onto various surfaces, and evaluating their properties to achieve stimuli-responsible materials. In this text, the term molecular machine usually represents a rather sophisticated molecule consisting of a molecular switch or motor that is connected via some linker to an anchoring group or groups.

Several examples of chromophores representing basic switches/motors that were lately incorporated into numerous sophisticated molecular machines are depicted in Figure 31.1. All of these photoswitches, like azobenzenes, diazocines, hydrazones, spiropyranes, fulgides, fulgimides, diarylethenes, or overcrowded alkenes (usually referred as molecular motors), are very well known from solution chemistry, and thus it is not surprising that there were many attempts to arrange them into (regular) 2-D arrays. In general, these photoswitches are in theory freely transferable between various surfaces, but the structure of linker and anchoring groups has to be properly tuned to fulfill the specific requirements of individual surfaces.

A crucial element to the success of switches and motors is the substrate as they are a key component of two-dimensional systems. The term substrate usually refers to surfaces that are capable of anchoring molecules. Based on their geometry, such substrates can be divided into either (i) planar or (ii) curved systems. Not surprisingly, they differ significantly in properties and will be thus discussed separately.

The following paragraphs will briefly mention characteristic representatives of selected substrates, SAMs that were grown on them, and the pros and cons of individual approaches.

*Molecular Photoswitches: Chemistry, Properties, and Applications*,
First Edition. Edited by Zbigniew L. Pianowski.


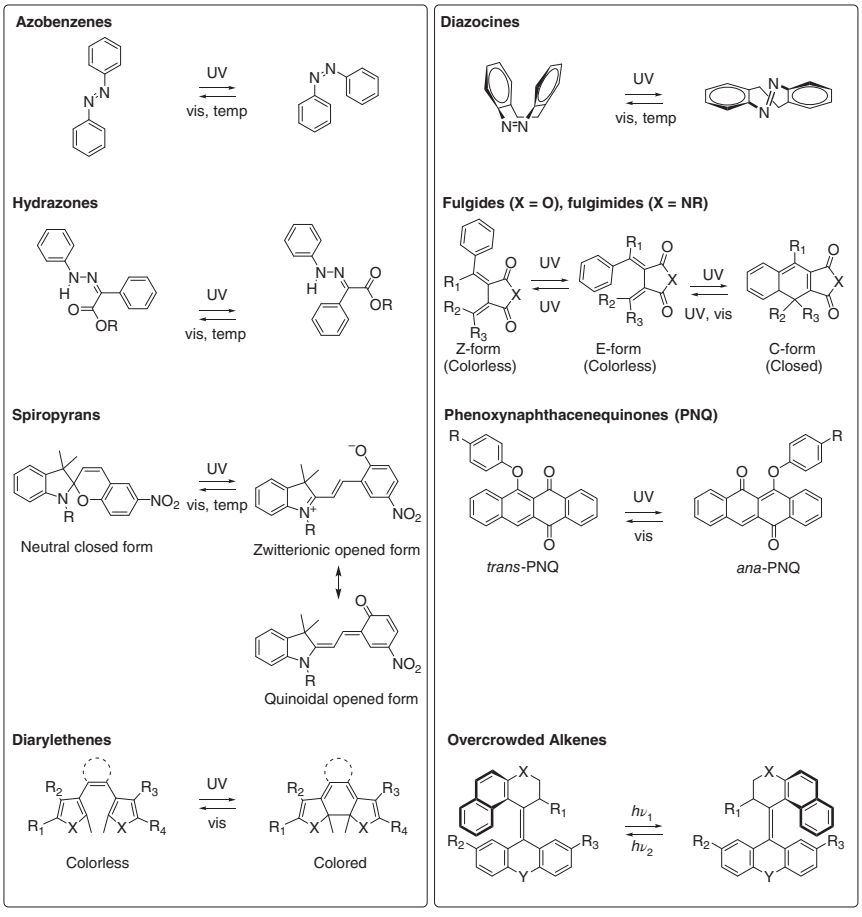


**Figure 31.1** Selected examples of molecular switches and motors that were attached to various surfaces.

## 31.1 2-D Arrays on Planar Substrates

The group of planar substrates covers a broad class of materials ranging from (i) thin films of various metals, to (ii) glass or silicon wafers, and to (iii) organic zeolite-like matrix. The criteria for selecting the type of substrate and method of preparation are highly dependent on the application for which these 2-D assemblies are used.

### 31.1.1 Molecular Machines on Flat Metallic Surfaces

So far, this is probably the most widely used approach. In general, corresponding substrates are easily accessible most frequently by the physical vapor deposition (PVD) methods, electrodeposition or electron beam evaporation of various coinage or noble metals on sheets of glass, mica, silicon, etc. In many cases (particularly if the PVD technique is applied), an interlayer of titanium, nickel, or chromium is

used to facilitate a sufficient adhesion of metals that do not form oxides readily to already-oxidized surfaces (for example glass or silicon with a native layer of oxides).

Although the pool of available coinage and noble metals is relatively broad, the usage of gold still dominates. It is historically the most studied substrate that, in most cases, supports formation of good SAMs. It also has several additional advantages. For one, it is a reasonably stable inert material, as it does not react with most chemicals and atmospheric oxygen. Thus, it can be handled outside the clean room environment. Another advantage is that it can be processed by various lithographic tools. Last but not least, gold (111) substrates are commonly used for numerous analytical techniques and spectroscopies such as X-ray photoelectron spectroscopy (XPS), polarization modulation-infrared reflection-adsorption spectroscopy (PM-IRRAS), Raman spectroscopy, contact-angle goniometry, near-edge X-ray absorption fine structure spectroscopy (NEXAFS), surface plasmon resonance (SPR), atomic force microscopy (AFM), scanning tunneling microscopy (STM), ellipsometry, among many others.

The bare surfaces of metals tend to readily adsorb various organic material because these (usually 2-D) structures lower the free energy of the interface between the metal and the solution [6]. Probably the most widely used anchoring groups that were installed on many molecular machines are still based on sulfur (thiols, thioethers, disulfides, etc.). However, different approaches will be discussed as well.

It is worth mentioning that although thiols have been widely used for decades to bind organic molecules to gold surfaces [1], the nature of this bond is a subject of profound debate. It was believed that a covalent sulfur-gold bond was formed during the SAMs formation, and the fate of the hydrogen atom originally attached to the sulfur remained unclear. However, recent discoveries suggest that the non-chemisorbed gold-sulfur binding probably prevails [7].

Not surprisingly, one of the first molecular machines attached to a gold surface was azobenzene [8] – probably the most studied photoswitch, whose first reversible isomerization in solution was reported already in 1937 [9]. These first prototypes consisted of an aliphatic chain terminated with a thiol group on one end and azobenzene core linked to its second end via an oxygen atom **1** (Figure 31.2) [10].

It was shown that **1** and related molecules form densely packed SAMs, and the packing itself is mostly driven by interactions between azobenzene units. Besides that, individual azobenzenes were ordered in a herringbone pattern, and their short axes were nearly parallel to each other [10–12]. Considering all these facts, it was believed and then also experimentally proven that such densely packed chromophores cannot undergo photoswitching. It is not surprising, since even parent azobenzene in solution requires ~127 $Å^3$ to freely perform *trans*-to-*cis* switching [13]. Later experiments confirmed that the borderline that separates the photochemically inactive SAMs from those that can already perform switching lies approximately at the value of ~40 $Å^2$ per molecule [4, 14, 15]. In other words, this is the minimal area that each linker carrying azobenzene has to occupy, allowing azobenzene to freely undergo *trans*-to-*cis* isomerization on a flat surface. Importantly, this rule does not apply to curved substrates: this number will be smaller for

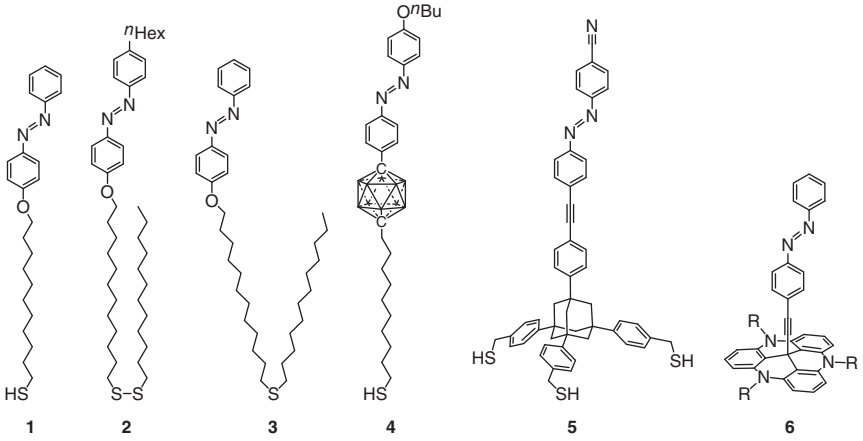


**Figure 31.2** Selected examples of azobenzene-based switches representing various approaches toward photochemically active SAMs.

surfaces with a positive curvature (nanoparticles [NPs]) [16] and larger for surfaces with a negative curvature (SAMs inside nanoporous materials) [17]. This topic was discussed in detail in an extensive review focused on azobenzene-based SAMs on different surfaces, published in 2010 [4].

A lot of effort has been invested into the development of SAMs to guarantee that each functional unit within the SAM will have sufficient free volume to allow for effective photoswitching. There have been several techniques developed during the last decades, and four of them are discussed with representative examples herein.

(1) The first approach was based on a "dilution" of SAMs with short thiols that acted as spacers [18, 19]. In reality, a mixture of two components (a molecular switch and a spacer) were adsorbed to a gold surface, but it was found that the composition of these SAMs sometimes did not reflect the ratio of both compounds in solution. The explanation is in different intermolecular interactions of individual components within SAMs [20]. Another complication that originates from this technique is a phase separation, a usually relatively slow process that turns originally homogeneous samples into systems with strictly phase-segregated domains [21]. Such reorganization also impacted the photoswitching capabilities of SAMs, because only azobenzene units located on the edges of crystalline domains can undergo *trans*-to-*cis* photoisomerization [4].

(2) Undesired phase segregation caused by a migration of thiolates could be in theory suppressed by covalent linkage of a molecular machine with a spacer. Synthetically less demanding approach is based on using either a disulfide or thioether bond (Figure 31.2, compounds **2** and **3**). This second strategy thus mimicked a 1 : 1 dilution, thus providing azobenzene switches a sufficient amount of free space for photoisomerization [4]. Unfortunately, disulfides proved to be unsuitable since their interaction with gold surface caused a splitting of the labile disulfide bond and the formation of a pair of two thiolates. Although the ratio of both components remained the same on the surface,

the phase segregation still remained an issue. In contrast, the use of thioether seems to be promising.

(3) The third technique was based on incorporating the (usually) bulky unit into the backbone of the molecule that generates steric bulkiness and thus separates photoactive units from its neighbors [22, 23]. Compound **3** depicted in Figure 31.2 represents one of these structures, and the steric bulkiness is generated by a spherically shaped 1,12-dicarba-*closo*-decaborane (*p*-carborane) cage. It was shown that SAMs built from **3** exhibit a higher photochemical response than structurally related compounds without a *p*-carborane unit [23].

(4) The fourth approach, which is from the synthetic point of view probably the most demanding, bet on the generation of free volume using specifically designed stands. Figure 31.2 (compounds **5** and **6**) shows only two selected examples [4]. The interchromophore spacing could be thus tuned by the geometry of the used linker/stand. The successful photoisomerization of SAMs formed from azobenzene attached to the adamantane-based tripod **5** was monitored by sum-frequency generation (SFG) vibrational spectroscopy [24]. The cyano group in the *para* position of the phenyl ring in **5** acted as a marker for SFG and permitted a direct measure of the switching states.

It is obvious that the structure of linkers plays a crucial role in designing molecular devices in general. Only intermolecular spacing has been discussed so far, but there is another similarly important factor that needs to be considered. This critical parameter is the strength of the electronic coupling of the molecule to the metallic substrate, since it determines the lifetime of molecular excited states. Switches and motors that are directly bound to a metallic surface are usually considered as photochemically inactive due to their strong coupling with surface. The insertion of a properly chosen linker between the anchoring group and functional unit usually leads to a considerable reduction of this coupling. Deactivation as well as a significant enhancement of photoisomerization was observed, and will be discussed in the following paragraphs.

The introduction of triazatriangulenium-based platforms (usually abbreviated as TATA) to the scientific community represented another milestone in mounting molecules onto surfaces [25]. These platforms act as pedestals that hold functional groups oriented perpendicularly toward the surface. This versatile concept utilizes stable and easily accessible TATA cations as starting units that can be converted to final products (like **6** in Figure 31.2) by reaction with corresponding acetylides. In contrast to previous approaches, the requirement for achieving free volume for photoisomerization is not due to packing constraints within the SAM, but instead due to a broad molecular stand [25]. The distance between individual stands can be tuned by side chains R (Figure 31.2) of different steric demands that can be easily incorporated into a TATA cation during its synthesis [25].

Further extension of this concept led to a broad family of TATA derivatives (Figure 31.3), sometimes with unexpected properties. The methoxy marker group in **7** allows monitoring of photoswitching in SAMs by IRRAS [26]. Based on the changes of intensity of $C_{(phenyl)}$–O(Me) stretching band in IRRAS, it was found

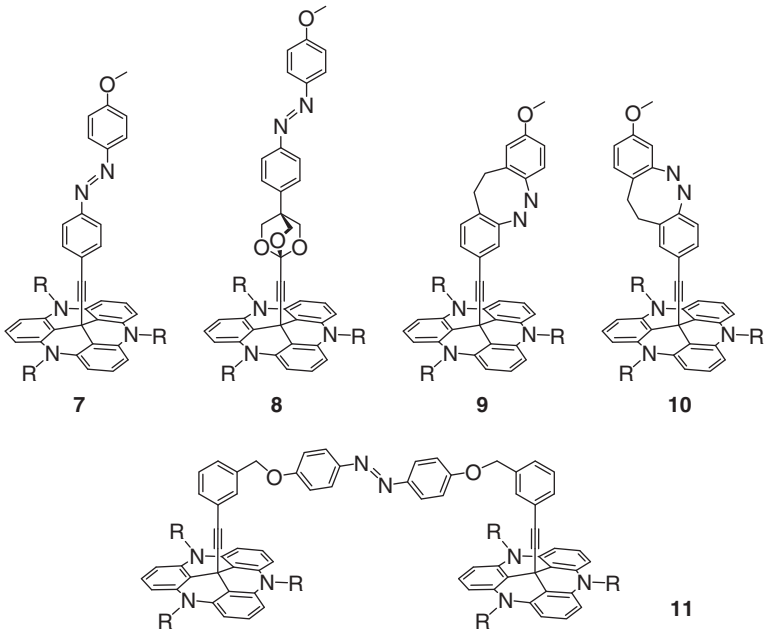


**Figure 31.3** Several examples of TATA-derived molecular switches and rotors that were anchored to Au(111) surface.

that a methoxy group is oriented perpendicular to the surface in *trans*- and tilted with respect to surface in *cis*-configuration. In combination with surface-enhanced Raman spectroscopy (SERS), it was also found that the *cis*-to-*trans* isomerization is roughly $10^3$ faster with respect to **7** in solution [26].

Further investigation of this phenomenon led to the discovery of an unusual case of surface catalysis involving azobenzenes in contact with an Au(111) surface [27]. A series of molecular switches containing both conjugated and non-conjugated units interconnecting azobenzenes with a TATA platform were synthesized. Conjugated units (like 1,4-disubstituted benzene) were responsible for a great acceleration of *cis*-to-*trans* isomerization (almost 1300 times compared to samples in solution), while incorporation of rigid aliphatic systems like 2,6,7-trioxabicyclo[2.2.2]octane in **8** (Figure 31.3) provided sufficient decoupling from the surface. The authors showed that for the strongly coupled systems, the relaxation rate depended on the spin-density distribution in the triplet states of the molecules. This suggested that an intersystem crossing is involved in the relaxation process [27].

To examine this mechanism in more detail, two diazocine derivatives **9** and **10** (Figure 31.3) were synthesized [28]. Diazocines, in contrast to azobenzenes, are stable in the *cis*-configuration (Figure 31.1), and their irradiation leads to an unstable *trans*-form. To investigate the *trans*-to-*cis* isomerization as a function of the conjugation to a metal surface, a diazocine core was linked to a TATA stand using acetylene unit in *meta* (**8**, weak conjugation) and in *para* (**9**, strong conjugation) positions. So far, only SAMs were prepared, and kinetics studies are a subject for further studies [28].

The interconnection of two TATA platforms using symmetrically *para*-substituted azobenzene led to derivative **11** acting both as a molecular switch and rotor [29]. This compound formed well-organized SAMs on Au(111) with the azobenzene units parallel to the surface. Spectroscopic data supported by the DFT computations suggested that in the *trans* configuration, the azobenzene unit is freely rotating. Irradiation with UV light caused reversible isomerization to the bent *cis* configuration, and rotation stopped [30].

Although simple aliphatic thiols have several drawbacks, they are still often used as linkers, mostly due to their relatively easy synthetic accessibility. As azobenzenes are probably the most studied of these systems, they have been discussed here at length. The paragraphs that follow discuss other types of photoswitches and motors.

The switching of a hydrazone derivative **12** containing a hexyl spacer (Figure 31.4) was tested on three different substrates: Au, Ag, and Cu. The half-life of thermal relaxation of **12** (Figure 31.1) in solution was found to be 789 years [31]. In contrast, corresponding SAMs exhibit drastic acceleration of half-life, and a value of 6.9 days was determined by tip-enhanced Raman spectroscopy (TERS) on a gold surface. It was also found that **12** can be switched on the Au and Cu surfaces once irradiated with 415 nm, although it cannot isomerize on an Ag surface unless higher energy light is used [31].

An approach based on co-adsorption of phenoxynaphthacenequinones (PNQ)-based photoswitches **13** (Figure 31.4) with tetradecanethiol to a flat surface of gold electrode led to a densely packed monolayer with rigidified orientation of the quinone units in the monolayer assembly [32]. PNQs undergo reversible photoisomerization between *trans*- and *ana*-form (Figure 31.1), and both forms also have a distinct electrochemical signature. The corresponding SAM thus gave a quasi-reversible redox wave of the quinone unit in the *trans*-form. Upon irradiation with UV light, the *ana*-form was formed, and the interface became

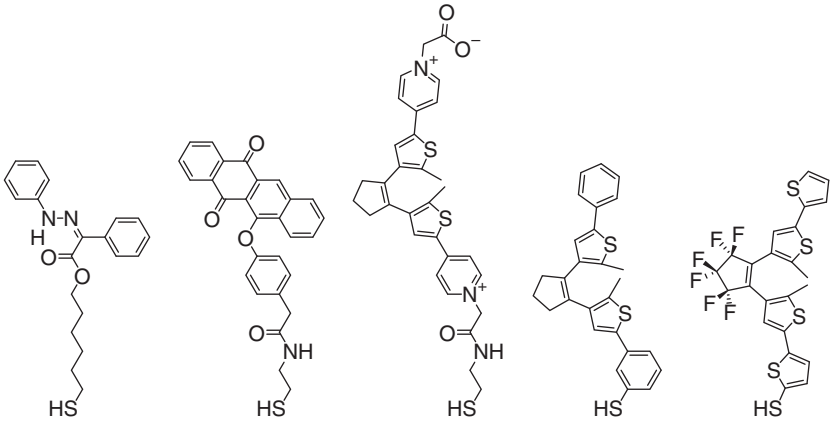


**12** **13** **14** **15** **16**

**Figure 31.4** Selected examples of molecular switches designed to form SAMs on a gold surface.

nearly redox inactive. Subsequent irradiation with visible light led to the restoration of *trans*-isomer and redox activity. This allows the application of such SAMs of molecular photoswitches as a read/write memory device, since both the writing and reading of information are done by two different physical signals [32].

Another group of widely studied chromophores belongs to the diarylethene family. They are represented by compounds **14**, **15**, and **16** in Figure 31.4. SAMs based on **14** (similarly as those formed from **13**) on gold electrodes were shown to be potential candidates for write-read-erase memory devices [33]. The open form of **14** was electrochemically cyclized. This process represented writing information, and the same technique was also used for its reading. Stored information was erased photochemically when the cyclized form of **14** was converted back to acyclic by simple illumination [33].

Examination of photochemical and electrochemical switching of structurally related **15** and **16** in SAMs on gold electrodes revealed that these properties are sensitive to the molecular structure of the switch [34]. For **15**, both the photochemical ring opening and closing were observed in SAM, while for **16**, the photochemical properties were changed markedly compared with those in solution. These results demonstrated that the distance between the surface and the photochromic unit is, in this particular case, less important than the nature of the specific interaction of the compound with the surface (weak conjugation mediated via *meta*-substituted benzene in **15** versus strong conjugation in 2,5-disubstituted thiophene **16**) [34].

Much effort has been directed toward anchoring molecular motors on metallic surfaces and evaluating their rotary properties to develop stimuli-responsive interfaces. The structure of enantiomerically pure **17** represents the first azimuthal molecular motor based on overcrowded alkene that was attached to a flat gold surface (Figure 31.5) [35]. Molecular motors in general consist of two parts: the stator and rotor. By definition, a stator is the immobilized part of a device, while the rotor is the rotating unit. Therefore, there are two aliphatic legs attached to the anthracene stator in **17**, ensuring that the light-driven rotation of the rotor will not cause a rotation of the whole molecular motor. These SAMs were grown on a semi-transparent 5 nm thin gold film deposited on quartz to minimize the optical absorbance of the metal layer. This allowed for the detection of the photochemical and thermal steps in the rotary cycle by circular dichroism spectroscopy. Unfortunately, it was shown that **17** cannot operate in single-component nor in mixed SAMs even once diluted with decanethiol in a 1 : 10 ratio. A plausible explanation for the absence of photochemical isomerization is an energy transfer from the excited state **17** to the gold surface (although phase segregation was not excluded) [35].

In contrast, the elongation of aliphatic legs in **17** gave compound **18**, whose molecular motor can already operate once organized into SAMs on flat gold surfaces. The full 360° rotation cycle was monitored by CD. The incorporation of an additional eight methylene units thus provided sufficient decoupling from the flat metallic surface [35].

To modulate physical surface properties like wettability or adhesion, the rotating part of the motor must change position dramatically toward the surface during its rotation cycle. Azimuthal motors (e.g. structures **17** and **18** in Figure 31.5) cannot

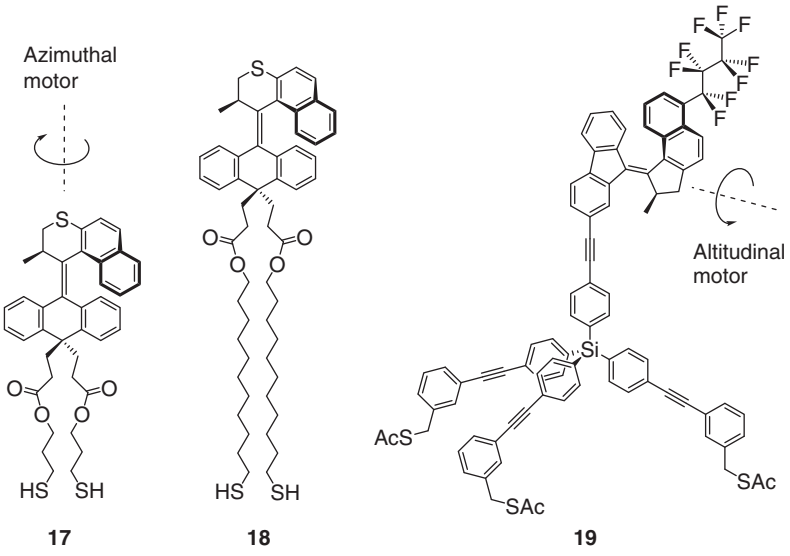


**Figure 31.5** Examples of azimuthal and altitudinal light-driven unidirectional molecular motors forming SAMs on Au(111) surface.

generate such a large effect. In contrast, the geometry of the longitudinal motor **19** (Figure 31.5) should guarantee more dramatic changes of the surface properties [36].

Compound **19** consists of a second-generation light-driven molecular motor whose indene rotor is equipped with a perfluorobutyl chain, while a fluorene-based stator was placed on the top of a tripodal stand. This tripodal stand effectively separates it from the metal surface. Water contact-angle measurements were performed on SAMs of **19** anchored to a gold surface to determine the wettability of the monolayer. The contact angle of $82 \pm 1°$ was achieved when hydrophobic perfluorobutyl chains were exposed to the interface. A light-triggered rotation then brought the perfluorinated unit closer to the gold surface, and the protiated part of the rotor was on the interface, making the surface more hydrophobic as demonstrated by a decrease of the contact angle to $68 \pm 1°$ [36].

### 31.1.2 Molecular Machines on Glass, Mica, or Silicon Wafers

While the formation of 2-D assemblies on noble metals mostly relies on sulfur-based ligands, different approaches were used to attach various molecular machines on glass, mica, or silicon substrates. These surfaces could be used either (i) neat, and thus SAMs are physisorbed on them, or (ii) chemically modified, allowing the covalent or electrostatic binding of ligands.

It is worth mentioning that the free volume requirements for successful switching/rotation on flat surfaces that was discussed a few paragraphs above only apply to molecules, which are strongly bound to substrates. In contrast, physisorbed molecules lack the strong interaction between the anchoring group and substrate, thus allowing molecular diffusion, which leads to the complete

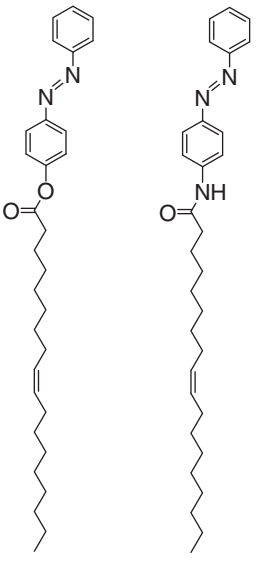


**Figure 31.6** Azobenzene switches forming physisorbed SAMs on mica.

(photo)isomerization of the molecules constituting the SAMs. This can be nicely demonstrated on the pair of compounds **20** and **21** that differ only in connection between azobenzene switch and aliphatic chain (Figure 31.6) [37]. The amide functionality in **21** is responsible for intermolecular hydrogen bonds that are stabilizing corresponding 2-D films. Both structures formed SAMs on a mica surface using a spin-coating technique, and the thickness of these films was found to be ca. 3.5 nm, based on AFM (the calculated length of molecules was ca. 3.1 nm meaning that they are vertically adsorbed at a distance between 0.2 and 0.5 nm from the mica surface). The scale or the density of SAMs was not affected by the absence (**20**) or presence (**21**) of hydrogen bonds. Illumination of the samples by UV light caused a reduction of thickness by 0.5 nm, as shown by the AFM profile measurement. This variation corresponded to the reduction of the length of the molecule due to *trans*-to-*cis* isomerization, since the length of *trans* isomer is ca. 3.1 nm, while the *cis* is only 2.7 nm. Loosely packed **20** resulted in homogeneous films, while **21**, whose films were interlinked by a network of hydrogen bonds, contained defects attributed to the formation of domains. Subsequent thermal relaxation led in both cases to a full retention of molecular thickness as well as to obtaining homogeneous 2-D films [37].

In many cases, there is a need for a strong anchoring of SAMs to a glass, quartz, or silicon substrate whose surface has to be thus properly activated, and current literature offers several ways to do that [3, 38]. The connection of molecular machines is then usually mediated via additional SAMs formed from aliphatic chains that are directly connected to the surface on one end, while the second end of chain is terminated with a reactive group. This concept will be demonstrated with four examples.

The silicon surface, modified with carboxylic functions, was coupled with an indolyl fulgimide-based switch **22** equipped with a primary amine anchor (Figure 31.7) [39]. Fulgimide photoswitching (Figure 31.1) was monitored by FTIR

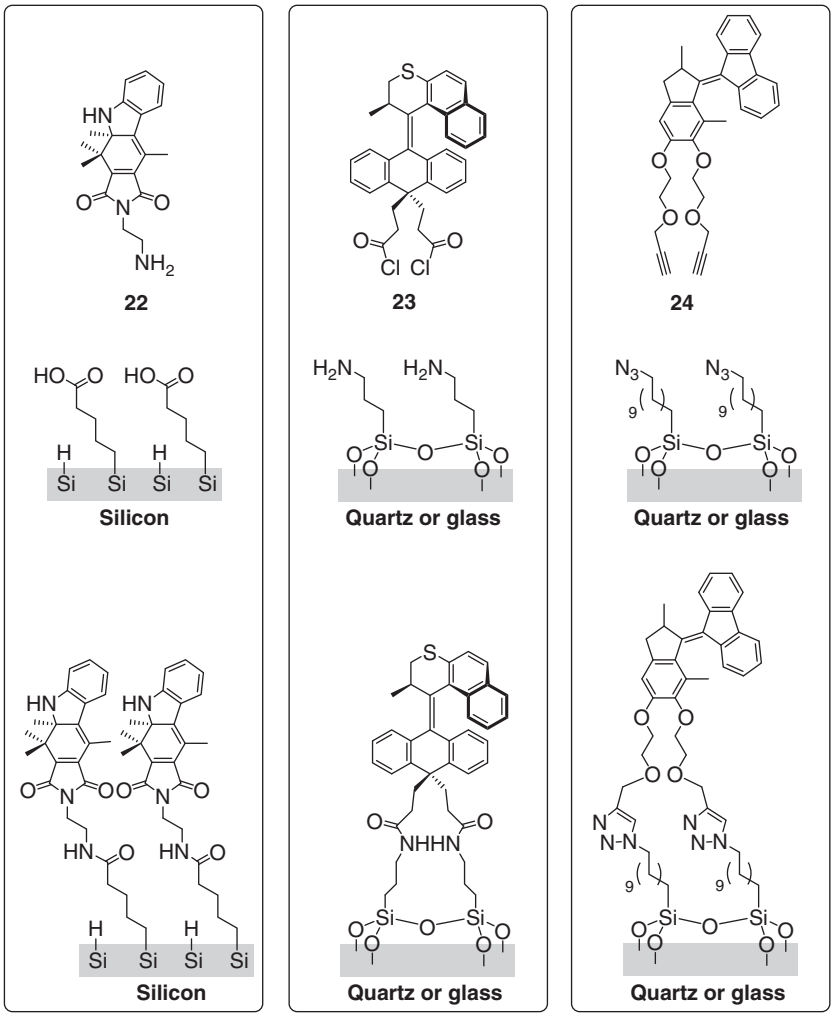


**Figure 31.7** Molecular switch **22** and azimuthal **23** and altitudinal **24** motors grafted onto silicon, quartz, or glass surface.

on the surface, and the data showed that the photoisomerization remained efficient and reversible, and the composition at the photostationary state was close to those found in solution [40].

The azimuthal molecular motor **23** was grafted onto quartz and glass surfaces using amide bonds. The substrate was coated with 3-aminopropyl groups, while **23** carried two legs terminated with acid chlorides [41]. The same strategy based on utilizing two anchors, which was already used in analogous **17**, guarantees the immobilization of stator. Light-triggered photoisomerization only caused a rotation of the naphthalene rotor and not of the whole motor unit. The advantage of quartz compared to gold is that the quenching of the photoisomerization by the surface can

be excluded. The full 360° rotation cycle of the anchored unidirectional **23** was then monitored by CD [41].

The Cu-catalyzed 1,3-dipolar cycloaddition between alkyne-terminated **24** and azide-substituted substrates (an inversed arrangement with alkyne-substituted surface and an azide carrying motor was also used) afforded a 2-D array of altitudinal motors (Figure 31.7) [42, 43]. The surface attachment was characterized by UV–vis, infrared (IR), and XPS. It was found that photochemical and thermal isomerizations are consistent with unidirectional rotation in solution. The rate-limiting step of rotation, the thermal isomerization, was dependent not only on surface coverage of the rotors, but also confinement that notably reduced the rate of the thermal isomerization process. The changes in kinetics from solution to surface were attributed to the interactions between the surface-bound motors [43].

Electrostatic interactions mediated via the amine-coated surface and four tetrapodal carboxylate legs guaranteed a relatively firm grafting of **25** to a glass substrate

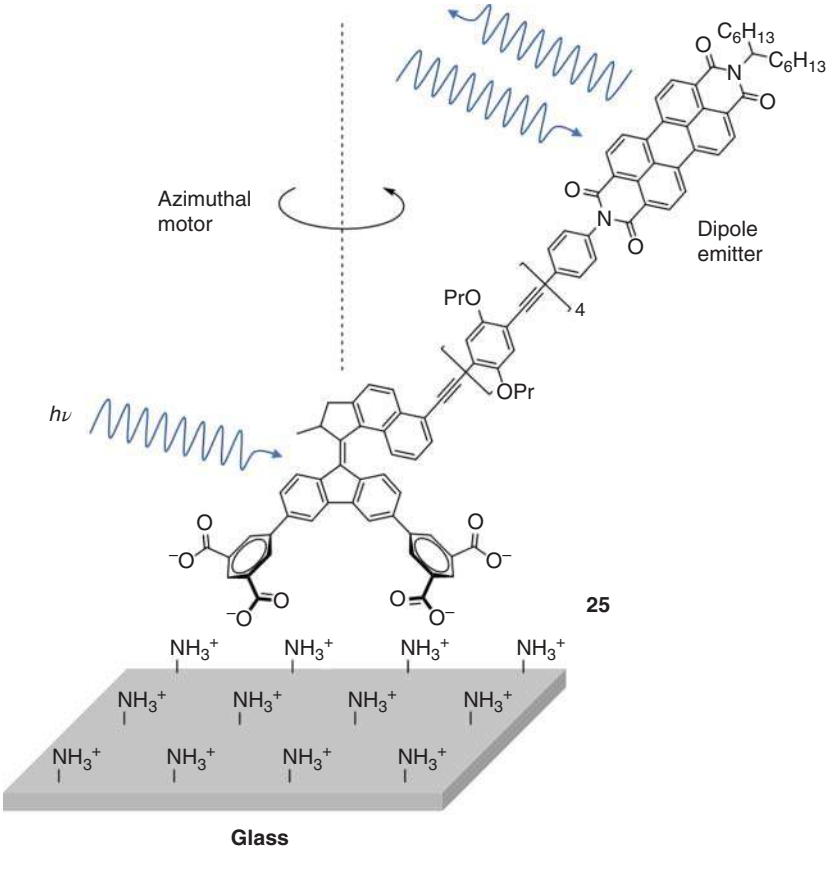


**Figure 31.8** Azimuthal molecular motor **25** bound to a modified glass surface. Source: Modified from Krajnik et al. [44].

(Figure 31.8). This complex azimuthal molecular motor, whose stator was immobilized on the surface, contained an indene-based rotator equipped with a long, rigid, phenyl-ethylene tentacle that was terminated with a perylene diimide fluorophore [44]. The main purpose of this long linker was to avoid fluorescence quenching of the motor by the perylene-based dipole emitter. The defocused wide-field imaging technique was used to monitor the rotational motion of individual synthetic molecular motor at interfaces for the first time. One laser beam ($\lambda_{ex} = 375$ nm) drove the rotation of the motor molecules, while a second one ($\lambda_{ex} = 532$ nm) induced fluorescence of the perylene diimide dipoles. One of the drawbacks of such electrostatically bound machines was their partial dissociation and reassociation with the surface during the ratcheted thermal helix inversion step [44].

### 31.1.3 Molecular Machines on a Zeolite-Like Matrix

This specific approach is based on attaching molecular machines to flat facets of a nanocrystalline hexagonal polymorph of an organic matrix called tris(*o*-phenylenedioxy)cyclotriphosphazene (usually abbreviated as TPP). This approach falls between a standard flat surface approach and an approach that uses nanoparticles because it combines certain aspects of both techniques: the regularly ordered surfaces that are characteristic for metallic substrates with small particle sizes that are typical for highly curved surfaces that will be discussed later.

The TPP is a spirocyclic compound that crystallizes in layers that contain pores with a trigonal cross-section. Each of these ~5 Å thick layers is rotated 60° toward the previous one, resulting in a mica-like material that contains a regular network of long, hexagonally shaped channels (Figure 31.9). They are in a trigonal arrangement, parallel to each other, and are interconnecting two opposite facets of TPP nanocrystals. The distance between the centers of the neighboring channels is ~11 Å and the internal diameter is ~5 Å [45].

This easily accessible white crystalline material is UV transparent above ca. 280 nm [46], thus allowing direct measurement of the UV–vis spectra of properly chosen mounted chromophores. It is also frequently used in perdeuteriated form (TPP-$d_{12}$), since the absence of protons simplifies the study of the guest molecules by solid-state NMR technique. Deuteriation suppresses the $^{13}C$ signals of the matrix

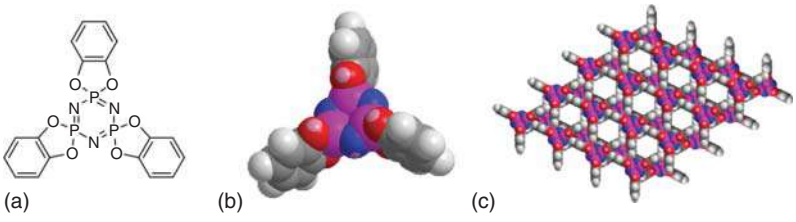


**Figure 31.9** Structure of TPP-$d_{12}$ molecule (a), space-filling model (b), and a top view of a fragment of two successive layers of a hexagonal polymorph (c) with characteristic channels in a trigonal arrangement.

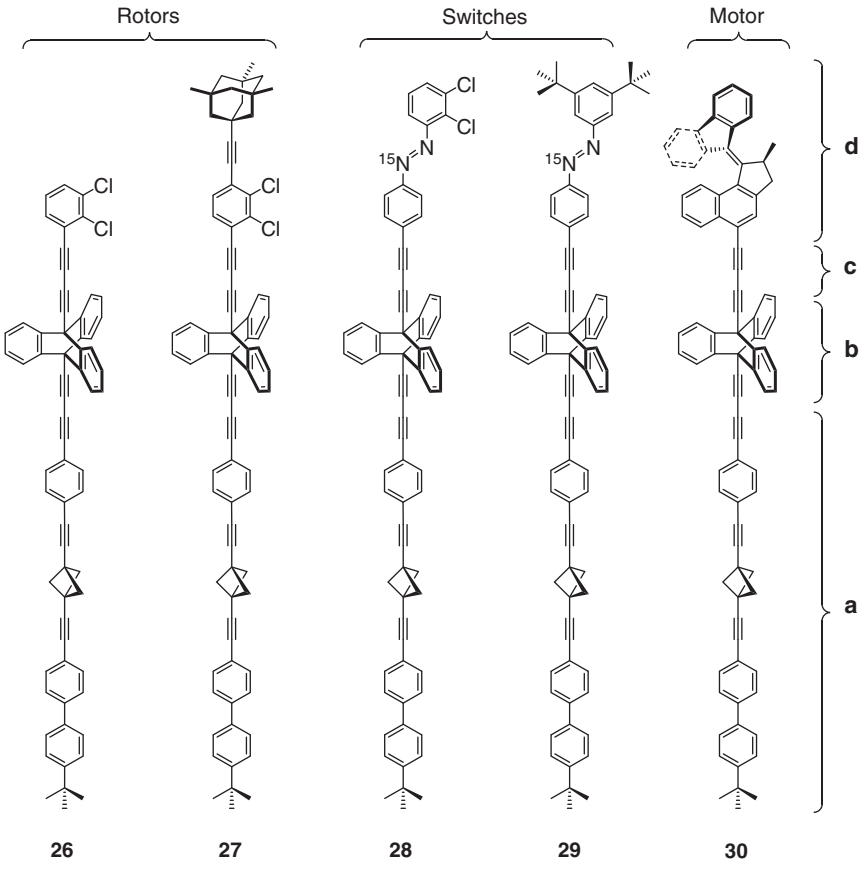


**Figure 31.10** Molecular dipolar rotors **26** and **27** [51], switches **28** and **29** [52], and motor **30** [53] specifically designed to form surface inclusions in TPP-$d_{12}$.

during $^{13}C$ cross-polarization NMR experiments and thus simplifies the assignment of the guest carbon atom resonances.

It has been known for decades that the zeolite-like structure of a hexagonal TPP polymorph can host various guest molecules that are accommodated inside its pores [47–50]. The specific design of the guest molecules leads to so-called surface inclusions, where only facets of TPP nanocrystals are decorated with molecular-level devices and the rest of the channel is empty. The first prototype leading to true surface inclusions was introduced in 2015 [51], and more advanced molecular machines were published later (Figure 31.10) [52, 53].

All these complex rod-like molecular-level devices share several characteristic motives:

(a) *Nonpolar shaft* that serves two main purposes – it firmly anchors molecules inside the TPP channel, and it contains two aliphatic units – *tert*-butyl group

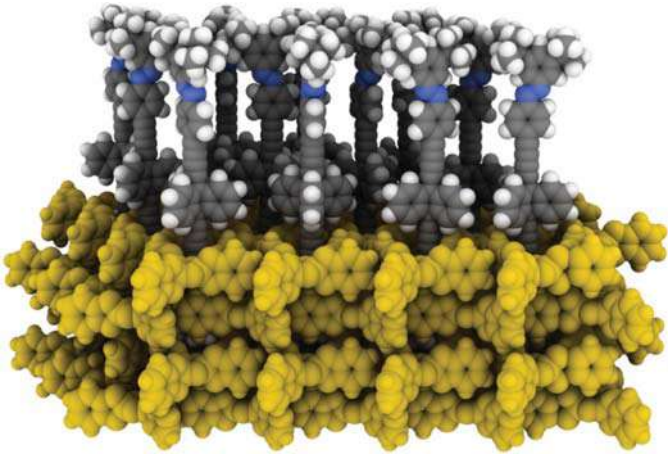

**Figure 31.11** Visualization of a regular array of molecular switches **29** anchored to a facet of hexagonal TPP-$d_{12}$. The TPP matrix is highlighted in yellow for clarity.

on one terminus and bicyclo[1.1.1]pentyl cage in the central part. Their characteristic $^{13}C$ chemical shifts are used to determine the depth of insertion into the matrix using solid-state NMR spectroscopy.

(b) *Triptycene*, whose equatorial van der Waals diameter (~11.6 Å) is significantly larger than the internal diameter of the TPP channel (~5 Å), acts as a stopper that prevents complete insertion into the matrix.

(c) *Butadiyne axis* separates functional units (d) from the surface, and facilitates synthetic manipulation.

(d) *Functional units* are the real heart of these molecular devices. Not surprisingly, their van der Waals diameter must be larger than the diameter of TPP channel to prevent insertion in a wrong direction. Structures **26** and **27** contain electrically driven dipolar rotors, and thus will not be discussed. In contrast, the remaining three structures are based on light-triggered systems (azobenzene-based switches **28** and **29**, and unidirectional molecular motor **30**).

Corresponding inclusions (Figure 31.11) are obtained during a mechanochemical reaction that is based on the ball-milling of both components (molecular machines and TPP matrix), and are usually followed by annealing at 80 °C for 24 hours.

The distribution of individual guest molecules on the TPP surface is dictated purely by the geometry of this matrix, since each molecular machine occupies one entrance to the channel in saturated systems. Their vertical axes that are defined by carbon–carbon triple bonds are thus ~11 Å apart within a 2-D film, and should be oriented perpendicular to the surface (although calculations suggest a slight tilting in some cases) [52]. Such separation guarantees enough free volume, and both molecular switches **28** and **29** as well as motor **30** can operate nearly as freely as individual molecules in solution. These experimental observations were confirmed also theoretically: the periodic boundary condition calculations predict a very

weak packing effect on the isomerization energy (up to ~2 kcal $mol^{-1}$) for arrays of switches **28** and **29**.

One of the advantages of using TPP instead of the previously discussed metallic surfaces is that the quenching of photoisomerization by the metallic surfaces can be completely ruled out. A relatively small size of discoidal TPP nanocrystals (~50 nm in diameter and ~20 nm thickness) [51–53], together with their relatively high monodispersity, allows the investigation of photoisomerizations in 2-D films using standard spectroscopic techniques like UV–vis (acquired on samples suspended in proper media) or solid-state NMR.

Selective installation of $^{15}N$ into the azobenzene moiety of **28** and **29** allowed for the detection of *cis*/*trans* isomerization for the first time in the 2-D film by the $^{15}N$ solid-state magic-angle spinning (MAS) technique.

The anchoring of molecules on the surface of TPP nanocrystals has several drawbacks, however. One of them directly originates from the mechanochemical reaction leading to these host–guest complexes. Ball milling reduces the size of TPP nanocrystals, and thus the size of available crystal facets. It was estimated that an ideal flat and defect-free facet of TPP can accommodate ca. 300–1100 molecules on each side [53]. The second issue is related to the (ir)regularity of occupancy of TPP channels. Although the degree of surface saturation is routinely controlled by mixing both components (solvent-free TPP and guest molecules) in defined ratios, the distribution of individual molecules within the surface is still a random process.

## 31.2 2-D Arrays on Curved Substrates

Surfaces with a positive curvature that are represented by nanoparticles (NPs) have been widely studied, as documented by a remarkable number of research articles published in recent years. Unfortunately, it is far beyond the scope of this chapter to discuss all aspects of such a dynamically expanding field. Thus, only a few representative examples demonstrating different behaviors of the SAMs of molecular machines on flat and curved metallic surfaces will be mentioned.

The coating of NPs with the SAMs of molecular switches is an attractive topic because it opens the possibility of making reversible changes to the properties of the NPs (solubility, fluorescence, etc.) by external stimuli like light [54]. Not only the coating, but also the size of NPs has a significant impact on their properties, thus allowing the fine tuning of the final materials by a careful selection of individual parameters.

The formation of SAMs on NPs is a relatively straightforward process: small gold NPs (< 10 nm), covered by a weakly bound "sacrificial" stabilizing ligand (that prevents them from undesired aggregation), are dispersed in a thiol-containing solvent. Initial ligands are then displaced due to the strong specific interaction between gold and alkanethiols. In contrast, larger gold NPs (> 10 nm) usually aggregate upon the coating with normal alkanethiols. Undesired aggregation is one of the drawbacks, which has traditionally been associated with NPs. Although the surface of gold NPs could be modified by a variety of ligands, the usage of simple linear aliphatic chains

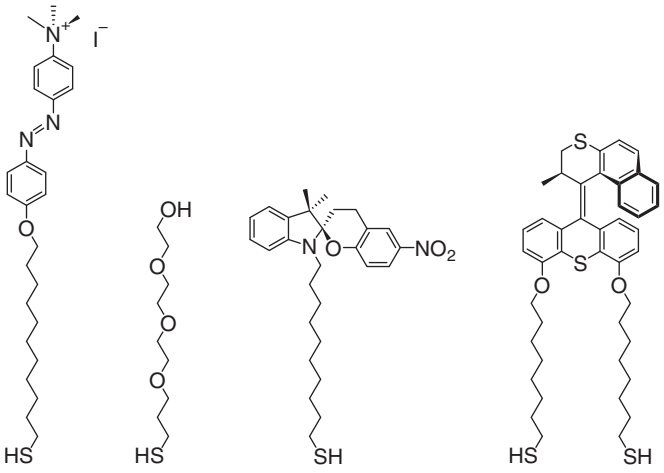


31 32 33 34

**Figure 31.12** Selected molecular switches and motor forming SAMs on gold nanoparticles.

carrying a functional group on one side and a thiol-based anchor on the other end still dominates (Figure 31.12).

One of the advantages of using nanoparticles in comparison with classical flat substrates is the fact that light-triggered switching or rotational movement in molecular machines can be monitored by traditional spectroscopic techniques such as UV–vis, CD, and NMR in solution/suspension in most cases.

Surface curvature is an important parameter that characterizes NPs, and it has to be seriously considered because it has a dramatic impact on the functionality of anchored molecular machines. For this reason, several comprehensive studies were dedicated to this phenomenon [56, 57]. Steric hindrance is not an issue even in single-component SAMs in case the curvature is large enough (in other words the diameter is small). In contrast, NPs with a small curvature resemble flat surfaces, and molecular machines within SAMs show a reduced activity due to a reduction in the degrees of freedom. It then becomes necessary to create a free volume by diluting SAMs with shorter ligands [4, 57].

Most of the gold NPs coated with photoactive SAMs are soluble in organic solvents. There has been a lot of effort invested into developing water-soluble systems that could be potentially used in biological systems [58]. A series of inherently hydrophobic azobenzenes were synthesized and coadsorbed with water-solubilizing background ligands onto gold NPs to fine-tune their properties. Compounds **31** and **32** (Figure 31.12) represented selected examples of switch and solubilizing ligands. The highly reversible photoisomerization was detected on such water-soluble NPs. Analysis of kinetics data revealed that hydroxy-terminated background ligands like **32** can enhance the *cis*-to-*trans* isomerization by almost 6000 times. It was found that efficient acceleration was achieved only in cases where the length of the ligand was similar to that of the azobenzene-based thiol. This suggested intermolecular interaction between these two species [58].

Spiropyrans (Figure 31.1) represent another group of widely studied photoswitches on NPs [59]. What makes spiropyrans unique among the broad class of molecular machines (Figure 31.1) is the fact that their two isomers have significantly different properties. This feature makes them perfect candidates for SAMs coating NPs since light-triggered switching induces dramatic changes of the physical properties of such nanoobjects. Unfortunately, spiropyrans are also vulnerable to photodegradation, a process that reduces the number of switching cycles [59]

The unique properties of spiropyrans are demonstrated in the following example. A novel class of light-responsible nanoobjects was obtained by anchoring **33** (Figure 31.12) on surfaces of gold and silver NPs. Such NPs reversibly self-aggregated into supramolecular assemblies upon irradiation of UV light in nonpolar solvents [60]. The nitro group was identified as a key component of this process, since analogous systems lacking the $NO_2$ unit showed distinctively different self-assembly properties relying on a reversible proton transfer. The resulting particles spontaneously aggregated into supramolecular assemblies in the dark, and readily disassembled upon exposure to blue light [60].

Molecular motors are another group of molecular machines that are an attractive target for immobilization on the surfaces of NPs due to their possible application as artificial propulsion systems. Compound **34** represents the first unidirectional light-driven molecular motor based on overcrowded alkene that was grafted to gold NPs (Figure 31.12) [55]. Two points of attachment represented by C8 legs were essential to prevent the uncontrolled thermal rotation of the entire system with respect to the surface. NMR, UV–vis, and CD spectroscopies confirmed that these motors can repetitively undergo full 360° unidirectional rotation cycle, although the rotation slowed down in comparison to an unbound motor (the $t_{1/2}$ of thermal helix inversion for free motor was $56 \times 10^2$ seconds at 293 K, and this value has almost doubled $12 \times 10^3$ seconds after immobilization to gold NPs). This can be attributed to the reduction in the degrees of freedom of the bound **34**, but a decrease in the rotation efficiency due to the energy transfer to the metallic surface can also retard the photochemical step [55].

Not surprisingly, the diametrically opposed behavior of molecular motors on flat and curved surfaces was described as well. The structurally related and previously mentioned azimuthal molecular motor **17** (Figure 31.5) was found to be inactive once anchored either neat or diluted with a decanethiol spacer on a flat gold surface. In sharp contrast, even single-component SAMs on gold NPs were able to undergo photoisomerization and subsequent thermal helix inversion as demonstrated by CD spectroscopy [35].

Although these motors showed function once attached to the surface of gold NPs dispersed in solvent, the gold particles themselves were subject to Brownian motion, thus making the applications of these molecular motors as an artificial propulsion system more difficult [35].

Substantial progress in the development of SAMs formed from various light-driven molecular machines has been accomplished in the past three decades. Many of these systems have evolved from a kind of laboratory curiosity to fully operational systems. At the same time, many promising routes toward future applications in the field of

nanoelectronics, catalysis, medicine, nanotechnology, etc. were outlined, and many others are still to be discovered.

## References


1 Love, C.J., Estroff, L.A., Kriebel, J.K. et al. (2005). Self-assembled monolayers of thiolates on metals as a form of nanotechnology. *Chem. Rev.* 105: 1103–1169.
2 García-López, V., Liu, D., and Tour, J.M. (2020). Light-activated organic molecular motors and their applications. *Chem. Rev.* 120: 79–124.
3 Ulman, A. (1996). Formation and structure of self-assembled monolayers. *Chem. Rev.* 96: 1533–1554.
4 Klajn, R. (2010). Immobilized azobenzenes for the construction of photoresponsive materials. *Pure Appl. Chem.* 82: 2247–2279.
5 Casalini, S., Bortolotti, C.A., Leonardi, F., and Biscarini, F. (2017). Self-assembled monolayers in organic electronics. *Chem. Soc. Rev.* 46: 40–71.
6 Adamson, A.W. and Great, A.P. (1997). *Physical Chemistry of Surfaces*, 6e. New York: Wiley-Interscience.
7 Inkpen, M.S., Liu, Z.-F., Li, H. et al. (2019). Non-chemisorbed gold-sulfur binding prevails in self-assembled monolayers. *Nat. Chem.* 11: 351–358.
8 Herr, B.R. and Mirkin, C.A. (1994). Self-assembled monolayers of ferrocenylazobenzenes: monolayer structure vs response. *J. Am. Chem. Soc.* 116: 1157–1158.
9 Hartley, G. (1937). The *cis*-form of azobenzene. *Nature* 140: 281.
10 Caldwell, W.B., Campbell, D.J., Chen, K. et al. (1995). A highly ordered self-assembled monolayer film of an azobenzenealkanethiol on Au(111): electrochemical properties and structural characterization by synchrotron in-plane X-ray diffraction, atomic force microscopy, and surface-enhanced Raman spectroscopy. *J. Am. Chem. Soc.* 117: 6071–6082.
11 Wang, R., Iyoda, T., Jiang, L. et al. (1996). Molecular arrangement in an azobenzene-terminated self-assembled monolayer film. *Chem. Lett.*: 1005–1006.
12 Tamada, K., Nagasawa, J., Nakanishi, F. et al. (1998). Structure and growth of hexyl azobenzene thiol SAM on Au(111). *Langmuir* 14: 3264–3271.
13 Victor, J.G. and Torkelson, J.M. (1987). On measuring the distribution of local free volume in glassy polymers by photochromic and fluorescence techniques. *Macromolecules* 20: 2241–2250.
14 Wang, Y.Q., Yu, H.Z., Cheng, J.Z. et al. (1996). End-group-dominated electrochemical kinetics of azobenzene self-assembled monolayers on gold. *Langmuir* 12: 5466–5471.
15 Karpe, S., Ocafrain, M., Smaali, K. et al. (2010). Oligothiophene-derivatized azobenzene as immobilized photoswitchable conjugated systems. *Chem. Commun.* 46: 3657–3659.
16 Shin, K.H. and Shin, E.J. (2008). Photoresponsive azobenzene-modified gold nanoparticles. *Bull. Korean Chem. Soc.* 29: 1259–1262.
17 Tanaka, T., Ogino, H., and Iwamoto, M. (2007). Photochange in pore diameters of azobenzene-planted mesoporous silica materials. *Langmuir* 23: 11417–11420.


**18** Evans, D.S., Johnson, S.R., Ringsdorf, H. et al. (2008). Photoswitching of azobenzene derivatives formed on planar and colloidal gold surfaces. *Langmuir* 14: 6436–6440.

**19** Kumar, A.S., Ye, T., Takami, T. et al. (2008). Reversible photo-switching of single azobenzene molecules in controlled nanoscale environments. *Nano Lett.* 8: 1644–1648.

**20** Heister, K., Allara, D.L., Bahnek, K. et al. (1999). Deviations from 1:1 compositions in self-assembled monolayers formed from adsorption of asymmetric dialkyl disulfides on gold. *Langmuir* 15: 5440–5443.

**21** Pace, G., Petitjean, A., Lalloz-Vogel, M.N. et al. (2008). Subnanometer-resolved patterning of bicomponent self-assembled monolayers on Au(111). *Angew. Chem. Int. Ed.* 47: 2518–2522.

**22** Tamada, K., Akiyama, H., Wei, T.X., and Kim, S.A. (2003). Photoisomerization reaction of unsymmetrical azobenzene disulfide self-assembled monolayers: modification of azobenzene dyes to improve thermal endurance for photoreaction. *Langmuir* 19: 2306–2312.

**23** Ito, M., Wei, T.X., Chen, P.-L. et al. (2005). A novel method for creation of free volume in a one-component self-assembled monolayer. Dramatic size effect of *para*-carborane. *J. Mater. Chem.* 15: 478–483.

**24** Wagner, S., Leyssner, F., Kördel, C. et al. (2009). Reversible photosiomerization of an azobenzene-functionalized self-assembled monolayer probed by sum-frequency generation vibrational spectroscopy. *Phys. Chem. Chem. Phys.* 11: 6242–6248.

**25** Baisch, B., Raffa, D., Jung, U. et al. (2009). Mounting freestanding molecular functions onto surfaces: the platform approach. *J. Am. Chem. Soc.* 131: 442–443.

**26** Jacob, H., Ulrich, S., Jung, U. et al. (2014). Monitoring the reversible photoisomerization of an azobenzene-functionalized molecular triazatriangulene platform on Au(111) by IRRAS. *Phys. Chem. Chem. Phys.* 16: 22643–22650.

**27** Schlimm, A., Löw, A., Rusch, T. et al. (2019). Long-distance rate acceleration by bulk gold. *Angew. Chem. Int. Ed.* 58: 6574–6578.

**28** Löw, R., Rusch, T., Röhrlich, F. et al. (2019). Diazocine-functionalized TATA platforms. *Beilstein J. Org. Chem.* 15: 1485–1490.

**29** Hammerich, M. and Herges, R. (2015). Laterally mounted azobenzenes on platforms. *J. Org. Chem.* 80: 11233–11236.

**30** Rusch, T.R., Schlimm, A., Krekiehn, N.R. et al. (2019). Ordered adlayers of a combined lateral switch and rotor. *J. Phys. Chem. C* 123: 13720–13730.

**31** Zheng, L.-Q., Yang, S., Lan, J. et al. (2019). Solution phase and surface photoisomerization of a hydrazone switch with a long thermal half-life. *J. Am. Chem. Soc.* 141: 17637–17645.

**32** Doron, A., Katz, E., Portnoy, M., and Willner, I. (1996). An electroactive photoisomerizable monolayer electrode: a command surface for the amperometric transduction of recorded optical signals. *Angew. Chem. Int. Ed.* 35: 1535–1537.

**33** Baron, R., Onopriyenko, A., Katz, E. et al. (2006). An electrochemical/photochemical information processing system using a monolayer-functionalized electrode. *Chem. Commun.*: 2147–2149.


**34** Browne, W.R., Kudernac, T., Katsonis, N. et al. (2008). Electro- and photochemical switching of dithienylethene self-assembled monolayers on gold electrodes. *J. Phys. Chem. C* 112: 1183–1190.

**35** Carrol, G.T., Pollard, M.M., van Delden, R., and Feringa, B.L. (2010). Controlled rotary motion of light-driven molecular motors assembled on a gold film. *Chem. Sci.* 1: 97–101.

**36** Chen, K.-Y., Ivashenko, O., Caroll, G.T. et al. (2014). Control of surface wettability using tripodal light-activated molecular motors. *J. Am. Chem. Soc.* 136: 3219–3224.

**37** Garah, M., Palmino, F., and Cherioux, F. (2010). Reversible photoswitching of azobenzene-based monolayers physisorbed on a mica surface. *Langmuir* 26: 943–949.

**38** Aswal, D.K., Lenfant, S., Guerin, D. et al. (2006). Self-assembled monolayers on silicon for molecular electronics. *Anal. Chim. Acta* 568: 84–108.

**39** de Villeneuve, C.H., Michalik, F., Chazalviel, J.N. et al. (2013). Quantitative IR readout of fulgimide monolayer switching on Si(111) surfaces. *Adv. Matter.* 25: 416–421.

**40** Klaes, S., de Villeneuve, C.H., Ozanam, F. et al. (2019). Influence of light polarizaiton on photoswitching of fulgimide monolayers on surfaces. *J. Phys. Chem. C* 123: 12223–12233.

**41** Pollard, M.M., Lubomska, M., Rudolf, P., and Feringa, B.F. (2007). Controlled rotary motion in a monolayer of molecular motors. *Angew. Chem. Int. Ed.* 46: 1278–1280.

**42** London, G., Caroll, G.T., Landaluce, T.F. et al. (2009). Light-driven altitudinal molecular motors on surfaces. *Chem. Commun.*: 1712–1714.

**43** Carroll, G.T., London, G., Landaluce, T.F. et al. (2011). Adhesion of photon-driven molecular motors to surfaces *via* 1,3-dipolar cycloadditions: effect of interfacial interactions on molecular motion. *ACS Nano* 5: 622–630.

**44** Krajnik, B., Chen, J., Watson, M.A. et al. (2017). Defocused imaging of UV-driven surface-bound molecular motors. *J. Am. Chem. Soc.* 139: 7156–7159.

**45** Comotti, A., Bracco, S., Ferretti, L. et al. (2007). A single-crystal imprints macroscopic orientation on xenon atoms. *Chem. Commun.*: 350–352.

**46** Allcock, H.R. (1964). Phosphonitrilic compounds. II. Reactions of phosphonitrilic chlorides with catechol and triethylamine. *J. Am. Chem. Soc.* 86: 2591–2595.

**47** Allcock, H.R. and Siegel, L.A. (1964). Phosphonitrilic compounds. III. Molecular inclusion compounds of tris(*o*-phenylenedioxy)phosphonitrile trimetr. *J. Am. Chem. Soc.* 86: 5140–5144.

**48** Sozzani, P., Bracco, S., Comotti, A. et al. (2005). Methane and carbon dioxide storage in a porous van der Waals crystal. *Angew. Chem.* 117: 1850–1854.

**49** Bracco, S., Comotti, A., Ferreti, L., and Sozzani, P. (2011). Supramolecular aggregation of block copolymers in the solid state as assisted by the selective formation of inclusion crystals. *J. Am. Chem. Soc.* 133: 8982–8994.

**50** Zhao, K., Dron, P.I., Kaleta, J. et al. (2014). Arrays of dipolar molecular rotors in tris(*o*-phenylenedioxy)cyclotriphosphazene. *Top. Curr. Chem.* 354: 163–212.


**51** Kaleta, J., Dron, P.I., Zhao, K. et al. (2015). Arrays of molecular rotors with triptycene stoppers: surface inclusion in hexagonal tris(*o*-phenylenedioxy)cyclotriphosphazene. *J. Org. Chem.* 80: 6173–6192.

**52** Santos Hurtado, C., Bastien, G., Mašát, M. et al. (2020). Regular 2-D arrays of surface-mounted molecular switches: switching monitored by UV-vis and NMR spectroscopy. *J. Am. Chem. Soc.* 142: 9337–9351.

**53** Kaleta, J., Chen, J., Bastien, G. et al. (2017). Surface inclusion of unidirectional molecular motors in hexagonal tris(*o*-phenylene-dioxy)cyclotriphosphazene TPP. *J. Am. Chem. Soc.* 139: 10486–10498.

**54** Grzelczak, M., Liz-Marzán, L.M., and Klajn, R. (2019). Stimuli-responsive self-assembly on nanoparticles. *Chem. Soc. Rev.* 48: 1342–1361.

**55** van Delden, R.A., Wiel, M.K.J., Pollard, M.M. et al. (2005). Unidirectional molecular motor on a gold surface. *Nature* 437: 1337–1340.

**56** Zdobinsky, T., Sankar, M.P., and Klajn, R. (2013). Support curvature and conformational freedom control chemical reactivity of immobilized species. *J. Am. Chem. Soc.* 135: 19135–19138.

**57** Moldt, T., Brete, D., Przyrembel, D. et al. (2015). Tailoring the properties of surface-immobilized azobenzenes by monolayer dilution and surface curvature. *Langmuir* 31: 1048–1057.

**58** Chu, Z., Han, Y., Bian, T. et al. (2019). Supramolecular control of azobenzene switching on nanoparticles. *J. Am. Chem. Soc.* 141: 1949–1960.

**59** Klajn, R. (2014). Spiropyran-based dynamic material. *Chem. Soc. Rev.* 43: 148–184.

**60** Kundu, P.K., Das, S., Ahrens, J., and Klajn, R. (2016). Controlling the lifetimes of dynamic nanoparticle aggregates by spiropyrans functionalization. *Nanoscale* 8: 19280–19286.

# 32 Light-Driven Molecular Machines

Alberto Credi, Serena Silvi, and Massimo Baroncini

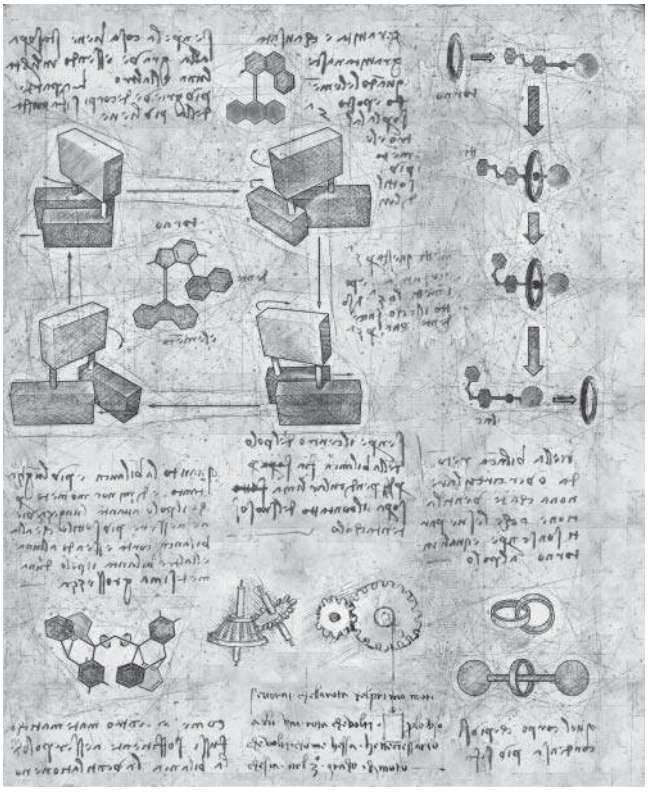

**Characteristic Features**

Nowadays, 500 years after the work of Leonardo da Vinci, artificial machines and devices of molecular size are routinely designed and constructed by chemists. In analogy to their macroscopic counterparts, light represents an ideal source of abundant, clean, and renewable energy to power their functions.

**Key References**

Corra, S., Curcio, M., Baroncini, M. et al. (2020). Photoactivated artificial molecular machines that can perform tasks. *Adv. Mater*. 32: 1906064–22.

Baroncini, M., Silvi, S., and Credi, A. (2019). Photo- and redox-driven artificial molecular motors. *Chem. Rev*. 120: 200–268.

Baroncini, M., Casimiro, L., de Vet, C., et al. (2018). Making and operating molecular machines: a multidisciplinary challenge. *ChemistryOpen* 7: 169–179.

# 32

# Light-Driven Molecular Machines

*Alberto Credi[1,4], Serena Silvi[2,4], and Massimo Baroncini[3,4]*

[1] *Università di Bologna, Dipartimento di Chimica Industriale "Toso Montanari", Viale del Risorgimento, 4, Bologna 40136, Italy*
[2] *Università di Bologna, Dipartimento di Chimica "G. Ciamician", via Selmi 2, 40126 Bologna, Italy*
[3] *Università di Bologna, Dipartimento di Scienze e Tecnologie Agro-alimentari, Viale Fanin 50, 40127 Bologna, Italy*
[4] *CLAN-Center for Light Activated Nanostructures, via Gobetti 101, 40129 Bologna, Italy*

## 32.1 Introduction

Molecular machines are (supra)molecular-based architectures in which the supply of an energy input results in the controlled and directed movement of some of their components with respect to the others [1, 2]. Living organisms harbor some of the most sophisticated examples of working molecular machines: motor proteins such as myosin and kinesin, energy-producing enzymes such as ATP synthase, DNA and RNA polymerases, which control gene replication and expression, and many other sophisticated multicomponent systems. Biological molecular machines are particularly remarkable for being able to bring forward all the fundamental functions, which define life by operating in the complex environment of a living cell [3–5]. The compelling level of functions performed by biomolecular machines represents sound scientific basis and a strong motivation for researchers attempting the development of entirely artificial molecular scale devices. Indeed, the inspiration brought by a deeper understanding of biological molecular machines, combined with chemical insight and an engineering mentality, has led to several ingenious achievements [6, 7]. In fact, during the past four decades, chemists have designed, synthesized, and investigated a large variety of artificial molecular machines, facing the many problems posed by the interfacing of nanoscale devices with the macroscopic world in terms of energy supply, information exchange, and, more recently, the task performed [8–10]. The award of the Nobel Prize in Chemistry 2016 "for the design and synthesis of molecular machines" is a clear recognition of the maturity and scientific significance of this research field [11–13].

*Molecular Photoswitches: Chemistry, Properties, and Applications*,
First Edition. Edited by Zbigniew L. Pianowski.


For molecular-scale machines, in analogy with their macroscopic counterparts, one of the most important aspects is the nature of the energy source employed to power their operation and of the stimuli adopted to monitor and control their action. Light is unique in being able to fulfill both these roles. Indeed, the absorption of photons by a chemical moiety can induce a large variety of chemical reactions that, through reversible structural and/or electronic modifications, allow to attain light-powered functionalities. Furthermore, light allows determining the state of a molecular machine along its working cycle, thus enabling the monitoring of its operation. This is possible because the chemical–physical transformations to which a molecular machine is subject during its working cycle are often reflected in marked modifications of its photophysical properties. Therefore, photons can be efficiently employed both for "writing," i.e. power, and "reading," i.e. control, artificial molecular machines [14, 15].

Besides the possibility to simultaneously fulfill two different roles, the use of light energy to power and control artificial molecular machines has several other advantages. First of all, the amount of light energy supplied to a system can be finely tuned by changing both its wavelength and intensity in relation to the absorption spectrum of the targeted species. Most important, light energy can be transferred to a molecular system without a physical connection since the only requisite for remote excitation is the transparency of the medium at the irradiation wavelength. In addition, the introduction of modern light sources such as lasers and LEDs coupled with the use of optical fibers and waveguides consents to investigate light-driven molecular machines with a high level of spatial and temporal resolution [16, 17]. Lastly, molecular machines powered solely by light energy, by relying on clean and reversible photochemical reactions, do not generate waste products. This is a most desirable aspect from a societal point of view. In fact, the development of a nanotechnology-based industry that uses only renewable and clean energy sources could help in addressing the unpostponable problems concerning energy supply and environmental pollution that our industrialized civilization is presently facing. In this frame, the construction of molecular machines capable of utilizing light, and in particular sunlight, to power their operation represents a most attractive and desirable achievement.

It has to be noted, however, that until about a decade ago, artificial nanomachines were mostly proof-of-principle systems, unable to perform even the most simple tasks that their biological counterparts so marvelously accomplish [18]. This scenario has started to change only in recent years when the work done by some leading research groups has demonstrated that synthetic molecular machines can provide the bases for groundbreaking applications in several areas of technology and medicine [19, 20]. In this chapter, we present the most recent developments along this direction by summarizing illustrative examples in which the photoinduced motion of synthetic molecular machines is exploited to achieve a sizeable and significant function or effect. After a brief description of the main types of photoinduced processes and chemical architectures, which are currently exploited

for the realization of light-driven molecular devices and machines, the discussion follows with an account on a selection of different types of advanced functionalities that have been achieved by harnessing light-induced molecular movements at the nanoscale.

### 32.1.1 Useful Photoinduced Processes

Artificial molecular machines powered by light exploit reversible photoinduced transformations able to trigger a sequence of chemical modifications or rearrangements, leading to the relative movement of some of the components of the machine itself. In general, molecular machines must be able to persistently repeat their motion to be of any use, which in turn dictates that only photoinduced processes, which are reversible and fatigue-resistant, can be exploited for their realization. Accordingly, research on reversible light-induced transformations is closely associated with the development of photochemically operated molecular machines [21]. Actually, all molecular machines activated by light are based on a rather small number of chemical species, which are able to support reversible and clean photoinduced processes [22, 23].

Lately the term "molecular photoswitch" has come into use to identify molecular species that can be reversibly switched between two (or more) states with light, widening, and partially overcoming the older definition of "photochromic compound." In fact, while photochromic compounds, or photochromes, by definition have different absorption spectra (i.e. color) among their interconvertible forms, photoswitches are not strictly required to adhere to this specific characteristic [24–26].

All molecular photoswitches share several common features (Figure 32.1). In general terms, by irradiation with light of proper wavelength ($h\nu$), the ***A*** and ***B*** forms of a photoswitchable moiety can be mutually interconverted. Moreover, since in nearly all cases one of the two states has a significantly higher thermodynamical stability than the other, a thermally activated (dark) process by which the high-energy form (***B***) reverts back to the stable one (***A***) can occur. While the photoinduced $\boldsymbol{A} \rightarrow \boldsymbol{B}$ transformation is usually very fast, the thermal $\boldsymbol{B} \rightarrow \boldsymbol{A}$ conversion may have a half-life as short as nanoseconds or as long as hundreds of years.

Usually, the quantitative photochemical conversion to either ***A*** or ***B*** is prevented because of the overlap of the absorption spectra of the ***A*** and ***B*** forms, which are both photoreactive (Figure 32.1). Under prolonged irradiation, a photostationary state enriched in one of the two forms is afforded, whose composition depends on the absorption coefficients of the ***A*** and ***B*** species, the quantum yield of the forward and backward photoreaction at the irradiation wavelength, and on the rate constant of the thermal back reaction.

Most molecular photoswitches known to date operate by undergoing a photoisomerization reaction: a light-induced chemical transformation leading to isomerization of the substrate, by bond rotation, skeletal rearrangement, or atom group

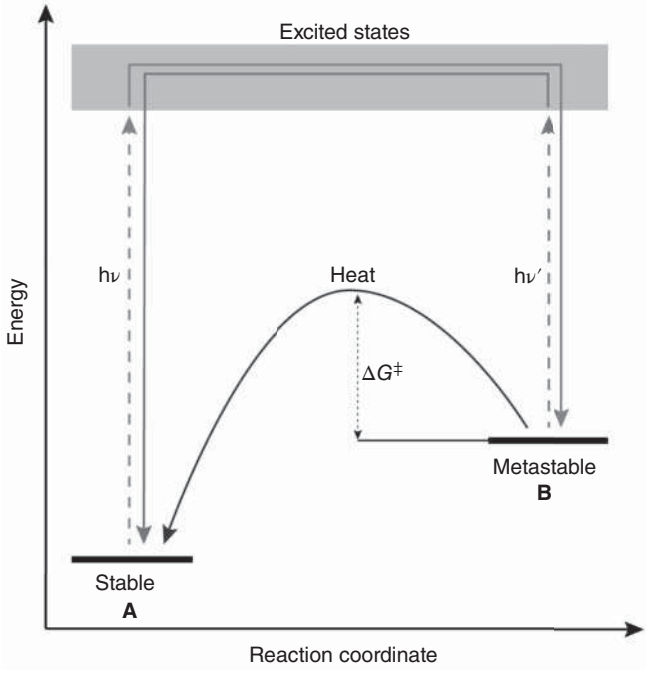


**Figure 32.1** Simplified energy profile describing the light- and thermally induced conversion between the two isomeric forms (***A*** and ***B***) of a generic molecular photoswitch.

transfer. In particular, the photoinduced *E*–*Z* configurational isomerization around an unsaturated bond is the prevailing photochemical mechanism in photoswitches and, consequently, at the core of the functioning of most light-activated molecular machines [26–29].

Photoswitches operating through a photoinduced *E*–*Z* isomerization can be suitably classified according to the nature of the isomerized multiple bond (Figure 32.2). In particular alkenes, with stilbene as the prototypical species, and polyenes such as indigoids [30] are examples of photoswitches in which light-induced bond rotation occurs about a carbon–carbon double bond (Figure 32.2a, see also Chapter 13 by Henry Dube). Azobenzene and its derivatives represent a class of compounds, presently one of the most explored and implemented ones, in which bond rotation intervenes about a nitrogen–nitrogen double bond. In particular heteroaryl azo compounds, due to their broad structural diversity, which is reflected in their vast range of spectral properties, are emerging as a new class of highly efficient and versatile molecular photoswitches (Figure 32.2b) [31, 32]. The photoswitching properties of imines, characterized by the isomerization of a carbon–nitrogen double bond, have only recently been investigated in detail. Their straightforward synthesis and structural diversity bode well for the future of this class of photoswitchable compounds (Figure 32.2c, see also Chapter 15 by Jean-Marie Lehn)

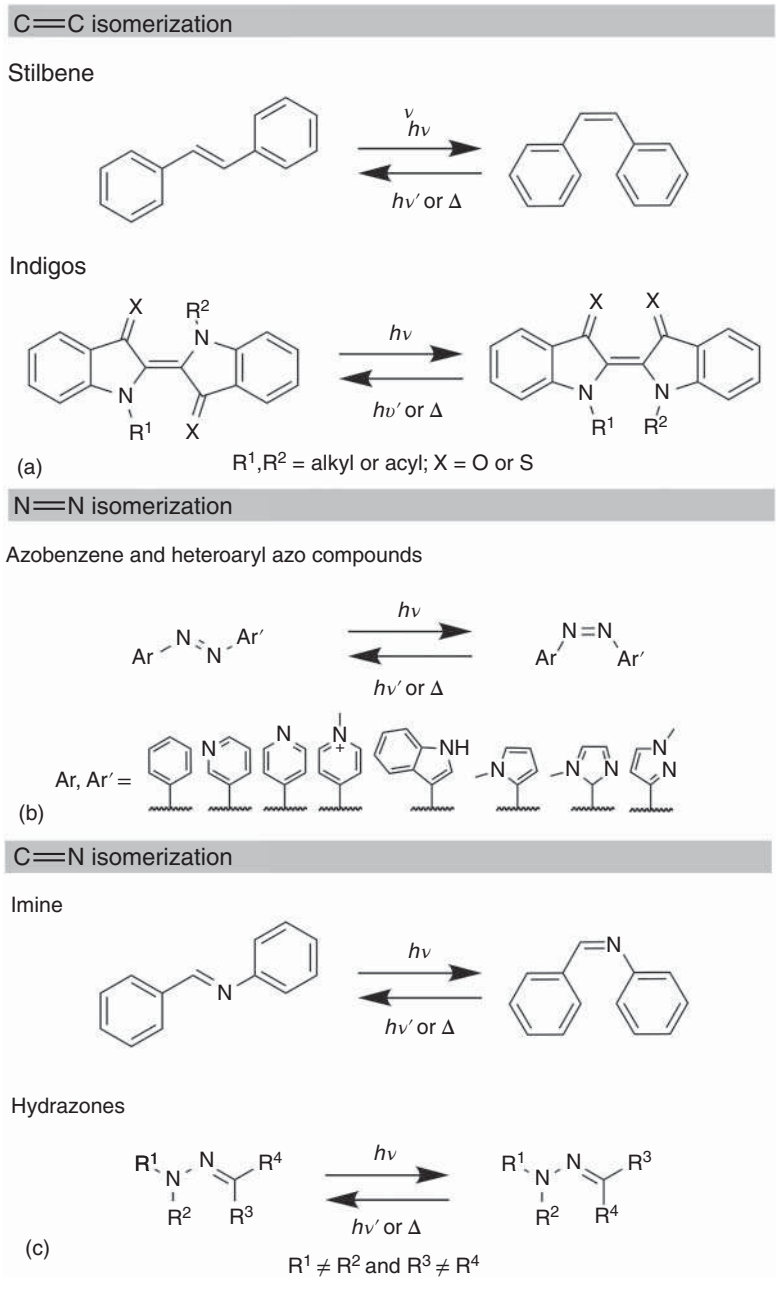


**Figure 32.2** The main classes of molecular photoswitches based on the *E*–*Z* isomerization about (a) C=C, (b) N=N, and (c) C=N double bonds.

[33, 34]. In addition to imines, hydrazone compounds, which exhibit extremely clean and highly reversible photoswitching behavior both in solution and in complex matrices, have also represented one of the last but most promising new entries in the ever-expanding photoswitch arena (Figure 32.2c, see also Chapter 6 by Ivan Aprahamian) [35, 36].

Closely related to photoisomerization, a photoinduced process that has found significant applications in the development of light-activated molecular machines is that of light-induced proton-transfer reactions [37]. In particular, metastable photoacids and photobases, i.e. photoswitchable compounds in which the structural rearrangement associated with a photoreaction is accompanied by a large difference in the acid–base properties, enable to implement photocontrol on any acid–base responsive processes [38]. Well-known classes of photoacids, which have been proved to be amenable for this approach, are 2-hydroxyazobenzenes [39, 40], merocyanine-based species [41], and switches based on the tricyanofuran unit (Figure 32.3) [42, 43].

Different examples are reported in the literature, which demonstrate that acid–base-controlled molecular machines can be rendered light-responsive by exploiting the proton-mediated intermolecular communication between the molecular machine itself and a photoacid (or photobase) [44–47]. This approach is particularly noteworthy since it enables to completely circumvent the synthetic hurdle of integrating a photoresponsive unit into the structure of the molecular machine itself.

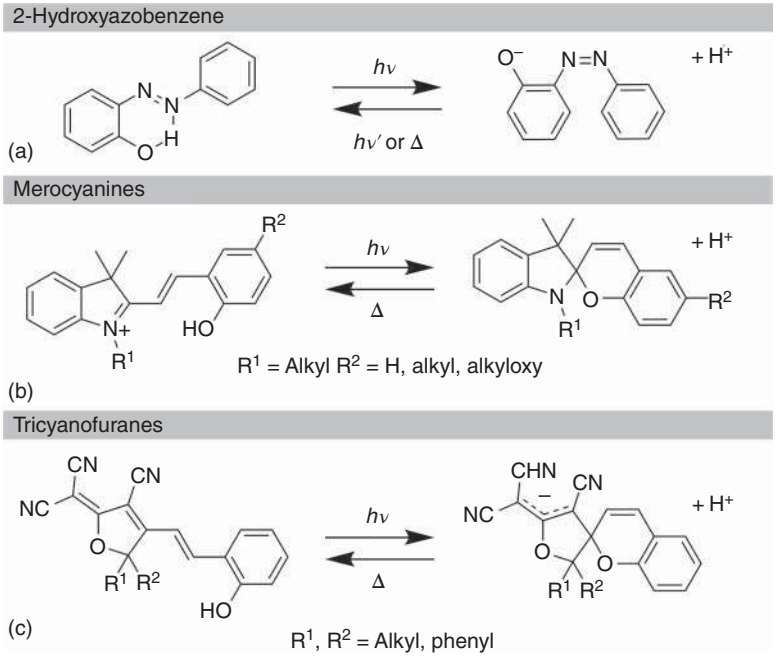


**Figure 32.3** Molecular structures of the main classes of metastable photoacids (a) 2-hydroxyazobenzene, (b) merocyanines and (c) tricyanofuranes.

## 32.2 Basic Types of Photochemically Driven Molecular Devices and Machines

Before describing specific examples regarding the application of light-driven molecular machines to develop materials and systems with advanced functionalities, it is worthwhile to introduce the fundamental classes of molecular architectures that have been exploited for their realization.

A fundamental distinction can be made between molecular machines that present in their constitution a mechanical bond and those that are based on completely covalent structures. In fact, most of the currently developed molecular machines are based on mechanically interlocked molecules (MIMs) [48–50]. This is because the mechanical bond present in MIMs adds an additional level of dynamic freedom that is absent in entirely covalent molecules [51, 52]. However, despite this clear advantage that MIMs architectures present in terms of dynamic freedom at the nanoscale, presently, some of the most efficient molecular machines are based on rather simple fully covalent species. Owing, mostly due to their constitutional simplicity and synthetic flexibility, molecular machines based on covalent architectures are some of the most robust and adaptable nanodevices currently available.

In the next paragraph, the structure of MIMs and of their precursors will be presented followed by relevant examples aimed at clarifying to the reader some of the basic mechanistic aspects of light-powered nanosystems based on MIMs. A short description of some basic types of light-driven nanomachines based on fully covalent architectures will follow.

For reasons of space, only the most representative examples relevant for the present discussion will be described. The interested reader is referred to the various books and comprehensive reviews available in the literature that deal specifically with the synthesis, mechanisms of operation, and applications of photochemically driven synthetic molecular machines [1, 8, 10, 14, 17, 20, 53–56].

### 32.2.1 Molecular Devices and Machines Based on Mechanically Interlocked Architectures

Starting from the 1970s, molecules that possess a mechanical bond, referred as mechanically interlocked molecules or MIMs for short, have rapidly evolved from laboratory oddities to synthetically accessible compounds with prospective applications in different areas of technology. In particular, the unique dynamic characteristics of MIMs make them ideal candidates for the realization of molecular devices and machines. In fact, the mechanical bond, while limiting the amplitude of the intercomponent motion in the three directions, enables different spatial arrangements of the molecular components, which in suitably designed MIMs can be selectively populated by external stimulation. Thus, it is not fortuitous that the most popular realization of the artificial molecular machine concept is based on MIM architectures.

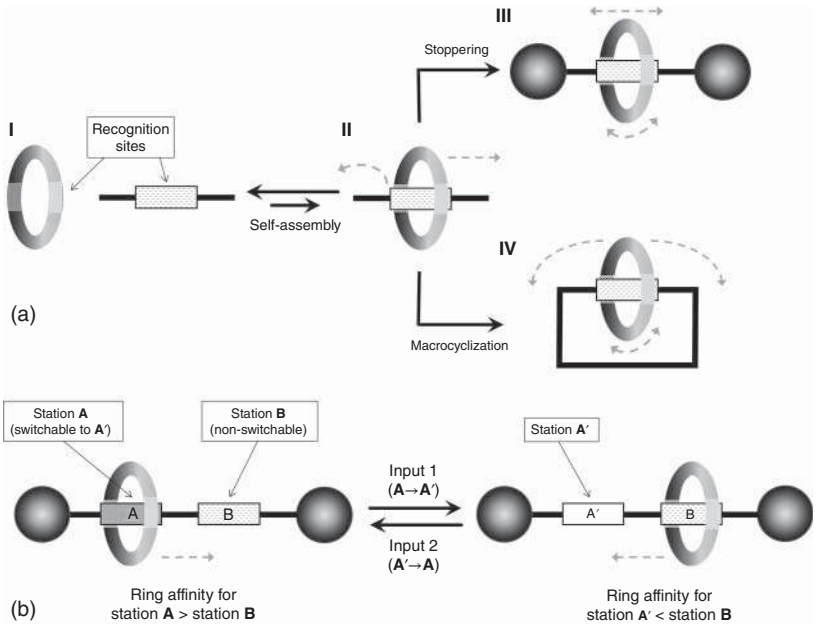


**Figure 32.4** (a) Schematic representation of ring and axle molecular components and of their complementary recognition sites (I), of the self-assembly process to yield a pseudorotaxane (II), and of its transformation into a mechanically interlocked molecule (MIM) either through stoppering with bulky groups to yield a rotaxane (III) or through macrocyclization to yield a catenane (IV). The dashed gray arrows indicate the intercomponent movements of interest for the realization of MIM-based molecular devices and machines. (b) Schematic representation of a two-station rotaxane operating as a controllable molecular shuttle. Left, the ring has a higher affinity for recognition site (i.e. station) A than B, thus the ring preferentially encircles station A. Right, station A′ has a lower affinity for the ring than B, thus the ring preferentially encircles station B. Station A can be reversibly switched into station A′ via orthogonal inputs that by inducing a shuttling movement control the relative position of the ring and axle components. The dashed gray arrows indicate the relative movements of the ring upon administration of input 1 (left) and input 2 (right).

MIMs are typically made starting from pseudorotaxanes, which result from the self-assembly of molecular macrocyclic (ring) and acyclic (axle) components (Figure 32.4a, I) into a threaded structure (Figure 32.4a, II). A pseudorotaxane is a dynamic structure in equilibrium with its non-threaded components, and its formation is possible because of the presence of noncovalent bonding interactions between the ring and the axle. A rotaxane can be obtained by attaching bulky groups (stoppering) at both extremities of a pseudorotaxane (Figure 32.4a, III). The stopper groups have to be selected large enough to impede the dethreading of the ring from the axle, thus resulting in a kinetically inert structure that does not disassemble even if the intercomponent interactions are switched off in some way.

Starting form pseudorotaxanes, through macrocyclization of its axle component, MIMs architectures with a different topology can be obtained, namely catenanes (Figure 32.4a, IV). In analogy to rotaxanes also in catenanes, owing to the presence of the mechanical bond, the two rings cannot be separated even after removal of the chemical interactions between them.

In the context of molecular devices and machines, a key feature of MIMs is represented by the possibility of modulating the mutual interaction between the component molecules via an external input. Indeed, a change in the affinity between the molecular constituents of a MIM can lead, through large amplitude movements, to the formation of distinct chemical species characterized by a different spatial distribution of the components. An emblematic example of a molecular machine based on an MIM architecture is represented by the two-station rotaxane schematized in Figure 32.4b. In this rotaxane, the ring has a higher affinity for recognition site A than B and thus encircles the first one (Figure 32.4b, left). In this kind of compounds, the recognition sites present on the axle are often termed stations. Upon application of a specific input able to transform station A into A′, which is characterized by a lower affinity for the ring than station B, the ring can find a new energy minimum by sliding along the axle toward station B (Figure 32.4b, right). If station A' is transformed back again to A by an opposite input, the ring returns to its starting position. Thus, by alternating the two control inputs, a forward and backward movement of the ring is obtained. MIMs like the one described, in which a shuttling motion of the ring is addressable by an external stimulus, are aptly named "molecular shuttles." Beside translational motion, in MIMs different kinds of large amplitude movements are possible, which can involve threading/dethreading, pirouetting, circumrotation, and/or rocking (Figure 32.4, dashed arrows) [2]. Furthermore, the rate of these rearrangements can also be controlled by incorporating appropriate subunits (for example, sterically hindering groups) in the components, which may also respond to stimulation. MIMs thus offer an ideal architecture to develop nanosystems in which intermolecular rearrangements and large-scale movements are controlled by external signals.

Based on these premises, it is evident that the introduction of photoswitchable moieties within the structure of a MIM, if the ensuing photoinduced transformation is able to influence the interactions between the components, is a practical way to achieve a level of control on the static and dynamic characteristics of these species using light [57–59].

Figure 32.5 shows a representative example of a rotaxane-based molecular machine, which makes use of a photoswitching azobenzene moiety to operate as a nanoscale light/current transducer [60]. Rotaxane (*E*)-**1**, which consists of a β-cyclodextrin macrocycle (β-CD) bearing a ferrocene unit threaded on an axle molecule comprising a photoisomerizable azobenzene moiety and a long alkyl chain, is self-assembled on a gold electrode. The β-CD ring is unable to dethread since the two extremities of the axle component are stoppered by the bulky anthracene group at one end and by the metal surface at the other end.

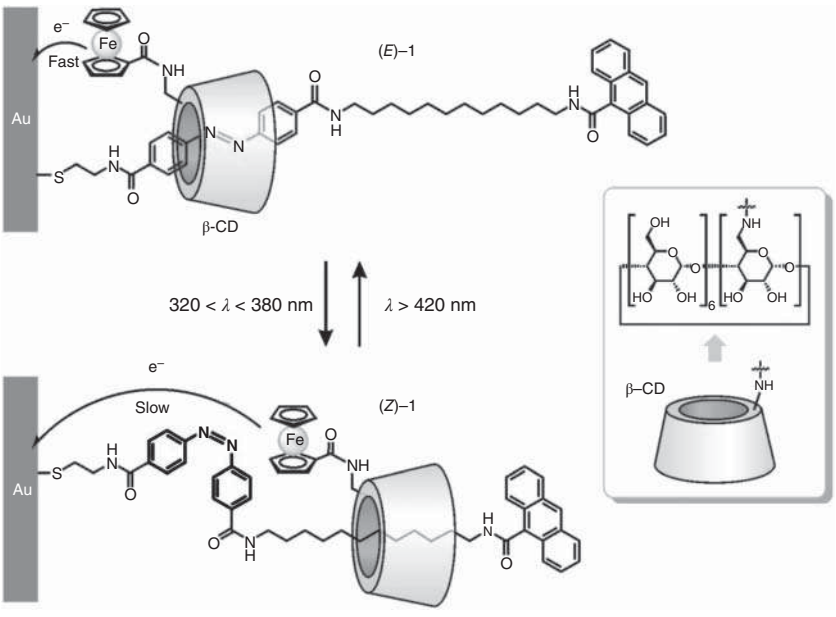


**Figure 32.5** Light-induced ring shuttling by *E*–*Z* isomerization of azobenzene in the surface-bound rotaxane **1**. Source: Willner et al. [60].

The azobenzene unit in the *E* configuration has a high affinity for the ring, which thus rests on it. Upon $E \rightarrow Z$ photoisomerization promoted by UV light irradiation, the isomerization of the azobenzene unit determines a movement of the β-CD ring toward the alkyl spacer. This is a consequence of the fact that the *Z* configuration of azobenzene is bulkier than the *E* form and cannot be encapsulated by β-CD; thus it has a negligible affinity toward the ring compared with the alkyl portion of the axle. Back $Z \rightarrow E$ photoisomerization, achieved by irradiation with visible light, triggers the return of the macrocycle to the starting position, which consequently completes a back and forth motion relative to the axle. Interestingly, this rather simple nanomachine is able to transduce optical information (light input) into an electrical signal (current output) via its shuttling motion. This happens because the current response for the oxidation of the appended ferrocene unit depends on its distance from the gold surface, thus enabling the electrochemical determination of the relative position of the β-CD ring along the axle, which is in turn controlled by the application of light stimuli.

An example of a more complex type of motion attainable in rotaxane-based MIM is exemplified by architectures constituted by two doubly interlocked molecular shuttles, which are usually referred to as [c2]daisy chains. These peculiar systems can undertake stimuli-induced contraction and extension movements [61] resembling those of the sarcomeres present in skeletal muscles, and for this reason they have been nicknamed "molecular muscles" [62, 63] The rotaxane dimer

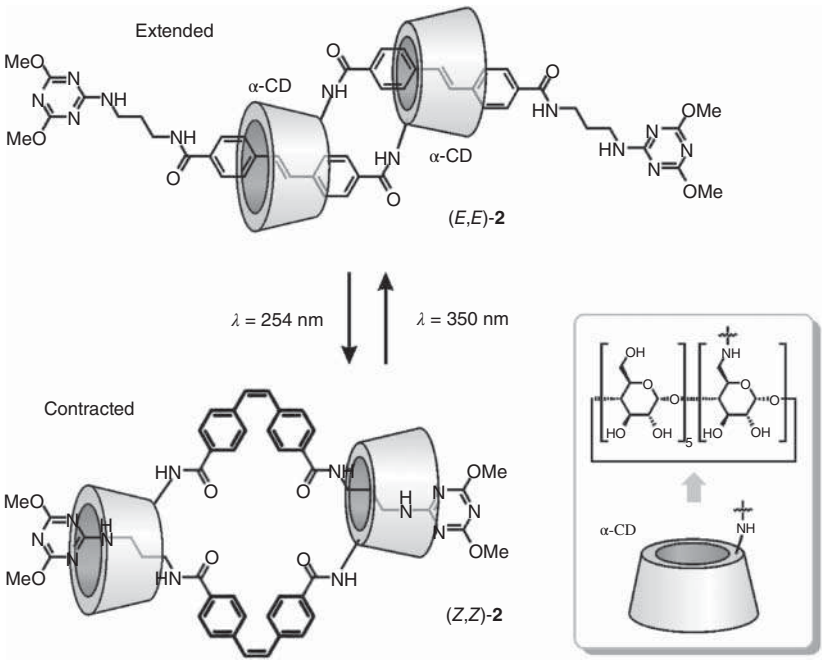


**Figure 32.6** Photochemical switching in a stilbene-containing rotaxane between extended and contracted forms. Source: Modified from Dawson et al. [64].

**2** (Figure 32.6), following the same operation principle of compound **1**, can be reversibly interconverted between an extended and contracted form as a result of the *E*–*Z* photoisomerization of the stilbene units incorporated in the axle [64]. While the stilbene unit in the *E* configuration is efficiently complexed by the α-cyclodextrin ring, its photoinduced isomerization to the *Z* form causes the macrocycle to move away. This change in the affinity between the axle and ring components results in an overall photocontrolled elongation/contraction of the whole molecular structure. Systems of this type are presently investigated as photo-addressable actuators in light-responsive advanced materials with foreseeable applications in micromechanics and soft robotics (see also Section 32.5.4).

Compound **3** (Figure 32.7) is another example of a photocontrollable bistable rotaxane motif, which exploits the photoisomerization of a fumaramide/maleamide

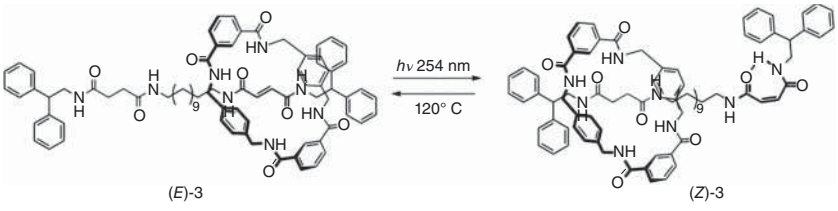


**Figure 32.7** Light-induced ring shuttling by *E*–*Z* isomerization of fumaramide in rotaxane **3**.

group to control the shuttling motion of the ring component (Figure 32.7) [65]. Rotaxane **3** is composed of an isophthalamide-based macrocycle and an axle moiety decorated with two recognition sites: a succinamide unit and a photo-isomerizable fumaramide group. The ring initially encircles the fumaramide group, which has a higher affinity for the amide macrocycle than the succinamide station. Photoisomerization by irradiation at 254 nm of the (*E*)-fumaramide moiety to its *Z* configuration induces the ring to move away and encircle the succinimide group. This is the result of the lower affinity of the macrocycle for the (*E*)-fumaramide station compared with the succinimide one. The thermally activated $Z \rightarrow E$ conversion of the fumaramide, by restoring the relative affinities of the two stations to their initial values, brings the ring back and completes a shuttling cycle controlled by light and thermal energy.

By employing the same recognition motifs present in rotaxane **3**, Leigh and coworkers were able to realize an outstanding example of complex movement in an MIM. Catenane **4** is one of the few existing examples of a molecular machine in which a combination of light and chemical stimuli is able to induce an overall directional rotation of a ring around another [66]. In catenane **4** (Figure 32.8), two rings are interlocked and held together by mechanical bond. The larger ring presents two recognition sites for the smaller encircling blue ring: a photoisomerizable fumaramide station (A) and a succinamide moiety (B). Station B presents on each side two bulky groups – a (*t*-butyl)dimethylsilyl group (C) and a triphenylmethyl group (D) – which act as kinetic barriers that impede any movement of the small ring around the larger one. Crucially, these two protecting groups can be orthogonally detached and reattached.

To operate this machine, a precise sequence of chemical and light stimuli has to be administered. In particular, in the starting state the small ring encircles the fumaramide binding site A, which, as in the case of the previously described rotaxane **3**, has a higher affinity for the ring than station B. Upon $E \rightarrow Z$ isomerization of the fumaramide station A promoted by light of 254 nm, its binding affinity for the small ring decreases in favor of binding site B. The subsequent removal of the silyl protecting group allows the small ring to move from A to B in a clockwise direction to encircle the succinamide station. Reattachment of the silyl protective group and successive back isomerization of the A station, followed by removal of the trityl group, result in another half-turn of the small ring that ends up surrounding the B station. Finally, tritylation of the free hydroxy group restores the initial state, thus concluding a full clockwise rotation powered by light irradiation and by two orthogonal chemical stimuli. Interestingly by inverting the sequence of silylation and tritylation attachment/detachment reactions, the movement of the smaller ring can be reversed affording counterclockwise rotation.

Despite the complex sequence of stimuli required for its operation drastically limiting the efficiency of this system, it represents an important milestone, which is highly representative of the advancements that the field of light-driven molecular machines based on MIMs has presently reached. In particular, the ability of this system to achieve a repetitive directional movement makes of it a noteworthy example of a full-fledged molecular motor. Molecular motors are a particularly valuable class

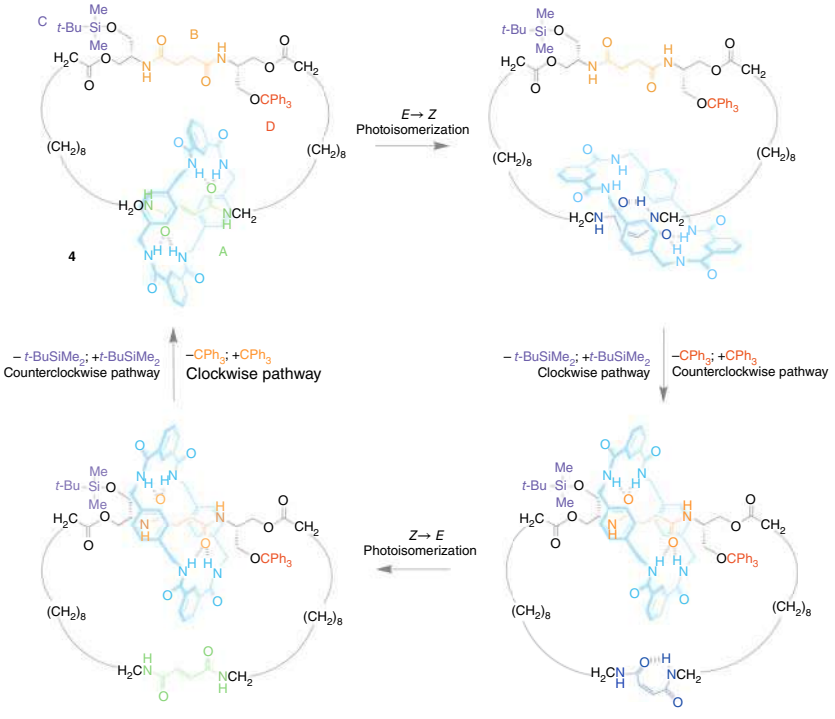


**Figure 32.8** Photochemically and chemically driven directional circumrotation in [2]catenane **4**. A and B indicate the fumaramide and succinamide stations, respectively. C and D indicate the (*t*-butyl) dimethylsilyl and triphenylmethyl stopper groups, respectively. Source: Adapted with permission from Baroncini et al. [17].

of nanomachines, since they are key components for the development of advanced molecular devices able to exploit a source of energy to produce mechanical work at the nanoscale.

### 32.2.2 Molecular Devices and Machines Based on Covalent Architectures

Despite lacking the large-amplitude dynamic features present in MIMs, light-activated molecular machines based on fully covalent architectures have yielded some of the most spectacular examples of control over molecular motion at the nanoscale.

Due to the large structural variety, for space requirements, a strict categorization based on their constitution is not practical. However, in general, fully covalent molecular machines display movements that are the result of either structural isomerization reactions – such as those that enable a peculiar class of nanomachines

known as "molecular walkers" to transport a cargo moiety along a track – or to conformational/configurational isomerization reactions – as in the class of molecular rotary machines.

A molecular rotary motor is a molecular machine capable of using an energy input to perform repeated directional 360° rotations of a rotor part of the molecule with respect to a stator part [67]. The directional control of rotation around a molecular bond has represented one of the most highly challenging tasks in nanoscience. Initial attempts were beset either by design shortcomings ascribable to the so-called Feynman's "ratchet and pawl" paradox [68, 69] or by only partial success [70]. Complete and repetitive unidirectional rotation remained an elusive goal until the peculiar stereochemical aspects of overcrowded alkene compounds were combined with their photochemical characteristics [71].

For an in-depth analysis of the operation and characteristics of overcrowded alkene molecular machines, the interested reader is referred to Chapter 11 (Feringa) of this book and to the many excellent review articles present in the literature [3, 9, 11, 17, 72, 73].

In the present context, it is enough to note that, nowadays, the totality of light-powered molecular rotary motors is based on the photochemically activated *E*–Z isomerization of either carbon–carbon or carbon–nitrogen double bonds. In these systems, a light-induced isomerization reaction is combined with particular stereochemical features that, by breaking the symmetry of the system, cause a directional preference in the relative sense of rotation of a portion of the molecule (rotor) with respect to another (stator).

Three main classes of molecular rotary motors have been developed in the last 20 years, namely: overcrowded alkenes, hemithioindigos, and imines (Figure 32.9).

Hemithioindigos (see also Chapter 13 by Henry Dube) [74, 75] and imine-based rotary machines (see also Chapter 15 by Jean-Marie Lehn) [76, 77] are still mainly investigated from a fundamental and mechanistic point of view. Instead,

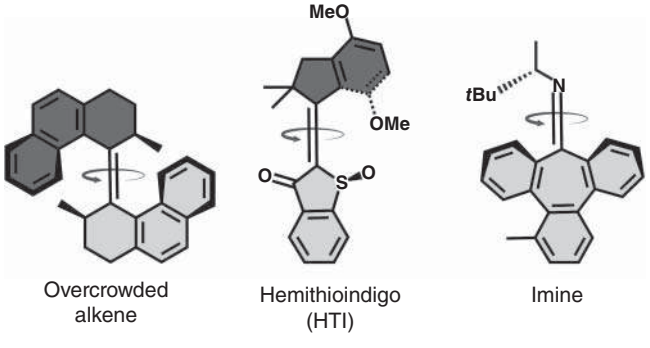


**Figure 32.9** Chemical structure of the three main classes of molecular rotary motors. The "stator" and "rotor" moieties are colored in dark and light gray, respectively.

overcrowded alkene-based rotary motors have advanced impressively in their range of applications over the past two decades [67, 73]. Nowadays, derivatives capable of rotating at room temperature with MHz frequencies, which work upon visible light irradiation and operate in aqueous environment, are available [78, 79]. As evidenced by the various examples reported in the following sections, the robustness, synthetic flexibility, and adaptability displayed by this class of molecular rotary motors have been a key enabler in the evolution of artificial molecular machines from laboratory oddities to potentially useful components in different areas of applied chemical research.

A structurally more complex class of covalent molecular machines, which is paradigmatic of systems where the moving part of the nanomachine is a substituent undergoing a rearrangement reaction, is represented by the so-called "molecular-walkers" [80]. In the simplest form, a molecular walker is composed of a bipedal moiety with "feet" that can bind and release from a "track" portion of the system through a series of successive chemical transformations. The stepwise administration of selective inputs enables the walking part of the system to progressively move along the track in a directional journey while keeping the walking portion of the molecule always bonded to the track to avoid missteps.

These systems have been inspired by the large number of bipedal motor proteins found in nature, the most famous examples being the kinesin and myosin V motor enzymes. Furthermore, interest in these systems has recently increased in response to the hypothesis that most viruses crawl on cellular surfaces following an analogous mechanism [81].

A prototypical example of an artificial molecular walker is shown, along with the sequence of reactions controlling its operation, in Figure 32.10a [82]. It is constituted by a walker component linked to the track by a hydrazone moiety, which is labile under acidic conditions, and a disulfide bridge that can be opened or closed with alternate redox stimuli. Thus, the two feet of the walker component can be orthogonally addressed in such a way that an opportune sequence of acid/base and redox inputs forces the two-legged molecule walker portion to move from the left to the right end of the track.

In a similar molecular walker, the introduction of a stilbene moiety between the two central footholds (Figure 32.10b) allows to control the overall direction of the walker motion by photoswitching the stilbene unit. This is possible since the configuration of the stilbene unit has a marked effect on the amount of ring strain present in the macrocycle formed when the walker unit bridges the stilbene linkage [83]. In particular, $E \rightarrow Z$ isomerization allows the walker to step onto the central stilbene unit, while subsequent $Z \rightarrow E$ isomerization results in a majority of the walkers being transported away from the stilbene group in a direction determined by which foot-track link is detached first. Thus, depending on the sequence of the two couples of orthogonal applied stimuli: acid or base, which control the dissociation of a "foot" of the walker from the track; UV or visible light (plus

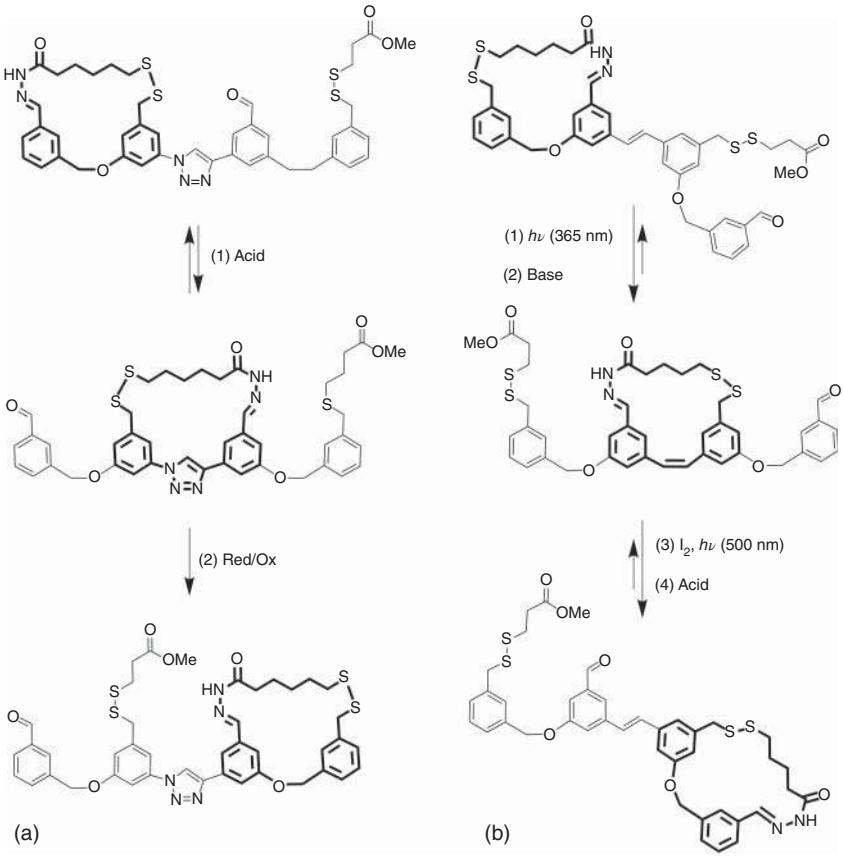


**Figure 32.10** Structure and sequence of transformations of a molecular walker that move directionally along a four-station molecular track in response to (1) acidification, and (2) chemical reduction and oxidation (a). Structure and sequence of transformation of a light-driven molecular walker that moves along a four-station molecular track. The reaction sequence transports the walker from left to the right end of the track; exchanging steps (2) and (4) causes the walker to be transported preferentially in the opposite direction (b).

iodine), which control the isomerization state of the stilbene unit, it is possible to control if the walker moves from the left to the right or vice versa, adding a further level of control on the movement displayed by the system.

Despite being remarkable examples of the control of linear movements at the nanoscale, all presently developed molecular walker systems are quite inefficient and operate on short and flexible tracks. Because of these shortcomings, such nanomachines have still not found applications besides proof-of-principle studies. Better systems with improved tracks that are rigid, polymeric, have junctions, and/or can be tethered to surfaces and walkers displaying better directional bias, binding chemistry, and directionality are presently a very active area of research.

## 32.3 From Movements to Functions

In the previous sections, the description of a few paradigmatic examples of light-driven molecular machines showcased some of the complex forms of movement that nowadays existing systems can attain. Research on nanomachines has reached a high level of sophistication that has driven researchers to move from proof-of-principle investigations, in which the movement performed by the machine is the only outcome, to studies aimed at demonstrating that useful work can be extracted from an operating molecular machine to accomplish a higher-level function.

Biological nanomachines admirably perform multiple useful tasks of great complexity and across different length scales, ranging from molecular (e.g. catalysis), microscopic (e.g. pumping and transport), to macroscopic level (e.g. muscle-based actuation and locomotion). It is not unthinkable that in the future artificial nanomachines could be able to replicate, and in certain tasks even surpass, the performance and complexity of operations of their natural counterparts, as happened in the case of macroscopic mechanical machines [84].

In the following paragraphs, relevant examples in the literature will be described in which the action of synthetic light-activated molecular machines is harnessed, transmitted, or collected such that a sizeable effect is detected beyond the machine operation itself. The different examples are organized according to the type of function enabled by the machine operation.

### 32.3.1 Catalysis

One of the major tasks accomplished by biomolecular machines is sustaining and controlling all the chemical processes that occur within a living organism through the precise catalytic regulation of metabolic reactions [4, 5]. This has served as an inspiration to develop artificial molecular machines able to exploit their movements to implement stimuli-responsive and dynamic catalytic mechanisms [85, 86].

Overcrowded alkene molecular rotary motors have been successfully employed to construct switchable catalysts that can selectively provide all the different stereoisomers in a given chemical transformation. These nanomachines exploit their molecular rotary portion as a multistage chiral switch, which in combination with appended catalytic moieties determines the ability to induce a degree of stereoselection in the product of a catalyzed transformation. In one of the first examples reported based on this approach, the stereodivergent Michael addition of a thiolate to an α,β-unsaturated ketone was accomplished with compound **5** (Figure 32.11), which consists of a molecular rotary part functionalized with aminopyridine and thiourea moieties [87]. In particular, as depicted in Figure 32.12, in the *E*-isomer the functional substituents responsible for the catalytic activity are far apart, resulting in a low catalytic activity and formation of a racemic product. Instead, the *Z*-isomer obtained by light irradiation presents the two functional substituents in close proximity; this arrangement causes a major increase of the reaction rate and a marked

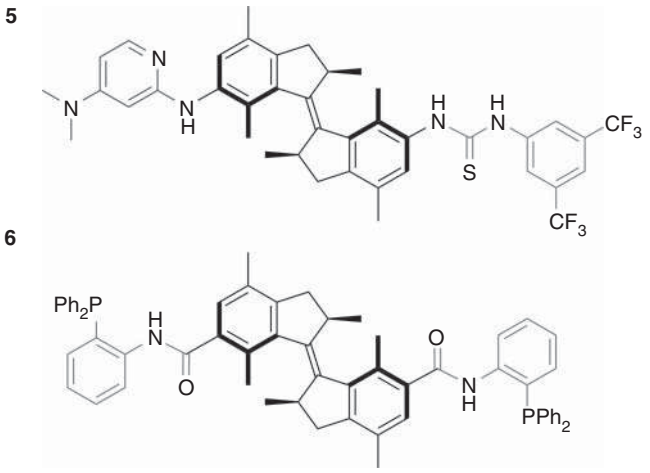


**Figure 32.11** Structure formula of the light switchable catalyst **5** and **6** in their (*P,P*)-(*E*) form. The light switchable moieties are colored in black, while the appended catalytic substituents in gray.

enantioselectivity. Furthermore, the relative helical orientation of the aminopyridine and thiourea moieties is able to determine the sign of the enantiomer obtained during the addition reaction. Specifically, the metastable (*M,M*)-(*Z*)-isomer affords prevalently the *S*-configuration of the product while the formation of the opposite enantiomer is catalyzed by the stable (*P,P*)-(*Z*)-form (Figure 32.12). Thus, **5** behaves as a light-responsive artificial catalyst whose product distribution can be controlled by the action of external photochemical and thermal stimuli, which are capable of directing the formation of either a racemate or one of the two enantiomers of the product.

In a following study [88], a compound identical to **5**, except for the absence of the phenyl spacers thus allowing a closer proximity of the catalytically active sites, was experimentally validated as a catalyst in the Henry reaction between nitromethane and trifluoroketones. It was proved that the formation of a more constrained pocket results in an enhanced activity and stereoselectivity of the switchable catalyst. By building on these concepts, a system was designed and synthesized in which each side of the rotary unit was decorated with chiral biphosphine moieties that could act as ligands for transition metals (compound **6** in Figure 32.11) [89]. As a test reaction for the enantioselectivity of the rotary-biphosphine catalyst **6** the palladium-catalyzed desymmetrization of *meso*-cyclopent-2-en-1,4-diol bis(carbamate) was chosen. In the presence of Pd, the (*P,P*)-(*E*)-isomer resulted in a nearly racemic oxazolidinone product in a moderate yield. Instead, the Pd complex of the (*M,M*)-(*Z*)-form, obtained by photochemical isomerization, resulted in a reaction yield of 90% and an enantiomeric ratio of 93 : 7 in favor of the (3*R*,4*S*) product. The opposite enantiomer (3*S*,4*R*) was obtained in a 85% yield and 6 : 94 enantiomeric ratio after thermal isomerization of the ligand to the (*P,P*)-(*Z*)-form. Despite its efficiency, this system proved to be rather delicate, in fact, in situ switching of the palladium catalyst proved to be

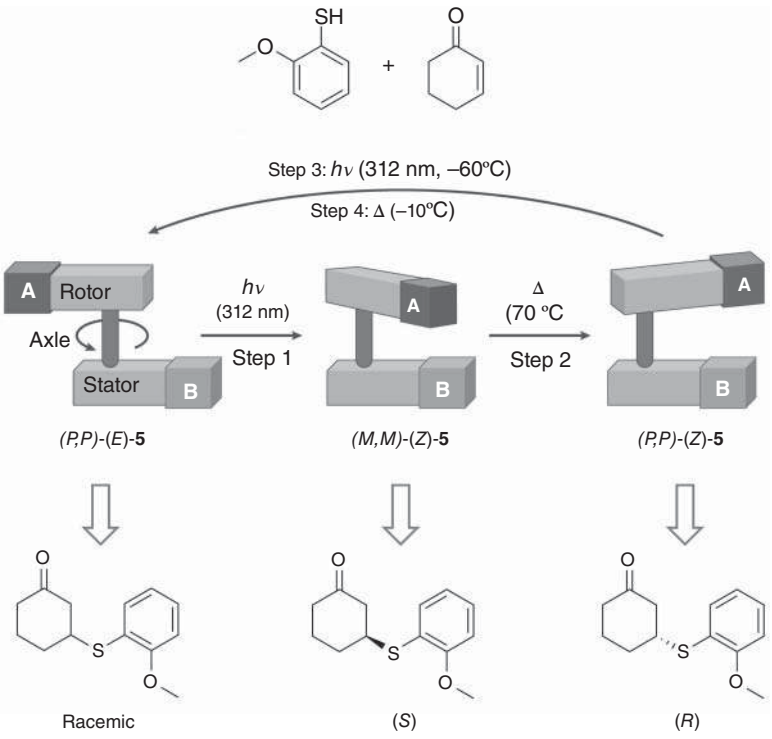


**Figure 32.12** The effect of the light- and thermally driven switching of **5** on the stereochemistry of the product of the Michael addition between 2-methoxythiophenol and 2-cyclohexen-1-one. Source: Adapted with permission from Wang and Feringa [87].

unrealizable due to the instability of the species generated by UV irradiation and heating.

A recent example of a multistate switchable catalyst was synthesized (**7**, Figure 32.13) by linking a bidentate 2,2′-biphenol ligand moiety to a photoactive molecular rotary photoswitch [90]. As a result of the spatial closeness of the photoresponsive and biphenol portions in this nanomachine, it was postulated that the favored atropoisomer of the biaryl moiety (highlighted in green in Figure 32.13) could be influenced by the helicity of the overcrowded alkene core (blue in Figure 32.13), which in turn is controlled by the configuration of the nearby stereogenic carbon atom (red circle in Figure 32.13). Detailed NMR, UV, and circular dichroism (CD) spectroscopic experiments proved that the reversible photoswitching between the ($R,P,S_a$) and ($R,M,R_a$) stereoisomers is indeed the result of the direct influence that the helicity of the motor part has on the chirality of the biphenol unit. The addition reaction of diethylzinc to aromatic aldehydes was used as a test for the catalytic properties of **7**. The active catalyst, formed upon coordination of the biphenol ligand of **7** to a zinc ion, presented good activity and light-switchable enantioselectivity on several substrates. This indicates that the metastable isomer ($R,M,R_a$) of the

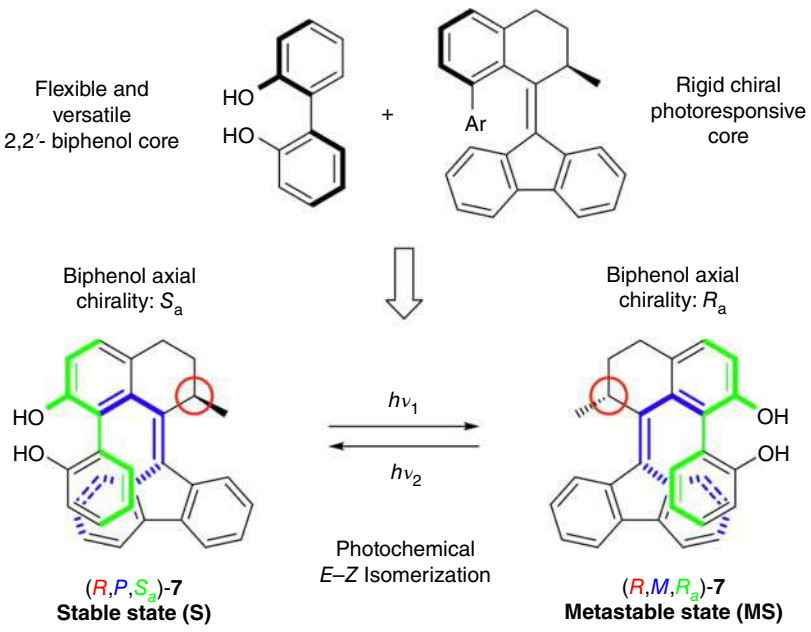


**Figure 32.13** Design, structural formula, and photoinduced switching of the catalyst **7**. This compound features point-to-helical-to-axial-to-point transfer of chirality, a property manifested in its catalytic activity. Source: Adapted with permission from Pizzolato et al. [90].

catalyst resembles in its catalytic activity the enantiomer of the stable isomer ($R,P,S_a$).

More recently, a photoswitchable overcrowded alkene appended with anion-binding triazole oligomers was demonstrated to enable stimuli-responsive anion-binding catalysis by means of supramolecular transfer of chirality (Figure 32.14) [91]. The relative positioning of the ion-binding units creates different chiral environments around the anion recognition site for each configuration of the photoswitchable central moiety, which translates into a different stereochemical product distribution for the catalyzed reaction. Triazoles oligomers were selected for their ability to adopt a helical supramolecular arrangement when engaged in hydrogen bonding with negatively charged anions. The switching of the photoactive part between its different states was expected to influence the helicity of the anion-bonded triazole moieties dictating, via a chirality transfer effect, the anion catalytic activity. NMR, UV–vis, and CD spectroscopy studies proved that while the (*R*,*R*)-(*P*,*P*)-*E*-**8** stereoisomer is unable to form a stable complex in the presence of chloride anions, the triazole oligomeric arms of the stereoisomers (*R*,*R*)-(*M*,*M*)-*Z*-**8** and (*R*,*R*)-(*P*,*P*)-*Z*-**8**, accessible via light- and heat-driven switching of the photoactive part, formed enantiomeric helical assemblies of opposite configuration in the presence of chloride anions. This observation demonstrates the transfer and amplification of chiral information from the photoswitchable moiety of the system to the supramolecular organization of the oligomeric anion-binding

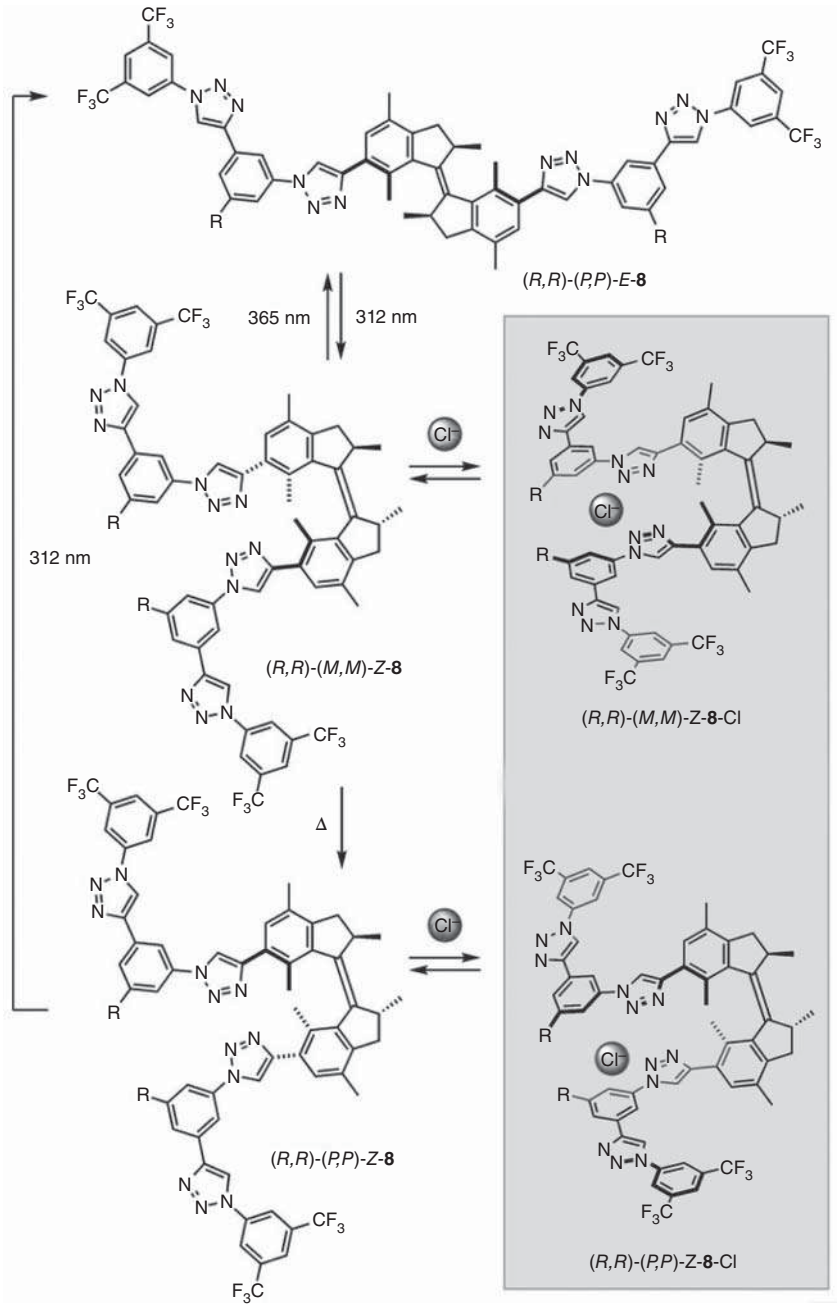


**Figure 32.14** Structure and phtoswitching behavior of a stereodivergent anion-binding catalysis based on an oligotriazole-functionalized overcrowded alkene type rotary motor. Source: Adapted with permission from Dorel et al. [91].

receptor portion. The catalytic activity of the assembly was tested on the addition reaction between silyl ketene acetal and 1-chloroisochroman showing, as expected, a modulable stereoselectivity in the addition product.

Indeed, the product was obtained as a racemate in the presence of the (*P,P*)-*E* state, while each of the *Z* states promoted the formation of opposite enantiomers: up to 80 : 20 e.r. for the (*M*,*M*)-*Z* state and 5 : 95 e.r. for the (*P*,*P*)-*Z*. These remarkable enantioselectivity reversal values highlight the potential of such systems in the field of photoswitchable catalysis but also, due to the underlying supramolecular chirality transfer concept, in the arena of supramolecular-responsive assemblies.

In general, the described systems exploit the possibility of overcrowded alkene photoswitches to be operated as multistate compounds with markedly different structures (e.g. size, shape, helicity) and features (e.g. polarity, optical properties). This has enabled, as shown, the development of different catalytic nanomachines able to closely mimic the allosteric regulation of the enzymes present in nature and to a certain extent even surpass them. Indeed, natural enzymes are unable to tune or switch the handedness of the synthesized products with the same capacity exhibited by these nanodevices. Thus, these systems could represent the first instance in which an artificial nanomachine has surpassed the functions of a natural one.

## 32.4 Transport of Molecular Substrates

The controlled transport of substrates is a fundamental function in all living organisms. Indeed, while ions and small molecules are able to freely diffuse across the cytosol within a living cell, larger cellular components such as vesicles and organelles need to be actively transported since they would move too slowly. This essential task is accomplished by protein-based biomolecular nanomachines such as kinesin and myosin [5]. These proteins are composed by a docking domain, capable of collecting or releasing a cargo moiety upon stimulation, and a motor portion that directionally transports the whole assembly along a track by consuming a fuel (ATP). Inspired by their biological counterparts, the design and synthesis of artificial molecular machines able to actively transport molecular substrates have always been a most ambitious goal in nanoscience. While synthetic DNA architectures capable of transporting and sorting cargos have reached a high level of sophistication [92], fully synthetic systems are still in their infancy. However, research activity in this area is rapidly advancing, pushed by the promises of disclosing unconventional new routes in energy conversion and storage, material science, and medical therapies [93, 94].

### 32.4.1 Rotaxane-Based Molecular Transporters

The reversible shuttling motion of the ring component along the axle in a switchable two-station rotaxane (see paragraph 32.2.1) readily suggests the possibility of its exploitation for the design of a nanomachine able to directionally transport a

molecular cargo. The development of such a system, however, requires a series of detailed considerations. Firstly, in a rotaxane-based transporter system, the macrocyclic ring has to be functionalized with a binding site to which the cargo can be attached and detached with the application of a stimulus. Furthermore, to properly operate, a rotaxane-based transporter nanomachine has to fulfill these design requirements: (i) the ring back and forth translation and cargo attachment and detachment processes have to be independent, reversible, and controlled by orthogonal (non-interfering) stimuli; (ii) the cargo has to remain bound to the macrocycle ring during the shuttling motion.

A proof-of-concept example of such a nanomachine was realized with the multicomponent rotaxane **9** (Figure 32.15b), which was designed to accomplish, via chemical and photochemical control, the capture, transport, and release of the metal complex **10** [95]. The rotaxane is constituted by a molecular axle containing a dibenzylammonium (A, green in Figure 32.15) and a 4,4′-bipyridinium (B, blue in Figure 32.15) station and an interlocked dibenzo[24]crown-8-type macrocycle (magenta in Figure 32.15). The ring encircles the dibenzylammonium site since it has a higher affinity for station A compared with B. Deprotonation of the ammonium center with a base induces the shuttling of the ring toward the bipyridinium station; the ring can be moved back to its initial position upon regeneration of the ammonium site with an acid [96]. These reversible ring movements, which can be controlled by acid/base chemical stimuli, occur on the timescale of milliseconds at room temperature in solution [97]. A nitrile group attached through a short chain to the crown ether ring plays the role of anchoring site for the cargo. The latter is a $[Ru(tpy)(bpy)]L^{2+}$ complex in which tpy (2,2′;6′,2″-terpyridine) and bpy (2,2′-bipyridine) are chelating ligands and L is a monodentate ancillary ligand (e.g. a solvent molecule). A combination of NMR and UV–visible spectroscopic and electrochemical studies enabled to elucidate and prove the accomplishment of the designed transporter function [95].

It was experimentally demonstrated that the ring in rotaxane **9**, initially located around the A station, is able to pick up from a solution the Ru complex **10** by replacing the monodentate ligand L with its nitrile tether. This reaction thus causes the loading of the cargo on the transporter. The successive deprotonation with a base of the dibenzylammonium station (+X in Figure 32.15a) provokes the movement of the ring toward B without affecting the linkage with the cargo. Irradiation with visible light (+Y) releases the Ru complex from the nitrile terminus of the rotaxane without affecting the position of the ring [98]. By regenerating the protonated A station (−X) by the addition of an acid, the ring is brought back to its starting position and another cycle, in principle, can restart. Unfortunately, the loading of a successive cargo molecule, i.e. re-coordination of **10** to **9**, was apparently hindered by adventitious ligands (most probably water) that by filling the vacant coordination position at the ruthenium center impede the binding of the nitrile moiety of **9**.

This system showcases an example of what could be more rightly defined as a light-operated rather than light-driven molecular machine, indeed light is not directly responsible for the movement of the components but is however able to

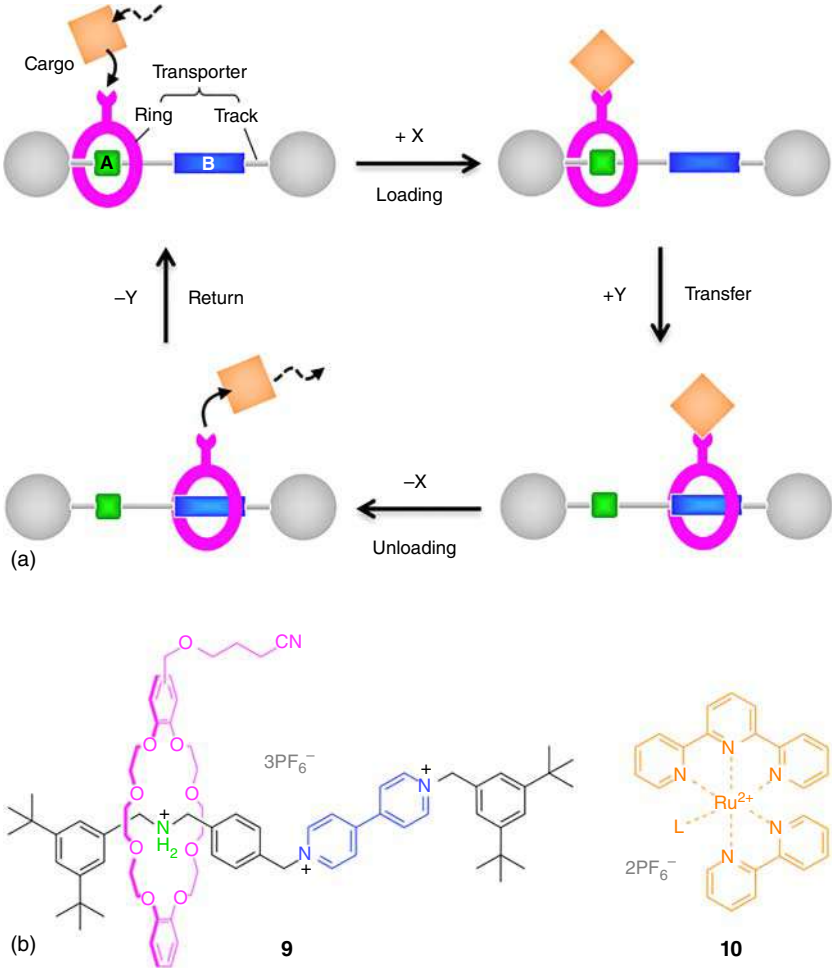


**Figure 32.15** Design of a "molecular transporter" based on a controllable molecular shuttle and operated by two independent external stimuli, X and Y (a). Structure formulas of the rotaxane transporter **9** and cargo **10** (b). Source: Adapted with permission from Baroncini et al. [17].

fulfill the key task related to cargo release. Moreover, it should be noted that the transport is unproductive since the cargo is picked up and released in the same homogeneous solution. Indeed, a physical separation between the site of collection and release of the cargo moieties is necessary to extract useful work from the operation of a molecular transporter, a role fulfilled by phospholipidic membranes in living cells. Recently, an artificial molecular machine capable of passively transport $K^+$ ions across a bilayer membrane, thus operating as a molecular scale "cable-car" has been demonstrated [99]. However, systems able to generate a concentration gradient by moving ions energetically uphill across a membrane are still unrealized.

Although still in their infancy, these examples can be seen as the forerunners of the next generation of molecular machines able to operate in compartmentalized environments and thus capable to accomplish tasks that could not be achieved otherwise.

### 32.4.2 Rotary Molecular Transporters

An innovative and not bioinspired design of a molecular transporter is based on nanomachines capable of performing a rotational motion that results in the intramolecular transport of a cargo moiety between two distinct positions located at the ends of a molecular scaffold. These systems are designed in such a way that, in response to an external stimulus, a molecular photoswitch changes the orientation of an attached "arm" with the effect of varying its distance from the extremities of a "platform." A successive orthogonal stimulus is then applied to induce the attachment/detachment of the cargo moiety from the moving arm portion of the nanomachine, thus allowing its controlled transfer in either direction. In such a system, it is crucial that, in analogy to "molecular walkers" (See paragraph 32.2.1), the cargo is connected to the machine during each step of the operation mechanism, to prevent its exchange with other molecules in solution.

An example of this type of nanomachine, which under the action of light transfers an acetyl group between two distant positions within the molecule, is shown in Figure 32.16 [100]. The transporter **11** is assembled from an overcrowded alkene rotary photoswitch decorated with three different components: (i) a phenoxy "departure site," to which the cargo acetyl group is linked at the start; (ii) a benzylamine "arrival site" on the opposite side of the lower portion of the system, where the cargo is transferred after rotation, and; (iii) a thiol group tethered to the upper half of the rotary photoswitch that acts as an arm to grasp the cargo and transfer it. The operational sequence (Figure 32.16) starts with the acid-catalyzed deprotection of the tritylated thiol and Boc-protected amine moieties in precursor **12**. Afterward, treatment with a base, which promotes the nucleophilic attack of the thiolate group on the tether to the phenolic ester on the nearby side yielding a thioacetate, induces the pickup of the cargo moiety by the arm. Then, the isomerization of the carbon–carbon double bond of the photoactive portion of the machine by irradiation at 312 nm brings the thioacetate close to the benzylamine site; finally, the nucleophilic attack of the benzylamine end on the thioacetate group, transfers the acetyl fragment from the arm to the lower half of the system. The net result of this series of reactions is the intramolecular transport of the acetyl group from one end to the opposite of this fairly rigid molecule, covering along the process a distance of about 2 nm.

### 32.4.3 Supramolecular Pumps

In addition to molecular transporters, the shuttling motion of the ring and axle components in (pseudo)rotaxane MIMs has enabled their exploitation for the development of artificial (supra)molecular pumps. In these devices, the ring and the axle

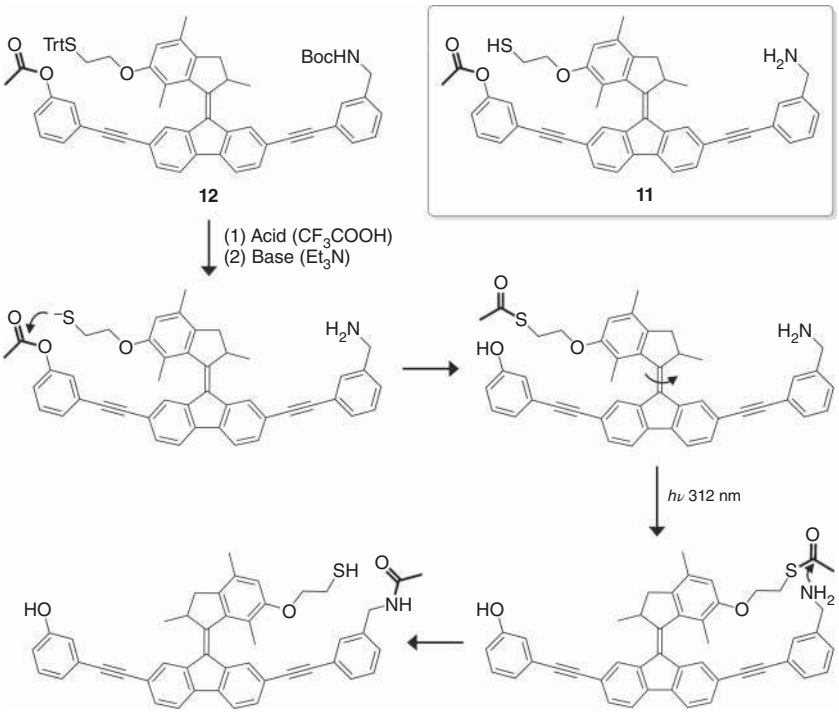


**Figure 32.16** Structure formulas of the molecular transporter **11** and its precursor **12**, based on a molecular rotary motor, and operation scheme for the chemically and photochemically triggered transport of an acetyl cargo (bold black) from a phenoxy "departure" site to a benzylamine "arrival" site. Source: Chen et al. [100].

move unidirectionally with respect to one another in response to an energy input. The scarcity of systems capable of implementing this apparently simple function is a clear indication of how challenging is to fulfill this seemingly trivial task. Indeed, artificial molecular pumps remain some of the most complex type of nanomachines both to realize and theoretically comprehend [101, 102].

The only reported example of a light-activated supramolecular pump based on a rotaxane architecture has been cleverly developed by exploiting the well-known recognition motifs represented by a crown ether encircling a secondary ammonium cation [103]. In a crucial preliminary work, it was reported that photoisomerization of the azobenzene units attached at both ends of the axle moiety $\mathbf{14}^+$ has a remarkable effect on both the kinetics and thermodynamics of the self-assembly process with the dibenzo[24]crown-8 (DB24C8) ring **13** that leads to the formation of a pseudorotaxane (Figure 32.17a) [104]. Specifically, photoisomerization of the azobenzene end groups in (*E*,*E*)-$\mathbf{14}^+$ to yield (*Z*,*Z*)-$\mathbf{14}^+$ results in both a reduction of the mutual binding interaction between the axle moiety and the ring and in a large decrease of the threading–dethreading rate constants. Furthermore, the process is fully reversible by irradiation with visible light or by heating thanks to the fatigue resistance typical of azobenzene photoswitches. These observations proved

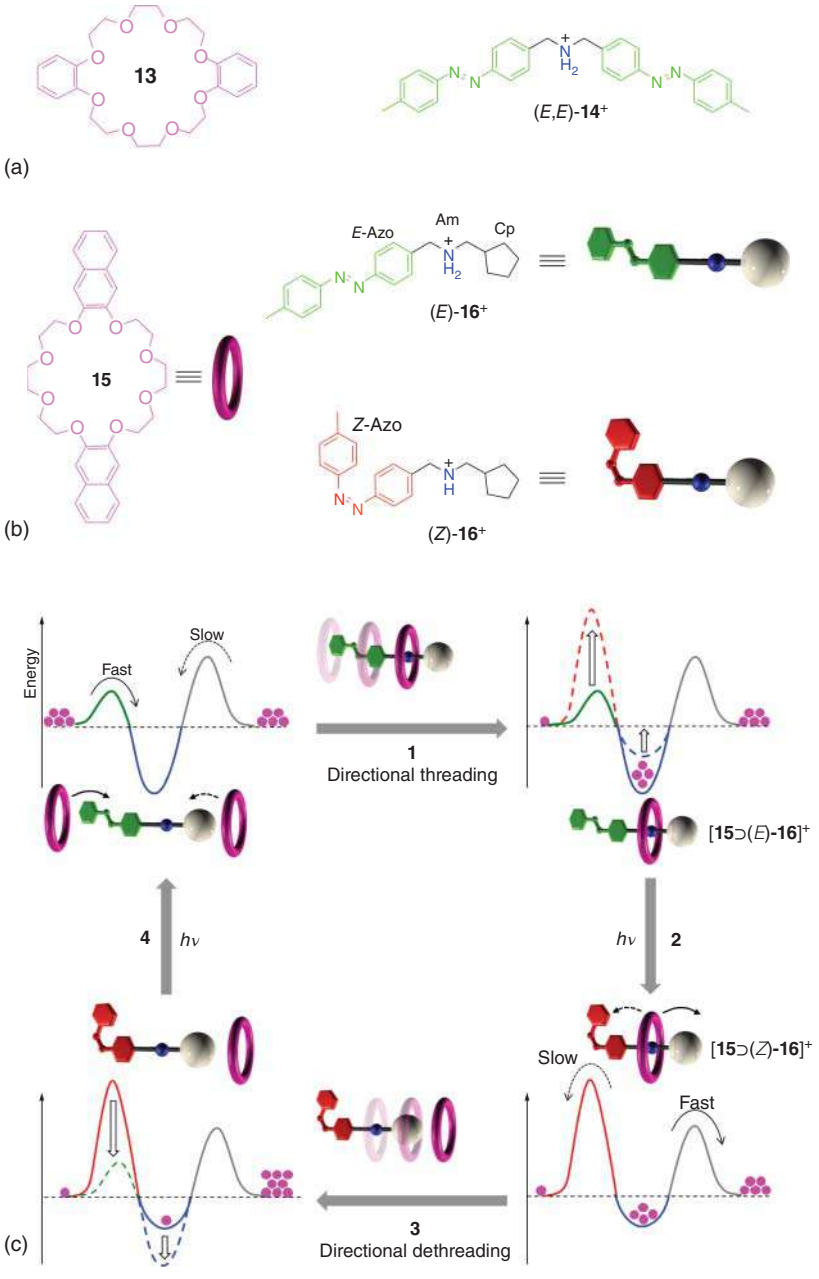


**Figure 32.17** (a) Structural formulas of the axle **14**$^+$, in its *E,E* configuration, and of the DB24C8 ring **13**. (b) Structural formula and schematized representation of the axle **15**$^+$, in its *E* and *Z* configurations, and of the ring **16**. (c) Schematic operation mechanism and simplified potential energy profiles, as a function of the ring-axle relative position, for each step (gray solid arrows) of the directional light-activated threading/dethreading motion (processes 1, 2, 3, and 4) of the ring and axle components. Dashed arrows indicate processes that are kinetically prevented. Source: Adapted with permission from Baroncini et al. [17].

that *Z*-azobenzene can behave as a photoswitchable inhibitor and negative catalyst for the self-assembly of the axle **14**$^+$ with ring **13**.

These preliminary results constituted the foundation for the design and synthesis of the nonsymmetric axle **15**$^+$ (Figure 32.17b), with the objective of developing a system where the ring would be forced to thread through the axle in a specific direction [105].

Critical for the operation of this simple model of a nanoscale molecular pump, axle **15**$^+$ hosts a secondary ammonium station (Am) bordered by a photoswitchable azobenzene unit (Azo) and a passive cyclopentyl moiety (Cp) [106] (Figure 32.17b), whose slippage rate for the macrocycle is intermediate between that of the Azo unit in the *E* and *Z* configurations.

Accurate kinetic experiments showed that the threading rate of the Cp moiety through the DB24C8 macrocycle is almost two orders of magnitude slower than that through the *E*-Azo end of (*E*)-**15**$^+$, while it is still considerably faster than that through the *Z*-Azo group of (*Z*)-**15**$^+$. However, a second pair of chemical stimuli had to be employed in order to complete a directionally controlled threading/dethreading cycle, since the photoisomerization of the Azo unit of **15**$^+$ did not affect the affinity of the axle for the macrocycle in the investigated solvent, hence preventing the realization of an autonomous operation cycle controlled solely by light.

In a successive work, ring **13** was replaced with a similar but strongly fluorescent macrocycle (compound **16** in Figure 32.17b) to study the self-assembly process by luminescence spectroscopy, a more sensitive technique than NMR [107]. The change in the ring component together with switching to dichloromethane as a solvent resulted in a binding constant of the ring **16** about four times larger with (*E*)-**15**$^+$ than (*Z*)-**15**$^+$, while the relative value of the rate constants for the threading and dethreading of the ring was unvaried. Hence, in the system composed of the ring **16** and the axle **15**$^+$, the light-induced switching of the Azo unit is able to affect simultaneously both the kinetics and thermodynamics of the self-assembly process between the ring and axle components.

Under light irradiation, the system operates as a supramolecular light-driven pump, which directionally carries rings from the Cp to the Azo end of the axle, as represented in Figure 32.17c. Along a cycle of operation, at the beginning, axle (*E*)-**15**$^+$ and ring **16** self-assemble into the pseudorotaxane architecture [**16**⊃(*E*)-**15**]$^+$ (Figure 32.17c, process 1). At this stage, the threading of the macrocycle is faster from the *E*-Azo end of the axle. Absorption of light by the *E*-Azo unit of [**16**⊃(*E*)-**15**]$^+$, yielding [**16**⊃(*Z*)-**15**]$^+$ (Figure 32.17c, process 2), results in two concomitant modifications: (i) a reduction of the affinity of the Am station toward **16**, and (ii) an increase of the energy barrier for dethreading from the Azo end of the axle. The combined effect of these two changes in the potential landscape of the system forces the ring to slip past the Cp end, thus exiting from the opposite side from which it threaded initially (Figure 32.17c, process 3). Finally, since both the *E* and *Z* isomers of **15**$^+$ are photoactive and their absorption spectra overlap, another photon of the same wavelength can trigger the $Z \rightarrow E$ photoisomerization of **15**$^+$, thus renovating the initial state

and completing the cycle (Figure 32.17c, process 4). It is interesting that in this system, one of the few shortcomings of azobenzene as a photoswitch, i.e. that the spectral features of the *E* and *Z* stereoisomers are overlapping, is positively exploited and actually fundamental for the proper operation of the machine. Indeed, upon continuous light irradiation, the ceaseless photoswitching between the *E* and *Z* configuration of the Azo end results in an out-of-equilibrium stationary state, which establishes a clockwise net flux of species along the closed network of reactions (gray arrows in Figure 32.17c), which continues as long as photons are absorbed. Hence, in this system under constant illumination, light energy powers a continuous relative unidirectional motion of the ring and axle components.

Presently, only another example of a light-activated supramolecular pump has been reported, which relies on a redox activated pump modified to be driven by a photoinduced electron transfer process. However, the delicate sequence of bimolecular reactions necessary to relay the electrons between the photosensitizer and the nanomachine and their concentration dependence severely hamper the fatigue resistance of the system when light operated [108].

It should be noted, however, that the free diffusion in solution of the pumped moieties in all present examples of light-operated supramolecular pumps rapidly dissipates any work done by the pump itself. Thus, despite the progress in this area being remarkable, further work still has to be done to turn these devices into systems able to perform useful work by generating, for example, concentration gradients across membranes or transport chemical moieties along predetermined pathways [109, 110].

## 32.5 Collective Effects and Macroscopic Actuation

The hierarchical organization of biological muscles is a prominent example of how nature has been extremely proficient in coupling and summing up in time and space the small force generated by individual biomolecular machines composed of single myosin and actin filaments by organizing them into a larger structure. Researchers have recently started to address the problem of amplifying the nanoscale mechanical movements of artificial molecular machines by organizing them into ordered and well-defined larger and more complex architectures [111].

In the past two decades, several research groups have devised methods to organize molecular machines at microscopic [112, 113] and macroscopic [114, 115] scales; these attempts have involved the deposition of molecular machines on surfaces [116–119], incorporation in membranes and interfaces [120], and integration with crystalline [121, 122] or polymeric [123, 124] structures. In the next sections, examples of light-powered synthetic molecular machines organized into larger assemblies aimed at combining their action in order to achieve effects at larger length scales will be presented.

### 32.5.1 Molecular Machines on Surfaces

The stimuli-induced structural and electronic changes of switchable molecular species deposited on a surface can be exploited to modulate macroscopic properties of the surface itself, such as wettability. This strategy, which has been extensively implemented with photoswitchable compounds [116], can be applied to molecular machines with the purpose of collecting and amplifying mechanical effects.

In a pioneering study, it was shown that light excitation of a rotaxane-based molecular shuttle adsorbed on an appropriately modified metal surface causes the displacement of a liquid droplet across the surface [125]. Rotaxane (*E*)-**17** (Figure 32.18a) consists of a tetralactam macrocycle threaded by an axle that comprises a photoactive fumaramide station and a tetrafluorosuccinamide station. The affinity of the macrocycle for the fumaramide site, arising from hydrogen bonding interactions, is larger than that for the fluorinated succinamide unit; thus, in the thermodynamically stable form of the rotaxane (*E*), the preferred station for the ring is the fumaramide one. Upon UV light excitation, however, the primary station undergoes $E \rightarrow Z$ isomerization forming the maleamide isomer, which is a very poor recognition site for the ring. As a result, the latter moves to encircle the tetrafluorosuccinamide site. The thermally activated $Z \rightarrow E$ back isomerization regenerates the starting structure, thus completing the shuttling cycle (Figure 32.18a). It should be noted that the stimuli-induced motion of the ring in **17** has the consequence of concealing or exposing the fluorinated moiety of the axle with respect to the environment. As the wettability of surfaces by polar or apolar liquids is highly sensitive to the presence of fluoroalkane groups on the surface, it was envisioned that the photoinduced shuttling process shown in Figure 32.18a could be exploited to change the contact angle of a liquid droplet placed on the surface.

The rotaxane was thus hydrogen-bonded on a monolayer of 11-mercaptoundecanoic acid self-assembled on a glass-supported Au(111) surface (Figure 32.18b). Indeed, the contact angle measured for small (0.5–5 μl) drops of low-volatility liquids (such as water, formamide, ethylene glycol, and diiodomethane) decreased significantly upon irradiation of the surface with ultraviolet light. Control experiments confirmed that the light-induced lowering of the contact angle is related to a reduction in the number of fluoroalkane residues exposed at the surface of the substrate (Figure 32.18b). Such a photoinduced dewetting was exploited to move the droplets across the surface: when the area above the droplet is irradiated, the liquid is attracted to the switched zone. The collective action of a monolayer of these molecular shuttles is powerful enough to move a droplet of diiodomethane for about 1 mm up to a 12° incline (Figure 32.18c). This effect is mediated by a change in a bulk physical property; as such, it is not the result of a direct amplification of motion from the nanometer to the macroscopic scale. Nevertheless, the work is fascinating because a millimeter-size movement is ultimately a consequence of molecular rearrangements in an organized assembly of molecular machines. From an applicative perspective, the transport of liquids using photoresponsive surfaces may prove useful for delivering analytes in lab-on-a-chip setup or for performing

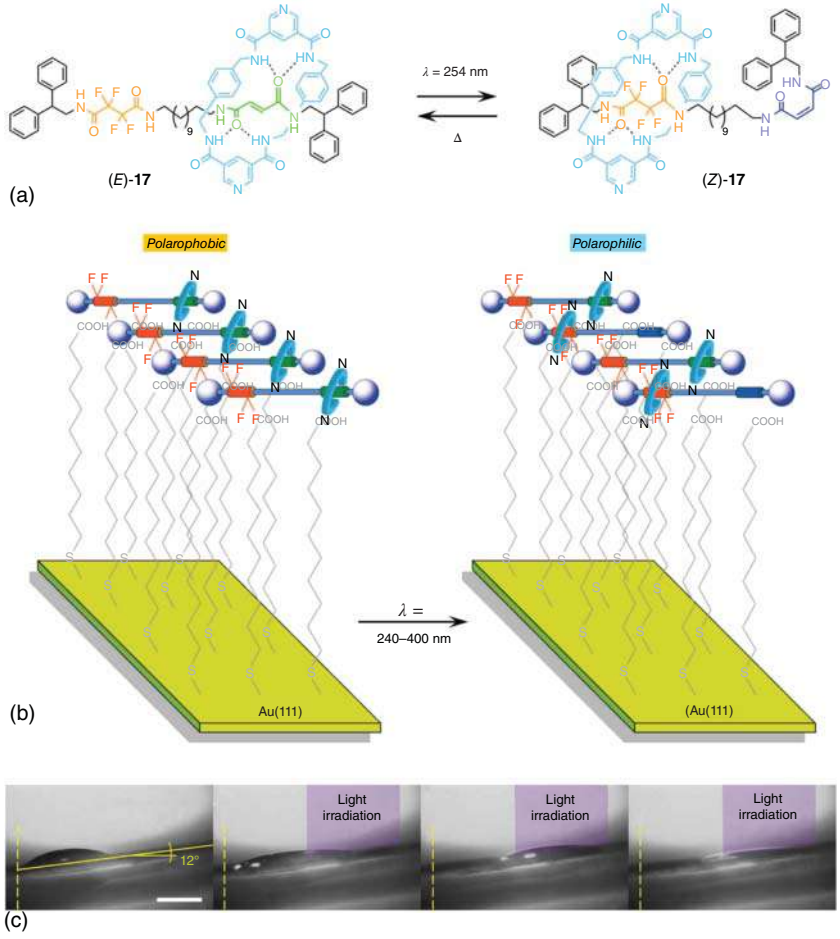


**Figure 32.18** Structural formula of rotaxane **17** and its operation as a photocontrolled molecular shuttle (a). Representation of the light-induced change of the hydrophobic/hydrophilic character of a gold surface covered with a self-assembled layer of rotaxane **17** and 11-mercaptoundecanoic acid (b). Lateral photographs showing the light-driven transport of a 1.25 µl drop of diiodomethane up a 12° incline on the surface of a substrate as shown in (b). From left to right: before irradiation [pristine (*E*)-**17**], after 160 seconds of irradiation with UV light (just before transport), after 245 seconds of irradiation (just after transport), and after 640 seconds irradiation (photostationary state) (c). Source: Berna et al. [125], figure 07 (p. 06)/Reproduced with permission from Springer Nature.

chemical reactions on a tiny scale without reaction vessels, simply by bringing individual drops containing different reactants together.

### 32.5.2 Molecular Machines Embedded in Metal–Organic Frameworks

While different examples of photoactive crystalline materials have been reported, in which the action of an included photoswitch is associated with macroscopic changes

in the crystalline structure leading to macroscopic mechanical actuation or phase transitions [126–129], only recently, with the advent of metal–organic frameworks (MOFs), the prospect of arranging and organizing molecular machines into solid state ordered architecture has become a real possibility. The reason is that the inclusion of a molecular machine into a crystalline architecture has to overcome particularly daunting obstacles. Crystals, in fact, are usually characterized by tightly packed structures without much free space available to allow large amplitude movements to an embedded moiety. Moreover, optical density and filter effects are of concern for the operation of light-actuated molecular machines included in a solid crystal structure, as both can severely limit the depth of penetration of light. In this context, MOFs have emerged as ideal candidates to overcome at least some of these limitations due to their porous skeleton, which allows nanoscale machines embedded in their structures to operate freely without the need to overcome large steric hindrances.

The first example of an MOF incorporating a functional molecular machine was obtained by applying a solvent-assisted linker exchange strategy, which enabled to incorporate dipyridyl-functionalized overcrowded alkene photoswitches (**18** in Figure 32.19) into the skeleton of a crystalline $Zn^{2+}$-coordinated MOF. The solid-state structure of the synthesized material is characterized by a vertical orientation of the stator portion of the rotary moiety **18** with respect to the plane of the tetrakis(4-carboxyphenyl)benzene (**TCPB**) co-ligand, leading to pillar-like arrays of photoswitching units confined in the interlayer space of the MOF [130]. Through a combination of X-ray and Raman spectroscopy studies, it was possible to prove the unrestricted rotation upon UV light irradiation of the overcrowded alkene units inside the MOF, allowed by the rigid and porous skeleton of the chosen framework, with rotary speeds comparable to those measured in solution. More recently, by replacing the TCPB co-ligand with a palladium porphyrin tetracarboxylic acid unit, the rotary motion could be driven with visible light, by taking advantage of an efficient energy transfer between the porphyrin and overcrowded alkene moieties [131]. In addition to being ideal scaffolds for investigating fundamental issues dealing with the spatial and temporal synchronization of the motion of arrays of nanomachines, these so-called "moto-MOFs" hold high promise in various applications ranging from controlling the diffusion of gases and small molecules in crystalline materials to the development of miniaturized light-driven chemical plants [132, 133].

### 32.5.3 Supramolecular Self-assembling Systems

It is well known that a high level of control on the orientation and mutual alignment of molecules, with the purpose of developing cooperative effects, can be attained by harnessing supramolecular association processes such as gelation and self-assembly of amphiphilic moieties. There are examples of simple photoswitches employed to obtain light controllable solvent gelators [134] and photo-regulate molecular aggregation [135]. This kind of system is of great interest for controlling biological processes and in drug release applications.

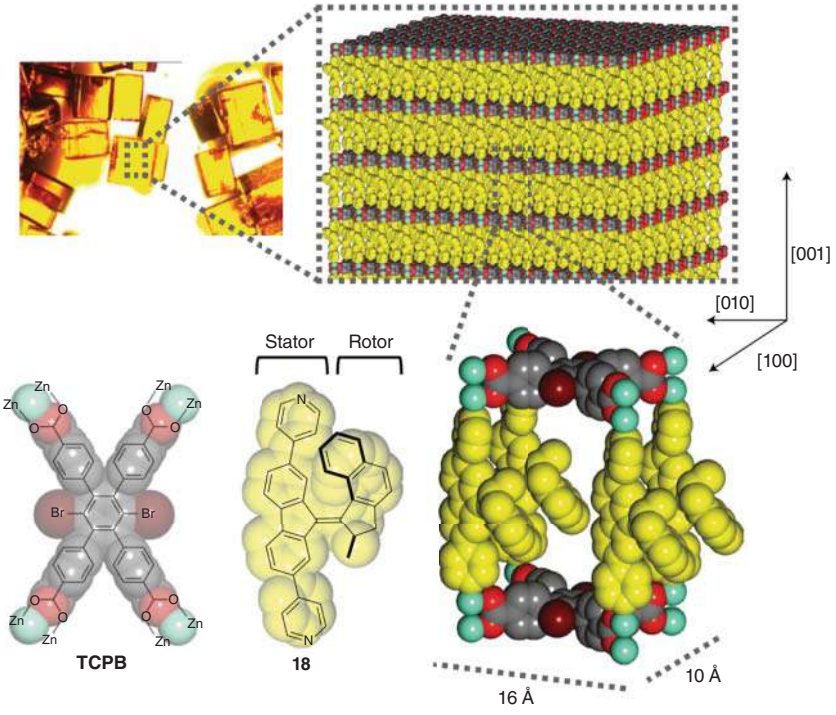


**Figure 32.19** Schematic representation of the 3D architecture of a "moto-MOF." The packing of the crystal, the elementary cell, and the structure of the linkers, tetracarboxylic acid (**TCPB**), and molecular motor (**18**) are shown. The stator of the motor (that is, the fluorene unit) is used to bridge the 2D layers constructed from Zn paddlewheel clusters and **TCPB**, while the rotor moiety (the naphthyl unit) can rotate freely with respect to the other half under light irradiation. Source: Danowski et al. [130], figure 01 (p. 02) / Reproduced with permission from Springer Nature.

Photoresponsive molecular rotary motors of the overcrowded alkene type, once properly functionalized to make them amphiphilic, have been shown to self-organize into hierarchical structures in water (Figure 32.20a) [136]. Compound **19** (Figure 32.20b) is constituted by a molecular rotary unit decorated with a dodecyl chain on the stator moiety and two carboxyl-terminated alkyl chains on the rotor end. At a concentration of 5% w/w in aqueous NaOH, molecules of **19** self-assemble yielding micrometric-length nanofibers with a diameter of about 5–6 nm (Figure 32.20a). Spectroscopic investigations prove that the photocontrolled rotary function of **19** is conserved in the assembled nanofibers.

Centimeter-long noodle-like strings of the self-assembled nanofibers were obtained by manually drawing the nanofiber suspension into a concentrated water solution of calcium chloride. The nanofibers become aligned in the bundles that constitute the strings because of the shear flow and the electrostatic screening of the $Ca^{2+}$ ions (Figure 32.20a). A string of self-assembled nanofibers irradiated with light of 365 nm while suspended into water readily bends toward the light source (Figure 32.20c), returning to its initial shape after three hours at 50 °C. The

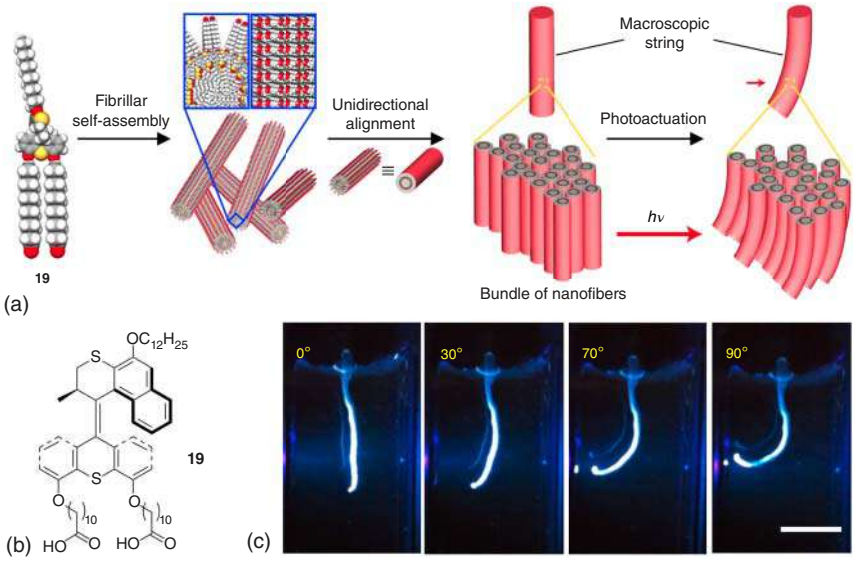


**Figure 32.20** Schematic representation of the hierarchical self-organization of the amphiphilic molecular rotary photoswitch **19** into nanofibers and bundles that make up macroscopic soft strings (a). Structural formula of the photoswitch **19**. (c) Photographic images of a supramolecular string in water subjected to UV irradiation with a source positioned on the left. Bending toward the source from 0° to 90° occurs within 60 seconds. Scale bar is 5 mm (b). Source: Chen et al. [136], figure 04 (p. 04)/Reproduced with permission from Springer Nature.

same photoinduced macroscopic motion is also observed in string removed from the aqueous solution and suspended in air. The force exerted by the motion of an air-suspended fiber is enough to lift a small piece of paper of 0.4 mg attached to its free end. Small-angle X-ray scattering (SAXS) experiments on the fiber bundles suggest that the photoinduced switching of the overcrowded alkene units in **19**, by increasing the local excluded volume that causes a perturbation of the packing arrangement, results in a thickening and shortening of the fibers. The bending toward the light source is due to the thickness of the string (~300 μm) and its optical density at the irradiation wavelength, which taken together limit light penetration and force the contraction to take place only at the irradiated side of the string [136].

The fact that this material can exert a macroscopic force upon light stimulation and self-organize in aqueous solution under ambient conditions surely makes it most interesting for biocompatible molecular machines-based soft robotics applications. Recently, with an analogous approach, multi-modal control over the self-assembly in aqueous media was demonstrated in amphiphilic rotary nanomachines able to alternatively organize into sheets, discs, micelles, or empty vesicles in response to chemical/light/heat stimuli [137]. The possibility to install macroscopic multi-state stimuli-responsive properties into foams, such as

foamability and foam stability, was also presented [138]. These works showcase the outstanding potential that self-assembly approaches have in achieving and controlling the amplification of the force exerted by a collection of nanoscale machines.

### 32.5.4 Polymers Integrating Molecular Machines

The integration of molecular machines into polymers is another emerging strategy for summing and scaling up the work done by a vast number of nanomachines to achieve macroscopic effects [62, 63, 117, 123, 124]. A design that has proved to be successful is that based on polymers containing doubly interlocked rotaxane species, i.e. [c2]daisy chains, which are MIMs able to expand and contract in response to an externally applied stimuli (also see paragraph 32.2.1).

Several examples exist in which molecular movements of chemically switchable [c2]daisy chains are translated to the microscopic domain in coordination [113] or supramolecular [139] polymers. Furthermore, cross-linked covalent polymers containing [c2]daisy chain functional moieties [115] have been shown to display macroscopic size changes as a result of the collective mechanical switching of the daisy chains units. The success of this design paradigm could be less surprising if one considers that also natural evolution has followed a similar blueprint in the form of the myofibrils constituting the skeletal muscles.

Macroscopic light-induced size changes in wet and dry gels were recently achieved by means of polymers incorporating [c2]daisy chain species, with a design similar to that of compound **3** (Paragraph 32.2.1, Figure 32.3). The polymer (Figure 32.21a) was prepared by condensing tetra(polyethylene glycol) cross-linkers with α-cyclodextrin-azobenzene [c2]daisy chains. Square-shaped fragment of hydrogel, prepared from the polymer, show a marked reduction of their volume upon exposure to UV light, while exposure to visible light restores the initial size (Figure 32.21b). The UV-light-promoted macroscopic deswelling and visible-light-induced swelling of the hydrogel were proved to be a result of the nanoscale expansion and contraction of the daisy chain monomers upon $E \rightarrow Z$ and $Z \rightarrow E$ isomerization, respectively (Figure 32.21c). In fact, a hydrogel containing only azobenzene switchable units showed an opposite behavior. Upon UV irradiation, in a gel containing only azobenzene moieties, the transition from the hydrophobic $E$ to the more polar $Z$-isomer causes a decrease in cross-linking density, with a consequent uptake of water and expansion of the material. Conversely, in the daisy chain-based gel, the swelling and deswelling are controlled by the change in the end-to-end distance of the molecular machine units (Figure 32.21c) [140].

The photoinduced actuation was also possible by irradiating a strip of gel suspended in water (Figure 32.21d). It was observed that under these conditions, the strip bends toward the light source upon illumination. As previously discussed for compound **19**, this phenomenon results from the partial penetration of light, which activates only the molecular machines on the illuminated side of the gel strip. Under the conditions employed, it took a few hours of exposure to UV

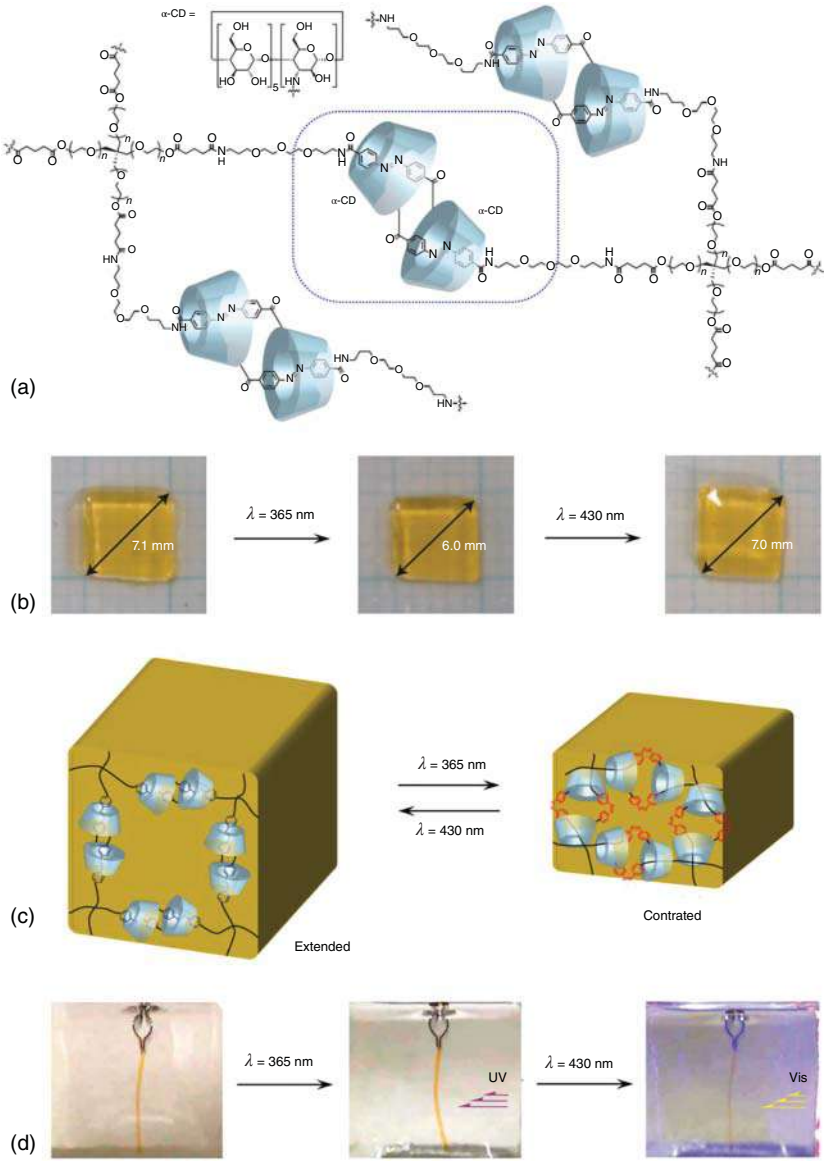


**Figure 32.21** Structural formula of a cross-linked polymer containing photoresponsive daisy chain units based on α-cyclodextrin hosts and azobenzene guests (one of them is highlighted in the box). The daisy chains are represented in the extended state, with the azobenzene moieties in the *E*-configuration (a). Photographs of a square-shaped fragment of the resulting hydrogel, showing the UV-light-induced shrinking and visible-light-induced expansion of the material (b). Schematic representation of the operation mechanism at the basis of the photoinduced actuation (c). Photographs of a strip of the hydrogel suspended in water and illuminated from the right-hand side, showing the reversible bending toward the irradiation source (d). Source: Iwaso et al. [140], figure 03b (p. 04), figure 04a (p. 05)/Reproduced with permission from Springer Nature.

light to reach the maximum bending amplitude, while the recovery of the initial shape by irradiation with visible light occurred in minutes. Importantly, the switching cycle could be repeated without loss of efficiency or degradation of the material.

Interestingly, a xerogel obtained by freezing-drying the hydrogel exhibited the same amount of bending toward the light source, but with a much faster response with respect to the hydrogel (Figure 32.21d). The ability to function also in a dry state is a remarkable property of this system, extremely rare in polymer-based actuators. Unfortunately, the xerogel presents a reduced fatigue resistance that results in a permanent reduction in size after a few cycles of operation.

In another series of investigations, Giuseppone and coworkers studied the influence of UV irradiation on polymeric gels containing overcrowded alkene-based photoswitches [141, 142]. Compound **20** (Figure 32.22) was prepared by linking alkyne- and azide-terminated oligomeric ethylene glycol chains to the stator and

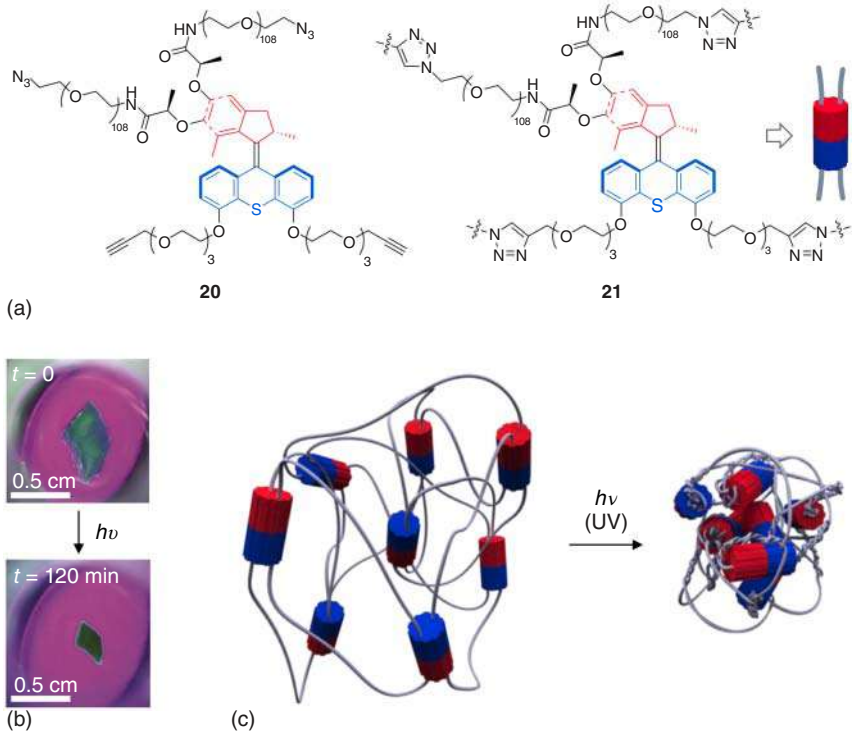


**Figure 32.22** The intermolecular "click" reaction between molecules of **20** yields the polymer conjugate **21** (a). Photographs showing the contraction of a piece of gel, consisting of **20** swollen with toluene, upon UV light irradiation (b). Schematic representation of the braiding of the polymer chains of **21**, caused by the photoinduced directional rotation of the photoswitchable units at the branching points, which results in the shrinkage of the gel (c). Source: Li et al. [141], figure 03c (p. 03)/Reproduced with permission from Springer Nature.

rotor halves of the enantiopure overcrowded alkene moiety, respectively. Successively, the cross-linked polymer **21** was prepared via copper-catalyzed Huisgen reaction of **20** under high concentration conditions (Figure 32.22a). In the resulting polymer **21**, the ethylene glycol chains attached to different photoswitching units are connected together by means of triazole rings. Polymer **21** was found to yield a gel in toluene, which was fully characterized by SAXS and atomic force microscopy (AFM). Upon UV irradiation, the resulting contraction of millimeter-sized pieces of gel is visible to the naked eye (Figure 32.22b). It was hypothesized that the light-driven unidirectional rotation of the photoswitch components results in a coiling up of the entangled polymer chains (Figure 32.22c). This interpretation was supported by AFM imaging experiments on a model compound prepared through the intramolecular macrocyclization of the arms of **20** to yield a bicyclic moiety. AFM observation of single molecules of the compound showed that under UV illumination, the individual eight-shaped objects exhibit a transition to a collapsed, more compact shape, a result fully consistent with the light-driven formation of a coiled structure.

This remarkable system is thus able to exploit the unidirectional movement of its embedded molecular photoswitches to convert the energy of incident photons into free energy in the form of entangled polymer chains. The overall efficiency was calculated to be quite low, about 0.15%, but more of concern was the fact that the accumulated energy could not be released because the light-driven braiding of the polymer is irreversible.

An improved system, depicted in Figure 32.23, was devised to overcome such an issue. The new design involved the presence of diarylethene photoswitches in the gel as "modulator elements" [143]. They perform as stimuli-responsive units able to release the elastic energy accumulated in the polymeric network by unbraiding the entangled macromolecular chains. This new polymer was obtained by reacting compound **22** (analogous to **20** but presenting only alkyne ends) with the azide-terminated diarylethene derivative **23** (Figure 32.23b) to yield a polymeric gel analogous to **21** but containing both modulator and rotary subunits. Key for the operation of the system is the fact that the rotary and modulator part can be activated by using light of different wavelength. Specifically, UV light drives the rotation of the overcrowded alkene units (Figure 32.23c) while it does not affect the diarylethene units in their closed (locked) form, thereby sustaining the coiling of the polymer chains. Conversely, visible light irradiation is ineffective for the actuation of the rotary units but switches the modulators to their open (unlocked) form (Figure 32.23c). Free rotation about carbon single bonds in the open modulator units can thus release the stored energy accumulated in the braided polymer.

Interestingly, if the system is irradiated with both UV and visible light, the rotary units coil the polymer chains and the modulators allow their unwinding. Thus, by adjusting the relative intensities of UV and visible light, it is possible to tune the winding and unwinding rates and control whether the gel is contracting or expanding. Hence, the energy stored in the material and its mechanical output can be tuned by optical modulation of the braiding and unbraiding frequencies. This system surely

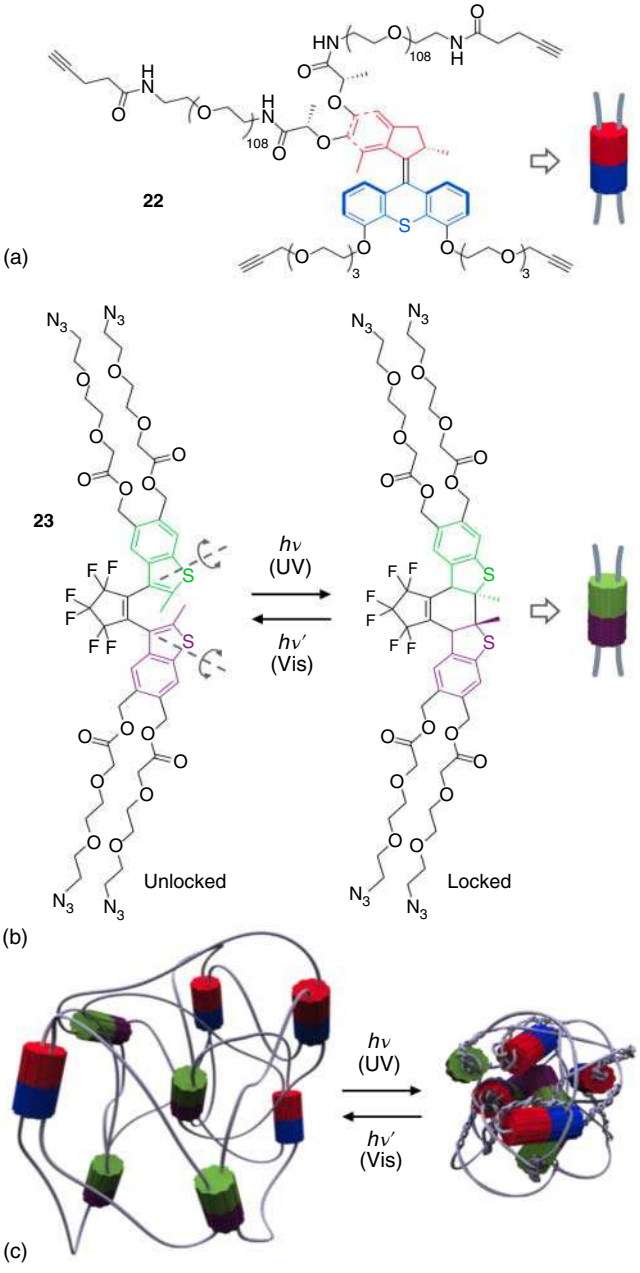


**Figure 32.23** Structure formula of the alkyne-terminated molecular rotary units **22** (a). Structure formula of the diarylethene-based compound **23** that, by a quadruple intermolecular 'click' reaction with **22**, yields a cross-linked polymer similar to **21** (Figure 32.22a) that contains both rotary and modulator units. The open (modulator unlocked; rotation axes shown in grey) and closed (modulator locked) forms can be interconverted by UV and visible light irradiation (b). Schematic representation of the gel obtained by co-polymerization of **22** and **23**, and of the UV-induced braiding and visible light-induced unbraiding of its chains (c). Source: Adapted with permission from Foy et al. [143].

represents an important milestone and outstanding achievement in the way toward the development of complex molecular machine-based systems capable of converting light energy into mechanical energy.

## 32.6 Conclusion

Research in the field of molecular machines has quickly evolved from an early stage, when the main focus was to develop simple prototypes able to emulate the type of movements present in macroscopic equivalents, to a more advanced period, in which a deeper knowledge of fundamental aspects of nanosystems shifted the focus of research to issues such as energy supply, collective effects, and practical applications. In fact, today, probably the most challenging and motivating issue associated with research on artificial molecular machines is the design of systems that can efficiently perform a useful function. Initially biomimetic designs (e.g. enzymatic systems, substrate transport, membrane operation) as well as techno-mimetic ones (catalysis, motion transmission, materials for mechanical actuation, and energy conversion) have certainly inspired and pushed forward the realm of possible applications of artificial nanomachines. Presently, these two approaches are often combined together. For example, the use of light as an energy source is a relatively rare occurrence for biological nanomachines, but extremely desirable from a technological point of view in artificial ones.

However, for real-world applications to emerge, many gaps still need to be filled in our understanding of how machines work at the nanoscale and synthetic limitations need to be solved. Among the relevant issues that should be prioritized is that of expanding the choice of molecular building blocks used in the construction of artificial molecular machines. This is particularly true for photoswitchable elements, which, as discussed here, are fundamental for the realization of nanosystems activated by light. In fact, most examples of molecular light-activated machines reported so far make use of overcrowded alkenes rotating photoswitches. The expansion of the number and type of photoactive moieties available could certainly contribute to the development of new architectures and working schemes. Furthermore, the vast majority of current photoactivated functional molecular machines are based on photoisomerization reactions. It might be interesting, in addition to considering new photoswitchable compounds, to explore the possibilities offered by underutilized light-induced processes, such as electron transfer or proton transfer.

Surely one of the aspects that requires the strongest research effort is the integration of molecular machines with their environment so that the molecular movement can produce an effect beyond the nanoscale. The examples discussed here demonstrate that this goal is now within the reach of scientists, and that the unique characteristics of the light–matter interaction can play a leading role in the development of advanced devices and materials based on molecular machines. The technological and biomedical advances anticipated since the dawn of this field of research could thus literally "see the light" in the next future.

## Acknowledgments

A.C. gratefully acknowledged financial support from the Ministero dell'Istruzione, Università e Ricerca (Fare "Ampli" R16S9XXKX3 and Prin "Nemo" 20173L7W8K), the University of Bologna, and the National Research Council of Italy. S.S. gratefully acknowledged financial support from the Ministero dell'Istruzione, Università e Ricerca (Prin "Pholies" 201732PY3X).

## References

1 Balzani, V., Credi, A., and Venturi, M. (2008). *Molecular Devices and Machines – Concepts and Perspectives for the Nanoworld*. Weinheim: Wiley-VCH.
2 Bruns, C.J. and Stoddart, J.F. (2016). *The Nature of the Mechanical Bond: From Molecules to Machines*. Wiley.
3 Schliwa, M. (ed.) (2003). *Molecular Motors*. Weinheim: Wiley-VCH.
4 Goodsell, D.S. (2004). *Bionanotechnology – Lessons from Nature*. Hoboken, NJ: Wiley-Liss.
5 Jones, R.A.L. (2008). *Soft Machines – Nanotechnology and Life*. Oxford: Oxford University Press.
6 Muraoka, T. and Kinbara, K. (2012). Development of photoresponsive supramolecular machines inspired by biological molecular systems. *J. Photochem. Photobiol. C* 13 (2): 136–147.
7 Baroncini, M., Casimiro, L., de Vet, C. et al. (2018). Making and operating molecular machines: a multidisciplinary challenge. *ChemistryOpen* 7: 169–179.
8 Erbas-Cakmak, S., Leigh, D.A., McTernan, C.T., and Nussbaumer, A.L. (2015). Artificial molecular machines. *Chem. Rev.* 115: 10081–10206.
9 Kassem, S., van Leeuwen, T., Lubbe, A.S. et al. (2017). Artificial molecular motors. *Chem. Soc. Rev.* 46: 2592–2621.
10 Pezzato, C., Cheng, C., Stoddart, J.F., and Astumian, R.D. (2017). Mastering the non-equilibrium assembly and operation of molecular machines. *Chem. Soc. Rev.* 46: 5491–5507.
11 Feringa, B.L. (2017). The art of building small: from molecular switches to motors (Nobel lecture). *Angew. Chem. Int. Ed.* 56: 11060–11078.
12 Sauvage, J.-P. (2017). From chemical topology to molecular machines (Nobel lecture). *Angew. Chem. Int. Ed.* 56: 11080–11093.
13 Stoddart, J.F. (2017). Mechanically interlocked molecules (MIMs) – molecular shuttles, switches, and machines (Nobel lecture). *Angew. Chem. Int. Ed.* 56: 11094–11125.
14 Silvi, S., Venturi, M., and Credi, A. (2011). Light operated molecular machines. *Chem. Commun.* 47: 2483–2489.
15 Ceroni, P., Credi, A., and Venturi, M. (2014). Light to investigate (read) and operate (write) molecular devices and machines. *Chem. Soc. Rev.* 43: 4068–4083.

**16** Katan, M. and Hecht, S. (2017). Photoswitchable molecules as key ingredients to drive systems away from the global thermodynamic minimum. *Chem. Soc. Rev.* 46: 5536–5550.

**17** Baroncini, M., Silvi, S., and Credi, A. (2019). Photo- and redox-driven artificial molecular motors. *Chem. Rev.* 119. https://doi.org/10.1021/acs.chemrev.9b00291.

**18** Coskun, A., Banaszak, M., Astumian, R.D. et al. (2012). Great expectations: can artificial molecular machines deliver on their promise? *Chem. Soc. Rev.* 41: 19–30.

**19** van Leeuwen, T., Lubbe, A.S., Štacko, P. et al. (2017). Dynamic control of function by light-driven molecular motors. *Nat. Rev. Chem.* 1: 0096.

**20** Wang, Q., Chen, D., and Tian, H. (2018). Artificial molecular machines that can perform work. *Sci. China Chem.* 61: 1261–1273.

**21** Balzani, V., Ceroni, P., and Juris, A. (2014). *Photochemistry and Photophysics: Concepts, Research, Applications*. Weinheim: Wiley-VCH.

**22** Aprahamian, I. (2020). The future of molecular machines. *ACS Cent. Sci.* 6: 347–358.

**23** Groppi, J., Baroncini, M., Venturi, M. et al. (2019). Design of photo-activated molecular machines: highlights from the past ten years. *Chem. Comm.* 55: 12595–12602.

**24** (2000). Special issue on photochromism: memories and switches. *Chem. Rev.* 100: 1683–1890.

**25** Dürr, H. and Bouas-Laurent, H. (2003). *Photochromism: Molecules and Systems*, Revised Edition. Elsevier.

**26** Pianowski, Z.L. (2019). Recent implementations of molecular photoswitches into smart materials and biological systems. *Chem. Eur. J.* 25: 5128–5144.

**27** Zhang, J., Zou, Q., and Tian, H. (2013). Photochomic materials: more than meets the eye. *Adv. Mater.* 25: 378–399.

**28** Bléger, D. and Hecht, S. (2015). Visible-light-activated molecular switches. *Angew. Chem. Int. Ed.* 54: 11338–11349.

**29** Wang, L. and Li, Q. (2018). Photochromism into anosystems: towards lighting up the future nanoworld. *Chem. Soc. Rev.* 47: 1044–1097.

**30** Petermayer, C. and Dube, H. (2018). Indigoid photoswitches: visible light responsive molecular tools. *Acc. Chem. Res.* 51: 1153–1163.

**31** Calbo, J., Weston, C.E., White, A.J.P. et al. (2017). Tuning azoheteroarene photoswitch performance through heteroaryl design. *J. Am. Chem. Soc.* 139: 1261–1274.

**32** Crespi, S., Simeth, N.A., and König, B. (2019). Heteroaryl azo dyes as molecular photoswitches. *Nat. Rev. Chem.* 3: 133–146.

**33** Fischer, E. and Frei, Y. (1957). Photoisomerization equilibria involving the C=N double bond. *J. Chem. Phys.* 27: 808–809.

**34** Dugave, C. and Demange, L. (2003). *Cis–trans* isomerization of organic molecules and biomolecules: implications and applications. *Chem. Rev.* 103: 2475–2532.


**35** Shao, B. and Aprahamian, I. (2020). Hydrazones as new molecular tools. *Chem* 6: 2162–2173.

**36** Su, X. and Aprahamian, I. (2014). Hydrazone-based switches, metallo-assemblies and sensors. *Chem. Soc. Rev.* 43: 1963–1981.

**37** Kumpulainen, T., Lang, B., Rosspeintner, A., and Vauthey, E. (2017). Ultrafast elementary photochemical processes of organic molecules in liquid solution. *Chem. Rev.* 117: 10826–10939.

**38** Peters, M.V., Stoll, R.S., Kühn, A., and Hecht, S. (2008). Photoswitching of basicity. *Angew. Chem. Int. Ed.* 47: 5968–5972.

**39** Haberfield, P. (1987). Phototropic molecules. 1. Phase transfer as a method for detecting transient species. *J. Am. Chem. Soc.* 109: 6177–6178.

**40** Emond, M., Le Saux, T., Maurin, S. et al. (2010). 2-Hydroxyazobenzenes to tailor pH pulses and oscillations with light. *Chem. Eur. J.* 16: 8822–8831.

**41** Shi, Z., Peng, P., Strohecker, D., and Liao, Y. (2011). Long-lived photoacid based upon a photochromic reaction. *J. Am. Chem. Soc.* 133: 14699–14703.

**42** Johns, V.K., Peng, P., DeJesus, J. et al. (2014). Visible-light-responsive reversible photoacid based on a metastable carbanion. *Chem. Eur. J.* 20: 689–692.

**43** Yang, C., Khalil, T., and Liao, Y. (2016). Photocontrolled proton transfer in solution and polymers using a novel photoacid with strong C–H acidity. *RSC Adv.* 6: 85420–85426.

**44** Credi, A., Dumas, S., Silvi, S. et al. (2004). Viologen-calix[6]arene pseudorotaxanes. Ion-pair recognition and threading/dethreading molecular motions. *J. Org. Chem.* 69: 5881–5887.

**45** Silvi, S., Arduini, A., Pochini, A. et al. (2007). A simple molecular machine operated by photoinduced proton transfer. *J. Am. Chem. Soc.* 129: 13378–13379.

**46** Tatum, L.A., Foy, J.T., and Aprahamian, I. (2014). Waste management of chemically activated switches: using a photoacid to eliminate accumulation of side products. *J. Am. Chem. Soc.* 136: 17438–11744.

**47** Yang, L.-P., Jia, F., Cui, J.-S. et al. (2017). Light-controlled switching of a non-photoresponsive molecular shuttle. *Org. Lett.* 19: 2945–2948.

**48** Bruns, C.J. and Stoddart, J.F. (2016). *The Nature of the Mechanical Bond*, 2e. Hoboken, NJ: Wiley.

**49** Stoddart, J.F. (2009). The chemistry of the mechanical bond. *Chem. Soc. Rev.* 38: 1802–1820.

**50** van Dongen, S.F.M., Cantekin, S., Elemans, J.A.A.W. et al. (2014). Functional interlocked systems. *Chem. Soc. Rev.* 43: 99–122.

**51** Barin, G., Forgan, R.S., and Stoddart, J.F. (2012). Mechanostereochemistry and the mechanical bond. *Proc. R. Soc. Lond.* 468: 2849–2880.

**52** Neal, E.A. and Goldup, S.M. (2014). Chemical consequences of mechanical bonding in catenanes and rotaxanes: isomerism, modification, catalysis and molecular machines for synthesis. *Chem. Comm.* 50: 5128–5142.

**53** Cheng, C. and Stoddart, J.F. (2016). Wholly synthetic molecular machines. *ChemPhysChem* 17: 1780–1793.


**54** Kay, E.R., Leigh, D.A., and Zerbetto, F. (2007). Synthetic molecular motors and mechanical machines. *Angew. Chem. Int. Ed.* 46: 72–191.

**55** Heard, A.W. and Goldup, S.M. (2019). Simplicity in the design, operation, and applications of mechanically interlocked molecular machines. *ACS Cent. Sci.* 1: 1–12.

**56** Abendroth, J.M., Bushuyev, O.S., Weiss, P.S., and Barrett, C.J. (2015). Controlling motion at the nanoscale: rise of the molecular machines. *ACS Nano* 9: 7746–7768.

**57** Stanier, C.A., Alderman, S.J., Claridge, T.D.W., and Anderson, H.L. (2002). Unidirectional photoinduced shuttling in a rotaxane with a symmetric stilbene dumbbell. *Angew. Chem. Int. Ed.* 41: 1769–1772.

**58** Qu, D.-H., Wang, Q.-C., Ma, X., and Tian, H. (2005). A [3]rotaxane with three stable states that responds to multiple-inputs and displays dual fluorescence addresses. *Chem. Eur. J.* 11: 5929–5937.

**59** Murakami, H., Kawabuchi, A., Matsumoto, R. et al. (2005). A multi-mode-driven molecular shuttle: photochemically and thermally reactive azobenzene rotaxanes. *J. Am. Chem. Soc.* 127: 15891–15899.

**60** Willner, I., Pardo-Yssar, V., Katz, E., and Ranjit, K.T. (2001). A photoactivated 'molecular train' for optoelectronic applications: light-stimulated translocation of a β-cyclodextrin receptor within a stoppered azobenzene-alkyl chain supramolecular monolayer assembly on a Au-electrode. *J. Electroanal. Chem.* 497: 172–177.

**61** Jiménez, M.C., Dietrich-Buchecker, C., and Sauvage, J.-P. (2000). Towards synthetic molecular muscles: contraction and stretching of a linear rotaxane dimer. *Angew. Chem. Int. Ed.* 39: 3284–3287.

**62** Bruns, C.J. and Stoddart, J.F. (2014). Rotaxane-based molecular muscles. *Acc. Chem. Res.* 47: 2186–2199.

**63** Goujon, A., Moulin, E., Fuks, G., and Giuseppone, N. (2019). [c2]Daisy chain rotaxanes as molecular muscles. *CCS Chem.* 1: 83–96.

**64** Dawson, R.E., Lincoln, S.F., and Easton, C.J. (2008). The foundation of a light driven molecular muscle based on stilbene and α-cyclodextrin. *Chem. Commun.* 3980–3982.

**65** Altieri, A., Bottari, G., Dehez, F. et al. (2003). Remarkable positional discrimination in bistable light- and heat-switchable hydrogen-bonded molecular shuttles. *Angew. Chem., Int. Ed.* 42: 2296–2300.

**66** Hernández, J.V., Kay, E.R., and Leigh, D.A. (2004). A reversible synthetic rotary molecular motor. *Science* 306: 1532–1537.

**67** Roke, D., Wezenberg, S.J., and Feringa, B.L. (2018). Molecular rotary motors: unidirectional motion around double bonds. *Proc. Natl. Acad. Sci. U.S.A.* 115: 9423–9431.

**68** Feynman, R.P., Leighton, R.B., and Sands, M. (1963). *The Feynman Lectures of Physics*, vol. I. Reading, MA: Addison-Wesley, Chapter. 46.

**69** Davis, A.P. (1998). Tilting at windmills? the second law survives. *Angew. Chem. Int. Ed.* 37: 909–910.


**70** Kelly, T.R., De Silva, H., and Silva, R.A. (1999). Unidirectional rotary motion in a molecular system. *Nature* 401: 150–152.

**71** Koumura, N., Zijlstra, R.W.J., van Delden, R.A. et al. (1999). Light-driven monodirectional molecular rotor. *Nature* 401: 152–155.

**72** Feringa, B.L. (2001). In control of motion: from molecular switches to molecular motors. *Acc. Chem. Res.* 34: 504–513.

**73** García-López, V., Liu, D., and Tour, J.M. (2019). Light-activated organic molecular motors and their applications. *Chem. Rev.* 120: 79–124.

**74** Guentner, M., Schildhauer, M., Thumser, S. et al. (2015). Sunlight-powered kHz rotation of a hemithioindigo-based molecular motor. *Nat. Commun.* 6: 1–8.

**75** Wilcken, R., Schildhauer, M., Rott, F. et al. (2018). Complete mechanism of hemithioindigo motor rotation. *J. Am. Chem. Soc.* 140: 5311–5318.

**76** Lehn, J.-M. (2006). Conjecture: imines as unidirectional photodriven molecular motors–motional and constitutional dynamic devices. *Chemistry* 12: 5910–5915.

**77** Greb, L. and Lehn, J.-M. (2014). Light-driven molecular motors: imines as four-step or two-step unidirectional rotors. *J. Am. Chem. Soc.* 136: 13114–13117.

**78** Lubbe, A.S., Böhmer, C., Tosi, F. et al. (2018). Molecular motors in aqueous environment. *J. Org. Chem.* 83: 11008–11018.

**79** Pfeifer, L., Scherübl, M., Fellert, M. et al. (2019). Photoefficient 2nd generation molecular motors responsive to visible light. *Chem. Sci.* 10: 8768–8773.

**80** Qu, D.-H. and Tian, H. (2013). Synthetic small-molecule walkers at work. *Chem. Sci.* 4: 3031–3035.

**81** Hamming, P.H.E., Overeem, N.J., and Huskens, J. (2019). Influenza as a molecular walker. *Chem. Sci.* 11: 27–36.

**82** von Delius, M., Geertsema, E.M., and Leigh, D.A. (2010). A synthetic small molecule that can walk down a track. *Nat. Chem.* 2: 96–101.

**83** Barrell, M.J., Campaña, A.G., von Delius, M. et al. (2010). Light-driven transport of a molecular walker in either direction along a molecular track. *Angew. Chem. Int. Ed.* 50: 285–290.

**84** Feringa, B.L. (2020). Vision statement: materials in motion. *Adv. Mat.* 32: 1906416.

**85** Blanco, V., Leigh, D.A., and Marcos, V. (2015). Artificial switchable catalysts. *Chem. Soc. Rev.* 44: 5341–5370.

**86** Vlatković, M., Collins, B.S.L., and Feringa, B.L. (2016). Dynamic responsive systems for catalytic functions. *Chem. Eur. J.* 22: 17080–17111.

**87** Wang, J. and Feringa, B.L. (2011). Dynamic control of chiral space in a catalytic asymmetric reaction using a molecular motor. *Science* 331: 1429–1432.

**88** Vlatković, M., Bernardi, L., Otten, E., and Feringa, B.L. (2014). Dual stereocontrol over the Henry reaction using a light- and heat-triggered organocatalyst. *Chem. Commun.* 50: 7773–7775.


**89** Zhao, D., Neubauer, T.M., and Feringa, B.L. (2015). Dynamic control of chirality in phosphine ligands for enantioselective catalysis. *Nat. Commun.* 6: 6652.

**90** Pizzolato, S.F., Štacko, P., Kistemaker, J.C.M. et al. (2018). Central-to-helical-to-axial-to-central transfer of chirality with a photoresponsive catalyst. *J. Am. Chem. Soc.* 140: 17278–17289.

**91** Dorel, R. and Feringa, B.L. (2020). Stereodivergent anion binding catalysis with molecular motors. *Angew. Chem.* 132: 795–799.

**92** See, e.g.Thubagere, A.J., Li, W., Johnson, R.F. et al. (2017). A Cargo-sorting DNA robot. *Science* 357, eeean6558.

**93** See, e.g.:O'Reilly, R.K., Turberfield, A.J., and Wilks, T.R. (2017). The evolution of DNA-templated synthesis as a tool for materials discovery. *Acc. Chem. Res.* 50: 2496–2509.

**94** See, e.g.:De Bo, G., Gall, M.A.Y., Kuschel, S. et al. (2018). An artificial molecular machine that builds an asymmetric catalyst. *Nat. Nanotechnol.* 13: 381–385.

**95** Schäfer, C., Ragazzon, B., Colasson, B. et al. (2016). An artificial molecular transporter. *ChemistryOpen* 5: 120–124.

**96** Ashton, P.R., Ballardini, R., Balzani, V. et al. (1998). Acid-base controllable molecular shuttles. *J. Am. Chem. Soc.* 120: 11932–11942.

**97** Garaudée, S., Silvi, S., Venturi, M. et al. (2005). Shuttling dynamics in an acid–base-switchable [2]rotaxane. *ChemPhysChem* 6: 2145–2152.

**98** Mobian, P., Kern, J.-M., and Sauvage, J.-P. (2004). Light-driven machine prototypes based on dissociative excited states: photoinduced decoordination and thermal recoordination of a ring in a ruthenium(II)-containing [2]catenane. *Angew. Chem. Int. Ed.* 43: 2392–2395.

**99** Chen, S., Wang, Y., Nie, T. et al. (2018). An artificial molecular shuttle operates in lipid bilayers for ion transport. *J. Am. Chem. Soc.* 140: 17992–17998.

**100** Chen, J., Wezenberg, S., and Feringa, B.L. (2016). Intramolecular transport of small-molecule cargo in a nanoscale devices operated by light. *Chem. Commun.* 52: 6765–6768.

**101** Astumian, R.D., Pezzato, C., Feng, Y. et al. (2020). Non-equilibrium kinetics and trajectory thermodynamics of synthetic molecular pumps. *Mater. Chem. Front.* 4: 1304–1314.

**102** Sabatino, A., Penocchio, E., Ragazzon, G. et al. (2019). Individual-molecule perspective analysis of chemical reaction networks: the case of a light-driven supramolecular pump. *Angew. Chem. Int. Ed.* 58: 14341–14348.

**103** Ashton, P.R., Campbell, P.J., Glink, P.T. et al. (1995). Dialkylammonium ion/crown ether complexes: the forerunners of a new family of interlocked molecules. *Angew. Chem. Int. Ed. Engl.* 34: 1865–1869.

**104** Baroncini, M., Silvi, S., Venturi, M., and Credi, A. (2010). Reversible photoswitching of rotaxane character and interplay of thermodynamic stability and kinetic lability in a self-assembling ring-axle molecular system. *Chem. Eur. J.* 16: 11580–11587.


**105** Baroncini, M., Silvi, S., Venturi, M., and Credi, A. (2012). Photoactivated directionally controlled transit of a non-symmetric molecular axle through a macrocycle. *Angew. Chem. Int. Ed.* 51: 4223–4226.

**106** Ashton, P.R., Baxter, I., Fyfe, M.C.T. et al. (1998). Rotaxane or pseudorotaxane? That is the question! *J. Am. Chem. Soc.* 120: 2297–2307.

**107** Ragazzon, G., Baroncini, M., Silvi, S. et al. (2015). Light-powered autonomous and directional molecular motion of a dissipative self-assembling system. *Nat. Nanotechnol.* 10: 70–75.

**108** Li, H., Cheng, C., McGonigal, P.R. et al. (2013). Relative unidirectional translation in an artificial molecular assembly fueled by light. *J. Am. Chem. Soc.* 135: 18609–18620.

**109** Casimiro, L., Groppi, J., Baroncini, M. et al. (2018). Photochemical investigation of cyanoazobenzene derivatives as components of artificial supramolecular pumps. *Photochem. Photobiol. Sci.* 17: 734–740.

**110** Sevick, E. (2015). Nanomachines: a light-driven molecular pump. *Nat. Nanotechnol.* 10: 18–19.

**111** Zhang, Q., Qu, D.-H., Tian, H., and Feringa, B.L. (2020). Bottom-up: can supramolecular tools deliver responsiveness from molecular motors to macroscopic materials? *Matter* 3: 355–370.

**112** Liu, Y., Flood, A.H., Bonvallet, P.A. et al. (2005). Linear artificial molecular muscles. *J. Am. Chem. Soc.* 127: 9745–9759.

**113** Du, G.Y., Moulin, E., Jouault, N. et al. (2012). Muscle-like supramolecular polymers: integrated motion from thousands of molecular machines. *Angew. Chem. Int. Ed.* 51: 12504–12508.

**114** Berna, J., Leigh, D.A., Lubomska, M. et al. (2005). Macroscopic transport by synthetic molecular machines. *Nat. Mater.* 4: 704–710.

**115** Goujon, A., Lang, T., Mariani, G. et al. (2017). Bistable [c2]daisy chain Rotaxanes as reversible muscle-like actuators in mechanically active gels. *J. Am. Chem. Soc.* 139: 14825–14828.

**116** Katsonis, N., Lubomska, M., Pollard, M.M. et al. (2007). Synthetic light-activated molecular switches and motors on surfaces. *Progr. Surf. Sci.* 82: 407–434.

**117** Silvi, S., Venturi, M., and Credi, A. (2009). Artificial molecular shuttles: from concepts to devices. *J. Mater. Chem.* 19: 2279–2294.

**118** Pathem, B.K., Claridge, S.A., Zheng, Y.B., and Weiss, P.S. (2013). Molecular switches and motors on surfaces. *Annu. Rev. Phys. Chem.* 64: 605–630.

**119** See, e.g.:Heinrich, T., Traulsen, C.H.H., Holzweber, M. et al. (2015). Coupled molecular switching processes in ordered mono- and multilayers of stimulus-responsive rotaxanes on gold surfaces. *J. Am. Chem. Soc.* 137: 4382–4390.

**120** Watson, M.A. and Cockroft, S.L. (2016). Man-made molecular machines: membrane bound. *Chem. Soc. Rev.* 45: 6118–6129.

**121** See, e.g.:Ohshima, S., Morimoto, M., and Irie, M. (2015). Light-driven bending of diarylethene mixed crystals. *Chem. Sci.* 6: 5746–5752.


**122** See, e.g.:Baroncini, M., d'Agostino, S., Bergamini, G. et al. (2015). Photoinduced reversible switching of porosity in molecular crystals based on star-shaped azobenzene tetramers. *Nat. Chem.* 7: 634–640.

**123** Fang, L., Olson, M.A., Benitez, D. et al. (2010). Mechanically bonded macromolecules. *Chem. Soc. Rev.* 39: 17–29.

**124** Yan, X., Zheng, B., and Huang, F. (2013). Integrated motion of molecular machines in supramolecular polymeric Scaffolds. *Polym. Chem.* 4: 2395–2399.

**125** Berna, J., Leigh, D.A., Lubomska, M. et al. (2005). Macroscopic transport by synthetic molecular machines. *Nat. Mater.* 4: 704–712.

**126** Naumov, P., Chizhik, S., Panda, M.K. et al. (2015). Mechanically responsive molecular crystals. *Chem. Rev.* 115: 12440–12490.

**127** Xu, W.C., Sun, S., and Wu, S. (2019). Photoinduced reversible solid-to-liquid transitions for photoswitchable materials. *Angew. Chem. Int. Ed.* 66: 1077–1087.

**128** Castiglioni, F., Danowski, W., Perego, J. et al. (2020). Modulation of porosity in a solid material enabled by bulk photoisomerization of an overcrowded alkene. *Nat. Chem.* 12 (7): 595–602.

**129** Baroncini, M., d'Agostino, S., Bergamini, G. et al. (2015). Photoinduced reversible switching of porosity in molecular crystals based on star-shaped azobenzene tetramers. *Nat. Chem.* 7: 634–640.

**130** Danowski, W., Leeuwen, T., Abdolahzadeh, S. et al. (2019). Unidirectional rotary motion in a metal–organic framework. *Nat. Nanotechnol.* 14: 488–494.

**131** Danowski, W., Castiglioni, F., Sardjan, A.S. et al. (2020). Visible-light-driven rotation of molecular motors in a dual-function metal-organic framework enabled by energy transfer. *J. Am. Chem. Soc.* 142: 9048–9056.

**132** Krause, S. and Feringa, B.L. (2020). Towards artificial molecular factories from framework-embedded molecular machines. *Nat. Rev. Chem.* 4: 550–562.

**133** Huang, H. and Aida, T. (2019). Towards molecular motors in unison. *Nat. Nanotechnol.* 14: 407.

**134** See, e.g.:Wezenberg, S.J., Feringa, B.L., Croisetu, C.M. et al. (2016). Reversible gel-sol photoswitching with an overcrowded alkene-based bis-urea supergelator. *Chem. Sci.* 7: 4341–4346.

**135** See, e.g.:Yu, J.-J., Cao, Z.-Q., Zhang, Q. et al. (2016). Photo-powered stretchable nano-containers based on well-defined vesicles formed by an overcrowded alkene switch. *Chem. Commun.* 52: 12056–12059.

**136** Chen, J., Leung, F.K.-C., Stuart, M.C.A. et al. (2018). Artificial muscle-like function from hierarchical supramolecular assembly of photoresponsive molecular motors. *Nat. Chem.* 10: 132–138.

**137** Xu, F., Pfeifer, L., Stuart, M.C.A. et al. (2020). *Chem. Commun.* 56: 7451–7454.

**138** Chen, S., Leung, F., Stuart, M., and the, C. W. J. O. (2020). Dynamic assemblies of molecular motor amphiphiles control macroscopic foam properties. *J. Am. Chem. Soc.* 2020 (142): 10163–10172.

**139** Goujon, A., Du, G., Moulin, E. et al. (2016). Hierarchical self-assembly of supramolecular muscle-like fibers. *Angew. Chem. Int. Ed.* 55: 703–707.

**140** Iwaso, K., Takashima, Y., and Harada, A. (2016). Fast response dry-type artificial molecular muscles with [c2]daisy chains. *Nat. Chem.* 8: 626–633.


**141** Li, Q., Fuks, G., Moulin, E. et al. (2015). Macroscopic contraction of a gel induced by the integrated motion of light-driven molecular motors. *Nat. Nanotechnol.* 10: 161–165.

**142** Colard-Itté, J.-R., Li, Q., Collin, D. et al. (2019). Mechanical behaviour of contractile gels based on light-driven molecular motors. *Nanoscale* 11: 5197–5202.

**143** Foy, J.T., Li, Q., Goujon, A. et al. (2017). Dual-light control of nanomachines that integrate motor and modulator subunits. *Nat. Nanotechnol.* 12: 540–545.

## 33 Molecular Photoswitches for Information Processing: From Simple to Complex

Joakim Andréasson and Uwe Pischel

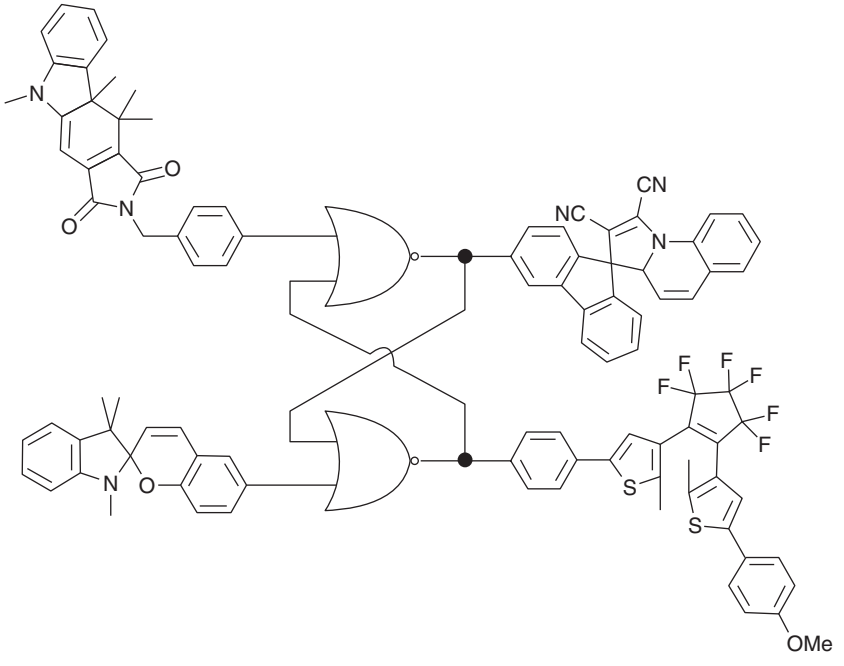


**Characteristic Features**

Photochromic compounds are ideal candidates for the realization of molecular logic and information processing. The ease and spatiotemporal precision by which light (inputs) can be delivered, the substantial differences in spectral properties (outputs) between the isomers, and the inherent memory effect are sought-after properties in this context and will be elaborated on in this chapter.

**Key References**

De Silva, A.P., Gunaratne, H.Q.N., and McCoy, C.P. (1993). A molecular photoionic and gate based on fluorescent signaling. *Nature* 364 (6432): 42–44.

Andreasson, J. and Pischel, U. (2015). Molecules with a sense of logic: a progress report. *Chem. Soc. Rev*. 44 (5): 1053–1069.

Andreasson, J. et al. (2011). All-photonic multifunctional molecular logic device. *J. Am. Chem. Soc*. 133 (30): 11641–11648.

Andreasson, J. et al. (2004). Molecule-based photonically switched half-adder. *J Am. Chem. Soc*. 126 (49): 15926–15927.

# 33

# Molecular Photoswitches for Information Processing: From Simple to Complex

*Joakim Andréasson*[1] *and Uwe Pischel*[2]

[1] *Chalmers University of Technology, Department of Chemistry and Chemical Engineering, Chemistry and Biochemistry, SE-412 96 Göteborg, Sweden*
[2] *University of Huelva, CIQSO – Center for Research in Sustainable Chemistry, Department of Chemistry, Campus de El Carmen s/n, E-21071 Huelva, Spain*

## 33.1 Introduction

Molecular logic, also referred to as molecular information processing, builds on the notion that molecular constructs can be used to mimic the functions typically performed by silicon-based microprocessors [1–7]. The proper function of the molecules most often relies on the *on–off* switching of an optically detectable property (output), such as absorption or emission, rather than the voltage-driven switching used in traditional silicon-based devices. The externally applied stimuli (inputs) used to trigger the spectral changes are often the addition of chemical species such as metal ions, protons, and oligonucleotides. Alternatively, photonic stimuli can be used, which is the case for the all-photonic molecular devices described in this chapter. We would like to emphasize already now that in terms of processor performance, the molecules are still far behind even the weakest CPU architecture. However, microprocessors are hardwired electronic circuits of millions of transistors and other components requiring sophisticated nanofabrication techniques to be used in the manufacturing process. The corresponding "platforms" used in molecular logic are, of course, the molecules. Any habile organic chemist can manufacture these entities in gram quantities using standard laboratory equipment, resulting in around $10^{21}$ *identical* copies of these logic platforms. Other upsides with the molecular approach include miniaturization, minimal power consumption, functional integration, and reconfiguration – some of which will be expanded on in this chapter. In these sections, we will mainly describe our approach to the realization of molecular logic devices using photochromic molecules, but also reference those springing from other research groups. We will start out with trivial one-input binary switches where the function relies on the *on–off* switching of energy and electron transfer reactions. Next, we will elaborate on a selection of two-input Boolean logic gates such as the AND-gate. Finally, molecules that perform the function of small logic circuits, including the half-adders

*Molecular Photoswitches: Chemistry, Properties, and Applications*,
First Edition. Edited by Zbigniew L. Pianowski.


(HAs)/half-subtractors (HSs), multiplexers (MUXs)/demultiplexers (DEMUXs), encoders/decoders, sequential logic devices, and other memory functions, will be illustrated. But first, back to where it all started!

## 33.2 Early Developments in Molecular Switches and Logic Gates

In 1993, de Silva and coworkers designed and characterized the first molecular logic gate [8]. The conceptual approach for this AND-gate has been followed numerous times by other research groups: The emission of a fluorophore is initially (before the application of any input) quenched by two molecular appendices such that both Input 1 AND Input 2 must be applied to silence the quenching processes of these two centers before emission (output) is being observed. In de Silva's design, protons and $Na^+$ ions were added as inputs to turn off the electron transfer (photoinduced electron transfer [PET]) quenching by an amine and a crown ether, respectively. Alteration of redox energies can conveniently be brought about also by the isomerization of molecular photoswitches [9]. Here, one isomeric form of the photoswitch should be easily oxidized/reduced, whereas the other form is not. Covalent attachment of the photoswitch to a fluorophore such that the distance between these units in the dyad is short enough to allow for efficient PET reactions to occur forms the basis of the design. Before the application of input light for isomerization, the photoswitch is in the redox-active form. Excitation of the fluorophore results in PET quenching that outcompetes the fluorescence so that the fluorescence output is *off* (*c.f.* **1o** in Figure 33.1). Exposing the dyad to light triggers isomerization to the redox-passive form, PET is thermodynamically disfavored, and bright fluorescence is observed (*c.f.* **1c** in Figure 33.1). The output is *on*. This approach is exemplified in Figure 33.1 by the dihydroindolizine-porphyrin dyad **1** from Gust, Moore, and Andréasson [10].

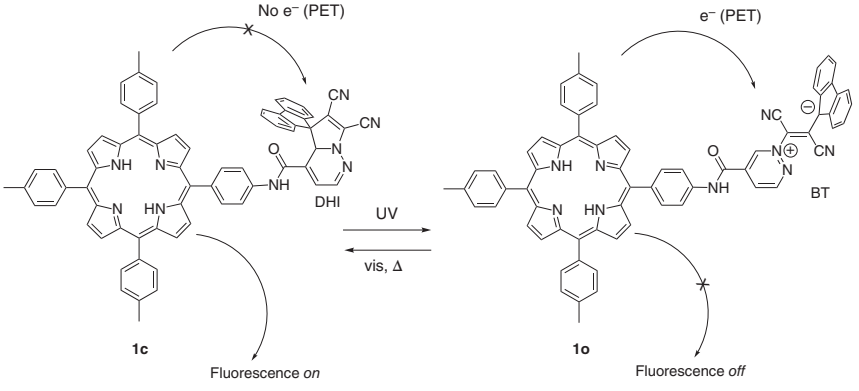


**Figure 33.1** Photochromic switching of PET and fluorescence in a porphyrin-dihydroindolizine dyad. DHI: dihydroindolizine; BT: betaine. Source: Based on Terazono et al. [10].

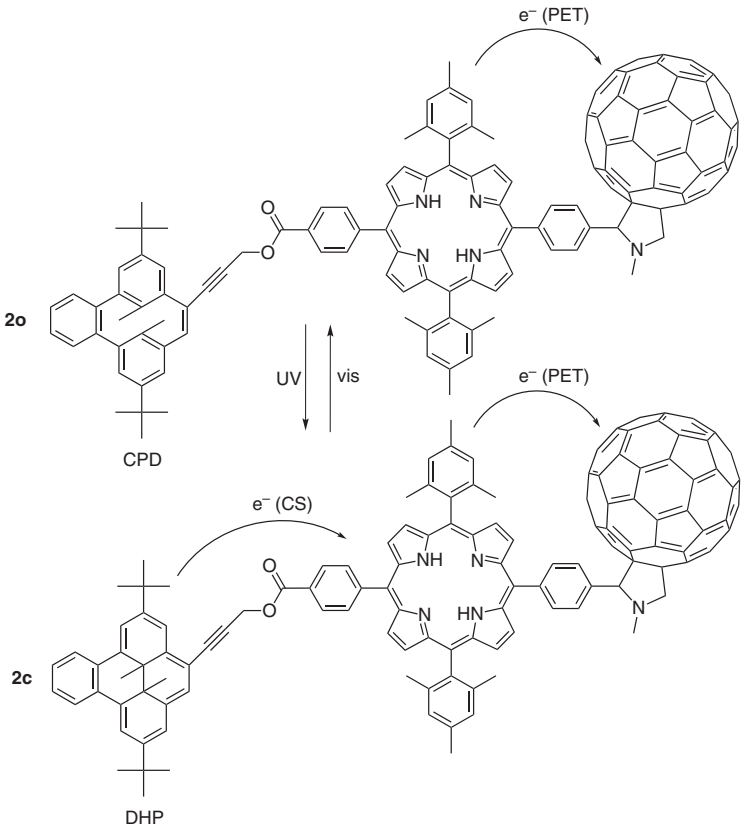


**Figure 33.2** Photochromic switching of electron transfer processes in a porphyrin-dimethyldihydropyrene-$C_{60}$ triad. DHP: dihydropyrene; CPD: cyclophanediene. Source: Based on Liddell et al. [11].

Photoinduced switching of redox energies can not only be used to control PET reactions, but also charge-shift (CS) reactions. A CS reaction is the development of one charge-separated state to another by transfer of electrons. This is illustrated in Figure 33.2 for triad **2** composed of a dimethyldihydropyrene photoswitch (DHP/CPD), a porphyrin (P), and a $C_{60}$ electron acceptor [11].

Excitation of the porphyrin is followed by rapid PET to $C_{60}$ to yield the initial charge-separated state where the porphyrin is carrying the positive charge and the $C_{60}$ the negative charge. This occurs irrespective of the state of the DHP. The DHP isomer is easy enough to oxidize for an electron to be transferred from DHP to the porphyrin in the DHP-P-$C_{60}$ form of the triad, that is, the time constant of this process is shorter than the lifetime of the initial charge-separated state. Hence, the fully charge-separated state $DHP^{+}$-P-$C60^{-}$ is formed (*cf*. **2c** in Figure 33.2). The CPD isomer, however, is too hard to oxidize, which implies that in the CPD-P-C60 form of the triad, the fully charge-separated state is not populated. Instead, the initial charge-separated state collapses rapidly to the ground state (*cf*. **2o** in Figure 33.2).

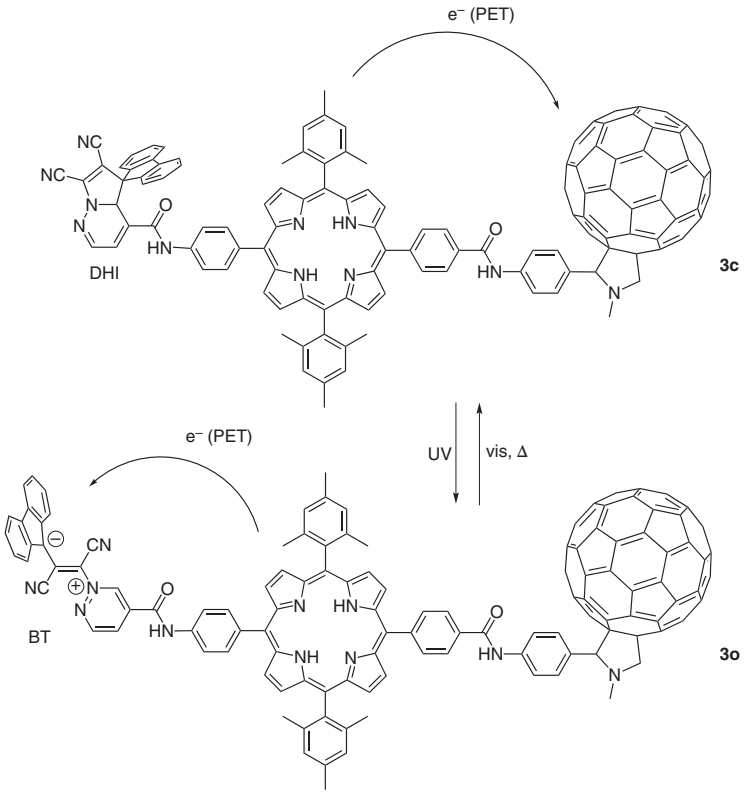


**Figure 33.3** Directional switching of PET in line with a double-throw switch.

One final example of electron transfer switching from the same groups is the double-throw switch in which the *direction* of the PET reaction can be controlled in a reversible fashion [12]. Triad **3** (see Figure 33.3) was devised such that a $C_{60}$ electron acceptor was covalently attached to a porphyrin core on the opposite side of the dihydroindolizine redox switch.

As indicated above, the BT form of this switch is much more easily reduced than the DHI form, so that the former can quench the singlet excited state of the porphyrin by PET (with a time constant of 56 ps), whereas the latter cannot. However, the $C_{60}$ acceptor is there to open up for another PET reaction between the porphyrin and $C_{60}$, with a time constant of 2 ns. Hence, the electron is transferred "to the right" when the dihydroindolozine redox switch is in the closed DHI form, but "to the left" when the switch is isomerized to the open BT form by UV light exposure (*cf*. **3c** and **3o** in Figure 33.3, respectively). The yields of the PET reactions are 82% and 99%, respectively, and in either form, no more than 1% of the electrons are transferred down the "wrong" branch.

Although the functions performed by the molecular designs presented above can be abstracted into one-input Boolean logic gates (i.e. BUFFER and NOT gates), the two-input versions are more useful and complex by nature. The most frequently

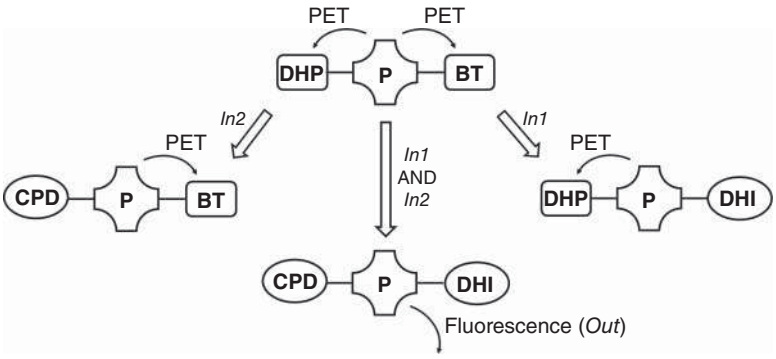


**Figure 33.4** Schematic depiction of the all-photonic molecular logic AND gate. Source: Based on Straight et al. [13].

mimicked two-input gate is the AND-gate that requires both inputs to be switched *on* to switch *on* the output. As indicated above, a commonly used design strategy of the molecular AND-gate is to append two quenchers to a fluorophore. Before intense emission is observed from the fluorophore (defined as the output, *Out*), both quenchers must be put in a non-quenching state, and if AND-logic is to be executed, the two quenching units must be effected orthogonally by the two inputs (*In1* and *In2*). These conditions are fulfilled by the triad schematically depicted in Figure 33.4, consisting of two photoswitches attached to a fluorescent porphyrin reporter [13].

The photoswitches are the dihydroindolizine (existing as DHI or BT) and the dimethyldihydropyrene (existing as DHP or CPD) that are known from above to quench the porphyrin fluorescence by PET reactions only in one of the respective isomeric forms. Initially, the triad is set to the DHP-P-BT state where both switches are PET-active. Now, the critical question is how to isomerize both these switches to the other form in an orthogonal fashion. Dimethyldihydropyrene displays P-type photochromism, whereas dihydroindolizine is of T-type, i.e. thermal isomerization occurs fairly rapidly for the latter but not the former. This is why heat (*In1*) can be used to isomerize dihydroindolizine from the BT to the DHI form without affecting dimethyldihydropyrene, whereas the latter can be almost selectively isomerized from DHP to CPD by red light (*In2*) due to the high efficiency of this process. This implies that orthogonal isomerization to the non-quenching forms is indeed possible, and the prerequisites for AND-gate function are met. It is worth mentioning that this triad can be reconfigured to perform also the function of the INHIBIT gate. Logic reconfiguration will be elaborated on in later sections.

## 33.3 Latches/Flip-Flops

In combinational logic, the order by which the inputs are applied does not affect the state of the output. For example, the AND gate described above switches the output to the *on*-state if both heat and red light are applied, irrespective of their order. On the other hand, sequential logic implies a memory function such that the output

is dependent on the input history of the device [14]. P-type photochromic compounds are the perfect candidates for the mimicry of logic functions with an inherent memory. Let's exemplify with the archetypical dithienylethene (DTE) photoswitch [15], where UV exposure yields the closed colored isomer and visible light yields the open colorless isomer: If you leave a colored DTE solution overnight in a dark cabinet, you would expect to find it colored also the next morning. Why? -Well, because the closed isomer is thermally stable, would probably be the answer from most people working with photochromic compounds. This is, of course, entirely correct. But an alternative answer would be that the DTE molecules *remember* that they were exposed to UV light, and not to visible light, before the sample was put in the cabinet last night. Please note that this would not be the case for T-type photochromic molecules such as the typical spiropyran derivative, where you would most likely find a colorless solution in the morning, although you gave it a good dose of 254 nm UV light the evening before. This may seem like a trivial example, but in fact, the memory function lends a touch of exclusiveness to P-type photoswitches. This refers to the comparison to the majority of all other chemical species that do not present a memory function (take away the reagent and the reaction is reversed) and to the silicon-based memory devices (where sophisticated feedback-loop circuits have to be used to result in the memory effect, see Figure 33.5).

The most straightforward memory function to implement with P-type photoswitches is the S/R latch that comes with two inputs (*Set* and *Reset*) and one output ($Q$) [16]. Application of *Set* (*Set* = 1) switches the output to the *on*-state ($Q = 1$), whereas application of *Reset* (*Reset* = 1) switches the output to the *off*-state ($Q = 0$). Applying none of the inputs leaves the system unchanged. This may appear rudimentary, but to be comprehensive the truth table shown in Table 33.1 must be applied, where $Q_{\text{current}}$ represents the current state of the output and $Q_{\text{next}}$ represents the state of the output after the respective next input. An implementation of the S/R latch using a DTE derivative was presented by the authors where *Set* was defined as UV light (for isomerization to the closed colored isomer), *Reset* defined as visible light (for isomerization to the open colorless isomer), and $Q$ was chosen as absorbance in the visible [17].

If the molecular implementation of the S/R latch is very straightforward, the function of other latches may at a first glance seem impossible to mimic using photoswitches or any other kind of molecule. The D-latch serves as an illustrating example. The D-latch has two inputs: a clock input (*Clock*) and a data input (*In*). From the

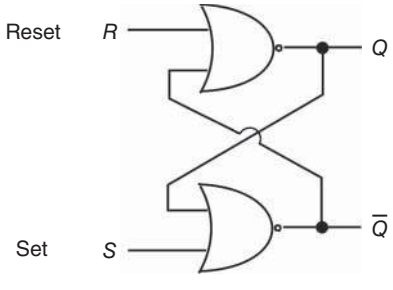


**Figure 33.5** Logic scheme for the S/R latch.

**Table 33.1** Truth table for the S/R latch.

| Entry | *Set* (*S*) | *Reset* (*R*) | $Q_{current}$ | $Q_{next}$ |
|---|---|---|---|---|
| 1 | 0 | 0 | 0 | 0 |
| 2 | 1 | 0 | 0 | 1 |
| 3 | 1 | 0 | 1 | 1 |
| 4 | 0 | 0 | 1 | 1 |
| 5 | 0 | 1 | 1 | 0 |
| 6 | 0 | 1 | 0 | 0 |

**Table 33.2** Truth table for the D-latch.

| Entry | *Clock* | *In* | $Q_{current}$ | $Q_{next}$ |
|---|---|---|---|---|
| 1 | 0 | 0 | 0 | 0 |
| 2 | 0 | 0 | 1 | 1 |
| 3 | 0 | 1 | 0 | 0 |
| 4 | 0 | 1 | 1 | 1 |
| 5 | 1 | 0 | 0 | 0 |
| 6 | 1 | 0 | 1 | 0 |
| 7 | 1 | 1 | 0 | 1 |
| 8 | 1 | 1 | 1 | 1 |

truth table of this device shown in Table 33.2, it is seen that whenever *Clock* is set to 1, the output $Q_{next}$ takes the value of *In*. On the contrary, when *Clock* is 0, the current output state ($Q_{current}$) is preserved so that $Q_{current} = Q_{next}$. Or in other words, application of *Clock* enables the state of *In* to be transmitted to the output *Q*.

It follows from entries 3 and 4 in the truth table that the application of *In* alone must not change the state of the system. If a photoswitch was to be used as a photonically driven molecular platform emulating the function of the D-latch, this would be equivalent to the condition that exposing the photoswitch to *In* does not trigger isomerization in any direction. Furthermore, from entries 5 and 6 it is seen that application of *Clock* alone sets the output *Q* to 0. If we assume that the output *Q* is defined as absorption in the visible region, the photoswitch should be isomerized to the colorless isomer upon exposure to *Clock*. The two prerequisites described above present no challenges, as *In* could in principle be chosen as anything that is not causing isomerization in any direction, whereas *Clock* is visible, light triggering isomerization to the colorless form. From entries 7 and 8 in the truth table, however, it is seen that the application of both *Clock* and *In* should result in isomerization to the colored isomer, i.e. in the opposite direction to application of *Clock* alone. The authors solved this seemingly impossible task by the use of a P-type

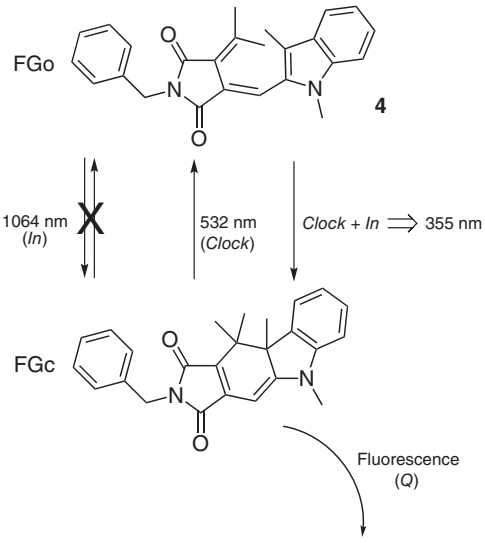


**Figure 33.6** A fulgimide photoswitch performing the function of the D-latch. Source: Based on Remon et al. [18].

photoswitch from the fulgimide (FG) family together with non-linear optics (**4** in Figure 33.6) [18].

More specifically, a third-harmonic generating (THG) crystal, that combines visible photons at 532 nm with IR photons at 1064 nm to yield 355 nm photons, was used. *Clock* and *In* were defined as laser light at 532 nm and 1064 nm, respectively, whereas the output $Q$ was defined as fluorescence from the closed isomer of the fulgimide, FGc. 1064 nm (*In* alone) is not triggering isomerization in any direction so that $Q_{\text{current}} = Q_{\text{next}}$. 532 nm (*Clock* alone) yields the open isomer FGo irrespective of the current state and no fluorescence ($Q_{\text{next}} = 0$). Application of both 1064 nm light and 532 nm light through the THG generates 355 nm UV photons that triggers isomerization to the fluorescent isomer FG(c). $Q_{\text{next}} = 1$ results, in perfect accordance with the truth table.

## 33.4 Keypad Locks

The keypad lock [19–22] is another example where the order by which the inputs are applied does influence the state of the output, i.e. a sequential logic device. This type of logic enters frequently in our daily life, as it forms the functional basis for all events where PIN-codes are used. Assuming that the correct PIN-code to your credit card is 1234, it is of course not supposed to grant access to your account if the entry would be 1243, 1324, 2134, or any other permutation of the four digits. A fairly trivial example of a keypad lock is the priority AND (PAND) gate that comes with two inputs. The difference between a regular AND-gate and the PAND-gate is that the input order matters for the latter. In 2009, the first all-photonic version of a molecular keypad lock was reported by Gust, Moore, and Andréasson [23]. Bi-photochromic triad **5** was designed comprising a FG and a DTE photoswitch covalently linked to a porphyrin (P) fluorescence reporter according to Figure 33.7.

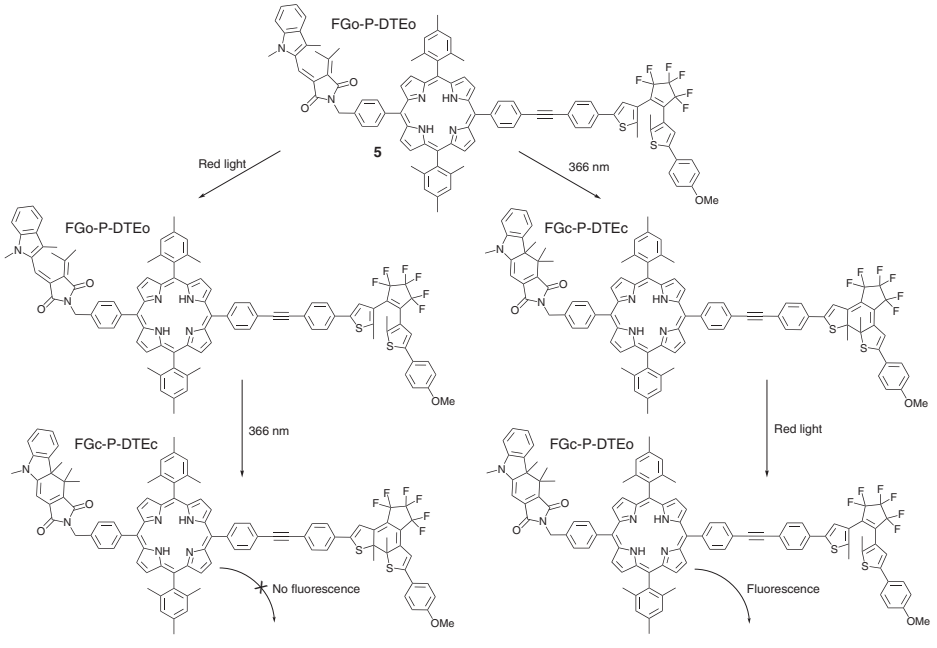


**Figure 33.7** Triad **5** performing the function of a two-input keypad lock.

Both FG and DTE exist in the open (FGo and DTEo) and the closed (FGc and DTEc) isomeric forms. The porphyrin interacts photophysically with the closed isomer of the photoswitches according to the following: The singlet excited state of FGc is efficiently quenched by P in a FRET (Förster resonance energy transfer) process. The singlet excited state of P is in turn FRET-quenched by DTEc. Moreover, exposure at 470 nm will almost only result in the direct excitation of FGc, as all other species display no or very low absorbance at this wavelength. Thus, for intense sensitized emission from P to be observed upon excitation at 470 nm, FG must be in the closed isomer FGc (for the 470 nm light to be absorbed at all) and DTE must be in the open isomeric form DTEo (not to FRET-quench the fluorescence from P). This implies that FGc-P-DTEo is the only fluorescent species out of the four possible forms of the triad upon excitation at 470 nm.

In the operation as a keypad lock, the triad is initially set to the all-open form FGo-P-DTEo. This is conveniently done by exposure to green light, irrespective of the isomeric form present. The two inputs are irradiation at $\lambda = 366$ nm (*Input A*) and red light (*Input B*), whereas the output is defined as the porphyrin fluorescence intensity at 650 nm upon excitation at 470 nm. 366 nm UV isomerizes both photoswitches to the closed isomer, whereas red light is only absorbed by DTEc, resulting in isomerization to yield DTEo. If the initial state FGo-P-DTEo is first exposed to red light, there will be no change in the isomeric distribution of any of the two photoswitches as this light is not being absorbed. Subsequent exposure to 366 nm UV will trigger isomerization to FGc-P-DTEc. This form displays no emission. On the contrary, if the initial state FGo-P-DTEo is instead initially exposed to 366 nm UV, the non-fluorescent isomer FGc-P-DTEc results. Subsequent irradiation with red light isomerizes exclusively DTEc to DTEo to yield FGc-P-DTEo, displaying intense emission upon excitation at 470 nm. 366 nm UV followed by red light corresponds to the input sequence "*Input A* followed by *Input B,*" and this is the only input sequence that switches the output to the *on*-state, equivalent to opening the lock.

Another example of a photochromically driven keypad lock was presented by the authors in 2011 [24]. A series of fluorescent reporter molecules, such as the aminonaphthalimide (**6** in Figure 33.8), were covalently attached to a spiropyran photoswitch.

The common denominator for the fluorescent reporter molecules is that their emission spectrum overlaps with the absorption spectrum of both the merocyanine (MC) and the protonated merocyanine ($MCH^+$) forms, whereas there is no overlap with the absorption spectrum of the spiro (SP) isomer. As the distance between the reporters and the photoswitch is considerably shorter than the critical Förster radius, the fluorescence from the reporters are quenched by the MC and the $MCH^+$ forms of the dyads, whereas fluorescence emission is observed for the SP form. Here, the fluorescence intensity was being used as the output. The dyads are initially set to the $MCH^+$ forms, and the two inputs are defined as base (*Input A*) and light of $\lambda > 530$ nm (*Input B*). To switch the output to the *on*-state, the dyads must be isomerized to the SP form. $MCH^+$ does not absorb light at $\lambda > 530$, which implies that base (*Input A*) must first be added to yield the non-protonated MC form that is photochromically active in this wavelength region. Subsequently, isomerization to the SP form occurs by application of $\lambda > 530$ (*Input B*). Thus, *Input A* followed by *Input B*

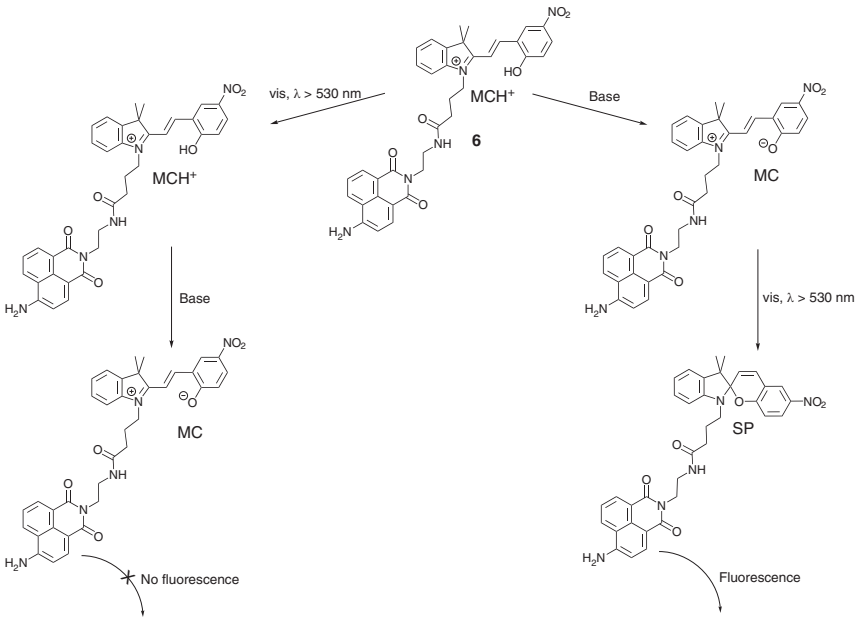


**Figure 33.8** Dyad 6 performing the function of a two-input keypad lock with photonic and chemical inputs.

is the only input sequence that results in fluorescence from the reporters, in line with the function of the keypad lock.

Additional features of a keypad lock, further strengthening the security, are *two-factor authentication* and *one-time passwords*. Both these functions are inherent to the security tokens issued for online banking, etc. The typical function of these tokens is that you start by entering your PIN to the security token that gives you back a six-digit number that you use to access your online bank account. This six-digit number is valid for one entry only, so that the next time you are doing internet banking, you must repeat the procedure to generate a new six-digit number. This increases the security dramatically, as a password stolen by intrusion will not give the intruder access to the protected system. This is the essence of one-time passwords, but also of two-factor authentication. As inferred by the name of the latter, two factors are needed for authentication. Typically, something that the user must *know* (the personal PIN number) and something that the user must *have* (the security token). In fact, withdrawing money from an ATM machine qualifies as two-factor authentication as you must *know* your PIN number and *have* your credit card. Andréasson and coworkers reported on a bi-photochromic molecular platform, composed of DTE and FG switches, where two-factor authentication and one-time passwords are inherent to the function [25]. In brief, only one out of the four possible isomeric forms of the molecule displays fluorescence (used as output), and the optical input sequences yielding this fluorescent state depend on the current state. Thus, the correct password varies with the current state, allowing for one-time password generation. Each of the initial isomeric states

presents characteristic absorption spectra. To arrive at the correct password, the user must have the "key" that connects the features in each absorption spectra to the password, in line with two-factor authentication.

## 33.5 Data Transmission

Several functions inherent to the transmission of digital data have been mimicked by molecular designs, including multiplexing/demultiplexing, encoding/decoding, and parity generators/checkers. On the molecular logic timeline, these molecular devices started to appear in the literature after a period of strong dominance by half- and full adders/subtractors, which will be the focus of section 33.6. Multiplexing was the first function to be reported in 2007 [26]. The function of a multiplexer is to merge two or more input channels into a common transmission medium. This merger must, of course, occur in a very controlled manner. Else, it would be impossible to disentangle, or demultiplex, the information from the two input channels at the receiving end after the data have been transmitted. What controls the merger of the data from the input channels is the selector input, *Sel*, and its action is schematically depicted in Figure 33.9 for the 2 : 1 multiplexer.

The molecule used for this purpose was designed by Gust, Moore, and Andréasson, consisting of two photoswitches attached to a fluorescent porphyrin reporter [26]. Indeed, this is the triad described above (Section 33.2) that was used as an AND gate in 2005 [13]. One and the same molecule performing several functions is the essence of logic reconfiguration and will be elaborated on in section 33.7. The 2 : 1 multiplexer (MUX) has two input channels referred to herein as *In1* and *In2*. Depending on the state of *Sel*, data from *In1* or *In2* are transmitted to the output, *Out*, representing the transmission medium. A condensed representation of this scheme is shown in the truth table in Table 33.3.

The molecular triad has two individual photoswitches that can each quench the fluorescence from the porphyrin reporter in one of the two isomeric forms. For the dimethyldihydropyrene, the DHP isomer is the quencher, whereas the CPD isomer has no effect on the porphyrin fluorescence intensity. The corresponding isomers for dihydroindolizine are BT and DHI. As mentioned in Section 33.2 above, BT and DHP can be selectively isomerized to the non-quenching isomers by exposure to heat and red light, respectively. Thus, the non-fluorescent isomer BT-P-CPD must be exposed

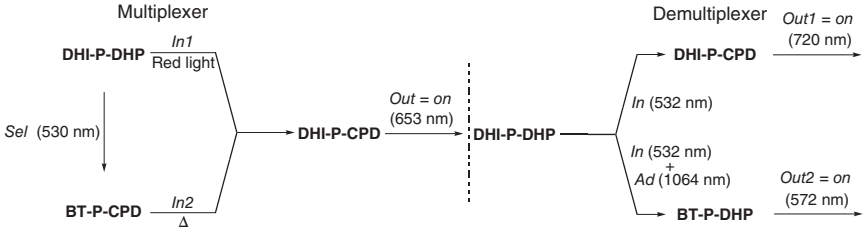


**Figure 33.9** Schematic depiction of the dihydroindolizine-porphyrin-dimethyldihydropyrene triad performing the functions of the 2 : 1 multiplexer and the 1 : 2 demultiplexer.

**Table 33.3** Truth table for the 2 : 1 multiplexer.

| Entry | *In1* | *In2* | *Sel* | *Out* |
|---|---|---|---|---|
| 1 | 0 | 0 | 0 | 0 |
| 2 | 0 | 1 | 0 | 0 |
| 3 | 1 | 0 | 0 | 1 |
| 4 | 1 | 1 | 0 | 1 |
| 5 | 0 | 0 | 1 | 0 |
| 6 | 0 | 1 | 1 | 1 |
| 7 | 1 | 0 | 1 | 0 |
| 8 | 1 | 1 | 1 | 1 |

to heat (triggering the BT → DHI process) to isomerize the triad to the fluorescent form DHI-P-CPD. For the "opposite" isomeric form DHI-P-DHP, red light must be used (triggering the DHP → CPD process) to yield DHI-P-CPD, and fluorescence is again observed. Interestingly, and seminal for the function as the 2 : 1 multiplexer, green light at 530 nm triggers isomerization from DHI-P-DHP to mainly CPD-P-BT, i.e. interconverting the two abovementioned non-fluorescent forms used in the operation as the MUX. Defining porphyrin fluorescence at 653 nm as *Out*, *Sel* as light at 530 nm, *In1* as red light, and *In2* as heat (that can be delivered as IR light), the function of the MUX is realized according to the following: In the absence of *Sel*, the triad is in the non-fluorescent DHI-P-DHP form. This form is thermally stable, implying that heat (*In2*) has no effect on the isomeric distribution, whereas red light (*In1*) isomerizes the triad to the fluorescent form DHI-P-CPD, switching *Out* to the *on*-state. Thus, the state of the *In1* channel is transmitted to the output, whereas the state of *In2* is irrelevant for the output. Switching *Sel* to the *on*-state isomerizes the triad to BT-P-CPD where BT is the quencher. Applying heat (switching *In2* to the *on*-state) to this isomer yields the fluorescent form DHI-P-CPD, whereas red light has no effect. Hence, after application of *Sel*, *Out* takes the value of *In2* in accordance with the function of the MUX.

The action of the MUX is being reversed by the demultiplexer (DEMUX) so that the data from the two input channels are separated to individual data streams again, after transmission. The two individual data streams are here represented by the two outputs, *Out1* and *Out2*. In the 1 : 2 DEMUX, the separation is made possible by the Address input *Ad* acting on the transmitted data, here represented by the input *In* (see Figure 33.9 above). When *Ad* is *off*, the state of *In* is directed to output *Out1* and *Out2* remains *off*. On the contrary, when *Ad* is switched *on*, *Out2* reports the state of *In*. Thus, if the output of the multiplexer serves as the input of the demultiplexer, and the selector input of the multiplexer and the address input of the demultiplexer are switched *on* and *off* in synchrony, demultiplexer output *Out1* will faithfully track the state of one of the multiplexer inputs, whereas demultiplexer output *Out2* will report the state of the second multiplexer input. Multiplexed data transmission follows.

Interestingly, Gust, Moore, and Andréasson devised a scheme where the dihydroindolizine-porphyrin-dimethyldihydropyrene triad also performs the function of the DEMUX [27]. *In* and *Ad* were defined as laser light at 532 and 1064 nm, respectively, whereas *Out1* and *Out2* were represented by intense porphyrin fluorescence at 720 nm (observed only from the DHI-P-CPD isomer) and strong absorbance from mainly BT at 572 nm, respectively. *In* and *Ad* are combined in a THG crystal, generating 355 nm when both lasers are on. If the initial state is chosen as the thermally stable isomer DHI-P-DHP, both outputs are *off*. Applying *In* while *Ad* is *off* yields mainly DHI-P-CPD which switches *Out1* to the *on*-state, whereas application of both *In* and *Ad* yields mainly BT-P-DHP, switching *Out2* to the *on*-state. Thus, the state of *In* is directed to *Out1* or *Out 2* depending on the state of *Ad*, which is the exact function of the DEMUX.

Encoding/decoding is frequently used in the context of data transmission, due to the inherent capacity for data compression. For example, the 4-2 encoder converts four bits of data into two bits according to the truth table in Table 33.4. More precisely, it converts the numbers 0, 1, 2, and 3 in 10-base (represented by the inputs *In*(0), *In*(1), *In*(2), and *In*(3)), to the corresponding binary numbers (comprised by *Out*(0) and *Out*(1)). The inputs can take the values 0 or 1 according to the truth table, i.e. only one input can be set to the *on*-state (1) at any time. As for the outputs, *Out*(0) is the sum digit and *Out*(1) is the carry digit implying that 0, 1, 2, and 3 in base 10 is represented by [*Out*(1)*Out*(0)] = [00, 01, 10, 11], respectively. So, what does it take for a photochromic molecular platform to emulate this function? First of all, two individual spectroscopically detectable features should be defined, corresponding to *Out*(0) and *Out*(1). Then, four input stimuli (*In*(0) –*In*(3)) are to be chosen so that the following applies: *In*(0) should not trigger the appearance of any of the spectral features chosen as the outputs. *In*(1) and *In*(2) should trigger the appearance of *Out*(0) and *Out*(1) respectively, whereas *In*(3) triggers both *Out*(0) and *Out*(1). This scheme is fairly straightforward to implement using two individual photoswitches, initially in the colorless form, where these switches are selectively isomerized to the colored isomers by the application of light at two different wavelengths corresponding to *In*(1) and *In*(2). The two colored isomers should have absorption features different enough to allow for spectral discrimination, presenting two wavelengths where to read *Out*(0) and *Out*(1). *In*(3) is light a third wavelength, isomerizing both switches to the colored form, whereas *In*(0) is not coloring any of the two switches. This is exactly the approach that was taken by Gust, Moore, and Andréasson in

**Table 33.4** Truth table for the 4–2 encoder.

| Entry | *In*(0) | *In*(1) | *In*(2) | *In*(3) | *Out*(1) | *Out*(0) |
|---|---|---|---|---|---|---|
| 1 | 1 | 0 | 0 | 0 | 0 | 0 |
| 2 | 0 | 1 | 0 | 0 | 0 | 1 |
| 3 | 0 | 0 | 1 | 0 | 1 | 0 |
| 4 | 0 | 0 | 0 | 1 | 1 | 1 |

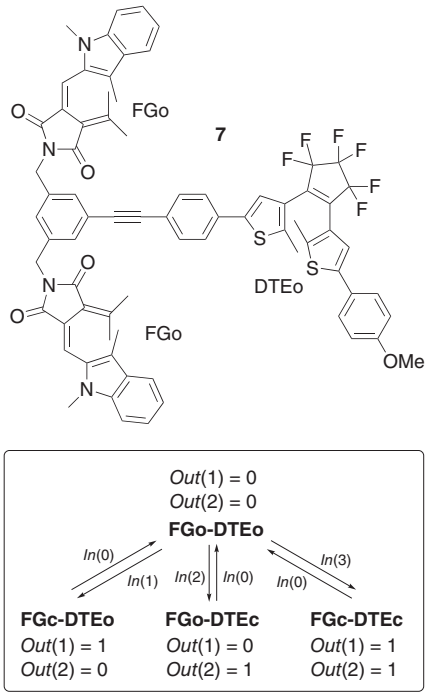


**Figure 33.10** FG-DTE triad **7** performing the function of the 4 : 2 encoder. Source: Modified from Andréasson et al. [28].

2008 when they reported the first molecular version of this device (see triad **7** in Figure 33.10) [28].

The triad consists of one DTE and two FG photoswitches covalently linked around a benzene core. The initial state is the all-open isomer FGo-DTEo with no absorption in the visible region. This state is formed by exposure to visible light, which also serves as input *In*(0). *In*(1) and *In*(2) were chosen as light at 397 and 302 nm isomerizing almost selectively FG and DTE, respectively, to the closed isomer. FGc is the main absorber at 475 nm, whereas DTEc is the exclusive absorber at 625 nm. The absorption at these two wavelengths was employed as the outputs. The last line in the truth table is fulfilled by defining 366 nm as *In*(3), isomerizing both FG and DTE to the closed isomer. This is equivalent to switching both outputs to the *on*-state.

The corresponding 2–4 decoder reverses the action of the 4–2 encoder, and this function was also performed by the same molecular triad [28]. Here, light at 302 and 397 nm was used as the two inputs and unique spectral signatures of the respective isomeric isomer formed after input application were chosen as outputs, correctly describing the decoder function.

Data transmission is never perfect, in the sense that it is inflicted with errors. This is true also for the entry of data to be transmitted. One corrupt bit may have severe implications, irrespective of being a result of erroneous entry of data or errors in the transmission process (how sure can you be that you got all digits in the account number right when you transferred money the last time?). Luckily, there are "control

points" in the form of check digits included in any string of transmitted data. These are extra digits added to the set of initial data in such a way that errors occurring in the entry or the transmission of the data will be detected. And errors do indeed occur; a bandwidth of 1 TB $s^{-1}$ implies that if 1 out of 100 billion bits is corrupted, 10 errors will occur each second.

A parity bit is an illustrative example of a check digit. Parity bits ($P$) are added to a string of binary data (data string = $D_n$ before added parity bit) so that the total number of 1s ($S$) is even (for even parity). This is the role of the parity generator, and the operation is executed before transmission of the data. After addition of the parity bit, the new string $D_nP$ is now transmitted to the receiving end, where the parity of $D_nP$ must be controlled before the data string can be delivered to the user. This is taken care of by the parity checker. If the parity remains even, fault-free data transmission has (likely) occurred,[1] whereas if the parity is odd, the checker must alert the user. The output from the parity checker is carrying this information. A "0" output signals that data transmission is OK, whereas a "1" output alerts the user that errors have occurred. The authors reported the first molecular version of the parity generator and the parity checker in 2013 [29], and other examples have followed [30]. The truth table for the described 2-bit parity generator is shown in Table 33.5, where it is seen that the two bits initially composing the initial data string ($D_1$ and $D_2$) serve as the inputs, and the parity bit $P$ serves as the output. As the number of 1s in the string to be transmitted ($D_1D_2P$) must always be an even number, the truth table of this device is identical to that of the XOR-gate, described in section 33.6. Thus, the logic situation translates straightforwardly into the following: only if exclusively one of the two inputs is *on*, the output switches *on*. This scheme can be realized using two principally different approaches: Degenerate (identical) inputs or non-degenerate (different from one another) inputs. The authors used degenerate all-optical inputs, implying that the output should describe a neuron-like *off–on–off* response with increasing light dose [29]. Two molecular triads consisting of FG and DTE photoswitches were used for this purpose, and

**Table 33.5** Truth table for the 2-bit parity generator.

| | Inputs | | Output | |
|---|---|---|---|---|
| **Entry** | $D_1$ | $D_2$ | $P$ | Σ |
| 1 | 0 | 0 | 0 | 0 (even) |
| 2 | 0 | 1 | 1 | 2 (even) |
| 3 | 1 | 0 | 1 | 2 (even) |
| 4 | 1 | 1 | 0 | 2 (even) |

Σ = number of 1s.

1 If two (or an even number) errors occur, the checker won't be able to detect the erroneous procedures.

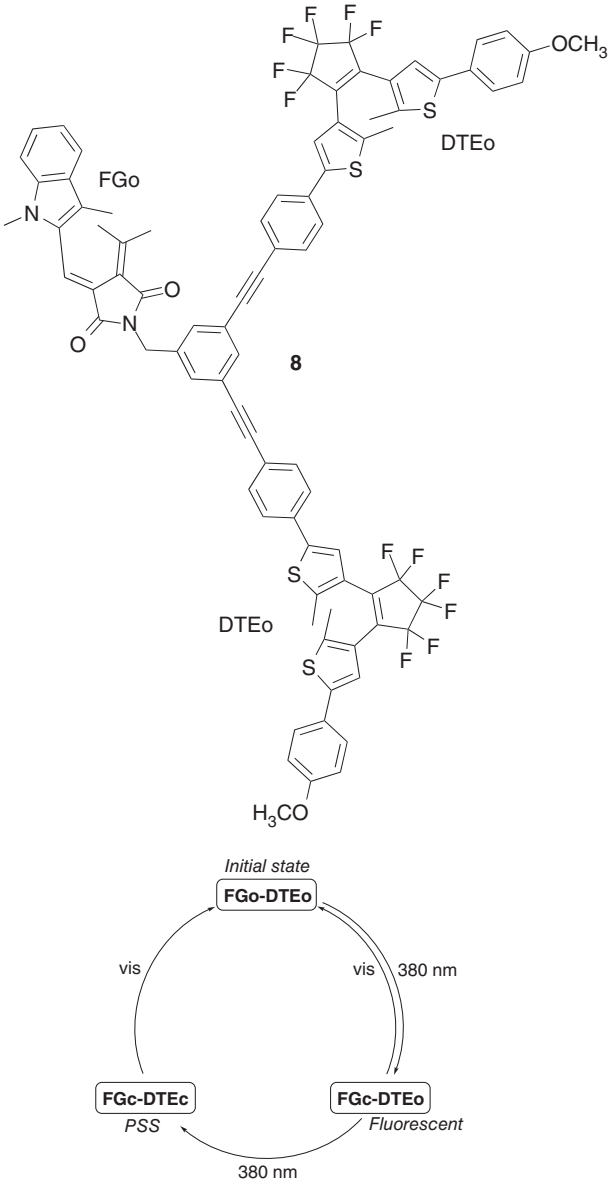


**Figure 33.11** Structure of FG-DTE triad **8** (top) and the functional principles of **8** performing the function of the 2-bit parity generator (bottom).

the structure and functional principles for one of these triads (**8**) are shown in Figure 33.11.

The initial state is chosen as the "all-open" form, where both the FG and the DTE are in the open isomer, FGo and DTEo, respectively. This form is non-fluorescent, as neither FGo nor DTEo emits significantly. Exposing the triad to UV light (380 nm, degenerate inputs $D_1$ and $D_2$) yields a photostationary state (PSS) enriched in the

**Table 33.6** Truth table for the 3-bit parity checker.

| | Inputs | | | Output | | |
|---|---|---|---|---|---|---|
| **Entry** | $D_1$ | $D_2$ | $P$ | $C$ | $\Sigma$ | **Result** |
| 1 | 0 | 0 | 0 | 0 | 0 (even) | Ok |
| 2 | 0 | 1 | 0 | 1 | 1 (odd) | Error |
| 3 | 1 | 0 | 0 | 1 | 1 (odd) | Error |
| 4 | 1 | 1 | 0 | 0 | 2 (even) | Ok |
| 5 | 0 | 0 | 1 | 1 | 1 (odd) | Error |
| 6 | 0 | 1 | 1 | 0 | 2 (even) | Ok |
| 7 | 1 | 0 | 1 | 0 | 2 (even) | Ok |
| 8 | 1 | 1 | 1 | 1 | 3 (odd) | Error |

$\Sigma$ = number of 1s in the $D_1D_2P$ data string.

"all-closed" form FGc-DTEc. Here, FGc is intrinsically fluorescent but the emission overlaps with the absorption of DTEc. FGc fluorescence is therefore quenched in an efficient FRET reaction, rendering this isomeric form non-fluorescent too. However, passing from the initial state FGo-DTEo to the FGc-DTEc-enriched PSS, the concentration of FGc-DTEo initially increases. After reaching the maximum concentration, it decreases again before the PSS is reached. In FGc-DTEo, FGc emits fluorescence as DTEo cannot act as a FRET quencher as the abovementioned spectral overlap is lacking. Thus, exposing the initial state FGo-DTEo to a 380 nm UV dose corresponding to only one of the two inputs switched to the *on*-state yields a substantial concentration of the fluorescent form FGc-DTEo and the output defined as FGc emission at 630 nm is switched *on*. On the contrary, applying both inputs shifts the isomeric distribution to the dominant presence of FGc-DTEc and the emission intensity is below the defined threshold level. Visible light resets the sample to the initial state FGo-DTEo. This is the function of the XOR-gate, and consequently also of the 2-bit parity generator. To realize the somewhat more complex function of the 3-bit parity checker (Table 33.6), a third input was defined as light at $\lambda > 540$ nm, whereas the emission from FGc at 630 nm was again used as the output.

## 33.6 Molecular-Scale Arithmetic

Addition of two bits by the half-adder (HA) is the most trivial of all arithmetic operations. At the same time, it forms the basis of modern computing. The HA has two inputs (representing the two bits to be added) and two outputs (the sum and the carry digit). As seen from the truth table in Table 33.7, the calculations performed by the HA is $0 + 0 = 00$, $0 + 1 = 01$, $1 + 0 = 01$, and $1 + 1 = 10$. In 10-base, this corresponds to $0 + 0 = 0$, $0 + 1 = 1$, $1 + 0 = 1$, and $1 + 1 = 2$.

Generation of the sum and the carry digits are equivalent to XOR-logic and AND-logic, respectively. In the context of molecular logic, this implies that the

**Table 33.7** Truth table for the half-adder.

| Entry | *In1* | *In2* | *Out 1* AND gate (Carry digit) | *Out 2* XOR gate (Sum digit) | Binary sum | 10-Base sum |
|---|---|---|---|---|---|---|
| 1 | 0 | 0 | 0 | 0 | 00 | 0 |
| 2 | 0 | 1 | 0 | 1 | 01 | 1 |
| 3 | 1 | 0 | 0 | 1 | 01 | 1 |
| 4 | 1 | 1 | 1 | 0 | 10 | 2 |

realization of a molecular HA requires a molecule that can perform the function of an AND gate and an XOR gate with shared inputs. The first version of such a device was presented by de Silva and McClenaghan in 2000 [31], and since then a plethora of alternative interpretations have been devised [32–34]. This development led ultimately to the realization of molecular designs capable of both adding and subtracting two bits (the so-called molecular calculators, or moleculators, composed of an HA and a half-subtractor, HS) [35] as well as full adders and full subtractors, which in principle allow for the addition/subtraction of N-bit numbers by cascading N full adder/subtractor circuits [36]. It is interesting to note that the adders/subtractors were the first complex logic devices that were targeted in molecular logic appearing after a period of strong dominance of individual logic gates, and it took until 2007 before other complex functions were reported, such as multiplexing/demultiplexing, encoding/decoding, and the sequential logic function of the keypad lock.

The first molecule-based all-photonic HA presented by Andréasson, Gust, and Moore in 2004 requires two distinct molecular species (the cocktail approach) and non-linear optics as integral part of the device [37]. This study was followed up by the first truly molecular all-photonic version in 2006 [38]. Here, one spiropyran and two identical quinoline-derived dihydroindolizine photoswitches were linked to a benzene core to constitute triad **9** shown in Figure 33.12.

As mentioned above, both photoswitches exist in a closed and an open form referred to as SP and MC for the spiropyran and DHI and BT for the dihydroindolizine. SP and DHI absorb almost exclusively in the UV region, and these are also the thermally stable isomers to which the sample isomerizes in the dark on the minute timescale. MC and BT are formed upon UV exposure and display strong absorption in the visible region. MC is intrinsically fluorescent, but in the triad the emission is quenched by BT in an efficient FRET process. Thus, the following distinguishing spectroscopic features of the triad can be identified that are all central for the function of the HA: The SP-DHI isomer displays no fluorescence at 690 nm and no absorption at 581 nm. MC-DHI displays strong emission at 690 nm and only moderately strong absorption at 581 nm. MC-BT displays no fluorescence at 690 nm but strong absorption at 581 nm. The effect of increased

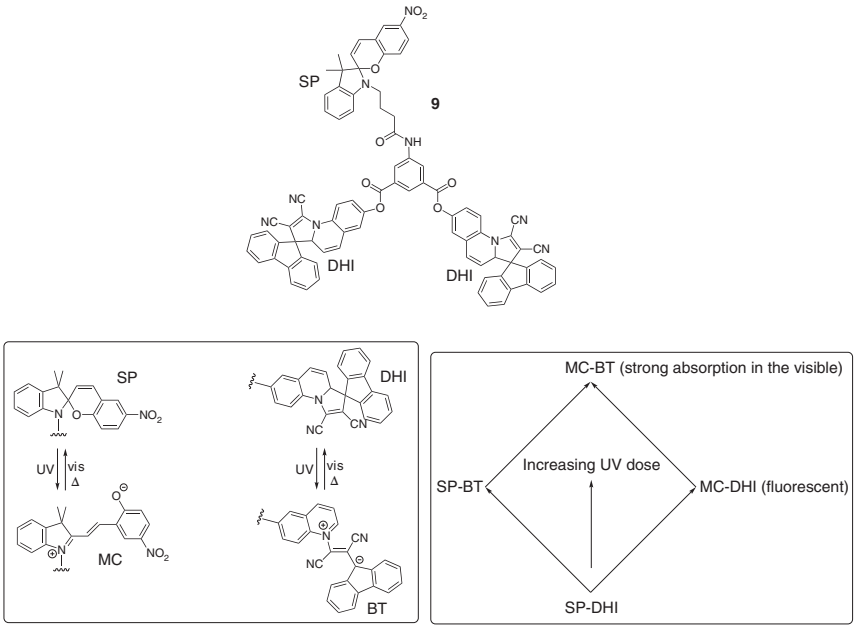


**Figure 33.12** Structure of the SP-DHI triad (top), isomerization of the SP and QDHI building blocks (bottom left), and the functional principle of the triad as a half-adder (bottom right).

UV intensity on the photothermal equilibrium position is shown in Figure 33.12: No UV implies exclusively SP-DHI, whereas sufficiently intense UV implies high enrichment in MC-BT. In between these extremes, SP-BT and MC-DHI dominate. UV light at 355 nm was used to represent both (degenerate) inputs. It follows that the absorbance at 581 nm increases with increasing UV intensity (switching *on* the output from the AND gate only when both UV inputs are applied), whereas the MC emission intensity describes an *off–on–off* response, which is required for the XOR gate function.

To realize the moleculator, the function of an HS must complement the function of the HA. As the HS is a combination between an XOR gate and an inhibit (INH) gate, this task boils down to designing a molecule that performs the functions of the AND gate, the XOR gate, and the INH gate with a shared set of two inputs. This matter intrigued the authors of this chapter for quite some time, and in the quest for this "trinity" it appeared that triad **7** described above is the best candidate to use in this context. After a careful analysis, including seven different input signals and a total of seven outputs, we realized that not only does the triad perform the functions of these three individual logic gates – it can be operated as any of 17 (!) digital logic devices [25, 28, 29, 39]. At that time, it was by far the most complex molecular logic device reported, and as of today it still is. We will devote section 33.7 to this story.

## 33.7 The All-Photonic Multifunctional Molecular Logic Device

In the transit from molecules capable of performing the functions of isolated individual logic gates to those of complex logic circuits described above, there are in principle two distinct ways to go: physical or functional integration. Physical integration would require wiring (concatenation) of simple logic switches and/or gates. This presents a long list of challenges such as input–output heterogeneity and massive signal losses, and only a few proof-of-principle examples of such concatenation are known in the literature [40]. In functional integration, the function of a complete logic circuit requiring several different concatenated logic gates is merged into one and the same molecular species. This means that a unimolecular system can mimic a complex logic circuit, composed of various logic gates, without the necessity of representing each logic gate by a different structural feature. Moreover, if a single substance performs several logic operations depending on the set of input and output signals, it is referred to as being logically reconfigurable [39, 41]. As indicated in the introduction, this feature lends a touch of exclusiveness to molecular logic devices compared to the more traditional hard-wired semiconductor-based devices that can only function as one logic device (without re-wiring).

The FG-DTE triad **7** is an extreme example of such a molecule, performing as the following devices: AND gate, XOR gate, INH gate, half-adder, half-subtractor, multiplexer, demultiplexer, encoder, decoder, keypad lock (with one-time password and two-factor authentication), parity generator, parity checker, and logically reversible transfer gates [25, 28, 29, 39]. All these operations have a common initial state, and the majority share the same two inputs, differing only in the choice of the optical output signal. This not only allows parallel logic operations with the same set of inputs but also makes switching (reconfiguration) between the various logic operations extremely rapid and convenient. The functions rely on the ability to control the excited state communication between the FG and the DTE photoswitches, as well as the selective isomerization of the individual photoswitches by the use of light at different wavelengths.

## 33.8 Summary and Outlook

At the time of writing, it's been 27 years since the first molecular logic device was demonstrated [8]. Since then, this research field has been going through several different phases, where the targeted logic functions have been increasing in complexity [1–7, 42, 43]. It seems, however, that the associated challenges to be overcome before molecular logic devices can be put into practice have remained the same over the last 10 years: Increasing the operational speed (clock frequency), the transition from fluid solution to the solid state, miniaturization, and the possibility to more efficiently concatenate separate molecular species to allow for cascading of input–output signals. The use of molecular photoswitches implies

that both the inputs and the outputs are of optical nature, that is, the input–output heterogeneity issue is at least formally already overcome. This will for sure facilitate any concatenation, but robust examples are still missing. The operational speed could also be dramatically increased if all-photonic devices, such as the molecular photoswitches, were used at the same time as small sample sizes were studied. The function is not limited by diffusion-controlled reactions to take place, and the photons can be delivered with the speed of light, with the possibility of addressing only a very small subset of the molecular ensemble. However, most studies are performed in macroscopic cuvettes containing the molecular system in a 3 ml solution. Even if the isomerization quantum yields are high enough not to waste the majority of all photons and powerful laser diodes are being used, the time required to isomerize the bulk sample is on the scale of seconds or more. This should be compared to the corresponding dynamics of the system, where each isomerization event is occurring on the ps to ns timescale. Miniaturization (optimally down to the single molecule scale) would therefore increase the clock frequency dramatically. At the same time, it is being argued that molecular logic should perhaps not benchmark the silicon-based predecessors, but instead try to find areas of applications where the traditional devices cannot go. Biological systems are promising environments due to the biocompatibility offered by the cleverly designed molecules. Theranostic devices [44], release-and-report [45], and photopharmacology [46] are concepts along these lines that appear frequently in today's scientific literature, and their appearance in clinical practice will likely be of more immediate use than any molecular design mimicking the function of microprocessors.

## References


1 Andréasson, J. and Pischel, U. (2015). Molecules with a sense of logic: a progress report. *Chem. Soc. Rev.* 44 (5): 1053–1069.
2 Balzani, V., Credi, A., and Venturi, M. (2003). Molecular logic circuits. *ChemPhysChem* 4 (1): 49–59.
3 de Silva, A.P. and Uchiyama, S. (2007). Molecular logic and computing. *Nat. Nanotechnol.* 2 (7): 399–410.
4 Erbas-Cakmak, S. et al. (2018). Molecular logic gates: the past, present and future. *Chem. Soc. Rev.* 47 (7): 2228–2248.
5 Katz, E. and Privman, V. (2010). Enzyme-based logic systems for information processing. *Chem. Soc. Rev.* 39 (5): 1835–1857.
6 Raymo, F.M. (2002). Digital processing and communication with molecular switches. *Adv. Mater.* 14 (6): 401–414.
7 Szacilowski, K. (2008). Digital information processing in molecular systems. *Chem. Rev.* 108 (9): 3481–3548.
8 De Silva, A.P., Gunaratne, H.Q.N., and McCoy, C.P. (1993). A molecular photoionic AND gate based on fluorescent signaling. *Nature* 364 (6432): 42–44.
9 Raymo, F.M. and Tomasulo, M. (2005). Electron and energy transfer modulation with photochromic switches. *Chem. Soc. Rev.* 34 (4): 327–336.


**10** Terazono, Y. et al. (2004). Photonic control of photoinduced electron transfer via switching of redox potentials in a photochromic moiety. *J. Phys. Chem. B* 108 (6): 1812–1814.

**11** Liddell, P.A. et al. (2004). Photonic switching of photoinduced electron transfer in a dihydropyrene-porphyrin-fullerene molecular triad. *J. Am. Chem. Soc.* 126 (15): 4803–4811.

**12** Straight, S.D. et al. (2005). Photochromic control of photoinduced electron transfer. Molecular double-throw switch. *J. Am. Chem. Soc.* 127 (8): 2717–2724.

**13** Straight, S.D. et al. (2005). Molecular AND INHIBIT gates based on control of porphyrin fluorescence by photochromes. *J. Am. Chem. Soc.* 127 (26): 9403–9409.

**14** de Ruiter, G. and van der Boom, M.E. (2011). Surface-confined assemblies and polymers for molecular logic. *Acc. Chem. Res.* 44 (8): 563–573.

**15** Irie, M. et al. (2014). Photochromism of diarylethene molecules and crystals: memories, switches, and actuators. *Chem. Rev.* 114 (24): 12174–12277.

**16** Baron, R. et al. (2006). An electrochemical/photochemical information processing system using a monolayer-functionalized electrode. *Chem. Commun.* (20): 2147–2149.

**17** Pischel, U. and Andréasson, J. (2010). A simplicity-guided approach toward molecular set-reset memories. *New J. Chem.* 34 (12): 2701–2703.

**18** Remon, P. et al. (2011). An all-photonic molecule-based D flip-flop. *J. Am. Chem. Soc.* 133 (51): 20742–20745.

**19** Chen, J.H., Zhou, S.G., and Wen, J.L. (2015). Concatenated logic circuits based on a three-way DNA junction: a keypad-lock security system with visible readout and an automatic reset function. *Angew. Chem. Int. Ed.* 54 (2): 446–450.

**20** Jiang, X.J. and Ng, D.K.P. (2014). Sequential logic operations with a molecular keypad lock with four inputs and dual fluorescence outputs. *Angew. Chem. Int. Ed.* 53 (39): 10481–10484.

**21** Margulies, D. et al. (2007). A molecular keypad lock: a photochemical device capable of authorizing password entries. *J. Am. Chem. Soc.* 129 (2): 347–354.

**22** Zou, Q. et al. (2012). Unsymmetrical diarylethenes as molecular keypad locks with tunable photochromism and fluorescence via $Cu^{2+}$ and $CN^-$ coordinations. *Chem. Commun.* 48 (15): 2095–2097.

**23** Andréasson, J. et al. (2009). An all-photonic molecular keypad lock. *Chem. Eur. J.* 15 (16): 3936–3939.

**24** Remon, P. et al. (2011). Molecular implementation of sequential and reversible logic through photochromic energy transfer switching. *Chem. Eur. J.* 17 (23): 6492–6500.

**25** Naren, G., Li, S.M., and Andréasson, J. (2017). One-time password generation and two-factor authentication using molecules and light. *ChemPhysChem* 18 (13): 1726–1729.

**26** Andréasson, J. et al. (2007). Molecular 2:1 digital multiplexer. *Angew. Chem. Int. Ed.* 46 (6): 958–961.

**27** Andréasson, J. et al. (2007). A molecule-based 1:2 digital demultiplexer. *J. Phys. Chem. C* 111 (38): 14274–14278.


**28** Andréasson, J. et al. (2008). Molecular all-photonic encoder-decoder. *J. Am. Chem. Soc.* 130 (33): 11122–11128.

**29** Bälter, M. et al. (2013). An all-photonic molecule-based parity generator/checker for error detection in data transmission. *J. Am. Chem. Soc.* 135 (28): 10230–10233.

**30** Fan, D.Q., Wang, E.K., and Dong, S.J. (2017). A DNA-based parity generator/checker for error detection through data transmission with visual readout and an output-correction function. *Chem. Sci.* 8 (3): 1888–1895.

**31** de Silva, A.P. and McClenaghan, N.D. (2000). Proof-of-principle of molecular-scale arithmetic. *J. Am. Chem. Soc.* 122 (16): 3965–3966.

**32** Guo, X.F. et al. (2004). Monomolecular logic: "half-adder" based on multistate/multifunctional photochromic spiropyrans. *J. Phys. Chem. B* 108 (32): 11942–11945.

**33** Liu, Y. et al. (2006). A multifunctional arithmetical processor model integrated inside a single molecule. *J. Phys. Chem. B* 110 (29): 14231–14235.

**34** Zhou, Y.C. et al. (2006). A new redox-resettable molecule-based half-adder with tetrathiafulvalene. *J. Phys. Chem. B* 110 (32): 15676–15679.

**35** Margulies, D. et al. (2004). Chemical input multiplicity facilitates arithmetical processing. *J. Am. Chem. Soc.* 126 (47): 15400–15401.

**36** Margulies, D., Melman, G., and Shanzer, A. (2006). A molecular full-adder and full-subtractor, an additional step toward a moleculator. *J. Am. Chem. Soc.* 128 (14): 4865–4871.

**37** Andréasson, J. et al. (2004). Molecule-based photonically switched half-adder. *J. Am. Chem. Soc.* 126 (49): 15926–15927.

**38** Andréasson, J. et al. (2006). All-photonic molecular half-adder. *J. Am. Chem. Soc.* 128 (50): 16259–16265.

**39** Andréasson, J. et al. (2011). All-photonic multifunctional molecular logic device. *J. Am. Chem. Soc.* 133 (30): 11641–11648.

**40** Silvi, S. et al. (2009). All-optical integrated logic operations based on chemical communication between molecular switches. *Chem. Eur. J.* 15 (1): 178–185.

**41** Chen, S.J. et al. (2012). Multi-addressable photochromic terarylene containing benzo[*b*]thiophene-1,1-dioxide unit as ethene bridge: multifunctional molecular logic gates on unimolecular platform. *J. Mater. Chem.* 22 (12): 5486–5494.

**42** Andréasson, J. and Pischel, U. (2010). Smart molecules at work-mimicking advanced logic operations. *Chem. Soc. Rev.* 39 (1): 174–188.

**43** Andréasson, J. and Pischel, U. (2018). Molecules for security measures: from keypad locks to advanced communication protocols. *Chem. Soc. Rev.* 47 (7): 2266–2279.

**44** Ai, X.Z., Mu, J., and Xing, B.G. (2016). Recent advances of light-mediated theranostics. *Theranostics* 6 (13): 2439–2457.

**45** Wu, T.Q. et al. (2012). Reporting the release of caged species by a combination of two sequential photoreactions, a molecular switch, and one color of light. *Angew. Chem. Int. Ed.* 51 (11): 2741–2744.

**46** Velema, W.A., Szymanski, W., and Feringa, B.L. (2014). Photopharmacology: beyond proof of principle. *J. Am. Chem. Soc.* 136 (6): 2178–2191.


# Section IV

# Photomodulation of Biological Systems

## 34 In Vivo Applications of Photoswitchable Bioactive Compounds

Alexandre M.J. Gomila and Pau Gorostiza

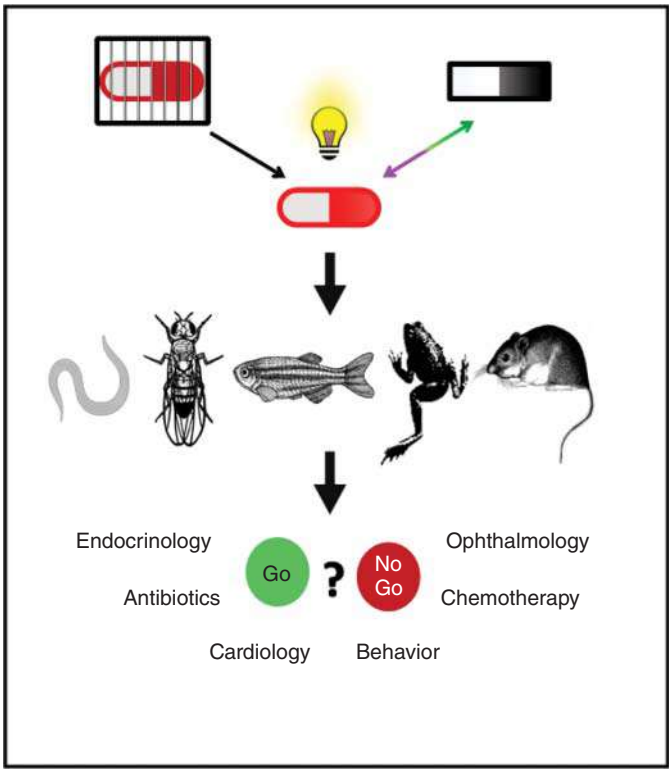


**Key References**

Ando, H., Furuta, T., Tsien, R.Y., and Okamoto, H. (2001). Photo-mediated gene activation using caged RNA/DNA in zebrafish embryos. *Nat. Genet*. 28, 317–325.

Lima, S.Q. and Miesenböck, G. (2005). Remote control of behavior through genetically targeted photostimulation of neurons. *Cell* 121, 141–152.

Szobota, S. et al. (2007). Remote control of neuronal activity with a light-gated glutamate receptor. *Neuron* 54, 535–545.

Caporale, N. et al. (2011). LiGluR restores visual responses in rodent models of inherited blindness. *Mol. Ther*. 19, 1212–1219.

Stein, M. et al. (2012). Azo-propofols: photochromic potentiators of GABAA receptors. *Angew. Chem. Int. Ed*. 51, 10500–10504.

Riefolo, F. et al. (2019). Optical control of cardiac function with a photoswitchable muscarinic agonist. *J. Am. Chem. Soc*. 141, 7628–7636.

# 34

# In Vivo Applications of Photoswitchable Bioactive Compounds

*Alexandre M.J. Gomila*[1,2,3] *and Pau Gorostiza*[1,2,3,4,*]

[1] *Institute for Bioengineering of Catalonia (IBEC), Nanoprobes and Nanoswitches, Baldiri i Reixac, 10 - 12, 08028 Barcelona, Spain*
[2] *The Barcelona Institute for Science and Technology (BIST), Carrer del Comte d'Urgell, 187, 08036 Barcelona, Spain*
[3] *Center for Network Biomedical Research in Bioengineering, Biomaterials and Nanomedicine (CIBER-BBN), Avenida Monforte de Lemos, 3-5, Pabellón 11, Planta 0, 28029, Madrid, Spain*
[4] *Catalan Institution for Research and Advanced Studies (ICREA), Passeig Lluís Companys, 23, 08010 Barcelona, Spain*

## 34.1 Photocontrol of Biological Processes

Precise control of biological functions has been the primary focus of all medical sciences ever since they were understood as downstream outcomes of cellular processes. These processes are inherently defined within a spatial and temporal rigorous fashion throughout all the biomolecular levels of all living creatures. Hence, the development of scientific tools for the study of biological processes has aimed to match their spatiotemporal scale. An important criterion is how one can precisely control a specific aspect of a cell process or an outcome on an organism. An advantageous strategy to spatiotemporally control a particular effect of a biologically active molecule is to lock the compound under the control of a conditional signal, internal or external. Light is an excellent controllable trigger. Light works as an orthogonal signal for biological systems and organisms, as most cells do not react to it. However, exceptions include highly specialized cells such as photoreceptors. Light wavelengths are harmless for biological tissues unless they are highly energetic. Moreover, light can be a convenient tool for investigations on many model organisms, such as zebrafish or nematodes, because they are transparent to visible and infra-red light. The use of light as a controllable stimulus has been essential for the manipulation of molecules, proteins, lipids, and oligonucleotides.

Historical precedents of the use of light to control biological outcomes, from specific molecular targets to clinical treatments, can be traced to at least four different fields: heliotherapy or phototherapy, photodynamic therapy (PDT) or photochemotherapy, optogenetics, and photopharmacology. Heliotherapy, the

*E-mail: pau@icrea.cat

*Molecular Photoswitches: Chemistry, Properties, and Applications*,
First Edition. Edited by Zbigniew L. Pianowski.


exposition to sun beams for treating illnesses, was already used in ancient Egypt, India, and Greece [1]. Heliotherapy has been refined as modern phototherapy since Niels Finsen, alongside one of his patients, developed an artificial ultraviolet (UV) light source for the treatment of *lupus vulgaris*. They were awarded the Nobel Prize in 1903 for this achievement [1]. Although it is now known that Finsen's lamp produced light in the violet and blue range, it unequivocally demonstrated to modern medicine and the world the antimicrobial effect of light [2]. Ever since, phototherapy has been defined as the exposure to daylight or to specific wavelengths to treat a disease. It has been used for seasonal affective disorder (SAD), circadian rhythm disorders, and skin disorders.

Historically parallel to phototherapy is photochemotherapy, now generally referred as photodynamic therapy (PDT). It involves the combination of a light-activated chemical (photosensitizing agent) and the selective use of light in target areas to induce cell death via formation of free radical molecules [3]. This technique dates back over 3000 years, when the natural products psoralens were used for the treatment of vitiligo in what is now India [4]. The term *photodynamic* was coined in 1904 by Tappeiner to describe how photosensitizing agents in biology produced oxygen-consuming chemical reactions [5]. PDT is the most common approach to couple light to therapeutic action using a photosensitizing dye molecule. Once the dye reaches its excited state, reactive oxygen species (ROS) are formed alongside a number of reactive intermediates.

With the discovery of light-dependent proteins in nature during the 1970s, a third category to light-control biological processes appeared. Although visual rhodopsins and many light-sensitive plant proteins were already known, their use as a manipulation tool started during the 1990s with the discovery of specific light-dependent channel proteins in algae and cyanobacteria. For the last 20 years, these proteins have been refined to alter biological processes. Since it is largely based on genetic manipulation methods to introduce exogenous proteins with light-sensitive constructs, the field was named optogenetics.

Lastly, in the 1970s a broad category emerged through photopharmaceutical agents. At the time, genetic manipulation was yet to become a reality, and pharmacological targets were still a concept debate. Nonetheless, even if nowadays this approach may in some cases take advantage of genetic modifications, it is based on externally supplied synthetic chromophores. These chemical constructions incorporate a photoresponsive moiety and enable configurational changes when exposed to specific light wavelengths, producing a biological action. This is referred as photopharmacology [6] and is commonly used to describe a photochemical event triggered by light that changes a molecule's pharmacological activity through structural alterations. Although other terms such as optopharmacology and optochemical agents are used sometimes, "photopharmacology" has become the prominent keyword encompassing all strategies where pharmacology and photochemistry are at the essence of their creation.

The idea of using photocontrollable compounds therapeutically against human diseases was also conceived in the 1970s [7]. The concept "photopharmacology" was initially described for the use of photoreactive species as therapeutic agents [8]

and is nowadays commonly used to describe any drug which has been modified by introducing a photolabile or photoisomerizable chemical construct or fragment. Notwithstanding, photopharmacology has demonstrated to be applicable not only for drug modification, but also for whole protein control, DNA and RNA modification, and peptidic or lipidic control and regulation. Their purposes have been largely fundamental as molecular tools to remotely control and study complex biological processes. For medical purposes, photopharmacology has been designed from two different strategies. Early approaches envisioned photoswitchable molecules to act as modulators for endogenously photosensitive processes, including degenerative diseases that tamper vision or circadian rhythm disorders. Most medical treatments are sustained with bioactive compounds that interact with a molecular target, such as enzymes, receptors, molecular and ionic carriers, ion channels, and membranes. Therefore, this view was expanded into a second strategy for medical photopharmacology by designing photocontrollable drugs as if they were conventional non-light-controllable drugs, to target a variety of pathological processes using *ad hoc* illumination methods.

The use of drugs offers the advantage to target endogenous biomolecules allowing the study of their physiology down to single protein scale, such as single receptors in dendritic spines. On top of that, the repertoire to study or treat endogenous targets, i.e. receptor channels, is not limited to genetic models of animals, but to any wild-type model that expresses the target and can be translated to specific organisms that may offer specific advantages of their own. Like with optogenetics, genetic targeting also holds out many intrinsic advantages, but they still differ from the mainstream of therapeutic purposes. Safety assessment and regulations are significant hurdles for genetic therapies, whereas drug testing is more compatible with current clinical standards and regulations, even if different isomers or prodrugs must be evaluated, as well as with established industrial processes.

Studying the interaction of any bioactive compound and its target leads unequivocally to the question of selectivity towards tissues and pharmacological pathways. Traditionally, selectivity has been pursued by (i) localized administration of the drug, (ii) earmarking target sites or overexpressing them, or (iii) when possible, as for antibiotics, avoiding any species-related cross-interaction and aiming to exogenous or structural/genetically far molecular targets. One of photopharmacology's goals is to improve the limited selectivity achieved with conventional drugs by adding light as an external controllable factor. The underlying hypothesis of photopharmacological applications to medicine is that drug safety parameters as tolerance and side effects will be higher than those for conventional drugs due to photocontrol, assuming that the inactive form of the drug can be very efficiently activated both with temporal and spatial precision at a desired site of action [9].

One of the first concerns to design photopharmacological compounds is photo-responsivity. Light, that is, photons, must be energetically high enough to alter the compound structurally, in an irreversible or reversible manner. Especially for in vivo applications, focus must be equally placed on the medicinal chemistry challenges associated with the development of photopharmacological agents. Last but not least, one must consider the technical and conceptual challenges associated with light delivery. Hence, when designing a plausible photoconvertible bioactive

molecule, the therapeutic optical window is an important limitation for future medical purposes. Biological tissues in the human body are sufficiently transparent toward X-ray and gamma wavelengths. For lower energy wavelengths used in photopharmacology (UV, visible, and near/infra-red (NIR/IR) spectra), biological tissues have a variety of molecular and supramolecular structures that scatter or absorb photons (melanin, collagen, lipids, hemoglobin, flavoproteins, myoglobin, bilirubin, cytochromes, DNA, RNA, etc. and water) [10]. These limitations for light penetration through tissue have caused criticism to light-based therapeutics; nonetheless, remarkable advances have been made and are being developed, such as wireless subdermal electronics and multi-modal optical fibers [11]. Ideally, a high intensity light source with a (two) narrow emission band(s) wavelength(s) for isomerization of the molecules would be the most suitable one for photopharmacology. It is commonly described that the optical therapeutic window wavelengths are in the range from 600 to 1700 nm, avoiding the water peak of absorption from 1400 to 1560 nm. NIR wavelengths (≈700 to 1400 nm) are much less absorbed by biological tissues and water. These wavelengths have lower scattering with reduced photodamage, they allow photons to penetrate deeper (>1 cm) [12] and to produce patterned illumination for faster scanning in biological time-lapse imaging [13, 14]. Because of this, two-photon (2P) techniques for isomerization and uncaging of photobioactive molecules have been pursued for the last thirty years [15]. Therefore, photons of double the wavelength than its original UV photon (i.e. in the NIR range) are used for photo(de)activation [16, 17]. 2P excitation has the additional advantage that suitable irradiation conditions only occur at the exact focus of the laser beam, adding a layer of spatial resolution as the optical *localization* is dramatically improved, with "activatable" volumes below 1 fl [15, 18].

Another way to meet biological criteria within the optical therapeutic window is using different wavelength-selective approaches. This is mainly applied in irreversible photopharmacology, or caged photopharmacology, where different wavelengths allow delivering different bioactive molecules at will, e.g. different neurotransmitters (glutamate and GABA) in rat brain slices with two-photon, two-color light at 720 and 830 nm [19].

All considered, several ideal points might be drawn when discussing in vivo applications of photopharmacology. Firstly, regarding their pharmacological properties, photoactive compounds should:

(i) have high potency, at least comparable to the parent drug when it is possible or to commercially available ones. Higher potencies of the active form will tolerate low photoconversion efficacy. The achieved concentration must surpass activity threshold regardless of the photoconversion efficacy.
(ii) The photoisomers should display different biological activity, if possible higher for the less thermodynamically stable isomer. For caged compounds, it is desirable that the photocleaved by-product produces no biological effects.

Secondly, as for the photochemical and photophysical properties, compounds must aim at:

(i) high molar attenuation coefficients for efficient photoactivation. Bearing in mind what light fluence is necessary to activate/isomerize the compounds, but

also, what is the achieved photoconversion (concentration of active form at the photostationary state or upon uncaging). Therefore, moderate light doses ensure that photodamage and/or photobiomodulation of third pathways are avoided, and that the observed effects are due to the concentration of the active photocompound in each condition.

(ii) Isomerization or uncaging should be done within the biological optical window and triggering exclusively a desired target protein or signaling pathway.

Thirdly and finally, in order to fulfill physicochemical requirements, the photopharmacological agents should be highly soluble and stable under physiological conditions, and the administration routes kept as simple as possible.

In some cases, it would be convenient to monitor the photoactivation process with a read-out signal like fluorescence or electrode recording for example. This is an optional characteristic that can be added at early research stages or be developed for specific medical interests like closed-loop systems.

As a result, and as described by Lerch et al. [20] one could classify photopharmacological treatments based on the difficulty to deliver the appropriate source of light to secure an efficient activation/deactivation of the photocontrolled drug. Hence, depending on how invasive the procedures are, it is possible to differentiate accessible regions (as skin or eyes) from those that require major surgery, such as brain or bone marrow. Nevertheless, as IR illumination and improvements on light-delivery devices progress, most regions would become accessible to photopharmacological treatments in the near or mid future.

## 34.2 Irreversible Photopharmacology – Cages

Photopharmacology can be classified according to the chemical and conformational reversibility of the incorporated photoresponsive fragment. Thus, for compounds that are photo-released or photoisomerized without possible recovery of the original conformation, the pharmacological change can only be produced once for each molecule. This is referred to as irreversible or caged photopharmacology, and the compounds are called caged ligands or phototriggers.

The term "caging" was coined by J. F. Hoffman in 1978 [21]. Caged photopharmacology can be defined as the incorporation of a photolabile "protecting" chemical structure which embeds a drug or biologically active compound. The photochemical protection is covalently attached to the biomolecule, preventing its functionality until the photolabile group is excited with light and the bond is broken (photoinactivation or photoactivation) [22].

Phototriggers have been a remarkable tool for neurobiology, especially those regulating neurotransmitters. Glutamate is the major excitatory neurotransmitter, and gamma-aminobutyric acid (GABA) is the principal inhibitory neurotransmitter in the central nervous system (CNS). The balance and coordination between both ensure a normal functioning of the CNS, and their deviation causes a number of neurological disorders. They are involved in the transmission of nerve impulses

and in cognitive functions such as learning and memory [23–25]. Before the first applicable optogenetic tool [26], photouncaging was used in vitro onto brain slices with light-dependent release of glutamate, demonstrating how complex neuronal networks could be manipulated with high spatiotemporal resolution [27]. Thereafter, several incursions to phototriggering in vivo neuronal systems and networks are to be outlined.

Caged glutamate was successfully used for 2P uncaging up to 200 μm into the cortex of adult mice paired with calcium imaging, proving to be a powerful technique to investigate functions of cortical synapses in animals [28]. Optofluidic uncaging (385 nm through epifluorescence pathway) of cloaked glutamate in freely moving mice has been reported to overcome off-target GABA-A receptor antagonism and to increase specific on-site high concentration of glutamate for dopamine neurons in the midbrain region at the ventral tegmental area (VTA), involved in reward-related behavior [29].

GABA has been caged within a ruthenium-based structure (RuBi-GABA) and administered onto cortical regions of anesthetized mice, inhibiting neuronal activity upon blue laser pulses [30]. Another RuBi derivative was also tested before inducing seizures with 4-aminopyridine (4-AP). Once a seizure episode started, blue illumination with an LED onto the neocortical region induced photouncaging of GABA and interrupted the seizure [31]. The authors continued exploring the optimal conditions and light delivery systems using implanted fibers for therapeutic treatment of epilepsy with irreversible photopharmacology [32].

Caging strategies have also been applied for gene and protein regulation. They proved to be not only a remarkable tool to study and understand specific developmental outcomes in any organism; furthermore, they can be applied for specific therapeutic approaches like cancer treatment or gene editing. Phototriggers were immediately envisioned as tools to control genes and protein expression. From an early approach that regulated estrogen receptors (ER) to promote transcription using caged estradiol in HEK293 cells [33], these techniques were rapidly applied in vivo.

Morpholino-based strategies have been widely used to alter gene expression. They consist of nucleosides onto a backbone of methylenemorpholine rings, around 25 base-oligomers, that interact with RNA strands interrupting splicing and translation. Caged morpholinos have been designed and studied to become conditional gene knockdown reagents. They are used for one- (UV) and two-photon stimulation to control embryonic gene function and pattering in zebrafish embryos [34–39] and xenopus tadpoles [37]. As many morpholinos had been already synthesized and used, a strategy to produce a light-dependent version of them was conceived. The original morpholino is kidnaped using a complementary oligonucleotide strand with a central photocleavable linker, which after UV illumination releases the conventional (known and tested) morpholino strand to act [40]. Another strategy for controlling gene expression was derived from the use of negative-charged peptide nucleic acids (ncPNAs), which down-regulate target genes by interrupting translation. As morpholinos, these have been caged with a photocleavable linker and a sense RNA strand, which once illuminated with UV releases the ncPNA and drives gene expression patterns in zebrafish embryos [41].

Small molecules to control gene expression using the modified $ER^{T2}$ have also been applied in vivo, although transgenic models or induced expressing models are needed. They are based on the caging of an inducer of ER (tamoxifen and its derivatives. These were applied in the zebrafish embryo model using caged cyclophen-OH as a transcriptional activator [42, 43] and in mice [44, 45]. From these studies the induction of tumors through the activation of a human oncogene was achieved transiently and constitutively in zebrafish embryos [46]. Labeling and tracing of heart muscle cells in zebrafish embryos using these photoinduction system was also demonstrated for three-photon uncaging [47]. The use of this system to label and monitor physiological outcomes in live animals has been discussed elsewhere [48].

Further improvements have been developed toward cancer treatment using light-activatable nanoparticles (NPs) that can be modified for better tissue recognition and stability of carried reagents. Even if light activates a non-pharmacologic target, the caging capacities onto NPs activity for cancer treatments must be recognized. One study showed how NIR illumination of gold particles could be used to denaturalized DNA constructs of doxorubicin as the chemotherapeutic agent in tumor-bearing mice [49]. Another study also used NIR illumination to disassemble large-size NP structures into ultrasmall units once they were accumulated onto the tumor region and internalized by cancerous cells. The single gold-NPs attached to the silencing sequence allowed tumor inhibition [50]. Finally, genome control

**Figure 34.1 Photocaged compounds.** (A) Reactions for RNA caging by Bhc-diazo and reactivation of the caged RNA by the photolytic removal (uncaging) of the Bhc moiety. Images of the effects of Eng2a overexpression by photoactivation of Bhc-caged eng2a mRNA in three-day-old larvae. Right, close-up views of the heads of the embryos shown at left. First row shows non-injected control larva with normal eye and body development. Below, larva injected with Bhc-caged eng2a mRNA and illuminated with ultraviolet light (10% of the maximum intensity for 10 seconds) at the shield stage. The eyes are significantly reduced in size or totally eliminated. Source: From Ando et al. [54]. (B) Photostimulation experiments were performed in a cylindrical arena (diameter 8: mm, height 2: mm) that could be homogeneously illuminated with 355 nm laser light. The arena was covered by a glass ceiling in (a–c) but left open in (d), as decapitated flies do not spontaneously walk, jump, or fly, making their confinement unnecessary. Caged ATP was microinjected into the CNS in (a–c) and applied directly to the nerve cord in (d). For each of the four experimental conditions (a–d), circuit diagrams on the left identify the neurons expressing P2X2 in black on dark backgrounds. These simplified schemes of the bilaterally symmetric circuit depict the neuronal elements responsible for jumping on top and the elements responsible for flight at the bottom. Selected individual frames of video recordings of photostimulation experiments are displayed on the right. (a) A fly expressing the UAS-P2X2 transgene under the control of the shakB-GAL4 driver in the TTMn-PSI-DLMns group of neurons in the thoracic ganglion responds to a 150 ms laser pulse with wing flapping. (b) A blind norpA7 fly expressing the UAS-P2X2 transgene under the control of the GAL4-c17 driver in the pair of GF neurons responds to a 250 ms laser pulse with wing flapping. (c) A fly lacking the UAS-P2X2 transgene is unresponsive to a 250 ms laser pulse. (d) Immobile, decapitated flies expressing the UAS-P2X2 transgene under the control of the shakB-GAL4 driver in the TTMn-PSI-DLMns group of neurons open their wings and fly (arrow) after photostimulation with a 150 ms laser pulse. Source: From Lima and Miesenböck [56].

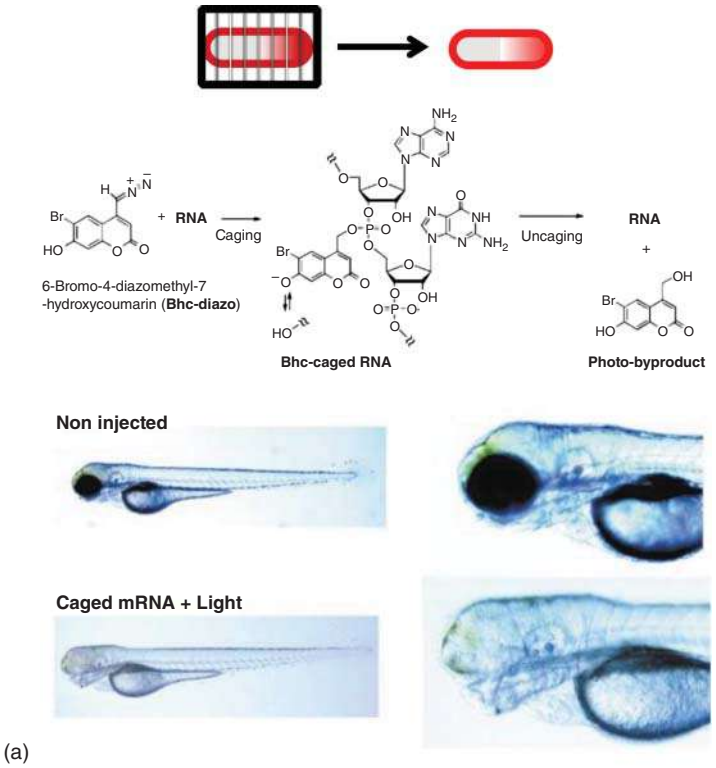


(a)

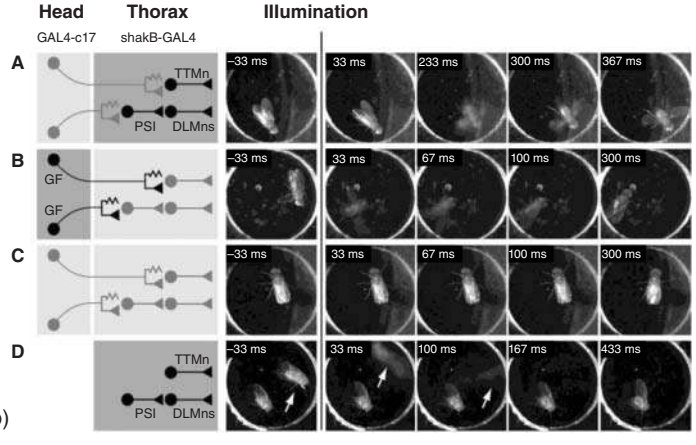


(b)

through upconversion nanoparticles (UCNPs) attached to Cas9-sgRNA complexes using a photolabile group has been developed to treat cancer in mice. The irradiation of NIR light to the UCNPs provoked the upconversion of UV toward the photolabile group and released CRISP-Cas9 system [51]. Another photocage example to treat cancer is based on photocleaved aptamers. Aptamers are single-stranded nucleic acids that bind to a specific target (proteins, cells, small molecules, etc.) and can also be conjugated to a drug. They are more resistant to enzymatic degradation

than other oligonucleotides and are folded into well-defined conformations with a relatively small molecular size (~10 KDa). Photocleavable aptamers were used in tumor-bearing mice to regulate their tumor-targeting capabilities, in terms of distribution and activity after illumination, as a proof of concept for future drug-delivery systems [52]. Regarding clinical treatment of tumors, doxorubicin (DOX) drug was caged with a photoremovable protecting group and optimized for membrane interaction to increase clearance rates. The photocage was solubilized with cyclodextrine and administered to tumor-induced athymic nude mice. Tumors were then irradiated with 365 nm wavelength fibers to release pure DOX [53]. Almost sixfold difference in DOX concentrations were found comparing irradiated and unirradiated tumors, with no release of DOX in the serum sample after irradiation, evidencing a controllable systemic exposure.

Photouncaging has also been applied to RNA and DNA molecules. RNA uncaging was applied in zebrafish to study the development of the telencephalon (combined with antisense morpholinos) and to interrupt eye development [54, 55] (Figure 34.1). The development of a caged anti-microRNA allowed to improve healing in diabetic mice without affecting protein silencing in other organs, as only illuminated regions enhanced cell proliferation and angiogenesis [57]. A caged DNA with the necessary translational and transcriptional machinery was loaded into a lipid vessel, which initiated protein production under UV illumination and induced luciferase production in vivo in mice [58]. Controlling specific tissue or organ development through phototriggers has been also achieved by caging retinoic acid (RA), a signaling molecule whose concentration during embryogenesis determine body axis and organ formation. To gain new insights of these phenomena several caged RA were designed and screened in zebrafish embryos [59]. One of those derivatives (cRA) produced developmental effects in zebrafish only when irradiated (from 364 to 414 nm wavelengths) and alongside active by-products. Nevertheless, the authors could effectively induce a described RA retina malformation at single cell level with two-photon excitation (750 nm).

Last but not least, a pioneering example halfway between caged photopharmacology and optogenetics was reported by uncaging of ATP molecules combined with genetic manipulation of TRPV1 and P2X receptors. These experiments allowed to control the behavior in flies and constituted the first demonstration of behavioral photomanipulation in vivo [56] (Figure 34.1).

## 34.3 Reversible Photopharmacology. Free and Tethered Photochromic Ligands

With regard to the conformational recurrence of the incorporated photoresponsive fragment, a second broad category can be defined as reversible photopharmacology or photoswitchable compounds. These compounds include a reversibly photoisomerizable structure, called a photoswitch, which can be bidirectionally regulated using two different wavelengths (and/or thermal relaxation). For biological scenarios, the first [60] and still most used photoswitch is azobenzene. It has a remarkable

performance in biological media, such as fast switching properties, high quantum yield, and stability regarding pH, temperature, and solubility [61, 62]. It has been embedded into the structure of drugs, dyes, lipids, enzymes, peptides, proteins, and nucleic acids, enabling these to photoisomerize between *trans*-to-*cis* configuration, undergoing geometrical and end-to-end distance changes, thereafter modifying their biological effect. Since its first applications in enzymology [60] and in the control of nicotine acetylcholine receptors [7] during the late 1960s and early 1970s, it has maintained its popularity in the biological and biomedical fields.

### 34.3.1 Cancer and Cytotoxicity

Several cancer and cytotoxic treatments relying on the use of light have emerged, mainly from the field of PDT. These approaches use photosensitizer molecules which, upon illumination, form ROS that cause cell death. One inconvenience is the need of oxygen as a necessary precursor, which can be scarce in certain environments, notably in hypoxic tumors. As an alternative, photopharmacology has explored direct photocontrol of cell death and cellular toxicity for over a decade now. In view of the vast extension of cancer targets studied in photopharmacology, with photocaging and photoswitchable compounds, readers might be interested in Dunkel and Ilaš recent work [63]. This section outlines published photopharmacological compounds specifically with *in vivo* results.

A recent study proposed and synthesized several photoswitches to control carbonic anhydrase (CA) activity [64]. This enzyme plays a key role in maintaining the balance between $CO_2$ production and acid-base homeostasis in cells, being overexpressed in several pathologies, such as cancer, epilepsy, or glaucoma. One of the proposed azobenzene photoswitches was tested with a phenotypical assay during zebrafish development for five days, with several illumination periods over 12–48 hours post fertilization (hpf), when $CO_2$ excretion is essential for normal development. It showed how the *trans* conformation impacted on the formation of the otoliths of the fish and caused several malformations, whereas *cis*-treated larvae developed normally [64]. The use of a *trans* active inhibitor of CA in suitable exposed cancer or glaucoma could be a new photopharmaceutical target in future years, as proposed by the authors.

Another target of interest has been the human dihydrofolate reductase, due to its role in single-carbon transfer reactions which are essential for cell viability. A photoswitchable derivative of methotrexate (named Phototrexate), a widely used chemotherapeutic agent, was designed introducing an azobenzene in the structure (azologization strategy). It showed how upon UV illumination, cell proliferation was terminated and induced methotrexate-like abnormalities and death to zebrafish embryos over five days postfertilization. The efficacy on human dihydrofolate reductase was shown in vitro with a fast switching compound, stable and non-toxic in the dark [65].

Histone deacetylases (HDACs) are involved in cell differentiation, cell proliferation, and apoptotic events. Their role is to deacetylase lysine residues at the histone tails, recovering positive charges and therefore enhancing electrostatic

attractions between histones. This process triggers chromatin condensation which silences gene expression and is of interest for the medical field, as shown with three new FDA-cleared drugs for clinical use in cancer (vorinostat, panobinostat, and belinostat). Due to their importance in cancer, HDACs have already produced several works in photopharmacology although they are yet to be tested in animal models. To mention a couple, Feringa and coworkers developed photoswitchable azobenzene-derivatives based on vorinostat structure and studied which influence the photoswitch positioning had on the pharmacological and photochemical properties [66]. A second strategy was envisioned by Reis group who designed azobenzene-derivative switches of small-molecule ligands for human HDACs as tools to control the epigenome [67].

Combretastatin A-4 (CA4) prodrug inhibits tubulin polymerization and exhibits selective cytotoxicity toward tumor vasculature. In an attempt to overcome the hypoxic environment of cancerous tissues, where PDT treatments are not suitable, several photoswitchable derivatives of CA4 were designed introducing an azobenzene [68]. Its active drug conformation was achieved upon UV illumination, but the authors observed a degradation of both compounds due to the action of glutathione reactions. Nevertheless, it was tested in *Caenorhabditis elegans* and mice [69]. In *C. elegans,* microtubule dynamics could be blocked during the cell cycle and in living mice the cytoskeleton was destroyed upon illumination. Notwithstanding, progress has been made to achieve desired photoderivatives based on CA4 treatments and several molecules already present improved photochemical properties in vitro, using visible and UV light and expanding the knowledge on the importance of pH for photoisomerization of the same compounds [70, 71]. A recent proposal to overcome UV tissue penetration and chemotherapy side effects describes the combination of Azo-CA4 and Phototrexate with upconversion nanoparticles, which upon NIR illumination emit UV light to activate these photoswitchable derivatives [72].

The use of gramicidin S (GS) as a cytotoxic agent against cancer [73] has been explored as a suitable backbone for photocontrollable cytotoxic peptide analogues. A set of diarylethene GS photoswitches were previously studied as antibiotics [74] and have been optimized into a second-generation photoswitchable GS red- and NIR-shifted compounds, stable in both closed and open forms, and displaying cytotoxic activity in vitro and in vivo. Tumors were reduced and even disappeared in one mouse in a 20-day period. The effect was oxygen-independent compared to a PDT-like treatment [75]. The authors expanded their investigation on GS photoderivatives for possible cancer treatments, and evaluated how compound modifications and administration techniques could improve safety parameters for in vivo photopharmacology in mice allograft models and zebrafish embryotoxic assays [76, 77]. Photopeptides and similar strategies to control biological functions have been reviewed recently [78].

Finally, a photoswitchable lipid vessel (based on spiropyran-merocanine conversion) was used for drug release in a tumor-bearing mice. The photoswitch altered the volume of the vessel in a reversible manner, decreasing it under UV illumination, thus liberating the drug to the medium [79].

### 34.3.2 Photopharmacology of Receptors and Ion Channels

Most photoswitchable compounds are designed to target a specific protein, often based on a known pharmaceutical agent or bioactive compound as scaffold. Many of these targets are membrane receptors, which are involved in diverse pathologies and their activity can be regulated with extracellular drugs. Due to the biomedical and pharmaceutical importance of G-protein-coupled receptors (GPCRs), photopharmacology has reasonably focused on controlling some of its family members [80] and testing them in vivo [81]. Since light offers rapid temporal control, a great number of photoswitchable compounds have been designed to alter neuronal excitability. One of the first compounds to control neurons was a maleimide azobenzene glutamate (MAG) photoswitch, which is tethered (chemically conjugated) to a modified ionotropic glutamate receptor (iGluR) that exposes cysteine near the ligand binding-site. These engineered receptors were named light- and ligand-gated GluRs (LiGluRs). A transgenic zebrafish line was produced and the MAG photoswitchable ligand tested, showing how larvae motility could be turned on and off under visible or UV illumination, respectively [82] (Figure 34.2). Recently, optimized MAG derivatives for 2P illumination have been used in *C. elegans* with calcium imaging, demonstrating NIR excitation and manipulation of neuronal activity [85]. These and other results regarding 2P excitation have been recently reviewed regarding the needs for in vivo all-optical imaging and manipulation techniques [17]. Photoswitchable, orthogonal, remotely tethered ligands (PORTLs) are a new class of tethered ligands that conjugate to a genetically encoded self-labeling tag. They have been used to modify metabotropic glutamate receptor (mGluRs) activity. One branched-PORTL was used to modulate mGluR2 activity in freely moving mice, showing an inhibition on working memory which could be reversed with green light illumination [86].

Regarding freely diffusible photochromic ligands (PCLs) in vivo, glutamate receptors were targeted by alloswitch-1, a photoswitchable allosteric modulator of metabotropic glutamate receptor $mGlu_5$. It produces an arrest of activity in freely swimming *Xenopus tropicalis* tadpoles when illuminated with UV light that is recovered under green illumination [87]. This library of photoswitchable mGluRs modulators yielded another compound that displayed fast relaxing allosteric photoswitch antagonism in $mGluR_4$, and was named Optoglunam4. It increases zebrafish larvae locomotion in dark and recovers normal behavior under UV illumination [88].

The major inhibitory neurotransmitters in the CNS are GABA and glycine. Both are indispensable for excitatory/inhibitory neuronal balance and play key roles in cognition and behavior. Both neurotransmitters act on chloride-ion-selective channels, thus hyperpolarizing neurons and inhibiting action potential firing. Photopharmacology was applied to gabaergic signaling in vitro [89] and in vivo [90] with the design of photoswitchable derivatives of propofol, an allosteric modulator of $GABA_A$Rs. One of them, Azopropofol2, potentiated GABA-induced chloride currents in its *trans* form and could be reversed under UV light. The compound ability to modulate neuronal networks was shown in anesthetized *Xenopus laevis*

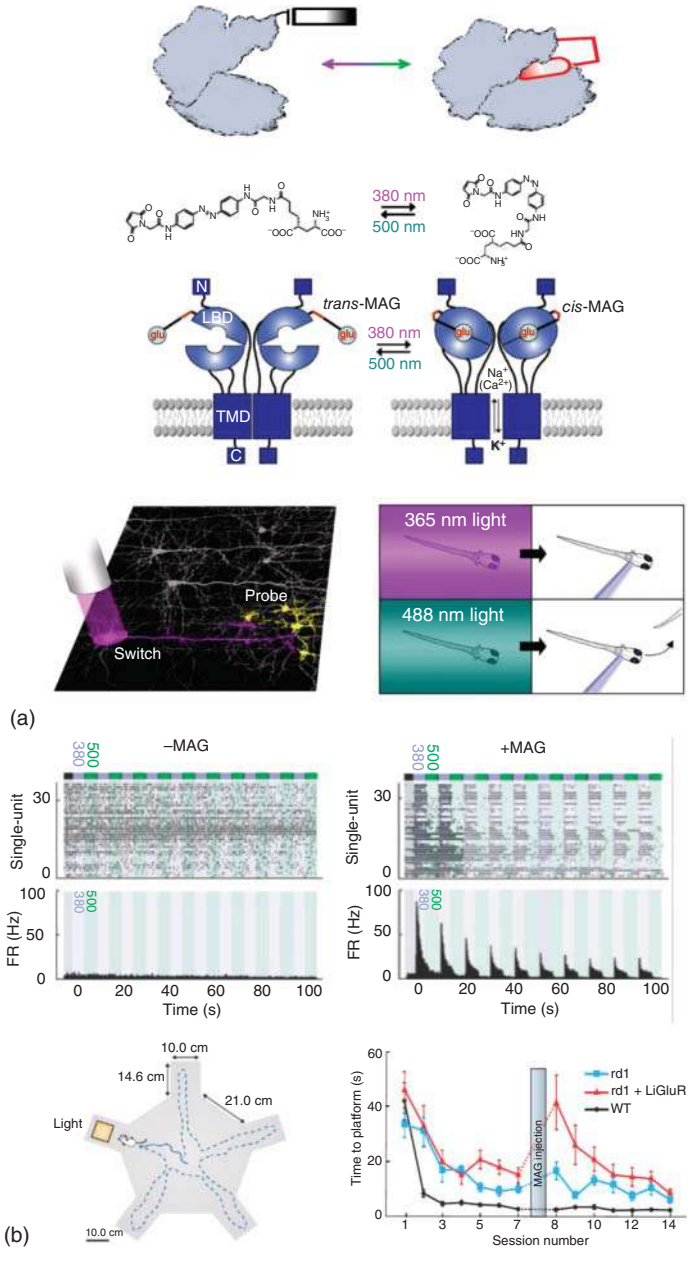
380 nm
500 nm
trans-MAG
cis-MAG
N
LBD
glu
TMD
C
Na+
(Ca2+)
K+
Probe
Switch
365 nm light
488 nm light
(a)
–MAG
+MAG
Single-unit
FR (Hz)
Time (s)
(b)
10.0 cm
14.6 cm
21.0 cm
Light
Time to platform (s)
MAG injection
rd1
rd1 + LiGluR
WT
Session number

tadpoles, which recovered the righting reflex (orient themselves in a ventral position) under UV illumination and even showed photoinduced motility, while anesthetic effects remained under darkness [90].

A new class of photoswitchable compounds to control $GABA_A$Rs was recently described to potentiate chloride currents under UV illumination. Their core structure is based on benzodiazepines and the photochromic moiety used was fulgimide, which compared to azobenzene, improves switching in aqueous solution between the stable forms (closed and open) with no thermal relaxation [91]. The compound was named Fulgazepam and its effect on GABA-chloride currents was observed in vitro and in wild-type zebrafish larvae. Locomotion activities were increased by 380 nm illumination and reversed by visible (500 nm) light, as generally desired in photopharmacology (*cis*-on photoswitch).

A small library of photoswitchable diazepam derivatives was developed by the same consortium that reported Fulgazepam, introducing azobenzene as the photochromic moiety. Although benzodiazepine-like activity was lost in all cases, two compounds showed significant light-dependent activity differences in zebrafish larvae. The first one, AzoNZ1, was characterized in vitro as a pore blocker of $GABA_A$Rs [92], and showed also subunit selectivity for glycine receptors [93]. A second compound, named Glyght, proved to be a *cis*-on negative allosteric modulator of the glycine receptor. It decreases glycinergic currents under UV illumination and increases the activity of zebrafish larvae. Normal behavior and chloride currents were recovered under blue light [94].

G-protein-coupled inwardly rectifying potassium channels (GIRK) have awakened interest in photopharmacology due to their role in neuronal excitability and their interactions with the major neurotransmitters in the CNS. With a newly

**Figure 34.2 Photoswitchable tethered ligands.** (a) Structure of MAG (maleimide-azobenzene-glutamate) compound in its *trans* state (dark and 500 nm) and *cis* state (380 nm). Source: From Volgraf et al. [83]. The light-gated glutamate receptor is based on the reversible photoisomerization of the tethered agonist maleimide-azobenzene-glutamate (MAG) between its *trans* configuration under 500 nm light and its *cis* configuration under 380 nm light. MAG is covalently attached by the maleimide moiety to a cysteine introduced into the ligand-binding domain (LBD) of the receptor. Photoswitching is driven by the reversible binding of the glutamate moiety of MAG, which is presented to the ligand-binding site in the *cis* configuration and withdrawn in *trans*. MAG binding under 380 nm light activates the receptor and opens its cation-selective channel, resulting in membrane depolarization. TMD, transmembrane domain; C, C terminus; N, N terminus. In combination with calcium- or voltage-sensitive dyes to measure neuronal activity, the light-gated glutamate receptor can be used as a remote, noninvasive neuronal switch for the electrode-free, all-optical analysis of neural circuits. When expressed in vivo, the light-gated glutamate receptor provides a tool for behavioral studies and circuit analysis. In the zebrafish larva, a touch-evoked escape response is assayed following activation of LiGluR (violet) or deactivation (blue). Source: From Szobota et al. [82]. (b) Example of multiunit recordings with light-gated glutamate receptor (liGlur) of rd1 retinas in the absence or presence of the photoswitch maleimide-azobenzene-glutamate (MAG). At the bottom, the diagram of the water maze-based light-avoidance behavior of adult rd1 mice, and the time to reach the platform for three experimental groups (rd1, LiGlur-rd1, WT). Source: From Caporale et al. [84].

selective GIRK1 inactivator, a small library of light-operated GIRK channel openers (LOGOs) was synthesized and characterized with azobenzene as the photochromic moiety [95]. One photoswitch (LOGO5) was further studied in zebrafish due to its desired solubility in water and photoswitching profile. It showed photocontrol of larvae motility in a reversible manner under UV and blue light illumination, exemplifying neuronal inactivation via endogenous GIRK channels upon visible illumination. The authors optimized LOGO with *ortho*-fluoro substitutions in the azobenzene moiety and displacing its isomerization wavelengths toward violet and green light, achieving visible light-control of zebrafish locomotion (violet light reduced activity, which was recovered under green light) [96].

Photocontrol of cardiac activity has been achieved in different animal models using various photopharmacological approaches. One study departed from a light-dependent (not reversible) small molecule identified in a large chemical screening assay using zebrafish larvae. This molecule, named Optovin [97], was found to be active in the transient receptor potential A1 (TRPA1) in zebrafish [98], which is involved in sensory systems including vision, taste, touch, and temperature. Based on optovin structure, a 1000 molecule screening assay in zebrafish identified two optovin analogs (TRPswitch A and B), which were further characterized in a zebrafish cardiac assay, showing heart beat arrest under violet light and recovery of cardiac activity after green light illumination [99].

A second strategy was based on rationally designing photoswitchable derivatives for muscarinic acetylcholine receptors (mAChR), using a dualsteric architecture. An azobenzene moiety was placed between an orthosteric muscarinic agonist (iperoxo) and an M2 receptor subtype-selective moiety (phthalimide). The photoswitchable derivative (named PAI for phthal-azo-iperoxo) enabled reversible photocontrol of cardiac activity in *Xenopus tropicalis* tadpoles: *trans*-PAI induced an arrest of heart beating which could be recovered with UV illumination or *cis*-PAI. In addition, the two isomers displayed significant differences in cardiac activity in rats and demonstrated NIR 2P switching in vitro [100] (Figure 34.3). Taking advantage of the presence of M2 receptors in the brain, PAI has been recently used to photocontrol brain waves in anesthetized mice [101]. Brain states are associated to characteristic oscillatory activities of neurons, which depend on neuromodulators, and are related to

**Figure 34.3 Photoswitchable chromic ligand (PCL).** Cardiac recordings in the presence or absence of PAI (phthalmide-azobenzene-iperoxo) in anesthetized Wistar rats, under white and UV light. In vivo effect of *trans*- and *cis*-PAI on the cardiac activity of rats is showed graphically. The activity of dark-relaxed (*trans*, gray plots) and UV-illuminated PAI (*cis*, purple plots) administered intraperitoneally in anesthetized rats was tested by means of electrocardiography. The heart rate (left panel) and PR interval (right panel) are plotted as a function of increasing doses of both isomers, which induced progressive bradycardia and PR lengthening in a dose-dependent manner. Significant differences between the dark-relaxed and UV-treated PAI were found in the heart rate and PR interval at the higher doses ($^{*}p < 0.05$; $^{***}p < 0.001$ *trans* vs. *cis*), in agreement with the higher agonist activity of the *trans* form observed in vitro and in tadpoles. Three rats in the *trans*-group died because of extreme bradycardia after the 100 μM/kg dose. The effects of PAI were reversible only upon administration of the muscarinic antagonist Atropine. Source: From Riefolo et al. [100].

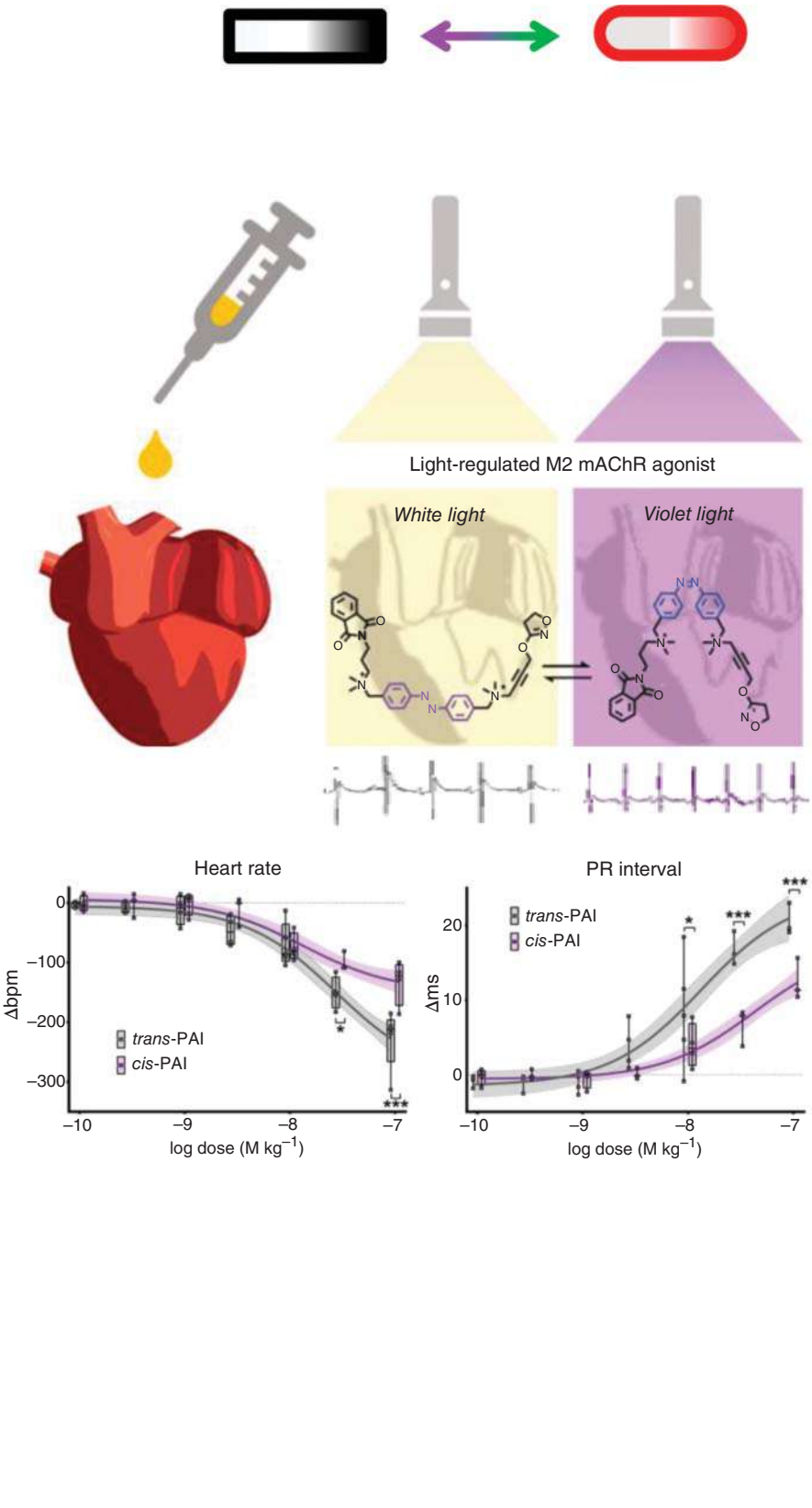
Light-regulated M2 mAChR agonist
White light
Violet light
Heart rate
PR interval
Δbpm
Δms
trans-PAI
cis-PAI
log dose (M kg−1)
log dose (M kg−1)

different behaviors. To study behavioral transitions and brain waves modulation in CNS treatments, tools to manipulate neuronal activity in a spatiotemporal manner are necessary. PAI allowed to remotely modify cortical brain waves using white light illumination, opening a new avenue for studying neuronal modulation in vivo.

Nicotinic acetylcholine receptors (nAChRs), which were the first target in photopharmacology [7], have been recently revisited with AzoCholine [102] (a derivative of the PCL BisQ from Bartels) to control dorsal root ganglion and hippocampal neuronal activity with UV and blue light. The compound allowed controlling swimming cycles in *C. elegans*, inducing freezing behaviors upon illumination with visible light.

Adrenergic modulation has also been explored in photopharmacology due to its essential role in most autonomous vital functions, such as heart and respiratory rhythm, digestion, papillary reflex, or glandular secretion. Several photoswitchable clonidine derivatives were characterized in a zebrafish larvae assay, and one, named Adrenoswitch-1, was further characterized in ophthalmic testing [103]. The fast-relaxing adrenergic photomodulator was tested in vivo for pupillary responses. Mice mydriasis was reversibly produced when exposed to UV light, which points to a way of improving conventional anticholinergic mydriatics used in ophthalmology without altering the pupil basal tone.

In a recent study, sphingosine-1-phosphate (S1P) receptors are controlled with light. These G-protein-coupled receptors are involved in the immune, vascular, and nervous systems, and are responsible in the modulation of acute and inflammatory pain. Evoked hypersensitivity to a noxious heat stimulus in mice was modulated with a photoswitchable compound targeting the sphingolipid metabolism and signaling [104].

Voltage-gated proton channels (Hv1) are present in macrophages, epithelial cells, and sperm and regulate pH of the media. They are also overexpressed in certain cancer types where their role is unclear, and it is suggested they are important for oocyte fertilization. Since several proton transport proteins are present in cells and regulate the pH, Hv1's importance in physiology and medicine is still unknown. An azobenzene derivative of a channel blocker was synthesized and tested in sperm and human macrophages demonstrating light-dependent proton currents modulation, and has been proposed as a tool for functional studies [105].

A remarkable application of photoswitches was developed for glucose homeostasis in type 2 diabetes. Based on sulfonylureas action on ATP-sensitive potassium channels that potentiate insulin release in beta cells, third-generation sulfonylureas were modified with azobenzene moieties. One of the compounds was tested in mice, monitoring their glucose concentration while illuminating pancreatic tissue with a blue laser coupled to an optic fiber. A reduction in glycemia was observed and could be significantly photocontrolled [106].

### 34.3.3 Protein and Gene Expression with Photoswitches

Remote control of protein expression and nucleic translation has also been achieved in vivo using photoswitchable compounds. One strategy is to conjugate an mRNA

molecule to a photocontrollable cap, which allows protein synthesis only under specific wavelength illumination (370 and 430 nm). This technique was applied to overcome single use caging methods and enabled modulating the formation of the secondary axis in zebrafish development by photocontrolling the synthesis of squint protein [107].

Another approach is to reversibly regulate G-quadruplexes, which are involved in transcription, translation, and telomere elongation processes, using blue and UV light [108]. The main role of G-quadruplexes is to arrest RNA polymerase activity by steric hindrance. This technique was previously demonstrated in thrombin aptamers [109] and was recently applied to promote transcription with a designed plasmid during zebrafish development.

### 34.3.4 Restoring Vision – Ion Channels and Switches

Significant efforts in photopharmacology have been devoted to restoring vision with photoswitchable small molecules. Two widespread retinal degeneration diseases are age-related macular degeneration and retinitis pigmentosa. Patients of either one become blind as a result of the irreversible loss of the photoreceptor cell layer, including both rods and cones [110, 111]. As these neurons from the outer layer die, the second- and third-class neuronal types (bipolar and horizontal; amacrine and ganglion cells, respectively) remain alive and functional for some time [112]. Hence, although the receptor for light is missing, the wiring for signal transmission is still operative and susceptible of photosensitization. Many strategies have been used to that aim, including optoelectronics, optogenetics, and photopharmacology.

Nowadays there are several optogenetics clinical trials for vision restoration (NCT02556736, NCT03326336, NCT04945772, and NCT04919473) [113–115] based on methods that have shown to restore vision in animals [116]. Nonetheless, the limitations of optogenetics include the need to inoculate exogenous receptors, which must be thoroughly tested for safety, and the requirement of bright light stimuli, in a range up to 3 log units of light intensity, in contrast to the 10 log units of photoreceptor cells [117].

The use of photoswitchable molecules for vision restoration was combined with genetic manipulation to specifically photocontrol retinal ganglion cells (RGCs). Using adeno-viral vectors (AAV), a modified ionotropic glutamate receptor (iGluR6) was introduced in degenerated mice retinas. The modified receptor (LiGluR6) carried a cysteine to conjugate the reactive maleimide of the photoswitchable glutamate ligand, thus allowing to photocontrol RGC activity and mimic photoresponses in the absence of photoreceptor cells [84] (Figure 34.2).

In order to avoid genetic manipulation and to target endogenous receptors, several diffusible PCLs were developed to achieve visual restoration in blinded mice by direct compound application. AAQ was the first to demonstrate a recovery of behavioral responses to light in open field and light avoidance tests in mice with degenerated retina. It showed to alter excitability in RGCs, bipolar and amacrine cells by blocking $K^+$ channels in a light-dependent manner [118]. Nonetheless, due to reduced vitreal retention over time after compound injection, and to the need of

high-intensity UV illumination, a red-shifted $K^+$ channel photoswitch (DENAQ) was subsequently developed [119]. DENAQ displays fast back-isomerization to *trans* in the dark and its *cis* configuration is achieved with visible light (450–550 nm). It also showed to recover some light-dependent behavior in blinded mice although high doses (300 μM) were required to elicit therapeutical effects. A third-generation photoswitch (BENAQ) [120], designed for the same channels, proved to last for over a month after one single in vivo injection in mice retinas. Although no behavioral tests were reported, toxic effects were not found in ex vivo retinae from mice and rabbit, and multielectrode array electrophysiology recordings showed a 20-fold potency increase when compared to DENAQ, retaining its photochemical properties. To avoid the permanent charges of DENAQ and BENAQ, another photoswitchable $K^+$ channel blocker named DAD was derived from the same concept. It switches under blue or white light and displays fast back-isomerization. It has a reduced functional lifetime (hours), similar to AAQ, and high solubility compared to BENAQ. It mainly acts on bipolar cells, but recovers light-dependent ganglion firing and functional vision in blind mice [121, 122]. Other photoswitchable compounds for vision restoration have been discussed elsewhere from a synthetic, chemical, or physiological perspective and many display remarkable in vitro properties [62, 121, 123–127].

## 34.4 Antibiotics and Insecticides in Photopharmacology

One of the major concerns in medicine is the resurfacing of infectious diseases that had been already eradicated by life-saving treatments in the past. Antimicrobial resistance and multidrug resistance (MDR) represent a significant global health threat due, in part, to the build-up of antibiotics in the environment as a result of their application in human medicine and animal farming, and on the other hand because of the long-term antibiotic treatments.

Photopharmacology has been explored as a way to produce antibiotic effects only where and when they are needed, and to release relatively inactivated compounds to the environment. A visible-light photocleavable fluoroquinolone derivative (BDP-Levofloxacin) has been used against Gram bacteria [128]. As a proof of concept for photoswitchable antimicrobial agents, photoswitchable quinolones were designed and pre-irradiated in order to control bacterial growth (365 nm) of *Escherichia coli* [129]. Photoswitchable ciprofloxacin derivatives (azofloxacin and spirofloxacin) were tested in *E. coli* and *Micrococcus luteus*. *Trans* Azofloxacin was 50 times more active than the unmodified antibiotic for *M. luteus*, but no difference between isomer activities was observed for *E. coli*. On the other hand, spirofloxacin showed more *cis*-isomer activity in minimum inhibitory concentration assays against *E. coli* than in its *trans* isomer, although ciprofloxacin continued to have more antibacterial activity [130]. Reversible action of diaminopyrimidines was demonstrated with visible light (green and red) in situ for *E. coli* [131]. A dithienylethene switchable scaffold was integrated into fluoroquinolones (ciprofloxacin and norfloxacin) and used as antibacterial in *E. coli*

and *Staphylococcus aureus* [132]. Incorporation of azobenzene or azopyrazole was also used to obtain photoswitchable amidohydrolase ligands as bacterial histone deacetylase (HDAC) inhibitors (mainly for *Pseudomonas aureginosa*) [133], and azobenzene in *meta*- or *para*-substitution was introduced in gramicidin S backbone and evaluated against *S. aureus* [134]. In addition, photoswitchable antimicrobial tetrapeptides against *S. aureus* were designed based on the methicillin-resistant *S. aureus* compound from Lau et al. [135] using an azobenzene photoswitch [136].

A recent trend in photopharmacology aims at improving insecticide action by confining their effects in space and time. Several photoswitchable azobenzene derivatives of the imidacloprid insecticide (a nAChR agonist) were tested in vitro and in vivo with *Musca domestica* (house fly), and one showed a five-fold difference in insecticide activity between its isomers (UV illumination reduced lethal dosage needed) [137]. Other photoswitchable insecticides have been proposed based on benzoylphenylurea (BPUs) insecticides and tested in armyworm *Mythimna separate*. As in the previous study, azobenzene modifications in *ortho*-, *meta*-, and *para*-substituents were analyzed, and one compound showed a five-fold increase in larval mortality under UV illumination [138].

## 34.5 Concluding remarks

Extensive efforts have been dedicated to develop photopharmacological compounds for a great variety of target proteins, and in vivo testing has become a way to demonstrate their advantages and envisaged clinical applications. Cancer, infections, and diseases of the nervous system are the fields that attracted most interest and that led to the molecules with most advanced properties. Small and transparent animal models have been advantageous to focus on conceptual proofs while passing over hurdles to deliver light and the drug itself. As more studies are carried out in mammalian models for pre-clinical demonstration, the questions regarding drug and light delivery are likely to be worked out to overcome the current limitations of photopharmacology. The required technologies are also of interest in other fields, like pharmacology (including systemic and local drug delivery), optogenetics (including invasive and non-invasive photostimulation), and photobiomodulation (focused on light delivery), and are expected to develop synergistically. For example, wireless and battery-free optofluidic systems have been demonstrated in vivo [139, 140] and could be optimized as is the case of other implants that are used clinically against cancer and pain. Red- and NIR-sensitive drugs bear the potential of being activated noninvasively through the tissue. Light upconversion materials can also be used for this purpose, as demonstrated with optogenetics.

Besides the generally reported efficacy and photocontrol, toxicity and safety assessment of photopharmacological drug candidates is essential to proceed toward real applications. In principle, all compounds to be administered, their by-products (as a result of uncaging or degradation), and isomers (in the case of photoswitches) must be characterized in order to be approved by drug agencies. However, it has been argued that if a reversible photoswitch displays only one stable configuration,

whereas the other is fast relaxing and unlikely to diffuse and act in farther regions or tissues, only the active stable conformation should be evaluated for toxicity and safety. On the contrary, when both isomers or states display long thermal lives, these must be evaluated as independent bioactive entities [11].

Overall, the in vivo studies compiled in this chapter set the stage to demonstrate in a clinically relevant context the basic hypothesis that photopharmacology enables (i) high efficacy with pharmacological and spatiotemporal selectivity, (ii) low systemic side effects, and (iii) novel therapies. Based on the reported advances, we speculate that the best-positioned applications for clinical trials may be ophthalmology (including vision restoration) due to the simplicity of light and drug application; antibiotics because of their medical importance; and photochemotherapy against cancer, which is fostered by clinically approved devices and related drugs for PDT in tissues exposed to light, including via natural orifices like throat, bladder, and large intestine.

In conclusion, the converging progress to develop caged and photoswitchable drugs (including design, synthesis, chemical, and pharmacological characterization in vitro and in vivo), to achieve robust pre-clinical efficacy and safety results, and to appeal investors, pharmaceutical industry, and clinicians, is paving the way for the first clinical trials of photopharmacology.

## References


1 Ackroyd, R., Kelty, C., Brown, N., and Reed, M. (2001). The history of photodetection and photodynamic therapy. *Photochem. Photobiol.* 74 (5): 656–669.

2 Enwemeka, C.S., Bumah, V.V., and Masson-Meyers, D.S. (2020). Light as a potential treatment for pandemic coronavirus infections: a perspective. *J. Photochem. Photobiol. B.* 207 (January): 111891.

3 Kalka, K., Merk, H., and Mukhtar, H. (2000). Photodynamic therapy in dermatology. *J. Am. Acad. Dermatol.* 42 (3): 389–413.

4 Fitzpatrick, T.B. and Pathak, M.A. (1959). Historical aspects of methoxsalen and other furocoumarins. *J. Invest. Dermatol* https://doi.org/10.1038/jid.1959.40.

5 Dougherty, T.J., Gomer, C.J., Henderson, B.W., Jori, G., Kessel, D., Korbelik, M., Moan, J., and Peng, Q. (1998) Photodynamic therapy. *J. Natl. Cancer Inst.* https://doi.org/10.1093/jnci/90.12.889

6 Meisel, P., Jährig, D., and Jährig, K. (1980). What is photopharmacology, and what can it do? *Pharmazie* 35 (7): 377–388.

7 Bartels, E., Wassermann, N.H., and Erlanger, B.F. (1971). Photochromic activators of the acetylcholine receptor. *Proc. Natl. Acad. Sci. U.S.A.* https://doi.org/10.1073/pnas.68.8.1820.

8 Gasparro, F.P., Chan, G., and Edelson, R.L. (1985). Phototherapy and photopharmacology. *Yale J. Biol. Med.* 58 (6): 519–534.

9 Yoon, I., Li, J.Z., and Shim, Y.K. (2013). Advance in photosensitizers and light delivery for photodynamic therapy. *Clin. Endosc.* https://doi.org/10.5946/ce.2013.46.1.7.


**10** Upputuri, P.K. and Pramanik, M. (2019). Photoacoustic imaging in the second near-infrared window: a review. *J. Biomed. Opt.* 24 (04): 1.

**11** Fuchter, M.J. (2020). On the promise of photopharmacology using photoswitches: a medicinal chemist's perspective. *J. Med. Chem.* https://doi.org/10.1021/acs.jmedchem.0c00629.

**12** Weissleder, R. and Ntziachristos, V. (2003). Shedding light onto live molecular targets. *Nat. Med.* 9 (1): 123–128.

**13** Oron, D., Papagiakoumou, E., Anselmi, F., and Emiliani, V. (2012). Two-photon optogenetics. In: *Progress in Brain Research*. (eds. Thomas Knöpfel, E.S.B.), Elsevier, pp. 119–143. https://doi.org/10.1016/B978-0-444-59426-6.00007-0.

**14** Watson, B.O., Nikolenko, V., and Yuste, R. (2009). Two-photon imaging with diffractive optical elements. *Front. Neural Circuits* 3: 6.

**15** Denk, W. (1994). Two-photon scanning photochemical microscopy: mapping ligand-gated ion channel distributions. *Proc. Natl. Acad. Sci. U.S.A.* 91 (14): 6629–6633.

**16** Bort, G., Gallavardin, T., Ogden, D., and Dalko, P.I. (2013). From one-photon to two-photon probes: 'caged' compounds, actuators, and photoswitches. *Angew. Chem. Int. Ed.* https://doi.org/10.1002/anie.201204203.

**17** Kellner, S. and Berlin, S. (2020). Two-photon excitation of azobenzene photoswitches for synthetic optogenetics. *Appl. Sci.* 10 (3): 805–820.

**18** Brieke, C., Rohrbach, F., Gottschalk, A. et al. (2012). Light-controlled tools. *Angew. Chem. Int. Ed.* 51: 8446–8476.

**19** Kantevari, S., Matsuzaki, M., Kanemoto, Y. et al. (2010). Two-color, two-photon uncaging of glutamate and GABA. *Nat. Methods* 7 (2): 123–125.

**20** Lerch, M.M., Hansen, M.J., van Dam, G.M. et al. (2016). Emerging targets in photopharmacology. *Angew. Chem. Int. Ed.* 55 (37): 10978–10999.

**21** Kaplan, J.H., Forbush, B., and Hoffman, J.F. (1978). Rapid photolytic release of adenosine 5′-triphosphate from a protected analogue: utilization by the Na:K pump of human red blood cell ghosts. *Biochemistry* https://doi.org/10.1021/bi00603a020.

**22** Passlick, S. and Ellis-Davies, G.C.R. (2019). Chromatically independent, two-color uncaging of glutamate and GABA with one- or two-photon excitation. *Physiol. Behav.* 176: 167–196.

**23** Riedel, G., Platt, B., and Micheau, J. (2003). Glutamate receptor function in learning and memory. *Behav. Brain Res.* https://doi.org/10.1016/S0166-4328(02)00272-3.

**24** Niswender, C.M. and Conn, P.J. (2010). Metabotropic glutamate receptors: physiology, pharmacology, and disease. *Annu. Rev. Pharmacol. Toxicol.* 50: 295–322.

**25** Bormann, J. (2000). The "ABC" of GABA receptors. *Trends Pharmacol. Sci.* 21 (1): 16–19.

**26** Nagel, G., Szellas, T., Huhn, W. et al. (2003). Channelrhodopsin-2, a directly light-gated cation-selective membrane channel. *Proc. Natl. Acad. Sci. U.S.A.* https://doi.org/10.1073/pnas.1936192100.


**27** Callaway, E.M. and Katzt, L.C. (1993). Photostimulation using caged glutamate reveals functional circuitry in living brain slices (neocortex/whole-cell recording/intrinsic circuits). *Neurobiology* 90 (August): 7661–7665.

**28** Noguchi, J., Nagaoka, A., Watanabe, S. et al. (2011). In vivo two-photon uncaging of glutamate revealing the structure-function relationships of dendritic spines in the neocortex of adult mice. *Aust. J. Phys.* 589 (10): 2447–2457.

**29** De Cuttoli, R.D., Chauhan, P.S., Reyes, A.P. et al. (2020). Optofluidic control of rodent learning using cloaked caged glutamate. *Proc. Natl. Acad. Sci. U.S.A.* 117 (12): 6831–6835.

**30** Lopes-dos-Santos, V., Campi, J., Filevich, O. et al. (2011). In vivo photorelease of GABA in the mouse cortex. *Brazilian J. Med. Biol. Res.* 44 (7): 688–693.

**31** Yang, X., Rode, D.L., Peterka, D.S. et al. (2012). Optical control of focal epilepsy in vivo with caged γ-aminobutyric acid. *Ann. Neurol.* 71 (1): 68–75.

**32** Wang, D., Yu, Z., Yan, J. et al. (2017). Photolysis of caged-GABA rapidly terminates seizures in vivo: concentration and light intensity dependence. *Front. Neurol.* 8 (May): 1–10.

**33** Cruz, F.G., Koh, J.T., and Link, K.H. (2000). Light-activated gene expression. *J. Am. Chem. Soc.* 122 (36): 8777–8778.

**34** Ouyang, X., Shestopalov, I.A., Sinha, S. et al. (2009). Versatile synthesis and rational design of caged morpholinos. *J. Am. Chem. Soc.* 131 (37): 13255–13269.

**35** Yamazoe, S., Shestopalov, I.A., Provost, E. et al. (2012). Cyclic caged morpholinos: conformationally gated probes of embryonic gene function. *Angew. Chem. Int. Ed.* 51 (28): 6908–6911.

**36** Shestopalov, I.A., Sinha, S., and Chen, J.K. (2007). Light-controlled gene silencing in zebrafish embryos. *Nat. Chem. Biol.* 3 (10): 650–651.

**37** Deiters, A., Garner, R.A., Lusic, H. et al. (2010). Photocaged morpholino oligomers for the light-regulation of gene function in zebrafish and xenopus embryos. *J. Am. Chem. Soc.* 132 (44): 15644–15650.

**38** Tallafuss, A., Gibson, D., Morcos, P. et al. (2012). Turning gene function ON and OFF using sense and antisense photo-morpholinos in zebrafish. *Development* 139 (9): 1691–1699.

**39** Yamazoe, S., Liu, Q., McQuade, L.E. et al. (2014). Sequential gene silencing using wavelength-selective caged morpholino oligonucleotides. *Angew. Chem. Int. Ed.* 53 (38): 10114–10118.

**40** Tomasini, A.J., Schuler, A.D., Zebala, J.A., and Mayer, A.N. (2009). PhotoMorphs™: a novel light-activated reagent for controlling gene expression in zebrafish. *Genesis* 47 (11): 736–743.

**41** Tang, X.J., Maegawa, S., Weinberg, E.S., and Dmochowski, I.J. (2007). Regulating gene expression in zebrafish embryos using light-activated, negatively charged peptide nucleic acids. *J. Am. Chem. Soc.* 129 (36): 11000–11001.

**42** Sinha, D.K., Neveu, P., Gagey, N. et al. (2010). Photocontrol of protein activity in cultured cells and zebrafish with one- and two-photon illumination. *ChemBioChem* 11 (5): 653–663.


**43** Sinha, D.K., Neveu, P., Gagey, N. et al. (2010). Photoactivation of the CreERT2 recombinase for conditional site-specific recombination with high spatiotemporal resolution. *Zebrafish* 7 (2): 199–204.

**44** Lu, X., Agasti, S.S., Vinegoni, C. et al. (2012). Optochemogenetics (OCG) allows more precise control of genetic engineering in mice with CreER regulators. *Bioconjugate Chem.* 23 (9): 1945–1951.

**45** Wong, P.T., Roberts, E.W., Tang, S. et al. (2017). Control of an unusual photo-claisen rearrangement in coumarin caged tamoxifen through an extended spacer. *ACS Chem. Biol.* 12 (4): 1001–1010.

**46** Feng, Z., Nam, S., Hamouri, F. et al. (2017). Optical control of tumor induction in the zebrafish. *Sci. Rep.* 7 (1): 1–12.

**47** Tekeli, I., Aujard, I., Trepat, X. et al. (2016). Long-term in vivo single-cell lineage tracing of deep structures using three-photon activation. *Light Sci. Appl.* 5 (6): e16084.

**48** Zhang, W., Hamouri, F., Feng, Z. et al. (2018). Control of protein activity and gene expression by cyclofen-OH uncaging. *ChemBioChem* 19 (12): 1232–1238.

**49** Xiao, Z., Ji, C., Shi, J. et al. (2012). DNA self-assembly of targeted near-infrared-responsive gold nanoparticles for cancer thermo-chemotherapy. *Angew. Chem. Int. Ed.* 51 (47): 11853–11857.

**50** Huo, S., Gong, N., Jiang, Y. et al. (2019). Gold-DNA nanosunflowers for efficient gene silencing with controllable transformation. *Sci. Adv.* 5 (10): eaaw6264.

**51** Pan, Y., Yang, J., Luan, X. et al. (2019). Near-infrared upconversion–activated CRISPR-Cas9 system: a remote-controlled gene editing platform. *Sci. Adv.* 5 (4): eaav7199.

**52** Li, L., Tong, R., Chu, H. et al. (2014). Aptamer photoregulation in vivo. *Proc. Natl. Acad. Sci. U.S.A.* 111 (48): 17099–17103.

**53** Ibsen, S., Zahavy, E., Wrasidlo, W. et al. (2013). Localized in vivo activation of a photoactivatable doxorubicin prodrug in deep tumor tissue. *Photochem. Photobiol.* 89 (3): 698–708.

**54** Ando, H., Furuta, T., Tsien, R.Y., and Okamoto, H. (2001). Photo-mediated gene activation using caged RNA/DNA in zebrafish embryos. *Nat. Genet.* 28 (4): 317–325.

**55** Ando, H., Kobayashi, M., Tsubokawa, T. et al. (2005). Lhx2 mediates the activity of Six3 in zebrafish forebrain growth. *Dev. Biol.* 287 (2): 456–468.

**56** Lima, S.Q. and Miesenböck, G. (2005). Remote control of behavior through genetically targeted photostimulation of neurons. *Cell* 121 (1): 141–152.

**57** Lucas, T., Schäfer, F., Müller, P. et al. (2017). Light-inducible antimiR-92a as a therapeutic strategy to promote skin repair in healing-impaired diabetic mice. *Nat. Commun.* 8 (May): 15162.

**58** Schroeder, A., Goldberg, M.S., Kastrup, C. et al. (2012). Remotely activated protein-producing nanoparticles. *Nano Lett.* 12 (6): 2685–2689.

**59** Neveu, P., Aujard, I., Benbrahim, C. et al. (2008). A caged retinoic acid for one- and two-photon excitation in zebrafish embryos. *Angew. Chem. Int. Ed.* 47 (20): 3744–3746.


**60** Kaufman, H., Vratsanos, S.M., and Erlanger, B.F. (1968). Photoregulation of an enzymic process by means of a light-sensitive ligand. *Science (80-.).* 162 (3861): 1487–1489.

**61** Beharry, A.A., and Woolley, G.A. (2011) Azobenzene photoswitches for biomolecules. *Chem. Soc. Rev.*https://doi.org/10.1039/c1cs15023e.

**62** Hüll, K., Morstein, J., and Trauner, D. (2018). In vivo photopharmacology. *Chem. Rev.* https://doi.org/10.1021/acs.chemrev.8b00037.

**63** Dunkel, P. and Ilaš, J. (2021). Targeted cancer therapy using compounds activated by light. *Cancers (Basel)* 13 (13): 3237.

**64** Aggarwal, K., Kuka, T.P., Banik, M. et al. (2020). Visible light mediated bidirectional control over carbonic anhydrase activity in cells and in vivo using azobenzenesulfonamides. *J. Am. Chem. Soc.* 142 (34): 14522–14531.

**65** Matera, C., Gomila, A.M.J., Camarero, N. et al. (2018). Photoswitchable antimetabolite for targeted photoactivated chemotherapy. *J. Am. Chem. Soc.* https://doi.org/10.1021/jacs.8b08249.

**66** Szymanski, W., Ourailidou, M.E., Velema, W.A. et al. (2015). Light-controlled histone deacetylase (HDAC) inhibitors: towards photopharmacological chemotherapy. *Chem. Eur. J.* https://doi.org/10.1002/chem.201502809.

**67** Reis, S.A., Ghosh, B., Hendricks, J.A. et al. (2016). Light-controlled modulation of gene expression by chemical optoepigenetic probes. *Nat. Chem. Biol.* https://doi.org/10.1038/nchembio.2042.

**68** Sheldon, J.E., Dcona, M.M., Lyons, C.E. et al. (2016). Photoswitchable anticancer activity via trans–cis isomerization of a combretastatin A-4 analog. *Org. Biomol. Chem.* 14 (1): 40–49.

**69** Borowiak, M., Nahaboo, W., Reynders, M. et al. (2015). Photoswitchable inhibitors of microtubule dynamics optically control mitosis and cell death. *Cell* 162 (2): 403–411.

**70** Imperatore, C., Scuotto, M., Valadan, M. et al. (2019). Photo-control of cancer cell growth by benzodiazo N-substituted pyrrole derivatives. *J. Photochem. Photobiol. Chem.* 377 (December 2018): 109–118.

**71** Imperatore, C., Valadan, M., Tartaglione, L. et al. (2020). Exploring the photodynamic properties of two antiproliferative benzodiazopyrrole derivatives. *Int. J. Mol. Sci.* 21 (4): 1246.

**72** Mulatihan, D., Guo, T., and Zhao, Y. (2020). Azobenzene photoswitch for isomerization-dependent cancer therapy via azo-combretastatin A4 and phototrexate. *Photochem. Photobiol.* 96 (6): 1163–1168.

**73** Okamoto, K., Tomita, Y., Yonezawa, H. et al. (1984). Inhibitory effect of gramicidin S on the growth of murine tumor cells in vitro and in vivo. *Oncology* 41 (1): 43–48.

**74** Babii, O., Afonin, S., Berditsch, M. et al. (2014). Controlling biological activity with light: Diarylethene-containing cyclic peptidomimetics. *Angew. Chem. Int. Ed.* 53 (13): 3392–3395.

**75** Babii, O., Afonin, S., Garmanchuk, L.V. et al. (2016). Direct photocontrol of peptidomimetics: an alternative to oxygen-dependent photodynamic cancer therapy. *Angew. Chem. Int. Ed.* 55 (18): 5493–5496.


**76** Babii, O., Afonin, S., Schober, T. et al. (2020). Peptide drugs for photopharmacology: how much of a safety advantage can be gained by photocontrol? *Futur. Drug Discov.* 2 (1): FDD28.

**77** Afonin, S., Babii, O., Reuter, A. et al. (2020). Light-controllable dithienylethene-modified cyclic peptides: Photoswitching the in vivo toxicity in zebrafish embryos. *Beilstein J. Org. Chem.* 16: 39–49.

**78** Albert, L. and Vázquez, O. (2019). Photoswitchable peptides for spatiotemporal control of biological functions. *Chem. Commun.* 55 (69): 10192–10213.

**79** Tong, R., Chiang, H.H., and Kohane, D.S. (2013). Photoswitchable nanoparticles for in vivo cancer chemotherapy. *Proc. Natl. Acad. Sci. U.S.A.* 110 (47): 19048–19053.

**80** Ricart-Ortega, M., Font, J., and Llebaria, A. (2019). GPCR photopharmacology. *Mol. Cell. Endocrinol.* 488 (October 2018): 36–51.

**81** Wijtmans, M., Josimovic, I., Vischer, H.F., and Leurs, R. (2022). Optical control of Class A G protein-coupled receptors with photoswitchable ligands. *Curr. Opin. Pharmacol.* 63: 102192.

**82** Szobota, S., Gorostiza, P., Del Bene, F. et al. (2007). Remote control of neuronal activity with a light-gated glutamate receptor. *Neuron* 54 (4): 535–545.

**83** Volgraf, M., Gorostiza, P., Numano, R. et al. (2006). Allosteric control of an ionotropic glutamate receptor with an optical switch. *Nat. Chem. Biol.* 2 (1): 47–52.

**84** Caporale, N., Kolstad, K.D., Lee, T. et al. (2011). LiGluR restores visual responses in rodent models of inherited blindness. *Mol. Ther.* 19 (7): 1212–1219.

**85** Cabré, G., Garrido-Charles, A., Moreno, M. et al. (2019). Rationally designed azobenzene photoswitches for efficient two-photon neuronal excitation. *Nat. Commun.* 10 (1): 907.

**86** Acosta-Ruiz, A., Gutzeit, V.A., Skelly, M.J. et al. (2020). Branched photoswitchable tethered ligands enable ultra-efficient optical control and detection of G protein-coupled receptors in vivo. *Neuron* 105 (3): 446–463.e13.

**87** Pittolo, S., Gómez-Santacana, X., Eckelt, K. et al. (2014). An allosteric modulator to control endogenous G protein-coupled receptors with light. *Nat. Chem. Biol.* 10 (10): 813–815.

**88** Rovira, X., Trapero, A., Pittolo, S. et al. (2016). OptoGluNAM4.1, a photoswitchable allosteric antagonist for real-time control of mGlu 4 receptor activity. *Cell Chem. Biol.* 23 (8): 929–934.

**89** Yue, L., Pawlowski, M., Dellal, S.S. et al. (2012). Robust photoregulation of GABA A receptors by allosteric modulation with a propofol analogue. *Nat. Commun.* 3 (May): 1012–1095.

**90** Stein, M., Middendorp, S.J., Carta, V. et al. (2012). Azo-propofols: Photochromic potentiators of GABAA receptors. *Angew. Chem. Int. Ed.* 51 (42): 10500–10504.

**91** Rustler, K., Maleeva, G., Gomila, A.M.J. et al. (2020). Optical control of GABA A receptors with a fulgimide-based potentiator. *Chem. Eur. J.* 26 (56): 12722–12727.

**92** Maleeva, G., Wutz, D., Rustler, K. et al. (2019). A photoswitchable GABA receptor channel blocker. *Br. J. Pharmacol.* 176 (15): 2661–2677.


**93** Maleeva, G., Nin-Hill, A., Rustler, K. et al. (2021). Subunit-specific photocontrol of glycine receptors by azobenzene-nitrazepam photoswitcher. *eNeuro* Vol. 8 https://doi.org/10.1523/ENEURO.0294-20.2020.

**94** Gomila, A.M.J., Rustler, K., Maleeva, G. et al. (2020). Photocontrol of endogenous glycine receptors in vivo. *Cell Chem. Biol.* 1–9.

**95** Barber, D.M., Schönberger, M., Burgstaller, J. et al. (2016). Optical control of neuronal activity using a light-operated GIRK channel opener (LOGO). *Chem. Sci.* 7 (3): 2347–2352.

**96** Trads, J.B., Burgstaller, J., Laprell, L. et al. (2017). Optical control of GIRK channels using visible light. *Org. Biomol. Chem.* 15 (1): 76–81.

**97** Kokel, D., Cheung, C.Y.J., Mills, R. et al. (2013). Photochemical activation of TRPA1 channels in neurons and animals. *Nat. Chem. Biol.* 9 (4): 257–263.

**98** Lam, P.Y., Mendu, S.K., Mills, R.W. et al. (2017). A high-conductance chemo-optogenetic system based on the vertebrate channel Trpa1b. *Sci. Rep.* 7 (1): 1–12.

**99** Lam, P.Y., Thawani, A.R., Balderas, E. et al. (2020). TRPswitch - a step-function chemo-optogenetic ligand for the vertebrate TRPA1 channel. *J. Am. Chem. Soc.* 142 (41): 17457–17468.

**100** Riefolo, F., Matera, C., Garrido-Charles, A. et al. (2019). Optical control of cardiac function with a photoswitchable muscarinic agonist. *J. Am. Chem. Soc.* 141 (18): 7628–7636.

**101** Barbero-Castillo, A., Riefolo, F., Matera, C. et al. (2021). Control of brain state transitions with a photoswitchable muscarinic agonist. *Adv. Sci.* 8 (14): 1–11.

**102** Damijonaitis, A., Broichhagen, J., Urushima, T. et al. (2015). AzoCholine enables optical control of alpha 7 nicotinic acetylcholine receptors in neural networks. *ACS Chem. Neurosci.* 6 (5): 701–707.

**103** Prischich, D., Gomila, A.M.J., Milla-Navarro, S. et al. (2021). Adrenergic modulation with photochromic ligands. *Angew. Chem. Int. Ed.* 60 (7): 3625–3631.

**104** Morstein, J., Hill, R.Z., Novak, A.J.E. et al. (2019). Optical control of sphingosine-1-phosphate formation and function. *Nat. Chem. Biol.* 15 (6): 623–631.

**105** Rennhack, A., Grahn, E., Kaupp, U.B., and Berger, T.K. (2017). Photocontrol of the Hv1 proton channel. *ACS Chem. Biol.* 12 (12): 2952–2957.

**106** Mehta, Z.B., Johnston, N.R., Nguyen-Tu, M.S. et al. (2017). Remote control of glucose homeostasis in vivo using photopharmacology. *Sci. Rep.* 7 (1): 1–11.

**107** Ogasawara, S. (2017). Duration control of protein expression in vivo by light-mediated reversible activation of translation. *ACS Chem. Biol.* 12 (2): 351–356.

**108** Ogasawara, S. (2018). Transcription driven by reversible photocontrol of hyperstable G-quadruplexes. *ACS Synth. Biol.* 7 (11): 2507–2513.

**109** Ogasawara, S., and Maeda, M. (2009) Reversible photoswitching of a G-quadruplex. Angew. Chem. Int. Ed. https://doi.org/10.1002/anie.200902183.

**110** Ferrari, S., Di Iorio, E., Barbaro, V. et al. (2011). Retinitis pigmentosa: genes and disease mechanisms. *Curr. Genomics* 12 (4): 238–249.


**111** Nowak, J.Z. (2006). Age-related macular degeneration (AMD): pathogenesis and therapy. *Pharmacol. Rep.* 58 (3): 353–363.

**112** Humayun, M.S., Prince, M., de Juan, E. et al. (1999). Morphometric analysis of the extramacular retina from postmortem eyes with retinitis pigmentosa. *Invest. Ophthalmol. Vis. Sci.* 40 (1): 143–148.

**113** Chaffiol, A., Caplette, R., Jaillard, C. et al. (2017). A new promoter allows optogenetic vision restoration with enhanced sensitivity in macaque retina. *Mol. Ther.* 25 (11): 2546–2560.

**114** Pan, Z.H., Ganjawala, T.H., Lu, Q. et al. (2014). ChR2 mutants at L132 and T159 with improved operational light sensitivity for vision restoration. *PLoS One* 9 (6): e98924.

**115** Ivanova, E., Hwang, G.S., Pan, Z.H., and Troilo, D. (2010). Evaluation of AAV-mediated expression of chop2-GFP in the marmoset retina. *Investig. Ophthalmol. Vis. Sci.* 51 (10): 5288–5296.

**116** Sahel, J.-A., Bennett, J., and Roska, B. (2019). Depicting brighter possibilities for treating blindness. *Sci. Transl. Med.* 11 (494): eaax2324.

**117** Dowling, J.E. (2020). Restoring vision to the blind. *Science (80-.)* 368 (6493): 827–828.

**118** Polosukhina, A., Litt, J., Tochitsky, I. et al. (2012). Photochemical restoration of visual responses in blind mice. *Neuron* 75 (2): 271–282.

**119** Tochitsky, I., Polosukhina, A., Degtyar, V.E. et al. (2014). Restoring visual function to blind mice with a photoswitch that exploits electrophysiological remodeling of retinal ganglion cells. *Neuron* 81 (4): 800–813.

**120** Tochitsky, I., Trautman, J., Gallerani, N. et al. (2017). Restoring visual function to the blind retina with a potent, safe and long-lasting photoswitch. *Sci. Rep.* 7: 1–8.

**121** Hüll, K., Benster, T., Manookin, M.B. et al. (2019). photopharmacologic vision restoration reduces pathological rhythmic field potentials in blind mouse retina. *Sci. Rep.* 9 (1): 1–12.

**122** Laprell, L., Tochitsky, I., Kaur, K. et al. (2017). Photopharmacological control of bipolar cells restores visual function in blind mice. *J. Clin. Invest.* 127 (7): 2598–2611.

**123** Marc, R., Pfeiffer, R., and Jones, B. (2014). Retinal prosthetics, optogenetics, and chemical photoswitches. *ACS Chem. Neurosci.* 5 (10): 895–901.

**124** Van Gelder, R.N. (2020). Optogenetic and photoswitch therapies for vision restoration. *Retin. Physician* 17 (Jan/Feb): 23–27.

**125** Laprell, L., Hüll, K., Stawski, P. et al. (2016). Restoring light sensitivity in blind retinae using a photochromic AMPA receptor agonist. *ACS Chem. Neurosci.* 7 (1): 15–20.

**126** Van Gelder, R.N. (2015). Photochemical approaches to vision restoration. *Vision Res.* 111 (Pt B): 134–141.

**127** Izquierdo-Serra, M., Bautista-Barrufet, A., Trapero, A. et al. (2016). Optical control of endogenous receptors and cellular excitability using targeted covalent photoswitches. *Nat. Commun.* 7: 12221.


**128** Kumari, P., Kulkarni, A., Sharma, A.K., and Chakrapani, H. (2018). Visible-light controlled release of a fluoroquinolone antibiotic for antimicrobial photopharmacology. *ACS Omega* 3 (2): 2155–2160.

**129** Velema, W.A., van der Toorn, M., Szymanski, W., and Feringa, B.L. (2013). Design, synthesis, and inhibitory activity of potent, photoswitchable mast cell activation inhibitors. *J. Med. Chem.* 56 (11): 4456–4464.

**130** Velema, W.A., Hansen, M.J., Lerch, M.M. et al. (2015). Ciprofloxacin-photoswitch conjugates: a facile strategy for photopharmacology. *Bioconjugate Chem.* 26 (12): 2592–2597.

**131** Wegener, M., Hansen, M.J., Driessen, A.J.M. et al. (2017). Photocontrol of antibacterial activity: shifting from UV to red light activation. *J. Am. Chem. Soc.* 139 (49): 17979–17986.

**132** Li, Z., Wang, Y., Li, M. et al. (2018). Synthesis and properties of dithienylethene-functionalized switchable antibacterial agents. *Org. Biomol. Chem.* 16 (38): 6988–6997.

**133** Weston, C.E., Krämer, A., Colin, F. et al. (2017). Toward photopharmacological antimicrobial chemotherapy using photoswitchable amidohydrolase inhibitors. *ACS Infect. Dis.* 3 (2): 152–161.

**134** Yeoh, Y.Q., Yu, J., Polyak, S.W. et al. (2018). photopharmacological control of cyclic antimicrobial peptides. *ChemBioChem* 19 (24): 2591–2597.

**135** Lau, Q.Y., Ng, F.M., Cheong, J.W.D. et al. (2015). Discovery of an ultra-short linear antibacterial tetrapeptide with anti-MRSA activity from a structure-activity relationship study. *Eur. J. Med. Chem.* https://doi.org/10.1016/j.ejmech.2015.10.015.

**136** Yeoh, Y.Q., Horsley, J.R., Yu, J. et al. (2020). Short Photoswitchable Antibacterial Peptides. *ChemMedChem* 15 (16): 1505–1508.

**137** Xu, Z., Shi, L., Jiang, D. et al. (2015). Azobenzene modified imidacloprid derivatives as photoswitchable insecticides: Steering molecular activity in a controllable manner. *Sci. Rep.* 5 (December 2014): 1–8.

**138** Tian, X., Zhang, C., Xu, Q. et al. (2017). Azobenzene-benzoylphenylureas as photoswitchable chitin synthesis inhibitors. *Org. Biomol. Chem.* 15 (15): 3320–3323.

**139** Qazi, R., Gomez, A.M., Castro, D.C. et al. (2019). Wireless optofluidic brain probes for chronic neuropharmacology and photostimulation. *Nat. Biomed. Eng.* 3 (8): 655–669.

**140** Noh, K.N., Park, S.I., Qazi, R. et al. (2018). Miniaturized, battery-free optofluidic systems with potential for wireless pharmacology and optogenetics. *Small* 14 (4): 1702479.

# 35 Molecular Photoswitches in Antimicrobial Photopharmacology

Mafalda Bispo, Jan Maarten van Dijl, and Wiktor Szymanski

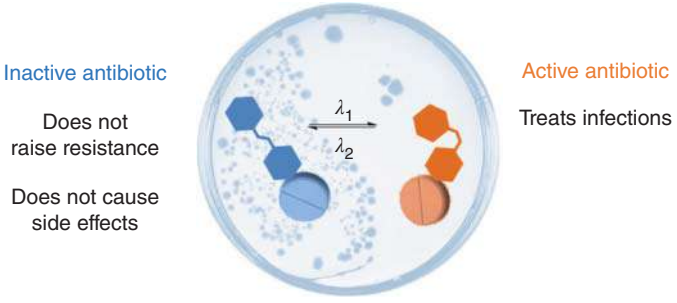


**Characteristic Features**

Photopharmacology, Antibiotic resistance, Harmful side effects, Penetration of light into human tissues, Red-light-responsive photoswitches, Photocontrol of small molecules and cyclic peptides

**Applied Molecular Photoswitches**

Azobenzenes, Diarylethenes, Spiropyranes, Stilbenes

**First Reported**

Velema, W.A., Van Der Berg, J.P., Hansen, M.J., et al. (2013). Optical control of antibacterial activity. *Nat. Chem.* **5** (11): 924–928. (First photocontrolled small molecule antibiotic).

Babii, O., Afonin, S., Berditsch, M., et al. (2014). Controlling biological activity with light: diarylethene-containing cyclic peptidomimetics. *Angew. Chem. Int. Ed.* **53** (13): 3392–3395 (First photocontrolled peptidic antibiotic).

**Key References**

Wegener, M., Hansen, M.J., Driessen, A.J.M., et al. (2017). Photocontrol of antibacterial activity: shifting from UV to red light activation. *J. Am. Chem. Soc.* **139** (49): 17979–17986.

Weston, C.E., Krämer, A., Colin, F., et al. (2017). Toward photopharmacological antimicrobial chemotherapy using photoswitchable amidohydrolase inhibitors. *ACS Infect. Dis.* **3** (2): 152–161.

Salta, J., Benhamou, R.I., Herzog, I.M., et al. (2017). Tuning the effects of nacterial membrane permeability through photo-isomerization of antimicrobial cationic amphiphiles. *Chem. Eur. J.* **23** (52): 12724–12728.

# 35

# Molecular Photoswitches in Antimicrobial Photopharmacology

*Mafalda Bispo[1], Jan Maarten van Dijl[1], and Wiktor Szymanski[2,3]*

[1] *University of Groningen, University Medical Center Groningen, Department of Medical Microbiology Hanzeplein 1, 9713GZ Groningen, The Netherlands*
[2] *University of Groningen, University Medical Center Groningen, Department of Radiology, Medical Imaging Center, Hanzeplein 1, 9713GZ Groningen, The Netherlands*
[3] *University of Groningen, Stratingh Institute for Chemistry, Nijenborgh 4, 9747 AG Groningen, The Netherlands*

## 35.1 Introduction

Since the beginning of the twentieth century, initiated with the seminal discovery of sulfonamides [1] by Domagk, and penicillin by Fleming [2], the mass production and routine application of antibiotics have revolutionized modern medicine, changing the therapeutic paradigm. Antibiotics enabled the execution and became essential for many medical interventions, such as organ transplantations, joint replacement surgery, and stem cell therapy [3]. However, the emergence of antimicrobial resistance (AMR) undermines all these therapeutic accomplishments, and it has become one of the most important public health threats of our century [4]. It is forecast that, by 2050, 300 million premature deaths and a loss of up to $100 trillion to the global economy may occur if the current spread of AMR is not effectively controlled [5]. Moreover, since 2007, no novel antibiotics classes have been brought to the market. Today, there are 22 classes of antibiotics, most of which were discovered between the 1930s and 1960s. The world's capacity for antibiotic discovery is thus seriously falling behind compared to the rate at which bacterial resistance emerges and spreads in hospitals and the community [6].

The emergence of AMR can be attributed to both the microbes and humans. Spontaneous mutations in bacterial genomes with subsequent inheritance by the following generations, and horizontal gene transfer of resistance genes between different bacterial species are key microbial mechanisms leading to AMR and facilitating its spread [7]. Regarding the human role in AMR, the world-wide overuse of antibiotics, be it for use in human healthcare, livestock farming, or agriculture, is a major problem, because prolonged exposure provides resistant microbes with a selective advantage [3].

*Molecular Photoswitches: Chemistry, Properties, and Applications*,
First Edition. Edited by Zbigniew L. Pianowski.


Another major challenge imposed by the currently available antibiotics is related to their side effects. Most types of antibiotics target a broad spectrum of microorganisms and, therefore, their administration affects bacterial communities in and on the human body as a whole, regardless of their pathogenic, mutualistic, or commensal properties [8]. In particular, some antibiotics have harmful effects on the gut microbiome, which creates a niche for opportunistic bacteria and pathogens, eventually leading to so-called dysbiosis and gut disorders. In turn, this may deregulate the immune system, leading to possible autoimmune or metabolic diseases [9]. In addition, several antibiotics display nephro- or ototoxicity, while others may elicit allergic responses [10]. Thus, to tackle these issues, there is a pressing need for the development of new antimicrobials with increased specificity for the site of infection and with fewer side effects. This need can be met by antimicrobial compounds with properties that can be specifically modulated or activated in a targeted area of infection.

## 35.2 Antimicrobial Photopharmacology

Most challenges associated with harmful antibiotic side effects and the emergence of resistance in bacteria stem from the same problem: the activity of the antibiotic outside the site of infection. Besides the adverse effects in the human body, *vide supra*, the activity of antibiotics released into the environment is also harmful. This is underscored by the finding that accumulation of antibiotics in surface fresh waters can be linked to the spread of resistance [11]. Therefore, methods that allow focusing of the antibacterial activity of new drugs exclusively to infected body sites offer a potential means to tackle these challenges. In principle, this can be achieved through the application of bioactive molecules that react to an external stimulus by reversibly altering their potency. In recent years, through the advent of photopharmacology [12–15], light has emerged as a preferred stimulus for external drug activation. Light is largely orthogonal to biological systems, and thus allows for the selective activation of photoresponsive molecules with unparalleled spatial and temporal resolution [16]. Recent developments in clinical instrumentation also enable minimally invasive delivery of light even deep within the tissues [17].

Photopharmacology relies on the introduction of photoresponsive moieties (such as molecular photoswitches) into the structure of bioactive molecules. This results in compounds that are both bioactive and photoactive, and the reversible switching between their photoisomers influences the molecular properties that are key to the drug potency, such as structure and polarity. This often enables switching between more and less active forms and, thus, connects the therapeutic effect to light irradiation in a spatially and temporally controlled way. In recent years, many examples of photopharmacological agents have been described, focusing on applications in vision restoration [18], neuronal transmission [19], chemotherapy [20], and antibiotic therapy, among others.

The use of photopharmacological antibiotics can be envisioned along two possible scenarios, presented in Figure 35.1. The first scenario relies on the use of T-type

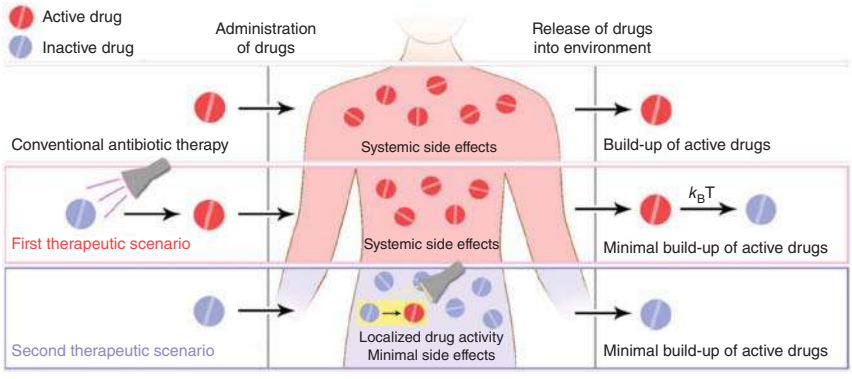


**Figure 35.1** Therapeutic scenarios enabled by photopharmacology to tackle the problem of antibiotic side effects and the development of bacterial resistance. In **conventional antibiotic therapy** (top), an active substance administered to the patient is systemically active and retains potency after leaving the body. The **first therapeutic scenario** in photopharmacological applications envisions light activation of the photoswitch-modified antibiotic prior to administration and then, by taking advantage of the back-isomerization of the photoswitch, loss of antibiotic potency by the time it is excreted. The **second therapeutic scenario** relies on local reversible activation of the photopharmacological agent inside the patient's body, thereby minimizing the side-effects. Source: Wegener et al. [21].

photoswitches that feature a metastable isomer and that are incorporated into bioactive molecules in such a way that this isomer is the more potent one. With these properties, the light-controlled drug can be transiently activated by irradiation prior to the administration to the patient, and it subsequently loses its activity due to thermal relaxation of the photoswitch to the less potent, thermodynamically stable form. This ensures that the active substance does not accumulate in the environment, potentially preventing the development and spread of resistance. In the first scenario, the key property of the photoswitch is the half-life of its metastable form, which should be in the same order of magnitude as the biological half-life of the drug. On the other hand, the wavelength (energy) of light used for activation is of less concern, as the activation happens before the administration.

The second therapeutic scenario (Figure 35.1) envisions the local activation of the antibiotic inside the patient's body, aiming to not only tackle the problem of resistance, but also to prevent any harmful side-effects. The key challenge here stems from the opacity of the human body to most energies of light in the UV-visible spectrum. Therefore, to enable this scenario, it is necessary to use molecular photoswitches that respond to irradiation with red/near-infrared (NIR) light, which penetrates deepest into the tissue (≈1 cm) and does not exhibit the phototoxicity that is characteristic for the more energetic UV light. Of note, deep-seated infections inside the human body can only be accessed by using a fiber-optic technology, which can reach infections at endoscopically accessible regions of the anatomy (e.g. the ears, nose, throat, gastrointestinal tract, lungs, urinary tract, or bowel) [22].

The first antibiotics that respond to light were designed by employing photocleavable protecting groups (PPGs) – moieties that undergo light-induced, irreversible

bond cleavage. This idea has emerged already in 2000 [23], and many other systems based on PPGs have followed since then [24–26]. However, these designs, while allowing for antibiotic (in)activation or orthogonal activation of multiple antibiotics, suffer from a lack of reversibility and, thus, they do not conform to the therapeutic scenarios presented in Figure 35.1.

## 35.3 Photoswitchable Small-Molecule Antibiotics

The development of photoswitchable small-molecule antibiotics has so far taken structural inspiration from a few privileged classes of antimicrobials. Here, we first introduce these classes and the respective challenges associated with them, and we discuss general methods for the evaluation of their efficacy. This is followed by a systematic introduction to the published examples of photoresponsive systems.

Since the 1920s, various synthetic and natural antibiotics were discovered, and they have become essential in today's healthcare. The discovery of the fluoroquinolones was one of the great milestones in science [27]. This class of antibiotics has a broad-spectrum activity against Gram-positive and -negative bacteria. Their ability to enter human cells via porins, which allows the elimination of intracellular pathogens, makes the fluoroquinolones very interesting antimicrobials. Fluoroquinolones (e.g. ciprofloxacin and norfloxacin; Figure 35.2) exert their antimicrobial action via the inhibition of homologous type II topoisomerases, DNA gyrase, and DNA topoisomerase IV. These enzymes are essential in replication, transcription, and repair of the bacterial DNA. Thus, when they are inhibited by an antimicrobial agent, it is expected that the bacterial growth is blocked [28]. The great success of fluoroquinolones is attributed to their good bioavailability after oral administration, relatively low toxicity, and favorable pharmacokinetics. However, with the increasing use of this class of antibiotics, both in human and veterinary medicines, resistance toward these agents started to emerge. The resistance to fluoroquinolones is a consequence of spontaneous mutations that may occur either in genes encoding the gyrase subunit A, or in the porin genes of Gram-negative bacteria. Mutations in the gyrase subunit A lower the affinity of this enzyme for fluoroquinolones. In contrast, porin mutations prevent the passage of these antibiotics through the Gram-negative bacterial outer membrane, allowing for efflux mechanisms to actively expel the drugs [29].

Another broad-spectrum antibiotic is trimethoprim (TMP; Figure 35.2), which is mainly used in the treatment of urinary tract infections. The administration of this antibiotic is normally done in combination with sulfamethoxazole to reduce the development of resistance. Moreover, both antibiotics have synergistic effects, since they both interfere with bacterial folic acid synthesis [30]. TMP inhibits bacterial growth by acting as a competitive inhibitor of dihydrofolate reductase (DHFR), which converts dihydrofolic acid into tetrahydrofolic acid (THF). THF is an essential cofactor in the synthesis of amino acids and purines [31]. Of note, bacterial and human DHFR are very different enzymes, and TMP is a selective inhibitor for the bacterial one. Unfortunately, also this antibiotic is plagued by resistance, which is

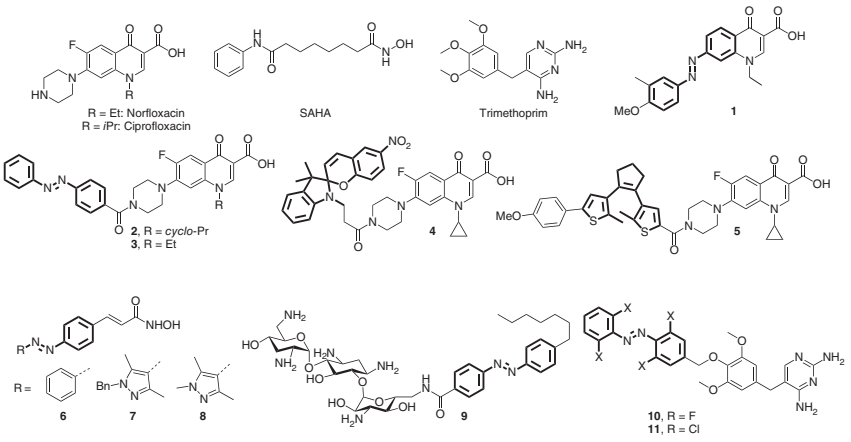


**Figure 35.2** Structures of photoswitchable antibiotics and the antimicrobial agents that inspired their design. Molecular photoswitches are highlighted in bold.

either due to the production of an altered DHFR that lacks the capacity to bind to TMP [32], or to overproduction of the normal DHFR [33, 34].

Polyamines are essential cationic compounds that act as virulence factors of important human bacterial pathogens, such as *Pseudomonas aeruginosa*, and influence their growth [35]. However, homeostasis of the polyamine levels is necessary since, in excess, polyamines become toxic to the bacteria. Therefore, polyamine-producing bacteria are able to acetylate these compounds, which lead to their quick excretion and degradation, and to deacetylate them for recycling [36]. Histone deacetylase-like amidohydrolases (HDAH) and acetylpolyamine amidohydrolases (APAHs) are homologues of the human histone deacetylase (HDAC), which are responsible for the deacetylation of acetylated polyamines. These enzymes are promising targets for antimicrobial therapy, since their inhibition can dysregulate the levels of polyamines and, therefore, impair the bacterial growth and virulence. However, only few in vitro studies were conducted so far [37–39] and none reported specific HDAH and APAH inhibitors. Nevertheless, suberanilohydroxamic acid (SAHA, Figure 35.2), a US Food and Drug Administration-approved chemotherapeutic agent that inhibits HDACs, was also able to inhibit both HDAH and APAH [37–39]. Accordingly, Krämer et al. reported that the inhibition of APAHs had an inhibitory effect on the growth of *P. aeruginosa* under glycose starvation conditions [38].

The efficacy of an antimicrobial drug depends on the susceptibility of the bacteria and its propensity to elicit bacterial resistance. The golden standard in determining the susceptibility of bacteria to drugs is the minimum inhibitory concentration (MIC), i.e. the lowest concentration of an antimicrobial that inhibits growth of a microorganism [40]. In addition to the MIC, it is also important to assess a drug's half-maximal inhibitory concentration (IC50), which is the concentration of a drug that causes 50% inhibition of a given biological process or component [41]. Both MIC and IC50 are essential parameters in determining the antimicrobial efficacy

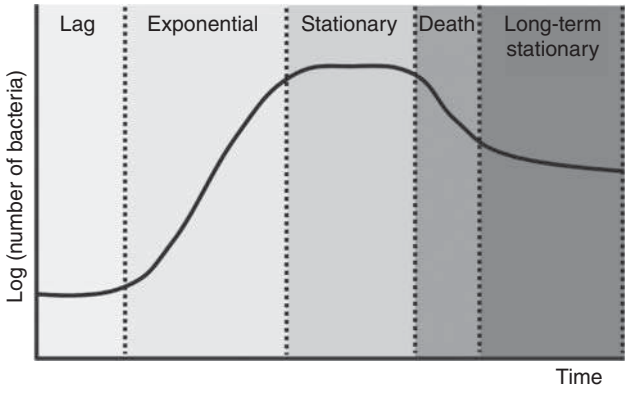


**Figure 35.3** Schematic representation of the five different phases in a typical bacterial growth curve.

of a drug but, for determining the development of susceptibility and resistance toward an investigated drug, it is also important to take the bacterial growth stage into account [42]. A typical bacterial growth curve consists of five distinct phases (Figure 35.3): the lag phase (i.e. the delay before exponential growth); the exponential phase (characterized by a constant rate of cell division); the stationary phase (where the population no longer expands due to nutrient limitation or otherwise unfavorable conditions); a death phase (where cells lose viability and lyse); and a long-term stationary phase (which can last for years) [43]. The important phase for assessing bacterial resistance to a drug is the lag phase, since in this phase the bacteria are still adapting to the new environment and unfold stress-responsive mechanisms to resist the killing by antibiotics [42]. Extended bacterial lag phases are closely related with the potential of the respective bacteria to develop tolerance for an antibiotic and to persist in its presence.

Photoswitchable antibiotics (Table 35.1) are characterized by their UV–vis spectra, in particular, the wavelengths that are used for switching between the two forms ($\lambda_1$, $\lambda_2$). Under irradiation, a kinetic equilibrium between the isomers develops, known as the photostationary state (**PSS**), with a certain distribution of the two forms (photostationary state distribution (**PSD**), expressed in the table as the ratio between the stable and metastable isomers). Once the irradiation ceases, the system usually returns to the thermodynamically more stable isomer, and this process proceeds with a certain **half-life**. The assessment of the antimicrobial potency of photoswitchable antibiotics is performed by measuring the **MIC** or **IC50** values usually for thermally adapted and PSS samples on a chosen **biological target**, including the bacteria *Escherichia coli*, *Micrococcus luteus*, *Staphylococcus aureus*, *P. aeruginosa,* and the enzyme amidohydrolase from *P. aeruginosa*. Successful designs show high potency (low MIC or IC50) and high-**fold difference** between the isomers, preferably with the thermally unstable isomer being the more potent one.

The first photoswitchable antibiotic, dating back to 2013, was based on the quinolone scaffold of ciprofloxacin (Figure 35.2). Recognizing the *N*-piperazine-

**Table 35.1** Photochemical and antibacterial properties of photoswitchable small-molecule antibiotics.

| Compound | $\lambda_1$ (nm) | PSD at $\lambda_1$ | $\lambda_2$ (nm) | PSD at $\lambda_2$ | Half-life | Biological target | MIC thermal (μM) | MIC PSS $\lambda_1$ (μM) | Fold difference |
|---|---|---|---|---|---|---|---|---|---|
| **Ciprofloxacin**[44] | — | — | — | — | — | *E. coli* | 0.38 | — | — |
| **Norfloxacin**[44] | — | — | — | — | — | *E. coli* | 0.39 | — | — |
| **TMP**[45] | — | — | — | — | — | *E. coli* | 1.7–6.9 | — | — |
| **1** [46] | 365 | 11:89 | nd | nd | 2.1 h | *E. coli* | >170 | 42 | >4 |
| | | | | | | *M. luteus* | 42 | 5 | 8 |
| **2** [47] | 365 | 39:61 | nd | nd | 4 h | | 0.25 | 0.50 | 0.5 |
| **3**/αCD[48] | 365 | 17:83 | WL | 84:16 | 58 h | *S. aureus* | 4.95 | 2.47 | 2 |
| **4** [47] | 365 | 18:82 | nd | nd | 17 h | *E. coli* | 1.25 | 0.625 | 2 |
| **5** [44] | 254 | 20:80 | >402 | >97:3 | bistable | | 44 | 2.7 | 16 |
| **6** [39] | 365 | 14:86 | 532 | 74:26 | 12.9 h | Amido-hydrolase from *P. aerugi-nosa* | 2.0[a)] | 0.21[a)] | 10 |
| **7** [39] | 365 | 5:95 | 532 | 93:7 | 17.8 h | | 0.53[a)] | 0.27[a)] | 2 |
| **8** [39] | 365 | 3:97 | 532 | 93:7 | 19.4 h | | 0.77[a)] | 0.13[a)] | 6 |
| **9** [49] | 365 | 39:61 | nd | nd | nd | *S. aureus*<br>*P. aerugi-nosa* | 10<br>20 | 10<br>5 | 1<br>4 |
| **10** [21] | 527 | 11:89 | 400 | 88:12 | >24 h | *E. coli* | 10 | 5 | 2 |
| **11** [21] | 652 | 13:87 | 400 | 87:13 | >24 h | | >80 | 10 | >8 |

a) in case of compounds **6–8**, their potency is expressed as IC50 – the concentration at which half of the enzyme activity is inhibited.

For the definition of terms and abbreviations, see the text in page 7.

substituted aromatic ring as a potential site to introduce an azobenzene photoswitch, Velema et al. [46] designed molecule **1** (Table 35.1, Figure 35.2) after careful optimization of the structure aimed at maximizing the difference in potency between the isomers and obtaining the *cis* isomer as the more potent one.

Upon irradiation with $\lambda = 365$ nm light, the potency of compound **1** against *M. luteus* increased eightfold and against *E. coli* >4-fold (Figure 35.4a,b). With a half-life of 2.1 hours, it was a good first design for use in the first therapeutic scenario (Figure 35.1), where the irradiation with UV light is not an obstacle and half-lives of the active isomer in the hour range are needed. This potential application was tested in an experiment (Figure 35.4c) where the irradiated compound **1** was allowed to thermally revert to the less potent *trans* isomer for increasing amount of time. While the freshly irradiated antibiotic showed high potency, after three hours of thermal relaxation, it had lost its antimicrobial properties.

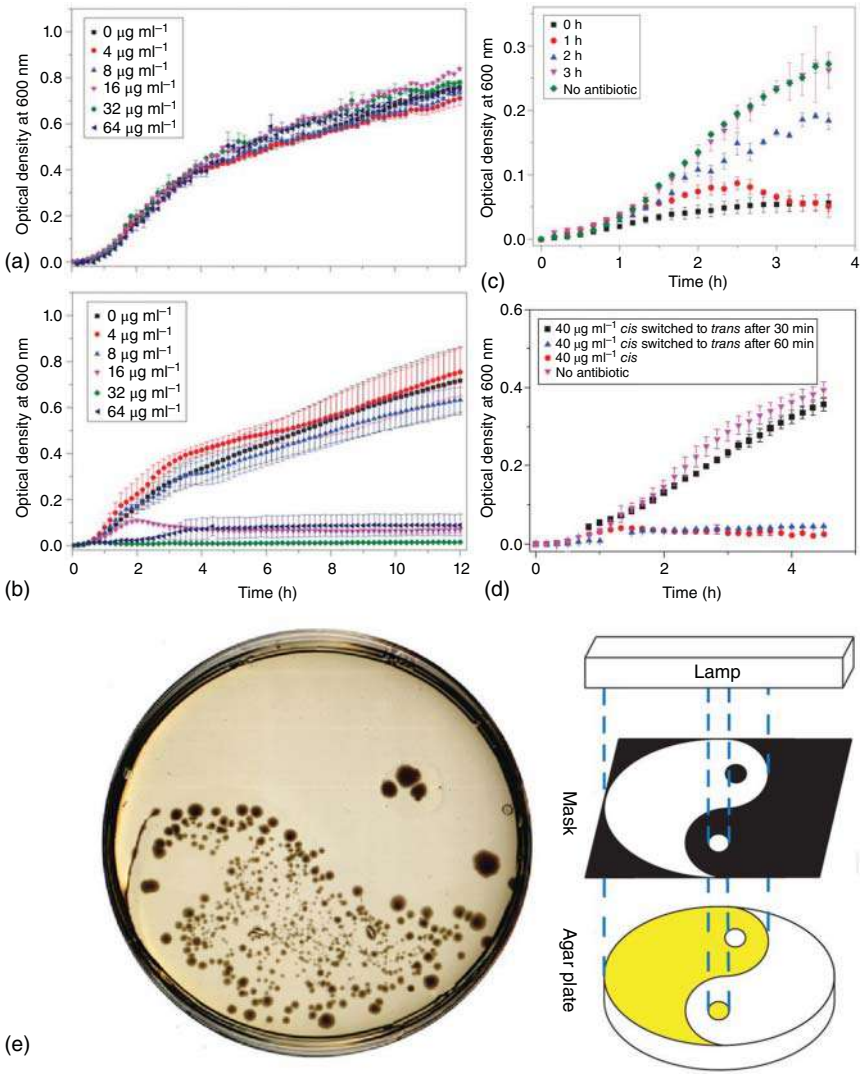


**Figure 35.4** Evaluation of the antibacterial activity of compound **1** using *E. coli*. (a, b): Growth curves of bacteria treated with increasing concentrations of compound **1**, thermally adapted (a) or irradiated at $\lambda = 365$ nm (b). (c): Growth curves of bacteria treated with compound **1** that had been thermally adapted for 0–3 hours after light activation. (d): The influence of bacterial exposure time to the active antibiotic, showing that the antibiotic had to be present in the exponential growth phase (>30 minutes) to affect the bacteria. (e): patterning experiment where light was applied to the part of a dish prior to the streaking of the bacteria, allowing for selective preservation of growth in the non-irradiated areas. Source: Velema et al. [46].

Furthermore, the use of compound **1** highlighted another important feature of photoswitchable bioactive molecules, namely the possibility to switch off their activity on demand by irradiation (in this case, with white light). Interestingly, this allowed for unprecedented experiments on the influence of the bacterial exposure time to antibiotics (Figure 35.4d), due to reversible temporal control over potency. Finally, bacterial patterning with light (Figure 35.4e) provided the first proof of spatial control using light.

In the follow-up report, Velema et al. explored another strategy to incorporate a molecular photoswitch into the structure of quinolone antibiotics [47], inspired by the fact that the secondary amine in the piperazine group of quinolone antibiotics can be largely modified without affecting their potency [50]. Instead of substituting a part of the pharmacophore with a photoswitch, the light-responsive molecule was simply attached to the drug, facilitating the synthesis and enabling the evaluation of other photoswitches besides azobenzene. The conjugates with azobenzene and spiropyrane (Figure 35.2; compounds **2** and **4**, respectively) were evaluated by the group of Feringa, and the diarylethene analogue (Figure 35.2; compound **5**) was presented later by Li et al. [44]. In all the cases, photocontrol over antibacterial activity was achieved (Table 35.1), and it was the most pronounced for compound **5**, showing 16-fold activation upon irradiation with $\lambda = 254$ nm light. This activation was attributed to the diminished flexibility of the closed diarylethene structure, which translates to better binding to the DNA gyrase.

Another strategy for photopharmacological activation was presented by Wang and coworkers [48] using compound **3**, a close structural analogue of azobenzene-appended quinolone **2** [47]. All photoswitchable antibiotics show potency in their "inactive" form, even though it is highly increased in their active form. Thus, to completely inhibit the antimicrobial activity of the inactive form, a method based on the well-known phenomenon of differential binding of the two forms of the azobenzene molecule to α-cyclodextrin (αCD), which would increase the difference between the photoisomers, was investigated. Since the *trans* isomer binds better, it can potentially be sequestered by αCD when the latter is added to the bacterial cultures. Upon switching, the *cis* isomer was expected to be removed from the complex and to show antimicrobial activity. Indeed, this predicted trend was reproduced experimentally: *trans*-**3** was shown to bind to αCD with binding constants in the $10^5$ range, and irradiation resulted in increased antibacterial potency, albeit that the difference was moderate. Nevertheless, this example [47] provides an alternative strategy to the photocontrol of molecule bioactivity that can be further explored, for example by taking advantage of orthogonal photoswitching systems where two light-responsive molecules can be controlled in parallel [51], e.g. one for αCD binding and the other for binding to the target.

Fuchter and coworkers focused on another target for antibiotic activity [39], relying on their discovery that inhibition of bacterial histone-deacetylase-like amidohydrolases influences the growth of *P. aeruginosa* strains under glucose starvation [38]. By modification of the SAHA-derived (Figure 35.2) structures reported earlier as histone deacetylase inhibitors [52], compounds **6**–**8** (Figure 35.2) were synthesized and evaluated, showing promising, sub-micromolar IC50 values for the inhibition of

target enzymes (Table 35.1). For initial designs based on a classical azobenzene scaffold (such as compound **6**), the *trans* isomer was up to 10-fold more potent. To test if the sub-optimal PSD values (85–90% *cis* under $\lambda = 365$ nm light and 74–82% *trans* under $\lambda = 532$ nm light) were limiting the influence of photoswitching on potency, the authors evaluated isosteric stilbene-based inhibitors. Such photoswitches need higher energy light for isomerization, but both forms are thermally stable and can be isolated and tested separately. The higher potency difference observed for stilbenes inspired the use of arylazopyrazoles as alternative molecular photoswitches, leading to compounds **7** and **8**. For these compounds, PSD values in the >90% range were obtained, with nanomolar potencies, albeit that only a 6-fold difference in bioactivity was observed with the *cis* isomer being more active.

Finally, the structural aspects of the molecular designs were studied in more detail through X-ray crystallography using complexes between the target proteins and compounds **6** and **8**. These investigations, very valuable for the photopharmacological field, revealed that the inhibitors modified with a photoswitch retain their crucial binding to the active-site $Zn^{2+}$ ion (Figure 35.5a). Furthermore, the inner phenyl group of the azobenzene was able to form favorable π-stacking interactions with two phenylalanine residues in the active site (Figure 35.5b). However, an important difference between azobenzene **6** and arylazopyrazole **8** is the bulkier nature of the latter, which was suggested to result in the twist of the outside ring out of planarity in the case of compound ***trans*-8** (Figure 35.5d). For compound ***trans*-6**, a preferred planar structure could be accommodated (Figure 35.5c), leading to better binding.

An alternative approach to control the activity of antibiotics with light is to modulate not their binding to the target, but the crossing of biological membranes. Fridman and coworkers presented photoswitchable cationic amphiphiles (such as compound **9**, Figure 35.2) [49], based on the structure of tobramycin, an aminoglycoside antibiotic that is positively charged under physiological conditions. The sample irradiated at $\lambda = 365$ nm, which contained 61% of the ***cis*-9** isomer, proved to be four times more potent on *P. aeruginosa* than the thermally adapted one (Table 35.1), with the differences being even more pronounced upon bacterial growth quantification (Figure 35.6a,b). Furthermore, while bacteria treated with

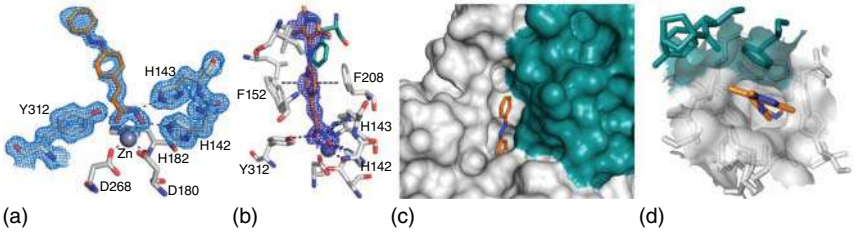


**Figure 35.5** Structural aspects of the binding of compounds **6** and **8** to *Bordetella/Alcaligenes* HDAH. (a): Key interactions of the hydroxamate group of compound **6** with the catalytic center. (b)**:** Geometry and interactions of compound **8** within the active site. (c and d): top view with the surface representation of the protein for the binding of compounds **6** (c) or **8** (d). Source: Weston et al. [39].

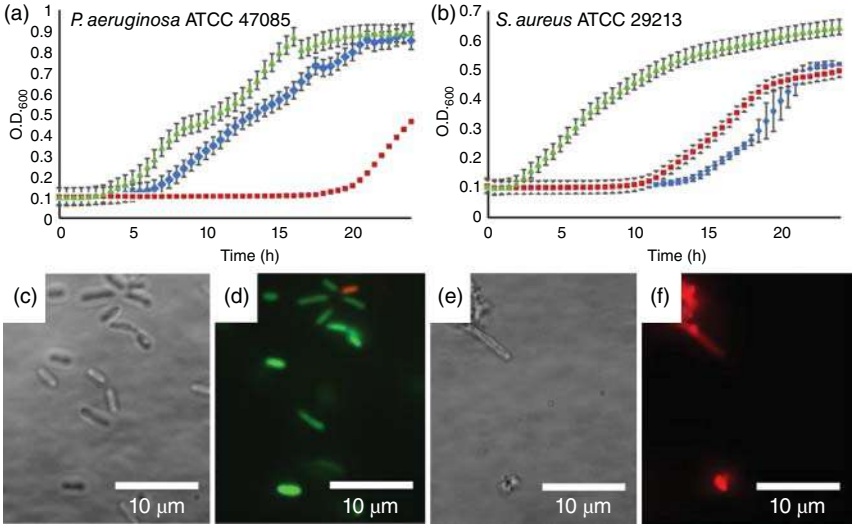


**Figure 35.6** Photocontrol of bacterial growth using the switchable amphiphilic tobramycin derivative **9**. (a, b)**:** growth curves of *P. aeruginosa* (a) and *S. aureus* (b) treated with mixtures containing mostly ***trans*-9** (blue) or ***cis*-9** (red); the growth of untreated bacteria is shown in green. (c–f): bright field (c, e) and fluorescence (d, f) images of *E. coli* treated with mostly ***trans*-9** (c, d) or ***cis*-9** (e, f). Fluorescence microscopy images were recorded upon bacterial staining with the membrane stability-indicative SYTO9 dye (green fluorescence) and the membrane damage-indicative propidium iodide dye (red fluorescence). Source: Salta et al. [49].

***trans*-9** showed indications of reduced cell division (Figure 35.6c), they still stained with the SYTO9 dye that binds to an intact cell membrane, indicating that this molecule did not alter membrane integrity (Figure 35.6d). Conversely, bacteria treated with the irradiated compound **9** showed almost no growth (Figure 35.6e), and they stained with propidium iodide (Figure 35.6f), which is indicative for vast membrane damage and loss of the proton-motive force. Altogether, the differences in potency between photoisomers of compound **9** were attributed to their different interactions with the bacterial cell membrane, providing a proof-of-principle for another approach in antibacterial photopharmacology.

All the photoswitchable antibiotics described up until this point require UV light ($\lambda = 254–365$ nm) for switching to active or inactive states, which limits their application potential in therapeutic settings that require local activation in the patient's body (Figure 35.1). Therefore, much effort has been devoted to developing molecular photoswitches that respond to visible/NIR light irradiation to enable safer operation and deeper tissue penetration [53–55]. Among those, the *tetra-ortho*-substituted azobenzenes have found the most applications in photopharmacology.

In the context of reversible antibiotic activation, Wegener et al. explored the modification of TMP (Figure 35.2) with *tetra-ortho*-fluoro- and *tetra-ortho*-chloro-azobenzene, leading to compounds **10** and **11** (Figure 35.2), respectively [21]. In both cases, the irradiated samples containing mostly the *cis* isomers were more potent than the thermally adapted ones (Table 35.1). Compound **10** could be

activated with green light ($\lambda = 532$ nm), enabling also the in situ activation in the presence of bacteria, without causing non-specific, light-induced damage to the cells (Figure 35.7a). However, only twofold increase in potency was observed upon irradiation. Much more promising results were obtained for compound **11**, which showed >8-fold increase in potency upon red-light ($\lambda = 652$ nm) irradiation (Table 35.1). Light of this energy falls into the so-called therapeutic window, in which the transparency of the human tissues is the largest, thus enabling their use in the second therapeutic scenario (Figure 35.1), where the antibiotics are activated inside the body. The use of visible light for switching the antibiotic in both directions was shown by first using red light for activation, followed by inactivation with violet light ($\lambda = 400$ nm), which resulted in the expected loss of potency (Figure 35.7b). However, it must be stated that the activation with red light was not efficient and irradiation times in the order of hours were needed. Nevertheless, this research represents the first application of deep-tissue-penetrating red light for the activation of a photopharmacological antibacterial agent.

In summary, the development of small-molecule antibacterial photopharmacological agents has so far focused on a small number of privileged targets (mostly fluoroquinolone antibiotics). With these designs, however, it was already possible to explore direct and indirect (e.g. through αCD complexation) photoactivation modes and the use of different photoswitch types. Azobenzenes are currently the most used photoswitches, especially since they can be implemented in visible-light-responsive systems, which allow deeper tissue penetration.

## 35.4 Photoswitchable Peptidic Antibiotics

Antimicrobial peptides (AMPs) are a promising class of compounds with an extraordinary broad-spectrum activity against Gram-positive and -negative bacteria, fungi, and even viruses. Importantly, AMPs generally present low susceptibility to bacterial resistance and protease digestion [56]. Gramicidin Soviet, usually referred to as Gramicidin S (GS), was one of the first peptide antibiotics discovered [57]. Its cationic cyclic structure forms an asymmetric macrocycle, based on two different sides with hydrophobic and cationic faces, respectively (Figure 35.8a). This feature allows GS to persist in solution and in a membrane-bound state [59]. GS has excellent antimicrobial properties against a wide range of Gram-positive bacteria [60] and, if combined with other antibiotics, it has a synergistic effect in the eradication of Gram-negative bacteria [61]. However, this antibiotic can only be applied topically due to its hemolytic activity [57]. Importantly, the mechanism of action of GS gives this antibiotic the biggest advantage, since no bacteria are known to have developed resistance to it with exception of the *Bacillus brevis* strains that naturally produce GS. The mode of action of GS relies on the permeabilization of phospholipid bilayers by forming transient pores (Figure 35.8b), which depolarize the membrane [62]. This depolarization disturbs the cellular homeostasis and leads to cell lysis. Thus, a possible resistance mechanism acquired by bacteria against GS becomes less likely, since multiple nonlethal changes in the target cell need to occur.

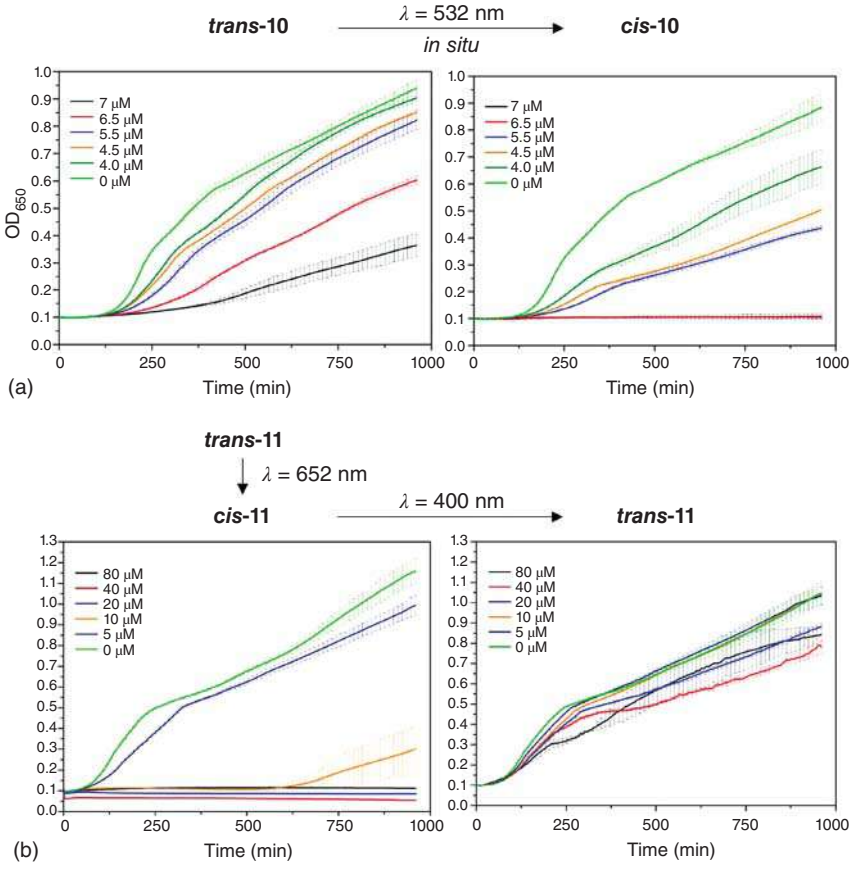


**Figure 35.7** Controlling the growth of *E. coli* with visible light-responsive photopharmacological agents. (a): bacterial growth curves in the presence of compound **10** before (left) and after (right) *in situ* irradiation with green light. (b): bacterial growth curves in the presence of compound **11**, which was activated in stock solution with red light (left) and subsequently inactivated with violet light (right). Source: Wegener et al. [21].

Photocontrol of peptide conformation and activity [63] is an established approach of using light-responsive molecules for manipulating biological systems [64]. In the context of antibacterial photopharmacology, this approach has been taken in modifying GS (Figure 35.8) by introduction of diarylethene [58, 65] and azobenzene [66] photoswitches into the cyclic peptide backbone.

The first reports on photoswitchable peptidic antibiotics date back to 2014. The molecular design reported by Babii et al. incorporates a diarylethene molecular photoswitch into the structure of GS (compound **12**, Figure 35.8c) [65]. While diarylethenes show less defined structural changes upon photoswitching as compared, e.g. to azobenzenes, their incorporation into cyclic peptide structures offers the possibility to influence the ring size, strain, and flexibility of the antibiotic, and these effects will strongly differ for the open and closed isomers of the switch [65]. Initial screening of the position in which the switch was incorporated into

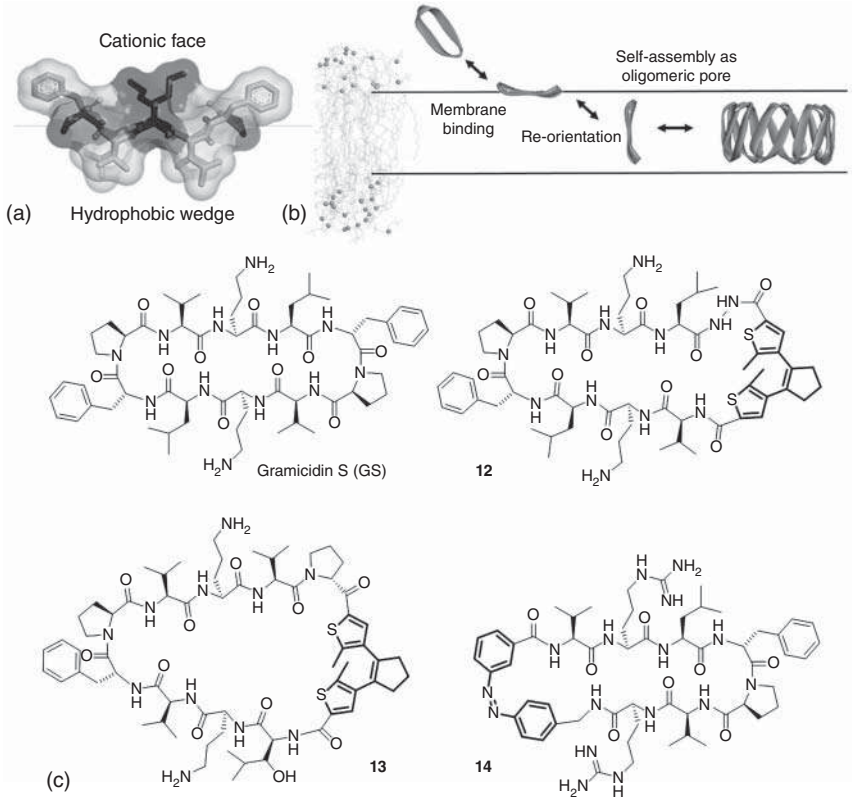


**Figure 35.8** GS-based photocontrolled peptidic antibiotics. (a): Molecular model of GS with highlighted amphipathicity of the two faces of (light gray: hydrophobic; dark gray: cationic). (b): Mechanism of GS pore formation in lipid bilayers. (c): Molecular structure of GS and photoswitchable peptidic antibiotics **12**–**14**. Molecular photoswitches are highlighted in bold. Source: Babii et al. [58].

GS revealed compound **12** as the preferred design (Table 35.2). The open form of this compound showed high potency against several *Staphylococcus* strains. Irradiation at $\lambda = 256\,\text{nm}$ provided up to 80% of the closed isomer, which in the case of diarylethene switches is thermally stable, and could be purified using RP-HPLC. The closed isomer proved to be four to eight times less potent than the open isomer, but it could be transformed into the more active form by irradiation with green light ($\lambda = 530\,\text{nm}$). The difference in potency has been exploited in a bacterial patterning experiment, once again highlighting the spatial control aspects in photopharmacology (Figure 35.9c).

The difference in potency between the isomers was explained based on the similarities that they show to the parental GS molecule with respect to the distribution of hydrophobic and hydrophilic regions (Figure 35.9a,b). In line with the experimental observations, the calculated hydrophobic moment of the open form was closer in value to that of GS, and the amphiphilicity of the closed form was less similar to that of the original antibiotic. These differences in amphiphilicity have been attributed

**Table 35.2** Photochemical and antibacterial properties of photoswitchable peptidic antibiotics.

| Compound | $\lambda_1$ (nm) | PSD at $\lambda_1$ | $\lambda_2$ (nm) | PSD at $\lambda_2$ | Half-life | Biological target | MIC PSS $\lambda_2$ (μM) | MIC PSS $\lambda_1$ (μM) | Fold difference |
|---|---|---|---|---|---|---|---|---|---|
| **12** [65] | 256 | <1:99 | 530 | >99:1[a)] | bistable | *S. aureus* | 3.2 | 26 | 8 |
| | | | | | | *S. epidermidis* | 6.4 | 52 | 8 |
| | | | | | | *S. xylosus* | 6.4 | 26 | 4 |
| | | | | | | human red blood cells | 5.2 | 58 | 11 |
| **13** [58] | 256 | <1:99 | 530 | >99:1 | >99:1[a)] | *B. subtilis* | 2 | 13 | 6.5 |
| | | | | | | *E. coli* | 100 | 200 | 2 |
| | | | | | | human red blood cells | 56 | 351 | 6.3 |
| **14** [66] | 352 | 29:71 | 405 | 75:25 | 4.2 d | *S. aureus* | 116 | 29 | 4 |

a) The pure closed isomers of compounds **12** and **13** were obtained by RP-HPLC purification from the irradiated samples.

to the changes in the conformation and flexibility of the cyclic peptide backbone, which influences the relative positioning of the side chains.

An important restriction to the use of GS, which limits it to topical application only, is its strong hemolytic activity [57]. Unfortunately, compound **12** showed toxicity toward human red blood cells at similar concentrations to its MIC against bacteria (Table 35.2), inspiring the further development toward compound **13** (Figure 35.8c) [58]. Careful optimization of photoswitch attachment and the nature of amino acids present in the cyclic peptide revealed a beneficial influence of hydroxylated side chains and inspired the introduction of a hydroxyleucine residue. Compound **13** not only showed slightly increased antibacterial potency as compared to its precursor **12**, but also evoked damage to red blood cells at much higher concentrations, increasing the potential for application.

While diarylethenes, as P-type photoswitches, offer an important alternative to the often-used azobenzene switches, enabling control over molecular flexibility and bistable operation, they suffer from the need for high-energy UV light irradiation (254 nm). The introduction of azobenzenes into the backbone of GS was explored by Abell and coworkers [66], inspired by the known ability of *cis*-azobenzene to mimic the β-turn in β-hairpin structures [67], such as those of GS. Among the evaluated molecules, compound **14** showed the most promising properties, providing a fourfold increase in potency upon activation with UV light of $\lambda = 352$ nm, despite the fact that there was only a moderate difference in the ratio of isomers upon irradiation (Table 35.2). Molecular modeling and NMR spectroscopy studies attributed the

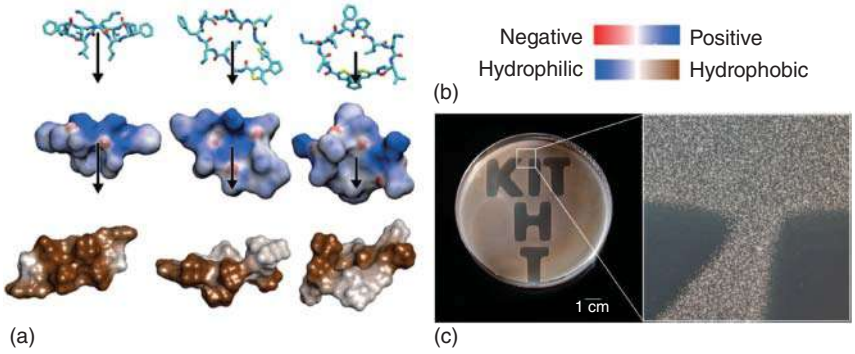


**Figure 35.9** The mechanism of action of diarylethene-modified cyclic peptide antibiotics based on GS. (a)**:** representative snapshots from molecular dynamics simulations of GS (left), ***open*-12** (middle) and ***closed*-12** (right). In the top panel, the amphiphilic molecules are aligned with their calculated hydrophobic moment vectors viewed from the side. The middle panel presents the solvent-accessible surfaces of the molecules with the electrostatic surface potentials. The lower panel shows Kyte–Doolittle hydrophobicities, viewed from the perspective of the membrane plane. (b): scales of charge distribution and hydrophobicity corresponding to panel A. (c): Bacterial patterning by through-mask irradiation of compound **12**, demonstrated using *Staphylococcus xylosus*. Source: Babii et al. [65].

difference to the well-defined β-sheet/β-turn secondary structure of the *cis* isomer, which could not be adopted by its thermally stable counterpart.

In summary, incorporation of molecular photoswitches into cyclic peptide antibiotics represents a viable alternative approach to using small-molecule antibacterial agents. While dealing with larger and more complex molecules, this approach often relies on more subtle changes in structure, polarity, and dynamics that can be achieved upon photoswitching. This sets limits to the possibilities for rational design, but also provides great opportunities for exploring different photoswitches and activation modes.

## 35.5 Other Applications of Molecular Photoswitches in the Context of Bacterial Infections

Molecular photoswitches are also being used for the fight against bacterial infections in ways that extend beyond the traditional definition of antimicrobial photopharmacology, where a photoresponsive element is introduced into the antibiotic structure. Thus, photoswitches have, for example, found application in light-responsive drug-delivery systems, such as those based on hydrogels [68], which release bioactive compounds upon irradiation. The incorporation of photoswitches into the hydrogels enables the photo-control of the drug release on the infection site (second therapeutic scenario, Figure 35.1) [68]. These hydrogels are composed of non-toxic compounds, which makes them interesting drug-delivery systems for antimicrobial photopharmacology.

Another area of applications relates to the formation of bacterial biofilms. Biofilms are multi-layered structures of bacteria embedded in a matrix of proteins, DNA, and host components. All these substances, present in the biofilm matrix, create a favorable environment for bacterial cell-to-cell and cell-to-surface adhesion, which provides protection against the host immune system and most antimicrobial agents [69]. Biofilm formation is therefore one of the bacterial survival strategies that lead to AMR, since targeted antigens may be hidden and key ligands may be repressed [70]. Moreover, cells in biofilms can communicate through the secretion of molecules (auto-inducers) that control quorum sensing (QS), thereby facilitating bacterial persistence [71]. Most of the biofilm-associated infections derive from implanted medical devices. After a device is implanted, host tissues, cells, and pathogenic bacteria compete for attachment to the surface of the device. If the bacteria "win," they initiate the biofilm formation thereby acquiring resistance to antibiotics [72]. The current treatment of such implant-related infections involves removal of the implant with subsequent surgical debridement of the infected tissues and wounds. Unfortunately, such necessary interventions are associated with substantial morbidity and mortality. Thus, the development of anti-biofilm agents, which could interfere with the QS signals and therefore inhibit or disperse the biofilm, or the coating of implants with substances that could prevent the bacterial attachment, are highly required. Wilkinson and coworkers used surfactants, which are based on carbohydrates that play an important role in bacterial adhesion [73]. The photoswitchable carbohydrate-based surfactants showed the dose-, bacteria-, and photoisomer-specific biological activity, suggesting a selective mode of action. Moreover, it was also observed that these surfactants influence the motility and swarming of bacteria [73]. Photofluidization was also investigated by other researchers [74] to soften the surface of a glassy material with rapid *trans–cis–trans* isomerization cycles of azobenzene groups, exposed to multiple wavelengths of light simultaneously, and thereby inhibiting the bacterial attachment. It seems very unlikely that bacteria will develop adaptive mechanisms against the photofluidization effects due to its rapid mode of action. Furthermore, azobenzene-based bacterial QS inducers have been reported [75] and optimized [76] to show very high levels of practically "on–off" responses to light exposure.

## 35.6 General Discussion and Outlook on Related Technologies

The design of photoswitchable antimicrobials was mainly inspired by the structure of currently used antibiotics. Fluoroquinolones (Figure 35.10) have been, by far, the most explored ones in photopharmacology, which is due to their *N*-piperazine-substituted aromatic ring that allows the introduction of photoswitches without largely compromising the antimicrobial properties. Azobenzene is the photoresponsive molecule that was mostly used [46–48]. However, other photoswitches were also attached to the fluoroquinolones, such as the diarylethene, which induced the highest change in antimicrobial activity after irradiation [44]. Of note, comparisons of the efficacy of different photoswitches rely on their

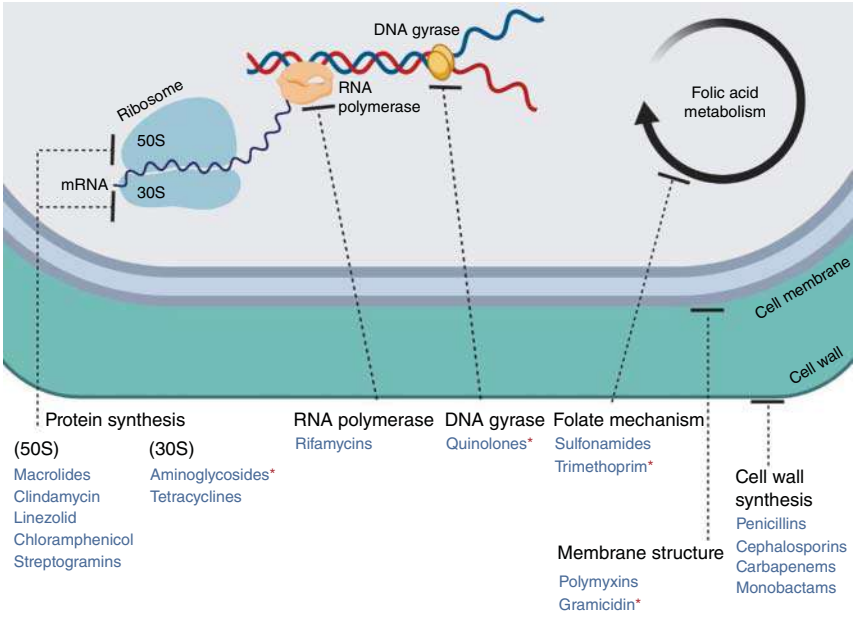


**Figure 35.10** Representation of the main targets for antibiotics. The antibiotics that inspired the design of photoswitchable variants are marked with*.

photo-conversion from an "inactive" form to the "active" form. It is also important though to emphasize that the MICs of "active forms" of most of the studied compounds are higher than the MICs of the antibiotics that inspired their design (Table 35.1). Nevertheless, the incremental changes in the MIC can be compensated by additional beneficial properties that the photoswitches can provide.

With the ambitious goal of developing drug combination treatments for infections caused by drug-resistant pathogens that overexpress efflux pump proteins, the synergistic effect between an antibiotic and an antimicrobial photoswitch was also explored in photopharmacology [49]. Tobramycin, an aminoglycoside that inhibits bacterial protein synthesis (Figure 35.10), was coupled to cationic amphiphilic photoswitches, which are well-known small-molecule-based membrane disruptors. Thus, the permeability induced by the cationic amphiphiles upon photo-conversion will disrupt the membrane and allow uptake of the antimicrobial agent through the membrane. Importantly, the possibility to modulate the membrane-disrupting effect of this type of antimicrobial agents allows the use of lower antibiotic concentrations, which reduces the toxic side effects related to these cationic amphiphiles.

Most of the commonly used antimicrobial photoswitches are activated by UV light, which makes their photoactivation only possible prior to administration due to the potential DNA damage caused by irradiation with UV light. However, in a clinical setting, the ideal scenario is the activation of a molecule inside the body (Figure 35.1), to minimize potential side effects. Thus, alternative photoswitches that can be activated by visible light, more importantly NIR light, were explored, to increase the penetration of the light into the infected tissue. *Tetra-ortho*-substituted

azobenzenes require lower energy excitation and were, therefore, studied in combination with TMP (Figure 35.10) [21]. However, the photo-conversion was not successful with red light *in situ,* and when it was performed before treating the bacteria, it was only efficient after a long period (hours) of light exposure. Chakrapani and coworkers also described a small molecule, which included a BODIPY-type PPG and which could be irreversibly activated by visible light at 470 nm to release a fluoroquinolone (levofloxacin) [77]. However, irradiation for 6 h was required to achieve complete growth inhibition of the bacteria and the photoconversion was not reversible.

AMPs are part of the first-line defense of the innate immune system against microbial attacks [78]. Their mode of action gives them advantages over other antibiotics, since resistance patterns are less likely to emerge. However, limited selectivity in the delivery of a peptide to its site of action and high hemolytic toxicity requires the design of novel approaches. Thus, photoswitches based on the AMP GS (Figure 35.10) have been explored, using diarylethenes and azobenzenes [58, 65]. With these photoswitches, modulation of the membrane polarization and, consequently, a reduction of GS-associated side effects was achieved, as well as the reversible photo-control of the secondary structure of this AMP and, hence, the binding affinity, aggregation, and folding properties [66].

It also has to be stated that, thus far, the development of photoresponsive antibiotics has largely been a trial-and-error endeavor, in which a chosen antibiotic was modified with a molecular photoswitch, leading to a series of molecules, which were then assayed and optimized. This process could be facilitated by more informed in silico design, along the lines of other medicinal chemistry projects, where docking and molecular dynamics studies enable the choice of a privileged ligand for a given protein target. However, this approach in photopharmacology is thus far challenged by the limited structural information on photoswitches, especially in their metastable states (such as *cis*-azobenzene) and by the flexibility of many of the switches in one of the forms.

### 35.6.1 Antimicrobial Photopharmacology and Photodynamic Therapy: Similarities and Synergies

A more clinically established light-dependent therapeutic avenue, already applied in a variety of pathologies, such as cancer, dermatological and ophthalmic diseases, is photodynamic therapy (PDT). The mechanism of action of PDT is based on the excitation of the photosensitizer with light of an appropriate wavelength, which results in intersystem crossing to the triple state, a further reaction with triplet molecular oxygen and the production of reactive singlet oxygen (Type II reaction). Another reaction that can take place (Type I reaction) relies on electron transfer from the photosensitizer's excited state to the molecular oxygen, producing superoxide anions, which can form hydrogen peroxide [79]. The discovery of photoantimicrobials for antimicrobial photodynamic therapy (aPDT) has accelerated since the early 1990s

after the emergence of the first drug-resistant infections [22]. aPDT has a broad spectrum in the treatment of infections caused by several microorganisms, such as bacteria, fungi, and viruses. Moreover, no resistance against aPDT by the microorganisms has been reported yet. Another important feature of aPDT relates to the particular properties of the photosensitizer. Ideally, the photosensitizer should be selective to the pathogen of interest with minimal damage to the host. The desired specificity has recently been accomplished by conjugating second-generation photosensitizers with biomolecular recognition motifs, such as carbohydrates, monoclonal antibodies, and bacteriophages. Additionally, the photosensitizer's absorption coefficient should be large in the visible spectrum, preferably in the long wavelength (NIR) region, because this will result in deeper penetration of the light into the infected tissue [80].

Although PDT does not strictly conform to the definition of photopharmacology due to the non-specific reactive oxygen species (ROS) damage that it relies on, it has been acknowledged as a source of inspiration for photopharmacology in the development of light-modulated drugs [12]. Therefore, some differences and similarities between these two light therapy-based approaches are hereby described. Of note, there are some disadvantages associated with PDT, which can relate to photopharmacology, but may also be potentially overcome by the latter. In particular, the systemic side effects (e.g. hypersensitivity, allergy, toxicity) upon intravenous administration of the photosensitizer have been limiting the clinical use of aPDT to topical applications. Photopharmaceuticals, after activation with light, can also cause adverse side effects while being cleared from the body. Nevertheless, efforts are being made to overcome such problems both in aPDT and photopharmacology. For aPDT, the solution relies on the development of targetable photosensitizers [81–83] to minimize their unpredictable distribution in easily light-exposed uninvolved tissues, such as the eyes and skin. Targeted aPDT would thus preclude phototoxicity and prolonged photosensitivity when treated patients are exposed to ambient light [84]. In photopharmacology, the implementation of reversible photochemical control of molecular entities, such as azobenzenes, spiropyrans, and diarylethenes, allows to switch off the respective antibiotic molecule in the body once it is no longer needed, thereby reducing the unwanted side effects [85]. The dependence of aPDT on the presence of molecular oxygen for the generation of ROS can also be a hurdle when treating biofilms. During the maturation of a biofilm, different microenvironments will be formed, such as oxygen- and substrate-rich zones on the surface of the biofilm and oxygen-depleted regions deep inside the biofilm, where so-called persister cells can develop [86, 87]. These persister cells have an important role in AMR, since their metabolic activity is low, making them less susceptible to the host immune system and the action of antibiotics. Thus, aPDT is generally limited to destruction of the cells on the surface of the biofilm, even though multiple cycles of aPDT treatment, or combination with antibiotics, may lead to the full eradication of the biofilm. On the other hand, photopharmaceuticals do not depend on the availability of oxygen or the presence of ROS scavengers [79], as is the case for aPDT. However, both aPDT and photopharmacology depend enormously on the delivery of light to the site of

therapeutic action. In photopharmacology, the best wavelengths to trigger isomerization are currently still in the UV range, which is only able to penetrate a few millimeters into the tissue and can cause mutations and burns. Thus, it is important to develop compounds that can be activated by light in the red and NIR wavelength range, allowing a deeper penetration into the tissue. Transdermal light delivery is the most approved procedure, but light does not penetrate efficiently into tissues, due to melanin pigmentation and the presence of light-absorbing molecules, such as heme and flavoproteins [79]. Consequently, the development of more sophisticated, smaller, and lighter light-delivery devices is currently being explored [88, 89]. New strategies to combine PDT and photopharmacology are being developed, such as the conjugation of photosensitizers with caged metal complexes, which include a photocleavable group on the ligand backbone [90]. However, studies related to this synergistic therapy with combined PDT and photopharmacology were, so far, only performed in relation to cancer diseases. There are no reports yet on the possible implementation of PDT and photopharmacology in the treatment of infectious diseases.

### 35.6.2 Antimicrobial Photopharmacology and Medical Imaging

Before initiating the appropriate medical treatment for fighting an infection, a rapid and accurate diagnosis is important. This is especially valid in case of light-activatable therapeutics, since the site of the irradiation must be identified through precise localization of the infection. Currently, the infection diagnosis relies on culture and/or molecular detection to identify the causative microbial species. This requires tissue biopsy for deep-seated infections, which can lead to morbidity and sampling error. Moreover, these traditional diagnostic approaches are costly and slow, which often leads to empiric infection management with broad-spectrum antibiotics [91]. The use of broad-spectrum antibiotics is not preferred as it makes the emergence of multi-drug-resistant bacteria more likely, which will complicate treatment and lead to worse outcomes. Thus, imaging modalities that could allow a reliable non-invasive detection of the infection, differentiate infection from inflammation and, if highly specific, identify the microorganism responsible for the infection, are necessary. The current imaging modalities applied in the diagnosis of infections are anatomical and functional imaging modalities, such as computed tomography, magnetic resonance imaging (MRI), ultrasound, positron emission tomography, single-photon emission computed tomography, and scintigraphy. However, these modalities do neither distinguish bacterial infections from other viral, fungal, or parasitic infections, nor from sterile inflammation. Bacteria-targeted imaging approaches, such as optical and optoacoustic imaging, are being explored to fill this gap in the diagnosis of infections [91–93].

The distribution and localized action of therapeutic molecules, such as photoactivated drugs and photosensitizers, can also be achieved by combining photopharmacology or aPDT with molecular imaging. One attribute of aPDT is that most of the photosensitizers that are currently used are also fluorescent, which

allows for optical imaging during therapy. The applicability of photopharmacology for diagnostic infection imaging is still largely unexplored, even though Li et al. described dithienylethene-functionalized switchable fluoroquinolones of which the blue fluorescence could be modulated upon excitation with UV light [44]. Spiropyrans represent promising molecules that may be applicable for molecular imaging of bacterial infections with photoswitches. In particular, their structural variability and photosensitivity allows the formation of a brightly colored merocyanine form (MC) upon UV light irradiation. This MC form absorbs light in the NIR range, similar to cyanine dyes [94]. Importantly, some studies have already supported the use of spiropyrans in molecular imaging as MRI contrast agents [95].

### 35.6.3 Concluding Remarks

In summary, antimicrobial photopharmacology is a promising alternative to the traditional therapies, which are starting to become increasingly less effective due to the emergence and spread of multi-drug resistant bacteria that remain fit in the presence of antibiotics. Importantly, the reversible photo-modulation of currently approved antibiotics has great potential to reduce the development of AMR and antibiotic-associated side effects inside the human body. There are still some areas of photopharmacology that need to be further explored, especially the development of better photoswitchable molecules activated by visible light, because the current ones still require long irradiation times for activation. Photoswitches have also great potential for implementation in the diagnosis of bacterial infections as "smart-activatable probes." By using light in an unprecedented manner, while still building on the experience and technical solutions offered by aPDT, antimicrobial photopharmacology has the potential to substantially aid in the struggle against AMR, which is one of the key challenges for mankind in the years to come.

## References


1 Otten, H. (1986). Domagk and the development of the sulphonamides. *J. Antimicrob. Chemother.* 17 (6): 689–696.

2 Fleming, A. (1929). On the antibacterial action of cultures of penicillium, with special reference to their use in the isolation of *B. influenzae*. *Br. J. Exp. Pathol.* 10: 226–236.

3 Subramaniam, G. and Girish, M. (2020). Antibiotic resistance – a cause for reemergence of infections. *Indian J. Pediatr.* https://doi.org/10.1007/s12098-019-03180-3.

4 World Health Organization. (2014). Antimicrobial resistance: global report on surveillance. https://www.who.int/antimicrobial-resistance/publications/surveillancereport/en

5 The Review on Antimicrobial Resistance, chaired by Jim O'Neill. Antimicrobial Resistance: Tackling a crisis for the health and wealth of nations. Dec 2014.


http://www.jpiamr.eu/wp-content/uploads/2014/12/AMR-Review-Paper-Tackling-a-crisis-for-the-health-and-wealth-of-nations_1-2.pdf.

6 Coates, A.R., Halls, G., and Hu, Y. (2011). Novel classes of antibiotics or more of the same? *Br. J. Pharmacol.* 163 (1): 184–194.

7 Sabtu, N., Enoch, D.A., and Brown, N.M. (2015). Antibiotic resistance: what, why, where, when and how? *Br. Med. Bull.* 116 (1): 105–113.

8 Escudeiro, P., Pothier, J., Dionisio, F. et al. (2019). Antibiotic resistance gene diversity and virulence gene diversity are correlated in human gut and environmental microbiomes. *mSphere* 4 (3): e00135–e00119.

9 Nikoopour, E. and Singh, B. (2014). Reciprocity in microbiome and immune system interactions and its implications in disease and health. *Inflamm. Allergy Drug Targets* 13 (2): 94–104.

10 Wargo, K.A. and Edwards, J.D. (2014). Aminoglycoside-induced nephrotoxicity. *J. Pharm. Pract.* 27 (6): 573–577.

11 Danner, M.-C., Robertson, A., Behrends, V. et al. (2019). Antibiotic pollution in surface fresh waters: occurrence and effects. *Sci. Total Environ.* 664: 793–804.

12 Velema, W.A., Szymanski, W., and Feringa, B.L. (2014). Photopharmacology: beyond proof of principle. *J. Am. Chem. Soc.* 136 (6): 2178–2191.

13 Hüll, K., Morstein, J., and Trauner, D. (2018). *In vivo* photopharmacology. *Chem. Rev.* 118 (21): 10710–10747.

14 Lerch, M.M., Hansen, M.J., van Dam, G.M. et al. (2016). Emerging targets in photopharmacology. *Angew. Chem. Int. Ed.* 55 (37): 10978–10999.

15 Broichhagen, J., Frank, J.A., and Trauner, D. (2015). A roadmap to success in photopharmacology. *Acc. Chem. Res.* 48 (7): 1947–1960.

16 Weissleder, R. and Ntziachristos, V. (2003). Shedding light onto live molecular targets. *Nat. Med.* 9 (1): 123–128.

17 Yun, S.H. and Kwok, S.J.J. (2017). Light in diagnosis, therapy and surgery. *Nat. Biomed. Eng.* 1 (1): 0008.

18 Tochitsky, I., Kienzler, M.A., Isacoff, E. et al. (2018). Restoring vision to the blind with chemical photoswitches. *Chem. Rev.* 118 (21): 10748–10773.

19 Bregestovski, P.D. and Maleeva, G.V. (2019). Photopharmacology: a brief review using the control of potassium channels as an example. *Neurosci. Behav. Physiol.* 49 (2): 184–191.

20 Reeβing, F. and Szymanski, W. (2017). Beyond photodynamic therapy: light-activated cancer chemotherapy. *Curr. Med. Chem.* 24 (42): 4905–4950.

21 Wegener, M., Hansen, M.J., Driessen, A.J.M. et al. (2017). Photocontrol of antibacterial activity: shifting from UV to red light activation. *J. Am. Chem. Soc.* 139 (49): 17979–17986.

22 Wainwright, M., Maisch, T., Nonell, S. et al. (2017). Photoantimicrobials – are we afraid of the light? *Lancet Infect. Dis.* 17 (2): e49–e55.

23 Lee, W., Li, Z.H., Vakulenko, S. et al. (2000). A light-inactivated antibiotic. *J. Med. Chem.* 43 (1): 128–132.

24 Velema, W.A., Van Der Berg, J.P., Szymanski, W. et al. (2014). Orthogonal control of antibacterial activity with light. *ACS Chem. Biol.* 9 (9): 1969–1974.

**25** Feng, Y., Zhang, Y.Y., Li, K. et al. (2018). Photocleavable antimicrobial peptide mimics for precluding antibiotic resistance. *New J. Chem.* 42 (5): 3192–3195.

**26** Velema, W.A., Van Der Berg, J.P., Szymanski, W. et al. (2015). Bacterial patterning controlled by light exposure. *Org. Biomol. Chem.* 13 (6): 1639–1642.

**27** Ronald, A.R. and Low, D.E. (2003). Fluoroquinolone antibiotics. Milestones in drug therapy. *J. Antimicrob. Chemother.* 52 (5): 880.

**28** Drlica, K. (1999). Mechanism of fluoroquinolone action. *Curr. Opin. Microbiol.* 2 (5): 504–508.

**29** Sharma, P.C., Jain, A., and Jain, S. (2009). Fluoroquinolone antibacterials: a review on chemistry, microbiology and therapeutic prospects. *Acta Pol. Pharm.* 66 (6): 587–604.

**30** Brogden, R.N., Carmine, A.A., Heel, R.C. et al. (1982). Trimethoprim: a review of its antibacterial activity, pharmacokinetics and therapeutic use in urinary tract infections. *Drugs* 23 (6): 405–430.

**31** Schnell, J.R., Dyson, H.J., and Wright, P.E. (2004). Structure, dynamics, and catalytic function of dihydrofolate reductase. *Annu. Rev. Biophys. Biomol. Struct.* 33 (1): 119–140.

**32** De Groot, R., Sluijter, M., De Bruyn, A. et al. (1996). Genetic characterization of trimethoprim resistance in *Haemophilus influenzae*. *Antimicrob. Agents Chemother.* 40 (9): 2131–2136.

**33** Dale, G.E., Broger, C., D'Arcy, A. et al. (1997). A single amino acid substitution in *Staphylococcus aureus* dihydrofolate reductase determines trimethoprim resistance. *J. Mol. Biol.* 266 (1): 23–30.

**34** Pikis, A., Donkersloot, J.A., Rodriguez, W.J. et al. (1998). A conservative amino acid mutation in the chromosome-encoded dihydrofolate reductase confers trimethoprim resistance in *Streptococcus pneumoniae*. *J. Infect. Dis.* 178 (3): 700–706.

**35** Canellakis, Z.N., Lande, L., and Bondy, P.K. (1989). Polyamines and their derivatives as modulators in growth and differentiation. *Yale J. Biol. Med.* 62 (5): 481–491.

**36** Parry, L., Lopez-Ballester, J., Wiest, L. et al. (1995). Effect of expression of human spermidine/spermine N1-acetyltransferase in *Escherichia coli*. *Biochemistry* 34 (8): 2701–2709.

**37** Hildmann, C., Ninkovic, M., Dietrich, R. et al. (2004). A new amidohydrolase from Bordetella or Alcaligenes strain FB188 with similarities to histone deacetylases. *J. Bacteriol.* 186 (8): 2328–2339.

**38** Krämer, A., Herzer, J., Overhage, J. et al. (2016). Substrate specificity and function of acetylpolyamine amidohydrolases from *Pseudomonas aeruginosa*. *BMC Biochem.* 17 (4): 1–10.

**39** Weston, C.E., Krämer, A., Colin, F. et al. (2017). Toward photopharmacological antimicrobial chemotherapy using photoswitchable amidohydrolase inhibitors. *ACS Infect. Dis.* 3 (2): 152–161.

**40** McKinnon, P.S. and Davis, S.L. (2004). Pharmacokinetic and pharmacodynamic issues in the treatment of bacterial infections diseases. *Eur. J. Clin. Microbiol. Infect. Dis.* 23 (4): 271–288.


**41** Soothill, J.S., Ward, R., and Girling, A.J. (1992). The IC50: an exactly defined measure of antibiotic sensitivity. *J. Antimicrob. Chemother.* 29 (2): 137–139.

**42** Li, B., Qiu, Y., Shi, H. et al. (2016). The importance of lag time extension in determining bacterial resistance to antibiotics. *Analyst* 141 (10): 3059–3067.

**43** Rolfe, M.D., Rice, C.J., Lucchini, S. et al. (2012). Lag phase is a distinct growth phase that prepares bacteria for exponential growth and involves transient metal accumulation. *J. Bacteriol.* 194 (3): 686–701.

**44** Li, Z., Wang, Y., Li, M. et al. (2018). Synthesis and properties of dithienylethene-functionalized switchable antibacterial agents. *Org. Biomol. Chem.* 16 (38): 6988–6997.

**45** Drugs.com. (2019). Proloprim - FDA prescribing information, side effects and uses. https://www.drugs.com/pro/proloprim.html

**46** Velema, W.A., Van Der Berg, J.P., Hansen, M.J. et al. (2013). Optical control of antibacterial activity. *Nat. Chem.* 5 (11): 924–928.

**47** Velema, W.A., Hansen, M.J., Lerch, M.M. et al. (2015). Ciprofloxacin-photoswitch conjugates: a facile strategy for photopharmacology. *Bioconjugate Chem.* 26 (12): 2592–2597.

**48** Fu, X., Bai, H., Qi, R. et al. (2019). Optically-controlled supramolecular self-assembly of antibiotic for antibacterial regulation. *Chem. Commun.* 55 (96): 14466–14469.

**49** Salta, J., Benhamou, R.I., Herzog, I.M. et al. (2017). Tuning the effects of bacterial membrane permeability through photo-isomerization of antimicrobial cationic amphiphiles. *Chem. Eur. J.* 23 (52): 12724–12728.

**50** Wolfson, J.S. and Hooper, D.C. (1989). Fluoroquinolone antimicrobial agents. *Clin. Microbiol. Rev.* 2 (4): 378–424.

**51** Lerch, M.M., Hansen, M.J., Velema, W.A. et al. (2016). Orthogonal photoswitching in a multifunctional molecular system. *Nat. Commun.* 7: 12054.

**52** Szymanski, W., Ourailidou, M.E., Velema, W.A. et al. (2015). Light-controlled histone deacetylase (HDAC) inhibitors: towards photopharmacological chemotherapy. *Chem. Eur. J.* 21 (46): 16517–16524.

**53** Bléger, D. and Hecht, S. (2015). Visible-light-activated molecular switches. *Angew. Chem. Int. Ed.* 54 (39): 11338–11349.

**54** Dong, M., Babalhavaeji, A., Collins, C.V. et al. (2017). Near-infrared photoswitching of azobenzenes under physiological conditions. *J. Am. Chem. Soc.* 139 (38): 13483–13486.

**55** Hemmer, J.R., Poelma, S.O., Treat, N. et al. (2016). Tunable visible and near infrared photoswitches. *J. Am. Chem. Soc.* 138 (42): 13960–13966.

**56** Seal, B.S., Drider, D., Oakley, B.B. et al. (2018). Microbial-derived products as potential new antimicrobials. *Vet. Res.* 49 (1): 66.

**57** Gause, G.F. and Brazhnikova, M.G. (1944). Gramicidin S and its use in the treatment of infected wounds. *Nature* 154: 703.

**58** Babii, O., Afonin, S., Ishchenko, A.Y. et al. (2018). Structure-activity relationships of photoswitchable diarylethene-based β-hairpin peptides as membranolytic antimicrobial and anticancer agents. *J. Med. Chem.* 61 (23): 10793–10813.


**59** Llamas-Saiz, A.L., Grotenbreg, G.M., Overhand, M. et al. (2007). Double-stranded helical twisted β-sheet channels in crystals of gramicidin S grown in the presence of trifluoroacetic and hydrochloric acids. *Acta Crystallogr. D* 63 (3): 401–407.

**60** Berditsch, M., Lux, H., Babii, O. et al. (2016). Therapeutic potential of gramicidin S in the treatment of root canal infections. *Pharmaceuticals* 9 (3): 56.

**61** Berditsch, M., Jäger, T., Strempel, N. et al. (2015). Synergistic effect of membrane-active peptides polymyxin B and gramicidin s on multidrug-resistant strains and biofilms of *Pseudomonas aeruginos*a. *Antimicrob. Agents Chemother.* 59 (9): 5288–5296.

**62** Ashrafuzzaman, M., Andersen, O.S., and Mcelhaney, R.N. (2008). The antimicrobial peptide gramicidin S permeabilizes phospholipid bilayer membranes without forming discrete ion channels. *Biochim. Biophys. Acta* 1778 (12): 2814–2822.

**63** Albert, L. and Vázquez, O. (2019). Photoswitchable peptides for spatiotemporal control of biological functions. *Chem. Commun.* 55 (69): 10192–10213.

**64** Szymański, W., Beierle, J.M., and Kistemaker, et al. (2013). Reversible photocontrol of biological systems by the incorporation of molecular photoswitches. *Chem. Rev.* 113 (8): 6114–6178.

**65** Babii, O., Afonin, S., Berditsch, M. et al. (2014). Controlling biological activity with light: diarylethene-containing cyclic peptidomimetics. *Angew. Chem. Int. Ed.* 53 (13): 3392–3395.

**66** Yeoh, Y.Q., Yu, J., Polyak, S.W. et al. (2018). Photopharmacological control of cyclic antimicrobial peptides. *ChemBioChem* 19 (24): 2591–2597.

**67** Podewin, T., Rampp, M.S., Turkanovic, I. et al. (2015). Photocontrolled chignolin-derived β-hairpin peptidomimetics. *Chem. Commun.* 51 (19): 4001–4004.

**68** Karcher, J. and Pianowski, Z.L. (2018). Photocontrol of drug release from supramolecular hydrogels with green light. *Chem. Eur. J.* 24 (45): 11605–11610.

**69** Mah, T.-F.C. and Toole, G.A.O. (2001). Mechanisms of biofilm resistance to antimicrobial agents. *Trends Microbiol.* 9 (1): 34–39.

**70** Parsek, M.R. and Singh, P.K. (2003). Bacterial biofilms: an emerging link to disease pathogenesis. *Annu. Rev. Microbiol.* 57 (1): 677–701.

**71** Jiang, Q., Chen, J., Yang, C. et al. (2019). Quorum sensing: a prospective therapeutic target for bacterial diseases. *Biomed. Res. Int.*: 2015879.

**72** Del Pozo, J.L. and Patel, R. (2007). The challenge of treating biofilm-associated bacterial infections. *Clin. Pharmacol. Ther.* 82 (2): 204–209.

**73** Hu, Y., Zou, W., Julita, V. et al. (2016). Photomodulation of bacterial growth and biofilm formation using carbohydrate-based surfactants. *Chem. Sci.* 7: 6628–6634.

**74** Kehe, G.M., Mori, D.I., Schurr, M.J. et al. (2019). Optically responsive, smart anti-bacterial coatings via the photofluidization of azobenzenes. *ACS Appl. Mater. Interfaces* 11 (2): 1760–1765.

**75** Van Der Berg, J.P., Velema, W.A., Szymanski, W. et al. (2015). Controlling the activity of quorum sensing autoinducers with light. *Chem. Sci.* 6: 3593–3598.

**76** Hansen, M.J., Hille, J.I.C., Szymanski, W. et al. (2019). Easily accessible, highly potent, photocontrolled modulators of bacterial communication. *Chem* 5 (5): 1293–1301.


**77** Kumari, P., Kulkarni, A., Sharma, A.K. et al. (2018). Visible-light controlled release of a fluoroquinolone antibiotic for antimicrobial photopharmacology. *ACS Omega* 3 (2): 2155–2160.

**78** Kościuczuk, E.M., Lisowski, P., Jarczak, J. et al. (2012). Cathelicidins: family of antimicrobial peptides. A review. *Mol. Biol. Rep.* 39 (12): 10957–10970.

**79** Morstein, J. and Trauner, D. (2019). New players in phototherapy: photopharmacology and bio-integrated optoelectronics. *Curr. Opin. Chem. Biol.* 50: 145–151.

**80** Hu, X., Huang, Y.Y., Wang, Y. et al. (2018). Antimicrobial photodynamic therapy to control clinically relevant biofilm infections. *Front. Microbiol.* 9: 1299.

**81** Embleton, M.L., Nair, S.P., Cookson, B.D. et al. (2002). Selective lethal photosensitization of methicillin-resistant *Staphylococcus aureus* using an IgG-in (IV) chlorin e6 conjugate. *J. Antimicrob. Chemother.* 50 (6): 857–864.

**82** Embleton, M.L., Nair, S.P., Heywood, W. et al. (2005). Development of a novel targeting system for lethal photo sensitization of antibiotic-resistant strains of *Staphylococcus aureus*. *Antimicrob. Agents Chemother.* 49 (9): 3690–3696.

**83** Wang, K.K., Shin, E.P., Lee, H.J. et al. (2018). Target-oriented photofunctional nanoparticles (TOPFNs) for selective photodynamic inactivation of methicillin-resistant *Staphylococcus aureus* (MRSA). *J. Photochem. Photobiol., B* 183: 184–190.

**84** Lee, H.H., Choi, M.-G., and Hasan, T. (2017). Application of photodynamic therapy in gastrointestinal disorders: an outdated or re-emerging technique? *Korean. J. Intern. Med.* 32 (1): 1–10.

**85** Arrue, L. and Ratjen, L. (2017). Internal targeting and external control: phototriggered targeting in Nanomedicine. *ChemMedChem* 12 (23): 1908–1916.

**86** Stewart, P.S. and Franklin, M.J. (2008). Physiological heterogeneity in biofilms. *Nat. Rev. Microbiol.* 6: 199–210.

**87** Wessel, C.K., Arshad, A.K., Fitzpatrick, M. et al. (2014). Oxygen limitation within a bacterial aggregate. *MBio* 5 (2): e992.

**88** Ray, T.R., Choi, J., and Bandodkar, et al. (2019). Bio-integrated wearable systems: a comprehensive review. *Chem. Rev.* 119 (8): 5461–5533.

**89** Veiseh, O., Doloff, J.C., Ma, M. et al. (2015). Size- and shape-dependent foreign body immune response to materials implanted in rodents and non-human primates. *Nat. Mater.* 14: 643–651.

**90** Reeßing, F. and Szymanski, W. (2017). Beyond photodynamic therapy: light-activated cancer chemo- therapy. *Curr. Med. Chem.* 24: 4905–4950.

**91** van Oosten, M., Hahn, M., Crane, L.M.A. et al. (2015). Targeted imaging of bacterial infections: advances, hurdles and hopes. *FEMS Microbiol. Rev.* 39 (6): 892–916.

**92** Heuker, M., Gomes, A., van Dijl, J.M. et al. (2016). Preclinical studies and prospective clinical applications for bacteria-targeted imaging: the future is bright. *Clin. Transl. Imaging* 4: 253–264.

**93** Wang, Y., Thompson, J.M., Ashbaugh, A.G. et al. (2017). Preclinical evaluation of photoacoustic imaging as a novel noninvasive approach to detect an orthopaedic implant infection. *J. Am. Acad. Orthop. Surg.* 25: S7–S12.


**94** Pugachev, A.D., Ozhogin, I.V., Lukyanova, M.B. et al. (2020). Visible to near-IR molecular switches based on photochromic indoline spiropyrans with a conjugated cationic fragment. *Spectrochim. Acta, Part A* 230: 118041.

**95** Kruttwig, K., Yankelevich, D.R., Brueggemann, C. et al. (2012). Reversible low-light induced photoswitching of crowned spiropyran-DO3A complexed with gadolinium(III) ions. *Molecules* 17 (6): 6605–6624.

# 36 Photoswitchable Cytotoxins

Oliver Thorn-Seshold

## Characteristic Features

Photoswitchable cytotoxins are research reagents that can optically modulate critical biological systems, from cytoskeleton dynamics to genomic integrity. Through recent applications in vivo in mouse, fish, worm, fly, and frog, these chemically diverse photopharmaceuticals are emerging as promising tools for high spatiotemporal precision manipulations across biology.

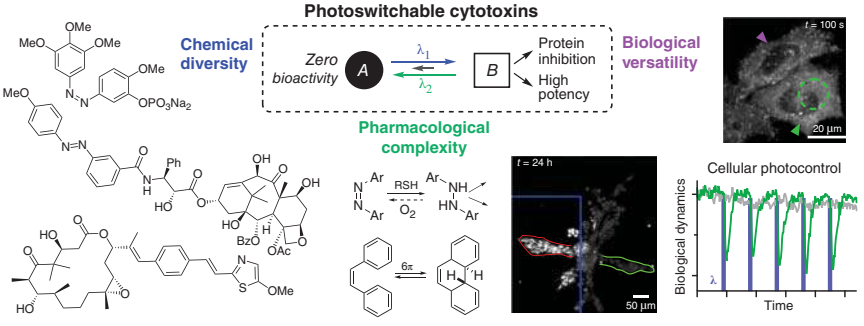


## First Reported

Hadfield, J., McGown, A., Mayalarp, S. et al. (2002). Substituted stilbenes, their reactions and anticancer activity. WO200250007.

Borowiak, M, Nahaboo, W, Reynders, M. et al. (2015). Photoswitchable inhibitors of microtubule dynamics optically control mitosis and cell death. *Cell 162*: 403–411.

## Key References

Babii, O., Afonin, S., Schober, T. et al. (2020). Peptide drugs for photopharmacology: how much of a safety advantage can be gained by photocontrol? *Future Drug Discovery* 2: FDD28.

Borowiak, M., Küllmer, F., Gegenfurtner, F. et al. (2020). Optical manipulation of F-actin with photoswitchable small molecules. *J. Am. Chem. Soc*. 142: 9240–9249.

Gao, L., Meiring, J., Varady, A. et al. (2021). *In vivo* photocontrol of microtubule dynamics and integrity, migration and mitosis. *bioRxiv* 10.1101/2021.03.26.437160.

# 36

# Photoswitchable Cytotoxins

*Oliver Thorn-Seshold*

*Ludwig-Maximilians University of Munich, Department of Pharmacy, Butenandtstrasse 5-13, Munich, 81377, Germany*

## 36.1 Introduction

### 36.1.1 The Rewards of Photoswitchable Cytotoxins

Cytotoxins include an enormous diversity of drug structures and mechanisms, united by one common feature: these drugs all address biological targets whose function is so critical to cell survival that their inhibition kills cells. Among others, cytotoxins affect DNA synthesis, reading, and replication; protein synthesis and recycling; metabolism; and cellular structure, motion, and division: in short, the most fundamental processes in biology. These processes have been so finely tuned by evolution and are so tightly controlled by error-checking mechanisms, that it is often impractical to use genetic engineering to manipulate them without significantly damaging or killing cells and model organisms. In such situations, cytotoxic drugs that can be administered exogenously are irreplaceable as practical tools, ensuring that cytotoxins occupy a privileged position in chemistry and biology. As their key biological targets are usually evolutionarily conserved across species and even kingdoms of life, cytotoxins also tend to translate well between model systems. This was crucial to the early development of DNA alkylators and antimitotics, and to this day makes cytotoxins particularly valuable as research reagents. Finally, as a class, cytotoxins include some of the most dangerous and powerful therapeutics for diseases in which these cellular processes run out of control. From tentative beginnings around the 1940s [1], cytotoxic therapeutic development has now led to DNA alkylators, antimetabolites, and microtubule inhibitors taking on massive clinical importance as cancer chemotherapeutics and as treatments for autoimmune diseases.

All cellular processes depend on spatiotemporal regulation of protein function; those targeted by cytotoxins are no exception. Photoswitchable cytotoxins (PSCs) to modulate these processes with cellular-scale spatial precision, and with the temporal precision to match their biology, would be extremely valuable for precise biological research – for much the same reasons as for the other drug classes discussed

*Molecular Photoswitches: Chemistry, Properties, and Applications*,
First Edition. Edited by Zbigniew L. Pianowski.


in this book [2, 3]. However, as reagents, cytotoxins face an additional challenge when compared to most other drug classes: their conserved biological targets are both present and required for normal function or survival, in all cells or tissues in study samples. Both research and therapeutic applications would greatly benefit from ensuring that only selected target cells are exposed to cytotoxic drug action, so avoiding side effects that either compromise study readouts or reduce therapeutic benefits. PSCs which could be applied globally to cells or organisms as an essentially inactive isomer to avoid these side effects, yet locally photoisomerized to apply their latent bioactivity only in a particular targeted cell (or tissue, or subcellular area) during a defined time window, would offer an elegant solution to this additional challenge and so would permit unique and powerful applications manipulating and studying the most crucial processes of life [4].

### 36.1.2 Scope of This Chapter

This chapter treats photoisomerizable cytotoxins whose bioactivity depends solely on their isomer state (Figure 36.1a). This excludes photoreactive compounds that are widely clinically used in photodynamic therapy (PDT) as well as chromophores that are clinically applied for photothermal therapy (PTT). Both PDT and PTT permit spatiotemporally localized generation of cytotoxicity in deep tissue in vivo [5, 6]. PSCs are unlikely ever to be clinically competitive with these highly effective, widespread, robust methods merely as cell-killing systems for therapeutic application. The unique advantage of PSCs is their ability to apply a biologically useful mechanism of action against a defined protein target (Section 36.2.1). Indeed, as of 2020, cytotoxic photopharmacology in cells or organisms remains firmly a research method. While PSCs may one day reach clinical applications that harness their mechanistic specificity, and several forward-looking discussions have been published [3], almost no clear data have yet been reported on therapeutically appropriate uses of PSCs (i.e. where the photopharmaceutical is systemically applied then locally photoisomerized to address pathological tissues). Therefore, this chapter focuses on the unique mechanistically defined applications that PSCs can enable in basic research, particularly as distinct from those enabled by photouncageable compounds (Sections 36.2.2–36.2.4).

This chapter will address cytotoxins for eukaryotic cells; bactericidal toxins have been addressed in Chapter 34. Cytotoxins are drugs that address a defined biological target whose correct functioning is so important that inhibiting it causes cell death in a variety of cell types. This chapter will therefore include photopharmaceutical analogs of clinically used cytotoxic therapeutics, such as antimitotics like the microtubule inhibitor paclitaxel, or antimetabolites like the dihydrofolate reductase inhibitor methotrexate. Photopharmaceutical analogs of cell-toxic drugs that target crucial biological systems but are not used clinically, such as the actin inhibitor jasplakinolide, will also be included. It will offer only selected examples of photopharmaceuticals that were not tested in cells, or which were applied in cells but without showing photocontrol of cell survival.

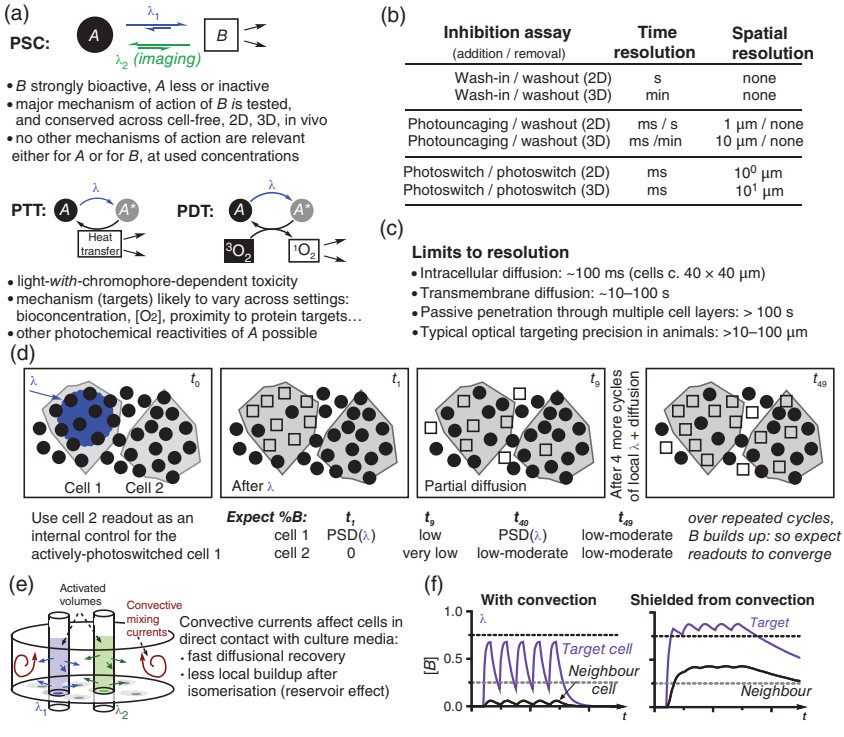


**Figure 36.1** Photoswitchable cytotoxins. (a) General concept of photoswitchable cytotoxins. (b) Estimates for typical spatial and temporal scales involved in using photoswitchable reagents. (c) Single-cell uses of PSCs. (d) Comparing optically targeted vs. nontargeted neighbor cells in 2D cell culture assays gives useful internal controls for many reagent and assay parameters. (e) Convective currents, combined with the reservoir effect of a large extracellular volume, permit rapid temporal reversibility after transmembrane diffusion of optically patterned reagents. (f) Blocking convective currents permits unidirectionally optically targeted reagents to apply photopatterned bioactivity over longer timescales.

To emphasize research uses, this chapter will focus on PSCs with strong experimental support indicating that their major mechanism of bioactivity in cells is indeed photoisomer-dependent inhibition of their intended biological target. This is a strict need for PSCs, much more than for any other class of bioactives. Cell-damaging and cytotoxic effects can be induced by deregulating or stimulating a very broad range of pathways, so the chances of misleading "positive" results are correspondingly high in PSC development. For example, it is far more likely that any given compound applied at sufficiently high concentrations will eventually suppress cell proliferation and/or kill cells, rather than causing the specific biological readouts that guide development of other classes of photopharmaceuticals (e.g. selectively opening specific ion channels, affecting lysine deacetylation, antagonizing neurotransmitter receptors). A PSC intended to inhibit a specific protein or pathway will have no value as a research reagent if at cellularly relevant concentrations it instead applies cytotoxicity by other, uncharacterized, mechanisms.

Therefore, the off-target effects that can be expected from PSCs, and the procedures that can be used for mechanism of action testing (Section 36.2.5), will be discussed before the principles of PSC reagent design are presented (Section 36.2.6), and the primary literature of PSCs is reviewed (Sections 36.3–36.5).

## 36.2 Photoswitchable Cytotoxins: Applications, Challenges, and Design

While cytotoxic drugs *can* be used to kill cells, this is never the goal of applying them in basic research: it is rather their ability to cleanly inhibit their critical biological targets that make them of interest [7]. Similarly, while demonstrating cytotoxicity is a typical step in the development of PSCs, their true applications lie in controlling biology in conceptually unique and/or practically simpler ways that are inaccessible to standard (always-active) cytotoxic drugs or to their photouncageable prodrugs. (Note that while photoinactivatable drugs can also be made, they have not had substantial impact – with the exception of the tubulin inhibitor colchicine, that is usefully photoinactivated to lumicolchicine in situ by UV.) To identify the most valuable opportunities for PSC use, it is instructive first to discuss the degree of spatial and temporal resolution of cytotoxic drug activity that it is useful to achieve and then to compare the spatiotemporal resolution that PSCs can achieve in practice, with that of standard (always-active) cytotoxic drugs and their photouncageable prodrugs: noting that resolution greatly depends on the assay setting (Figure 36.1b) as well as the protein target they address.

### 36.2.1 The Spatiotemporal Specificity Needed for Photoswitchable Cytotoxins

There are theoretical limits to the spatiotemporal resolution that cytotoxins should aim to achieve, since resolution below the limits of assay sensitivity or of the biological response being targeted is not useful. Due to the biology of their targets, most cytotoxins only produce useful biological readouts on timescales of minutes or more (e.g. DNA-interacting compounds, metabolic inhibitors), and it seems difficult to spatially target them with subcellular resolution since these timescales are far longer than those of small-molecule diffusion throughout cells.

Among the cytotoxins, the greatest rewards for spatiotemporally resolved PSCs may lie with inhibitors of cytoskeletal processes, as these have the fastest biological responses (lower useful limit of c. 100 ms) and the greatest meaningful spatial resolution (biologically differentiated at the optical limit). However, even for these PSCs, *subcellularly spatially resolved* applications have rarely been reported (see Sections 36.3–36.5) [8]. Therefore, spatial targeting to the single-cell level, and temporal resolution to ≥100 ms, may be the highest useful standards for PSCs (Figure 36.1c). This impacts PSC design, favoring metastable isomer half-lives on the scale of c. ≥100 ms to give useful temporal resolution without needing re-isomerization cycles (Section 36.2.6): a differentiating feature from other photopharmaceutical

classes (e.g. for ion channels, which often benefit from submillisecond relaxation half-lives [2]).

### 36.2.2 Use of Photoswitchable Cytotoxins in 2D

Optical approaches are required in almost all cases where spatial resolution to individual cells is needed to deliver meaningful results. There are many examples of this resolution using either PSCs or photouncaging approaches, on timescales from seconds to hours. Assays on cell lines in 2D cell culture rarely require this spatial precision since, often, the isolated cells act as "replicate experiments" giving identical outcomes whether cells are addressed one by one, or in parallel. However, cell-specific biological modulation in 2D culture is a valuable proof of concept for optical targeting in more complex systems and provides a useful internal control for nonspecific assay interferences [9] (Figure 36.1d).

In 2D cell culture, rapid transmembrane diffusion of reagents can combine with convective mixing currents in the medium that contact the cell surface [9], to ensure rapidly temporally reversible patterning of reagent bioactivity (Figure 36.1e,f). For both PSCs and photouncaging reagents [10], cell-precise patterning can be achieved by using illumination pulses directed at the target cell to inhibit protein function, then waiting for typically c. 1 minute to allow extracellular diffusion and equilibration with the medium to reduce intracellular concentrations of the active species below inhibitory thresholds [11]. (If a 2D cell culture assay aims at cell-specific targeting over an *extended* period of time, the reversibility of PSCs can be advantageous compared to photouncaging, since photopatterning can be repeated as needed: but if convective transport is eliminated, as is often done by embedding or overlaying cells with viscous hydrogel media such as carboxymethylcellulose or agarose, photouncageable compounds too may achieve persistent cell specificity (Figure 36.1f).) Similarly, for always-active drugs, wash-in/washout experiments can also deliver good temporal resolution of drug activity in 2D cell culture: although they have no possibility of targeting selected cells [9]. Taken together, this leads to the first conceptually unique opportunity for PSCs: rapid response modulation in 2D culture assays.

Opportunity 1: Faster Switch-Off in 2D: Consider PSCs whose biological targets support readouts on timescales faster than washout (i.e. seconds or less, such as inhibitors of cytoskeletal dynamics), which permit either bidirectional photoisomerizations or else spontaneously relax on a timescale of milliseconds to seconds. Such reagents can deliver uniquely improved temporal resolution of bioactivity control by being faster to "switch both on *and* off" than the cellular diffusional recovery timescale (Figure 36.2a). While this seems superficially simple and is frequently performed with fast-relaxing ion channel switches, for PSCs it relies on near-complete switching to a nearly inactive isomer, as well as limiting the scope of biological targets. Indeed, there has been only one demonstration of a PSC operated in this mode (**PSTs**, see Section 36.3.1.2). This opportunity for PSCs may be amplified in the case of drugs with long target residence times or with

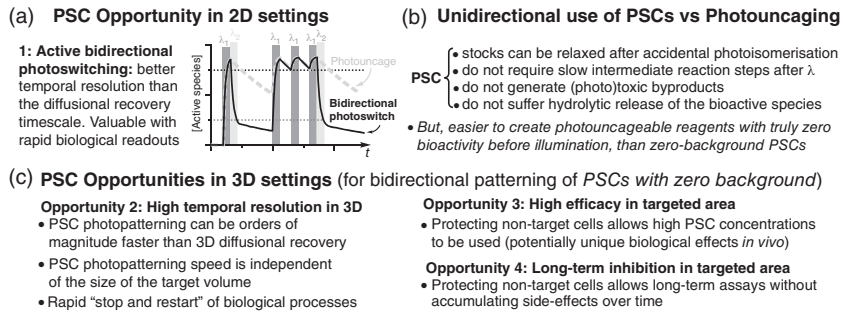


**Figure 36.2** Unique opportunities for photoswitchable cytotoxins. (a) Modulating bioactivity faster than the diffusional recovery timescale in cell culture. (b) Unidirectional photoswitching of a PSC from a fully inactive to an active isomer reproduces the performance of photouncageable compounds, although with several conceptual advantages. (c) Unique opportunities for PSCs in 3D settings or in vivo in model organisms rely on combining highly efficient isomerization to a nearly inactive isomer, with efficient isomerization to the bioactive isomer. These opportunities are fast bioactivity modulation in arbitrary volumes, generating high concentrations of the bioactive species at the desired site, and long-term maintenance of bioactivity without side effects outside the target zone.

slow transmembrane partitioning [12–14]. However, biological targets which give assay-relevant effects more slowly, as are addressed by e.g. antimetabolites, topoisomerase inhibitors or protein degradation reagents, can be sufficiently temporally resolved in 2D culture without requiring optical targeting.

### 36.2.3 Opportunities and Limitations of Photoswitchable Cytotoxins in 3D

3D systems such as organoids, tissue explants, and live animals, represent conceptually more challenging as well as more biologically rewarding systems and bring the true opportunities for optically controlled cytotoxins. Here, effects applied in one area propagate through the system to various degrees, so it becomes crucial to prevent the cytotoxic drug from inhibiting its conserved and critical protein target in nontargeted cells (see e.g. Section 36.3.1).

In most of these 3D uses, always-active reagents cannot achieve spatial targeting. An exception is that in adult model organisms (>10 g), slow exchange can be harnessed to obtain a degree of spatial specificity by local injection (for example, intratumoral injection of antimitotics) or local drug release from porous materials (which is clinically used). These simple and relatively noninvasive local treatments act as fast- or slow-release point sources of the active drug in larger organisms. In practice, they deliver comparable spatiotemporal profiles of the active drug as what could theoretically, in a very favorable scenario, be delivered by optical approaches. The unique spatial uses of PSCs therefore lie in "small 3D systems" (3D cell culture or organoids, tissue explants, and small early-stage embryos/larvae).

In 3D settings, diffusional exchange of drugs is much slower than in 2D, since they must typically cross several cell layers between the medium (or the bloodstream) and

the target cell, and there are no convective currents to speed access to the cell surface (compare Figure 36.1f). A similar situation of shielding from convection arises when samples are embedded in e.g. collagen or agarose gels, which is often performed both with 3D cell cultures and with small animals in imaging studies. Through a combination of these effects, the temporal resolution achievable with always-active reagents in wash-in/washout experiments on 3D systems decreases drastically, to the scale of minutes or hours, leaving great opportunities for PSCs.

The unique uses of optical methods in small 3D systems therefore lie in spatially and/or temporally restricted applications. The conceptually unique opportunities for PSCs compared to photouncaging again center on their potential to be passively or actively switched off, by spontaneous relaxation or photoisomerization in the reverse direction to a less active isomer. However, now the residual activity of the less bioactive isomer must also be considered.

If a PSC's less active isomer is essentially inactive, then it can give the same photopatterning of bioactivity as a photouncaged compound, if it is operated simply by unidirectional localized photoswitching to the active isomer in the target volume ("photoactivation mode"; Figure 36.2b). In this case, the maximum concentration of the PSC or the photouncageable compound that can be applied and photoactivated in an assay will depend on the maximum acceptable degree of toxicity that they apply while diffusing out through cells surrounding the photoactivation zone. However, in the ideal case, the PSC's active isomer could be nearly completely isomerized back to its nearly inactive isomer either by quasi-instantaneous switch-off photoisomerization *or* by spontaneous relaxation that is competitive to diffusion timescales in 3D systems (minutes scale) (Figure 36.2a). This would enable *steep spatiotemporal gradients* of bioactivity to be applied and maintained in the long term just by photoswitching a PSC and would bring unique opportunities in 3D (Figure 36.2c):

Opportunity 2: Faster, High-Volume Switch-Off in 3D: Similarly to the case in 2D settings (Opportunity 1), active switch-off of PSCs within a target volume could remove bioactivity with sub-second resolution. However, as diffusional recovery is slower in 3D systems, this active PSC control now provides orders of magnitude better temporal resolution than what would be possible with photouncaged reagents; and it can also be used in volumes of arbitrary size. This unique resolution may be helpful to study the acute and chronic consequences of inhibiting processes that occur on temporal scales faster than diffusion in 3D systems (minutes scale), such as cell division.

Opportunity 3: Stronger Inhibition in 3D: A much higher concentration of the PSC could be applied overall, since switch-off in cells surrounding a targeted zone can avoid them experiencing substantial, assay-limiting inhibition. This may bring biological advantages by more completely and reproducibly inhibiting processes in the target zone than photouncaging approaches can permit. Note that this usually has no counterpart in 2D cell culture settings, where photoactivated compounds can be harmlessly diluted out into a large reservoir of medium, and where it is usually of little interest what happens in neighboring cells.

Opportunity 4: Longer Assay Timescales in 3D: Repeated targeted isomerizations of PSCs could maintain targeted volumes in an inhibited state over much longer

periods than diffusion timescales, without accumulating the bioactive isomer in surrounding cells as photouncaging would. This permits much more long-term studies than can be possible with photouncaging.

However, if photoisomerization to the less active isomer of a PSC is incomplete and relaxation is also insignificant on the timescale of diffusion in 3D, then even if the PSC's less active isomer is essentially inactive, it cannot maintain steep spatiotemporal gradients of bioactivity. For example, if a bistable PSC has at best 80% photoconversion to its inactive isomer, then the greatest possible fold change of concentration of the bioactive isomer that could be maintained by differential photoswitching in targeted vs. nontargeted areas would be fivefold (photopatterning of regions at 100% vs. 20% of the active isomer). This useful property of the photoswitch is called its *maximum* functional dynamic range upon photoswitching ($FDR_{max}$) [13]. The FDR that is obtained in practice is additionally limited by the available photoisomerization wavelengths in the experimental setup, which in biological studies in small 3D systems are typically restricted to lasers at 405, 488, and 561 nm. If the practical FDR is relatively small (perhaps <10-fold), then bidirectional photoswitching may even cause more inhibition in nontarget areas than would result from diffusional recovery, so "photoactivation mode" may bring the best spatiotemporal performance of the PSC in 3D. This offers no *unique conceptual* applications as compared to photouncaging, but in practice there remain several advantages for such PSCs (see Section 36.2.4) [11].

Finally, if a PSC's less active isomer has significant residual bioactivity, then even if it features a good practical FDR and/or appropriately fast relaxation, it will be of very limited value for 3D uses. The inhomogenous concentration profiles that arise by treating limited diffusion 3D systems with small molecules (highest concentrations in the most-accessible cells), combined with the need to avoid significant background activity in nontargeted zones, will strictly limit the reagent concentrations that can be used: in the same way that the concentrations of always-active cytotoxins are limited. It has always proven possible to generate photouncageable prodrugs of those drugs that have been adapted into PSCs (in most cases, the photouncageable variant has preceded the PSC). As long as those photouncageable prodrugs are well designed for activity quenching and for efficient practical photoactivation, in 3D applications they are conceptually superior to residual activity PSCs, and they are likely to be more powerful in practice too. The penalty caused by residual activity in PSC designs is discussed further in Section 36.2.6.

### 36.2.4 Practical Considerations for Optical Methods

As well as the four conceptually unique opportunities outlined above, PSCs share the advantages and drawbacks of all photopharmaceutical classes. These have been reviewed elsewhere in this volume. Briefly, the greatest disadvantage of PSCs as compared to photouncaging approaches (Figure 36.2b) is that it is far more difficult to design an ideal PSC having highly complete conversion to an essentially inactive photoisomer yet still featuring satisfactory potency as the active isomer:

whereas near-ideal application of photocages, with large activity quenching and then efficient unmasking, is often straightforward to achieve [10]. However, the practical advantages of PSCs include avoiding both chemically toxic and phototoxic photouncaging byproducts, ability to harness longer wavelengths and lower light intensities for isomerization, which ensures better spatial specificity in 3D systems (that suffer optical scattering at short wavelengths) as well as better biological tolerance of illuminations, population-level photoswitching speeds that are limited only by photon flux and not by post-illumination hydrolysis and/or fragmentation (see below), avoiding nonoptical drug-release mechanisms (e.g. enzymatic hydrolysis of photocages) [10], ensuring that compound stocks are not irreversibly damaged by accidental exposure to light, which simplifies practical handling, and potentially suffering lower penalties of molecular weight for including photoresponse (particularly with photoswitch-*included* designs) [15], which can be crucial for achieving reliably high solubility and permeability as needed for small 3D uses.

These many advantages provide additional motivation for the development and use of PSCs in certain settings. Particularly, as long as reagent solubility, and comparable potency to that of standard drugs, can be ensured, these advantages can also motivate using unidirectional photoswitches in "photoactivation mode" (Figure 36.2b) as a valuable alternative to improve both on the performance and the ease of use as compared to photouncageable inhibitors.

*Regarding photoswitching speeds*: on the single-molecule level, all photoswitch scaffolds have picosecond photoswitching timescales that are orders of magnitude faster than the biological processes they can be used to target (milliseconds to minutes). These single-molecule timescales are irrelevant for photopharmaceuticals, as the relevant timescale is that for photoisomerizing a *bulk population* of a PSC. However, under typical illumination conditions in research settings (high light intensities), bulk isomerizations too are more rapid than any relevant biological processes, so most photoswitches can be considered "suitably" fast.

### 36.2.5 Mechanism of Action Testing and Off-Target Effects

From a medicinal chemistry viewpoint, it would be surprising if a drug's potency and major cellular mechanism of action could routinely be retained despite derivatizing optimized drug structures with relatively large molecular photoswitches. As well as the starting potency of the drug, the manner of its derivatization plays a key role in if/how this modification is tolerated. Photoswitches are usually designed into bioactives either by *appending* the entire photoswitch or by *extending* an aryl ring with one half of a photoswitch [16]. In these cases, the photoswitch will bring significant extra rigidity, molecular size, and surface area that can risk off-target effects. Only in rare cases can a photoswitch be *included* entirely within the pharmacophore, which minimizes these overall changes to molecular properties [17].

*Solubility* is the drug-like property of most concern to medicinal chemistry in early development, as "compounds that are not fully soluble in bioassays can result in erratic assay results, erroneous SAR, and discrepancies between assays, such as enzyme and cell-based assays" [18]. Nearly, all drugs classed as cytotoxins have

cytosolic binding targets, and most are somewhat polar if not hydrophilic. However, nearly all photoswitches used in cellular photopharmaceuticals – azobenzenes, stilbenes, hemithioindigos (HTIs), dithienylethenes, etc. – have large, flat aromatic surfaces which cause low aqueous solubility and make aggregate formation, particularly during dilution steps, likely. Not only are they intrinsically hydrophobic, which also impacts overall reagent polarity and partitioning into the cytosol where their targets are usually found, but they are typically planar in at least one isomer, and π-stacking may further reduce solubility in an isomer-dependent manner [19]. Indeed, Hartley's first report of azobenzene isomerization relied on differences of polarity and solubility to separate *E* and *Z* isomers. PSCs are typically much less potent than their parent drugs and so require use at higher concentrations to elicit similar on-target responses; and the combination of higher applied concentrations with lower intrinsic solubility can cause multiple undesired off-target effects which may even become the primary mechanism of action.

A broad spectrum of inhibitory and cytotoxic effects can be caused in cell-free and cellular settings by compounds whose poor solubility prevents them from addressing defined protein targets or binding sites [18], which therefore have no value as research reagents or therapeutics. In medicinal chemistry, such compounds are classed as pan-assay interference compounds (PAINS); surfactant-like effects, aggregate formation, membrane disruption, and protein aggregation are some of the target- and assay-independent effects that they cause. Similar, off-target biological effects that may also be isomer-dependent can be expected from photopharmaceuticals when they are used at moderate to high concentrations (e.g. ≥10 μM). Shoichet has campaigned for 20 years for awareness of kinetic aggregation effects even below expected solubility limits; several of the typical "aggregating nuisance compounds"are classic azobenzenes [20]. Unfortunately, such effects are rarely [12] considered or controlled for in PSC design [13]; and some reports of PSCs may have observed only PAINS mechanisms (e.g. isomer-dependent aggregators and membrane disruptors, or photoswitchable surfactants) (Figure 36.3b) [21].

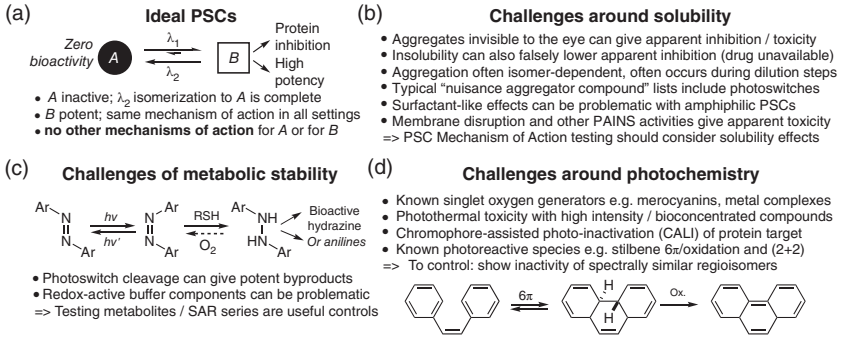


**Figure 36.3** Toward "ideal" photoswitchably cytotoxic reagents. (a) Properties of an ideal PSC. (b–d) Challenges for delivering a clean cellular mechanism of action: solubility, metabolic stability, and photochemical toxicity.

*Metabolic stability* is a second drug-like property of some concern [18]. In short-term 2D applications, it may not pose problems, but in long-term use, and particularly toward uses in model organisms, both metabolic stability and potential off-target effects of likely metabolic byproducts must be considered. Some aspects of metabolic stability are similar to those for general compound development. For example, attaching photoswitches to drug cores via enzymatically instable bonds can also give confounding effects which may be isomer-dependent [21], without this indicating that a PSC has photoswitchable potency on its target.

Other metabolism aspects are unique to photoswitches. Most of these aspects have been reviewed elsewhere [12]. In brief, C=C-based photoswitches appear metabolically robust [11, 13], but azobenzenes have known metabolic labilities [22]. Their N=N double bond is electrophilic and oxidizing and can be reductively degraded even by uncatalyzed attack of monothiols. Typically, *Z*-azobenzenes are c. 100-fold more reactive to thiols than *E* [23], and at cellular thiol concentrations they may have a half-life under an hour [11]; therefore, historical data testing the stability and toxicity of fast-relaxing azobenzene dyes as their *E*-isomers are not useful for evaluating the liabilities of azobenzene PSCs that must be photopatterned as both *E* and *Z*. The *Z*-azobenzene is also the more basic isomer and its electrophilicity is greatly enhanced by protonation, which can provide the second pathway for faster reductive destruction of the *Z*-isomer [24]. Matching this picture of their reductive lability, an azobenzene PSC was substantially destroyed upon culturing cells under low-oxygen conditions, with the expected detection of aniline cleavage products [25]. Thus, problems can be particularly anticipated for PSCs that are constructed by *extending* an azobenzene onto a drug, such that even fractional isomer-dependent reductive cleavage to the aniline is likely to give significantly greater bioactivity than the intact PSC. For these PSC designs, evaluating the potency of the expected aniline cleavage product can indicate whether *Z*-isomer-specific reductive cleavage should be investigated as a potential source of light-specific bioactivity. Other studies of heteroaryl azobenzene reagents have revealed *Z*-isomer-dependent reduction to diarylhydrazines as a source of bioactivity, arguing for some caution with azobenzene PSCs [26, 27] (Figure 36.3c).

*Cytotoxic photochemical activity* is a constant threat in developing PSCs. Illumination can cause phototoxicity not only via endogenous cellular chromophores, but also by a variety of PSC-dependent mechanisms. These include a drug's ability to damage targets in its environment either by its photochemical reactivity or by phototoxicity (e.g. photocatalyzing singlet oxygen generation). These effects have been well studied in medicinal chemistry, since some very useful drugs also have cell-toxic photochemical activity, such as DNA-crosslinking heavy metal complexes based on Pt(II) and Ru(II), the myosin inhibitor blebbistatin, and anthracycline topoisomerase inhibitors like doxorubicin. It is unlikely that such photochemically active cytotoxins can be adapted as PSCs without photochemical toxicity complicating or overriding their desired mechanisms. While photoswitches such as azobenzenes, heterostilbenes, HTIs, and dithienylethenes seem to cause no appreciable phototoxic effects when illuminated with low photon fluxes, other photoswitches such as nitrospiropyrans and heterostilbeniums are known

singlet oxygen generators and should therefore be avoided for mechanism-specific reagents [28]. Note that cellular sensitivity to phototoxicity mechanisms is strongly dependent on the subcellular localization of the chromophore [29] as well as other complex factors. Therefore, apparent structure-dependent bioactivity is to be expected for phototoxic PSCs maintained under lit conditions and need not indicate any differences in binding affinity or potency toward a proposed target.

Under high photon flux conditions, two additional illumination-dependent processes can cause confounding readouts with any PSCs, in cell-free or cellular conditions. Firstly, under high light intensities, photochemically unreactive chromophores cause cytotoxicity even in vivo by PTT. This can be expected if fast-relaxing PSCs are tested under high-intensity illuminations that are intended to maintain a high population of the metastable isomer [5]; and it may be severe if the PSC concentrates into environments whose integrity is critical to cell survival (such as mitochondria for delocalized lipid cations, or membranes for hydrophobic/surfactant-like compounds). Secondly, in cell-free as well as cellular conditions, "chromophore-assisted laser inactivation" (CALI) with high photon fluxes can cause *on-target but photon-dependent, irreversible damage* to protein binding partners that are in closest proximity to the PSC. This CALI effect is widely exploited in cell biology for targeted protein inactivation [30] and should be anticipated with focused lasers on microscopes, or with long high-intensity sample illumination in cell-free settings. Both these sources of phototoxicity can give misleading results that appear to show cytotoxic or cell-free protein inhibitory activity under illuminated conditions which can be expected to feature apparent structure-dependent potency based on subtle differences of biodistribution or binding affinity, so careful controls are needed if high light intensities are unavoidable (Figure 36.3d).

Straightforward methods can test whether a PSC retains its desired mechanism of action and avoids these off-target effects. Isomer-dependent solubility effects [31] can easily be checked before and after assays by UV–vis spectroscopy. Showing that regioisomeric control compounds are biologically inactive is a particularly important step [9, 11]; alternatively, showing that sign inversion designs have sign-inverted bioactivity [32], and/or that using different photoswitch scaffolds gives similar isomer-dependent bioactivity patterns [4, 11], all support that the PSC's cellular mechanism of action is indeed photoisomer-dependent rather than photon-dependent. In situ photoswitching results should also match those from pre-illuminated stocks of PSCs. These and other guidelines to control for sources of irreproducibility are recently becoming available [9].

### 36.2.6 General Design Features of PSCs

The design logic for PSCs is similar to that of the other photopharmaceuticals reviewed in this volume and elsewhere [12, 16, 33]. Primarily, a photoswitch must ensure isomer-dependent biological potency. Typically, this is achieved using changes of molecular shape at a key region to modulate binding affinity, although polarity and hydrogen bonding have also been employed [14, 34, 35]. Changes

in molecular shape that propagate from an intracyclic photoswitch through macrocyclic systems have also proven compelling [35, 36]. While solubility and therefore cytosolic bioavailability can also be isomer-dependently modulated (e.g. up to 40-fold greater solubility of *Z*- than *E*-azobenzenes [31]), photopharmaceuticals exploiting these changes are not likely to deliver reproducible biological effects in increasingly complex models, and even their photoresponse may be unpredictably suppressed by aggregation, so such designs should be avoided where possible. Since residual bioactivity in a PSC blocks the unique research applications that it could otherwise attain in 3D systems (Section 36.2.3), it is most valuable to design PSCs for low residual bioactivity in the less active isomer (e.g. <5% of that of the other isomer) even some potency must be sacrificed.

Photoswitchably bioactive inhibitors were first reported for azobenzenes in 1968 [37], and to date, most PSCs have relied on the large isomer-dependent shape changes associated with double bond photoisomerization photoswitches. Of these, azobenzene is the scaffold with the most-advanced molecular engineering, such as near-quantitative bidirectional photoswitching and photoresponse to 500–700 nm light, installed by heteroaryl, tetra-ortho-substituted, and cyclic analogs [12]. However, PSCs remain the class of photopharmaceuticals that are least dominated by azobenzene derivatives.

Depending on the desired assay setting, a favorable relaxation half-life may be targeted during PSC design (e.g. from hundreds of milliseconds to minutes in 2D cell culture; from seconds to minutes/hours in 3D applications). A high completeness of photoswitching *toward the less bioactive isomer* must also be emphasized for PSCs, to suppress residual bioactivity; and to favor completeness of photoisomerization, azobenzenes, stilbenes, and indigoids are increasingly being replaced by their heteroaryl derivatives [12, 13, 15]. Azobenzenes have clear advantages for rationally designing combinations of relaxation rates and completeness, since their photostationary state isomer distributions (PSDs) are well studied and predictable, and relaxation rates can often be estimated to within an order of magnitude. However, a notable exception are those PSCs designed for "photoactivation mode" use (see Section 36.2.4), since relaxation and bidirectional isomerization are irrelevant for that mode, a broader range of scaffolds can be employed, particularly those that are differentiated from azobenzenes by greater metabolic stability or orthogonality to selected imaging wavelengths. Examples of such reagents being rapidly transitioned through all assay settings from 2D to animal models have recently appeared [15] (see Section 36.3.1.3).

In conclusion, the most valuable uses of PSCs depend on their ability to pattern mechanistically defined drug bioactivity with spatiotemporal resolution on the time and length scales which are relevant to their underlying biological targets and assay parameters.

The next sections now review the PSCs that have been applied in cells to address defined and critical biological targets. The intention here is not just to present the performance of these PSCs, since they have been reviewed several times [2, 3, 16, 33], but particularly, to pick out features from each class to illustrate the opportunities and challenges for PSCs as high-precision reagents, an aspect which has been

much less discussed. Therefore, special emphasis will be given to aspects where deeper evaluations, further chemical developments, or alternative approaches could improve the contributions of PSCs to biological research.

## 36.3 Photopharmaceutical Analogs of Cytotoxic Drugs

### 36.3.1 Microtubule Structure and Dynamics (Antimitotics)

Microtubules (MTs) are giant tube-like noncovalent polymers that are used as intracellular scaffolds and tracks for hundreds of critical cellular processes. Each MT is built from tens of thousands of α/β-tubulin heterodimers, and tens of thousands of MTs are organized into the cellular MT network. Key roles of MTs, most of which are spatiotemporally differentiated, include maintaining cell shape, generating forces, serving as tracks for transport of cargos and mitochondria by motor proteins, and acting as an organizing system for proteins and structures within the cell. MTs require constant remodeling to drive or perform these cellular functions; MT inhibitors are compounds that block the necessary remodeling dynamics. These act either by stabilizing MTs (preventing necessary depolymerization) or by destabilizing them (removing necessary MT polymers), which have different biological consequences particularly in vivo [38]. Since the segregation of chromosomes relies on MT dynamics, MT inhibitors also block cell division, causing cell cycle arrest and committing cells to apoptosis. While MT inhibitors can be cytotoxic to all cells, and indeed were mostly discovered as cytotoxic natural products, many of them have found valuable therapeutic uses against cancer (paclitaxel, vinca alkaloids, and epothilones) relying in part on the impact of MT inhibition during cell division; others are applied in inflammatory diseases (colchicine).

MT inhibitors are also used very widely in basic research as reagents to manipulate cytoskeleton-dependent processes: with applications in diverse fields from cargo trafficking and cell migration, to cell division, embryonic development, and neurodegeneration [38]. However, since these inhibitors cannot be applied with the spatiotemporal precision needed to address their biological roles, PSCs that can optically modulate MT dynamics and stability have been hotly pursued. Ten families of MT-inhibiting PSCs have been developed; about 10 further reports applied the reagent **PST-1** for studies of the roles of MTs in e.g. cell migration, cargo transport, cell polarity, and embryonic development. These compounds illustrate several aspects of general importance to PSC development and use, which will now be reviewed.

#### 36.3.1.1 Microtubule Stabilizers: Taxanes and Epothilones

***Taxanes***

MT stabilizers typically have large and complex structures, where no motif can be identified for isosteric replacement by a photoswitch. Accordingly, Trauner and Thorn-Seshold used an azobenzene extension design to modify the sterically tolerant side chain benzamide of paclitaxel, creating **AzTax** (Figure 36.4a) [8].

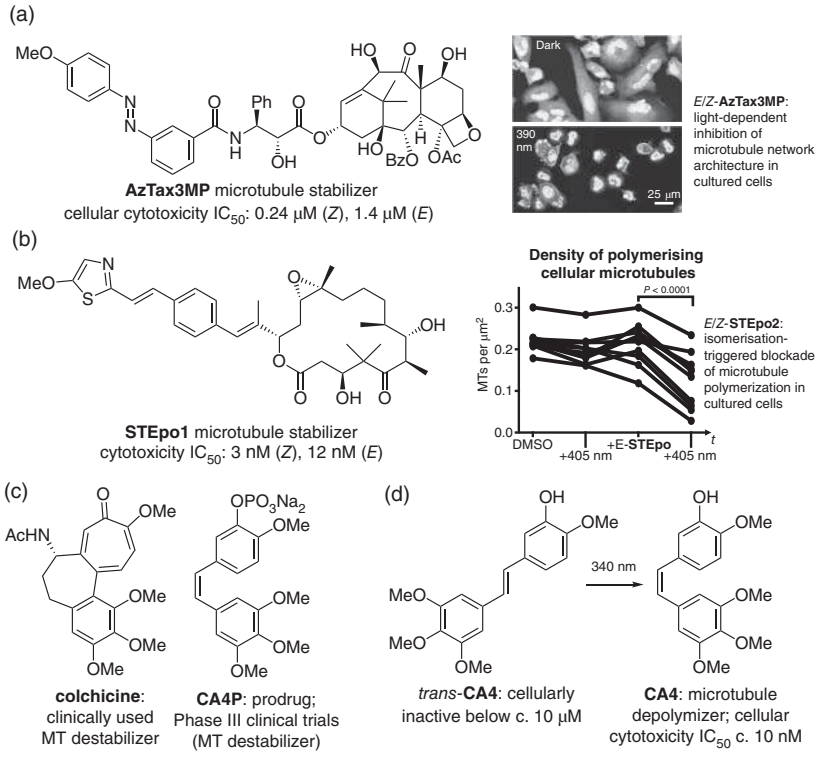


**Figure 36.4** Photoswitchably toxic microtubule-targeting natural product derivatives. (a) Trauner and Thorn-Seshold's azobenzene-extended taxane **AzTax3MP**, a moderately potent *Z*-active microtubule stabilizer enabling subcellular spatial targeting (microtubules shown in gray, nuclei in white). (b) Thorn-Seshold's epothilone-inspired styrylthiazole extension photopharmaceutical **STEpo2**: a potent, *Z*-active microtubule stabilizer. (c) Colchicine and structurally similar, *cis* natural product combretastatin A-4 (shown as its phosphate prodrug **CA4P**) are microtubule depolymerizing agents. (d) Hadfield, Bisby, and Scherer advanced *trans*-**CA4** as a photoactivation mode PSC. Source: Müller-Deku et al. [8].

An SAR series of 10 **AzTax** identified the three-carboxamide orientation as giving greater isomer-dependent difference of bioactivity than four-substituted analogs (*E/Z* equipotent) and better potency than two-substituted analogs. A *para*-methoxy substituent was used in the lead reagent **AzTax3MP** to give satisfactory PSDs (determined in buffer without cosolvent, by using soluble carboxamide analogs). Cell-free tubulin polymerization assays confirmed their MT-inhibiting ability, and a combination of long-term (cytotoxicity and cell cycle arrest) and short-term (MT network structure, and MT polymerization dynamics) cellular assays supported that isomer-dependent disruption of MT dynamics and structure was their major cellular mechanism of action, at concentrations matching their cytotoxicity. A drawback was that its difference of cytotoxic potency between all-*E* and the best-*Z*-PSD was moderate (sixfold); this is often seen with photoswitch extension designs where the photoswitch configuration brings only minor impact to the overall molecular structure. **AzTax** solubility was also poor, preventing its use outside

2D cell culture. Nonetheless, the reagent showed high spatial precision: repeated 60 second cycles of cell-specific photoisomerization and diffusional recovery could reversibly modulate MT polymerization in single selected cells without affecting dynamics in neighboring cells; and a degree of subcellular MT targeting was also shown by localized inhibition of MT polymerization dynamics in selected dendrite regions of individual rat hippocampal neurons [8].

***Epothilones***

Orthogonality to GFP/YFP imaging, and metabolic resistance, are desirable features for photopharmaceuticals intended for use in 3D models and in vivo. As azobenzenes do not typically perform well in these respects, Thorn-Seshold pursued heterostilbene-extended analogs of the MT stabilizer epothilone, which, beneficially, is more potent and soluble than paclitaxel [14]. In these designs, a styrylthiazole photoswitch was attached at a sterically challenging position, where the thiazole's preferences for a hydrogen bonding interaction to tubulin protein as well as the *Z*-photoswitch's preferred nitrogen-out geometry, were harnessed to design low nanomolar **STEpos** that were more active as the lit *Z*-isomers (Figure 36.4b). Through a small SAR series, an *E*-active regioisomer was also demonstrated, supporting that there were no significant effects from phototoxicity. The spatial precision of **STEpo** bioactivity photoswitching was shown on a 10-μm scale in cell-free assays, and live cell assays supported photocontrol of MT dynamics as the cellular bioactivity mechanism [14]. A notable feature of the styrylthiazole is its orthogonality to GFP imaging. Since it is an isostere of the widely used azobenzene photoswitch, it should be possible to adopt it in designs known for azobenzene photopharmaceuticals, in order to harness this beneficial feature for biological studies (see also Section 36.4.2 and [7]). A drawback was that its steep absorption cutoff resulted in photoisomerization with the standard 405-nm microscopy laser line being 1–2 orders of magnitude slower than for other photoswitches, although this can likely be addressed with substituent tuning.

#### 36.3.1.2 Microtubule Destabilizers 1: Combretastatins and Azocombretastatins

By contrast to the complex structures of MT stabilizers that have limited potential for even photoswitch extension designs, the structure and the SAR of the MT destabilizer colchicine offer an opportunity that is rare in photopharmacology and is probably unique for PSCs. The pharmacophore of colchicine is simple: two polysubstituted aromatic rings held rigidly in proximity to each other. Structurally similar natural products include the mid-nanomolar potency *cis*-stilbene, combretastatin A-4 (**CA4**; Figure 36.4c); crucially, it was shown by Pettit that *trans*-**CA4** has no tubulin-inhibiting activity (c. 20 000-fold less affinity) [39, 40]. Although *trans*-**CA4** has other bioactivity in the mid-micromolar range, this suggests a broad window within which local *trans*-to-*cis*-isomerization of colchicine-like **CA4** analogs could locally target MT inhibition, against a background of essentially zero inhibition.

***Combretastatins***

Hadfield, Bisby, and Scherer identified this PSC concept in the early 2000s and performed seminal studies with the stilbene **CA4**. Having treated cells with *trans*-**CA4**

(Figure 36.4d), they applied increasing photon fluxes of UV light in a photodose response study, showing that the cytotoxicity was maximized after reaching the photostationary state (c. 6-minutes single-photon UV illumination, c. 10 000-fold toxicity increase). In an interesting "double cage" concept, they also employed a UV-photocleavable protecting group to further reduce the toxicity of *trans*-**CA4**, this being the easiest route to improve the pre-/post-illumination toxicity ratio [41]. These studies confirmed the feasibility of using in situ photoisomerisation to light specifically apply bioactivity from an MT inhibitor, but the wavelengths needed ($\lambda_{max} \sim 335$ nm) were inaccessible to the microscopy studies which could have made use of the PSC's potential spatiotemporal specificity. Therefore, they also examined two-photon isomerization at 640 nm, which can be performed on specialized microscopes. Noting that the lipophilic *trans*-**CA4** is intracellularly bioconcentrated into membranes and lipid droplets, reaching up to 200× the extracellularly applied concentration [42] (an effect that is probably relevant for many photopharmaceuticals), they theorized that *trans*-to-*cis* photoconversion of even femtolitre intracellular volumes could apply meaningful effects, given the high tolerated doses of *trans*-**CA4**. In situ two-photon isomerization in 2D cell culture was inconclusive however: 48 hours after two-photon irradiation, only cells which had been irradiated had been killed (i.e. not their neighbors) [43]. Since diffusion on the seconds to minutes scale is observed after single-photon photouncaging, this persistent effect suggests that toxicity had been applied irreversibly by photochemical means (see Section 36.2), rather than pharmacologically by the in situ generated *Z*-**CA4**: i.e. in situ two-photon activation was unsuccessful.

#### *Azocombretastatins*

In 2014, Thorn-Seshold reported azobenzene analogs of **CA4**, intended to allow reversible bidirectional photoswitching as well as spontaneous relaxation to a biologically inactive *trans* isomer [44]. These analogs included the simple isostere **PST-1** and its faster-relaxing amino analog **PST-2**; as well as phenolic phosphate ester **PST-1P** and serinamide **PST-2S** which are their water-soluble prodrugs, intended for in vivo use (analogous to the water-soluble **CA4**-like prodrugs that reached human Phase III clinical trials; Figure 36.5a). In situ illuminations of lead **PST-1**, continued over several days (390 nm pulses every five minutes to maintain a *cis*-rich PSD), could photocontrol cell proliferation, cell cycle arrest, and induction of apoptosis in a range of cell lines, with a > 20-fold ratio of lit to dark cytotoxic potency being reached, although the *Z*-azobenzenes had a 25-fold loss of potency compared to *Z*-**CA4**. Uniquely, experiments using a double-illumination "rescue" protocol wherein each UV pulse was immediately followed by a pulse at 505 nm to reduce the *cis* proportion (applied globally throughout the sample) showed significantly reduced cytotoxicity despite applying more photons overall. This important result supported that **PST-1** toxicity was only dependent on the photoisomer ratio and did not involve phototoxicity; and showed that multiple cycles of reversible photoisomerizations could be used in long-term experiments with the azobenzene analogs, to reach unique outcomes inaccessible to the irreversible stilbene photoswitches.

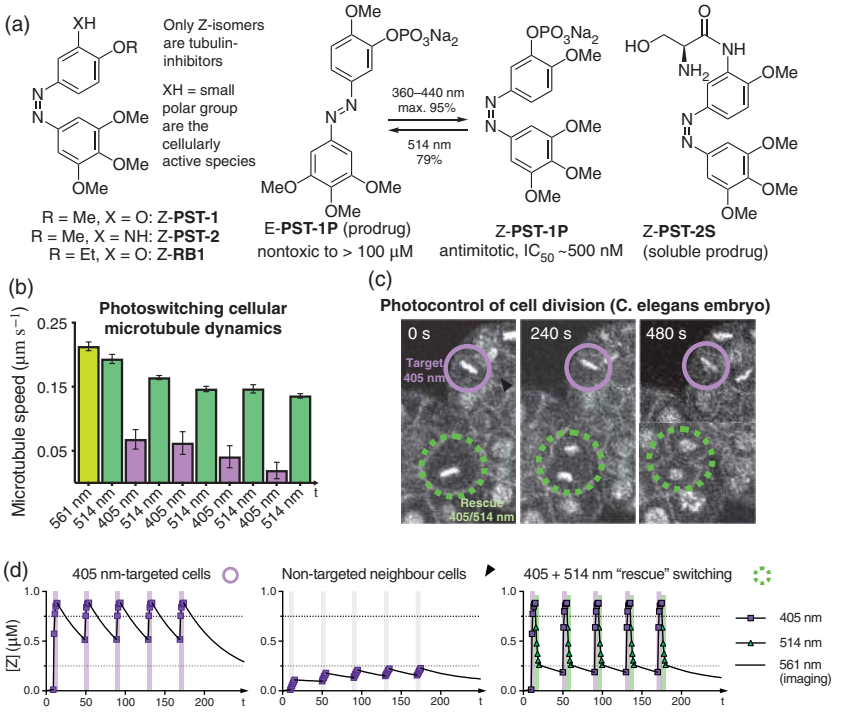


**Figure 36.5** Azocombretastatins as reversibly photoisomerizable antimitotics and microtubule inhibitors for cell culture and early embryo use. (a) **PST-1** and related azocombretastatins give photoisomer-dependent cellular cytotoxicity. (b) Optical control over cellular microtubule dynamics, using active bidirectional photoswitching of **PST-1**. (c) Cell-precise optical control over cell division in embryonic development of the worm *C. elegans*, using both 405 nm targeting, and dual 405/514 nm "rescue" pulsing cycles, with **PST-1**. (d) Particularly in the absence of convectional currents (e.g. in the eggshell-surrounded worm embryo), slower global *Z*→*E* isomerization by 561-nm imaging light can be a significant factor in maintaining the spatially precise division between uninhibited and highly inhibited cells or regions (after 405 and/or 514 nm patterning) despite transmembrane diffusion.

In 2015, Trauner and Thorn-Seshold reported cellular and embryonic uses of the bidirectional photoreversibility of **PST** [4], showing the value of the fast switch-off that PSCs enable but that photouncageable inhibitors or wash-in/washout experiments cannot (Opportunities 1 and 2; Sections 36.2.2–36.2.3). Multiple cycles of alternating 405 and 514 nm in situ illuminations on the microscope were used to reversibly control microtubule polymerization dynamics in live cells in 2D cell culture, with temporal resolution on the scale of seconds, relying on active photoswitching at 514 nm for **PST** switch-off (Figure 36.5b). Then, to test applications in an early-stage animal model, individual dividing cells within intact worm embryos were optically targeted with repeated pulses of 405 nm for inhibition, or with repeated 405/514 nm rescue protocol cycles. 405-targeted cells were blocked in mitosis, while their division-synchronized nearest-neighbr cells divided unaffected,

showing precise spatial targeting maintained over minutes in the embryo. The 405/514 nm rescue cells were also unaffected; this stringent test showed that reverse photoisomerizations fully release MT inhibition on timescales faster than diffusion, highlighting the temporal precision of the PSC approach (Figure 36.5c,d).

Interestingly, although the PSD at 514 nm still contains c. 21% of the bioactive *Z*-**PST** (threefold change compared to c. 76% at 405 nm), it was shown that imaging at 561 nm, a wavelength that is ineffective for photoisomerization in cuvette characterization, slowly isomerized the whole sample toward c. 9% *Z*-isomer PSD (ninefold change compared to the PSD at 405 nm) [45]. This is probably a general effect for most azobenzenes when imaged on confocal microscopes, due to the high intensity of the microscopes' focused lasers (typical intensities 30 mW $mm^{-2}$, compared to c. 0.01 mW $mm^{-2}$ for long-term LED illumination in cell culture [9, 15, 46]). This can be a drawback, limiting useful **PST** concentrations to those for which c. 9% *Z* remains biologically inactive (the problems of this non-orthogonality to imaging wavelengths are discussed later). However, at low **PST** concentrations where 9% *Z* does not pass the threshold for MT inhibition, this global isomerization during 561-nm imaging can counteract the diffusion of *Z*-isomer from 405-nm-targeted cells into neighboring cells, so ensuring that all nontargeted cells escape MT inhibition (Figure 36.5d). This enables steeper spatiotemporal bioactivity gradients than are possible from 405/514 nm patterning alone; and it may be useful to exploit this effect more broadly with other azobenzene PSCs.

Simultaneously, Streu reported the azocombretastatin **PST-1** as synthesized by an improved route. They confirmed that the cellular cytotoxic potency of *Z*-**PST-1** is c. 20 times lower than that of *Z*-**CA4**; intriguingly, they showed that its potency of inhibiting tubulin polymerization in cell-free conditions is only two times lower [47]. It was possible that the azobenzene's more polar N=N bridge may reduce its tendency to be intracellularly bioconcentrated, lowering apparent potency. Rastogi and Brittain therefore compared **PST-1** with **RB1**, its *para*-ethoxy analog, noting that its slightly slower photoisomerization in aqueous media could reflect desirably greater hydrophobicity (Figure 36.5a). *Z*-**RB1** indeed proved to be c. threefold more potent than *Z*-**PST-1** in 2D cell culture, but it was still one order of magnitude less potent than *Z*-**CA4** [48]. Other studies indicated that the electron-rich *Z*-azobenzene's lower cellular potency may be due to its biodegradation to non-inhibiting byproducts. Hartman observed fast degradation of *Z*-**PST-1** by GSH [46], although *E*-**PST-1** resists GSH degradation [11] (when TCEP is excluded). This could align with the earlier observation of isomer-*independent* **PST** toxicity to highly metabolically active liver cells, probably due to their extensive reductive cleavage of the N=N bond to toxic aniline byproducts [44]. Recently, Zhao and Wang studied **PST-1** in cells cultured under hypoxia (oxygen-deficiency), a characteristic feature of all solid tumors. Hypoxia upregulates reductive repair pathways and could also prevent re-oxidation of diphenylhydrazine reduction intermediates (Figure 36.3c). They showed that *Z*-**PST-1** no longer causes cell cycle arrest (a consequence of MT inhibition) under hypoxia and identified the aniline reductive cleavage byproducts as the major species left in cell culture media

after incubation in hypoxia [25], which highlights a likely dynamic liability of azobenzenes in cells.

Despite these limitations, a range of successful biological studies have relied on bidirectionally reversible photoswitching of **PST-1** as a unique method to apply spatially defined MT inhibition within temporally defined windows, even in the context of undergraduate biology practical courses [9]. Four selected research examples will be given. Plachta used **PST-1** to reveal the origins of microtubule organization in early-stage mouse embryos, which had remained an unsolved issue since mammalian embryos lack centrosomes [49]. Matis uncovered the crucial role of MT-based force generation as a complement to actin-based mechanics in driving morphogenesis in *Drosophila* embryos [50]. Theisen showed the role of MT-supported intracellular cargo transport in permitting neuronal migration within the developing zebrafish, a study that was enabled only by the fully soluble prodrug **PST-1P** due to the fish's intolerance to organic cosolvents [45]. On still more precise spatial scales, Sixt used targeted photoswitching to show the subcellular role of microtubule structure and dynamics in permitting individual dendritic cells to retain overall cohesion during migration [51].

Taken together, the **PSTs** have proven powerful reagents for high-precision MT control in 2D cell culture and early embryo applications, and they also vouch for the potential of PSCs in general. Notably, the specificity of the **PSTs**' cellular/in vivo mechanism of action has been validated by 6 independent chemical reports and 10 additional biological reports across a variety of model organisms, representing the highest level of translation of any PSC to date.

The research on **PST**s in comparison to **CA4** has more broadly highlighted liabilities and opportunities for PSCs based on azobenzenes or stilbenes. In 2D cell culture, the azobenzene **PSTs** have succeeded as reproducible and easily accessible reagents with lower complexity than photouncageable inhibitors. In cell culture and in early-stage embryos, azobenzene **PSTs** have enabled reversible spatiotemporal targeting that has demonstrated the first two unique opportunities of PSCs. However, the model-dependent metabolic liability and the attendant low apparent potency of **PST-1** are severe restrictions that can block systemic uses of this azobenzene reagent in larger animals. In these respects, stilbene **CA4** offers 10-to-50-fold better potency and metabolic robustness which have enabled its application even in humans (though not as a PSC). The main problems with stilbene **CA4** are its photochemical degradation, e.g. by 6π-electrocyclization oxidation to a phenanthrene, and its nonresponse to 405-nm light which means that it cannot be optically targeted on microscopes. At the other end of the spectrum, the long-wavelength absorption tail of the **PST-1** azobenzene's $n \rightarrow \pi^*$ band causes extensive spectral overlap across GFP, YFP, and even RFP imaging bands. While this *can* in special circumstances be exploited, it is a limitation particularly for in vivo studies since (i) typically several fluorescent proteins should be imaged at once for multiplexed readouts, which will globally interfere with PSC bioactivity, and (ii) limiting PSC concentrations to those where e.g. 9% *Z* is inactive in *any* cells is particularly problematic in 3D systems and in vivo where drug concentrations strongly vary with cell distance from the surface [9].

#### 36.3.1.3 Microtubule Destabilizers 2: Heteroaryl Colchicine Analog PSCs

Given the drawbacks of azobenzene-based PSCs in specific settings, the Thorn-Seshold group has explored several C=C photoswitch scaffolds for MT-inhibiting PSC colchicinoids.

***Hemithioindigos (HTIs)***

The C=C-based HTI photoswitch is well known in materials sciences but has been barely utilized in cellular photopharmacology. However, HTIs feature all-visible-light photoswitching, near-complete $E \rightarrow Z$ photoswitching in the 510–550 nm region ($\gg$95%), and lower molecular symmetry than azobenzene, all of which can be exploited in appropriate designs. A set of HTI-based colchicine-mimic **HOTubs** were first reported in 2019 [32]. Exploiting asymmetry, both *E*-active and *Z*-active **HOTubs** were designed, with one aim being to use near-complete photoisomerization of *E*-active compounds (such as **HOTub-81**; Figure 36.6a) back to a less bioactive *Z* to generate steeper spatial gradients of bioactivity than azobenzene **PSTs** permit. The **HOTubs** indeed featured both *E*- and *Z*-active representatives as desired, and their MT-inhibiting cellular mechanism of action was supported by light-dependent cell cycle arrest. **HOTub** reagents faced two drawbacks: low potency and low photoswitchability of bioactivity. The most potent **HOTub** had a cellular $IC_{50}$ of only 1 μM, which is problematic as the solubility of HTIs is much poorer than that of azobenzenes.

Thus, the second generation study optimized potency by hopping toward a different parent drug scaffold, giving an SAR series of **HITubs** [17] (Figure 36.6b). The *para*-hydroxy group ensures relaxation on the seconds-to-minutes timescale which is appropriate for cellular use; and the most potent representative **HITub-4** improved cellular potency down to 100 nM while retaining its cellular mechanism of action. Still, its residual bioactivity in the less active PSD was still 1/4 of that in the more-active PSD, just like the best of the **HOTubs**. However, this residual bioactivity correlated well with the c. 25%–30% residual *Z* isomer content at the PSD [17]. This motivated a search for HTI analogs with still-lower-*Z*-PSDs in order to generate high photoswitchability of bioactivity.

Therefore, the third generation SAR study used pyrrole HTI as the photoswitch, which features c. 95% $Z \leftrightarrow E$ photoconversions which is optimally photoisomerized by 442/532 nm laser lines. The lead compound of this series, **PHTub-7** (Figure 36.6c), now reached c. 12-fold photoswitchability of cytotoxic bioactivity and showed long-term photocontrol over cell cycle arrest and cellular MT network structure [13]. Short-term photocontrol of MT dynamics was also demonstrated in live cells (the first such use of HTIs in photopharmacology). Exceptionally, this was shown with both *E*- and *Z*-active **PHTubs**, which united with the SAR series exploration, supported the cellular mechanism of action and excluded off-target effects. As well as providing a useful reagent toolbox, these studies can motivate the use of HTI or pyrrole HTI photoswitches in photopharmaceuticals for other targets.

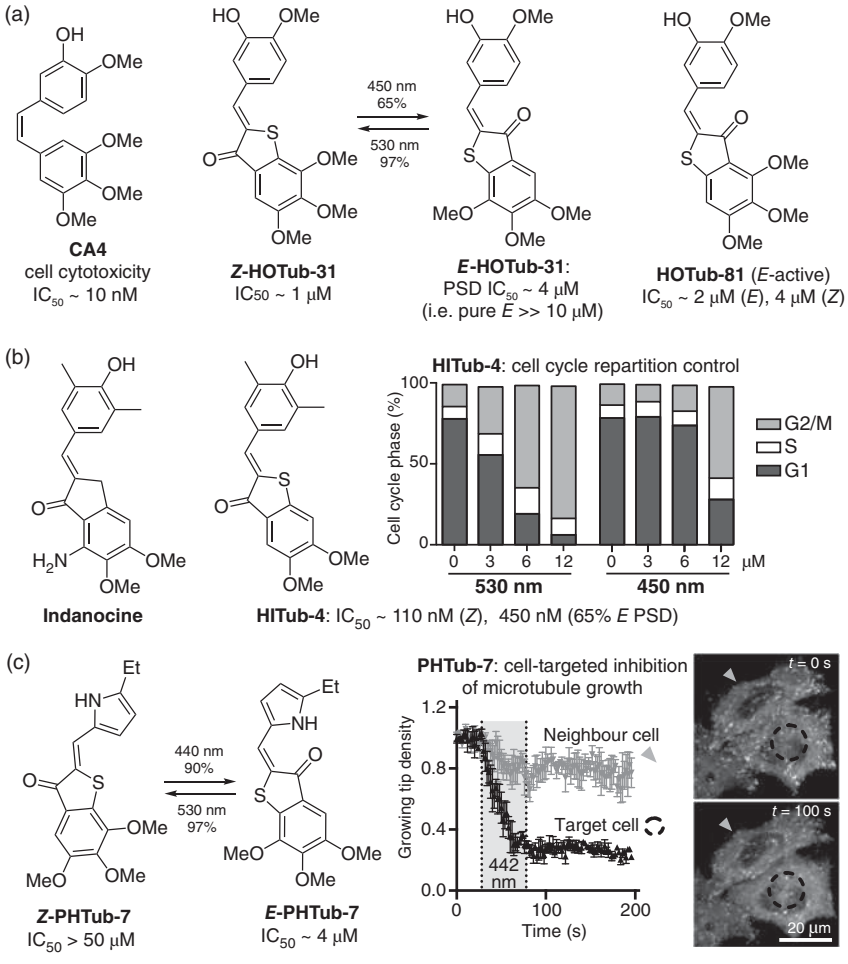


**Figure 36.6** Hemithioindigo-based photoswitchable cytotoxins addressing microtubules. (a) Thorn-Seshold used the asymmetry of the HTI photoswitch to design both *E*- and *Z*-active PSCs inhibiting microtubule dynamics, with good photoswitching completion in the $E \rightarrow Z$ direction only. (b) SAR development for moderately relaxing, potency-optimized **HITub** reagents. (c) Heteroaryl HTI **PHTubs** with improved photoswitching completion in both $Z \leftrightarrow E$ directions could be used for cell-precise photocontrol of microtubule dynamics in live cells.

### *Styrylbenzothiazoles (SBTs) and Styrylthiazoles (STs)*

These heterostilbenes have proven ideally suited to address most of the challenges facing azobenzene PSC antimitotics [11, 15]. The caveat for using Styrylbenzothiazoles/Styrylthiazoles SBTs/STs in cellular photopharmacology is that they are unidirectional photoswitches useful in photoactivation mode, since $Z \rightarrow E$ photoisomerization is incomplete and current SBTs are slow-relaxing at physiological pH [11] (see Section 36.2.4). Still, SBT-based MT-inhibiting PSCs have proven to be powerful reagents for cellular and true in vivo studies across a variety of animal models:

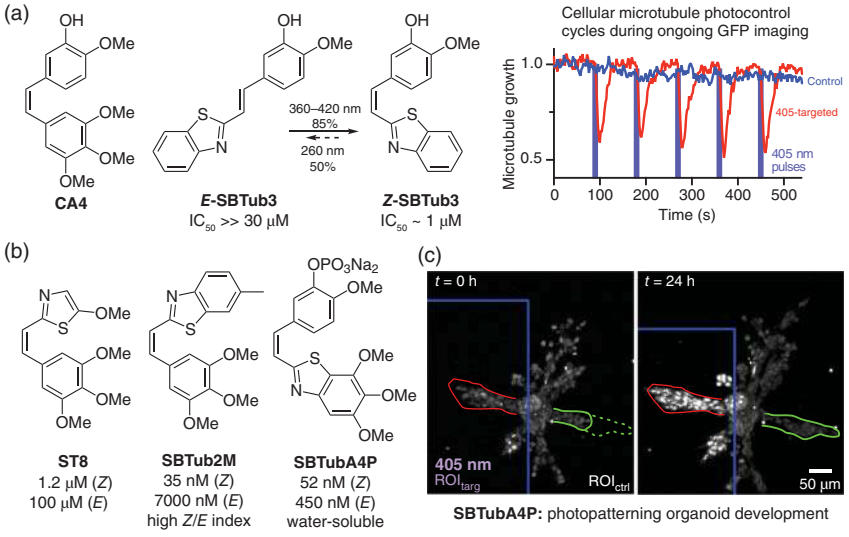


**Figure 36.7** Heterostilbene inhibitors of the microtubule cytoskeleton. (a) Thorn-Seshold's heterostilbene analogs of colchicine/combretastatin as isomer-dependent microtubule inhibitors. (b) SAR development of **SBTubs** for potency, solubility, and photoswitchability of bioactivity. (c) Buffer-soluble **SBTubA4P** photocontrols cell migration and division with cell-scale precision over 24 hours in 3D organoid culture.

The first generation of **SBTub** reagents was designed to isomer-dependently map the SBT photoswitch to the colchicine pharmacophore (Figure 36.7a), with scaffold inversion and regioisomeric controls completing a small SAR set [11]. GSH resistance, liver microsome resistance, and photochemical stability even in a photoreactor were shown to be excellent. *Z*-**SBTubs** were crystallized into tubulin and inhibited tubulin assembly in cell-free settings; their cellular mechanism of action was then validated in assays of cytotoxicity, MT network integrity, and cell cycle arrest. Unlike the HTI-based PSCs, the *E*-**SBTubs** had no detectable cellular effects of up to 50 times the $IC_{50}$ concentration of their *Z*-isomers which was the threshold for aggregation [11].

The second generation of SBT- and ST-based **SBTub** reagents were then produced, including a large SAR series that optimized *Z*-potency down to 35 nM, ensured aqueous solubility up to 2 mM and demonstrated *E/Z*-bioactivity ratios in excess of 200-fold (Figure 36.7b) [15]. Their near-UV absorption maxima (~370 nm) give strong absorption at the 405-nm microscopy laser ($\varepsilon_{405} \sim 10\,000\ M^{-1}\ cm^{-1}$), but their $\pi \rightarrow \pi^*$ band is narrow, so SBT and ST both have $\varepsilon < 10\ M^{-1}\ cm^{-1}$ above 470 nm: making them nonresponsive to high-intensity imaging of GFP (488 nm) or YFP/RFP (514/561 nm), unlike azobenzenes. By combining this total nonresponse to imaging wavelengths with their very high photoswitchability of bioactivity and metabolic stability, the **SBTubs** permitted unique applications inaccessible to the **PST** series, as follows.

High concentrations of *E*-**SBTub** could be applied with many repeated cycles of low-photon-flux 405-nm illuminations (each of which isomerizes only a small

fraction of the **SBTub** in the targeted cell), to repeatedly inhibit or to sustain the inhibition of MT dynamics over very long experimental time courses, without photobleaching and photodamage in the target. Initially, this was shown in 2D cell culture, by repeated cycles of MT polymerization inhibition, where reversibility was ensured by transmembrane diffusion. This was then reproduced subcellularly in sensitive primary neurons, where continuous pulsing in regions of individual neurites maintained a blockade of MT polymerization down the neurite [11]. Then, using the highly soluble **SBTubA4P**, applications in 3D organoids (hundreds of cells) embedded in collagen gels were shown, where repeated UV illuminations maintained cell-precise blockade of invasion and cell division over 24 hours, with precision to the single-cell level (Figure 36.7c). In intact whole-brain explants of dual mCherry/GFP-labeled developing fly embryos, the potency-optimized **SBTub2M** allowed time-specific depolymerization of centrosomal microtubules just before cell division, modifying the sequence of neuroblast development. Last, **SBTubA4P** was applied for both short- and long-term studies in whole animals. In the developing frog, PSC targeting could be used either to stop embryonal development entirely, or else more sensitively to suppress sensorimotor responses. Interestingly, **PST-1P** could not be used for such targeting as it was similarly toxic as both *E* and *Z* isomers in these models, probably reflecting the metabolic liabilities of its azobenzene core. Finally, in two-day-old zebrafish, **SBTubA4P** allowed optically targeted inhibition of the dynamics of intracellular microtubules with reversibility on the timescale of c. 10 minutes and nearly single-cell spatial precision [15].

This range of SBT applications across species, and on different time and length scales, illustrates the research potential of such PSCs which combine efficient photoresponse, metabolic and photochemical stability, imaging orthogonality, and above all a high *E/Z*-bioactivity ratio. It is likely that refined SBT scaffolds permitting either bidirectional photoisomerizations (e.g. at 405/442 nm) or else appreciable $Z \rightarrow E$ relaxation on a ~minutes timescale would represent an ideal "general photoswitch" allowing research to be seamlessly translated from cell-free, to 2D cell culture, 3D, tissue, and through to intact animal settings.

### 36.3.2 Actin Structure and Dynamics

Actin is the most abundant cellular protein and is used to power cell motility, mechanostasis, force generation, shape maintenance, endocytosis, and intracellular transport. As it is both highly conserved and critical to cellular survival, natural product actin inhibitors are widespread as toxins and chemical deterrents. Some were identified early because of their lethality, such as phalloidin from the iconic death cap mushroom. Marine organisms proved a particularly rich source of actin inhibitors, yielding e.g. latrunculin, swinholide, and jasplakinolide in cellular screens for cytotoxicity (Figure 36.8a) [52]. Given the ubiquitous importance of the dynamics and stability of the actin cytoskeleton, and the diversity of processes it supports, reagents that could harness the exquisite target selectivity and high potency of these inhibitors while adding spatiotemporal precision would be highly desirable as tools, to suppress their lethality against organisms or to target their

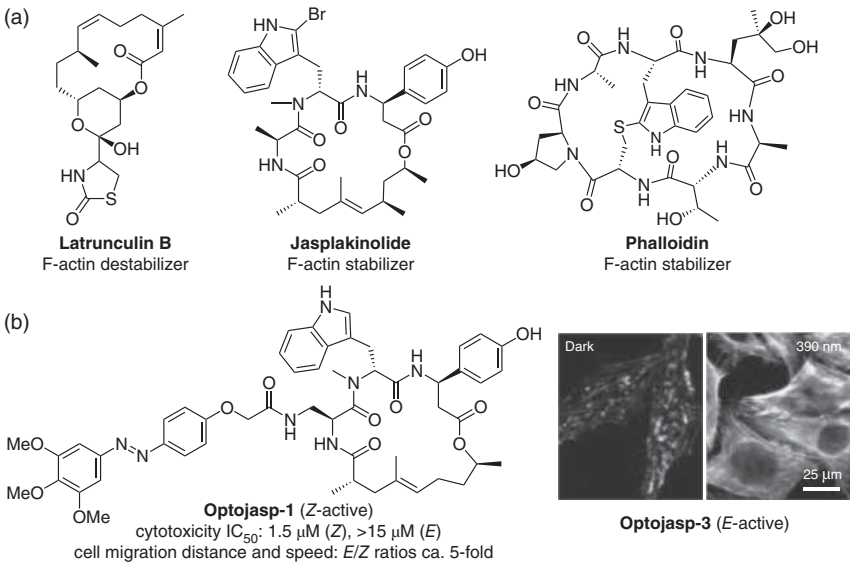


**Figure 36.8** Photoswitchable inhibitors of the actin cytoskeleton. (a) Actin inhibitors are complex natural products. (b) Trauner and Arndt's photoswitchable azobenzene **optojasps**, based on jasplakinolide (cellular F-actin network shown in gray). Source: Allingham et al. [52].

effects to selected cells. A challenge for adapting these actin-targeting inhibitors to photopharmacology lies in their typically large, complex, and flexible structures, in which rigid substructures to replace with photoswitches are rarely apparent [52].

Trauner and Arndt have made the only report of photoswitchable actin inhibitors to date [53]. Using SAR data for fluorescent actin-binding probes based on the inhibitor jasplakinolide, a series of derivatives was prepared attaching azobenzene photoswitches peripherally, via a linker, at a tolerated position in order to retain binding affinity. Variable linker lengths and photoswitch orientations were employed in an SAR series. Matching the design, all **optojasps** (Figure 36.8b) were cellularly bioactive. The anti-actin mechanism of action was confirmed for lead compounds by combining cellular assays to test both direct actin-disrupting effects (on actin polymerization, actin network structure, cell shape and motility), as well as downstream consequences of inhibiting actin-dependent processes with spatiotemporal resolution (nuclear translocation and gene transcription). Notably, some of the reagents had higher cellular potency as *Z* (≥6-fold), others as *E* (1.5-fold), and some were *E/Z*-equipotent. This range of isomer-dependent potencies also gave confidence that phototoxicity or isomer-dependent bioavailability effects, which should be similar across analogs, were not confounding factors.

Arndt and Raunser examined the structural basis of these *E/Z*-differences in detail, in one of the only two studies to yet succeed in obtaining separate structures of both the *E*- and *Z*-isomers of a photoswitchable ligand bound to its protein target [34]. Their results are of great interest toward designing photoswitchable inhibitors in general. The large, flexible macrocycle had essentially identical conformation

and interactions on the protein as both the *E* and *Z* isomers. This is probably unavoidable given the high affinity of the jasplakinolide. Indeed, it is likely that most photoswitch attachment and even extension strategies (e.g. **AzTax** in Section 36.3.1.1) will give the same behavior, unless a region that is crucial for high-affinity binding is derivatized with the photoswitch (though that risks losing affinity altogether). Two unexpected features emerged however. Firstly, on the ligand level, the *Z*-**optojasp** featured a CNNC torsion angle of nearly 90°, whereas free *Z*-azobenzenes typically have ca. 60° torsion angles. This indicates that surprisingly flexible photoswitch geometries may be seen if stabilized by protein interactions: i.e. the photoswitch may contribute actively to binding, rather than merely being tolerated or clashing with the protein. This can be particularly relevant for photoswitch extension designs, where the photoswitch is often held closer to critical interaction sites. Secondly, on the complex level, the conformation of the actin D-loop (an important loop at the interface of actin–actin interactions in the polymer) was markedly affected by the photoswitch. The *Z*-**optojasp** stabilized the closed D-loop conformation much more than *E*-**optojasp** did and showed interactions more like those of phalloidin than jasplakinolide [34]. This indicates that even if the binding affinities of two photoisomers are similar, their biological *potencies* may be different if their binding gives functionally relevant differences in the structure of the complex. While this has been known for decades in e.g. neurotransmitter and channel ligand research, it will no doubt become relevant to photopharmaceutical design, particularly where structural biology or SAR precedent indicates it.

### 36.3.3 DNA Synthesis and Integrity (Antimetabolites and DNA Lesion Agents)

Compounds that damage DNA act on cells from all tissues of origin, and some are among the strongest known cytotoxins. The major cancer chemotherapeutics include agents from diverse chemical classes that directly or catalytically damage DNA (alkylators, crosslinkers, topoisomerase inhibitors, bleomycin, etc.) or prevent DNA synthesis and thus block cell replication (antimetabolites). Independently of potential use as photoswitchable therapeutics, it is likely that photoswitchable, mechanistically defined DNA-damaging agents will prove valuable in e.g. studying the time- and tissue-specific basis of the side effects arising from these cytotoxic chemotherapeutics.

Cisplatin is an archetype for metal complex cytotoxins that crosslink DNA. Many reports have examined photoswitching of ligands for potentially cytotoxic metal complexes, although the field remains at early stages. Branda used photoisomer-dependent electronic communication across diarylethenes (DAE) to modulate coordination strength of a monodentate ligand for ruthenium [54], although on-metal photoswitching was suppressed. Gamez [55] employed the same ligand with platinum (II) coordinating two chlorides and DMSO and applied it to cells. Future work in photoisomer-dependent cytotoxicity based on modulating ligand exchangeability will probably seek to complete the coordination sphere with fewer isomer-independently exchangeable ligands; tuning steps such as increasing

solubility and preventing complex polymerization through the bifunctional ligand might increase the reliability of this approach.

Rather than directly attacking DNA integrity, other approaches target the upstream synthesis of nucleobases, which prevents replication and is ultimately also cytotoxic.

A photoswitchable analog of the eukaryotic DNA synthesis inhibitor methotrexate has been studied by Gorostiza, designed by deleting two ring nitrogens and replacing its bridging aminomethyl group with a diazene to give **phototrexate** [56] (Figure 36.9a). This photopharmaceutical is rather unusual as it is fully water-soluble and is also likely to have good cellular delivery (by benefiting from folate receptor-mediated uptake), which are both excellent design features that could be adopted more widely. **Phototrexate** was light-dependently active against purified DHFR in a cell-free assay system; its lit state also gave greater cellular toxicity and was more toxic to developing zebrafish embryos; in each case, similar potencies as methotrexate were reached for the lit drug. Surprisingly, the *E*-isomer was almost dose-independently active in the cell-free and cellular assays. This nitrogen-rich design does face unusual challenges dictated by its structure and its protein target. Electron-poor aza-heterocyclic azobenzenes are liable to *Z*-specific reductive degradation, and some have been shown to act in vitro by *Z*-isomer-specific reduction with thiols that are standard assay buffer components, generating potent but non-photoswitchable diphenylhydrazines (see Section 36.4.2 and [26, 27]). **Phototrexate**'s target enzyme is also a NADPH-powered reductase that hydrogenates the C=N in alpha to the bridge of its substrate, folic acid. Therefore, during the next development steps of **phototrexate**, it will be interesting to use a similar evaluation procedure as with kinase photopharmaceuticals: e.g. testing its diphenylhydrazine and its non-reducible *E*- and *Z*-stilbene analogs for activity and examining whether both isomers remain intact in cells and in the DHFR assay buffer despite the reductants that are present, to exclude partial reduction as an activity mechanism. Rationalizing *E*-isomer activity through a SAR series could also be valuable; and as elsewhere, results will ideally be complemented by readouts of the cellular mechanism of action (DNA synthesis inhibition). In these ways, **phototrexate** may serve not only as a tool, but more broadly as a valuable test case for the redox robustness of azobenzene approaches, about which much uncertainty persists.

Feringa, Szymanski and coworkers have adapted antibiotics that selectively inhibit prokaryotic DNA synthesis into bactericidal photopharmaceuticals. Such investigations have driven substantial innovations in photopharmaceutical reagent designs (see e.g. [57] and references therein) and are presented separately in Chapter 34. However, it is worth noting here some of the conceptual differences between PSCs for eukaryotic cells and photopharmaceutical antibiotics that arise primarily because of the differences in the intended use of these compounds, and that drive different needs and opportunities for the two classes of reagents.

Firstly, bacteria are much smaller than eukaryotic cells, making spatial targeting by photoswitching more difficult: although as single-celled organisms, the rewards of cell-scale spatial targeting may also be lower (see Section 36.2.2). Secondly,

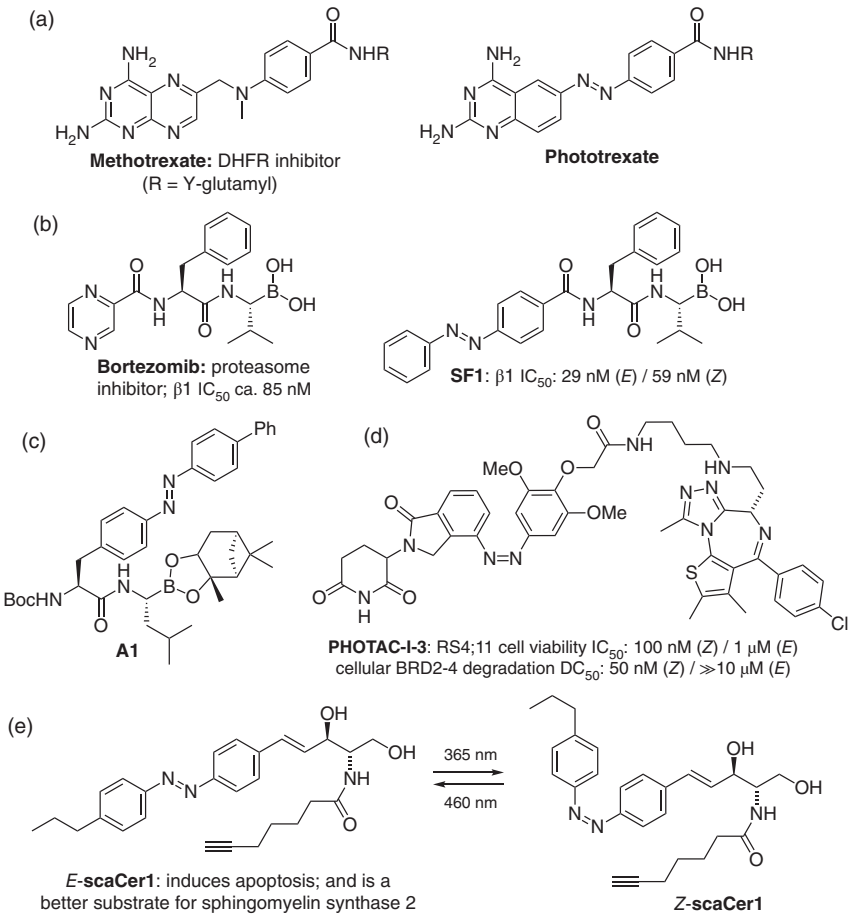


**Figure 36.9** Photoswitchable reagents targeting other critical cellular processes. (a) Gorostiza's azobenzene-incorporating analog of DNA synthesis inhibitor methotrexate. (b) Szymanski and Feringa's distal photoswitch approach to photopharmaceutical bortezomib analogs, **SF1**. (c) Abell's truncated, boronate ester prodrugs of proteasome inhibitor analogs, **A1**. (d) Trauner and Pagano's **PHOTAC** design for optically targeted protein degradation via photoisomer-dependent E3 ligase recruitment. (e) Trauner's photoswitchable ceramide **scaCer1** which isomer-dependently induces apoptosis. Source: Matera et al. [56].

photoswitchable antibiotics have so far been designed as light-dependent toxins, not as reagents to spatiotemporally address conserved targets for research; and so far, on-target potency has been prioritized rather than minimizing off-target effects. Thirdly, the desired duration of antibacterial action has typically been measured in hours, rather than seconds, which deprioritises the seconds-scale temporal targeting that PSCs emphasize. Lastly, PSCs as reagents can enable novel assays already in 2D cell culture or model embryos by modulating spatiotemporally regulated protein function on the microns-and-seconds scale. Photoswitchable antibiotics however have been intended to reach novel uses when applied systemically to humans,

as tissue-selective therapeutics against bacterial infection, and/or when deactivated on a timescale of hours after treatment, to prevent selecting for resistant bacteria in the environment. Whole-animal use brings stringent requirements for their safety profile on both organ and organism levels (see Sections 36.5.1 and 36.5.2), including accounting for both photoisomers as well as likely metabolic byproducts (e.g. anilines arising from bacterial azoreductase activity on azobenzene [58]). The criteria on which photoswitchable therapeutic antibiotics have to compete against alternative approaches are also different to those areas in which research reagent PSCs can differentiate themselves (Section 36.2). Notably, for antibiotics, spatial targeting on the large scale of human tissues faces conceptual comparisons to reagents whose on-target binding can be locally photouncaged; and temporal deactivation on the excretion timescale faces comparisons to excretion-associated mechanisms such as enzymatic cleavage in kidney, liver, or even bladder. These are exciting challenges for synthetic and medicinal chemistry that are also likely to interface strongly with innovations in medical technology and materials sciences; and it is likely that different chemistries will ultimately be needed for antibiotics as compared to PSCs in order to fill these different needs.

### 36.3.4 Protein Degradation

The proteasome is the protein complex needed by all cells to degrade proteins that have been flagged for destruction by ubiquitinylation, whether because of damage or misfolding, or from normal rates of protein turnover. Proteasome inhibitors, such as the approved anticancer drugs bortezomib and delanzomib, cause the accumulation of ubiquitinylated proteins that ultimately triggers cell death by apoptosis. Szymanski and Feringa [59] synthesized bortezomib analogs derivatized with azobenzenes distally to the boronic acid, at the P3 residue (e.g. **SF1**, Figure 36.9b). These gave c. twofold difference in competitive binding to the proteasome in cell lysates, although cellular cytotoxicities were nearly isomer-independent. Abell also investigated derivatives truncating the P3 residue and installing the photoswitch at P2, that were conveniently applied as the boronate ester prodrugs [60]. These were up to fivefold more affine as *E*-isomers in lysate (e.g. **A1**,Figure 36.9c). The most hydrophobic derivative was applied to cells but unexpectedly gave cytotoxicity that was greater for its *Z*-isomer, raising a question for future studies, of whether bioavailability was the determinant of apparent cellular potency as has been seen elsewhere [21] (see too Section 36.4.1). Further refinement of *E/Z*-potency differentials that should be conserved between cell-free and cellular settings is desirable for further development of these mechanistically exciting compounds.

Upstream of the proteasome, heterobifunctional "PROTAC" ligands that recruit ubiquitinylating E3 ligases to a chosen target protein to cause its proteasomal degradation have been a highly active area of research. Though not typically applied as cytotoxins, they also have potential for cytotoxicity by clogging the proteasome with abundant proteins. The mechanistic value of being able to noninvasively modulate levels of a selected protein in optically targeted cells was recognized by multiple laboratories, with designs from Trauner and Pagano [61], Crews and Carreira [62], and

You and Jiang [63], appearing in short succession (Figure 36.9d). PROTACs comprise an E3 ligase ligand, attached via a linker, to a ligand for the protein of interest (POI) that is to be ubiquitinylated and ultimately degraded. This offers three obvious sites for photoswitch incorporation toward "PHOTACs" (photosensitive PROTACs): the E3 ligand, the linker, or the POI ligand. Of these, endowing the E3 ligase ligand with photoisomer-dependent affinity could seem to be the most valuable, since it should permit this motif to be integrated modularly into any existing PROTACs to rationally install photocontrol. By contrast, PROTACs are sensitive to linker length, geometry, flexibility, and polarity and require variable linkers according to their POI target, so photoswitch integration into the linker seems likely to require case-by-case screening of linker libraries for each target pair.

Trauner and Pagano merged an azobenzene into the E3 ligase ligand lenalidomide giving photoisomer-dependent E3 ligase binding and compared the resulting PHOTACs with the second design placing the azobenzene in the linker [61]. Through an SAR series of 19 compounds, representatives of both designs were identified that demonstrated excellent *E/Z*-bioactivity ratios for photodependent cellular protein degradation, and both bromodomain proteins (BRDs, e.g. **PHOTAC-I-3**; Figure 36.9d) and the prolyl *cis-trans* isomerase FKBP12 could be targeted according to the terminal ligand. "Rainbow assays" [4] of protein-degrading bioactivity as a function of cellular illumination wavelengths matched cell-free photostationary state measurements over the full range 370–545 nm, showing maximum activation at 390 nm and maximum photodeactivation around 545 nm and illustrating the possibility of using illumination wavelengths to sensitively modulate bioactivity ("color dosing"). Time-dependent in situ illumination protocols also illustrated the expected photoreversibility of bioactivity, and an appropriate timescale for biological recovery in the dark of c. nine hours. Taken together, this study showed comprehensive proof that these PHOTACs are isomer-dependent bioactives with "clean" mechanisms of action.

Crews and Carreira's photoPROTAC was based on installing an azobenzene into the linker of a BRD2 degrader [62]. They instead used tetra-*ortho*-fluoro-azobenzene, which in contrast to polymethoxylated azobenzenes should have a more *Z*-rich photostationary state at 415 nm, but which cannot be relaxed to a biologically inactive all-*E* state and so requires washout for complete switch-off of bioactivity; the *E/Z*-bioactivity ratio achieved by this photoPROTAC could benefit from improvements through structure–activity tuning to reach the ratios of the optimized PHOTACs. You and Jiang inserted an azobenzene into the linker but instead used a terminal ligand targeting the BCR-ABL fusion protein that is a driver of leukemia, again illustrating cellular photocontrol of protein degradation [63]. These approaches illustrate the broader potential for photoswitches to be employed at the forefront of biological control methods. The conceptual challenge of photoisomer-dependent ubiquitinylation having been met, expansion to target different POIs, and research applications where PHOTAC spatiotemporal specificity or color dosing are critical to assay performance, are now expected.

### 36.3.5 Apoptosis

Photoswitchable ceramides remain a rare example of lipid photopharmaceuticals that apply photoisomer-dependent cytotoxicity through a defined molecular mechanism (compare Section 36.5.1). After exploring long-lipid-chain photoswitchable ceramides for applications to membrane biophysics and to sphingolipid metabolism, Trauner and coworkers developed short-lipid-chain azobenzene-based photoswitchable ceramides such as **scaCer1** (Figure 36.9e). These were not only photoisomer-dependent substrates for sphingolipid metabolism, but also photoisomer-dependently caused PARP cleavage and apoptosis, presumably by hijacking the intracellular lipid signaling pathway by which ceramide insertion to the outer mitochondrial membrane induces programmed cell death [64]. These cleverly designed PSCs are ideal research reagents to probe for sphingolipid-mediated metabolism and signaling.

More broadly, nature employs a variety of signaling lipids and hydrophobic hormones in regulating critical cellular processes, including proliferation and cell death. These rely on lipid bioconcentration out of aqueous environments (that can be a severe drawback for synthetic photoswitchable ligands against cytosolic targets) as an inherent part of the lipid detection and response mechanisms, which can particularly suit photopharmaceutical adaptation. Indeed, there are exciting prospects for research into photopharmaceutical lipids far beyond biophysical/structural roles. Several synthetic hormones used as cancer chemotherapy drugs, including tamoxifen, are themselves photoisomerizable; but only very recently have true photopharmaceuticals for e.g. targeting nuclear hormone receptors and controlling gene expression been developed [65, 66]; and further developments are eagerly awaited.

## 36.4 Selected Photopharmaceuticals with Cytotoxic Potential Against Defined Targets

A number of photopharmaceuticals have been designed as photoswitchable analogs of therapeutically useful drugs that have the *potential* for cytotoxic activity, even if the photopharmaceuticals were not used to apply cytotoxicity (or even applied in cells). Though these do not fit the definition of PSCs, they illustrate the scope of drugs and targets that could be considered. Selected examples will now be presented, aiming to use each class to also introduce key considerations for PSC development in general.

### 36.4.1 KDAC Enzymatic Activity (HDACs and SIRTs)

Histone deacetylases (HDACs) and sirtuins (SIRTs) are KDACs: enzymes that can deacetylate lysine. Most of them operate on histones, where by unmasking the basic lysine side chain amine, polyanionic DNA can be more tightly packed, so reducing its accessibility for transcription. By inhibiting this ubiquitous method of

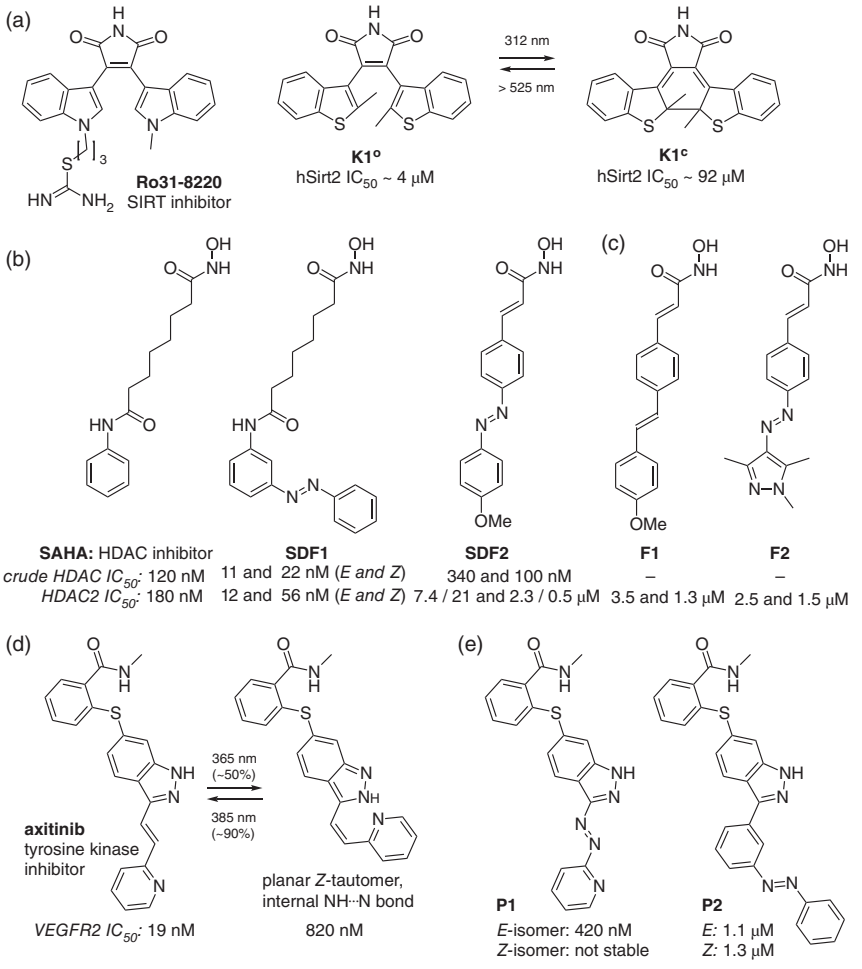


**Figure 36.10** Photoswitchable inhibitors of lysine deacetylases and kinases. (a) König's diarylethene **K1**, inspired by SIRT inhibitor **Ro31–8220**. (b) Szymanski, Dekker, and Feringa's azobenzene hydroxamic acids **SDF1–SDF2**, inspired by the HDAC inhibitor **SAHA**. (c) Fuchter's related HDAC photoswitches **F1–F2**, to extend substituent and photoswitch SAR. (d) Axitinib is an inherently photoswitchable tyrosine kinase inhibitor that responds to near-UV light. (e) Peifer and coworkers' azobenzene-derivatized axitinib analogs **P1–P2**.

regulating gene expression, KDAC inhibitors can also exert antiproliferative effects. Clinically used KDAC inhibitors (such as vorinostat/SAHA and romidepsin) are indeed antiproliferative both in cell culture and in vivo.

Inspired by the report of a bisindolylmaleimide SIRT inhibitor **Ro31–8220**, from 2014 König developed analogs incorporating either DAE (in the nearly isosteric **K1**; Figure 36.10a), or later fulgimide, 6π-electrocyclization photoswitches. So far, these compounds were only demonstrated in cell-free conditions; increased solubility, potency, and photoswitchability of bioactivity in cellular settings would be desirable to improve usability [67, 68].

Other groups focused on developing photoswitchable HDAC inhibitors. HDACs feature a zinc ion at the end of their active site tunnel, that is a Lewis acid for catalyzing acetamide hydrolysis; HDAC inhibitors typically use zinc coordination as a powerful driver of inhibitor binding.

Szymanski, Dekker, and Feringa reported both rigid and flexible azobenzene-bearing hydroxamic acids as photoswitchable HDAC inhibitors [69] (Figure 36.10b). Most of the flexible reagents had similar potency to the parent inhibitor **SAHA**, with zero to moderate isomer dependency (e.g. **SDF1**). The rigid reagents displayed isomer dependency of bioactivity in specific cases when on-target potency was sacrificed unequally from each isomer (**SDF2**: 39-fold *E/Z* ratio reported against HDAC2 in a cell-free assay, by loss of *E*-activity).

As the *E*-**SDF2** $IC_{50}$ values were much lower than the rest of the series (*E*-**SDF2** $IC_{50}$ 21 μM vs. **SAHA** 0.18 μM), Meyer-Almes and Fuchter expanded a SAR study around **SDF2**, varying the photoswitch (stilbene, azobenzene, and heteroazobenzene) and its substituents (H, OMe, and tBu) (e.g. **F1**–**F2**; Figure 36.10c), and including controls for spontaneous relaxation during the assay. This study found only threefold photoswitchability of bioactivity for **SDF2**, matching trends through a series of nine related compounds [70]. A recent work also suggests only ca. threefold photoswitchability of bioactivity can be expected from rigid hydroxamates [71]. It is possible that isomer dependency of context- and kinetics-dependent parameters, rather than binding affinity, may underlie the discrepancies (e.g. the expected lower solubility/bioavailability of the *E*-isomer). Future work may resolve whether the rigid or flexible approaches are best adapted to tackle photoswitchable KDAC modulation.

### 36.4.2 Kinase Activity

Around 60 kinase inhibitors have been clinically approved, most for use in cancer as suppressors of tumor proliferative signaling. Early noncovalent inhibitors usually with low kinase selectivity were later complemented by drugs using covalent-reactive motifs to target selected kinases on the basis of endogenous cysteines around their ATP-binding sites. Photopharmacology has, with the exception of an initial report in 1969 [72], mainly used covalent-reactive approaches only with engineered reactive residues (Chapter 41); but the success of covalent kinase inhibitors may motivate future developments in a similar direction.

Peifer identified that the tyrosine kinase inhibitor axitinib is an inherently bidirectionally photoswitchable heterostilbene (Figure 36.10d), and their investigation into its activity contains five features of general interest to PSC development [7]. (i) The initially surprising result that preswitched *E* and *Z* isomers returned almost identical selectivity profiles over a panel of 300 kinases was conclusively traced to in situ $E \rightarrow Z$ isomerization by ambient light in the high-throughput assay. Elsewhere, results initially attributed to *E*-heterostilbenes but in reality arising from their *Z* isomers [11] have also been found; this can be a particularly likely issue in projects where biological evaluations are performed externally, unless UV–vis or HPLC spectra of assay solutions are acquired both before and after assays [7, 9]. (ii) Peifer then showed

that the *E/Z* bioactivity ratio of axitinib against its major target, the kinase VEGFR2, is approximately 40 in cell-free conditions, and outstandingly, that this translates into a 31-fold ratio of antiproliferative potency in cellular assays where proliferation is highly controlled by VEGFR2. This strong correspondence between cellular and cell-free assay results indicates that no significant confounding features affect the assay outcomes. (iii) They noted that the apparent steep dose–response curve for the less active *Z*-axitinib could be understood as precipitation of the poorly soluble planar molecule, rather than specific action against the target addressed by its *E* isomer. (iv) Minor amounts of the inactive [2+2] cycloaddition byproduct were identified after *in* situ illumination of treated cells, highlighting the potential limitations of photoswitch scaffolds that are prone to undergo aggregation-driven intermolecular photoreaction. (v) Lastly, while the UV/violet wavelengths needed for $E \rightarrow Z$ photoswitching of the heterostilbene definitively exclude use in deep tissue, they actually favor research uses since imaging can be performed over a wide wavelength range without affecting the photoswitch (see also Section 36.3.1.3) [7, 9, 11].

Toward alternatives that could be bidirectionally photoswitched using microscopy wavelengths, Peifer and others evaluated azobenzene analogs of axitinib (e.g. **P1**–**P2**, Figure 36.10e). Interesting complications arose, with severe potency losses and reduction of *E/Z* bioactivity ratios, as well as problematic tautomerism involving the N=N double bond [73, 74]. To some degree these are specific to kinase inhibitors, which tend to feature nitrogen-rich heterocyclic substructures that have proven difficult to adapt for azobenzene reagents, since heteroaromatic and/or bicyclic aromatic rings can make azobenzenes particularly prone to reductive degradation that may be detected in cell-free assays with careful controls [26, 27] but may also arise only in cellular conditions. Therefore, an alternative design approach has attached the azobenzene peripherally, so avoiding these liabilities, but not reaching 10-fold photoswitchability of potency [75]. Taken together, these selected examples show the sometimes unexpected complications facing photoswitch integration for robust PSC design.

## 36.5 Selected Toxic Photopharmaceuticals Acting Against Less-Defined or Cell-Type-Specific Targets

### 36.5.1 Membrane Porosity (Cytolytic Toxins)

The physical integrity of both the plasma membrane and internal membranes is crucial to cellular survival. Membrane disruption can rapidly kill cells by permitting the free exchange of ions and water to the extracellular space and by breaking down intracellular compartmentalization: soap is an excellent toxin in 2D cell culture. Photoswitchable surfactants will likewise be toxic in 2D cell culture, potentially with isomer dependency and even high apparent potency, since their concentration from 3D volumes onto 2D membrane surfaces increases their effective concentration at the site of action (an effect that does not translate to 3D settings). However, as research tools for biology, there is little value in applying photoswitchable soaps

as cytotoxins. Surfactant-like reagents proposed as PSCs against a putative-specific target should be treated with extreme caution and carefully assessed for nonspecific toxicity if used at high concentrations. By contrast, the many successes of nontoxic photoswitchable lipids as research tools, even in vivo, should be noted [76].

Several groups have published light-dependent membrane pore formation reagents, which is precedented by work from the 1970s, particularly in photoswitchable ionophores of Shinkai and Manabe, and Irie and Kato. The gramicidins are pore-forming peptides that have been the focus of much antibiotic research. Although they are toxic to all cells and so cannot be applied systemically, they can be topically used as bactericidal agents. Schreiber reported photoswitchable azobenzene gramicidins in 1991 [77] as models for photocontrolled ion pores; developments from Woolley in the 2000s included introducing HTI as a photoswitch with greater geometric rearrangement upon photoswitching [36]. Since 2004 however, when Erlanger's 1960s concept for photoswitchable ion channel ligands was revolutionized by Trauner and coworkers who genetically engineered a covalent photoswitch ligation site (see Chapter 41), biological channels have instead been used to modulate transmembrane ion currents in living systems with mechanistic selectivity.

However, unspecific artificial pores have seen continued development as photoisomer-specific toxins [78]. Though they lack a defined biological target and so do not match the definition of a PSC, two cases are notable. Firstly, Komarov and Ulrich introduced DAE as a photoswitch motif for gramicidin in 2014 [79]; this was a significant step toward in vivo applications, since the metabolic stability of the DAE can be significantly greater than that of the N=N bond of azobenzene [78] and potentially than that of the HTI C=C (an aldol condensation product). After optimizing a series of analogs [80], they performed the most advanced in vivo studies of a systemically applied photoisomer-dependent cytotoxin that have ever been reported [35, 81], aiming to use the optimized gramicidin as a cytotoxic therapeutic in vivo, whose toxicity should be spatially targeted by local illumination. Their excellent study of derivative **LMB002** (Figure 36.11a) in the mouse included performing and proving tissue-localized photoisomerization in vivo and evaluating isomer-dependent ADME and toxicity [35]. Despite the c. 10-fold difference of cellular potency seen in 2D cell culture, **LMB002** gave only a 1.5-fold difference of $LD_{50}$ dosing in vivo. This indicates a substantial loss of any potential "therapeutic window" upon the transition to in vivo use, which seems entirely reasonable and which underlines the extreme importance of minimizing the bioactivity of the less active isomer if in vivo applications of PSCs are to be realized (see Section 36.2). This study contains much medicinal chemistry detail that will be essential reading for those developing PSCs toward in vivo applications. Secondly, Maglia and coworkers reported a photoswitch-appended analog of the pore-forming peptide toxin FraC [82], featuring nearly fourfold change of hemolytic activity in cell culture between photoisomers; the insertion of an ionic azobenzene photoswitch at a residue contacting the membrane is a clever feature that should find wider application in rational design of photopharmaceuticals.

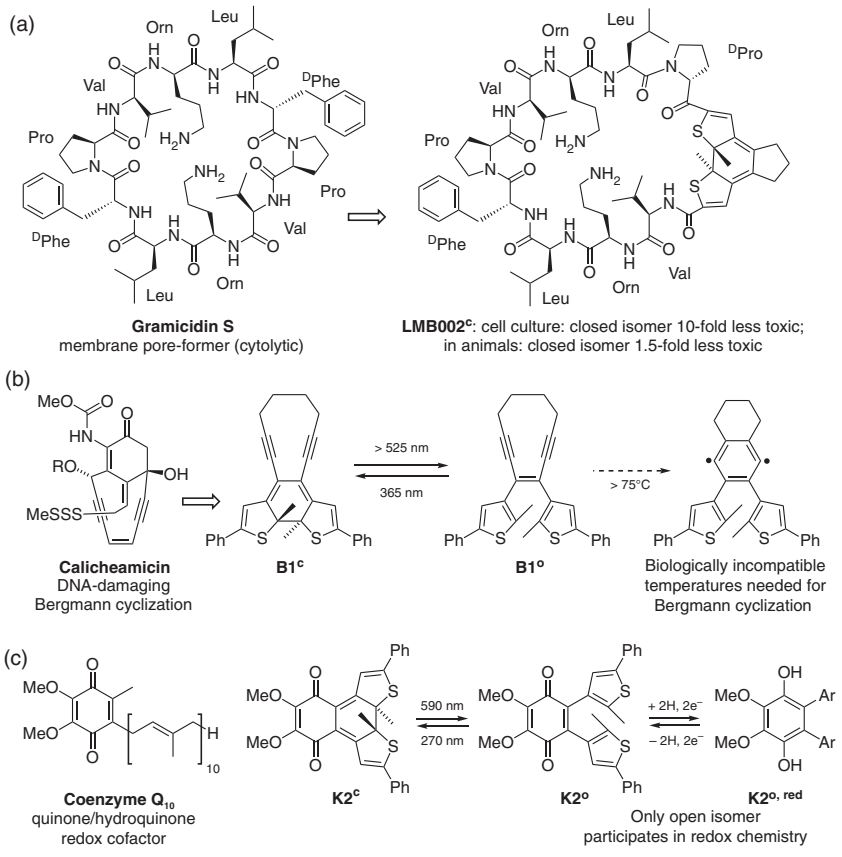


**Figure 36.11** Diarylethene photopharmaceuticals. (a) Komarov and Ulrich's photoswitchably cytolytic gramicidin derivative **LMB002**. (b) Branda's photoswitchable Bergmann cyclization design **B1**. (c) König's photoswitchable analog of redox cofactor $CoQ_{10}$, **K2**.

### 36.5.2 Agents with In Vivo Lethality (Neurotoxins/Myotoxins)

Cytotoxins are compounds that kill the broadest possible range of cell types. Drugs with survival critical targets that are tissue-specifically expressed or drugs that cause organ-level malfunctions that are lethal to organisms do not fit this definition, but they can also benefit from adaptation as high-precision photopharmaceuticals in order to exclude off-target effects in biological studies. This includes many ion channel modulators that can act as neurotoxins or myotoxins. For example, Gorostiza has observed isomer-specific lethal bradycardia in rats locally treated with photoswitchable muscarinic acetylcholine receptor agonists, which could also be used to control heart rate in frog tadpoles [83]. Similarly, Shao created photoswitchable ligands for the insect ryanodine receptor that have isomer-specific insecticidal activity [84].

Such photopharmaceuticals often have less stringent performance standards than for PSCs, as undesired effects in untargeted cells may be avoided simply by relying on target expression patterns rather than requiring near-zero bioactivity in the less

active isomer. This makes it easier both to create such photopharmaceuticals and to assay them for mechanistic selectivity. These photopharmaceuticals are also in many cases more urgently needed in their target research field, since a number of these organ- or organism-level toxins affect faster response systems (compared to the targets of PSCs) that have correspondingly higher need for fast response tools. However, the toxic activity of such drugs can be seen only on specific cell types in culture or on an organism level, and the scope for applications of these tools is restricted to the specific fields where their targets are biologically most relevant. Therefore, they will not be further discussed here but are primarily covered in Chapters 40 and 41.

### 36.5.3 The Underutilized Potential of Ring-Opening/-Closing Photoswitches

Most photopharmaceutical designs have focused on photoswitching ligand sterics. This is well suited to double-bond isomerization photoswitches, which have been used in nearly all the PSCs presented here. By comparison, photoreversible modulation of conjugation in DAEs remains an under-explored method for photopharmacology. However, by acting as photoreversible masking groups for the bridging alkene bond, DAEs offer exciting prospects for irreversibly triggering, or else reversibly permitting, chemical reactivity which can affect biological systems. A major challenge for DAEs is their extreme hydrophobicity, which has prevented applications against cytosolic targets, let alone in vivo, unless derivatized with large hydrophilic groups [35, 79]. This still leaves opportunities open for their use in membrane-bound environments, but it is certain that further-evolved DAE-type scaffolds with better solubility could be employed against the full range of biological targets. Three notable examples of DAEs will illustrate some of the scope for such design.

Inspired by antitumor agents of the calicheamicin class, in which Bergmann cyclization of an enediyne triggers irreversible formation of a highly toxic DNA-crosslinking benzene diradical, Branda developed a diethynyl DAE (**B1**) where the alkene-unmasked ring-open isomer has the enediyne structure needed for Bergmann cyclization (Figure 36.11b). While the hydrophobic compounds were not applied biologically, and while they were not shown to undergo Bergmann cyclization at temperatures below 75 °C [85], it is likely that this chemically appealing design can be modified to enable cellular uses.

König used one of the C=C bonds of the 2,3-dimethoxyquinone ring of the redox cofactor $CoQ_{10}$ as the bridging alkene of a DAE (**K2**; Figure 36.11c). This prevented the alkene-masked ring-closed isomer from participating in redox chemistry, while the ring-open isomer can be reversibly reduced to the hydroquinone. Isomer-dependent participation in mitochondrial redox relays (which occur in and along lipid membranes) was indicated in cell-free conditions using isolated mitochondria [86]. Though $CoQ_{10}$ is not toxic, this report presents significant aspects: the DAE was applied to a membrane-bound target that matches the DAE's own likely biolocalization, and the DAE acted as a catalytic transfer agent: together offering the ability to give strong responses from even small applied doses. It is

likely that similar or π-extended systems could be adapted for e.g. isomer-dependent redox cycling, which is both a significant cytotoxicity mechanism for several classes of bioactives and may have promising research applications in light-dependently affecting metabolic status in cells.

Entropically irreversible release of masked Michael acceptor dienophiles from DAEs can be ensured by photoisomerisation to the ring-open alkene isomer, as has been demonstrated in cell-free conditions by Branda (dienophile at the bridging alkene [54]) and by Hecht [87] (dienophile at an aryl ring). As Michael acceptors are valuable biological ligation motifs, it would be exciting to test if adapting this release to be an equilibrium process (e.g. by tethering the dienophile to the photoswitch) would result in photoreversibly alkylating DAEs that might be used for a variety of light-triggered applications, from simple protein labeling, to CALI, metal coordination, protein degradation, and beyond.

## 36.6 Outlook for Photoswitchable Cytotoxins

The recent progress in harnessing PSCs as spatiotemporally precise research reagents for modulating critical biological processes has been rapid. Mostly within just the last five years, a range of unique proof-of-concept biological applications of PSCs have already been reached, and the key step of translating PSCs from 2D cell culture into mechanistically validated applications in 3D cell culture, explants, and in vivo has been taken. The stage of their being employed in biological research, without being themselves the *subject* of research, has been recently entered. Further progress is also well precedented by the development and commercialization of photoswitchable lipid reagents [76], and it should not be long before PSCs can likewise be said to have truly entered the reagent arena.

The pace of chemical PSC development is still accelerating and its creativity is increasing. The expanding set of molecular photoswitches that have been validated as appropriate for in situ photocontrol in cell biology makes up a multifaceted toolbox for reagent design. The scope of drug chemotypes and protein targets that have been addressed with PSC reagents and the increasingly sophisticated manner in which these reagents have been designed or are now understood to act should continue to spur the next innovations in the field.

On a practical level, many barriers for synthetic chemists to enter the field, which were significant a decade ago, have now fallen: (i) after gradual identification of which photochemical and which biological performance parameters are or are not cellularly relevant, accepted practices are now beginning to appear for determining them and for validating tools [9]. This has greatly increased the chances of turning a successful synthesis into a successful biological application. (ii) LED technology has revolutionized the possibilities to easily conduct early PSC screening against any target over any time frame. Cheap and robust systems for multiwell plate screening of PSCs in cell culture under arbitrary in situ illumination wavelengths and timing patterns over many days can be built or purchased for total costs of less than 50€ [4] or can be retrofitted onto microscopes [12]. (iii) Most crucially, cell and in

vivo biology is equipped to take on photopharmaceutical reagents in ways that were unthinkable a decade ago. Biologists are primed to photoswitch, since optogenetics has become a workhorse method in biology, and the illumination methods it requires are almost [9] perfectly suited to photopharmacology. Microscope technology has also blossomed: the expensive, slow, insensitive, bleach-prone, and relatively rare laser scanning microscopes of the 2000s have been succeeded by widely distributed spinning disk confocal, light sheet, and TIRF microscopes, now at a fraction of the cost, and increasingly boasting "white-light" lasers that are tunable over the visible spectrum for optimal visible light photoswitching.

Thus the "establishment phase" of PSCs has largely reached its goals and is well set up to tackle the challenges that now lie ahead, from which two features in particular stand out.

(1) Good Targets: Some degree of photoisomerization-dependent control over bioactivity is possible in cell culture, for a very broad range of targets, but the biological utility of applying this control varies widely. To paraphrase one famous synthetic chemist, it is "better to develop a B-grade solution to an A-grade problem, than the other way around." It is the value of *addressing a particular biological target with a photopharmaceutical* that should guide and focus tool development efforts, rather than chemical aspects of synthetic access, or good PSDs, or easy proof-of-concept readout. It is likely that most of the PSC classes discussed above will not go on to play significant roles in biological research. Some may fail because of chemical or photochemical liabilities, but these could in many cases be addressable by subsequent chemical refinements. However, the reagent classes for which there is no great biological need for the unique aspects that photoswitching can bring (Section 36.2) face a conceptual dead-end that no chemistry can address.
It seems likely that directing PSCs against biological targets with the most significant and most steep spatiotemporal activity gradients is likely to be a very good use of their potential; and that those targets for which optogenetic systems are unavailable will continue to have the most urgent needs for PSCs. Separately to the targets presented so far, the greatest value could lie in new photopharmaceutical inhibitors of cell structure (cytoskeletal motors, structurally associated proteins, and adhesion proteins) and critical functions (enzymes that perform post-translational modifications, enzymes involved in redox and metabolism).
(2) Good Reagents: Following Whitesides' quip, that "if the science of something is still interesting, the something is probably not ready to be a product," impactful PSCs will ultimately need to be as available (commercially distributed), and as unexciting (i.e. workhorse approaches, not temperamental curiosities), as the drugs on which they are based. In particular, PSCs will need to work *reliably* in their various biological applications. This does not need high potency or even high photoswitchability of potency, although both are helpful. However, assay outcomes must be reliably reproducible across different labs and settings to convince the biology community that PSCs are useful and valuable methods of manipulation.

Relatedly, tools should be pharmacologically as "clean" as possible to avoid that bioactivity seen in one assay could later need re-interpretation as additional bioactivity mechanisms come to light. This reliability requires high standards for proving on-target mechanism of action, and for benchmarking and excluding sources of assay artifacts (aggregation/bioavailability, phototoxicity, etc.: Section 36.2). Even in the earliest stages of reagent development, Shokat's criteria for evaluating the reliability of a new probe can be a useful guide: "[showing] a consistent dose-dependent relationship between biochemical target engagement and cellular activity... [and,] proof that the first drug can be modified and its biochemical and cellular activity improved in a manner consistent with the structural model" [88]. The value of a well-constructed structure–activity relationship series, of finding a consistent relationship between cell-free and cellular activity, and of using the *most stringent possible* controls (e.g. regioisomers, rather than cosolvent-only), is undeniable. Optimizing the practical usability of PSCs will also be crucial for this, e.g. by designing for performance at available wavelengths, for metabolic stability, and for good solubility. Finally, it should be noted that all these aspects of *good reagents* are absolute prerequisites for any PSC to transition out of pure research uses and aim at therapeutic applications. The more thoroughly that these standards are brought into practice, the greater the chances will for PSCs to cross that challenging divide.

In Summary: The conceptual value of PSCs as highly spatiotemporally precise research reagents for modulating critical biological processes is clear. Due to their ubiquitously important targets, PSCs face intriguing challenges in their design and validation that do not as greatly affect other classes of photopharmaceuticals, but the rewards of developing PSCs may be correspondingly greater. Photoswitch chemistry and the applications of chemical photoswitches in biology have experienced massive developments in the last decade; and the challenges of PSC design and application have in many cases been a driving force for these innovations. The validity of the PSC approach has been confirmed by a number of proof of concept and early research applications across a range of biological settings, involving targets from cytoskeleton to signaling and structural to genomic integrity. The stage is now set for further development and broader applications of PSCs throughout the physical and life sciences, particularly to harness their unique Opportunities for assays that are faster, stronger, and higher precision than conventional approaches allow.

## Acknowledgment

I wish to thank Martin Maier for constructive criticism and help with figure preparation and Zbigniew Pianowski for helpful critique and support in the editing process.

## References


1 Goldacre, R.J., Loveless, A., and Ross, W.C.J. (1949). Mode of production of chromosome abnormalities by the nitrogen mustards the possible role of cross-linking. *Nature* 163 (4148): 667–669.

2 Hüll, K., Morstein, J., and Trauner, D. (2018). In vivo photopharmacology. *Chem. Rev.* 118 (21): 10710–10747.

3 Welleman, I.M., Hoorens, M.W.H., Feringa, B.L. et al. (2020). Photoresponsive molecular tools for emerging applications of light in medicine. *Chem. Sci.* 11 (43): 11672–11691.

4 Borowiak, M., Nahaboo, W., Reynders, M. et al. (2015). Photoswitchable inhibitors of microtubule dynamics optically control mitosis and cell death. *Cell* 162 (2): 403–411.

5 Jung, H.S., Verwilst, P., Sharma, A. et al. (2018). Organic molecule-based photothermal agents: an expanding photothermal therapy universe. *Chem. Soc. Rev.* 47 (7): 2280–2297.

6 Robertson, C.A., Evans, D.H., and Abrahamse, H. (2009). Photodynamic therapy (PDT): a short review on cellular mechanisms and cancer research applications for PDT. *J. Photochem. Photobiol. B* 96 (1): 1–8.

7 Schmidt, D., Rodat, T., Heintze, L. et al. (2018). Axitinib: a Photoswitchable approved tyrosine kinase inhibitor. *ChemMedChem* 13 (22): 2415–2426.

8 Müller-Deku, A., Meiring, J.C.M., Loy, K. et al. (2020). Photoswitchable paclitaxel-based microtubule stabilisers allow optical control over the microtubule cytoskeleton. *Nat. Commun.* 11 (1): 4640.

9 Thorn-Seshold, O. and Meiring, J. (2021). Photocontrolling microtubule dynamics with photoswitchable chemical reagents. *in Microtubules-Methods and Protocols* (ed. H. Inaba; Springer, 2022).

10 Josa-Culleré, L. and Llebaria, A. (2021). In the search for photocages cleavable with visible light: an overview of recent advances and chemical strategies. *ChemPhotoChem* 5: 298–316.

11 Gao, L., Meiring, J.C.M., Kraus, Y. et al. (2021). A robust, GFP-orthogonal photoswitchable inhibitor scaffold extends optical control over the microtubule cytoskeleton. *Cell Chem. Biol.* 28: 1–14.

12 Fuchter, M.J. (2020). On the promise of photopharmacology using photoswitches: a medicinal Chemist's perspective. *J. Med. Chem.* 63 (20): 11436–11447.

13 Sailer, A., Meiring, J., Heise, C. et al. (2021). Pyrrole hemithioindigo antimitotics with near-quantitative bidirectional photoswitching photocontrol cellular microtubule dynamics with single-cell precision. *Angew. Chem.* 60 (44): 23695–23704.

14 Gao, L., Meiring, J.C.M., Heise, C. et al. (2021). Photoswitchable epothilone-based microtubule stabilisers allow GFP- orthogonal, optical control over the microtubule cytoskeleton. *Angew. Chem.* 61 (10): e202114614.

15 Gao, L., Meiring, J.C.M., Varady, A. et al. (2021). In vivo photocontrol of microtubule dynamics and integrity, migration and mitosis, by the potent GFP-imaging-compatible photoswitchable reagents SBTubA4P and SBTub2M. *bioRxiv* http://dx.doi.org/10.1101/2021.03.26.437160.


**16** Broichhagen, J., Frank, J.A., and Trauner, D. (2015). A roadmap to success in photopharmacology. *Acc. Chem. Res.* 48 (7): 1947–1960.

**17** Sailer, A., Ermer, F., Kraus, Y. et al. (2020). Potent hemithioindigo-based antimitotics photocontrol the microtubule cytoskeleton in cellulo. *Beilstein J. Org. Chem.* 16: 125–134.

**18** Di, L., Kerns, E.H., and Carter, G.T. (2009). Drug-like property concepts in pharmaceutical design. *Curr. Pharm. Des.* 15 (19): 2184–2194.

**19** Fitz, J. and Mammana, A. (2020). Spectroscopic study of the pH dependence of the optical properties of a water-soluble molecular photo-switch. *Spectrochim. Acta, Part A* 227: 117576.

**20** McGovern, S.L., Helfand, B.T., Feng, B. et al. (2003). A specific mechanism of nonspecific inhibition. *J. Med. Chem.* 46 (20): 4265–4272.

**21** Thorn-Seshold, O. (2020). Comment on "photo-controlled reversible microtubule assembly mediated by paclitaxel-modified cyclodextrin". *Angew. Chem. Int. Ed.* 59 (20): 7652–7654.

**22** Gavin, J., Ruiz, J.F.M., Kedziora, K. et al. (2012). Structure requirements for anaerobe processing of azo compounds: implications for prodrug design. *Bioorg. Med. Chem. Lett.* 22 (24): 7647–7652.

**23** Boulègue, C., Löweneck, M., Renner, C. et al. (2007). Redox potential of azobenzene as an amino acid residue in peptides. *ChemBioChem* 8 (6): 591–594.

**24** Beharry, A.A., Sadovski, O., and Woolley, G.A. (2011). Azobenzene photoswitching without ultraviolet light. *J. Am. Chem. Soc.* 133 (49): 19684–19687.

**25** An, Y., Chen, C., Zhu, J. et al. (2020). Hypoxia-induced activity loss of a photo-responsive microtubule inhibitor azobenzene combretastatin A4. *Front. Chem. Sci. Eng.* 14 (5): 880–888.

**26** Kolarski, D., Sugiyama, A., Rodat, T. et al. (2021). Reductive stability evaluation of 6-azopurine photoswitches for the regulation of CKIα activity and circadian rhythms. *Org. Biomol. Chem.* 19: 2312–2321.

**27** Schehr, M., Ianes, C., Weisner, J. et al. (2019). 2-Azo-, 2-diazocine-thiazols and 2-azo-imidazoles as photoswitchable kinase inhibitors: limitations and pitfalls of the photoswitchable inhibitor approach. *Photochem. Photobiol. Sci.* 18 (6): 1398–1407.

**28** Ji, J., Li, X., Wu, T. et al. (2018). Spiropyran in nanoassemblies as a photosensitizer for photoswitchable ROS generation in living cells. *Chem. Sci.* 9 (26): 5816–5821.

**29** Hoebeke, M., Piette, J., and van de Vorst, A. (1991). Photosensitized production of singlet oxygen by merocyanine 540 bound to liposomes. *J. Photochem. Photobiol., B* 9 (3): 281–294.

**30** Jacobson, K., Rajfur, Z., Vitriol, E. et al. (2008). Chromophore-assisted laser inactivation in cell biology. *Trends Cell Biol.* 18 (9): 443–450.

**31** Brown, C., Rastogi, S.K., Barrett, S.L. et al. (2017). Differential azobenzene solubility increases equilibrium cis/trans ratio in water. *J. Photochem. Photobiol., A* 336: 140–145.


**32** Sailer, A., Ermer, F., Kraus, Y. et al. (2019). Hemithioindigos as desymmetrised molecular switch scaffolds: design control over the isomer-dependency of potent photoswitchable antimitotic bioactivity in cellulo. *ChemBioChem* 20: 1305–1314.

**33** Velema, W.A., Szymanski, W., and Feringa, B.L. (2014). Photopharmacology: beyond proof of principle. *J. Am. Chem. Soc.* 136 (6): 2178–2191.

**34** Pospich, S., Küllmer, F., Nasufovic, V. et al. (2021). Cryo-EM resolves molecular recognition of an optojasp photoswitch bound to actin filaments in both switch states. *Angew. Chem. Int. Ed.* 60 (16): 8678–8682.

**35** Babii, O., Afonin, S., Schober, T. et al. (2020). Peptide drugs for photopharmacology: how much of a safety advantage can be gained by photocontrol? *Future Drug Discovery* 2 (1): FDD28.

**36** Lougheed, T., Borisenko, V., Hennig, T. et al. (2004). Photomodulation of ionic current through hemithioindigo-modified gramicidin channels. *Org. Biomol. Chem.* 2 (19): 2798–2801.

**37** Kaufman, H., Vratsanos, S.M., and Erlanger, B.F. (1968). Photoregulation of an enzymic process by means of a light-sensitive ligand. *Science* 162 (3861): 1487–1489.

**38** Peterson, J.R. and Mitchison, T.J. (2002). Small molecules, big impact: a history of chemical inhibitors and the cytoskeleton. *Chem. Biol.* 9 (12): 1275–1285.

**39** Pettit, G.R., Rhodes, M.R., Herald, D.L. et al. (1998). Antineoplastic agents 393. Synthesis of the trans-isomer of combretastatin A-4 prodrug. *Anticancer Drug Design.* 13 (8): 981–993.

**40** Gaspari, R., Prota, A.E., Bargsten, K. et al. (2017). Structural basis of *cis*- and *trans*-combretastatin binding to tubulin. *Chem* 2 (1): 102–113.

**41** Hadfield, J., McGown, A., Mayalarp, S. et al. (2002). Substituted stilbenes, their reactions and anticancer activity. WO200250007.

**42** Roger, H.B., Stanley, W.B., Greg, M.G. et al. (2012). Time-resolved nanosecond fluorescence lifetime imaging and picosecond infrared spectroscopy of combretastatin A-4 in solution and in cellular systems. *Meas. Sci. Technol.* 23 (8): 084001.

**43** Scherer, K., Bisby, R., Botchway, S. et al. (2014). Anticancer phototherapy using activation of E-combretastatins by two-photon–induced isomerization. *J. Biomed. Opt.* 20 (5): 051004.

**44** Thorn-Seshold, O., Borowiak, M., Trauner, D., et al. (2014). Azoaryls as reversibly modulatable tubulin inhibitors. WO2015166295, .

**45** Theisen, U., Ernst, A.U., Heyne, R.L.S. et al. (2020). Microtubules and motor proteins support zebrafish neuronal migration by directing cargo. *J. Cell Biol.* 219 (10): e201908040.

**46** Sheldon, J.E., Dcona, M.M., Lyons, C.E. et al. (2016). Photoswitchable anticancer activity via *trans–cis* isomerization of a combretastatin A-4 analog. *Org. Biomol. Chem.* 14 (1): 40–49.

**47** Engdahl, A.J., Torres, E.A., Lock, S.E. et al. (2015). Synthesis, characterization, and bioactivity of the photoisomerizable tubulin polymerization inhibitor azo-combretastatin A4. *Org. Lett.* 17 (18): 4546–4549.


**48** Rastogi, S.K., Zhao, Z., Barrett, S.L. et al. (2018). Photoresponsive azo-combretastatin A-4 analogues. *Eur. J. Med. Chem.* 143: 1–7.

**49** Zenker, J., White, M.D., Templin, R.M. et al. (2017). A microtubule-organizing center directing intracellular transport in the early mouse embryo. *Science* 357 (6354): 925–928.

**50** Singh, A., Saha, T., Begemann, I. et al. (2018). Polarized microtubule dynamics directs cell mechanics and coordinates forces during epithelial morphogenesis. *Nat. Cell Biol.* 20 (10): 1126–1133.

**51** Kopf, A., Renkawitz, J., Hauschild, R. et al. (2020). Microtubules control cellular shape and coherence in amoeboid migrating cells. *J. Cell Biol.* 219 (6): e201907154.

**52** Allingham, J.S., Klenchin, V.A., and Rayment, I. (2006). Actin-targeting natural products: structures, properties and mechanisms of action. *Cell. Mol. Life Sci.* 63 (18): 2119–2134.

**53** Borowiak, M., Küllmer, F., Gegenfurtner, F. et al. (2020). Optical manipulation of F-actin with photoswitchable small molecules. *J. Am. Chem. Soc.* 142 (20): 9240–9249.

**54** Samachetty, H.D. and Branda, N.R. (2006). Integrating molecular switching and chemical reactivity using photoresponsive hexatrienes. *Pure Appl. Chem.* 78 (12): 2351–2359.

**55** Presa, A., Brissos, R.F., Caballero, A.B. et al. (2015). Photoswitching the cytotoxic properties of platinum(II) compounds. *Angew. Chem. Int. Ed.* 54 (15): 4561–4565.

**56** Matera, C., Gomila, A.M.J., Camarero, N. et al. (2018). Photoswitchable antimetabolite for targeted photoactivated chemotherapy. *J. Am. Chem. Soc.* 140 (46): 15764–15773.

**57** Wegener, M., Hansen, M.J., Driessen, A.J.M. et al. (2017). Photocontrol of antibacterial activity: shifting from UV to red light activation. *J. Am. Chem. Soc.* 139 (49): 17979–17986.

**58** Tian, Y., Li, Y., Jiang, W.-L. et al. (2019). In-situ imaging of azoreductase activity in the acute and chronic ulcerative colitis mice by a near-infrared fluorescent probe. *Anal. Chem.* 91 (16): 10901–10907.

**59** Hansen, M.J., Velema, W.A., de Bruin, G. et al. (2014). Proteasome inhibitors with photocontrolled activity. *ChemBioChem* 15 (14): 2053–2057.

**60** Blanco, B., Palasis, K.A., Adwal, A. et al. (2017). Azobenzene-containing photoswitchable proteasome inhibitors with selective activity and cellular toxicity. *Bioorg. Med. Chem.* 25 (19): 5050–5054.

**61** Reynders, M., Matsuura, B.S., Bérouti, M. et al. (2020). PHOTACs enable optical control of protein degradation. *Sci. Adv.* 6 (8): eaay5064.

**62** Pfaff, P., Samarasinghe, K.T.G., Crews, C.M. et al. (2019). Reversible spatiotemporal control of induced protein degradation by bistable PhotoPROTACs. *ACS Cent. Sci.* 5 (10): 1682–1690.

**63** Jin, Y., Lu, M., Wang, Y. et al. (2020). Azo-PROTAC: novel light-controlled small-molecule tool for protein knockdown. *J. Med. Chem.* 63 (9): 4644–4654.

**64** Morstein, J., Kol, M., Novak, A.J.E. et al. (2021). Short photoswitchable ceramides enable optical control of apoptosis. *ACS Chem. Biol.* 16 (3): 452–456.


**65** Hinnah, K., Willems, S., Morstein, J. et al. (2020). Photohormones enable optical control of the peroxisome proliferator-activated receptor gamma (PPARγ). *J. Med. Chem.* 63 (19): 10908–10920.

**66** Morstein, J., Trads, J.B., Hinnah, K. et al. (2020). Optical control of the nuclear bile acid receptor FXR with a photohormone. *Chem. Sci.* 11 (2): 429–434.

**67** Falenczyk, C., Schiedel, M., Karaman, B. et al. (2014). Chromo-pharmacophores: photochromic diarylmaleimide inhibitors for sirtuins. *Chem. Sci.* 5 (12): 4794–4799.

**68** Simeth, N.A., Altmann, L.-M., Wössner, N. et al. (2018). Photochromic indolyl fulgimides as chromo-pharmacophores targeting sirtuins. *J. Organomet. Chem.* 83 (15): 7919–7927.

**69** Szymanski, W., Ourailidou, M.E., Velema, W.A. et al. (2015). Light-controlled histone deacetylase (HDAC) inhibitors: towards photopharmacological chemotherapy. *Chem. Eur. J.* 21 (46): 16517–16524.

**70** Weston, C.E., Krämer, A., Colin, F. et al. (2017). Toward photopharmacological antimicrobial chemotherapy using photoswitchable amidohydrolase inhibitors. *ACS Infect. Dis.* 3 (2): 152–161.

**71** Kobauri, P., Szymanski, W., Cao, F. et al. (2021). Biaryl sulfonamides as cisoid azosteres for photopharmacology. *Chem. Commun.* 57: 4126–4129.

**72** Bieth, J., Vratsanos, S.M., Wassermann, N. et al. (1969). Photoregulation of biological activity by photochromic reagents, II. Inhibitors of acetylcholinesterase. *Proc. Natl. Acad. Sci. U.S.A.* 64 (3): 1103–1106.

**73** Wei, N., Liang, J., Peng, S. et al. (2018). Design, synthesis, and biological evaluation of axitinib derivatives. *Molecules* 23 (4): 747.

**74** Heintze, L., Schmidt, D., Rodat, T. et al. (2020). Photoswitchable azo- and diazocine-functionalized derivatives of the VEGFR-2 inhibitor axitinib. *Int. J. Mol. Sci.* 21 (23): 8961.

**75** Hoorens, M.W.H., Ourailidou, M.E., Rodat, T. et al. (2019). Light-controlled inhibition of BRAFV600E kinase. *Eur. J. Med. Chem.* 179: 133–146.

**76** Morstein, J., Impastato, A.C., and Trauner, D. (2021). Photoswitchable lipids. *ChemBioChem* 22: 73–83.

**77** Stankovic, C.J., Heinemann, S.H., and Schreiber, S.L. (1991). Photo-modulated ion channels based on covalently linked gramicidins. *Biochim. Biophys. Acta* 1061 (2): 163–170.

**78** Peddie, V. and Abell, A.D. (2019). Photocontrol of peptide secondary structure through non-azobenzene photoswitches. *J. Photochem. Photobiol., C* 40: 1–20.

**79** Babii, O., Afonin, S., Berditsch, M. et al. (2014). Controlling biological activity with light: diarylethene-containing cyclic peptidomimetics. *Angew. Chem.* 126 (13): 3460–3463.

**80** Babii, O., Afonin, S., Ishchenko, A.Y. et al. (2018). Structure–activity relationships of photoswitchable diarylethene-based β-hairpin peptides as membranolytic antimicrobial and anticancer agents. *J. Med. Chem.* 61 (23): 10793–10813.

**81** Afonin, S., Babii, O., Reuter, A. et al. (2020). Light-controllable dithienylethene-modified cyclic peptides: photoswitching the in vivo toxicity in zebrafish embryos. *Beilstein J. Org. Chem.* 16: 39–49.


**82** Mutter, N.L., Volarić, J., Szymanski, W. et al. (2019). Reversible photocontrolled nanopore assembly. *J. Am. Chem. Soc.* 141 (36): 14356–14363.

**83** Riefolo, F., Matera, C., Garrido-Charles, A. et al. (2019). Optical control of cardiac function with a photoswitchable muscarinic agonist. *J. Am. Chem. Soc.* 141 (18): 7628–7636.

**84** Wang, L., Chen, M., Xia, S. et al. (2020). Azobenzene-diamides as photopharmacological ligands for insect ryanodine receptor. *J. Agric. Food. Chem.* 68: 14409–14416.

**85** Sud, D., Wigglesworth, T.J., and Branda, N.R. (2007). Creating a reactive Enediyne by using visible light: photocontrol of the Bergman cyclization. *Angew. Chem. Int. Ed.* 46 (42): 8017–8019.

**86** Simeth, N.A., Kneuttinger, A.C., Sterner, R. et al. (2017). Photochromic coenzyme Q derivatives: switching redox potentials with light. *Chem. Sci.* 8 (9): 6474–6483.

**87** Göstl, R. and Hecht, S. (2015). Photoreversible prodrugs and protags: switching the release of maleimides by using light under physiological conditions. *Chem. Eur. J.* 21 (11): 4422–4427.

**88** Dang, C.V., Reddy, E.P., Shokat, K.M. et al. (2017). Drugging the 'undruggable' cancer targets. *Nat. Rev. Cancer* 17 (8): 502–508.

## 37 Photopharmacology of G-Protein-Coupled Receptors

Silvia Panarello, Xavier Rovira, Amadeu Llebaria, and Xavier Gómez-Santacana

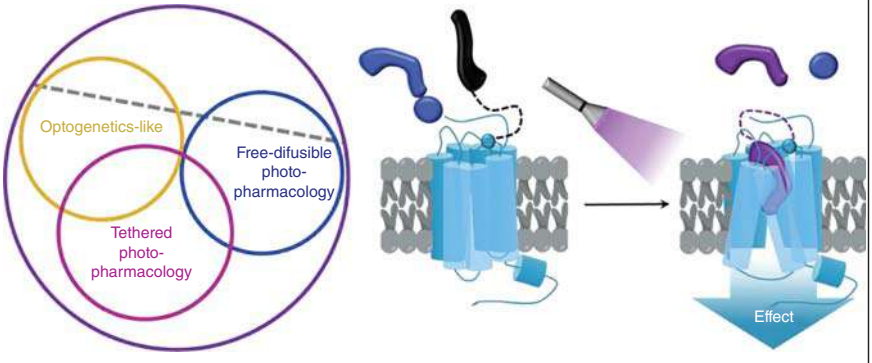


### Characteristic Features

G-protein-coupled receptor (GPCR) photopharmacology is based on light-regulated molecules to switch "on" and "off" GPCR activation states. The photoswitching can be reversible or irreversible, and it may involve genetically modified receptors or wild type. Moreover, the light-regulated molecules can be classified as photochromic or caged ligands, *T*-on/*M*-on affinity ligands, or efficacy switches.

### Characterization Methods

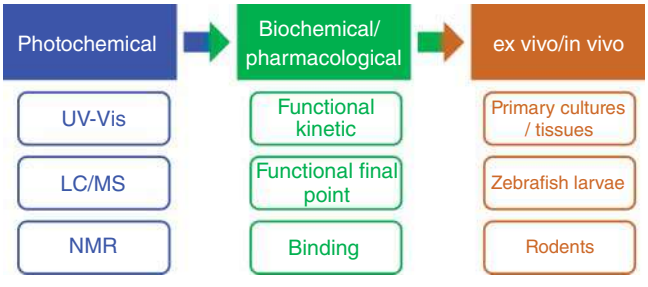


### First Reported

Levitz, J. et al. (2013). *Nat. Neurosci*. 16 (4): 507–516.

Schönberger, M. and Trauner, D. (2014). *Angew. Chem. Int. Ed*. 53 (12): 3264–3267.

Pittolo, S. et al. (2014). *Nat. Chem. Biol*. 10 (10): 813–815.

Zussy, C. et al. (2018). *Mol. Psychiatry* 23 (3): 509–520.

### Key References

Kramer, R.H., Mourot, A., and Adesnik, H. (2013). *Nat. Neurosci*. 16: 816–823.

Hüll, K., Morstein, J., and Trauner, D. (2018). *Chem. Rev*. 118 (21): 10710–10747.

Ricart-Ortega, M., Font, J., and Llebaria, A. (2019). *Mol. Cell. Endocrinol*. 488: 36–51.

# 37

# Photopharmacology of G-Protein-Coupled Receptors

*Silvia Panarello[1], Xavier Rovira[1,3], Amadeu Llebaria[1], and Xavier Gómez-Santacana[1,2]*

*[1]MCS, Institute for Advanced Chemistry of Catalonia – CSIC, Jordi Girona 18-26, 08034, Barcelona, Spain*
*[2]Université de Montpellier, Institut de Génomique Fonctionnelle, UMR5203 CNRS, U1191 INSERM, 141, rue de la Cardonille, 34094 Montpellier cedex 5, France*
*[3]University of Vic – Central University of Catalonia, Molecular Photopharmacology Research Group, The Tissue Repair and Regeneration Laboratory (TR2Lab), Faculty of Sciences and Technology, Vic, C. de la Laura, 13, 08500 Spain*

## 37.1 Introduction

G-protein-coupled receptors (GPCRs) are the largest family of membrane receptors targeted by commercial drugs. However, the proportion of approved small molecules targeting GPCRs has slowed down in comparison to the total number of other therapeutic approaches, such as biologicals. This is in large part due to adverse effects or lack of efficacy found in clinical trials [1, 2]. Many of these problems have been attributed to the lack of selectivity or the ubiquitous expression of receptors in non-targeted tissues and organs, thus eliciting undesired actions. Therefore, innovative research strategies are necessary to distinctly define the spatial and temporal action of GPCR drugs that will help unravel the receptor function in physiologically relevant areas. To that aim, new chemical approaches are currently under development to confine a specific drug activity in a localized region during the right time period [3]. One of these strategies, named photopharmacology, is based on the use of light-regulated drugs to control receptor activation states and represents an unprecedented opportunity inasmuch as light can be controlled with an unparalleled spatial and temporal precision. Indeed, driving the drug action through the use of light has demonstrated to allow for an accurate restriction of its effect to specific organs, tissues, or even subcellular locations with strictly defined time applications [4, 5]. This precision has permitted the study of the link between biological structures, a particular GPCR, and the physiological responses elicited by its activation or inactivation [6, 7]. Importantly, diffusible photopharmacological tools can be used as conventional drugs in cells, tissues, and alive animals without the need to genetically modify the biological system to light-control the GPCR activity. The unique regulation of the receptor state offered by photopharmacology opens new opportunities to study the kinetic component of GPCRs mechanisms of

*Molecular Photoswitches: Chemistry, Properties, and Applications*,
First Edition. Edited by Zbigniew L. Pianowski.


activation and the underlying molecular processes. A comprehensive compilation and classification of the different photopharmacological strategies, the methods used to analyze and characterize light-regulated molecules, and some examples of the impact that this field may have in drug discovery will be disclosed in this review.

## 37.2 Enabling Light as an Actuator for GPCR Research

When analyzing the reported strategies to control GPCR activity with light, it is essential to consider the following: (i) Does the approach require genetic manipulation of the organism or can be applied to native receptors? (ii) Is the light-induced reaction reversible (i.e. photoswitching)? and (iii) Are the light-sensitive molecules freely diffusible or covalently bound to the GPCR protein? Depending on these properties, light strategies to control biological function of GPCRs can be classified in three generic groups of approaches: **Optogenetics**, **Freely Diffusible Photopharmacology**, and **Tethered Photopharmacology** [4].

### 37.2.1 Optogenetics-Like Approaches

**Optogenetic** approaches comprise a group of strategies that involve genetic modification to achieve light-control of well-defined biological events in specific cells that can be translated to living tissues and live animals [8]. Optogenetics was defined as "Nature Method of the Year 2010" [9] and was originally based on the use of genetically encoded photoreceptors already present in nature (rhodopsin [10], channelrhodopsins [11], halorhodopsin [12], and bacteriorhodopsin [13]) to excite a neuron upon illumination. These photoreceptors covalently bind to retinal and can be classified into two groups based on their photoisomerization: bistable and monostable pigments (MSP). While MSP are only thermally stable before light application, bistable pigments are thermally stable in both isomers of retinal [14].

Optogenetic approaches have evolved in the last years to include a broader variety of biological processes in neuroscience [15, 16]. Among the large number of optogenetic tools currently developed, **opto-XRs** represent an interesting approach for the development of light-sensitive GPCRs. It is based on the development of chimeric GPCRs in which the extracellular part corresponds to that of the light-sensitive rhodopsin, whereas the intracellular component interacting the G protein is derived from other GPCRs. An recent example is the opto-$\beta_2$AR receptor, which is a chimeric rhodopsin/$\beta_2$-adrenergic receptor [17]. Opto-$\beta_2$AR kinetically behaves similar to endogenous $\beta_2$AR in terms of G protein and mitogen-activated protein (MAP) kinase activation, as well as receptor internalization. However, Opto-$\beta_2$AR activity is triggered by light thanks to the light-sensitive region of rhodopsin. Of note, this construct demonstrated to be able to control Gs signaling in vivo after genetic modification of the animal and by the use optical fibers and wireless light application. Other receptor chimeras have been developed coupled to $G_q$ and $G_i$ proteins, based on $\alpha_1$ adrenoceptors [8] and GPR37 [18], respectively, and thus demonstrate in that this is a generalizable strategy for the different signaling pathways activated by GPCRs.

Optogenetic tools have become important to improve our understanding of biological processes, providing *fully reversible* photoactivation in most cases, with high specificity and fast temporal responses when compared with pharmacological methodologies using drugs. However, the presence of an exogenous protein can alter the cell physiology, thus hampering the possibility of drawing certain conclusions about the function of the endogenous biological system. Moreover, the need for genetic manipulation to introduce a photoactivable protein in the targeted organism implies ethical concerns and limits their therapeutic use in humans.

### 37.2.2 GPCR Photopharmacology Approaches

**GPCR Photopharmacology** offers an alternative to optogenetics based on the use light-regulated small molecules, such as receptors agonists, antagonists, or modulators [19]. Two general strategies have emerged by using small synthetic photoswitches: freely diffusible photopharmacology and tethered photopharmacology.

#### 37.2.2.1 Freely Diffusible Photopharmacology

Since it was first used to study sodium/potassium channels in the 1970s [20], caged ligands (**CLs**) have become a well-established approach for the study of cell physiology [21]. This strategy is based on ligands equipped with a photolabile protecting group (i.e. cage) that prevents a correct ligand–receptor interaction, rendering the drug pharmacologically inactive. The cage can be photochemically cleaved under suitable light exposure to *irreversibly* release the biologically active ligand [22]. This approach has been classically applied for the development of several photoactivable neurotransmitters acting on different GPCRs, such as glutamate, gamma-butyric acid (GABA), histamine, and dopamine, or second messengers, such as cyclic adenosine monophosphate (cAMP), cyclic guanosine monophosphate (cGMP), $Ca^{2+}$, $IP_3$ [23], but it is not that common for ligands with higher selectivity or optimized drug properties.

For the design of caged ligands, several properties need to be considered. First, a negligible bioactivity of the caged compound is needed, including the presence of impurities from synthesis that often correspond to the bioactive ligand, which is usually very active. Purities above 3 orders of magnitude are desirable to have a good operativity window where no activity is found for the cage, whereas full activity is recovered upon illumination. Additionally, the drug photoreleasing (uncaging) reaction upon illumination has to be fast reaction and with a high yield. This can be achieved with the use of a suitable cage type and optimizing the illumination wavelength and intensity [23, 24]. Importantly, the active compounds must be chemically and metabolically stable at these illumination conditions. That is, it does not degrade or promote a reaction that forms other molecules.

In the following example, a caged antagonist selective for dopamine $D_2/D_3$ receptor was described [25] (Figure 37.1a) based on the crystal structure of the dopamine $D_3$ receptor in complex with eticlopride. However, the caged eticlopride was found to be photochemically unstable. Therefore, the authors designed a analog photostable under the illumination conditions applied for photorelease (dechloroeticlopride) with similar binding properties, functional behavior, and uncaging properties after interaction with dopamine receptors. However, the development of caged drugs

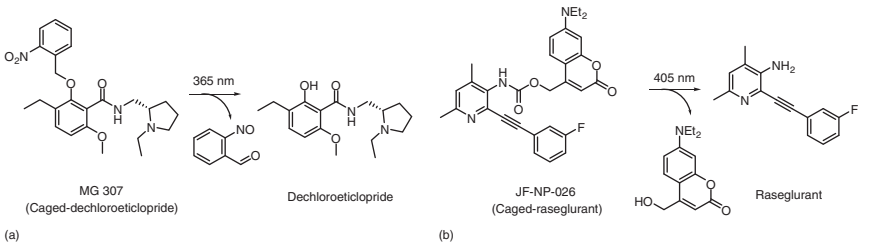


**Figure 37.1** Structure and photochemistry of the photo-caged compounds (a) MG307 (caged-dechloroeticlopride) and (b) JF-NP-026 (caged-raseglurant). Upon irradiation with 365 and 405 nm of light respectively, the $D_2/D_3$ receptor antagonist, (a) dichloeticlopride, and the $mGlu_5$ NAM, (b) raseglurant, are irreversibly released. Source: Giengeret al. [25].

for GPCRs in more complex systems, such as in vivo studies, has been poorly developed, except for few examples. One of these examples is JF-NP-026 (Figure 37.1b), a caged analog of Raseglurant, a negative allosteric modulator (NAM) selective for $mGlu_5$ receptor [7]. JF-NP-026 was proven inactive in rodent models but violet illumination either peripherally or in the central nervous system (CNS) (thalamus) triggered raseglurant uncaging and produced a highly significant analgesic behavior. Thanks to the spatiotemporal control offered by light, the authors could highlight the specific anatomic distribution of $mGlu_5$ receptors involved in pain transmission.

The strategies based on caged compounds are excellent approaches to release effective concentrations of active compounds at the site of action with precise control while avoiding undesired effects in other tissues. Moreover, the design and development of caged compounds can be simpler than using other light-control strategies since the photoreleased drug is usually well characterized. However, uncaging is an irreversible process and, therefore, the drug cannot be inactivated once released, thus limiting a precise light control. In addition, the released by-products from the cage can have off-target or toxic effects [26].

Freely diffusible photochromic ligands (**PCLs**) can be reversibly activated and inactivated upon illumination. Indeed, PCLs carry a photochromic moiety in their molecular scaffold that can be reversibly switched between two isomers upon irradiation. If these isomers have different binding affinities or efficacies for the targeted receptor, the PCL can be used to *reversibly* photoswitch the receptor-associated biological effect. The design of this PCLs is generally more challenging than caged compounds since the ligand structure must include a photoswitch without compromising the affinity of the ligand. There are different types of depending on the different isomerization mechanisms: *cis/Z* and *trans/E* isomers (azobenzenes, stilbenes, and hemithioindigos) and open and closed forms (spiropyrans, diarylethenes, and thiophenefulgides). These chemical transformations result in remarkable changes in geometry, flexibility, polarity, and charge distribution of the compound.

To date, chemistry efforts have provided a large number of synthetic photoswitches among which azobenzene derivatives are the most commonly used for biological applications. This is due to the advantages offered by the physicochemical properties of azobenzenes, which are fulfilling many important requirements of photopharmacology: azobenzene synthesis is well established [27], are stable under

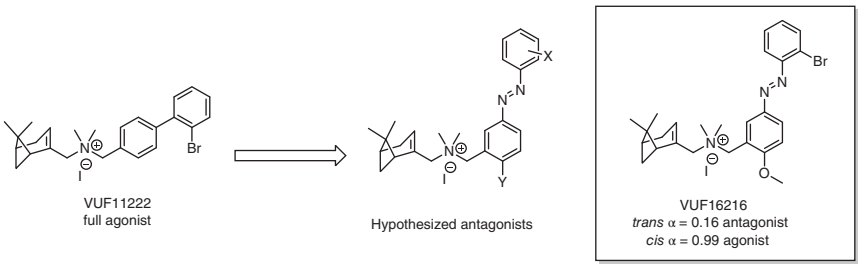


**Figure 37.2** The compound VUF11222 is an example of biaryl CXCR3 ligands. Azologization of the scaffold of VUF11222 and proper Y and X groups gave rise to photoisomerizable analogs with efficacies depending on the Y substituents. Light at 360 nm promoted a switch from *trans* to *cis* configuration. Using [$^{35}$S]-GTPγS functional assay, the authors determined different efficacies for the *trans* and the *cis*. Among all molecules reported, VUF16216 represents the highest photoinduced efficacy switch for a GPCR azo-ligand reported to date.

physiological conditions, and the photoisomerization rates can be tuned for the regulation of GPCR biological processes [28]. To date, freely diffusible PCLs have been synthesized targeting all major GPCR classes acting at the orthosteric and allosteric sites or both at the same time, ligands named dualsteric [29].

PCL photoisomerization usually affects binding properties of the ligand due to a lower affinity of one isomer. However, there are examples, where the photoswitching affects the intrinsic activity of the ligand without substantially modifying ligand affinity. A recent example of this last-mentioned type of PCL has been reported for chemokine receptor CXCR3 [30]. In this study, a series of azobenzene-based compounds was reported of which VUF16216 (Figure 37.2) demonstrated to perform as a real-time reversible efficacy trigger from antagonism to agonism [31].

#### 37.2.2.2 GPCRs Tethered Photopharmacology

Tethered photopharmacology is based on photochromic ligands that are covalently bound to the target protein through a specific nucleophilic residue upon a bioconjugation reaction. The most frequent approach for GPCRs is based on the use of genetic engineering to introduce a residue (usually a cysteine) or a suicide enzyme-based tag (SNAP, CLIP, etc.) to provide the receptor with an anchor point that allows the bioconjugation of the ligand [4, 32]. Therefore, tethered photopharmacology can be considered as a merging strategy between optogenetic and PTL approaches, taking advantage of the best features of both, such as the receptor specificity provided by genetic manipulation (optogenetics), and the applicability of PCL photopharmacology (Figure 37.3), which allows the use of minimally modified receptors that maintain the biological functions of native ones. On the other hand, a few tethered pharmacology approaches have been used with wild-type proteins, but they are scarce in the GPCR field.

There are different tethered approaches reported in literature, with the common features above described. Depending on bioconjugation strategy and the anchor point placement, tethered photopharmacology can be divided into:

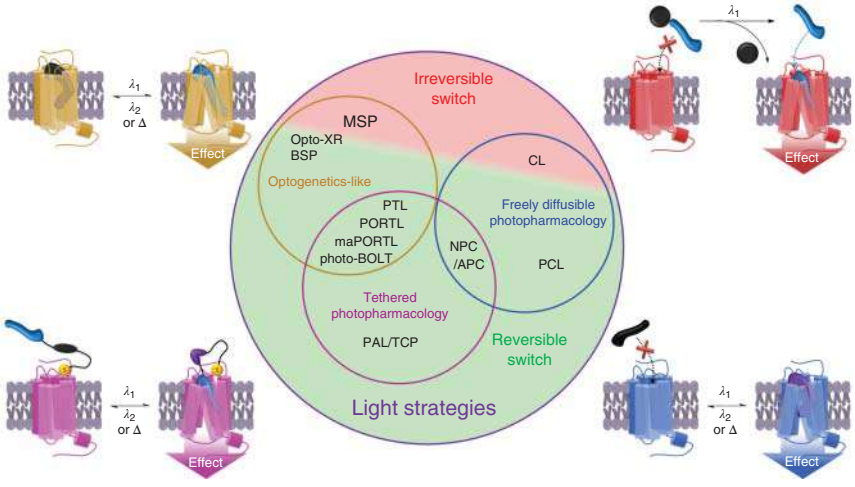


**Figure 37.3** Venn diagram showing all relationships between light-technologies currently described to control GPCR function. Strategies are first classified depending on the nature of the photoswitching (reversible in green background or irreversible in red). The second classification depends on the following factors: (1) the target is a receptor genetically introduced or modified (optogenetics-like), (2) the ligand is free-diffusible or (3) the ligand covalently bound to the target protein (tethered). The strategies that have been developed for GPCRs are in bold. Side schematic representations represent the following approaches: an optogenetic approach in yellow, a caged ligand (CL) in red, a photochromic ligand (PCL) in blue, and a photoswitchable tethered ligand (PTL) in magenta.

(1) Photoswitchable tethered ligands (PTLs) that will conjugate the receptor through a genetically introduced amino acid.
(2) Photoswitchable bioorthogonal ligand tethering (photo-BOLTs) that conjugate to introduced unnatural amino-acid residues.
(3) Photoswitchable orthogonal remotely tethered ligands (PORTLs) or membrane-anchored photoswitchable orthogonal remotely tethered ligands (maPORTLs) that conjugate to fused protein domains.
(4) Photoswitchable affinity labels (PALs) or targeted covalent photoswitches (TCPs) that react with nucleophiles of native/unmodified receptors.
(5) Antibody/nanobody-photoswitch conjugates (APCs/NPCs), which are based on tethering an antibody or a nanobody that binds the target receptor through a *strong* and specific non-covalent interaction.

However, between these approaches, only PAL, PTLs, PORTLs, maPORTLs, and NPC are described in the GPCR field and all them involving engineered proteins, except OptogluNAM4.1, which is a photoswitchable NSM of $mGlu_4$ that binds covalently [33]. In this PAL approach, the authors proved the covalently labeling of nonmodified $mGlu_4$ receptor by pharmacological methodologies, but not at a molecular level.

PTL compounds are designed as maleimide-azobenzene ligand derivatives that react by affinity labeling with genetically engineered protein receptors, commonly

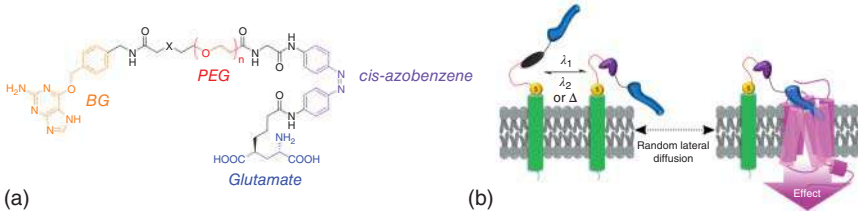


**Figure 37.4** Targeting unmodified native mGluRs with benzylguanine-azoglutamate (BGAG). (a) SNAP-tag binding photoswitchable receptor agonist BGAG in its *cis* active form upon 380 nm illumination, with polyethylene glycol (PEG) linker of different lengths between benzylguanine (BG) and azobenzene-glutamate. "X" indicates distinct spacer elements within the several analogs of BGAG. (b) The active isomer of BGAG, *cis*-BGAG, tethered to a SNAP-tag fused to a single-pass transmembrane segment (SNAP-TM) randomly approaches and photoactivates a native (unmodified) mGluR. Source: Reproduced with permission from Donthamsetti et al. [43]. Copyright (2019) American Chemical Society.

introducing a cysteine amino acid. This single-point mutation must not alter the function of the protein or its membrane trafficking. The photoswitchable unit is generally located in the linker, close to the ligand moiety [34]. This approach has been applied to class A and class C GPCRs, as recently described for dopamine $D_1/D_2$ receptors (DAR) [35] and $mGlu_2$ receptor [34] This strategy has demonstrated to be very efficient due to the high selectivity of the ligand for the modified receptor but also possess some limitations. The presence of native cysteines on the surface of the cells may reduce the bioconjugation selectivity. Moreover, maleimide stability is limited in cellular environments due to slow hydrolysis and possible reaction with cytosolic glutathione [32].

To overcome those limitations, the **PORTL** strategy was developed as an evolution of PTLs for mGlu receptors. In this study, the tether is large chain that will covalently attach to a fusion protein tag based on suicide enzymes that covalently react with benzyl guanines (BC), benzyl cytosines (BC), or haloalkanes (SNAP-[36], CLIP-[37], and HALO [38]-tag, Figure 37.4a). This strategy provides an orthogonal bioconjugation with a very high selectivity [39–41].

An approach derived from PORTL and related to APCs has been applied also to mGlu Receptors [42]. In this research, a selective nanobody and a SNAP-tag were fused for receptor recognition and ligand tethering, respectively. The nanobody recognized with high affinity a green fluorescent protein (GFP) domain that was fused to the *N*-terminus of $mGlu_2$ receptor. It is worth noting that the authors suggested the possibility of using this same method with nanobodies recognizing endogenous receptors for future developments in native tissues. Along these lines, in a recent study, the same authors applied the PORTL strategy to native receptors by placing the labeling tag in a proximal module. That is a single transmembrane helix domain fuses to a SNAP tag, which can be a genetically encoded and expressed in biological systems. This module can diffuse to a close proximity of the endogenous target receptor and enable the photoswitchable ligand binding (Figure 37.4b) [43].

## 37.3 Characterization of GPCR Photopharmacological Tools

In the process of development of photopharmacological tools, such as caged or PCLs (free diffusible or tethered), the characterization of compounds needs to be carefully addressed before testing them in physiologically relevant environments. However, since the biological activity of these compounds is illumination-dependent, further considerations are necessary. First, the compound photoisomerization and photorelease (uncaging) under different light conditions have to be well determined. Subsequently, the translation of these light-induced molecular changes to biological activities requires to be fully addressed. Additionally, the intrinsic properties of compounds that make them sensitive to light must be carefully taken into consideration as they might interfere with the readout of the biological assay. All these theoretical and methodological considerations are covered in this section.

### 37.3.1 Photoisomerization and Uncaging Characterization

The three most common methodologies to measure compound photoisomerization or photorelease are ultraviolet-visible (UV-vis) spectroscopy, liquid chromatography coupled to a photodiode array or mass spectroscopy (LC/PDA/MS), and nuclear magnetic resonance (NMR). These techniques allow the detection of photoisomers or caged compound components by their differential profile in the output (i.e. spectrum, chromatogram). Although these methods can provide complementary information, depending on the photosensitive compound, it might not be amenable in some cases, as explained in Sections 37.3.1.1–37.3.1.4.

#### 37.3.1.1 UV–vis Spectroscopy

The UV–vis spectra of photochromic isomers are generally very different. Similarly, caged compounds and their photoreleased protecting groups often have a differential UV-vis profile. This makes this technique one of the basic experimental procedures for photoisomerization and photo-uncaging detection. Moreover, UV-vis spectroscopy is a robust, unambiguous, and inexpensive methodology that also allows monitoring different photoisomeration cycles, determining the thermal relaxation of the metastable isomer, or measuring the photoreleasing rate of a caged compounds. On the other hand, evaluating the isomerization of photochromic compounds with low bistability might represent a challenge, but this technique allows to use a wide range of solvents that often modify the stability of the different isomeric forms. Usually, the concentrations needed to evaluate the UV-vis spectrum range between 10 and 100 μM. However, the main limitation of this methodology is that the quantitative detection of the amount of each isomer in a mixture is problematic. Some deconvolution methodologies have been described to overcome this issue. However, to apply these methods, the spectrum of a pure sample for each isomer is needed, which represents a methodological challenge with some photochromic compounds having low bistability.

#### 37.3.1.2 LC/PDA/MS

Liquid chromatography (LC) is a powerful methodology that allows to quantitatively detect a mixture of molecules, such as caged compounds or photoisomers. If LC is coupled to a photodiode detector (PDA), the UV-vis absorption spectra of each of the separated peaks can be obtained to properly identify the isomer/compound. Moreover, if LC is subsequently coupled to a mass spectrometer (MS), it is possible to determine the mass of each molecular entity, which will be identical in the case of photoisomers. To quantify the isomeric ratio, the separated peaks must be integrated using the PDA channel at the wavelength of the isosbestic point (i.e. wavelength with equal absorbance of both species), which can be previously determined by UV-vis spectroscopy. Methods based in LC have high sensitivity requiring small sample quantities (c. 1 nmol) to quantify photoisomerization but are low throughput. Moreover, only bistable photochromic compounds can be analyzed using this method because the metastable isomer should not relax before or during the time of measurement (c. 1–10 minutes), which would result in detecting only the thermodynamically stable isomer.

#### 37.3.1.3 NMR

NMR is a nondestructive technique that can be very useful to detect mixtures of isomers of a photochromic compound or a caged compound release. This technique allows a direct sample illumination with an optical fiber or a laser while measuring, what can be very useful for the characterization of photochromic compounds with low bistability. Using $^{1}$H-NMR, the hydrogen peaks of different species or isomers can be integrated, and their ratio corresponds the molar ratio. The main disadvantage of this technique is that it requires samples at high concentrations (>1 mM), at which some GPCR ligands may not be soluble in deuterated aqueous solutions.

### 37.3.2 Characterization of the Receptor Photoswitching

The main objective of photopharmacological compounds is to gain control on the target protein activity through light. This activity switch is generally related to a molecular lysis or isomerization prompted by a specific light exposure. However, the effect of this chemical reaction is not always evident in biological experiments. Therefore, a proper pharmacological characterization is needed to correctly evaluate the differential activities of light-controllable molecules under different illumination conditions.

Many pharmacological and biochemical assays have been used to date in GPCR photopharmacology. Among these, only kinetic assays allow to measure real-time photoswitching. Indeed, when a spatiotemporally controllable molecular tool is evaluated, such as photopharmacological drugs, a time resolution of the method is an important parameter to be considered since in some assays long incubations are needed. Other relevant points to consider are the complexity of the setup needed and the robustness of the data obtained since the application of light will likely alter the assay readout. Indeed, this is a very important point to contemplate since light-based assays (fluorescence, bioluminescence…) may lead to artifacts due to

ligand high absorbance resulting in signal quenching. Taking into consideration all these properties, the assays used for photopharmacological characterization can be organized in four main categories:

- *Kinetic functional assays*, which are based on the measurement of a biological substance concentration variations (second messenger, ions, etc.) or on the interaction of two protein units that associate or dissociate upon a GPCR activation. These methods offer the possibility to perform dynamic measurements, including real-time measurement while the system is being irradiated with different light wavelengths.
- *Endpoint functional assays*, which are based on the measurement of an accumulated biological substance (second messengers or proteins). These, usually provide good specific signal-to-noise ratio. However, since the measurement is stopped at a certain time point, these methods do not allow a continuous dynamic measurement of biological events (including photoisomerization).
- *Binding assays*, which measure ligand binding to the target GPCR and can be kinetic or endpoint.
- *Conformational assays,* which are kinetic and measure a change of conformation of the target GPCR.

#### 37.3.2.1 Kinetic Functional Assays

***cAMP and Calcium Sensors (Figure 37.5(1))***

A common strategy in photopharmacology is based on the use of second messenger sensors, which can be fluorescent, bioluminescent, or produce Förster resonance energy transfer (FRET)/BRET (bioluminescence resonance energy transfer) upon binding to a second messenger such as cAMP or $Ca^{2+}$. The kinetic nature of these sensors offers advantages such as the possibility of measuring the receptor photoswitching in real time. However, a possible interference in fluorescence or luminescence assay responses due to quenching by the photosensitive ligands can be a drawback. This involves the need to carefully consider the addition of control experiments to avoid assay interferences or subtract them from final results. Several assays with cAMP sensors in photopharmacology have been described, such as sensors fused with luciferase proteins [44] and cAMP exchange proteins directly activated by cAMP (EPAC) FRET sensors [45]. Also cytosolic calcium concentration has been monitored upon GPCR photoswitching with chemical $Ca^{2+}$ sensors (Fura-2, Fluo2, X-Rhod-5F) [33, 46–51] or genetically encoded sensors (GCaMP, R-GECO, aqueorin, OGB1AM) [41, 52–56].

***BRET to Monitor G Protein Activation and β-Arrestin Recruitment (Figure 37.5(2))***

G protein activation methods based on BRET assays are cell-based assays in which different protein constructs have to be co-transfected: $G_\alpha$ subunit fused to a luciferase and the $G_\beta$ or $G_\gamma$ fused to a fluorescent protein (GFP, yellow fluorescent protein (YFP), Venus V1/V2). In proximity, the two elements in presence of the luciferase substrate give rise to resonance energy transfer from the bioluminescent luciferase to the fluorescent protein. Therefore, upon G protein activation $G_\alpha$ and $G_{\beta\gamma}$ subunits

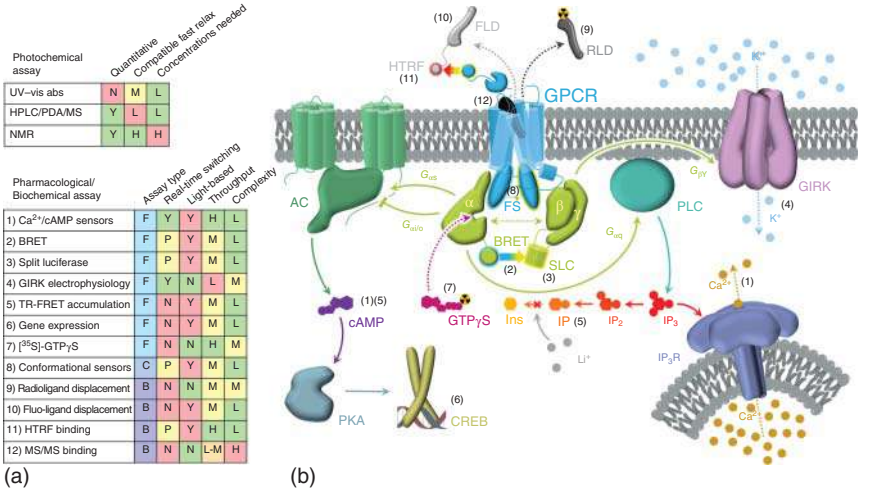

| Photochemical assay | Quantitative | Compatible fast relax | Concentrations needed |
|---|---|---|---|
| UV–vis abs | N | M | L |
| HPLC/PDA/MS | Y | L | L |
| NMR | Y | H | H |

| Pharmacological/ Biochemical assay | Assay type | Real-time switching | Light-based | Throughput | Complexity |
|---|---|---|---|---|---|
| 1) $Ca^{2+}$/cAMP sensors | F | Y | Y | H | L |
| 2) BRET | F | P | Y | M | L |
| 3) Split luciferase | F | P | Y | M | L |
| 4) GIRK electrophysiology | F | Y | N | L | M |
| 5) TR-FRET accumulation | F | N | Y | M | L |
| 6) Gene expression | F | N | Y | M | L |
| 7) [$^{35}$S]-GTPγS | F | N | N | H | M |
| 8) Conformational sensors | C | P | Y | M | L |
| 9) Radioligand displacement | B | N | N | M | M |
| 10) Fluo-ligand displacement | B | N | Y | M | L |
| 11) HTRF binding | B | P | Y | H | L |
| 12) MS/MS binding | B | N | N | L-M | H |



**Figure 37.5** Summary of assays to characterize of GPCR phopharmacological tools. (a) List of the different assays used in GPCR photopharmacology with a summary of the main features of each assay: assay type (*F* for functional, *B* for binding, and *C* for conformational), ability to detect reversible photoswitching, if it is based on light, degree of throughput, and complexity. The suitability of each feature to characterize photopharmacological tools responds to a color code: green for very good suitability, yellow for good or medium suitability, and red for a lower suitability or a need for a careful examination. Letter codes are the following ones: *Y* for *yes*, *N* for *no*, *H* for *high*, *M* for *medium*, *L* for *low*, *P* for *theoretically possible but not done in GPCR photopharmacology*. (b) Graphic scheme of the different events present in GPCR signaling that can be object of measurement in different pharmacological/biochemical assays. The events are related to the assays listed on the left part with a number code from (1) to (12). β-arrestin recruitment assays are not represented in the scheme.

dissociate leading to a decrease of the BRET and an increased emission from the luciferase. Similar assay has been also applied to β-arrestin recruitment in which both, the receptor and β-arrestin, are labeled with BRET donors and acceptors [57]. BRET-based assays are very common in GPCR pharmacology, however, in the photopharmacology field have not been widely used, except in few reports [35]. The possible compatibility of luciferase substrates with an external illumination must be examined, since some are unstable and prone to photodegradation, such as coelenterazine. However, this assay is completely amenable for bistable photoswitchable compounds and caged molecules using pre-illumination protocols. Moreover, as an assay with bioluminescent and fluorescent components, the interference with photosensitive ligands must be assessed.

### *Split Luciferase Complementation (Figure 37.5(3))*

Split luciferase complementation assays are commonly used to measure protein–protein interactions. Both interacting proteins have a fragment that reconstitute into a functional luciferase when the complex is formed. This method can be applied to monitor interactions between $G_{\alpha}$ and $G_{\beta\gamma}$ subunits, G proteins and receptors, G proteins and effectors, and β-arrestins recruitment by GPCRs.

However, photoregulated ligands could still quench luminescence from luciferases although it has been found to be less likely. In addition, as previously mentioned, external illumination might degrade the luciferase substrate, thus limiting its use in photopharmacology protocols. Despite not being widely used, this method has been recently reported in GPCR photopharmacology [54, 58].

***GIRK Channel Activation (Figure 37.5(4))***

One of the most common techniques to detect activity of a GPCR upon stimulation with light-controlled ligands is the measurement of a G-protein-coupled inwardly-rectifying potassium channel (GIRK) opening, which is induced by its interaction with the $G_{\beta\gamma}$ subunit after G protein activation and dissociation. This technique needs the co-transfection of the receptor of interest and the GIRK channel in cell cultures or in *Xenopus tropicalis* oocytes. Channel opening is usually detected by electrophysiology experiments (e.g. voltage clamp, patch-clamp) using a buffer with high concentration of potassium to monitor depolarization upon GIRK channel opening. The main advantage of this technique is that the measurement is performed in a dynamic real-time mode. Moreover, the response recording is completely independent of the applied light, thus giving rise to robust results free of artifacts, which has promoted its wide use in GPCR photopharmacology [30, 34, 35, 39–43, 50, 52, 59–61]. These advantages have allowed the development of protocols with a variety of light conditions, thus making this method an excellent option to prove reversibility of a receptor photoswitching. However, the low throughput makes difficult testing large number of compounds.

#### 37.3.2.2 Endpoint Functional Assays

***TR-FRET IP and cAMP Accumulation (Figure 37.5(5))***

One method to characterize GPCR light-regulated ligands is based on the measurement of the concentration of second messengers upon G protein activation. Second messengers accumulate when the natural degradation is inhibited. In the case of $G_{\alpha q}$ activation, phospholipase C (PLC) activation produces an increase of inositol triphosphate ($IP_3$), which is stepwise dephosphorylated to myo-inositol (Ins). However, the presence of lithium ions in the culture media inhibits the last dephosphorylation step, leading to an accumulation of inositol monophosphate (IP). Similarly, $G_{\alpha s}$ activates the adenylyl cyclase (AC) and produces an increase in the concentration of cAMP, which is accumulated in the presence of a phosphodiesterase inhibitors. In contrast, $G_{\alpha i/o}$ and the other inhibitory G proteins inhibit the AC activity leading to a decrease of cAMP levels. A commonly used method in photopharmacology to quantify IP or cAMP accumulation in the cytosol is based on Homogeneous Time-resolved FRET (HTRF) using labeled antibodies and second messengers. In this method, during cell lysis it is used a buffer implemented with fluorescently labeled IP or cAMP with a FRET acceptor and an IP- or cAMP-recognizing antibody labeled with a lanthanide cryptate/chelate. A competition between labeled and the endogenously produced IP or cAMP can be analyzed by time-resolved FRET signal after incubation of the cells using different light conditions [6, 7, 25, 33, 46–49, 62–64]. The main limitation of this method is that photoswitches and photocages

may interfere or quench the FRET signal between donor and acceptor molecules. However, since this is an endpoint assay, photoactive ligands can be washed out previous to the addition of the FRET fluorophores.

***Gene Reporter Assays (Figure 37.5(6))***

Activation of GPCRs can promote gene expression through second messenger-responsive transcription factors. For instance, upon activation of $G_{\alpha s}$ GPCRs, the activity of AC is enhanced resulting in an increase of the cAMP cytosolic concentration, which will subsequently promote the enzymatic activity of Protein kinase A (PKA). One of the PKA's reported actions is the phosphorylation of cAMP response element-binding (CREB) transcription factor that will lead to an increase of the expression of CREB-target genes, such as secreted alkaline phosphatase (SEAP). Thus, a $G_{\alpha s}$ GPCR activation can be monitored in cells transfected with SEAP adding a phosphorylated substrate that becomes fluorescent or chemiluminescent upon SEAP dephosphorylation. Other similar methods that detect cAMP-mediated expression of other CREB-target genes by immunofluorescence are also available. In GPCR photopharmacology, this endpoint assay has been successfully used to characterize caged compounds [65–68]. However, these methods require long receptor stimulations of 24–48 hours. Therefore, the use of these types of assay for the analysis of the activity of photochromic compounds that usually require high intensity and continuous illumination could result in cell phototoxicity or to light-induced biological effects that lead to activity-biased measurements.

***[$^{35}$S]-GTPγS Binding (Figure 37.5(7))***

[$^{35}$S]-GTPγS binding assays are classical radiolabeling functional methods to quantify the activation of G proteins in cell membrane preparations. The assay, not specific for a $G_{\alpha}$ subtype, is based on the non-hydrolyzable analog guanosine triphosphate (GTP) with a radiolabeled sulfur in γ position binding, which will bind the $G_{\alpha}$ subunit upon receptor and G protein activation. The ineffective hydrolysis results in a slow reversible binding of [$^{35}$S]-GTPγS and its accumulation that can be measured by counting the amount of [$^{35}$S]-label incorporated by $G_{\alpha}$ subunits. The radioactive basis of these type of techniques has limited their use in GPCR photopharmacology. However, some remarkable examples have found in these methods with several advantages, such as the low complexity of the protocols used and the lack of interference with light-regulated ligands [30, 31, 61, 68].

#### 37.3.2.3 Conformational Assays

***Conformational Biosensors (Figure 37.5(8))***

Although being a method of increasing interest to study activation mechanisms, GPCR conformational sensors have been only used in one photopharmacology study [69]. These sensors are based on FRET-compatible fluorescent protein domains fused into two regions of the receptor. A differential FRET can be measured upon conformational changes of the GPCR linked to the activation state. They were initially developed for mechanistic studies using pharmacology and microscopy and usually have a low signal/noise ratio although remarkable examples in class

C GPCRs demonstrate very high accuracy and excellent robustness. Like many fluorescence-based assays, the possible interaction between the photosensitive ligands and the fluorophores needs to be explored. Nevertheless, they provide very useful information of the GPCR dynamics upon ligand binding, which may be different depending on the photoisomers regardless of their pharmacological activity.

#### 37.3.2.4 Binding Assays

***Radiolabeled Ligand Displacement (Figure 37.5(9))***

This assay is the most common binding assay used for GPCRs. It is a straightforward method based on the competition of the assayed ligand with a radiolabeled tracer. Treating membranes containing the target GPCR, the bound ligand can be estimated by measuring the remaining radioactivity after a rapid and thorough washing. As an assay based on radiolabeled ligands, it is generally compatible with photopharmacological ligands if the photosensitive ligands do not quench scintillation processes. However, this method retains the major drawbacks of using radioactive isotopes (health and waste risks, need of appropriate infrastructure and equipment). Several reports in GPCR photopharmacology include binding information obtained by this type of assays [25, 30, 31, 54, 58, 60, 61, 68, 70].

***Fluorescent Ligand Displacement and HTRF Binding (Figure 37.5(10, 11))***

These assays are based on similar principles to that of radiolabeled ligand displacement, with the difference that the ligand is fluorescently instead of radioactively labeled, thus avoiding the problems related to the use of radioactivity. They also offer the possibility to monitor kinetic measurements but the photosensitive ligands may interact with the components of the assay [64]. A related approach with fluorescent ligand displacement makes use of tagged GPCRs with an HTRF donor (Tb or Eu cryptates). This can induce time-resolved FRET with the fluorescent ligand bound, thus reducing the background signal [35].

***Mass Spectrometry Binding Assay (Figure 37.5(12))***

This assay is based on the detection by MS/MS spectrometry of a ligand bound to the target receptor alone or in competition with another one. Since the detection of the ligand does not require any irradiation or light detection, the assay is fully compatible with photopharmacological applications. However, the sensitivity of the assay can be variable due to the different capacities of ionization of the compounds and needs to be set up for every ligand to be detected. It represents a powerful binding assay that has been used only very recently in the field of photopharmacology [71].

## 37.4 *T*-on/*M*-on Photochromic Ligands

In the photopharmacology field, the term photoswitching refers to a change in the biological activity of a pharmacological target (in the case concerning here, a GPCR) due to a light-prompted ligand isomerization. This ligand isomerization may lead

to a change in affinity that generally is traduced in change of the receptor activity. Indeed, changes of ligand affinity are generally translated in changes on potency that is the dose of ligand needed to observe a specific functional effect. Most publications reporting on GPCR PCLs describe a change of potency or affinity, usually expressed as a photoinduced shift (PAS or PPS, for affinity or potency, respectively) [46, 60]. The larger is this shift, the larger is the photoswitching resulting in higher chances to find a ligand dose to enable a complete *on/off* effect upon photoisomerization. However, the maximal effect that a ligand can produce upon binding, which is only related to the ligand efficacy, is also a relevant pharmacological parameter that can be differentially regulated by photoswitchable ligands. Depending on the intrinsic activity, a ligand can be described as a full agonist, partial agonist, neutral antagonist, or inverse agonist, and two isomers of the same molecule may behave differently upon binding to the receptor.

With these assumptions, most of the GPCR-directed PCLs can be classified into following three main subgroups that we propose:

- ***Affinity T-on* ligands**, which are PCLs, whose ***T***hermodynamically more stable isomer is binding to the target GPCR with higher affinity. This would correspond to the *trans* isomers for common azobenzenes, *cis* isomers for cyclic azobenzenes, spiro isomer for spiropyrans, or open isomer of dithienylethenes (Figure 37.6a).
- ***Affinity M-on* ligands**, which are PCLs, whose ***M***etastable isomer is binding to the target GPCR with higher affinity. This would correspond to the *cis* isomers in common azobenzenes, *trans* isomers in cyclic azobenzenes, merocyanine isomer for spiropyrans, or closed isomer for dithienylethenes (Figure 37.6b).
- ***Efficacy photoswitches***, which are PCLs that bind to the target receptor both with the thermodynamically stable and the metastable isomer, but each photoisomer has different intrinsic activity (i.e. full agonist, partial agonist, antagonist, partial/full inverse agonist).

The *T-on* approach provides PCLs that perform their biological activity in the dark and, by the illumination with a specific light wavelength, they lose their affinity. This affinity can also be eventually rescued with the use of another wavelength of illumination. Generally, the development of this type of ligands (especially using azobenzenes) is not arduous since, the azologization approaches [72] have good chances to be successful. The use of different illumination wavelengths can provide photostationary states (PSS) with different proportions of the two isomers. This allows adjusting the active ligand dose by means of light, therefore providing a spatiotemporal control of the GPCR activity. This makes *T-on* PCLs excellent tool compounds to control the activity of GPCRs in physiological studies, which is not possible with most of the currently available chemical biology tools. From the therapeutic point of view, this approach is however limited. Nonetheless, it could be designed to treat a disease that is spread throughout the organism, whereas the drug activity is "disconnected" in specific regions of the body to prevent off-target side effects.

On the other hand, the use of the *M-on* approach for PCLs can improve the previous therapeutic limitations of *T-on* ligands, since they show a lower activity in the

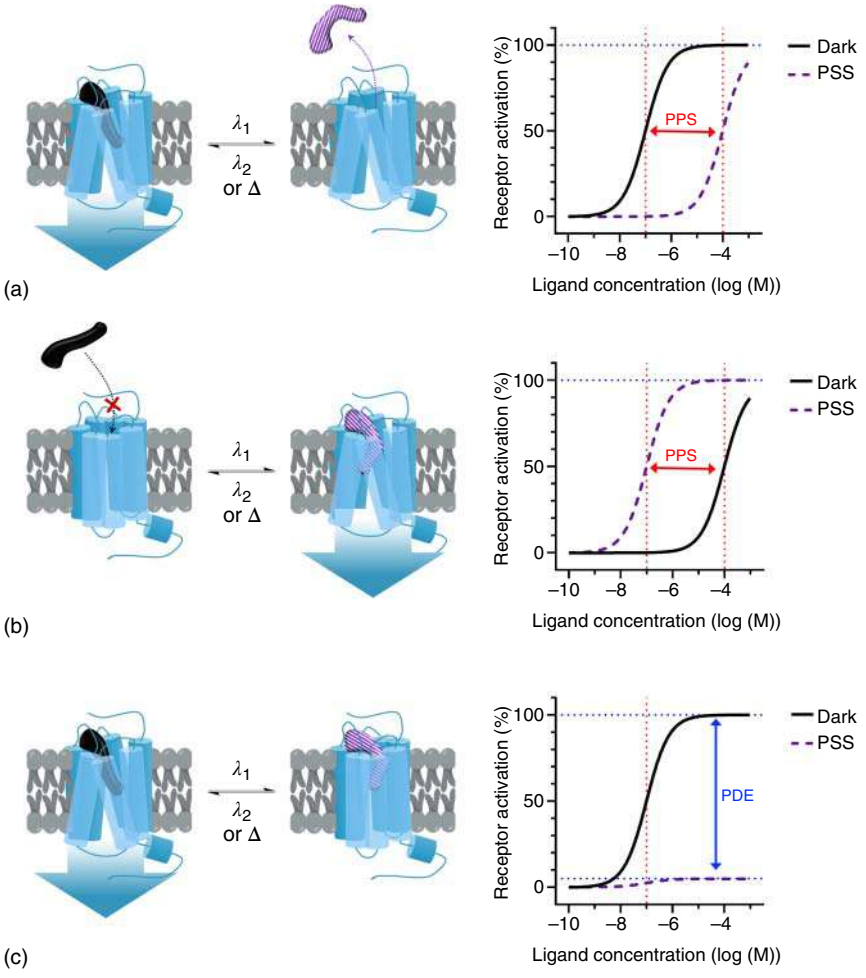


**Figure 37.6** Pharmacological classification of GPCR photochromic ligands. Graphical scheme and model dose–response curves of types of GPCR photoswitching ligands: (a) *M-on* Affinity switch, (b) *T-on* affinity switch, (c) efficacy photoswitch from a *T-full* agonist to an *M-antagonist*.

dark and can be activated with a light of specific wavelengths in a precise time and location. Moreover, *T-on* ligands may be also advantageous in research applications to study the implication of a receptor activity with precision in cells, tissues, and organs. The development of *T-on* ligands has been proved to be more challenging especially for *E–Z* photoswitches due to the particular angle between the aromatic rings of the isomers, such as *cis*-azobenzene, which is barely found in the binding mode of conventional GPCR drugs. Nonetheless, the spatiotemporal control of the ligand activity provides an extra local selectivity, which would prevent possible side effects if the GPCR is expressed in non-targeted regions of the body. This aspect of

photopharmacology will be further discussed in the "therapeutic prospects" section of this chapter.

The most prominent example of efficacy photoswitching in GPCRs is retinal. For this molecule, the 11-*cis* isomer acts as an inverse agonist after covalently binding bistable pigments, such as parapinopsin [14]. In contrast, after absorption of a photon, the ligand isomerizes to all-*trans*-retinal, which as an agonist activates the receptor and initiates the transducing signaling cascades. However, retinal cannot be considered a formal PCL for MSP, such as vertebrate rhodopsin, since this photoswitching is not reversible with a second light wavelength [14]. Synthetic PCLs have demonstrated differences of intrinsic efficacy between isomers and photoswitching from antagonism to full agonism (Figure 37.6c). These differences in intrinsic activity are usually expressed as PDE (photoinduced difference of efficacy) [30, 31, 62].

From the chemical biology point of view, light-regulated ligands controlling the receptor efficacy are excellent tool compounds to study the response of a particular GPCR. Indeed, the differential binding of photoisomers allows for a fine control of its functional activity, enabling a real *on/off* switch that is dependent on their relative ratio. However, this approach involves a continuous action of the ligand toward the targeted receptors regardless the isomer acting. This can be a limitation of the approach from the therapeutic point of view since the activity of receptors expressed in cells or tissues nonrelated to the treatment will be also altered.

## 37.5 Translation to In Vivo and Therapeutic Prospects

The translation of the photochemical and photophysical properties of a biologically active molecule to a precise control of biological activity constitutes the essence of photopharmacology. The use of light-triggered stimulus to manipulate the molecular activation of GPCRs in living animals opens the opportunity to study of molecular and biological mechanisms with unprecedented spatial and temporal resolution. On the one hand, in vivo photopharmacology allows to study a particular anatomical location of the receptor with a specific physiological response or stimulus at molecular and cellular levels, allowing to accurately establish the GPCR function, mechanism, and dynamics in living organisms [5]. On the other hand, the high resolution of optical manipulation techniques offers the opportunity to develop light-regulated drugs acting on GPCRs with a degree of control unattainable with conventional drugs. This fine control allows to therapeutically restore specific receptor dysfunctional states, which are related to a defined pathophysiological situation.

A critical element for in vivo applications of photopharmacology is the existence of a suitable device to deliver light to a localized target tissue or organ to promote the photoresponse of molecules and proteins [73, 74]. Undoubtedly, there are organs where light delivery is relatively straightforward, for example, in external organs such as the skin, the auditory system, and organs related to light transfer or light stimulus processing (i.e. eye and retina) [75]. In contrast, some

other locations present more difficulties because are deep and non-transparent tissues, such as the brain or the heart. Indeed, photopharmacological manipulation on these locations requires invasive devices to transfer the light from the source [76]. The type of organism involved is also relevant and small animal models such as tadpoles or zebrafish, which are relatively transparent, offer advantages for light delivery over bigger organisms such as rodents or humans, which usually require implantable systems involving surgery. In addition, for specific applications, the light parameters (wavelengths, intensity, illumination time and area, tissue penetration) and the photomolecular properties define also the requirements of the illumination system. However, as a consequence of the advent of optogenetics, the development of bioelectronic devices and illumination systems for optical regulation and light delivery is in constant progress and can be applied into the photopharmacology field.

Therapeutic proofs of concept for GPCR photopharmacological pain control in wild-type animals have been successful using mGlu photoswitchable azobenzenes, [6, 46] caged allosteric modulators [7], or azobenzene lipids [50]. Photopharmacological approaches for visual impairment or blindness appear specially promising. A striking demonstration has been obtained using a white light photoswitchable azobenzene acting on ion channels of retinal ganglion cells. In these reports, ON and OFF responses were induced by utilizing intrinsic circuitry in mice blind retina showing promising effects in behavioral mice experiments [77]. However, the use of photoresponsive drugs to regulate the dynamic molecular architecture and cellular complexity of the vision machinery is an enormous challenge, which will require deep and sustained efforts for effective restoration of responses in damaged retina. Finally, among the excitement of many potential applications of light to improve drug effects, the control of bacterial growth with red-light-operated antibiotics [78] the regulation of pancreatic function for glucose homeostasis in anesthetized mice [79], or the development of molecules acting on cancer cells are particularly remarkable.

## 37.6 Concluding Remarks and Future Perspectives of Photopharmacology

Photopharmacology promises to improve drug specificity and regulation demands the convergent knowledge of different science disciplines. Light-operated molecules play an essential role and therefore medicinal chemists have been attracted and actively involved in the design and synthesis of photocontrolled protein ligands [80]. These molecules will require high selectivity and affinity for the target protein combined with the biophysical, metabolic, and efficacy properties of a drug and the necessary photochemical properties for exerting a light-induced switch in the protein activity, which must be compatible with cellular and tissue environments and amenable to be used in living animals. An aspect of particular importance is the dynamic role that light plays in drug action, which needs to encompass the molecule photochemical and photophysical properties with the activation and deactivation

receptor kinetics that ultimately has an effect on its biological role in a particular physiological process [81]. Therefore, apart from the classical optimization parameters of a drug (affinity, functional activity, and selectivity, ADME, toxicity, etc.), the response of the drug to light must also be fine-tuned to obtain an effective biological regulation.

A critical point in photopharmacology is the validation of the biological activity under different light conditions. The development of biochemical and pharmacological assays for testing molecules needs the implementation of different approaches that may involve isolated proteins or receptors, cellular assays, tissues, or in vivo models. The adaptation of the conventional pharmacology tests is a possibility usually employed, although the use of light sources and illumination devices increases in many cases the complexity and the number of optimization parameters for the assay. For instance, many enzyme or receptor assays use fluorescence, absorbance, or luminescence readouts in multiwell plate formats. In photopharmacology, these assays need to be compatible with the light source used for activating the photoresponsive molecules, avoiding interferences with the photochemical processes operating over the drug. A relatively underestimated aspect of photopharmacological assays is the lack of standardization of the equipment and light parameters, which needs a careful future consideration to increase reproducibility, robustness, and reliable quantification of the biological activities. Photopharmacology is based on the simultaneous operation of molecules and light in biological systems, and the dosing regimens are both very important in obtaining the final drug effects. In vivo testing, as mentioned before, is requiring a strong bioengineering effort to build light sources and systems for applying light and drugs at the required anatomical location or organs under strict controlled conditions. The use of chronic or long-lasting treatments or behavioral tests where the animals need to be free of movement has ended in implantable devices many times externally operated under wireless control [82].

Beyond the improvement of drug therapeutics, photopharmacology is opening new avenues in basic science. Biological function takes place in a strict spatially and temporally regulated manner on a cell and organism level. From a molecular perspective, biology involves a concatenation of chemical events in a defined temporal sequence and with strict spatial confinement. Understanding and manipulating this dynamic and precise machinery is an enormous scientific challenge. The real-time remote control of protein activity in a reversible manner is a scientific challenge that has a great potential for the study and manipulation of biological processes. The spatial and temporal control of protein activity obtained in photopharmacology provides unique opportunities for studying basic biochemical mechanisms, biological function, and cellular interaction. For example, the structure of receptors in active or inactive states and its conformational evolution can be regulated using photoswitchable ligands [83]. As such, scientist can use molecular switches for understanding molecular interactions and to link to receptor functional activity. Moreover, photoactive molecules can be used to operate over a specific receptor allowing the study of its role in organism development, biological functions, and disease progression.

Overall, light provides an ideal external control element for reversibly regulating proteins in living systems, combining safety, easy delivery, and high spatial and temporal resolution not interfering to most cellular processes, which combined with optogenetics is opening a wide perspective for high-precision light-operated biology.

## References


1 Guo, D., Hillger, J.M., IJzerman, A.P., and Heitman, L.H. (2014). *Med. Res. Rev.* 34: 856–892.
2 Saikia, S., Bordoloi, M., and Sarmah, R. (2019). *Curr. Drug Targets* 20: 522–539.
3 Xue, Y., Bai, H., Peng, B. et al. (2021). *Chem. Soc. Rev.* https://doi.org/10.1039/D0CS01061H.
4 Kramer, R.H., Mourot, A., and Adesnik, H. (2013). *Nat. Neurosci.* 16: 816–823.
5 Hüll, K., Morstein, J., and Trauner, D. (2018). *Chem. Rev.* 118: 10710–10747.
6 Zussy, C., Gómez-Santacana, X., Rovira, X. et al. (2018). *Mol. Psychiatry* 23: 509–520.
7 Font, J., López-Cano, M., Notartomaso, S. et al. (2017). *Elife* 6: e23545.
8 Airan, R.D., Thompson, K.R., Fenno, L.E. et al. (2009). *Nature* 458: 1025–1029.
9 Deisseroth, K. (2011). *Nat. Methods* 8: 26–29.
10 Li, X., Gutierrez, D.V., Hanson, M.G. et al. (2005). *Proc. Natl. Acad. Sci. U.S.A.* 102: 17816–17821.
11 Rappleye, M. and Berndt, A. (2019). *Curr. Opin. Struct. Biol.* 57: 176–184.
12 Mukohata, Y. (1977). *Biochem. Biophys. Res. Commun.* 78: 7.
13 Oesterhelt, D. and Stoeckenius, W. (1971). *Nature. New Biol.* 233: 149–152.
14 Tsukamoto, H. and Terakita, A. (2010). *Photochem. Photobiol. Sci.* 9: 1435–1443.
15 Deisseroth, K. (2015). *Nat. Neurosci.* 18: 1213–1225.
16 Weitzman, M. and Hahn, K.M. (2014). *Curr. Opin. Cell Biol.* 30: 112–120.
17 Siuda, E.R., McCall, J.G., Al-Hasani, R. et al. (2015). *Nat. Commun.* 6: 8480.
18 Zheng, W., Zhou, J., Luan, Y. et al. (2018). *Front. Mol. Neurosci.* 11: https://doi.org/10.3389/fnmol.2018.00095.
19 Velema, W.A., Szymanski, W., and Feringa, B.L. (2014). *J. Am. Chem. Soc.* 136: 2178–2191.
20 Kaplan, J.H., Forbush, B., and Hoffman, J.F. (1978). *Biochemistry* 17: 1929–1935.
21 Ellis-Davies, G.C.R. (2020). *Acc. Chem. Res.* 53: 1593–1604.
22 Fehrentz, T., Schönberger, M., and Trauner, D. (2011). *Angew. Chem. Int. Ed.* 50: 12156–12182.
23 Weinstain, R., Slanina, T., Kand, D., and Klán, P. (2020). *Chem. Rev.* 120: 13135–13272.
24 Josa-Culleré, L. and Llebaria, A. (2020). *ChemPhotoChem* 4, ahead of print.
25 Gienger, M., Hübner, H., Löber, S. et al. (2020). *Sci. Rep.* 10: 829.
26 Falvey, D.E. (2005). *J. Am. Chem. Soc.* 127: 16747–16747.
27 Merino, E. (2011). *Chem. Soc. Rev.* 40: 3835.


**28** Szymański, W., Beierle, J.M., Kistemaker, H.A.V. et al. (2013). *Chem. Rev.* 113: 6114–6178.

**29** Ricart-Ortega, M., Font, J., and Llebaria, A. (2019). *Mol. Cell. Endocrinol.* 488: 36–51.

**30** Gómez-Santacana, X., de Munnik, S.M., Vijayachandran, P. et al. (2018). *Angew. Chem. Int. Ed.* 57: 11608–11612.

**31** Gómez-Santacana, X., de Munnik, S.M., Mocking, T.A.M. et al. (2019). *Beilstein J. Org. Chem.* 15: 2509–2523.

**32** Leippe, P., Koehler Leman, J., and Trauner, D. (2017). *Biochemistry* 56: 5214–5220.

**33** Rovira, X., Trapero, A., Pittolo, S. et al. (2016). *Cell Chem. Biol.* 23: 929–934.

**34** Levitz, J., Pantoja, C., Gaub, B. et al. (2013). *Nat. Neurosci.* 16: 507–516.

**35** Donthamsetti, P.C., Winter, N., Schonberger, M. et al. (2017). *J. Am. Chem. Soc.* 139: 18522–18535.

**36** Keppler, A., Gendreizig, S., Gronemeyer, T. et al. (2003). *Nat. Biotechnol.* 21: 86–89.

**37** Gautier, A., Juillerat, A., Heinis, C. et al. (2008). *Chem. Biol.* 15: 128–136.

**38** Los, G.V., Encell, L.P., McDougall, M.G. et al. (2008). *ACS Chem. Biol.* 3: 373–382.

**39** Broichhagen, J., Damijonaitis, A., Levitz, J. et al. (2015). *ACS Cent. Sci.* 1: 383–393.

**40** Levitz, J., Broichhagen, J., Leippe, P. et al. (2017). *Proc. Natl. Acad. Sci. U.S.A.* 114: E3546–E3554.

**41** Acosta-Ruiz, A., Gutzeit, V.A., Skelly, M.J. et al. (2020). *Neuron* 105: 446–463.e13.

**42** Farrants, H., Gutzeit, V.A., Acosta-Ruiz, A. et al. (2018). *ACS Chem. Biol.* 13: 2682–2688.

**43** Donthamsetti, P.C., Broichhagen, J., Vyklicky, V. et al. (2019). *J. Am. Chem. Soc.* 141: 11522–11530.

**44** Bahamonde, M.I., Taura, J., Paoletta, S. et al. (2014). *Bioconjugate Chem.* 25: 1847–1854.

**45** Duran-Corbera, A., Catena, J., Otero-Viñas, M. et al. (2020). *J. Med. Chem.* 63: 8458–8470.

**46** Gómez-Santacana, X., Pittolo, S., Rovira, X. et al. (2017). *ACS Cent. Sci.* 3: 81–91.

**47** Pittolo, S., Gomez-Santacana, X., Eckelt, K. et al. (2014). *Nat. Chem. Biol.* 10: 813–815.

**48** Broichhagen, J., Johnston, N.R., Von Ohlen, Y. et al. (2016). *Angew. Chem. Int. Ed.* 55: 5865–5868.

**49** Broichhagen, J., Podewin, T., Meyer-Berg, H. et al. (2015). *Angew. Chem. Int. Ed.* 54: 15565–15569.

**50** Morstein, J., Hill, R.Z., Novak, A.J.E. et al. (2019). *Nat. Chem. Biol.* 15: 623–631.

**51** Morstein, J., Dacheux, M.A., Norman, D.D. et al. (2020). *Chem. Soc.* https://doi.org/10.1021/jacs.0c02154.

**52** Carroll, E.C., Berlin, S., Levitz, J. et al. (2015). *Proc. Natl. Acad. Sci. U.S.A.* 112: E776–E785.


**53** Frank, J.A., Yushchenko, D.A., Fine, N.H.F. et al. (2017). *Chem. Sci.* 8: 7604–7610.

**54** Lachmann, D., Konieczny, A., Keller, M., and König, B. (2019). *Org. Biomol. Chem.* 17: 2467–2478.

**55** Riefolo, F., Matera, C., Garrido-Charles, A. et al. (2019). *J. Am. Chem. Soc.* 141: 7628–7636.

**56** Wagner, N., Schuhmacher, M., Lohmann, A., and Nadler, A. (2019). *Chem. Eur. J.* 25: 15483–15487.

**57** Donthamsetti, P., Quejada, J.R., Javitch, J.A. et al. (2015). *Curr. Protoc. Pharmacol.* 70: 2.14.1–2.14.14.

**58** Agnetta, L., Bermudez, M., Riefolo, F. et al. (2019). *J. Med. Chem.* 62: 3009–3020.

**59** Schönberger, M. and Trauner, D. (2014). *Angew. Chem. Int. Ed.* 53: 3264–3267.

**60** Hauwert, N.J., Mocking, T.A.M., Da Costa Pereira, D. et al. (2018). *J. Am. Chem. Soc.* 140: 4232–4243.

**61** Hauwert, N.J., Mocking, T.A.M., Da Costa Pereira, D. et al. (2019). *Angew. Chem. Int. Ed.* 58: 4531–4535.

**62** Gómez-Santacana, X., Dalton, J.A.R., Rovira, X. et al. (2017). *Eur. J. Med. Chem.* 127: 567–576.

**63** Westphal, M.V., Schafroth, M.A., Sarott, R.C. et al. (2017). *J. Am. Chem. Soc.* 139: 18206–18212.

**64** Taura, J., Nolen, E.G., Cabré, G. et al. (2018). *J. Controlled Release* 283: 135–142.

**65** Banghart, M.R. and Sabatini, B.L. (2012). *Neuron* 73: 249–259.

**66** Banghart, M.R., Williams, J.T., Shah, R.C. et al. (2013). *Mol. Pharmacol.* 84: 687–695.

**67** Banghart, M.R., He, X.J., and Sabatini, B.L. (2018). *ACS Chem. Neurosci.* 9: 684–690.

**68** Dolles, D., Strasser, A., Wittmann, H.-J. et al. (2018). *Adv. Ther.* 1: 1870003.

**69** Agnetta, L., Kauk, M., Canizal, M.C.A. et al. (2017). *Angew. Chem. Int. Ed.* 56: 7282–7287.

**70** Prischich, D., Gomila, A.M.J., Milla-Navarro, S. et al. (2021). *Angew. Chem. Int. Ed.* 60: 3625–3631.

**71** Ricart-Ortega, M., Berizzi, A.E., Pereira, V. et al. (2020). *ACS Pharmacol. Transl. Sci.* 3: 883–895.

**72** Broichhagen, J., Frank, J.A., and Trauner, D. (2015). *Acc. Chem. Res.* 48: 1947–1960.

**73** Morstein, J. and Trauner, D. (2019). *Curr. Opin. Chem. Biol.* 50: 145–151.

**74** Ray, T.R., Choi, J., Bandodkar, A.J. et al. (2019). *Chem. Rev.* 119: 5461–5533.

**75** Dieter, A., Keppeler, D., and Moser, T. (2020). *EMBO Mol. Med.* 12: e11618.

**76** Paoletti, P., Ellis-Davies, G.C.R., and Mourot, A. (2019). *Nat. Rev. Neurosci.* 20: 514–532.

**77** Laprell, L., Tochitsky, I., Kaur, K. et al. (2017). *J. Clin. Invest.* 127: 2598–2611.

**78** Wegener, M., Hansen, M.J., Driessen, A.J.M. et al. (2017). *J. Am. Chem. Soc.* 139: 17979–17986.

**79** Mehta, Z.B., Johnston, N.R., Nguyen-Tu, M.-S. et al. (2017). *Sci. Rep.* 7: 291.

**80** Fuchter, M.J. (2020). *J. Med. Chem.* 63: 11436–11447.


**81** Welleman, I.M., Hoorens, M.W.H., Feringa, B.L. et al. (2020). *Chem. Sci.* 11: 11672–11691.
**82** Qazi, R., Gomez, A.M., Castro, D.C. et al. (2019). *Nat. Biomed. Eng.* 3: 655–669.
**83** Arkhipova, V., Fu, H., Hoorens, M.W.H. et al. (2021). *J. Am. Chem. Soc.* 143: 1513–1520.

# 38 Photoswitching of Ion Channels

Timm Fehrentz and Johannes Broichhagen

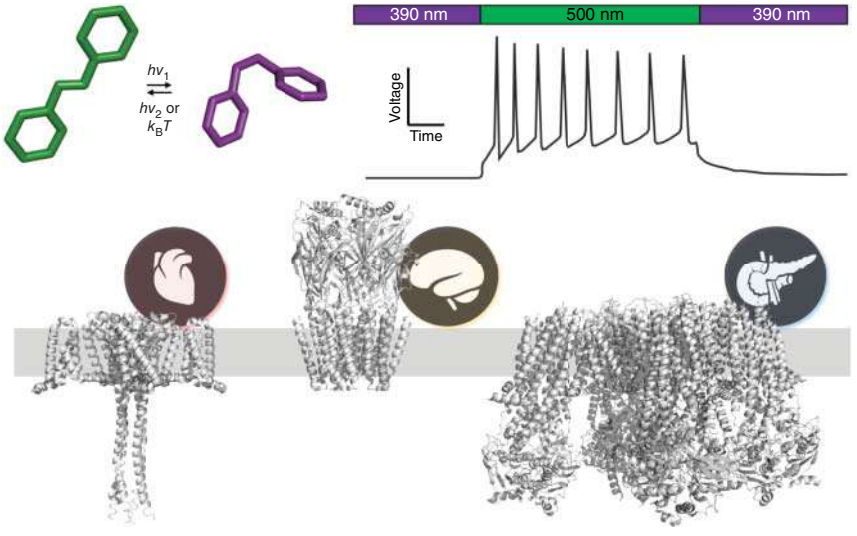


**Characteristic Features**

Ion channels allow ions to cross a cell's lipid bilayer membrane, maintaining membrane potential while allowing to transmit information between extracellular space and cytosol. They respond to many stimuli (e.g. light, ligands, voltage, force, temperature) and are responsible for action potential firing in excitable tissue. Different organs, including the heart, the pancreas, and the brain, are able to communicate by this fundamental mechanism in physiology.

**First Reported**

Bartels et al. (1971). *PNAS*, 68: 1820–1823; Banghart et al. (2004). *Nat. Neurosci*.; Volgraf et al. (2006). *Nat. Chem. Bio*.

**Key References**

Broichhagen et al. (2014). *Nat. Commun*. Fehrentz et al. (2018). *Nat. Chem. Bio*. Hüll et al. (2018). *Chem. Rev*. Mourot et al. (2012). *Nat. Meth*. Paoletti et al. (2019). *Nat. Rev. Neurosci*.

# 38

# Photoswitching of Ion Channels

*Timm Fehrentz*[1] *and Johannes Broichhagen*[2]

[1] *Department of Cardiology, Angiology and Pneumology, University Hospital Heidelberg, Im Neuenheimer Feld 410, 69120 Heidelberg, Germany*
[2] *Leibniz-Forschungsinstitut für Molekulare Pharmakologie, Department of Chemical Biology, Robert-Rössle-Str. 10, 13125 Berlin, Germany*

## 38.1 Introduction

### 38.1.1 Ion Channels and Their Function in Excitable Tissue

Ion channels are transmembrane proteins that are most relevant for physiological processes and bestow electrical excitability to different tissue based on their ion permeability. This excitability allows for rapid transportation of information and represents a fundamental concept in physiology. For instance, neuronal information of the motor cortex in the brain is transmitted to muscles that control movement, while cardiac excitation triggers heart contraction and pancreatic excitation results in insulin secretion.

In principle, ligand-, voltage-, temperature-, and pressure-gated ion channels can be distinguished. However, as an introductive example, voltage-gated $K^+$ ($K_v$) channels are discussed hereafter in more detail as these play an important role for the excitability of neurons, cardiomyocytes, and pancreatic β-cells. $K_v$ channels assemble in the cell membrane as tetramers out of four subunits, which build the selectivity filter in the center (Figure 38.1a,b) [2, 3]. Each subunit owns six transmembrane helices called S1–S6. Helices S5 and S6 together with the P-helix form the selectivity filter and gates, two important properties of the channel. The GYG sequence within the P-helix is the $K^+$ selectivity-determining motif and conserved in all $K^+$ channels. Lastly, S1–S4 function as a voltage sensor of the channel. As ions are unevenly distributed across the membrane, they build up an electrical potential, a characteristic for any given cell type. Once membrane depolarization opens the channel, $K^+$ ions follow their electrochemical gradient and generate a current across the cell membrane, which repolarize and even hyperpolarize the membrane potential under physiological conditions.

After a first glimpse at the structure and function of one ion channel, it is equally important to notice their function as a dynamic ensemble within a specific cell that

*Molecular Photoswitches: Chemistry, Properties, and Applications*,
First Edition. Edited by Zbigniew L. Pianowski.


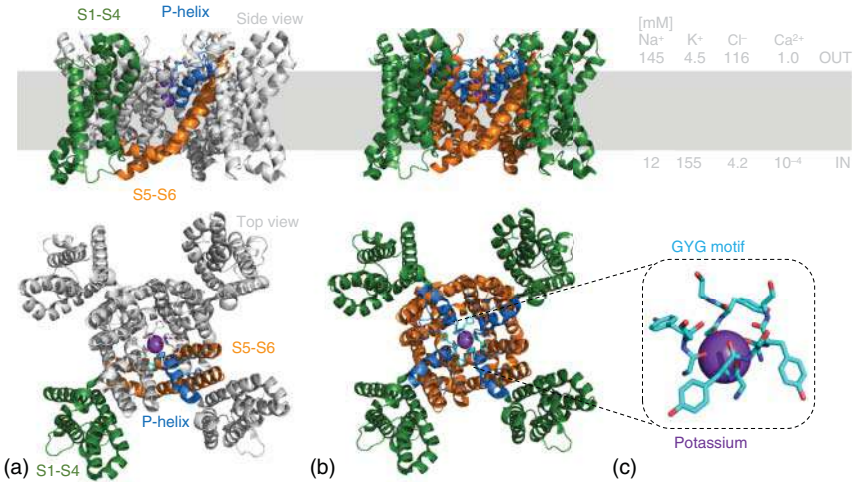


**Figure 38.1 Voltage-gated $K^+$ channel ($K_v$) as an example for channel characteristics (pdb: 2r9r)** [1]. (a) The channel consists of a tetramer sitting in the plasma membrane (side view, top). One subunit is colored on the top left, consisting of voltage-sensing S1–S4 helices (green), pore-forming helices S5–S6 (orange), selectivity-defining P-helix (blue), and GYG motif (cyan). Lower structure depicts 90° rotation around the x-axis. (b) As in (a) but all subunits are colored, highlighting the fourfold symmetry, and with zoom-in on the $K^+$-(purple) bound GYG motif. (c) Physiological distribution of ions across the plasma membrane is noted on the top right corner in millimolar (mM) concentration. Source: Modified from Long et al. [1].

defines the electrical excitability. In particular, each excitable cell contains a specific subset of ion channels and pumps that determine the electrical properties, including the action potential (AP) and the resting membrane potential. The latter is mainly based on an unequal distribution of $Na^+$ and $K^+$ across the cell membrane. This distribution (Figure 38.1c) is maintained by the $Na^+/K^+$ ATPase, which pumps 3 $Na^+$ ions out of and 2 $K^+$ ions into the cell under ATP hydrolysis. $K^+$ leak channels are constitutively open and comprise, depending on the tissue, two-pore-domain $K^+$ ($K_{2P}$) and inward rectifier $K^+$ ($K_{ir}$) channels. These channels set the resting membrane potential to approximately –90 mV for working cardiomyocytes, –70 mV for neurons, and –70 mV for pancreatic β-cells. Confirmed by experimental investigations, theoretical consideration led to the derivation of the Goldman–Hodgkin–Katz equation that allows to calculate the resting membrane potential, based on the contributing ions $Na^+$, $K^+$, $Cl^-$, and $Ca^{2+}$ [4, 5]. In excitable tissue, if the membrane is depolarized, an AP can be triggered with specific biophysical properties depending on the cell type. It is important to realize that the AP represents the key unit of the electrical cellular communication and a fine interplay between the spatiotemporal control of different ion channels, such as voltage-gated $Na^+$, $K^+$, and $Ca^{2+}$ channels ($Na_v/K_v/Ca_v$). In a simplified view, an AP is divided into a phase where the resting membrane potential is constant. Afterwards, a rapid depolarization follows after reaching a threshold potential, carrying the rising phase. This is the "all-or-nothing" response in excitable tissue that determines if an AP is generated or not. Afterwards,

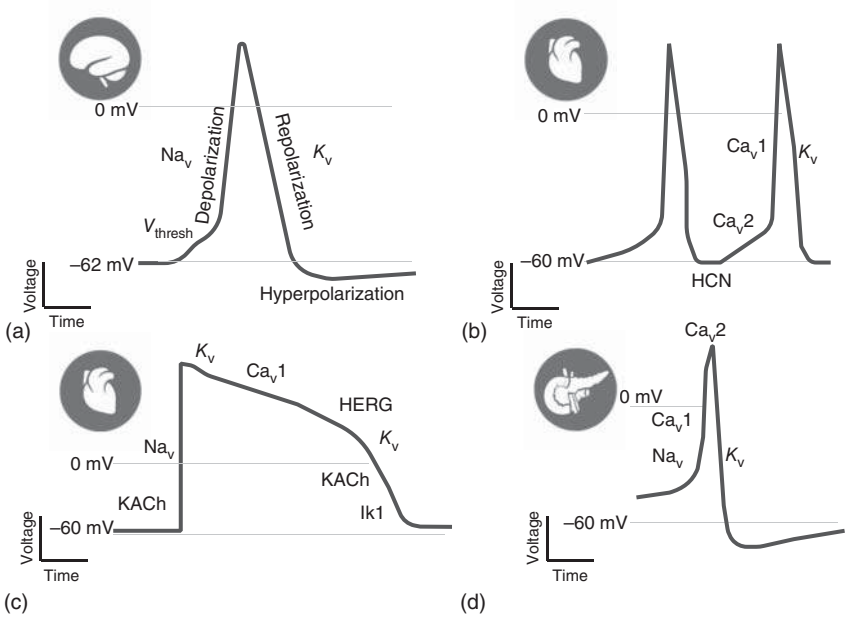


**Figure 38.2 Schematic depictions of cell-specific action potentials.** (a) Illustration of an action potential of a hippocampal pyramide neuron. (b) Cardial actions potential of pacemakers cell within the sinoatrial node. (c) Action potential of the working myocard. (d) Pancreatic action potential of a β-cell. Source: Based on The Human Protein Atlas [7].

a repolarization falling phase follows, which returns to the resting potential by a rapid repolarization [6]. Duration, kinetics, and amplitude of APs differ significantly between neurons, cardiomyocytes, and pancreatic β-cells (Figure 38.2).

### 38.1.2 Electrophysiology: Patch Clamping and Other Methods

The interest to study the function of electric excitable tissue sparked the need to develop scientific methods for its measurement. Within the last decades, several techniques were established and help to tremendously extend our knowledge; however, the complexity of physiology is a challenging task and requires further technological developments as of today. Still, the patch-clamp technique represents a key method to determine the membrane potential and currents across the membrane of a cell [8]. For this reason, one electrode remains in the bath solution of a cell, and the second electrode is present in a fine glass pipette, known as the patch-pipette. Once it is moved close to a cell membrane, it forms a tight seal with high resistance. From this point on, the experimenter can choose different recording modes. For instance, the voltage-clamp mode allows to detect either macroscopic currents of ion channel ensembles of a single cell, or even single-channel currents. In the current-clamp mode, changes of the membrane potential can be recorded, including action potentials. The importance of the technique is reflected in the award of the Nobel Prize to its developers Erwin Neher and Bert Sakmann in 1991.

More recently, optical techniques were introduced that allow to study cytosolic $Ca^{2+}$ levels and membrane potential changes of single cells and cellular ensembles [9–11]. These fluorescent sensors are based on dyes and genetically modified proteins [9]. Thus, the electrical activity of many coupled excitable cells can now be studied with high spatiotemporal resolution using a microscope coupled to a fast recording camera. For instance, this allowed to visualize the excitation propagation within the heart, opening new options for the understanding of cardiac physiology [12].

### 38.1.3 Neurons

Neurons form networks that underlie brain function. A single neuron distinguishes action potentials from the dendritic tree, including postsynapses, the cell soma, and axons. As such, communication within a neuron is transmitted via electrical activity, whereas the communication between neurons is transmitted and processed chemically by neurotransmitters [13]. Once released at the presynapse, the neurotransmitter is detected at the postsynapse and triggers modulation of the postsynaptic potential.

Glutamate is the key excitatory neurotransmitter in the central nervous system and is detected by ionotropic glutamate receptors (iGluRs), including AMPA, NMDA, kainate, and δ receptors [14]. They belong to the class of ligand-gated ion channels, which also comprise nicotinic acetylcholine (nACh), serotonin- ($5\text{-}HT_3$), glycine-, γ-aminobutyric-acid ($GABA_A$), and P2X receptors [15]. iGluRs arrange as tetramers within cell membranes, whereas each subunit comprises an extracellular amino-terminal and ligand-binding domain, a transmembrane domain, and an intracellular carboxyl-terminal domain. Upon ligand binding, they open their gate and allow cations to follow their electrochemical gradient. This leads to a cation inward current, which depolarizes the postsynapse and is called an excitatory postsynaptic potential (EPSP) [14]. In the context of memory storage, strengthening and weakening of glutamate detection leads to long-term potentiation or depression, respectively. Here, the phosphorylation state of receptors and possibly up or downregulation of AMPA and NMDA receptor expression are key mechanisms, which modify postsynaptic glutamate detection [14]. In contrast, ligand-gated $GABA_A$ receptors function as inhibitory ion channels detecting GABA. Here, the selectivity filter of the pore is permeable to $Cl^-$ ions that hyperpolarize the postsynaptic membrane and induce inhibitory postsynaptic potentials (IPSPs). EPSPs and IPSPs are perceived all over the dendritic tree and become integrated. A resulting depolarization at the axon initial segment will trigger an action potential once reaching threshold exceedance ($V_{tresh}$), which lasts in the case of hippocampal neurons for approximately 2 ms (Figure 38.2a) [6]. Initially, voltage-gated $Na^+$ channels ($Na_v$) open and $Na^+$ influx occurs. This triggers the rapid depolarization phase of an action potential (AP) (Figure 38.2a). After the opening of $Na_v$ channels, delayed $K_v$ channels open and the outward $K^+$ triggers the repolarization phase of the action potential. For some neurons, a hyperpolarization is monitored, which is

based on $Ca^{2+}$-dependent $K^+$ channels. At the end of the cycle, the $Na^+/K^+$ ATPase restores the resting membrane potential.

Sensory neurons represent a specialized part of the nervous system. They act as primary detectors of environmental stimuli, including temperature, light, pressure, itch, auditory signals, and taste [15]. All these stimuli modulate the membrane potential and trigger an action potential, resulting in further information processing toward the central nervous system (CNS). For instance, detection of painful stimuli depends on nociceptors that express transient receptor potential (TRP) channels [16]. Especially subtype TRPV1 functions as detector of heat above 37 °C and $H^+$ resulting from tissue damage. Once this tetrameric ion channel opens, cellular cation influx results in a depolarization that triggers AP firing. Analogously, in another set of sensory fibers, the ion channel transient receptor potential ankyrin (TRPA1) is required for the sensation of a distinct itch form [17]. Given the multitude of sensations and perceptions, one can only imagine the fine-tuned interplay and resulting complexity of ion channels in the human body.

### 38.1.4 Cardiomyocytes

The mammalian heart ensures perfusion of all organs with oxygenated blood and nutriment by rhythmic contraction. This muscular organ is mainly composed of cardiomyocytes, which are electrically interconnected by tight junctions and form the so-called syncytium. These synchronized cells allow for a defined electrical excitation in form of electrical conduction waves that precede cardiac contraction, whereas the sinus node represents the main pacemaker center of the heart. Conduction cardiomyocytes activate working cardiomyocytes, which, upon depolarization, carry out the cross-bridge cycle leading to contraction of the cell and thus the heart. Every type of cardiomyocytes owns a specific set of ion channels resulting in a cell-defined action potential [18]. Primary pacemaker cells within the sinoatrial node, which belong to the class of conduction cardiomyocytes, is discussed below in more detail. At a hyperpolarized membrane potential, activation of the hyperpolarized cyclic nucleotide-gated ion channels HCN-2 and HCN-4 results in cation inward currents that depolarize the cell (Figure 38.2b). This process triggers the opening of T-type and L-type $Ca^{2+}$ channels (LTCCs, $Ca_v1$), which forms a fast and diastolic (i.e. at heart rest between beats) depolarization of the action potential. Conversely, the repolarization of the AP is dependent on delayed rectifier $K^+$ channels. In contrast to conduction cardiomyocytes, the AP of working cardiomyocytes is initiated by a membrane depolarization that opens $Na_v1.5$ (Figure 38.2c) [19]. The resulting influx of $Na^+$ ions triggers rapid depolarization, which is counteracted by a rapid repolarization carried by $K^+$ efflux through $K_v4.2/K_v4.3$. Opening of $Ca_v1.2$ leads to a long plateau phase, and in order to return to the resting membrane potential of the cardiomyocyte, rapid repolarization is carried by different $K^+$ channels (including $K_v1.5/3.1$ HERG, $K_v$LQT1, $K_{ir}2.1/2.2$). In total, the working cardiomyocyte action potential lasts between 200 and 300 ms, and as such about 100-times longer than a neural AP. Severe consequences are the result of malfunctions in this orchestrated interplay, and as such, cardiac

arrhythmia represent diseases that often constitute with a pathological heartbeat. For instance, atrial fibrillation affects at least 2% of the western population [20]. Thus, antiarrhythmic drugs that specifically target ion channels in the heart have been developed and represent an ongoing pursuit in medicinal chemistry and translational programs.

### 38.1.5 Pancreatic β-Cells

The pancreas represents an abdominal organ with exocrine and endocrine gland functions. Whereas the secretion of enzymes is involved in digestive system processes, the endocrine function lies within the control of the blood sugar level [21]. Here, pancreatic α- and β-cells located within pancreatic islets of Langerhans, a mini organ itself, represent the major contributor to mass and key cells for hormonal response. In a simplistic view, pancreatic α-cells secrete glucagon, increasing blood sugar concentration, while β-cells release insulin, decreasing blood sugar levels. Interestingly, β-cells show electrical activity in a glucose-dependent manner. At lower glucose concentrations (<5 mM) electrical activity is missing, while at higher concentrations (~6 mM) β-cells start firing action potentials, which can lead to oscillatory situations at even higher glucose levels [21]. This is the result of elevated intracellular glucose and the uptake into cells by the low-affinity glucose transporter GLUT2, which is broken down to pyruvate and further processed into AcetylCoA, entering the Krebs' cycle to generate NADH and $FADH_2$. These cofactors are needed in the oxidative phosphorylation steps in mitochondria to ultimately generate ATP under ADP consumption. This increasing ATP/ADP ratio leads to closing of ATP-sensitive $K^+$ ($K_{ATP}$) channels, a hetero-octameric assembly of a tetrameric structure of heterodimers, $(K_{ir}6.2/SUR1)_4$. The resulting reduction of $K^+$ efflux leads to membrane depolarization, which in turn leads to opening of LTCC, $Ca^{2+}$ influx, and thus $Ca^{2+}$-dependent exocytosis of insulin. In addition, tetrodotoxin-sensitive $Na_v$ channels open and the resulting influx of $Na^+$ ions triggers the upstroke of the β-cell action potential [22, 23]. L-type, T-type, and P/Q-type $Ca^{2+}$ channels open and carry the peak phase of the action potential (i.e. above −20 mV at 20 mM glucose), which lasts about 200 ms [22]. Afterwards, A-type $K^+$-currents and opening of delayed rectifying $K^+$ channels initiate repolarization of the membrane. As such, β-cells are the prime example of coupling metabolism to electrical excitability, and their malfunction has profound consequences, most prominently in type II diabetes [24, 25].

## 38.2 Principle of Photopharmacology

### 38.2.1 Historical and Modern Genetic Strategies

The idea to allow ions pass a lipid bilayer triggered by light can be dated back to the early 1970s, when Erlanger in his pioneering work used positively charged azobenzene scaffolds bearing quaternary ammonium moieties to activate acetylcholine receptors with light (Figure 38.3a). In the mid-2000s, ion channels with

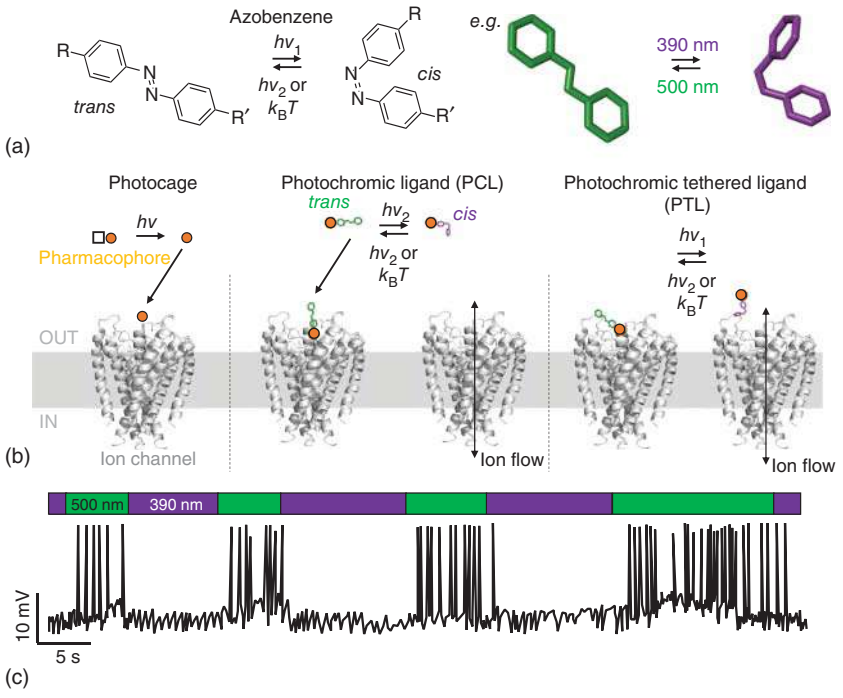


**Figure 38.3 Strategies to endow ion channels with light.** (a) Azobenzenes can be toggled reversibly from their *trans*- and *cis*-isomer by applying two orthogonal wavelengths of light (and sometimes also by thermal relaxation). Example is depicted on the right. (b) Schematic representation of controlling ion channels (pdb: 1j95) [26] with light by caged compounds, photochromic ligands (PCLs), and photochromic tethered ligands (PTLs). (c) Optical control of action potential firing. Source: Based on Zhou et al. [26].

native light-sensitivity have been discovered, and recombinant, artificial channels have been engineered, defining the field of optogenetics. These proteins have been widely applied in neuroscientific research and were recently reviewed elsewhere in great detail [27–29]. As such, we will focus on strategies to endow ion channels with light by synthesized chemicals that target a particular channel or a subset thereof. These strategies can be divided into chemical and hybrid (Figure 38.3b), thereby also separating the targeting approach: using photopharmacophores that can diffuse in solution yield their selectivity through their pharmacological unit (termed photochromic ligand, PCL [30, 31]), while hybrid techniques introduce attachment points to a channel by mutations (termed photochromic tethered ligand, PTL [30, 31]), by fusion of a self-labeling suicide enzyme for covalent attachment [32] (termed (membrane associated) photochromic orthogonal remotely tethered ligand, (ma)PORTL [33–35]) or by delivery via immunochemistry (e.g. nanobody-photoswitch conjugate, NPC [36]) of a photodrug. It should be noted that the two latter have been applied to G-protein-coupled receptors, which, upon activation, downstream to G protein inwardly rectifying $K^+$ (GIRK) channels. As such, they indirectly control ion channels and are listed here to outline future

possibilities. Importantly, by controlling ion channels with light, one can evoke and/or suppress AP firing in cells, thereby remote controlling a cell's excitability (Figure 38.3c).

## 38.2.2 Chemical Strategies

### 38.2.2.1 Caged Compounds

One straightforward way to use light as a translator for drug action is the use of caged compounds. These compounds are pharmacophores that are fused to a photolabile chemical group (usually an *ortho*-nitrobenzyl or a coumarin) that undergoes a chemical degradation reaction when exposed to UV to blue light, thereby liberating the active compound (Figure 38.3b) [37]. MNI-glutamate serves as the best and most used example [38]; however, the reaction is not reversible and therefore switching is only possible once. Caged molecules for the optical control of biological function are reviewed elsewhere in great detail [37, 39].

### 38.2.2.2 Photochromic Ligands (PCLs)

To obtain reversible switching modes, azobenzenes, among other photoswitches, have proven their usefulness (Figure 38.3a): they are found in two different isomeric states, the *cis*- and *trans*-forms, and these forms can be reversibly interconverted by two distinct wavelengths of light (UV and visible, usually blue to green light unsubstituted azobenzene) [31, 40]. In addition, for high spatial control, two-photon excitation has been used, either directly on the azobenzene's cross-section [41] or via a sensitizer [42]. The change in geometrical form does not only vary the shape and end-to-end distance of an azobenzene from ~9 to ~6 angstroms, but also drastically changes the dipole moment (from 0 to 3 Debye). Yet, azobenzenes have more advantageous properties, such as fast switching kinetics (femtoseconds for a molecule [43]) and high photostationary states under illumination (~90%) with $\tau$ values in the seconds to days (tunable to years) range. Repeating cycles can be performed without fatigue, quantum yields and extinction coefficients are sufficiently high (quantum yield $\Phi = 0.3$; $\varepsilon$ ~20 000 $M^{-1}$ $cm^{-1}$) and bistability (i.e. staying in the desired form when irradiation is ceased) is given. With several possible routes to synthesize azobenzenes, which are increasing as of today, many of these mentioned features can be fine-tuned, which makes this molecular class attractive for its use in photopharmacology. Some important parameters are: (i) adding electron-donating substituents (possible also in conjunction with electron-withdrawing group to induce "push–pull-systems") to the aromatic cores results in red-shifting and faster thermal relaxation [30], (ii) installing halogen atoms or tetramethoxy in the *ortho*-positions leads to red-shifts and bistability [44–46], (iii) closing a ring to obtain a diazocine reverses the light dependence and makes the *cis*-form the energetically favorable isomer [47], and (iv) using heterocycles instead of phenyl rings may lead to extreme bistability [48] or red-shift [49].

Once it has been decided on the properties of the azobenzene photoswitch, a pharmacophore has to be found that has desirable properties toward an ion channel, which can be for instance an activator, a blocker, or an allosteric modulator. High

affinity and selective pharmacology are of importance, as installing a photoswitch will certainly reduce the molecule's binding constant, efficacy, and selectivity. Accordingly, it is important to learn about the structure activity relationship, and ideally, crystal structures are available that give insights on the atomic level of how the drug acts on its target. In our hands, the most success to endow a drug with light sensitivity was to modify a benchmark pharmacophore, which is established in the community for research purposes, to an azobenzene. The chemical fusion to the ligand can be accomplished by two major approaches, known as azologization (usually adding a phenyl azo unit to an existing aromatic unit, or replacing "azosteres") or azo-extension (adding a complete azobenzene scaffold to a solvent-exposed part of the parent molecule) [31]. The synthesized PCL is usually applied to ion channels that are heterologously expressed in cells for initial assessment of their activity and channel-switching properties (Figure 38.3b), before their use in cells or organs that express the targeted channel endogenously, and, ultimately, in vivo.

### 38.2.3 Photoswitchable Tethered Ligands (PTLs)

Spatiotemporal resolution is achieved when PCLs are isomerized by pointing light to a certain area; however, as they diffuse and exhibit bistability they act globally in their setting even when illumination is restricted to a small area. To overcome this, measures were taken to tether the photoswitch directly and selectively onto its target with the support of genetic engineering. In early studies dating back to the 1970s, free cysteines were targeted as an attachment point for covalent conjugation with benzyl bromides (Figure 38.3b) [50, 51]. Today, maleimides with their inherent Michael system are used to target free cysteines in a "click chemical" fashion. To achieve photocontrol, the idea is to precisely place the PTL to the protein target's ligand-binding site by a covalent link. As such, the head group can reach the binding site in one isomeric state, while it cannot in the other. This strategy can be imagined as an extension of PCL that are endowed by a reactive group toward a target. Another advantage of using PTLs is the power of genetic precision, that is, under an appropriate promoter, cell subtypes can be genetically targeted. As selectivity is gained, other factors need to be considered working with PTLs: (i) the amino acid that is mutated to a cysteine should not be crucial for channel properties and has to be surface exposed and on the extracellular side (as PTL permeability might be hampered, and, more importantly intracellular reductive environment would quench the maleimide), and (ii) the distance between the cysteine and the orthosteric-binding site needs careful evaluation, sometimes aided by computational approaches. As such, the PTL design with its molecular flexibility and length might have an effect on the pharmacological properties. Although PTLs have been applied in vivo [52, 53], their limited stability in aqueous environments makes them less suitable for studies in animals. This has led to other targeting strategies, such as the use of self-labeling protein tags (SNAP-, CLIP-, and Halo-tags) that (i) can be genetically fused to the protein of interest, or (ii) can be membrane-anchored to deliver the photoswitch, as shown for metabotropic glutamate receptors that signal on GIRK ion channels downstream after activation. This further development resulted in an

extended acronym, PORTL, standing for the photoswitchable orthogonal remotely tethered ligand approach and has shown to overcome thiol-maleimide chemistry, at least for G protein-coupled receptors (GPCRs) [33, 35]. A NPC was employed on the same target, adding another layer of specificity [36]. Indeed, this concept consists of a SNAP-fused nanobody, where the SNAP tag is reacted with a PORTL and the nanobody's antigen is green fluorescent protein (GFP). This construct can be made in vitro and then finds its GFP-fused mGluR2-expressing cell. A similar angle, termed drugs acutely restricted to tethering (DART), was applied by using a membrane-anchored Halo-tag labeled with an AMPA receptor antagonist in vivo, however not photoswitchable, to elucidate the role of D1 and D2 cells in akinesia and movement execution deficits [54]. Merging the desirable properties of small-molecule photoswitches with genetic targeting (e.g. Cre-dependent [35] or by CRISPR/Cas9 technology [55, 56]) and biomolecular techniques (e.g. SNAP-, CLIP-, and Halo-tags [57]; nano- [58] or sybodies [59, 60]) is the path to choose if in vivo (defined as in the intact and living animal) photopharmacology is desired eventually.

## 38.3 Photoswitchable Ion Channels

### 38.3.1 Photopharmacology in Neurons and in the Brain

Neuronal function, connectivity, and signaling remains enigmatic, mostly due to its complexity. As such, photocontrol focused very early on neural cells, with a special focus on pathological states that natively have to do with sensing light. This resulted in promising applications in programs for vision restoration.

#### 38.3.1.1 SPARK and AQs

In 2004, Isacoff, Trauner, and Kramer reported a light-switchable potassium channel, termed synthetic photoisomerizable azobenzene-regulated $K^+$ (SPARK) channel (Figure 38.3b, right) [61]. This was the start of a renaissance in using azobenzenes as photoswitches for the control of biological activity after reports have ceased in the 1980s. It is the first PTL system, with a genetically introduced cysteine for ligand attachment to control the $K_v$ channel shaker. The SPARK system furthermore needed a photoswitch named MAQ (Figure 38.4a) to optically control $K^+$ conductance of the shaker channel. For this reason, tertraethylammonium (TEA), a quaternary ammonium group (Q), which blocks $K_v$ channels at two distinct positions of the channel, is fused to an azobenzene (A) and a maleimide (M). One binding site of TEA is located above the selectivity filter, whereas the other position is found below the selectivity filter within the inner vestibule. The SPARK system was first characterized in *Xenopus laevis* ooyctes. Covalently bound MAQ rests in its elongated *trans*-state that blocks conductance under 500 nm light, whereas in the *cis*-state under 380 nm light the block is reversed by movement of the azobenzene, shortening the M–Q distance, and resulting in removal of the blocker from the pore. Application of SPARK to hippocampal pyramidal neurons allowed to reversibly control neuronal activity by light and represents a key step in the development of photopharmacology. Here, action potential firing of neurons

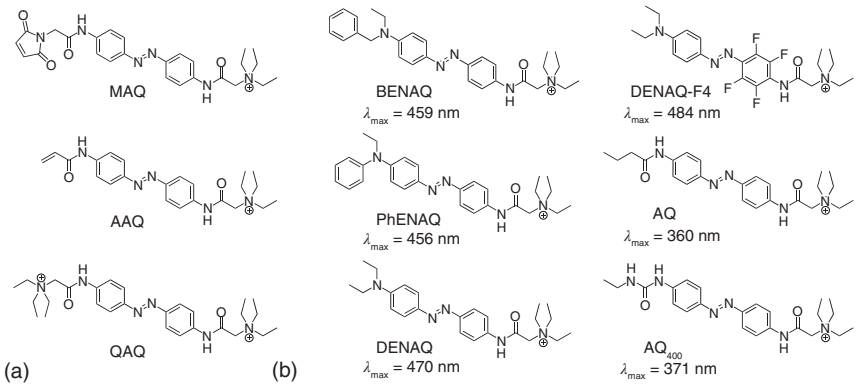


**Figure 38.4 TEA-based photoswitches for remote control of neural activity.** (a) MAQ and AAQ represent photoswitches for $K_v$ channels and QAQ a PCL for $Na_v$ channels. (b) Photoswitches for $K_v$ channels that were tuned for their spectral and photophysical properties. Maximal absorbance wavelengths in aqueous buffers are listed.

was triggered under 500 nm light, whereas 380 nm illumination stopped neuronal activity.

PCLs of $K_v$ channels have been designed in the logic of MAQ, whereas the maleimide was replaced by variable groups, with some derivatives shown in Figure 38.4a. One of the most prominent representatives is AAQ, consisting of an acrylamide, an azobenzene, and a quaternary ammonium group [62]. Externally applied on shaker- and other $K_v$ channel family members, *trans*-AAQ blocks conductance, which is relieved under UV light. In the context of neuronal excitability, *trans*-AAQ initiates AP firing of dissociated hippocampal neurons, whereas *cis*-AAQ prevents neuronal activity. Later on, it was demonstrated that AAQ and other derivatives function as open-channel blocker of $K_v$ channels [63]. A dose response curve of AAQ determined the $IC_{50}$ of *trans*-AAQ to be 2 μM and for *cis*-AAQ to be 64 μM, indicating a change of 30-fold block potency. The translational potential of PCLs became visible as AAQ was applied to restore vision of blind mice [64]. *Retinitis pigmentosa* and macular degeneration represent eye diseases, which induce the loss of rods and cones, where photoreceptors reside in the retina. Application of these PCLs in a mouse model of *Retinitis pigmentosa* indicated that light sensitivity of the retinal cells was increased [64]. Furthermore, pupillary light reflex and light avoidance behavior of blind mice could be restored [64].

Notably, the $K_v$ channel blocker TEA linked to an azobenzene also resembles the structure of lidocaine to a high degree, a typical $Na_v$ channel blocker and clinically applied local anesthetics [15]. Based on this, another derivative of MAQ/AAQ called QAQ was introduced and applied as an optically $Na_v$ channel blocker with additional activity on $K_v$ and $Ca_v$ channels (Figure 38.4a). With its double positive charge, the compound is membrane impermeable and can act only from the internal side when a strategy to load cells expressing the ion channel TRPV1 or P2X receptors is applied [65]. Interestingly, the heat-sensing ion channel TRPV1, which is activated by capsaicin, and the ATP-sensitive receptors $P2X_2$, $P2X_4$, and $P2X_7$ allow for

the uptake of dyes and midsized drugs into the cytosol of cells once their agonists are present [66, 67]. Indeed, this loading strategy was applied to TRPV1 expressing pain-sensing neurons, including c-fibers. Thus, in tissue, the electrical activity of these fibers could be specifically controlled by light, leaving the activity of other neurons untouched. This allowed the successful photocontrolled application of QAQ on explanted murine ganglia and on the eye-blinking reflex of mice in vivo.

The development of AQs reflects an example to explore the chemical space of photopharmaceuticals. Congeners have been described, first to maximally red-shift the switching characteristics by implementing amines as electron-pushing substituents. In a study in 2011, several AQs were synthesized and tested toward $K_v$ channels, bearing different alkylated amines, ranging from benzyl/ethyl (BENAQ) over phenyl/ethyl (PhENAQ) to bis-ethyl (DENAQ) groups (Figure 38.4b), including a fluorinated AQ (DENAQ-F4) [68]. While these approaches yielded red-shifts to wavelengths of 484 nm for photocontrolling conductance of $K_v$ channels, other AQ derivatives have been synthesized that are switchable in the UV to blue region, like compound 5 (also termed AQ) [63]. A subtle modification from an amide linkage to a urea moiety yielded $AQ_{400}$, which significantly improved the behavior under irradiation in terms of channel-switching amplitude and kinetics with a slight red-shift, exemplified in dorsal root ganglion neurons (Figure 38.4b) [69]. Together, there is a large chemical space that can be modified and explored concerning red-shifting, bistability, and allowing the use of different laser lines.

#### 38.3.1.2 Ionotropic Glutamate Receptors

Glutamate is an amino acid with a plethora of functions in the body and is commonly known as the main excitatory neurotransmitter [14]. As such, it is the endogenous ligand for iGluRs, ion channels that are responsible for synaptic transmission. Consisting of tetramers, iGluRs were historically distinguished by their pharmacology and were later matched in their respective families by sequence alignments [70]. To date, δ receptors have not been photocontrolled, while the photoswitchable agonist ATA and the photoswitchable antagonist ShuBQX-3, both PCLs, have been developed for AMPA receptors (Figure 38.5a) [71, 72]. Depending on their light activation and deactivation, action potential firing was induced and suppressed in a reversible manner with these switches, as shown in hippocampal neurons by patch-clamping. ATA was used in further studies in vision restoration programs, where it targets retinal ganglion and amacrine cells in blind mouse retinae. Similarly, the NMDA receptor has been addressed with ATG as a switchable agonist and PNRA as switchable antagonist [73, 74], both PCLs, and the L-MAGs, employing the PTL approach to derive photosensitivity [75] (Figure 38.5b). Experiments to manipulate glutamate-induced currents were conducted in several test systems, such as HEK293T cells, explanted neurons and brain slices, *Xenopus* oocytes, and zebrafish larvae. A different approach for NMDA photocontrol was pursued and successfully shown by Paoletti et al., who incorporated the azobenzene-bearing, unnatural amino acid PSAA into different subunits of NMDARs in HEK293 cells [76]. Not only were the authors able to endow this channel with light sensitivity by genetic code expansion, but they also

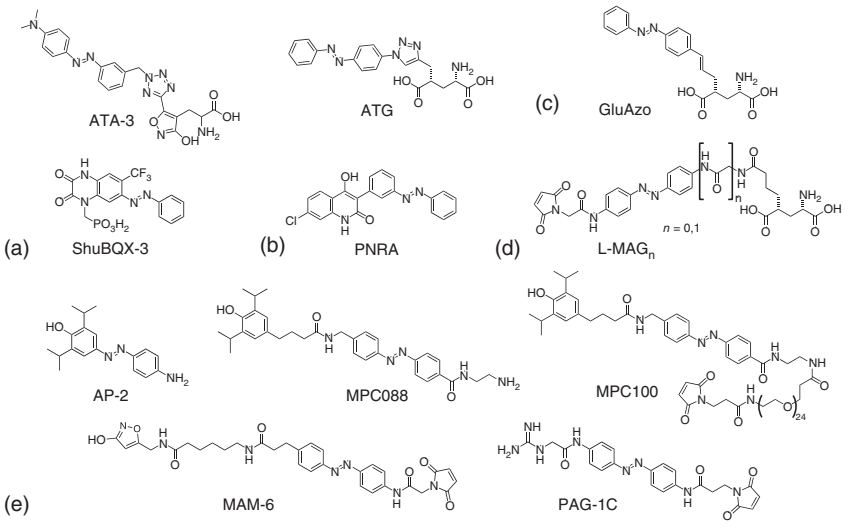


**Figure 38.5 Photoswitchable (tethered) ligands for remote controlling neural function targeting ligand-gated ion channels.** Among many targets, examples are depicted for (a) AMPA-, (b) NMDA-, (c) NMDA- and kainate, (d) kainate-, and (e) $GABA_A$-receptors.

recorded dynamic changes in protein movement upon azobenzene isomerization, demonstrating the power of photopharmacology on a different stage. The largest body of data, however, has been generated on the kainate receptor. The PCL GluAzo (Figure 38.5c), which was evaluated in 2007 as a photoswitchable agonist in HEK293T cells, rat hippocampal neurons, and lastly in Purkinje cells, a class of GABAergic neurons [77]. L-MAG (Figure 38.5d) was also employed for this receptor class and developed over the years and mirrors the efforts of fine tuning photoswitches for a particular demand. First published as "LiGluR," [78] which allows allosteric control with an optical switch in 2006, various congeners have been reported. In particular, they differ in linker length [79], bear different substitution patterns on the azobenzene scaffold for a red-shift in photoresponse (i.e. tetra-*ortho*-chloro [80], electron rich *para*-amine [81]), carry a handle for improved 2-photon absorption [82], and deliver reactive esters to target endogenous receptors covalently [83]. MAGs were allowed to be used in numerous applications, such as blocking zebrafish touch response by light [84] or vision restoration in mice with inherited blindness [85], and helped to resolve fundamental questions in cell biology in relating the Kolmer–Agduhr neuron to spontaneous locomotion in zebrafish [52]. Furthermore, it has been expanded to the chimeric system HyLighter, a $K^+$-selective glutamate receptor [86].

#### 38.3.1.3 Ionotropic GABA Receptors

Similar to the excitatory neurotransmitter, the glutamate receptors, the inhibitory counterparts have been in the focus of being photocontrolled. First success on the ionotropic $GABA_A$ receptor was reported in 2012 with a PCL approach by Trauner using AP-2 [87], and independently by Pepperberg with a PCL and PTL approach,

using MPC088 and MPC100 [88] (Figure 38.5e). All of these compounds were azobenzenes comprising a propofol analogue, which is a positive allosteric modulator of $GABA_A$. As such, and upon activation of the channel, the membrane potential is even more hyperpolarized, and accordingly making it less probable to reach the threshold potential upon stimulation (depolarization). In later studies from the Kramer laboratory, two more PTLs were designed to photocontrol $GABA_A$ receptors (MAM-6 and PAG-1C), and together, these studies showed robust photocontrol in different experimental setups, from transfected cells in culture, to neurons, and even in vivo (Figure 38.5e) [89, 90].

#### 38.3.1.4 Other Channels: Nicotinic Acetylcholine Receptors, TREK1 and GIRKs

Regarding the great variety of ion channels in different neurons, together with the straightforward design in photopharmacology, other families have been successfully targeted to be switched with light. Prominent examples are mentioned here, e.g. nicotinic acetylcholine receptors [87–90] (which are pentameric ligand-gated ion channels comparable to $GABA_A$), TRP [91, 92] ion channels, and GIRK [93, 94] ion channels, and have been reviewed in more detail elsewhere [40]. It should be noted that some channels are not exclusively expressed in the brain, but can also be found in other tissue, where they were not investigated photopharmacologically.

### 38.3.2 Photopharmacology on Cardiomyocytes and in the Heart

The human heart is a contractive organ that has to work in a constant manner over the lifespan. Malfunctions in the heart beat can bear severe risks for patients. Several approaches, including pharmacotherapy, cardiac pacemaker, and cardiac ablation, have become standard procedures to target arrhythmia. However, there is still a need for improvement and to expand the present approaches. Using light with its spatiotemporal precision in conjunction with photodrugs seems to be an attractive effort to minimize invasive procedures and extend the possibilities of cardiac pharmacology.

#### 38.3.2.1 LTCC Control with FHU-779

First attempts to control heart function by light have been carried out with optogenetic techniques in zebrafish and mice [95]. The first application of PCLs on cardiac tissue of mice was carried out by LTCCs photoswitch called FHU-779 [96]. Indeed, voltage-gated LTCCs play important roles in cardiac, neuronal, and pancreatic tissue [97]. In the heart, they are expressed in primary pacemaker cells within the sinoatrial node and determine the diastolic depolarization of the action potential. As such, pharmacological block of these channels lowers the heart rate. In addition, LTCCs form the plateau phase of action potentials in working cardiomyocytes, and the resulting $Ca^{2+}$ influx determines cardiac contraction. From a pharmacological point of view, dihydropyridines, verapamil, and diltiazem represent common LTCC blockers, which are in clinical use to treat for instance hypertension and cardiac arrhythmia [97]. FHU-779 is based on diltiazem equipped with an azobenzene moiety (Figure 38.6a, b). The *trans*-state of FHU-779 can be converted into its *cis*-state

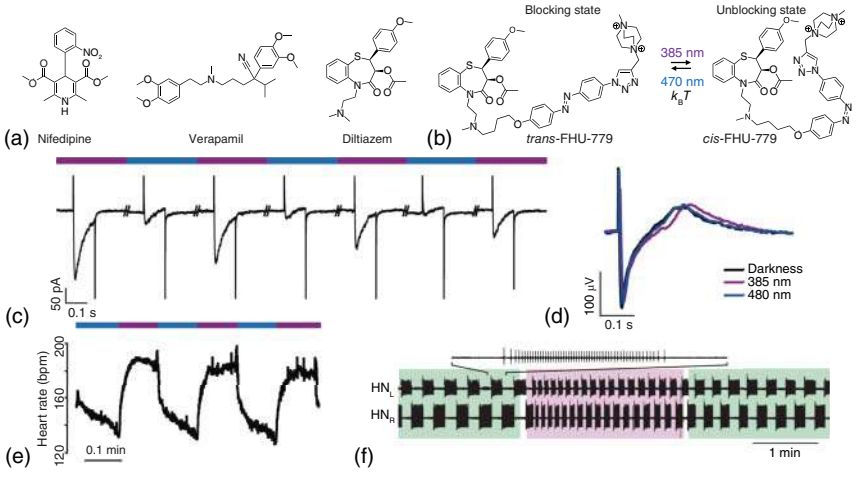


**Figure 38.6 Optical control of the heart.** (a) Classical blocker of LTCCs, including nifedipin, verapamil, and diltiazem. (b) FHU-779, a diltiazem-based PCL for LTCCs. (c) Representative trace of $Ca_v1.2$ inward currents in the presence of FHU-779, recorded under changing illumination conditions. (d) FHU-779-based field potential modulation of human stem cell–derived cardiomyocytes. (e) FHU-779-based optical modulation of the heart beat of mouse in the Langendorff configuration. Source: Fehrentz et al. [96]. (f) Light control of heart central pattern generator interneurons (HN) by AAQ. Source: Fortin et al. [62].

upon 385 nm illumination, whereas 480 nm light reverses the process. Patch-clamp characterization on $Ca_v1.2$ and $Ca_v1.3$ further revealed selective photoswitching (Figure 38.6c) with an $IC_{50}$ of *trans*-FHU779 in the range of diltiazem itself (2.7 µM) [96]. Application of FHU-779 on human stem cell–derived cardiomyocytes in a multielectrode array setup revealed that stimulated field potentials (FPs) showed longer plateau phase under 380 nm in comparison to 480 nm light (Figure 38.6d). This FP plateau phase resembles the LTCC-dependent plateau phase of action potential within working cardiomyocytes and is in line with the view that blocking of LTCCs shortens the action potential. In a further step, FHU-779 was applied on explanted mouse hearts in the Langendorff configuration, where the beating heart was perfused retrograde into the coronary arteries and the electrocardiogram was recorded (Figure 38.6e) [96]. The right atrium, including the sinoatrial node, was illuminated and resulted under 480 nm in heart beat decrease, which was reversed under 380 nm light (Figure 38.6f).

#### 38.3.2.2 AAQ Application

Another PCL application on cardiac tissue was performed in the leech *Hirudo medicinalis* [62]. Here AAQ, a PCL for $K_v$ channels, was applied on heart central pattern generator interneurons (HN). These cells control the contraction of the heart by activity patterns that control heart motor neurons. As mentioned above, $K_v$ channel blocks by *trans*-AAQ triggered neuronal activity, whereas *cis*-AAQ suppressed firing. This finding was also found in the context of HN neurons. Here, UV light–reduced bursting patterns, which were increased under 480 nm light illumination.

### 38.3.3 Photopharmacology on Pancreatic β-Cells

β-Cells in the pancreas are linking metabolism to electrical excitability. During and after a meal, elevated glucose in the blood is taken up by β-cells and metabolized to increase the ATP/ADP, which then blocks the $K_{ATP}$ channel, which can be considered the leak channel to suppress AP firing in the unstimulated state. Blockage causes depolarization, which acts downstream on voltage-dependent LTCCs to increase intracellular $Ca^{2+}$ concentration, driving insulin release. Given the pulsatile nature of insulin exocytosis, putting $K_{ATP}$ and LTCC under spatiotemporal optical control to mimic physiological release is an attractive goal to treat type II diabetes, and minimizing the risk of hypoglycemia, which is a concern with classical pharmacological treatment.

#### 38.3.3.1 $K_{ATP}$ Control with JB253 and JB558

The $K_{ATP}$ channel, also known as Kir6.2/SUR1, was first described in the 1980s in several tissues, such as the heart and the pancreas [98], and the link between glucose uptake and insulin release was established in due course [99]. Within that time, pharmacology was established by using sulfonylureas (SUs), such as glimepiride, as channel blockers and diazoxide as channel openers [100] (Figure 38.7a). In 2014, the $K_{ATP}$ channel was successfully optically controlled by using a SU-based PCL, dubbed JB253 [101] (Figure 38.7b). Responding to blue light, its *cis*-form was able to

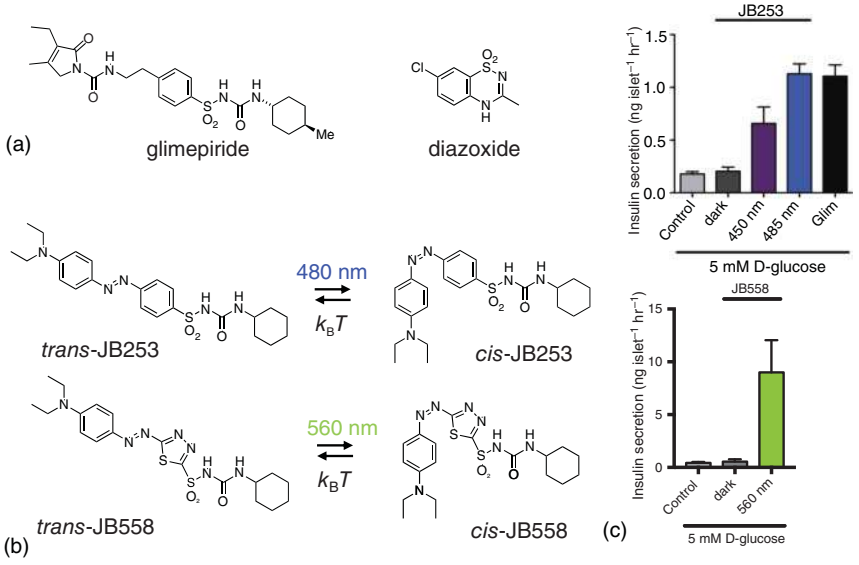


**Figure 38.7 Optical control of β-cell function and insulin release.** (a) $K_{ATP}$ channel blocker glimepiride and channel opener diazoxide. (b) JB253 and JB558, sulfonylurea-based PCLs for $K_{ATP}$ channel photocontrol. (c) Insulin release from β-cells can be triggered with purple to blue or with yellow to green light when using JB253 or JB558, respectively. Source: Modified from Broichhagen et al. [49]. Licensed under CC BY-3.0.

close the $K_{ATP}$ channel and triggered insulin release in cellular systems, as well as in the islet of Langerhans (Figure 38.7c). Starting from this promising study, and being used as a chemical biology tool to dissect islets signaling to identify so-called β-cell hubs that act as pacemakers for hormone release [102], JB253 was further evaluated pharmacologically [103]. Optimization of the two-step synthetic route yielded JB253 in multigram quantities without the need for chromatographic purification in high purity, and it was demonstrated that bacterial azoreductase from *Escherichia coli* was not able to reduce the diazene bond, which would destroy the PCL. This would be a serious drawback, if it happened in the stomach of potential patients. Ultimately, toxicology was established in rats and did not show significant changes in body weight or by food uptake at maximum tolerated doses by oral gavage. Most importantly, glucose homeostasis was optically controlled in vivo in mice by exposing the pancreas to 470 nm of blue light, lowering blood glucose levels, and increasing insulin release, making JB253 a robust and valuable photopharmacophore for β-cell and islet research. A congener, JB558, which bears a heterocyclic diazathiophene in the azobenzene scaffold, was developed in 2015, which could recapitulate the findings of JB253 in vitro, but in response to green–yellow (520–560 nm) light, considerably red-shifting the action spectrum (Figure 38.7) [49].

#### 38.3.3.2 LTCC Control with FHU-779

In line with the application of JB253 and JB558 to optical manipulate β-cell function, targeting of LTCC was performed with FHU-779. In one set of experiments, modulation of cellular $Ca^{2+}$ influx by FHU-779 was monitored by $Ca^{2+}$ imaging using Fluo-8 [96]. Here, *trans*-FHU-779 blocked LTCCs and prevented cellular $Ca^{2+}$ influx; however, under *cis*-FHU-779 channel block was released and resulted in an increased cytosolic $Ca^{2+}$ concentration. Furthermore, *cis*-FHU-779 allowed for $Ca^{2+}$-dependent insulin secretion, whereas *trans*-FHU-779 reduced β-cell insulin release. In another setting, FHU-779 was applied to demonstrate that high spatiotemporal control of compartmental $Ca^{2+}$ influx in β-cells within pancreatic islets can be performed. Together, PCLs for $K_{ATP}$ channels and LTCCs extended the tool box for β-cell research with a translational aspect.

## 38.4 Outlook

The field of photopharmacology had seen the light of day in the late 1960s and early 1970s by pioneering studies from the Erlanger and Lester laboratories. It took another 30 years before this field experienced its renaissance, with the help of modern achievements and techniques in chemistry and molecular biology, such as progress in synthesis and cloning. While picking up speed in the mid-2000s, the translational potential quickly shifted into focus, especially to treat diseases that were affected by ion channels. With a main obstacle to overcome, i.e. the delivery of light into deep tissue, PCLs have to prove that they can meet the clinical parameters needed as approved drugs, in terms of pharmacodynamics and -kinetics, absorption, distribution, metabolism and excretion (ADME), and low toxicity. The use of PTLs

that target genetically introduced cysteines has an even higher bar to achieve for bioavailability. It is worth discussing, however, what the next steps should be, to give photopharmacology the leap for its next destiny: the human body.

### 38.4.1 Targeting of Photopharmaceuticals

Targeting of drugs and photodrugs has to be precise to its target to minimize off-target effects, and this can be best achieved by delivery of a payload that is fused to a tight and selective binder. Antibody–drug conjugates (ADCs) have been developed to deliver toxic substances to tumors [104] and offer an attractive method to also deliver photoswitches to endogenous proteins with subtype selectivity. Given the large size of antibodies and thus, the higher effort to obtain and derivatize these, other smaller targeting proteins have been described, including nanobodies, affibodies, sybodies, and aptamers. While these can be expressed from bacterial cultures in large quantities and yields, their modification with a photoswitch can be straightforward by means of self-labeling protein tag fusion [36] (SNAP- or Halo-tag), incorporation of unnatural amino acids for biorthogonal click chemistry, or side-chain labeling (e.g. cysteines, lysines) with modern techniques. Nanobodies have been raised to be subtype selective for metabotropic glutamate receptor 2 [105] and using the protein scaffold of nanobodies, libraries of sybodies have been created to target cell surface proteins in an unprecedented fast manner [59, 60]. Although many advantages can be listed, one has to bear in mind that foreign peptides and proteins might provoke immune responses, which has to be carefully evaluated.

### 38.4.2 Light Delivery

One of the most discussed questions in photopharmacology is the delivery of light. While topical or subcutaneous application demands are easily met, deeper tissue light delivery, including through the cranium to access the brain, remains problematic. 2-Photon activation of photopharmaceuticals has been described [41, 82], but the use of a 2-photon laser for therapy remains illusional given its complicated setup. While tumors are ablated with photodynamic therapy, using light to kill cancer cells, it is difficult to achieve similar delivery if one wants to replicate for instance pulsatile insulin release on a daily basis. In mice, light delivery by surgery and use of LED light to exposed organs or fiber optic implants into the brain have been described [103], both with confront borders for human use. Novel instruments for light delivery have been portrayed [106], and other light-delivering systems can be envisioned, such as the use of luciferases. These enzymes convert chemical energy to light and delivery could be achieved by genetic fusion to a targeting anti- or nanobody, and thus systemic application of the luciferase substrate would only engage on site. The toxicity and long-term use of such chemicals need of course to be taken into consideration.

Future developments in these directions are needed to allow photopharmacology to emerge from a research tool on excitable tissue to direct and beneficial applications in human health.

## References


1 Long, S.B., Tao, X., Campbell, E.B., and MacKinnon, R. (2007). Atomic structure of a voltage-dependent K+ channel in a lipid membrane-like environment. *Nature* 450 (7168): 376–382. https://doi.org/10.1038/nature06265.

2 Tombola, F., Pathak, M.M., and Isacoff, E.Y. (2006). How does voltage open an ion channel? *Annu. Rev. Cell Dev. Biol.* 22: 23–52. https://doi.org/10.1146/annurev.cellbio.21.020404.145837.

3 Gutman, G.A., Chandy, K.G., Grissmer, S. et al. (2005). International Union of Pharmacology. LIII. Nomenclature and molecular relationships of voltage-gated potassium channels. *Pharmacol. Rev.* 57 (4): 473–508. https://doi.org/10.1124/pr.57.4.10.

4 Goldman, D.E. (1943). Potential, impedance, and rectification in membranes. *J. Gen. Physiol.* 27 (1): 37–60. https://doi.org/10.1085/jgp.27.1.37.

5 Hodgkin, A.L. and Katz, B. (1949). The effect of sodium ions on the electrical activity of giant axon of the squid. *J. Physiol. (Lond.)* 108 (1): 37–77. https://doi.org/10.1113/jphysiol.1949.sp004310.

6 Bean, B.P. (2007). The action potential in mammalian central neurons. *Nat. Rev. Neurosci.* 8 (6): 451–465. https://doi.org/10.1038/nrn2148.

7 The Human Protein Atlas. http://v19.3.proteinatlas.org. (accessed 18 August 2020).

8 Liem, L.K., Simard, J.M., Song, Y., and Tewari, K. (1995). The patch clamp technique. *Neurosurgery* 36 (2): 382–392. https://doi.org/10.1227/00006123-199502000-00020.

9 Grienberger, C. and Konnerth, A. (2012). Imaging calcium in neurons. *Neuron* 73 (5): 862–885. https://doi.org/10.1016/j.neuron.2012.02.011.

10 Fan, L.Z., Kheifets, S., Böhm, U.L. et al. (2020). All-optical electrophysiology reveals the role of lateral inhibition in sensory processing in cortical layer 1. *Cell* 180 (3): 521–535.e18. doi:https://doi.org/10.1016/j.cell.2020.01.001.

11 Efimov, I.R., Nikolski, V.P., and Salama, G. (2004). Optical imaging of the heart. *Circ. Res.* 95 (1): 21–33. https://doi.org/10.1161/01.RES.0000130529.18016.35.

12 Berenfeld, O. and Efimov, I. (2019). Optical mapping. *Card. Electrophysiol. Clin.* 11 (3): 495–510. https://doi.org/10.1016/j.ccep.2019.04.004.

13 Jessell, T.M. and Kandel, E.R. (1993). Synaptic transmission: a bidirectional and self-modifiable form of cell-cell communication. *Cell* (72 Suppl): 1–30. https://doi.org/10.1016/s0092-8674(05)80025-x.

14 Traynelis, S.F., Wollmuth, L.P., McBain, C.J. et al. (2010). Glutamate receptor ion channels: structure, regulation, and function. *Pharmacol. Rev.* 62 (3): 405–496. https://doi.org/10.1124/pr.109.002451.

15 Hille, B. *Ionic Channels of Excitable Membranes*; 1984: Macmillan Education Australia.

16 Ramsey, I.S., Delling, M., and Clapham, D.E. (2006). An introduction to TRP channels. *Annu. Rev. Physiol.* 68: 619–647. https://doi.org/10.1146/annurev.physiol.68.040204.100431.


**17** Wilson, S.R., Gerhold, K.A., Bifolck-Fisher, A. et al. (2011). TRPA1 is required for histamine-independent, Mas-related G protein-coupled receptor-mediated itch. *Nat. Neurosci.* 14 (5): 595–602. https://doi.org/10.1038/nn.2789.

**18** Schram, G., Pourrier, M., Melnyk, P., and Nattel, S. (2002). Differential distribution of cardiac ion channel expression as a basis for regional specialization in electrical function. *Circ. Res.* 90 (9): 939–950. https://doi.org/10.1161/01.res.0000018627.89528.6f.

**19** Grant, A.O. (2009). Cardiac ion channels. *Circ. Arrhythm. Electrophysiol.* 2 (2): 185–194. https://doi.org/10.1161/CIRCEP.108.789081.

**20** January, C.T., Wann, L.S., Alpert, J.S. et al. (2014). 2014 AHA/ACC/HRS guideline for the management of patients with atrial fibrillation: a report of the American College of Cardiology/American Heart Association Task Force on Practice Guidelines and the Heart Rhythm Society. *J. Am. Coll. Cardiol.* 64 (21): e1–e76. https://doi.org/10.1016/j.jacc.2014.03.022.

**21** Rorsman, P., Braun, M., and Zhang, Q. (2012). Regulation of calcium in pancreatic α- and β-cells in health and disease. *Cell Calcium* 51 (3–4): 300–308. https://doi.org/10.1016/j.ceca.2011.11.006.

**22** Rorsman, P. and Ashcroft, F.M. (2018). Pancreatic β-cell electrical activity and insulin secretion: of mice and men. *Physiol. Rev.* 98 (1): 117–214. https://doi.org/10.1152/physrev.00008.2017.

**23** Herrington, J., Zhou, Y.-P., Bugianesi, R.M. et al. (2006). Blockers of the delayed-rectifier potassium current in pancreatic beta-cells enhance glucose-dependent insulin secretion. *Diabetes* 55 (4): 1034–1042. https://doi.org/10.2337/diabetes.55.04.06.db05-0788.

**24** Eizirik, D.L., Pasquali, L., and Cnop, M. (2020). Pancreatic β-cells in type 1 and type 2 diabetes mellitus: different pathways to failure. *Nat. Rev. Endocrinol.* 16 (7): 349–362. https://doi.org/10.1038/s41574-020-0355-7.

**25** Frank, J.A., Broichhagen, J., Yushchenko, D.A. et al. (2018). Optical tools for understanding the complexity of beta-cell signalling and insulin release. *Nat. Rev. Endocrinol.* 14 (12): 721–737. https://doi.org/10.1038/s41574-018-0105-2.

**26** Zhou, M., Morais-Cabral, J.H., Mann, S., and MacKinnon, R. (2001). Potassium channel receptor site for the inactivation gate and quaternary amine inhibitors. *Nature* 411 (6838): 657–661. https://doi.org/10.1038/35079500.

**27** Wiegert, J.S., Mahn, M., Prigge, M. et al. (2017). Silencing neurons: tools, applications, and experimental constraints. *Neuron* 95 (3): 504–529. https://doi.org/10.1016/j.neuron.2017.06.050.

**28** Deisseroth, K. (2015). Optogenetics: 10 years of microbial opsins in neuroscience. *Nat. Neurosci.* 18 (9): 1213–1225. https://doi.org/10.1038/nn.4091.

**29** Govorunova, E.G., Sineshchekov, O.A., Li, H., and Spudich, J.L. (2017). Microbial rhodopsins: diversity, mechanisms, and optogenetic applications. *Annu. Rev. Biochem.* 86 (1): 845–872. https://doi.org/10.1146/annurev-biochem-101910-144233.

**30** Fehrentz, T., Schönberger, M., and Trauner, D. (2011). Optochemical genetics. *Angew. Chem. Int. Ed.* 50 (51): 12156–12182. https://doi.org/10.1002/anie.201103236.


**31** Broichhagen, J., Frank, J.A., and Trauner, D. (2015). A roadmap to success in photopharmacology. *Acc. Chem. Res.* 48 (7): 1947–1960. https://doi.org/10.1021/acs.accounts.5b00129.

**32** Leippe, P., Koehler Leman, J., and Trauner, D. (2017). Specificity and speed: tethered photopharmacology. *Biochemistry* 56 (39): 5214–5220. https://doi.org/10.1021/acs.biochem.7b00687.

**33** Broichhagen, J., Damijonaitis, A., Levitz, J. et al. (2015). Orthogonal optical control of a G protein-coupled receptor with a SNAP-tethered photochromic ligand. *ACS Cent. Sci.* 1 (7): 383–393. https://doi.org/10.1021/acscentsci.5b00260.

**34** Donthamsetti, P.C., Broichhagen, J., Vyklicky, V. et al. (2019). Genetically targeted optical control of an endogenous G protein-coupled receptor. *J. Am. Chem. Soc.* 141 (29): 11522–11530. https://doi.org/10.1021/jacs.9b02895.

**35** Acosta-Ruiz, A., Gutzeit, V.A., Skelly, M.J. et al. (2020). Branched photoswitchable tethered ligands enable ultra-efficient optical control and detection of G protein-coupled receptors in vivo. *Neuron* 105 (3): 446–463. https://doi.org/10.1016/j.neuron.2019.10.036.

**36** Farrants, H., Gutzeit, V.A., Acosta-Ruiz, A. et al. (2018). SNAP-tagged nanobodies enable reversible optical control of a G protein-coupled receptor *via* a remotely tethered photoswitchable ligand. *ACS Chem. Biol.* 13 (9): 2682–2688. https://doi.org/10.1021/acschembio.8b00628.

**37** Klán, P., Šolomek, T., Bochet, C.G. et al. (2013). Photoremovable protecting groups in chemistry and biology: reaction mechanisms and efficacy. *Chem. Rev.* 113 (1): 119–191. https://doi.org/10.1021/cr300177k.

**38** Paoletti, P., Ellis-Davies, G.C.R., and Mourot, A. (2019). Optical control of neuronal ion channels and receptors. *Nat. Rev. Neurosci.* 20 (9): 514–532. https://doi.org/10.1038/s41583-019-0197-2.

**39** Ankenbruck, N., Courtney, T., Naro, Y., and Deiters, A. (2018). Optochemical control of biological processes in cells and animals. *Angew. Chem. Int. Ed.* 57 (11): 2768–2798. https://doi.org/10.1002/anie.201700171.

**40** Hüll, K., Morstein, J., and Trauner, D. (2018). *In vivo* photopharmacology. *Chem. Rev.* 118 (21): 10710–10747. https://doi.org/10.1021/acs.chemrev.8b00037.

**41** Carroll, E.C., Berlin, S., Levitz, J. et al. (2015). Two-photon brightness of azobenzene photoswitches designed for glutamate receptor optogenetics. *Proc. Natl. Acad. Sci. U.S.A.* 112 (7): E776–E785. https://doi.org/10.1073/pnas.1416942112.

**42** Cabré, G., Garrido-Charles, A., Moreno, M. et al. (2019). Rationally designed azobenzene photoswitches for efficient two-photon neuronal excitation. *Nat. Commun.* 10 (1): 907. https://doi.org/10.1038/s41467-019-08796-9.

**43** Nägele, T., Hoche, R., Zinth, W., and Wachtveitl, J. (1997). Femtosecond photoisomerization of *cis*-azobenzene. *Chem. Phys. Lett.* 272 (5): 489–495. https://doi.org/10.1016/S0009-2614(97)00531-9.

**44** Bléger, D., Schwarz, J., Brouwer, A.M., and Hecht, S. (2012). O-fluoroazobenzenes as readily synthesized photoswitches offering nearly quantitative two-way isomerization with visible light. *J. Am. Chem. Soc.* 134 (51): 20597–20600. https://doi.org/10.1021/ja310323y.

**45** Konrad, D.B., Frank, J.A., and Trauner, D. (2016). Synthesis of redshifted azobenzene photoswitches by late-stage functionalization. *Chem. Eur. J.* 22 (13): 4364–4368. https://doi.org/10.1002/chem.201505061.

**46** Konrad, D.B., Savasci, G., Allmendinger, L. et al. (2020). Computational design and synthesis of a deeply red-shifted and bistable azobenzene. *J. Am. Chem. Soc.* 142 (14): 6538–6547. https://doi.org/10.1021/jacs.9b10430.

**47** Thapaliya, E.R., Zhao, J., and Ellis-Davies, G.C.R. (2019). Locked-azobenzene: testing the scope of a unique photoswitchable scaffold for cell physiology. *ACS Chem. Neurosci.* 10 (5): 2481–2488. https://doi.org/10.1021/acschemneuro.8b00734.

**48** Weston, C.E., Richardson, R.D., Haycock, P.R. et al. (2014). Arylazopyrazoles: azoheteroarene photoswitches offering quantitative isomerization and long thermal half-lives. *J. Am. Chem. Soc.* 136 (34): 11878–11881. https://doi.org/10.1021/ja505444d.

**49** Broichhagen, J., Frank, J.A., Johnston, N.R. et al. (2015). A red-shifted photochromic sulfonylurea for the remote control of pancreatic beta cell function. *Chem. Commun. (Camb.)* 51 (27): 6018–6021. https://doi.org/10.1039/c5cc01224d.

**50** Bartels, E., Wassermann, N.H., and Erlanger, B.F. (1971). Photochromic activators of the acetylcholine receptor. *Proc. Natl. Acad. Sci. U.S.A.* 68 (8): 1820–1823. https://doi.org/10.1073/pnas.68.8.1820.

**51** Lester, H.A., Krouse, M.E., Nass, M.M. et al. (1980). A covalently bound photoisomerizable agonist: comparison with reversibly bound agonists at electrophorus electroplaques. *J. Gen. Physiol.* 75 (2): 207–232. https://doi.org/10.1085/jgp.75.2.207.

**52** Wyart, C., Bene, F.D., Warp, E. et al. (2009). Optogenetic dissection of a behavioural module in the vertebrate spinal cord. *Nature* 461 (7262): 407–410. https://doi.org/10.1038/nature08323.

**53** Broichhagen, J. and Trauner, D. (2014). The in vivo chemistry of photochromic tethered ligands. *Curr. Opin. Chem. Biol.* 21: 121–127.

**54** Shields, B.C., Kahuno, E., Kim, C. et al. (2017). Deconstructing behavioral neuropharmacology with cellular specificity. *Science* 356 (6333) https://doi.org/10.1126/science.aaj2161.

**55** Nishiyama, J., Mikuni, T., and Yasuda, R. (2017). Virus-mediated genome editing via homology-directed repair in mitotic and postmitotic cells in mammalian brain. *Neuron* 96 (4): 755–768.e5. https://doi.org/10.1016/j.neuron.2017.10.004.

**56** Gao, Y., Hisey, E., Bradshaw, T.W.A. et al. (2019). Plug-and-play protein modification using homology-independent universal genome engineering. *Neuron* 103 (4): 583–597.e8. https://doi.org/10.1016/j.neuron.2019.05.047.

**57** Xue, L., Karpenko, I.A., Hiblot, J., and Johnsson, K. (2015). Imaging and manipulating proteins in live cells through covalent labeling. *Nat. Chem. Biol.* 11 (12): 917–923. https://doi.org/10.1038/nchembio.1959.

**58** Dong, J.-X., Lee, Y., Kirmiz, M. et al. (2019). A toolbox of nanobodies developed and validated for use as intrabodies and nanoscale immunolabels in mammalian brain neurons. *eLife* 8: e48750. https://doi.org/10.7554/eLife.48750.


**59** Zimmermann, I., Egloff, P., Hutter, C.A. et al. (2018). Synthetic single domain antibodies for the conformational trapping of membrane proteins. *eLife* 7: e34317. https://doi.org/10.7554/eLife.34317.

**60** Zimmermann, I., Egloff, P., Hutter, C.A.J. et al. (2020). Generation of synthetic nanobodies against delicate proteins. *Nat. Protoc.* 15 (5): 1707–1741. https://doi.org/10.1038/s41596-020-0304-x.

**61** Banghart, M., Borges, K., Isacoff, E. et al. (2004). Light-activated ion channels for remote control of neuronal firing. *Nat. Neurosci.* 7 (12): 1381–1386. https://doi.org/10.1038/nn1356.

**62** Fortin, D.L., Banghart, M.R., Dunn, T.W. et al. (2008). Photochemical control of endogenous ion channels and cellular excitability. *Nat. Methods* 5 (4): 331–338. https://doi.org/10.1038/nmeth.1187.

**63** Banghart, M.R., Mourot, A., Fortin, D.L. et al. (2009). Photochromic blockers of voltage-gated potassium channels. *Angew. Chem. Int. Ed.* 48 (48): 9097–9101. https://doi.org/10.1002/anie.200904504.

**64** Polosukhina, A., Litt, J., Tochitsky, I. et al. (2012). Photochemical restoration of visual responses in blind mice. *Neuron* 75 (2): 271–282. https://doi.org/10.1016/j.neuron.2012.05.022.

**65** Mourot, A., Fehrentz, T., Le Feuvre, Y. et al. (2012). Rapid optical control of nociception with an ion-channel photoswitch. *Nat. Methods* 9 (4): 396–402. https://doi.org/10.1038/nmeth.1897.

**66** Chung, M.-K., Güler, A.D., and Caterina, M.J. (2008). TRPV1 shows dynamic ionic selectivity during agonist stimulation. *Nat. Neurosci.* 11 (5): 555–564. https://doi.org/10.1038/nn.2102.

**67** Pelegrín, P. (2011). Many ways to dilate the P2X7 receptor pore. *Br. J. Pharmacol.* 163 (5): 908–911. https://doi.org/10.1111/j.1476-5381.2011.01325.x.

**68** Mourot, A., Kienzler, M.A., Banghart, M.R. et al. (2011). Tuning photochromic ion channel blockers. *ACS Chem. Neurosci.* 2 (9): 536–543. https://doi.org/10.1021/cn200037p.

**69** Gutzeit, V.A., Acosta-Ruiz, A., Munguba, H. et al. (2021). A fine-tuned azobenzene for enhanced photopharmacology in vivo. *Cell Chem. Biol.* 28 (11): 1648–1663.e16. https://doi.org/10.1016/j.chembiol.2021.02.020.

**70** Reiner, A. and Levitz, J. (2018). Glutamatergic signaling in the central nervous system: ionotropic and metabotropic receptors in concert. *Neuron* 98 (6): 1080–1098. https://doi.org/10.1016/j.neuron.2018.05.018.

**71** Stawski, P., Sumser, M., and Trauner, D. (2012). A photochromic agonist of AMPA receptors. *Angew. Chem. Int. Ed.* 51 (23): 5748–5751. https://doi.org/10.1002/anie.201109265.

**72** Barber, D.M., Liu, S.-A., Gottschling, K. et al. (2016). Optical control of AMPA receptors using a photoswitchable quinoxaline-2,3-dione antagonist. *Chem. Sci.* 8 (1): 611–615. https://doi.org/10.1039/C6SC01621A.

**73** Laprell, L., Repak, E., Franckevicius, V. et al. (2015). Optical control of NMDA receptors with a diffusible photoswitch. *Nat. Commun.* 6 (1): 8076. https://doi.org/10.1038/ncomms9076.


**74** Hartrampf, F.W.W., Barber, D.M., Gottschling, K. et al. (2017). Development of a photoswitchable antagonist of NMDA receptors. *Tetrahedron* 73 (33): 4905–4912. https://doi.org/10.1016/j.tet.2017.06.056.

**75** Berlin, S., Szobota, S., Reiner, A. et al. (2016). A family of photoswitchable NMDA receptors. *eLife* 5: e12040. https://doi.org/10.7554/eLife.12040.

**76** Klippenstein, V., Hoppmann, C., Ye, S. et al. (2017). Optocontrol of glutamate receptor activity by single side-chain photoisomerization. *eLife* 6: e25808. https://doi.org/10.7554/eLife.25808.

**77** Volgraf, M., Gorostiza, P., Szobota, S. et al. (2007). Reversibly caged glutamate: a photochromic agonist of ionotropic glutamate receptors. *J. Am. Chem. Soc.* 129 (2): 260–261. https://doi.org/10.1021/ja067269o.

**78** Volgraf, M., Gorostiza, P., Numano, R. et al. (2006). Allosteric control of an ionotropic glutamate receptor with an optical switch. *Nat. Chem. Biol.* 2 (1): 47–52. https://doi.org/10.1038/nchembio756.

**79** Gorostiza, P., Volgraf, M., Numano, R. et al. (2007). Mechanisms of photoswitch conjugation and light activation of an ionotropic glutamate receptor. *Proc. Natl. Acad. Sci. U.S.A* 104 (26): 10865–10870. https://doi.org/10.1073/pnas.0701274104.

**80** Rullo, A., Reiner, A., Reiter, A. et al. (2014). Long wavelength optical control of glutamate receptor ion channels using a tetra-*ortho*-substituted azobenzene derivative. *Chem. Commun.* 50 (93): 14613–14615. https://doi.org/10.1039/C4CC06612J.

**81** Kienzler, M.A., Reiner, A., Trautman, E. et al. (2013). A red-shifted, fast-relaxing azobenzene photoswitch for visible light control of an ionotropic glutamate receptor. *J. Am. Chem. Soc.* 135 (47): 17683–17686. https://doi.org/10.1021/ja408104w.

**82** Izquierdo-Serra, M., Gascón-Moya, M., Hirtz, J.J. et al. (2014). Two-photon neuronal and astrocytic stimulation with azobenzene-based photoswitches. *J. Am. Chem. Soc.* 136 (24): 8693–8701. https://doi.org/10.1021/ja5026326.

**83** Izquierdo-Serra, M., Bautista-Barrufet, A., Trapero, A. et al. (2016). Optical control of endogenous receptors and cellular excitability using targeted covalent photoswitches. *Nat. Commun.* 7 (1): 12221. https://doi.org/10.1038/ncomms12221.

**84** Szobota, S., Gorostiza, P., Del Bene, F. et al. (2007). Remote control of neuronal activity with a light-gated glutamate receptor. *Neuron* 54 (4): 535–545. https://doi.org/10.1016/j.neuron.2007.05.010.

**85** Caporale, N., Kolstad, K.D., Lee, T. et al. (2011). LiGluR restores visual responses in rodent models of inherited blindness. *Mol. Ther.* 19 (7): 1212–1219. https://doi.org/10.1038/mt.2011.103.

**86** Janovjak, H., Szobota, S., Wyart, C. et al. (2010). A light-gated, potassium-selective glutamate receptor for the optical inhibition of neuronal firing. *Nat. Neurosci.* 13 (8): 1027–1032. https://doi.org/10.1038/nn.2589.

**87** Stein, M., Middendorp, S.J., Carta, V. et al. (2012). Azo-propofols: photochromic potentiators of GABAA receptors. *Angew. Chem. Int. Ed.* 51 (42): 10500–10504. https://doi.org/10.1002/anie.201205475.


**88** Yue, L., Pawlowski, M., Dellal, S.S. et al. (2012). Robust photoregulation of GABA a receptors by allosteric modulation with a propofol analogue. *Nat. Commun.* 3 (1): 1095. https://doi.org/10.1038/ncomms2094.

**89** Lin, W.-C., Davenport, C.M., Mourot, A. et al. (2014). Engineering a light-regulated GABAA receptor for optical control of neural inhibition. *ACS Chem. Biol.* 9 (7): 1414–1419. https://doi.org/10.1021/cb500167u.

**90** Lin, W.-C., Tsai, M.-C., Davenport, C.M. et al. (2015). A comprehensive optogenetic pharmacology toolkit for in vivo control of GABAA receptors and synaptic inhibition. *Neuron* 88 (5): 879–891. https://doi.org/10.1016/j.neuron.2015.10.026.

**91** Stein, M., Breit, A., Fehrentz, T. et al. (2013). Optical control of TRPV1 channels. *Angew. Chem. Int. Ed.* 52 (37): 9845–9848. https://doi.org/10.1002/anie.201302530.

**92** Frank, J.A., Moroni, M., Moshourab, R. et al. (2015). Photoswitchable fatty acids enable optical control of TRPV1. *Nat. Commun.* 6 (1): 7118. https://doi.org/10.1038/ncomms8118.

**93** Barber, D.M., Schönberger, M., Burgstaller, J. et al. (2016). Optical control of neuronal activity using a light-operated GIRK channel opener (LOGO). *Chem. Sci.* 7 (3): 2347–2352. https://doi.org/10.1039/C5SC04084A.

**94** Trads, J.B., Burgstaller, J., Laprell, L. et al. (2016). Optical control of GIRK channels using visible light. *Org. Biomol. Chem.* 15 (1): 76–81. https://doi.org/10.1039/C6OB02153K.

**95** Arrenberg, A.B., Stainier, D.Y.R., Baier, H., and Huisken, J. (2010). Optogenetic control of cardiac function. *Science* 330 (6006): 971–974. https://doi.org/10.1126/science.1195929.

**96** Fehrentz, T., Huber, F.M.E., Hartrampf, N. et al. (2018). Optical control of L-type Ca2+ channels using a diltiazem photoswitch. *Nat. Chem. Biol.* 14 (8): 764–767. https://doi.org/10.1038/s41589-018-0090-8.

**97** Zamponi, G.W., Striessnig, J., Koschak, A., and Dolphin, A.C. (2015). The physiology, pathology, and pharmacology of voltage-gated calcium channels and their future therapeutic potential. *Pharmacol. Rev.* 67 (4): 821–870. https://doi.org/10.1124/pr.114.009654.

**98** Yan, H., Dan, H., Congxin, H., and Nichols Colin, G. (2019). Genetic discovery of ATP-sensitive K+ channels in cardiovascular diseases. *Circ. Arrhythm. Electrophysiol.* 12 (5): e007322. https://doi.org/10.1161/CIRCEP.119.007322.

**99** Ashcroft, F.M. and Rorsman, P. (2013). K ATP channels and islet hormone secretion: new insights and controversies. *Nat. Rev. Endocrinol.* 9 (11): 660–669. https://doi.org/10.1038/nrendo.2013.166.

**100** Trube, G., Rorsman, P., and Ohno-Shosaku, T. (1986). Opposite effects of tolbutamide and diazoxide on the ATP-dependent K+ channel in mouse pancreatic beta-cells. *Pflügers Arch.* 407 (5): 493–499. https://doi.org/10.1007/BF00657506.

**101** Broichhagen, J., Schonberger, M., Cork, S.C. et al. (2014). Optical control of insulin release using a photoswitchable sulfonylurea. *Nat. Commun.* 5: 5116. https://doi.org/10.1038/ncomms6116.


**102** Johnston, N.R., Mitchell, R.K., Haythorne, E. et al. (2016). Beta cell hubs dictate pancreatic islet responses to glucose. *Cell Metab.* 24 (3): 389–401. https://doi.org/10.1016/j.cmet.2016.06.020.

**103** Mehta, Z.B., Johnston, N.R., Nguyen-Tu, M.S. et al. (2017). Remote control of glucose homeostasis in vivo using photopharmacology. *Sci. Rep.* 7 (1): 291. https://doi.org/10.1038/s41598-017-00397-0.

**104** Chau, C.H., Steeg, P.S., and Figg, W.D. (2019). Antibody–drug conjugates for cancer. *Lancet* 394 (10200): 793–804. https://doi.org/10.1016/S0140-6736(19)31774-X.

**105** Scholler, P., Nevoltris, D., de Bundel, D. et al. (2017). Allosteric nanobodies uncover a role of hippocampal MGlu2 receptor homodimers in contextual fear consolidation. *Nat. Commun.* 8 (1): 1967. https://doi.org/10.1038/s41467-017-01489-1.

**106** Frank, J.A., Antonini, M.-J., Chiang, P.-H. et al. (2020). In vivo photopharmacology enabled by multifunctional fibers. *bioRxiv*:https://doi.org/10.1101/2020.03.28.012567.

# 39 Molecular Switches as Building Blocks for DNA and RNA

Hans-Achim Wagenknecht

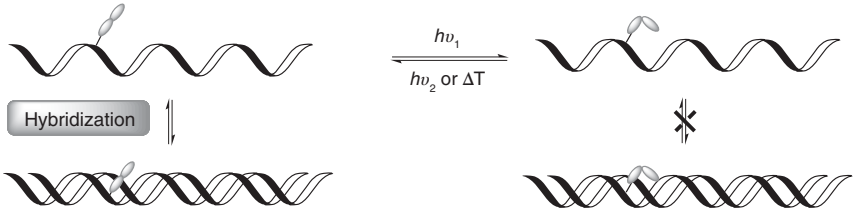


**Characteristic Features**

The well-defined photoinduced switching is an important task in the development of new photoresponsive DNA and RNA architectures for applications in chemical biology and nanotechnology. Three types of photochromic compounds were elucidated for DNA and RNA: (i) In 1998, Komiyama published the first DNA strands with an azobenzene substituting a nucleobase. (ii) Later, Heckel et al. solved the problem of the incompatibility of the spiropyrans with DNA photochemistry by pyridopyrans. (iii) Most recently, Jäschke et al. published nucleosides in which the aromatic heterocycle of the nucleobase replaces one of the thienyl groups for diaryl photoswitches.

**Key References**

Asanuma, H., Ito, T., and Komiyama, M. (1998). *Tetrahedron Lett*. 39: 9015–9018.

Brieke, C., and Heckel, A. (2013). *Chem. Eur. J*. 19: 15726–15734.

Sarter, C., Dey, S., and Jäschke, A. (2019). *ACS Omega* 4: 12125–12129.

Cahova, H., and Jäschke, A. (2013). *Angew. Chem. Int. Ed*. 52: 3186–3190.

# 39

# Molecular Switches as Building Blocks for DNA and RNA

*Hans-Achim Wagenknecht*

*Karlsruhe Institute of Technology (KIT), Institute of Organic Chemistry, Fritz-Haber-Weg 6, 76131 Karlsruhe, Germany*

## 39.1 Introduction

In biology, nucleic acids play the central role for storage of genetic information (DNA) and for transfer of genetic information into regulatory processes and functional proteins (RNA). Beyond their pure biology purpose, nucleic acids are able to serve as unique structural basis to create nanometer-sized one-, two-, and three-dimensional objects. Representatively, the DNA nanoobjects of Seeman et al [1] and the DNA origamis by Rothemund [2] are important structures. DNA/RNA architectures apply self-assembly of DNA or RNA single strands to form molecular architectures in a highly programmed fashion. The canonical base pairing between C and G, and between T/U and A, in combination with stacking interactions enable researchers to create supramolecular objects of impressive complexity, size, physico-chemical stability, rigidity, and monodispersity [3]. These could not be achieved by simple organic-chemical building blocks without nucleic acids. So far, the majority of such advanced nanoarchitectures were solely built by the four natural building blocks (A, C, T/U, and G). RNA and DNA are synthesized from building blocks [4], and a greater potential for DNA and RNA architectures arises from using synthetically modified and artificial building blocks that add functionalities, in particular photoresponsitivity, to those architectures. The well-defined photoinduced switching is a significant goal for the development of new photoreactive nanostructured DNA and RNA architectures. Among the known and structurally diverse photochromic compounds, in particular, azobenzenes, spirobenzopyrans, and diarylethenes were recently used to introduce photoswitching functionality into nucleic acids by the building-block approach. Such nucleic acid architectures are able to photoregulate biological activity and nanostructures [5].

From the structural point of view, DNA and RNA can be synthetically modified with organic photoswitches by five different approaches (Figure 39.1): [6] (i) DNA/RNA base substitutes/surrogates: The photoswitch substitutes one of the natural nucleobases and is attached to the anomeric center of the

*Molecular Photoswitches: Chemistry, Properties, and Applications*,
First Edition. Edited by Zbigniew L. Pianowski.


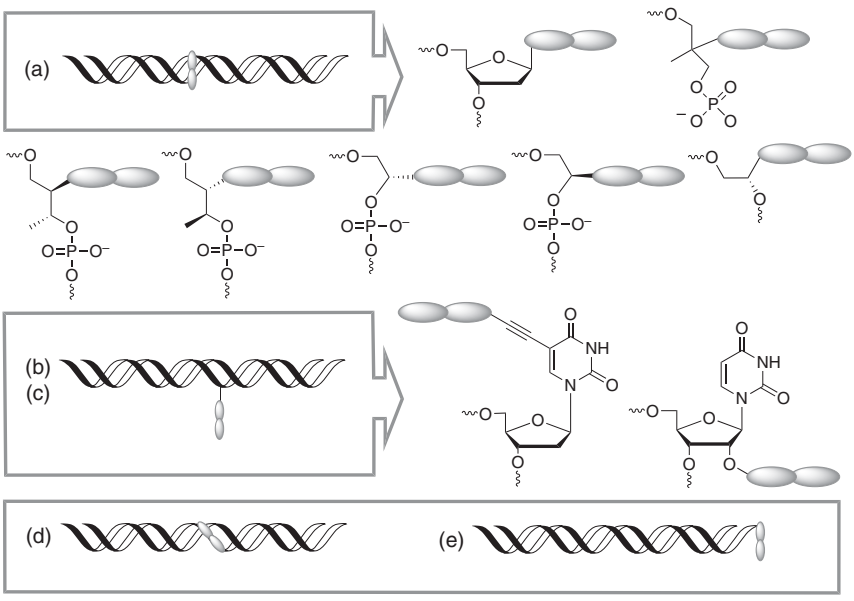


**Figure 39.1** Principal ways of incorporation of molecular switches (red) into DNA and RNA by (a) base surrogates, (b) base modifications, (c) sugar modifications, (d) phosphodiester modifications, and (e) 5′-caps. Source: Based on Schmucker and Wagenknecht [6].

2′-deoxyribofuanoside/ribofuranoside. In some cases, the sugar moiety was replaced by an acyclic linker between the phosphodiester bridges to enhance chemical stability and facilitate chemical synthesis. This approach places the photoswitch inside the DNA or RNA base stack. (ii) DNA/RNA base modifications: The photoswitch is attached to the aromatic core of a nucleobase and placed outside the DNA/RNA base stack. The 5-position of pyrimidines (C and T/U) is preferred due to the good synthetic accessibility and the assumption that Watson–Crick base pairing is not significantly altered. The 8-position of purines (A and G) must not be modified because the normal anti-conformation of the unmodified nucleotide is then switched to the syn-conformation with irregular consequences for the nucleic acid conformation. To prevent these structural changes, 7-deazapurine nucleotides are important alternatives because they may be modified at their 7-position. (iii) DNA/RNA sugar modifications: The photoswitch is attached to the 2′-position and places it into the groove. The alkylation of the 2′-hydroxy group stabilizes the RNA. Additionally, there are two ways of modifications that were not often applied for molecular switches. (iv). The phosphodiester bridge is modified by the photoswitch. This approach places the photoswitch into the backbone of the nucleic acid and has a strong structural impact. The synthetic incorporation requires modification of the phosphordiester coupling chemistry. (v) The photoswitch is attached to the 5′-terminus of DNA or RNA. From the synthetic point of view, this is probably the easiest way to modify nucleic acids with photoswitches because it is a postsynthetic methodology, which means that the photoswitch is attached to the presynthesized

nucleic acids, e.g. by amide coupling to a 5′-terminal amino modifier as building block. Many of such terminal modifiers are commercially available.

Herein, we summarize the currently available DNA and RNA building blocks with photoswitches of the three main classes – azobenzenes, spiropyrans, and diarylethenes. We present only those building blocks that were covalently attached to DNA and RNA strands to elucidate their nucleic-acid-switching properties.

## 39.2 Azobenzenes in DNA/RNA Building Blocks

The photoinduced *trans–cis* isomerization of azobenzene derivatives is a fully reversible process that induces a significant geometrical change and enlarges the distance between both ends of substituted azobenzenes. Azobenzenes can be easily synthesized, e.g. from diazonium salts as precursors or by Mills reaction in a great variety. The *cis*-to-*trans* isomerization is also initiated by thermal energy, not only by light, which is the major disadvantage of this photoswitch. This combination of unique properties makes this type of photoswitch attractive for photoregulation of nucleic acids. In 1998 and 1999, Komiyama published the first DNA strands with the building block **1** in which the azobenzene substitutes a nucleobase and was attached to a prochiral and acyclic linker between the phosphodiester bridges (Figure 39.2) [7], and with the building block **3**, in which the azobenzene was attached to the 2′-position of the sugar [8]. The DNA with building block **1** was fully switchable and the geometric change of the switching had a dramatic impact on the melting temperatures of the 8mer DNA duplexes. The *cis* form lowered the melting temperature by ∼9 °C, which led the two strands to dissociate at room temperature [9]. Rehybridization was achieved by visible-light irradiation to the *trans*-form. The DNA duplexes with the building block **3** were more stable and showed a less intense switching effect, presumably by the intact A-U base pair. Since these early discoveries, azobenzenes have attracted much interest as photoswitches in DNA and RNA. Basic applications of building block **1** included photoregulation of DNA polymerase reaction [10] and photocontrol of DNA triplex formation [11]. The modification by a dimethylamino group at the outer benzene part of the azobenzene in building block **2** gains a push–pull system and allows visible-light photocontrol of this switch in DNA. One of the major disadvantages of these early studies, however, was the use of a racemic linker as substitute for the 2′-deoxyribofuranoside, although the diastereomeric mixtures of DNA strands could be resolved. In 2001, Asanuma, Komiyama et al. replaced the linker by optically pure D- and L-threoninol in DNA building blocks **4** and **5**; D-threoninol gained the bigger melting temperature differences [12]. Advanced applications in chemical biology, such as the photoregulation of RNA digestion by RNAse H [13] and photoregulation of transcription [14], and in DNA nanotechnology, such as a DNA nanomachine powered by light irradiation [15], and light-driven DNA nanomachines with a photoresponsive molecular engine [16], were demonstrated by using **4** and **5**. The introduction of methyl groups (see building blocks **7**–**12**) into two *ortho* positions at the outer benzene ring of the azobenzene in building block

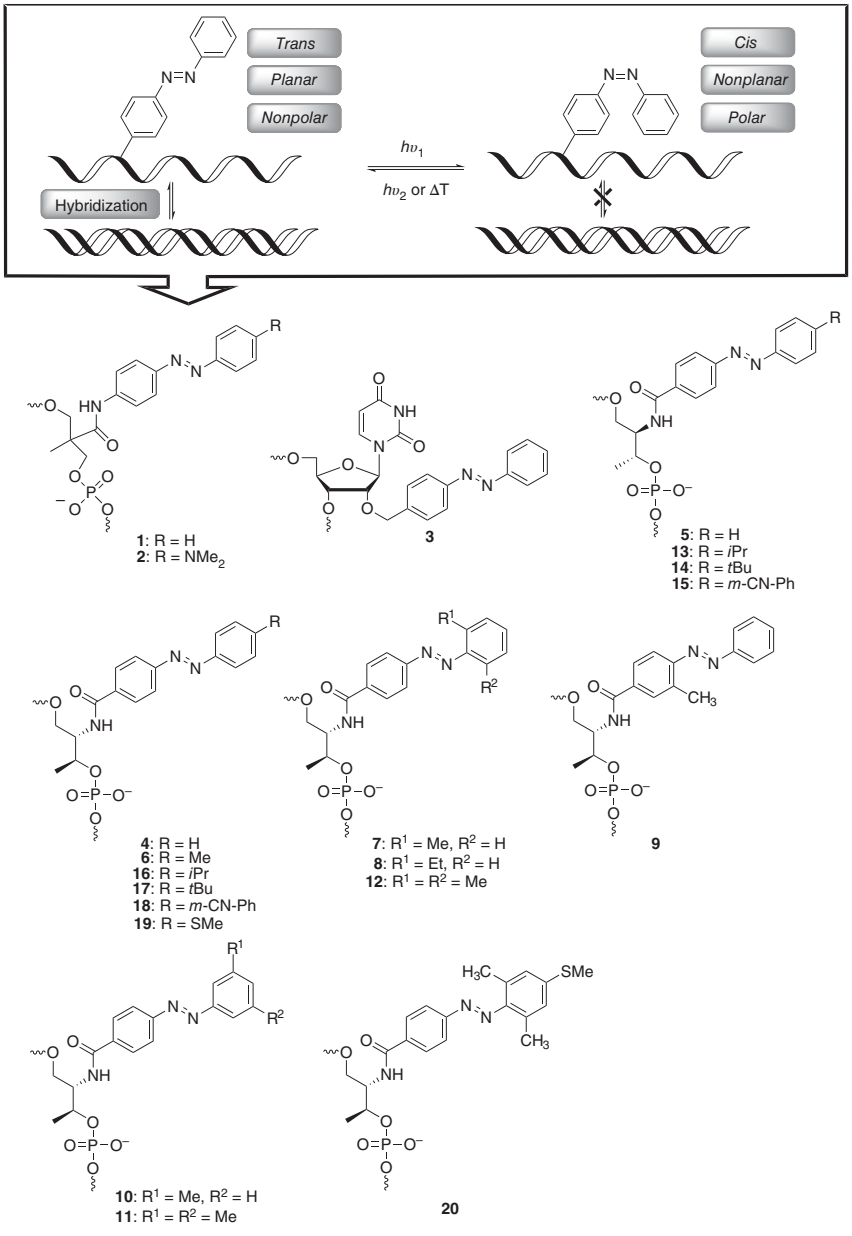


**Figure 39.2** DNA and RNA building blocks **1**–**20** with azobenzenes and similar derivatives as photoswitches. Source: Based on Asanuma et al. [7].

**12** remarkably raised both its photoregulation ability and the thermal stability of the *cis*-form [17]. The building block **12** was recently applied to photoregulate the isothermal DNA amplification by template-mediated ligation [18]. The azobenzene building blocks **4**, **7**, and **12** were also incorporated into RNA to obtain photoresponsive RNA for efficient photocontrol of the formation and dissociation of RNA duplexes. The observed differences in melting temperature between the *trans* and *cis* forms were higher than those of comparable photoresponsive DNA duplexes [19]. The introduction of bulky substituents to the D- and L-threolinol-based building blocks **4** and **5** gave building blocks **13**–**15** and **16**–**18**, respectively, which modulate the photoswitching in the DNA even to a reverse behavior [20]. The original building blocks **4** and **5** were also further developed to the building blocks **19** and **20**. A new DNA nanodevice combined building blocks **4** and **20** and showed seesaw-like movement that is driven by light [21]. These results demonstrate that these azobenzene building blocks are also useful for DNA nanotechnology.

Although the D-threoninol-based building blocks were the first choice for introducing azobenzenes as photoswitches to DNA and RNA, the following other structural attempts were published as important alternatives (Figure 39.3): (i) The C-nucleoside building blocks **21** and **22** that were developed by Heckel, Asanuma et al. resemble the 2′-deoxyribofuranoside structure of natural nucleotides and should have minimal perturbance on the duplex structure. In fact, they showed improved photoswitching properties in DNA at room temperature [22]. These building blocks exhibit high thermal stability and excellent fatigue resistance, which makes them excellent photoswitches also for RNA [23]. (ii) Another acyclic alternative to the threoninole linkers is the glycerol tether that links the azobenzene via an ether bond [24]. The (R)-configured building block **23** shows better photoregulation properties than the (S)-configured **24**. The *cis–trans* isomerization induces a melting temperature of 45 °C difference in a 12mer oligonucleotide bearing five building blocks **23**. This effect was attributed to the reduced number of carbons (two) of the glycol linker between the phosphodiester bridges in comparison to the threoninol linker (three). Furthermore, the dimethylated building block **25** was applied for light-driven reversible strand displacement [25]. (iii) The cyclic azobenzene in DNA building block **26** should reverse the relative stabilities. Due to ring strain, the *cis* isomer should be more stable than the *trans* isomer [26]. However, experiments in DNA were not yet fully successful because the *trans–cis* isomerization was too fast to determine melting temperature differences. (iv) The described building blocks **1**-**2** and **4**-**26** place the azobenzene into the base stack and the photoswitching ability may be diminished due to lack of space inside DNA or RNA. In building blocks **27**-**32**, the azobenzenes are attached to the 5-position of 2′-deoxyuridine. The correspondingly modified 12mer oligonucleotides showed only moderate melting temperature differences of the matched DNA duplexes (2–5 °C) between the *trans* and *cis* form of building block **27**. Further derivatization at the outer benzene ring in DNA building blocks **28**–**32** did not increase the melting temperature differences [27]. Locking the sugar pucker in DNA building block **33** did expectedly not change the photoswitching abilities. (v) Finally, the azobenzene switch was attached to the 2′-position of one uridine in a DNA oligonucleotide

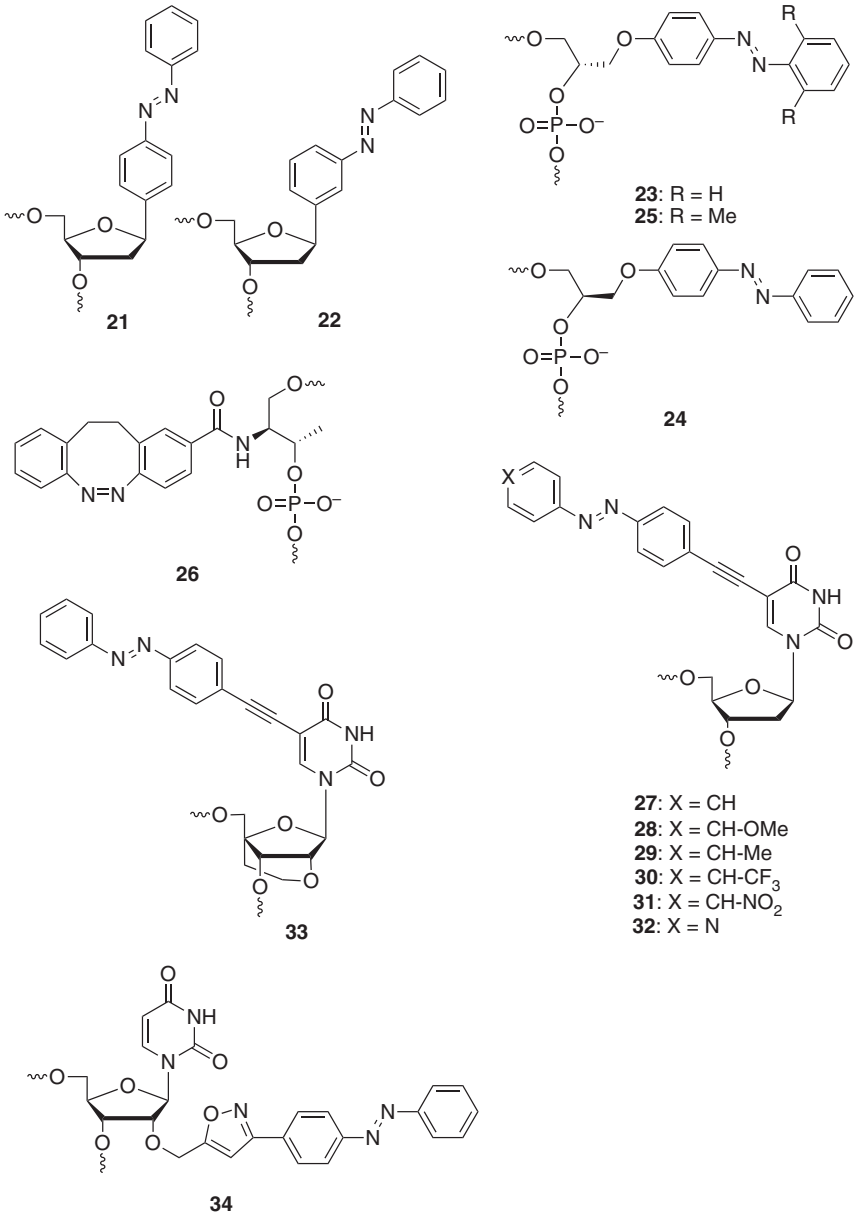


**Figure 39.3** DNA and RNA building blocks **21**–**34** with azobenzenes and similar derivatives as photoswitches.

using postsynthetic nitrile oxide-alkyne cycloaddition. This postsynthetic approach has the advantage that is not necessary to develop a new synthetic route to the corresponding phosphoramidite of building block **34**. However, the photoswitching abilities are hampered in the DNA duplex and the reason for this is not clear [28]. This result tracks well with the first studies by Komiyama who decided to use the building block **1** instead of building block **2**, as described above.

## 39.3 Spiropyrans in DNA/RNA Building Blocks

Spiropyrans contain – as the name already implies – a spiro center that connects the indolene part with the pyrane part of the chromophore. As a result, the closed form of the chromophore is unipolar, but bears a molecular twist that makes it non-planar. Upon irradiation, the spiropyran opens to the zwitterionic and planar merocyanine form, which yields a large change in polarity [29]. The closed spiropyran is formed back either by thermal activation or by visible-light irradiation. These strong geometric and polarity changes make spiropyran an attractive photoswitch for nucleic acids. It was expected that the closed spiropyran form of this photoswitch is not able to insert into the base stack due to its twisted structure, but the open merocyanine form could intercalate in coplanar orientation to the adjacent base pairs with regard to its planarity and polarity. This assumption was experimentally verified by synthetic spiropyrans and their photoregulation as non-covalent DNA binders [30], G-quadruplex binders [31], and as non-covalent binders in special RNA aptamers [32]. Electrostatic interactions play a key role for non-covalent DNA binding of spiropyran photoswitches [33]. Ground-state interactions between the non-covalently bound photoswitch and the DNA base stack were detected by circular dichroism (CD) spectroscopy for the merocyanine form, but not for the spiropyran form. There are only very few reports in literature on covalent conjugation of spiropyrans to DNA (Figure 39.4); there is no report for RNA modification. The first DNA example was published by Asanuma et al. in 2001 [34]. The spiropyran **35** was postsynthetically attached to the 5′-terminus of DNA and should serve as 5′-cap that photoregulates the DNA hybridization. The melting temperature of the open merocyanine cap of **35** was significantly higher than the closed spiropyran cap, which indicates the expected exclusive base stack interaction of the merocyanine. We incorporated the spiropyran chromophore into DNA by three different structural approaches, as DNA base substitute **36** [35], as 2′-modification **37** of the ribofuranoside of uridine [35], and as DNA modification at the 5-position of 2′-deoxyuridine **38** [36]. Building blocks **36** and **38** were incorporated into oligonucleotides by their phosphoramidites using automated DNA synthesis on solid phase, whereas spiropyran **37** was postsynthetically attached using the Cu(I)-catalyzed alkyne-azide cycloaddition between spiropyran azides [37] and presynthesized DNA with a propargyl group at the central 2′-position of the sequence. We found out, however, that the spiropyran chromophore loses its photoswitching ability when covalently conjugated into

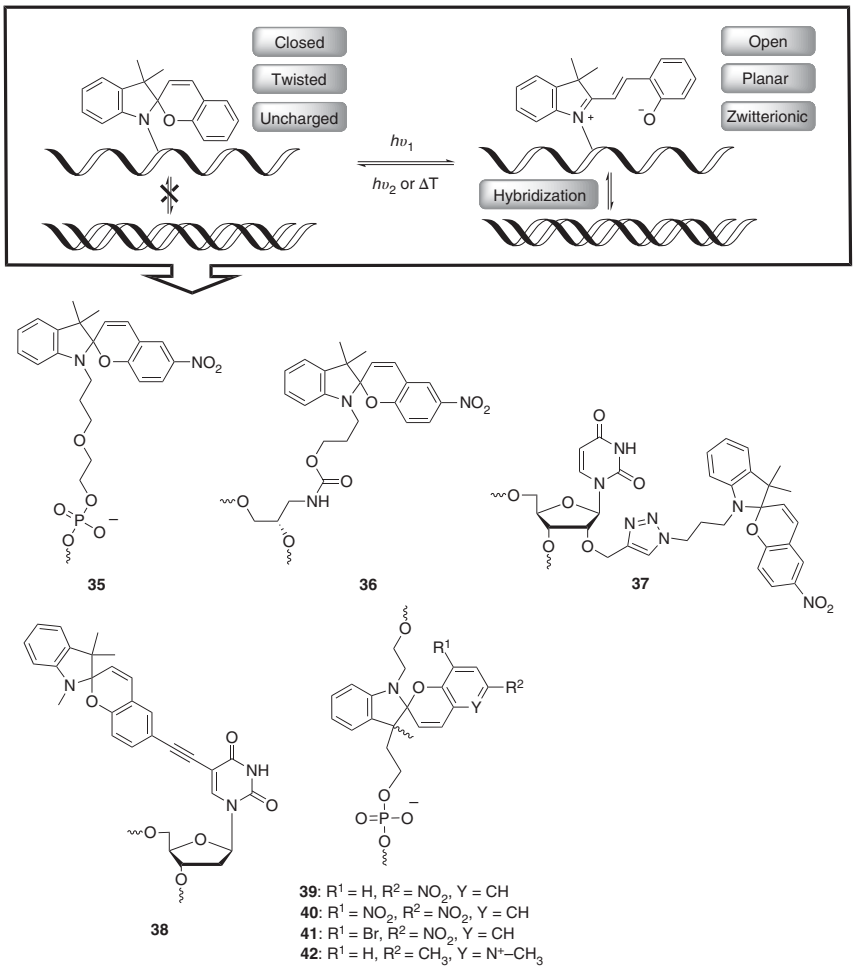


**Figure 39.4** DNA and RNA building blocks **35**–**42** with spiropyrans and similar derivatives as photoswitches.

the DNA environment [35]. It can be assumed that charge transfer processes with the DNA quench the excited state of the spiropyran chromophore and inhibit the switching process [38]. Moreover, Stafforst et al. reported that spiropyrans in general decompose in aqueous buffer solution [39]. Taken together, these results make the use of spiropyran photoswitch in nucleic acid quite questionable. There is one example, however, of a spiropyran that was successfully switched after conjugation to DNA. Heckel et al. solved the photophysical problem by replacing the conventional benzopyrans by pyridopyrans [40]. DNA was synthesized with the spiropyran **39** as phosphoramidite for modification in the phosphodiester backbone. The advanced postsynthetic conversion with different aldehyde precursors gave the spiropyridopyran building blocks **40**–**42** in the phosphodiester backbone. Only the DNA strand with building block **42** converted to the merocyanine form upon

irradiation in the UV-A range, and the merocyanine forms showed improved thermal stability and could only be converted back to the spiroform by irradiation at 530 nm. This is, to the best of our knowledge, the only successful example of photoswitching by a covalently linked spiropyran–DNA conjugate.

## 39.4 Diarylethenes in DNA/RNA Building Blocks

The third alternative structures for photoswitches are the diarylethenes [41], which are still rather unexplored with respect to nucleic acids. This is surprising because the advantage of this type of photoswitch is that not only the forward reaction to the closed isomer needs light but also the back reaction (reopening of the central ring) needs light and cannot be obtained in a thermally induced way. As a result, a fully reversible colorless-to-colorful transition and backwards is achieved by diarylethenes. Moreover, diarylethenes exhibit good fatigue resistance, rapid response, and good quantum yields, which make this class of photoswitch broadly applicable [42]. The assumption with regard to nucleic acids is that open and closed forms of the diarylethenes differ by the steric demand and thereby photoregulate DNA hybridization and other structural changes. The use of diarylethenes as photoswitches for nucleic acid started much later than the azabenzene building blocks. There are several examples in the literature that describe the use of diarylethenes as non-covalent DNA binders, e.g. for chiroptical DNA complexes [43], and as fluorescent switches for DNA by the use of two thiazole orange fluorophores [44]. Jäschke et al. published several nucleosides in which the aromatic heterocycle of the nucleobase replaces one of the thienyl groups of dithienyl photoswitches. Those nucleoside–photoswitch hybrids were prepared with 2′-deoxyuridine [45], 2′-deoxycytidine,[45] 7-deaza-2′-deoxyadenosines [46], and 7-deaza-2′-deoxyguanosines [47], and carefully studied to gain a detailed understanding of the photophysical properties [48]. Only the photoswitch hybrids with 2′-deoxyuridine and 2′-deoxycytidine as building blocks **43** and **44** were synthetically incorporated into DNA (Figure 39.5). In 2013, Jäschke et al. developed a postsynthetic protocol to prepare these photoswitch–DNA conjugates by postsynthetic Suzuki–Miyaura coupling with presynthesized oligonucleotides that contain 5-iodo-2′-deoxyuridine and 5-iodo-2′-deoxycytidine, respectively, as reactive precursors. The yielded DNA hybrid with the 2′-deoxycytidine building block **44** was highly thermally unstable in its closed form.[45] But the modified DNA with the building block **43** was fully photoswitchable. One of such modifications decreased the melting temperature of a 15mer double strand by 2.3 °C, both in the open and closed forms of the photoswitch. In a recent study, the photochemical properties were tuned by different substituents in DNA building blocks **43**, **45,** and **46**. The incorporation of up to three such modifications into one DNA strand leads to an additive DNA absorbance of the closed form in the visible range. The photostationary state of ∼50%, however, limits the applicability of this type of DNA photoswitches. We chose a slightly different approach and attached a full diarylethene photoswitch to the 5-position of 2′-deoxyuridine and incorporated

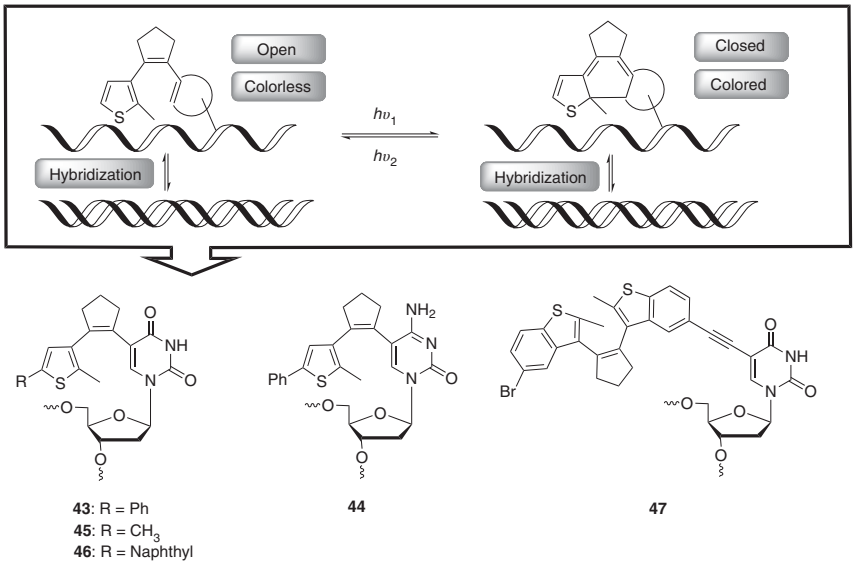


**Figure 39.5** DNA and RNA building blocks **43**–**47** with diarylethenes and similar derivatives as photoswitches.

the DNA building block **47** by standard phosphoramidite chemistry [36, 49]. The resulting DNA double strands were fully switchable in both directions. The modification **47** shows a high destabilization of the 17mer DNA double strands by 7.4 °C, which is enhanced to 11.2 °C after irradiation at 310 nm and formation of the closed form [49]. According to the noncovalently bound diarylethenes reported by Feringa et al., only the closed form is able to penetrate the DNA base stack [43]. This could explain our observations because the inserted closed form of the photoswitch interferes with stacking by the neighboring DNA base pairs. In conclusion, diarylethenes represent promising photoswitches for nucleic acids, but their photophysical properties and the structure of the DNA conjugates must be improved before applications in chemical biology and nanotechnology can be envisioned.

## 39.5 Conclusion

There are many building blocks available for incorporation of photoswitches into DNA and RNA. The vast majority of these building blocks are based on the azobenzene switch. The major purpose is the photocontrol of DNA hybridization from single strands to duplexes. This goal has been achieved with the azobenzene switches, and many applications in chemical biology and nanotechnology have been realized over the last two decades. In contrast, DNA and RNA building blocks based on spiropyrans and diarylethenes are still underdeveloped, although these types of photoswitches have significant and characteristic advantages. In particular,

the big polarity and geometric change between the closed spiropyrans and the open merocyanins is an attractive feature. The diarylethenes have the advantage that both directions of isomerization are exclusively induced by light and not by thermal energy. These advantages have to be explored for nucleic acids in the future and require more organic–synthetic efforts.

## Acknowledgments

Financial support by the Deutsche Forschungsgemeinschaft (grant Wa 1386/9-4) and KIT is gratefully acknowledged.

## References

1 Seeman, N.C. (1982). *J. Theor. Biol.* 99: 237–247.
2 Rothemund, P.W.K. (2006). *Nature* 440: 297–302.
3 (a) Simmel, F.C. (2008). *Angew. Chem. Int. Ed.* 47: 5884–5887; (b) Sacca, B. and Niemeyer, C.M. (2012). *Angew. Chem. Int. Ed.* 51: 58–66; (c) Tian, Y. and Mao, C. (2004). *J. Am. Chem. Soc.* 126: 11410–11411; (d) Jones, M.R., Seeman, N.C., and Mirkin, C.A. (2015). *Science* 347: 1260901; (e) Zhang, F., Nangreave, J., Liu, Y., and Yan, H. (2014). *J. Am. Chem. Soc.* 136: 11198–11211; (f) Simmel, S.S., Nickels, P.C., and Liedl, T. (2014). *Acc. Chem. Res.* 47: 1691–1699; (g) Torring, T., Voigt, N.V., Nangreave, J. et al. (2011). *Chem. Soc. Rev.* 40: 5636–5646.
4 (a) Reese, C.B. (2005). *Org. Biomol. Chem.* 3: 3851–3868; (b) Beaucage, S.L. and Caruthers, M.H. (1981). *Tetrahedron Lett.* 22: 1859–1862.
5 (a) Lubbe, A.S., Szymanski, W., and Feringa, B.L. (2017). *Chem. Soc. Rev.* 46: 1052–1079; (b) Wu, Z. and Zhang, L. (2019). *Biomater. Sci.* 7: 4944–4962.
6 Schmucker, W. and Wagenknecht, H.-A. (2012). *Synlett* 23: 2435–2448.
7 Asanuma, H., Ito, T., and Komiyama, M. (1998). *Tetrahedron Lett.* 39: 9015–9018.
8 Asanuma, H., Yoshida, T., Ito, T., and Komiyama, M. (1999). *Tetrahedron Lett.* 40: 7995–7998.
9 Asanuma, H., Ito, T., Yoshida, T. et al. (1999). *Angew. Chem. Int. Ed.* 38: 2393–2395.
10 Yamazawa, A., Liang, X., Asanuma, H., and Komiyama, M. (2000). *Angew. Chem. Int. Ed.* 39: 2356–2357.
11 Liang, X., Asanuma, H., and Komiyama, M. (2002). *J. Am. Chem. Soc.* 123: 1877–1883.
12 Asanuma, H., Takarada, T., Yoshida, T. et al. (2001). *Angew. Chem. Int. Ed.* 40: 2671–2673.
13 Matsunaga, D., Asanuma, H., and Komiyama, M. (2004). *J. Am. Chem. Soc.* 126: 11452–11453.
14 Liu, M., Asanuma, H., and Komiyama, M. (2006). *J. Am. Chem. Soc.* 128: 1009–1015.

**15** Liang, X., Nishioka, H., Takenaka, N., and Asanuma, H. (2008). *ChemBioChem* 9: 702–705.
**16** Kamiya, Y. and Asanuma, H. (2014). *Acc. Chem. Res.* 47: 1663–1672.
**17** Nishioka, H., Liang, X., Kashida, H., and Asanuma, H. (2007). *Chem. Commun.*: 4354–4356.
**18** Cheng, B., Kashida, H., Shimada, N. et al. (2019). *Chem. Commun.* 55: 1080–1083.
**19** Ito, H., Nishioka, H., and Asanuma, H. (2010). *Org. Biomol. Chem.* 8: 5519–5524.
**20** Liang, X., Takenaka, N., Nishioka, H., and Asanuma, H. (2008). *Chem. Asian J.* 3: 553–560.
**21** Nishioka, H., Liang, X., Kato, T., and Asanuma, H. (2012). *Angew. Chem. Int. Ed.* 51: 1165–1168.
**22** Goldau, T., Murayama, K., Brieke, C. et al. (2015). *Chem. Eur. J.* 21: 17870–17876.
**23** Goldau, T., Murayama, K., Brieke, C. et al. (2015). *Chem. Eur. J.* 21: 2845–2854.
**24** Kou, B., Guo, X., Xiao, S.-J., and Lang, X. (2013). *Small* 9: 3939–3943.
**25** Kou, B., Zhang, J., Huai, X. et al. (2015). *RSC Adv.* 5: 5055–5058.
**26** Eljabu, F., Dhruval, J., and Yan, H. (2015). *Bioorg. Med. Chem. Lett.* 25: 5594–5596.
**27** Mori, S., Morihori, K., Kasahira, Y. et al. (2015). *Chemosensors* 3: 36–54.
**28** Freeman, C., Vyle, J.S., and Heaney, F. (2013). *RSC Adv.* 3: 1652–1655.
**29** (a) Berkovic, G., Krongauz, V., and Weiss, V. (2000). *Chem. Rev.* 100: 1741–1753; (b) Sakata, T., Yan, Y., and Marriott, G. (2005). *J. Org. Chem.* 70: 2009–2013.
**30** (a) Hammarson, M., Andersson, J., Li, S. et al. (2010). *Chem. Commun.* 46: 7130–7132; (b) Andersson, J., Li, S., Lincoln, P., and Andreasson, J. (2008). *J. Am. Chem. Soc.* 130: 11836–11837.
**31** Livendahl, M., Jamroskovic, J., Hedenström, M. et al. (2017). *Org. Biomol. Chem.* 15: 3265–3275.
**32** (a) Young, D.D. and Deiters, A. (2008). *ChemBioChem* 9: 1225–1228; (b) Zhang, X., Zhang, J., Ying, Y.-L. et al. (2014). *Chem. Sci.* 5: 2642–2646.
**33** Avagliano, D., Sánchez-Murcia, P.A., and González, L. (2019). *Phys. Chem. Chem. Phys.* 21: 8614–8618.
**34** Asanuma, H., Shirasuka, K., Yoshida, T. et al. (2001). *Chem. Lett.* 30: 108–109.
**35** Beyer, C. and Wagenknecht, H.-A. (2010). *Synlett*: 1371–1376.
**36** Barrois, S., Beyer, C., and Wagenknechrt, H.-A. (2012). *Synlett* 23: 711–716.
**37** Beyer, C. and Wagenknecht, H.-A. (2010). *J. Org. Chem.* 75: 2752–2755.
**38** Avagliano, D., Sánchez-Murcia, P.A., and González, L. (2019). *Phys. Chem. Chem. Phys.* 21: 17971–17977.
**39** Stafforst, T. and Hilvert, D. (2009). *Chem. Commun.*: 287–288.
**40** Brieke, C. and Heckel, A. (2013). *Chem. Eur. J.* 19: 15726–15734.
**41** Irie, M. (2000). *Chem. Rev.* 100: 1685–1716.
**42** Kathan, M. and Hecht, S. (2017). *Chem. Soc. Rev.* 46: 5536–5550.
**43** Mammana, A., Carroll, G.T., Areephong, J., and Feringa, B.L. (2011). *J. Phys. Chem. B* 115: 11581–11587.
**44** Liu, K., Wen, Y., Shi, T. et al. (2014). *Chem. Commun.* 50: 9141–9144.


**45** (a) Sarter, C., Dey, S., and Jäschke, A. (2019). *ACS Omega* 4: 12125–12129; (b) Cahova, H. and Jäschke, A. (2013). *Angew. Chem. Int. Ed.* 52: 3186–3190.
**46** (a) Singer, M. and Jäschke, A. (2010). *J. Am. Chem. Soc.* 132: 8372–8377; (b) Sarter, C., Heimes, M., and Jäschke, A. (2016). *Beilstein J. Org. Chem.* 12: 1103–1110.
**47** Singer, M., Nierth, A., and Jäschke, A. (2013). *Eur. J. Org. Chem.*: 2766–2769.
**48** (a) Li, Y., Lustres, L.P., Volpp, H.-R. et al. (2018). *Phys. Chem. Chem. Phys.* 20: 22867–22876; (b) Buckup, T., Sarter, C., Volpp, H.-R. et al. (2015). *J. Phys. Chem. Lett.* 6: 4717–4721.
**49** Barrois, S. and Wagenknecht, H.-A. (2012). *Beilstein J. Org. Chem.* 8: 905–914.

# 40 Photoswitchable Peptides and Proteins

Susanne Kirchner, Anna-Lena Leistner, and Zbigniew L. Pianowski

**Key Aspects**

Molecular architecture that reversibly transforms light energy into function or activity changes in peptides, peptide-like molecules and proteins.

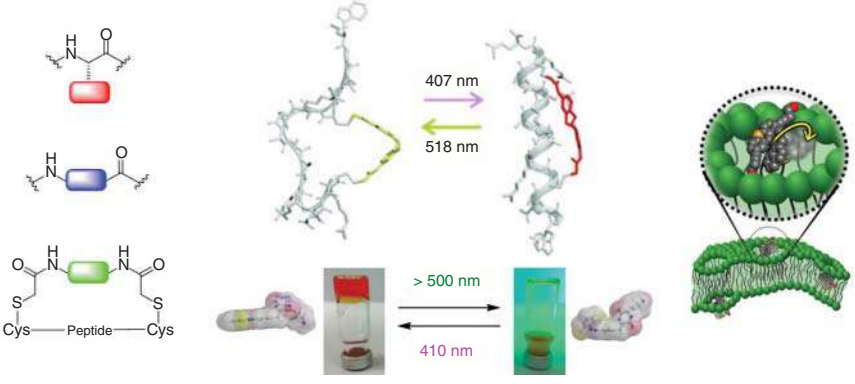


**Key References**

Babii, O., Afonin, S., Berditsch, M. et al. (2014). Controlling biological activity with light: diarylethene-containing cyclic peptidomimetics. *Angew. Chem. Int. Ed*. 53: 3392–3395.

Hüll, K., Morstein, J., and Trauner, D. (2018). *In vivo* photopharmacology. *Chem. Rev*. 118: 10710–10747.

Albert, L. and Vàzquez, O. (2019). Photoswitchable peptides for spatiotemporal control of biological functions. *Chem. Commun*. 55: 10192–10213.

# 40

# Photoswitchable Peptides and Proteins

*Susanne Kirchner[1], Anna-Lena Leistner[1], and Zbigniew L. Pianowski[1,2]*

*[1] Institute of Organic Chemistry IOC, Karlsruher Institut für Technologie (KIT), Fritz-Haber-Weg 6, 76131, Karlsruhe, Germany*
*[2] Institute of Biological and Chemical Systems – Functional Molecular Systems IBCS-FMS, Karlsruher Institut für Technologie (KIT), Hermann-von-Helmholtz-Platz 1, 76344, Eggenstein-Leopoldshafen, Germany*

## 40.1 Introduction

Peptides and proteins are key components of cellular and intercellular processes in every living organism – just to name enzymatic catalysis, signal transduction, processing of cellular information by hormones or antibodies, but also cytoskeleton formation and supply of energy. Selective ways to control their activity enable researchers to precisely dissect their particular roles in the cellular and organismal context. In case of proteins, numerous small-molecule inhibitors have been invented to control their activity. Other means of identification of protein functions are development of knockout organisms or engineering of fusion proteins with GFP variants. Shorter peptides can be radiolabeled, caged, or appended with small fluorophores. However, fusion of molecular photoswitches with peptidic molecules of various complexity level provides a complementary method for activity photomodulation, with the level of spatiotemporal control often inaccessible for the previously mentioned techniques. Light is unreactive toward almost all biomolecules, it does not permanently contaminate the samples, and it can be dosed with high precision. These features make it an almost ideal "reagent" for precise interventions in complex biological setups. Additionally, the reversibility inherent to photochromism allows in principle for an independent control over multiple subsequent or parallel processes within one organism. It also brings an additional dynamic component, which goes beyond the simple two-state systems (e.g. "enzyme on" – "enzyme off"). This, in turn, can provide an insight into scarcely explored biological oscillatory processes.

In this chapter, we would like to focus on several types of architectures that combine molecular photoswitches with peptides, peptide-like molecules, and ultimately with proteins. We want to demonstrate successful applications and known limitations of such hybrid systems. For that, we collected a range of representative examples of light-triggered conformational control of peptides,

*Molecular Photoswitches: Chemistry, Properties, and Applications*,
First Edition. Edited by Zbigniew L. Pianowski.


modulation of activity and structural features, as well as biosynthetic incorporation of photoswitches into biopolymers.

## 40.2 Functionalization of Peptides and Proteins with Photochromic Residues

Activity of proteins (Scheme 40.1) critically depends on their 3D-structure. Some proteins can even assume multiple active structures and interact with various partners, yielding different biochemical functions [1]. Photoisomerization often induces changes in molecular geometry and polarity. Thus, a properly located molecular photoswitch can transform the energy of light into significant conformational changes of the adjacent peptide chains, which in turn strongly influence activity or function of the protein. However, such a selective functionalization faces the same set of problems as any other selective protein labeling. Chemical synthesis of properly folded full-size proteins with a sequence-specific photochromic modification would be extremely challenging. While several successful syntheses of fully functional proteins based on native chemical ligation (NCL) or analogous protocols raise much hope, this technique is still far from routine. Currently, a more successful approach is chemoselective labeling of thiol side chains in reactive cysteine residues with photoswitches, mostly activated azobenzene derivatives. An emerging alternative is biosynthetic incorporation of unnatural photochromic amino acids into proteins, which will be discussed in the last section of this chapter in more detail. That technique seems to be particularly suitable for following *in vivo* studies.

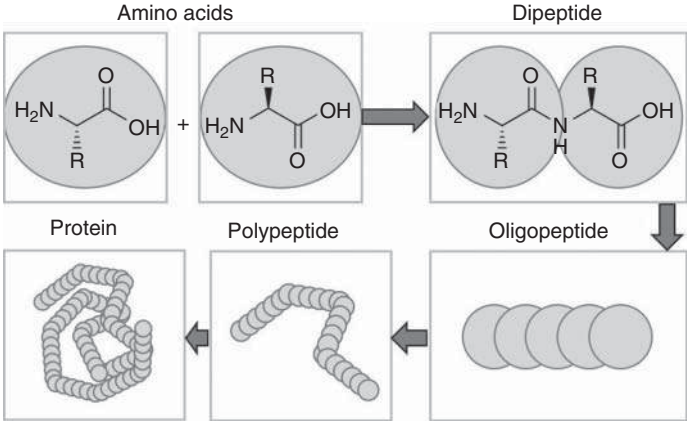


**Scheme 40.1** Hierarchy of the amino acid oligomers.

On the other hand, synthetic accessibility of peptides (or peptide analogs) decorated with photochromic residues enables research on photomodulation of their activity *in vitro*, and in some cases also *in vivo*. The majority of proteins and peptides are biosynthesized in course of ribosomal synthesis, where single amino

acids activated on tRNA "adapters" are subsequently added to the C-terminus of a growing peptide in the order templated by mRNA sequences ("N-to-C" synthesis direction). Non-ribosomal peptide synthetases are mRNA-independent enzymes that can also synthesize peptides (usually very specific ones). The ribosomal peptide synthesis inspired Robert B. Merrifield to develop solid-phase peptide synthesis (SPPS), for which he was awarded the Chemistry Nobel prize in 1984. Since then, this process is constantly optimized. In its current form, it enables efficient synthesis of up to 60–70-meric oligopeptides with satisfactory yields and purity. The key advantage of SPPS methodology is its large tolerance on the use of non-proteinogenic amino acids (e.g. D-amino acids, β-amino acids) and unnatural building blocks (including molecular photoswitches), as long as orthogonal conditions for activation and deprotection can be developed [2]. Due to its standardization and speed, SPPS almost fully outcompeted earlier peptide synthesis protocols in solution, based on iterative cycles of chemoselective coupling followed by isolation and deprotection.

The carboxylic acid group of a protected monomer (an amino acid, or a photochromic molecule with matching reactive groups) is initially activated to form an acyl azide, halide, anhydride, or – most often – an active ester. The last one is generated using carbodiimides (DCC, DIC, and EDC), phosphonium (BOP, PyBOP) or uronium reagents (HBTU, HATU), often in combination with the racemization inhibitor 1-hydroxybenzotriazole (HOBt). The activated first monomer is then coupled via a reactive linker, which later acts as a C-terminal protecting group, to the solid support, usually called resin. Chain elongation is now possible by iterative deprotection of the N-terminus on the growing peptide chain, coupling the resulting free amino group with the next activated monomer, and washing steps. The peptide grows from its C- to its N-terminus (opposite way as in protein biosynthesis), while being constantly linked to the resin. First resins, developed by Merrifield, consisted of cross-linked polystyrene modified with $CH_2Cl$ groups as linkers. A variety of resins (Rink, Wang) with improved chemical properties and polarity better suited for reagent penetration have been developed since then.

Two most common SPPS protocols differ in regard of used combination of protecting groups and deprotecting reagents. The "Fmoc-protocol" uses N-terminally Fmoc-protected monomers with acid-labile protecting groups (Boc, Bhoc, Pbf) on the amino acid side chains (Figure 40.1). Here, deprotection of the N-terminus occurs upon addition of basic reagents (e.g. 20% piperidine solution in DMF). When the oligopeptide synthesis is finished, the product is cleaved from the resin with concomitant deprotection of all the side chains using acidic conditions (typically 50–80% solutions of trifluoroacetic acid (TFA)). In the "Boc-protocol," the TFA-labile Boc-group is used to protect the N-terminus of monomers and is iteratively removed after each coupling step. Side chains are protected with TFA-resistant benzyl-based groups. Their removal at the end of synthesis with concomitant detachment from the resin is accomplished using anhydrous hydrogen fluoride. The "Boc-protocol" reduces peptide aggregation during synthesis. It is also used if peptides contain base-sensitive moieties. The "Fmoc-protocol" is preferred elsewhere, due to less aggressive reagents that do not need specific laboratory setup.

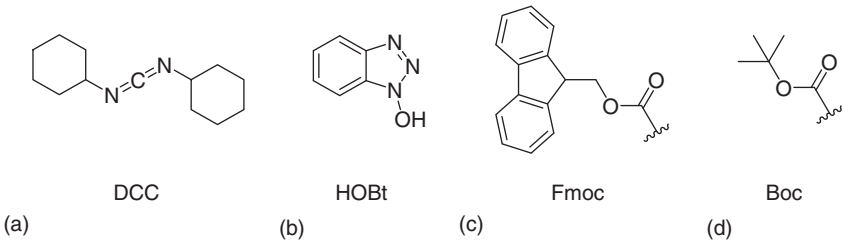


**Figure 40.1** Common reagents and protection groups applied in the solid-phase peptide synthesis process: (a) Dicyclohexylcarbodiimide (DCC), (b) 1-hydroxybenzotriazole (HOBt), (c) fluorenylmethoxycarbonyl (Fmoc) group, and (d) *tert*-butyloxycarbonyl (Boc) group.

As an iterative process, SPPS can be often performed in an automatized manner (peptide synthesizers).

The first challenge in synthesis of a photoswitchable peptide is efficient incorporation of the photochromic building block. This unit can be implemented as a side chain, inside of the peptide backbone, or as a cross-linker (Scheme 40.2).

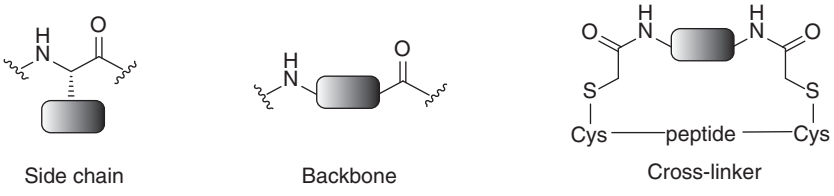


**Scheme 40.2** Possible positions for incorporation of molecular photoswitches into peptides.

Goodman et al. first introduced azobenzenes into peptides via amino acids containing an azobenzene side chain [3]. They synthesized (*S*)-4-(phenylazo)phenylalanine (PAP), which is derived from the natural amino acid phenylalanine (Scheme 40.3).

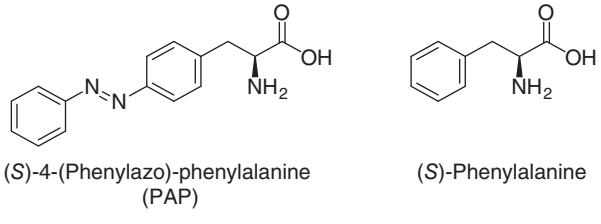


**Scheme 40.3** (*S*)-4-(Phenylazo)phenylalanine (PAP) – a photochromic derivative of (*S*)-phenylalanine.

PAP can be protected on the N-terminus with an Fmoc group and then effectively used as a building block in the SPPS. However, many other photoswitches undergo degradation when exposed to the deprotection conditions used in SPPS. In such

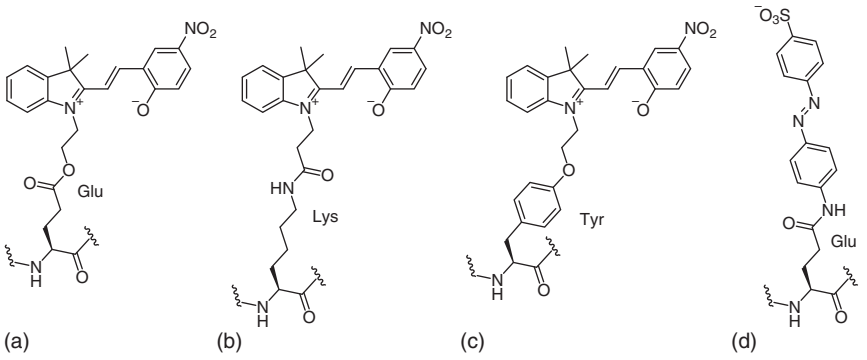


**Figure 40.2** Monomeric fragments of spiropyran-linked (a) poly-L-glutamic acid [4c], (b) poly-L-lysine [4b], (c) poly-L-tyrosine [4e], and (d) azobenzene-modified poly-L-glutamic acid [4a].

cases, a different synthetic strategy has been implemented [4]. At first, SPPS is used to synthesize a nonphotochromic peptide containing a reactive group (for example a side chain of glutamic acid, aspartic acid, lysine, or tyrosine). This peptide is cleaved from the resin, then it reacts in solution with the properly activated photoswitch, and it is finally purified. This strategy has been particularly successful in decorating peptides with multiple photochromic units (Figure 40.2).

Incorporation of photoswitches into the peptide backbone is usually accomplished with molecules bearing a carboxylic group and an Fmoc-protected amine on their opposite terminus. This backbone modification is particularly useful for inducing large structural transformations in polypeptide chains and presents a tool to investigate folding mechanisms and conformational dynamics. These effects are especially pronounced with azobenzenes due to their high quantum efficiencies and large geometrical changes induced upon isomerization [5] (Figure 40.3).

On the other hand, diarylethenes (DAEs) proved to be effective in the modulation of activity in cyclic oligopeptides. Although molecular geometry of DAE remains almost unaffected upon photoisomerization, it seriously alters rigidity of the system, which in turn influences flexibility and strain of the peptide, and consequently its biological activity [6].

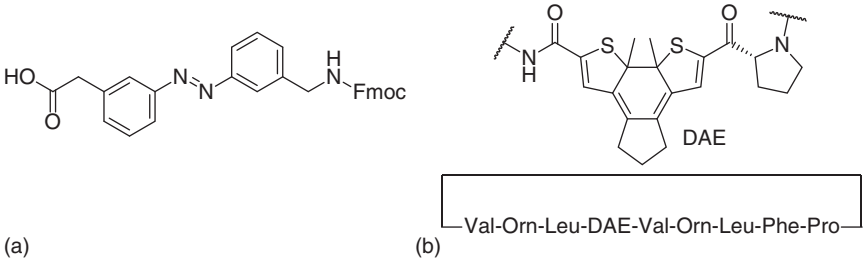


**Figure 40.3** Photoswitches incorporated into a peptide backbone: (a) a Fmoc-protected azobenzene SPPS building block "AMPP"; (b) a diarylethene (DAE) motif incorporated into a cyclic peptide gramicidin S.

Yet another technique of introducing photochromic residues into peptides, based on the NCL reactivity, has been demonstrated by the group of Rück-Braun with hemithioindigos and azobenzenes [7]. The N-terminally protected photochromic molecules are activated in the form of thioesters. Transthioesterification followed by an irreversible S→N acyl transfer results in an efficient peptide bond formation, as depicted in Scheme 40.4. Here, it was particularly important to develop conditions that prevent reductive degradation of the photochromes.

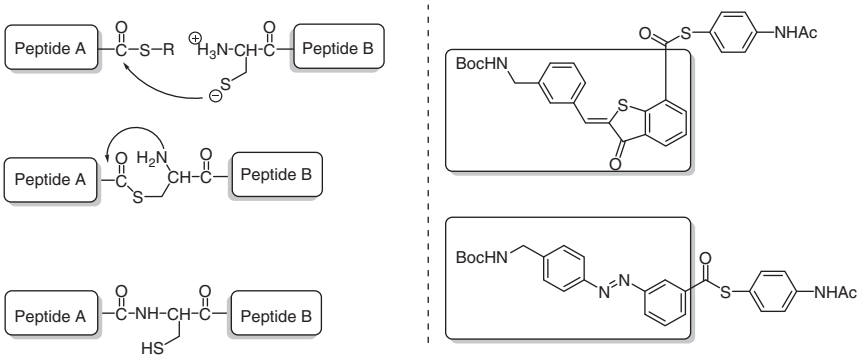


**Scheme 40.4** Mechanism of the native chemical ligation (NCL) (left); *N*-Boc-protected hemithioindigo and azobenzene thioesters as building blocks for NCL (right).

The third type of molecular architecture for incorporation of photochromes, dubbed "cross-linking" (Scheme 40.2) relies on a two-point attachment of the photoswitch to side chains of the targeted peptide. In contrary to the first method (a photochromic side chain with single attachment point), this architecture enables more efficient transfer of the strain generated upon photoisomerization onto the peptide chain. And in contrary to the backbone incorporation (the second "architecture"), the canonical peptide backbone and the resulting conformational constraints remain largely unaffected.

While, in principle, every pair of reactive amino acid side chains (e.g. from lysine, glutamic, or aspartic acid) can be used for the cross-linking, longer linkers with high flexibility do not transmit well the photoisomerization strain changes. Therefore, short cysteine side chains are used most often in such systems, also due to their reactivity in click reactions with bifunctional thiol-reactive switches (most often azobenzenes) (Scheme 40.5) (Figure 40.4) [9]. The structure of photochromic cross-linkers has been carefully optimized to achieve maximal photocontrol, when one photoisomer maintains the α-helical conformation of the adjacent peptide while the other causes denaturation of the helix [10].

Another way of reducing unwanted flexibility of the system is decoration of peptides with unnatural amino acids with short alkylamine side chain, such as (*S*)-2,3-diaminopropionic acid (Dpr). In that case, carboxylic groups of the respective bifunctional photoswitch are activated as *N*-hydroxysuccinimide esters, which chemoselectively react with alkylamine groups under aqueous conditions in the presence of other nucleophilic amino acid side chains. The groups of Herges

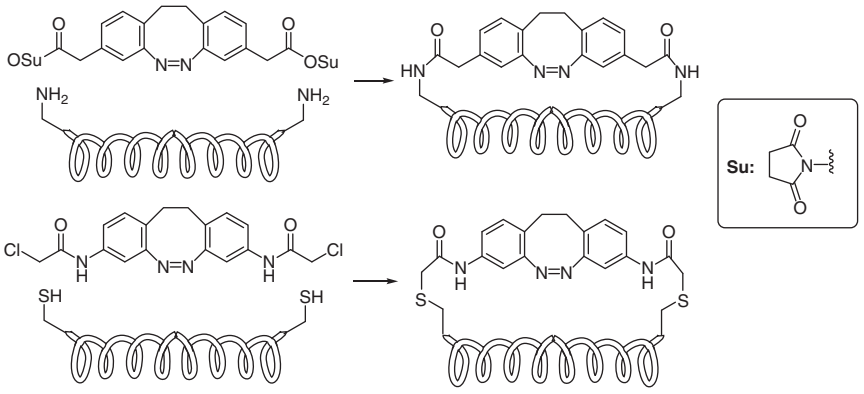


**Scheme 40.5** Comparison of a primary amine-reactive cross-linker with a thiol-reactive cross-linker. Source: Modified from Preußke et al. [8].

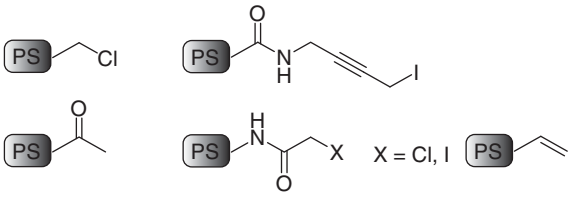


**Figure 40.4** An overview of thiol-reactive functional groups appended on bifunctional molecular photoswitches for efficient cross-linking with cysteine side chains of the targeted peptide.

and Sönnichsen [8] demonstrated feasibility of this concept with a bifunctional diazocine (cyclic azobenzene), and compared it with the cysteine/chloroacetemide linker (Scheme 40.5).

## 40.3 Selected Applications of Photochromic Peptides

Due to the modular synthesis, the rich spectrum of functions, and decades of structural investigations, peptides are among the most interesting scaffolds for decoration with photochromic residues. In this section, we want to demonstrate the scope of photomodulation of peptide structure or activity, as well as the variety of molecular photoswitches applicable in this task.

To demonstrate induction of a biological effect upon photomodulation of a dipole moment, photoswitches with substantial dipole moment changes, such as azobenzenes (0 D (*E*) ↔ 3 D (*Z*)) or hemithioindigos (2.8 D (*Z*) ↔ 1.2 D (*E*)), have been appended to the N-terminus of gramicidin A. Upon exposure to light, a decrease in the dipole moment caused increase of the ionic current of gramicidin channels in lipid bilayers [11].

Light-induced structure and polarity change can also cause reversible denaturation of the adjacent helical polypeptide. This was realized on poly(L-glutamic acid),

known to preferentially form α-helices, decorated with multiple nitrospiropyrans. The helical structure was still preserved upon this modification. In the dark, the closed nitrospiropyrans transformed to the open merocyanines, which formed dimers with neighboring merocyanine molecules. This, in turn, forced the affected area to assume the random coil structure [4c].

Another method to trigger reversible changes in peptides' secondary structures is incorporation of a photochromic residue into the main peptide chain. The resulting photoisomerization-induced geometry changes have been applied for peptide aggregation studies [12]. Hilvert group inserted an azobenzene unit into the backbone of loop region of a β-hairpin-forming peptide. This enabled light-driven switching between the β-hairpin conformation and an aggregated oligomer [5, 13]. Molecular dynamics simulations indicated that the β-turn geometry is most optimally emulated by the 3-[(3-aminomethyl)-phenylazo]phenylacetic acid (AMPP, Figure 40.3) [13]. A similar system, proposed by Dong et al., could be switched between a soluble disordered (*E*) and a β-hairpin (*Z*) peptide [14]. Further studies on light-induced dynamic of β-hairpin-forming peptides [15] and amyloid-like structures [16] have been reported by the groups of Zinth and Hoffmann-Röder.

Marafon et al. recently demonstrated a light-induced α-synuclein aggregation – a process associated with Parkinson's disease etiopathogenesis – using a photoactive foldamer containing two 3-aminoprop-2-enoic acid units as switchable elements in the short peptidic backbone (Figure 40.5). These units can interconvert from the *Z*-isomer stabilized with internal hydrogen bonds to the *E*-isomer with 290–320 nm (UV-B), and back to the *Z*-isomer with 254 nm (UV-C). The (*E,E*)-configured foldamers efficiently form aggregates with an intramolecular hydrogen bonding network, which are then seeding the following aggregation of α-synuclein. This process is followed by ECD and visualized with electron microscopy of the α-synuclein fibers [17].

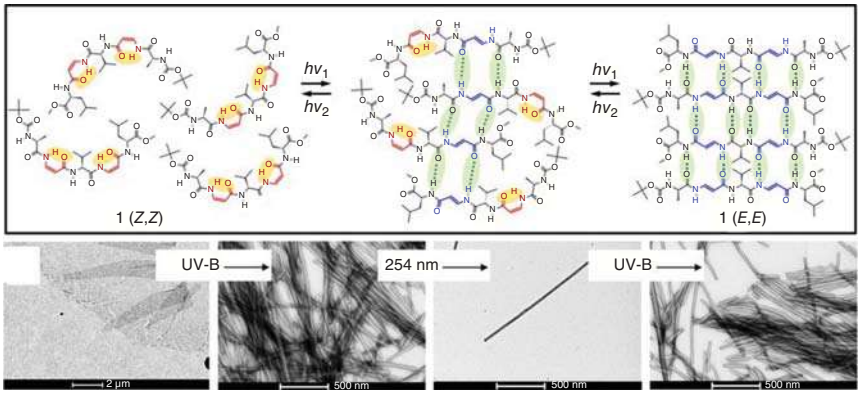


**Figure 40.5** A photoactive foldamer containing two photochromic 3-aminoprop-2-enoic acid units can interconvert from the *Z*-isomer stabilized with internal hydrogen bonds to the *E*-isomer with 290–320 nm ($h\nu_1$), and back to the *Z*-isomer with 254 nm ($h\nu_2$). The (*E,E*)-form can efficiently aggregate and seed the following aggregation of α-synuclein. Source: Marafon et al. [17]. Reproduced with permission from John Wiley & Sons, Inc.

Torner and Arora recently demonstrated photocontrol over the protein tertiary structure, by designing a conformationally defined coiled coil system. It was based on short so-called "cross-linked helix dimers" derived from tropomyosin, where the two helical peptides have been linked with an azobenzene unit in the backbone. A reversible 50% reduction in helicity was observed on CD spectra (at 222 nm) upon photoswitching (up to 90% of the *Z*-isomer was obtained upon irradiation with 370 nm). The conformational change did not require binding to a receptor, as in similar previously reported systems [18].

In addition to photocontrol over the peptide aggregation process, peptides with photochromic backbone segment can undergo light-induced activity modulation, resulting in, e.g. photoswitchable hormones. There, Podewin, Broichhagen, et al. designed and synthesized a small library of photoswitchable peptidomimetics based upon human atrial natriuretic peptide, containing AMPP in the backbone. One of the peptides – TOP271 – exhibited a fourfold difference in NPR-A-mediated cGMP synthesis *in vitro* upon photoisomerization, which is sufficient to cause large optically-induced conformational changes *ex vivo,* and transforms the NPR-A into an endogenous photoswitch [19]. Liraglutide is another peptide, whose backbone was appended with the AMPP unit. It is an agonist of a glucagon-like peptide 1 receptor, an incretin mimetic, and a promising agent in type 2 diabetes treatment. Its photochromic analog LirAzo afforded isomer-biased GLP-1R signaling as a result of differential activation of second messenger pathways in response to light. While the *E*-isomer primarily engages calcium influx, the *Z*-isomer favors cAMP generation. LirAzo thus allows optical control of insulin secretion and cell survival (Figure 40.6) [20].

Also the backbone of cyclic peptides has been appended with photoswitchable fragments, most often with azobenzenes [21]. An illustrative example is photocontrol over contracting muscle fibers. In skeletal muscles, the neural nitric oxide synthase (nNOS) interacts with α-1-syntrophin to recruit nNOS to the dystrophin-associated protein complex in the plasma membrane, which ultimately leads to muscle contraction. Replacing the natural α-1-syntrophin with its photochromic analog in the *E*-configuration enabled regular muscle contraction, unless the majority of it was photoisomerized to the respective *Z*-isomer. The shortening amplitude of the muscle fibers was then reduced to 96% of its initial value. This effect was comparable to the effect of the nonphotochromic nNOS inhibitor 3-bromo-7-nitroindazole. Additionally, a negative control confirmed that irradiation in the absence of the photochromic version of α-1-syntrophin had no effect [22]. Another example is the incorporation of diarylethene switches into the cyclic backbone of gramicidin S. It yielded a range of derivatives with photomodulated antibacterial and anticancer activity, as well as hemolytic cytotoxicity [23].

Apart from introduction into the peptide's backbone, or into its side chain, photochromic residues can also cross-link a peptide chain – usually an α-helix. This concept has been introduced by G.A. Woolley. In 2000, his group reported an azobenzene decorated in both *para*-positions with iodoacetamide rests, reactive

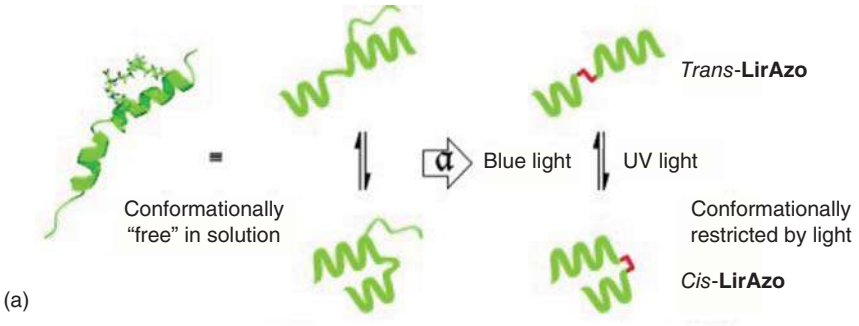


(a)

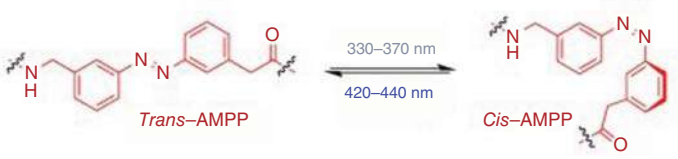


(b)

(c)

| | 7 | | | 17 | | | | | | | 27 | | | | 37 |
|---|---|---|---|---|---|---|---|---|---|---|---|---|---|---|---|
| **GLP–1 (7–37):** | $H_2N$–HAEGT | FTSDV | SSYLE | GQ--AAK | | | | | | | EFIAW | LVKGR | G–OH | | |
| **Liraglutide:** | $H_2N$–HAEGT | FTSDV | SSYLE | GQ--AAK (γEp) | | | | | | | EFIAW | LVRGR | G–OH | | |
| **Lira:** | $H_2N$–HAEGT | FTSDV | SSYLE | GQ--AAK | | | | | | | EFIAW | LVRGR | G–OH | | |
| **LirAzo:** | $H_2N$–HAEGT | FTSDV | SSYLE | AMPPAAK | | | | | | | EFIAW | LVRGR | G–OH | | |
| | ***** | ***** | ***** | | | | | | | | ***** | **:** | * | | |

**Figure 40.6** Logic, design, and primary structure of LirAzo. (a) The liraglutide NMR structure (PDB ID: 4apd) served as a template for the synthesis of LirAzo, which differs in the placement of AMPP (red) between the helices (α = azologization). (b) *Z*-AMPP and *E*-AMPP are formed upon illumination with UV and blue light, respectively. (c) The amino acid sequence of LirAzo, showing the replacement of 22G–23Q by AMPP (p = palmitoyl). Source: Reproduced with permission from Broichhagen et al. [20].

toward thiols and in particular – cysteine side chains [24]. The preliminary analysis demonstrated that its *Z*-photoisomer possesses optimal geometry for coupling simultaneously to two cysteine residues located in the distance of 7 amino acids (positions: *i, i + 7*) within an α-helix peptide, while the strain in the respective *E*-photoisomer would result in destabilization of the helix. Indeed, the reversible helix-coil transition has been observed for the peptide cross-linked with this bifunctional azobenzene. As the *Z*-photoisomer is in most cases not generated quantitatively, and is thermally unstable, the same group presented a complementary design with the coupling distance of 11 amino acids (positions *i, i + 11*), which comfortably accommodates the *E*-azobenzene cross-linker, while being distorted upon its photoisomerization to the *Z*-form [10]. The scope of this design has been expanded with water-soluble cross-linkers [25], azobenzenes switchable entirely with visible light [26], and alternative photochromic residues (Figure 40.7) [8, 27]. A detailed overview of applications of this system has been recently provided by Albert and Vázquez in their review on spatiotemporal control of biological functions [28].

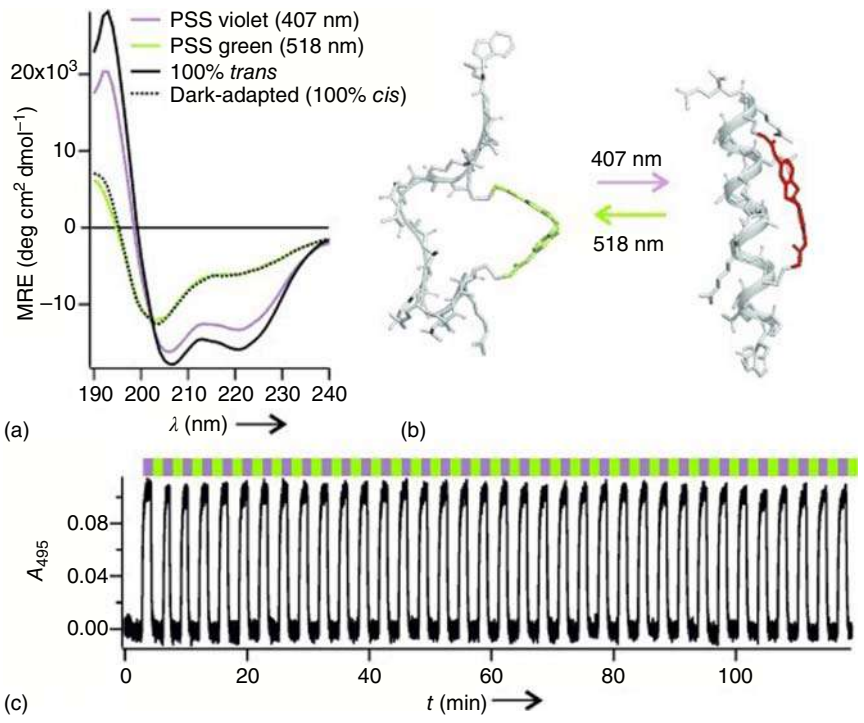


**Figure 40.7** Photoswitching of helical peptide conformation with a bridged azobenzene derivative. (a) CD spectra (5 mM PBS pH 7.0); (b) models showing the cross-linked peptide FK-11 (AcWGEACAREAAAREAACRQ-NH2) in the *Z* (left) and *E* (right) conformations; (c) multiple rounds of photoswitching in the presence of 5 mM reduced glutathione. Source: Reproduced with permission from the Samanta et al. [27].

## 40.4 Light-Activated Cell-Penetrating and Antimicrobial Peptides

For over 20 years, cell-penetrating peptides (CPPs) enable intracellular transport of all sorts of cargo particles, spanning from fluorophores and drugs, to nanoparticles. One of its most important applications is selective cargo delivery, for instance cytotoxic molecules into cancer cells. Selectivity of the delivery process toward particular cell types, or inside of an organism, can be tuned using specific recognition patterns. This approach is exemplified by oligoarginine CPPs protected with an oppositely charged oligoglutamate linked together with a MMP-2-sensitive loop. Latent cell penetration propensity of this construct is activated only in proximity of cancer cells, which overproduce the MMP-2 protease. This causes cleavage of the oligoglutamate fragments, and exposure of the oligoarginine motif [29]. From this angle, the idea of precise spatiotemporal photocontrol over the delivery process is a particularly interesting alternative.

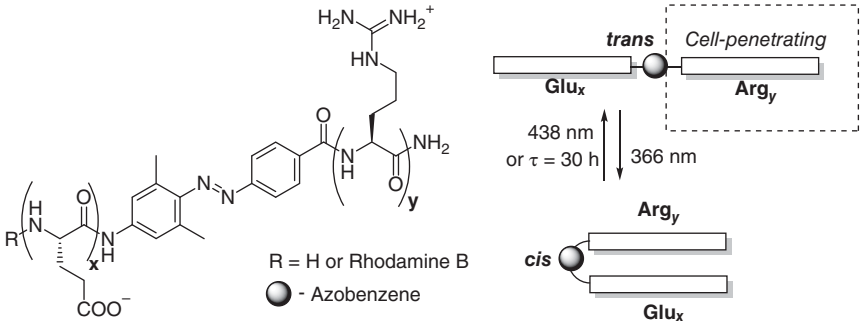


**Figure 40.8** The oligopeptide bearing oligoglutamate and oligoarginine fragments linked with an azobenzene efficiently penetrates HeLa cells as *E*-isomer. Upon irradiation with 366 nm and HPLC separation, the metastable *Z*-isomer does not penetrate the cells, until irradiated with 438 nm or thermally back-isomerized to the *E*-form. Source: Prestel and Möller [30].

Based on the successful "MMP-2" architecture, Prestel and Möller reported [30] oligoarginine CPPs stapled with an azobenzene linker to oligoglutamates. The *E*-isomer efficiently penetrates cells. In the *Z*-isomer, however, the oligoglutamate approaches the oligoarginine, neutralizes its charge, and, in consequence, inhibits the cell penetration (Figure 40.8). As the *E-Z* photoisomerization is not quantitative, full inhibition of the cell penetration can be only achieved upon HPLC purification of the impermeable *Z*-form.

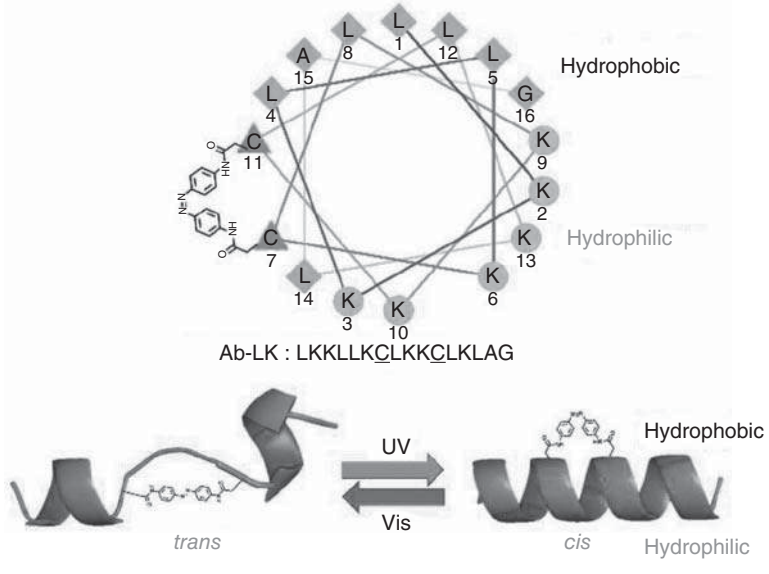


**Figure 40.9** Wheel diagram of the azobenzene-stapled LK peptide (Ab-LK) and principle for photoswitching of the helical structure. The *Z*-form is cell-permeable. Source: Reproduced with permission from the Kim et al. [31].

Using the concept of peptide cross-linking with an azobenzene unit, Kim et al. reported [31] photomodulation of cell penetration ability for an amphiphilic α-helical peptide composed of lysine and leucine units. The helical conformation is preserved for the *Z*-isomer and distorted in the *E*. The *E*-form penetrates mammalian cells (HeLa, HEK 293T, CHO-K1) only slightly (27% fluorescence-positive cells), while the *Z*-isomer – correctly folded – was significantly more efficient (76%), already at submicromolar concentrations (Figure 40.9).

Schober et al. synthesized a series of fluorescently labeled cationic cyclic oligopeptides (9–14-meric) containing diarylethene units in the backbone. The efficiency of cell penetration varied up to 6.5-fold between the closed and the open form [32].

García-López et al. demonstrated that molecular motors can open cell membranes by UV light-induced nanomechanical action. If the motor is additionally combined with directing peptide sequences, such as a short peptide targeting integrins or GRP78 occurring at the surface of particular cell types (e.g. cancer cells), this nanomechanical action can selectively target these cell-surface recognition sites [33]. This design has been extended to two-photon NIR activation, which enables deep tissue penetration, and can target cells with high spatiotemporal precision by adjusting the light focal plane (Figure 40.10) [34].

In 2014, the teams of Wu and Tian reported that lysine-containing oligopeptides decorated with spiropyrans at both termini demonstrated certain antimicrobial activity, mostly against Gram-positive bacteria. The activity was affected by the nature of spiropyran-peptide linker. However, its photomodulation was not reported [35]. Recently, Abell group demonstrated that replacement or addition of an azobenzene in a known antibacterial tetrapeptide bearing two *p*-phenyl-phenylalanine residues yielded compounds active against *Staphylococcus aureus,* where the activity increased fourfold upon UV-light-driven equilibration from the *E*- to the *Z*-enriched composition [36]. Similar activity photomodulation was observed earlier for several derivatives of a cyclic antimicrobial peptide gramicidin S bearing azobenzenes as a fragment of their cyclic backbones [37]. This design was complemented by the groups of Komarov and Ulrich with a collection of diarylethene-decorated gramicidin S analogs. Meaningful differences in antimicrobial activity upon photoisomerization, as well as selectivity toward bacterial vs. mammalian cells, have been reported [23] (Figure 40.11).

## 40.5 Photochromic Gelators

Gels are soft materials that use solid 3D-cross-linked polymeric networks (covalent or supramolecular) to immobilize solvents, which often exceed 99% of its total mass. Gelatin, agar, or silicone-based gelators form stable covalent hydrogels with a broad range of applications in biology and medicine (e.g. implants, contact lenses). Supramolecular gels, on the other hand, are formed by self-assembly of low-molecular-weight gelators (LMWGs). Gelation in supramolecular systems is usually reversible, and such materials are often self-healing. Combination of supramolecular hydrogelators with molecular photoswitches results in smart

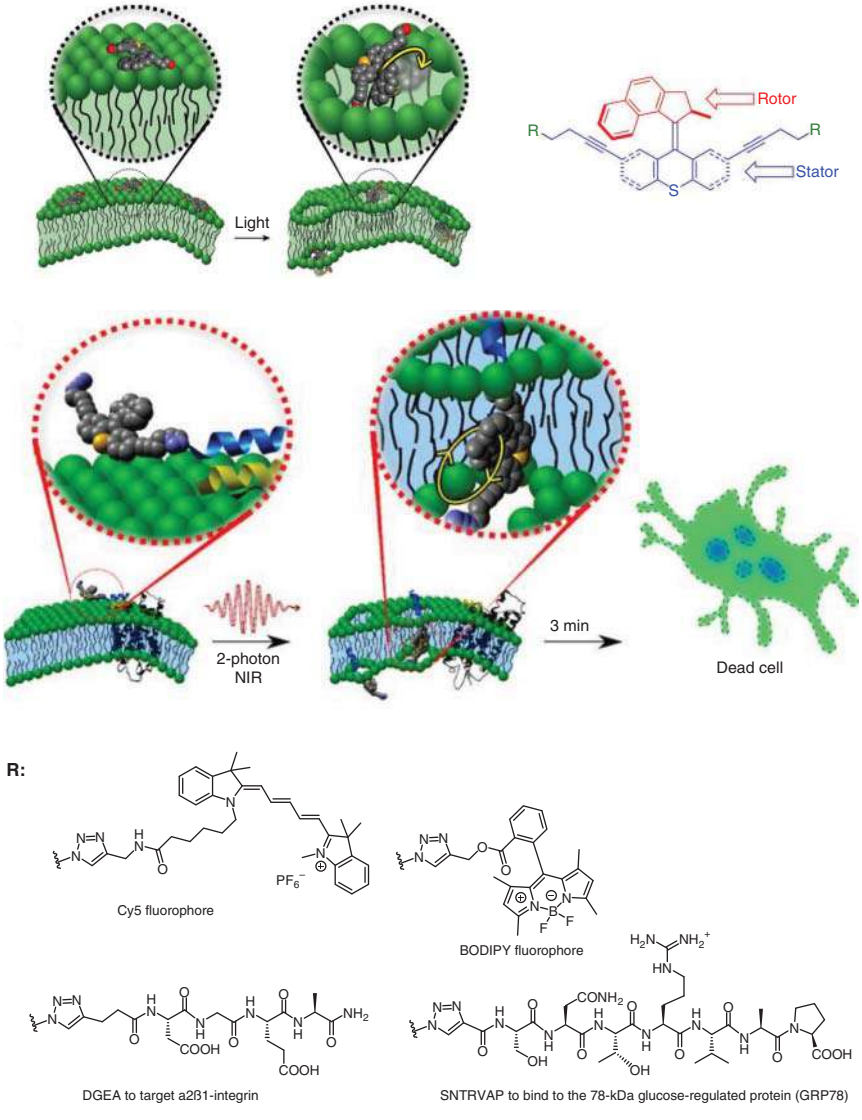


**Figure 40.10** Molecular nanomachines activated with UV- (top) or NIR-light (middle) for disruption of lipid bilayers through molecular mechanical action. The substituents **R** bear fluorophores for tracking the molecular movement, or peptides which target proteins overexpressed on surface of cancer cells (PC3 or MCF7). Source: Reprinted with permission from García-López et al. [33] and from Liu et al. [34].

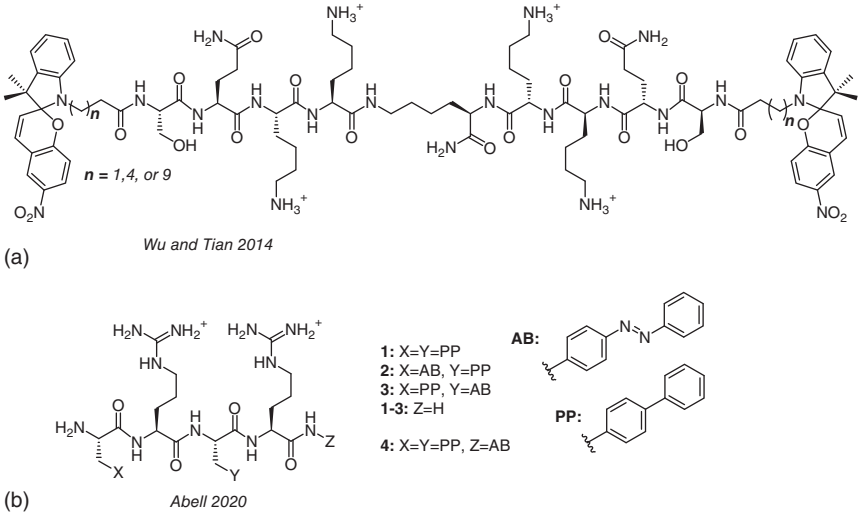


**Figure 40.11** Antimicrobial photochromic peptides based on (a) spiropyrans or (b) azobenzenes.

materials, which change their physical properties reversibly upon irradiation, and can be used, e.g. for light-controlled cargo release with potential for therapeutic applications [38]. Several systems of that nature, based on photochromic peptides, have been reported. The group of Díaz Díaz demonstrated a range of azobenzene-decorated peptide LMWG with light-modulated self-assembly process in organic solvents, which formed multistimuli-responsive organogels [39]. Later, the same group applied some of the tetrapeptides as LMWG for removal of organic solvents and toxic dyes from the surface of aqueous phases, with the long-term goal to create a material that could deal with oils spills on rivers and oceans [40]. The teams of Browne and Feringa demonstrated a tripeptide motif decorated with dithienylethene, which could gelate water under acidic and neutral conditions. While photoisomerization did not cause gel dissipation, it resulted in color change between red and bright yellow. This effect was used to write a message on the gel using masks upon sample irradiation [41]. The group of Zhang reported that a dipeptide D-Ala-D-Ala decorated with spiropyran forms a hydrogel, which exhibits dual response – to light and ligand–receptor interactions (with 1 eq. vancomycin) [42]. The group of Ravoo demonstrated a hierarchical supramolecular hydrogel (Fmoc-RGDS + Fmoc-RGDS-AAP) with the tetrapeptide partially (10%) labeled with arylazopyrazole (AAP). An efficient and reversible switching between gel and liquid state with UV and visible light, respectively, has been demonstrated, along with light-controlled release of encapsulated fluorescein and cyclodextrin vesicles filled with fluorescent cholesterol derivatives [43]. Later on, the same group reported AAP-decorated FGDS tetrapeptide, which in combination with covalent nonresponsive agarose network, yields a robust hybrid hydrogel with phototunable mechanical properties and shape memory [44]. The group of Pianowski proposed an alternative design, based on the report from the Nachtsheim

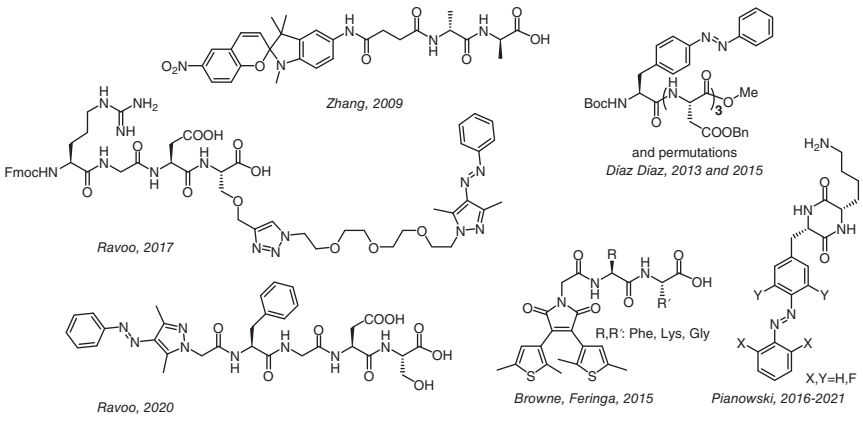


**Figure 40.12** Photochromic peptide-based supramolecular gelators.

group [45] who demonstrated that phenylalanine-containing cyclic dipeptides (2,5-diketopiperazines, DKP) bearing polar side chains are efficient low-MW hydrogelators. Replacement of the nonpolar phenyl ring with azobenzene residues, which reversibly change their polarity upon photoisomerization, enabled effective photocontrol over the self-assembly process of the gel-forming supramolecular fibers. Initially, UV [46] and later also visible light (by using fluorinated azobenzenes) [47] was applied to dissipate hydrogels into non-viscous fluids. Using a hydrogel loaded with an antibiotic, bacterial growth could be controlled with green light [47a]. By exploiting the supramolecular nature of the gel, it was doped it with a potent anticancer agent that was quickly released with green light, but showed negligible leaking in darkness [47b]. The latter material rises hope for further therapeutic applications. Later, it has been discovered that *ortho*-fluorinated azobenzenes with conjugated unsaturated substituents (–CHO, –C=C–) can be efficiently $E \rightarrow Z$ isomerized with red light (>630 nm) – within the "therapeutic window" [48]. A DKP gelator analog bearing this photochromic motif forms a viscous material that dissipated with red light to nonviscous fluid. This observation may also enhance the scope of therapeutic applications for azobenzene-based materials (Figure 40.12).

## 40.6 Photochromic Peptide-Derived Structures and Their Applications

Numerous peptide-derived oligomers with various degrees of structural modifications have been applied in biological context. Their function can be also photomodulated by the incorporation of molecular photoswitches using synthetic strategies similar to the preparation of photochromic peptides. This class of compounds is exemplified by photochromic peptoids and peptide nucleic acids (PNAs).

Peptoids and PNAs are synthetic oligomers with polyamide backbones that can mimic biopolymers and can be sequence-specifically synthesized via solid phase

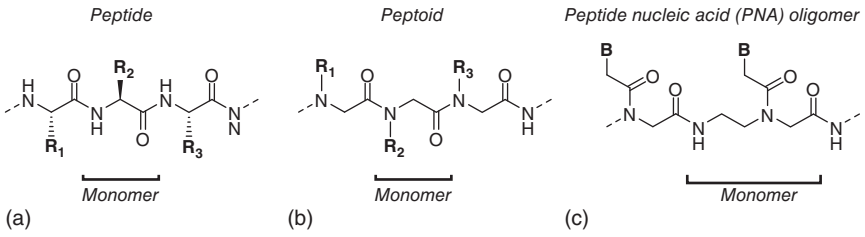


**Figure 40.13** Comparison between structures of (a) a polypeptide, (b) a peptoid and (c) a peptide nucleic acid (PNA) oligomer. Marked monomeric units correspond to one amino acid, an *N*-substituted glycine, or to a 2-(2′-aminoethyl)glycine unit, respectively. The residues $\mathbf{R}_n$ usually correspond to side chains of proteinogenic amino acids, while **B** stands for canonical DNA nucleobases (adenine, cytosine, guanine, or thymine).

synthesis [49]. Whereas in peptides the side chains are appended to the α-carbon, PNA oligomers and peptoids carry the side chains connected to the nitrogen atoms (Figure 40.13). Peptoids, alternatively described as poly-*N*-substituted glycines, are usually decorated with side chains similar to those in peptides and are applied as peptidomimetics – for example antimicrobial or anticancer agents resistant to proteolysis [49, 50]. PNAs are synthetic analogs of oligonucleotides. The side chains of PNA oligomers contain canonical purine and pyrimidine nucleobases. In combination with proper chain geometry of the 2-(aminoethyl)glycine backbone this results in sequence-specific hybridization to complementary DNA or RNA strands, yielding highly stable duplet or triplet helices (through Watson-Crick and Hoogsteen base pairing, respectively). PNAs are resistant on both nucleases and proteases. Therefore, they can be used for *in vivo* oligonucleotide sensing [51], or as potent antisense agents [52].

Photoswitchable peptoids are attractive scaffolds for photomodulation of biological activity. In 2008, Shah and Kirshenbaum reported the successful synthesis of a peptoid bearing an azobenzene side chain that can be interconverted between an *E* and a *Z* form [53].

To constrain the overall flexibility, peptoid macrocycles of various sizes have been synthesized in the Bräse group. Octameric macrocycles have been decorated, and ultimately also cross-linked with double azobenzene units using biorthogonal copper-catalyzed alkyne-azide [3+2] cycloaddition (CuAAC). Alternating irradiation with UV and blue light reversibly changed the conformation of such systems [54].

By incorporating photoswitchable groups into the PNA oligomer, the hybridization to complementary strands can be controlled in a reversible manner. Stafforst and Hilvert demonstrated an Fmoc-protected PNA monomer that bears an azobenzene moiety instead of a nucleobase. This monomer was incorporated site specifically into PNA oligomers. It was observed that the melting temperature of an examined $PNA_2$/DNA triplex of the photoswitchable PNA with complementary DNA strands was lowered upon *E*-to-*Z* isomerization. Formation of the *E*-$PNA_2$/DNA triplex efficiently blocked the transcription of two investigated genes by the T7 RNA polymerase, while inhibition with the corresponding *Z*-isomers

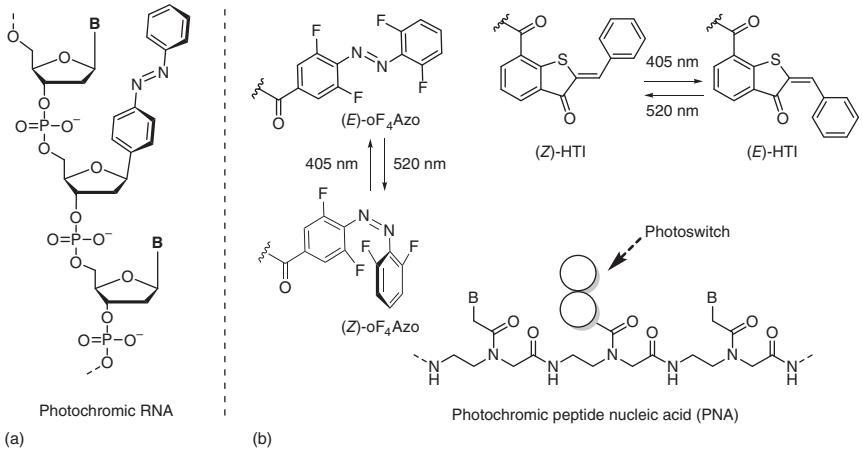


**Figure 40.14** Comparison between structures of a photochromic RNA oligomer decorated with (a) azobenzene [57], and (b) photochromic peptide nucleic acid (PNA) oligomers decorated either with a fluorinated azobenzene (*o*$F_4$Azo) or hemithioindigo (HTI) photoswitch. **B** stands for canonical nucleobases – adenine, cytosine, guanine, and either uracil (RNA) or thymine (PNA).

was observed to be two times weaker [55]. Sawada et al. were able to control the formation of $PNA_2$/DNA triplex structures by implementing tail-clamp PNA that contain azobenzene in the ethylene glycol-type linker that connects two homopyrimidine PNA strands. Upon irradiation, the dimeric TC-PNA/DNA complex was converted to a trimeric TC-PNA/DNA complex [56]. Vàzquez group expanded this methodology and designed two new types of photoswitchable PNA by incorporating a fluorinated azobenzene (F4Azo) and hemithioindigo (HTI) photoswitch (Figure 40.14), both responsive to visible light, and demonstrating reversible control over hybridization to complementary DNA [58].

Another type of polyamides that can interact with DNA are minor groove-binding imidazole/pyrrole polyamides that selectively bind to distinct sequences of double-stranded DNA. Sewald group synthesized azobenzene-bearing analogs of these polyamides that enable light-induced binding. Their results showed that the thermodynamically more stable *E*-isomer of the polyamide does not bind to the respective DNA sequence. Upon irradiation, the corresponding *Z*-isomers are formed and bind to hairpin structures of double-stranded DNA [59].

## 40.7 Pathways to Photochromic Proteins

Site-selective incorporation of small photochromic molecules into proteins in order to photomodulate biological processes (such as e.g. catalytic activity of enzymes) is, as mentioned earlier, a much more complex challenge than in the case of short peptides. Chemoselective functionalization of proteins for the photopharmacology purposes has been pioneered by the group of Trauner. It can be

exemplified by appending nicotinic acetylcholine receptors with photoswitchable tethered agonists and antagonists. The modified receptors showed activation or inhibition, respectively, caused with deep-violet light, but responded normally to acetylcholine in darkness [60]. This approach required engineering of additional cysteine residues in the receptor at the optimal positions to install the photochromic ligand functionalized with maleimide or other thiol-reactive groups. Recently, Trauner group published an excellent review on *in vivo* photopharmacology, where numerous successful approaches to chemoselective protein functionalization with photochromic molecules have been systematically described [61]. Particular areas of applications have been also described by Gorostiza, Fehrentz and Broichhagen in the respective chapters of this book.

An alternative to the chemoselective attaching of photoswitchable ligands is biosynthetic incorporation of molecular photoswitches in the form of unnatural amino acids using amber codon suppression technology and its modifications. In this technique, the host organism is enriched with two components coming from a distant and usually unrelated organism – an engineered tRNA with the anticodon to the UAG sequence (the "amber" stop codon) and an enzyme (an aminoacyl-tRNA synthetase) that is capable of loading this and only this tRNA molecule with the unnatural amino acid (and none of the 20 proteinogenic ones). Both of these species are not recognized by the native enzymatic set of the host organism, and thus considered "orthogonal." Various combinations of host cells and sources of the "orthogonal pair" have been demonstrated, including bacterial, archeal, yeast, and mammalian origin. For each new photochrome (or any other unnatural amino acid), this method requires a selection process of a new orthogonal tRNA/aminoacyl-tRNA synthetase pair. Then, the orthogonal tRNA loaded with the photochromic amino acid recognizes the UAG codon, which under normal conditions terminates biosynthesis of the peptide chain growing on a ribosome. The UAG codon is introduced into the gene transcript at the position of the desired modification. The canonical meaning of "UAG" in that particular case is re-assigned by introduction of the orthogonal tRNA/synthethase pair. If the unnatural amino acid is provided in the cell culture medium, the desired photochromic mutant of the protein is biosynthesized [62]. Deficit of the unnatural substrate, and/or its inefficient incorporation results in the truncated version of the protein, which can be often separated from the desired product after isolation from cells. This idea has been illustrated with photochromic modification of a glutamate receptor NMDA, where one of the two subunits was appended with an azobenzene-bearing unnatural amino acid (PSAA). Significant photomodulation of the modified receptor's activity has been demonstrated upon alternating irradiation with 365 nm and 460 nm light (Figure 40.15) [63].

The biosynthesis of a mutant protein containing an azobenzene side chain was first demonstrated by the group of P. Schultz in 2006. For this purpose, an orthogonal tRNA/aminoacyl tRNA synthetase pair derived from an archaeon *M. jannaschii* was engineered to accept the (*S*)-4-(phenylazo)-phenylalanine (AzoPhe, also abbreviated as PAP at the Scheme 40.3) inside of the *Escherichia coli* (bacteria) host organism, and translate it in response to the amber codon [64]. This system was applied for the

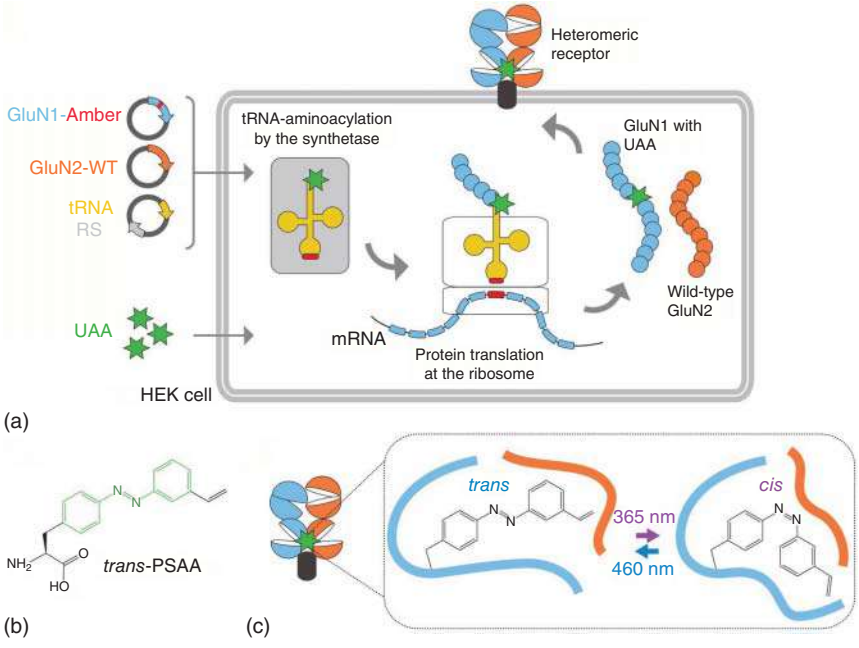


**Figure 40.15** Schematic representation for synthesis of a photochromic protein heterodimer using the amber codon suppression methodology. (a) Cells are transfected with a targeted gene containing an introduced amber stop codon (*red*) at a desired position, and with an orthogonal suppressor tRNA (*yellow*)/aminoacyl synthetase (RS; *gray*) pair. The cells are incubated in the presence of the photochromic unnatural amino acid (UAA) (here – azobenzene-based PSAA, *green asterisks*), and produce the desired UAA-protein. (b) Structure of the PSAA. (c) Diagram of a NMDAR GluN1/GluN2 heterodimer carrying a PSAA at the ABD dimer interface. Remarkable structural changes that impact the receptor activity occur reversibly upon photoisomerization. Source: Klippenstein et al. [63].

biosynthesis of a photoswitchable analog of the *E. coli* catabolite activator protein (CAP) (a transcriptional activator). The activity of CAP correlates with the concentration of cAMP. The binding of cAMP to CAP induces conformational changes in the homodimeric protein that leads to an increased binding affinity to its promoter. In consequence, the transcription from CAP-dependent promoters is enhanced. The introduction of AzoPhe in close proximity to amino acids that are involved in the binding of cAMP resulted in a mutant CAP whose binding affinity to its promoter could be photomodulated. After irradiation with 334 nm UV light, a fourfold reduction of the binding constant of the mutated CAP to the promoter was observed.

Since then, AzoPhe and its red-shifted analogs were site-specifically incorporated via amber codon suppression into various proteins in *E. coli* [65] and in mammalian cells [66]. The group of Deiters genetically encoded two fluorinated AzoPhe analogs (Figure 40.16) in bacteria and mammalian cells with archaeal *Methanosarcina barkeri* $tRNA_{CUA}$/pyrrolysyl-tRNA synthetase pairs, which are orthogonal in both types of the host organisms. The introduction of fluorine substituents in azobenzene promotes an increased thermal stability of the respective *Z*-isomer and allows reversible

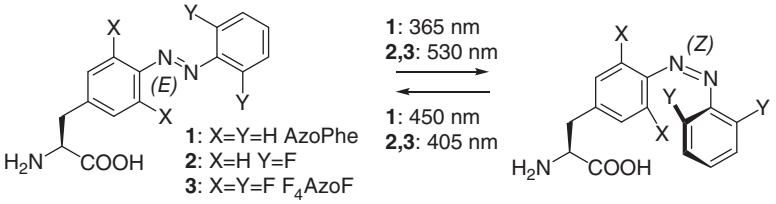


**Figure 40.16** Genetically encoded azobenzene-decorated amino acids. The $E \rightarrow Z$ isomerization of AzoPhe (sometimes also abbreviated as "PAP") **1** is triggered with UV light, while the fluorinated analogs **2** and **3** can be switched with more biocompatible visible light frequencies (green). Source: Modified from Luo et al. [67].

photoswitching with visible light, which is more suitable for biological applications, than UV frequencies [67]. Especially $F_4$AzoPhe (an AzoPhe analog with four fluorine atoms located *ortho* to the azo bond) proved to be optimal for the reversible control of biological functions at longer time spans (hours/days). It was incorporated into the bioluminescent firefly luciferase. Upon irradiation with green light, the chemiluminescence was significantly reduced. This effect was stable for a minimum of 24 hours under physiological conditions and reversible over five switching cycles.

Yet another strategy to incorporate molecular photoswitches site-specifically into proteins in living mammalian cells is the genetically encoded bioorthogonal ligand tethering (BOLT). In this case, the incorporated unnatural amino acid is not photoswitchable itself, but it contains a biorthogonal reactive group. After biosynthesis of the respective mutant protein, a molecular photoswitch can be covalently attached to the side chain via a suitable linker in a bioorthogonal ligation reaction (Figure 40.17) [68]. In 2015 the group of Chin reported the selective inhibition of MEK1, which is a kinase involved in a signaling pathway that regulates growth and development. A mutant of MEK1 with a genetically encoded reactive amino acid was biosynthesized and an inhibitor of MEK1 was coupled to an azobenzene-containing linker that specifically reacts with the unnatural amino acid in presence of other amino acid side chains and biomolecules. After this bioorthogonal ligation, the inhibitor is covalently attached to MEK1 via a photoswitchable linker. In the *E*-configuration, the relative position of MEK1 and its inhibitor promotes the binding and results in inhibition of the kinase activity of MEK1. Irradiation with 360 nm causes *E*-to-*Z* photoisomerization of the azobenzene linker, which due to the geometry change causes dissociation of the bound inhibitor. After irradiation of the cells with 440 nm or thermal relaxation of the *Z*- to the respective *E*-isomer, the inhibition is re-established. Overall, this architecture enabled reversible photocontrol of the inhibitor activity.

The two previously presented approaches can be complemented with genetic incorporation of an unnatural amino acid that contains azobenzene side chain decorated with an additional biocompatible reactive group. After biosynthesis of the respective mutant protein, spatial proximity to a reactive position (e.g. a cysteine side chain) can lead to spontaneous formation of covalent bonds, resulting in azobenzene bridges that later enable optical modulation of the protein conformation [66]. The group of Wang designed four azobenzene-derived amino

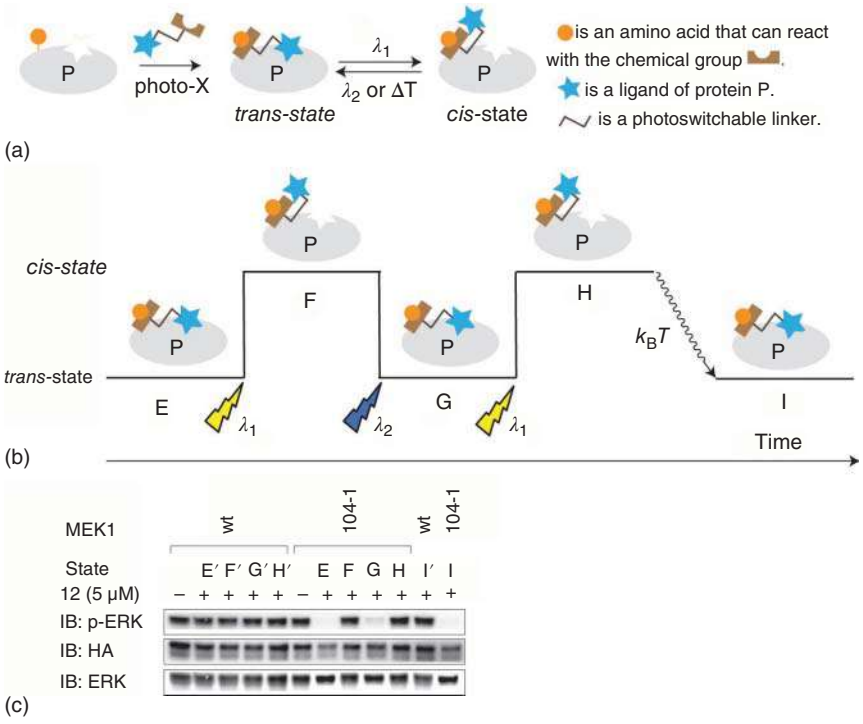


**Figure 40.17** The biorthogonal ligand tethering (BOLT) strategy to install a photochromic ligand on a protein. (a) The protein is expressed with a reactive unnatural amino acid, which bioorthogonally reacts with an added photochromic ligand. The geometry of one photoisomer promotes binding of an attached ligand to the active site, while the other photoisomer with unfavorable geometry cannot efficiently inhibit the site; (b) the isomers can be switched by irradiation or thermally (H→I). Source: Reproduced with permission from Tsai et al. [68]. Copyright (2015), SpringerNature.

acids that bear thiol-reactive groups and the corresponding tRNA/pyrrolysyl-tRNA synthetase pairs that allow their biosynthetic incorporation into proteins in bacteria and mammalian cells (Figure 40.18) [65b].

## 40.8 Summary

The combination of light and photoswitchable peptides or proteins provides researchers with a plethora of previously unattainable ways to precisely control biological systems or peptide-based materials. In this chapter, we summarized synthetic and biosynthetic methods of introducing photochromic residues into peptide-based systems. We have demonstrated, how photochromic systems can be used to photomodulate complex biological setups and how they were applied in peptide aggregation studies. We have demonstrated the ways of photocontrol over antimicrobial activity, cell penetration, or gelation processes based on photochromic peptides, as well as possible applications of photochromic

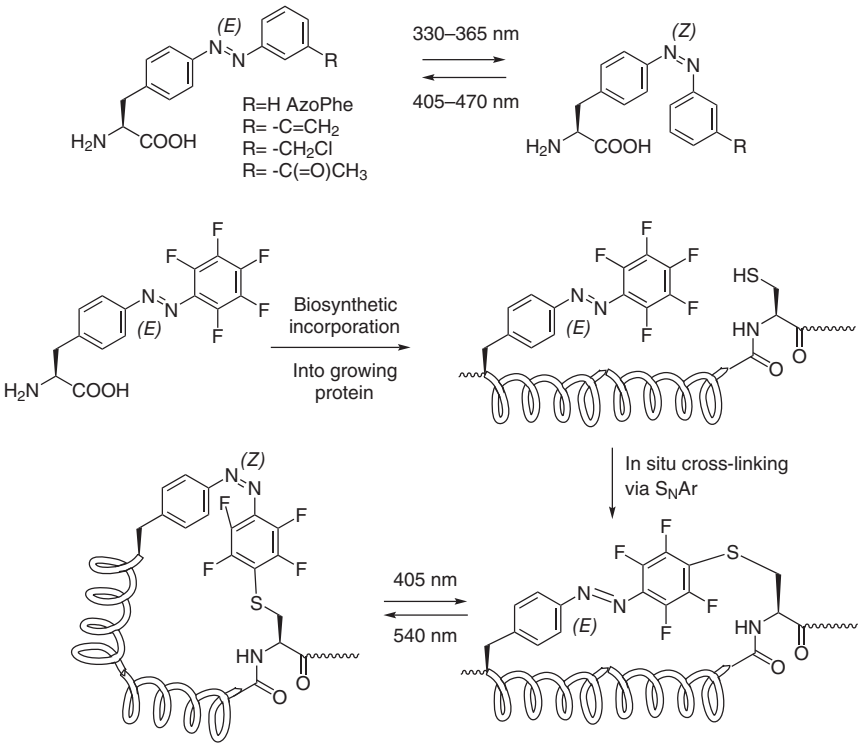


**Figure 40.18** Genetic incorporation of unnatural amino acids bearing reactive azobenzene derivatives. Upon subsequent cyclization, the cross-linked proteins can reversibly change their conformation, and undergo activity photomodulation with UV, or entirely within visible light frequencies. Source: Modified from Hoppmann and Wang [69].

peptide-derived structures – peptoids and PNAs. Finally, we provided an overview over available methods to combine molecular photoswitches with proteins, and the scope of applications for the resulting photochromic proteins. We believe that this chapter will inspire our readers to develop new methodologies and applications in this extremely interesting and vibrant area of research.

## References


1 Tuinstra, R.L., Peterson, F.C., Kutlesa, S. et al. (2008). *Proc. Natl. Acad. Sci.* 105: 5057–5062.

2 Palomo, J.M. (2014). *RSC Adv.* 4: 32658–32672.

3 Goodman, M. and Kossoy, A. (1966). *J. Am. Chem. Soc.* 88: 5010.

4 (a) Sato, M., Kinoshita, T., Takizawa, A. et al. (1989). *Polym. J.* 21: 533–541. (b) Fissi, A., Pieroni, O., Ruggeri, G., and Ciardelli, F. (1995). *Macromolecules* 28: 302–309. (c) Angelini, N., Corrias, B., Fissi, A. et al. (1998). *Biophys. J.* 74: 2601–2610. (d) Fissi, A., Pieroni, O., Ciardelli, F. et al. (1993). *Biopolymers* 33:

1505–1517. (e) Vandewyer, P.H. and Smets, G. (1970). *J. Polym. Sci., Part A: Polym. Chem.* 8: 2361–2374.

**5** Aemissegger, A. and Hilvert, D. (2007). *Nat. Protoc.* 2: 161–167.

**6** Babii, O., Afonin, S., Berditsch, M. et al. (2014). *Angew. Chem. Int. Ed. Engl.* 53: 3392–3395.

**7** (a) Zeyat, G. and Rück-Braun, K. (2012). *Beilstein J. Org. Chem.* 8: 890–896. (b) Kitzig, S. and Ruck-Braun, K. (2017). *J. Pept. Sci.* 23: 567–573.

**8** Preußke, N., Moormann, W., Bamberg, K. et al. (2020). *Org. Biomol. Chem.* 18: 2650–2660.

**9** (a) Kusebauch, U., Cadamuro, S.A., Musiol, H.-J. et al. (2006). *Angew. Chem.* 118: 7170–7173. (b) Woolley, G.A. (2005). *Acc. Chem. Res.* 38: 486–493. (c) Zhang, F., Zarrine-Afsar, A., Al-Abdul-Wahid, M.S. et al. (2009). *J. Am. Chem. Soc.* 131: 2283–2289.

**10** Flint, D.G., Kumita, J.R., Smart, O.S., and Woolley, G.A. (2002). *Chem. Biol.* 9: 391–397.

**11** (a) Lougheed, T., Borisenko, V., Hennig, T. et al. (2004). *Org. Biomol. Chem.* 2: 2798–2801. (b) Lien, L., Jaikaran, D.C.J., Zhang, Z., and Woolley, G.A. (1996). *J. Am. Chem. Soc.* 118: 12222–12223. (c) Borisenko, V., Burns, D.C., Zhang, Z., and Woolley, G.A. (2000). *J. Am. Chem. Soc.* 122: 6364–6370.

**12** Nuti, F., Gellini, C., Larregola, M. et al. (2019). *Front. Chem.* 7: 180.

**13** Aemissegger, A., Krautler, V., van Gunsteren, W.F., and Hilvert, D. (2005). *J. Am. Chem. Soc.* 127: 2929–2936.

**14** Dong, S.-L., Löweneck, M., Schrader, T.E. et al. (2006). *Chem. Eur. J.* 12: 1114–1120.

**15** (a) Rampp, M.S., Hofmann, S.M., Podewin, T. et al. (2018). *Chem. Phys.* 512: 116–121. (b) Schrader, T.E., Cordes, T., Schreier, W.J. et al. (2011). *J. Phys. Chem. B* 115: 5219–5226. (c) Hofmann, S.M., Frost, C.V., Podewin, T. et al. (2020). *J. Phys. Chem. B* 124: 5113–5121.

**16** Deeg, A.A., Schrader, T.E., Kempter, S. et al. (2011). *ChemPhysChem* 12: 559–562.

**17** Marafon, G., Crisma, M., Masato, A. et al. (2021). *Angew. Chem. Int. Ed.* 60: 5173–5178.

**18** Torner, J.M. and Arora, P.S. (2021). *Chem. Commun.* 57: 1442–1445.

**19** Podewin, T., Broichhagen, J., Frost, C. et al. (2017). *Chem. Sci.* 8: 4644–4653.

**20** Broichhagen, J., Podewin, T., Meyer-Berg, H. et al. (2015). *Angew. Chem. Int. Ed.* 54: 15565–15569.

**21** (a) Renner, C., Kusebauch, U., Loweneck, M. et al. (2005). *J. Pept. Res.* 65: 4–14. (b) Renner, C. and Moroder, L. (2006). *ChemBioChem* 7: 868–878.

**22** Hoppmann, C., Schmieder, P., Domaing, P. et al. (2011). *Angew. Chem. Int. Ed. Engl.* 50: 7699–7702.

**23** Babii, O., Afonin, S., Ishchenko, A.Y. et al. (2018). *J. Med. Chem.* 61: 10793–10813.

**24** Kumita, J.R., Smart, O.S., and Woolley, G.A. (2000). *Proc. Natl. Acad. Sci.* 97: 3803–3808.

**25** Zhang, Z., Burns, D.C., Kumita, J.R. et al. (2003). *Bioconjugate Chem.* 14: 824–829.

**26** (a) Beharry, A.A., Sadovski, O., and Woolley, G.A. (2011). *J. Am. Chem. Soc.* 133: 19684–19687. (b) Samanta, S., Babalhavaeji, A., Dong, M.-x., and Woolley, G.A. (2013). *Angew. Chem. Int. Ed.* 52: 14127–14130.

**27** Samanta, S., Qin, C., Lough, A.J., and Woolley, G.A. (2012). *Angew. Chem. Int. Ed.* 51: 6452–6455.

**28** Albert, L. and Vázquez, O. (2019). *Chem. Commun.* 55: 10192–10213.

**29** Jiang, T., Olson, E.S., Nguyen, Q.T. et al. (2004). *Proc. Natl. Acad. Sci. U.S.A.* 101: 17867–17872.

**30** Prestel, A. and Möller, H.M. (2016). *Chem. Commun.* 52: 701–704.

**31** Kim, G.C., Ahn, J.H., Oh, J.H. et al. (2018). *Biomacromolecules* 19: 2863–2869.

**32** Schober, T., Wehl, I., Afonin, S. et al. (2019). *ChemPhotoChem* 3: 384–391.

**33** García-López, V., Chen, F., Nilewski, L.G. et al. (2017). *Nature* 548: 567–572.

**34** Liu, D., García-López, V., Gunasekera, R.S. et al. (2019). *ACS Nano* 13: 6813–6823.

**35** Chen, L., Zhu, Y., Yang, D. et al. (2014). *Sci. Rep.* 4: 6860.

**36** Yeoh, Y.Q., Horsley, J.R., Yu, J. et al. (2020). *ChemMedChem* 15: 1505–1508.

**37** Yeoh, Y.Q., Yu, J., Polyak, S.W. et al. (2018). *ChemBioChem* 19: 2591–2597.

**38** Draper, E.R. and Adams, D.J. (2016). *Chem. Commun.* 52: 8196–8206.

**39** Fatás, P., Bachl, J., Oehm, S. et al. (2013). *Chem. Eur. J.* 19: 8861–8874.

**40** Bachl, J., Oehm, S., Mayr, J. et al. (2015). *Int. J. Mol. Sci.* 16: 11766–11784.

**41** van Herpt, J.T., Stuart, M.C., Browne, W.R., and Feringa, B.L. (2014). *Chemistry* 20: 3077–3083.

**42** Qiu, Z., Yu, H., Li, J. et al. (2009). *Chem. Commun.* 3342–3344.

**43** Chu, C.-W. and Ravoo, B.J. (2017). *Chem. Commun.* 53: 12450–12453.

**44** Nowak, B.P. and Ravoo, B.J. (2020). *Soft Matter* 16: 7299–7304.

**45** Kleinsmann, A.J. and Nachtsheim, B.J. (2013). *Chem. Commun.* 49: 7818–7820.

**46** Pianowski, Z.L., Karcher, J., and Schneider, K. (2016). *Chem. Commun.* 52: 3143–3146.

**47** (a) Karcher, J. and Pianowski, Z.L. (2018). *Chem. Eur. J.* 24: 11605–11610. (b) Karcher, J., Kirchner, S., Leistner, A.-L. et al. (2021). *RSC Adv.* 11: 8546–8551.

**48** Leistner, A.-L., Kirchner, S., Karcher, J. et al. (2021). *Chem. Eur. J*. 27: 8094–8099.

**49** Zuckermann, R.N. (2011). *Biopolymers* 96: 545–555.

**50** Yoo, B. and Kirshenbaum, K. (2008). *Curr. Opin. Chem. Biol.* 12: 714–721.

**51** Pianowski, Z., Gorska, K., Oswald, L. et al. (2009). *J. Am. Chem. Soc.* 131: 6492–6497.

**52** Thomas, S.M., Sahu, B., Rapireddy, S. et al. (2013). *ACS Chem. Biol.* 8: 345–352.

**53** Shah, N.H. and Kirshenbaum, K. (2008). *Org. Biomol. Chem.* 6: 2516–2521.

**54** Herlan, C.N., Sommer, K., Weis, P. et al. (2021). *Molecules* 26: 150.

**55** Stafforst, T. and Hilvert, D. (2010). *Angew. Chem. Int. Ed.* 49: 9998–10001.

**56** Sawada, S., Takao, T., Kato, N., and Kaihatsu, K. (2017). *Molecules* 22.

**57** Goldau, T., Murayama, K., Brieke, C. et al. (2015). *Chem. Eur. J.* 21: 2845–2854.


**58** Zhang, L., Linden, G., and Vazquez, O. (2019). *Beilstein J. Org. Chem.* 15: 2500–2508.
**59** Muller, S., Paulus, J., Mattay, J. et al. (2020). *Beilstein J. Org. Chem.* 16: 60–70.
**60** Tochitsky, I., Banghart, M.R., Mourot, A. et al. (2012). *Nat. Chem.* 4: 105–111.
**61** Hüll, K., Morstein, J., and Trauner, D. (2018). *Chem. Rev.* 118: 10710–10747.
**62** Noren, C.J., Anthonycahill, S.J., Griffith, M.C., and Schultz, P.G. (1989). *Science* 244: 182–188.
**63** Klippenstein, V., Hoppmann, C., Ye, S. et al. (2017). *eLife* 6.
**64** Bose, M., Groff, D., Xie, J. et al. (2006). *J. Am. Chem. Soc.* 128: 388–389.
**65** (a) John, A.A., Ramil, C.P., Tian, Y.L. et al. (2015). *Org. Lett.* 17: 6258–6261. (b) Hoppmann, C., Maslennikov, I., Choe, S., and Wang, L. (2015). *J. Am. Chem. Soc.* 137: 11218–11221.
**66** Hoppmann, C., Lacey, V.K., Louie, G.V. et al. (2014). *Angew. Chem. Int. Ed.* 53: 3932–3936.
**67** Luo, J., Samanta, S., Convertino, M. et al. (2018). *ChemBioChem* 19: 2178–2185.
**68** Tsai, Y.H., Essig, S., James, J.R. et al. (2015). *Nat. Chem.* 7: 554–561.
**69** Hoppmann, C. and Wang, L. (2019). *Methods Enzymol.* 624: 249–264.

# 41 Photochromic Carbohydrate Conjugates

Guillaume Despras, Vivek Poonthiyil, and Thisbe K. Lindhorst

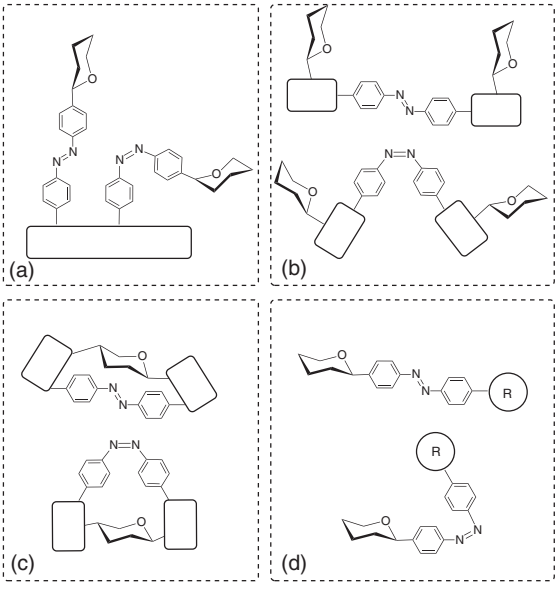


**Characteristic Features**

Optoglycomics: *Cis/trans* isomerization of azobenzene-based glycoconjugates (ABGs) can be used to modulate carbohydrate function on different levels: the orientation of a carbohydrate ligand can be controlled on a surface (glyco-SAMs) (a), the overall shape of a linear or cyclic molecule can be altered (b, c) or the ligand properties/affinities of azobenzene glycosides can be tuned; mechanisms of carbohydrate recognition on cell surfaces (glycocalyx) can be addressed.

**Key References**

Weber, T., Chandrasekaran, V., Stamer, I., et al. (2014). Switching of bacterial adhesion to a glycosylated surface by reversible reorientation of the carbohydrate ligand. *Angew. Chem. Int. Ed. 53*: 14583–14586.

Despras, G., Hain, J., and Jaeschke, S.O. (2017). Photocontrol over molecular shape: synthesis and photochemical evaluation of glycoazobenzene macrocycles. *Chem. Eur. J.* **23**: 10838–10847.

Despras, G., Möckl, L., Heitmann, A. et al. (2019). A photoswitchable trivalent cluster mannoside to probe the effects of ligand orientation in bacterial adhesion. *ChemBioChem 20*: 2373–2382.

Fast, E., Schlimm, A., Lautenschläger, I., et al. (2020). Improving the switching capacity of glyco-self-assembled monolayers on Au(111). *Chem. Eur. J. 26*: 485–501.

# 41

# Photochromic Carbohydrate Conjugates

*Guillaume Despras, Vivek Poonthiyil, and Thisbe K. Lindhorst*

*Christiana Albertina University of Kiel, Otto Diels Institute of Organic Chemistry, Otto-Hahn-Platz 3-4 24118, Kiel, Germany*

Carbohydrates, in addition to nucleic acids and proteins, constitute one of the major biopolymer classes, which are fundamental to life. However, due to the complexity of carbohydrates and a lack of methods for their proper investigation within the supramolecular environment of a living cell, the glycomics lag far behind the genomics and proteomics, respectively.

In the glycomics, the role of carbohydrates and glycoconjugates in cell–cell recognition and communication is investigated rather than their more well-known function in energy storage and as biomaterials (cellulose, chitin). A pivotal role in cell–cell communication is taken by the glycocalyx, a layer of complex glycoconjugates surrounding every cell.

## 41.1 The Glycocalyx and Mysteries of Carbohydrate Recognition

The glycocalyx is a highly individual feature of a cell, mediating information about its phenotype, its developmental and current status, and in addition, the glycocalyx structure is significant for health and disease states of a cell. In fact, the glycocalyx has to be considered as an extracellular cell organelle, with a major function in information exchange and transfer. It consists of various sugars that are conjugated to proteins and lipids, forming complex classes of, i.e. glycoproteins and glycosphingolipids, respectively [1]. A cell's glcocalyx interacts with other cells, microbes, viruses [2], and bacteria, with proteins and antibodies as well as with various smaller molecules like hormones, drugs, and toxins, leading to distinct biological responses [3]. However, it has remained unclear until today how carbohydrate recognition is orchestrated within a cell organelle that is characterized by a substantial molecular heterogeneity that lacks an apparent fold and does not obey any obvious structural order.

*Molecular Photoswitches: Chemistry, Properties, and Applications*,
First Edition. Edited by Zbigniew L. Pianowski.


To understand the biological functionality of the glycocalyx and to decipher what has been called the sugar code of the cell [4], different levels of molecular complexity have to be inspected. First of all, the monosaccharide constituents of the glycocalyx and their oligomerization into highly complex and oligoantennary saccharides have to be considered. Here, a structural and stereochemical complexity is formed, which is unprecedented in cell biology [5]. This complexity finds a corresponding counterpart in the lectins, a wide class of carbohydrate-specific proteins that mediate biological events by specific interactions with saccharide epitopes [6]. In a second level of complexity, multivalency effects in carbohydrate recognition have to be considered, including homo- as well as heteromultivalency. Tailor-made multivalent glycoconjugates, often referred to as glycoclusters, serve as excellent tools for the investigation of multivalent interactions between carbohydrate ligands and their lectins that themselves also often display multiple carbohydrate recognition domains [7, 8]. The functional advantage of multivalency in carbohydrate recognition lies in the enhancement of affinity (avidity, respectively) and of specificity as well as in the enabling of fine-tuning of biological response.

However, numerous multivalency studies have suggested that there are additional structural features regulating carbohydrate recognition. Hence, we have recently used photosensitive azobenzene glycoconjugates to investigate the meaning of carbohydrate orientation in carbohydrate–lectin interactions (*vide infra*). The idea about the importance of carbohydrate orientation on the cell surface indeed goes back to Sen-itiroh Hakomori, who has just recently passed away on 11 November 2020 at the age of 91. Hakomori's work has shown that carbohydrate-to-carbohydrate interactions (CCIs) between glycospingolipids lead to clustering of carbohydrate epitopes [9] that form so-called glycosynaptic domains on the cell surface when properly oriented [10]. Based on this work, Nicklas Strömberg et al. have reported that the orientation of glycosphingolipid saccharide chains relative to the cell surface influences bacterial adhesion to the respective sugar receptors [11]. And Boons and colleagues have concluded recently that binding of lectins to carbohydrate microarrays is "modulated by presentation of minimal [sugar] epitopes in the context of complex N-glycans" [12]. Even if such findings appear rather specialized for a book chapter intelligible to non-specialized chemists, it is of general importance to widen our general appreciation of the carbohydrate-dependent recognition processes at the cell surface.

## 41.2 The Potential of Azobenzene-Based Glycoconjugates

To address the unsolved mysteries of the glycocalyx, photosensitive glycoconjugates have recently come into play. Indeed, especially azobenzene is now used as an effective photoswitch to be incorporated into glycoconjugates. The reversible photoisomerization of the azobenzene N=N double bond between a *trans* and a *cis* state is known for decades, but today it serves as a process that is highly profitable for investigations in biological systems [13] as well as in medicine and to build molecular

devices for chemical engineering [14]. This chapter focuses on azobenzene-based glycoconjugates (ABGs) as the principal and most often investigated photochromic carbohydrates synthesized and employed today.

A carbohydrate attached to an azobenzene photoswitch can be reversibly reoriented upon photoisomerization of the azo group, which serves the role of a hinge within an ABG. The orientational control of carbohydrate presentation in space can come into effect on a surface (Figure 41.1a), within a polymer or a supramolecular arrangement (Figure 41.1b), or in a glycoazobenzene macrocycle (Figure 41.1c), for example. Furthermore, individual AGBs can exert specific properties in one isomeric state, whereas in the other state they are inactive, for example as lectin ligands or enzyme inhibitors (Figure 41.1d). Thus, the orientational control of carbohydrate presentation can translate into a biological or another functional

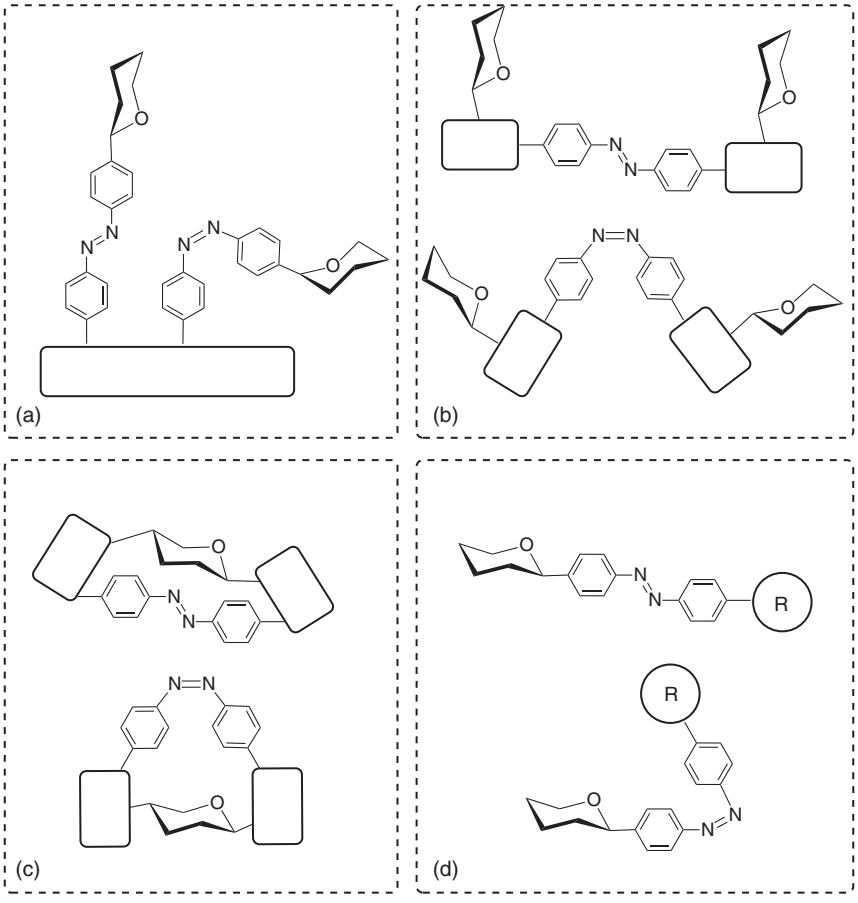


**Figure 41.1** Azobenzene-based glycoconjugates (ABGs) are photosensitive tools to manipulate and control the orientation of carbohydrates and their relative presentation through reversible *cis/trans* isomerization. Four examples are abstracted referring to surfaces (a), azobenzene-containing polymers (b), glycoazobenzene macrocyles (c), and simple ligands and substrates, respectively (d).

effect with spatiotemporal resolution and accordingly find applications in basic research as well as in medical treatment, reminding of the approaches taken in optogenetics.

## 41.3 Optoglycomics

The term optogenetics refers to a research field where light is used to control and study genetically modified neurons [15]. When this approach is combined with synthetic chemistry, hybrid devices can be obtained to serve the same purpose. Hence, the wisdom of nature is joined with the potential of chemistry to study highly complex biological systems and possibly repair malfunction. This approach has been brought forward by Dirk Trauner and colleagues, who coined the term "optochemical genetics," a semantic reminiscence of "optogenetics" [16]. In optochemical genetics, the potential of azobenzene-based designer molecules has been impressively employed in neuroscience.

Here, we would like to consider the expression "optoglycomics" for a research field where photochromic carbohydrate conjugates are employed to unravel the mystery of the glycosciences and to employ, in particular, ABGs for the design of novel light-sensitive glyco-probes. Photoresponsive glycoconjugates are ideal molecular tools to investigate important parameters of the three-dimensional presentation of carbohydrates. Moreover, also the conformational properties of carbohydrate epitopes can be investigated and manipulated when combined into photochromic glycoconjugates. Such photochromic glycoconjugates open the door into the investigation of carbohydrate recognition with a new twist, using light to manipulate, control, and investigate function.

In view of the biological functions encoded in the stereochemistry and dynamics of naturally occurring carbohydrates, a photoswitchable azobenzene unit enables the study of the following functional changes in carbohydrates:

- the relative multivalency of carbohydrates
- the orientation and presentation of carbohydrates on a surface
- the relative stereochemistry of carbohydrates and
- the relative orientation of carbohydrates within a functional conjugate.

## 41.4 First Examples – Azobenzene Glycoconjugates Altering Multivalency Effects

Surprisingly, in the glycosciences, azobenzene-based conjugates have not yet received as much attention as in other fields of chemistry. However, since approximately 2010, the field is emerging. In their visionary work, Jayaraman and coworkers synthesized the first azobenzene-based photoresponsive glycoclusters back in 2002 (Figure 41.2) and investigated their affinities with various lectins [17]. They attached mono- and divalent mannose and lactose ligands to a

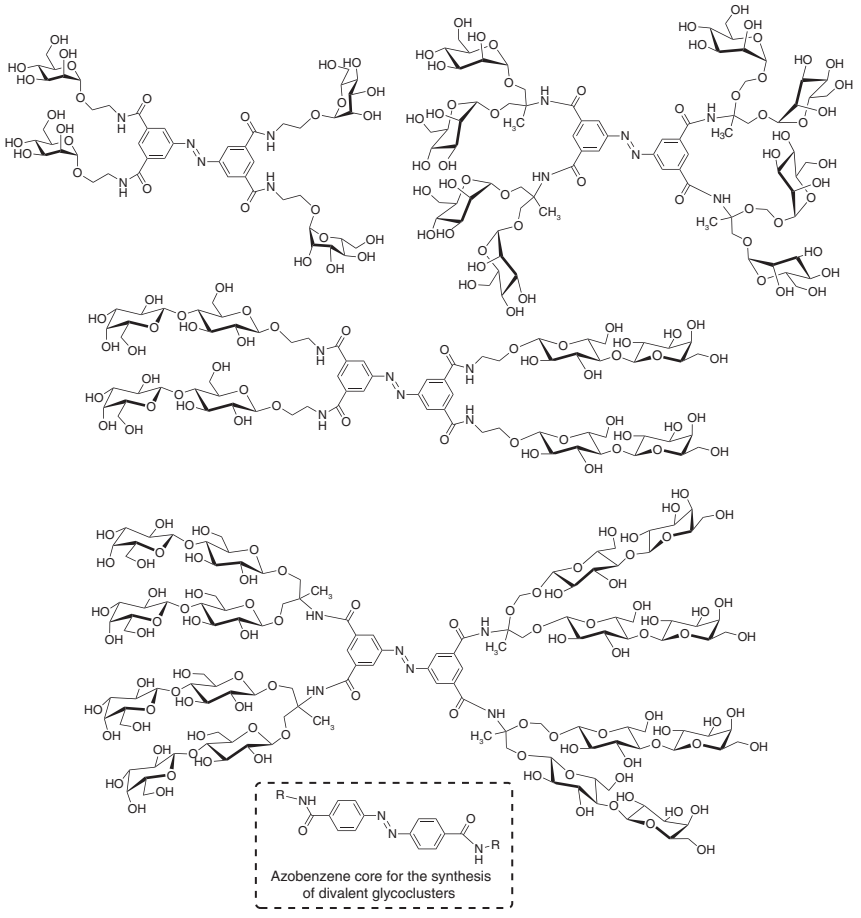


**Figure 41.2** The first azobenzene glycoconjugates were prepared by Jayaraman et al. and investigated in binding assays with mannose- and lactose-specific plant lectins [17, 18]. These studies suggested that photoswitching of the azobenzene core is suited to optimize the spatial orientation of glycoligands for cooperative lectin binding. Source: Srinivas et al. [17, 18].

di- or tetrafunctional azobenzene core, respectively, using peptide coupling. Then, multivalency effects of the synthetic azobenzene-based glycoclusters with the respective lectins, peanut agglutinin (PNA) and concanavalin A, were assessed. Isothermal titration calorimetry showed cooperative binding between tetravalent mannose-azobenzene conjugates and ConA on one hand and on the other hand between bi- and tetravalent lactose-azobenzene conjugates with PNA [17, 18]. More interestingly, the *cis* isomers showed a higher affinity to the investigated lectins than the *trans* isomers. Cooperativity was significantly higher with *cis* isomers than with the respective *trans* isomers, suggesting that suitable spatial orientation of clustered glycoligands is one of the prerequisites for cooperative carbohydrate recognition.

In line with the findings of Jayaraman and colleagues, researchers around Laura Hartmann have also detected altering of multivalency effects upon isomerization of

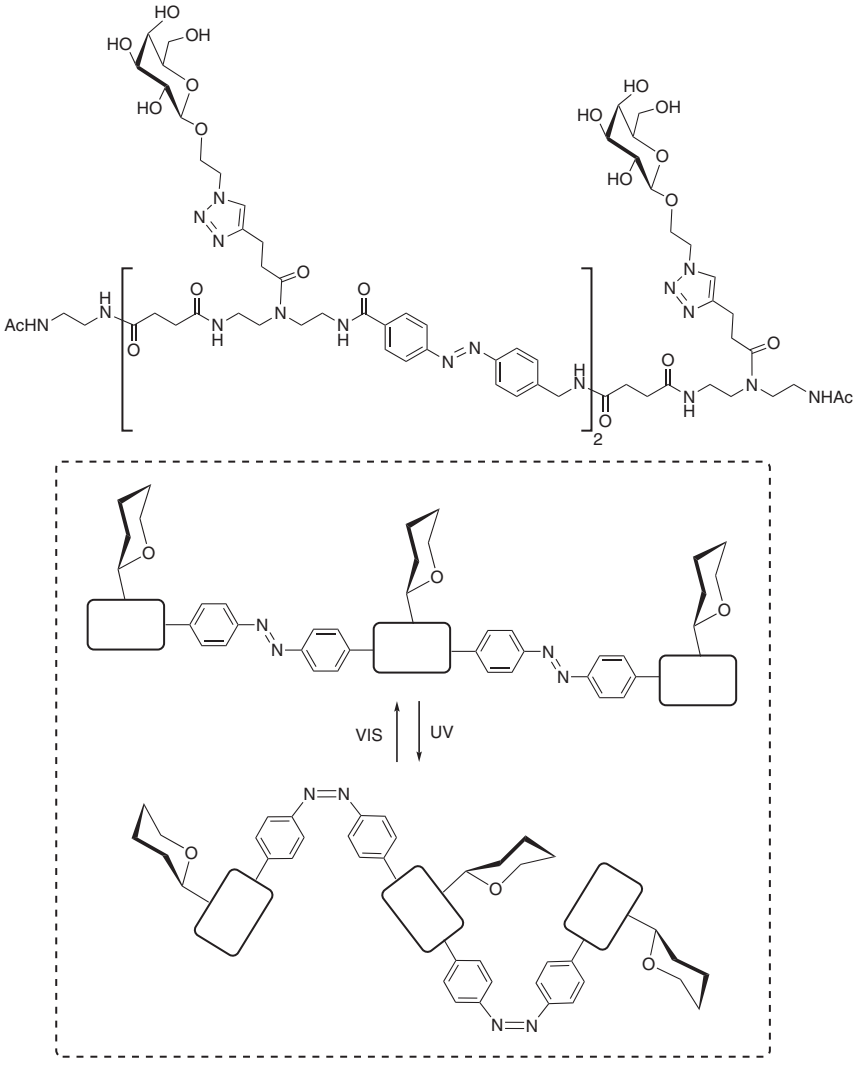


**Figure 41.3** Precision glycopolymers with incorporated azobenzene units allow switching of multivalency effects upon irradiation as shown in lectin-binding assays. Source: Modified from Ponader et al. [19].

azobenzene units incorporated into glycooligomers [19]. They recently presented the synthesis of photoswitchable glycooligomers by including azobenzene units into their precision oligomers, which expose β-galactoside moieties at defined positions of the oligomeric chain (Figure 41.3). By irradiation with light, the geometry of these photochromic glycooligomers can be switched between two states, resulting in reduction of their affinity to the tetrameric galactose-specific lectin *Pseudomonas aeruginosa* 1st lectin (PA-IL) upon *trans* to *cis* isomerization. The researchers suggest that photoisomerization changes the geometry of the glycooligomer such that multivalent binding to the lectin is compromised. This results in reduced binding. Here it

can be concluded that relative stereochemistry of carbohydrates, relative multivalency of carbohydrates, and the mode of ligand presentation seem to be altered.

## 41.5 Synthesis and Photochromic Properties of ABGs

Because any project on the application of azobenzene glycoconjugates relies on the feasibility of synthetic approaches, this subchapter summarizes the basic avenues to synthetic ABGs. Since the first report about the synthesis of AGBs by Jayaraman and coworkers, their preparation as well as the design of AGBs has progressed significantly. Various ligation chemistries were utilized, also considering the consequences for the photochromic properties of the resulting azobenzene derivatives.

To structure the various entries into AGBs, two general strategies can be distinguished, a "direct" and an "indirect strategy." Following a direct strategy, the azobenzene derivatives are completed first and then directly attached to carbohydrates (Scheme 41.1). In the indirect strategy, carbohydrates are first functionalized with "one half" of the later azobenzene unit, preferably a phenyl substituent, and in a second part of the synthesis they are coupled with a suitably substituted "second half" to obtain the target ABGs (Scheme 41.1). A couple of representative examples are explained below, including information about the photochromic and relaxation properties of ABGs.

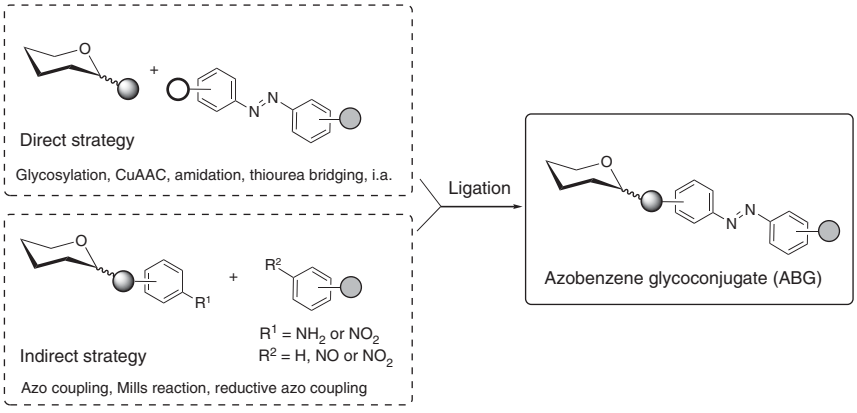


**Scheme 41.1** Azobenzene glycoconjugates can be achieved following two principal approaches, a direct and an indirect strategy. Both entries hold great potential for various modifications regarding structural design and optimization of photochromic properties.

Back in 2012, CuAAC (copper-catalyzed azide-alkyne cycloaddition) was utilized in a direct strategy to achieve mono-, di-, and trivalent ABGs to study multivalency effects in carbohydrate recognition in dependence of the relative orientation of the ligated sugar ligands [20]. For the synthesis of these "sweet switches," 2-azidoethylmannoside building blocks were coupled with propargylated *p*,*p*′-dihydroxyazobenzene to gain, for example, glycoclusters **1** and **2** (Scheme 41.2).

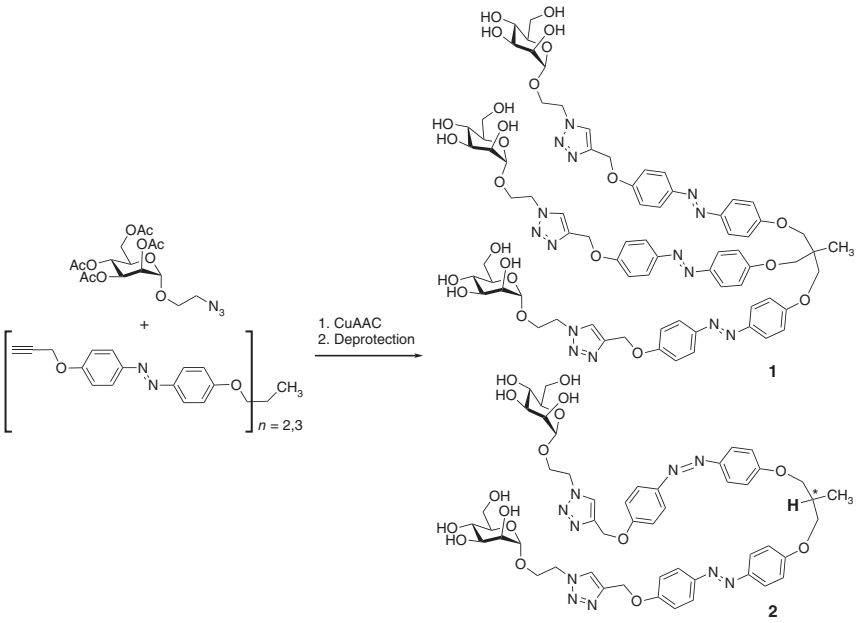


**Scheme 41.2** Direct approach to di- and trivalent "sweet switches" using "click chemistry" (CuAAC) as introduced by the Lindhorst group [20]. Glycocluster **2** is depicted as a mixture of diastereomeric *cis/trans*-configured isomers (see text for details). Source: Based on Chandrasekaran et al. [20].

Investigation of the photochromic properties of these ABGs revealed that in the ground state (GS) they all existed exclusively in the *trans* state. However, the results obtained after irradiation at 365 nm revealed that photoswitching was influenced by intramolecular electronic effects such as quenching and excitonic coupling. Hence, there remains a need for multivalent AGBs, in which the individual glycoazobenzene branches can be photochemically addressed without such detrimental effects. Another interesting aspect of that work relates to the divalent AGB **2**. As irradiation with 365 nm does not result in complete isomerization of both branches, a pair of diastereomers is seen for the *trans*/*cis*-configured glycoazobenzene cluster **2**. Hence, a mixture of four isomers, a double *trans*, a double *cis*, and two *trans/cis* isomers are obtained as seen in the $^{1}$H NMR spectrum from four doublets for the proton at the focal point of the cluster.

Another obvious direct approach to AGBs is glycosylation of hydroxy-azobenzene derivatives. The synthesis of such azobenzene glycosides also provides a direct connection between a carbohydrate ligand and the azobenzene photoswitch allowing for an immediate transmission of the geometrical effect of N=N isomerization into the orientation of the attached glycoligand.

Hence, (*O*-glycosyl)trichloroacemidates were employed as glycosyl donors to glycosylate hydroxyazobenzene. This is a straightforward and high-yielding approach into azobenzene glycosides, which show excellent photochromic properties. Interestingly, the photochromic properties of azobenzene glycosides depend on

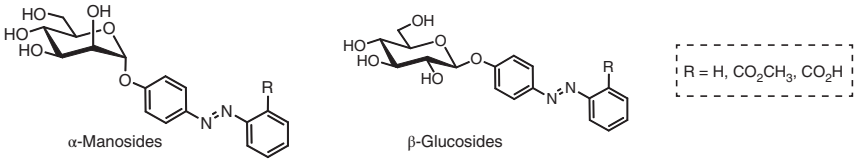


**Figure 41.4** Azobenzene glycosides can be directly obtained by glycosylation of hydroxyazobenzene. Their properties depend on the nature of the sugar glycone and the stereochemistry of the anomeric linkage. Source: Chandrasekaran et al. [21].

the stereochemistry of the sugar glycone, namely the sugar series and the anomeric configuration. This was studied in 2014 together with the effect of *ortho*-substitution of the azobenzene ring [21]. A series of anomeric azobenzene mannosides and glucosides were prepared (Figure 41.4) showing that *ortho*-substitution of the azobenzene with carboxy or methoxycarbonyl groups shortens the half-life of the *cis* isomer from approx. 90 hours to 2 to 5 hours, respectively. Significantly different effects arose from the different anomeric linkages and the nature of the pyranoside, belonging either to the *manno* or *gluco* series. These results demonstrate that with suitable substitutions either in the sugars or in the azobenzene part of ABGs, the *cis* to *trans* thermal isomerization rate can be tuned. This is important since both the slow and fast *cis* to *trans* isomerization are useful depending on the desired application. For instance, slow relaxation is required when both isomers have to be independently investigated in biological assays. On the other hand, fast relaxation is essential to use ABGs in real-time information transmitting systems.

To investigate bacterial adhesion of type 1 fimbriae of *Escherichia coli* bacteria (*vide infra*), photochromic α-D-mannopyranosides were synthesized as ligands for the bacterial lectin FimH. The trichloroacetimidate **3** was used to glycosylate the azobenzene alcohol **4** and obtain the mannoside **5**. After protecting group manipulations and a further mannosylation step, the mannobioside **6** was achieved (Scheme 41.3). The *trans* to *cis* isomerization of compound **6** was almost quantitative, and the resulting *cis* isomer had a long half-life of 178 hours. Standard bacterial adhesion inhibition assays showed that both the *trans* and *cis* forms of **6** had equal inhibitory potency, being almost two orders of magnitude higher than that of the standard inhibitor methyl mannoside [22].

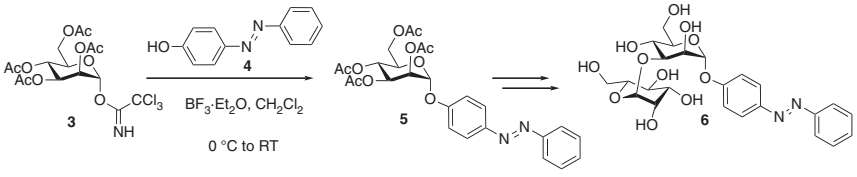


**Scheme 41.3** Synthesis of an azobenzene dimannoside as a photoswitchable ligand for the lectin FimH. Source: Based on Chandrasekaran et al. [22].

While glycosylation of monohydroxyazobenzene derivatives is very effective, the one of 4,4′-dihydroxyazobenzene (DHAB) is found to be tricky. Lindhorst

and Despras employed this reaction in several projects aiming at symmetrical azobenzene bis-glycosides (*vide infra*) and frequently were confronted with poorly reproducible results and unsatisfying yields. Hence, recently, they investigated this reaction in greater detail to outline its scope and limitations [23]. Among a number of different glycosyl donors, sugar trichloroacetimidates and in particular 6-functionalized thioglycosides proved suitable for the bis-glycosylation of DHAB; however, this reaction remains difficult as DHAB is a rather poor glycosyl donor.

An alternative to glycosylation of azobenzene derivatives is the Mitsunobu reaction. It was employed to directly connect 4-hydroxyazobenzene **7** to the anomeric center of both unprotected and protected mannopyranosides (Scheme 41.4) [24]. Interestingly, unprotected D-mannose led to the corresponding α-mannoside **8** (no β-product observed), although in low yield, while di-isopropylidene-protected D-mannose **9** provides the β-product **10** in excellent yield and anomeric selectivity. The latter result is especially important as selective β-mannosylation is notoriously very challenging. Employing a similar Mitsunobu strategy, Hain et al. directly ligated 4,4′-dihydroxyazobenzene **11** to the primary alcohol of an unprotected propargyl mannoside (**12**) to give the symmetrical ABG **13** in a fair yield after acetylation [25].

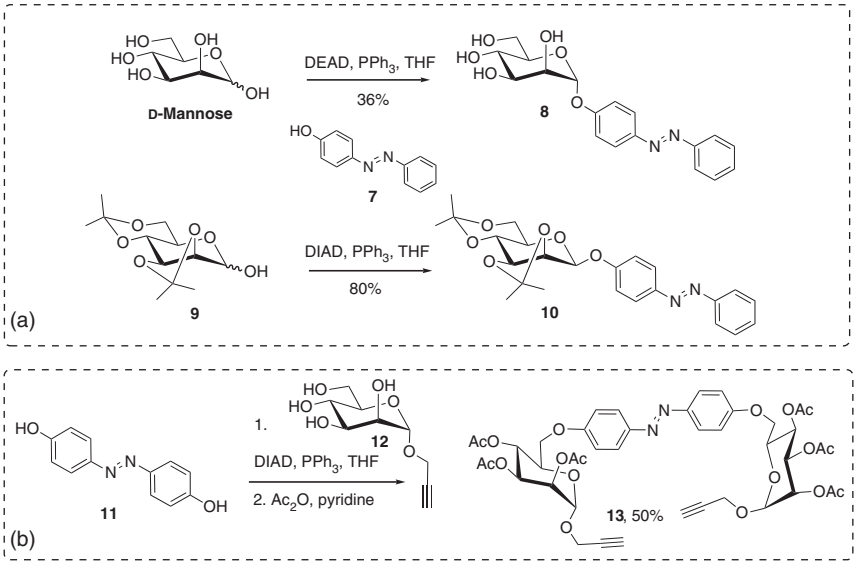


**Scheme 41.4** The Mitsunobu reaction can be employed for the direct synthesis of ABGs via glycosylation (a), or via substitution at the primary position of monosaccharides (b). Source: Based on Hain et al. [24].

Díaz-Lobo et al. investigated an anomeric mixture of azobenzene glucosides, which was obtained via a Mitsunobu reaction, to selectively photoregulate the catalytic activity of key enzymes of the glycogen metabolism. Indeed, they found that the more stable *trans* isomer of the azobenzene glucoside had a slight inhibitory effect on rat muscle glycogen phosphorylase (RMGP) as well as on *Escherichia coli*

glycogen synthase (EcGS). The effect of the respective *cis* isomer, obtained after irradiation, did not significantly change for RMGP, but its effect on EcGS increased 50-fold. This approach holds potential for treatment of glycogen metabolism disorders [26].

A study published by König et al. also aimed at the regulation of enzyme activity. Various azobenzene β-galactosyl thioglycosides were prepared as photochromic inhibitors of β-galactosidase. In an optimized case, a photochromic thiogalactoside proved as strong competitive inhibitor of β-galactosidase from *E. coli* with its inhibition constant ($K_i$) changing from 60 nM in the *trans* state to 290 nM in the *cis* state [27].

Although the direct coupling of azobenzene and sugars is a straightforward approach, an indirect approach is more relevant for the preparation of unsymmetrical AGBs. Obviously, one of the most common methods to form azophenyl compounds is the classic diazo coupling, i.e. the formation of a diazonium salt from an aniline followed by the nucleophilic addition of an aryl derivative. This was used by Laurent et al. to form amphiphilic ABGs comprising a dialkyl aniline moiety (Scheme 41.5a) [28]. Lindhorst et al. reported that the synthetically difficult 1,2-*cis*-glycoside-type ABGs can be synthesized following an indirect strategy [21]. To synthesize compounds **15** and **16** (Scheme 41.5b), a Mills reaction consisting of acid-promoted condensation of the amino-substituted aryl glycoside **14** and nitrosoarenes was employed, affording the target compounds in excellent yields. In another report, a reductive coupling method was employed to form

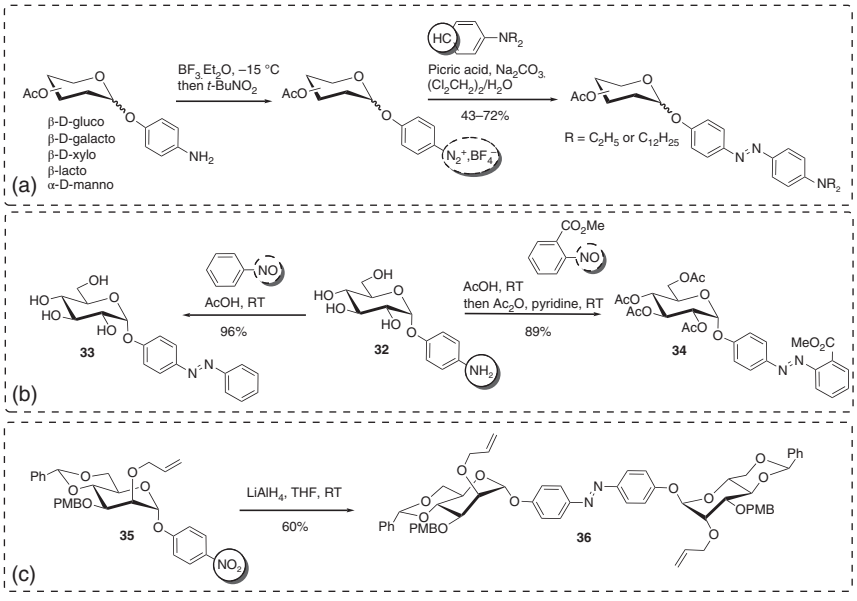


**Scheme 41.5** Preparation of ABGs via indirect strategies. (a) Azobenzene glycosides via diazo coupling; (b) α-azobenzene glucosides via Mills reaction; (b) α-azobenzene bis-mannoside via reductive self-coupling of a *p*-nitro phenyl glycoside.

the bis-azobenzene glycoside **18** (Scheme 41.5c), otherwise hardly accessible by a glycosylation approach [29]. The *p*-nitrophenyl mannoside **17** was treated with lithium aluminum hydride (LAH) to provide **18** in 60% yield.

It might be mentioned here that recently photoswitchable carbohydrate-based azoalkenes were studied as "new protagonists in the azo chemical space" and achieved in an indirect two-step approach [30]. For their preparation, unprotected monosaccharides were condensed with aryl hydrazines, the resulting hydrazones *O*-acetylated and then heated to obtain stable diazo-dienes with interesting unusual switching properties.

In conclusion, there are plenty of approaches to the synthesis of AGBs. Additional potential lies in the late stage modification of the azobenzene unit to achieve red-shifted ABGs, as recently shown by Poonthiyil et al. [31]. Furthermore, the glycosidic linkage can be altered from *O*- to *S*-glycosides, i.e. with a perspective to alternative synthetic entries as well as altered photochromic properties of the respective AGBs.

## 41.6 Peptides Modified with ABGs

The secondary structure and the function of proteins and peptides can be photo-regulated by intramolecular cross-linking of the oligomeric chain with azobenzene derivatives [13, 32, 33], and more specifically with ABGs. Hence, in 2015, we reported the successful ligation of ABGs to the cysteine side chains of peptides by nucleophilic substitution and thiol-ene reactions [29]. First, the chloroacetamido ABG **19** and the allyl-functionalized derivative **22** were synthesized. These molecules exhibited good photoswitching properties. Upon UV

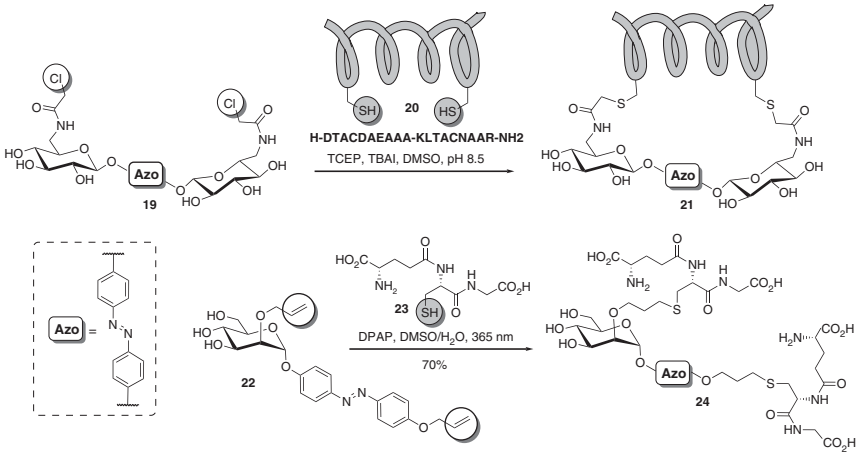


**Scheme 41.6** Ligation of photoswitchable carbohydrate-derived cross-linkers with peptides. Top: the chloroacetamido derivative **19** was conjugated to the cysteine-bearing oligopeptide **20** via nucleophilic substitution; bottom: the allyl-armed ABG **22** reacted with tripeptide **23**, presenting a cysteine residue, in a thiol-ene addition to form **24**.

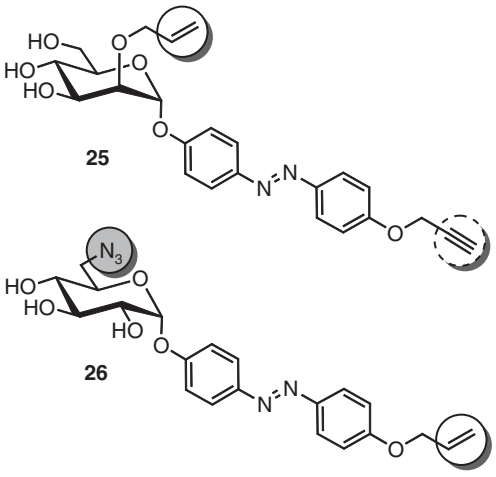


**Figure 41.5** Hetero-bifunctional ABGs bearing functional groups suitable for click chemistry or thiol-ene ligation. Source: Based on Müller and Lindhorst [34].

irradiation, the *trans* isomers underwent quantitative conversion to the respective *cis* isomers with half-lives ranging from one to two days. Compound **19** was successfully used to cross-link the synthetic nonapeptide **20**, bearing two cysteine residues, hence giving the photoswitchable peptide **21** (Scheme 41.6). Following a thiol-ene coupling procedure, also the diallyl derivative **22** was conjugated with glutathione **23** to form the glycopeptide **24**.

In a subsequent work, the synthesis of hetero-bifunctional ABGs **25** and **26** was reported, which could be used for bioorthogonal cross-linking of proteins (Figure 41.5) [34].

## 41.7 Glycoazobenzene Macrocycles

Macrocycles represent a fascinating class of molecules that exhibit unique properties due to their specific shape and their conformational strain [35]. The incorporation of one or more azobenzene units into cyclic frameworks enables the possibility to modulate the molecular shape and therefore the properties of macrocycles in a controlled and reversible manner [36]. Importantly, the ring strain also influences both the photochromism and the relaxation of the *cis* azobenzene.

The use of carbohydrate-building blocks for the preparation of photoswitchable macrocycles presents great advantages [37]. In addition to their biocompatibility and water solubility, the multiple functional groups displayed by carbohydrates (alcohol, amino, and carboxy groups) allow the installation of functional handles onto the corresponding macrocycles. Also, when used in their cyclic forms (pyranoside or furanoside), sugars are frequently locked in a single-ring conformation, which may result in macrocycles with a well-defined and stable molecular shape. Finally yet importantly, the chirality of glycosides can be transferred to the photoswitch, which can thus function as a chiroptical switch, also influencing the overall conformation of the macrocycle.

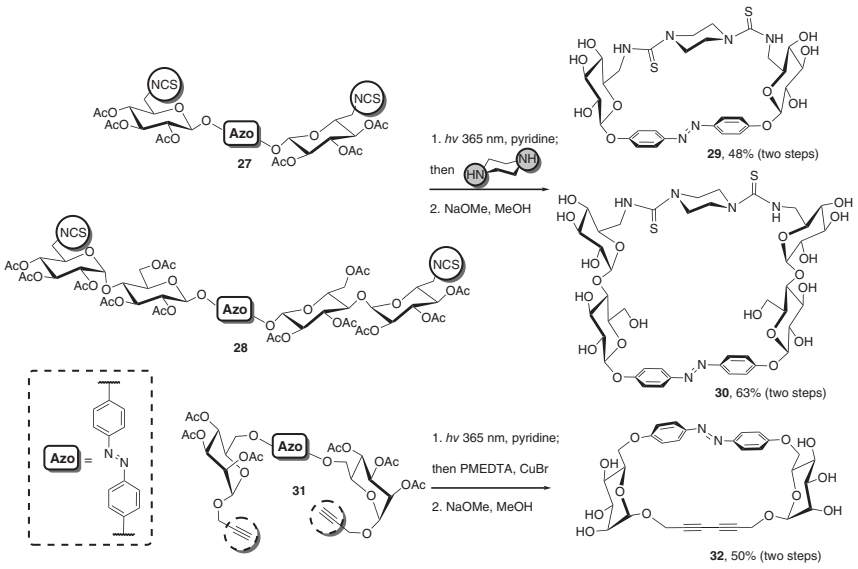


**Scheme 41.7** Synthesis of thiourea- and diyne-bridged glycoazobenzene macrocycles according to Despras and coworkers [25, 38]. Source: Refs. [25, 38].

The investigation of glycoazobenzene macrocycles has been recently started by Despras et al. who described the macrocycles **29**, **30**, and **32** (Scheme 41.7), with differing molecular architectures. In a first report, the cyclization of 6-isothiocyanato-azobenzene bis-glycosides **27** and **28** with piperazine was introduced, using thiourea bridging for cyclization [38]. It is interesting to note that the cyclization was effective only when the open-chain substrates were pre-organized by isomerization of azo bond to its *cis* state prior to the cyclization. In a further work, the cyclization of propargyl mannosides connected to an azobenzene unit at the primary position was achieved [25]. Here, an intramolecular Glaser–Hay coupling was employed for the key macrocyclization step. Also in this case, it was necessary to pre-organize the substrate **31** by photoisomerization to bring the alkyne functions close to each other.

Glycoazobenzene macrocycles **29**, **30**, and **32** exhibit good photoswitching ability, especially in the *trans* to *cis* isomerization caused by UV light irradiation. The back *cis* to *trans* photoisomerization (435–530 nm) is however dependent on the ring strain, with a decreased efficiency if the azobenzene is connected to the anomeric position of the saccharide. NMR studies, supported by molecular modeling, indicated a drastic change in conformation of the macrocycle upon isomerization of the azobenzene hinge. This also gave a hint about the conformational restriction of the ring and thereby the stability of the molecular shape. The chiroptical behavior of glycoazobenzene macrocycles was also investigated by circular dichroism spectroscopy. Circular dichroism spectra measured in water and DMSO before and after isomerization evidenced a chirality transfer from the carbohydrate to the azobenzene moieties. The photoswitch shows strong dichroic signals, both in the *trans* and the *cis* states, differing in intensity and also in sign in case of

the maltoside derivative **30**. On the one hand, the *trans* azobenzene is no longer planar and has a preferential helical twist. On the other hand, the inherently chiral *cis* azobenzene no longer exists as a racemate, but instead one helical conformer (*M* or *P*) is predominant depending on the stereochemistry of the attached sugar. According to the strength of the observed Cotton effect, we assumed that one helical *cis* conformer is negligible in solution and the photoisomerization may be a unidirectional process. In addition to the photomodulation of the chiroptical response, we also found out that it is possible to switch the solubility of macrocycle **32** in water. Thus, a suspension of insoluble *trans*-**32** turns to a clear yellow solution of *cis*-**32** after irradiation with UV light, while the suspension is recovered upon exposure to green light or heating.

Also, Xie's group has developed glycoazobenzene macrocycles. They implemented a macrolactonization strategy to synthesize a first series of photoswitchable glycomacrocycles comprising a single monosaccharide unit in the backbone (**34–37**, Scheme 41.8) [39, 40]. Hence, thioglycosides bearing two adjacent bromoacetyl groups were cyclized in moderate yields, in the presence of 2,2′-dihydroxyazobenzene (**33**) under basic conditions. In a next paper, the same group employed a photoresponsive template with a view to control the stereoselectivity of an intramolecular glycosylation reaction [41]. Both a benzyl-protected glycosyl donor and an acceptor were connected to 2,2′-dihydroxyazobenzene via ester linkages, using either an aryl or an alkyl spacer, respectively. Overall, excellent α-selectivity was achieved in the glycosylation step in most cases, regardless of the configuration of the azobenzene template. Only the yields were lower when the two sugar partners were closer (in *cis* azobenzene).

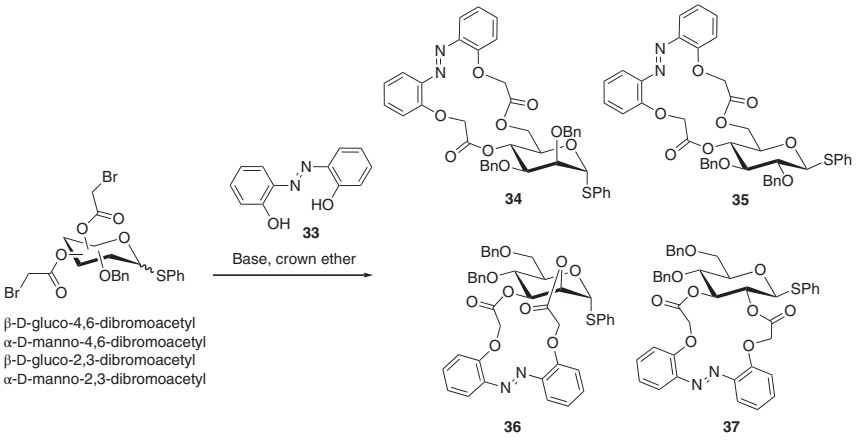


**Scheme 41.8** Synthesis of azobenzene glycomacrolactones by Xie and coworkers [39, 40]. Source: Lin et al. [39, 40].

Glycoazobenzene macrocycles reported by Xie and colleagues present similar photochromic properties as the structures published by Despras and coworkers, associated with very slow thermal relaxation processes in the *cis* state (up to 72 days

at 20 °C). It is noteworthy that neither flipping of the chair conformation nor distortion occurs upon photoisomerization of macrocycles embedding a single sugar unit [39, 40].

Xie's macrocycles also display equivalent chiroptical features as compounds **29** to **32** (Scheme 41.7), due to chirality transfer from the carbohydrate to the azobenzene unit. The prototype macrocycle **34** exhibits gelation ability in organic solvents, and the resulting gels are sensitive to diverse stimuli (light, temperature, shaking), for example in undergoing reversible sol to gel transition [39]. Interestingly, the chiroptical signal corresponding to an organogel formed in cyclohexane undergoes a helical inversion in response to light exposure or temperature increase. In a very recent study, Xie's macrocycles **34** and **37** were used as photoswitchable chiral dopants in cholesteric liquid crystals (CLCs) [42]. With a twisting helical power increase by up to 500% upon *trans* → *cis* photoisomerization, the macrocycles were able to drive rotational motion of microscale objects on the surface of CLC films.

## 41.8 Amphiphilic ABGs and Their Biological Applications

ABGs have also been designed as amphiphiles, mainly as mimetics of the naturally occurring glycosphingolipids. A specific class of glycosphingolipids, the α-galactosylceramides are known to activate natural killer cells after presentation by the protein CD1d. This results in the production of a variety of proinflammatory and immunomodulatory cytokines. Colleagues around Dirk Trauner and Anja Hoffmann-Röder synthesized the photoswitchable ceramide **α-GalACer-4**, which was designed after a synthetic ceramide called **KRN-7000** and which is known as a strong immunostimulant (Figure 41.6) [43]. Synthetic **α-GalACer-4** was found to serve as very potent immunomodulator that elicits very low cytokine production in its *trans* configuration, whereas after irradiation to the *cis* state, it triggers significant cytokine secretion. Therefore, **α-GalACer-4** is a candidate for the investigation of spatiotemporal activation of cytokine production and might find important biological applications, for example in cancer treatment.

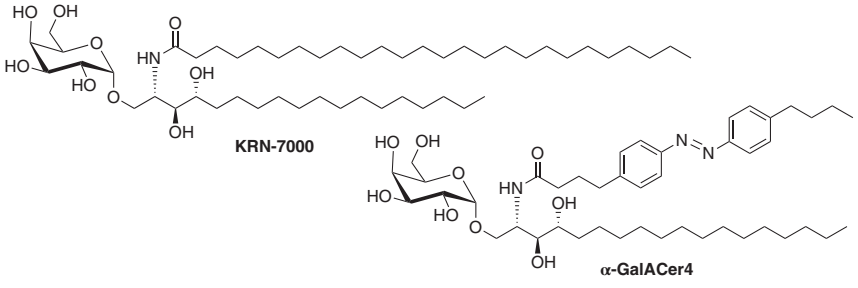


**Figure 41.6** **α-GalACer-4**, which was designed after the known immunostimulant KRN-700, serves as promising immunomodulator in the *cis* state, whereas as *trans* isomer (shown) its biological activity is weak. Source: Modified from Hartrampf et al. [43].

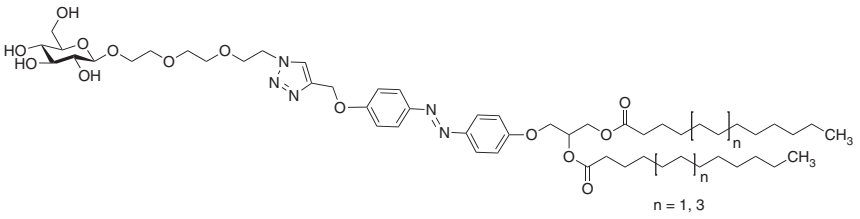


**Figure 41.7** A modular synthetic approach led to azobenzene glycolipid mimetics comprising a hydrophilic glycoside and a lipophilic azobenzene diacylglycerol moiety, which can both be varied employing click-type triazole conjugation and Steglich esterification. Source: Reise et al. [44].

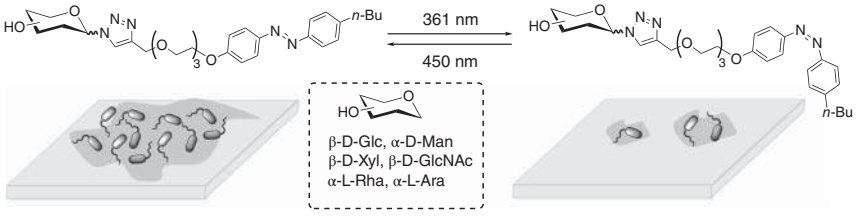


**Figure 41.8** Photocontrolled reversible inhibition of bacterial biofilm formation with ABG-based surfactants. Source: Modified from Hu et al. [45].

Reise and colleagues have reported the modular synthesis of a library of photoswitchable glycolipid mimetics (Figure 41.7). These glycoazobenzene amphiphiles were designed for incorporation into cell membranes to study and manipulate their function. So far, photoswitching of Langmuir films comprising the synthetic photosensitive glycoamphiphiles was shown by Langmuir isotherm studies [44].

In 2016, Hu et al. reported the photo-regulated antibacterial and biofilm modulatory activity of a group of ABG-based surfactants (Figure 41.8) [45]. They exhibited isomer-specific and concentration-dependent inhibition of the growth of both *E. coli* and *Staphylococcus aureus*. In antibacterial and biofilm inhibition studies, surfactants at low concentrations exhibited similar effects in both *trans*- and *cis*-dominated photostationary states (PSSs), while at higher concentrations the difference in activity between the two states became more pronounced.

Most recently, Salta et al. reported the synthesis of ABG-based cationic amphiphiles and their application in photo-regulated bacterial membrane permeabilization [46]. Antimicrobial cationic amphiphiles **40** and **41** were synthesized (Scheme 41.9). The aminoglycoside **40** was obtained through peptide coupling of **38** and the azobenzene unit **39**. It was found that their bacterial membrane permeabilization property depends not only on their concentration but also on their conformation. The membrane permeabilization caused by the *trans* isomer of **41** was higher than by its *cis* isomer, while the *cis* isomer of **40** had a more pronounced membrane permeabilizing effect than its *trans* isomer.

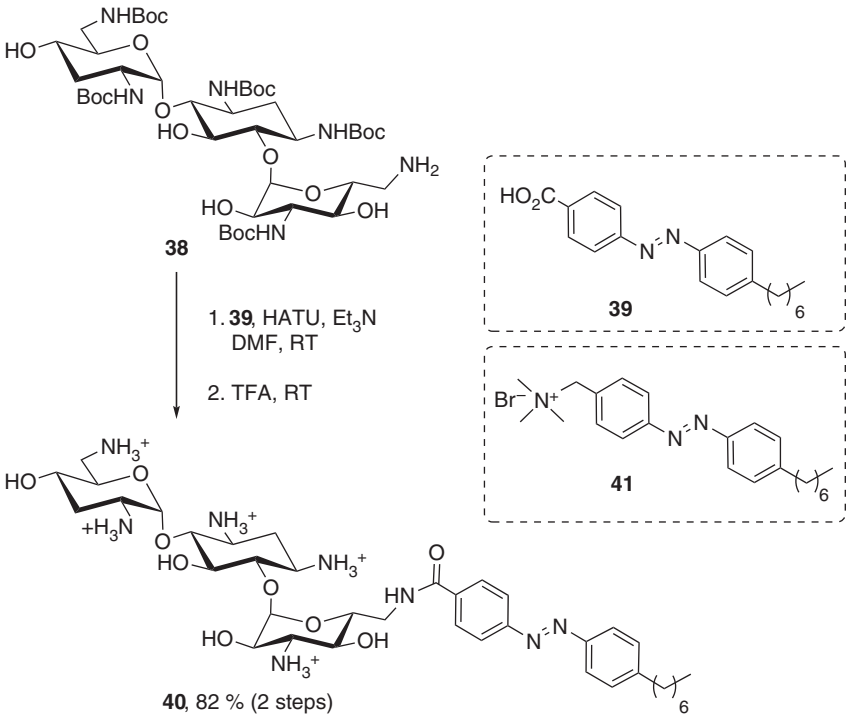


**Scheme 41.9** Preparation of a photoswitchable polycationic aminoglycoside for bacterial membrane permeabilization. Source: Modified from Salta et al. [46].

## 41.9 Photoswitchable Glyco-SAMs

An important tool in the glycosciences is the so-called glycoarrays [47–50]. Glycoarrays are artificial glycosylated surfaces where saccharide ligands are mounted onto a suitable material of different dimension. The saccharide ligands can be attached to the surface either covalently or by chemi- or physisorption, respectively. Glycoarrays can be investigated by a number of analytical techniques and have evolved as a powerful methodology to study carbohydrate–lectin interactions or glycoenzyme specificity, antibody specificity, and cell–cell adhesion [51].

Glyco-self-assembled monolayers (SAMs) are a special type of glycoarrays where well-ordered monolayers self-assemble on gold when alkanethiol derivatives are employed, forming of S—Au bonds on the surface. The alkanethiols employed for SAM fabrication can be terminated with sugar ligands to achieve carbohydrate-presenting SAMs, hence glyco-SAMs. We have combined the knowledge about SAMs on the one hand and on azobenzene photoswitches on the other hand, to fabricate photoswitchable glyco-SAMs to control the orientation of surface-bound carbohydrate ligands (Figure 41.9). Although SAMs of various

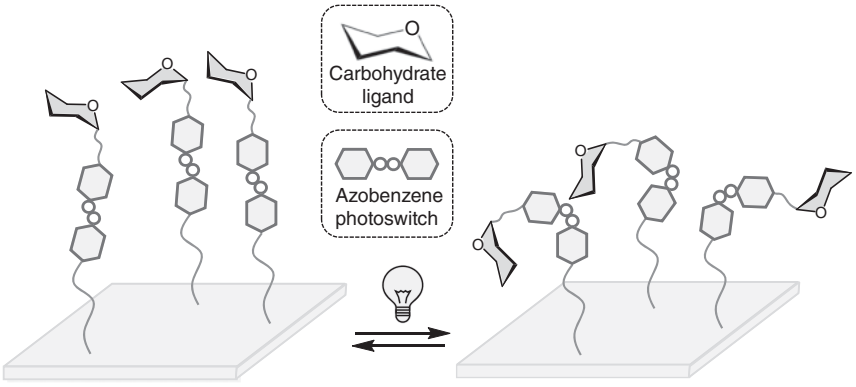


**Figure 41.9** Photoresponsive glyco-SAMs are a means to reversibly control the orientation of carbohydrate ligands on a surface.

photoresponsive azobenzene derivatives have been prepared before [52–54], our study using AGB alkanethiols marked the first preparation of photosensitive glyco-SAMs [55].

In glyco-SAMs, the complexity of the presented sugars can be varied as well as the architecture of the backbone of the SH-modified anchoring group. However, to study the biological effect of altered sugar orientation within the supramolecular environment of a glycoarray, the photoswitching on the surface has to be effective. Here, it is important to consider that the *trans* to *cis* isomerization of the azobenzene moiety requires enough free volume on the surface to allow a successful process. This is even more relevant when relatively bulky and hydrophilic carbohydrate head groups are covering the monolayer. Various solutions to the problem were shown with diverse azobenzene-containing SAMs (cf. this book). We have investigated three different approaches, compatible with a biological study. Firstly, we used so-called diluter alkanethiols lacking the azobenzene photoswitch and, thus, not demanding any additional space on the surface upon irradiation (Figure 41.10a) [55].

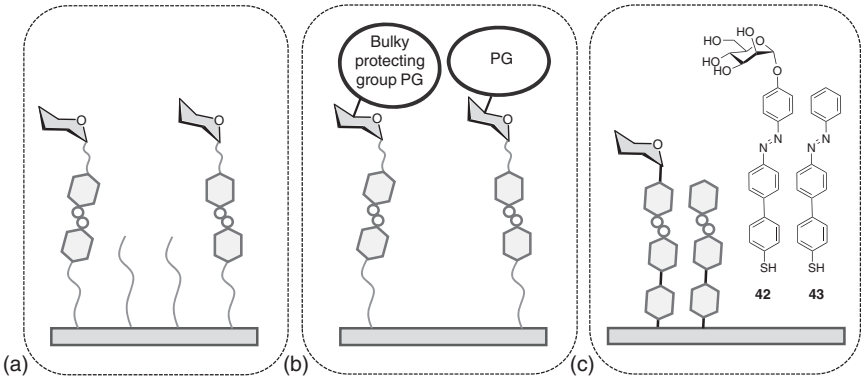


**Figure 41.10** Three approaches implemented to optimize ABG switching on surface: (a) diluting linker molecule; (b) bulky labile group on the carbohydrate moiety; (c) aromatic stiff linker.

In a second approach, we have installed bulky protecting groups on the sugar head groups, occupying additional space in the self-assembly process. After SAM formation, these protecting groups can be cleaved, providing the required spatial freedom for photoswitching while leaving the monolayer intact. The latter approach was called "self-diluting" (Figure 41.10b). Thirdly, in a somewhat counterintuitive approach, rigid backbones were chosen for the synthesis of photoswitchable glycoazobenzene thiols. SAMs fabricated from ABGs based on rigid biphenyl backbones lead to densely packed monolayers supported by intermolecular π–π interactions (Figure 41.10c).

When the biphenyl glycoazobenzene thiol **42** was self-assembled together with the diluter molecule **43**, thus combining the dilution approach with rigid backbones to achieve effective photoswitching on the surface, almost half of the assembled molecules underwent reversible *trans*/*cis* isomerization. This finding constitutes an important advance in the field of photoswitchable glyco-SAMs [56]. The fabricated SAMs were investigated in great spectroscopic detail, employing IRRAS (infrared absorption reflection spectroscopy), X-ray photoelectron spectroscopy (XPS), and near edge X-ray absorption fine structure (NEXAFS). Especially IRRASs is an effective IR method to determine orientational changes on metal surfaces. Surface selection rules dictate that only those vibrations with a component of the transition dipole moment (TDM) perpendicular to the surface plane can interact with the incident light and be detected in IRRAS. Thus, vibrational bands with TDMs perpendicular to the Au surface appear more intense than those with TDMs, which are parallel to the Au surface. This can be directly applied to the intensity of the band at 1250 $cm^{-1}$ corresponding to $C_{aryl}–O_{aryl}$ stretching vibrations of the azobenzene unit, indicating its successful *trans* to *cis* conversion and vice versa.

The investigation of mannose-specific lectin binding to a mixed SAM fabricated from **42** and **43** (Figure 41.10c) employing concanavalin A showed that lectin binding to the SAM was reduced by one-third in the *cis* state when in comparison to the *trans* state.

## 41.10 Inhibition of Bacterial Adhesion

In a next step, photocontrol of carbohydrate-specific cell adhesion is desirable. A relevant example is the spatiotemporal resolution of bacterial adhesion in the context of biofilm formation and infection, respectively. The interest in inhibition of bacterial adhesion has grown significantly due to the increased antibiotic resistance seen in bacteria, approaching what has been called an "antiadhesion therapy" against bacterial infection [57, 58].

As the glycocalyx is a target for bacteria and viruses adhering to it by means of specific carbohydrate–lectin interactions, the inhibition of this adhesion process as the first and fundamental step of infection is an obvious idea to prevent disease. On the other hand, the microbiome of a target organism must not be completely inhibited as it forms an integral part of a healthy organism. Hence, a specific and possibly spatiotemporal resolution of microbial adhesion is desired. Here, photochromic glycoconjugates come into play.

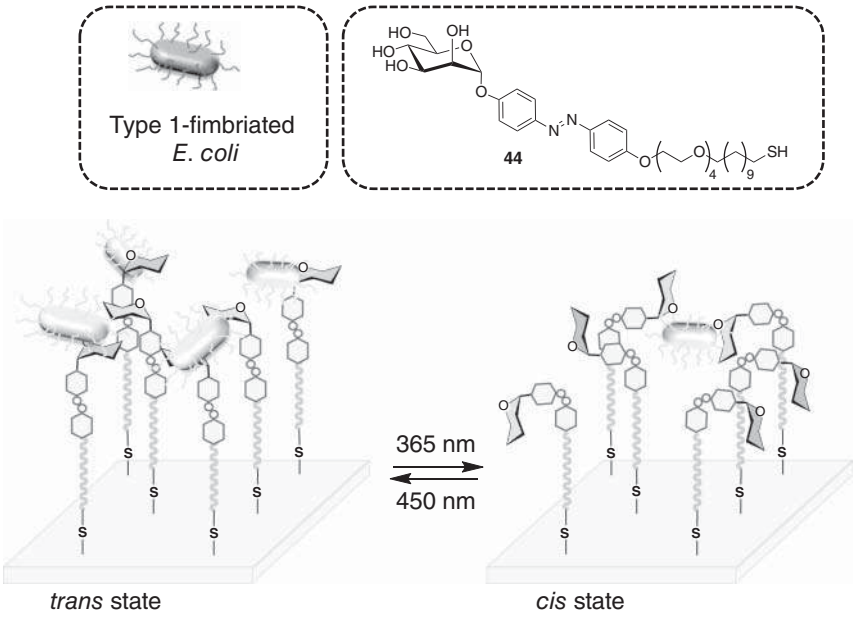


**Figure 41.11** Photocontrol of FimH-mediated adhesion of live *E. coli* cells to a photoswitchable glyco-SAM fabricated from AGB **44**. In the *cis* state, bacterial adhesion is reduced by a factor of approx. five. Source: Modified from Weber et al. [63].

Many bacteria, such as *E. coli*, express several hundreds of proteinaceous filaments on their surface, called fimbriae, which mediate tight adhesion to the host cell surface by protein–carbohydrate interactions [59]. A special type, so-called type 1 fimbriae, is terminated with the lectin FimH [60], which specifically recognizes α-D-mannopyranoside ligands [61]. In particular in uropathogenic *Escherichia coli* (UPEC), type 1 fimbriae constitute important virulence factors [62].

Using α-mannoside-decorated ABG-glyco-SAMs, it was possible to reversibly switch bacterial adhesion by photoisomerization of the azobenzene units and thus altering the orientation of carbohydrate ligands exposed on the surface (Figure 41.11) [63]. It had been shown earlier that azobenzene mannosides are potent ligands for the type 1 fimbrial lectin FimH, independent of the configuration of the N=N double bond of the azo group [64]. Therefore, the difference seen in bacterial adhesion to a glyco-SAM fabricated from **44** must be due to orientational change rather than to a change in ligand affinity.

The ABG **44** used for glyco-SAM fabrication comprises an undecane moiety to stabilize the SAM in addition to an oligoethylene glycol chain (OEG) to suppress unspecific surface recognition and the glycophotoswitch. When the exposed azobenzene mannoside head groups of the SAM were irradiated to effect *trans cis* isomerization, the number of adherent bacteria decreased by a factor of five (Figure 41.11).

Hence, with α-mannoside-decorated ABG-glyco-SAMs, it was possible to reversibly switch bacterial adhesion by altering the orientation of carbohydrate ligands exposed on the surface (Figure 41.11) [63]. This finding once again underlines

Hakomori's prediction that carbohydrate recognition is controlled by the mode of ligand presentation on the cell surface.

In line with those studies, Zhang et al. exploited analogous photoswitchable SAMs as "smart surfaces" [65] and investigated selective lectin and cell adhesion via electrochemistry. SAMs were fabricated on gold electrodes using azobenzene-conjugated galactoside and mannoside thiols, respectively. They exploited adhesion of PNA and liver cancer cells, i.e. in dependence of the azobenzene configuration of the respective SAMs and showed that "these two smart surfaces showed the ability to take orders from different light signals to operate controllable recognition of selective lectins and cells" [65].

Chen and coworkers prepared a photoresponsive SAM system capable of capturing and releasing bacterial cells [65]. A mixed SAM made of mercapto-functionalized OEG linkers, including those terminating with an azobenzene moiety (**73**), was prepared (Figure 41.12). A multivalent β-cyclodextrin (CD)-mannose glycoconjugate was immobilized on the SAM through host–guest interaction. It is known that the host–guest recognition of CDs with azobenzenes can be reversibly regulated by photoirradiation. The *trans* isomer of azobenzene fits well inside the CD cavity, forming a stable complex, whereas the *cis* isomer does not fit in it and thus the complex breaks [66, 67]. The SAM system prepared by the Chen group exhibited excellent capability for the selective capture of type 1 fimbriated *E. coli* through the formation of a ternary complex between the *trans*-azobenzene glycoside, the cyclodextrin-mannose

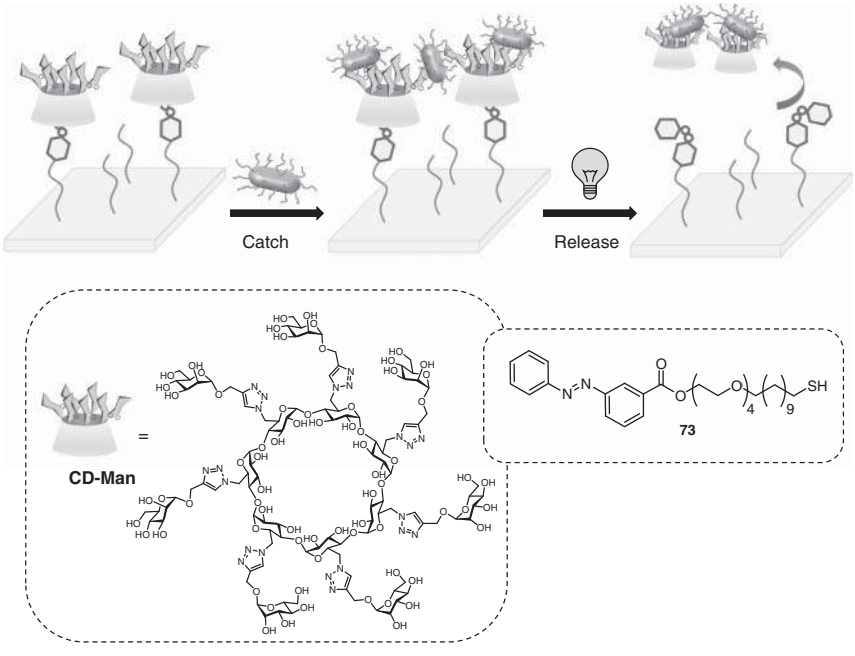


**Figure 41.12** The photocontrolled inclusion of an azobenzene derivative into the cavity of an α-mannoside-decorated cyclodextrin for the selective catch and release of bacteria. Source: Modified from Zhang et al. [65].

glycoconjugate, and type 1-fimbriated bacteria, binding to mannose ligands with the fimbrial lectin FimH. Upon UV irradiation of the SAM, causing *trans* to *cis* isomerization of the azobenzene moiety, the azobenzene–CD complexes dissociated, releasing the captured bacteria from the SAM.

In related work, Chen and coworkers used β-CD derivative decorated with seven quaternary ammonium salt groups as the host molecule instead of the CD-mannose glycoconjugate used before [68]. Ammonium salt-decorated CDs are known to be strong bactericidal compounds [69]. This allowed to construct a dynamic supramolecular platform capable of switching roles reversibly between bacterial killing and bacterial releasing upon UV–Vis light irradiation.

In a somewhat similar approach published by Li et al. the spatiotemporal interrogation and intervention with biofilms was shown [70]. Bacteria tend to organize into networks such as biofilms that offer all advantages of a multicellular community and are relevant for infection. Again D-mannose was used as ligand of the bacterial lectin FimH. Another important element of the work was the use of upconverting nanoparticles (UCNPs), which were modified with the cyclodextrin β-CD, yielding UCNP-CD. Again, the molecular recognition between UCNP-CD and photoswitchable azobenzene glycoconjugates formed the basis of this approach. The UCNPs, however, allow excitation with near-infrared light (NIR) and hence, the intercalation of UCNP-CD and the ABGs could be NIR-controlled, paralleling with bacterial assembly and disassembly both in vitro and in vivo conditions.

## 41.11 Metabolic Oligosaccharide Engineering and AGBs

Metabolic oligosaccharide labeling is a methodology that has greatly complemented the toolbox of the glycosciences. Based on the early findings of Werner Reutter that the biosynthesis of neuraminic acid constituents of the glycocalyx can be chemically altered when modified *N*-acetyl-mannosamin (ManNAc) precursors are fed to a cell [71], the group of Carolyn Bertozzi used ManNAc derivatives equipped with bioorthogonal functionalities such as azido groups to enable labeling of the glycocalyx sugars [72]. This method has paved the way to the biophysical investigation of the glycosylated surface of live cells to finally gain a bigger picture of the biological function of the glycocalyx [73].

In greater detail, *N*-azidoacetyl mannosamin (ManNAz) serves as precursor in neuraminic acid biosynthesis. Neuraminic acid is typically found at terminal positions of glycocalyx oligosaccharides. The azido group in ManNAz is accepted by the biosynthetic machinery and hence appears in neuraminic acid termini of the glycocalyx after metabolic engineering of the cell surface glycans. Likewise, it is possible to apply *N*-azidoacetyl-galactosamin (GalNAz) in the same approach to incorporate the azido label at the core position of mucin-type O-linked glycoproteins [74]. When the $N_3$-functionalized precursors are *O*-acetylated, they can penetrate the cell membrane and are deacetylated by cellular esterases before they enter the glycan biosynthetic pathway.

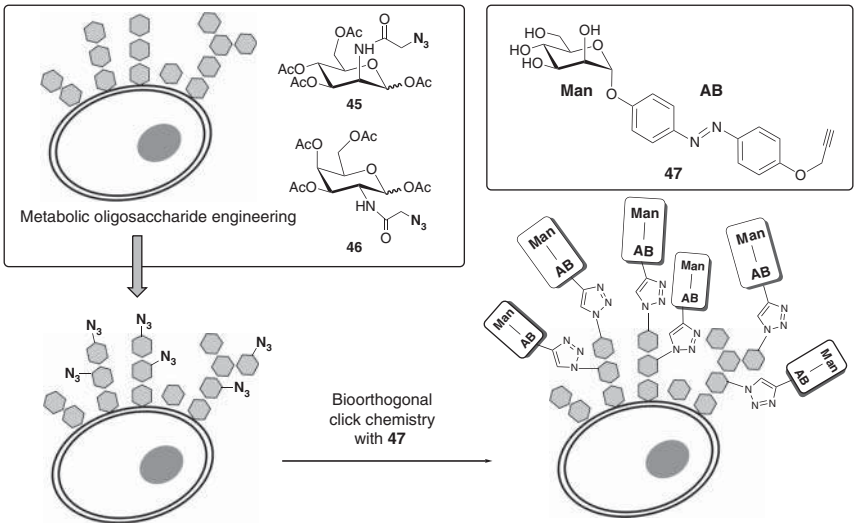


**Figure 41.13** Bioorthogonal labeling of HMEC-1 cell surface with the azobenzene mannoside **44** via metabolic oligosaccharide engineering. Source: Modified from Möckl et al. [75].

We had the obvious idea to combine metabolic oligosaccharide engineering (MOE) with optoglycomics. Building on our results about photoswitching of bacterial adhesion to glyco-SAMs on gold [75], we applied the azobenzene mannoside derivative **47** to prove that photoswitching of bacterial adhesion with small molecules also works in the complex environment of the cell surface (Figure 41.13) [75]. Human microvascular endothelial cells, variant 1 (HMEC-1), were incubated with either tetraacetylated *N*-azidoacetyl-D-mannosamine **45** ($Ac_4$ManNAz) or $Ac_4$GalNAz (**46**) to install bioorthogonal azido functional groups on the cell surface. When $Ac_4$ManNAz is employed and taken up by the cells, azido labeling of terminal neuraminic acid residues is accomplished. When $Ac_4$GalNAz is used in MOE, the azido group appears in *N*-azidoacetyl lactosamine (LacNAc) constituents of mucin-type oligosaccharides, which are not as exposed at the cell surface as neuraminic acid.

We then applied the alkyne-functionalized azobenzene α-D-mannoside **47** for conjugation with the azido-functionalized HMEC-1 surface by copper-catalyzed azide-alkyne cycloaddition (click chemistry). Thus, an effective ligand for type 1 fimbriae-mediated adhesion of *E. coli* was installed and bacterial adhesion tested. When $Ac_4$ManNAz was applied, leading to labeling at the outer regions of the cell surface, conjugation with azobenzene mannoside **47** led to a 50% increase of bacterial adhesion when the azobenzene hinge in *cis* state was photoswitched to the *trans* state. When the cells were labeled with $Ac_4$GalNAz, leading to labeling of inner regions of the cell surface, isomerization of the photoswitchable mannose ligand did not lead to significant differences in bacterial adhesion.

The results showed that the ABG **47** is suited to influence adhesion of *E. coli* to HMEC-1. Bacterial adhesion is most likely mediated through the specific interaction

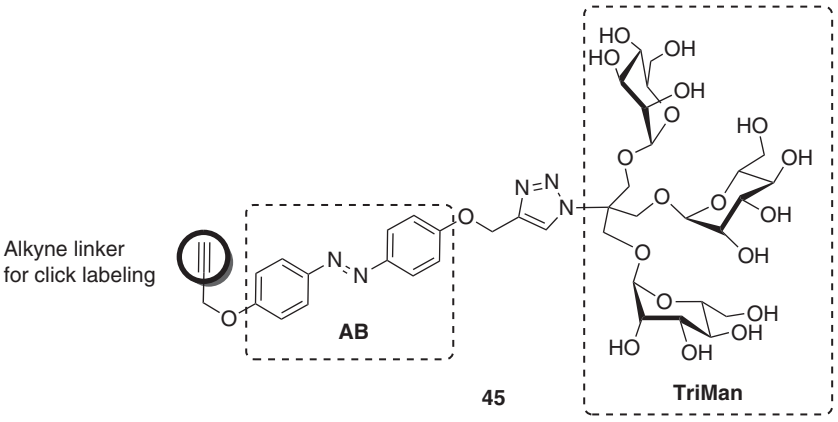


**Figure 41.14** Photoswitchable cluster trimannoside **45** equipped with a terminal alkyne function for further ligation via click chemistry, e.g. on azide-labeled cell surfaces. Source: Modified from Despras et al. [38].

of the bacterial lectin FimH with the azobenzene mannose ligand. Control studies proved that the effect is sugar-specific. Bacterial binding is reduced when the ligand adopts a disadvantageous orientation in the *cis* configuration. Furthermore, it was shown that the FimH ligand must be localized at terminal glycans to ensure that the orientation change upon *cis*/*trans* isomerization is not too small for a biological effect.

Taken together, a combination of MOE, biophysics and the synthesis of smart photosensitive glycoconjugates might pave the way into a new era in the glycosciences.

A second example along the same lines was published in 2019 [38]. When the trivalent photoswitchable FimH ligand **45** (Figure 41.14) was applied with cells labeled with $Ac_4$ManNAz, the trivalent cluster served as ligand for the bacterial lectin FimH in bacterial adhesion studies as expected. In line with previous results with monovalent photoswitchable ligands, bacterial adhesion was found approx. 50% higher in the case of the *trans*-configured ligands than in the *cis* state.

Notably, the conformational flexibility of the cluster mannoside **45** does not prevent the effect of orientational control of sugar presentation, once again underlining the importance of the orientation of carbohydrate ligands in the interaction process between bacterial cells and eukaryotic cells. It appears that relatively small ABGs hold a great potential for further "optoglycomics"-type studies to shed light into the function of the glycocalyx.

## 41.12 Conclusion

It is obvious that the combination of light and tailor-made ABGs of various architectures is a means to shed light into the mysteries of the glycocalyx, the extracellular cell organelle mediating cell–cell communication and cell–cell adhesion. We have suggested the term "optoglycomics" to highlight the power of this new approach in the glycosciences.

With the examples reviewed in this chapter, it becomes clear that ABGs can play an important role in the glycosciences and in biological chemistry, specifically in the spatiotemporal modulation of the relative multivalency of carbohydrates, their presentation in space, the influencing of the properties of macrocycles, and in particular their orientation on surfaces, which was shown to critically effect cell adhesion. Notably, bacterial adhesion and biofilm formation was reversibly controlled successfully.

The new field of the optoglycomics has to be further advanced to reach the power of, for example, MOE. Nevertheless, ABGs have already been successfully combined with MOE to show that the orientational control of cell adhesion is also effective within the environment of the glycocalyx. The photochromic properties of AGBs are often very advantageous, and there are plenty of synthetic entries into various ABG architectures for multiple applications. The synthesis of ABGs also bears the potential for their further modification into red-shifted analogues, suggesting their eventual employment in the biomedical field.

## References


1 Varki, A. and Kornfeld, S. (2017). Historical background and overview, *in Essentials of Glycobiology*, 3rd ed., (Eds. Varki, A., Cummings, R.D., Esko, J.D., Stanley, P., Hart, G. W., Aebi, M., Darvill, A.G., Kinoshita, T., Packer, N.H., Prestegard, J.H., Schnaar, R.L., and Seeberger, P.H.) Cold Spring Harbor, NY: Cold Spring Harbor Laboratory Press.

2 Casalino, L., Gaieb, Z., Goldsmith, J.A. et al. (2020). Beyond shielding: the roles of glycans in the SARS-CoV-2 spike protein. *ACS Cent. Sci.* 6: 1722–1734.

3 Zeng, Y., Zhang, X.F., Fu, B.M., and Tarbell, J.M. (2018). The role of endothelial surface glycocalyx in mechanosensing and transduction. *Adv. Exp. Med. Biol.* 1097: 1–27.

4 Bernardi, A. and Sattin, S. (2020). Interfering with the sugar code: ten years later. *Eur. J. Org. Chem.*: 4652–4663.

5 Werz, D.B., Ranzinger, R., Herget, S. et al. (2007). Exploring the structural diversity of mammalian carbohydrates ("glycospace") by statistical databank analysis. *ACS Chem. Biol.* 2: 685–691.

6 Arnaud, J., Audfray, A., and Imberty, A. (2013). Binding sugars: from natural lectins to synthetic receptors and engineered neolectins. *Chem. Soc. Rev.* 42: 4798–4813.

7 Müller, C., Despras, G., and Lindhorst, T.K. (2016). Organizing multivalency in carbohydrate recognition. *Chem. Soc. Rev.* 45: 3275–3302.

8 González-Cuesta, M., Ortiz Mellet, C., and García Fernández, J.M. (2020). Carbohydrate supramolecular chemistry: beyond the multivalent effect. *Chem. Commun.* 56: 5207–5222.

9 Hakomori, S. (2004). Carbohydrate-to-carbohydrate interaction in basic cell biology: a brief overview. *Arch. Biochem. Biophys.* 426: 173–181.


**10** Todeschini, A.G. and Hakomori, S. (2008). Functional role of glycosphingolipids and gangliosides in control of cell adhesion, motility, and growth, through glycosynaptic microdomains. *Biochim. Biophys. Acta* 1780: 421–433.

**11** Stromberg, N., Nyholm, P.G., Pascher, I., and Normark, S. (1991). Saccharide orientation at the cell surface affects glycolipid receptor function. *Proc. Natl. Acad. Sci. U.S.A.* 88: 9340–9344.

**12** Wang, Z., Chinoy, Z.S., Ambre, S.G. et al. (2013). A general strategy for the chemoenzymatic synthesis of asymmetrically branched N-glycans. *Science* 341: 379–383.

**13** Beharry, A.A. and Woolley, G.A. (2011). Azobenzene photoswitches for biomolecules. *Chem. Soc. Rev.* 40: 4422–4437.

**14** Welleman, I.M., Hoorens, M.W.H., Feringa, B.L. et al. (2020). Photoresponsive molecular tools for emerging applications of light in medicine. *Chem. Sci.* 11: 11672–11691.

**15** Zhang, F., Wang, L.P., Brauner, M. et al. (2007). Multimodal fast optical interrogation of neural circuitry. *Nature* 446: 633–639.

**16** Fehrentz, T., Schönberger, M., and Trauner, D. (2011). Optochemical genetics. *Angew. Chem. Int. Ed.* 50: 12156–12182.

**17** Srinivas, O., Mitra, N., Surolia, A., and Jayaraman, N. (2002). Photoswitchable multivalent sugar ligands: synthesis, isomerization, and lectin binding studies of azobenzene–glycopyranoside derivatives. *J. Am. Chem. Soc.* 124: 2124–2125.

**18** Srinivas, O., Mitra, N., Surolia, A., and Jayaraman, N. (2005). Photoswitchable cluster glycosides as tools to probe carbohydrate-protein interactions: synthesis and lectin-binding studies of azobenzene containing multivalent sugar ligands. *Glycobiology* 15: 861–873.

**19** Ponader, D., Igde, S., Wehle, M. et al. (2014). Photoswitchable precision glycooligomers and their lectin binding. *Beilstein J. Org. Chem.* 10: 1603–1612.

**20** Chandrasekaran, V. and Lindhorst, T.K. (2012). Sweet switches: azobenzene glycoconjugates synthesized by click chemistry. *Chem. Commun.* 48: 7519–7521.

**21** Chandrasekaran, V., Johannes, E., Kobarg, H. et al. (2014). Synthesis and photochromic properties of configurationally varied azobenzene glycosides. *ChemistryOpen* 3: 99–108.

**22** Chandrasekaran, V., Kolbe, K., Beiroth, F., and Lindhorst, T.K. (2013). Synthesis and testing of the first azobenzene mannobioside as photoswitchable ligand for the bacterial lectin FimH. *Beilstein J. Org. Chem.* 9: 223–233.

**23** Berry, J., Despras, G., and Lindhorst, T.K. (2020). A compatibility study on the glycosylation of 4,4′-dihydroxyazobenzene. *RSC Adv.* 10: 17432–17437.

**24** Hain, J., Chandrasekaran, V., and Lindhorst, T.K. (2015). Joining hydroxyazobenzene and mannose under Mitsunobu conditions. *Isr. J. Chem.* 55: 383–386.

**25** Hain, J. and Despras, G. (2018). A two-step approach to a glycoazobenzenemacrocycle with remarkable photoswitchable features. *Chem. Commun.* 54: 8563–8566.

**26** Díaz-Lobo, M., Garcia-Amorós, J., Fita, I. et al. (2015). Selective photoregulation of the activity of glycogen synthase and glycogen phosphorylase, two key enzymes in glycogen metabolism. *Org. Biomol. Chem.* 13: 7282–7288.


**27** Rustler, K., Mickert, M.J., Nazet, J. et al. (2018). Development of photoswitchable inhibitors for β-galactosidase. *Org. Biomol. Chem.* 16: 7430–7437.

**28** Laurent, N., Lafont, D., Dumoulin, F. et al. (2003). Synthesis of amphiphilic phenylazophenyl glycosides and a study of their liquid crystal properties. *J. Am. Chem. Soc.* 125: 15499–15506.

**29** Müller, A., Kobarg, H., Chandrasekaran, V. et al. (2015). Synthesis of bifunctional azobenzene glycoconjugates for cysteine-based photosensitive cross-linking with bioactive peptides. *Chem. Eur. J.* 21: 13723–13731.

**30** Sánchez-León, A.M., Cintas, P., Light, M.E., and Palacios, J.C. (2020). Thermal and photochemical switching of chiral sugar azoalkenes: a mechanistic interrogation. *Eur. J. Org. Chem.*: 2827–2841.

**31** Poonthiyil, V., Reise, F., Despras, G., and Lindhorst, T.K. (2018). Microwave-assisted facile synthesis of red-shifted azobenzene glycoconjugates. *Eur. J. Org. Chem.*: 6241–6248.

**32** Renner, C., Kusebauch, U., Löweneck, M. et al. (2005). A photo-controlled β-hairpin. *J. Pept. Res.* 65: 4–14.

**33** Volgraf, M., Gorostiza, P., Szobota, S. et al. (2007). Reversibly caged glutamate: a photochromic agonist of ionotropic glutamate receptors. *J. Am. Chem. Soc.* 129: 260–261.

**34** Müller, A. and Lindhorst, T.K. (2016). Synthesis of hetero-bifunctional azobenzene glycoconjugates for bioorthogonal cross-linking of proteins. *Eur. J. Org. Chem.*: 1669–1672.

**35** Liu, Z., Nalluri, S.K.M., and Stoddart, J.F. (2017). Surveying macrocyclic chemistry: from flexible crown ethers to rigid cyclophanes. *Chem. Soc. Rev.* 46: 2459–2478.

**36** Geng, W.C., Sun, H., and Guo, D.S. (2018). Azo group(s) in selected macrocyclic compounds. *J. Inclusion Phenom. Macrocyclic Chem.* 92: 1–79.

**37** Xie, J. and Bogliotti, N. (2014). Synthesis and applications of carbohydrate-derived macrocyclic compounds. *Chem. Rev.* 114: 7678–7739.

**38** Despras, G., Hain, J., and Jaeschke, S.O. (2017). Photocontrol over molecular shape: synthesis and photochemical evaluation of glycoazobenzene macrocycles. *Chem. Eur. J.* 23: 10838–10847.

**39** Lin, C., Maisonneuve, S., Métiver, R., and Xie, J. (2017). Photoswitchable carbohydrate-based macrocyclic azobenzene: synthesis, chiroptical switching, and multistimuli-responsive self-assembly. *Chem. Eur. J.* 23: 14996–15001.

**40** Lin, C., Maisonneuve, S., Theulier, C., and Xie, J. (2019). Synthesis and photochromic properties of azobenzene-derived glycomacrolactones. *J. Org. Chem.*: 1770–1777.

**41** Lin, C., Jiao, J., Maisonneuve, S. et al. (2020). Stereoselective synthesis and properties of glycoazobenzene macrocycles through intramolecular glycosylation. *Chem. Commun.* 56: 3261–3264.

**42** Kim, Y., Mafy, N.N., Maisonneuve, S. et al. (2020). Glycomacrocycle-based azobenzene derivatives as chiral dopants for photoresponsive cholesteric liquid crystals. *ACS Appl. Mater. Interfaces* 12: 52146–52155.

**43** Hartrampf, N., Seki, T., Baumann, A. et al. (2020). Optical control of cytokine production using photoswitchable galactosylceramides. *Chem. Eur. J.* 26: 4476–4479.


**44** Reise, F., Warias, J.E., Chatterjee, K. et al. (2018). Photoswitchable glycolipid mimetics: synthesis and photochromic properties of glycoazobenzene amphiphiles. *Chem. Eur. J.* 24: 17497–17505.

**45** Hu, Y., Zou, W., Julita, V. et al. (2016). Photomodulation of bacterial growth and biofilm formation using carbohydrate-based surfactants. *Chem. Sci.* 7: 6628–6634.

**46** Salta, J., Benhamou, R.I., Herzog, I.M., and Fridman, M. (2017). Tuning the effects of bacterial membrane permeability through photo-isomerization of antimicrobial cationicamphiphiles. *Chem. Eur. J.* 23: 1–6.

**47** Feizi, T. and Chai, W. (2004). Oligosaccharide microarrays to decipher the glyco code. *Nat. Rev. Mol. Cell Biol.* 5: 582–588; b).

**48** Laurent N, Voglmeir J, Flitsch SL. Glycoarrays-tools for determining protein-carbohydrate interactions and glycoenzyme specificity. 2008;37:4400–12.

**49** Rillahan, C.D. and Paulson, J.C. (2011). Glycan microarrays for decoding the glycome. *Annu. Rev. Biochem.* 80: 797–823.

**50** Love, K.R. and Seeberger, P.H. (2002). Carbohydrate arrays as tools for glycomics. *Angew. Chem. Int. Ed.* 41: 3583–3586.

**51** Kind, M. and Wöll, C. (2009). Organic surfaces exposed by self-assembled organothiol monolayers: preparation, characterization, and application. *Prog. Surf. Sci.* 84: 230–278.

**52** Pace, G., Ferri, V., Grave, C. et al. (2007). Cooperative light-induced molecular movements of highly ordered azobenzene self-assembled monolayers. *Proc. Natl. Acad. Sci. U.S.A.* 104: 9937–9942.

**53** Ferri, V., Elbing, M., Pace, G. et al. (2008). Light-powered electrical switch based on cargo-lifting azobenzene monolayers. *Angew. Chem. Int. Ed.* 120: 3455–3457.

**54** Siemeling, U., Bruhn, C., Bretthauer, F. et al. (2009). Photoresponsive SAMs on gold fabricated from azobenzene-functionalised asparagusic acid derivatives. *Dalton Trans.* 40: 8593–8604.

**55** Chandrasekaran, V., Jacob, A., Petersen, F. et al. (2014). Improving the switchin capacity of glyco-self-assembled monolayers on Au(111). *Chem. Eur. J.* 20: 8744–8752.

**56** Fast, E., Schlimm, A., Lautenschläger, I. et al. (2020). Improving the switching capacity of glyco-self-assembled monolayers on Au(111). *Chem. Eur. J.* 26: 485–501.

**57** Asadi, A., Razavi, S., Talebi, M., and Gholami, M. (2019). A review on anti-adhesion therapies of bacterial diseases. *Infection* 47: 13–23.

**58** Ofek, I., Hasty, D., and Sharon, N. (2003). Anti-adhesion therapy of bacterial diseases: prospects and problems. *FEMS Immunol. Med. Microbiol.* 38: 81–181.

**59** Knight, S.D. and Bouckaert, J. (2009). Structure, function, and assembly of type 1 fimbriae. *Top. Curr. Chem.* 288: 67–107.

**60** Waksman, G. and Hultgren, S.J. (2009). Structural biology of the chaperone-usher pathway of pilus biogenesis. *Nat. Rev. Microbiol.* 7: 765–774.

**61** Ohlsen, K., Oelschlaeger, T.A., Hacker, J., and Khan, A.S. (2009). Carbohydrate receptors of bacterial adhesins: implications and reflections. *Top. Curr. Chem.* 288: 109–120.


**62** Hartmann, M. and Lindhorst, T.K. (2011). The bacterial lectin FimH, a target for drug discovery – carbohydrate inhibitors of type 1 fimbriae-mediated bacterial adhesion. *Eur. J. Org. Chem.*: 3583–3609.

**63** Weber, T., Chandrasekaran, V., Stamer, I. et al. (2014). Switching of bacterial adhesion to a glycosylated surface by reversible reorientation of the carbohydrate ligand. *Angew. Chem. Int. Ed.* 53: 14583–14586.

**64** Hartmann, M., Papavlassopoulos, H., Chandrasekaran, V. et al. (2012). Inhibition of bacterial adhesion to live human cells: activity and cytotoxicity of synthetic mannosides. *FEBS Lett.* 586: 1459–1465.

**65** Zhang, J., Ma, W., He, X.P., and Tian, H. (2017). Taking orders from light: photo-switchable working/inactive smart surfaces for protein and cell adhesion. *ACS Appl. Mater. Interfaces* 9: 8498–8507.

**66** Samanta, A., Stuart, M.C.A., and Ravoo, B.J. (2012). Photoresponsive capture and release of lectins in multilamellar complexes. *J. Am. Chem. Soc.* 134: 19909–19914.

**67** Nalluri, S.K.M., Voskuhl, J., Bultema, J.B. et al. (2011). Light-responsive capture and release of DNA in a ternary supramolecular complex. *Angew. Chem. Int. Ed.* 50: 9747–9751.

**68** Wei, T., Zhan, W., Yu, Q., and Chen, H. (2017). Supramolecular platform with switchable multivalent affinity: photo-reversible capture and release of bacteria. *ACS Appl. Mater. Interfaces* 9: 25676–25774.

**69** Wei, T., Zhan, W., Cao, L. et al. (2016). Multifunctional and regenerable antibacterial surfaces fabricated by a universal strategy. *ACS Appl. Mater. Interfaces* 8: 30048–30057.

**70** Li, W., Donga, K., Wanga, H. et al. (2019). Remote and reversible control of in vivo bacteria clustering by NIR-driven multivalent upconverting nanosystems. *Biomaterials* 217: 119310.

**71** Keppler, O.T., Stehling, P., Herrman, M. et al. (1995). Biosynthetic modulation of sialic acid-dependent virus-receptor interactions of two primate polyoma viruses. *J. Biol. Chem.* 270: 1308–1314.

**72** Laughlin, S.T. and Bertozzi, C.R. (2007). Metabolic labeling of glycans with azido sugars and subsequent glycan-profiling and visualization via Staudinger ligation. *Nat. Protoc.* 2: 2930–2944.

**73** Möckl, L. (2020). The emerging role of the mammalian glycocalyx in functional membrane organization and immune system regulation. *Front. Cell Dev. Biol.* 8: 253.

**74** Hang, H.C., Yu, C., Kato, D., and Bertozzi, C.R. (2003). A metabolic labeling approach toward proteomic analysis of mucin-type O-linked glycosylation. *Proc. Natl. Acad. Sci. U.S.A.* 100: 14846–14851.

**75** Möckl, L., Müller, A., Bräuchle, C., and Lindhorst, T.K. (2016). Switching first contact: photocontrol of *E. coli* adhesion to human cells. *Chem. Commun.* 52: 1254–1257.


## 42 Building a Smart Molecular Robot by Combining a Motor Protein and a Molecular Photo-Switch

Nobuyuki Tamaoki

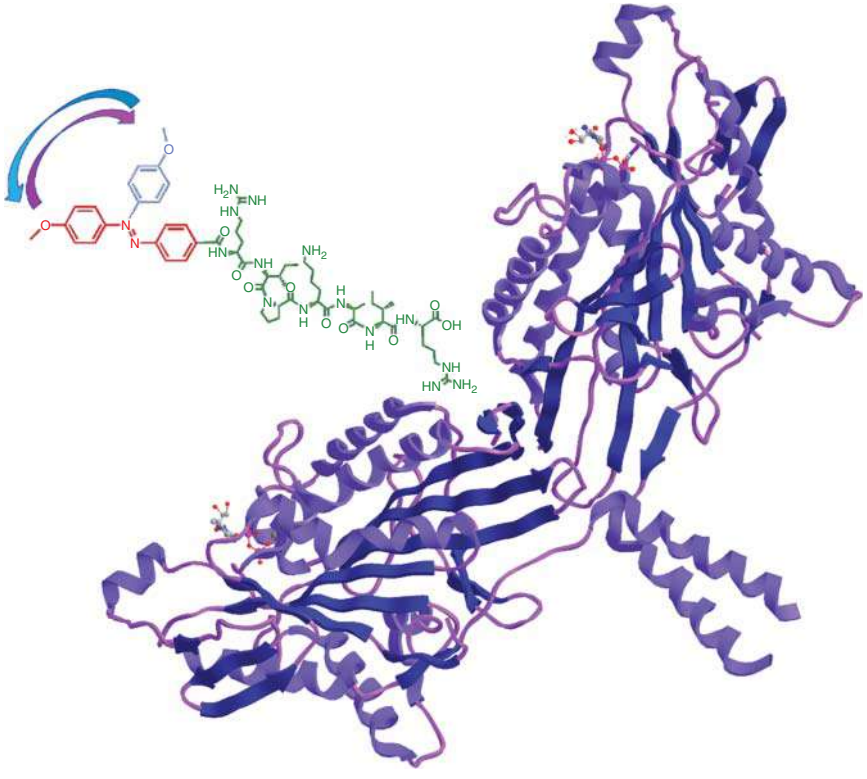

**Characteristic Features**

A smart molecular robot that can "see, judge, and do actions" is constructed by a combination of a motor protein and a suitably designed molecular photo-switches that work as an energy source or an inhibitor.

**Key References**

Perur, N., Yahara, M., Kamei, T. et al. (2013). A non-nucleoside triphosphate powering kinesin-microtubule motility with photo-tunable velocity. *Chem. Commun.* 49: 9935–9937.

Kumar, K.R.S., Kamei, T., Fukaminato, T. et al. (2014). Complete ON/OFF photoswitching of the motility of a nanobiomolecular machine. *ACS Nano* 8: 4157–4165.

Kumar, K.R.S., Amrutha, A.S., Tamaoki, N. (2016). Spatiotemporal control of kinesin motor protein by photoswitches enabling selective single microtubule regulations. *Lab Chip* 16: 4702–4709.

# 42

# Building a Smart Molecular Robot by Combining a Motor Protein and a Molecular Photo-Switch

*Nobuyuki Tamaoki*

*Hokkaido University, Research Institute for Electronic Science, N20, W10, Kita-ku, Sapporo 001-0020, Japan*

When we encounter danger, we visually catch the information, process the information in the brain, and take actions to avoid the danger autonomously according to the result of the information processing. Such smartness seems to be a characteristic of higher organisms that have the brain, nerves, and means of transportation such as feet. However, similar smartness, though more primitive, has also been achieved in unicellular organisms without brains or nerves. For example, Euglena can freely swim in the water using flagella, and when exposed to strong blue light, they move away from it, and when exposed to green light, they gather there (Figure 42.1) [1]. In other words, Euglena feels the light stimulus from the outside, processes the information, makes its own judgment, and takes action. This shows that the brain and nerves are not needed to "see, judge, and act." Then, what is the minimum molecular mechanism required to realize the smartness of "....seeing, judging, and acting"? The author and the coworkers aimed to build a smart molecular robot by combining a motor protein working in the living body with a photoreactive molecule obtained by synthesis [2]. Such a molecular robot is positioned as a prototype of an artificial intelligence molecular robot and is expected to be the first step to realize a drug that autonomously gathers and works in the affected area in the living body and a soft and human-friendly robot in the future.

We selected a motor protein, "kinesin-1/microtubule,", as a movable molecular system. The kinesin-1/microtubule system realizes the generation of forces during mass transfer and cell division within cells. Kinesin-1 has a protein dimer structure with a head group at each N-terminus. The head group catalyzes the hydrolysis of adenosine triphosphate (ATP) and moves on two legs in one direction on microtubules that serve as rails. In the 1980s, Vale et al. established a motility assay method that reproduces the movement of kinesin-1/microtubules in vitro [3]. A flow cell containing a buffer solution is constructed between a pair of glass substrates with kinesin-1 fixed on the inner surface, and the fluorescence-labeled microtubules adsorbed on the kinesin surface slide in one direction due to the movement of the kinesin head due to the action of ATP as shown in Figure 42.2.

*Molecular Photoswitches: Chemistry, Properties, and Applications*,
First Edition. Edited by Zbigniew L. Pianowski.


(A)

(a)

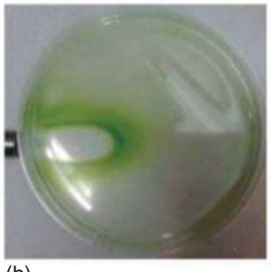

(b)

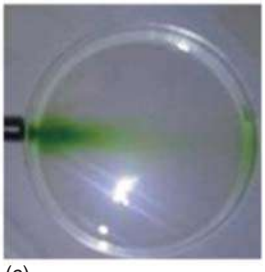

(c)

(B)

**Figure 42.1** (A) Single Euglena, (B) (a) Euglena in a Petri dish, initial state, (b) Euglena after irradiating strong blue light from the left side for 24 hours, (c) Euglena after irradiating strong green light from the left side for 24 hours. Source: Ooka et al. [1]. Reprinted with permission from Royal Society of Chemistry.

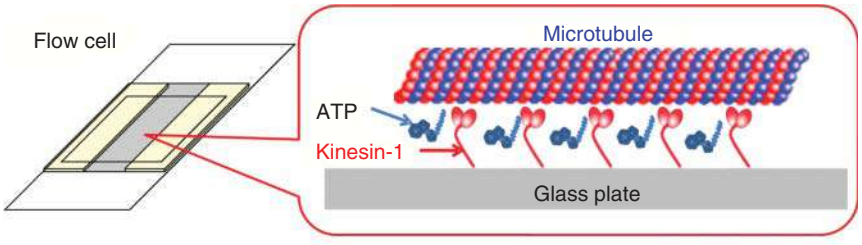



**Figure 42.2** Structure of flow cell for invitro motility assay (top) and a fluorescent image of microtubules (bottom).

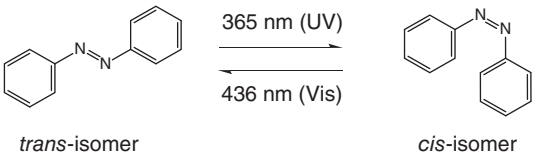


**Figure 42.3** Chemical structures and photoisomerization of *trans*- and *cis*-azobenzenes.

We considered imparting synthetic photoresponsive molecules that could interact with the protein for the purpose of giving vision to this biomolecular machine. As a photoresponsive molecule, we focused on azobenzene, which has been used for photocontrol of various functional molecules. Azobenzene has a structure in which two benzenes are connected by an N=N double bond and have a *trans*- and a *cis*- isomers with respect to the double bond (Figure 42.3). These isomers undergo photo-isomerization reactions upon photoexcitation. In general, the *trans* isomer shows a strong π–π* transition near 330–380 nm, and the *cis* isomer shows a stronger n–π * transition near 400–500 nm. As a result, it is possible to preferentially cause a *trans*-to-*cis* photoisomerization reaction by irradiating near-ultraviolet light around 365 nm and a *cis*-to-*trans* photoisomerization reaction by irradiating blue light around 440 nm. *Trans* and *cis* isomers exhibit a variety of different properties. For example, the molecular length of the *trans* isomer is 9.0 Å and that of the *cis* isomer is as short as 5.5 Å, and the dipole moment is almost 0 for the *trans* isomer while it is 3 D (Debye) for the *cis* isomer. Therefore, by incorporating azobenzene into parent molecules, it becomes possible to reversibly switch the distance between two parts in the molecule and the affinity with other molecules with light.

In order to introduce vision into motor proteins, it is necessary to have a mechanism for relating the above-mentioned synthetic optical switches with the movement of motor proteins. So far, attempts have been made to introduce azobenzene into the microtubule binding site of kinesin-1 by a covalent bond [4]. However, the hydrolysis rate changed only by about 50% by light irradiation, which was incomplete as an optical switch and any photo-switches in the motile functions of kinesin-1/microtubule were not confirmed in the work. As a simpler method, we tried an optical switch of motion by introducing a monolayer containing an azobenzene terminal group on the surface of the substrate that kinesin contacts [5, 6]. Although the gliding speed of microtubules changes reversibly in conjunction with the photoisomerization reaction of the azobenzene monolayer, the magnitude of the change is about 15%. The incomplete optical switching with the photoisomerizable surface probably comes from the fact that the surface that kinesin touches doesn't play a decisive role to the motile function of kinesin.

In order to completely switch the movement of kinesin-1, it is necessary to have a mechanism that works on the function of the hydrolysis site itself while retaining the motor function. So, first, we tried to synthesize a photoresponsive high-energy molecule to replace ATP.

As the first photoresponsive high-energy molecule, ATP-azo was synthesized by introducing azobenzene into the ribose site of ATP, which is the original substrate of kinesin-1 (Figure 42.4, center) [7]. Despite the introduction of azobenzene, ATP-azo was found to act as a substrate to drive the movement of kinesin-1. Furthermore, by

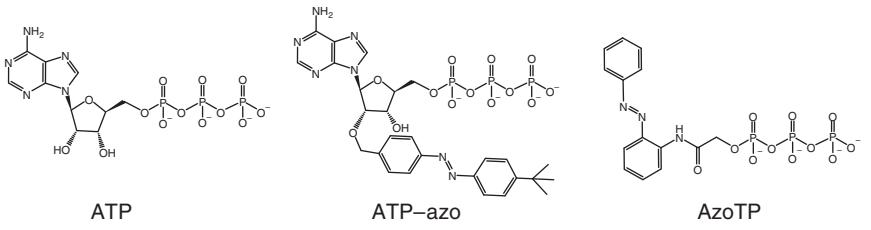


**Figure 42.4** Chemical structures of ATP, ATP-azo, and AzoTP.

the photoreaction from the *trans* isomer to the *cis* isomer by ultraviolet irradiation (actually, the photoreaction proceeds in both directions of the *trans* isomer ↔ *cis* isomer, and the photo-stationary state of 90% *cis* isomer and 10% *trans* isomer is achieved under 365 nm light). It was found that the gliding speed of microtubules increased by 30%. Subsequently, when irradiated with visible light of 436 nm, the gliding speed of microtubules returned to almost the original value. That is, in ATP-azo, the activity as a high-energy molecule changed due to the change in the molecular geometry of the compound, and as a result, the gliding velocity of the microtubule propelled by kinesins fixed on the surface of the substrate could be reversibly changed. However, the magnitude of the change in speed is only 30%, which is not enough. It is known that the ribose site of ATP does not interact with the amino acid residue of kinesin. In ATP-azo, azobenzene was introduced into the ribose site, so that the properties as a substrate of kinesin-1 were not lost. It can be interpreted that the substitution onto the ribose site is also the reason why the characteristics as an energy molecule could not be significantly changed by the photo-isomerization reaction of the azobenzene unit in the molecule. Therefore, we designed a completely new triphosphate derivative in which the adenine ring and ribose moiety were replaced with an azobenzene amide, aiming at a high-energy molecule whose activity is greatly changed by a photoisomerization reaction [8]. The structure of the synthesized compound, AzoTP, is shown on the right side in Figure 42.4. Surprisingly, the compound was a good substrate for kinesin-1/microtubule and induced a maximum kinetic velocity of about half that of ATP (Km is about 10 times that of ATP). Furthermore, when the azobenzene moiety was converted to the *cis* form by irradiating with ultraviolet light (92% *cis* form and 8% *trans* form in a photo-stationary state under ultraviolet light), the gliding speed of microtubules decreased by about 80%. The gliding speed was restored by the subsequent irradiation with visible light, and the switching of the gliding speed by the irradiation with ultraviolet light and visible light could be repeated for at least 10 cycles (Figure 42.5). Detailed analysis has also revealed that the reason why gliding does not stop completely under ultraviolet irradiation is due to the *trans* isomer remained at 8% concentration even at the photo-stationary state under ultraviolet light. The reason why AzoTP shows high activity in the *trans* form and almost no activity in the *cis* form is probably related to the fact that the recognition of the adenine ring at the recognition site of kinesin-1 utilizes hydrophobic interaction and π-π stacking. Compared to *trans* azobenzene, which is a hydrophobic, plate-like π-conjugated system like the adenine ring, *cis*-azobenzene,

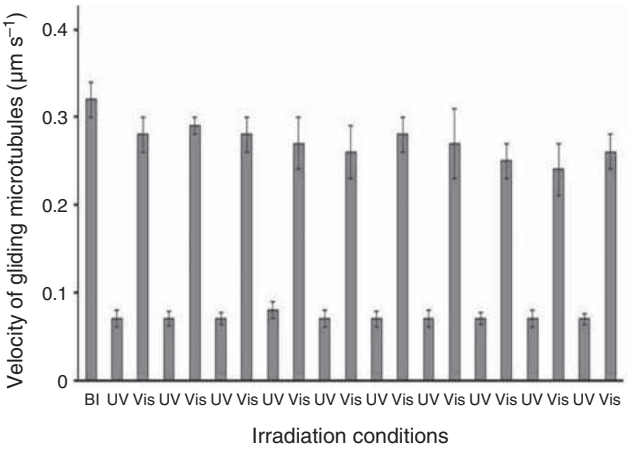


**Figure 42.5** Change of the velocity of the gliding microtubules responding to the irradiation conditions. BI means "before irradiation". UV means "after 366 nm irradiation for 10 seconds". Vis means "after 436 nm irradiation for 30 seconds".

which has a hydrophilic and nonplanar structure, may show a lower affinity for kinesin recognition sites.

AzoTP has also been shown to drive not only kinesin-1 but also other motor proteins such as F1-ATPace and myosin with photoresponsiveness [9]. When AzoTP is added to muscle fibers containing myosin-1, it does not have the ability to contract muscle fibers in the *cis* form, but when it is converted to *trans* form by irradiating blue light on the spot, the muscle fibers contract immediately. That is, AzoTP is a rare non-nucleoside type high-energy compound that widely acts as a substitute for ATPase, and its activity as a high-energy compound can be reversibly changed by light irradiation, in addition to that macroscale events like the contraction of muscle fibers could be induced by the activity of it. Recently, some compounds related to AzoTP have also been synthesized [10]. The structures are shown in Figure 42.6. By introducing substituents to the azobenzene unit or changing the structure of the linker that connects the azobenzene moiety and the triphosphate moiety in AzoTP, compounds (**1e** and**1f**) that selectively exhibits higher activity toward the motor proteins myosin-1 than kinesin-1 were also found.

Aiming at a perfect optical switch that controls with "complete ON and OFF" of the gliding speed of microtubules, we next tried to synthesize a photoresponsive inhibitor. It is known that the C-terminus of the kinesin-1 heavy chain interacts with the head part in the molecule and inhibits the hydrolysis of ATP when it is not loaded with any cargos. Therefore, in kinesin-1 used in the mortality assay, the C-terminus in the molecule is genetically engineered. We synthesized a novel photoresponsive inhibitor (**2a** in Figure 42.7) in which azobenzene was introduced at the amino terminus of a 12-amino acid peptide based on the amino acid sequence of the C-terminus of kinesin-1, and its inhibitory effect and photo-responsiveness were investigated [11]. As a result, the compound **2a** in the *trans* form was found to be a potent inhibitor that completely stops the movement of the kinesin-1/microtubule

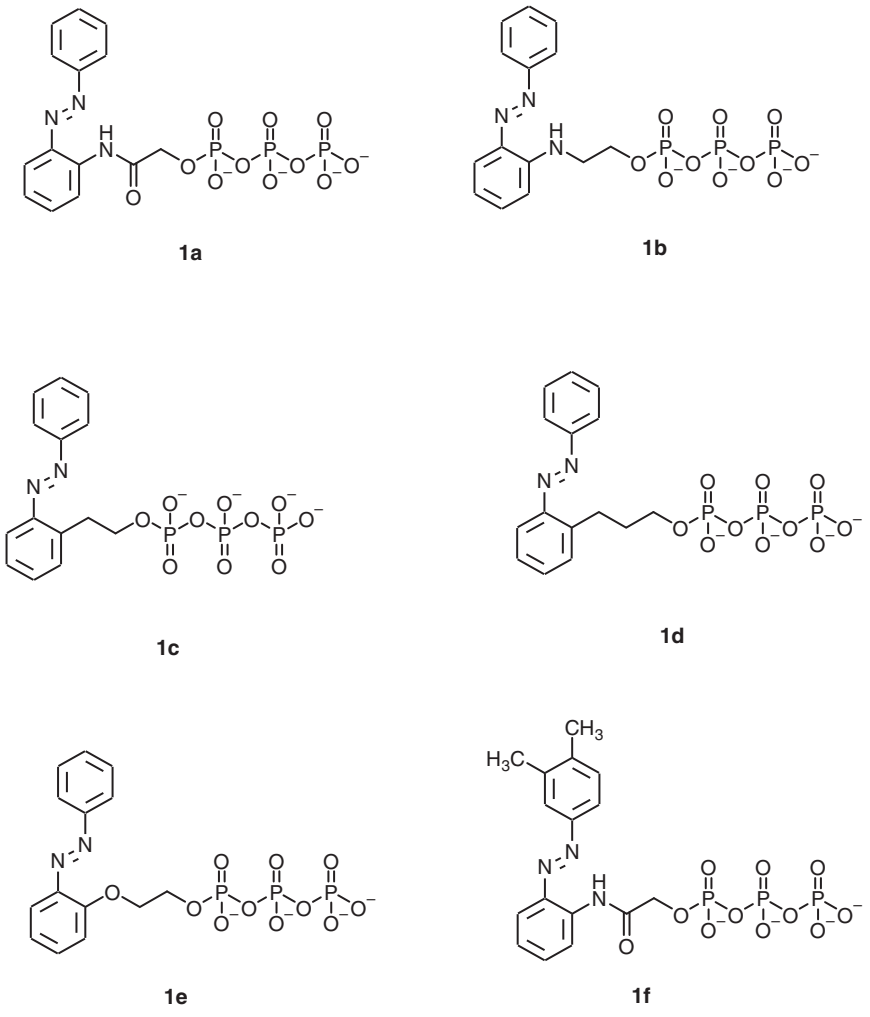


**Figure 42.6** Chemical structures of AzoTP (**1a**) and its analogs.

system even in the presence of ATP. Moreover, in the photo-stationary state achieved by ultraviolet irradiation, almost the same speed as the sliding speed of microtubules in the absence of an inhibitor was observed. Furthermore, by irradiating with visible light, the gliding of microtubules was completely stopped again. That is, the motion of the kinesin-1/microtubule system was repeatedly switched between ON and OFF by alternate irradiations with ultraviolet light and visible light (Figure 42.8).

The properties of the azobenzene-peptide photoresponsive inhibitor acting on kinesin-1 can be tuned by changing the structure of the peptide moiety and the substituents on azobenzene. Figure 42.7 shows the structures of various synthesized azobenzene peptides. First, by optimizing the peptide structure (**2b**) and introducing a methoxy group onto azobenzene (**2**), we have succeeded in producing a strong photoresponsive inhibitor that exhibits an inhibitory effect

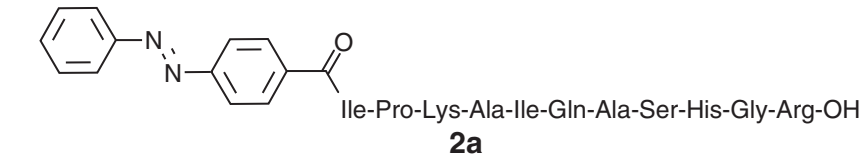


**2a**

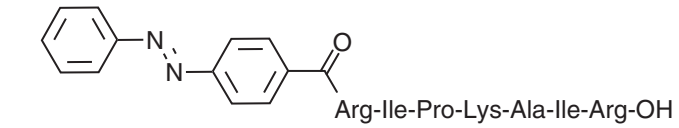


**2b**

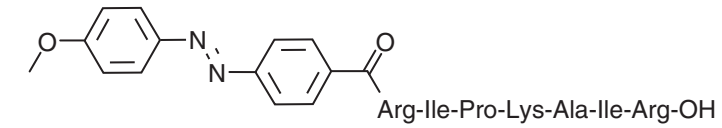


**2c**

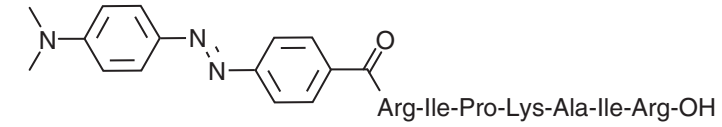


**2d**

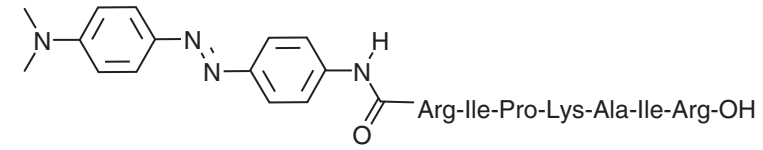


**2e**

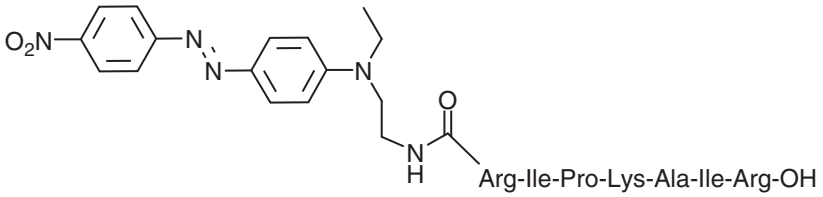


**2f**

**Figure 42.7** Chemical structures of azobenzene-peptides showing photo-switchable inhibition property toward kinesin-1.

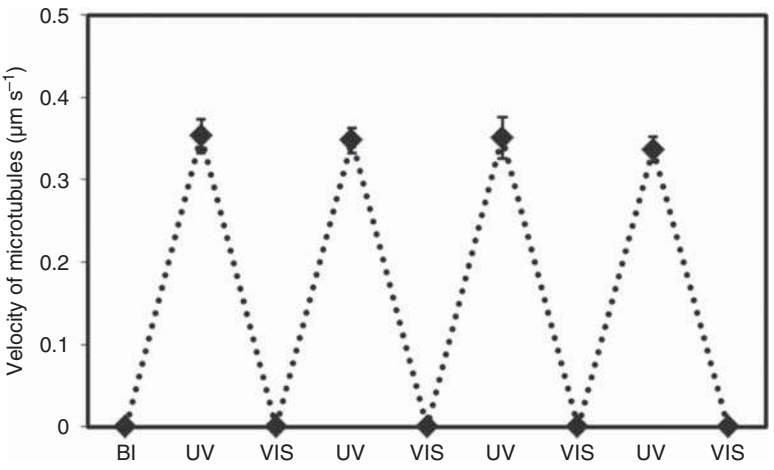


**Figure 42.8** Complete ON–OFF photo-switching of the velocity of microtubules in the presence of 1 mM ATP and the photoresponsive inhibitor **2a** (2 mM). Source: Reprinted with permission from Kumar et al. [11].

even at a low concentration of several tens of micro molar [12]. Further, in the azobenzene-peptide in which an amino group is introduced on azobenzene, the absorption region of the *trans* isomer is shifted toward a long wavelength, and the *trans-cis* isomerization reaction is exhibited with light in the visible light region of about 480 nm (**2d–f**) [13]. In addition, since the *cis* isomer spontaneously returns to the *trans* isomer in less than 1 ms in a dark place, the property enable us to switch between the active state and the inhibitory state of kinesin movement by illuminating and cutting off the light with only one single-wavelength light in the visible range. A combination of a device for irradiating a minute area an argon

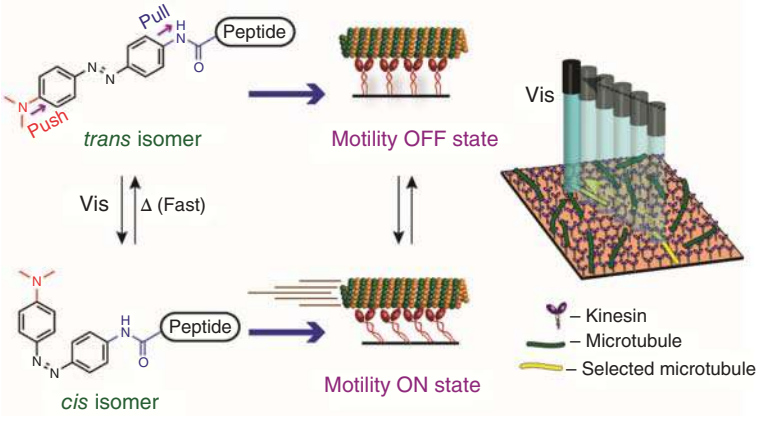


**Figure 42.9** An illustration showing the mechanism of the transportation of a selected single microtubule driven by kinesin-1 whose motile function is photo-regulated by amino-substituted azobenzene-peptide. Source: Reprinted with permission from Amrutha et al. [13].

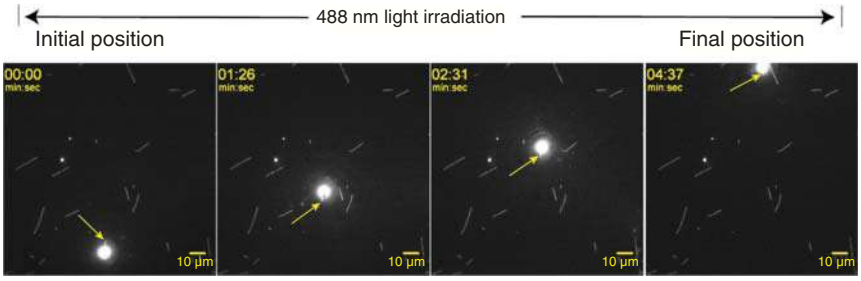


**Figure 42.10** Manipulation of a single microtubule by a visible laser. **2e** was used as a photoresponsive inhibitor. Source: Amrutha et al. [13]. Reprinted with permission from American Chemical Society.

ion laser in a scanning mode (Figure 42.9) and the compound shown here made it possible to selectively let only a single microtubule glide (Figure 42.10).

Finally, using the kinesin-1-microtubule-ATP system containing this photoresponsive inhibitor **2c**, the behavior as a smart molecular robot that discriminates the wavelength of light and shows gathering and scattering were evaluated. As shown in Figure 42.11, ultraviolet light that turn off the inhibitory effect of the inhibitor on the entire flow cell from above the cell and visible light that turns on the inhibitory effect only in a circular area with a diameter of about 25 μm are simultaneously applied [14]. Observation of the movement of microtubules under these irradiation conditions with the fluorescent optical microscope revealed that, all the microtubules inside the circle with a diameter of 25 μm that are exposed to visible light are stopped, while the microtubules outside the circle that are exposed to only ultraviolet light are gliding at a high speed. In addition, as a result that the microtubules outside of the circle sliding in random directions immediately stopped sliding when they entered the circle, the density of microtubules in the circle increased significantly compared to the outside after six minutes. When only the visible light irradiation was stopped after six minutes, all the microtubules in the circle started to slide again, and two minutes after the visible light irradiation was stopped, the microtubules were redistributed over the entire visual field. Theses assembly and redistribution were repeated even after changing the position of visible light. Microtubules seemingly sense the wavelength of light in the environment and, depending on the wavelength, decide whether to escape or stay there. Of course, the ability to glide was in fact brought about by kinesin-1 on the substrate and ATP in the system, and the photosensitivity and gliding ON–OFF functions were attained by the photo-responsive inhibitor interacting with the kinesin-1/microtubule system. Organisms are often perceived as systems that work on their own. However, since various functions of living organisms are also made up of various substances taken in from the outside and the help of symbiotic organisms, it is not special that the molecular robot this time does not express all the functions independently. Namely, the present molecular system composed of kinesin-1, microtubule, ATP and a photoresponsive inhibitor could be regarded as one molecular robot system. In other words, it can be said that this research has

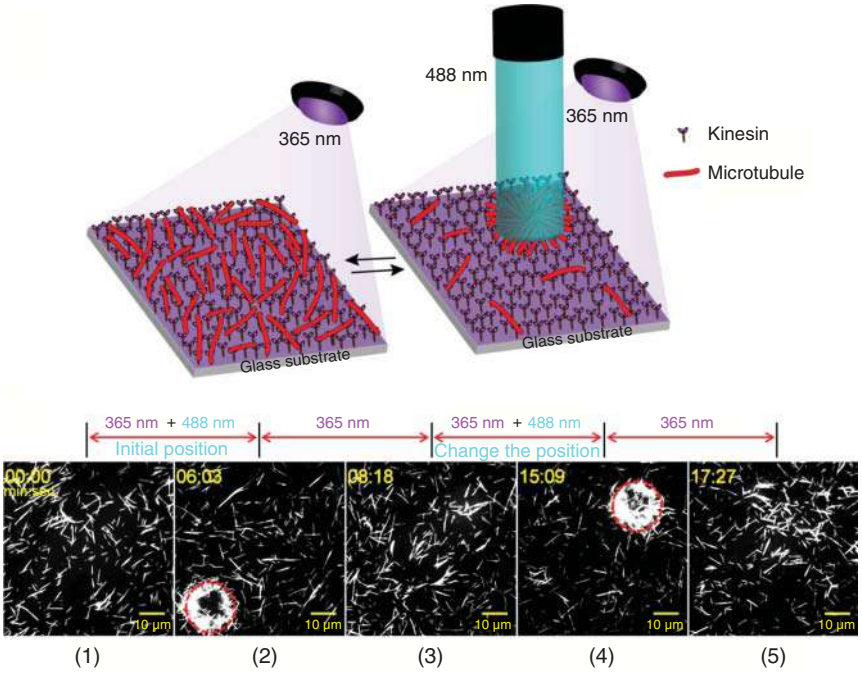


**Figure 42.11** (a) Schematic representation of the irradiation set-up and the dispersion and concentration of microtubules on a kinesin-coated glass substrate under the irradiation with light at 365- and 488-nm. (b) Sequential fluorescence images of gliding microtubules over kinesin in the presence of Azo-peptide and ATP during the in situ photocontrol process: (1) prior to irradiation with 488-nm light; (2) after irradiation with both 488- and 365-nm light; (3) after terminating irradiation with 488-nm light but maintaining irradiation of the entire imaging area with only 365-nm light; (4) after changing the location of 488-nm light irradiation and maintaining irradiation of the entire imaging area under 365-nm light; (5) after terminating irradiation with 488-nm light but maintaining irradiation of the entire imaging area with only 365-nm light. Red circles: Regions of 488-nm light. Source: Kumar et al. [14]. Reprinted with permission from Royal Society of Chemistry/CC BY 3.0.

revealed that a molecular robot that "sees, judges, and acts" can be constructed with a simple mechanism at the molecular level.

## References


1 Ooka, H., Ishii, T., Hashimoto, K., and Nakamura, R. (2014). Light-induced cell aggregation of Euglena gracilis towards economically feasible biofuel production. *RSC Adv.* 4 (40): 20693–20698.

2 Amrutha, A.S., Kumar, K.R.S., and Tamaoki, N. (2019). Azobenzene-based photoswitches facilitating reversible regulation of kinesin and myosin motor systems for nanotechnological applications. *ChemPhotoChem* 3 (6): 337–346.

3 Vale, R.D., Reese, T.S., and Sheetz, M.P. (1985). Identification of a novel force-generating protein, kinesin. *Cell* 42 (1): 39–50.


4 Yamada, M.D., Nakajima, Y., Maeda, H., and Maruta, S. (2007). Photocontrol of kinesin ATPase activity using an azobenzene derivative. *J. Biochem.* 142 (6): 691–698.

5 Rahim, M.K.A., Fukaminato, T., Kamei, T., and Tamaoki, N. (2011). Dynamic photocontrol of the gliding motility of a microtubule driven by kinesin on a photoisomerizable mono layer surface. *Langmuir* 27 (17): 10347–10350.

6 Rahim, M.K.A., Kamei, T., and Tamaoki, N. (2012). Dynamic photo-control of kinesin on a photoisomerizable monolayer - hydrolysis rate of ATP and motility of microtubules depending on the terminal group. *Org. Biomol. Chem.* 10 (16): 3321–3331.

7 Kamei, T., Fukaminato, T., and Tamaoki, N. (2012). A photochromic ATP analogue driving a motor protein with reversible light-controlled motility: controlling velocity and binding manner of a kinesin-microtubule system in an in vitro motility assay. *Chem. Commun.* 48 (61): 7625–7627.

8 Perur, N., Yahara, M., Kamei, T., and Tamaoki, N. (2013). A non-nucleoside triphosphate for powering kinesin-microtubule motility with photo-tunable velocity. *Chem. Commun.* 49 (85): 9935–9937.

9 Menezes, H.M., Islam, M.J., Takahashi, M., and Tamaoki, N. (2017). Driving and photo-regulation of myosin-actin motors at molecular and macroscopic levels by photo-responsive high energy molecules. *Org. Biomol. Chem.* 15 (42): 8894–8903.

10 Islam, M.J., Matsuo, K., Menezes, H.M. et al. (2019). Substrate selectivity and its mechanistic insight of the photo-responsive non-nucleoside triphosphate for myosin and kinesin. *Org. Biomol. Chem.* 17 (1): 53–65.

11 Kumar, K.R.S., Kamei, T., Fukaminato, T., and Tamaoki, N. (2014). Complete ON/OFF photoswitching of the motility of a nanobiomolecular machine. *ACS Nano* 8 (5): 4157–4165.

12 Amrutha, A.S., Kumar, K.R.S., Matsuo, K., and Tamaoki, N. (2016). Structure-property relationships of photoresponsive inhibitors of the kinesin motor. *Org. Biomol. Chem.* 14 (30): 7202–7210.

13 Amrutha, A.S., Kumar, K.R.S., Kikukawa, T., and Tamaoki, N. (2017). Targeted activation of molecular transportation by visible light. *ACS Nano* 11 (12): 12292–12301.

14 Kumar, K.R.S., Amrutha, A.S., and Tamaoki, N. (2016). Spatiotemporal control of kinesin motor protein by photoswitches enabling selective single microtubule regulations. *Lab Chip* 16 (24): 4702–4709.


# 43 Computational Design of Photochromic Proteins

Elliott M. Dolan and Sagar D. Khare

**Characteristic Features**

Computational design endows photocontrol over proteins for biotechnological and pharmacological applications. Photochromic protein design provides novel techniques for investigating biological systems.

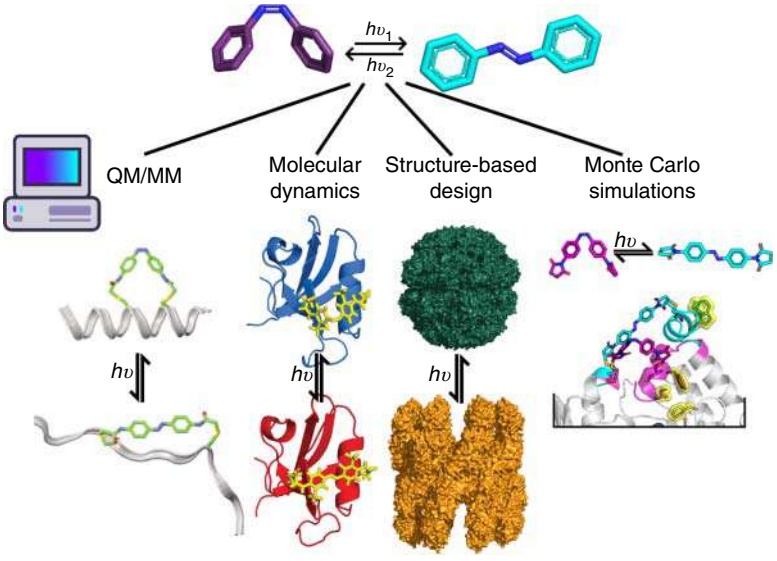


**Key References**

Flint, D.G., Kumita, J.R., Smart, O.S., and Woolley, G.A. (2002). Using an azobenzene cross-linker to either increase or decrease peptide helix content upon *trans*-to-*cis* photoisomerization. *Chem. Biol.* 9: 391–397.

Hoersch, D., Roh, S.-H., Chiu, W., and Kortemme, T. (2013). Reprogramming an ATP-driven protein machine into a light-gated nanocage. *Nat. Nanotechnol.* 8: 928–932.

Blacklock, K.M., Yachnin, B.J., Woolley, G.A., and Khare, S.D. (2018). Computational design of a photocontrolled cytosine deaminase. *J. Am. Chem. Soc.* 140: 14–17.

Guntas, G., Hallett, R.A., Zimmerman, S.P., et al. (2015). Engineering an improved light-induced dimer (iLID) for controlling the localization and activity of signaling proteins. *Proc. Natl. Acad. Sci.* U.S.A. 112: 112–117.

# 43

# Computational Design of Photochromic Proteins

*Elliott M. Dolan and Sagar D. Khare*

*Rutgers The State University of New Jersey, Institute for Quantitative Biomedicine, Department of Chemistry and Chemical Biology, NJ 08854, Piscataway, USA*

## 43.1 Introduction

Key phenomena in the biological world, e.g. photosynthesis, vision, and phototaxis, are reliant on light-responsive proteins. Designing proteins that respond in predictable ways to light – a cheap, external, highly spatio-temporally controllable means of energy transfer – has the potential to endow exquisite control over biological processes. Photocontrolling proteins can aid in the study of enzyme cascades with high precision, disease-like protein aggregation and dissolution, and directed organization of cellular morphologies [1–3]. Beyond using naturally evolved proteins for photoswitching, developing methods to endow photocontrol over any protein of choice would lead to many new applications in diverse areas, e.g. synthetic biology, biocatalysis, and biomedicine.

Natural photocontrollable proteins provide a conceptual blueprint as inspiration for engineering and design. The light-responsive opsins are a class of channel proteins, which pump ions in response to light [4]. Ion conduction is a result of the photoisomerization of a lysine-bound retinal derivative (Figure 43.1a), which leads to conformational changes resulting in the opening of the opsin channel permitting ions to flow across the membrane, allowing for light-controllable neuron depolarization. The photo-oligomerizing cryptochrome proteins function as blue-light responsive regulators [7]. Similar to opsins, cryptochrome proteins bind the chromophore flavin adenine dinucleotide, which induces protein structural shifts resulting in oligomerization when irradiated by blue-light (Figure 43.1b). Opsins and cryptochrome proteins, among others, are foundational to the field of optogenetics. Optogenetics has been illuminating for neurology, but the limited set of photocontrollable proteins restricts applications [12].

Several synthetic approaches have attempted to mimic the natural blueprint of coupling photoresponsiveness of cofactors to propagated conformational changes by conjugating synthetic photo-responsive chemicals to proteins in chosen

*Molecular Photoswitches: Chemistry, Properties, and Applications*,
First Edition. Edited by Zbigniew L. Pianowski.


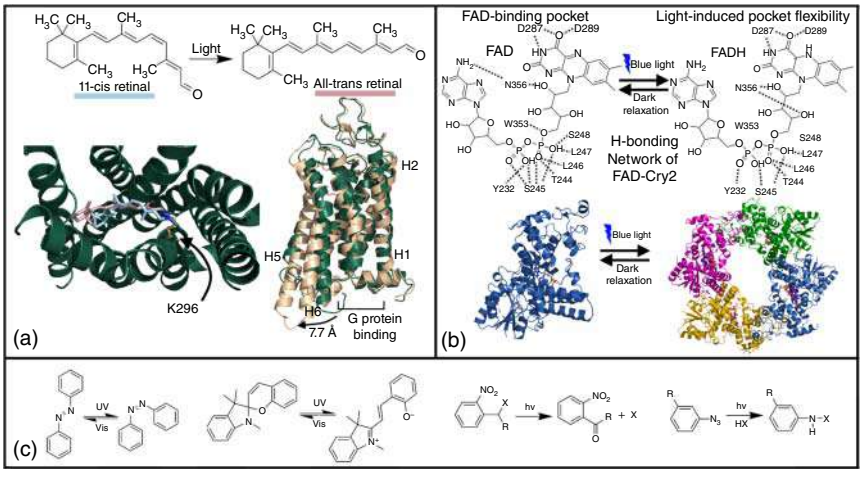


**Figure 43.1** (a) Photoisomerization of 11-*cis*-retinal to all-*trans*-retinal, conjugated to K296 in rhodopsin, photoexcitation results in a conformational shift to all-*trans*-retinal propagating this isomerization (from *cis*-blue to all-*trans*-pink) to allow G protein binding. Source: Refs. [4–6]. (b) Cryptochrome 2 flavin adenine dinucleotide photoactivation and the changes in residue interactions alter tetramerization. Source: Refs. [7–9]. (c) Photoresponsive molecules that have been used for protein photocontrol, including the photoisomerizing molecules azobenzene and spiropyran, and photolabile molecules, including nitrobenzene- and azidobenzene-based chromophores [10]. Source: Refs. [5, 6, 8–11].

locations [13]. Strategies that have been used include irreversible modifications by photolabile groups, and reversible conformational changes by photoisomerizing moieties (Figure 43.1c) [10]. The bio-orthogonality of this approach avoids the use of fusion with recombinant natural photosensitive protein domains (which can have unpredictable effects on protein expression and stability) and expands the parts of the visible spectrum accessible to proteins through modifying the photochromic conjugates themselves. Additionally, this strategy broadens possible protein targets for photosensitizing as the photosensitive component is not endogenous. The Woolley group at the University of Toronto pioneered the field of photocontrolling peptides and proteins, primarily through the conjugation of azobenzene derivatives at select locations on proteins [14].

Computational protein modeling allows for energetic and structural understanding of protein function and enzyme activity and is a powerful tool in rationally designing proteins. Introducing bio-orthogonal photochromic chemicals into computational protein design has yielded a range of successful strategies to create photocontrollable proteins. In this chapter, we present these various computational strategies to design photocontrol into protein secondary structure, inter-domain folding, domain–domain interactions, protein oligomerization, and enzyme activity. We conclude with a short discussion of optogenetic protein design and highlight avenues for improving photochromic protein design.

## 43.2 Designed Photocontrol Over Protein Secondary Structure with Azobenzene

Azobenzene gained the interest of protein scientists when its isomerization energy was determined to be around 10 kcal $mol^{-1}$, approaching the folding energy of many protein structures [15]. Woolley's group soon synthesized an unfolding helical peptide with a thiol-conjugated azobenzene [16]. The helical peptide contained two cysteines located six residues apart ($i$, $i+7$) conjugated by a diiodoacetimide azobenzene crosslinker. The dark-adapted crosslinked peptide exhibited characteristic helical signature at 222 nm in its circular dichroism (CD) spectra. This 222 nm minimum increased significantly when the crosslinked peptide was irradiated with 380 nm light, photoisomerizing the crosslink into the *cis*-state and losing the α-helical structure.

From this proof-of-principle, Woolley and coworkers hypothesized that the spacing between crosslinked cysteines impacts secondary structure preference. The peptide structure would be helical if both the crosslinked isomer and the cysteine spacing were compatible. This compatibility could be tested by modeling crosslinked helical peptides with different cysteine spacing and crosslink isomers; the lower-energy isomer of a given cysteine spacing should be the preferred isomer (Figure 43.2a) [17]. To test this hypothesis, they modeled eight helical peptides, each containing two cysteines positioned at $i$, $i+x$, $x$ ranging from 4–8 and 10–12 onto which the crosslink was conjugated. The azobenzene crosslink was modeled with a B3LYP/6-31G* density functional theory (DFT) method to optimize *cis*- and *trans*-geometries. Crosslinkers were added to each polypeptide in either isomeric state for a total of 16 crosslinked models. The models were first minimized with a molecular mechanics forcefield and then further optimized with QM/MM simulations; the isomer of the crosslink was maintained throughout. The final energies of the models were determined through a single-point energy calculation of the azobenzene conjugated to the cysteines using the B3LYP/6-31G* basis set.

The energy differences between the models indicated that cysteine spacing indicates crosslink isomer preference (Figure 43.2b). *cis*-Azobenzene yielded lower energies with shorter cysteine spacings, and *trans*-azobenzene yielded lower energies with longer cysteine spacings. Experimental validation of two cysteine spacings was performed with $i$, $i+4$ for the *cis*-crosslink and $i,i+11$ for the *trans*-crosslink. The $i,i+4$ spacing was selected for the *cis*-isomer peptide as simulations showed the largest energy difference between isomers and a lower total energy than the $i,i+5$ crosslink. For the *trans*-isomer peptide, the $i,i+11$ spacing was selected to prevent the crosslinker from twisting around the helix (as it would in $i+10$) and the $i+11$ spacing included more residues to destabilize upon isomerization.

The cysteine-spacing validation was conducted on two helical peptides, one with an $i,i+4$ Cys-spacing and one with $i,i+11$ Cys-spacing. The $i,i+4$ peptide was predicted to have $\alpha$-helical conformation in the *cis*-crosslinker state. As predicted, the CD spectrum showed helical content when *cis*-isomerized with 370 nm light and a decrease in helical content under a dark-adapted (*trans*) state (Figure 43.2c). Following this, the $i,i+11$ peptide was predicted to show helical structure in the

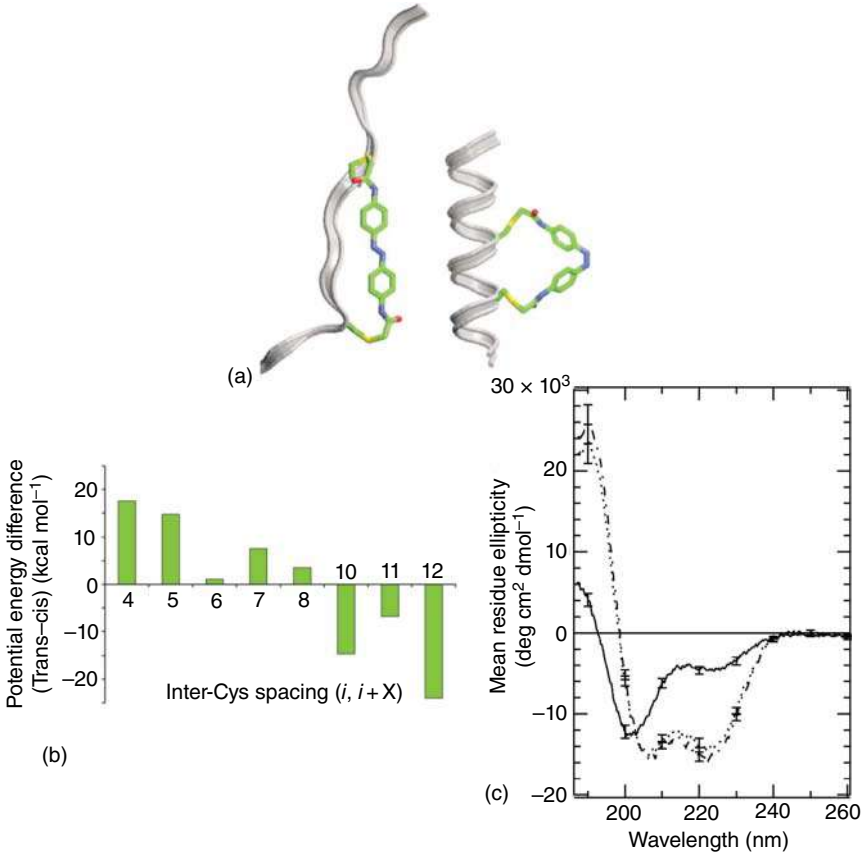


**Figure 43.2** Computational and experimental results of diiodoacetimide-azobenzene conjugated to dual-cysteine mutants of the peptide Ac-$(EAAAK)_3$-A-$NH_2$ peptide. (a) Energy-optimized models of Cys-*i,i* + 4 peptide conjugated to a *cis*- or *trans*-azobenzene crosslinker. (b) Energy differences between *trans*- and *cis*-crosslinked peptides with different cysteine spacings. The more positive or negative the energy is, the greater a *cis*- or *trans*-crosslinker, respectively, will stabilize an α-helical structure. (c) Circular dichroism spectra of the crosslinked Cys-*i,i* + 4 peptide when dark-adapted – *trans*-crosslink (solid line) and when irradiated – *cis*-crosslink (dotted line). Calculated CD spectra for a 100% *cis*-crosslink peptide are shown as a dash–dot line [17]. Source: Flint et al. [17].

dark state and a disordered structure in the excited state. Similarly, the *i,i* + 11 peptide demonstrated an increase in helical content under the dark-adapted state and a decrease in helical content in the excited state. This experimental change in helical content matched the study design goals. This modeling and validation were the first designing of photocontrol into protein structure. The design method Flint et al. used is computationally expensive but was functional and practical as their total design set was small – only a few peptides were tested.

Waldauer et al. pursued an analogous method when designing a minimal photoswitchable β-sheet peptide to investigate amyloid fibril aggregation [2]. Their goal was to design a minimal photocontrollable peptide capable of β-sheet formation

in one state and a soluble monomer in the other. The minimal peptide length was determined to be five residues with azobenzene as the crosslinker between cysteines at $X_1$ and $X_5$. With a minimal peptide selected, their computational design strategy was to create a peptide that will β-aggregate in the *trans*-state and resolubilize in the *cis*-state.

Computational design was performed as a series of rounds of molecular dynamics simulations. Each round sampled a different peptide sequence, with subsequent rounds further simulating previous best sequence designs. The peptide simulations were performed with the CHARMM program with either implicit or explicit solvents and models were ranked by a set of order parameters. These parameters calculate the propensity of the *trans*-state crosslinked peptides to adopt β-sheet conformations ($P_2$) and the number of inter-chain hydrogen bonding between peptides to occur ($P_1$). For *cis*-state crosslinked peptides, the radius of gyration was also computed throughout the trajectory as a measure of solubility.

An initial round of simulations was conducted on crosslinked pentapeptides at the $X_3$ position to determine its effect on β-sheet aggregation formation. Trimer simulations of the *trans*-crosslinked peptides CAGAC and CAAAC revealed alanine hinders β-aggregation, yielding glycine as the most optimal $X_3$ amino acid. The second round of design explored modeling all possible residue combinations at positions $X_2$ and $X_4$ of the *trans*-crosslinked pentapeptide. Trimer simulations were performed to sample each mutant's propensity for β-sheet formation ($P_2$) with fast implicit solvent simulations. The average propensity for this β-sheet formation ($P_2$) was used to rank designs, and the top 15% went to the next round of design. In the third round, hexapeptide variants with crosslinkers fixed in the *cis*- or *trans*-states were considered. *Trans*-crosslinked simulations were ranked according to average inter-hexapeptide hydrogen bond number to favor β-aggregation, and *cis*-crosslinked simulations were ranked by average radius of gyration ratio analogous to solubility. These rankings were summed for each hexapeptide, and the 15% best-ranked mutants were further modeled. The fourth set of simulations contained eight replicates of the hexapeptides modeled in either *cis*- or *trans*-states (Figure 43.3a). The *trans*-state simulations determined the hexapeptide CHGQCK had the highest amount of intermolecular backbone hydrogen bonds and highest scoring-order parameters P1 and P2 (Figure 43.3b). The *cis*-state simulations indicated the hexapeptides all formed disordered aggregates with their radius of gyration metric independent of sequence. Three final eight-peptide-containing simulations were performed on the *trans*-crosslinked hexapeptide CHGQCK with explicit waters. In all three simulations, an octameric β-aggregate morphology formed and was stable with a single simulation modeling fibril breakage as a monomer separated from the oligomer and remained monomeric. These aggregate models also included azobenzene contributing to oligomer packing through benzene pi-stacking and diazene hydrogen bond formation.

Waldauer et al. then synthesized the crosslinked CHGQCK peptide for experimental validation. The models predict aggregation in the dark-adapted *trans*-state and dissolution in the UV irradiated *cis*-state. Light-scattering experiments indeed demonstrated oligomerization in the absence of UV light and dissociation when

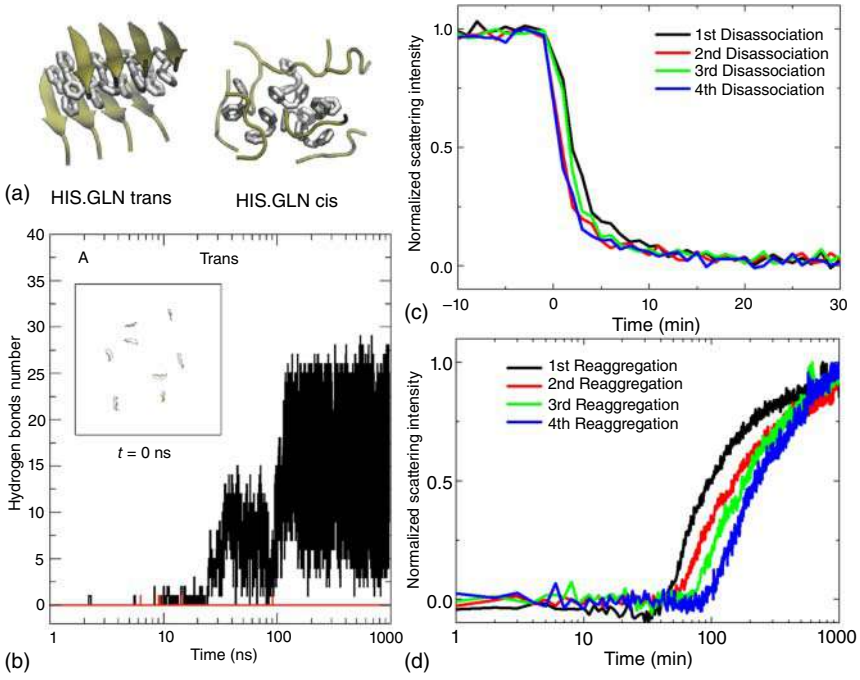


**Figure 43.3** Simulation and experimental results of the minimal photoswitchable peptide that undergoes light-dependent aggregation. (a) Simulation snapshots of the HIS.GLN hexapeptide in the aggregate state (*trans*) and soluble state (*cis*). (b) Hydrogen bond count of a simulation trajectory of the octamer HIS.GLN hexapeptide with a *trans*-crosslinker. Increasing hydrogen bonds form during aggregation. (c) Light scattering of 4 disassociation events of the His. Gln hexapeptide by UV light. (d) Light scattering of 4 reaggregation events. (c, d) were performed in one 165 hour experiment on the same set of peptides [2]. Source: Waldauer et al. [2].

exposed to UV light. An amyloid-like fibril indicator (polythiophene acetic acid) detected the *trans*-state hexapeptide aggregation, indicating the hexapeptide oligomers are similar to amyloid-like fibrils [18]. The indicator fluorescence decreased after the hexapeptide was exposed to UV light, corresponding to similar shifts observed in polythiophene acetic acid binding to amyloid-like fibrils. Oligomerization required 35 to 100 minutes to be measurable and 12 hours to reach a maximal aggregation equilibrium, but complete dissociation occurred in five to ten minutes upon irradiation (Figure 43.3c,d). Oligomerization and dissociation were found to be reversible and repeatable four times over a period of one week, but there was a noticeable decrease in oligomerization rate after repeated bouts. This work shows evidence that through multiple rounds of design selection utilizing molecular dynamics simulations, β-sheet oligomerization can be designed for photocontrol. Proper analysis of molecular dynamics simulations appears to be a good design strategy for small peptide systems. However, performing simulations with many computational trajectories becomes prohibitively expensive as the system size grows.

## 43.3 Computationally Guided Structural Design of Photoswitching Protein Domains

Design of azobenzene crosslinking can be performed by examining the structure of the protein domain and selecting possible crosslink residue pairs that fit a set of geometric criteria (e.g. end-to-end distance) corresponding to the chemical structures of the photoswitch and the crosslinking residues. This method for computational design has proved quite successful, though it does not explicitly evaluate the effect of crosslinking on protein structure or stability.

Zhang et al. used this approach to conjugate a FynSH3 protein domain with an azobenzene derivative and the altered stability bestowed photocontrol over peptide binding [19]. The design strategy was to determine candidate residue pairs within *cis*- or *trans*-azobenzene end-to-end distances. From this first set of candidates, each pair was mutated to cysteine, and all possible interatomic S—S distances were calculated. Three candidate pairs were selected from the set, each pair satisfying the inter-cysteine sulfur distance, which matches either the *cis*- or *trans*-azobenzene state (Figure 43.4a). These mutants were created in the laboratory, crosslinked, and screened for photocontrol. Of the three mutants, the crosslinked candidate L3C-L29C FynSH3 (LLF) displayed the highest amount of CD spectral shift upon photoisomerization, which was further enhanced by introducing the FynSH3 destabilizing T47A substitution. The LLF CD spectrum indicated a near native fold when excited to the *cis*-state conformation and a loss of fold in the dark-adapted state. Upon *trans*-to-*cis* isomerization (Figure 43.4b), NMR chemical shifts became more similar to the chemical shifts of the folded, un-crosslinked protein. This indicates that the *trans*–*cis*-isomerization induces an unfolded to a near-native folded state transition. Previous work show that peptide binding to the FynSH3 domain is dependent on foldedness [23]. Isothermal titration calorimetry was performed to measure affinity of the *cis*- and *trans*-LLF. Dark-adapted *trans*-LLF attenuated binding by more than a threefold over the uncrosslinked LLF ($K_d = 3.4\,\mu M$ down from $1.0\,\mu M$). Irradiated *cis*-LLF enhanced binding with a twofold increase ($K_d = 0.56\,\mu M$ up from $1.0\,\mu M$). From these experiments, the authors concluded the *cis*-LLF has a native-like folded structure, which is lost upon isomerization.

While lacking the detailed picture obtainable from MD or quantum mechanics (QM) simulations, Zhang et al. showed that structure-based rational design methods can result in photocontrol over domain folding, even though the dynamic range for the obtained switches is small. Hoersch et al. utilized similar photoswitches to control bulk conformational shifts in a larger protein (Figure 43.4c–e) [20, 21]. By designing interfaces in an oligomeric protein, they employed similar structural-guided design to create photocontrolled protein machines. The group II chaperonin from *Methanococcus maripaludis* is a 16-mer protein composed of two opposingly stacked C-symmetric octamers [20, 21]. This chaperonin resides in an "open" state until adenosine triphosphate (ATP) binding and hydrolysis triggers a conformational shift to a "closed" state. Hydrolyzed ATP release returns the chaperonin to an open state. Conformational and functional changes such as the change observed in the chaperonin are common in nature but are difficult to design. Hoersch et al.'s strategy to control the conformational shift was to design in an

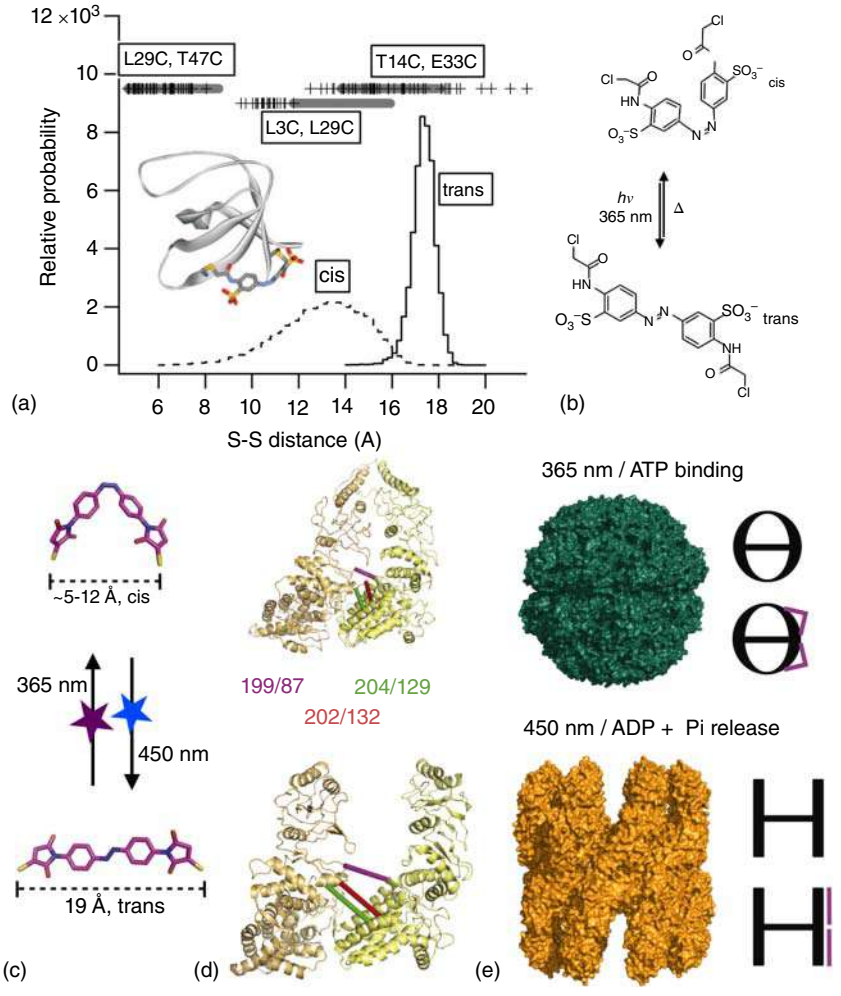


**Figure 43.4** Photoswitch structural design in the FynSH3 domain and the *M. maripaludis* chaperonin. (a) Interatomic S—S distance distributions for *cis*- and *trans*-crosslinkers on the FynSH3 protein from molecular dynamics (MD) simulations of X-ray and NMR structures (solid bars and crosses, respectively) [19]. (b) The BSBCA crosslinker in its *cis*- and *trans*-orientation [19]. (c) The ABDM crosslinker in its *cis*- and *trans*-isomer, illustrating distance changes induced by photoisomerization for inducing mechanism action [20, 21]. (d) Inter-monomer crosslink locations structurally identified for photo-induced chaperonin opening and closing [20]. (e) Open–close models of the *M. maripaludis* Group II chaperonin protein under both natural conditions and crosslinked photoisomerizing conditions, represented by Θ (closed) and H (open) with a straight or crooked purple line (*trans*- or *cis*-ABDM crosslinker) [20, 21]. Images of proteins with PDB accession codes 3LOS and 3IYF were made with Pymol [11, 22]. Source: (a, b) Zhang et al. [19]. (c–e) Modified from Hoersch et al. [20].

azobenzene photoswitch between proteins in both symmetric octamers to control the open or closed state of the chaperonin (Figure 43.4e).

The azobenzene-dimaleimide photoswitching crosslinker was selected due to its maximum end-to-end distance change of 5 Å (*cis*) to 18 Å (*trans*; Figure 43.4c). Residue pairs were first selected that satisfied the geometry of the *cis*-azobenzene between monomers of the closed-state chaperonin. Residue pairs were then selected satisfying the geometry of *trans*-azobenzene between monomers in the open-state chaperonin. The authors required that the designed cysteines must be solvent-accessible to allow for azobenzene-dimaleimide conjugation, so a minimum amount of Cys-S solvent-accessible surface area was required for a valid pair. Between the open and closed set of residue pairs, three sets were selected.

The designed chaperonin did not suffer loss of function and was still capable of ATP-dependent opening and closing in the uncrosslinked state. The chaperonin was then crosslinked by the photoswitch in the closed state by increasing the population of the closed state by incubation with a phosphate mimic ($AlF_X$). Once suitably labeled, the azo-chaperonin demonstrated the designed opening with irradiation of 450 nm light to shift the azobenzene into the *trans*-conformation (Figure 43.4e). Azo-chaperonin was exposed to 365 nm light, closing the azo-chaperonin with the *trans*-to-*cis* photoisomerization of the conjugated azobenzene. Experimental evidence showed this light-based conformational shifting to be reversible and repeatable. The addition of $AlF_x$ to azo-chaperonin triggered the functional conformation change to the closed state. Exposure of 450 nm light predominantly drove the azo-chaperonin into the open-*trans*-state and overrode the $AlF_x$-driven closed state. The *cis*-state of the azo-chaperonin conformationally shifted between the closed–open state (upon ATP binding and hydrolysis, respectively), yet the energy transduced by azobenzene isomerization is sufficient to overcome the ATP-binding barrier.

Structure-guided rational design strategy for the chaperonin was a good choice due to its size – performing explicit atomistic modeling, e.g. MD simulations on a > 230 kDa protein is impractical. These examples of designing photocontrol over protein conformation and function highlight the strengths of structure-guided design. However, protein functions, which require subtle interactions, e.g. cofactor binding, may require a more sophisticated consideration of the conformational landscape of the protein.

## 43.4 Protein Activity Modulation with Photoswitchable Crosslinkers

Many proteins gain or lose function upon binding to certain cofactors. Ritterson et al. set out to design a photoswitchable cadherin based on that principle [24]. Cadherins are cell–cell adhesion proteins, which oligomerize upon binding to calcium. The design strategy was to use photoisomerization of an azobenzene derivative to modulate calcium binding and thus cadherin oligomerization.

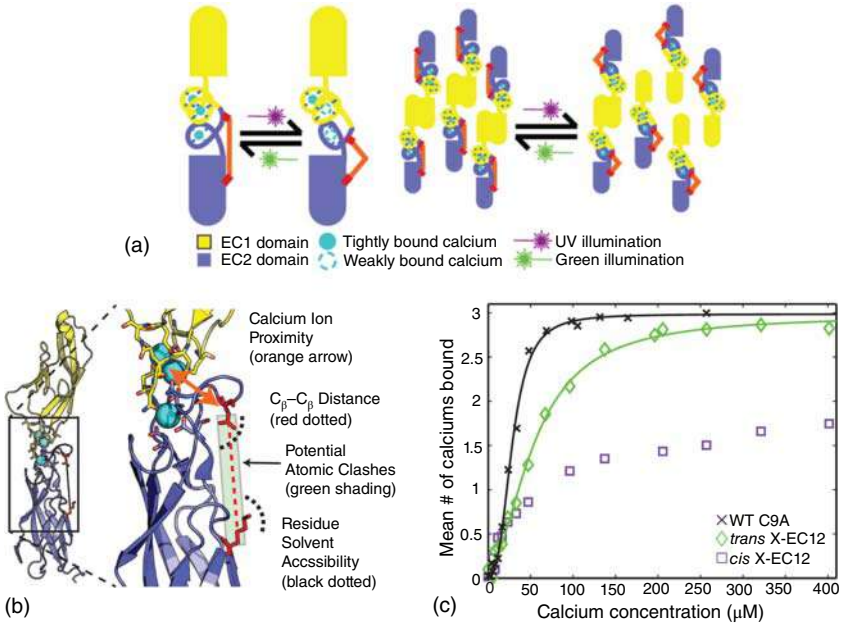


**Figure 43.5** (a) Cartoon design strategy for conjugation of a photoswitch to calcium-binding loops for reversible oligomerization of cadherin. (b) Target of the BSBCA photoswitch to modulate calcium binding of cadherin, labels indicating design considerations. (c) $Ca^{2+}$ binding by mass spec of the Wild Type (WT), *trans*-crosslinker, and *cis*-crosslinker states of the designed cadherin [24]. Source: Ritterson et al. [24].

Their design targets were the $Ca^{2+}$-binding loops in the cadherin, shown to be important for function (Figure 43.5a). The design strategy was based on a combination of structural and energetic computational methods (Figure 43.5b). To identify potential Cys substitutions, they first mutated (*in silico*) all residues in a set of cadherin structures to alanine and removed residues from consideration if the alanine substitution destabilized the protein by >1 kcal $mol^{-1}$. Next, they selected residue pairs with geometrically compatible distances to the azobenzene derivative BSBCA, between 17 and 20 Å for $C_\beta$ distances. Positions were then rejected for lack of solvent accessibility for photoswitch conjugation and predicted steric clashes upon conjugation. With this strategy, 11 pairs were selected. Experimental characterization showed one pair with the best switchability and function. This azo-cadherin was further characterized.

The azo-cadherin underwent repeated reversible isomerization of the photoswitch through oscillating irradiation of 370 and 500 nm light (Figure 43.5c). With the photoswitch bound and photoisomerizable, *cis*-azo-cadherin was predicted to have lower $Ca^{2+}$ affinity than *trans*-azo-cadherin. *Trans*-azo-cadherin demonstrated twofold weaker affinity than the wild type. *Cis*-azo-cadherin $Ca^{2+}$ binding was diminished to a point not measurable by the assay. *Cis*-state $Ca^{2+}$ binding was thus quantitatively determined through correlating $Ca^{2+}$ binding as a function of *cis*-photoswitch half-life. This experiment yielded a $Ca^{2+}$-binding $K_d$ nearly 18-fold

higher in the *cis*-state than the *trans*. The authors sought to measure oligomerization affinity changes when oligomerized under a *cis*- or *trans*-azo-cadherin. The wild-type $EC_{50}$ was measured to be 72 μM. The *trans*-azo-cadherin $EC_{50}$ was slightly reduced to 176 μM, and the *cis*-azo-cadherin $EC_{50}$ was further reduced to 619 μM. This reduction in $EC_{50}$ correlates with the $Ca^{2+}$ binding in the photoswitching azo-cadherin.

Cadherin cofactor binding is analogous to enzyme activity in that the binding pocket can be destabilized to alter activity. Using similar structural design methods to both identify residues near an active site and determine energetically beneficial crosslinker placements can aid in designing enzyme photocontrol. This approach was extended by Blacklock et al. in their design of a photoswitchable yeast cytosine deaminase (yCD) [25]. Blacklock et al.'s computational protocol was designed to locate residue pairs around an enzyme active site, conjugate a photoswitch to those residues, and explicitly evaluate the impact of isomerization on active site geometry to determine if the enzyme can be photomodulated. Their design target was the enzyme yCD – a zinc-containing dimeric metalloenzyme cytosine deaminase. This enzyme is of therapeutic interest as it generates the toxin 5-fluorouracil from non-toxic 5-fluorocytosine. If yCD could be photocontrolled, it could provide a powerful chemotherapeutic tool when used in conjunction with 5-fluorocytosine.

To control yCD activity, a computational tool was developed to design for photocontrol with the 4,4′-bis(maleimide)azobenzene (ABDM). First, the RosettaMatch algorithm was used to determine all geometrically possible placements of the photoswitch on yCD. The photoswitch and corresponding cysteines were modeled into location and designed further using RosettaDesign. Final designs were selected based on several parameters: distance from the active site, total Rosetta energy units, conformational strain on the crosslink, and the *cis–trans* isomerization's potential to disrupt the model active site (Figure 43.6a).

The top mutants were produced in the lab and crosslinked with ABDM, and then tested with a cytosine consumption assay [26]. A crosslinked mutant, yCD-Opt1, increased enzyme activity upon 370 nm irradiation compared to dark-adapted state. Another mutant, yCD-Opt2, demonstrated no activity changes upon irradiation but higher activity when crosslinked. Further simulations were performed on each of the crosslinked mutants to identify the structural effects of *cis–trans* isomerization (Figure 43.6b). This computational isomerization was performed by isomerizing the crosslink and minimizing the structure. While yCD-Opt1 *trans*-isomerization simulations featured protein backbone shifts from the wild-type structure, the yCD-Opt2 simulations did not, supporting the experimental data reported.

yCD-Opt1 showed a 2.5-fold increase in activity under UV-light compared to the dark-adapted state (Figure 43.6c). The authors presented a high degree of yCD-Opt1 photocontrol by switching the light repeatedly over the course of a single assay, resulting in corresponding changes in activity (Figure 43.6d). yCD-Opt1 acted on 5-fluorocytosine in a photocontrollable manner with a ~ 1.5 fold activity difference in the UV-excited state over the dark-adapted state. CD experiments showed similar melt curves between yCD-Opt1 and the wild type. Such similarity indicates that the crosslink isomerization caused a localized disruption of enzyme activity rather

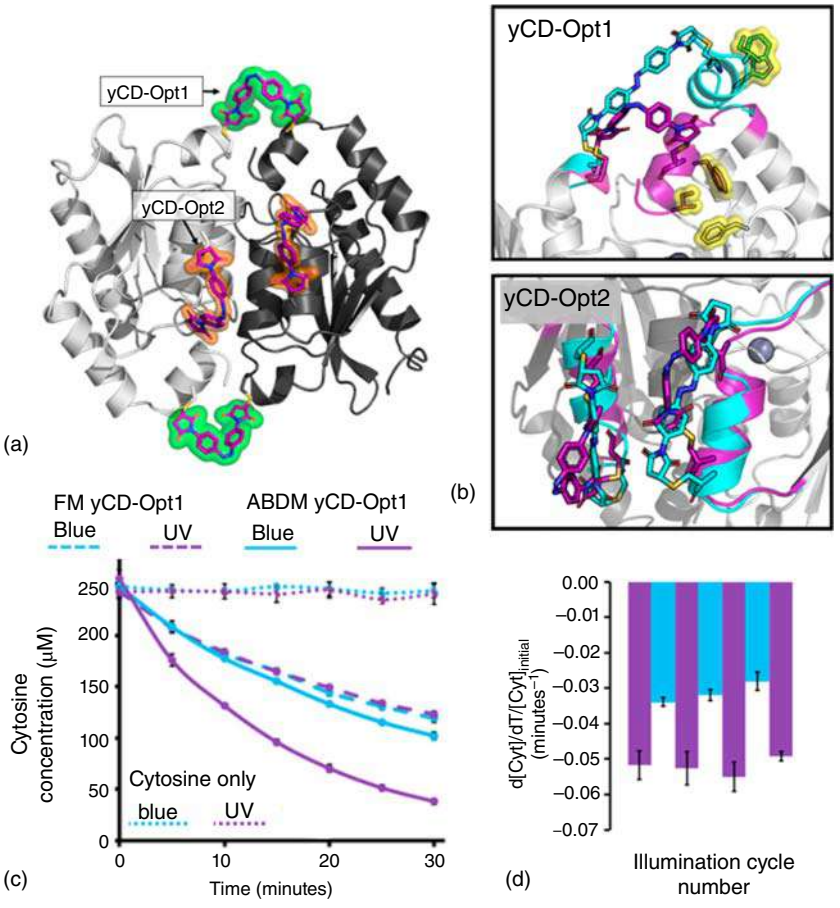


**Figure 43.6** (a) yCD dimer incorporating ABDM at two designed locations, designated yCD-Opt1 and yCD-Opt2. (b) Lowest-energy structures of *cis*- and *trans*-isomerization simulations for yCD-Opt1 and yCD-Opt2 designs – note yCD-Opt1 has significantly more backbone disruption than yCD-Opt2 during crosslink isomerization. (c) Cytosine concentration vs. time of labeled yCD-Opt1 with either free maleimide (FM) or ABDM. (d) The slopes of cytosine consumption assays with ABDM-labeled yCD-Opt1 demonstrating UV and Blue light radiation switching dynamically switches ABDM-yCD-Opt1 activity [25]. Source: Blacklock et al. [25].

than global destabilization. This combination of structurally informed design with additional all-atom simulations for further analysis is a promising strategy when designing photocontrol into enzyme-like systems.

One challenge the previous studies encountered when designing photocontrol is an inability to fully isomerize azobenzene from *cis*- to *trans*-state. This is because many azobenzene chromophores are unable to undergo a complete population *trans*-to-*cis* isomerization due to thermal *cis*-to-*trans* relaxation. This deficiency may be overcome with other *cis*-stabilizing photoswitches or modifying the crosslinked protein to enhance *cis*-isomer stability. Yasuike et al. computationally

designed a destabilizing photoswitch into a fynomer to photocontrol inhibition of the serine protease chymase [27]. Fynomers are small proteins from the Fyn SH3 domain capable of specific-binding through strategies of randomly sampling the binding-interface residues of the fynomer with selection techniques (e.g. phage display). The number of possible designs increases when both the protein and the photoswitch can be manipulated. Previous work conferred poor photocontrol over a chymase-inhibiting fynomer, with greatly reduced affinity and a twofold degree of affinity switching [28]. The authors endeavored to remedy these shortcomings.

The first focus was on improved computational methods and selecting alternative crosslink sites. The design goal was developing an "On" state with the irradiated *cis*-azobenzene and an "Off" state with the dark-adapted *trans*-azobenzene. The RosettaMatch algorithm was used to determine possible *cis*-state crosslink placements of the two selected crosslinking photoswitches, IAC and PIP (detailed in Scheme 43.1). IAC is an established photoswitch crosslinker and PIP is an azonium-ion based crosslinker with red-shifted excitation spectrum. Each set of cysteine pairs were computationally conjugated by both the *cis*-IAC and *cis*-PIP crosslinkers and minimized with Rosetta FastRelax. The crosslinked models were isomerized and minimized to model *trans*-state fynomers and evaluate the crosslink's effect on its structure. Designs were scored by deviations from the ideal crosslink geometries.

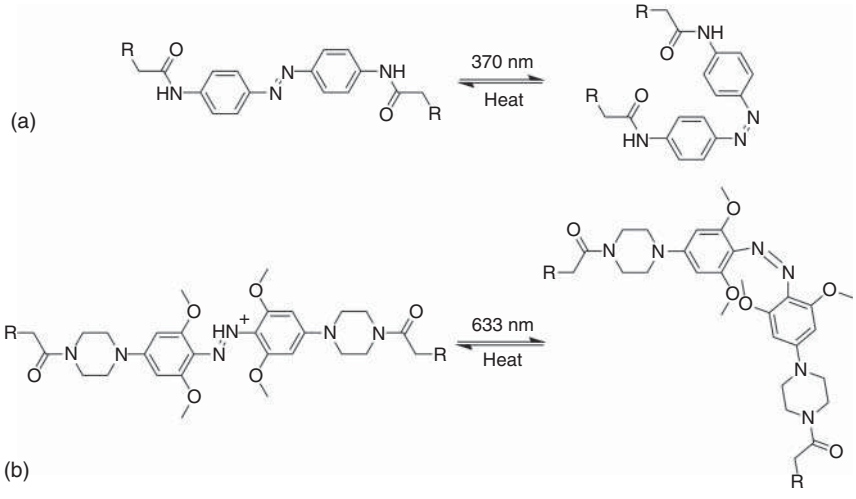


**Scheme 43.1** Photoisomerization of azo-based crosslinkers (a) IAC, azobenzene-iodoacetamide, and (b) PIP, piperazino-tetra-*ortho*-methoxy azobenzene. Both photoswitches are conjugated to a fynomer for photocontrol. Notably, IAC has a 150-fold longer *cis*-to-*trans* relaxation half-life than PIP, while PIP has a more biologically amenable excitation wavelength than IAC. Source: Yasuike et al. [27].

Five fynomer mutants were expressed and crosslinked. The IAC crosslinked mutants displayed varying effects on chymase inhibition when compared to the wild-type fynomer $IC_{50}$ of ~10 nM. The strongest inhibitor of the IAC mutants

yielded a *cis*-$IC_{50}$ of 26 nM and a *trans*-$IC_{50}$ of 36 nM, while the remaining IAC mutants attenuated inhibition and a range of lesser photoswitchable affinities. Several crosslinked mutants showed no inhibition. Computational models of these poor inhibitors exhibited minor structural shifts, implying allosteric shifts rather than gross structural changes must alter the binding mode of the fynomer. The inhibition and photocontrollable affinity were altered by replacing IAC with PIP, indicative of these design possibilities when selecting between a range of photoswitches. Further, the fast-relaxing PIP photoswitch enhanced its *cis*-to-*trans* relaxation half-life by 16-fold. This effect was likely from designing the photoswitching moiety close to a positively charged region of the fynomer, destabilizing the azonium ion and promoting *cis*-isomer stability. Finally, between two PIP mutants with the shortest and longest half-lives, the authors measured a ~60-fold half-life change with the same photoswitch. While PIP allows for fast relaxation between the *cis*- and *trans*-state, this work presented design of both protein photocontrol and further photoswitch response modification.

## 43.5 Non-canonical Photochromic Amino Acid Design

The previously described computational designs of photoswitchable proteins utilize post-translational modifications of cysteines by thio-reactive photoswitches. These strategies require some amount of solvent-exposed surface area of the conjugating residues and photoswitches with reactive moieties. Recent strategies to get around these requirements include genetically encoding the proteins with unnatural amino acids capable of photoisomerization. Luo et al. worked toward this goal through encoding the azobenzene-phenylalanine (AzoF) amino acid into mammalian cells to reversibly control a firefly luciferase (FLuc) [29]. To this end, two additional unnatural amino acids $F_2$AzoF and $F_4$AzoF were genetically encoded, both demonstrating enhanced optical properties and improved *cis*-isomer thermal stability (Figure 43.7a). $F_2$AzoF and $F_4$AzoF contain fluorine substitutions at the *ortho* positions of the one or both benzenes. These halogen substitutions increased both the excitation wavelength of photoisomerization and the *cis*-state thermal stability. The unnatural amino acids were genetically encoded by engineering the *Methanosarcina barkeri* pyrrolysyl-tRNA synthetase/$tRNA_{CUA}$ to incorporate AzoF at the Amber stop codon TAG. As proof of principle, the encoding was successful when TAG was placed in the linker between the dual fluorescent reporter protein mCherry-enhanced green fluorescent protein (EGFP).

With a functional synthetase for AzoF in hand, the authors then designed a photoswitchable FLuc using Eris software [30]. The computational design strategy was to analyze each residue in FLuc to find potential allosteric residues. This was conducted with the Eris software to identify residues with a high number of conformational states theoretically accessible with respect to their surrounding residues. Per-residue energies were calculated into an allostery score with this conformational state metric incorporated and ranked, highlighting residues with an allostery score greater than two. This yielded eight mutants as potential candidates for AzoF mutation.

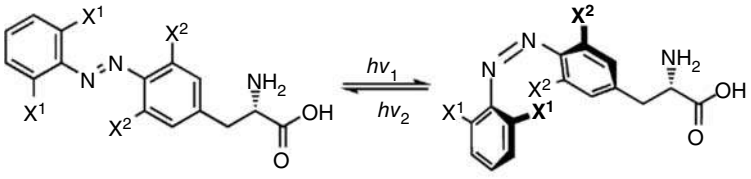


(a) AzoF: $X^1$ = H, $X^2$ = H, $hv_1$ = 365 nm, $hv_2$ = 450 nm;
$F_2$AzoF: $X^1$ = F, $X^2$ = H, $hv_1$ = 530 nm, $hv_2$ = 405 nm;
$F_2$AzoF: $X^1$ = F, $X^2$ = F, $hv_1$ = 530 nm, $hv_2$ = 405 nm.

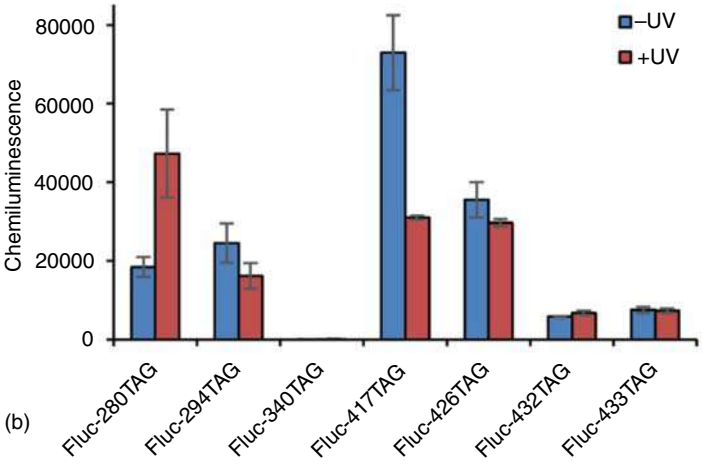


(b)

**Figure 43.7** (a) Photoisomerization of unnatural amino acid azobenzenes and their respective *ortho* substitutions. (b) AzoF-containing firefly luciferase assay for reversible chemiluminescence [29]. Source: Luo et al. [29].

Seven of the eight mutants were selected for AzoF incorporation. Most either showed activity regardless of irradiation or complete loss of activity (Figure 43.7b). Two mutants appeared to have photoresponsive activity, with W417AzoF demonstrating the highest activity. W417AzoF had 2.5-fold higher chemiluminescence in the *trans*-isomeric state than the *cis*-isomeric state. This correlated with Eris calculations indicating a destabilizing effect on FLuc activity, with higher instability in the *cis*-isomeric state. The binding energy of D-luciferyl-adenosine monophosphate (AMP) was evaluated with MedusaScore, and it was found the *cis*-FLuc-W417AzoF was less favorable in the active states of FLuc than wild-type FLuc [31]. This interaction energy was also evaluated to be better in the *cis*-state than in the *trans*-state of FLuc-W417AzoF. The FLuc-W417AzoF cells presented reversible chemiluminescence intensities corresponding to exposure of alternating UV and white light. AzoF was replaced with the two analogues $F_2$AzoF and $F_4$AzoF to overcome the drawbacks of AzoF. *Cis*-$F_4$AzoF enhanced thermostability when incorporated into cells by maintaining *cis*-state chemiluminescence of FLuc for 24 hours after introduction.

The *cis*-F-$_4$AzoF mutant of Fluc allowed reversible photocontrol of chemiluminescence in cells through irradiation of alternating 530 and 405 nm light.

This work designed a photocontrollable enzyme with precise control over photoswitch incorporation by genetically encoding a photoswitchable unnatural amino acid. Further designing the photoswitch for stability illustrates improved control over photoswitch incorporation, removing the necessity of adding conjugating moieties to the photoswitch. Designing photocontrol in this manner gives control over chromophore placement and mimics the evolved selection of naturally occurring photochromic and optogenetic proteins.

## 43.6 Computational Redesign of Photochromic Proteins

The field of optogenetics has leveraged and repurposed naturally occurring photochromic proteins for a range of applications, with many reviews detailing these advances [12, 13, 32]. While reengineering photochromic proteins has been successful, de novo design of photochromic proteins remains elusive. Computer simulations of photochromic proteins have been used in unraveling the underlying conformational mechanisms of photocontrol, but designing for a similar photo-activated conformational change has yet to be accomplished. However, modifying these photochromic proteins using computational design tools to improve their photophysical properties has been accomplished. Guntas et al. redesigned the *Avena sativa* light-oxygen-voltage 2 (LOV2) domain to improve affinity for its binding partner SspB protein from a difference of twofold to 50-fold [33].

The LOV2 domain senses blue light with a bound flavin mononucleotide chromophore. Upon irradiation, a LOV2 cysteine residue covalently binds the chromophore - inducing structural rearrangement and unfolding of the flanking Jα helix. Once the cysteine–chromophore adduct breaks, the Jα helix returns to its dark-adapted state. The LOV2 domain was previously modified by Kuhlman and colleagues such that the unfolded helix binds to the SspB protein, resulting in the LOV2-SspB light-inducible dimer (LID) [34]. The low change in affinity between the dark state and light state was hypothesized to be from dark-state undocking of the Jα helix [34]. To improve this binding affinity, a combined strategy was pursued of computational library design and phage-display screening. Based on the crystal structure of the dark-state LOV2 domain, all residues within 6 Å of the Jα helix were modeled using the pmut_scan protocol in Rosetta (Figure 43.8a) [35]. This protocol performs every possible point mutation across a given set of residues, returning energies for each point mutant. This set was filtered to mutations that lowered the total energy or slightly destabilized the structure (less than one or two Rosetta Energy Units). An oligonucleotide library was created from this mutational set of 743 mutations at 49 positions and used in a phage display screen for binding under both blue light and dark conditions (Figure 43.8a). Single-point mutants exhibited minimal improvements, so top mutants were pooled and combined, yielding a recombined library. From subsequent rounds of phage display, the four sequences with the highest dynamic ranges were further characterized.

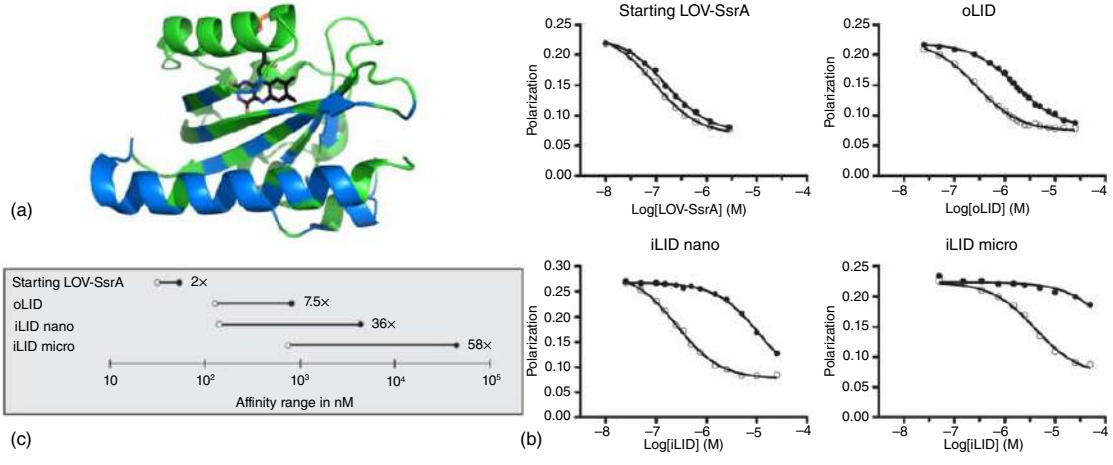


**Figure 43.8** (a) The AsLOV2 domain with selected positions (blue) for computational point-mutant sampling with pmut_scan in Rosetta. (b) Characterization of the starting LOV-SsrA domain and a Jα-stabilized version (oLID), to the improved iLID nano- and iLID microversions. (c) Comparison of light and dark affinities of the respective LIDs [33]. Source: Guntas et al. [33].

The highest dynamic range LID mutant achieved affinity changes from the irradiated state to the dark state of 132 nM to 4.7 μM, named the improved light-induced dimer (iLID). The iLID protein affinity shifted a magnitude upward with a point mutation on SspB, bringing the irradiated-state and dark-state affinities to 800 nM and 47 μM, respectively (Figure 43.8b,c). Based on the structure of the iLID, a selection of mutant reversions to wild-type residue identities were performed. These reversions yielded similar or reduced dynamic range, but the pair Y502Q/H521R resulted in a threefold tighter affinity in both states. This iLID was the first computationally redesigned photo-oligomerizing heterodimer and highlights the utility of computational point-mutant analysis screening. Because photoactivation in proteins has repeatedly been reported as fragile, the group here utilized computational modeling to filter possible mutants to an experimentally reasonable set to further screen and recombine [32]. Interestingly, the iLID protein structure contained features deviating from the original LID that were not designed. Further computational analysis of these and other photochromic proteins could identify similar interactions or motifs for the design of novel photoresponsive proteins.

## 43.7 Computational Analyses of Photocontrollable Proteins

As the set of proteins engineered to be photochromic grows and the discovery of photoresponsive proteins continues, these optogenetic tools are being computationally probed to discern the conformational landscape of phototriggered protein conformational shifts [12, 13, 32, 36]. These analyses have yet to result in the de novo creation of a photoresponsive protein but have yielded important structural insights that may be useful for future work. The methods used include quantum mechanical, molecular dynamics, and Monte Carlo-based simulations. Analyses with each technique describe potential mechanisms of function that can improve design.

Quantum mechanical simulations on photochromic proteins can be useful to examine the chromophore and the surrounding protein environment to determine the photochemical effects that propagate and cause structural reconfiguration. To that end, a model photoswitchable protein system is Dronpa, a reversibly switchable fluorescent protein. Dronpa's tripeptide chromophore induces a structural change upon irradiation resulting in tetramerization (Figure 43.9a). Morozov et al. investigated the photochemical changes incurred by this chromophore in its protein environment with quantum mechanics and molecular dynamics simulations [37]. These simulations were performed on the Dronpa M159T mutant to increase the quantum yield and demonstrated that in eight of twelve 50 ps QM/MM simulations the chromophore remained planar after excitation. This planar chromophore is stabilized by two water molecules and Ser142 hydrogen bonding with the phenolate oxygen of the chromophore (Figure 43.9a). The remaining trajectories revealed a deactivation and isomerization of the chromophore when the phenolate oxygen forms only one hydrogen bond in the excited state. This deactivation further

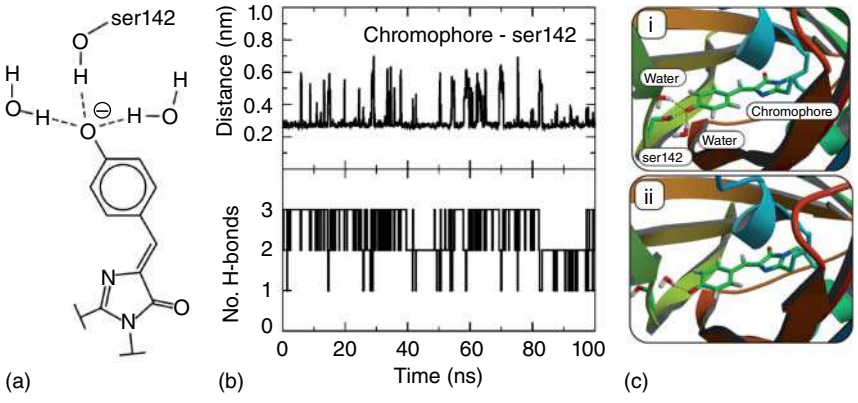


**Figure 43.9** (a) The Dronpa chromophore formed from the Cys62, Tyr63, Gly64 triplet stabilized by the Ser142 hydroxyl hydrogen and two endogenous water molecules. (b) Time evolution over a 100 ns MD simulation of the chromophore-Ser142 hydroxy group distance and the total number of hydrogen bonds to the phenolate moiety. (c) Models of the Dronpa M159T chromophore with intact (i) and destabilized (ii) hydrogen bonds [37]. Source: Morozov and Groenhof [37].

stabilizes the imidazolinone ring, introducing an energetic barrier to photoisomerize the chromophore into its active state. A 100 ns MD simulation reveals these three hydrogen bonds transiently break with enough frequency to deactivate the chromophore (Figure 43.9b,c). These QM and MM simulations highlight the importance of including these stabilizing and destabilizing interactions in design.

Molecular dynamics simulations can be beneficial in understanding structural and conformational fluctuations in proteins. An investigation into allostery by Buchli et al. involved the use of azobenzene as a tool to mimic protein response to peptide binding. PDZ domains are a class of C-terminal peptide-binding proteins, which play a key role in signal transduction. Their allosteric interactions are important in the context of regulation. The PDZ domain from human tyrosine-phosphatase 1E was selected as it possesses allosteric properties. It contains a binding groove between an α-helix and a β strand, and allosteric changes are propagated in the protein upon peptide binding [38]. To investigate these allosteric effects involved in peptide binding, two residues across this binding groove were mutated to cysteines for conjugation by azobenzene-iodoacetimide (Figure 43.10a). Protein structures were determined using NMR spectroscopy with the conjugated photoswitch in the *cis*- and *trans*-orientations, respectively. Transient IR spectroscopy indicated the protein responded to the azobenzene isomerization by undergoing small but far-reaching conformational shifts (Figure 43.10b). Molecular dynamic simulations were used to visualize conformational shifts resulting from crosslinker isomerization. Simulations depicted a continuous protein shift rather than a two-state transition as the structure moves from the initial *cis*-state to the final *trans*-state.

The explicit solvent MD simulations exhibited water-density shifts around the protein at longer time scales than the protein structural shifts. The reorganization

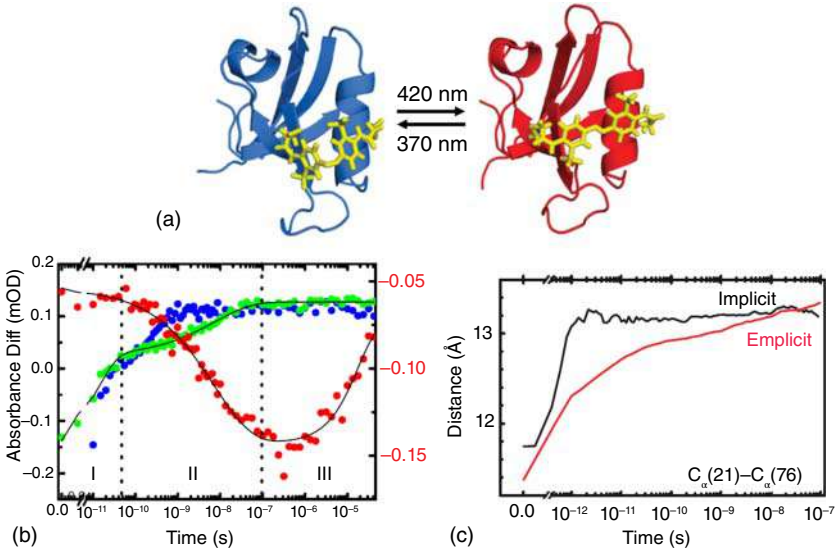


**Figure 43.10** (a) NMR-derived structures of the crosslinked PDZ2 domains in the *cis*- and *trans*-crosslinked state (*cis*, protein databank (PDB) ID 2M0Z, *trans*, PDB ID 2M10). (b) Transient IR spectroscopy of the PDZ2 amide I band in red (1640 $cm^{-1}$) and the band originating from the photoswitch (1491 $cm^{-1}$) when conjugated to the protein (green) and free in solution (blue). (c) Distance vs. time data for the α-carbons of the crosslinked cysteines in PDZ2 from explicit and implicit MD simulations. The response in phase II of (b) is qualitatively similar to the explicit MD simulation results in (c), implying water molecules are important in the protein structure response of crosslink isomerization [38]. Source: Buchli et al. [38].

of the protein structure explored via IR experiments is comparable in time scales to the water reorganization seen in the explicit water simulations (Figure 43.10c). These results suggest that allostery observed in PDZ domain is a result of changing the conformational landscape as a consequence of an altered water shell around the protein rather than a structural change in the PDZ domain itself. Therefore, consideration of solvent structure and dynamics and coupling between protein and solvent conformational ensembles may also be key factors for predicting and designing photocontrolled proteins.

## 43.8 Conclusion

Predictive design of photochromic proteins remains a challenging problem. Some considerations include designing for chromophore binding and for a protein environment that will chemically respond to the excitation of the chromophore. This designed photochemical response must then propagate into a protein structure change, which needs to result in the desired protein response. To some extent, success has been achieved by using a photoisomerizing azobenzene molecule as both the chromophore and structural actuator. Other non-azobenzene

photoswitches have been used for photocontrolling proteins but have yet to be included in computational design [39]. Computational methods have been used for determining locations where the resulting structural perturbation in the protein as a result of the isomerization can be most impactful. Going forward, the plethora of computational analyses at multiple time and length scales should be utilized toward design. A fast analysis of chromophore conjugation and/or crosslinking based on the native-state structure can be complemented by computationally intensive quantum mechanical/molecular dynamics simulations of selected variants for further validation. Experiments should inform computational simulations, which should guide further experimentation in a *design–build–test* cycle.

The studies reviewed here point toward several key computational methods that may be useful for photochromic protein design. When designing or repurposing a photochromic protein, modeling the point-mutational landscape for chromophore attachment narrows the sequence search space for experimental trials. Performing QM/MM simulations can then further narrow the sample space to ensure the photophysical properties of the chromophore are not disrupted. For designs incorporating a photoisomerizing molecule, computational determination of photoswitch placement based strictly on inter-residue distances and solvent accessibility can be reliable. However, more detailed computational methods, such as RosettaMatch, in determining photoswitch placement may be more effective. While many design assumptions target "flexible" protein regions, evidence reviewed here indicates this may target overly flexible structures and avoid more effective placement of the chromophores. Additionally, modeling both (*cis* and *trans*) states of a photoswitch-protein conjugate has yielded better agreement with experimental results. Photochromic protein design remains difficult in view of the requirement for considering multiple states in the design process. However, the development of tools reviewed here promises to make photochromic protein design more robust and useful.

## References


1 Zhao, E.M., Suek, N., Wilson, M.Z., et al. (2019). Light-based control of metabolic flux through assembly of synthetic organelles. *Nat. Chem. Biol.* 15 (6): 589–597. https://doi.org/10.1038/s41589-019-0284-8.

2 Waldauer, S.A., Hassan, S., Paoli, B. et al. (2012). Photocontrol of reversible amyloid formation with a minimal-design peptide. *J. Phys. Chem. B* 116 (30): 8961–8973. https://doi.org/10.1021/jp305311z.

3 Polstein, L.R., Juhas, M., Hanna, G. et al. (2017). An engineered optogenetic switch for spatiotemporal control of gene expression, cell differentiation, and tissue morphogenesis. *ACS Synth. Biol.* 6 (11): 2003–2013. https://doi.org/10.1021/acssynbio.7b00147.

4 Zhou, X.E., Melcher, K., and Xu, H.E. (2012). Structure and activation of rhodopsin. *Acta Pharmacol. Sin.* 33 (3): 291–299. https://doi.org/10.1038/aps.2011.171.


5 Palczewski, K., Kumasaka, T., Hori, T. et al. (2000). Crystal structure of rhodopsin: a G protein-coupled receptor. *Science* 289 (5480): 739–745. https://doi.org/10.1126/science.289.5480.739.

6 Choe, H.-W., Kim, Y.J., Park, J.H. et al. (2011). Crystal structure of metarhodopsin II. *Nature* 471 (7340): 651–655. https://doi.org/10.1038/nature09789.

7 Ma, L., Guan, Z., Wang, Q. et al. (2020). Structural insights into the photoactivation of Arabidopsis CRY2. *Nat. Plants* 6 (12): 1432–1438. https://doi.org/10.1038/s41477-020-00800-1.

8 Ma, L., Wang, X., Guan, Z. et al. (2020). Structural insights into BIC-mediated inactivation of Arabidopsis cryptochrome 2. *Nat. Struct. Mol. Biol.* 27 (5): 472–479. https://doi.org/10.1038/s41594-020-0410-z.

9 Ma, L., Guan, Z.Y., and Yin, P. (2020). Cryo-EM structure of Arabidopsis CRY under blue light-mediated activation. https://www.rcsb.org/structure/6M79.

10 Wang, G. and Zhang, J. (2012). Photoresponsive molecular switches for biotechnology. *J. Photochem. Photobiol. C Photochem. Rev.* 13 (4): 299–309. https://doi.org/10.1016/j.jphotochemrev.2012.06.002.

11 Schrodinger LLC (2020). The PyMOL Molecular Graphics System, Version 2.4.1.

12 Fenno, L., Yizhar, O., and Deisseroth, K. (2011). The development and application of optogenetics. *Annu. Rev. Neurosci.* 34: 389–412. https://doi.org/10.1146/annurev-neuro-061010-113817.

13 O'Banion, C.P. and Lawrence, D.S. (2018). Optogenetics: a primer for chemists. *ChemBioChem* 19 (12): 1201–1216. https://doi.org/10.1002/cbic.201800013.

14 Beharry, A.A. and Woolley, G.A. (2011). Azobenzene photoswitches for biomolecules. *Chem. Soc. Rev.* 40 (8): 4422–4437. https://doi.org/10.1039/c1cs15023e.

15 Dias, A.R., Minas Da Piedade, M.E., Martinho Simões, J.A. et al. (1992). Enthalpies of formation of *cis*-azobenzene and *trans*-azobenzene. *J. Chem. Thermodyn.* 24 (4): 439–447. https://doi.org/10.1016/S0021-9614(05)80161-2.

16 Kumita, J.R., Smart, O.S., and Woolley, G.A. (2000). Photo-control of helix content in a short peptide. *Proc. Natl. Acad. Sci. U.S.A.* 97 (8): 3803–3808. https://doi.org/10.1073/pnas.97.8.3803.

17 Flint, D.G., Kumita, J.R., Smart, O.S., and Woolley, G.A. (2002). Using an azobenzene cross-linker to either increase or decrease peptide helix content upon *trans*-to-*cis* photoisomerization. *Chem. Biol.* 9 (3): 391–397. https://doi.org/10.1016/S1074-5521(02)00109-6.

18 Nilsson, K.P.R., Åslund, A., Berg, I. et al. (2007). Imaging distinct conformational states of amyloid-β fibrils in Alzheimer's disease using novel luminescent probes. *ACS Chem. Biol.* 2 (8): 553–560. https://doi.org/10.1021/cb700116u.

19 Zhang, F., Zarrine-Afsar, A., Al-Abdul-Wahid, M.S. et al. (2009). Structure-based approach to the photocontrol of protein folding. *J. Am. Chem. Soc.* 131 (6): 2283–2289. https://doi.org/10.1021/ja807938v.

20 Hoersch, D. (2016, 2016). Engineering a light-controlled F1 ATPase using structure-based protein design. *PeerJ* (7): 1–11. https://doi.org/10.7717/peerj.2286.


**21** Hoersch, D., Roh, S.-H., Chiu, W., and Kortemme, T. (2013). Reprogramming an ATP-driven protein machine into a light-gated nanocage. *Nat. Nanotechnol.* 8 (12): 928–932. https://doi.org/10.1038/nnano.2013.242.

**22** Zhang, J., Baker, M.L., Schröder, G.F. et al. (2010). Mechanism of folding chamber closure in a group II chaperonin. *Nature* 463 (7279): 379–383. https://doi.org/10.1038/nature08701.

**23** Feng, S., Kasahara, C., Rickles, R.J., and Schreiber, S.L. (1995). Specific interactions outside the proline-rich core of two classes of Src homology 3 ligands. *Proc. Natl. Acad. Sci. U.S.A.* 92 (26): 12408–12415. https://doi.org/10.1073/pnas.92.26.12408.

**24** Ritterson, R.S., Kuchenbecker, K.M., Michalik, M., and Kortemme, T. (2013). Design of a photoswitchable cadherin. *J. Am. Chem. Soc.* 135 (34): 12516–12519. https://doi.org/10.1021/ja404992r.

**25** Blacklock, K.M., Yachnin, B.J., Woolley, G.A., and Khare, S.D. (2018). Computational design of a photocontrolled cytosine deaminase. *J. Am. Chem. Soc.* 140 (1): 14–17. https://doi.org/10.1021/jacs.7b08709.

**26** Mahan, S.D., Ireton, G.C., Knoeber, C. et al. (2004). Random mutagenesis and selection of *Escherichia coli* cytosine deaminase for cancer gene therapy. *Protein Eng. Des. Sel.* 17 (8): 625–633. https://doi.org/10.1093/protein/gzh074.

**27** Yasuike, N., Blacklock, K.M., Lu, H. et al. (2019). Photoswitchable affinity reagents: computational design and efficient red-light switching. *ChemPhotoChem* 3 (6): 431–440. https://doi.org/10.1002/cptc.201900016.

**28** Babalhavaeji, A. and Woolley, G.A. (2018). Modular design of optically controlled protein affinity reagents. *Chem. Commun.* 54 (13): 1591–1594. https://doi.org/10.1039/C7CC07391G.

**29** Luo, J., Samanta, S., Convertino, M. et al. (2018). Reversible and tunable photoswitching of protein function through genetic encoding of azobenzene amino acids in mammalian cells. *ChemBioChem* 19 (20): 2178–2185. https://doi.org/10.1002/cbic.201800226.

**30** Yin, S., Ding, F., and Dokholyan, N.V. (2007). Eris: an automated estimator of protein stability. *Nat. Methods* 4 (6): 466–467. https://doi.org/10.1038/nmeth0607-466.

**31** Yin, S., Biedermannova, L., Vondrasek, J., and Dokholyan, N.V. (2008). MedusaScore: an accurate force field-based scoring function for virtual drug screening. *J. Chem. Inf. Model.* 48 (8): 1656–1662. https://doi.org/10.1021/ci8001167.

**32** Banerjee, S. and Mitra, D. (2020). Structural basis of design and engineering for advanced plant optogenetics. *Trends Plant Sci.* 25 (1): 35–65. https://doi.org/10.1016/j.tplants.2019.10.002.

**33** Guntas, G., Hallett, R.A., Zimmerman, S.P. et al. (2015). Engineering an improved light-induced dimer (iLID) for controlling the localization and activity of signaling proteins. *Proc. Natl. Acad. Sci. U.S.A* 112 (1): 112–117. https://doi.org/10.1073/pnas.1417910112.

**34** Lungu, O.I., Hallett, R.A., Choi, E.J. et al. (2012). Designing photoswitchable peptides using the AsLOV2 domain. *Chem. Biol.* 19 (4): 507–517. https://doi.org/10.1016/j.chembiol.2012.02.006.


**35** Leaver-Fay, A., Tyka, M., Lewis, S.M. et al. (2011). Rosetta3: an object-oriented software suite for the simulation and design of macromolecules. *Methods Enzymol.* 487: 545–574. https://doi.org/10.1016/B978-0-12-381270-4.00019-6.

**36** Acharya, A., Bogdanov, A.M., Grigorenko, B.L. et al. (2017). Photoinduced chemistry in fluorescent proteins: curse or blessing? *Chem. Rev.* 117 (2): 758–795. https://doi.org/10.1021/acs.chemrev.6b00238.

**37** Morozov, D. and Groenhof, G. (2016). Hydrogen bond fluctuations control photochromism in a reversibly photo-switchable fluorescent protein. *Angew. Chem.* 128 (2): 586–588. https://doi.org/10.1002/ange.201508452.

**38** Buchli, B., Waldauer, S.A., Walser, R. et al. (2013). Kinetic response of a photoperturbed allosteric protein. *Proc. Natl. Acad. Sci. U.S.A* 110 (29): 11725–11730. https://doi.org/10.1073/pnas.1306323110.

**39** Peddie, V. and Abell, A.D. (2019). Photocontrol of peptide secondary structure through non-azobenzene photoswitches. *J. Photochem. Photobiol. C Photochem. Rev.* 40: 1–20. https://doi.org/10.1016/j.jphotochemrev.2019.05.001.

# Index



*Molecular Photoswitches: Chemistry, Properties, and Applications*,
First Edition. Edited by Zbigniew L. Pianowski.


## *b*

## *d*



## *e*

## *f*

## *g*

## *k*



## *l*

## *m*



## *t*